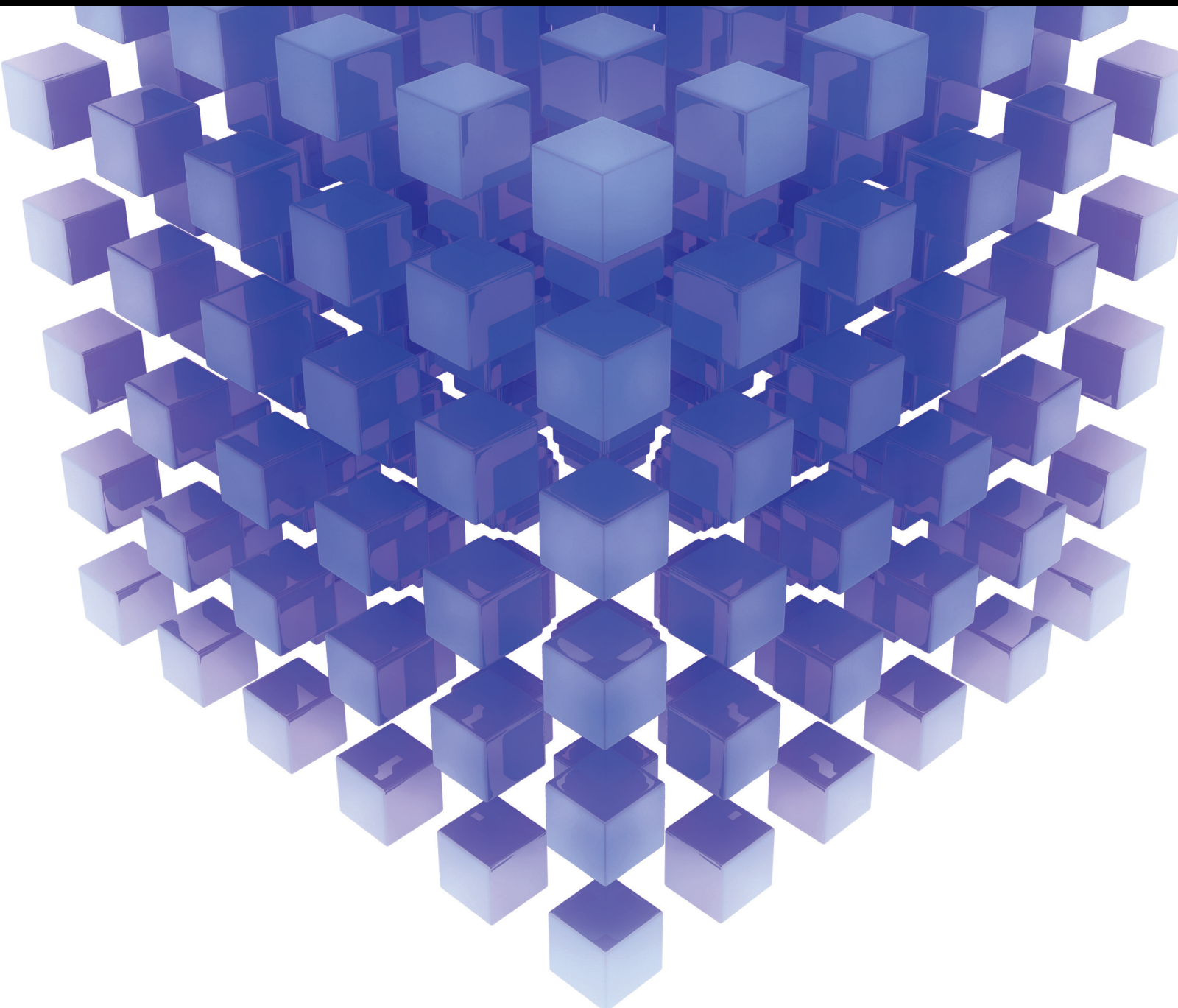


# Advanced Optimization Models For Smart City Applications

Lead Guest Editor: Dinesh Kumar Saini

Guest Editors: Punit Gupta and Kashif Zia





---

# **Advanced Optimization Models For Smart City Applications**

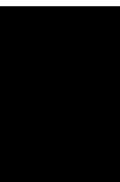
Mathematical Problems in Engineering

---

## **Advanced Optimization Models For Smart City Applications**

Lead Guest Editor: Dinesh Kumar Saini

Guest Editors: Punit Gupta and Kashif Zia




---

Copyright © 2023 Hindawi Limited. All rights reserved.

This is a special issue published in “Mathematical Problems in Engineering.” All articles are open access articles distributed under the Creative Commons Attribution License, which permits unrestricted use, distribution, and reproduction in any medium, provided the original work is properly cited.

# Chief Editor

Guangming Xie , China

## Academic Editors

Kumaravel A , India  
Waqas Abbasi, Pakistan  
Mohamed Abd El Aziz , Egypt  
Mahmoud Abdel-Aty , Egypt  
Mohammed S. Abdo, Yemen  
Mohammad Yaghoub Abdollahzadeh  
Jamalabadi , Republic of Korea  
Rahib Abiyev , Turkey  
Leonardo Acho , Spain  
Daniela Addessi , Italy  
Arooj Adeel , Pakistan  
Waleed Adel , Egypt  
Ramesh Agarwal , USA  
Francesco Aggogeri , Italy  
Ricardo Aguilar-Lopez , Mexico  
Afaq Ahmad , Pakistan  
Naveed Ahmed , Pakistan  
Elias Aifantis , USA  
Akif Akgul , Turkey  
Tareq Al-shami , Yemen  
Guido Ala, Italy  
Andrea Alaimo , Italy  
Reza Alam, USA  
Osamah Albahri , Malaysia  
Nicholas Alexander , United Kingdom  
Salvatore Alfonzetti, Italy  
Ghous Ali , Pakistan  
Nouman Ali , Pakistan  
Mohammad D. Aliyu , Canada  
Juan A. Almendral , Spain  
A.K. Alomari, Jordan  
José Domingo Álvarez , Spain  
Cláudio Alves , Portugal  
Juan P. Amezcua-Sanchez, Mexico  
Mukherjee Amitava, India  
Lionel Amodeo, France  
Sebastian Anita, Romania  
Costanza Arico , Italy  
Sabri Arik, Turkey  
Fausto Arpino , Italy  
Rashad Asharabi , Saudi Arabia  
Farhad Aslani , Australia  
Mohsen Asle Zaem , USA

Andrea Avanzini , Italy  
Richard I. Avery , USA  
Viktor Avrutin , Germany  
Mohammed A. Awadallah , Malaysia  
Francesco Aymerich , Italy  
Sajad Azizi , Belgium  
Michele Bacciocchi , Italy  
Seungik Baek , USA  
Khaled Bahlali, France  
M.V.A Raju Bahubalendruni, India  
Pedro Balaguer , Spain  
P. Balasubramaniam, India  
Stefan Balint , Romania  
Ines Tejado Balsera , Spain  
Alfonso Banos , Spain  
Jerzy Baranowski , Poland  
Tudor Barbu , Romania  
Andrzej Bartoszewicz , Poland  
Sergio Baselga , Spain  
S. Caglar Baslamisli , Turkey  
David Bassir , France  
Chiara Bedon , Italy  
Azeddine Beghdadi, France  
Andriette Bekker , South Africa  
Francisco Beltran-Carbajal , Mexico  
Abdellatif Ben Makhlof , Saudi Arabia  
Denis Benasciutti , Italy  
Ivano Benedetti , Italy  
Rosa M. Benito , Spain  
Elena Benvenuti , Italy  
Giovanni Berselli, Italy  
Michele Betti , Italy  
Pietro Bia , Italy  
Carlo Bianca , France  
Simone Bianco , Italy  
Vincenzo Bianco, Italy  
Vittorio Bianco, Italy  
David Bigaud , France  
Sardar Muhammad Bilal , Pakistan  
Antonio Bilotta , Italy  
Sylvio R. Bistafa, Brazil  
Chiara Boccaletti , Italy  
Rodolfo Bontempo , Italy  
Alberto Borboni , Italy  
Marco Bortolini, Italy

Paolo Boscariol, Italy  
Daniela Boso , Italy  
Guillermo Botella-Juan, Spain  
Abdesselem Boulkroune , Algeria  
Boulaïd Boulkroune, Belgium  
Fabio Bovenga , Italy  
Francesco Braghin , Italy  
Ricardo Branco, Portugal  
Julien Bruchon , France  
Matteo Bruggi , Italy  
Michele Brun , Italy  
Maria Elena Bruni, Italy  
Maria Angela Butturi , Italy  
Bartłomiej Błachowski , Poland  
Dhanamjayulu C , India  
Raquel Caballero-Águila , Spain  
Filippo Cacace , Italy  
Salvatore Caddemi , Italy  
Zuowei Cai , China  
Roberto Caldelli , Italy  
Francesco Cannizzaro , Italy  
Maosen Cao , China  
Ana Carpio, Spain  
Rodrigo Carvajal , Chile  
Caterina Casavola, Italy  
Sara Casciati, Italy  
Federica Caselli , Italy  
Carmen Castillo , Spain  
Inmaculada T. Castro , Spain  
Miguel Castro , Portugal  
Giuseppe Catalanotti , United Kingdom  
Alberto Cavallo , Italy  
Gabriele Cazzulani , Italy  
Fatih Vehbi Celebi, Turkey  
Miguel Cerrolaza , Venezuela  
Gregory Chagnon , France  
Ching-Ter Chang , Taiwan  
Kuei-Lun Chang , Taiwan  
Qing Chang , USA  
Xiaoheng Chang , China  
Prasenjit Chatterjee , Lithuania  
Kacem Chehdi, France  
Peter N. Cheimets, USA  
Chih-Chiang Chen , Taiwan  
He Chen , China

Kebing Chen , China  
Mengxin Chen , China  
Shyi-Ming Chen , Taiwan  
Xizhong Chen , Ireland  
Xue-Bo Chen , China  
Zhiwen Chen , China  
Qiang Cheng, USA  
Zeyang Cheng, China  
Luca Chiapponi , Italy  
Francisco Chicano , Spain  
Tirivanhu Chinyoka , South Africa  
Adrian Chmielewski , Poland  
Seongim Choi , USA  
Gautam Choubey , India  
Hung-Yuan Chung , Taiwan  
Yusheng Ci, China  
Simone Cinquemani , Italy  
Roberto G. Citarella , Italy  
Joaquim Ciurana , Spain  
John D. Clayton , USA  
Piero Colajanni , Italy  
Giuseppina Colicchio, Italy  
Vassilios Constantoudis , Greece  
Enrico Conte, Italy  
Alessandro Contento , USA  
Mario Cools , Belgium  
Gino Cortellessa, Italy  
Carlo Cosentino , Italy  
Paolo Crippa , Italy  
Erik Cuevas , Mexico  
Guozeng Cui , China  
Mehmet Cunkas , Turkey  
Giuseppe D'Aniello , Italy  
Peter Dabnichki, Australia  
Weizhong Dai , USA  
Zhifeng Dai , China  
Purushothaman Damodaran , USA  
Sergey Dashkovskiy, Germany  
Adiel T. De Almeida-Filho , Brazil  
Fabio De Angelis , Italy  
Samuele De Bartolo , Italy  
Stefano De Miranda , Italy  
Filippo De Monte , Italy



































José António Fonseca De Oliveira  
Correia , Portugal  
Jose Renato De Sousa , Brazil  
Michael Defoort, France  
Alessandro Della Corte, Italy  
Laurent Dewasme , Belgium  
Sanku Dey , India  
Gianpaolo Di Bona , Italy  
Roberta Di Pace , Italy  
Francesca Di Puccio , Italy  
Ramón I. Diego , Spain  
Yannis Dimakopoulos , Greece  
Hasan Dinçer , Turkey  
José M. Domínguez , Spain  
Georgios Dounias, Greece  
Bo Du , China  
Emil Dumic, Croatia  
Madalina Dumitriu , United Kingdom  
Premraj Durairaj , India  
Saeed Eftekhar Azam, USA  
Said El Kafhali , Morocco  
Antonio Elipe , Spain  
R. Emre Erkmen, Canada  
John Escobar , Colombia  
Leandro F. F. Miguel , Brazil  
FRANCESCO FOTI , Italy  
Andrea L. Facci , Italy  
Shahla Faisal , Pakistan  
Giovanni Falsone , Italy  
Hua Fan, China  
Jianguang Fang, Australia  
Nicholas Fantuzzi , Italy  
Muhammad Shahid Farid , Pakistan  
Hamed Faruqi, Iran  
Yann Favennec, France  
Fiorenzo A. Fazzolari , United Kingdom  
Giuseppe Fedele , Italy  
Roberto Fedele , Italy  
Baowei Feng , China  
Mohammad Ferdows , Bangladesh  
Arturo J. Fernández , Spain  
Jesus M. Fernandez Oro, Spain  
Francesco Ferrise, Italy  
Eric Feulvarch , France  
Thierry Floquet, France

Eric Florentin , France  
Gerardo Flores, Mexico  
Antonio Forcina , Italy  
Alessandro Formisano, Italy  
Francesco Franco , Italy  
Elisa Francomano , Italy  
Juan Frausto-Solis, Mexico  
Shujun Fu , China  
Juan C. G. Prada , Spain  
HECTOR GOMEZ , Chile  
Matteo Gaeta , Italy  
Mauro Gaggero , Italy  
Zoran Gajic , USA  
Jaime Gallardo-Alvarado , Mexico  
Mosè Gallo , Italy  
Akemi Gálvez , Spain  
Maria L. Gandarias , Spain  
Hao Gao , Hong Kong  
Xingbao Gao , China  
Yan Gao , China  
Zhiwei Gao , United Kingdom  
Giovanni Garcea , Italy  
José García , Chile  
Harish Garg , India  
Alessandro Gasparetto , Italy  
Stylianios Georgantzinou, Greece  
Fotios Georgiades , India  
Parviz Ghadimi , Iran  
Ştefan Cristian Gherghina , Romania  
Georgios I. Giannopoulos , Greece  
Agathoklis Giaralis , United Kingdom  
Anna M. Gil-Lafuente , Spain  
Ivan Giorgio , Italy  
Gaetano Giunta , Luxembourg  
Jefferson L.M.A. Gomes , United Kingdom  
Emilio Gómez-Déniz , Spain  
Antonio M. Gonçalves de Lima , Brazil  
Qunxi Gong , China  
Chris Goodrich, USA  
Rama S. R. Gorla, USA  
Veena Goswami , India  
Xunjie Gou , Spain  
Jakub Grabski , Poland















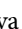








Antoine Grall , France  
George A. Gravvanis , Greece  
Fabrizio Greco , Italy  
David Greiner , Spain  
Jason Gu , Canada  
Federico Guarracino , Italy  
Michele Guida , Italy  
Muhammet Gul , Turkey  
Dong-Sheng Guo , China  
Hu Guo , China  
Zhaoxia Guo, China  
Yusuf Gurefe, Turkey  
Salim HEDDAM , Algeria  
ABID HUSSANAN, China  
Quang Phuc Ha, Australia  
Li Haitao , China  
Petr Hájek , Czech Republic  
Mohamed Hamdy , Egypt  
Muhammad Hamid , United Kingdom  
Renke Han , United Kingdom  
Weimin Han , USA  
Xingsi Han, China  
Zhen-Lai Han , China  
Thomas Hanne , Switzerland  
Xinan Hao , China  
Mohammad A. Hariri-Ardebili , USA  
Khalid Hattaf , Morocco  
Defeng He , China  
Xiao-Qiao He, China  
Yanchao He, China  
Yu-Ling He , China  
Ramdane Hedjar , Saudi Arabia  
Jude Hemanth , India  
Reza Hemmati, Iran  
Nicolae Herisanu , Romania  
Alfredo G. Hernández-Díaz , Spain  
M.I. Herreros , Spain  
Eckhard Hitzer , Japan  
Paul Honeine , France  
Jaromir Horacek , Czech Republic  
Lei Hou , China  
Yingkun Hou , China  
Yu-Chen Hu , Taiwan  
Yunfeng Hu, China  
Can Huang , China  
Gordon Huang , Canada  
Linsheng Huo , China  
Sajid Hussain, Canada  
Asier Ibeas , Spain  
Orest V. Iftime , The Netherlands  
Przemyslaw Ignaciuk , Poland  
Giacomo Innocenti , Italy  
Emilio Insfran Pelozo , Spain  
Azeem Irshad, Pakistan  
Alessio Ishizaka, France  
Benjamin Ivorra , Spain  
Breno Jacob , Brazil  
Reema Jain , India  
Tushar Jain , India  
Amin Jajarmi , Iran  
Chiranjibe Jana , India  
Łukasz Jankowski , Poland  
Samuel N. Jator , USA  
Juan Carlos Jáuregui-Correa , Mexico  
Kandasamy Jayakrishna, India  
Reza Jazar, Australia  
Khalide Jbilou, France  
Isabel S. Jesus , Portugal  
Chao Ji , China  
Qing-Chao Jiang , China  
Peng-fei Jiao , China  
Ricardo Fabricio Escobar Jiménez , Mexico  
Emilio Jiménez Macías , Spain  
Maolin Jin, Republic of Korea  
Zhuo Jin, Australia  
Ramash Kumar K , India  
BHABEN KALITA , USA  
MOHAMMAD REZA KHEDMATI , Iran  
Viacheslav Kalashnikov , Mexico  
Mathiyalagan Kalidass , India  
Tamas Kalmar-Nagy , Hungary  
Rajesh Kaluri , India  
Jyotheeswara Reddy Kalvakurthi, India  
Zhao Kang , China  
Ramani Kannan , Malaysia  
Tomasz Kapitaniak , Poland  
Julius Kaplunov, United Kingdom  
Konstantinos Karamanos, Belgium  
Michal Kawulok, Poland



Irfan Kaymaz , Turkey  
Vahid Kayvanfar , Qatar  
Krzysztof Kecik , Poland  
Mohamed Khader , Egypt  
Chaudry M. Khalique , South Africa  
Mukhtaj Khan , Pakistan  
Shahid Khan , Pakistan  
Nam-Il Kim, Republic of Korea  
Philipp V. Kiryukhantsev-Korneev ,  
Russia  
P.V.V Kishore , India  
Jan Koci , Czech Republic  
Ioannis Kostavelis , Greece  
Sotiris B. Kotsiantis , Greece  
Frederic Kratz , France  
Vamsi Krishna , India  
Edyta Kucharska, Poland  
Krzysztof S. Kulpa , Poland  
Kamal Kumar, India  
Prof. Ashwani Kumar , India  
Michal Kunicki , Poland  
Cedrick A. K. Kwuimy , USA  
Kyandoghere Kyamakya, Austria  
Ivan Kyrchei , Ukraine  
Márcio J. Lacerda , Brazil  
Eduardo Lalla , The Netherlands  
Giovanni Lancioni , Italy  
Jaroslaw Latalski , Poland  
Hervé Laurent , France  
Agostino Lauria , Italy  
Aimé Lay-Ekuakille , Italy  
Nicolas J. Leconte , France  
Kun-Chou Lee , Taiwan  
Dimitri Lefebvre , France  
Eric Lefevre , France  
Marek Lefik, Poland  
Yaguo Lei , China  
Kauko Leiviskä , Finland  
Ervin Lenzi , Brazil  
ChenFeng Li , China  
Jian Li , USA  
Jun Li , China  
Yueyang Li , China  
Zhao Li , China































Zhen Li , China  
En-Qiang Lin, USA  
Jian Lin , China  
Qibin Lin, China  
Yao-Jin Lin, China  
Zhiyun Lin , China  
Bin Liu , China  
Bo Liu , China  
Heng Liu , China  
Jianxu Liu , Thailand  
Lei Liu , China  
Sixin Liu , China  
Wanquan Liu , China  
Yu Liu , China  
Yuanchang Liu , United Kingdom  
Bonifacio Llamazares , Spain  
Alessandro Lo Schiavo , Italy  
Jean Jacques Loiseau , France  
Francesco Lolli , Italy  
Paolo Lonetti , Italy  
António M. Lopes , Portugal  
Sebastian López, Spain  
Luis M. López-Ochoa , Spain  
Vassilios C. Loukopoulos, Greece  
Gabriele Maria Lozito , Italy  
Zhiguo Luo , China  
Gabriel Luque , Spain  
Valentin Lychagin, Norway  
YUE MEI, China  
Junwei Ma , China  
Xuanlong Ma , China  
Antonio Madeo , Italy  
Alessandro Magnani , Belgium  
Toqeer Mahmood , Pakistan  
Fazal M. Mahomed , South Africa  
Arunava Majumder , India  
Sarfranz Nawaz Malik, Pakistan  
Paolo Manfredi , Italy  
Adnan Maqsood , Pakistan  
Muazzam Maqsood, Pakistan  
Giuseppe Carlo Marano , Italy  
Damijan Markovic, France  
Filipe J. Marques , Portugal  
Luca Martinelli , Italy  
Denizar Cruz Martins, Brazil

Francisco J. Martos , Spain  
Elio Masciari , Italy  
Paolo Massioni , France  
Alessandro Mauro , Italy  
Jonathan Mayo-Maldonado , Mexico  
Pier Luigi Mazzeo , Italy  
Laura Mazzola, Italy  
Driss Mehdi , France  
Zahid Mehmood , Pakistan  
Roderick Melnik , Canada  
Xiangyu Meng , USA  
Jose Merodio , Spain  
Alessio Merola , Italy  
Mahmoud Mesbah , Iran  
Luciano Mescia , Italy  
Laurent Mevel , France  
Constantine Michailides , Cyprus  
Mariusz Michta , Poland  
Prankul Middha, Norway  
Aki Mikkola , Finland  
Giovanni Minafò , Italy  
Edmondo Minisci , United Kingdom  
Hiroyuki Mino , Japan  
Dimitrios Mitsotakis , New Zealand  
Ardashir Mohammadzadeh , Iran  
Francisco J. Montáns , Spain  
Francesco Montefusco , Italy  
Gisele Mophou , France  
Rafael Morales , Spain  
Marco Morandini , Italy  
Javier Moreno-Valenzuela , Mexico  
Simone Morganti , Italy  
Caroline Mota , Brazil  
Aziz Moukrim , France  
Shen Mouquan , China  
Dimitris Mourtzis , Greece  
Emiliano Mucchi , Italy  
Taseer Muhammad, Saudi Arabia  
Ghulam Muhiuddin, Saudi Arabia  
Amitava Mukherjee , India  
Josefa Mula , Spain  
Jose J. Muñoz , Spain  
Giuseppe Muscolino, Italy  
Marco Mussetta , Italy

Hariharan Muthusamy, India  
Alessandro Naddeo , Italy  
Raj Nandkeolyar, India  
Keivan Navaie , United Kingdom  
Soumya Nayak, India  
Adrian Neagu , USA  
Erivelton Geraldo Nepomuceno , Brazil  
AMA Neves, Portugal  
Ha Quang Thinh Ngo , Vietnam  
Nhon Nguyen-Thanh, Singapore  
Papakostas Nikolaos , Ireland  
Jelena Nikolic , Serbia  
Tatsushi Nishi, Japan  
Shanzhou Niu , China  
Ben T. Nohara , Japan  
Mohammed Nouari , France  
Mustapha Nourelfath, Canada  
Kazem Nouri , Iran  
Ciro Núñez-Gutiérrez , Mexico  
Włodzimierz Ogryczak, Poland  
Roger Ohayon, France  
Krzysztof Okarma , Poland  
Mitsuhiro Okayasu, Japan  
Murat Olgun , Turkey  
Diego Oliva, Mexico  
Alberto Olivares , Spain  
Enrique Onieva , Spain  
Calogero Orlando , Italy  
Susana Ortega-Cisneros , Mexico  
Sergio Ortobelli, Italy  
Naohisa Otsuka , Japan  
Sid Ahmed Ould Ahmed Mahmoud , Saudi Arabia  
Taoreed Owolabi , Nigeria  
EUGENIA PETROPOULOU , Greece  
Arturo Pagano, Italy  
Madhumangal Pal, India  
Pasquale Palumbo , Italy  
Dragan Pamučar, Serbia  
Weifeng Pan , China  
Chandan Pandey, India  
Rui Pang, United Kingdom  
Jürgen Pannek , Germany  
Elena Panteley, France  
Achille Paolone, Italy

George A. Papakostas , Greece  
Xosé M. Pardo , Spain  
You-Jin Park, Taiwan  
Manuel Pastor, Spain  
Pubudu N. Pathirana , Australia  
Surajit Kumar Paul , India  
Luis Payá , Spain  
Igor Pažanin , Croatia  
Libor Pekař , Czech Republic  
Francesco Pellicano , Italy  
Marcello Pellicciari , Italy  
Jian Peng , China  
Mingshu Peng, China  
Xiang Peng , China  
Xindong Peng, China  
Yuexing Peng, China  
Marzio Pennisi , Italy  
Maria Patrizia Pera , Italy  
Matjaz Perc , Slovenia  
A. M. Bastos Pereira , Portugal  
Wesley Peres, Brazil  
F. Javier Pérez-Pinal , Mexico  
Michele Perrella, Italy  
Francesco Pesavento , Italy  
Francesco Petrini , Italy  
Hoang Vu Phan, Republic of Korea  
Lukasz Pieczonka , Poland  
Dario Piga , Switzerland  
Marco Pizzarelli , Italy  
Javier Plaza , Spain  
Goutam Pohit , India  
Dragan Poljak , Croatia  
Jorge Pomares , Spain  
Hiram Ponce , Mexico  
Sébastien Poncet , Canada  
Volodymyr Ponomaryov , Mexico  
Jean-Christophe Ponsart , France  
Mauro Pontani , Italy  
Sivakumar Poruran, India  
Francesc Pozo , Spain  
Aditya Rio Prabowo , Indonesia  
Anchasa Pramuanjaroenkij , Thailand  
Leonardo Primavera , Italy  
B Rajanarayan Prusty, India

Krzysztof Puszynski , Poland  
Chuan Qin , China  
Dongdong Qin, China  
Jianlong Qiu , China  
Giuseppe Quaranta , Italy  
DR. RITU RAJ , India  
Vitomir Racic , Italy  
Carlo Rainieri , Italy  
Kumbakonam Ramamani Rajagopal, USA  
Ali Ramazani , USA  
Angel Manuel Ramos , Spain  
Higinio Ramos , Spain  
Muhammad Afzal Rana , Pakistan  
Muhammad Rashid, Saudi Arabia  
Manoj Rastogi, India  
Alessandro Rasulo , Italy  
S.S. Ravindran , USA  
Abdolrahman Razani , Iran  
Alessandro Reali , Italy  
Jose A. Reinoso , Spain  
Oscar Reinoso , Spain  
Haijun Ren , China  
Carlo Renno , Italy  
Fabrizio Renno , Italy  
Shahram Rezapour , Iran  
Ricardo Rianza , Spain  
Francesco Riganti-Fulginei , Italy  
Gerasimos Rigatos , Greece  
Francesco Ripamonti , Italy  
Jorge Rivera , Mexico  
Eugenio Roanes-Lozano , Spain  
Ana Maria A. C. Rocha , Portugal  
Luigi Rodino , Italy  
Francisco Rodríguez , Spain  
Rosana Rodríguez López, Spain  
Francisco Rossomando , Argentina  
Jose de Jesus Rubio , Mexico  
Weiguo Rui , China  
Rubén Ruiz , Spain  
Ivan D. Rukhlenko , Australia  
Dr. Eswaramoorthi S. , India  
Weichao SHI , United Kingdom  
Chaman Lal Sabharwal , USA  
Andrés Sáez , Spain

Bekir Sahin, Turkey  
Laxminarayan Sahoo , India  
John S. Sakellariou , Greece  
Michael Sakellariou , Greece  
Salvatore Salamone, USA  
Jose Vicente Salcedo , Spain  
Alejandro Salcido , Mexico  
Alejandro Salcido, Mexico  
Nunzio Salerno , Italy  
Rohit Salgotra , India  
Miguel A. Salido , Spain  
Sinan Salih , Iraq  
Alessandro Salvini , Italy  
Abdus Samad , India  
Sovan Samanta, India  
Nikolaos Samaras , Greece  
Ramon Sancibrian , Spain  
Giuseppe Sanfilippo , Italy  
Omar-Jacobo Santos, Mexico  
J Santos-Reyes , Mexico  
José A. Sanz-Herrera , Spain  
Musavarah Sarwar, Pakistan  
Shahzad Sarwar, Saudi Arabia  
Marcelo A. Savi , Brazil  
Andrey V. Savkin, Australia  
Tadeusz Sawik , Poland  
Roberta Sburlati, Italy  
Gustavo Scaglia , Argentina  
Thomas Schuster , Germany  
Hamid M. Sedighi , Iran  
Mijanur Rahaman Seikh, India  
Tapan Senapati , China  
Lotfi Senhadji , France  
Junwon Seo, USA  
Michele Serpilli, Italy  
Silvestar Šesnić , Croatia  
Gerardo Severino, Italy  
Ruben Sevilla , United Kingdom  
Stefano Sfarra , Italy  
Dr. Ismail Shah , Pakistan  
Leonid Shaikhet , Israel  
Vimal Shanmuganathan , India  
Prayas Sharma, India  
Bo Shen , Germany  
Hang Shen, China

Xin Pu Shen, China  
Dimitri O. Shepelsky, Ukraine  
Jian Shi , China  
Amin Shokrollahi, Australia  
Suzanne M. Shontz , USA  
Babak Shotorban , USA  
Zhan Shu , Canada  
Angelo Sifaleras , Greece  
Nuno Simões , Portugal  
Mehakpreet Singh , Ireland  
Piyush Pratap Singh , India  
Rajiv Singh, India  
Seralathan Sivamani , India  
S. Sivasankaran , Malaysia  
Christos H. Skiadas, Greece  
Konstantina Skouri , Greece  
Neale R. Smith , Mexico  
Bogdan Smolka, Poland  
Delfim Soares Jr. , Brazil  
Alba Sofi , Italy  
Francesco Soldovieri , Italy  
Raffaele Solimene , Italy  
Yang Song , Norway  
Jussi Sopanen , Finland  
Marco Spadini , Italy  
Paolo Spagnolo , Italy  
Ruben Specogna , Italy  
Vasilios Spitas , Greece  
Ivanka Stamova , USA  
Rafał Stanisławski , Poland  
Miladin Stefanović , Serbia  
Salvatore Strano , Italy  
Yakov Strelniker, Israel  
Kangkang Sun , China  
Qiuqin Sun , China  
Shuaishuai Sun, Australia  
Yanchao Sun , China  
Zong-Yao Sun , China  
Kumarasamy Suresh , India  
Sergey A. Suslov , Australia  
D.L. Suthar, Ethiopia  
D.L. Suthar , Ethiopia  
Andrzej Swierniak, Poland  
Andras Szekrenyes , Hungary  
Kumar K. Tamma, USA

Yong (Aaron) Tan, United Kingdom  
Marco Antonio Taneco-Hernández , Mexico  
Lu Tang , China  
Tianyou Tao, China  
Hafez Tari , USA  
Alessandro Tasora , Italy  
Sergio Teggi , Italy  
Adriana del Carmen Téllez-Anguiano , Mexico  
Ana C. Teodoro , Portugal  
Efstathios E. Theotokoglou , Greece  
Jing-Feng Tian, China  
Alexander Timokha , Norway  
Stefania Tomasiello , Italy  
Gisella Tomasini , Italy  
Isabella Torcicollo , Italy  
Francesco Tornabene , Italy  
Mariano Torrisi , Italy  
Thang nguyen Trung, Vietnam  
George Tsiatas , Greece  
Le Anh Tuan , Vietnam  
Nerio Tullini , Italy  
Emilio Turco , Italy  
Ilhan Tuzcu , USA  
Efstratios Tzirtzilakis , Greece  
FRANCISCO UREÑA , Spain  
Filippo Ubertini , Italy  
Mohammad Uddin , Australia  
Mohammad Safi Ullah , Bangladesh  
Serdar Ulubeyli , Turkey  
Mati Ur Rahman , Pakistan  
Panayiotis Vafeas , Greece  
Giuseppe Vairo , Italy  
Jesus Valdez-Resendiz , Mexico  
Eusebio Valero, Spain  
Stefano Valvano , Italy  
Carlos-Renato Vázquez , Mexico  
Martin Velasco Villa , Mexico  
Franck J. Vernerey, USA  
Georgios Veronis , USA  
Vincenzo Vespri , Italy  
Renato Vidoni , Italy  
Venkatesh Vijayaraghavan, Australia

Anna Vila, Spain  
Francisco R. Villatoro , Spain  
Francesca Vipiana , Italy  
Stanislav Vitek , Czech Republic  
Jan Vorel , Czech Republic  
Michael Vynnycky , Sweden  
Mohammad W. Alomari, Jordan  
Roman Wan-Wendner , Austria  
Bingchang Wang, China  
C. H. Wang , Taiwan  
Dagang Wang, China  
Guoqiang Wang , China  
Huaiyu Wang, China  
Hui Wang , China  
J.G. Wang, China  
Ji Wang , China  
Kang-Jia Wang , China  
Lei Wang , China  
Qiang Wang, China  
Qingling Wang , China  
Weiwei Wang , China  
Xinyu Wang , China  
Yong Wang , China  
Yung-Chung Wang , Taiwan  
Zhenbo Wang , USA  
Zhibo Wang, China  
Waldemar T. Wójcik, Poland  
Chi Wu , Australia  
Qihong Wu, China  
Yuqiang Wu, China  
Zhibin Wu , China  
Zhizheng Wu , China  
Michalis Xenos , Greece  
Hao Xiao , China  
Xiao Ping Xie , China  
Qingzheng Xu , China  
Binghan Xue , China  
Yi Xue , China  
Joseph J. Yame , France  
Chuanliang Yan , China  
Xinggang Yan , United Kingdom  
Hongtai Yang , China  
Jixiang Yang , China  
Mijia Yang, USA  
Ray-Yeng Yang, Taiwan

Zaoli Yang , China  
Jun Ye , China  
Min Ye , China  
Luis J. Yebra , Spain  
Peng-Yeng Yin , Taiwan  
Muhammad Haroon Yousaf , Pakistan  
Yuan Yuan, United Kingdom  
Qin Yuming, China  
Elena Zaitseva , Slovakia  
Arkadiusz Zak , Poland  
Mohammad Zakwan , India  
Ernesto Zambrano-Serrano , Mexico  
Francesco Zammori , Italy  
Jessica Zangari , Italy  
Rafal Zdunek , Poland  
Ibrahim Zeid, USA  
Nianyin Zeng , China  
Junyong Zhai , China  
Hao Zhang , China  
Haopeng Zhang , USA  
Jian Zhang , China  
Kai Zhang, China  
Lingfan Zhang , China  
Mingjie Zhang , Norway  
Qian Zhang , China  
Tianwei Zhang , China  
Tongqian Zhang , China  
Wenyu Zhang , China  
Xianming Zhang , Australia  
Xuping Zhang , Denmark  
Yinyan Zhang, China  
Yifan Zhao , United Kingdom  
Debao Zhou, USA  
Heng Zhou , China  
Jian G. Zhou , United Kingdom  
Junyong Zhou , China  
Xueqian Zhou , United Kingdom  
Zhe Zhou , China  
Wu-Le Zhu, China  
Gaetano Zizzo , Italy  
Mingcheng Zuo, China

# Contents

**Retracted: Application of Data Warehouse Technology Based on Neural Network in Physical Education Quality Management**

Mathematical Problems in Engineering

Retraction (1 page), Article ID 9863480, Volume 2023 (2023)

**Retracted: Research on Mobile Ideological and Political Teaching in Universities Based on the Android Platform**

Mathematical Problems in Engineering

Retraction (1 page), Article ID 9848072, Volume 2023 (2023)

**Retracted: Evaluation Method of Writing Fluency Based on Machine Learning Method**

Mathematical Problems in Engineering

Retraction (1 page), Article ID 9780319, Volume 2023 (2023)

**Retracted: Quality Assessment Method of Information Model Reform of Higher Mathematics Education Based on Big Data**

Mathematical Problems in Engineering

Retraction (1 page), Article ID 9805925, Volume 2023 (2023)

**Novel Architecture for Transactive Energy Management Systems with Various Market Clearing Strategies**

S. L. Arun [ID](#), Kishore Bingi [ID](#), R. Vijaya Priya [ID](#), I. Jacob Raglend [ID](#), and B. Hanumantha Rao

Research Article (15 pages), Article ID 3979662, Volume 2023 (2023)

**Violation Punishment and Total Factor Productivity, Based on the Spillover Effect between Director-Interlocked Firms**

Yang Lu [ID](#), Xiangge Meng [ID](#), and Haitao Song

Research Article (10 pages), Article ID 8977265, Volume 2023 (2023)

**Research on Optimization of Air Defense Firepower Configuration for Warship Cooperating with Strategic Location on the Sea**

W. F. Zhao [ID](#), H. J. Sun [ID](#), M. Li, and K. N. Teng [ID](#)

Research Article (16 pages), Article ID 5297688, Volume 2023 (2023)

**An Efficient Approach of Face Detection and Prediction of Drowsiness Using SVM**

Ratnesh Kumar Shukla, Arvind Kumar Tiwari, and Ashish Kumar Jha [ID](#)


Research Article (12 pages), Article ID 2168361, Volume 2023 (2023)

**Deep Neural Network for Accurate Age Group Prediction through Pupil Using the Optimized UNet Model**

Swathi Gowroju [ID](#), Sandeep Kumar [ID](#), Aarti [ID](#), and Anshu Ghimire [ID](#)


Research Article (24 pages), Article ID 7813701, Volume 2022 (2022)

**Study on the Level of Integration of Equipment Manufacturing Industry and Producer Service Industry in the Region Transforming Provinces and Its Influencing Factors: Taking Shanxi Province as an Example**

Tao Ding , Guoxin Bai, and Han Xu


Research Article (16 pages), Article ID 1309293, Volume 2022 (2022)

**Regional Economic Forecasting Method Based on Recurrent Neural Network**

E. Liu , Haiou Zhu, Qing Liu, and Thomas Bilaliib Udimal


Research Article (6 pages), Article ID 3058947, Volume 2022 (2022)

**Application of Computer Vision in Intelligent Manufacturing under the Background of 5G Wireless Communication and Industry 4.0**

Yan Li 


Research Article (9 pages), Article ID 9422584, Volume 2022 (2022)

**[Retracted] Application of Data Warehouse Technology Based on Neural Network in Physical Education Quality Management**

Bo Zhao and Yanjin Liu 


Research Article (10 pages), Article ID 4456885, Volume 2022 (2022)

**[Retracted] Evaluation Method of Writing Fluency Based on Machine Learning Method**

Sheng Gao 


Research Article (12 pages), Article ID 1253614, Volume 2022 (2022)

**Analysis of the Impact of Energy Factor Allocation Efficiency on Green Total Point Productivity from a Low-Carbon Perspective**

Jiegang Sun 


Research Article (11 pages), Article ID 6000948, Volume 2022 (2022)

**Normality Test for Influence Function of Mining Surface Subsidence Based on Network Observation Station**

Pengyu Li, Zhenqi Hu , Yaokun Fu, Gensheng Li, Jiaxin Guo, and Dongzhu Yuan



Research Article (12 pages), Article ID 2201996, Volume 2022 (2022)

**Modeling and Optimizing Based on OTCPN in Multi-Tier Shuttle Warehousing System**

Huishuang Zhu, Meng Wang , and Huaijin Gao

Research Article (15 pages), Article ID 9773212, Volume 2022 (2022)

**Fuzzy Analysis of SVIRS Disease System with Holling Type-II Saturated Incidence Rate and Saturated Treatment**



Hu Zhang, V. Madhusudanan , B. S. N. Murthy, M. N. Srinivas, and Biruk Ambachew Adugna 

Research Article (19 pages), Article ID 1330875, Volume 2022 (2022)







## Contents

### **A Digital Assessment Method for Multisource Influence Factors on Corrosion Characteristics in the Karst Areas**

Zhanfei Gu  and Zhikui Liu 


Research Article (11 pages), Article ID 8130609, Volume 2022 (2022)

### **A Novel Architecture for Diabetes Patients' Prediction Using K-Means Clustering and SVM**

Nitin Arora , Anupam Singh , Mustafa Zuhaer Nayef Al-Dabagh , and Sumit Kumar Maitra 









Research Article (9 pages), Article ID 4815521, Volume 2022 (2022)

### **Research on Vehicle-Mounted Electromagnetic Ejection Remote Fire Extinguishing System**

Xing Wang, Yadong Li, Zhenrui Shi, Baoshan Cao, Yanjie Cao, Hui Zhao, and Xun Gong 



Research Article (9 pages), Article ID 2129942, Volume 2022 (2022)

### **Nonisolated DC to DC Converters for High-Voltage Gain Applications Using the MPPT Approach**

C. Subba Rami Reddy , Bharath Kumar Narukullapati , M. Uma Maheswara Rao , Sangu Ravindra , P. M. Venkatesh , T. Ch. Anil Kumar , B. Mouli Chandra , and Afework Aemro Berhanu 

Research Article (12 pages), Article ID 9227651, Volume 2022 (2022)

### **An Epidemic Patch-Enabled Delayed Model for Virus Propagation: Towards Evaluating Bifurcation and White Noise**

Zhigang Liu, V. Madhusudanan , M. N. Srinivas, ChukwuNonso H. Nwokoye, and Tadele Degefa Geleto 

Research Article (19 pages), Article ID 3763858, Volume 2022 (2022)

### **Parameter Calibration of Sediment Transport Capacity Formula of the Third Entrance of Xinqiman Reservoir in Tarim River Based on CCHE2D Model**

Yixin Geng, Yujian Li , Liang Mao, and Peng An


Research Article (9 pages), Article ID 4227059, Volume 2022 (2022)

### **Influence of Urban Atmospheric Ecological Environment on the Development of Outdoor Sports**

Linqiang Xu  and Gia Lyu 

Review Article (6 pages), Article ID 1931075, Volume 2022 (2022)

### **Granger Causality Analysis of Foreign Trade in Cement Products and Ecological Impact in China**

Chen Feng 


Research Article (11 pages), Article ID 3467483, Volume 2022 (2022)

### **Prediction of Fault Occurrences in Smart City Water Distribution System Using Time-Series Forecasting Algorithm**

Maheswari Chenniappan , Divya Gnanavel , Kavi Priya Gunasekaran , R.R. Rajalakshmi , A.S. Ramya , Albert Alexander Stonier , Geno Peter , and Vivekananda Ganji 



Research Article (13 pages), Article ID 9678769, Volume 2022 (2022)

**A Decision-Making Model for Selection of the Suitable FDM Machine Using Fuzzy TOPSIS**

S. Raja and A. John Rajan 

Research Article (15 pages), Article ID 7653292, Volume 2022 (2022)

**Visual Object Tracking Based on Adaptive Background-Awareness and Spatial Constraint**

Keqi Fan , Qianqian Yu, Yiyang Wang, Deng Chen , and Yuhui Zheng


Research Article (11 pages), Article ID 6062283, Volume 2022 (2022)

**A Comparative Study on Detection of Malware and Benign on the Internet Using Machine Learning Classifiers**

J. Pavithra  and S. Selvakumara Samy 





Research Article (8 pages), Article ID 4893390, Volume 2022 (2022)

**A Threshold Segmentation Algorithm for Sculpture Images Based on Sparse Decomposition**

Zhao Yang and Jixin Wan 

Research Article (8 pages), Article ID 8523370, Volume 2022 (2022)

**Discriminating the Pneumonia-Positive Images from COVID-19-Positive Images Using an Integrated Convolutional Neural Network**

Vetrithangam D , V. Indira, Syed Umar , Bhaskar Pant, Mayank Kumar Goyal , and Arunadevi B 



Research Article (9 pages), Article ID 5643977, Volume 2022 (2022)

**Psychological Mechanism and Exercise Intervention of College Students' Problematic Internet Use Based on IoT Technology**

Zhiqiang Chen  and Pu Sun


Research Article (14 pages), Article ID 3615217, Volume 2022 (2022)

**Fault Diagnosis Using Data Fusion with Ensemble Deep Learning Technique in IIoT**

S Venkatasubramanian, S Raja, V Sumanth, Jaiprakash Narain Dwivedi , J Sathiaparkavi, Santanu Modak, and Mandefro Legesse Kejela 



Research Article (8 pages), Article ID 1682874, Volume 2022 (2022)

**[Retracted] Research on Mobile Ideological and Political Teaching in Universities Based on the Android Platform**

Jinxin Chen  and Yuanyuan Guan


Research Article (8 pages), Article ID 1214684, Volume 2022 (2022)

**CRUN-Based Leaf Disease Segmentation and Morphological-Based Stage Identification**

J. Sujithra  and M. Ferni Ukrit 

Research Article (13 pages), Article ID 2546873, Volume 2022 (2022)

**Research on Dance Teaching Based on Motion Capture System**


Yuan Peng 

Research Article (8 pages), Article ID 1455849, Volume 2022 (2022)

# Contents

---

**Research on College English Teaching Evaluation Based on Neural Network**

Yuanyuan Zhao 


Research Article (10 pages), Article ID 7653986, Volume 2022 (2022)

**[Retracted] Quality Assessment Method of Information Model Reform of Higher Mathematics Education Based on Big Data**

Jiao Li, Jiao Xue , and Hongjuan Fu


Research Article (8 pages), Article ID 5932902, Volume 2022 (2022)

**A Traffic Scheduling Method Based on SDN**

Li Wang 


Research Article (7 pages), Article ID 1819202, Volume 2022 (2022)

**Evaluation Model of Sports Culture Industry Competitiveness Based on Fuzzy Analysis Algorithm**

Guoqiang Sun , Xinxin Zhang, and Yu Lin

Research Article (8 pages), Article ID 9708646, Volume 2022 (2022)

**A Multiobjective Allocation Method for High-Quality Higher Education Resources Based on Cellular Genetic Algorithm**

Tianshu He 

Research Article (8 pages), Article ID 4322078, Volume 2022 (2022)

## Retraction

# Retracted: Application of Data Warehouse Technology Based on Neural Network in Physical Education Quality Management

### Mathematical Problems in Engineering

Received 17 October 2023; Accepted 17 October 2023; Published 18 October 2023

Copyright © 2023 Mathematical Problems in Engineering. This is an open access article distributed under the Creative Commons Attribution License, which permits unrestricted use, distribution, and reproduction in any medium, provided the original work is properly cited.

This article has been retracted by Hindawi following an investigation undertaken by the publisher [1]. This investigation has uncovered evidence of one or more of the following indicators of systematic manipulation of the publication process:

- (1) Discrepancies in scope
- (2) Discrepancies in the description of the research reported
- (3) Discrepancies between the availability of data and the research described
- (4) Inappropriate citations
- (5) Incoherent, meaningless and/or irrelevant content included in the article
- (6) Peer-review manipulation

The presence of these indicators undermines our confidence in the integrity of the article's content and we cannot, therefore, vouch for its reliability. Please note that this notice is intended solely to alert readers that the content of this article is unreliable. We have not investigated whether authors were aware of or involved in the systematic manipulation of the publication process.

In addition, our investigation has also shown that one or more of the following human-subject reporting requirements has not been met in this article: ethical approval by an Institutional Review Board (IRB) committee or equivalent, patient/participant consent to participate, and/or agreement to publish patient/participant details (where relevant).

Wiley and Hindawi regrets that the usual quality checks did not identify these issues before publication and have since put additional measures in place to safeguard research integrity.

We wish to credit our own Research Integrity and Research Publishing teams and anonymous and named external researchers and research integrity experts for contributing to this investigation.

The corresponding author, as the representative of all authors, has been given the opportunity to register their agreement or disagreement to this retraction. We have kept a record of any response received.

### References

- [1] B. Zhao and Y. Liu, "Application of Data Warehouse Technology Based on Neural Network in Physical Education Quality Management," *Mathematical Problems in Engineering*, vol. 2022, Article ID 4456885, 10 pages, 2022.

## *Retraction*

# **Retracted: Research on Mobile Ideological and Political Teaching in Universities Based on the Android Platform**

### **Mathematical Problems in Engineering**

Received 26 September 2023; Accepted 26 September 2023; Published 27 September 2023

Copyright © 2023 Mathematical Problems in Engineering. This is an open access article distributed under the Creative Commons Attribution License, which permits unrestricted use, distribution, and reproduction in any medium, provided the original work is properly cited.

This article has been retracted by Hindawi following an investigation undertaken by the publisher [1]. This investigation has uncovered evidence of one or more of the following indicators of systematic manipulation of the publication process:

- (1) Discrepancies in scope
- (2) Discrepancies in the description of the research reported
- (3) Discrepancies between the availability of data and the research described
- (4) Inappropriate citations
- (5) Incoherent, meaningless and/or irrelevant content included in the article
- (6) Peer-review manipulation

The presence of these indicators undermines our confidence in the integrity of the article's content and we cannot, therefore, vouch for its reliability. Please note that this notice is intended solely to alert readers that the content of this article is unreliable. We have not investigated whether authors were aware of or involved in the systematic manipulation of the publication process.

Wiley and Hindawi regrets that the usual quality checks did not identify these issues before publication and have since put additional measures in place to safeguard research integrity.

We wish to credit our own Research Integrity and Research Publishing teams and anonymous and named external researchers and research integrity experts for contributing to this investigation.

The corresponding author, as the representative of all authors, has been given the opportunity to register their agreement or disagreement to this retraction. We have kept a record of any response received.

### **References**

- [1] J. Chen and Y. Guan, "Research on Mobile Ideological and Political Teaching in Universities Based on the Android Platform," *Mathematical Problems in Engineering*, vol. 2022, Article ID 1214684, 8 pages, 2022.

## *Retraction*

# **Retracted: Evaluation Method of Writing Fluency Based on Machine Learning Method**

### **Mathematical Problems in Engineering**

Received 26 September 2023; Accepted 26 September 2023; Published 27 September 2023

Copyright © 2023 Mathematical Problems in Engineering. This is an open access article distributed under the Creative Commons Attribution License, which permits unrestricted use, distribution, and reproduction in any medium, provided the original work is properly cited.

This article has been retracted by Hindawi following an investigation undertaken by the publisher [1]. This investigation has uncovered evidence of one or more of the following indicators of systematic manipulation of the publication process:

- (1) Discrepancies in scope
- (2) Discrepancies in the description of the research reported
- (3) Discrepancies between the availability of data and the research described
- (4) Inappropriate citations
- (5) Incoherent, meaningless and/or irrelevant content included in the article
- (6) Peer-review manipulation

The presence of these indicators undermines our confidence in the integrity of the article's content and we cannot, therefore, vouch for its reliability. Please note that this notice is intended solely to alert readers that the content of this article is unreliable. We have not investigated whether authors were aware of or involved in the systematic manipulation of the publication process.

Wiley and Hindawi regrets that the usual quality checks did not identify these issues before publication and have since put additional measures in place to safeguard research integrity.

We wish to credit our own Research Integrity and Research Publishing teams and anonymous and named external researchers and research integrity experts for contributing to this investigation.

The corresponding author, as the representative of all authors, has been given the opportunity to register their agreement or disagreement to this retraction. We have kept a record of any response received.

### **References**

- [1] S. Gao, "Evaluation Method of Writing Fluency Based on Machine Learning Method," *Mathematical Problems in Engineering*, vol. 2022, Article ID 1253614, 12 pages, 2022.

## *Retraction*

# **Retracted: Quality Assessment Method of Information Model Reform of Higher Mathematics Education Based on Big Data**

### **Mathematical Problems in Engineering**

Received 1 August 2023; Accepted 1 August 2023; Published 2 August 2023

Copyright © 2023 Mathematical Problems in Engineering. This is an open access article distributed under the Creative Commons Attribution License, which permits unrestricted use, distribution, and reproduction in any medium, provided the original work is properly cited.

This article has been retracted by Hindawi following an investigation undertaken by the publisher [1]. This investigation has uncovered evidence of one or more of the following indicators of systematic manipulation of the publication process:

- (1) Discrepancies in scope
- (2) Discrepancies in the description of the research reported
- (3) Discrepancies between the availability of data and the research described
- (4) Inappropriate citations
- (5) Incoherent, meaningless and/or irrelevant content included in the article
- (6) Peer-review manipulation

The presence of these indicators undermines our confidence in the integrity of the article's content and we cannot, therefore, vouch for its reliability. Please note that this notice is intended solely to alert readers that the content of this article is unreliable. We have not investigated whether authors were aware of or involved in the systematic manipulation of the publication process.

Wiley and Hindawi regrets that the usual quality checks did not identify these issues before publication and have since put additional measures in place to safeguard research integrity.

We wish to credit our own Research Integrity and Research Publishing teams and anonymous and named external researchers and research integrity experts for contributing to this investigation.

The corresponding author, as the representative of all authors, has been given the opportunity to register their agreement or disagreement to this retraction. We have kept a record of any response received.

### **References**

- [1] J. Li, J. Xue, and H. Fu, "Quality Assessment Method of Information Model Reform of Higher Mathematics Education Based on Big Data," *Mathematical Problems in Engineering*, vol. 2022, Article ID 5932902, 8 pages, 2022.

## Research Article

# Novel Architecture for Transactive Energy Management Systems with Various Market Clearing Strategies

S. L. Arun <sup>1</sup>, Kishore Bingi <sup>2</sup>, R. Vijaya Priya <sup>1</sup>, I. Jacob Raglend <sup>1</sup>  
and B. Hanumantha Rao<sup>3</sup>

<sup>1</sup>*School of Electrical Engineering, Vellore Institute of Technology, Vellore, India*

<sup>2</sup>*Department of Electrical and Electronic Engineering, Universiti Teknologi PETRONAS, 31750 Seri Iskandar, Malaysia*

<sup>3</sup>*School of Electrical and Electronic Engineering, University College Dublin, Dublin, Ireland*

Correspondence should be addressed to Kishore Bingi; [bingi.kishore@ieee.org](mailto:bingi.kishore@ieee.org)

Received 11 September 2022; Revised 23 November 2022; Accepted 5 April 2023; Published 24 April 2023

Academic Editor: Punit Gupta

Copyright © 2023 S. L. Arun et al. This is an open access article distributed under the Creative Commons Attribution License, which permits unrestricted use, distribution, and reproduction in any medium, provided the original work is properly cited.

The recent advancements in demand-side management techniques add significant benefits to the distribution systems. One such technique is transactive energy management systems (TEMS) which motivate the energy end-users to take part in local energy trading. The end-users can effectively increase the monetary benefits by trading the surplus generation/demand within the local energy market (LEM). The LEM operator frames a viable market clearing strategy to fix the market clearing price to enhance the monetary benefits of all the market players. In this study, LEM architecture with different market clearing strategies is proposed for TEMS to ensure profitable power transactions between the neighboring end-users. An optimal energy management algorithm is also proposed for time scheduling the operation of flexible loads and batteries, considering dynamics in end-users' behavior, variations in utility parameters, and the intermittent nature of renewable power generation. Further, an optimal load scheduling algorithm is developed at the end-users' premises to improve the profits in the LEM. Correspondingly, the trading strategies are extended to increase market reliability by penalizing participants for their abnormal activities in energy trading. The proposed framework is validated with different case studies considering ten residential participants in a locality.

## 1. Introduction

Demand side management (DSM) techniques are proven to achieve remarkable benefits in smart distribution systems [1]. For instance, the end-users can avail considerable incentives from the grid operator by actively responding (demand response) to the utility DSM control schemes. An energy management system helps the end-users easily track and regulate the operation of home appliances to avail the maximum economic benefits [2]. Also, the end-users can further minimize their electricity bill by significantly reducing and meeting the demand through energy storage devices, especially during peak intervals. Since these storage devices are charged from the grid, they may not result in a substantial reduction in the electricity bill, especially when the utility charges at a flat-rate tariff. As an alternate solution, the end-users adopt in-house renewable energy

resources (RERs), for instance, rooftop solar photovoltaic (PV) arrays and small wind turbines, to meet the residential demand either partly or entirely. Nevertheless, the power generation from the RERs is site-specific and profoundly intermittent. Henceforth, the net demand profile of such residential buildings is highly unpredictable.

On the other hand, utilities encourage the end-users to trade their excess power generation to the utility with considerable incentives and call these types of users as prosumers. Generally, prosumers prefer to export the excess generation into the grid during peak intervals to enhance electricity bill savings. Further, to reduce their dependency on the grid during high price intervals, prosumers optimally reschedule the operation of home appliances for low-price intervals. To enhance the control mechanism of home appliance operation, the smart energy management system (SEMS) is indispensable [2]. Generally, SEMS is devised to



schedule the operating time of household appliances concerning end users' requirements, utility operational dynamics, and the intermittent nature of RERs.

*1.1. Literature Review.* Several research works have been addressed in the literature to schedule household appliances through energy management systems optimally. To lower the residential consumer's electricity bill, a load scheduling algorithm using a mixed-integer linear program is proposed in [3]. Considering the uncertainty of home appliances' operation times, energy storage systems, and the sporadic nature of renewable energy generation, an efficient energy management scheme is devised in [4]. A DSM with prosumer participation is developed in [5], where the consumer's electricity bill is reduced by exporting power to the utility. Also, the residential electricity demand pattern is synthesized based on the probability of appliances' times of operation. Incorporating RERs and electric vehicles with appropriate DSM in residential buildings substantiates microgrid stability and lessens utility dependence [6]. A load scheduling algorithm to maximize operational savings as a primary objective function is discussed in [7], employing a simple linear program. In [8], an optimization technique is presented to schedule the load demand of PV-installed residential buildings as the output power variation is unpredictable.

The feed-in tariff (FiT) scheme in the traditional market is intended to motivate small-scale prosumers. However, the number of new installations over a decade increased unexpectedly. The governing bodies started to decrease the FiT price significantly, which resulted in a lengthy investment pay-back period for prosumers. FiT schemes have been discontinued in some parts of the world, like the state of Queensland in Australia [9]. As the distribution grid operators face additional operational challenges with integrating RERs-based residential buildings [10], utilities are showing a lack of interest in purchasing surplus generation from the end-users. However, few utilities regulate end-users' support by initiating a time-varying power injection limit (PIL) [11]. In this regulation, an end-user benefits economically by injecting the excess generation into the grid without exceeding the predefined utility PIL. In such scenarios, the excess power generation beyond the utility PIL should either be stored in the battery for subsequent usage or drained via a dump load. Further, the end-users are recommended to lessen the power evacuation from RERs by disconnecting the in-house resources from the system when the surplus power generation exceeds PIL.

Although introducing PIL at the end-user premises significantly reduces the operational difficulties of utilities, this regulation may decrease the profit gained by the end-user. Further, the generated green energy may not be fully utilized when surplus generation exceeds the utility PIL. Hence, the PIL constraint indirectly restricts the installation capacity of in-house RERs at the end-user side. To overcome this limitation, end-users are preferred to participate in transactive energy management systems (TEMS) [12, 13]. TEMS is an advanced technique in DSM schemes that intend

to develop a deregulated market between the end-users to trade their excess generation and demand with neighboring users to attain more profit compared to utility [14]. This kind of market is called the local energy market (LEM).

In [15], a game theory-based reverse auction model is developed as a multiagent system including prosumers of the corresponding locality and utility. However, neither the prosumers are modeled as individual agents, nor the flexible loads are considered. An individual agent-based simulation environment is structured in [16] to share the energy among participants in the community energy market. In such a community, a recursive least squares learning algorithm is framed to find the dynamic pricing and initiate decision-making. Nevertheless, modeling of flexible loads is not considered in the considered work. In [17], a peer-to-peer (P2P) energy trading technique is devised between electric vehicles. A game theory method is employed in the considered work to maintain the dynamic equity between demand and supply at peak and off-peak intervals. A similar game theory approach is discussed in [18], which has initiated a P2P energy trading technique considering a multiagent coordinated zone-based energy trading network. Also, this study details the energy trading between prosumers in the smart neighborhood.

In [19], a P2P energy sharing mechanism is developed using a game theory method for off-grid and on-grid microgrid systems. A game-theory method based on a bilevel optimization algorithm and a two-stage distributed optimization algorithm using Nash bargaining is discussed in [20, 21], respectively, for P2P power trading. Different P2P power trading techniques are explained in [22–24]. A novel multilevel transactive energy optimization model is proposed in [25] for the optimal scheduling of distributed generation units within the considered virtual power plant (VPP). The model supports energy transfers inside a specific VPP as well as between the linked VPPs. Further, a blockchain-based smart contract layer is being developed to automate and store the energy transaction information. In [26], a market model based on the double auction technique is developed to facilitate P2P energy trading. The proposed market architecture's benefits are highlighted by comparing it with the manager-based centralized energy market in terms of social welfare, total payment, and energy trade volume outcomes. The overview of blockchain-based decentralized energy market architecture and its components for TEMS is detailed in [27]. Consecutively, the blockchain-based intra- and inter-VPP-P2P energy market is realized in [28]. Besides mixed-integer linear programming-based optimization, it is proposed to compute the optimal cost for energy exchange.

A comprehensive review of transactive energy systems is presented in [29], emphasizing the control techniques, topologies, and simulators available for the design, assessment, and analysis of the systems. Further, a hierarchical framework which comprised four main levels is used to evaluate the transactive energy control strategies and controller's concepts. A decentralized architecture is developed in [30] to integrate the retail and wholesale energy markets in the context of wind and demand uncertainty, as well as the

financial risks provided by these sources. The results of simulation studies show that the suggested structure has a strong potential to create integrated power markets with maximum performance and efficiency despite multiple system restrictions. The impact of numerous uncertainties (created by pricing, generation, and demand) on direct energy trading is examined in [31]. Additionally, a Nash bargaining game-based direct transactive energy trading framework is implemented to mitigate the effects of uncertainty. A detailed evaluation of previous research studies and pilot projects on P2P energy trading in terms of implementation approaches with mathematical formulations is presented in [32].

*1.2. Research Gap and Motivation.* Based on the literature survey, it is foreseen that the optimum scheduling of flexible loads and batteries, including the expected renewable generation and utility dynamics, results in significant savings in end-users' electricity bills. Further, injecting excess power into the utility, especially during peak intervals, assures end-users of high incentives from the utility. Additionally, the active participation of end-users in energy trading under LEM increases the profit considerably. On the other hand, developing suitable market clearing strategies by the LEM operators (LEMO) attracts many end-users to participate in transactive energy systems, increasing the installation and optimal utilization of RERs.

An optimal energy management algorithm is developed in this study to enhance the operational and monetary perks of end-users and utilities. The algorithm is framed to control the operating time of flexible loads and batteries, considering end-users' operational dynamics and requirements, utility parameter variations, and renewable power generation. Further, the scheduling method has been upgraded to assist the end-users in taking part in LEM. The upgraded system optimally determines the expected demand/generation for the upcoming intervals based on the dynamics of end-users' behavior and climatic changes. In addition, the proposed system reschedules the operations of home appliances in real time to reduce the forfeit imposed by the market operator for not supporting the grid with quoted power. LEM is also devised with different market clearing strategies to manage the power trading between the neighboring end-users. The proposed LEM scheme ensures the individuals' profit in energy trading based on their participation and consistency in quoted demand. Further, the proposed LEM scheme identifies the abnormal activities of participants in quoted power and penalizes them accordingly.

*1.3. Contributions and Paper Organization.* The major contributions of this study are described as follows:

- (1) An optimal energy management algorithm is proposed for time scheduling the operation of flexible loads and batteries considering
  - (a) Dynamics in end-users' behavior
  - (b) Variations in utility parameters (consumer demand limit and PIL)

- (c) Intermittent nature of renewable power generation
- (2) An energy trading algorithm is developed to enable the participants to participate in LEM to enhance their profits through transactive energy.
- (3) A new local energy market with different market clearing strategies is presented to ensure profitable power transactions between the neighboring end-users
- (4) The proposed trading strategies are extended to increase the market's reliability by penalizing the participants for their abnormal activities in energy trading

The remaining sections of the manuscript are organized as follows: the detailed architecture of the proposed local energy market and the mathematical modeling of the end-user's demand pattern are discussed in Section 2; as part of the P2P energy market, two different pricing strategies are developed in Section 3; the proposed market clearing strategies are validated through case studies in Section 4. The conclusions and future scope are given in Section 5.

## 2. Architecture of the Local Energy Market

A group of residential consumers and prosumers in close proximity forms a LEM. In LEM, the market participants (consumer/prosumer) are encouraged to trade their surplus generation/demand within the locality along with the upstream utility grid. The proposed conceptual architecture of LEM is shown in Figure 1, which consists of market participants, LEMO, and a utility grid. The objective of LEMO is to maintain a real-time balance between local demand and generation with the appropriate pricing strategies within the locality. This led to the development of TEMS with different market clearing strategies within the locality.

Nowadays, residential consumers are intelligently operating electrical and electronic household appliances to fulfill their tasks timely. Based on the operating pattern, residential loads are categorized into two groups: nonflexible loads (NFLs) and flexible loads (FLs). The loads which are essential and anticipated to respond instantly are classed as NFLs. The inheritance and comfort highly persuade the end-user's operational profiles of the NFLs. Loads that are flexible to operate between user-defined periods are categorized under FLs. The net demand of an end-user  $n$  ( $n \in \mathcal{N} \triangleq [1, 2, \dots, N]$ ) for the time interval  $t$  ( $t \in \mathcal{T} \triangleq [1, 2, \dots, T]$ ) is as  $ND_n^t$ , and it is mathematically expressed as follows:

$$ND_n^t = NFL_n^t + FL_n^t + ES_n^t - DC_n^t, \quad \forall n \in \mathcal{N}; \forall t \in \mathcal{T}, \quad (1)$$

where

- (i)  $N$  is the locality's cumulative end-users
- (ii)  $T$  is the maximum number of time intervals over a period
- (iii)  $NFL_n^t$  and  $FL_n^t$  represent the overall demand of the entire NFLs and FLs, respectively

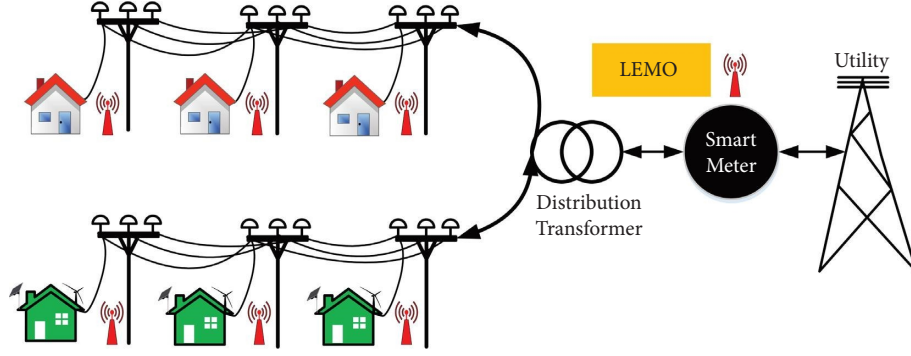


FIGURE 1: Conceptual diagram of the local energy market.

$FL_n^t$  can be computed as follows:

$$FL_n^t = \sum_{l \in FLs} \mathcal{S}_{l,n}^t \cdot P_{l,n}, \quad (2)$$

where  $\mathcal{S}_{l,n}^t$  denotes operating status of flexible load  $l$  during an interval  $t$ . The value of  $\mathcal{S}_{l,n}^t$  is assigned to 0 and 1 for the respective load status of OFF and ON.  $P_{l,n}$  represents the power rating of flexible load  $l$ .

$ES_n^t$  refers to the battery power exchange during different modes of battery operation, and it is described as follows:

$$ES_n^t > 0; \left\{ \begin{array}{l} \mathfrak{B}_{C,n}^t = 1, \mathfrak{B}_{D,n}^t = 0, \mathfrak{B}_{F,n}^t = 0 \\ \text{Battery in charging mode} \end{array} \right\},$$

$$ES_n^t < 0; \left\{ \begin{array}{l} \mathfrak{B}_{C,n}^t = 0, \mathfrak{B}_{D,n}^t = 1, \mathfrak{B}_{F,n}^t = 0 \\ \text{Battery in discharging mode} \end{array} \right\}, \quad (3)$$

$$ES_n^t = 0; \left\{ \begin{array}{l} \mathfrak{B}_{C,n}^t = 0, \mathfrak{B}_{D,n}^t = 0, \mathfrak{B}_{F,n}^t = 1 \\ \text{Battery in floating mode} \end{array} \right\},$$

where  $\mathfrak{B}_{C,n}^t$ ,  $\mathfrak{B}_{D,n}^t$ , and  $\mathfrak{B}_{F,n}^t$  are battery operating mode status during charging, discharging, and floating, respectively.

$DG_n^t$  represents the power generation from installed in-house distributed energy resources. These days, residential buildings are mostly equipped with renewable power generation systems such as rooftop solar PV or small wind turbines. Hence, considering the RERs, the total power generation ( $DG_n^t$ ) can be computed as follows:

$$DG_n^t = P_{PV,n}^t + P_{WT,n}^t, \quad (4)$$

where  $P_{PV,n}^t$  and  $P_{WT,n}^t$  represent the installed solar PV and wind turbine power generation, respectively.

Currently, utilities are introducing various electricity pricing schemes as part of the DSM program to maintain a flat load profile. One such pricing scheme is real-time pricing (RTP), where the end-user will be informed about the interval's electricity price and other incentives just before the interval begins [33]. Hence, the prediction strategies of end-users play a vital role in reducing end-users' electricity bills. The total electricity bill of any user  $n$  ( $TEB_n$ ) will be computed based on the utility cost function as expressed in

$$TEB_n = \sum_{t=1}^T C^t(ND_n^t), \quad (5)$$

$$C^t(ND_n^t) = \begin{cases} GSP^t \cdot ND_n^t \cdot \Delta t; & \text{if } 0 \leq ND_n^t \leq CDL^t, \\ \left( \begin{array}{l} GSP^t \cdot CDL^t \cdot \Delta t + \\ (ND_n^t - CDL^t) \cdot \beta^t \cdot GSP^t \cdot \Delta t \end{array} \right); & \text{if } ND_n^t > CDL^t, \\ GBP^t \cdot ND_n^t \cdot \Delta t; & \text{if } ND_n^t < 0, \end{cases} \quad (6)$$

where  $GSP^t$  and  $GBP^t$  are the  $t^{\text{th}}$  interval grid selling and buying prices, respectively.  $CDL^t$  represents the consumer demand limit (CDL) for the interval  $t$ , which the grid operator imposes to regulate the energy utilization at the consumer zone [34].

The consumer will be fined only when the total demand exceeds the utility-defined CDL. Hence, the electricity bill will be increased based on the CDL factor ( $\beta^t$ ) of that

interval ( $t$ ). To limit the usage of the peak power plant and increase profit, the utilities are imposing higher energy prices during peak intervals. Further, the end-users are also incentivized by the utilities to export their surplus, especially during peak intervals. Hence, the prosumers are showing more interest in optimally altering their demand pattern to avail of possible utility benefits. This optimal scheduling problem can be analytically calculated considering the

objective function as minimizing the overall debt of the electricity bill as expressed in

$$\min. \left( \text{TEB}_n = \sum_{t=1}^T \mathbb{C}^t(\text{ND}_n^t) \right), \quad (7)$$

subject to

$$\mathcal{S}_{l,n}^t = 0 \quad t \notin \Psi_{l,i} \forall l \in \text{FL}, \quad (8)$$

$$\sum_{t=1}^T \mathcal{S}_{l,n}^t = \lambda_{l,n} \forall l \in \text{FL}, \quad (9)$$

$$\mathfrak{B}_{C,n}^t + \mathfrak{B}_{D,n}^t + \mathfrak{B}_{F,n}^t = 1 \forall t \in T, \quad (10)$$

$$\text{SoC}_{\min,n} < \text{SoC}_{B,n}^t < \text{SoC}_{\max,n}, \quad (11)$$

$$\text{ES}_{\min,n} < |\text{ES}_n^t| < \text{ES}_{\max,n}, \quad (12)$$

where  $\Psi_{l,n}$  is the user-predefined time for flexible load  $l$  and  $\lambda_{l,n}$  is the number of intervals needed to fulfill the flexible load  $l$  task. Battery operational parameter  $\text{SoC}_{B,n}^t$  represents the feasible state of charge (SoC) at the beginning of the time interval  $t$ . The minimum and maximum SoC boundary values are represented as  $\text{SoC}_{\min,n}$  and  $\text{SoC}_{\max,n}$ , respectively. Similarly, the battery power exchange minimum and maximum boundaries are given as  $\text{ES}_{\min,n}$  and  $\text{ES}_{\max,n}$ , respectively.

The distribution grid operators face many operational challenges due to the high penetration of grid-connected small-scale RERs. Hence, the utilities regulate the end users' support by introducing a time-varying PIL. To utilize the maximum amount of generated renewable power and to increase the economic profit through energy export, the end-users are expected to optimally schedule their household appliances with due consideration to the dynamics in renewable energy generation. Accounting for this, the objective function defined in (7) is updated with the modified cost function as shown in

$$\mathbb{C}^t(\text{ND}_n^t) = \begin{cases} \text{GSP}^t \cdot \text{ND}_n^t \cdot \Delta t; & \text{if } 0 \leq \text{ND}_n^t \leq \text{CDL}^t, \\ \left( \begin{array}{l} \text{GSP}^t \cdot \text{CDL}^t \cdot \Delta t + \\ (\text{ND}_n^t - \text{CDL}^t) \cdot \beta^t \cdot \text{GSP}^t \cdot \Delta t \end{array} \right); & \text{if } \text{ND}_n^t > \text{CDL}^t, \\ \text{GBP}^t \cdot \text{ND}_n^t \cdot \Delta t; & \text{if } (-\text{PIL}^t) \leq \text{ND}_n^t < 0, \\ \text{GBP}^t \cdot (-\text{PIL}^t) \cdot \Delta t; & \text{if } \text{ND}_n^t < (-\text{PIL}^t). \end{cases} \quad (13)$$

In addition to the constraints discussed from (8) to (12), the modified objective function is also subjected to the power injection constraint. The constraint imposes that the excess energy shared with the utility during a particular interval ( $t$ ) should not exceed the utility's predefined power export limit of that interval ( $\text{PIL}^t$ ). The hard constraint shall be mathematically expressed as follows:

$$\text{ND}_n^t \geq (-\text{PIL}^t), \quad \forall t \in T. \quad (14)$$

To overcome the limitation due to utility PIL, it is preferred that the end-users take part in TEMS. As part of TEMS, the LEM operator invites the end-users to trade the power (surplus generation/demand) within the locality. The expected net demand  $\text{END}_n^t$  of any participant  $n$  for the time interval  $t$  is computed as follows:

$$\text{END}_n^t = \text{ENFL}_n^t + \text{EFL}_n^t + \text{EES}_n^t - \text{EDG}_n^t \forall n \in \mathcal{N}; \forall t \in \mathcal{T}, \quad (15)$$

where  $\text{ENFL}_n^t$  represents the expected nonflexible load demand for interval  $t$ , which will be decided based on the users' comfort and desire.

$\text{EFL}_n^t$  and  $\text{EES}_n^t$  are the expected demands of flexible load and battery banks which can be obtained as the result of the optimal scheduling problem defined in (7) and (13).  $\text{EDG}_n^t$  is the expected power generation from in-house RERs, which can be predicted either by devising a dedicated algorithm or

analyzing the local renewable resources variables such as solar irradiation, atmospheric temperature, and wind speed provided by the LEM operator. Based on the quoted demand of individuals, the LEM operator will clear the market so that all the localities and the grid participants would benefit.

End-users' active participation will build successful TEMS. Further, adopting suitable marketing strategies for LEM may increase the participants' interest in TEMS. The LEM should be designed with due consideration for participants' consumption patterns and utility dynamics in operational parameters (selling price, buying price, CDL, and PIL). However, the developed LEM should deliver adequate economic benefit to the participants without violating the utility power constraints. Different market strategies are proposed in the upcoming section to have a profitable power transaction between participants through TEMS.

### 3. Local Energy Market Pricing Strategies

The reliability of any LEM is merely based on the pricing strategy used to clear the market. Therefore, the proposed LEM shall be managed by either a utility or a third party in this work. However, the utility considers all the end-users participating in LEM as single users whose power demand varies continuously. Hence, the individual users' utility constraint parameters, such as CDL and PIL, should be

aggregated. This study proposes two different market clearing strategies: average market clearing (AMC) and generation-to-demand ratio-based market clearing (GDRMC) strategies.

**3.1. Average Market Clearing (AMC) Strategy.** Let us consider a locality where all the users participate in LEM. Considering individuals' expected net demand, the aggregated locality demand ( $TDE^t$ ), locality generation ( $TGE^t$ ), and locality net demand ( $LND^t$ ) for an interval  $t$  can be calculated as follows:

$$\begin{aligned} TDE^t &= \sum_{N \in \mathcal{N}} END_n^t \forall END_n^t \geq 0, \\ TGE^t &= \sum_{N \in \mathcal{N}} |END_n^t| \forall END_n^t < 0, \\ LND^t &= TDE^t - TGE^t = \sum_{N \in \mathcal{N}} END_n^t. \end{aligned} \quad (16)$$

The computed value of  $LND^t$  expresses the entire locality's grid dependency. Hence, two substrategies are proposed under AMC for different values of  $LND^t$ .

**3.1.1. AMC Strategy-1:  $LND^t \geq 0$ .** When the locality's total demand is more than its total generation ( $TDE^t \geq TGE^t$ ), the locality will act as an importer for utilities. The locality should depend on the grid to meet the excess demand in this scenario. However, LEM allows the exporter (having excess generation) and importer (having excess demand) to trade the surplus power with others for more profit than the utility. The exporter market clearing price ( $\lambda_{sell}^t$ ) for an interval  $t$  under AMC strategy-1 is expressed as follows:

$$\lambda_{sell}^t = \frac{GSP^t + GBP^t}{2}. \quad (17)$$

Based on the computed price of  $\lambda_{sell}^t$ , importer market clearing price ( $\lambda_{buy}^t$ ) for an interval  $t$  under AMC strategy-1 can be calculated as follows:

$$\lambda_{buy}^t = \begin{cases} \frac{(LND^t \times GSP^t) + (\lambda_{sell}^t \times TGE^t)}{TDE^t} & \text{if } |LND^t| \leq (N \times CDL^t), \\ \frac{(N \times CDL^t \times GSP^t) + (\lambda_{sell}^t \times TGE^t)}{(N \times CDL^t)} & \text{if } |LND^t| > (N \times CDL^t). \end{cases} \quad (18)$$

**3.1.2. AMC Strategy-2:  $LND^t < 0$ .** When the total generation of a locality is more than the total demand ( $TGE^t > TDE^t$ ), the locality will act as an exporter of utility. Further, the locality is allowed to share the surplus generation with the grid until the magnitude of  $LND^t$  reaches the aggregated value of all participants' PIL. The ( $\lambda_{buy}^t$ ) under AMC strategy-2 is expressed as follows:

$$\lambda_{buy}^t = \frac{GSP^t + GBP^2}{2}. \quad (19)$$

Based on the computed price of  $\lambda_{buy}^t$ , the  $\lambda_{sell}^t$  for an interval  $t$  under AMC strategy-2 can be calculated as follows:

$$\lambda_{sell}^t = \begin{cases} \frac{(TDE^t \times \lambda_{buy}^t) + (LND^t \times GBP^t)}{TGE^t}; & \text{if } |LND^t| \leq (N \times PIL^t), \\ \frac{(TDE^t \times \lambda_{buy}^t) + (N \times PIL^t \times GBP^t)}{(N \times PIL^t)}; & \text{if } |LND^t| > (N \times PIL^t), \end{cases} \quad (20)$$

The proposed AMC strategy is simple; hence, the computational time for market clearing is less for any number of participants. Further, the AMC-based LEM is easily predictable, making the participants more interested in energy trading. However, the exporters (in AMC strategy-1) and importers (AMC strategy-2) have more profit irrespective of the amount of contribution in the locality net demand. To overcome this weakness and make profitable

transactions for all participants, the generation-to-demand ratio is proposed as a market clearing approach in the following subsection.

**3.2. GDR-Based Market Clearing Strategy.** Considering the net demand of individual participants, the locality generation-to-demand ratio (GDR) for an interval  $t$  can be computed as follows:

$$\text{GDR}^t = \frac{\text{TGE}^t}{\text{TDE}^t}. \quad (21)$$

The value of  $\text{GDR}^t$  decides the nature of locality with respect to utility as an importer ( $\text{GDR}^t < 1$ ) or exporter ( $\text{GDR}^t > 1$ ). Hence, two strategies are proposed under the generation-to-demand ratio market clearing (GDRMC) strategy.

**3.2.1. GDRMC Strategy-1.** When the locality acts as an importer for utility ( $\text{GDR}^t < 1$ ), the market clearing price for exporters and importers of the locality can be computed as follows:

$$\lambda_{\text{sell}}^t = \frac{\text{GSP}^t + \text{GBP}^t(1 - \text{GDR}^t)}{2}, \quad (22)$$

$$\lambda_{\text{buy}}^t = (\lambda_{\text{sell}}^t \times \text{GDR}^t) + (\text{GSP}^t(1 - \text{GDR}^t)).$$

The demand of individual importers highly influences the economic benefit of the individual participants in the proposed strategy. Further, quoting more demand in LEM may lead to nonprofitable trading. Hence, the proposed strategy will be used only when the net locality demand is maintained within the utility's defined locality demand limit. If the demand constraint is violated, the importers are restricted from sharing the excess demand in LEM. Considering this limitation, the proposed GDRMC strategy-1 is modified concerning the importer demand limit. The modified generation-to-demand ratio for an interval  $t$  is computed as follows:

$$\text{MGDR}^t = \frac{\text{TGE}^t}{N \times \text{CDL}^t}. \quad (23)$$

Considering  $\text{MGDR}^t$ , the market clearing price for the exporter ( $\lambda_{\text{sell}}^t$ ) and the importer ( $\lambda_{\text{buy}}^t$ ) of an interval  $t$  can be calculated as follows:

$$\lambda_{\text{sell}}^t = \frac{\text{GSP}^t + \text{GBP}^t(1 - \text{MGDR}^t)}{2}, \quad (24)$$

$$\lambda_{\text{buy}}^t = (\lambda_{\text{sell}}^t \times \text{MGDR}^t) + (\text{GSP}^t(1 - \text{MGDR}^t)).$$

**3.2.2. GDRMC Strategy-2.** When the value of  $\text{GDR}^t$  is greater than 1, the locality will act as an exporter concerning utility, and the market clearing prices for importers and exporters can be calculated as given in (25) and (26), respectively:

$$\lambda_{\text{buy}}^t = \frac{\text{GSP}^t - \text{GBP}^t(1 - 1/\text{GDR}^t)}{2}, \quad (25)$$

$$\lambda_{\text{sell}}^t = \frac{\lambda_{\text{buy}}^t + \text{GBP}^t(\text{GDR}^t - 1)}{\text{GDR}^t}. \quad (26)$$

Consequentially, the utilities are imposing time-varying PIL limits to reduce operational difficulties. Hence, the exporters are constrained to trade their excess generation by considering the utility-defined locality net export limit. The modified GDR for the locality when the net export exceeds the utility limit can be computed as follows:

$$\text{MGDR}^t = \frac{N \times \text{PIL}^t}{\text{TDE}^t}. \quad (27)$$

Subsequently, the market clearing prices for importers and exporters can be calculated as expressed in (28) and (29), respectively:

$$\lambda_{\text{buy}}^t = \frac{\text{GSP}^t - \text{GBP}^t(1 - 1/\text{GDR}^t)}{2}, \quad (28)$$

$$\lambda_{\text{sell}}^t = \frac{\lambda_{\text{buy}}^t + \text{GBP}^t(\text{MGDR}^t - 1)}{\text{MGDR}^t}. \quad (29)$$

Considering different pricing strategies, the traded electricity bill of participant  $n$  during a trading interval  $t$  can be computed as follows:

$$\begin{aligned}
\text{TEB}_n^t = & \left\{ \begin{array}{l} \text{ND}_n^t \cdot \lambda_{\text{buy}}^t \cdot \Delta t; \\ \left[ \frac{N \times \text{CDL}^t}{N_I} + \lambda_{\text{buy}}^t \left( \text{ND}_n^t - \frac{N \times \text{CDL}^t}{N_I} \right) \cdot \beta^t \cdot \text{GSP}^t \right] \cdot \Delta t; \\ \text{ND}_n^t \cdot \lambda_{\text{sell}}^t \cdot \Delta t; \\ \frac{N \times \text{PIL}^t}{N_E} \cdot \lambda_{\text{sell}}^t \cdot \Delta t; \end{array} \right. \\
& \left\{ \begin{array}{l} \left\{ \begin{array}{l} \text{ND}_n^t \geq 0 \\ \text{TDE}^t \leq (N \times \text{CDL}^t) \end{array} \right. \\ \text{or} \\ \left\{ \begin{array}{l} 0 \leq \text{ND}_n^t \leq \frac{N \times \text{CDL}^t}{N_I} \\ \text{TDE}^t > (N \times \text{CDL}^t), \end{array} \right. \\ \left\{ \begin{array}{l} \text{ND}_n^t > \frac{N \times \text{CDL}^t}{N_I} \\ \text{TDE}^t > (N \times \text{CDL}^t), \end{array} \right. \\ \left\{ \begin{array}{l} \text{ND}_n^t < 0 \\ \text{TGE}^t \leq (N \times \text{PIL}^t) \end{array} \right. \text{ or } \left\{ \begin{array}{l} \frac{N \times \text{PIL}^t}{N_E} \leq \text{ND}_n^t < 0 \\ \text{TGE}^t > (N \times \text{PIL}^t), \end{array} \right. \\ \left\{ \begin{array}{l} \frac{N \times \text{PIL}^t}{N_E} > \text{ND}_n^t \\ \text{TGE}^t > (N \times \text{PIL}^t). \end{array} \right. \end{array} \right. \quad (30)
\end{aligned}$$

The proposed market strategies are developed based on the participants' quoted demand. The quoted electricity demand of individual participants merely depends upon the accurate prediction of RERs and the optimal scheduling of flexible loads. However, the user cannot maintain the quoted demand strictly for all the trading intervals due to sudden changes in end-users' requirements. Hence, false demand quotations may ruin the LEM's profitable power trading in TEMS. To overcome this

issue, a trading agreement violation cost ( $\Gamma_n^t$ ) is introduced for the calculation of the electricity bill. Further, the deviation in quoted demand may increase or decrease the trading electricity bill. The change in electricity bill is referred to as the deviation cost ( $\text{DC}_n^t$ ). The values of  $\Gamma_n^t$  and  $\text{DC}_n^t$  for any user  $n$  during an interval  $t$  can be computed with due consideration to actual net demand ( $\text{AND}_n^t$ ), quoted demand, market clearing prices, and false data penalty rate ( $\delta^t$ ) as shown in

$$\Gamma_n^t = \left| \left( \text{AND}_n^t - \text{END}_n^t \right) \cdot \frac{\lambda_{\text{buy}}^t + \lambda_{\text{sell}}^t}{2} \cdot \delta^t \right|, \quad (31)$$

$$\text{DC}_n^t = \begin{cases} \left( \text{AND}_n^t - \text{END}_n^t \right) \cdot \lambda_{\text{buy}}^t; & \text{if } \text{AND}_n^t > 0 & \text{END}_n^t > 0 \\ \left( \text{AND}_n^t - \text{END}_n^t \right) \cdot \lambda_{\text{sell}}^t; & \text{if } \text{AND}_n^t < 0 & \text{END}_n^t < 0 \\ \left( \text{AND}_n^t \cdot \lambda_{\text{sell}}^t \right) - \left( \text{END}_n^t \cdot \lambda_{\text{buy}}^t \right); & \text{if } \text{AND}_n^t < 0 & \text{END}_n^t > 0 \\ \left( \text{AND}_n^t \cdot \lambda_{\text{buy}}^t \right) - \left( \text{END}_n^t \cdot \lambda_{\text{sell}}^t \right); & \text{if } \text{AND}_n^t > 0 & \text{END}_n^t < 0. \end{cases} \quad (32)$$

Considering the trading electricity bill, deviation cost, and agreement violation cost, the net electricity bill of a user during a trading interval can be computed as follows:

$$\text{EB}_n^t = \text{TEB}_n^t + \text{DC}_n^t + \Gamma_n^t. \quad (33)$$

#### 4. Simulation Study

The proposed market strategies are validated concerning various case studies to emphasize the significance of TEMS on the end-user's electricity bill savings.

*4.1. Study Environment.* The considered locality consists of ten residential prosumers actively participating in TEMS. Currently, residential buildings are furnished with a numerous modern electrical equipment to make life easier. The most common and essential appliances and their power ratings are given in Table 1 [35].

To lessen the dependency on the grid and improve electricity bill savings, residential consumers are recommended to build in-house RERs. Considering various resources, for instance, residential consumers highly prefer renewable power generation using rooftop solar PV and small wind turbines. Further, the residents are interested in battery storage to reduce the electricity bill by meeting essential demands during peak intervals [24]. The RERs and batteries are optimally sized with due consideration to the total investment cost, space availability, and intermittence in renewable resources as formulated in the author's previous work [35]. The variations in utility energy selling and buying prices over a month are depicted in Figure 2. For a better view of utility dynamics, per day variations in electricity prices are given in Figure 3. The utility CDL factor for crossing CDL is considered as 2.5 times the nominal cost. The false data penalty rate for violating the trading agreement (not supporting the grid with quoted generation/demand) is 0.2.

On account of the end-users' comfort and desire, the operation of various household appliances is optimally scheduled by solving the objective function defined in (7), subject to the constraints given in (8)–(12) and (14). Considering the individual user inside the studied locality, the optimal demand pattern and available generation from RERs over a month are shown in Figure 4.

*4.2. Study Results.* The economic analysis of individual participants is evaluated in the following cases: prosumers under the peer-to-grid (P2G) scheme without PIL (Case 1); prosumers under the P2G scheme with PIL (Case 2); prosumers under the P2P scheme with the AMC strategy (Case 3); and prosumers under the P2P scheme with the GDRMC strategy (Case 4). The participants' per day electricity bills for different cases are shown in Figure 5. To show the effectiveness of the proposed architecture, the study is extended for a period of one month and the monthly electricity bills for different cases are listed in Table 2.

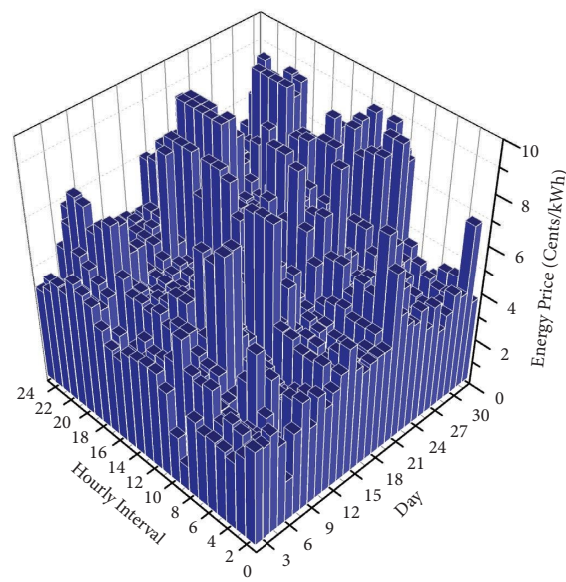
In-house RER installation merely depends on the consumers' economic background and space availability. Few consumers in the locality may not afford it. However, those users can also actively participate in LEM as consumers and reduce their electricity bills significantly. To validate this, the simulation study has been extended to the locality in which 50% of the residential buildings are not installed with any additional energy resources. The monthly electricity bill of all the participants under different market cases is listed in Table 3.

Active participation and accurate prediction of expected electricity demand significantly increase the participants' profits. However, deviations in the quoted electricity demand and injecting false data will severely affect the electricity market. Hence, the market operators introduce trading agreement violation costs to regulate the participant's deviations from the quoted demand. To validate this, the case study is evaluated for a trading interval considering

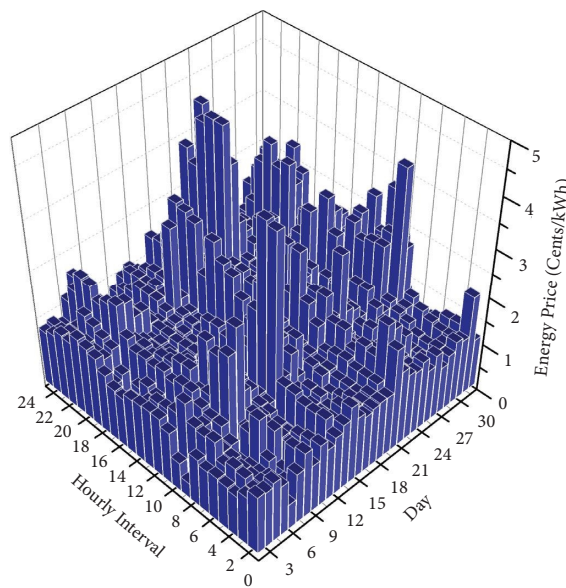


TABLE 1: Household appliances.

S. no.	Load	Power (kW)	Type
1	Fan	0.10	NFL
2	Lighting	0.02	NFL
3	Television	0.25	NFL
4	Mobile and laptop charger	0.05	NFL
5	Air conditioner	1.0	NFL
6	Refrigerator	0.5	NFL
7	Cloth washer	0.8	FL
8	Cloth dryer	2.2	FL
9	Dish washer	1.5	FL
10	Well pump	1.2	FL
11	PHEV charging	2.3	FL



(a)



(b)

FIGURE 2: Utility monthly electricity price variation. (a) Selling price. (b) Buying price.

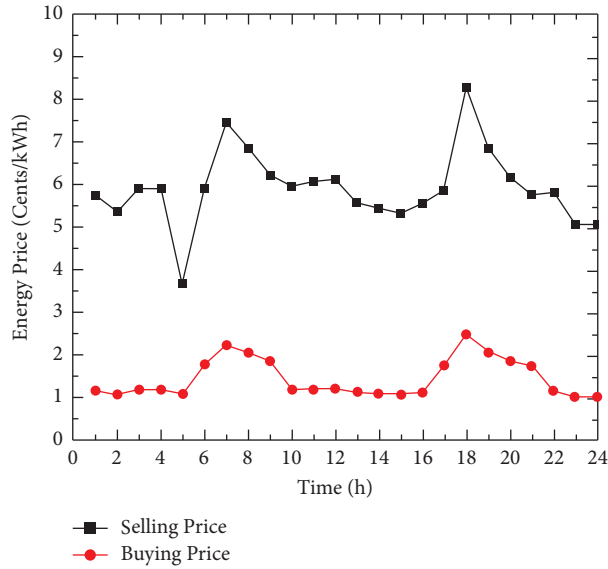


FIGURE 3: Utility energy price variation.

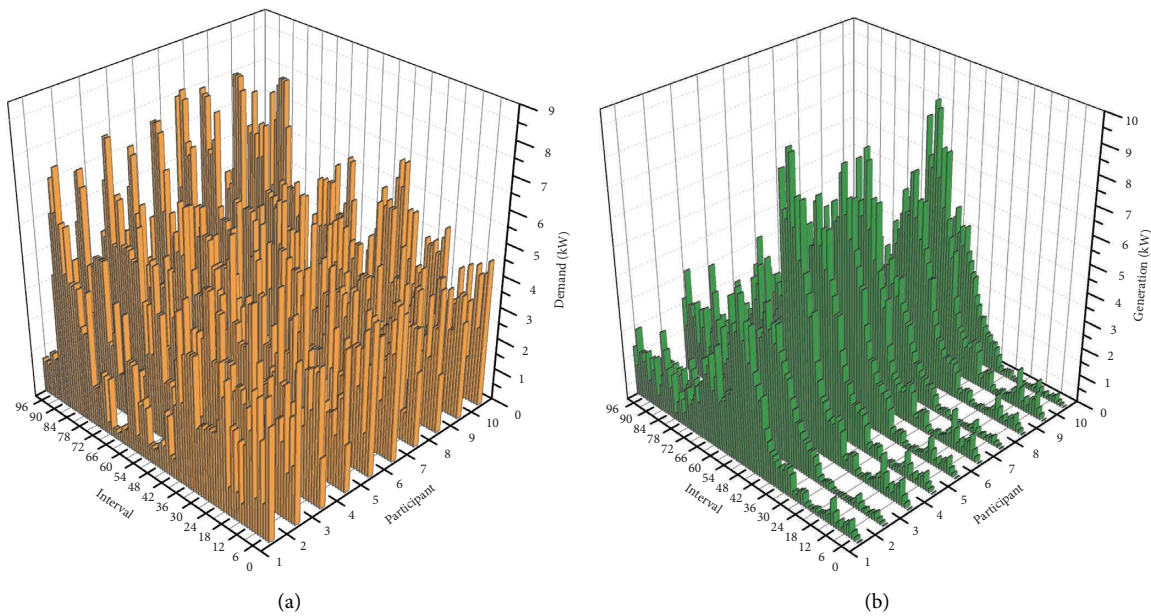


FIGURE 4: Monthly variations. (a) Optimal demand pattern. (b) Available generation.

different deviations, and the corresponding results are tabulated in Tables 4 and 5.

4.3. *Discussions.* The outcomes shown in Tables 2 and 3 express the economic significance of the transactive energy systems in the smart grid paradigm. Cases 1 and 2 are examined using the P2G scheme, whereas Cases 3 and 4 are evaluated using the P2P scheme. Furthermore, in Case 1, the participants saved more money on their electricity bills since the utility provides unconditional grid assistance. However, in order to address operational issues caused by the significant penetration of small scale in-house RERs, utilities

are placing numerous constraints in the P2G system. Case 2 results show that implementing grid limits such as the PIL constraint has a detrimental impact on end consumers' electricity bills. Participants in P2P schemes using AMC (Case 3) and GDRMC (Case 4) approaches save significantly more than in P2G schemes (Case 2). Furthermore, the percentage reductions in electricity bill for the AMC and GDRMC schemes compared to the P2G scheme demonstrate the usefulness of the recommended market strategies. Participants can increase this proportion by optimizing the timing of domestic appliance use while considering end-user dynamics, power generation from in-house RERs, utility limits, and predicted market net demand. Aside from the

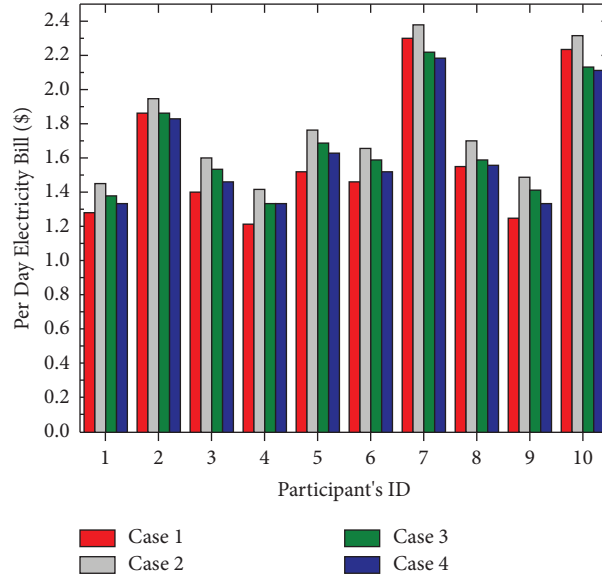


FIGURE 5: Participants' per day electricity bill.

TABLE 2: Participants' monthly electricity bill.

PID	Case-1	Case-2	Case-3		Case-4	
	$\mathcal{B}_{\text{PID}}$ (\$)	$\mathcal{B}_{\text{PID}}$ (\$)	$\mathcal{B}_{\text{PID}}$ (\$)	$\mathcal{S}_{\text{PID}}$ (%)	$\mathcal{B}_{\text{PID}}$ (\$)	$\mathcal{S}_{\text{PID}}$ (%)
1	96.53	98.91	94.8	4.16	92.76	6.22
2	97.67	100.18	96.16	4.02	93.78	6.39
3	78.07	85.17	82.17	3.53	79.55	6.6
4	81.59	87.23	84.22	3.46	81.48	6.6
5	79.96	87.12	83.34	4.34	80.52	7.58
6	82.96	87.49	84.05	3.94	81.62	6.71
7	99.87	101.85	96.4	5.36	94.42	7.3
8	85.66	90.21	87.13	3.42	84.61	6.21
9	80.25	86.04	83.25	3.25	80.76	6.14
10	99.14	101.61	97.28	4.27	94.96	6.55

PID: participant's ID.  $\mathcal{B}_{\text{PID}}$ : participant's monthly electricity bill.  $\mathcal{S}_{\text{PID}}$ : percentage saving of electricity bill when compared to Case-2.

TABLE 3: Participants' monthly electricity bill.

PID	Case-1	Case-2	Case-3		Case-4	
	$\mathcal{B}_{\text{PID}}$ (\$)	$\mathcal{B}_{\text{PID}}$ (\$)	$\mathcal{B}_{\text{PID}}$ (\$)	$\mathcal{S}_{\text{PID}}$ (%)	$\mathcal{B}_{\text{PID}}$ (\$)	$\mathcal{S}_{\text{PID}}$ (%)
1	96.53	98.91	94.9	4.06	90.4	8.61
2	97.67	100.19	95.49	4.7	91.75	8.43
3	78.07	85.17	78.97	7.28	75.53	11.32
4	81.59	87.23	81.4	6.69	77.95	10.64
5	79.96	87.13	79.88	8.33	76.43	12.29
6	148.93	148.93	135.13	9.27	125.58	15.68
7	147.26	147.26	133.44	9.39	124.54	15.43
8	149.81	149.81	136.25	9.06	127.17	15.12
9	150.76	150.76	137.3	8.93	127.91	15.16
10	153.74	153.74	139.58	9.22	129.76	15.6

economic benefits, the recommended strategies protect end-users' privacy by supporting them in sharing just demand information.

The extended case study assumes that 50% of the community's participants do not have any in-house RERs, and the recommended techniques result in considerable

TABLE 4: Penalty analysis for fault data injection attack under the AMC strategy.

UEM	GSP = 5.4 cents/kWh		LND = 4 kW		LEM	$\lambda_{\text{sell}}^t = 3.5$ cents/kWh	
	GBP = 1.6 cents/kWh		CDL = 3 kW			$\lambda_{\text{buy}}^t = 4.4$ cents/kWh	
PID	END (kW)	EEBill (cents)	AND (kW)	UEBill (cents)	TEBill (cents)	P-cost (cents)	TEB (cents)
1	1.5	6.6	1.7	9.18	7.48	0.24	7.72
2	-1	-3.5	-0.8	-1.28	-2.8	0.24	-2.56
3	1.5	6.6	1.5	8.1	6.6	0	6.6
4	2	8.8	2.5	13.5	11	0.6	11.6
5	-1.5	-5.25	0.5	2.7	2.2	2.37	4.57
6	2.5	11	1.5	8.1	6.6	1.19	7.79
7	0.5	2.2	0.8	4.32	3.52	0.36	3.88
8	-2	-7	-2	-3.2	-7	0	-7
9	-0.5	-1.75	-1.8	-2.88	-6.3	1.55	-4.75
10	1	4.4	1	5.4	4.4	0	4.4

EEBill: expected electricity bill under P2P scheme. UEBill: expected electricity bill under P2G scheme. TEBill: trading electricity bill; P-cost-agreement violation cost.

TABLE 5: Penalty analysis for fault data injection attack under the GDRMC strategy.

UEM	GSP = 5.4 cents/kWh		LND = 4 kW		LEM	$\lambda_{\text{sell}}^t = 3.1$ cents/kWh	
	GBP = 1.6 cents/kWh		CDL = 3 kW			$\lambda_{\text{buy}}^t = 4.2$ cents/kWh	
PID	END (kW)	EEBill (cents)	AND (kW)	UEBill (cents)	TEBill (cents)	P-cost (cents)	TEB (cents)
1	1.5	6.3	1.7	9.18	7.14	0.22	7.36
2	-1	-3.1	-0.8	-1.28	-2.48	0.22	-2.26
3	1.5	6.3	1.5	8.1	6.3	0	6.3
4	2	8.4	2.5	13.5	10.5	0.55	11.05
5	-1.5	-4.65	0.5	2.7	2.1	2.19	4.29
6	2.5	10.5	1.5	8.1	6.3	1.1	7.4
7	0.5	2.1	0.8	4.32	3.36	0.33	3.69
8	-2	-6.2	-2	-3.2	-6.2	0	-6.2
9	-0.5	-1.55	-1.8	-2.88	-5.58	1.43	-4.15
10	1	4.2	1	5.4	4.2	0	4.2

electricity bill reductions for both prosumers and consumers. These findings support the viability of the proposed P2P energy market. Furthermore, the computations required by the suggested market strategies are straightforward for any number of players which makes the real-time implementation of LEMO simple. Finally, the penalty analysis findings in Tables Z and W demonstrate the impact of erroneous demand quotations on the electricity bill. Participants are penalized based on the percentage divergence from the real demand. Furthermore, the participants' misleading data have a significant influence on the market clearing parameters  $\lambda_{\text{sell}}^t$  and  $\lambda_{\text{buy}}^t$ . However, the participant is strongly penalized to make up for the economic loss. This expense can be used for operation and maintenance by the LEMO and/or grid operator. Even if any advanced computing technique precisely anticipates the predicted demand and generation of the participants, variations in the user demand pattern are unavoidable. Participants must reschedule battery operations depending on market conditions to overcome variances and thereby decrease penalty costs.

## 5. Conclusions and Future Scope

An optimal scheduling algorithm is proposed at the end-users' premises, considering the depreciation of the total electricity bill as the objective function. Considering the end-user's requirements, utility dynamics, and expected generation from the installed in-house RERs, the proposed algorithm assisted the end-user in controlling the operation of flexible loads and batteries. Further, the end-users are motivated through the transactive energy technique to share the surplus generation/demand with other participants in the community for a higher profit than the utility. To manage the local energy trading, a framework for the locality electricity market is also proposed with two strategies: an average market clearing strategy and a generation-to-demand ratio-based market clearing strategy. The proposed architectures are validated through various case studies considering ten residential participants. Compared to the P2G approach with utility-defined PIL, the AMC technique increases the community average savings in participants' monthly electricity bills by 3.97%. However, by using the

GDRMC approach, the average percentage savings is increased to 6.63%. Furthermore, the percentage savings for the community with 50% of participants who do not own any in-house RERs are 7.69% and 12.83% for AMC and GDRMC approaches, respectively. These findings highlight the significance of TEMS in improving end-user social welfare. Furthermore, the penalty analysis for fault data injection threats to provide the cyber security and reliability of the P2P energy market.

Since the recommended techniques anticipate co-operation from all players, the profit obtained by each member during every trading interval is restricted in relation to the community's net demand. When community demand exceeds generation, importers may not get significant economic gains from LEM. On the other hand, exporters may earn less when the generation is higher. In the future, as an extension of this work, TEMS shall be developed with more complex market clearing strategies to overcome the abovementioned issue. Besides, with the proposed centralized power management system, the third-party agent (LEMO) is required to coordinate the power balance between local generation and demand. Hence, a decentralized system can be incorporated to eliminate third-party intervention (LEMO) while implementing P2P power trading in a microgrid community.

## Nomenclature

AMC:	Average market clearing
CDL:	Consumer demand limit
DSM:	Demand side management
FiT:	Feed-in tariff
FLs:	Flexible loads
GDR:	Generation-to-demand ratio
GDRMC:	Generation-to-demand ratio-based market clearing
LEM:	Local energy market
LEMO:	Local energy market operator
NFLs:	Nonflexible loads
PIL:	Power injection limit
PID:	Participant's ID
P2G:	Peer-to-grid
P2P:	Peer-to-peer
RERs:	Renewable energy resources
RTP:	Real-time pricing
SEMS:	Smart energy management system
SoC:	State of charge.
TEMS:	Transactive energy management systems.

## Data Availability

The data used to support the findings of this study are available from the corresponding author upon request.

## Conflicts of Interest

The authors declare that they have no conflicts of interest.

## Acknowledgments

This research work was supported by the School of Electrical Engineering, Vellore Institute of Technology.

## References

- [1] P. Palensky and D. Dietrich, "Demand Side Management: Demand Response, Intelligent Energy Systems, and Smart Loads," *IEEE Transactions on Industrial Informatics*, vol. 7, 2011.
- [2] S. L. Arun and M. P. Selvan, "Smart residential energy management system for demand response in buildings with energy storage devices," *Frontiers in Energy*, vol. 13, no. 4, pp. 715–730, 2019.
- [3] T. Hubert and S. Grijalva, "Modeling for residential electricity optimization in dynamic pricing environments," *IEEE Transactions on Smart Grid*, vol. 3, no. 4, pp. 2224–2231, 2012.
- [4] X. Chen, T. Wei, and S. Hu, "Uncertainty-aware household appliance scheduling considering dynamic electricity pricing in smart home," *IEEE Transactions on Smart Grid*, vol. 4, no. 2, pp. 932–941, 2013.
- [5] C. O. Adika and L. Wang, "Autonomous appliance scheduling for household energy management," *IEEE Transactions on Smart Grid*, vol. 5, no. 2, pp. 673–682, 2014.
- [6] P. Mesarić and S. Krajcar, "Home demand side management integrated with electric vehicles and renewable energy sources," *Energy and Buildings*, vol. 108, pp. 1–9, 2015.
- [7] E. L. Ratnam, S. R. Weller, and C. M. Kellett, "Scheduling residential battery storage with solar PV: assessing the benefits of net metering," *Applied Energy*, vol. 155, pp. 881–891, 2015.
- [8] C. Wang, Y. Zhou, B. Jiao, Y. Wang, W. Liu, and D. Wang, "Robust optimization for load scheduling of a smart home with photovoltaic system," *Energy Conversion and Management*, vol. 102, pp. 247–257, 2015.
- [9] Solar Bonus Report Department of Natural Resources, "Mines and Energy," 2018, [https://www.dnrm.qld.gov.au/\\_\\_data/assets/pdf\\_file/0005/1379678/](https://www.dnrm.qld.gov.au/__data/assets/pdf_file/0005/1379678/).
- [10] I. Colak, S. Sagiroglu, G. Fulli, M. Yesilbudak, and C.-F. Covrig, "A survey on the critical issues in smart grid technologies," *Renewable and Sustainable Energy Reviews*, vol. 54, pp. 396–405, 2016.
- [11] N. Liu, X. Yu, C. Wang, C. Li, L. Ma, and J. Lei, "Energy-sharing model with price-based demand response for microgrids of peer-to-peer prosumers," *IEEE Transactions on Power Systems*, vol. 32, no. 5, pp. 3569–3583, 2017.
- [12] M. F. Zia, M. Benbouzid, E. Elbouchikhi, S. M. Muyeen, K. Techato, and J. M. Guerrero, "Microgrid Transactive Energy: Review, Architectures, Distributed Ledger Technologies, and Market Analysis," *IEEE Access*, vol. 8, 2020.
- [13] N. Gupta, B. R. Prusty, O. Alrumayh, A. Almutairi, and T. Alharbi, "The role of transactive energy in the future energy industry: a critical review," *Energies*, vol. 15, no. 21, p. 8047, 2022.
- [14] O. Abrishambaf, F. Lezama, P. Faria, and Z. Vale, "Towards transactive energy systems: an analysis on current trends," *Energy Strategy Reviews*, vol. 26, Article ID 100418, 2019.
- [15] M. H. Cintuglu, H. Martin, and O. A. Mohammed, "Real-time Implementation of Multiagent-Based Game Theory Reverse Auction Model for Microgrid Market Operation," *IEEE Transactions on Smart Grid*, vol. 6, 2015.

- [16] P. Shamsi, H. Xie, A. Longe, and J.-Y. Joo, "Economic Dispatch for an Agent-Based Community Microgrid," *IEEE Transactions on Smart Grid*, vol. 34, 2016.
- [17] R. Alvaro-Hermana, J. Fraile-Ardanuy, P. J. Zufria, L. Knapen, and D. Janssens, "Peer to Peer Energy Trading with Electric Vehicles," *IEEE Intelligent Transportation Systems Magazine*, vol. 8, 2016.
- [18] B. Celik, R. Roche, D. Bouquain, and A. Miraoui, "Coordinated Neighborhood Energy Sharing Using Game Theory and Multi-Agent Systems," *IEEE Manchester PowerTech*, vol. 21, pp. 1–6, 2017.
- [19] W. Amin, Q. Huang, K. Umer et al., "A motivational game-theoretic approach for peer-to-peer energy trading in islanded and grid-connected microgrid," *International Journal of Electrical Power & Energy Systems*, vol. 123, Article ID 106307, 2020.
- [20] E. Fernandez, M. Hossain, K. Mahmud, M. S. H. Nizami, and M. Kashif, "A bi-level optimization-based community energy management system for optimal energy sharing and trading among peers," *Journal of Cleaner Production*, vol. 279, Article ID 123254, 2021.
- [21] A. Jiang, H. Yuan, and D. Li, "A two-stage optimization approach on the decisions for prosumers and consumers within a community in the peer-to-peer energy sharing trading," *International Journal of Electrical Power & Energy Systems*, vol. 125, Article ID 106527, 2021.
- [22] C. Zhang, J. Wu, M. Cheng, Y. Zhou, and C. Long, "A bidding system for peer-to-peer energy trading in a grid-connected microgrid," *Energy Procedia*, vol. 103, pp. 147–152, 2016.
- [23] T. Morstyn, N. Farrell, S. J. Darby, and M. D. McCulloch, "Using peer-to-peer energy-trading platforms to incentivize prosumers to form federated power plants," *Nature Energy*, vol. 3, no. 2, pp. 94–101, 2018.
- [24] B. H. Rao, S. L. Arun, and M. P. Selvan, "Framework of locality electricity trading system for profitable peer-to-peer power transaction in locality electricity market," *IET Smart Grid*, vol. 3, no. 3, pp. 318–330, 2020.
- [25] M. Gough, S. F. Santos, A. Almeida et al., "Blockchain-based transactive energy framework for connected virtual power plants," *IEEE Transactions on Industry Applications*, vol. 58, no. 1, pp. 986–995, 2022.
- [26] C. Liu and Z. Li, "Comparison of centralized and peer-to-peer decentralized market designs for community markets," *IEEE Transactions on Industry Applications*, vol. 58, no. 1, pp. 67–77, 2022.
- [27] V. Hosseinnezhad, B. Hayes, B. O'regan, and P. Siano, "Practical insights to design a blockchain-based energy trading platform," *IEEE Access*, vol. 9, pp. 154827–154844, 2021.
- [28] S. Seven, Y. Yoldas, A. Soran et al., "Energy trading on a peer-to-peer basis between virtual power plants using decentralized finance instruments," *Sustainability*, vol. 14, no. 20, p. 13286, 2022.
- [29] A. J. Onumanyi, S. J. Isaac, C. P. Kruger, and A. M. Abu-Mahfouz, "Transactive energy: state-of-the-art in control strategies, architectures, and simulators," *IEEE Access*, vol. 9, pp. 131552–131573, 2021.
- [30] A. Bagheri and S. Jadid, "Integrating wholesale and retail electricity markets considering financial risks using stochastic programming," *International Journal of Electrical Power & Energy Systems*, vol. 142, Article ID 108213, 2022.
- [31] G. Li, Q. Li, X. Yang, and R. Ding, "General nash bargaining based direct p2p energy trading among prosumers under multiple uncertainties," *International Journal of Electrical Power & Energy Systems*, vol. 143, Article ID 108403, 2022.
- [32] S. Suthar, S. H. C. Cherukuri, and N. M. Pindoriya, "Peer-to-peer energy trading in smart grid: frameworks, implementation methodologies, and demonstration projects," *Electric Power Systems Research*, vol. 214, Article ID 108907, 2023.
- [33] P. Centolella, "The integration of price responsive demand into regional transmission organization (RTO) wholesale power markets and system operations," *Energy*, vol. 35, no. 4, pp. 1568–1574, 2010.
- [34] G. T. Costanzo, G. Zhu, M. F. Anjos, and G. Savard, "A system architecture for autonomous demand side load management in smart buildings," *IEEE Transactions on Smart Grid*, vol. 3, no. 4, pp. 2157–2165, 2012.
- [35] S. L. Arun and M. P. Selvan, "Intelligent residential energy management system for dynamic demand response in smart buildings," *IEEE Systems Journal*, vol. 12, no. 2, pp. 1329–1340, 2018.

## Research Article

# Violation Punishment and Total Factor Productivity, Based on the Spillover Effect between Director-Interlocked Firms

Yang Lu , Xiangge Meng , and Haitao Song

*School of Accounting, Harbin University of Commerce, Harbin 150028, Heilongjiang, China*

Correspondence should be addressed to Yang Lu; 20160639@ayit.edu.cn

Received 10 August 2022; Accepted 23 September 2022; Published 20 April 2023

Academic Editor: Dinesh Kumar Saini

Copyright © 2023 Yang Lu et al. This is an open access article distributed under the Creative Commons Attribution License, which permits unrestricted use, distribution, and reproduction in any medium, provided the original work is properly cited.

Using the sample of A-share listed firms in China from 2008 to 2019, we empirically test the spillover effect of violation punishment on the total factor productivity of director-interlocked firms. We find that violation punishment can significantly aggravate the violation of director-interlocked firms and preliminarily verify the spillover effect of violation punishment among director-interlocked firms. We also find that violation punishment will significantly reduce the total factor productivity of director-interlocked firms. The result is still stable after replacing the measurement method of total factor productivity, and its impact has a certain continuity, which can affect for two consecutive years. Further research shows that the R&D investment plays a mediation role between the violation punishment and the total factor productivity of the director interlocked firms. The violation punishment can reduce the R&D investment of the director-interlocked firms and then reduce the total factor productivity of the director-interlocked firms. In addition, after distinguishing the type of firm ownership, we find that compared with state-owned enterprises, violation punishment has a more significant inhibitory effect on the total factor productivity of private enterprises' director-interlocked firms. Based on the perspective of the director network, we investigate the spillover effect of violation punishment on the total factor productivity of director-interlocked firms, which provides a new theoretical perspective for the in-depth understanding of the economic consequences of violation punishment, improves the total factor productivity of listed firms, and has important theoretical and practical significance.

## 1. Introduction

Nowadays, the phenomenon of interlocking directors is very prominent in the global capital market, especially in China, indicating that it is unique and it is urgent to study the relationship of the director network in China's capital market. There has been a great deal of empirical evidence that interlocking directors can transmit information [1–3], knowledge, and experience [4] among listed firms and generate convergence of financing decisions, investment decisions, and M&A decisions [5–7]. Therefore, based on the role of interlocking directors in the information bridge between listed firms, it is increasingly important to study the spillover effect between listed firms with interlocking directors.

In recent years, financial fraud and stock price manipulation of listed firms such as Ruixing Coffee have emerged

one after another, which has greatly damaged the overall image of Chinese enterprises. To prevent and control the illegal behaviors of enterprises and establish an enterprise system with clear property rights, clear rights and responsibilities, separation of government and enterprises, and scientific management, we need not only to improve the internal governance structure of enterprises but also to play the regulatory role of external supervision. The role of regulators is mainly to timely check the violations of firms and punish them. Strengthening market supervision is the main theme of China's capital market in recent years. With the strengthening of law enforcement and the improvement of the regulatory system, more and more listed firms have been investigated for violations of laws and regulations. Figure 1 illustrates the changing trend of violation punishment of listed firms in China from 2008 to 2019. The samples of violation punishment from 2008 to 2015 showed

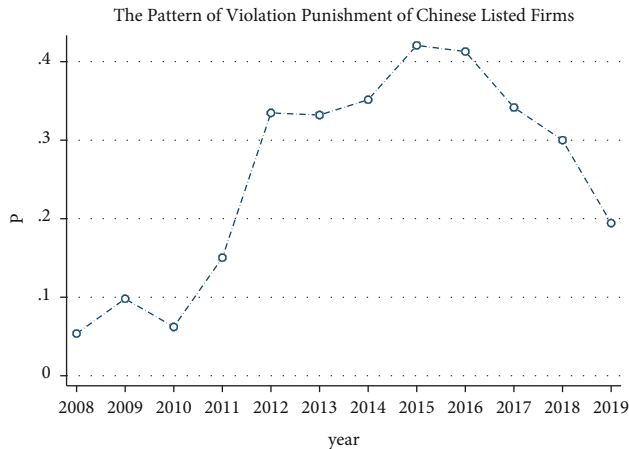


FIGURE 1: The pattern of violation punishment of Chinese listed firms from 2008–2019.

an obvious upward trend and showed a slow downward trend from 2016 to 2019. However, the results of violation punishment in 2019 show that the samples of violation punishment of listed firms accounted for about 20% of the samples. Violations of listed firms are subject to inspection and punishment by the regulatory authorities and will have a negative impact on the continuing operation of listed firms. Large amounts of compensation can easily lead to the rupture of the company's capital flow, causing financial risks. At the same time, violation punishment is negative news for firms [8]. The firms will face the pressure of public opinion, and the reputation of the firms will be damaged [9], which is very harmful to the sustainable development of the firms. Then, based on the director network, questions such as does the violation punishment of listed firms have a spillover effect on the director-interlocked firms and what impact will the violation punishment of listed firms have on the violation punishment of director-interlocked firms arise.

At the macrolevel, total factor productivity is an important indicator and basis to measure the quality of a country's economic growth and technological progress. The report of the 19th National Congress of the Communist Party of China pointed out that "China's economy has changed from the stage of high-speed growth to the stage of high-quality development. We must adhere to quality first and benefit first, take the supply side structural reform as the main line, promote the quality, efficiency, and power changes of economic development, and improve the overall productivity." High-quality development is the transformation of China's economic development stage and a new stage of development, following the historical development law of "quantitative change to qualitative change." In the past, the model of relying on excessive investment to support China's rapid economic growth has been unsustainable. The extensive development model is facing the challenges of diminishing marginal returns and disappearing demographic dividends, which has reached the limit of environmental tolerance. Therefore, there is an urgent need to explore a new driving force leading China's economic growth and quality change, and its core is the improvement of total factor productivity.

At the microlevel, the improvement of total factor productivity is closely related to enterprise management activities, such as the use of advanced production equipment, increasing R&D investment, improving export and financing behavior, adjusting organizational structure, and improving management level. As the main body of national economic development, the operation and development of enterprises have become an important symbol to measure the quality of an industry, field, and even national economic development. Improving enterprise efficiency can not only help enterprises improve their business performance and core competitiveness and win greater development space for enterprises but also promote the quality and efficiency of the national economy and achieve high-quality development. In fact, in China's economic practice, subject to factors such as the distorted system and imperfect market system, the innovation ability of enterprises is not strong, and the capital-labor and other factor input combination need to be optimized, which leads to the low total factor productivity of Chinese enterprises.

Figure 2 reports the changing trend of China's total factor productivity from 2008 to 2019. As shown in Figure 2, except for a brief increase in total factor productivity from 2009 to 2010, total factor productivity showed an obvious downward trend from 2008 to 2019. Therefore, it is very important to explore the influencing factors of total factor productivity and promote high-quality development. Then, the following questions arise: Does the violation punishment of listed firms have a spillover effect on the total factor productivity of director-interlocked firms? What is the path of the spillover effect of violation punishment on the total factor productivity of director-interlocked firms? What are the other heterogeneous factors of the spillover effect of violation punishment on the total factor productivity of director-interlocked firms?

In order to answer the abovementioned questions, taking China's A-share listed firms from 2008 to 2019 as a sample, we use logistic regression to test whether the violation punishment has spillover effect among the director interlocked firms and uses the ordinary least square method to test the impact of violation punishment on the total factor productivity of the director-interlocked firms. We found that violation punishment can significantly aggravate the violation of director-interlocked firms, which proves that violation punishment has the spillover effect among director-interlocked firms. Violation punishment will inhibit the total factor productivity of director-interlocked firms. This effect still exists after replacing the total factor productivity measurement method, and it can last for two periods. Further research shows that R&D investment plays a mediation role in violation punishment and total factor productivity. Violation punishment can reduce the total factor productivity of director-interlocked firms by reducing R&D investment of director-interlocked firms. After distinguishing the type of firm ownership, we found that compared with state-owned enterprises, violation punishment can significantly reduce the total factor productivity of private enterprise director interlocked firms. The existing study did not focus on consideration of the contrasting effect



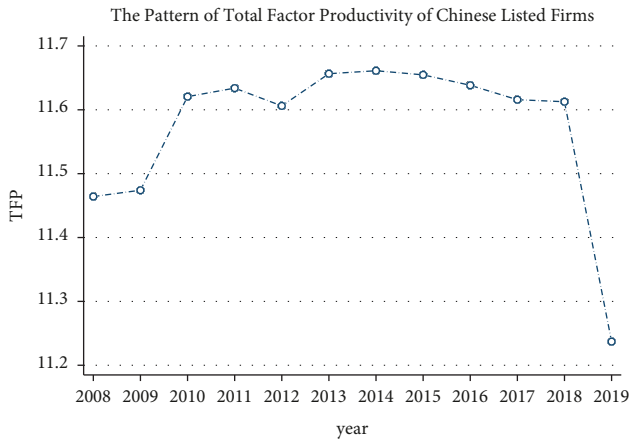


FIGURE 2: The pattern of total factor productivity of Chinese listed firms from 2008–2019.

of information transmission among interlocking directors, which is also warranted and so is the provision of operational suggestions to help businesses establish a good image and transmit positive signals within the company network.

The main contributions of this study are as follows: First, from the perspective of the director network, we investigate the spillover effect of violation punishment on the total factor productivity of director interlocked firms. Compared with China, the research on the measurement of total factor productivity abroad started earlier, and the research results are quite abundant. It is possible that the measurement of total factor productivity can be divided into technological progress, technical efficiency, and scale efficiency. The research on the influencing factors of total factor productivity at home and abroad mainly includes internal factors such as financing constraints [10, 11], human capital [12, 13], and R&D investment [14, 15]. In addition, external factors such as government subsidies [16, 17], industrial policies [18, 19] and financial development [20, 21] ignore the impact of violation punishment on total factor productivity. Therefore, this study puts the violation punishment and total factor productivity in the same research framework. Based on the perspective of the director network, we study the impact of violation punishment on the total factor productivity of director-interlocked firms, which not only expands the research on the economic consequences of violation punishment and the influencing factors of total factor productivity but also improves the research on the relationship between violation punishment and total factor productivity.

Second, we analyze the transmission path of the spillover effect of violation punishment on the total factor productivity of director interlocked firms. From the path of R&D investment, we study the impact mechanism of violation punishment on the spillover effect of total factor productivity of director-interlocked firms. Violation punishment can reduce the total factor productivity of director-interlocked firms by reducing R&D investment of director-interlocked firms. The in-depth analysis of this study has accumulated new experience for studying the spillover effect

of violation punishment on total factor productivity of director-interlocked firms and deepened and expanded the relevant empirical research.

Third, we explore the heterogeneous influencing factors of the spillover effect of violation punishment on the total factor productivity of director-interlocked firms. From the aspect of firm ownership, we reveal the heterogeneous effect of different firm ownership on the impact of violation punishment on the total factor productivity of director-interlocked firms. Compared with state-owned enterprises, violation punishment has a more significant effect on the reduction of total factor productivity of director-interlocked firms of private enterprises. This heterogeneity study makes the spillover effect of violation punishment on total factor productivity of director-interlocked firms more comprehensive and systematic, provides reference for empirical research in this field, and provides policy suggestions for the improvement of total factor productivity of listed firms.

The remainder of this study is structured as follows: Section 2 conducts our theoretical analysis and research hypotheses. Section 3 describes our research design. Section 4 presents our empirical results and analysis. Section 5 conducts further analysis, and Section 6 presents our conclusions.

## 2. Theoretical Analysis and Research Hypotheses

Nowadays, the phenomenon of interlocking directors is very prominent in the global capital market, especially in China. There has been a great deal of empirical evidence that interlocking directors can transmit information [1–3], knowledge, and experience [4] among listed firms and generate convergence of financing decisions, investment decisions, and M&A decisions [5–7]. Therefore, based on the role of interlocking directors in the information bridge between listed firms, question such as what impact will the violation punishment have on the violation punishment of the director-interlocked firms arises.

According to the information transmission theory of experience accumulation mechanism, social learning theory, and attribution theory, the violation punishment of listed firms will affect the violation punishment of interlocked firms. A large number of literatures have shown that personal experience accumulation will have an impact on corporate behavior. The punishment of listed firms for violation of regulations will significantly affect the capital market performance and investment and financing behavior of peer companies [22, 23]. Xin et al. [9] found that the punishment of listed firm for violations can significantly affect the market response and performance of other unpunished member enterprises in the group. Therefore, based on the accumulation of directors' personal experience and the transmission of information among interlocked firms, the behavior and decision-making of directors among interlocked firms are similar, and then the decision-making of firms is similar. Based on the above analysis, we put forward the first research as follows:

H1: violation punishment can significantly aggravate the violation of director interlocked firms.

Previous studies have shown that internal factors such as the level of financing constraints and R&D investment can directly affect the level of total factor productivity. A large number of empirical studies show that financing constraints inhibit total factor productivity. Badia and Sloommaekers [24] took Estonia as the research sample, and they found that young enterprises and highly indebted enterprises are subject to higher levels of financing constraints, and the financing constraints are significantly negatively correlated with total factor productivity. Chen and Guariglia [11] took Chinese enterprises as research samples and found that in the case of difficult external financing, informal finance and internal cash flow are important influencing factors of total factor productivity. Most literatures show that R&D investment plays an important role in promoting the improvement of total factor productivity. Helpman [25] emphasized that investment in research and development activities is the main way to improve a country's total factor productivity and achieve overall technological progress. Bloom et al. [26] found that R&D investment and inter-enterprise technology spillover effect can significantly improve enterprise total factor productivity. In addition, studies by Amable et al. [14] and Baumann and Kritikos [15] also confirmed the effect of R&D investment on total factor productivity.

However, a large number of literatures show that violation punishment can have negative consequences. The punishment of violations by the regulatory authorities is a major negative news for listed firms, which will produce a significant negative market reaction in the short term, which shows the effectiveness of government supervision to a certain extent [8]. The punishment of violation will directly lead to the decline of stock price [27], market value loss, and reputation loss [28], and then the punishment of violation will inhibit the company's risk-taking behavior [29], reduce the enterprise's investment level [30], and affect the enterprise's investment behavior. In addition, the punishment for violation also damages the value of the creditor's rights of the firm [31].

Therefore, the violation punishment of listed firms will have a negative impact on the director interlocked firms. The company punished for violation can obtain less bank loans, higher interest rate, shorter term, higher guarantee requirements [32], and higher debt financing cost [33, 34], which will result in financing constraints. When the firm faces financing difficulties, it will reduce R&D investment, which will affect the total factor productivity of the director interlocked firms. Based on the abovementioned analysis, we put forward the first research as follows:

H2: violation punishment can significantly reduce the total factor productivity of director interlocked firms.

### 3. Research Design

*3.1. Sample Selection and Data Sources.* This article selects all A-share listed firms in Shanghai and Shenzhen of China from 2008 to 2019 as the initial samples. In order to ensure

the validity of the research data, the samples were screened according to the following criteria: (1) Excluding ST and ST\* firms. (2) Excluding financial listed firms. (3) Excluding samples with asset-liability ratios less than 0 and greater than 1. (4) Excluding samples with missing financial data. (5) Excluding samples where directors do not hold concurrent positions in other listed firms. After the abovementioned treatment, we obtain a total of 94717 firm-year observations. Furthermore, in order to study the spillover effect of violation punishment on director-interlocked firms, we exclude the samples of violation punishment of director-interlocked firms and finally obtain 8813 firm-year observations.

The data of this study are mainly from WIND database and CSMAR database. The China Stock Market and Accounting Research (CSMAR) Database offers data on the China stock markets and the financial statements of China's listed companies. In order to control the influence of extreme values, Winsorize tailing was performed on 1% and 99% of all continuous variables. In addition, robust command is used to correct the standard errors in multivariate regression, so that the results are more robust.

*3.2. Definition of Violation Punishment.* Listed firms are subject to regulatory punishments and announcements for violating relevant laws and regulations of the CSRC or other regulatory authorities. We choose the year of announcement of punishment for violations as the year of punishment for violations of listed firms. When listed firms are punished for many violations within one year, only one sample of punishment is retained.

According to the codes of listed firms with interlocking directors in CSMAR database, all listed firms in the same year are paired together and then merged with the data of violation punishment, that is, the punishment information of the director interlocked firms. In this study, we set violation punishment as a dummy variable  $P$ . When the firm has been punished for violations, the value is 1; otherwise, it is 0.

And we set violation punishment of the director interlocked firms as a dummy variable  $A$ . When listed firm has more than one interlocked firm to be punished for violations in one year, as long as there is an interlocked firm to be punished for violations, the value is 1; otherwise, it is 0.

*3.3. Definition of Total Factor Productivity.* Based on the existing literature, this study uses the Olley-Pakes method (OP) to calculate total factor productivity (TFP). Referring to Qian et al. [35] and Zhao and Lu [36], the natural logarithm of operating income is used to measure the total output, the natural logarithm of the number of employees is used to measure the labor input, the net value of fixed assets is used to measure the capital input, and the cash paid for services received by buyers is used as a substitute for the input price of intermediate products. The natural logarithm of the difference between the cash paid for the purchase and construction of long-term assets such as fixed assets and the disposal of long-term assets such as fixed assets is used to measure the capital investment. The total output is reduced

TABLE 1: Definition of control variables.

Age of the firm	The natural logarithm of the firm's listing years
Lev (asset-liability ratio)	Ratio of total liabilities to total assets.
Size (size of the firm)	Natural logarithm of total assets.
State (firm ownership)	If it is a state-owned enterprise, the value of A is 1; otherwise, it 0.
Grow (Gross revenue growth rate)	Ratio of total gross revenue at the end of the year minus total gross revenue at the end of last year to total gross revenue at the end of last year.
ROE (return on equity)	Ratio of net profit to shareholder equity balance.
Independ (proportion of independent directors)	Proportion of independent directors to the total number of directors.
Dual (duality)	If the chairman and general manager are concurrently appointed, the value of A is 1; otherwise, is 0.
Industry (industry characteristics)	Industry dummy variables
Year (Year characteristics)	Year dummy variables

by the industrial product price index (PPI) of the province where the company is located, and the capital input is reduced by the fixed asset investment price index of the province where the company is located.

3.4. *Control Variables.* As for the control variables, according to the existing literature, we choose the age of the firm (Age), the asset-liability ratio (Lev), the size of the firm (Size), firm ownership (State), growth rate of total operating revenue (Grow), return on equity (ROE), the proportion of independent directors (Independ), and duality (Dual). In addition, the industry and year fixed effects are also controlled. See Table 1 for details.

3.5. *Research Model.* In order to prove the spillover effect of violation punishment among interlocked firms with concurrent directors, we construct the following logit regression model:

$$A_{i,t+1} = \alpha_0 + \alpha_1 P_{i,t} + \alpha_2 \text{Control}_{i,t} + \varepsilon_{i,t}. \quad (1)$$

Among them, in order to avoid endogenous problems,  $A$  is whether the director interlocked firms is subject to violation punishment in year  $t + 1$ .  $P$  is whether the listed firm is subject to violation punishment in year  $t$ . Control is the relevant control variable in year  $t$ .  $\alpha_0$  is a constant term;  $\alpha_1$  is the regression coefficient between the violation punishment of the listed firm and the violation punishment of the director-interlocked firms;  $\alpha_2$  is the regression coefficient of the control variable.; and  $\varepsilon_{i,t}$  is the residual term.

In order to better verify the spillover effect of violation punishment of listed firms on the total factor productivity of director-interlocked firms, we delete the sample observations of violation punishment of director-interlocked firms themselves. We construct the following multiple regression model:

$$\text{TFP\_OP}_{i,t+1} = \alpha_0 + \alpha_1 P_{i,t} + \alpha_2 \text{Control}_{i,t} + \varepsilon_{i,t}. \quad (2)$$

Among them, in order to avoid endogenous problems, TFP adopts the year of  $t + 1$ , and TFP\_OP is the total factor productivity of the director-interlocked firms calculated by the OP method.  $P$  is whether the listed firm is punished for violation in year  $t$ . Control is the relevant control variable in year  $t$ .

TABLE 2: Descriptive statistics.

Variable	N	Mean	Sd	Min	Median	Max
<i>Before deleting the violation punishment sample of the director interlocked firms themselves</i>						
A	94717	0.079	0.269	0	0	1
P	94717	0.392	0.488	0	0	1
Age	94717	2.828	0.327	1.792	2.833	3.526
Lev	94717	0.470	0.198	0.070	0.477	0.905
Size	94717	22.486	1.323	19.790	22.307	26.262
State	94717	0.510	0.500	0	1	1
Grow	94717	0.204	0.565	-0.540	0.110	4.666
ROE	94717	0.072	0.101	-0.455	0.073	0.339
Independ	94717	0.371	0.052	0.333	0.333	0.571
Dual	94717	0.198	0.398	0	0	1
<i>After deleting the violation punishment sample of the director interlocked firms themselves</i>						
TFP_OP <sub>t+1</sub>	7202	7.590	0.874	5.573	7.515	9.862
P	8813	0.288	0.453	0	0	1
Age	8813	2.782	0.348	1.609	2.833	3.497
Lev	8813	0.437	0.197	0.0620	0.431	0.863
Size	8813	22.411	1.386	20.028	22.186	26.647
State	8813	0.503	0.500	0	1	1
Grow	8813	0.172	0.364	-0.492	0.115	2.445
ROE	8813	0.084	0.081	-0.238	0.081	0.310
Independ	8813	0.372	0.0530	0.333	0.333	0.571
Dual	8813	0.207	0.405	0	0	1

In the robustness test, we use the LP method to calculate the total factor productivity of director interlocked firms (TFP\_LP) for replacement. Besides, we use TFP\_OP and TFP\_LP which are in year  $t + 2$  and  $t + 3$  for regression to test whether the impact of violation punishment on the total factor productivity of director interlocked firms has a time effect. The regression model is as follows:

$$\frac{\text{TFP\_OP}_{i,t+2}/\text{TFP\_LP}_{i,t+2}}{\text{TFP\_OP}_{i,t+3}/\text{TFP\_LP}_{i,t+3}} = \alpha_0 + \alpha_1 P_{i,t} + \alpha_2 \text{Control}_{i,t} + \varepsilon_{i,t}. \quad (3)$$

## 4. Empirical Results and Analysis

4.1. *Descriptive Statistics.* Table 2 reports the descriptive statistics. Before excluding the samples of violation punishment of director-interlocked firms themselves, it can be

TABLE 3: Regression results of violation punishment and violation punishment of director interlocked firms.

	$A_{t+1}$	$A_{t+1}$
	(1)	(2)
P	0.151*** (5.97)	0.155*** (6.09)
Age		0.262*** (5.53)
Lev		1.539*** (17.97)
Size		-0.163*** (-12.68)
State		-0.259*** (-8.70)
Grow		0.012 (0.54)
ROE		-1.675*** (-14.85)
Independ		-0.333 (-1.33)
Dual		0.153*** (4.91)
Constant	-1.241*** (-4.67)	1.149*** (2.79)
Ind/Year	Yes	Yes
N	94717	94717

Note. \*\*\*, \*\*, and \* indicate that the variables pass the test at the significance level of 1%, 5%, and 10%, respectively. The numbers in parentheses are  $t$  values, which are all two tailed.

found that the total sample has 94717 observations. The mean value of violation punishment of listed firm  $P$  is 0.392, and the standard deviation is 0.488, which is greater than the average value, indicating that violation punishment is common in listed firms and the difference is large. The mean value of violation punishment of director interlocked firms ( $A$ ) is 0.079, and the standard deviation is 0.269, which is far greater than the average value, indicating that violation punishment is also common in director-interlocked firms, and the difference is also large.

After excluding the sample of violation punishment of the director-interlocked firms themselves, the sample has 8813 observations, and the sample has 7202 observations in year  $t+1$ . The mean value of punishment for violation of listed firms  $P$  is 0.288, and the standard deviation is 0.453, which is greater than the average value. The mean value of total factor productivity of director-interlocked firms in  $t+1$  year ( $TFP\_Op_{t+1}$ ) is 7.590, the standard deviation is 0.874, and the median is 7.515, which is less than the mean value, indicating that there are many samples with low total factor productivity of director-interlocked firms.

**4.2. Regression Results and Analysis.** Table 3 reports the regression results of violation punishment and violation punishment of director interlocked firms. Columns (1) and (2) report the regression results with and without control variables, respectively. In column (1), the coefficient of violation punishment  $P$  is 0.151, which is significant at the level of 1%. In column (2), the coefficient of violation

TABLE 4: Regression results of violation punishment and total factor productivity of director-interlocked firms.

	$TFP\_Op_{t+1}$
P	-0.032** (-2.24)
Age	-0.867*** (-38.07)
Lev	0.710*** (15.11)
Size	0.381*** (55.13)
State	0.109*** (6.97)
Grow	0.126*** (5.85)
ROE	1.484*** (14.78)
Independ	0.010 (0.08)
Dual	-0.008 (-0.49)
Constant	0.450** (2.11)
Ind/year	Yes
Adj_ $R^2$	0.624
F	208.471
N	7202

Note. \*\*\*, \*\*, and \* indicate that the variables pass the test at the significance level of 1%, 5%, and 10%, respectively. The numbers in parentheses are  $t$  values, which are all two tailed.

TABLE 5: Variance expansion factors of relevant variables.

Variable	VIF	1/VIF
Size	2.04	0.490526
Lev	1.86	0.538282
State	1.54	0.648321
Age	1.50	0.668705
ROE	1.20	0.832948
Dual	1.14	0.874629
Grow	1.12	0.892393
P	1.11	0.902003
Independ	1.10	0.907377
Mean VIF	1.40	

Note. In the following other regression analysis, the variance inflation factor of relevant variables is less than 10, so there is no collinearity problem. Considering the space limitation, it will not be listed.

punishment  $P$  is 0.155, which is greater than that in column (1) and is also significant at the 1% level. The results show that violation punishment can significantly aggravate the violation of director interlocked firms, which prove that violation has the spillover effect among director interlocked firms.

Table 4 reports the regression results of violation punishment and total factor productivity of director interlocked firms. As shown in Table 4, the coefficient of violation punishment  $P$  is -0.032, which is significant at the level of 5%. The results show that violation punishment can significantly reduce the total factor productivity of director-interlocked firms.

TABLE 6: Regression results of violation punishment and total factor productivity of director-interlocked firms measured by the LP method.

	TFP_LP <sub>t+1</sub>
<i>P</i>	-0.027* (-1.86)
Age	0.192*** (8.64)
Lev	0.782*** (16.55)
Size	0.553*** (78.50)
State	0.076*** (4.79)
Grow	0.102*** (4.82)
ROE	1.974*** (19.10)
Independ	0.010 (0.08)
Dual	-0.005 (-0.32)
Constant	-2.753*** (-13.34)
Ind/Year	Yes
Adj_R <sup>2</sup>	0.739
<i>F</i>	390.652
<i>N</i>	7202

Note. \*\*\*, \*\*, and \* indicate that the variables pass the test at the significance level of 1%, 5%, and 10%, respectively. The numbers in parentheses are *t* values, which are all two tailed.

Table 5 reports the variance inflation factors (VIF) for the relevant variables. We can see from the table that the variance inflation factor of the size of the firm (Size) is the largest, that is, only 2.04, and the mean of the variance inflation factor of each variable is 1.40, which is far less than 10. It indicates that there is no collinearity problem between variables.

Table 6 reports the robustness test results of the regression between the violation punishment and the total productivity of the director interlocked firms measured by the LP method. As shown in Table 6, the coefficient of violation punishment *P* is -0.027, which is significant at the level of 10%. It shows that violation punishment can inhibit the total factor productivity of director-interlocked firms, which verifies the abovementioned conclusion again and shows the robustness of this conclusion.

Table 7 reports the regression results of violation punishment and total factor productivity of director-interlocked firms in *t* + 2 and *t* + 3 period. In the *t* + 2 period, the coefficients of violation punishment *P* in column (1) and (2) are -0.029 and -0.032, respectively, which are significant at the level of 10%. In the *t* + 3 period, the coefficients of violation punishment *P* in column (3) and (4) are -0.009 and -0.023, respectively, which are not statistically significant. The results show that the reduction effect of violation punishment on the total factor productivity of director-interlocked firms can last for two periods and has a time effect.

TABLE 7: Results of time effect of violation punishment on total factor productivity of director-interlocked firms.

	<i>t</i> + 2		<i>t</i> + 3	
	TFP_OP (1)	TFP_LP (2)	TFP_OP (3)	TFP_LP (4)
<i>P</i>	-0.029* (-1.78)	-0.032* (-1.87)	-0.009 (-0.47)	-0.023 (-1.15)
Age	-0.878*** (-34.25)	0.161*** (6.22)	-0.872*** (-30.43)	0.140*** (4.71)
Lev	0.732*** (13.77)	0.800*** (14.44)	0.761*** (12.84)	0.814*** (12.59)
Size	0.372*** (46.88)	0.538*** (64.05)	0.358*** (39.80)	0.518*** (52.84)
State	0.105*** (5.98)	0.073*** (4.00)	0.085*** (4.31)	0.055** (2.57)
Grow	0.084*** (3.63)	0.079*** (3.39)	0.030 (1.15)	0.027 (1.03)
ROE	1.184*** (10.73)	1.705*** (14.58)	0.961*** (8.05)	1.474*** (11.43)
Independ	-0.076 (-0.55)	-0.025 (-0.17)	-0.026 (-0.16)	0.099 (0.57)
Dual	0.007 (0.35)	0.018 (0.90)	0.004 (0.16)	0.015 (0.62)
Constant	0.570** (2.08)	-2.395*** (-8.63)	0.948*** (3.90)	-1.465*** (-5.09)
Ind/Year	Yes	Yes	Yes	Yes
Adj_R <sup>2</sup>	0.598	0.705	0.572	0.671
<i>F</i>	163.053	281.972	143.055	211.304
<i>N</i>	6023	6023	5102	5102

Note. \*\*\*, \*\*, and \* indicate that the variables pass the test at the significance level of 1%, 5%, and 10%, respectively. The numbers in parentheses are *t* values, which are all two tailed.

## 5. Further Analysis

5.1. *Mediation Effect of R&D Investment.* According to the previous analysis, the violation punishment can aggravate the violation punishment of director-interlocked firms and further aggravate the financing constraints of director-interlocked firms. Financing difficulties will reduce R&D investment, which will lead to the reduction of total factor productivity of director-interlocked firms. Therefore, we will further test the mediating role of R&D investment in violation punishment and total factor production of director-interlocked firms.

We use the natural logarithm of R&D investment amount to measure R&D investment. Referring to the mediating effect test method of Wen et al. [37], the following regression model is constructed to test the mediating effect of R&D investment in the relationship between violation punishment and total factor productivity of director-interlocked firms:

$$R\&D_{i,t} = \alpha_0 + \alpha_1 P_{i,t} + \alpha_2 Size_{i,t} + \alpha_3 Grow_{i,t} + \alpha_4 Cash_{i,t} + \alpha_5 TA_{i,t} + \alpha_6 CFO_{i,t} + \varepsilon_{i,t},$$

$$\frac{TFP\_OP_{i,t+1}}{TFP\_LP_{i,t+1}} = \alpha_0 + \alpha_1 P_{i,t} + \alpha_2 R\&D_{i,t} + \alpha_3 Control_{i,t} + \varepsilon_{i,t}. \tag{4}$$

TABLE 8: Mediating effect test of violation punishment on total factor productivity of interlocked firms: R&amp;D investment.

	R&D	TFP_OP <sub>t+1</sub>	TFP_LP <sub>t+1</sub>
	(1)	(2)	(3)
<i>P</i>	-0.340** (-2.50)	-0.032** (-2.21)	-0.026* (-1.79)
R&D		0.002 (1.38)	0.004*** (3.35)
Age		-0.865*** (-37.82)	0.197*** (8.85)
Lev		0.714*** (15.18)	0.792*** (16.72)
State		0.111*** (7.10)	0.081*** (5.13)
ROE		1.480*** (14.76)	1.965*** (19.05)
Independ		0.012 (0.10)	0.016 (0.13)
Dual		-0.009 (-0.52)	-0.006 (-0.39)
Size	0.470*** (8.10)	0.380*** (54.86)	0.551*** (77.73)
Grow	0.320 (1.61)	0.126*** (5.81)	0.100*** (4.74)
Cash	3.357*** (5.52)		
TA	-7.655*** (-10.70)		
CFO	4.361*** (4.07)		
Constant	-12.522*** (-5.62)	0.468** (2.20)	-2.708*** (-13.21)
Ind/Year	Yes	Yes	Yes
Adj_R <sup>2</sup>	0.600	0.624	0.740
<i>F</i>	349.048	205.571	387.281
<i>N</i>	8805	7202	7202

Note. \*\*\*, \*\*, and \* indicate that the variables pass the test at the significance level of 1%, 5%, and 10%, respectively. The numbers in parentheses are *t* values, which are all two tailed.

Table 8 reports the mediating effect of R&D investment on the impact of violation punishment on the total factor productivity of director-interlocked firms. In column (1), the coefficient of violation punishment *P* is -0.340, which is significant at the level of 5%. It shows that violation punishment can significantly reduce the R&D investment of director-interlocked firms. In column (2), the coefficient of violation punishment *P* is -0.032, which is significant at the level of 5%. The coefficient of R&D investment (R&D) is 0.002, which is not statistically significant, indicating that R&D investment does not play a mediating role between violation punishment and total factor productivity of director-interlocked firms. In column (3), the coefficient of violation punishment *P* is -0.026, which is significant at the level of 10%. The coefficient of R&D investment (R&D) is 0.004, which is significant at the level of 1%, indicating that R&D investment plays a mediating role between violation punishment and total factor productivity of director-interlocked firms, and it is part of the mediating role. To sum up, the punishment violation can inhibit the total factor

TABLE 9: Property right heterogeneity test of violation punishment affecting total factor productivity of interlocked firms.

	State = 1 TFP_OP <sub>t+1</sub>	State = 0 TFP_OP <sub>t+1</sub>	State = 1 TFP_LP <sub>t+1</sub>	State = 0 TFP_LP <sub>t+1</sub>
	(1)	(2)	(3)	(4)
<i>P</i>	0.002 (0.09)	-0.058*** (-2.95)	0.001 (0.05)	-0.050*** (-2.63)
Age	-0.783*** (-23.49)	-0.931*** (-28.50)	0.211*** (6.27)	0.193*** (6.21)
Lev	0.475*** (7.56)	0.839*** (11.95)	0.549*** (8.29)	0.863*** (12.99)
Size	0.390*** (42.60)	0.369*** (30.03)	0.555*** (60.33)	0.551*** (44.39)
Grow	0.115*** (4.09)	0.115*** (3.61)	0.108*** (3.86)	0.075** (2.45)
ROE	1.534*** (11.87)	1.531*** (9.81)	1.797*** (12.98)	2.243*** (14.93)
Independ	0.054 (0.32)	0.213 (1.13)	0.251 (1.41)	-0.064 (-0.34)
Dual	-0.019 (-0.69)	-0.007 (-0.33)	-0.031 (-1.10)	0.007 (0.34)
Constant	0.941*** (3.56)	1.766*** (5.03)	-2.225*** (-8.35)	-2.433*** (-8.49)
Ind/year	Yes	Yes	Yes	Yes
Adj_R <sup>2</sup>	0.651	0.555	0.738	0.735
<i>F</i>	143.849	66.178	247.138	146.136
<i>N</i>	3803	3399	3803	3399
Chi <sup>2</sup>	4.54**	3.32*		

Note. \*\*\*, \*\*, and \* indicate that the variables pass the test at the significance level of 1%, 5%, and 10%, respectively. The numbers in parentheses are *t* values, which are all two tailed.

productivity of the director-interlocked firms by reducing the R&D investment of the director-interlocked firms.

**5.2. Heterogeneity of Property Rights.** Furthermore, the impact of property right heterogeneity on violation punishment and total factor productivity of director-interlocked firms is analyzed. Many papers show that private enterprise in China might suffer from “credit discrimination” [38]. Li and Liu [39] found that private enterprise has higher debt financing costs than state-owned enterprise. Therefore, compared with state-owned enterprises, the financing constraints of private enterprises are more serious. Private enterprises will have less funds for R&D investment, resulting in low total factor productivity.

Table 9 reports the impact of property right heterogeneity on violation punishment and total factor productivity of director-interlocked firms. Columns (1) and (2) are the regression results of total factor productivity measured by the OP method. Columns (3) and (4) are the regression results of total factor productivity measured by the LP method. For state-owned enterprises, in columns (1) and (3), the coefficients of violation punishment *P* are 0.002 and 0.001, respectively, which are not statistically significant. The results show that the violation punishment will not have a significant impact on the total factor productivity of the director-interlocked firms of state-owned enterprises. For private enterprises, in columns (2) and (4), the coefficients of

violation punishment  $P$  are  $-0.058$  and  $-0.050$ , respectively, which are significant at the level of 1%. The results show that violation punishment can significantly reduce the total factor productivity of director-interlocked firms of private enterprises.

In addition, the Chi square value of columns (1) and (2) is 4.54, which is significant at the 5% level. The Chi square value of columns (3) and (4) is 3.32, which is significant at the 10% level. It shows that the impact of violation punishment on the total factor productivity of director-interlocked firms is significantly different between state-owned enterprises and private enterprises. Therefore, compared with state-owned enterprises, violation punishment can significantly reduce the total factor productivity of director-interlocked firms of private enterprise.

## 6. Conclusions

Based on the perspective of the spillover effect of the director network, this study takes China's nonfinancial listed firms from 2008 to 2019 as a sample to theoretically analyze and empirically test the spillover effect of violation punishment on total factor productivity of director-interlocked firms. The study found that the violation punishment will aggravate the violation punishment of director-interlocked firms and preliminarily verified that the violation punishment has the spillover effect among director-interlocked firms based on the director network. Violation punishment can significantly reduce the total factor productivity of director-interlocked firms, and this effect has a time effect and can last for two years. Further study found that violation punishment can inhibit the total factor productivity of director-interlocked firms by reducing the R&D investment of director-interlocked firms. In addition, after distinguishing the type of firm ownership, it is found that compared with state-owned enterprises, violation punishment has a more significant impact on the total factor productivity of director-interlocked firms of private enterprise.

This study has important practical significance for deeply understanding the economic consequences of violation punishment and the influencing factors of total factor productivity and promoting the high-quality development of listed firms. According to the research results of this study, violation punishment can significantly reduce the total factor productivity of director-interlocked firms. The results provide a reference for listed firms. Listed firms should pay attention to the regulatory penalties of the CSRC, correct deficiencies, and reduce the occurrence of violations, which will help to ensure the healthy growth of enterprises and promote the sustainable development of China's capital market. Last year, as part of China's increased efforts to manage financial risks, the country's securities regulator issued heavy fines to individuals and businesses. In addition, the report states that the CSRC banned 66 individuals from the securities market and issued 296 administrative penalties during the same time period. Since China's financial sector has expanded rapidly, regulatory authorities have increased their oversight in recent years to limit the associated financial risks. This has coincided with a severe crackdown on

illegal practices. In addition, when the violation punishment occurs, there are differences in the total factor productivity level of director-interlocked firms of different firm ownership. Listed firms can take different measures according to their own situation to improve total factor productivity and promote the high-quality development of Chinese enterprises.

## Data Availability

The dataset can be accessed from the corresponding author upon request.

## Conflicts of Interest

The authors declare that they have no conflicts of interest.

## Acknowledgments

This work was supported by Basic Scientific Research Business Cost Project of Heilongjiang Provincial Undergraduate Colleges and Universities in 2022, Research on the Development Path of Green Innovation of Strategic Emerging Industries in Heilongjiang Province under Carbon Constraints. (Project No. 2022-KYYWF-E003).

## References

- [1] S. Battiston, G. Weisbuch, and E. Bonabeau, "Decision spread in the corporate board network," *Advances in Complex Systems*, vol. 06, no. 04, pp. 631–644, 2003.
- [2] A. Barnea and I. Guedj, *Director Networks*, Social Science Electronic Publishing, Rochester, NY, USA, 2009.
- [3] X. S. Zhou, L. Wang, and C. Chen, "Inter-corporate top managers' ties and accounting information comparability: an empirical study on the perspective of inter-organizational imitation," *Nankai Business Review*, vol. 20, no. 3, pp. 100–112, 2017.
- [4] X. W. Lu, J. Q. Wang, and D. Y. Dong, "Board network, information transmission and the debt financing costs," *Journal of Management Science*, vol. 26, no. 03, pp. 55–64, 2013.
- [5] J. Engelberg, P. Gao, and C. A. Parsons, "Friends with money," *Journal of Financial Economics*, vol. 103, no. 1, pp. 169–188, 2012.
- [6] C. Fracassi and G. A. Tate, "External networking and internal firm governance," *The Journal of Finance*, vol. 67, no. 1, pp. 153–194, 2012.
- [7] J. Ishii and Y. Xuan, "Acquirer-target social ties and merger outcomes," *Journal of Financial Economics*, vol. 112, no. 3, pp. 344–363, 2014.
- [8] G. M. Chen and N. Gao, "An empirical study of the effectiveness of securities regulation in China," *Management World*, no. 07, pp. 40–47, 2005.
- [9] Y. Xin, F. Teng, and X. L. Gu, "Information and performance transfer effects of fraud regulation in business group," *Journal of Management Science*, vol. 32, no. 01, pp. 125–142, 2019.
- [10] J. Antony, T. Klarl, and A. Maubner, "Firm heterogeneity, credit constraints, and endogenous growth," *Journal of Economics*, vol. 105, no. 3, pp. 199–224, 2012.
- [11] M. Chen and A. Guariglia, "Internal financial constraints and firm productivity in China: do liquidity and export behavior

- make a difference?" *Journal of Comparative Economics*, vol. 41, no. 4, pp. 1123–1140, 2013.
- [12] Y. Che and L. Zhang, "Human capital, technology adoption and firm performance: impacts of China's higher education expansion in the late 1990s," *The Economic Journal*, vol. 128, no. 614, pp. 2282–2320, 2018.
- [13] M. Bagheri, S. Mitchelmore, V. Bamiatzi, and K. Nikolopoulos, "Internationalization orientation in SMEs: the mediating role of technological innovation," *Journal of International Management*, vol. 25, no. 1, pp. 121–139, 2019.
- [14] B. Amable, I. Ledezma, and S. Robin, "Product market regulation, innovation, and productivity," *Research Policy*, vol. 45, no. 10, pp. 2087–2104, 2016.
- [15] J. Baumann and A. S. Kritikos, "The link between R&D, innovation and Productivity: Are micro firms different?" *Research Policy*, vol. 45, no. 6, pp. 1263–1274, 2016.
- [16] A. Howell, "Picking 'winners' in China: do subsidies matter for indigenous innovation and firm productivity?" *China Economic Review*, vol. 44, no. 44, pp. 154–165, 2017.
- [17] C. Criscuolo, R. Martin, H. G. Overman, and J. Van Reenen, "Some causal effects of an industrial policy," *The American Economic Review*, vol. 109, no. 1, pp. 48–85, 2019.
- [18] P. Aghion, J. Cai, M. Dewatripont, L. Du, A. Harrison, and P. Legros, "Industrial policy and competition," *American Economic Journal: Macroeconomics*, vol. 7, no. 4, pp. 1–32, 2015.
- [19] A. Howell, "Picking 'winners' in space: impact of spatial targeting on firm performance in China," *Journal of Regional Science*, vol. 60, no. 5, pp. 1025–1046, 2020.
- [20] R. B. Freeman, "It's Financialization," *International Labour Review*, vol. 149, no. 2, pp. 163–183, 2010.
- [21] V. Midrigan and D. Y. Xu, "Finance and misallocation: evidence from plant-level data," *The American Economic Review*, vol. 104, no. 2, pp. 422–458, 2014.
- [22] A. Durnev and C. Mangen, "Corporate investments: learning from restatements," *Journal of Accounting Research*, vol. 47, no. 3, pp. 679–720, 2009.
- [23] A. Beatty, S. Liao, and J. J. Yu, "The spillover effect of fraudulent financial reporting on peer firms' investments," *Journal of Accounting and Economics*, vol. 55, no. 2-3, pp. 183–205, 2013.
- [24] M. Moreno Badia and V. Sloommaekers, "The missing link between financial constraints and productivity," *IMF Working Papers*, vol. 09, no. 72, pp. 1–39, 2009.
- [25] E. Helpman, "Trade, FDI and the organization of firms," *Journal of Economic Literature*, vol. 44, no. 3, pp. 589–630, 2006.
- [26] N. Bloom, M. Schankerman, and J. V. Reenen, "Identifying technology spillovers and product market rivalry," *Econometrica*, vol. 81, no. 4, pp. 1347–1393, 2013.
- [27] X. Chen, Q. Cheng, and A. K. Lo, "Accounting restatements and external financing choices," *Contemporary Accounting Research*, vol. 30, no. 2, pp. 750–779, 2013.
- [28] J. M. Karpoff, D. Scott Lee, and G. S. Martin, "The consequences to managers for financial misrepresentation," *Journal of Financial Economics*, vol. 88, no. 2, pp. 193–215, 2008.
- [29] M. Pan and H. R. Wei, "Bank risk-taking and supervision: does the intensity of supervision matter? Evidence from China's banking industry," *Journal of Financial Research*, no. 12, pp. 64–80, 2015.
- [30] Q. B. Yuan and Y. Y. Zhang, "The real effects of corporate fraud: evidence from class Action lawsuits," *Accounting and Finance*, vol. 56, no. 3, pp. 879–911, 2016.
- [31] X. H. Zhou and R. M. Reesor, "Misrepresentation and capital structure: quantifying the impact on corporate debt value," *Journal of Corporate Finance*, vol. 34, pp. 293–310, 2015.
- [32] J. R. Graham, S. Li, and J. P. Qiu, "Corporate misreporting and bank loan contracting," *Journal of Financial Economics*, vol. 89, no. 1, pp. 44–61, 2008.
- [33] W. Dou, X. M. Hao, and P. Y. Li, "Will the violation of a listed company Affect its debt financing? An analysis based on regional legal environment differences," *Scientific Decision Making*, no. 01, pp. 1–22, 2018.
- [34] T. K. Lai, A. C. H. Lei, and F. M. Song, "The impact of corporate fraud on director-interlocked firms: evidence from bank loans," *Journal of Business Finance & Accounting*, vol. 46, no. 1-2, pp. 32–67, 2019.
- [35] X. S. Qian, J. Kang, Y. L. Tang, and X. P. Cao, "Industrial policy, efficiency of capital allocation and firm's total factor productivity—evidence from a natural experiment in China," *China Industrial Economics*, no. 08, pp. 42–59, 2018.
- [36] J. Y. Zhao and Z. F. Lu, "Does pension contribution rate affect firm productivity?" *Economic Research Journal*, vol. 53, no. 10, pp. 97–112, 2018.
- [37] Z. L. Wen, L. Zhang, J. T. Hou, and H. Y. Liu, "Testing and application of the mediating effects," *Acta Psychologica Sinica*, vol. 36, no. 05, pp. 614–620, 2004.
- [38] L. Chen, S. Luo, and T. Zhao, "Financial constraints, trade mode transition, and global value chain upgrading of Chinese firms," *Sustainability*, vol. 11, no. 17, p. 4527, 2019.
- [39] G. Z. Li and L. Liu, "Debt financing cost and private firms credit discrimination," *Journal of Financial Research*, vol. 12, pp. 137–150, 2009.



## Research Article

# Research on Optimization of Air Defense Firepower Configuration for Warship Cooperating with Strategic Location on the Sea

W. F. Zhao , H. J. Sun , M. Li, and K. N. Teng 

Naval Aviation University, Yantai, 2H J Sun 64001, Shandong, China

Correspondence should be addressed to H. J. Sun; 14118420@bjtu.edu.cn

Received 5 August 2022; Revised 15 September 2022; Accepted 3 October 2022; Published 20 April 2023

Academic Editor: Dinesh Kumar Saini

Copyright © 2023 W. F. Zhao et al. This is an open access article distributed under the Creative Commons Attribution License, which permits unrestricted use, distribution, and reproduction in any medium, provided the original work is properly cited.

Aiming at the problem of optimizing the firepower configuration for warships cooperating with strategic locations on the sea, the influence of air defense elements on firepower configuration is analyzed comprehensively, and the constraints of firepower configuration are put forward. Combined with factors such as the forward distance of the warship, the depth of the defense, the angle of the combat sector, and the direction of the enemy's attack, based on the coastal defense forces and the warship, the firepower configuration models of air defense at a strategic location on the sea for a single warship and two warships' coordinated air defense at important places are established, respectively. The forward range of a single warship and two warships' cooperative air defense at sea is determined, and the defense depth expectation calculation formula is given. And according to the configuration of air defense firepower of the warship cooperating with strategic locations on the sea, the warship cooperating with maritime key area defense effectiveness model is constructed by using the random service system theory. Finally, under the hypothetical conditions, the numerical simulation experiments show that the proposed model and calculation formula are reasonable and effective, which can provide a certain theoretical basis for the firepower configuration of warships cooperating with strategic locations on the sea.

## 1. Introduction

Strategic locations on the sea are often far away from the mainland, with small areas, scattered locations, harsh environments, and limited natural resources, but of significant potential military value [1]. The main combat modes of offensive and defensive operations at a strategic location on the sea are as follows: under the unified command of airborne early-warning aircraft; guided by enemy space-based satellites and long-range reconnaissance aircraft; covered by electromagnetic suppression of electronic warfare aircraft, the troops used various combat weapons (such as manned/unmanned attack aircraft and warships, submarine-launched long-range cruise missiles, precision-guided bombs, and shore-based medium- and short-range tactical missiles/long-range rockets) to carry out multidirectional, multistage, and multiform saturation attack. One of the bottlenecks of air defense/antimissile operations at a

strategic location on the sea is the independent operation of a single strategic location on the sea. Because of the short defense depth, the troops cannot deploy a defense system with a large depth and cascade interception at a strategic location on the sea [2]. Therefore, to further expand the defense depth of important locations on the sea and build a defense system for multibatch interception of important locations on the sea, this paper studies the optimization of firepower configuration for coordinated air defense operations between warships and ground air defense forces at a strategic location on the sea.

The configuration of anti-aircraft firepower units is not only the key link of air defense on the ground but also a hot issue in air defense/antimissile research [3–8]. At present, the research on the air defense firepower configuration of warships mainly focuses on the air defense formation configuration of aircraft carrier formations [9–11], ship formations [12–14], and air defense ships in maritime areas

[15–18]. Among these studies, Zhao and Liu [12] analyzed the basic principles of the formation of air defense area and established an optimization model and algorithm for the formation deployment of two ships in a maritime formation. Rao and Ravishankar [17] proposed a three-stage method based on game theory to study the deployment of air defense resources to maximize the coverage and performance of radar systems under various terrain conditions. Aiming at the problem of coordinated deployment of air defense weapon systems in multiple important bases to defend against UAV attacks, Xue et al. [18] constructed a multiweapon cooperative defense model according to the performance of each defense system, and further designed a genetic algorithm to solve it. However, few studies were conducted on the formation configuration of the naval formation and the cooperative air defense operations of the strategic locations on the sea. Limited literature [19] studied the issue of combat firepower distribution of island-ship integrated air defense dynamic weapons. With the support of warships, the decision-making model of island-ship cooperative dynamic weapon utilization was established. But there was no quantitative analysis of the firepower configuration of warships and islands and reefs for cooperative air defense operations. Ma et al. [20] studied the deployment of warships to support islands and reef air defense operations. Taking the maximum cover angle as the criterion, they established a configuration model of a single ship supporting air defense operations on islands and reefs and a two-ship configuration model. But they did not consider the firepower configuration of warships and air defense forces deployed at strategic locations on the sea for coordinated air defense operations.

Aiming at optimizing the configuration of warships in coordination with coastal air defense firepower units at strategic locations on the sea, this paper firstly builds a firepower unit configuration model of the ground air defense system to deal with the small area of strategic locations on the sea and analyzes the defense depth of the end defense line. Secondly, this paper builds a coordinated air defense configuration model between warships and air defense forces deployed at strategic locations on the sea and quantitatively analyzes the defense depth of the midrange defense line constructed in front of the warships to construct the maximum defense depth at strategic locations on the sea. Thirdly, according to the air defense firepower configuration of the ship's coordinated maritime strategic location; this paper constructs the ship's coordinated maritime strategic location defense effectiveness model according to the random service system theory. Finally, based on the midrange and terminal double-layer defense model constructed in this paper, an example simulation analysis is carried out, verifying that the model is reasonable and effective.

## 2. The Configuration Model of the Air Defense Firepower Unit at a Strategic Location on the Sea

The air attack weapons in air defense operations at strategic locations on the sea include various combat aircraft, tactical missiles, aerial bombs, and rocket bombs [21]. In this paper,

aircraft are considered as incoming targets to study the configuration of antiaircraft fire units. The air defense operations of strategic locations on the sea are not only related to the cover capability of ground air defense weapon systems but also the performance of enemy aviation equipment, the distance to drop bombs, and the location of the ground antiaircraft weapon fire unit configuration.

**2.1. Enemy Mission Line.** During air defense operations at strategic locations on the sea, enemy aircraft carrying aviation munitions must be eliminated outside the enemy mission line. The enemy mission line [22] is a critical line for the defense of strategic locations on the sea. Once the enemy plane flies over this boundary line, it can attack the target at strategic locations on the sea and complete its air strike mission, as shown in Figure 1.

When the enemy plane launches air-to-ground missiles (or drops bombs) at a point  $T_1(T_2)$ , the distance between the enemy mission line and the center of the protected object is given as follows:

$$R_{rwx} = r_0 + r_s + r_k(r_f). \quad (1)$$

$r_0$  is the radius of the defended object, and  $r_s$  is the effective radius of the air-to-ground missile (bomb)

$r_k$  is the horizontal distance of the air-to-ground missile or cruise missile after launch

$r_f$  is the horizontal flight distance of the bomb dropped by the aircraft

**2.2. Defensive Depth and Route Shortcut.** To protect strategic locations on the sea, antiaircraft fire units must destroy incoming targets outside the enemy mission line. To improve defense efficiency, when the air defense firepower unit is configured, it is necessary to configure a certain defense depth according to the incoming direction of the enemy. The size of the defense depth determines the number of shots fired by the antiaircraft fire units on incoming targets. Assuming that the time interval of the continuous firing of an antiaircraft fire unit is  $t_0$ , and the flight speed of the incoming target is  $v_0$ , the defense depth required by the antiaircraft fire unit to shoot  $n$  times can be estimated as follows:

$$L_{zs} = \Delta L + v_0 t_0 (n - 1), \quad (2)$$

where  $\Delta L$  represents the possible horizontal distance reduction of the kill zone under complex conditions. If the antiaircraft fire unit adopts the shooting-observing-shooting mode, the defense depth required for  $n$  shots can be estimated as follows:

$$L_{zs} = \Delta L + v_0 \left( t_{gc} (n - 1) + \sum_{k=2}^n t_k \right). \quad (3)$$

$t_{gc}$  is the observation and evaluation time of the air defense weapon system

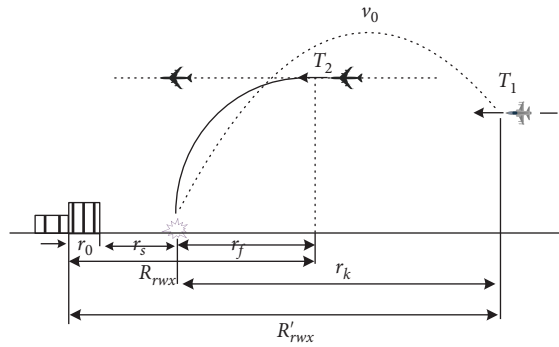


FIGURE 1: Enemy mission line.

$t_k$  is the flight time between the  $k$ -th interceptor missile and the incoming target, which is related to factors such as the route shortcut and flight height of the incoming target

Route shortcut refers to the vertical distance from the center of the fire launch unit to the projection line or the tangent of the projection line of the air attack target track at sea level. As shown in Figure 2, the route shortcut  $|O_1P|$ , usually denoted by  $P$ , is an important parameter to determine whether the projectile can be launched or fired. In fact, as the route shortcut of the incoming target increases, the interception ballistic curvature will increase, and the required overload of the ship-to-air missile will also increase. But the available overload of the ship-to-air missile is unchanged. These will reduce the ratio of available overload to required overload, and increase the guidance error of the missile, thereby reducing the single-shot kill probability of the ship-to-air missile [23].

**2.3. Configuration Model of Antiaircraft Firepower Units for Strategic Locations on the Sea.** The configuration of air defense firepower units is a key link in air defense/antimissile defense operations at strategic locations on the sea. Due to the special geographical and natural environment conditions, only limited air defense forces can be deployed in strategic locations on the sea, and some small areas can only be equipped with portable air defense missiles. When establishing an antiaircraft fire unit, we must position the antiaircraft weapon platform at a certain distance from the target being defended to maximize the combat capability of the antiaircraft weapon system and ensure that it can be fired multiple times in front of the enemy mission line. For the air defense operations of strategic locations on the sea, considering its small area, we should try to deploy the fire units along the coastline according to the main combat direction of the enemy when configuring the air defense fire units, expanding the defense depth of air defense fire units (as shown in Figure 2).

Assuming that the center of the important sea area is  $O$ , and the horizontal main combat direction of the important sea area is  $BOD$ , where  $\angle BOD = 2\varphi$ .  $O_1$  is the configuration point of the antiaircraft firepower unit,  $d_{pz} = |OO_1|$  is the configuration distance from the center of the defended

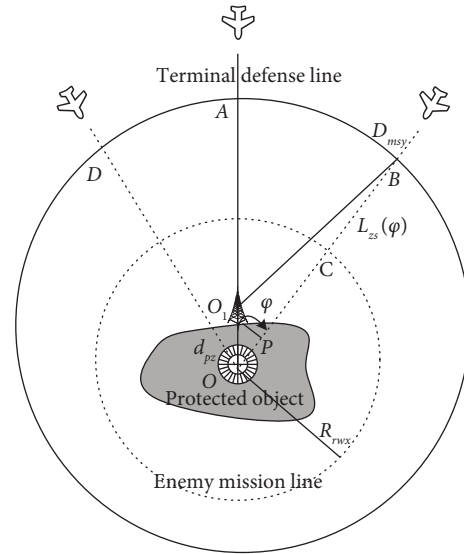


FIGURE 2: Schematic diagram of air defense firepower configuration in a strategic location on the sea.

object. The enemy mission line is  $R_{rwx}$ . The kill zone far boundary of the antiaircraft fire unit is  $D_{msy} = |O_1B|$ , and the antiaircraft fire unit has a border defense depth of  $L_{zs}(\varphi) = |BC|$ . In  $\Delta O_1OB$ , using the triangular cosine theorem, we can obtain as follows:

$$D_{msy} = d_{pz}^2 + (R_{rwx} + L_{zs}(\varphi))^2 - 2d_{pz}(R_{rwx} + L_{zs}(\varphi)). \quad (4)$$

From formula (4), it can be calculated that when air defense firepower is deployed on the coastline of important coastal areas, the minimum defense depth in the main combat direction is  $L_{zs}(\varphi)$ , and the corresponding route shortcut is  $P_{\max} = (L_{zs}(\varphi) + R_{rwx})\sin\varphi$ . In addition, it can be seen from Figure 2 that the maximum defense depth is  $L_{zs} = D_{msy} - R_{rwx}$ . when the route shortcut is zero.

### 3. The Air Defense Firepower Configuration Model of Warships Cooperating with the Strategic Location on the Sea

**3.1. The Air Defense Firepower Configuration Model of a Single Warship Cooperating with the Strategic Location on the Sea.** Figure 3 is a schematic diagram of the air defense firepower configuration of a single ship supporting a strategic position on the sea. The warship is preconfigured  $O'$ , which forms a double-layer interception defense system with antiaircraft firepower at the strategic position on the sea. Taking into account the large forward distance of the warship and the range far boundary of the ship-to-air missile, and the relatively small area of the strategic position on the sea, the configuration distance  $|OO_1|$  between the center and the antiaircraft firepower mentioned in Section 2.3, compared to ship forward distance and missile range boundaries, is negligible. For the convenience of modeling and analysis, it is assumed that the terminal defense line and the enemy mission line at the strategic position on the sea are concentric circles. The forward distance of the warship is  $d_{pz} =$



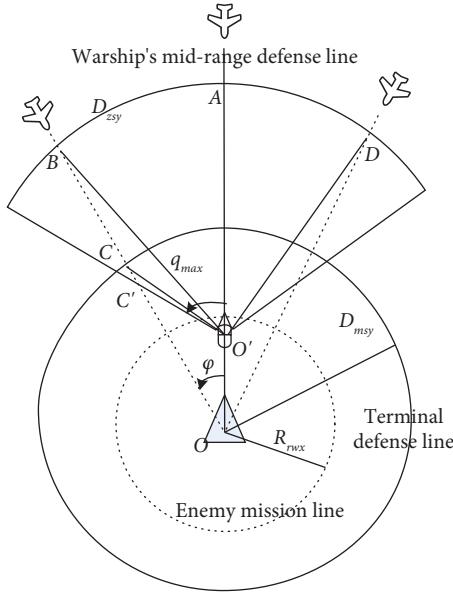


FIGURE 4: Schematic diagram 2 of the air defense configuration of a single warship cooperating with a strategic location on the sea.

$$f(\theta) = \begin{cases} \frac{1}{b-a}, & a \leq \theta \leq b, \\ 0, & \text{otherwise.} \end{cases} \quad (8)$$

Assuming that the azimuth of the warship deployment is  $\alpha$ . It can be seen from Figure 5 that the effective defense depth of the warship is defined as follows:

$$L_{zs}(\theta) = \frac{D_{zsy} \sin(q_{max} + \alpha - \theta - \theta_1)}{\sin(q_{max} + \alpha - \theta)}, \quad (9)$$

where  $\theta_1 = \arcsin(d_{pz} \sin \theta / D_{zsy})$ . Then, the expected defense depth of a warship in the main combat sector is defined as follows:

$$\begin{aligned} E(L_{zs}(a, b)) &= \int_a^b L_{zs}(\theta) f(\theta) d\theta \\ &= \int_a^b \left( \frac{D_{zsy} \sin(q_{max} + \alpha - \theta - \theta_1)}{\sin(q_{max} + \alpha - \theta)} \right) f(\theta) d\theta. \end{aligned} \quad (10)$$

The defense depth of the overlapping kill area of the warship's coordinated antiaircraft fire  $L'_{zs}(\theta) = |CC'|$  is given as follows:

$$\begin{aligned} L'_{zs}(\theta) &= D_{msy} - (|OB| - |BC|) \\ &= D_{msy} - D_{zsy} \left( \frac{\sin(\theta + \theta_1)}{\sin \theta} - \frac{\sin(q_{max} + \alpha - \theta - \theta_1)}{\sin(q_{max} + \alpha - \theta)} \right). \end{aligned} \quad (11)$$

As can be seen from Figure 5, when there comes to a different target attack angle, there needs a different method to calculate the air defense firepower defense depth of the warship cooperating with strategic positions on the sea.

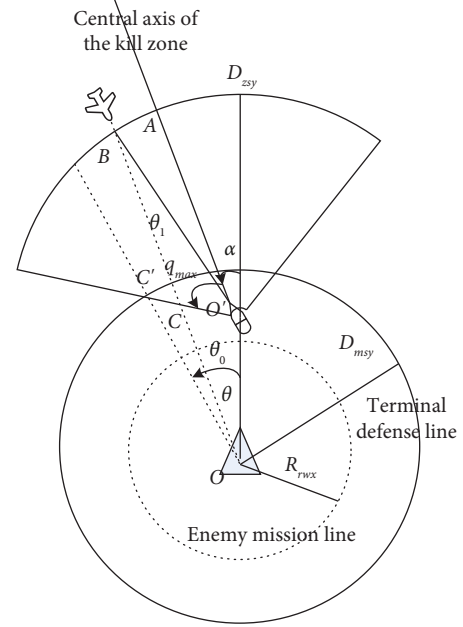


FIGURE 5: The defense depth of a single warship cooperating with a strategic location on the sea.

The specific calculation formula is defined as follows:

$$l_{zs}(\theta) = \begin{cases} L_{zs}(\theta) + (D_{msy} - R_{rwx} - L'_{zs}(\theta)), & \theta \leq \theta_0; \\ L_{zs}(\theta) + D_{msy} - R_{rwx}, & \theta_0 < \theta < \varphi, \end{cases} \quad (12)$$

where  $\theta_0 = q_{max} + \alpha - \arcsin(d_{pz} \sin(\alpha + q_{max}) / D_{msy})$ . Then, the formula for calculating the expected defense depth of a single warship cooperating with strategic positions on the sea is given as follows:

$$E(l_{zs}(a, b)) = \int_a^b l_{zs}(\theta) f(\theta) d\theta. \quad (13)$$

### 3.3. The Air Defense Firepower Configuration Model of the Two Warships Cooperating with Strategic Positions on the Sea.

In the air defense operations of warship formations cooperating with strategic positions on the sea, the defense configuration includes linear configuration and circular configuration, etc. In the air defense of two warships cooperating with strategic positions on the sea, the central axis of the main combat direction of strategic positions on the sea, which can maximize the defense sector of the warship formation, as shown in Figure 6. The larger the configuration distance between the two ships, the larger the defense sector and the smaller the overlapping area of firepower. Conversely, the smaller the configuration distance between the two ships, the smaller the defensive sector and the larger the overlapping area of firepower. Meanwhile, the larger the forward configuration distance of the two ships, the smaller the defense sector and the greater the defense depth. Conversely, the smaller the forward configuration distance, the larger the defense sector and the smaller the defense depth. Therefore, when configuring the antiaircraft fire unit of the two warships cooperating

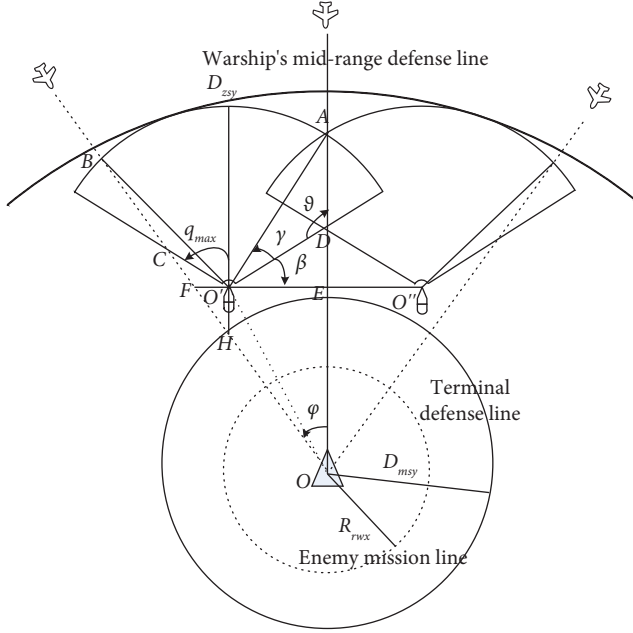


FIGURE 6: The configuration model of air defense firepower of two warships cooperating with a strategic location on the sea.

with strategic positions on the sea, one needs to consider the configuration distance between the two ships, as well as the forward configuration distance.

**3.3.1. The Configuration Distance between the Two Warships.** The limiting condition for the configuration distance between two warships is under the condition that the sum of the defense depths of the two warships' overlapping firepower area should not be less than the defense depth of a single ship's zero route shortcut, the configuration distance between the two warships should be as large as possible to expand the defense sector [24].

The far boundary of the warship defense is  $D_{zsy}$ , that is,  $|AD| = 0.5D_{zsy}$  in Figure 6. In  $\triangle AO'D$ , by the law of sine, we obtain

$$\frac{|AD|}{\sin \gamma} = \frac{|AO'|}{\sin \vartheta}, \frac{|O'D|}{\sin(\gamma + \vartheta)} = \frac{|AO'|}{\sin \vartheta}, \quad (14)$$

where  $\vartheta = \pi - q_{\max} = |AO'| = 2|AD| = D_{zsy}$ , thus

$$|O'D| = D_{zsy} \left( \sqrt{1 - \frac{1}{4}\sin^2 q_{\max}} - \frac{1}{2}\cos q_{\max} \right). \quad (15)$$

Then, the configuration distance between the two warships is defined as follows:

$$\begin{aligned} d_{O'O''} &= |O'O''| \\ &= 2D_{zsy} \left( \sqrt{1 - \frac{1}{4}\sin^2 q_{\max}} - \frac{1}{2}\cos q_{\max} \right) \sin q_{\max}. \end{aligned} \quad (16)$$

**3.3.2. The Model of the Forward Configuration Distance between the Two Warships.** The principle of configuring the forward distance between two warships is the same as that of a

single warship. When the configuration distance between the two warships and the main combat sector is determined, the distance between the two warships and the strategic positions on the sea gradually increases, and the air defense depth between the two warships and strategic positions on the sea becomes larger. When the forward configuration distance of the two warships reaches a certain level, the defense depth shows a decreasing trend with the greater forward configuration distance of the warships. As shown in Figure 6, the two warships are deployed at points  $O', O''$  (outside the terminal defense line at strategic positions on the sea), and the main combat sector angle of the strategic positions on the sea is  $2\varphi$ . Assuming that the minimum value of the horizontal defense depth of the warships is  $L_{zs}$ , then when the boundary of the combat sector is  $|BC| = L_{zs}$ , the configuration distance  $|OO'| = |OO''|$  between the warship and the strategic positions on the sea reaches its maximum value.

At this moment, using the triangle sine theorem, we can obtain

$$\begin{cases} \frac{|BC|}{\sin \angle CO'B} = \frac{|O'B|}{\sin \angle BCO'}, \\ \frac{|O'C|}{\sin \angle CBO'} = \frac{|O'B|}{\sin \angle BCO'}, \\ \frac{|O'H|}{\sin \angle O'CH} = \frac{|O'C|}{\sin \varphi}, \end{cases} \quad (17)$$

where  $\angle BCO' = \pi + \varphi - q_{\max} = |BC| = L_{zs}$ ,  $|O'B| = D_{zsy}$ , after simplification,

$$|O'H| = \frac{D_{zsy} \sin(q_{\max} - \varphi - \angle CO'B)}{\sin \varphi}, \quad (18)$$

where  $\angle CO'B = \arcsin(L_{zs} \sin(q_{\max} - \varphi)/D_{zsy})$ . From the proportional relationship between  $|O'H|$  and  $|OE|$ , the distance from the strategic position on the sea to the configuration center  $E$  of the two warships can be obtained.

$$|OE| = \frac{D_{zsy} \sin(q_{\max} - \varphi - \angle CO'B) + 0.5d_{O'O''} \cot \varphi}{\sin \varphi}. \quad (19)$$

The maximum value of the distance from the strategic position on the sea to the two warships.

$$d_{oo'}^{\max} = \sqrt{\frac{1}{4}d_{O'O''}^2 + |OE|^2}. \quad (20)$$

When the deployment point  $O', O''$  of the two warships is located within the terminal defense line at strategic positions on the sea, as shown in Figure 7, the overlapping airspace of anti-aircraft firepower of warships cooperating with the strategic position on the sea is relatively large, as well as the defense sector angle. When the two warships are at the boundary distance  $|BC| = L_{zs}$  of the main combat sector, the forward configuration distance of the warships takes the minimum value.

According to the geometric relationship in Figure 7, we can get



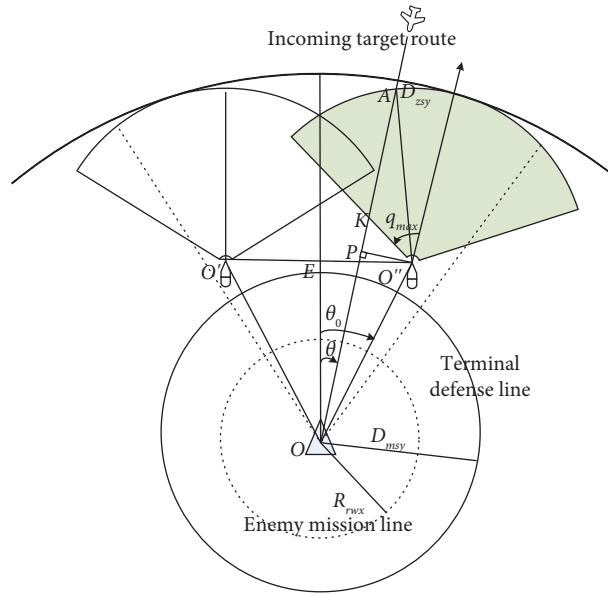


FIGURE 8: The defense depth of the two warships cooperating with a strategic location on the sea.

Comparing Figures 6 and 7, the forward distance of the two warships in Figure 6 is relatively large, and the defense depth of the two warships cooperating with the strategic position on the sea is large as well. In Figure 7, however, the overlapping area of the air defense firepower between the two warships and the strategic position on the sea is large,

and the defense depth of the two warships cooperating with the strategic position on the sea is small. In fact, according to the forward distance  $d_{OO''} \in (d_{OO''}^{\min}, d_{OO''}^{\max})$ , the defense depth of the two warships cooperating with the strategic position on the sea can be obtained as follows:

$$l_{zs}(\theta) = \begin{cases} L_{zs}(\theta) + D_{msy} - R_{rwx}; \\ \quad \text{if } d_{OO''}(\cos(\theta_0 - \theta) + \sin(\theta_0 - \theta)\cot q_{\max}) \geq D_{msy} \\ \sqrt{D_{zy}^2 - d_{OO''}^2 \sin^2(\theta_0 - \theta)} + d_{OO''} \cos(\theta_0 - \theta) - R_{rwx}; \text{ other.} \end{cases} \quad (27)$$

The expected defense depth of the two warships cooperating with the strategic position on the sea is given as follows:

$$E(L_{zs}(a, b)) = \int_a^b l_{zs}(\theta) f(\theta) d\theta. \quad (28)$$

#### 4. Efficiency Analysis of the Air Defense of Warships Cooperating with the Strategic Position on the Sea

4.1. Efficiency Model of Air Defense of the Strategic Position on the Sea. The main air strikes faced by the strategic position on the sea are multidirectional, multistage, and multiform saturation attacks. In the event of a large-scale air attack, the defense system at the strategic position on the sea can be regarded as a random service system. The arrival process of the incoming target obeys the Poisson distribution with parameter  $\lambda$ , that is,

$$P_k(t) = \frac{(\lambda t)^k}{k!} e^{-\lambda t}. \quad (29)$$

$k = 0, 1, 2, \dots$  and  $t > 0$ ,  $P_k(t)$  demonstrates the probability that  $k$  targets will strike within time  $t$ . The anti-air defense at the strategic position on the sea adopts the principle of “first to come, first to be served” and uses the shooting method of “shooting-observing-shooting.” Each anti-aircraft fire unit is regarded as a “service counter,” and the “service” time for incoming targets obeys the negative exponential distribution of a parameter  $\mu$ , that is,

$$P(\tau < t) = 1 - e^{-\mu t}, t \geq 0, \quad (30)$$

where  $\mu = 1/t_{smean}$ ,  $t_{smean}$  represents the average “service” time to the target. It is assumed that the time of the incoming target flying over the kill zone obeys a negative exponential distribution with parameter  $\nu$ , that is,

$$P(\tau < t) = 1 - e^{-\nu t}, t \geq 0, \quad (31)$$



where  $v = 1/w_{mean}$  and  $t_{wmean}$  is the average time that the target stays in the kill zone, which depends on the incoming target's flight speed  $v_0$  and the defense depth  $L_{zs}$  of the anti-aircraft weapon fire units defending it. Incoming targets stay and fly in the launch area, which is equivalent to "customers" queuing for service in the service system. The incoming target flew away from the launch area and successfully penetrated the defense, which is equivalent to that of a "customer" who has been queuing for too long in the service system automatically left.

According to the above-mentioned analysis and assumptions, the air defense of the strategic position on the sea can be regarded as the M/M/n/c queuing model with a limited waiting time. Assuming that  $N(t)$  represents the number of targets in the air defense weapon system at the  $t$  epoch, the possible states of the system are given as follows:

$A_0$ : There are  $n$  firepower channels idle in the system, and there are 0 targets;

$A_1$ : The system has 1 fire channel firing and 1 target;

.....

$A_n$ : All fire channels of the system are under firing, there are  $n$  targets;

$A_{n+1}$ : All fire channels of the system are under firing, and there is 1 target waiting to be fired;

.....

$A_{n+s}$ : All fire channels of the system are under firing, and there are  $s$  targets waiting to be fired.

According to the principle of equilibrium state, the equation system can be obtained as follows:

$$\begin{cases} A_0: \mu p_1 - \lambda p_0 = 0; \\ A_1: 2\mu p_2 - (\lambda + \mu)p_1 + \lambda p_0 = 0; \\ \dots \\ A_k: (k+1)\mu p_{k+1} - (\lambda + k\mu)p_k + \lambda p_{k-1} = 0; \\ \dots \\ A_n: (n\mu + v)p_{n+1} - (\lambda + n\mu)p_n + \lambda p_{n-1} = 0; \\ A_{n+1}: (n\mu + 2v)p_{n+2} - (\lambda + n\mu + v)p_{n+1} + \lambda p_n = 0; \\ \dots \\ A_{n+i}: (n\mu + (i+1)v)p_{n+i+1} - (\lambda + n\mu + v)p_{n+i} + \lambda p_{n+i-1} = 0; \\ \dots \\ A_{n+s}: (n\mu + sv)p_{n+s} - \lambda p_{n+s-1} = 0. \end{cases} \quad (32)$$

According to  $p_0 + p_1 + p_2 + \dots + p_n + \dots + p_{n+s} = 1$ , the probability of stability can be obtained as follows:

$$\begin{cases} p_0 = \left[ \sum_{k=0}^n \frac{\rho^k}{k!} + \frac{\rho^n}{n!} \cdot \sum_{s=1}^{\infty} \frac{\rho^s}{\prod_{m=1}^s (n+m\vartheta)} \right]^{-1}; \\ p_k = \frac{\rho^k}{k!} \cdot p_0, 0 \leq k \leq n; \\ p_{n+s} = \frac{\rho^n}{n!} \left( \rho^i \left( \prod_{k=1}^i (n+k\vartheta) \right)^{-1} \right) \cdot p_0, 1 \leq i \leq s, \end{cases} \quad (33)$$

where  $\rho = \lambda P_f / \mu = \lambda P_f t_{smean}$ ,  $\vartheta = v / \mu = v_0 t_{smean} / L_{zs}$ , and  $P_f$  is the probability that the target is detected by the radar. The probability of successful penetration of the incoming target

without being shot is denoted as  $P_{ref}$ . When there are on average  $m$  targets in the system waiting to be fired, the probability of the target not being fired is given as follows:

$$P_{ref} = \frac{v}{\lambda} \sum_{s=1}^{\infty} s p_{n+s} = \frac{v/\mu}{\lambda/\mu} \sum_{s=1}^{\infty} s p_{n+s} = \frac{\vartheta}{\rho} \sum_{s=1}^{\infty} s p_{n+s} = \frac{\vartheta}{\rho} \cdot \frac{\rho^n / n! \cdot \sum_{s=1}^{\infty} s \rho^s / \prod_{k=1}^s (n+k\vartheta)}{\sum_{k=0}^n \rho^k / k! + \rho^n / n! \cdot \sum_{s=1}^{\infty} \rho^s / \prod_{m=1}^s (n+m\vartheta)} \quad (34)$$

Thus, the probability of the incoming target being shot is:  $P_{shoot} = 1 - P_{ref}$ . assuming the killing probability of the air defense firepower unit to the incoming target is  $P_{kill}$ , the defense efficiency of the strategic position on the sea is  $DF = P_{shoot} \cdot P_{kill}$ .

4.2. Efficiency Model of the Defense of the Warship Cooperating with the Strategic Position on the Sea. The defense of the warships cooperating with the strategic position on the sea can be regarded as a double-layer air defense/antimissile defense system. It is the forward-configured warship that carries out the midrange interception defense at first, and

it is the strategic position on the sea that performs terminal interception on targets that the warship has not effectively intercepted. Each layer of the defense system is treated as an M/M/n/c queuing model with a limited waiting time. Therefore, the efficiency model of the ship-

ground double-layer air defense/antimissile defense is described as follows:

The efficiency model of the warship's midrange defense is given as follows:

$$JT: \begin{cases} \rho_1 = \lambda \cdot t_{smean}^{(jt)} \cdot P_{f_1}; \vartheta_1 = \frac{v_0 t_{smean}^{(jt)}}{L_{zs}^{(jt)}}, \\ P_{shoot}^{(jt)} = 1 - \frac{\vartheta_1 / \rho_1 \sum_{m=1}^{\infty} m \rho_1^{n_1} / n_1! (\rho_1^m (\prod_{k=1}^m (n_1 + k \vartheta_1))^{-1})}{(\sum_{i=0}^{n_1} \rho_1^i / i! + \rho_1^{n_1} / n_1! \sum_{s=1}^{\infty} (\rho_1^s (\prod_{m=1}^s (n_1 + m \vartheta_1))^{-1})}); \\ DF_1 = P_{shoot}^{(jt)} P_{kill}^{(jt)}; \end{cases} \quad (35)$$

Based on the warship interception, the efficiency model of the terminal interception defense of the warship

cooperating with the strategic position on the sea is given as follows:

$$YD: \begin{cases} \rho_2 = (1 - DF_1) \lambda \cdot t_{smean}^{(dj)} \cdot P_{f_2}; \vartheta_2 = \frac{v_0 t_{smean}^{(dj)}}{L_{zs}^{(dj)}}, \\ P_{shoot}^{(dj)} = 1 - \frac{\vartheta_2 / \rho_2 \sum_{m=1}^{\infty} m \rho_2^{n_2} / n_2! (\rho_2^m (\prod_{k=1}^m (n_2 + k \vartheta_2))^{-1})}{(\sum_{i=0}^{n_2} \rho_2^i / i! + \rho_2^{n_2} / n_2! \sum_{s=1}^{\infty} (\rho_2^s (\prod_{m=1}^s (n_2 + m \vartheta_2))^{-1})}); \\ DF_1 = P_{shoot}^{(dj)} P_{kill}^{(dj)}; \end{cases} \quad (36)$$

Overall, the efficiency model of the warship cooperating with the strategic position on the sea is given as follows:

$$DF = DF_1 + (1 - DF_1) DF_2. \quad (37)$$

$\rho_i$  ( $i = 1, 2$ ) is the number of incoming targets found in the average firing time of warships and the strategic position on the sea.  $\vartheta_i$  ( $i = 1, 2$ ) represents the number of successful penetrations due to exceeding the waiting time during the average firing time.  $n_i$  ( $i = 1, 2$ ) represents the number of anti-aircraft fire units on the warship and at the strategic position on the sea, respectively. The rest of the parameters are the same as those defined above.

## 5. Simulation Experiments

It is assumed that the coordinated air defense between a strategic position on the sea and a warship forms an effective double-layer interception defense system, with the warship's front-mounted ship-to-air missiles performing the mid-range defense, and the air defense weapon systems deployed at the strategic position on the sea performing the terminal defense. Table 1 shows the performance of the relevant parameters of the firepower unit of each air defense weapon platform. The anti-aircraft firepower units configured on

warships and the strategic position on the sea are set to 4 and 6, respectively, and the probability of finding the target and the probability of killing are random numbers in the corresponding interval.

It is assumed that the maximum radius of the bombing circle of the enemy air attack weapon is 60 km, the flying height of the enemy air attack aircraft is 300 m at a flight speed  $v_0 = 300$  m/s, and the attack intensity  $\lambda = 8$  of planes per minute. The main combat sector angle at the strategic position on the sea  $2\varphi = 120^\circ$ , and the defensive combat shooting mode adopts the method of "shoot-look-shoot," and the observation and evaluation time  $t_0 = 15$  s. When configured with firepower, the warship is required to intercept the incoming targets in the main combat sector at least 2 times. Tables 2 and 3 show the relevant conclusions obtained from the air defense firepower configuration model of the warship cooperating with the strategic position on the sea constructed in Section 3.

As can be seen from Table 2, in the "shooting-observing-shooting" mode, the warship's defense depth in the main combat direction cannot be less than 30.9 km. To meet this requirement, when conducting the air defense of a single warship cooperating with the strategic position on the sea, the minimum forward distance is 27 km and the maximum

TABLE 1: Relevant parameters of firepower unit of air defense weapon system.

Parameter	Antiaircraft fire unit of the surface-to-air missile in the strategic position on the sea	Antiaircraft fire unit of warship surface-to-air missile
Kill zone far boundary (km)	80	100
Kill zone near the boundary (km)	5	3
Maximum course angle $q_{max}$ (*)	75	80
Maximum route shortcut (km)	77	98
Observation evaluation time (s)	15	15
Antiaircraft fire transfer time (s)	10	10
Average flight speed of antiaircraft missiles (m/s)	900	900
Antiaircraft fire unit	8	6
Probability of finding the target $P_f$	Rand (0.8, 1)	Rand (0.8, 1)
Single-shot missile kill probability $P_{kill}$	Rand (0.5, 0.9)	Rand (0.5, 0.9)

TABLE 2: Conclusions about the distance of firepower configuration between the warship cooperating with a strategic location on the sea.

Parameter	Minimum value (km)	Maximum value (km)	Remarks (km)
The forward distance of air defense of single-warship cooperating with the strategic position on the sea	27	75	$L_{zs}^{min} = 30.9$
The distance between the two warships	$d_0$	154	$d_{oo'} = 60$
The distance between the coordinated air defense of two warships and the strategic position on the sea	40	98	
The vertical distance between the configuration line of the two warships and the strategic position on the sea	33	75	

TABLE 3: Results of cooperative defense in depth.

Parameter	Single-warship	Two-warship	Remarks
Warship defense depth expectation (km)	90.5	98.4	
Depth expectation in the overlapping area of coordinated antiaircraft fire (km)	39.8	22.7	Depth expectation of independent air defense of the strategic position on the sea: 51.2 km
Coordinated air defense depth expectation (km)	100.7	125.7	

is 75 km. When conducting the air defense of two warships cooperating with the strategic position on the sea, without considering the communication distance and other factors, the maximum distance between the two warships is 154 km, and the minimum value is the minimum distance between the two warships under electromagnetic interference. When the distance between the two warships is 60 km, the configuration distance between the warships and the strategic position on the sea ranges from 40 km to 98 km, and the vertical distance between the two warships' configuration line and the strategic position on the sea ranges from 33 km to 55 km. Simulation parameters: when the single-warship coordinated air defense forward distance is 40 km, the two-warship coordinated air defense distance is 60 km, and the distance between the two warships is 60 km, to calculate the expected value of the defense depth within the range of the enemy's incoming direction. It is not difficult to see from Table 3 that the horizontal air defense depth of the two warships' coordinated air defense is better than that of the

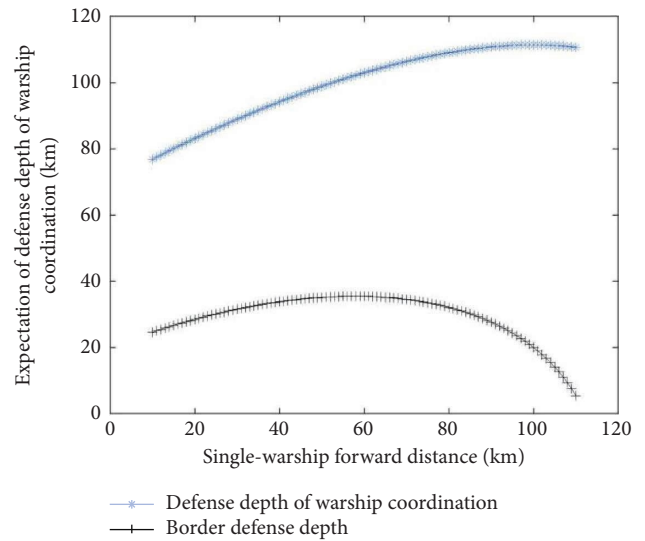


FIGURE 9: Single lead distance and defense depth.

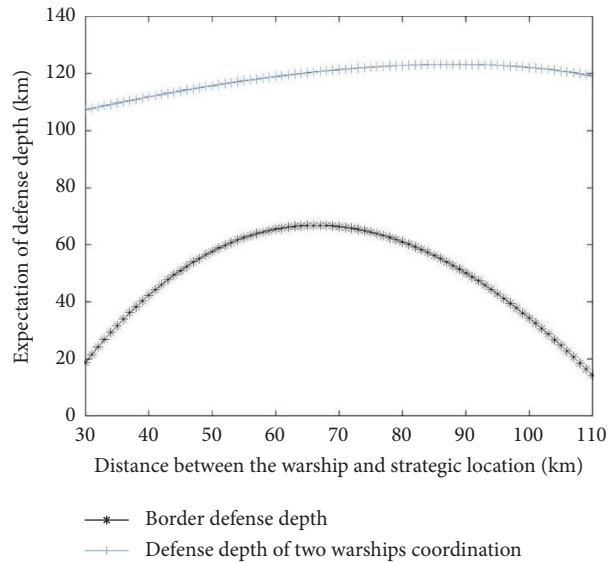


FIGURE 10: The forward distance and defense depth of the two warships.

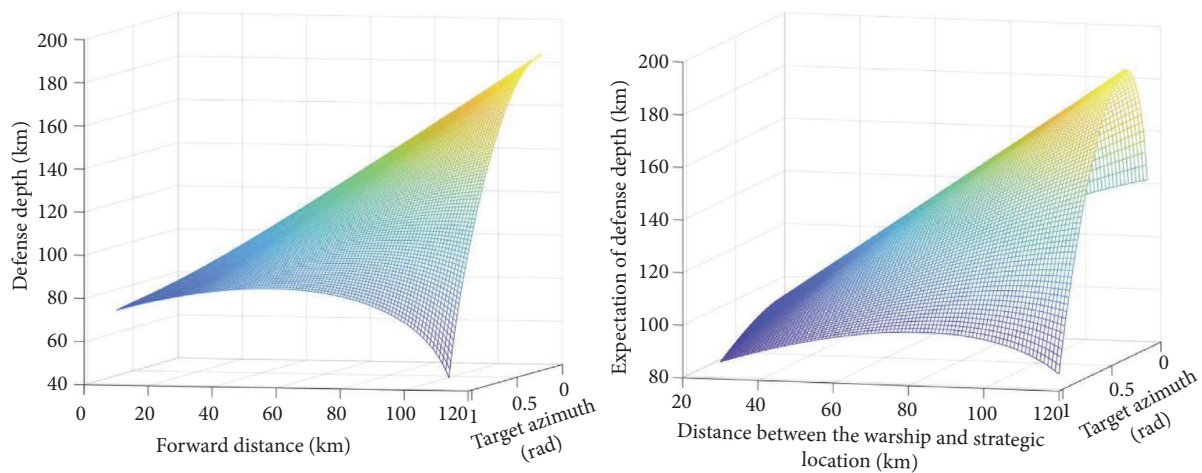


FIGURE 11: Schematic diagram of the depth, forward distance, and target azimuth of the warship cooperating with a strategic location on the sea.

single warship's coordinated air defense. The expected value of the horizontal defense depth of a single warship cooperating with the strategic position on the sea is 100.7, while that of two warships cooperating with the strategic position on the sea is 125.7. In the independent air defense operation of the strategic position on the sea, the expected defense depth is 51.2 km. The fact is that the conclusions of Table 3 are obtained when the configuration distance is determined. To further analyze the relationship between the defense depth and the configuration distance of air defense firepower units, this paper uses the configuration distance as a variable in the simulation, and obtains a schematic diagram of the horizontal defense depth, the border defense depth, and the configuration distance, as shown in Figures 9 and 10.

It can be seen from the figure that whether the coordinated air defense is conducted by a single warship or two warships, the expected value of the horizontal defense depth increases with the increase of the warship configuration

distance. When the configuration distance reaches a certain level, the defense depth tends to be stable. However, if the forward distance is too large or too small, the border defense depth in the main combat direction cannot meet the requirements of warships for performing two interceptions. Combining Table 2 and Figures 9 and 10, it can be seen that under a single-warship coordinated defense, the configuration distance is less than 27 km or greater than 75 km, or under a two-warship coordinated defense, the configuration distance is less than 40 km or greater than 97 km. In this case, the border defense depth is less than 30.9 km, which does not meet the defense requirements.

The horizontal defense depth of air defense of warships cooperating with the strategic position on the sea is not only related to the configuration distance but also related to parameters such as the azimuth angle of the incoming target, the azimuth angle of warship deployment, and the configuration distance between the two warships. Figure 11 reflects

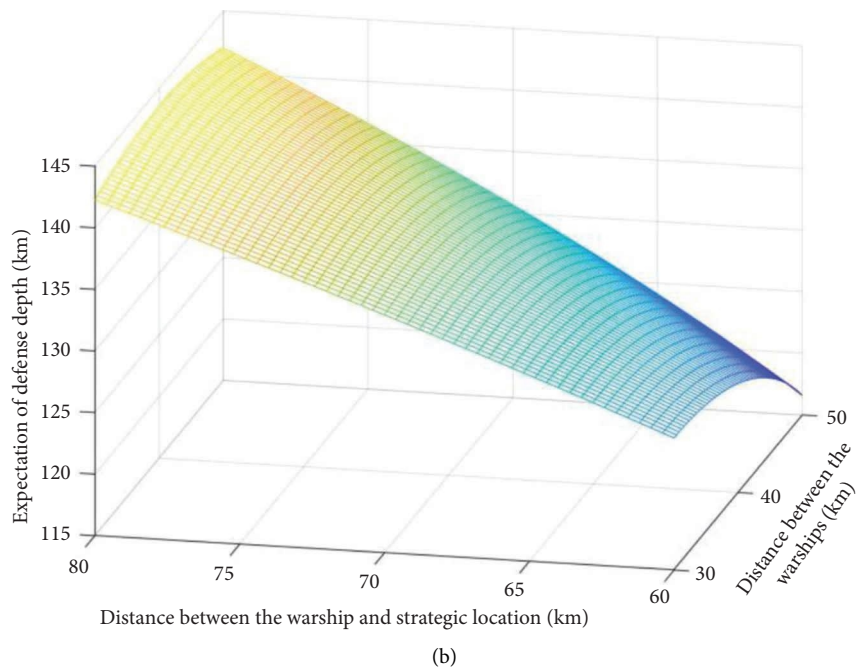
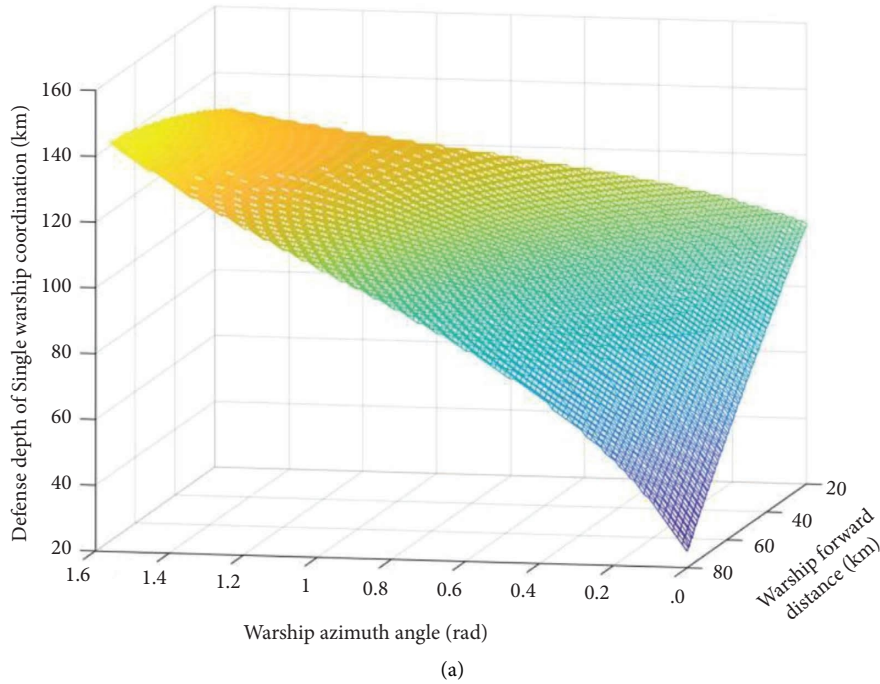


FIGURE 12: The relationship between the depth of defense for the azimuth of the warship, and the configuration distance of warship-ground.

the relationship between the defense depth, the configuration distance, and the direction of the incoming target under air defense of the single warship and the two warships cooperating with the strategic position on the sea. As can be seen from the figure, when the incoming direction is facing the center of the defense kill zone, the defense depth is relatively large, and the configuration distance gradually increases. When the attack angle is relatively large and close to the boundary of the combat direction, the defense depth first increases and then decreases with the configuration distance. In addition, the depth expectation of two-warship

coordinated defense is significantly higher than the data of single-warship coordinated defense.

Figure 12(a) takes the direction angle of the incoming target as an example and shows the relationship between the air defense depth of the warship cooperating with the strategic position on the sea, the warship's deployment azimuth, and the forward distance. The smaller the warship's deployment azimuth angle and the incoming direction angle, the greater the defense depth. As the deployment azimuth increases, the greater the deployment distance, the greater the defense depth.

TABLE 4: Simulation results of cooperative defense effectiveness between the warship and strategic location on the sea.

Coordinated defense type		$\rho$	$\vartheta$	$P_{ref}$	$P_{shoot}$	$DF$
Single-warship coordinated defense	Single-warship medium-range defense effectiveness	10.08	0.2913	0.6296	0.3704	0.3148
	Terminal defense effectiveness at the strategic position on the sea	6.4050	0.2388	0.1337	0.8663	0.7797
	Total	—	—	—	—	0.8491
Two-warship coordinated defense	Two-warship medium-range defense effectiveness	9.3600	0.2453	0.1709	0.8291	0.7047
	Terminal defense effectiveness at the strategic position on the sea	2.7603	0.2388	0.0043	0.9957	0.8962
	Total	—	—	—	—	0.9693

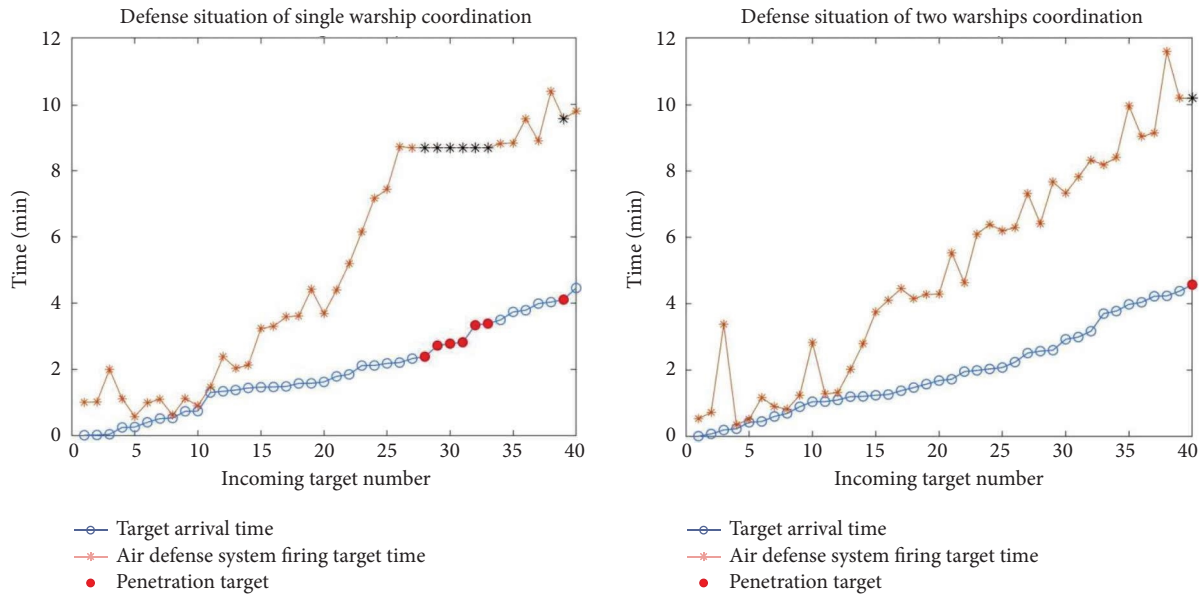


FIGURE 13: Target arrival time and penetration.

Figure 12(b) reflects the relationship between the defense depth, the configuration distance between the two warships, and the distance between the warship and the ground under the air defense of two warships cooperating with the strategic position on the sea. As can be seen from the figure, as the distance between the two warships increases, the defense depth decreases. But in fact, the larger the defense sector of the two warships, the greater the distance between the two warships and the strategic position on the sea, and the defense depth also increases.

Therefore, ignoring other factors, when optimizing the configuration of air defense firepower units of a single warship cooperating with the strategic position on the sea, the azimuth angle of the warship should maintain a small angle with the direction of the incoming target. Premised by meeting the requirements of the warship's defense depth in the main combat direction, the forward distance of the warship should be as forward as possible. Under the defense of two warships cooperating with the strategic position on the sea, the configuration distance between the two warships is determined according to the enemy's main attack sector and the antiaircraft far boundary of the antiaircraft fire unit. On the premise of meeting the defense depth requirements of the main combat sector, the small distance between the two warships is conducive to the coordinated defense of the

two warships. It effectively increases the overlapping area of air defense firepower in the center of the combat sector and increases the probability of intercepting incoming targets. In addition, under the condition of meeting the defense depth requirements of the main combat sector, the greater the distance between the two warships and the strategic position on the sea, the greater the expected value of the defense depth.

According to the abovementioned analysis of the coordinated defense depth of warships cooperating with the strategic position on the sea, the efficiency model of coordinated defense, and the parameters of the combat scenario, this paper uses MATLAB to conduct random simulations. After 100 simulations, the conclusions related to cooperative defense effectiveness between the warship and strategic location on the sea are shown in Table 4 and Figure 13.

It can be seen from the simulation results that the cooperative defense effectiveness between two warships and strategic locations on the sea is 0.9693, which is superior to that between a single warship and strategic location on the sea at 0.8491. This is because the defense depth in the defense of two warships cooperating with the strategic position on the sea is larger than that in a single-warship coordinated defense. Moreover, the two-warship coordinated defense usually has a large number of air defense firepower units, which can effectively form alternate echelon interceptions,

thereby improving interception efficiency. It can be seen from Figure 13 that when the number of attacking warships reaches 40, in the single-warship coordinated defense system, 7 attacking targets penetrated the defense without being shot, while only 1 penetrated the defense in the two-warship cooperated defense system. In fact, among the plans on warships supporting the air defense of the strategic location on the sea, the independent air defense of the strategic location on the sea shows an efficiency of 0.6218, which is far lower than the efficiency of the air defense of warships cooperating with the strategic position on the sea. It can be seen that under the simulation background, the defense efficiency of the two-warship coordinated defense is 96.93%, which is much higher than that of the independent air defense at the strategic location on the sea. Furthermore, when the strength of the incoming target is A (frames/min), the defense efficiency of two-warship coordinated defense remains above 80%, while that of the independent defense at the strategic location on the sea is less than 50%. Overall, it is fair to say that the two-warship coordinated air defense can greatly improve defense efficiency.

## 6. Conclusion

Aiming at the optimization of the firepower configuration for air defense operations at a strategic location on the sea, this paper comprehensively analyzes the influence of various elements of air defense on the firepower configuration according to the actual situation of the air defense combat battlefield environment. Based on the coastal defense forces and warship anti-aircraft firepower units deployed at the strategic location on the sea, this paper constructs a firepower configuration model for coordinated air defense operations between warships and the strategic location on the sea. Accordingly, the calculation formulas of the forward distance and the expected value of the defense depth of the single warship and two warship air defenses cooperating with the strategic position on the sea are proposed. In addition, through simulation examples, this paper also analyzes the influence of parameters such as the azimuth angle, forward distance, and incoming target azimuth angle of warship deployment on the configuration optimization of air defense firepower units. The optimization model and calculation formulas constructed in this paper can provide a certain theoretical basis for the configuration of coordinated air defense firepower units between warships and the strategic location on the sea. In the follow-up research, we will further discuss the configuration optimization of the integrated air defense firepower unit of reefs, seas, and air under the coordination of long-range aviation, early-warning aircraft, and other forces.

## Data Availability

The data that support the findings of this study are available within the article.

## Conflicts of Interest

The authors declare that there are no conflicts of interest regarding the publication of this paper.

## Acknowledgments

This research was supported by grant JY2020A016 from the Military Postgraduate Funding Projects.

## References

- [1] X. X. Ma, K. N. Teng, and X. L. Hou, "Models to calculate the deployment distance of reef air defense fire units," *Ordnance Industry Automation*, vol. 36, no. 10, pp. 38–41, 2017.
- [2] F. Han and G. Chen, "Characters and countermeasures of island air defense," *The 4th China command and Control Conference*, vol. 1, no. 1, pp. 338–342, 2016.
- [3] P. Z. Shen, L. B. Yang, and P. Y. Wang, "Research on operational effectiveness of surface-to-air missile air defense system deployed in multiple fire units," *Fire Control and Command Control*, vol. 45, no. 1, pp. 1–6, 2020.
- [4] O. Karasakal, "Air defense missile-target allocation models for a naval task group," *Computers & Operations Research*, vol. 35, no. 6, pp. 1759–1770, 2008.
- [5] L. Li, F. Liu, G. Long, H. Zhao, and Y. Mei, "Performance analysis and optimal allocation of layered defense M/M/N queueing systems," *Mathematical Problems in Engineering*, vol. 2016, no. 5, 21 pages, Article ID 5915918, 2016.
- [6] J. Wang, S. C. Lou, Y.-long Wang, and Fa-wen Wu, "Quantitative analysis of deployment distance between fire units based on the composite disposition of the air defense missiles," *Systems Engineering and Electronics*, vol. 28, no. 2, pp. 263–265, 2006.
- [7] E. Johansson and S. Karlsson, *Deployment of Air Defense*, Chalmers University of Technology, Gothenburg, Sweden, 2019.
- [8] H. W. Sun, X. F. Xie, and W. Pang, "Integrated air defense firepower intelligence optimal assignment based on improved firepower assignment model," *Control and Decision*, vol. 35, no. 5, pp. 1102–1112, 2020.
- [9] C. R. Piao, "Disposition method of long-range anti-aircraft forces for aircraft-carrier formation," *Ship Electronic Engineering*, vol. 40, no. 8, pp. 19–23, 2020.
- [10] Y. S. Zhang and N. N. Yang, "Investigation on air defense force requirement of short-range guard vessel in aircraft carrier formation," *Ship Science and Technology*, vol. 33, no. 7, pp. 112–114, 2011.
- [11] Y. L. Han, J. G. Yan, Y. Lin, Q. Y. Zhang, and Q. S. Huo, "Air ship missile carrier aircraft attack array model research," *Applied Mechanics and Materials*, vol. 687–691, pp. 1436–1442, 2014.
- [12] J. Y. Zhao and F. Liu, "Deployment optimization of two warships formation for air defense," *Acta Armamentarii*, vol. 31, no. 6, pp. 865–869, 2010.
- [13] X. Liu, "Air defense formation modeling and air defense capability evaluation of sea fleet," *Journal of North University of China (Natural Science Edition)*, vol. 40, no. 6, pp. 531–536, 2019.
- [14] M. Z. Ruan, Q. M. Li, and T. H. Liu, "Modeling and optimization on fleet anti-aircraft firepower allocation," *Acta Armamentarii*, vol. 31, no. 11, pp. 1525–1529, 2010.

- [15] H. Shan and Yan, "Research on modeling method of firepower collaborative process for shipboard cooperative air defense," *30th Chinese Control and Decision Conference*, vol. 1, no. 1, pp. 2069–2074, 2018.
- [16] J. Qin and X. Wu, "Modeling and simulation on the earliest launch time of ship-to-air missile of warship formation in cooperative air-defense," *IMCEC*, vol. 1, no. 1, pp. 375–379, 2016.
- [17] D. V. Rao and M. Ravishankar, "A methodology for optimal deployment and effectiveness evaluation of air defense resources using game theory," *Sadhana*, vol. 45, no. 1, pp. 1–15, 2020.
- [18] N. Xue, D. Ding, J. Ding, B. Ma, and Y. Jia, "Optimization method for coordination deployment of air defense system based on improved genetic algorithm," in *Proceedings of the 2021 IEEE 4th Advanced Information Management, Communicates, Electronic and Automation Control Conference (IMCEC)*, vol. 4, pp. 1658–1664, Chongqing, China, June, 2021.
- [19] Z. Liu and W. B. Liu, "Island and warship integrated cooperation anti-air dynamic decision model and its algorithm," *Command Control & Simulation*, vol. 41, no. 1, pp. 20–25, 2019.
- [20] X. X. Ma, K. N. Teng, and J. J. Dai, "Research on reasonable configuration simulation of warship in supporting operations of reef air defense," *Computer Integrated Manufacturing Systems*, vol. 36, no. 5, pp. 21–25, 2019.
- [21] W. Z. Jiang, W. Gong, and Y. Y. Lei, "Reef battlefield air defense combat environment model," *Computer and Digital Engineering*, vol. 11, pp. 2034–2036, 2014.
- [22] T. Lin, J. J. Zhao, J. P. Zheng, and B. Lai, *Russian Ground to Air Missile Tactics*, Electronic Industry Press, Oregon, USA, 2005, in Chinese.
- [23] A. S. Tan, *Operational Research Analysis of Surface Ship Formation*, National Defence Industry Press, Arlington, Virginia, (in Chinese), 2009.
- [24] X. Gu and L. H. Tan, *The Tactics of Naval Surface Vessels Formation*, Naval Publishing Company, Beijing, China, 2001, in Chinese.



## Research Article

# An Efficient Approach of Face Detection and Prediction of Drowsiness Using SVM

Ratnesh Kumar Shukla,<sup>1</sup> Arvind Kumar Tiwari,<sup>2</sup> and Ashish Kumar Jha <sup>3</sup>

<sup>1</sup>Dr. APJ Abdul Kalam Technical University Lucknow, Lucknow, India

<sup>2</sup>Kamla Nehru Institute of Technology, Sultanpur, Uttar Pradesh, India

<sup>3</sup>Nepal Engineering College, Pokhara University, Lekhnath, Nepal

Correspondence should be addressed to Ashish Kumar Jha; ashishkj@nec.edu.np

Received 27 August 2022; Revised 7 October 2022; Accepted 10 October 2022; Published 17 April 2023

Academic Editor: Dinesh Kumar Saini

Copyright © 2023 Ratnesh Kumar Shukla et al. This is an open access article distributed under the Creative Commons Attribution License, which permits unrestricted use, distribution, and reproduction in any medium, provided the original work is properly cited.

This article investigates an issue of road safety and a method for detecting drowsiness in images. More fatal accidents may be averted if fatigued drivers are using this technology accurately and the proposed models provide quick response by recognising the driver's state of falling asleep. There are the following drowsiness models for depicting the possible eye state classifications as VGG16, VGG19, RESNET50, RESNET101 and MobileNetV2. The absence of a readily available and trustworthy eye dataset is perceived acutely in the realm of eye closure detection. On extracting the deep features of faces with VGG16, 98.68% accuracy has been achieved, VGG19 provides an accuracy of 98.74%, ResNet50 works with 65.69% accuracy, ResNet101 has achieved 95.77%, and MobileNetV2 is achieving 96.00% accuracy with the proposed dataset. The put forth model using the support vector machine (SVM) has been used to evaluate several models, and the present results in terms of loss function and accuracy have been obtained. In the proposed dataset, 99.85% accuracy in detecting facial expressions has been achieved. These experimental results show that the eye closure estimation has a higher accuracy and cheap processing cost, as well as the ability of the proposed framework for drowsiness.

## 1. Introduction

As people reside for comforts, circumstances keep on getting improved. Nowadays, everyone feels a primary requirement for a vehicle and thus the number of vehicles has grown rapidly in the society. It has resulted in the growth of a number of enterprises and enhanced economic prosperity.

As the number of vehicles on the road are increasing, the possibilities of the traffic accidents increase particularly due to the reason of sleepy drivers. Long-distance driving requires drivers to travel for extended periods of time to improve the efficiency of driving. Driving a car for an extended period of time exhausts and distracts the driver. It may lead to a fatal traffic accident. Drivers not getting enough sleep on a consistent basis may feel sleepy while driving. Most often such drivers may become victims of accident. Drowsy driving is the leading cause of automobile

accidents globally. The best approach to avoid sleepy driving accidents is to warn the motorist ahead of time. Drowsiness can be diagnosed using a variety of methods. Drowsiness is detected using the face detection and eye recognition [1]. These have sparked scholarly interest in sleepiness detection and deployment of insurance and productivity industries. Facial recognition algorithms have been improved to recognise drowsiness occlusions, and hair and skin color has some of the sources of drowsiness. The possible downstream has impacts of performance on drowsiness, based on potential sleepiness detection technologies, misapplications for driving safety, insurance claim skimming, coverage avoidance, worker monitoring, and job instability. Driver related characteristics are commonly used in the current techniques for identifying a driver's drowsiness. As a result of autonomous driving, the availability of these measures is limited. Physiological signal-based techniques have

appeared to be a feasible choice [2]. Only minimally intrusive methods are appropriate in a dynamic driving environment and convolutional neural network (CNN) has tried to solve this problem in the form of deep learning. The performance of open-source brain-computer interface (OpenBCI) Cyton electroencephalogram (EEG) has detected device and the Arduino open source electrical platform. The driver plays such a crucial part in the vehicle operation on the road. To prevent road accidents, the early warning system will help to wake a driver from the state of sleepiness. Drowsiness detection differs based on the equipment and the method used [3]. Deep learning-based systems have detected tiredness that decreases the road accidents. A tiredness detection technique based on the CNN has been suggested in the article [4]. People might suffer from a variety of mental diseases, such as schizophrenia, depression, and intellectual difficulties. In today's world, social media is the one thing that cannot be replaced. Through online chats, users may express their feelings, opinions, and thoughts to others on this platform. The data that are gathered everyday on the internet and are growing daily are the focus of many different strategies today [5]. The system discriminated human and nonhuman person's eyes by training the first network, then used the second network to identify the location of the feature points of the eye. Estimating the eye opening position based on the features, the network points out the score of the driver's sleepiness state [6]. The most prevalent kind of "synthetic media," which includes images, sounds, and films that appear to be created using conventional techniques but actually were created using the cutting-edge software, appears to be Deepfakes. In this chapter, we looked at a few publications to learn more about DF and its uses [7].

## 2. Related Work

One of the leading causes of accidents is drowsy driving. Major accidents can occur when sleepy drivers are unable to react to hazardous conditions. It is critical to identify driver's tiredness early and correctly in order to reduce accidents caused by sleepy driving. Early identification of sleepy driving is crucial to reduce such incidents. The effects of driver sleepiness on driving performance, behavioural indicators, and physiological markers have been found. This demonstrates the feasibility of implementing a sleepiness detection model based on the hybrid sensing and without contact sensors, as well as the prospect of extremely accurate early identification of a fatigued driver [8]. This model has detected sleepiness which in turn detected all levels of exhaustion from mild to severe. The posture index was especially beneficial when paired with the blink data since it was more sensitive to mild tiredness than traditional information and could compensate for the limitations of blink data [9]. Practical application of the proposed technique is one of the work limitations. Using 32 channels in a real-world context is not an opinion, this is a physical constraint that makes these devices hard to commercialize [10]. This technique is used for detecting tiredness based on the detection yawns and blinks at the same time. Establishment and foundation have many

discriminating physiological inputs at the same time. These are identified automatically from sources to merge corresponding multioutputs, short-term energy, and kurtosis. Finally, tiredness is recognised by monitoring many yawn and blink signals at the same time [11]. To discriminate between tiredness and alertness, deep neural networks (DNNs) are used. The best suited channels of brain activity detection are determined by CNN using colour map pictures. DNNs from the right lateral prefrontal cortex are used to get the findings. The CNN architecture has achieved a 99.3% average accuracy, showing that the model can distinguish between sleepy and nondrowsy pictures [12]. CNN has employed different aims in real-time application to obtain high accuracy and recognise the driver's falling asleep status as an indication of tiredness. The outcomes of the experiments reveal that eye closure estimate has high accuracy and low processing complexity. The proposed framework is able to detect sleepiness [13]. Twitter is the biggest storehouse for data collected from various blogging platforms including Facebook, Weibo, YouTube, Instagram, and others. Additionally, text, audio, and video were gathered from repositories. The sentiment analysis collects user attitudes through opinion mining and categorises them as favourable, negative, or neutral [14]. By feeding, the recurrences are plotted as input features into a CNN. The efficiency has been found for drowsy/awake categorization studied in CNN. In drowsy/awake categorization, the CNN models based on rectified linear units and recurrence plots outperformed other conventional models, with ECG accuracy enhanced by 6–17% and photo pothys monogram accuracy is observed to have been improved by 4–14% [15]. The wearable dry electrode prototype, a rather pleasant forehead setup, which captures images in vigilance dynamics easily. The suggested approach achieves the best mean and correlation coefficients of 71.18% and 66.20%, respectively, in real-time circumstances and practically in laboratory. To assess the simulated-to-real generalisation, cross-environment tests are applied, and the best correlation coefficient is determined to be 53.96% [16]. Mathematics of SVM, tree-based classifiers, and neural networks will go into great detail about ensemble algorithms with appropriate applications [17]. A deep cascaded convolutional neural network (DCNN) has been created to recognise face area and it overcomes the problem in low accuracy using an artificial feature extraction. The Dlib toolkits are utilised to identify the frontal facial landmarks in frame. In this process, the authors have used a new parameter known as eyes aspect ratio (EAR) to analyse the tiredness in the current frame, according to the eyes landmarks. Practically, there are different modules to identify the changes in the size with the help of EAR. The first module used SVM with the EAR as input to build a unique weariness state classifier [18]. After the features have been determined, they are classified using the following classifiers: bagging reduced error pruning, K-closest neighbour, AdaBoost, Gaussian Naive Bayes (GNB), stochastic gradient descent, and SVM. Thus, stacking of LGBM and random forest has been found to produce the best forecasts across all three datasets [19].

The above Table 1 shows the different positions of sleepiness and expected levels thereof. In the article, all of the expected eye positions have been provided for the calculation of the current position of opened and closed eyes using the EAR. The main aspect of this table is to carry out the investigation of the position of eye for assessing the state of sleepiness [20]. The position of eyelids is the outcome of the calculation of EAR for detecting sleepiness. Actually eyes present different states such as open eyes, closed eyes, and partially open or closed in a random time. The closed and partially opened or closed levels are marked as sleepiness [21].

### 3. Methods and Data Description

Drowsiness detection systems have been developed by using subjective, vehicle-based, behavioural, and physiological data. The subjective measurements have been commonly used to establish a sleepy baseline or reference point. Observation and self-ratings are examples of these measurements. Experts or qualified ratters' keep an eye on the driver to assess his or her present level of sleepiness based on observer evaluations. A driver's sleepiness can be detected by monitoring the driver. The upper body or facial region of the driver is examined for sleep-induced drowsiness. Measures like steering wheel movement and lane position standard deviation are used by vehicle-based systems to assess driving behaviour. In behavioural-based approaches, a camera is utilised to monitor the driver's face. Image processing technologies have been utilised to discover drowsiness signs and early symptoms [21]. The eye movements, facial emotions, and head posture are all evaluated. Data from brain activity, heart activity, eye activity, and muscle tone are used in the physiological methods.

*3.1. Datasets of Drowsiness.* The facial drowsiness dataset is included for closed and open eyes, and to design for an improved performance of facial recognition in the existing models. There are several sleepiness datasets that can offer decent results in real-time. There are the following datasets used in sleepiness detections.

*3.1.1. ZJU Dataset.* ZJU gallery from the ZJU eye blink database has a collection of photos of 80 video clips in video libraries. They made the following four movies for each participant: first without including glasses, second one has thin rim glasses, third one has black frame glasses, and fourth one with and without spectacles of left and right eyes photographed individually. Table 2 are containing 4,841 photos of the collection, including 2,458 open and 2,383 closed eyes and the trained networks with subsample pictures with their shots geometrically normalised to  $24 \times 24$  pixels [22].

*3.1.2. MRL Dataset.* The recognition of eyes, their components, estimation of the gaze, and frequency of eye-blinking are all critical challenges in computer vision. Solving the

issues in the field of driver behaviour, which has resulted in the acquisition of a huge quantity of testing data acquired in real world scenarios. The MRL eye dataset possesses a large database of human eye pictures. These collections are included for low and high resolution infrared images captured in a variety of lighting conditions and a variety of equipment. Table 3 contains 4,841 images, comprising of 24,000 closed eyes and 24,000 open eyes. The dataset is suitable for testing a wide range of features or trainable classifiers [23].

*3.1.3. Proposed Dataset.* The proposed dataset in Table 4 contains 3,893 images of open eyes and closed eyes, and they are cropped and labelled by using the annotations supplied. 2,701 open-eye pictures and 1,192 closed-eye shots have been covered up. The authors cropped the annotated faces with margin around the face and eye bounding boxes in their suggested datasets. Figure 1 depicts the collection of the proposed dataset pairings of closed eyes and open eyes pictures.

*3.2. Model Description.* This article has used the previous pertained models as feature extractors of the faces to extract eyes features from informative regions. The driving time is critical for improving the model's performance. Obviously, the longer a driver drives in monotonous conditions, the more likely he or she is to fall asleep. This is why highway drivers are usually advised to take a rest after two hours of driving. As a consequence, the model has been made to learn a linear relationship between elapsed time and the amount of time before the critical state occurs. Some people may feel drowsy at one point, and then get awake again. The behaviour shows that there is no obvious linear relationship between the driving duration and the time before reaching a certain degree of drowsiness.

*3.2.1. VGG16.* The VGG model is using the ImageNet dataset for image classification. K. Simonyan and A. Zisserman from the University of Oxford who proposed VGG16 have used a CNN model in their article "Very Deep Convolutional Networks for Large-Scale Image Recognition." ImageNet dataset contains 14 million pictures divided into thousand classes, and this model achieved 92.7% accuracy in the top-5 tested model. ImageNet dataset comprises of more than 15 million high-resolution images organised into more than 22,000 categories. The photographs are collected from the Internet and categorised by users using Amazon's Mechanical Turk crowd-sourcing technology [21].

*3.2.2. VGG19.* A deep learning has made use of CNN architecture for image categorization. The VGG architecture has included with 16 convolutional layers and three fully linked layers. The next great step has been put forward after Alexnet's ImageNet Challenge triumph in 2012. The VGG19 abbreviation refers to the fact that there are 19 different strata in all. VGG19 is a 19-layer convolutional neural network that has trained on millions of image samples that

TABLE 1: Description of different subject and level of sleepiness position in images.

Level	Subject	Level of sleepiness
1	Feel busy	Not feeling sleepy
2	Critical, alert and wakeful	Extremely sleepy and fighting sleep
3	Work smart but not concentrate on the peak level	Some effort for sleep alert
4	Wakeful and relaxed but not alert	Optimal sleepiness of open
5	Small sparkle	Showing sleepiness features
6	Difficult to wake up, foggy, and lose the track	Alert
7	Woozy and sleepy	Very alert
8	Struggling for sleep	Extremely sleep
9	Not awake after alert	Alert at extreme level

TABLE 2: Analysis of open eyes and closed eyes in ZJU dataset.

Open eyes	Closed eyes	Total images
2383	2458	4841

TABLE 3: Extraction of open eyes and closed eyes in MRL dataset.

Open eyes	Closed eyes	Total images
24000	24000	48000

TABLE 4: Proposed dataset classification with open and closed eyes.

Open eyes	Closed eyes	Total images
2701	1192	3893



FIGURE 1: Sample set of the proposed dataset with open eyes and closed eyes.

normalise images using the zero-centre architectural style. The fully linked layer has included ReLU, Dropout, Softmax, and classification output.

**3.2.3. RESNET50.** A CNN with 50 layers like the frequently used ResNet-50 model is a deep residual network. ResNet has artificial neural networks (ANNs) that build networks by stacking residual blocks on top of each other. ResNet comes in a variety of flavours, each with a different number of layers but the same basic idea. ResNet 50 is a ResNet variation capable of working with up to 50 neural network layers. ResNet was built specifically to address this issue. To increase model accuracy, deep residual nets use residual blocks. The strength of this form of neural network is the notion of “skip connections,” which lies at the heart of the residual blocks [24]. As a reference architecture for learning food-domain

properties, we used a residual network with 50 layers. The proposed database features outperform over the learnt ones from previous food databases and the massive ImageNet picture database [25].

**3.2.4. RESNET101.** ResNet101 is a deep convolutional neural network with 101 layers. ResNet101 is trained with ImageNet database including million photographs with a pretrained version of the network. This network can classify photographs into thousands distinct image categories, such as mouse, keyboards, pencils, and a wide range of animals. ResNet101 has amassed a library of rich feature extraction for a wide range of images including  $224 \times 224$  pixels size images [26].

**3.2.5. CNN.** CNN is a computationally efficient model that analyses features to discover image-related issues using specific convolution and pooling procedures. CNN is a classification framework that divides the pictures into labelled categories. The many layers of CNN extract picture information before learning to identify the images. As a result, typical outputs of CNN indicate the classes or labels of the classes that the CNN has learned to categorise [27].

**3.2.6. SVM.** SVM is a linear model used for classification and regression problems of the objects. SVM is very useful for solving the problems of linear and nonlinear categories and may be used in a variety of situations. The approach separates the data into classes by creating a line or hyperplane, which is a core notion in SVM. The SVM is a machine learning method that takes data and, if possible, draws a line that separates the classes. Assuming that the user supplies a dataset of red rectangles and blue ellipses (positives from negatives) to SVM to differentiate, and the SVM creates a hyperplane to identify the dataset into two groups (red and blue) [28].

**3.2.7. MobileNetV2.** MobileNetV2 is an extended version of CNN designed to function on mobile devices. It has included residual networks to solve the problem of inverted residual structure with bottleneck. MobileNetV2 has intermediate expansion layer filters that extract features using lightweight and depth wise convolutions as a source of nonlinearity. It boosts mobile model performance across a wide range of

activities and benchmarks, as well as model sizes. A new module with an inverted residual structure has been added to MobileNetV2. Nonlinearity in thin layers is no longer an issue. The state-of-the-art object recognition and semantic segmentation results are also achieved using MobileNetV2 as the backbone for feature extraction [29].

#### 4. Approaches of the Proposed Model

The proposed model is working on detection of the drowsiness position. The authors are applying different steps to find out the correct position of the eyes in the faces of the persons. Eye is identified as the exact value of the driver, when driving the car. Another feature is not giving good result to identify the position of drivers. To begin, the authors are collecting the input image using camera or database and detect the face image.

After collection of face image, the useful image is identified. Then, multitask cascaded convolutional networks (MTCNN) is applied for classifying the faces with their features like eyes, mouth, and nose from the facial region. MTCNN having been applied can detect the eyes and apply the EAR theorem to detect the accurate position of the eyes such as open or close [30]. In the previous section, there is a different level of position to identify the status of the eyes and new metric termed as eyes aspect ratio (EAR) is created [31]. It is determined with the use of facial landmark coordinates (open or closed). Two sets of the EAR are fetched from the face recognised by MTCNN in images and trained for particular face, representing eyes-open and eyes-closed. After that, the SVM classifier compares the features of eyes and classifies if drowsiness exists or not. The landmarks of the face are then obtained using the Dlib toolkit [32]. The detection is carried out with the help of logistic regression. The image orientation detection algorithm was tested using over 100,000 pictures from the Scene UNderstanding (SUN) collection. This technique surpasses similar algorithms utilizing art, and it recognises the accuracy of correct orientation of visual contents comparable to human observers [33]. The aspect ratio of the eyes may be computed using the eye coordinates. Finally, the one-of-a-kind SVM can classify the present condition of the frame's eyes [34]. The performance of the algorithms may be significantly improved by using the SVM and the primary contributions in this investigation are as follows:

- (1) Detection of face from image dataset using digital camera.
- (2) Application of MTCNN to classify the faces from images, which improves the performance significantly.
- (3) Detection of the eyes and application of EAR to determine the accurate position of the eyes. EAR works in different levels and the suggested technique improves significantly in both accuracy and speed.
- (4) Application of SVM to classify the eyes feature for their openness or closeness.
  - (a) If eyes are closed, next step is followed.
  - (b) If eyes are open, step 1 is followed.
- (5) Finding a way out of the sleepiness position.

The suggested method takes individual differences into account, and it is more reasonable and accurate, according to the results of comparative studies. It is the same as a start-up procedure. Face traits, particularly the size of the eyes, exhibit notable variances, as is commonly observed. As a result, a simulator is employed to collect data by asking the user to open and close his or her eyes for a brief interval of time. MTCNN is built to detect the face of the driver in the current frame by applying the picture data. Facial landmarks can also be retrieved using the Dlib toolbox. As illustrated in Figure 2, the following two types of EAR may be determined: when the eyes are open, EAR1 is computed, and when the eyes are closed, EAR2 is calculated. Finally, a customised SVM is trained for the given person to determine whether the eyes are open or closed using the two forms of EAR as positive and negative examples.

*4.1. MTCNN (Multitask Cascaded Convolutional Networks).* Face detection is one of the most significant computer vision methods for sleepiness detection. In practice, a system for detecting sleepiness must not only be accurate but also be rapid. Deep learning technologies, notably the convolutional neural network model, improves photo recognition accuracy dramatically, and the algorithm performance, on the other hand, is delayed by the intricate network structure. The MTCNN has been developed for face detection. Different loss functions are employed for different tasks. The loss function quantifies the difference between index of expected output and input label that was actually marked and applied face classification tasks, as well as face area box bounding fitting tasks, are part of the training process, and the image is converted into matrix form with height, width, and colour [35]. After that, a rectangle box is drawn around the face and crucial spots such as the eyes, nose, and mouths are chosen. It is a straightforward approach to tackle and apply traditional feature-based algorithms such as the MTCNN classifier. An excellent job in image datasets has been proven by it [36]. Deep learning algorithms have set a desired level performance in the recently state-of-the-art on common benchmark for face detection datasets. Face detection and recognition is a challenging task in computer vision problem that entails recognising and finding persons in image photographs.

Figure 3 is showing the output after applying the OpenCV package and the traditional feature-based cascade classifier may be used to recognise faces. MTCNN has undergone three tasks to train the used CNN detectors like face/nonface classification, bounding box regression, and facial landmark localization.

*4.2. Face Classification.* The learning goal of expression has made use of two-classified problems for cross-entropy loss. Cross-entropy determines the amount of bits necessary to describe and transmit to average event from one distribution and compared to another distribution based on the concept

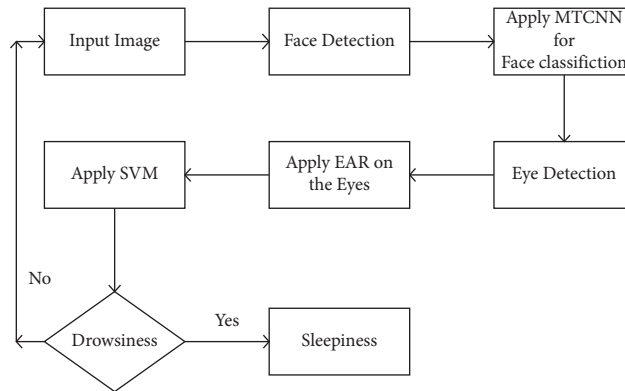


FIGURE 2: Apply proposed model to detect drowsiness condition.

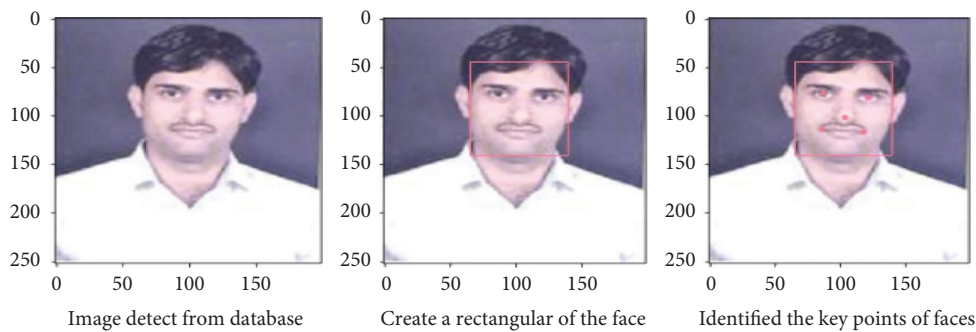


FIGURE 3: The figure given above is showing output after applying the MTCNN and found out the rectangular and key points of the faces.

of entropy in the information theory. There are additional bits necessary in cross-entropy of  $Q$  from  $P$  which is the number to represent an event, and it used  $Q$  instead of  $P$  when analysing a target of underlying probability distribution  $P$  and a close approximation of the target distribution  $Q$  is carried out.

$$H(P, Q) = -\sum x \ln x P(x) * \log(Q(x)), \quad (1)$$

where  $H(P, Q)$  is indicating a cross-entropy function,  $P$  indicates a target distribution, and  $Q$  indicates approximation of the target distribution.  $P(x)$  is the probability of event  $x$  in  $P$ ,  $Q(x)$  is the probability of event  $x$  in  $Q$ ,  $\log$  is the base-2 logarithm, and the results are calculated in bits.

**4.3. Bounding Box Regression.** It predicts the candidate window and the nearest ground truth bounding boxes left top, height, and breadth in images. Each sample is treated with the Euclidean loss, and the learning goal is stated as a regression problem. The Euclidean loss is minimised by posing facial landmark recognition as a regression problem, similar to the bounding box regression task. Three variables absolutely necessary are set up as follows:

- (i) To detect the faces, the frontal face detector method can identify one or more faces.
- (ii) A predictor that can recognise keypoints in faces inside the variable and shape.

- (iii) For capturing photos from the webcam, the cv2.Video is used to capture the object. A parameter with the value 0 was also specified for taking photographs from a camera.

**4.4. EAR (Eye Aspect Ratio).** Using the Dlib toolbox, face landmarks were collected. As indicated in Figure 4, there are six dots dispersed around each eye to identify its location. Between open and closed states, the distribution of ocular landmarks differs significantly. The programme eye aspect ratio was used to track the frequency of blinking.

The following formula may be used to calculate EAR based on the position of ocular landmarks:

$$EAR = \frac{(P2 - P6) + (P3 - P5)}{2(P1 - P4)}. \quad (2)$$

The coordinates of eye landmarks are indicating  $P_i$  where integer  $i$  equals to 1, 2, 3, 4, 5, and 6. When the eyes are observed to be open, the EAR is more than 0.2, as demonstrated in Figure 4. The EAR, on the other hand, is less than 0.2 for the closure of the eye. As previously mentioned, the condition of the eyes might indicate whether or not he or she is sleepy, because there are huge disparities in the amount of time that eyes are closed while he or she is awake and when he or she is tired. To define the shape of the pupil, a method of ellipse fitting is presented. This approach is segmenting the pupil using a standard imaging process as seen in Figure 4 given above. The white pixels indicate a form

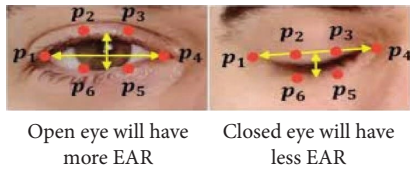


FIGURE 4: Detecting the value of open eyes and closed eyes after applying eye aspect ratio (EAR).

of eyes that are then placed into the ellipse. Finally, the eyes were assessed using the ratio of major and minor axes of ellipse.

**4.5. Drowsiness Detection.** An experiment is conducted to show the detection. Individual distinct events are taken into account in this experiment to create a unique classifier. It is a soft hand start-up procedure and an adjustable threshold rather than a set one. To make it work, images for open and close eyes for a few seconds are taken, and then the MTCNN and Dlib toolbox to acquire two sets of EAR are applied. The SVM classifier is trained by using two sets of data as input. The structural risk minimization criteria are applied in SVM, a machine learning model. It is a linear classifier model with a feature of being the biggest interval of defined space. We leverage deep features derived by CNNs linked with support vector machines as an alternative to end-to-end classification because the labelled data is typically scarce in real-world applications. Data with open eyes are labelled as positive, whereas data with closed eyes are labelled as negative. In an images eyes cannot abruptly changes, i.e., eyes cannot shifted from open to closed and closed to open in a single frame with immediate time. The EAR is containing six consecutive frames, which are concatenating into a single feature vector.

## 5. Experimental Analysis and Results

Face detection is an essential study direction in this target detection publication. The face's position in the provided picture is returned. Facial recognition using deep learning requires three phases: data input, feature extraction, and face feature detection (including eye and mouth), with feature extraction being the most important. Rather than a complex network, the design is made up of subnetworks. The algorithm can run quicker since each subnetwork has fewer filters but better filter discrimination. However, we observed that having worthless facial landmark information might be an impediment to its performance. As a result, we create a one-of-a-kind convolutional neural network that can recognise a driver's face. Because of the lightweight frame and the lack of facial landmarks, it is more efficient. We are building an image drowsiness model in the figure given above to see if the driver is drowsy or not. The authors utilise a number of algorithms to classify the driver's weariness. The recommended model will provide a better image drowsiness result. As a result, scaling the original image to various sizes is an option. The data from video or picture is initially collected in the proposed diagram. Then they use MTCNN to figure out who is in the video or picture. We apply the

facial landmarks algorithm on the faces after successfully collecting the real-time image. This programme recognises the many features of the faces. This algorithm recognises facial features such as stance, eye, and mouth. These three facial features are crucial in determining whether or not someone is drowsy. We use CNN to extract the features of the face, mouth, and eyes after collecting these three characteristics. The eyes are a very crucial part of the faces when they are drowsy. So, in order to get the exact value of the eyes, we are using the EAR. We use SVM once we have collected these three characteristics. Machine learning (ML) algorithms for classification are known as SVM and SVM has a supervised learning method for classifying objects including many categories. We use EAR in SVM to determine if the eyes are closed or open, as well as whether the mouth is yawning or not. Following this identification, we apply the SVM on the faces and if the faces are not facing forward, they are in a drowsy position. If these characteristics are true, then they forward it to the next stage as sleepiness, and another on is sent to step one and the procedure continues to the next image. It has the ability to alter the behaviour and pose a significant risk of injury to other users. By tracking the length to identify the state of objects, it is feasible to prevent the accidents caused by the driver's fatigue to some extent. However, this technology cannot determine whether or not an object is sleepy in real time. A detecting system has emerged as a realistic option with the progress of information technology. As a result, research into intelligent drowsy object detection has real-world ramifications. In general, regularisation is the only necessity when our network is at risk of overfitting. This can occur if a network is too large, and if the user trains for too long or if the user lacks sufficient data. Dropout is simple to create if the convolutional network has fully linked layers at the end. Convolutional layers require less regularisation to begin with since they have fewer parameters. Activations can also become strongly linked as a result of the spatial correlations stored in feature maps. Dropout becomes unsuccessful as a result of this. VGG16, VGG19, RESNET50, RESNET101, and MobileNetV2 were large models with completely linked layers at the network's conclusion. Dropout between completely linked layers was used to counteract overfitting. Modern convents have decreased the model size while enhancing performance by replacing dense layers with global average pooling. The batch-normalized the model's good performance backup the idea, that batch normalisation should be utilised between convolutions. Furthermore, dropout between convolutions should be avoided, as models with dropout performed worse than the control model. Generic dropouts are working well, when nodes/pixels have spatial relationship, dropping whole activations/features at random works extremely well. It is a simple Keras Dropout layer parameter change that works with a variety of convolutional models.

In the above Figure 5 is showing the model accuracy of VGG16, VGG19, RESNET50, RESNET101, MobileNeV2, and SVM model using proposed dataset. This performance ratio is performing better result using SVM. Also Figure 6, graphs are showing the comparative analysis of the

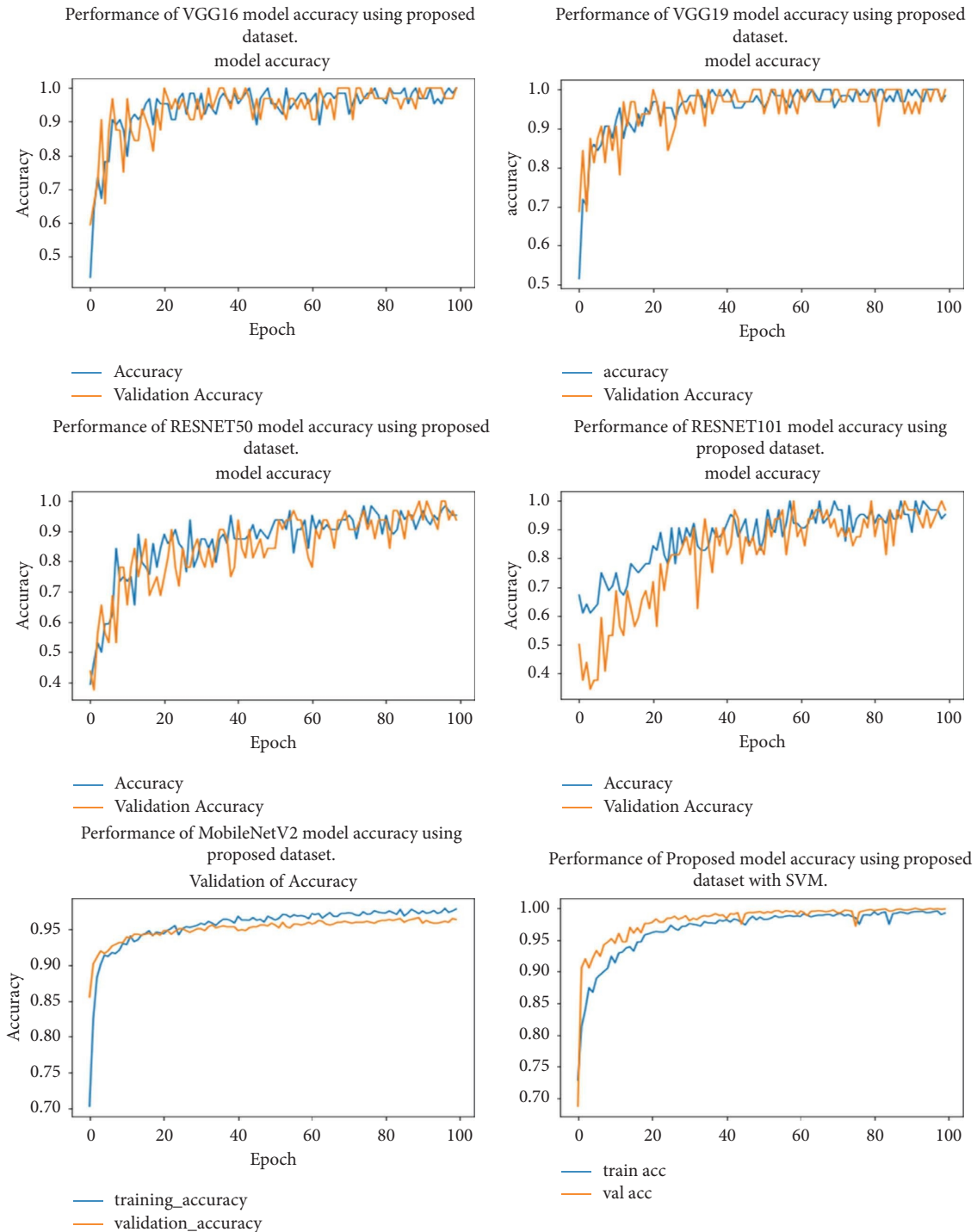


FIGURE 5: Performance accuracy of VGG16, VGG19, RESNET50, RESNET101, MobileNetV2 and proposed model using proposed dataset.

performance of loss function and validation loss in different models. VGG16, VGG19 is performing better than RESNET50 and RESNET101. These models are pretrained models perform with proposed datasets. But they are not providing good result compare than MobileNetV2 and proposed model with SVM. The pretrained model is working on softmax to categories the object in proposed model with SVM to identifying the object. SVM is classifying the features of the object in different class. The proposed model

with SVM is providing better result in loss-function and validation loss-function in compare the above VGG16, VGG19, RESNET50, RESNET101 and MobileNetV2. The proposed model with SVM is providing better result in loss function and in accuracy compare to above five pretrained models.

The Figure 7 is showing the result of after compiling 100 and 500 epochs in proposed model with proposed dataset. When the epochs are increasing the value of loss function is



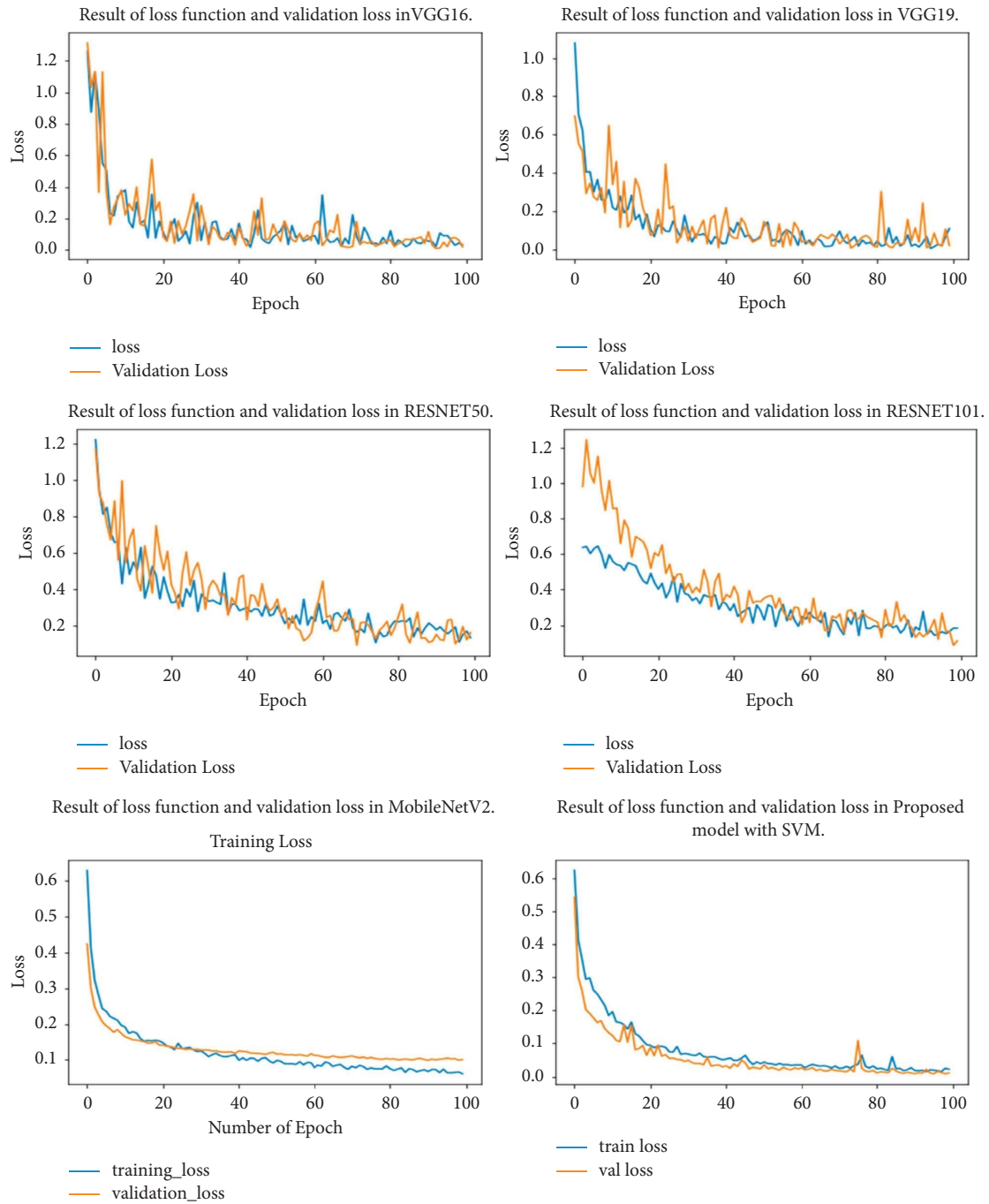


FIGURE 6: Performance of loss function in VGG16, VGG19, RESNET50, RESNET101, MblenetV2, and proposed model with proposed dataset.

decreasing and accuracy is also increasing, after comparing the 100 and 500 epochs. Epochs are working a set of feature called cluster to work together. After compiling the 500 epochs, we find an accurate performance in loss function and accuracy. So we can say the proposed model with SVM is working well compare to VGG16, VGG19, RESNET50, RESNET101 and MobileNetV2. Proposed approach has provided better performance compare to another five pre-trained model showing in the Figure 8. They will be providing exact value with proposed dataset.

## 6. Comparative Analysis of Different Models with Datasets

The Table 5 and Figure 8 exhibit the performance of the VGG16, VGG19, RESNET50, RESNET101, MobileNetV2 and proposed model with SVM. VGG16 and VGG19 yield a better result compared to RESNET50 and RESNET101. But proposed model generates better result compared to VGG16, VGG19, RESNET50, RESNET101 and MobileNetV2. They show different model with working different

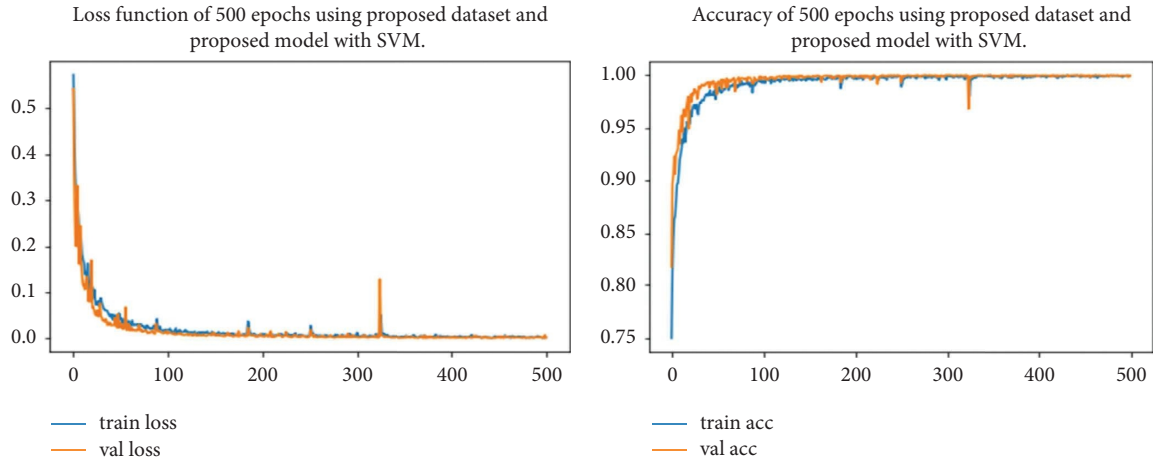


FIGURE 7: Performance of accuracy and loss function of proposed model with proposed dataset using 500 epochs.

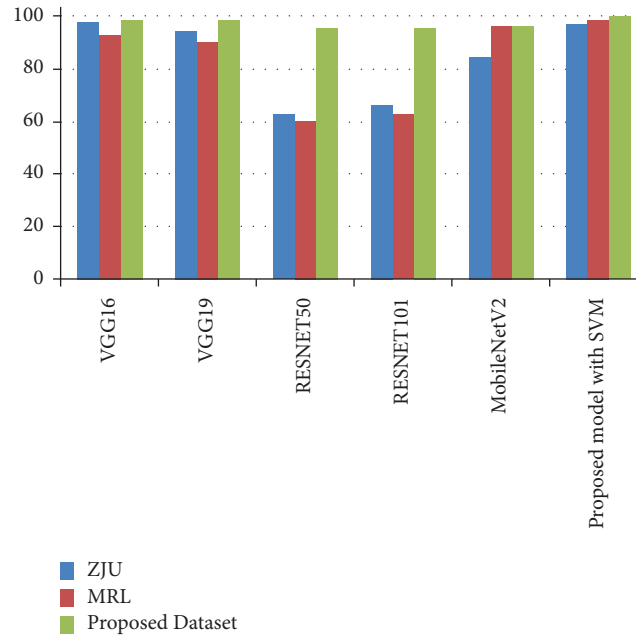


FIGURE 8: Above figure is showing the graphical representation of the VGG16, VGG19, RESNET50, RESNET101, MOBILENETV2, and the proposed model with SVM.

TABLE 5: Performance of the models VGG16, VGG19, RESNET50, RESNET101 and proposed model including different dataset.

S.No.	Technique	Dataset	Epochs	Accuracy
1	VGG 16	ZJU [22]	100	98.15
		MRL [23]	100	92.56
		Proposed dataset	100	98.68
2	VGG19	ZJU [22]	100	94.96
		MRL [23]	100	90.23
		Proposed dataset	100	98.74
3	RESNET50	ZJU [22]	100	62.50
		MRL [23]	100	60.33
		Proposed dataset	100	95.69
4	RESNET101	ZJU [22]	100	65.89
		MRL [23]	100	62.31
		Proposed dataset	100	95.77

TABLE 5: Continued.

S.No.	Technique	Dataset	Epochs	Accuracy
5	MobileNetV2	ZJU [22]	100	84.70
		MRL [23]	100	95.88
		Proposed dataset	100	96.00
6	Proposed model with SVM	ZJU [22]	100	97.54
		MRL [23]	100	98.76
		Proposed dataset	100	99.56
			500	99.85

datasets. The proposed approach is applied to the datasets from ZJU, MRL and proposed database; they have achieved recognition accuracy of 99.85% with proposed dataset. This article employs the five preprogrammed models VGG16, VGG19, ResNet50 and ResNet101. Extracting the deep features of eyes with VGG16 has resulted in 98.68% accuracy, VGG19 shows 98.74% accuracy, ResNet50 shows 95.69% accuracy, ResNet101 exhibits 95.77% accuracy and MobileNetV2 shows accuracy of 96.00% with own dataset. All result shown in this paper with accuracy complies with their approved results.

## 7. Conclusion

Research on sleepy driving detection algorithms is one of the most essential strategies to prevent road accidents. As it is aware to all, there are substantial individual variances between people, particularly when it comes to the eyes. While researching computer vision algorithms, individual modifications of Table 5 and Figure 8 must be addressed. In this paper, a novel picture of sleepiness detection technique takes individual attributes into account. To begin, an MTCNN is created to retrieve a face from an image, avoiding the artificial feature extraction process used in typical face identification algorithms. According to experimental data, face detection accuracy can reach 99.65% in 100 epochs and 99.85% in 500 epochs. In comparison to VGG16, VGG19, RESNE50, RESNET101, and MobileNetV2, the proposed model with SVM produced superior results. Based on the Dlib toolkit, a new parameter EAR is offered to analyse the status of the object's eyes. Experiments indicate a high association between the EAR and the size of an object's eyes, confirming our assumptions. Finally, in the study, a module is developed while taking individual variances in the eyes into account. A unique classifier based on SVM is constructed for each image, and the condition of the eyes is analysed using a prelearned classifier. Experiment findings show that put forth approaches consistently outperforms state-of-the-art methods while retaining real-time performance on both publicly available and self-built datasets. The comparative study reveals for the suggested model to have outperformed all five previous existing models. The fundamental contribution of this study is to monitor with drowsiness.

## Data Availability

ZJU dataset is available at (<https://github.com/elmino9ykl/ZJU-Dataset>) and MRL dataset (<https://mrl.cs.vsb.cz/eyedataset>).

## Conflicts of Interest

The authors declare that they have no conflicts of interest regarding the publication of this study.

## References

- [1] M. Zhu, J. Chen, H. Li, F. Liang, L. Han, and Z. Zhang, "Vehicle driver drowsiness detection method using wearable EEG based on convolution neural network," *Neural Computing & Applications*, vol. 33, no. 20, pp. 13965–13980, 2021.
- [2] X. Zhao, C. Meng, M. Feng, S. Chang, and Q. Zeng, "Eye feature point detection based on single convolutional neural network," *IET Computer Vision*, vol. 12, no. 4, pp. 453–457, 2018.
- [3] S. S. Sharan, R. Viji, R. Pradeep, and V. Sajith, "Driver fatigue detection based on eye state recognition using convolutional neural network," in *Proceedings of the 2019 International Conference on Communication and Electronics Systems (ICCES)*, pp. 2057–2063, IEEE, Singapore, July, 2019.
- [4] F. Zhang, J. Su, L. Geng, and Z. Xiao, "Driver fatigue detection based on eye state recognition," in *Proceedings of the 2017 International Conference on Machine Vision and Information Technology (CMVIT)*, pp. 105–110, IEEE, Singapore, February, 2017.
- [5] B. Chilwal and A. K. Mishra, "Extraction of depression symptoms from social networks," *The Smart Cyber Ecosystem for Sustainable Development*, vol. 29, pp. 307–321, 2021.
- [6] J. Gwak, A. Hirao, and M. Shino, "An investigation of early detection of driver drowsiness using ensemble machine learning based on hybrid sensing," *Applied Sciences*, vol. 10, no. 8, p. 2890, 2020.
- [7] S. Rastogi, A. K. Mishra, and L. Gaur, "Detection of DeepFakes using local features and convolutional neural network," in *DeepFakes* CRC Press, Boca Raton, FL, USA, 2022.
- [8] M. Sunagawa, S. I. Shikii, W. Nakai, M. Mochizuki, K. Kusukame, and H. Kitajima, "Comprehensive drowsiness level detection model combining multimodal information," *IEEE Sensors Journal*, vol. 20, no. 7, pp. 3709–3717, 2020.
- [9] J. R. Paulo, G. Pires, and U. J. Nunes, "Cross-subject Zero calibration driver's drowsiness detection: exploring

- spatiotemporal image encoding of EEG signals for convolutional neural network classification," *IEEE Transactions on Neural Systems and Rehabilitation Engineering*, vol. 29, pp. 905–915, 2021.
- [10] C. Zhang, X. Wu, X. Zheng, and S. Yu, "Driver drowsiness detection using multi-channel second order blind identifications," *IEEE Access*, vol. 7, pp. 11829–11843, 2019.
- [11] M. A. Tanveer, M. J. Khan, M. J. Qureshi, N. Naseer, and K. S. Hong, "Enhanced drowsiness detection using deep learning: an fNIRS study," *IEEE Access*, vol. 7, pp. 137920–137929, 2019.
- [12] M. Hashemi, A. Mirrashid, and A. B. Shirazi, "Driver safety development: real-time driver drowsiness detection system based on convolutional neural network," *SN Computer Science*, vol. 1, no. 5, pp. 1–10, 2020.
- [13] H. Lee, J. Lee, and M. Shin, "Using wearable ECG/PPG sensors for driver drowsiness detection based on distinguishable pattern of recurrence plots," *Electronics*, vol. 8, no. 2, p. 192, 2019.
- [14] V. Arya, A. K. M. Mishra, and A. González-Briones, "Analysis of sentiments on the onset of COVID-19 using machine learning techniques," *Advances in Distributed Computing and Artificial Intelligence Journal*, vol. 11, no. 1, pp. 45–63, 2022.
- [15] W. L. Zheng, K. Gao, G. Li et al., "Vigilance estimation using a wearable EOG device in real driving environment," *IEEE Transactions on Intelligent Transportation Systems*, vol. 21, no. 1, pp. 170–184, 2020.
- [16] F. You, X. Li, Y. Gong, H. Wang, and H. Li, "A real-time driving drowsiness detection algorithm with individual differences consideration," *IEEE Access*, vol. 7, pp. 179396–179408, 2019.
- [17] H. Khan, A. Srivastav, and A. K. Mishra, "Use of classification algorithms in health care," in *Big Data Analytics and Intelligence: A Perspective for Health Care* Emerald Publishing Limited, West Yorkshire, UK, 2020.
- [18] A. Dasgupta, D. Rahman, and A. Routray, "A smartphone-based drowsiness detection and warning system for automotive drivers," *IEEE Transactions on Intelligent Transportation Systems*, vol. 20, no. 11, pp. 4045–4054, 2019.
- [19] A. K. Mishra and A. K. Dash, "Development impact bonds in developing countries: an emerging innovation for achieving social outcomes," *Journal of Social and Economic Development*, vol. 21, pp. 1–27, 2022.
- [20] M. Ramzan, H. U. Khan, S. M. Awan, A. Ismail, M. Ilyas, and A. Mahmood, "A survey on state-of-the-art drowsiness detection techniques," *IEEE Access*, vol. 7, pp. 61904–61919, 2019.
- [21] S. Kaplan, M. A. Guvensan, A. G. Yavuz, and Y. Karalurt, "Driver behavior analysis for safe driving: a survey," *IEEE Transactions on Intelligent Transportation Systems*, vol. 16, no. 6, pp. 3017–3032, 2015.
- [22] M. Singh and A. S. Arora, "A novel face liveness detection algorithm with multiple liveness indicators," *Wireless Personal Communications*, vol. 100, no. 4, pp. 1677–1687, 2018.
- [23] S. Mohanty, S. V. Hegde, S. Prasad, and J. Manikandan, "Design of real-time drowsiness detection system using dlib," in *Proceedings of the 2019 IEEE International WIE Conference on Electrical and Computer Engineering (WIECON-ECE)*, pp. 1–4, IEEE, Bangalore, India, November, 2019.
- [24] A. Jain, R. Kumar Dwivedi, H. Alshazly, A. Kumar, S. Bourouis, and M. Kaur, "Design and simulation of ring network-on-chip for different configured nodes," *Computers, Materials & Continua*, vol. 71, no. 2, pp. 4085–4100, 2022.
- [25] S. Zhou, C. Chen, G. Han, and X. Hou, "Deep convolutional neural network with dilated convolution using small size dataset," in *Proceedings of the 2019 Chinese Control Conference (CCC)*, pp. 8568–8572, IEEE, Guangzhou, China, July, 2019.
- [26] K. Crowston, "Amazon mechanical turk: a research tool for organizations and information systems scholars," in *Shaping the Future of Ict Research. Methods and Approaches* Springer, Berlin, Germany, 2012.
- [27] A. Jain and A. Kumar, "Desmogging of still smoggy images using a novel channel prior," *Journal of Ambient Intelligence and Humanized Computing*, vol. 12, no. 1, pp. 1161–1177, 2021.
- [28] K. Simonyan and A. Zisserman, "Very deep convolutional networks for large-scale image recognition," 2014, <https://arxiv.org/abs/1409.1556>.
- [29] S. Kumar, A. Jain, A. Kumar Agarwal, S. Rani, and A. Ghimire, "Object-based image retrieval using the U-Net-Based neural network," *Computational Intelligence and Neuroscience*, vol. 2021, Article ID 4395646, 14 pages, 2021.
- [30] K. Zhang, Z. Zhang, Z. Li, and Y. Qiao, "Joint face detection and alignment using multitask cascaded convolutional networks," *IEEE Signal Processing Letters*, vol. 23, no. 10, pp. 1499–1503, 2016.
- [31] C. Wang, Y. Xiao, X. Gao, L. Li, and J. Wang, "A framework for behavioral biometric authentication using deep metric learning on mobile devices," *IEEE Transactions on Mobile Computing*, vol. 22, no. 1, pp. 19–36, 2023.
- [32] A. M. R. Tolba, "Trust-based distributed authentication method for collision attack avoidance in VANETs," *IEEE Access*, vol. 6, pp. 62747–62755, 2018.
- [33] A. Bhola and S. Singh, "Visualisation and modelling of high-dimensional cancerous gene expression dataset," *Journal of Information and Knowledge Management*, vol. 18, no. 1, Article ID 1950001, 2019.
- [34] N. Alioua, A. Amine, M. Rziza, and D. Aboutajdine, "Driver's fatigue and drowsiness detection to reduce traffic accidents on road," in *Proceedings of the International Conference on Computer Analysis of Images and Patterns*, pp. 397–404, Springer, Berlin, Heidelberg, August, 2011.
- [35] R. Jabbar, K. Al-Khalifa, M. Kharbeche, W. Alhajyaseen, M. Jafari, and S. Jiang, "Real-time driver drowsiness detection for android application using deep neural networks techniques," *Procedia Computer Science*, vol. 130, pp. 400–407, 2018.
- [36] A. Bhola and S. Singh, "Gene selection using high dimensional gene expression data: an appraisal," *Current Bioinformatics*, vol. 13, no. 3, pp. 225–233, 2018.

## Research Article

# Deep Neural Network for Accurate Age Group Prediction through Pupil Using the Optimized UNet Model

Swathi Gowroju <sup>1,2</sup>, Sandeep Kumar <sup>3</sup>, Aarti <sup>4</sup> and Anshu Ghimire <sup>5</sup>

<sup>1</sup>Lovely Professional University, Phagwara, Punjab, India

<sup>2</sup>Department of Computer Science and Engineering, Sreyas Institute of Engineering and Technology, Hyderabad, India

<sup>3</sup>Department of Computer Science and Engineering, Koneru Lakshmaiah Educational Foundation, Vaddeswaram, Andhra Pradesh, India

<sup>4</sup>Department of Computer Science and Engineering, Lovely Professional University, Phagwara, Punjab, India

<sup>5</sup>Department of Computer Science and Engineering, Nepal Engineering College, Kathmandu, Nepal

Correspondence should be addressed to Anshu Ghimire; [anshug@nec.edu.np](mailto:anshug@nec.edu.np)

Received 3 August 2022; Revised 14 September 2022; Accepted 15 September 2022; Published 13 October 2022

Academic Editor: Dinesh Kumar Saini

Copyright © 2022 Swathi Gowroju et al. This is an open access article distributed under the Creative Commons Attribution License, which permits unrestricted use, distribution, and reproduction in any medium, provided the original work is properly cited.

Predicting age automatically from the image is a difficult task and shortening the challenge to be more concise is also a challenging task. Nevertheless, the existing implementations using manually designed features using a wide variety of input features using benchmark datasets are unsatisfactory as they suffer from unknown subject information. It is challenging to judge CNN's performance using such approaches. The proposed system performs the segmentation through UNet without using a dense layer to perform the segmentation and classification. The proposed system uses the skip connection to hold the loss at the max-pooling layer. Also, the morphological processing and probabilistic classification served as the proposed system's novelty. The proposed method used three benchmark datasets, MMU, CASIA, and UBIRIS, to experiment with building a training model and tested using various optimization techniques to perform an accurate segmentation. To further test and improve the quality of the proposed method, we experimented with random images. The proposed system's accuracy is 96% when experimented on random images of subjects collected purely for experimentation. Three optimizers, namely, Stochastic Gradient Descent, RMS Prop, and Adaptive Moment Optimizer, were experimented with in the proposed system to fit the system. The average accuracy we received using optimizers is 71.9, 84.3, and 96.0 for the loss value of 2.36, 2.30, and 1.82, respectively.

## 1. Introduction

Over the decade, most methods were built based on statistical models, various features of the face such as wrinkles, freckles, spots on the skin, etc. Every human has to face these changes in the body as it is uncontrollable and inevitable [1]. Aging patterns may differ due to their personalized patterns, such as makeup, individual lifestyle, environmental conditions, and health [2, 3]. These attributes may instead create difficulty in estimating the age of the person. With the introduction of FGNet, this problem has been alleviated slightly by using the age dataset. For facial images, we have anthropometric models which measure the distance between

facial points from the image [4]. These are called landmark points of the face. One can define up to 132 facial measurements from the face at different locations on it. Another model, the active appearance model, is statistically and programmatically defined landmarks on the face [5–7]. These models consider both facial and texture to predict the shape of the face. These techniques are well suited for age and gender predictions. Although these methods perform well and are used widely in several applications, they need manual measurements and classification, which takes time and effort [8]. In the early 2000s, as said in Demirjian-Chaillet et al.'s method, the individual's age estimation took 10 min.

In the past decade, deep learning techniques have been used in many implementations of images. They show their accuracy well in performing segmentation, classification, and feature extractions [9–11]. We experimented with this to perform pupil segmentation to predict the age through it computationally. Age estimation based on biometric traits is attracting many researchers. One of the safe-to-use biometric traits is the eye. Eye not only authenticates a person but also hides much information needed in most applications [12–15]. One of the best applications is the result of this research paper. We proposed a rare computer application using scarce research characteristics that gave a 98% satisfying result in the experimentation. We believed in pupil dilation and used this property to estimate the person's age computationally accurately. Few researchers experimented on the proposed prediction. Most of the predictions were analyzed in the literature survey and the results were based upon the medical predictions. The computer model-based prediction was becoming problematic in terms of accuracy as the input images are always noisy due to occlusion and eyelashes. Furthermore, face detection followed by Pupil needs proper training on individual elements of the face, which is rarely available in the market [16–18]. Hence the work done on the proposed system in terms of deep learning became tough. The proposed system worked on deep and traditional methods to segment the Pupil by training the eye model of the face and generating the masked images of it for the training, through which segmentation is achieved [19–23]. The novelty of the proposed system, when compared to the existing systems, in summary, is described in the below points.

- (1) The proposed UNet can accurately identify pupil boundaries even in low illumination and noise with occlusion.
- (2) To identify the pupil boundary accurately, we performed segmentation in the first stage, followed by morphological processing in the second stage, where we can reduce segmentation errors.
- (3) The mean error rate is reduced compared to the existing state-of-the-art methods as the system is well checked with various optimizers to identify the problem.
- (4) To eliminate the overfitting problem due to the high pixel values of the image, we implemented Leaky ReLu and modified Leaky ReLu to address the problem of vanishing Gradient and dying ReLu to make the training process quicker.

The literature survey is described in Section 2 to give the paper's road map. The proposed method is discussed in Section 3. To check the accuracy level of training with UNet, we trained the system using the most popular deep learning architectures such as ResNet 50 and VGGNet along with UNet, and the training details and the pretrained models were discussed in the first subsection of Section 3. The flowchart is explained in subsections of the proposed method. Section 4 discussed the results using all possible input operations of the proposed system. Subsections of

Section 4 describe the segmentation of images from benchmark datasets, input face images, and the live video. After obtaining the segmented Pupil, we predicted the age in the 4.2 section. The accuracy of the proposed system is compared to the existing systems in Section 6.

## 2. Literature Survey

We studied various methods of predicting age. Characteristics that are used to predict age are, using eyes, using wrinkle features, and using dental characteristics. Age prediction using Pupils was medically proposed in 2013 by Erbilek et al. using iris biometric. They took young and old age groups collected from the University of Notre Dame, which is publicly available. They collected iris data from all 50 subjects based on the scalar distance between the iris and Pupil. According to the ratio obtained from twelve feature points, they were categorized into three age groups less than 25, 25–60, and greater than 60. In 2004, Lanitis et al. proposed AAM based method which predicts age using geometric and texture features. This methodology has a drawback: it faces difficulty if the image illumination is improper. Gao et al. in 2009 used pixel intensity and Local binary patterns to predict the age. The Gabor filter for the image used the following equation:

$$\Psi_{\mu,v}(z) = \frac{x_{u,v}^2}{\sigma^2} e^k \left[ e^i x_{u,v}^2 e^{-\sigma}, 2 \right], \quad (1)$$

where  $x_{u,v} = x_v e^{i\phi}$  and  $\phi_u = (\pi\mu/8)$ . In order to define the age membership function, he used LPB, which defines the third-order derivative of  $\mu$ . The author classified the person using SVM into three classes, baby, child, adult and old. The accuracy of the proposed classification was 78.9%. As an extension to work, Guo et al. used the Gabor filter defined above with a small size, using the following equation:

$$4(x, y) = e \left( -\frac{(x^2 + y^2)}{q\sigma^2} \right) \times \cos \left( \frac{q\pi}{\lambda} k \right), \quad (2)$$

where  $q$  is 2.,  $x \cos \theta + y \sin \theta$  and  $y = -x \cos \theta + y \cos \theta$  which rotates the filter with an angle of  $\theta$  at different intervals. To decrease the further dimension of the input image, the author used PCA (principal component analysis), which works well for bio-inspired features. The classification was made for 0–9, 10–19, 20–29, 30–39, 40–49, 50–59, and 60–69 age groups using their own dataset of 1002 images, with an accuracy of 79%. Agbo-Ajala et al. proposed a deep learning classifier to predict the age and gender of the subject using an unfiltered face. The author used a CNN model using landmarks detection and face alignment to predict age, and the binary classification is calculated using the following equation:

$$H_p(x) = \frac{1}{k} \sum_{i=1}^n \left[ R_j \log(p(\dot{x}_j)) + (1 - x_j) \log(1 - P(\dot{x}_j)) \right], \quad (3)$$

where  $x$  is the binary class label for predicted points on the face, IMDB -WIKI and MORPH-II datasets were used in the

training dataset. At the same time, the testing is done on a random dataset collected from random users. The accuracy was 81% while testing the data. Xie et al., 2015, experimented with ensemble learning from facial images to predict a person's age. He formed team-based learning, which is correlated with a specific age group. ResNet is used for the implementation. For the  $x^{\text{th}}$  learner, the probability distribution is calculated using the following equation:

$$\begin{aligned} \int_{-\infty}^{\infty} e^{-x^2} dx &= \left[ \int_{-\infty}^{\infty} e^{-x^2} dx \int_{-\infty}^{\infty} e^{-y^2} dy \right]^{(1/2)} \\ &= \left[ \int_0^{2\pi} \int_0^{\infty} e^{-r^2} r dr d\theta \right]^{(1/2)} \\ &= \left[ \pi \int_0^{\infty} e^{-u} du \right]^{(1/2)}. \end{aligned} \quad (4)$$

The probabilistic loss function is defined using equations (3) and (4) as follows:

$$\sum_{n=1}^n f^k = \frac{1}{N} \sum_{k=1}^k \sum_{i=0}^{n-1} \sum_{j=0} P_i^{kj} \log(p_i^k, j). \quad (5)$$

The system achieved an accuracy of 89.6%, with a loss of 2.9 at each level, which is very high for a CNN to consider it the best. The parameters such as tooth are also considered to predict the age by Kim et al. in 2020, using CNN while training the dataset using dental X-ray images. The first four molar images were captured using an X-ray. Using a heat map of the 16<sup>th</sup>, 26<sup>th</sup>, 36<sup>th</sup>, and 46<sup>th</sup> tooth is extracted to train the model to check the first molar presence. It was a pretty different trial of age prediction. Gradient weighted class activation mapping algorithm. The CNN of ResNet is used to train its own dataset of 2025 patients received by radiologists. The ages of only 20–29, 30–39, and 40–49 were used in the experimentation as tooth selection is mandatory to predict the age. The prediction accuracy was 89.05% for all three age groups. Age prediction using wrinkles present on the face was used by Sharma et al. in the year 2021 using CACD and UTK Face datasets with RGB images using FGNet CNN architecture to build a model. The model was executed for 200 epochs for the aging process. The author used the classes of 20–40, 41–60, and 60+ ages. Using the following equation, the output function is defined.

$$G(x) = \sum_{i=1}^{n-1} (C_y^f A_y^f) + x A_y^f, \quad (6)$$

where the first term represents the attention mask,  $x$  is the input image, and  $f$  is the respective class. The content mask is generated for each image, and the mouth portion is cropped. The error rate obtained was 0.001%, with an age prediction accuracy of 74. Using on UTKFace dataset, age prediction is experimented with by Sheoran et al., Sari et al., and Lobato et al., using deep CNN using transfer learning on the VGGFace2 pretrained model and ResNet50-f. The mean average error is calculated using the following equation:

$$\frac{1}{n} \sum_{i=1}^n |y_i - \hat{y}_i|, \quad (7)$$

where  $y_i$  is the ground truth and  $\hat{y}_i$  is the predicted age of the  $i$ th sample. The mean error obtained was 6.098, and the accuracy was 5.91. We studied a survey on age prediction and tabularized in Table 1 the predictions of the literature about the findings. Most of the models use the face as a parameter to predict age. There were less number of articles that studied other parameters, such as predicting age using wrinkles and skin. These other medical articles [10–15] studied the prediction through a pupillometer. Gowroju et al. [16–18] proposed a method to segment the Pupil using a deep learning technique accurately.

The authors studied various age groups and concluded that pupil diameter changes as age grow up to the mid-40s and then the size of the Pupil decreases significantly as age increases [19]. The calculation also depends upon the luminance and refractive index of the eye. In the proposed system, we experimented on different aged people from benchmark datasets and a few randomly selected images as well as the live video to predict the age computationally to add it to the list of parameters to predict the age.

### 3. Proposed Method

Since the deep neural network has been proving its ability and intelligence in many feature extraction and segmentation applications, we considered one of the best performing architectures in the field of medicine was taken to implement the proposed method. We optimized the existing architecture of UNet and experimented with various optimizers and classifiers to finalize the proposed methodology. The overall block of the algorithm is listed in brief using 11 step process. The corresponding flowchart of the above algorithm is depicted in Figure 1.

**3.1. Create a Trained Model.** In this section, we described the datasets used for the experimentation and the pretrained models used for the efficiency calculation of the proposed method. In this section, we described the datasets used for the experimentation and the pretrained models used for the efficiency calculation of the proposed method. Deep Learning techniques may be taught more quickly by performing all controlling operations rather than sequentially. The proposed system used GPU for training the model. A GPU (Graphics Processing Unit) is a specific processor with dedicated secondary storage that performs the floating-point computations necessary for graphics translation. Regularization, such as dropout and early stopping of the GPU, helps increase the accuracy in the minimum number of epochs and decreases validation loss.

**3.1.1. Datasets Used.** The proposed system used three benchmark datasets: CASIA Ver-1, UBIRIS ver-2, and MMU. CASIA version 4 (Chinese Academy of Sciences' Institute of Automation) is one of the open databases containing 2639 infrared light images extracted from 239

TABLE 1: Pupil diameter according to the age group.

S. No	Age group	No of subjects	Diameter
1	15–19	12	2.0–2.1
2	20–29	15	2.3–3.5
3	30–39	23	4.1–5.12
4	40–49	23	5.21–6.15
5	50–59	21	4.81–5.77
6	60–69	12	3.58–4.63

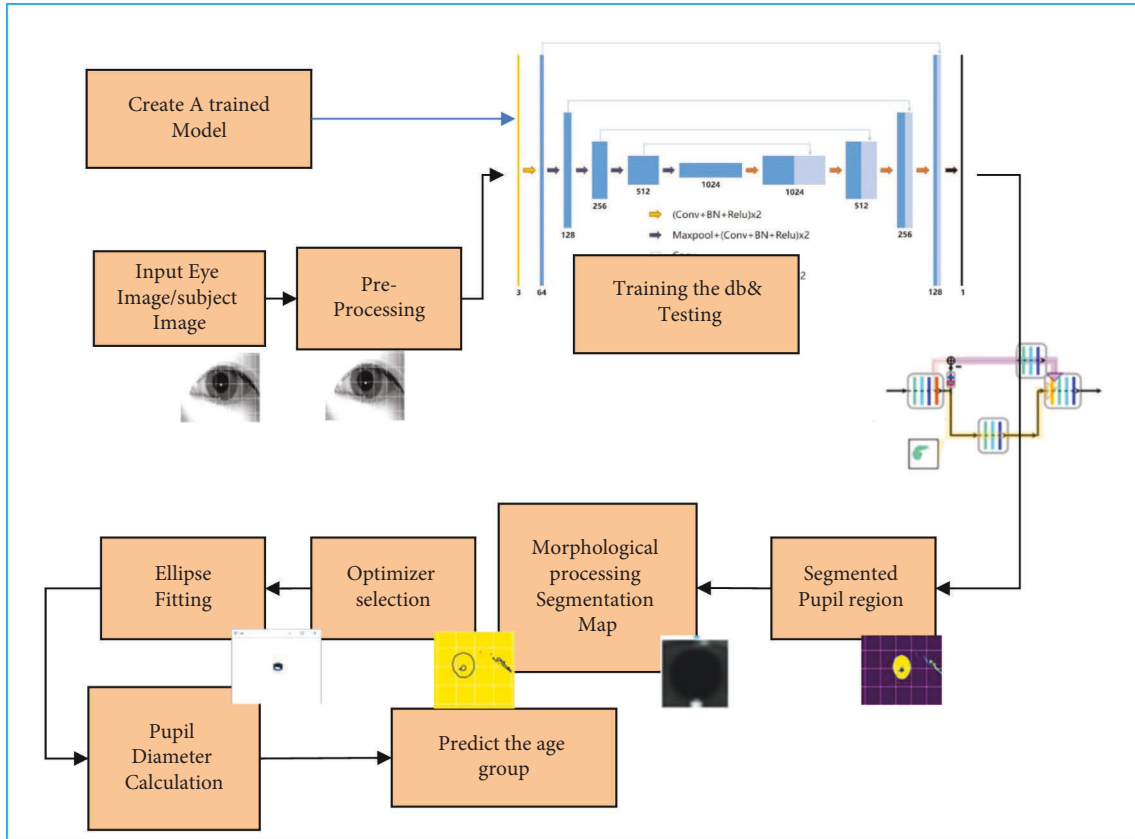


FIGURE 1: Flowchart of the proposed system.

subjects and eye images of different subjects of age groups 18–50 with a storage of 1.86 GB. UBIRIS is Noisy Visible Wavelength Iris Image Databases. The UBIRIS ver-2 is an open-source database that contains 10199 eye images collected from 241 subjects that contain detailed information on the eye, age, gender, and several other parameters. Multimedia University collects the MMU dataset for the iris biometric system, which contains 575 images with a high noise ratio. The three datasets were used individually for the proposed system to know the accuracy of the proposed system in different environments to predict the Pupil. The CASIA dataset is a noise dataset with infrared illumination, which makes automatic segmentation easier. UBIRIS is a colored dataset with significant occlusion and noise, and MMU is a collection of binary images with occlusion and noise. We experimented on three pretrained models to decide on the proposed UNet implementation. To experiment, we considered three CNN models, ResNet, UNet, and VGGNet.

**3.1.2. Using ResNet 50.** The deep neural network is hard to build because of the vanishing gradient problem where the Gradient is backpropagated in the layers, increasing the network's depth even more. As the ResNet is already built with 50 layers, as shown in Figure 2, the network's performance decreased numerously. In order to overcome this problem, we added skip connections in the network, which did not increase the network's performance, but the number of layers (depth) did not increase.

**3.1.3. Using VGGNet.** As the input to the VGG is fixed in size, i.e., of  $224 \times 224$  image, the preprocessing of the image is mandatory since the image's input is  $128 \times 128$  in the training dataset. The image is processed through the convolutional layers with a small receptive field of  $3 \times 3$ , which makes the task of capturing Pupil very slowly. In the configuration of VGG, it also has the convolution filter of size  $1 \times 1$ , where the pixel size is restricted to 1 in the spatial



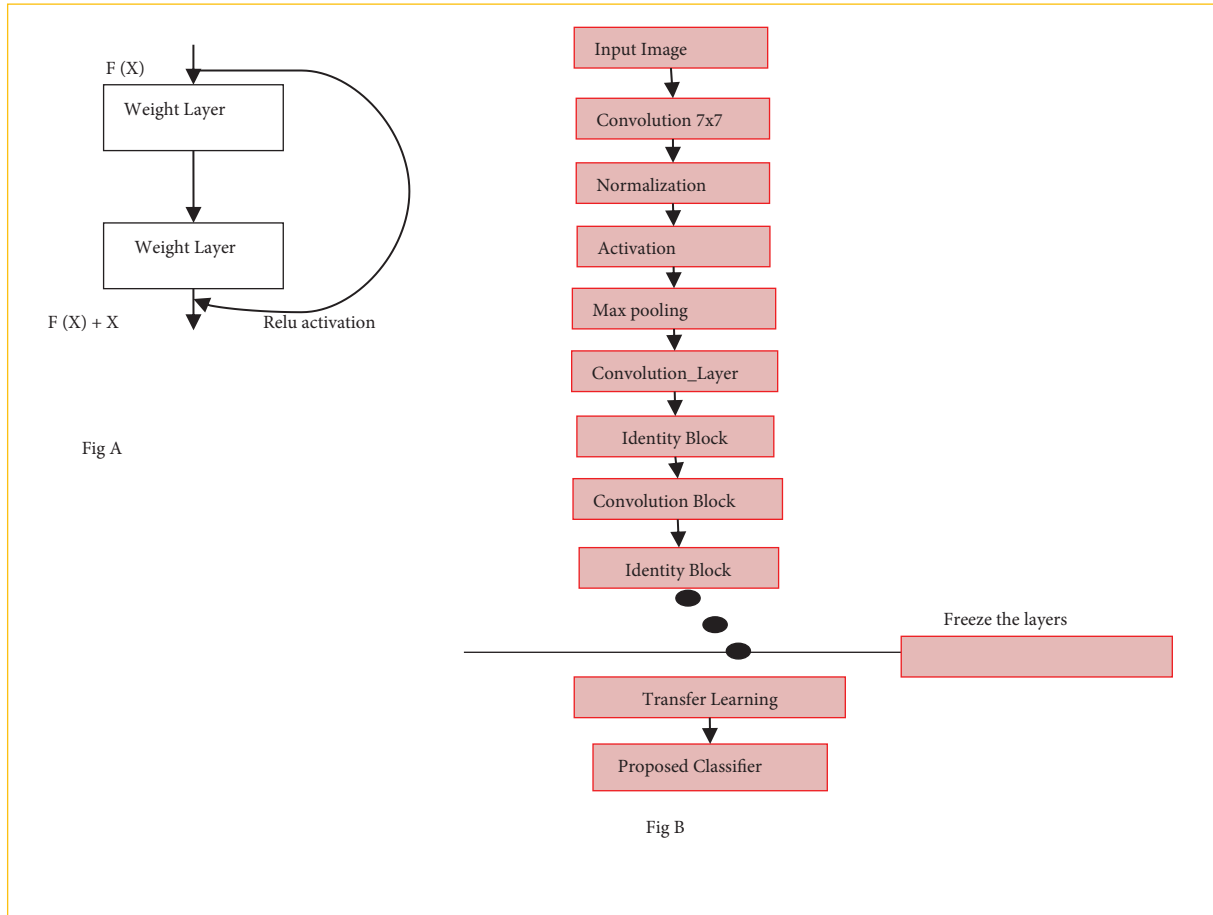


FIGURE 2: Resnet model.

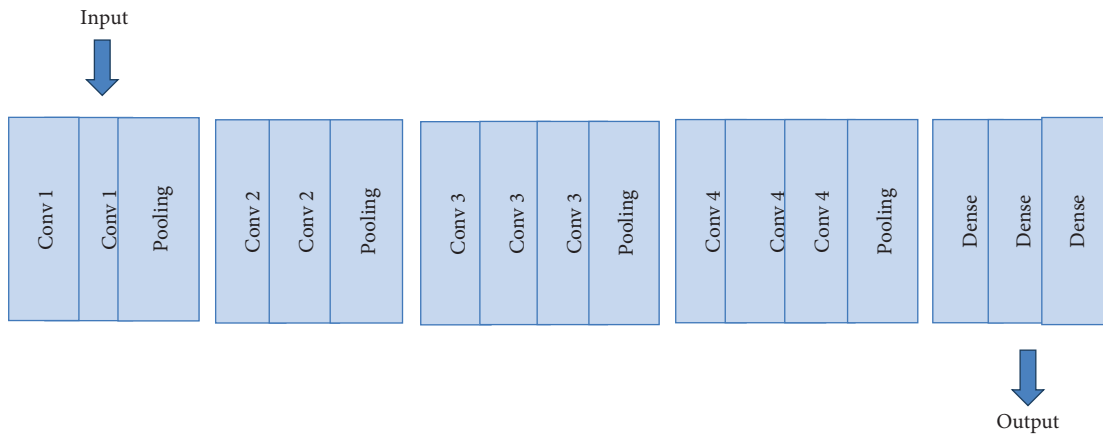


FIGURE 3: VGG architecture.

pooling. By the end of the architecture, due to the fully connected dense layers, the model is about to have 4096 channels where each fully connected layer classifies 1000 channels for the class, as shown in Figure 3. With the weight of 19 layers, it processes input with two conv3-64 layers and max-pooling between two conv3-128 layers, four conv3-256 layers, four conv3-512 layers, four conv3-512 layers, and three fully connected layers and a SoftMax layer with 144 number of parameters.

3.1.4. *Using UNet.* Next, we implemented UNet architecture for the same set of data. The UNet architecture is shown in Figure 4. The advantage of UNet is that it helps us to perform localization and classification together. The other existing models can also do the task, but due to overlapping redundancies, no accuracy in localization, and the need for a fully connected layer at the end of the connection, which leads to excessive network size, we opted UNet. The conventional UNet is modified and is used in the proposed

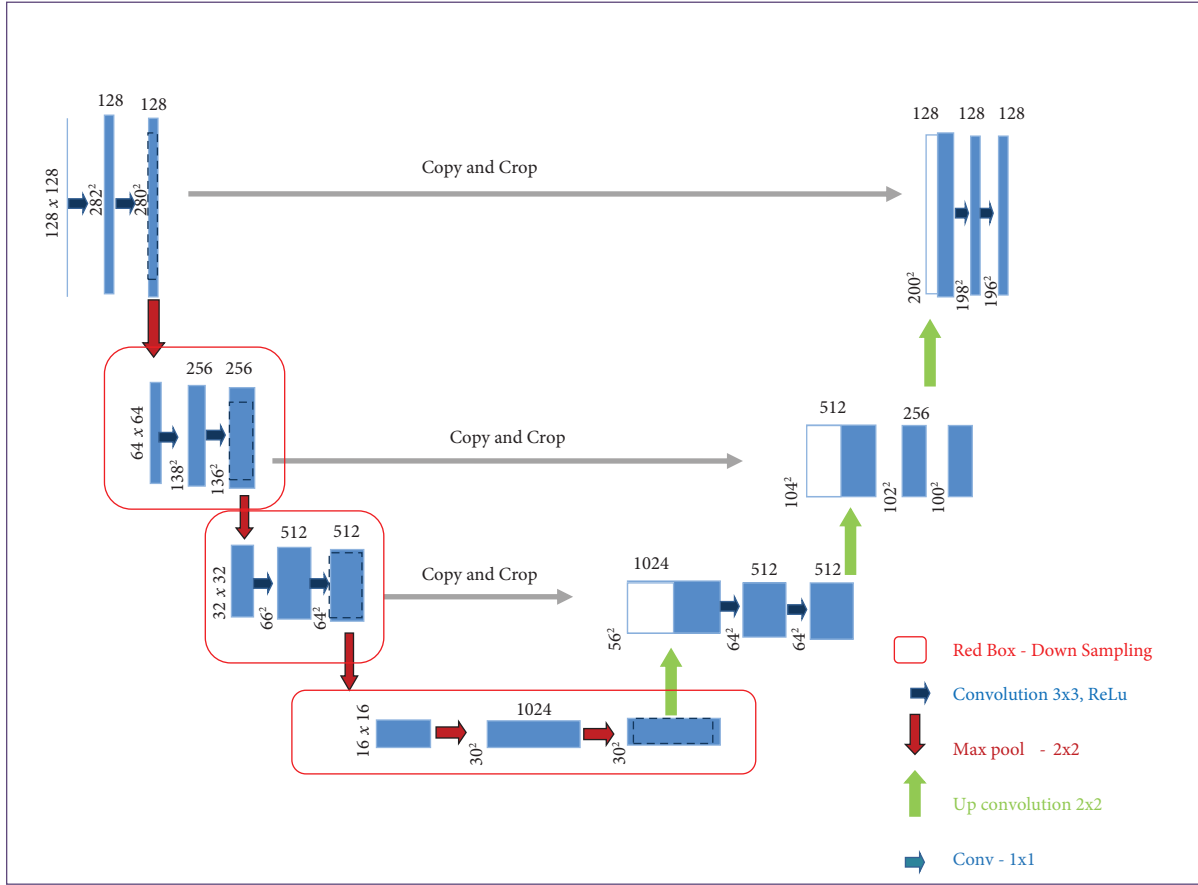


FIGURE 4: Proposed UNet model.

system. The edge mapping feature of the system uses equation (8). In the optimized model of UNet, the first two layers are used to collect the low-level features, and the last three are used for extracting high-level features.

$$L_e = - \sum_{i=1}^x \sum_{j=1}^y [G_e \log(s_e) + (1 - G_e) \log(1 - S_e)], \quad (8)$$

where  $(i, j)$  represents the pixel points from the predicted edge map  $s$  and  $G_e$  is the truth map,  $x, y$  are the width and height of the feature map, to extract the segmented part of the pupil. The sigmoid function activates the concatenation at the end to generate the segmentation feature map. The conventional UNet consists of five encoders, five decoder networks, and a fully connected SoftMax classifier. At each layer, while downsampling, it follows  $3 \times 3$  convolutions and  $2 \times 2$  ReLU function which is followed by max-pooling window with a stride value of 2. This downsampling extracts the features that double at each downsampling path. The low-resolution feature maps are replaced with high-level feature maps during the upsampling path while restoring the features to their original size to produce an output feature map. The concatenation is performed at each layer of encoding and decoding. This process is followed by ReLU activation to generate dense feature maps. After five consecutive encoding and decoding, the final fully connected SoftMax classifier classifies pixel by pixel classification. The conventional UNet

used in medical image processing to segment the tumor was a great attempt. However, this conventional UNet has a drawback regarding segmenting the Pupil from the eye. However, the conventional UNet suffers from 3 significant drawbacks when used with the pupil dataset. Firstly, UNet architecture eliminates redundancy by duplicating the low-resolution features to the next stage. This causes the edge information of the segmented object to be very rough and spiky. As in the proposed application, we need to find the edge of the Pupil accurately to determine the diameter. However, high-resolution edge data does not pass through the downsampling layers and does not contain enough information about those objects. A sample example is shown in Figure 5 because edge information is not appropriate to determine the Pupil for segmentation. The model is shown in Table 2: trains on a total of 1,928,322 trainable parameters that return the dimension of features of Pupil in the feature map. This feature map contains the noise and pupil information approximated with the edge map, as shown in Figure 6.

Hence, we modified conventional UNet to the proposed UNet model with Adaptive Movement Estimation optimization to perform segmentation.

**3.2. Input an Image.** Secondly, the input image is too small to get trained and generate feature maps. As the expected

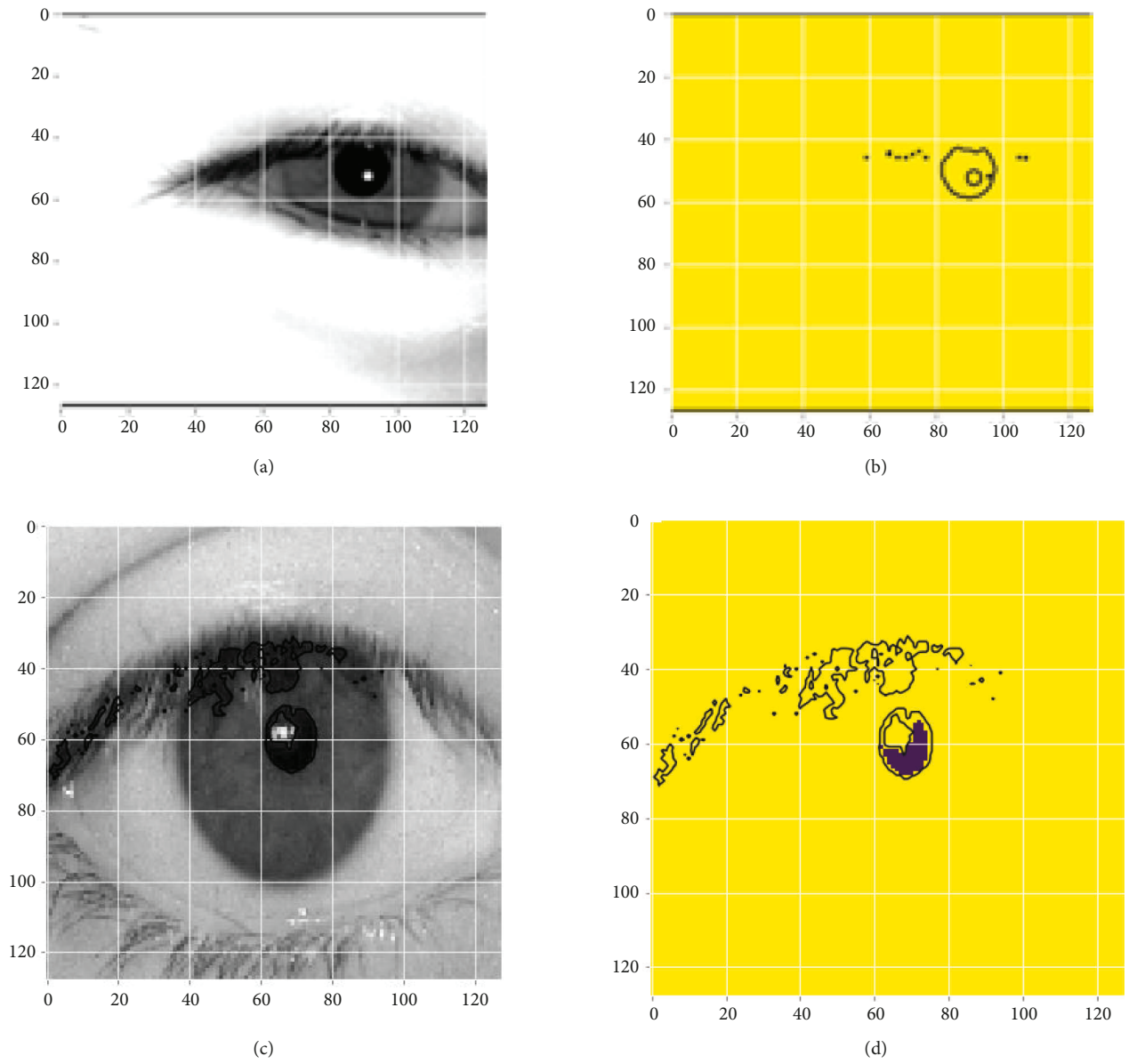


FIGURE 5: Feature map of Predicted Pupil along with noise information.

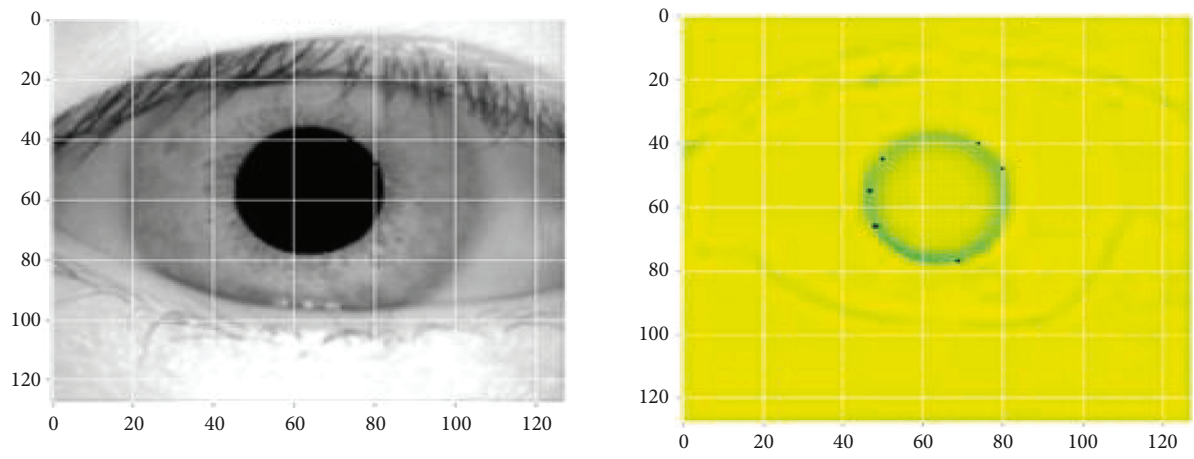


FIGURE 6: Edge Information extracted by Conventional UNet.

output is a single segmented pupil, and there is no chance of other outputs, the SoftMax used in the training model trains the model for a longer time. Instead, the proposed method uses a sigmoid function that works on two-class logistic regression to produce the feature map of the Pupil, followed by morphological thresholding to produce the accurate segmentation of the Pupil. Thirdly, when the input dataset is noisy, such as UBIRIS, the convolutional layers and the presence of max-pooling layers in the encoding path and decoding path increases the receptive field of the input image, with which the pixels around the Pupil are also classified as pupil area as the negative part in the feature map is set to 1. The sample images are shown in Figure 7, and this decreases the accuracy of segmentation of Pupil.

To address this situation, we trained the network with Leaky ReLU to preserve the pixels around the Pupil in a slow-decreasing part of the pupil area to prevent the dying ReLU problem caused by the second addressed problem caused by conventional UNet. Using the above steps, the UNet is reconstructed for the proposed system.

### 3.3. Preprocessing

**3.3.1. Dataset and Training.** The benchmark datasets CASIA and MMU were taken to train the model. For the segmentation, we considered the masks of each dataset to know the Pupil from each image. We divided the model into train and test folders. For each dataset, 80–20 ratio is considered for training-testing, respectively. The GPU-based system with an AMD processor is taken for training the model. We took 50 epochs and batch normalization while training the model. Sample images of each dataset are specified in Figure 8.

**3.4. Training.** We divided the data into training and testing sets. The image is converted into binary, and each dataset's masks are generated separately for training the model. While giving the input, each image is resized to  $128 \times 128$ , as the convolution and max-pooling operations will generate the values of feature map parameters. The training is performed with a proper system configuration and generates a segmentation map. The following sections describe the system configuration and segmentation of Pupil in detail. Table 2 describes the summary of training proposed UNet. We cannot obtain a constant efficiency for the model because when the randomized state of the split changes, so does the model's accuracy. To prevent data leaking, keeping the testing data separate from the training data is best. The performance of the ML model must be assessed while it is being created using the training data. Here is when the value of cross-validation data becomes apparent. We split the data into training and validation sets with 80% and 20% images. The proposed system used a kernel (filter) size of  $2 \times 2$ , batch size of 30, several epochs of 50, leaky relu as the activation, split ration as 80:20, and the learning rate as 0.001. Three optimizers were tested and checked the performance to use Adaptive moment estimation for training the model.

**3.4.1. System Configuration.** We used the GPU-based laptop hardware with 8 GB RAM, AMD processor and software configuration using Keras, Tensorflow, and OpenCV 3 using Python.

The datasets were considered according to the difficulty level of prediction, and the model is trained with ground truth pupil images of each dataset. The output is compared to the ground truth of the image to correct itself. We tested on three optimizers Gradient descent, RMS Prop, and Adaptive moment estimation. Based on the effectiveness shown by the Adaptive momentum algorithm while training, we chose this technique for the optimization in the proposed model. We evaluated training accuracy, recall, Precision, and F1 score for each trail we performed using the optimization. The hyperparameters are calculated using the confusion matrix defined as follows, and Table 3 shows the confusion matrix used in evaluating hyperparameters.

A positive label corresponds to the actual class of interest. Negative is anything apart from it. True positive is the corresponding accurate prediction from the collection of pixels. False negative corresponds to the other classes apart from the actual prediction class. Accuracy is calculated using the following equation:

$$\text{accuracy} = \frac{\text{TP} + \text{TN}}{\text{TP} + \text{FN} + \text{TN} + \text{FP}}. \quad (9)$$

It is the fraction that measures the correctly classified pixels. The Precision can be calculated using the following equation:

$$\text{precision} = \frac{\text{tp}}{\text{tp} + \text{FP}}. \quad (10)$$

The approximate factual information can be calculated through Precision. It is the degree to which the class can be accurate. The recall is another hyperparameter that can be calculated through a confusion matrix using equation (11), which specifies the actual metric of several positives in the prediction:

$$\text{recall} = \frac{\text{TP}}{\text{TP} + \text{FN}}. \quad (11)$$

Another parameter we need is the balancing between Precision and recall. It can be calculated using the F1-score of the model using the following equation:

$$f1\text{score} = \frac{2(P * R)}{P + R}, \quad (12)$$

where  $P$  is Precision and  $R$  is recall.

**3.5. Segmentation of Pupil.** The segmentation map is constructed from pooling operations in the encoding path followed by the skip connections on the input image. The process is shown in Figure 9. It describes the process of executing 2D. We start with a kernel and “stride” (slide) it over the 2D input data, multiplying the portion of the input it is currently on element-wise and then adding the results into a single output cell. Every area the kernel slides over is subjected to this same procedure, which creates a new 2D

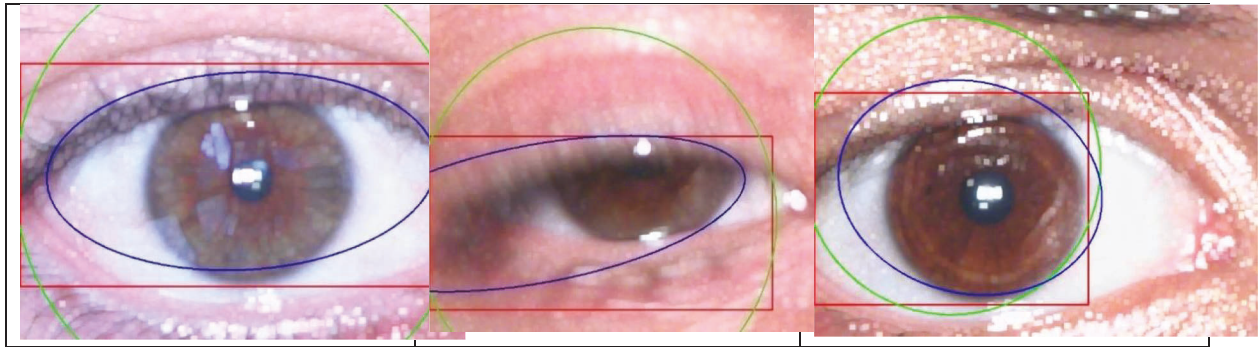


FIGURE 7: False nonpupil area detection in Noisy Images.

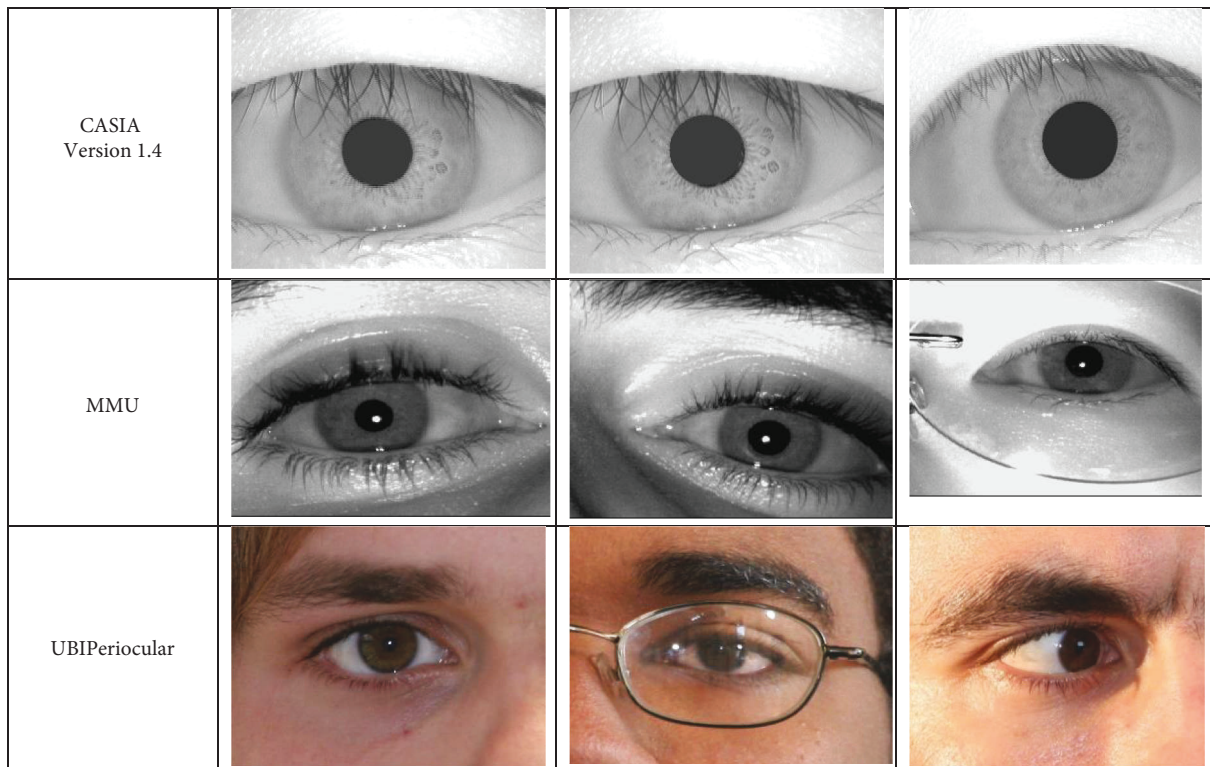


FIGURE 8: Sample image from Datasets.

feature matrix. Stride describes the amount by which the kernel moves on the input feature matrix. In the animation below, the input matrix gets an additional stripe of zeros added from each of its four sides to guarantee that the output matrix is the same size as the input matrix. (Zero) padding is the term for this. The encoder module reduces the resolution by half for every pooling operation and increases the receptive field. The skip connections in the model reconstruct the original image to restore the changes in the image. Due to this, we generated the feature map, as shown in Figure 5. However, the feature maps that we obtained were noisy.

**3.6. Morphological Processing and Segmentation Map.** The main aim of the morphological operation is to reduce the

noise on the feature map. This process is described in Figure 10, and this process enhanced the image resolution by removing noise caused by eyelashes to give the feature map ready for ellipse fitting. We first applied a median filter to remove general noise caused, followed by erosion and dilation to enhance the pupil area. We applied thresholding on the enhanced pupil area to form a segmentation map to fit the ellipse.

**3.7. Optimizer Selection.** The main challenge in the machine learning algorithm is to minimize the loss at every epoch from the weights of each neuron. The optimizer helps to modify the weights and learning rate, which directly helps in reducing the overall loss. We experimented with three optimizers in the proposed method to predict the system's

TABLE 2: Training summary of UNet.

Layer (depth -index)	Output shape	Training parameters
Downsampling		
Conv2d: 3-1	32, 512, 512	320
BatchNorm2d: 3-3	32, 512, 512	64
Conv2d: 3-4	32, 512, 512	9,248
Conv2d: 3-8	64, 256, 256	18,496
BatchNorm2d: 3-10	64, 256, 256	128
Conv2d: 3-11	64, 256, 256	36,928
Conv2d: 3-15	128, 128, 128	73,856
BatchNorm2d: 3-17	128, 128, 128	256
Conv2d: 3-18	128, 128, 128	147,584
BatchNorm2d: 3-20	128, 128, 128	256
Conv2d: 3-22	256, 64, 64	295,168
BatchNorm2d: 3-24	256, 64, 64	512
Conv2d: 3-25	256, 64, 64	590,080
BatchNorm2d: 3-27	256, 64, 64	512
Upsampling		
ConvTranspose2d: 3-28	128, 128, 128	131,200
BatchNorm2d: 3-30	128, 128, 128	256
Conv2d: 3-32	128, 128, 128	295,040
BatchNorm2d: 3-34	128, 128, 128	256
Conv2d: 3-35	128, 128, 128	147,584
BatchNorm2d: 3-37	128, 128, 128	256
ConvTranspose2d: 3-38	64, 256, 256	32,832
BatchNorm2d: 3-40	64, 256, 256	128
Conv2d: 3-42	64, 256, 256	73,792
BatchNorm2d: 3-44	64, 256, 256	128
Conv2d: 3-45	64, 256, 256	36,928
BatchNorm2d: 3-47	64, 256, 256	128
ConvTranspose2d: 3-48	32, 512, 512	8,224
BatchNorm2d: 3-50	32, 512, 512	64
Conv2d: 3-52	32, 512, 512	18,464
BatchNorm2d: 3-54	32, 512, 512	64
Conv2d: 3-55	32, 512, 512	9,248
BatchNorm2d: 3-57	32, 512, 512	64

TABLE 3: Confusion matrix.

		Predicted class	
		Positive pred	Negative pred
True prediction class	Positive	TP (true positive)	FN (false negative)
	Negative	FP (false positive)	TN (true negative)

accuracy. The discussion and resultant loss values are explained in detail in the respective subsections.

**3.7.1. Stochastic Gradient Descent Algorithm.** This fundamental algorithm is commonly used in many deep learning techniques. It is the first-order derivative function to calculate the loss value. The weights of neurons are continuously altered so that they can reach minima. The Gradient is calculated using the following equation:

$$\text{for } i \text{ in range } (k): w_j := w_j - \alpha \frac{\partial J_i}{\partial w_j}, \quad (13)$$

where  $j$  is the cost of the  $i$ th training sample. Due to its nature of updating every time at every epoch, all parameters of the dataset were updated at every epoch, which increased

the time and loss. The corresponding result while training is shown in Table 4.

The loss using the SGD equation is calculated at every epoch; by the end of 40 epochs, the loss value is 2.36. The corresponding accuracy and loss graphs are shown in Figure 11. As we cannot directly test on the large dataset, we took the training sample of 700 images and their masks and a test sample of 140 images to perform the modeling.

The obtained loss value is 2.36. The confusion matrix can be drawn as shown in Figure 11. The hyperparameters for the SGD are shown in Table 5.

**3.7.2. RMS Prop.** Unlike the SGD, RMS Prop uses the decaying average of the gradients while adapting the parameter. It updates the weight for each input variable.

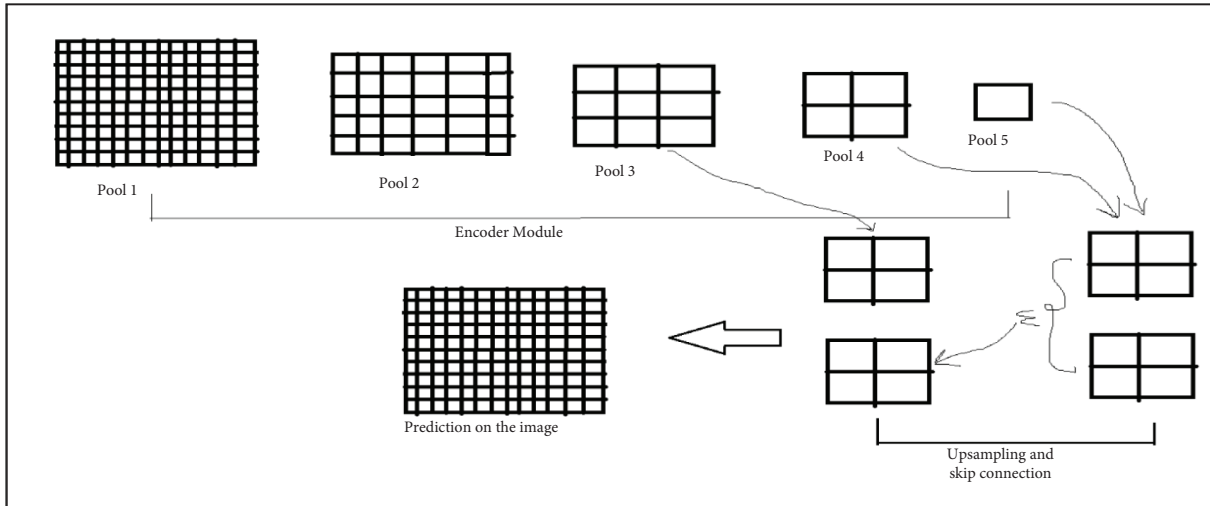


FIGURE 9: Segmentation feature map.

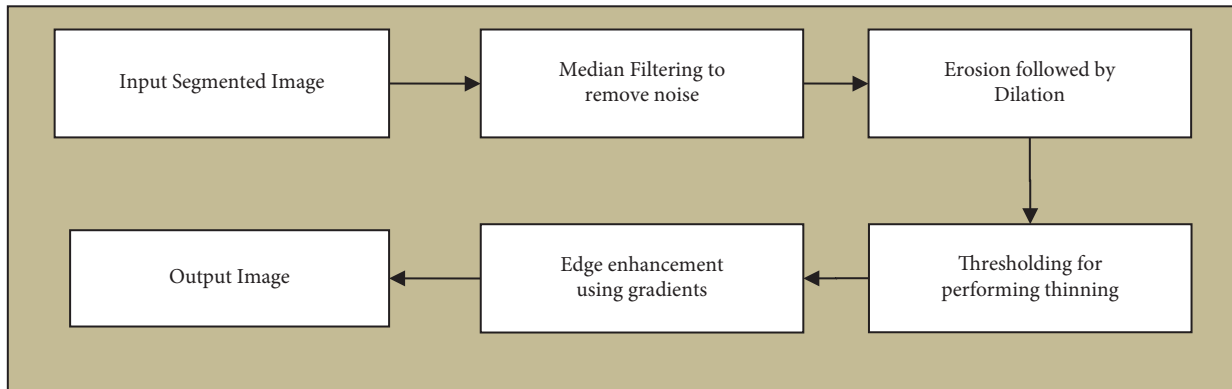


FIGURE 10: Flow chart for Morphological Processing.

TABLE 4: Training parameters using SGD in the model.

CNN layer	Operation	Output	Stride	Kernel	In	Out	Trainable variables
$64 \times 64 \times 32$	Convolution	$32 \times 32 \times 32$	2	2	32	32	0
$32 \times 32 \times 32$		$32 \times 32 \times 64$	2	3	32	64	0
$32 \times 32 \times 64$	Max pooling	$16 \times 16 \times 64$	2	3	64	64	9465
$16 \times 16 \times 64$	Conv	$16 \times 16 \times 128$	2	3	64	128	0
$16 \times 16 \times 128$	Conv	$8 \times 8 \times 128$	2	3	128	128	35642
$8 \times 8 \times 128$	Max pooling	$8 \times 8 \times 256$	2	3	128	256	32456
$8 \times 8 \times 256$	Conv	$16 \times 16 \times 128$	2	3	256	128	0
$16 \times 16 \times 128$	Conv	$16 \times 16 \times 256$	2	3	128	256	0
$16 \times 16 \times 256$	Conv	$16 \times 16 \times 128$	2	3	256	128	78954
$16 \times 16 \times 128$	Max pooling	$32 \times 32 \times 64$	2	3	128	64	123487
$32 \times 32 \times 64$	Conv	$32 \times 32 \times 128$	2	3	64	128	145863
$32 \times 32 \times 128$	Conv	$32 \times 32 \times 64$	2	3	128	64	754623
$32 \times 32 \times 64$	Conv	$64 \times 64 \times 32$	2	3	64	32	0
$64 \times 64 \times 32$	Max pooling	$64 \times 64 \times 64$	2	3	32	64	0
$64 \times 64 \times 64$	Conv	$64 \times 64 \times 32$	2	3	63	32	458692
$128 \times 128 \times 16$	Conv	$128 \times 128 \times 32$	2	3	16	32	459896
$128 \times 128 \times 32$	Conv	$128 \times 128 \times 16$	2	3	32	16	595656
$14 \times 14 \times 512$	Flatten	$7 \times 7 \times 512$	1	3	512	512	674569
$1 \times 1 \times 4096$	FC2	$1 \times 1 \times 1000$	7	2	4096	1000	745892

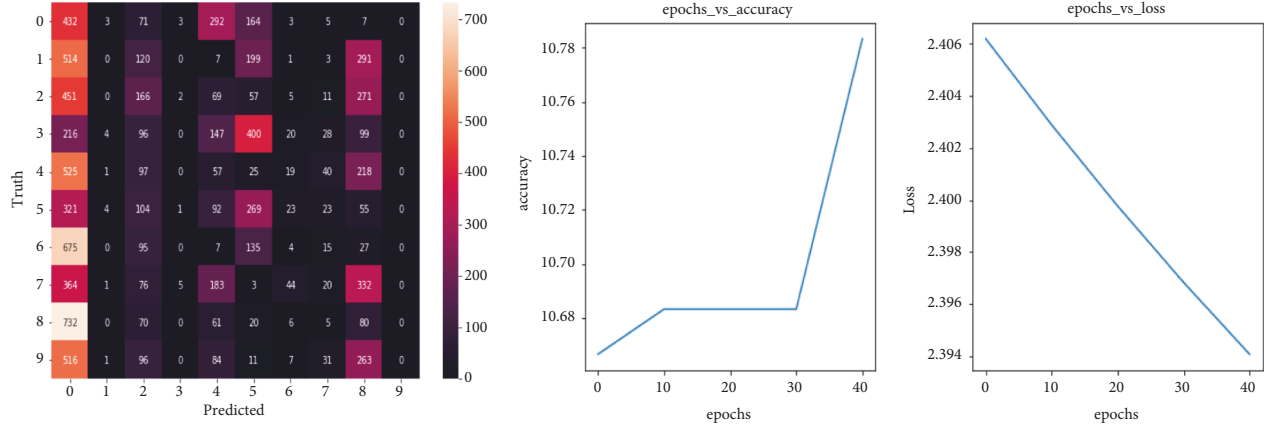


FIGURE 11: Confusion Matrix and Accuracy, Loss plots for SGD optimization.

TABLE 5: Hyperparameters of SG algorithm.

Stochastic gradient	
Precision	75.9
Specificity	74.2
F-score	76.2
Accuracy	71.9

Because of this property, we increased our learning rate with its beta value (Value of momentum) set to 0.9. The corresponding weights hence will be changed by the partial derivative functions equations (14) and (15) and weight  $w$  and gradient  $b$  can be calculated with equations (16) and (17).

$$v_{d_i} = \beta \cdot \partial_{d_i} + (1 - \beta) d_i^2, \quad (14)$$

$$v_{d_j} = \beta \cdot \partial_j + (1 - \beta) d_j^2, \quad (15)$$

$$w = w - \alpha \cdot \frac{d_i}{\sqrt{v_{d_i}} + \epsilon}, \quad (16)$$

$$b = b - \alpha \cdot \frac{d_i}{\sqrt{v_{d_j}} + \epsilon}. \quad (17)$$

For the proposed system, when the residual path carries the low-resolution value,  $v_{d_i}$  can be very low, with which the weight value may become zero. To prevent that, we are adding  $\epsilon$  to prevent the denominator loss. The average of squared gradients balances the step size to avoid the vanishing gradient problem. The training using RMS Prop is shown in Table 6.

Because of the automatic adjusting of the learning rate, the trainable parameters increased more than the SGD implementation. Hence the loss value obtained is 2.30. The number of epochs is 50, the accuracy is 57% and the loss is 2.30. The confusion matrix and the learning curve are shown in Figure 12. The hyperparameters for the RMS Prop are shown in Table 7.

**3.7.3. Adaptive Momentum Optimization.** The adaptive moment optimizer uses squared gradients similar to the

RMS but calculates the moving averages. Due to the free selection of the learning rate for the neural network, it is easier to implement the technique. We took the initial moving averages in the proposed system as 0.9 and 0.999 for the minibatch and beta of the following equations:

$$m_i = \beta m_{i-1} + (1 - \beta) g_i, \quad (18)$$

$$v_i = \beta_2 v_{i-1} + l' - \beta_2 g_i^2, \quad (19)$$

where  $m$  and  $v$  the mean and variance of moving averages of minibatch and betas? These values express the first and second moments. The weights from the corrected moments can be calculated using the following equation:

$$w_t = w_{t-1} - \eta. \quad (20)$$

With the epsilon value as  $1e-7$ , the training values obtained for the proposed method are described in Table 8.

The loss and accuracy of the sample-tested data are shown in Figure 13. The loss value is 1.82, significantly less than the other two optimizers. The confusion matrix is represented in Figure 13.

The hyperparameters are calculated using the confusion matrix for Adaptive moment estimation and the values are tabularized as shown in Table 9.

When comparing the three optimizers, as shown in Table 10, plotted in Figure 14, we chose the adaptive momentum estimation as the suitable optimizer for the current dataset to perform the segmentation with minimum loss.

**3.8. Ellipse Fitting.** On the feature map obtained in the previous stage, we called a natural ellipse fitting algorithm using algebraic least squares using the following equation:

$$J(\theta, x_1, x_2, x_3 \dots x_1) = \sum_{n=1}^N \frac{\theta^i u(x_j) u(x_j)^i \theta}{\theta^2}, \quad (21)$$

where  $j$  is the Jacobian function,  $\theta$  is the vectorized parameters,  $x$  is the vector variable, and  $u(x_j)$  is the conic equation. The estimated pupil diameter can be corrected using the regression equation:



TABLE 6: Training parameters using RMS Prop in the model.

CNN layer	Operation	Output	Stride	Kernel	In	Out	Trainable variables
$64 \times 64 \times 32$	Convolution	$32 \times 32 \times 32$	2	2	32	32	0
$32 \times 32 \times 32$		$32 \times 32 \times 64$	2	3	32	64	1352
$32 \times 32 \times 64$	Max pooling	$16 \times 16 \times 64$	2	3	64	64	0
$16 \times 16 \times 64$	Conv	$16 \times 16 \times 128$	2	3	64	128	4256
$16 \times 16 \times 128$	Conv	$8 \times 8 \times 128$	2	3	128	128	45897
$8 \times 8 \times 128$	Max pooling	$8 \times 8 \times 256$	2	3	128	256	0
$8 \times 8 \times 256$	Conv	$16 \times 16 \times 128$	2	3	256	128	75686
$16 \times 16 \times 128$	Conv	$16 \times 16 \times 256$	2	3	128	256	77568
$16 \times 16 \times 256$	Conv	$16 \times 16 \times 128$	2	3	256	128	145689
$16 \times 16 \times 128$	Max pooling	$32 \times 32 \times 64$	2	3	128	64	0
$32 \times 32 \times 64$	Conv	$32 \times 32 \times 128$	2	3	64	128	214563
$32 \times 32 \times 128$	Conv	$32 \times 32 \times 64$	2	3	128	64	458796
$32 \times 32 \times 64$	Conv	$64 \times 64 \times 32$	2	3	64	32	8458923
$64 \times 64 \times 32$	Max pooling	$64 \times 64 \times 64$	2	3	32	64	0
$64 \times 64 \times 64$	Conv	$64 \times 64 \times 32$	2	3	63	32	7589666
$128 \times 128 \times 16$	Conv	$128 \times 128 \times 32$	2	3	16	32	47996669
$128 \times 128 \times 32$	Conv	$128 \times 128 \times 16$	2	3	32	16	47987642
$14 \times 14 \times 512$	Flatten	$7 \times 7 \times 512$	1	3	512	512	75852252
$1 \times 1 \times 4096$	FC2	$1 \times 1 \times 1000$	7	2	4096	1000	14256335

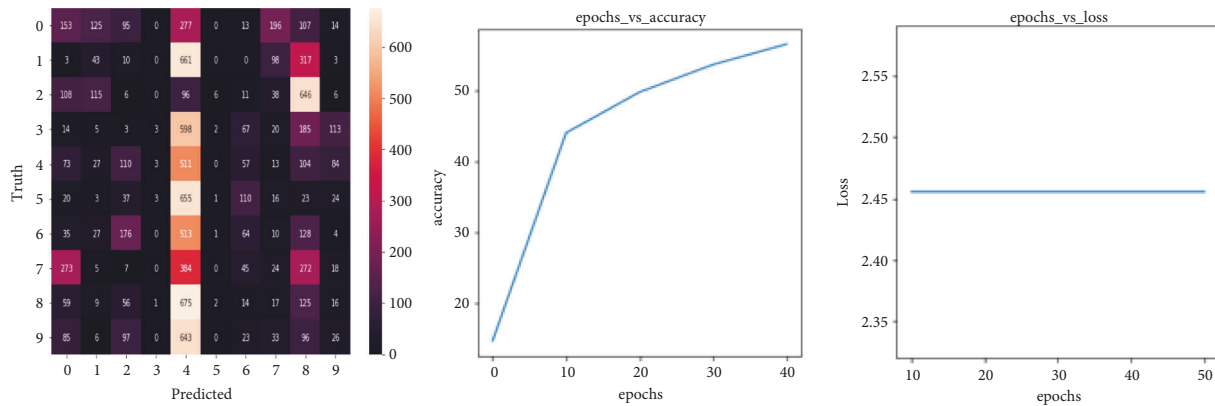


FIGURE 12: Confusion matrix and accuracy, loss plots for RMS prop.

$$E_c = P - k_0 - k_1x - k_2y, \quad (22)$$

where  $E_c$  is the corrected diameter,  $P$  is the predicted diameter values,  $x$  and  $y$  are horizontal and vertical gaze axes, and  $k_{0,1,2}$  are regression parameters.

3.9. Age Prediction. In the last phase of the proposed methodology, we presented the age prediction using Figure 15, in which the calculated diameter is compared with specific values predicted using pupilometer to classify the age. Section 4.2 clearly shows the estimated Pupil and the age-predicted out of it.

#### 4. Results & Discussion

Once the optimizer selection is finalized, we tried the proposed system’s segmentation, and it is accurate. We trained the system to segment the pupil part carefully to predict the diameter of the Pupil and the age. We considered three different step cases using the proposed method. First,

TABLE 7: Hyperparameters of RMS prop algorithm.

RMS prop	
Precision	75.3
Specificity	88.4
F-score	80.2
Accuracy	84.3

we analyzed the proposed system using the benchmark datasets, followed by checking the prediction on the image. Third, by using the live video. In these three cases, we calculated the accuracy for three cases by considering benchmark datasets from images and live videos. Three scenarios are explained in the following subsections.

##### 4.1. Three Possible Cases of Input

4.1.1. Case I: Considering Benchmark Datasets for Segmentation. The benchmark datasets CASIA and MMU were considered to perform the segmentation of Pupil.

TABLE 8: Training parameters using adaptive moment optimizer prop in the model.

CNN layer	Operation	Output	Stride	Kernel	In	Out	Trainable variables
$64 \times 64 \times 32$	Convolution	$32 \times 32 \times 32$	2	2	32	32	0
$32 \times 32 \times 32$		$32 \times 32 \times 64$	2	3	32	64	0
$32 \times 32 \times 64$	Max pooling	$16 \times 16 \times 64$	2	3	64	64	9465
$16 \times 16 \times 64$	Conv	$16 \times 16 \times 128$	2	3	64	128	0
$16 \times 16 \times 128$	Conv	$8 \times 8 \times 128$	2	3	128	128	35642
$8 \times 8 \times 128$	Max pooling	$8 \times 8 \times 256$	2	3	128	256	32456
$8 \times 8 \times 256$	Conv	$16 \times 16 \times 128$	2	3	256	128	0
$16 \times 16 \times 128$	Conv	$16 \times 16 \times 256$	2	3	128	256	0
$16 \times 16 \times 256$	Conv	$16 \times 16 \times 128$	2	3	256	128	78954
$16 \times 16 \times 128$	Max pooling	$32 \times 32 \times 64$	2	3	128	64	123487
$32 \times 32 \times 64$	Conv	$32 \times 32 \times 128$	2	3	64	128	145863
$32 \times 32 \times 128$	Conv	$32 \times 32 \times 64$	2	3	128	64	754623
$32 \times 32 \times 64$	Conv	$64 \times 64 \times 32$	2	3	64	32	0
$64 \times 64 \times 32$	Max pooling	$64 \times 64 \times 64$	2	3	32	64	0
$64 \times 64 \times 64$	Conv	$64 \times 64 \times 32$	2	3	63	32	458692
$128 \times 128 \times 16$	Conv	$128 \times 128 \times 32$	2	3	16	32	459896
$128 \times 128 \times 32$	Conv	$128 \times 128 \times 16$	2	3	32	16	595656
$14 \times 14 \times 512$	Flatten	$7 \times 7 \times 512$	1	3	512	512	652342
$1 \times 1 \times 4096$	FC2	$1 \times 1 \times 1000$	7	2	4096	1000	687519

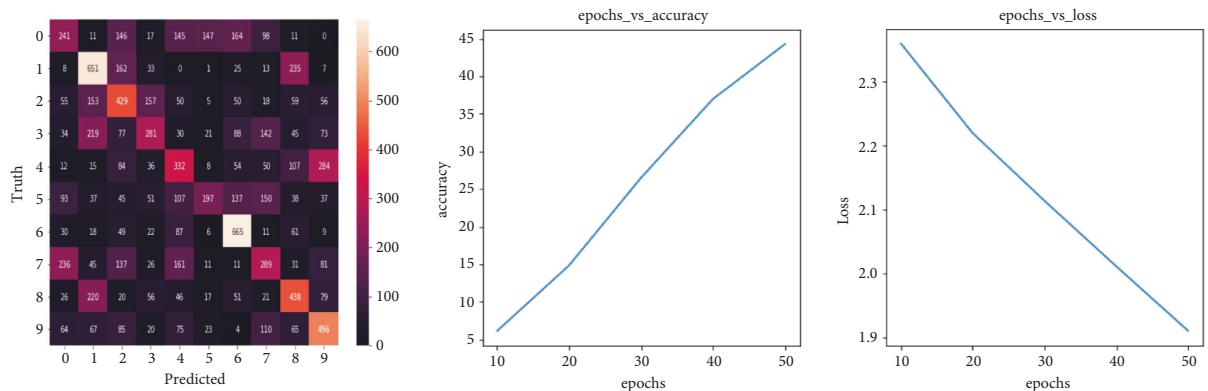


FIGURE 13: Confusion matrix and accuracy, loss plots for adaptive moment optimizer.

TABLE 9: Hyperparameters of adaptive moment algorithm.

Adaptive movement estimation	
Precision	93.0
Specificity	96.4
F-score	94.7
Accuracy	96.0

TABLE 10: Comparison graph of optimizers.

	Stochastic gradient	Root mean square prop	Adaptive movement estimation
Precision	75.9	75.3	93.0
Specificity	74.2	88.4	96.4
F-score	76.2	80.2	94.7
Accuracy	71.9	84.3	96.0

Figure 16 shows the segmented part of the Pupil after fitting an ellipse to it.

The original input images are taken from six subjects in the CASIA database of different age groups. The low-intensity values from Figure 16 are carefully discarded due to

the morphological processing after the feature map generation. The edges of subjects are also carefully taken without any further loss of resolution due to the residual path we added to the architecture. CASIA is no noise database, as it is captured through infrared near the camera.

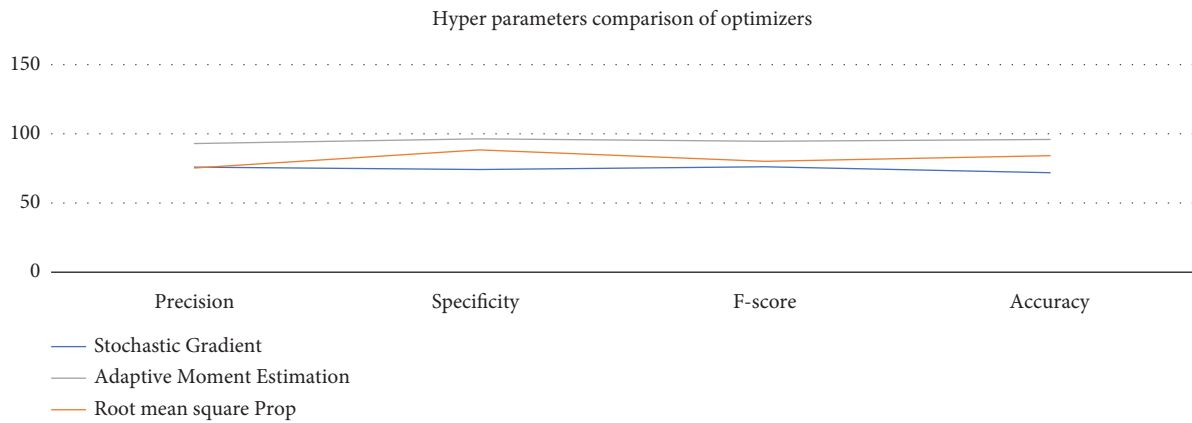


FIGURE 14: Graph of hyperparameters.

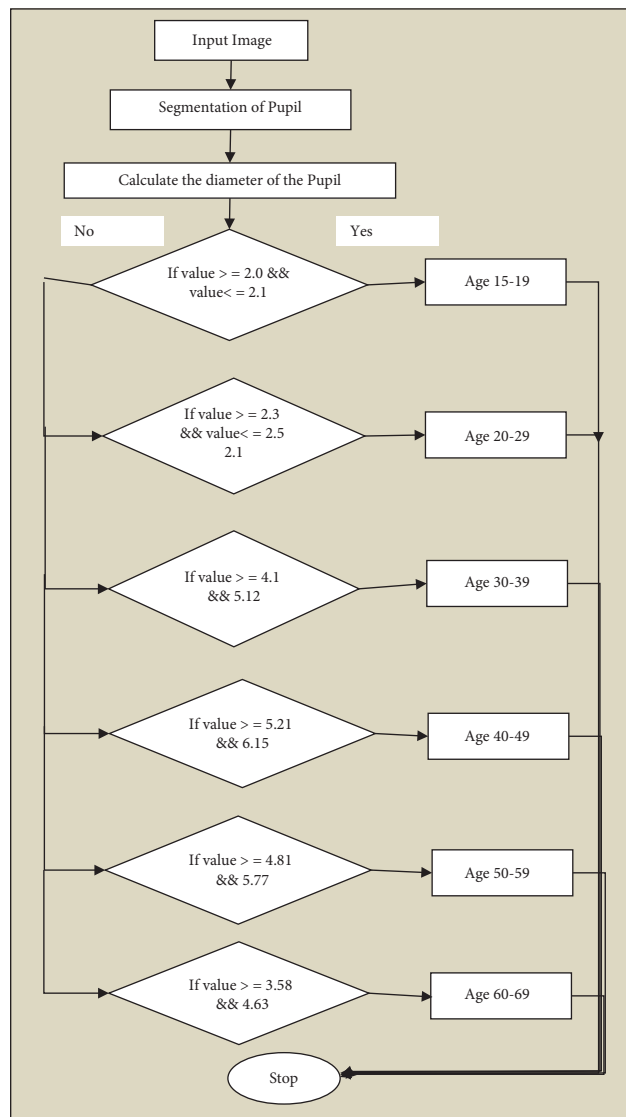


FIGURE 15: Flowchart of age classification.

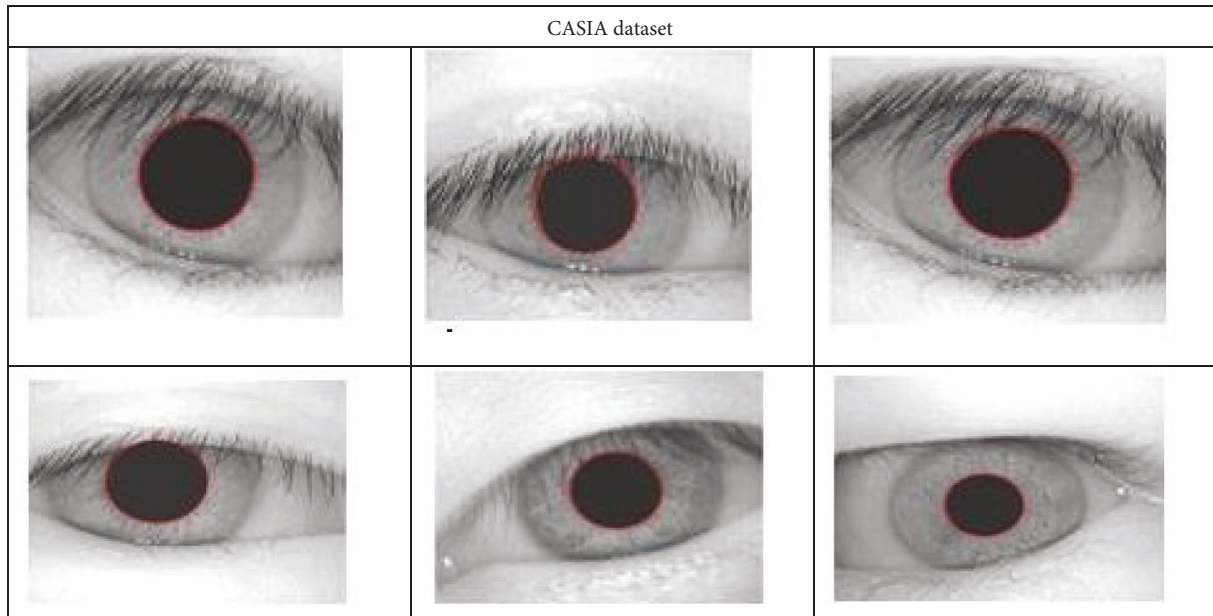


FIGURE 16: Ellipse fitting on CASIA dataset.

The segmentation of Pupil is almost accurate to 100% due to significantly less noise. The same experimentation is performed on the MMU dataset and UBIRIS also. The resultant fitted images are shown in Figure 17. Due to the occlusion and noise present in the images, the prediction was not 100% accurate. However, the accuracy we obtained for the CASIA dataset is 98%. For the MMU dataset, it is 94%, and for UBIRIS, it is 91%. By understanding the results obtained with the benchmark datasets, we designed the model to suit live video. There were three challenges we needed to face for live video. Those are as follows: .

- (1) A video is a moving object. Performing segmentation needs a static image.
- (2) We will receive a full image of the Subject. We directly cannot see the eye image of the person.
- (3) The clarity of the input video is random, which depends upon the background and lighting conditions of the room. Because of these three challenges, we first considered segmentation on the image, which aided in proceeding to the live video. We discussed the result analysis of the image in the following case. The model accuracy and loss graphs are shown in Figure 18. The proposed implementation is then tested on benchmark datasets. Surprisingly the output was at most accurate on the noisy dataset, as shown in Figure 19. Hence the proposed system then trained on the input eye without segmentation by generating the mask to identify the pupil part. In case II, we explained the corresponding scenario.

*4.1.2. Case II: Confirming Age Prediction from the Image.* For this case, we considered the dataset of UBIRIS and periocular images to localize the pupil area. As the input

image is noisy with other features such as skin eyebrows, segmentation of the Pupil is a complex task. Hence, we generated the eye masks to train the network for pupil segmentation. The experiment was quite working and the segmentation was successful for all the images. The resultant prediction is shown in Figure 20. With this advancement, we moved on to the segmentation of live video. The analysis is discussed in the following case.

*4.1.3. Case III: Segmentation on Live Video.* We considered the specification of the system as an ASUS gaming laptop, with a GPU-based processor and 8 GB of Ram capacity to run the algorithm. The localization process is a bit difficult in the case of live video. In the proposed algorithm, we performed preprocessing to remove the noise from the full facial image to generate pixel data of the eye. The preprocessing steps are as follows.

*Step 1.* Predict the face of the Subject.

*Step 2.* Locate facial points using landmarks detection.

*Step 3.* Localize the eye portion out of the region.

*Step 4.* Load the model to predict the Pupil.

*Step 5.* Segment the pupil part.

*Step 6.* Fit the ellipse.

We explained each step in detail in further discussion. In Step 1, we used the voila Jones face detection algorithm, which used the Haar cascade frontal face classifier to detect the face's  $x$ ,  $y$ ,  $w$ , and  $h$  parameters to define the rounded box using ROI selection. As the viola Jones algorithm suffers only

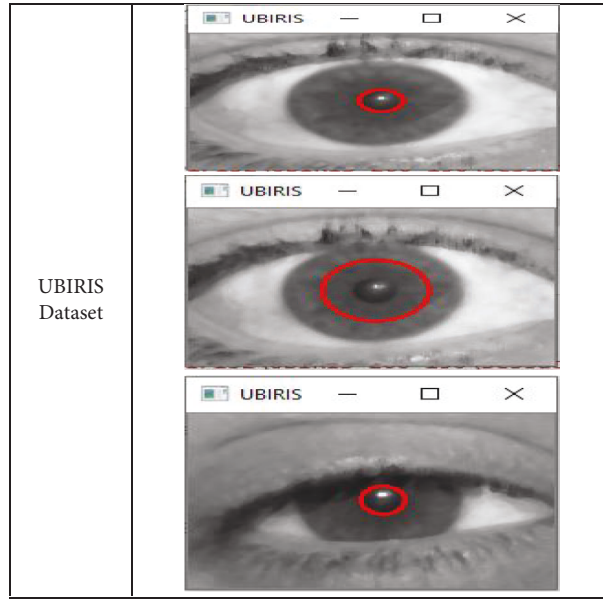


FIGURE 17: Result of segmentation on MMU and UBIRS datasets.

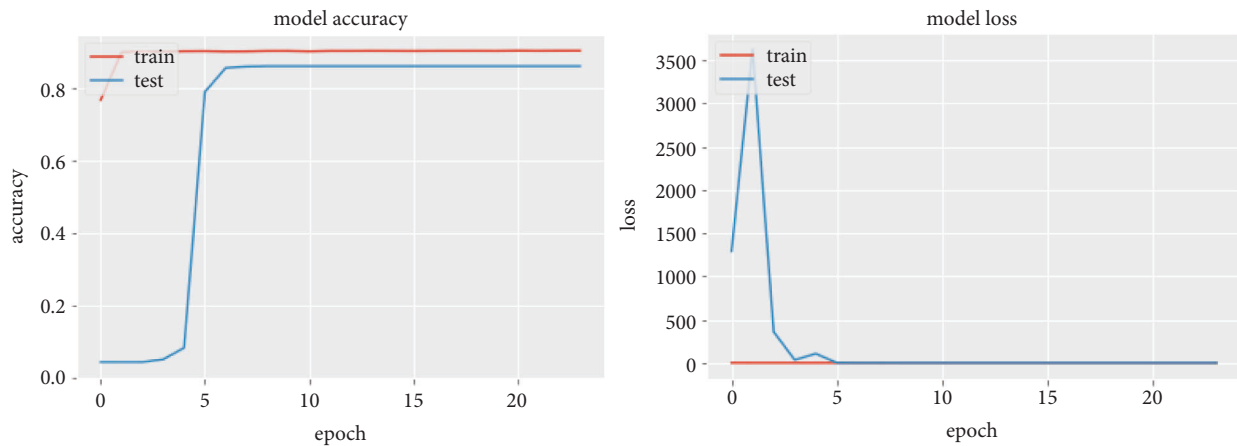


FIGURE 18: Plots are drawn against accuracy and loss.

binary classification and is too sensitive for low and high brightness and high false detection rates in further classification of facial parts, we did not consider this for eye localization. The resultant image after facial detection  $s$  is shown in Figure 21.

Once we obtain the face from the input video, the top part of the work is done. Then we proceeded to the next step, locating facial points using 49 landmarks. We checked the various landmark detection algorithms from the literature and selected the best detection using 49 landmarks to predict various parts of the face, as shown in Figure 22.

The 49 landmarks estimation algorithm is processed to produce the feature map of the proposed system. The corresponding feature map is shown in Figure 23(a). We figured out the eye position to perform the segmentation. In Step 3, the Eye position is localized, as shown in Figure 23(b). The proposed method is pupil segmentation. As the clarity is less in the live video, we implemented thresholding to perform the

segmentation. As we implemented thresholding on the binary image, as proposed, we could analyze the image quickly. The resultant segmentation is shown in Figures 23(c) & 23(d).

The pupil positions were extracted from the video using key points. Sample key point selection from the console is shown in Figure 24. The key points help us to locate the ellipse out of the face. In Step 5, we called the ellipse fitting algorithm to fit the ellipse. The segmented part of the Pupil is further processed from the image to perform age prediction. The diameter of the Pupil is shown in Figure 25.

It is calculated to check the age of the person. From the literature as we reviewed several articles written by researchers to check the pupil diameter variation according to age, we confirmed our research from various authors as shown in the literature. The diameter of the Pupil is calculated from the segmented Pupil to predict the subject's age. We experimented on random images collected from the Internet on live video.

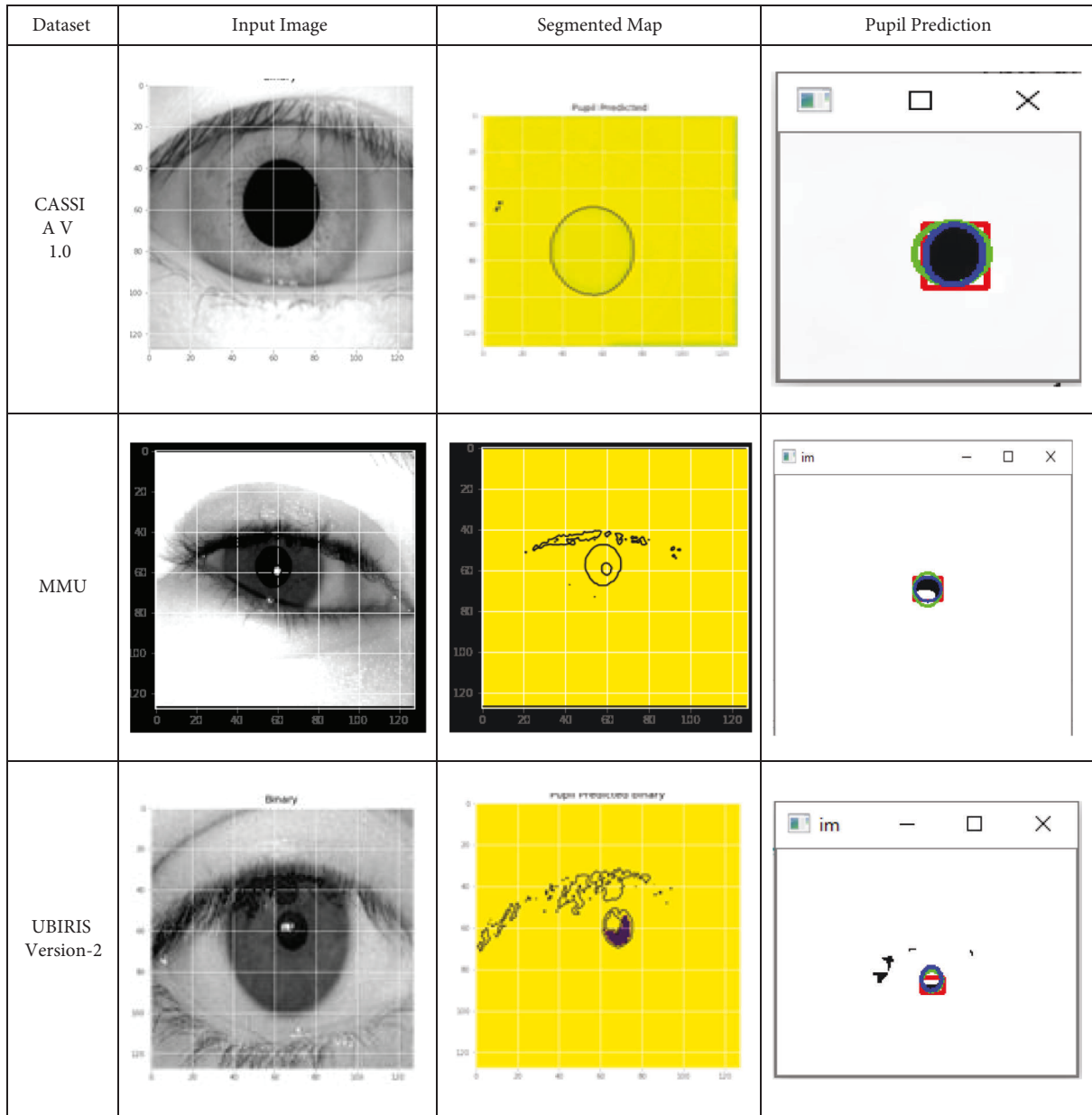


FIGURE 19: Pupil segmentation and fitting the ellipse on segmented pupil on standard datasets, CASIA and MMU.

**4.2. Age Prediction.** We took sample images from various subjects on the Internet with different age groups to analyze the proposed system. We tabularized different people's ages and pupil diameters using a pupillometer. We calculated the Pupil's diameter from the ellipse obtained in the segmentation process. The estimated pupil sizes of different age groups are listed in Table 11. Using the mean data obtained from various kinds of literature, we predicted the diameter of the Pupil: Using the above analysis, the person's age group is predicted. The accuracy of the proposed system is 97.4%. We considered 7 age groups, i.e., '1-2', '3-9', '10-20', '21-27', '28-45', '46-65', and '66-100'. The corresponding ages we considered for the experimentation were tested under the proposed system. The calculated ages and pupil diameters are shown

in Table 11. The resultant image after calculating the age is shown in Figure 24.

Figures 24(a) and 24(b) explain the correctness of predicting age. Figures 24(b) and 24(c) show the incorrect prediction due to an unidentified Pupil. We tested nearly 80 images using the proposed system. The graph explains that the pupil diameter is in specific diameters for different age groups. There is a clash in identifying the pupil diameter calculated for the age group 30 to 60 with individual age groups of 28-45. We are trying to find a way to eliminate this redundancy using another parameter to calculate the age.

We considered the dataset of 800 subjects of different age groups. We divided them into six groups for easier calculation. The groups are grp 0: '1-9', grp 1: '10-20', grp 2:

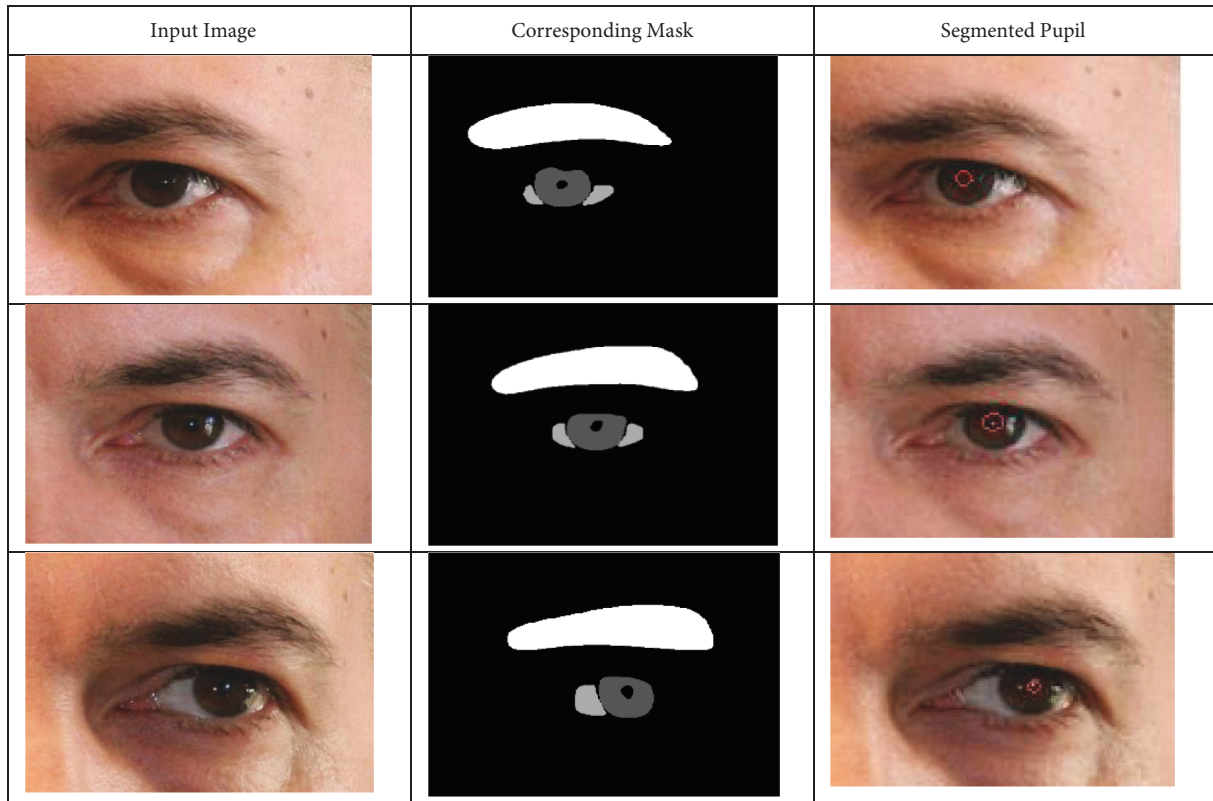


FIGURE 20: Input image from UBIRIS dataset and its corresponding mask.

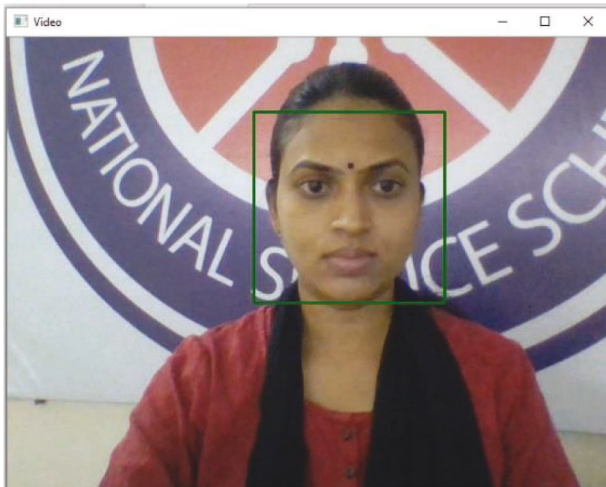


FIGURE 21: Input video from webcam—detecting face using classifier.

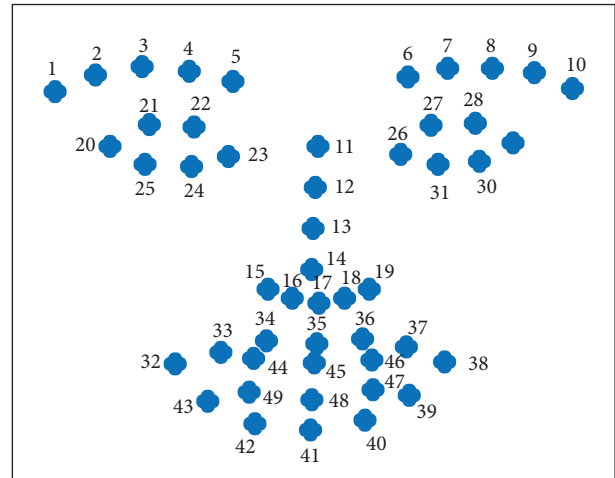


FIGURE 22: 49 landmarks to detect the eye portions of the Subject.

'21–27', grp 3: '28–45', grp 4: '46–65', grp 5: '66–100'. However, we did not consider the grp 0 for the experimentation. Few images were collected from the UBIRIS periocular dataset. Moreover, few were collected on their own at university premises and from the Internet. For various age groups, the diameter is recorded and plotted in Figure 26. The graph of the entire testing set database is

shown in Figure 27. The diameter values are different for different age groups and can be identified here. The hyperparameters of the proposed system were calculated and shown in Table 12.

### 5. Analysis of Hyperparameters

The proposed system has experimented on four different datasets, three benchmark datasets CASIA, UBIRIS, MMU,

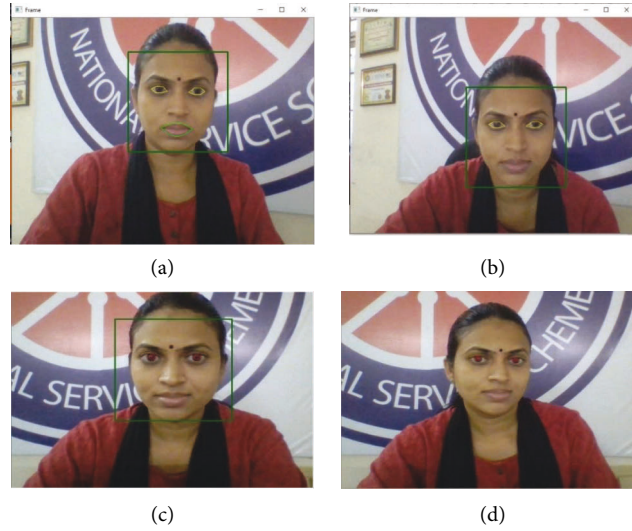


FIGURE 23: (a) Detected landmarks 23. (b) Localizing the eye portion. (c & d) Resultant segmentation of Pupil.

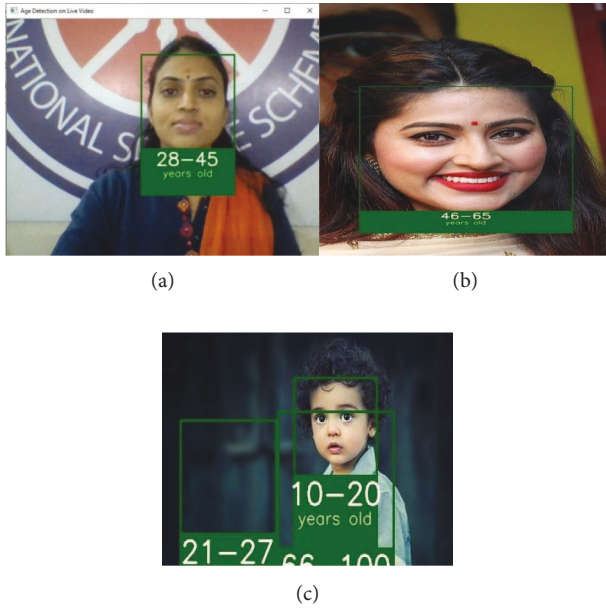


FIGURE 24: (a) Input live video-resultant age group. (b & c) Random image from the Internet.

and Own dataset. Table 12 shows the accuracy obtained on each dataset. The benchmark datasets have achieved the accuracy of 89.6, 95.3, 93.1, and 95.62, respectively. The accuracy for each dataset varied according to the occlusion present in the data.

## 6. Comparison

In this section, we compared the proposed system accuracy with existing systems, and the graphs were drawn on the comparison in the subsequent section. As stated in the literature, several other parameters predict a person's age. We calculated the mean error using the following equation:



FIGURE 25: Diameter of pupil.

$$\frac{1}{n} \sum_{i=1}^n |y_i - \hat{y}_i|, \quad (23)$$

where  $y_i$  is the ground truth and  $\hat{y}_i$  is the predicted age of the  $i$ th sample. The error obtained by various authors is collected and compared with the proposed method to check the accuracy. It is shown that the error rate is more for small kids of age 0–9. As the age grows, the error value is decreased and reaches the minimum value. The error rate increased slowly up to 3.08 for ages above 70.

Comparatively, the proposed system has shown better accuracy than the existing systems. The accuracy of the existing systems is also compared and shown in Table 13.

Table 14 shows the proposed system's accuracy over other state-of-the-art methods. The proposed system shows better accuracy over existing systems and prediction parameters.



TABLE 11: Predicted diameter values of pupil.

Sl. No	Age of the subject	Width and height of the ellipse	Diameter calculated by the proposed method
1	24	63.93853759765625 65.2686996459961	2.765833
2	27	68.04349517822266 69.22743225097656	3.030417
3	27	61.34874725341797 65.39747619628906	2.765833
4	27	62.53804016113281 65.19945526123047	2.765833
5	20	57.815773010253906 61.56900405883789	2.236667
6	24	87.5483169555664 90.62991333007812	5.67625
7	35	83.653076171875 85.93659973144531	5.411667

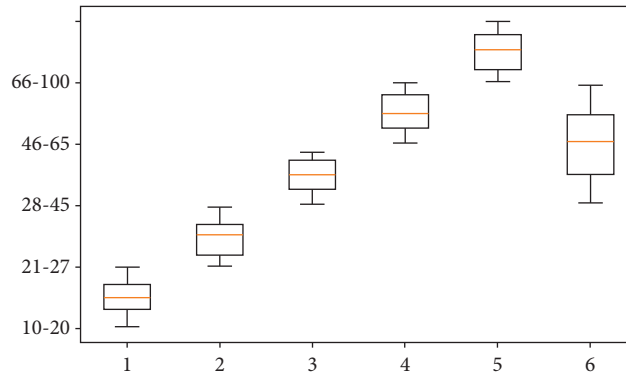


FIGURE 26: Plot representing pupil measurements and corresponding age group distribution.

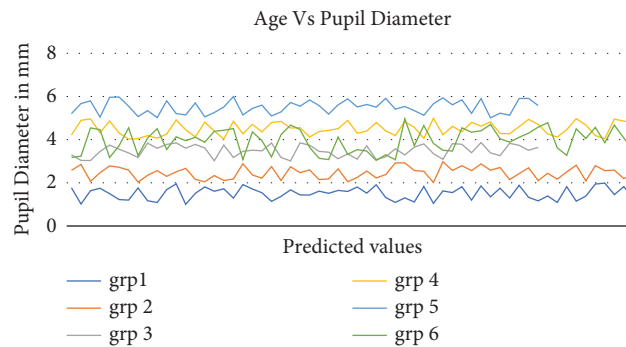


FIGURE 27: Graph of Predicted values from the proposed system.

TABLE 12: Hyperparameters of the proposed system.

Dataset	Age grp	Size of the data	Rate of accuracy	Overall classification rate
Test data	'10-20'	60	80%	88.6%
	'21-27'	50	86%	
	'28-45'	100	98%	
	'46-65'	50	82%	
	'66-100'	50	97%	
Training data	'10-20'	20	94.7	89.6
	'21-27'	20	88.5	
	'28-45'	24	89.6	
	'46-65'	36	84.5	
	'66-100'	14	83.6	

TABLE 12: Continued.

Dataset	Age grp	Size of the data	Rate of accuracy	Overall classification rate
UBER IS	'10-20'	30	89.4	95.3
	'21-27'	25	98.3	
	'28-45'	21	97.3	
	'46-65'	35	96.8	
	'66-100'	29	94.9	
MMU	'10-20'	10	87.6	93.1
	'21-27'	10	89.3	
	'28-45'	20	97.4	
	'46-65'	20	95.4	
	'66-100'	25	96.1	
Random dataset	'10-20'	60	97.5	95.62
	'21-27'	50	89.3	
	'28-45'	100	95.3	
	'46-65'	50	98.4	
	'66-100'	60	97.6	
Avg				93.40

TABLE 13: Comparison of Accuracy with state-of-the-art methods.

	[3]	[5]	[4]	[6]	[7]	[9]	Ours
Accuracy (%)	78.9	79	81	89.6	89.05	74	93.40

TABLE 14: Comparison of various parameters and their mean error rate using various parameters.

Age group	Using other parameters			Using face parameter				
	Ours using pupil parameter	Using molar parameter [3]	Using wrinkles as a parameter [5]	[4]	[6]	[7]	[9]	[11]
0-9	6.84	11.21	6.33	11.97	14.33	9.86	13.63	14.08
10-19	3.46	6.23	4.32	9.85	8.78	7.75	10.45	9.56
20-29	3.36	7.95	6.31	9.78	9.96	8.42	10.45	9.74
30-39	2.22	8.17	7.3	9.69	9.25	7.12	9.45	8.12
40-49	1.71	8.64	1.23	10.35	8.75	8.56	11.63	9.79
50-59	2.35	9.43	2.31	10.56	9.63	11.55	13.75	10.63
60-69	2.82	11.12	6.32	13.78	10.12	12.78	15.96	13.85
70-89	3.08	15.56	8.12	19.96	16.45	16.96	20.13	19.68
Total	3.23	9.78875	7.37	11.9925	10.90875	10.375	13.18125	11.93125

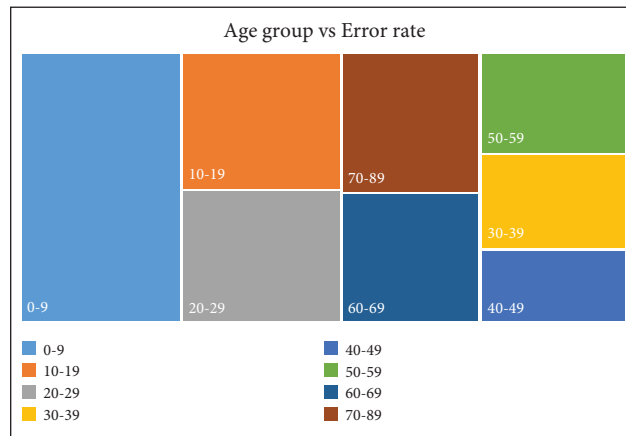


FIGURE 28: Age group and the corresponding error rate.

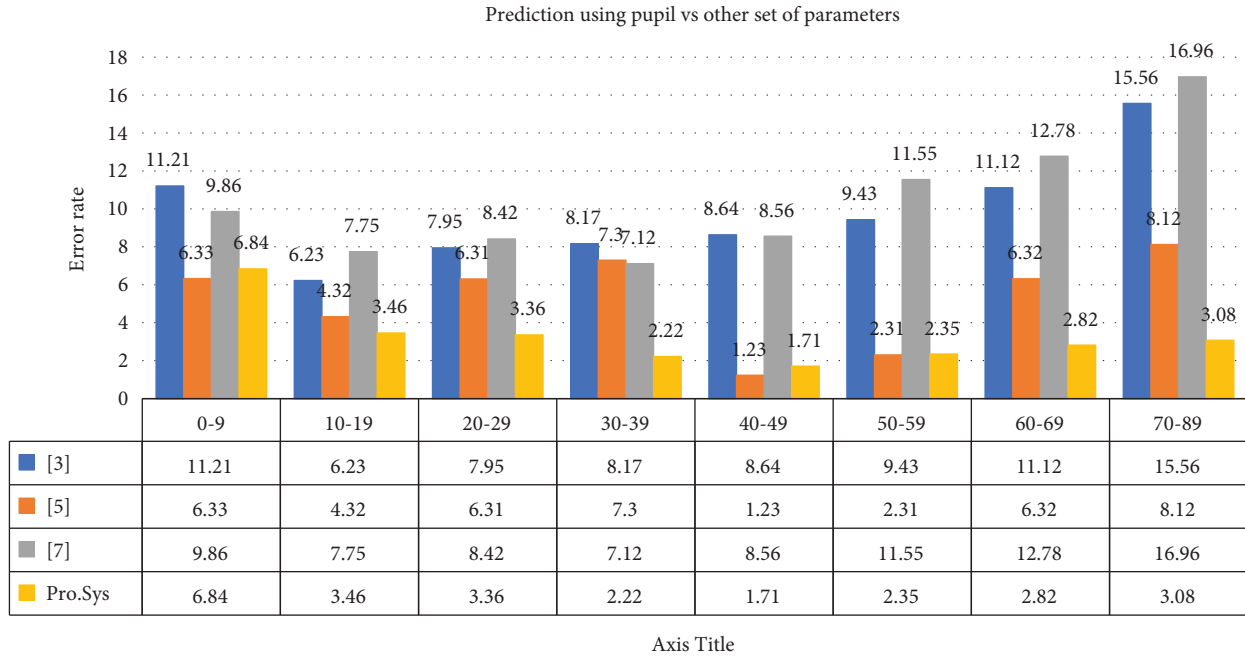


FIGURE 29: Comparison of an error rate of age prediction using Pupil with another set of parameters.

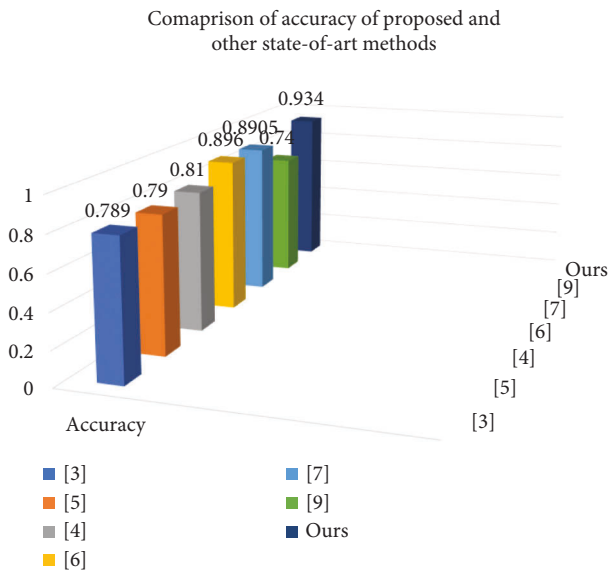


FIGURE 30: Accuracy comparison graph.

6.1. *Comparison Graphs of Parameters.* As stated in the previous section, the mean error and the accuracy were calculated for the proposed system and compared with other state-of-the-art methods to evaluate the performance of the proposed system. This section shows the comparison graph of the mean error rate of the proposed system against the state-of-the-art methods. When compared with the error rates of various age groups, as shown in Figure 28, the youngest age groups have an error rate compared to the old age subjects.

We compare the state-of-the-art methods of various parameters such as the Subject’s wrinkles, face, and

molar data. We gave a comparison chart of the error rate for all these parameters in Figure 29. There is a fair set of distinguishing error rates using the proposed methodology. Compared with the other existing methods, the proposed system shows better accuracy. Figure 30 compares the existing methods and the proposed method’s accuracy.

## 7. Conclusion

The proposed method is designed given the anonymous data we receive in forensic departments and criminal analysis. There were several methods to retrieve the age of the person. However, this proposed methodology is unique in predicting the Pupil’s age. The method has proven smooth implementation with an approximate accuracy of 95.6% on the random Subject. The proposed algorithm is compared with pretrained models such as ResNet and VGGNet to perform the efficiency check. The optimizers such as Gradient Descent, RMS Prop, and ADAM were used to check the Accuracy, Precision, *F*-score, and Specificity. We predicted the hyperparameter values of the proposed system using Adam as, Precision- 93.0%, Specificity- 96.4%, *F*-score 94.7%, and Accuracy- 96.0%, which were noted as higher compared to the other optimization techniques. ADAM was selected to perform the segmentation as the proposed system needs the accurate segmentation of pupils to predict the person’s age. Benchmark datasets such as CASIA, MMU, UBIRIS, and a few random images were collected to exhibit the system’s efficiency. The random dataset is chosen from Internet sources, where the image clarity and noise are almost near zero. Hence the resultant experimentation gave us a fruitful result. The experimentation succeeded while executing the proposed methodology on a random dataset,

which increased our confidence level in experimenting on live video. The classification accuracy for CASIA, UBIRIS, MMU, and random datasets was 89.6, 95.3, 93.1, 95.62, and 93.40, respectively. The proposed system has more than 20% accuracy compared to the other state-of-the-art methods. We want to extend the study to the noisiest datasets or else an excuse for training the system to generate the most accurate results. Age estimation based on biometric traits is attracting many researchers. One of the safe-to-use biometric traits is an eye. Eye not only authenticates a person but also hides much information needed in most applications. This application can be used in future security verification scenarios such as passport verification, border applications, age-restricted goods dispatch applications, etc.

### Data Availability

The data used to support the findings of this study can be obtained from the corresponding author upon request.

### Conflicts of Interest

The authors declare that they have no conflicts of interest.

### References

- [1] K. Zhang, C. Gao, L. Guo et al., "Age group and gender estimation in the wild with deep RoR architecture," *IEEE Access*, vol. 5, Article ID 22492, 2017.
- [2] M. Erbilek, M. Fairhurst, and M. C. Da Costa Abreu, "Age prediction from iris biometrics," in *Proceedings of the 5th International Conference on Imaging for Crime Detection and Prevention (ICDP 2013)*, pp. 1–5, London, UK, December 2013.
- [3] S. Kim, Y.-H. Lee, Y.-K. Noh, F. C. Park, and Q. S. Auh, "Age-group determination of living individuals using first molar images based on artificial intelligence," *Scientific Reports*, vol. 11, no. 1, pp. 1073–1111, 2021.
- [4] F. Gao and H. Ai, "Face age classification on consumer images with Gabor feature and fuzzy LDA method," in *Proceedings of the International Conference on Biometrics*, Springer, Alghero, Italy, June 2009.
- [5] G. Guo, G. Mu, Y. Fu, and T. S. Huang, "Human age estimation using bio-inspired features," in *Proceedings of the IEEE Conference on Computer Vision and Pattern Recognition*, pp. 112–119, Miami, FL, USA, June 2009.
- [6] O. Agbo-Ajala and S. Viriri, "Deeply learned classifiers for age and gender predictions of unfiltered faces," *The Scientific World Journal*, vol. 2020, pp. 1–12, 2020.
- [7] S. Huang, N. Haiminen, A. P. Carrieri et al., "Human skin, oral, and gut microbiomes predict chronological age," *mSystems*, vol. 5, no. 1, pp. 006300-19–e719, 2020.
- [8] V. Sheoran, S. Joshi, and T. R. Bhayani, "Age and gender prediction using deep CNNs and transfer learning," in *Proceedings of the International Conference on Computer Vision and Image Processing*, pp. 293–304, Prayagraj, India, December 2020.
- [9] N. Sharma, R. Sharma, and N. Jindal, "Prediction of face age progression with generative adversarial networks," *Multimedia Tools and Applications*, vol. 80, no. 25, Article ID 33911, 2021.
- [10] M. M. Lavezzo, S. A. Schellini, C. R. Padovani, F. E. Hirai, and F. E. Hirai, "Evaluation of pupillary diameter in preschool children," *Neuro-Ophthalmology*, vol. 33, no. 6, pp. 313–317, 2009.
- [11] J. Zeng, H. Ling, L. Jan Latecki, S. Fitzhugh, and G. Guo, "Analysis of Facial Images across Age Progression by Humans," *International Scholarly Research Notices*, vol. 2012, Article ID 505974, 7 pages, 2012.
- [12] B. Winn, D. Whitaker, D. B. Elliott, and N. J. Phillips, "Factors affecting light-adapted pupil size in normal human subjects," *Investigative Ophthalmology & Visual Science*, vol. 35, no. 3, pp. 1132–1137, 1994.
- [13] H. Husniye, H. Erdol, and A. Turk, "The effects of age on pupil diameter at different light amplitudes," *Beyoglu Eye J*, vol. 10, pp. 31–37, 2018.
- [14] J. N. Sari, A. N. Hanung, E. N. Lukito, P. InsapSantosa, and R. Ferdiana, "A study on algorithms of pupil diameter measurement," in *Proceedings of the 2nd International Conference on Science and Technology-Computer (ICST)*, pp. 188–193, Yogyakarta, Indonesia, October 2016.
- [15] S. Gowroju and S. Kumar, "Robust deep learning technique: U-Net architecture for pupil segmentation," in *Proceedings of the 11th IEEE Annual Information Technology, Electronics and Mobile Communication Conference (IEMCON)*, pp. 0609–0613, Vancouver, BC, Canada, October 2020.
- [16] A. Swathi and S. Kumar, "A Smart Application to Detect Pupil for the Small Dataset with Low Illumination," *Innovations in Systems and Software Engineering*, vol. 17, pp. 1–15, 2021.
- [17] A. Swathi and S. Kumar, "Review on pupil segmentation using CNN-region of interest," *Intelligent Communication and Automation Systems*, vol. 1, pp. 157–168, 2021.
- [18] S. Gowroju and S. Kumar, "Robust pupil segmentation using UNET and morphological image processing," in *Proceedings of the 2021 International Mobile, Intelligent, and Ubiquitous Computing Conference (MIUCC)*, pp. 105–109, Cairo, Egypt, October 2021.
- [19] L. L. Lobato-Rincón, M. D C. Cabanillas-Campos, C. Bonnin-Arias, E. Chamorro-Gutiérrez, A. Murciano-Cespedosa, and C. Sánchez-Ramos Roda, "Pupillary behavior in relation to wavelength and age," *Frontiers in Human Neuroscience*, vol. 8, no. 2, p. 221, 2014.
- [20] N. R. Misra, S. Kumar, and A. Jain, "A review on E-waste: fostering the need for green electronics," in *Proceedings of the 2021 International Conference on Computing, Communication, and Intelligent Systems (ICCCIS)*, pp. 1032–1036, Noida, India, November 2021.
- [21] A. Jain and A. Kumar, "Desmogging of still smoggy images using a novel channel prior," *Journal of Ambient Intelligence and Humanized Computing*, vol. 12, no. 1, pp. 1161–1177, 2021.
- [22] S. Kumar, A. Jain, A. Kumar Agarwal, S. Rani, and A. Ghimire, "Object-based image retrieval using the U-Net-Based neural network," *Computational Intelligence and Neuroscience*, vol. 2021, no. 2, 14 pages, Article ID 4395646, 2021.
- [23] A. K. Agarwal and A. Jain, "Synthesis of 2D and 3D NoC mesh router architecture in HDL environment," *Journal of Advanced Research in Dynamical and Control Systems*, vol. 11, no. 4, pp. 2573–2581, 2019.

## Research Article

# Study on the Level of Integration of Equipment Manufacturing Industry and Producer Service Industry in the Region Transforming Provinces and Its Influencing Factors: Taking Shanxi Province as an Example

Tao Ding , Guoxin Bai, and Han Xu

*School of Economics and Management, Taiyuan University of Science and Technology, Taiyuan 030024, Shanxi, China*

Correspondence should be addressed to Tao Ding; 20152911317@stu.qhnu.edu.cn

Received 13 July 2022; Revised 15 August 2022; Accepted 20 August 2022; Published 13 October 2022

Academic Editor: Punit Gupta

Copyright © 2022 Tao Ding et al. This is an open access article distributed under the Creative Commons Attribution License, which permits unrestricted use, distribution, and reproduction in any medium, provided the original work is properly cited.

At present, China's equipment manufacturing industry and producer service industry are gradually ushered in the leapfrog high-quality development of the rising period. It is particularly important how Shanxi, as the vanguard of the transformation and development, positively responds to the national call to break the shackles of the current integrated development of equipment manufacturing and producer services, for Shanxi Province and even the country's future industrial integration, transformation, and upgrading to accumulate "Shanxi Experience." Therefore, this paper measures and analyzes the integration level of equipment manufacturing and production services between 2012 and 2017 using the input-output method. Then, by constructing the model of the factors influencing the integration of Shanxi's equipment manufacturing industry and producer service industry, selecting the relevant indicators and bringing in the relevant data from 2009 to 2019, by using the principal component regression analysis method, and thus clarifies the main factors that influence the convergence of the equipment manufacturing industry and production service industry in Shanxi. Finally, this paper has provided targeted countermeasures and suggestions to further promote the integration of the two industries in Shanxi Province.

## 1. Introduction

As a core sector of the national industrial system, equipment manufacturing is the fundamental for us to achieve the "Chinese dream," and to improve our Comprehensive National Power and international competitiveness. As an important part of the modern service industry, producer services are the supporting service sector for enterprise production, commercial operation and social development, equipment manufacturing industry, and other industrial sectors indispensable to the important cooperation and complementary sectors. Nowadays, the world is going through the biggest change in a century, in particular, under the test of the global epidemic in 2020, the interconnectedness and interdependence of the global regions have become more prominent, and the economies of all countries have been hit hard to varying degrees. However, among

other countries, China has taken the lead in the recovery of manufacturing and service industries and putting the economy back on the right track. At the same time, with the publication of relevant documents such as the 14th Five-Year Plan for Economic and Social Development of the Nationality Law of the People's Republic of China and the outline of vision 2035 and the views on accelerating the high-quality development of manufacturing services, it proves that China's equipment manufacturing industry and producer service industry are striding into the sequence of high-quality development.

Shanxi, a significant educational and resource province, has taken steps to support the growth of producer services and has seen some success in doing so. The promotion of deep manufacturing and service industry integration and the development of service manufacturing are key strategic goals of the Shanxi provincial initiative "China produced 2025." In

Shanxi, the added value of producer services increased by more than four times between 2004 and 2014. The value added by the financial, retail, and transportation sectors rose by 9.5, 3.5, and 1.5 times, respectively. The financial sector is growing the fastest, and its yearly growth rate is far faster than the province's overall level of economic activity. Although Shanxi's productive service sector is quickly expanding, there are still a number of issues, including tiny businesses, a shaky foundation, and a lack of understanding of innovation. Additionally, it directly contributes to the promotion and integration of the manufacturing sector. Thus, for Shanxi Province, a model of the rise of central China and a leader in the transformation of energy cities across the country, if it wants to continue to forge its own path of transformation in this highly competitive and fast-changing international environment, it is necessary to make clear the integration level of equipment manufacturing industry and producer service industry and its main influencing factors in order to promote these two industries to become an important pulling force for local economic development.

This paper is organized into five sections. Section 1 presents the introduction, and section 2 highlights the related study. Section 3 focuses on the empirical analysis, and section 4 presents the evaluation index of the study. Section 5 presents the conclusion and enlightenment.

## 2. Literature Review

The concept of "industry convergence" originated from the "technology convergence" phenomenon discovered by American scholar Rosenberg [1] in the study of the evolution of the American machine tool industry in 1963; according to this, it is pointed out that industrial convergence is the process of technology diffusion and convergence to different industries. Since then, with the innovation of computer technology, digitalization and informatization have gradually become the focus of discussion. In 1978, Negreouponte systematically described the technological boundary among computer, print publishing, and radio and television industry, and further found that the intersection of these three industries is the most concentrated place of enterprise innovation and development, which leads to the industrial boundaries of the vague idea, and for the subsequent interaction of industries to lay a preliminary theoretical foundation. Then, in the late 1990s, the pace of academic research on industrial convergence continued to increase, and foreign Scholars Geum et al. [2], Kim et al. [3], Abreu and Mendes [4], and others have explained and analyzed the concept from different dimensions such as technology, representation, and process. At the same time, although the initial research on industrial convergence in China is still relatively late compared with that in foreign countries, a large number of domestic scholars such as Xin [5], Zhou and Ning [6], Su et al. [7], and so on have also conducted supplementary studies from these three dimensions, so that the connotation of industrial integration is a more rich and more perfect theoretical system.

As for the influence factors of the integration of equipment manufacturing and production services, most domestic and foreign scholars focus on the internal and external factors. Van Der Merweren [8] argues that the level of integration between manufacturing and production services is mainly driven by customer demand. By studying the service types of service-oriented equipment manufacturing industry, Ren [9] points out that the service strategy of manufacturing industry will be influenced by the change in its external business environment, and these changes include the continuous and significant pressure of interfirm product competition, the increasing demand for customer value, and the increasing demand for profit. Leiponen [10] through the empirical analysis of the factors influencing the integration of the manufacturing and the service industries in Finland, it is found that the difference in R&D efficiency between the manufacturing and the service industries affects and promotes the integration of the two industries. Li [11] by discussing the internal and external conditions of the development and upgrading of equipment manufacturing industry, this paper further expounds the relationship between equipment manufacturing industry and production service industry, and points out the relevant influencing factors, including policies, funds, etc. Wang and Li [12] analyze the main influencing factors of the service level of China's manufacturing industry from the angles of input and output, including market competitive intensity, service economy level, resource dependence degree, enterprise market structure, capital distribution structure, enterprise scale, service business profit level, etc., and empirical analysis of various factors in promoting the transformation of manufacturing services.

In addition, scholars also focus on the equipment manufacturing and producer service integration model. As early as the 1980s, with the gradual rise and expansion of the information industry, some enterprises began to combine and apply it to the construction of enterprise information systems; as a result, the production process becomes more efficient and transparent; and the manufacturing process becomes more flexible and complex. Aiming at this situation, Vandermerve and Rada first put forward the integration mode of "manufacturing service," after which a large number of scholars devoted themselves to the study of this mode. Garciam [13] studies the development process of the service industry and the manufacturing industry, and considers that modularization and coordinated development are the best models for the integration and development of the two industries. Taking the general group as an example, Gebauer et al. [14] illustrate that service-oriented manufacturing is one of the important means of industrial convergence, which can promote the interactive development of the two industries. He and Sun [15] further improve and deepen the concept and attributes of service manufacturing on the basis of previous studies, and emphasize the objective importance of the development of manufacturing industry in China under the current situation; on this basis, it is necessary to constantly strengthen the development of service-oriented manufacturing model, and promote the transformation and upgrading of Chinese

manufacturing. Wu [16] believes that the operation mode of the integrated system of equipment manufacturing and producer services in China is a multifactor coordinated operation mode; furthermore, it puts forward the multifactor cooperation-oriented operation mode of “equipment manufacturing enterprise—market—government.” Zeng [17] based on the background of “Internet +” and Industry 4.0, through the empirical research on the industrial integration degree of China’s equipment manufacturing industry and its branches and high-tech service industry, furthermore, a new model of network manufacturing in equipment manufacturing industry is proposed. Generally speaking, although the research contents and fields of these two industrial integration models are becoming more and more extensive, they are all centered on “manufacturing service.”

Based on substantial numbers of literature amount in China and other countries, many valuable achievements have been made in the study of industrial convergence and the integration of equipment manufacturing and production services, and this has provided the enormous help to this article’s follow-up research. However, at present, the level of integration of China’s equipment manufacturing industry and production service industry is still at the initial stage of development compared to other countries, and domestic scholars still mainly focus on the national level or the more developed cities and regions, while in the central transition provinces such as Shanxi, the integration of the two industries is still relatively slow. In addition, some empirical research studies are still at the level of a few years ago, the selection of relevant data is also relatively slow, which is now fast-growing China, and the reference is declining. To this end, it is necessary to use more recent data to study current developments and to supplement relevant research on the convergence of the two industries.

Thus, this paper intends to use the input-output method to calculate the overall integration degree of equipment manufacturing and production services in Shanxi Province, with the latest input-output table data, and find closer to the level of industrial integration in Shanxi Province, the impact of factors for empirical analysis, and finally for reference to Shanxi countermeasures.

### 3. Analysis on the Integration Level of Equipment Manufacturing Industry and Producer Service Industry in Shanxi Province

**3.1. Selection of Measurement Methods for Industrial Convergence.** According to the research results of related scholars and the actual research situation of this paper, the authors believe that the input-output method can explore the source and direction of input and output among industries and facilitate the study of the links between industrial sectors. At the same time, the results of this method can provide an important reference for economic analysis and policy research in Shanxi Province. Therefore, this article first chooses the input-output method to study the Shanxi Province equipment manufacturing industry and the production service industry fusion level’s present situation.

**3.2. Index Selection and Data Sources of Industrial Convergence Measurement.** The input-output table was first born in America in the 1930s, but the work of compiling the input-output table in China started a little later into the 1990s. Domestic input-output tables are now typically prepared on a five-year cycle. So far, Shanxi Province’s latest published input-output table is for 2017, and the previous three published input-output tables were for 2002, 2007, and 2012. But given that the National Bureau of Statistics of the People’s Republic of China began to fine-tune some industry classification standards after 2012, to take full account of the completeness and validity of the data, finally, this paper chooses to use the latest two periods of 2012 and 2017 input-output table data to calculate, so as to explore its equipment manufacturing and production service industry levels of integrated development. In particular, the following indicators will be used in this paper, based on the research of Wu [18]:

(1) Intermediate input rate

The intermediate input rate refers to the ratio of the sum of the other industries’ intermediate inputs to the national economy. The formula is as follows:

$$F_j = \frac{\sum_{i=1}^n x_{ij}}{\sum_{i=1}^n x_{ij} + N_j}, \quad (j = 1, 2, \dots, n). \quad (1)$$

In the formula,  $F_j$  represents the intermediate input rate of other industrial sectors of the national economy to the  $J$  industry, and  $X$  represents the intermediate input of the  $I$  industry to the  $J$  industry.  $\sum_{i=1}^n x_{ij}$  is the sum of the intermediate inputs to the  $J$  industry from other industrial sectors in the national economy;  $N_j$  is the added value of the  $J$  industry; and  $\sum_{i=1}^n x_{ij} + N_j$  represents the total input of each industrial sector to the  $J$  industry in the national economy.

The intermediate input rate reflects the proportion of raw materials purchased from other industrial sectors in the total input of each industrial sector in the productive activities. Here, the total input is represented by the intermediate input value added. Therefore, the higher the intermediate input rate is, the lower the added value is.

(2) Intermediate demand rate

The intermediate demand rate refers to the ratio of the intermediate demand of other industries to the total demand of the industries in the national economy. The formula is as follows:

$$G_i = \frac{\sum_{j=1}^n x_{ij}}{\sum_{j=1}^n x_{ij} + Y_i}, \quad (i = 1, 2, \dots, n). \quad (2)$$

In the formula,  $G_i$  represents the intermediate demand rate of other industrial sectors of the national economy for the  $I$  industry, and  $x_{ij}$  represents the intermediate demand of  $J$  industry for the  $I$  industry.

$\sum_{i=1}^n x_{ij}$  represents the sum of the intermediate demands for the  $I$  industry by other industrial sectors in the national economy, and  $Y_i$  represents the final demand for the  $I$  industry.  $\sum_{i=1}^n x_{ij} + Y_i$  represents the total demand of each industrial sector for the  $I$  industry in the national economy.

In general, the intermediate demand rate objectively reflects the proportion of intermediate products in the total products in each industry sector, that is, the quantity served by each industry sector as raw materials. The higher the intermediate demand rate of an industry product, the more productive materials it provides, the rawer material it tends to be, and the higher the degree of integration with other industries.

### (3) Degree of industrial convergence

According to the above formula, we can establish the model of industry convergence degree. Based on the research results of Wang [19], this paper uses the intermediate demand rate and intermediate input rate to construct the integration model of equipment manufacturing industry and producer service industry as follows:

$$C_i = \frac{1}{2} \left( \frac{1}{2} (F_{i \rightarrow j} + F_{j \rightarrow i}) + \frac{1}{2} (G_{i \rightarrow j} + G_{j \rightarrow i}) \right). \quad (3)$$

In the formula,  $C_i$  represents the level of integration between the two industries;  $G_{i \rightarrow j}$  represents the intermediate demand rate of industry  $I$  for industry  $J$ ; and  $G_{j \rightarrow i}$  represents the intermediate demand rate of industry  $J$  for industry  $I$ .  $F_{i \rightarrow j}$  represents the intermediate input rate of  $I$  to industry  $j$ ;  $F_{j \rightarrow i}$  represents the intermediate input rate of industry  $J$  to industry  $I$ .

In addition, the value range of  $C_i$  is between 0 and 1, but the closer the value of  $C_i$  is to 1, the higher the degree of integration between the two industries, and the better the situation of integration; otherwise, the lower the degree of integration, the worse the situation of integration. When the value of  $C_i$  is close to 1, it means that the two industries are completely integrated to form a new industry. In order to compare and identify the characteristic level of the degree of industrial convergence, this paper divides the degree of industrial convergence according to the degree of industrial convergence and makes the evaluation table of the degree of industrial convergence, as shown in Table 1.

**3.3. Empirical Analysis of Industrial Convergence Measurement.** Based on the national economic industrial classification (GB/T4754-2017) and according to the latest statistical classification of production services (2019), this paper reasonably divides and selects equipment manufacturing industry and production service industry. Then, combined with the actual development of equipment manufacturing industry and producer service industry in

TABLE 1: Industrial integration rating scale.

Degree of industrial convergence	Level of industrial convergence
$0.8 < C \leq 1.0$	High fusion
$0.7 < C \leq 0.8$	Basic fusion
$0.5 < C \leq 0.7$	Moderate fusion
$0.3 < C \leq 0.5$	Partial fusion
$0 < C \leq 0.3$	It has not fused yet

Shanxi Province, seven subsectors of producer service industry and seven subsectors of equipment manufacturing industry are selected as the research object. Among them, production services specifically include the following: wholesale and retail; transportation, warehousing, and postal services; information transmission, software, and information technology services; finance; real estate; leasing and business services; and scientific research and technology services. The equipment manufacturing industry specifically includes the following: metal product manufacturing, general equipment manufacturing, special equipment manufacturing, transportation equipment manufacturing, electrical machinery and equipment manufacturing, communication equipment, computer and other electronic equipment manufacturing, and instrumentation manufacturing. The following paper will further measure and analyze the overall level of integration between equipment manufacturing and production services in Shanxi Province:

Based on the input-output data of Shanxi Province in 2012 and 2017, the integration degree of equipment manufacturing and production services can be calculated (Table 2).

From the perspective of input, the intermediate input rates of equipment manufacturing industry in Shanxi Province in 2012 and 2017 were 0.5864 and 0.5493, respectively, while the corresponding intermediate input rates of production services in the same years were 0.3337 and 0.4141, respectively. It is not difficult to find that the input rate of the equipment manufacturing industry in Shanxi Province in these two years is greater than the input rate of the production service industry in the corresponding years, it shows that the development input of equipment manufacturing industry in Shanxi Province in recent years plays a leading role in the development of production service industry in Shanxi Province, and its driving capacity is far greater than that of production service industry. In addition, this is also verified from the side that the production service industry has a very high added value. From the vertical time point of view, the input rate of the equipment manufacturing industry in Shanxi Province in 2017 is less than that in 2012, which shows that the local equipment manufacturing industry has got a qualitative leap and upgraded under the constant attention and hard development of Shanxi Province, and the added value of the industry is constantly rising. Although the input rate of production services in Shanxi Province has slightly increased, it can show that the driving capacity of this industry to the equipment manufacturing industry in Shanxi Province has significantly increased.



TABLE 2: 2012 and 2017 integration of equipment manufacturing industry and production service industry in Shanxi Province.

Year	Intermediate input rate of equipment manufacturing industry	Intermediate input rate of production service industry	Intermediate demand rate of equipment manufacturing industry	Intermediate demand rate of production service industry	Degree of fusion
2012	0.5864	0.3337	0.1891	0.2993	0.3521
2017	0.5493	0.4141	0.1876	0.4159	0.3917

Note. The above data are calculated by the author himself.

In terms of consumption, the intermediate demand rate of production services in Shanxi Province increased from 0.2993 to 0.4159 in 2012 and 2017. It is obvious that the equipment manufacturing industry's intermediate demand for production services is on the rise, and it is shown that with the accelerating transformation and upgrading of equipment manufacturing industry in Shanxi Province, the production service industry is integrating into the production and development of equipment manufacturing industry, and further deepening the dependence of equipment manufacturing industry on producer service industry. In addition, the demand rate for production services in both years was higher than the demand rate for equipment manufacturing in the corresponding years, indicating that the production service sector is also mainly dependent on intermediate consumption in equipment manufacturing, and the equipment manufacturing industry plays a significant role in its pull. In addition, by contrast, the change in the intermediate demand rate of equipment manufacturing industry is relatively stable and not very volatile.

Finally, according to the calculated fusion degree, the fusion degrees of equipment manufacturing industry and producer service industry in 2012 and 2017 are 0.3521 and 0.3917, respectively. Compared with the evaluation table of industrial integration grade, it can be found that in these two years, the equipment manufacturing industry and producer service industry in Shanxi Province are in a state of partial integration, and the degree of industry convergence in 2017 is higher than that in 2012, which indicates the degree of integration of these two industries is deepening.

All in all, in recent years, with the unremitting efforts of Shanxi Province, the integration trend of local equipment manufacturing industry and producer service industry has been strengthening, gradually moving toward medium integration, and the overall development of the two industries is getting better and better.

#### 4. An Empirical Analysis of the Factors Influencing the Integration of Equipment Manufacturing and Production Services in Shanxi Province

After measuring and analyzing the integration level of equipment manufacturing industry and production service industry in Shanxi Province, this paper will further explore the main factors that affect the integration development of these two industries. On this basis, we select the evaluation index of each influencing factor and build the model of the influencing factor of industrial convergence. Finally, we use the principal component regression analysis to make an

empirical analysis, in order to explore the real impact of the two industries in Shanxi factors.

##### 4.1. Establishment of Evaluation Index System of Influencing Factors

*4.1.1. Analysis of Influencing Factors and Selection of Indicators.* Based on the domestic and foreign scholars' research on the influence factors of industrial convergence, we can know that the convergence level of the two industries is often caused by many factors. Therefore, after fully considering the availability and interpretability of data, and combining the theoretical research of relevant scholars and the actual development of regional industries, this paper sums up the factors affecting the level of integration of the two industries in Shanxi Province, and there are three dimensions: fusion basic dimension, fusion condition dimension, and fusion environment dimension. Among them, the basic dimensions of integration include R&D investment, talent reserve, and technological innovation; the dimensions of integration conditions include market demand, industrial upgrading, and industrial competition, and the dimension of fusion environment includes economic environment, investment environment, and policy environment.

- (1) R&D investment: as an important index to measure the development of enterprises, R&D investment is not only an important source for equipment manufacturing enterprises to enhance their competitiveness but also a source of profits for production service enterprises to pursue. In addition, R&D investment needs the enough R&D funds to support, which is one of the key factors for the integration of the two industries, but also an important guarantee for production and operation, technological innovation, and other related activities. Especially for the internal R&D departments of equipment manufacturing enterprises and high-tech R&D enterprises in the production service industry, in the process optimization, product innovation, service quality improvement, and so on, there is no doubt that there is the need for adequate R&D funds as an important support for the sustainable development of their enterprises. Based on this, this paper chooses R&D investment intensity to measure R&D investment degree. In addition, since the investment of R&D funds in a specific region is often relatively limited, the proportion of R&D funds allocated is also relatively stable;

considering the difficulty of obtaining data on R&D funds in specific industries, therefore, this paper selects the total expenditure of R&D funds of Shanxi Province to calculate; and the specific formula is as follows: R&D funds expenditure/GDP total value.

- (2) Talent reserve: the integration and development of any industry cannot be separated from the accumulation and investment of talents. Human resource is not only an important long-term strategic reserve resource for enterprises but also an important soft power for enterprises to move to a higher level of development. In terms of the specific impact on industrial integration, high-quality human resources can indirectly affect the overall development of the industry, and at the same time raise the level of interindustry integration and speed up the process of interindustry integration, finally, to promote the birth of new forms of business and the transformation and upgrading of industrial structure. At present, with the rapid development of equipment manufacturing industry and the continuous deepening of the service level of manufacturing industry, the industry's own human resource reserve has long been unable to meet its development needs; meanwhile, the compound innovative talents with a large amount of knowledge and technology reserve are becoming the important footstone to support the development of science and technology. At this time, with the high-tech enterprises in the producer service industry continuously sending high knowledge and technical talents to the equipment manufacturing sector, they will effectively allocate their talent resources, thus better serving the integration of the two industries. Therefore, the reserve of high-quality talents is one of the important factors affecting the integration of the two industries. Based on this, this paper selects the proportion of R&D personnel to measure the talent reserve factor in Shanxi Province, and the specific formula is as follows: R&D personnel number/year-end employment number.
- (3) Technological innovation: technological innovation plays a vital role in promoting the integration of equipment manufacturing and production services, and is an important technical support for the integration of the two industries. Technological innovation with its strong penetration gradually blurred the boundaries between the two industries, and enhanced exchanges and cooperation between the two industries, thus promoting the integration of industries. In addition, technological innovation is also one of the important factors to promote the transformation of technological structure and industrial structure. After technological innovation, it will trigger the adjustment and upgrading of technological structure, and then further trigger the

change in industrial structure, and at the same time, technological changes will stimulate the new needs of users. In the face of the new market demand, the equipment manufacturing enterprises will actively develop new products, and then cross-penetrate with the high-tech enterprises in the production service industry to continuously meet the new market demand and expand the market volume ratio, thus creating the broad market demand space for the industrial fusion. Therefore, technological innovation constitutes an important internal thrust to promote the integrated development of equipment manufacturing and production services. As one of the important forms of technological innovation, the number of patent applications can directly reflect the achievements of scientific and technological innovation in a region. Based on this, this paper chooses the patent application volume to measure the factors of technological innovation in Shanxi Province.

- (4) Market demand: market demand, as an important factor in the integration of the two industries, is an important impetus to accelerate the development of their integration. With the development of social economy and the improvement of market order, consumers will be stimulated to change from traditional, single, and passive consumption demand to new consumption demand. Under the guidance of the emerging trend of demand, equipment manufacturing enterprises and producer service enterprises began to cooperate actively to deduce new fusion products, thus accelerating market consumption and bringing new market profit space, and finally, further deepen the equipment manufacturing and production service industry integration development trends. Combined with the above analysis, this paper thinks that the proportion of gross output value of secondary and tertiary industries in a region can reflect the market maturity and market demand of the region. The higher the proportion of the total output value of secondary and tertiary industries, the better the market development, the more exploitable the consumer demand, and the greater the potential market demand space. In addition, for the equipment manufacturing industry and production service industry, it is more convenient for the equipment manufacturing industry to obtain the necessary production services, and large production service enterprises can also use this condition to extend the industrial chain; furthermore, it is beneficial to the integration and development of the two industries. Based on this, this paper uses the ratio of the secondary and tertiary industries' gross output value to the regional gross output value to measure the market demand of Shanxi. The specific formula is as follows: gross output value of

secondary and tertiary industries/gross output value of regions.

- (5) Industrial upgrading: here, the industrial upgrading is mainly reflected in the upgrading of the industrial structure. The upgrading of industrial structure generally refers to the dynamic process of the gradual evolution of industrial structure from low level to high level, technological innovation and upgrading, optimization of management system, and improvement of product quality and production efficiency are often accompanied by this process. In addition, there is a close relationship between industrial structure upgrading and industrial integration development. In general, most scholars thought that the upgrading of industrial structure was promoted by industrial convergence, that is, industrial convergence existed before further industrial upgrading. However, there is a two-way interaction between industrial upgrading and industrial convergence, that is, industrial convergence promotes industrial structure upgrading, and industrial structure upgrading deepens industrial convergence. As far as the equipment manufacturing industry and production service industry are concerned, in the early stage of their development, the two industries will gradually realize the initial integration in products, technologies, markets, management, and organization through interaction and integration; then, when the overall industrial structure is upgraded, it will, in turn, promote the joint development of the two industries and further deepen the integration of their products and technologies, and simultaneously causes the market and the organization management fusion level to stride over a new step. Based on this, this paper chooses the energy consumption rate of GDP to reflect the factors of industrial upgrading, because this indicator takes into account that Shanxi Province is a typical energy-intensive province, so it will consume a lot of energy in the course of its development; therefore, the energy consumption rate of GDP can better reflect the upgrading of industrial structure in Shanxi Province.
- (6) Industrial competition: the intraindustry competition is the micromotivation to promote industrial integration, but also to strengthen cooperation between each other and enhance the overall competitiveness of the industry. At present, both the equipment manufacturing industry and the production service industry are facing huge competition, especially when the domestic industrial policy is constantly adjusted, the market is constantly improved, and the barriers to entry in related subsectors are constantly falling, which led to a variety of enterprises have poured into the industry market and launched a fierce competition. In addition, as China's overall economy continues to grow in size, the consumption potential of the market, and the business and investment environment have been significantly enhanced, and the opening-up efforts have also been significantly increased, this has attracted a variety of foreign investors to join, and a variety of large multinational foreign enterprises have poured into China and further exacerbated the competition in China's industrial market. Under this influence, some local equipment manufacturing industries and production service industries will take the initiative to accelerate the pace of independent innovation through industrial integration and concentration ratio, to further optimize the industrial structure, to realize industrial upgrading, and finally, to expand the competitive advantage. Based on this, this paper selects the number of equipment manufacturing and production service enterprises to measure the industry competition index.
- (7) Economic environment: the improvement of the level of economic development in a region can provide a stable and good economic environment for the integration of local industries and speed up the process of interindustry integration. After the reform and opening up, China's economies in various regions have made considerable progress, and the overall economic level of society has significantly improved. In particular, China has entered a new era with a sound socialist market economy system with Chinese characteristics, and it is also an important support and guarantee for the integrated development of the industry. In addition, a region's economic development level can also reflect the local human, capital, technology, and other production input factors of the basic stock, related infrastructure conditions, and potential market demand scale. Combining relevant studies at home and abroad and examples of regional economic development, it is not difficult to find that most industries in economically developed regions have sufficient input of production factors, convenient infrastructure conditions, and huge market consumption demand, and as a result, the possibility of industrial convergence and the overall level of convergence are also higher than other backward areas. As for the equipment manufacturing industry and producer service industry, which are highly concentrated production factors, a good economic development environment can expand their industrial scale, enhance production efficiency, and deepen the level of integration. Based on this, this paper chooses per capita GDP to measure the economic and environmental factors in Shanxi Province.
- (8) Investment environment: the quality of the regional investment environment often directly affects the enthusiasm of investors and the absorptive capacity of investors, and it is also an important external

environmental factor that affects and restricts the development of regional industry. American scholar Stobaugh [20], in how to analyze the climate of foreign investment, divided the contents of the investment environment into eight factors, including foreign investment factors. This paper argues that foreign investment in China will often be invested in the region of the overall investment environment is extremely careful study and evaluation, and will ultimately make investment decisions. Therefore, foreign investment can indirectly reflect the advantages and disadvantages of a regional investment environment to a certain extent. In addition, the integrated development of equipment manufacturing and production services also needs the support of a good investment environment and external investors. Foreign investment can bring its international management model, sufficient capital, and advanced technology into the development of the two local industries, speed up the integration process of the two industries, and improve the integration quality of the industries, to boost the local economy. In addition, under the new situation, the state has also continuously advocated that local governments should actively face the new situation of foreign investment changes, while appropriately lowering the threshold of foreign investment and expanding the scope of foreign investment under the premise of guaranteeing the overall economic security of the country, and finally, the environment for foreign investment has been further optimized. Therefore, it is quite reasonable to use foreign investment to measure the overall investment environment of Shanxi Province and to use the ratio of foreign direct investment to GDP to quantify the calculation, and the formula is as follows: foreign direct investment/GDP.

- (9) Policy environment: the policy environment is an important external influence factor for the development of industrial interaction and integration. A good policy environment can not only reflect the local government's support for industrial development but also promote the degree of industrial integration. Here, the policy environment mainly embodies in the relaxation of government regulation and the coordination of industrial policy. From the above analysis, the deregulation of government can break down industry entry barriers, reduce market access, and reduce the transaction costs between industries, thus accelerating the process of interindustry integration. The coordination of industrial policy mainly shows that the government actively meets the needs of industrial development, and gives appropriate policy support to the industry by promulgating or amending relevant policies, regulations, and rules; for example, we should strengthen financial subsidies or give preferential tax treatment to key development areas, so as to

encourage and support the continuous innovation and development of related industries, and accelerate the industrial upgrading and integration. In addition, from another point of view, the current market operation mechanism in China, the government's intervention and impact on market development are still greater. Therefore, the integration of the development of various industries on the need for government policy support and guidance. Of course, it can be predicted that the new industrial policies will provide support and guidance for the development of industrial integration under the gradual transformation of the current government functions and the deepening of the reform of "supervision and service." Based on this, this paper uses the financial science and technology expenditure as the proportion of the general budget expenditure to measure the policy environment.

*4.1.2. Establishment of an Indicator System.* After a thorough analysis of the factors affecting the integration of equipment manufacturing and production services in Shanxi Province, this paper is based on the selection principles of scientific, feasible, and representative indicators, and finally, the paper constructs the evaluation index system of influencing factors on the integration of equipment manufacturing and production services in Shanxi Province. In particular, the evaluation index system is divided into three target dimensions: fusion foundation, fusion condition, and fusion environment. Each target dimension is subordinate to three criterion dimensions, altogether nine criterion dimensions, and at the same time, an evaluation index is designed for each criterion dimension, as shown in Table 3.

*4.2. Model Building.* Based on the abovementioned in-depth analysis of the factors influencing the integration of equipment manufacturing industry and production service industry in Shanxi Province and the establishment of the evaluation index system of the factors influencing the integration degree, below, this article will further construct the Shanxi Province equipment manufacturing industry and the production service industry fusion influence factor theory model, as follows:

$$Y_t = \beta_0 + \beta_1 X_{1t} + \beta_2 X_{2t} + \beta_3 X_{3t} + \dots + \beta_8 X_{8t} + \beta_9 X_{9t} + \mu_t. \quad (4)$$

Among them, the  $Y$  represents the explanatory variable—the convergence degree of the equipment manufacturing industry and the production service industry in Shanxi Province, and  $X_1$  through  $X_9$  stands for explanatory variable—the R&D investment intensity, the proportion of R&D personnel, patent application volume, the ratio of the secondary and tertiary industries' gross output value to the regional gross output value, the energy consumption rate of GDP, the number of equipment manufacturing and production service enterprises, per

TABLE 3: Evaluation index system of influencing factors on the integration of equipment manufacturing and production services in Shanxi Province.

Target layer	Criterion layer	Index layer	Method of measurement	Mark	Expected impact
Fusion foundation	R&D investment	R&D investment intensity (%)	R&D fund expenditure/GDP total value	X1	+
	Talents reserve	The proportion of R&D personnel (%)	R&D personnel number/year-end employment number	X2	+
	Technological innovation	Patent application volume (piece)	From the Statistical Bulletin of Shanxi National Economy and Social Development	X3	+
Fusion condition	Market demand	The ratio of the secondary and tertiary industries' gross output value to the regional gross output value (%)	Gross output value of secondary and tertiary industries/gross output value of regions	X4	+
	Industrial upgrading	The energy consumption rate of GDP (%)	Directly from Shanxi Statistical Yearbook	X5	-
	Industrial competition	The number of equipment manufacturing and production service enterprises (One)	Directly from Shanxi Statistical Yearbook	X6	+
Fusion environment	Economic environment	Per capita GDP (yuan)	Directly from Shanxi Statistical Yearbook	X7	+
	Investment environment	The ratio of foreign direct investment to GDP (%)	Foreign direct investment/GDP	X8	+
	Policy environment	The financial science and technology expenditure as the proportion of the general budget expenditure (%)	From Shanxi Province Science and Technology Funds Investment Statistical Bulletin directly obtained	X9	+

Note. "+" indicates a positive influence.

capita GDP, the ratio of foreign direct investment to GDP, and the financial science and technology expenditure as the proportion of the general budget expenditure. The  $t$  represents the year from 2009 to mid-2019,  $\beta_0$  represents a constant term,  $\beta_1$  to  $\beta_9$  represents the regression coefficient of the explanatory variable, in turn, and  $\mu_t$  represents a random perturbation term.

### 4.3. Sources of Data and Methodology

4.3.1. *Establishment of an Indicator System.* This paper takes the equipment manufacturing industry and producer service industry of Shanxi Province as the research object, and selects the related data of Shanxi Province from 2009 to 2019, in order to make an in-depth analysis on the influencing factors of the convergence of these two industries, most of the original data for the fusion of the measurement of influencing factors come directly from the "China Statistical Yearbook," "China Science and Technology Statistical Yearbook," and "Shanxi Statistical Yearbook," and the official website of Shanxi Provincial Bureau of Statistics issued by the past years, "Shanxi Province national economy and Social Development Bulletin," and "Shanxi Province Science and Technology Funds Investment Statistical Bulletin," and the remaining data by the author consulted the information collated. It should also be noted that data for 2019 and prior years are currently available only owing to the slow production of the relevant statistical yearbooks and the delay in their release dates, considering the timeliness and availability of the data.

In addition, this paper takes the degree of integration between equipment manufacturing and production services

in Shanxi Province as the explanatory variable, and on the choice of its data, this paper takes full account of the fact that the input-output method used in the preliminary analysis of the fusion level has no data continuity; that is, only the latest two-stage input-output table can be used to calculate the fusion data in 2012 and 2017; therefore, this paper adopts Wu [18] the measurement method and adopts the coordination degree model to calculate the coupling degree between the equipment manufacturing industry and the producer service industry in Shanxi Province, thus approximately replacing its industrial integration degree, based on this analysis of the relevant factors and industrial integration of the relationship and impact. At the same time, the order parameter model of the model is further constructed as follows:

$$u_j(e_{ji}) = \frac{e_{ji} - \alpha_{ji}}{\beta_{ji} - \alpha_{ji}} \tag{5}$$

In the formula,  $\alpha_{ji}$  and  $\beta_{ji}$  represent the maximum and minimum of the order variable, respectively, the  $j$  represents the region, and the  $i$  represents the specific year. In addition, both equipment manufacturing and production services consist of 11 time-series variables, and then,  $u_1$  and  $u_2$  are calculated using a simple weighted average formula, and their coupling is further defined by the following formula:

$$C = \frac{2u_1u_2}{u_1 + u_2} \tag{6}$$

The integration of equipment manufacturing and production services in 2009–2019 is further calculated by combining formula (6), as shown in the following Table 4.

TABLE 4: 2009–2019 integration of equipment manufacturing and production services in Shanxi Province.

Year	Degree of fusion
2009	0.2314
2010	0.2448
2011	0.2612
2012	0.2549
2013	0.2696
2014	0.2734
2015	0.2956
2016	0.2997
2017	0.3251
2018	0.3441
2019	0.3654

Data source: it is calculated and collated.

*4.3.2. Selection of Research Methods.* Through the above analysis, we can find that there are many factors affecting the integration of equipment manufacturing and production services in Shanxi Province. If these variables are brought into the model for simple regression analysis, the multicollinearity between variables will easily appear, thus making the analysis meaningless. In view of this, in order to overcome this problem as far as possible, this paper chooses to use the principal component analysis method to extract several important principal component factors from the nine influencing factors of the convergence degree of these two industries; then, this paper makes a quantitative analysis on the influence level of each principal component factor on the degree of industrial integration, and finally finds out the factors that really affect the integration of equipment manufacturing and production services in Shanxi Province through regression analysis.

*4.4. Empirical Process Analysis.* In this paper, the related variable indexes and their data were compiled by Excel and entered into SPSS20.0. The new standardized data variables  $ZY$  and  $X_i$  ( $i = 1, 2, \dots, 9$ ) can be obtained after the data are standardized. Then, the principal component analysis will be carried out in this paper. But before the analysis, we need to check the variables and sample data to determine whether it is suitable for the one-step principal component analysis. Therefore, the KMO and Bartlett sphericity tests are used to verify whether the following principal component analysis can be performed, and the results are shown in Table 5.

In general, KMO measures the partial correlation between variables, with values ranging from 0 to 1. The principal component analysis is generally not recommended if the KMO value is below the threshold of 0.5. As can be seen from Table 5, the KMO value between variables is 0.368, slightly less than 0.5. At this point, the Bartlett sphericity test needs to be taken into account. The approximate chi-square value is 101.167, the degree of freedom is 36, and the significance level is  $\text{Sig.} = 0.000 < 0.05$ , indicating that the variables are not independent, but have some significant correlation. Therefore, based on the results of KMO and Bartlett's tests, it is suggested that these sample variables can be used for the principal component analysis.

TABLE 5: KMO and Bartlett's tests.

Kaiser–Meyer–Olkin measurement of sampling adequacy		0.368
Bartlett's sphericity tests	Approximate chi-square	101.167
	Degree of freedom DF	36
	Sig.	0.000

Furthermore, from the matrix of correlation coefficient of main variables automatically drawn by SPSS20.0 software, we can find that there are higher correlation coefficients among some variables, showing some significant correlation, so we can continue to extract common factors, and the results are shown in Table 6.

The following is a further analysis of the common factor variance table. Table 7 shows that under the principal component analysis method, the original 9 variables can be preliminarily extracted corresponding to the 9 characteristic roots; that is, the variance of the original variables can be explained, and each variable has a common degree of 1. Then, looking at the common degree of the variables after extracting the feature root, we can find that the common degree of each variable begins to appear different. Generally speaking, the larger the common degree value after extraction, the better the variable can be expressed by the common factor. In general, the value greater than 0.7 is enough to show that the variable can be reasonably expressed by the common factor. Comparing with the common degree of variables extracted from Table 7, we can find that the total value of each variable is more than 0.8, which indicates that more than 80% of the information of the original variable can be well interpreted and expressed by the principal component, and the information of the original variable is less lost.

Next, the principal component analysis is needed to extract the main common components. In general, the principal component can be synthetically extracted by two methods, one is by observing whether the characteristic root of the common component is more than 1, the other is by observing whether the cumulative variance contribution of the common component is more than 85%, and after considering the results of the two methods, the principal components can be extracted. In particular, the total variance explained in Table 8 shows that the characteristic roots of the first three principal components are all greater than 1, 4.488, 2.275, and 1.331, respectively. The variance contribution rates were 49.867%, 25.277%, and 14.785%, respectively. The cumulative variance contribution rates were 49.867%, 75.144%, and 89.929%, respectively. From this synthesis, the first three principal components can reflect the original 9 variables to 89.929% of the information, basically covering all the sample size of the original data information.

Further to the principal component analysis of the lithotripsy in Figure 1, we can find that the characteristic values of the first three principal components are relatively large. Among them, the first principal component has the largest contribution to the interpretation of the original variables, followed by the second and third principal components. In addition, from the 4th and later principal

TABLE 6: Correlation coefficient matrix table of principal component analysis variables.

	ZX1	ZX2	ZX3	ZX4	ZX5	ZX6	ZX7	ZX8	ZX9
ZX1	1.000	0.189	0.145	-0.279	-0.102	-0.280	0.110	0.413	0.694
ZX2	0.189	1.000	0.180	0.444	-0.399	0.061	0.256	-0.485	0.239
ZX3	0.145	0.180	1.000	0.789	-0.846	0.842	0.957	0.013	0.273
ZX4	-0.279	0.444	0.789	1.000	-0.812	0.804	0.844	-0.280	0.064
ZX5	-0.102	-0.399	-0.846	-0.812	1.000	-0.640	-0.884	-0.067	-0.307
ZX6	-0.280	0.061	0.842	0.804	-0.640	1.000	0.796	-0.281	0.030
ZX7	0.110	0.256	0.957	0.844	-0.884	0.796	1.000	0.092	0.410
ZX8	0.413	-0.485	0.013	-0.280	-0.067	-0.281	0.092	1.000	0.494
ZX9	0.694	0.239	0.273	0.064	-0.307	0.030	0.410	0.494	1.000

TABLE 7: Common factor variance.

	Initial	Extraction
ZX1 (R&D investment intensity)	1.000	0.839
ZX2 (the proportion of R&D personnel)	1.000	0.964
ZX3 (patent application volume)	1.000	0.932
ZX4 (the ratio of the secondary and tertiary industries' gross output value to the regional gross output value)	1.000	0.930
ZX5 (the energy consumption rate of GDP)	1.000	0.852
ZX6 (the number of equipment manufacturing and production service enterprises)	1.000	0.882
ZX7 (per capita GDP)	1.000	0.982
ZX8 (the ratio of foreign direct investment to GDP)	1.000	0.883
ZX9 (the financial science and technology expenditure as the proportion of the general budget expenditure)	1.000	0.829

TABLE 8: Total variance as explained.

Ingredients	Initial eigenvalue			Extract square sum load		
	Total	Variogram %	Accumulation %	Total	Variogram %	Accumulation %
1	4.488	49.867	49.867	4.488	49.867	49.867
2	2.275	25.277	75.144	2.275	25.277	75.144
3	1.331	14.785	89.929	1.331	14.785	89.929
4	0.444	4.938	94.867			
5	0.328	3.643	98.510			
6	0.083	0.920	99.430			
7	0.027	0.303	99.733			
8	0.023	0.259	99.992			
9	0.001	0.008	100.000			

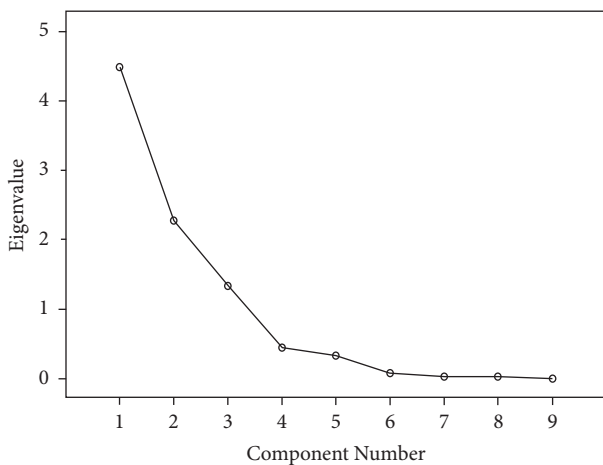


FIGURE 1: Macadam map.

component eigenvalues less than 1, the contribution to the interpretation of the original variable is gradually weakened.

Based on the above analysis, three principal components can be extracted.

After obtaining the three principal components, the following three principal component score expressions can be derived from the values in the matrix of principal component scores in Table 9:

TABLE 9: Principal component score coefficient matrix.

	Principal component		
	F1	F2	F3
ZX1 (R&D investment intensity)	0.026	0.865	0.301
ZX2 (the proportion of R&D personnel)	0.393	-0.044	0.899
ZX3 (patent application volume)	0.945	0.089	-0.178
ZX4 (the ratio of the secondary and tertiary industries' gross output value to the regional gross output value)	0.918	-0.293	0.045
ZX5 (the energy consumption rate of GDP)	-0.915	-0.122	-0.014
ZX6 (the number of equipment manufacturing and production service enterprises)	0.845	-0.310	-0.268
ZX7 (per capita GDP)	0.970	0.154	-0.135
ZX8 (the ratio of foreign direct investment to GDP)	-0.103	0.772	-0.526
ZX9 (the financial science and technology expenditure as the proportion of the general budget expenditure)	0.310	0.837	0.179

TABLE 10: Model fit.

Model	R	R <sup>2</sup>	Adjusted R <sup>2</sup>	Standard estimate error
1	0.933	0.870	0.814	0.43077234

TABLE 11: Results of multiple regression analysis.

Model	Sum of squares	df	F	Sig.
1				
Regress	8.701	3	15.630	0.002
Residual error	1.299	7		
Total	10.000	10		

$$\begin{aligned}
 F1 &= 0.026ZX1 + 0.393ZX2 + 0.945ZX3, \\
 F2 &= 0.865ZX1 - 0.044ZX2 + 0.089ZX3 - 0.122ZX5 \\
 &\quad - 0.310ZX6 + 0.154ZX7 - 0.772ZX8 + 0.837ZX9 \\
 &\quad + 0.918ZX4 - 0.915ZX5 + 0.845ZX6 + 0.970ZX7 \\
 &\quad - 0.103ZX8 + 0.310ZX9, \\
 F3 &= 0.301ZX1 + 0.899ZX2 - 0.178ZX3 - 0.045ZX4 \\
 &\quad - 0.014ZX5 + 0.268ZX6 - \\
 &\quad 0.0135ZX7 - 0.526ZX8 + 0.179ZX9,
 \end{aligned} \tag{7}$$

where F1, F2, and F3 in the three formulas represent the specific scores of the principal components, respectively, and the ZX1 to ZX9 are the normalized variables corresponding to the X1 to X9.

Using ZY as a dependent variable and F1, F2, and F3 as independent variables, a regression model is established, which is as follows:

$$ZY_t = \alpha_1 F_1 + \alpha_2 F_2 + \alpha_3 F_3 + \mu_t. \tag{8}$$

In the formula,  $\alpha_1$ ,  $\alpha_2$ , and  $\alpha_3$  are regression coefficients,  $\mu_t$  is a random error, and  $t$  represents a year from 2009 to 2019. <https://fanyi.so.com/javascript;>

Furthermore, using SPSS20.0 software to test the estimated model parameters, the specific results are as follows:

Table 10 shows that the  $R^2$  of the regression model is 0.870, and the adjusted  $R^2$  is 0.814, which indicates that the degree of the three principal component variables in the

regression model can explain that the dependent variables are 81.4%, reflecting the overall fit of the sample.

From Table 11, the  $F$  value is 15.630 and the SIG value is 0.002, which shows that the regression equation is significant at the level of 1%.

As can be seen from Table 12, the normalized coefficients of F1, F2, and F3 are 0.980, -0.034, and -0.206, and the  $t$ -test shows that the model setting has some significance. Further regression model formula (10) can be determined from the principal component variable coefficients, as shown below as follows:

$$ZY_t = 0.980F_1 - 0.034F_2 - 0.206F_3. \tag{9}$$

In order to further express the regression equation in terms of standardized independent variables, the matrix composed of the first three principal component coefficient vectors and the principal component regression coefficient estimator matrix are multiplied to obtain the following:



TABLE 12: Results of multivariate regression coefficients.

Model	Nonstandard coefficient		Standard coefficient	t	Sig.
	B	Standard error			
(Constant quantity)	-9.044E-008	0.130		0.000	1.000
1 F1	0.218	0.033	0.980	6.584	0.000
F2	-0.030	0.146	-0.034	-0.206	0.842
F3	-0.156	0.134	-0.206	-1.165	0.282

TABLE 13: Impact coefficient table of explanatory variables for industrial convergence.

Explanatory variable	Coefficient of influence	Direction of action
ZX1 (R&D investment intensity)	-0.066	-
ZX2 (the proportion of R&D personnel)	0.201	+
ZX3 (patent application volume)	0.96	+
ZX4 (the ratio of the secondary and tertiary industries' gross output value to the regional gross output value)	0.9	+
ZX5 (the energy consumption rate of GDP)	-0.89	-
ZX6 (the number of equipment manufacturing and production service enterprises)	0.894	+
ZX7 (per capita GDP)	0.973	+
ZX8 (the ratio of foreign direct investment to GDP)	0.183	+
ZX9 (the financial science and technology expenditure as the proportion of the general budget expenditure)	0.238	+

$$\beta_i = \begin{pmatrix} 0.026 & 0.865 & 0.301 \\ 0.393 & -0.044 & 0.899 \\ 0.945 & 0.089 & -0.178 \\ 0.918 & -0.293 & 0.045 \\ -0.915 & -0.122 & -0.014 \\ 0.845 & -0.310 & -0.268 \\ 0.970 & 0.154 & -0.135 \\ 0.103 & 0.772 & -0.526 \\ 0.310 & 0.837 & 0.179 \end{pmatrix} * \begin{pmatrix} 0.980 \\ -0.034 \\ -0.206 \end{pmatrix} \tag{10}$$

$$= \begin{pmatrix} -0.066 \\ 0.201 \\ 0.960 \\ 0.900 \\ -0.890 \\ 0.894 \\ 0.973 \\ 0.183 \\ 0.238 \end{pmatrix} .$$

Finally, according to the final regression equation, we can get the influence coefficient and the general action direction of each variable index in the following Table 13:

4.5. *Analysis of Empirical Results.* Based on the principal component regression analysis above, this paper concludes the regression equation between the standardized degree of industrial convergence and the related impact variables, and Table 13 shows the following results:

- (1) Industrial integration basis: according to the regression coefficient of R&D expenditure intensity (ZX1), there is a slight negative correlation between R&D expenditure intensity (ZX1) and industrial integration degree (ZY). For every 1 percentage point increase in ZX1, the degree of industrial convergence (ZY) decreases by 0.066%. This paper suggests that the reason for this phenomenon may be related to the size of the data, so the theoretical inference hypothesis of this indicator has not been fully verified. According to the regression coefficient of the ratio of R&D personnel (ZX2), the ratio of R&D personnel (ZX2) has a positive correlation with the degree of industrial convergence (ZY). When the ratio of R&D personnel (ZX2) increases by 1 percentage point, the degree of industrial convergence (ZY) increases by 0.201%. It shows that the reserve and proportion of high-knowledge talents have a positive effect on promoting the integration of equipment manufacturing and production services. Finally, according to the regression coefficient of the number of patent applications (ZX3), there is a significant positive correlation between the number of patent applications (ZX3) and the degree of industrial convergence (ZY). When the number of

From this, the coefficients before the standardized variable can be obtained, and then, the regression equation expressed by the standardized independent variable can be obtained as follows:

$$ZY = -0.066ZX1 + 0.201ZX2 + 0.96ZX3 + 0.9ZX4 - 0.089ZX5 + 0.894ZX6 + 0.973ZX7 + 0.183ZX8 + 0.238ZX9. \tag{11}$$

patent applications (ZX3) increases by 1 percentage point, the degree of industrial convergence (ZY) increases by 0.96%. It can be seen that the more patent applications, the stronger the close relationship between the equipment manufacturing industry and the production services industry; the deeper integration of these two industries has a good role in promoting; and at the same time, it also reflects that technological innovation has an important influence on the promotion of industrial convergence.

- (2) The conditions of industrial convergence: according to the regression coefficient of the ratio of the gross output value of the secondary industry to the total output value of the region (ZX4), there is a significant positive correlation between the ratio of the gross output value of the secondary industry to the total output value of the region (ZX4) and the degree of industrial convergence (ZY); that is, each increase of 1 percentage point in the ratio of the secondary and tertiary industries to the total regional output (ZX4) will increase the degree of industrial convergence (ZY) by 0.9%. This shows that the better the overall development of the secondary and tertiary industries, and the higher their proportion in the GDP of the region, the more they can reflect the vigorous demand of the local consumer market, and for equipment manufacturing and production services to further integration to provide a huge market demand conditions, and further deepen the two industries of interaction and relevance. From the regression coefficient of the rate of reduction of energy consumption of the gross product (ZX5), we can see that the rate of reduction of energy consumption of the gross product (ZX5) has a significant negative correlation with the degree of industrial convergence (ZY); that is, when the rate of energy consumption of the gross product (ZX5) increases by 1 percentage point, it would reduce industrial integration by 0.89%. This shows that when the GDP energy consumption rate is greatly reduced, the overall industrial efficient energy use will be greatly increased; while indirectly reflecting the progress of energy-saving technology and the upgrading of the overall industrial structure of enterprises, it also provides a good upgrade condition for the deep integration of equipment manufacturing and production services. Finally, according to the regression coefficient of the number of enterprises in equipment manufacturing and production services (ZX6), there is a significant positive correlation between the number of enterprises in equipment manufacturing and production services (ZX6) and the degree of industrial convergence (ZY), namely, each increase in the number of equipment manufacturing and production service enterprises (ZX6) by 1 percentage point will increase the degree of industrial integration (ZY) by 0.894%.

This shows that when the number of equipment manufacturing and production service enterprises is growing, the resulting fierce internal competition can effectively promote the integration level of the two industries.

- (3) Industrial convergence environment: from the regression coefficient of per capita regional gross product (ZX7), we can see that there is a significant positive correlation between per capita regional gross product (ZX7) and industrial convergence degree (ZY); that is, when per capita regional gross product (ZX7) increases by 1 percentage point, industrial convergence (ZY) will increase by 0.973%. This shows that the higher the level of per capita regional gross domestic product, the greater the market development and consumption potential, which is more conducive to promoting the deep integration of equipment manufacturing and production services, and for its development has provided a good economic development environment and the huge market development space. According to the regression coefficient of the ratio of foreign direct investment to GDP (ZX8), there is a positive correlation between the ratio of foreign direct investment to GDP (ZX8) and the degree of industrial convergence (ZY); that is, every 1 percentage point increase in the foreign direct investment share of GDP (ZX8) is associated with a 0.183 percentage increase in the degree of industrial convergence (ZY). This shows that the increase in the foreign direct investment can promote the deep integration of manufacturing and production services, which further reflects the improvement and optimization of the investment environment that can deepen the level of integration of the two industries. Finally, it can be seen from the regression coefficient of the proportion of local fiscal science and technology expenditure in the local general budget expenditure (ZX9) that there is a positive correlation between the proportion of science and technology expenditure of local finance in local general budget expenditure (ZX9) and industrial convergence degree (ZY); that is, each increase of 1 percentage point in the proportion of local fiscal expenditure on science and technology (ZX9) will increase the degree of industrial convergence (ZY) by 0.238%. It is concluded that the higher the proportion of local fiscal expenditure on science and technology is, the better the integration level of equipment manufacturing and production services is. At the same time, it also reflects that a good regional policy environment can provide strong policy impetus for the development of the two industries and enhance the deep-level integration between industries.

Combined with the above empirical results, we can determine that R&D investment divided by R&D expenditure intensity is not expected to be verified, and other indicators have been verified, basically consistent with the

previous theoretical analysis. It shows that talent reserve, technological innovation, market demand, industrial upgrading, industry competition, economic environment, investment environment, and policy environment are the important factors that affect the integration of equipment manufacturing and production services in Shanxi Province. Therefore, Shanxi Province should continue to make efforts in these areas, formulate appropriate development planning, and vigorously promote the local equipment manufacturing industry and production service deep integration.

## 5. Conclusions and Enlightenment

The purpose of this paper is to study the level of integration development between equipment manufacturing industry and producer service industry in Shanxi Province and its influencing factors. Therefore, this paper uses the input-output method to calculate and analyze the integration degree of two big industries in Shanxi Province in 2012 and 2017. Finally, on this basis, this paper further uses the principal component regression analysis to empirically analyze the two industrial convergence levels of the main factors and find their ultimate impact factors. Two conclusions can be drawn as follows:

- (1) *Measurement part.* In this paper, the input-output method is used to calculate the integration degree of equipment manufacturing industry and producer service industry in Shanxi Province in 2012 and 2017. It is further found that in these two years, the equipment manufacturing industry and the producer service industry of Shanxi Province are in the state of partial integration on the whole, and the degree of industrial integration in 2017 has significantly increased compared with that in 2012; it shows that the integration trend of equipment manufacturing industry and producer service industry is strengthening; the two industries are moving toward medium integration; and the overall development trend is getting better.
- (2) *Empirical part.* This paper explores and analyzes the related influencing factors of the integrated development of the equipment manufacturing industry and production service industry in Shanxi Province, and on this basis, selects the evaluation indexes and data of each influencing factor; at the same time, this paper further establishes the influence factor model of industrial convergence and finally uses the principal component regression analysis to carry on the empirical analysis to it. The empirical results show that except R&D investment, which is measured by R&D expenditure intensity, which has not been verified, all other indexes have been verified, which is basically consistent with the previous theoretical analysis. As a result, it can be proved that talent reserve, technological innovation, market demand, industrial upgrading, industry competition, economic environment, investment environment, and policy environment are the important factors

that affect the integration of equipment manufacturing and production services in Shanxi Province.

Based on the above analysis, we can find that the two major industrial convergence of the impact of almost every factor are closely related to the government. It can be said that the government is the future to promote the development of equipment manufacturing and production services an important hand and support basis. Therefore, the government departments of Shanxi Province should take on the task of industrial integration and actively play the role of government macroeconomic regulation and control to provide a good policy environment for local equipment manufacturing and production services. In addition, as far as equipment manufacturing and producer services are concerned, the talent factor is an important intellectual foundation to ensure the long-term development and deep integration of the two industries. At present, Shanxi is in an important critical period of transformation and development, and the degree of craving for high-quality R&D, management, innovation, and vocational and technical talents is much greater than ever before. Therefore, the Shanxi provincial government needs to establish a comprehensive talent training, reserve, attraction, and incentive mechanism in order to constantly enhance the human intelligence advantage [21].

## Data Availability

The experimental data used to support the findings of this study are available from the corresponding author upon request.

## Conflicts of Interest

The authors declare that they have no conflicts of interest to report regarding the present study.

## Acknowledgments

This work was supported by the Shanxi Province Science and Technology Strategy Research Special Key Project, Research on Ecological Assessment of Innovation in Shanxi Province (project no. 202104031401001).


## References

- [1] N. Rosenberg, "Technological change in the machine tool industry, 1840–1910," *The Journal of Economic History*, vol. 23, no. 4, pp. 414–443, 1963.
- [2] Y. Geum, M. S. Kim, and S. Lee, "How industrial convergence happens: a taxonomical approach based on empirical evidences," *Technological Forecasting and Social Change*, vol. 107, pp. 112–120, 2016.
- [3] N. Kim, H. Lee, W. Kim, H. Lee, and J. H. Suh, "Dynamic patterns of industry convergence: e," *Research Policy*, vol. 44, no. 9, pp. 1734–1748, 2015.
- [4] M. Abreu and V. Mendes, *Commercial Bank Interest Margins and Profitability: Evidence for Some EU Countries*, Porto Working Paper series, USA, 2002.

- [5] X. Xin, *A Study on the Integration of Cultural Industry and Tourism Industry: Mechanism, Path and Model--Taking Kaifeng as an Example [D]*, Henan University, Minglun St, Shun He Hui Zu Qu, 2013.
- [6] Yu Zhou and H. Ning, "On the reasons and types of industrial convergence and its influence on economic development [J]," *Journal of Shanxi Normal University (Philosophy and Social Sciences edition): Social Sciences*, vol. 5, pp. 56–60, 2014.
- [7] Y. Su, Y. You, and Z. Wang, "Integrated Development of rural primary, secondary and tertiary industries: theoretical discussion, status analysis and countermeasures [J]," *Chinese soft science*, vol. 8, pp. 17–28, 2016.
- [8] S. Vandermerwe and J. Rada, "Servitization of business: a," *European Management Journal*, vol. 6, no. 4, pp. 314–324, 1988.
- [9] G. Ren, *Service Business Development in Manufacturing Companies [D]*, pp. 56–82, University of Cambridge, PhD Dissertation, Cambridge, 2009.
- [10] A. I. J. A. Leiponen, "The benefits of R&D and breadth in innovation strategies: a comparison of Finnish service and manufacturing firms," *Industrial and Corporate Change*, vol. 21, no. 5, pp. 1255–1281, 2012.
- [11] Li man, "Interaction between equipment manufacturing upgrading and production services and its influencing factors," *Century Bridge*, vol. 2, pp. 95-96, 2014.
- [12] X. Wang and J. Li, "Service level and influencing factors of Chinese manufacturing industry [J]," *Journal of the Xiangtan University*, vol. 40, no. 5, pp. 53–60, 2016.
- [13] J. Garciam, "Towards modular and coordinated manufacturing systems oriented to services[J]," *Dynacolumbia*, vol. 77, no. 163, pp. 201–210, 2010.
- [14] H. Gebauer, G. J. Ren, A. Valtakoski, and J. Reynoso, "Service-driven manufacturing: provision, evolution and financial impact of services in industrial firms[J]," *Journal of Service Management*, vol. 23, no. 1, pp. 120–136, 2012.
- [15] Z. He and L. Sun, "Service discussion analysis and service manufacturing proposal [J]," *Journal of Management*, no. 10, pp. 15–23, 2012.
- [16] J. Wu, *Study on the Interactive Integration System of Equipment Manufacturing and Producer Services Based on Industrial philosophy[D]*, Harbin University of Science and Technology, Nangang, Harbin, 2017.
- [17] Z. Zeng, *A Study on the Impact of Industrial Convergence on the Industrial Competitiveness of China's Equipment Manufacturing Industry [D]*, Chongqing University of Technology, Chongqing, China, 2020.
- [18] H. Wu, *A Study on the Integration of Production Services and Manufacturing in Anhui [D]*, Anhui University of Finance and Economics, Beng Shan Qu, 2015.
- [19] C. Wang, *Study on Integration Mechanism and Support Strategy of Equipment Manufacturing and Production Services in China [D]*, Harbin University of Science and Technology, Heilongjiang, 2014.
- [20] R. B. Stobaugh, "How to analyze foreign investment climates [J]," *Harvard Business Review*, vol. 47, no. 5, pp. 100–108, 1969.
- [21] X. Chen and J. F. Huang, "Division of labor, interaction and integration: an empirical study on the evolution of the relationship between service industry and manufacturing industry," *China Soft Science*, vol. 10, pp. 65–71, 2004.

## Research Article

# Regional Economic Forecasting Method Based on Recurrent Neural Network

E. Liu <sup>1</sup>, Haiou Zhu,<sup>2</sup> Qing Liu,<sup>3</sup> and Thomas Bilaliib Udimal<sup>1</sup>

<sup>1</sup>College of Economics and Management, Southwest Forestry University, Kunming 650224, Yunnan, China

<sup>2</sup>School of Design and Creative Arts, Loughborough University, LE11 3TU, Leicestershire, UK

<sup>3</sup>School of Information Engineering, Yunnan Forestry Technological College, Kunming 650224, Yunnan, China

Correspondence should be addressed to E. Liu; [liue@swfu.edu.cn](mailto:liue@swfu.edu.cn)

Received 11 August 2022; Revised 14 September 2022; Accepted 19 September 2022; Published 6 October 2022

Academic Editor: Dinesh Kumar Saini

Copyright © 2022 E. Liu et al. This is an open access article distributed under the Creative Commons Attribution License, which permits unrestricted use, distribution, and reproduction in any medium, provided the original work is properly cited.

Macroeconomic situation is the overall performance of the economic situation of a country and region. Making accurate forecasts of macroeconomic trends is of great significance for analyzing the success or failure of macroeconomic control policies, evaluating the quality of economic system operation, and correctly formulating future development planning strategies. The macroeconomic system is a nonlinear system, the environment is constantly changing, and additional disturbing factors directly affect the operation of the macroeconomic system, which has a great impact on the forecast results. The historical information required for macroeconomic modeling is unstable, unclear, and incomplete, which makes it very difficult to solve such problems with traditional forecasting methods. In response to the multivariate and nonlinear characteristics of macroeconomic forecasting, this paper proposes the application of artificial neural networks for forecasting. This paper introduces the recurrent neural network into the field of economic forecasting to solve the problems of the traditional BP (back propagation) neural network method. The experimental data are verified and the experimental results prove that the studied scheme based PSO-GRU improve the performance of economic forecasting.

## 1. Introduction

Macroeconomic system is the comprehensive performance of the overall economic situation of a country or region; finance is an important part of the national economy and an important macro-control tool [1]; macro-control is a complex system project, and to make active and effective regulation, we must first make forecasts. Forecasting is based on historical information and the current situation and infers the development trend of things according to certain theories and methods [2].

Economic phenomena can be recognized and used. Economic forecast is a scientific forecast based on the knowledge of the inner laws of economic phenomena. The development of economic phenomena is influenced by many factors, which are intrinsically linked and will continue to have an impact on the development of economic phenomena for a long period of time, which makes the occurrence and

development of economic phenomena have objective regularity [3, 4]. The degree of accuracy of economic forecasting is relative and limited. The development of economic phenomena is influenced not only by factors that people already know and can grasp, but also by factors that people have not yet recognized and cannot grasp, such as sudden changes in major economic policies, huge natural disasters and other events that have a great impact on economic life [5]. Therefore, the future development of economic phenomena has uncertainty, and due to the existence of uncertainty, there are inevitable deviations in economic forecasting, coupled with the fact that sometimes the statistics and economic information available are insufficient or not accurate enough, and the forecasting methods chosen are not appropriate, which may also cause the failure of economic forecasting [6, 7]. As the development of economic phenomena change both by chance and necessity, the changes affected by chance are random fluctuations, and the necessity behind the chance

determines the development process of things. Therefore, under the premise of ensuring the accuracy and completeness of survey statistics and economic information, the accuracy of economic forecasting can be maximized by constantly studying and improving the forecasting methods [8].

The deviation of the results of economic forecasting from the actual economic operation does not necessarily mean the failure of forecasting [9]. The purpose of economic forecasting is to guide economic production activities by making appropriate economic decisions. In other words, by analyzing the results of economic forecasts, government departments or individual entities make necessary adjustments and interventions in economic activities and take corresponding economic measures to make economic activities develop in the direction of profit and avoid harm, which inevitably leads to the situation that the forecast results are not consistent with the actual economic operation [10–12]. However, in this case, the deviation of the forecast results from the actual economic operation indicates the usefulness of the forecast, which is a kind of inconsistency beneficial to economic life.

Among the existing forecasting methods, time series forecasting and regression forecasting are the two most commonly used statistical methods. The macroeconomic system is essentially a nonlinear system, and the environment in which it is located is in a state of constant change, and additional disturbances act directly on the operating process of the macroeconomic system, which has a great impact on the forecasting results [13–15]. The historical information required for macroeconomic modeling is unstable, unclear, and incomplete, which makes it very difficult to solve such problems using traditional forecasting methods, and the application of artificial neural networks is proposed for forecasting [16].

Artificial neural network is a nonlinear dynamic system that can realize nonlinear relationships between variables within arbitrary accuracy [17–20]. It has the ability to solve nonlinear problems, network learning ability, and system fitting ability, and can meet the macroeconomic pointer forecasting requirements, so that the system has the ability to deal with nonlinear and uncertainty problems. Macroeconomic system is a complex system, and under the guidance of economic theory, the characteristics of macroeconomic system are analyzed and the macroeconomic pointer is discussed [21–23]. Under the guidance of economic theory, the characteristics of macroeconomic system are analyzed, and the macroeconomic pointer system is discussed. Based on the characteristics of macroeconomic system such as nonlinearity and uncertainty, a comprehensive and integrated approach combining qualitative and quantitative analysis is proposed to analyze macroeconomics [24]. A system modeling method combining polynomial fitting and BP neural network is proposed to improve the accuracy of system forecasting. The system modeling method combining polynomial fitting and BP neural network is proposed to improve the forecast accuracy of the system, realize the forecast of regional macroeconomic pointers, and describe the macroeconomic development trend.

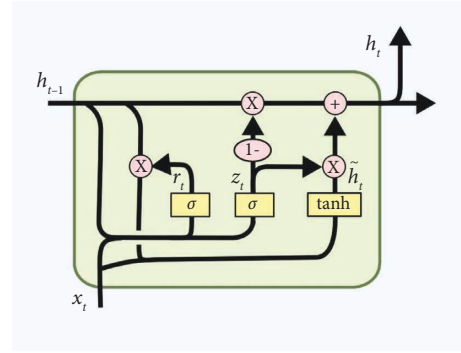


FIGURE 1: GRU model structure.

## 2. Methodology

**2.1. GRU.** Recurrent neural network (RNN) is a neural network structure for sequential data, the core of which is to recycle the parameters of network layers to avoid the parameter surge caused by the increase of time step, and to introduce the hidden state for recording historical information to effectively deal with the before and after correlation of data [25–28]. RNN is very effective for data with sequential characteristics, and it can mine the temporal information as well as semantic information in the data. Using this capability of RNN, it enables deep learning models to make a breakthrough in solving problems in NLP fields such as speech recognition, language modeling, machine translation, and temporal analysis.

Gated recurrent units (GRU) is a typical RNN model [29–31]; the GRU network model and its structure is shown in Figure 1. Please rephrase the part for clarity, the structure of GRU is similar to the LSTM, but much simpler than the LSTM, which only contains two kinds of gates: the reset gate and the update gate. The reset gate is responsible for getting the short-term dependencies in the temporal data, i.e., the reset gate controls how much information in the past is forgotten and the update gate controls the state information of the previous moment, which is substituted into the current state and is helpful to get the long-term dependencies in the temporal data and it updates all candidate implicit states.

**2.2. PSO.** Particle swarm optimization (PSO) is a population intelligence optimization algorithm inspired by the feeding process of birds, also known as flock foraging algorithm [26, 32]. In PSO, each potential solution of the optimization problem is considered as a particle, similar to a bird in a flock. Each particle has a velocity that determines its flight direction and distance [19], as well as a fitness value, and then all particles find the optimal value in the solution space using the current optimal particle as the criterion. Suppose that in a D-dimensional search space, the number of particles is  $N$  and a particle  $x$  in the particle population, the velocity of a particle  $X$  in the swarm can be expressed as follows:

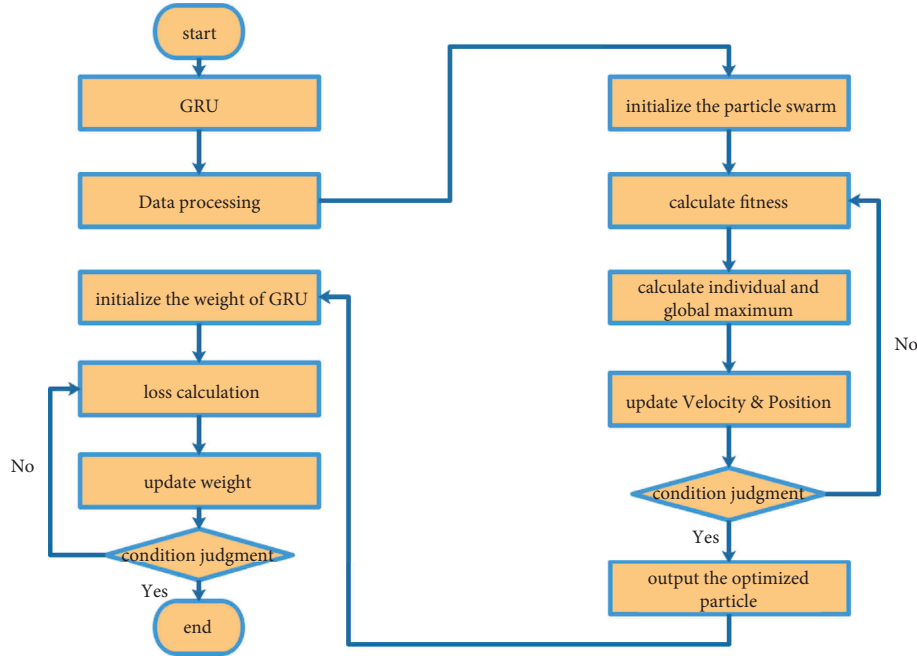


FIGURE 2: PSO-GRU model structure.

$$\begin{aligned} X_i &= [x_{i1}, x_{i2}, \dots, x_{iN}], \\ V_i &= [v_{i1}, v_{i2}, \dots, v_{iN}]. \end{aligned} \quad (1)$$

The optimal position found by an individual particle is called the individual pole, denoted by  $p_{id}$ , and the optimal position found by the whole particle swarm is called the global pole, denoted by  $p_{gd}$ , after which the particles are updated according to equation:

$$\begin{aligned} v_{id}(t) &= \Lambda \cdot v_{id}(t) + c_1 r_1(t) [p_{id}(t) - x_{id}(t)] \\ &\quad + c_2 r_2(t) [p_{gd}(t) - x_{id}(t)], \\ x_{id}(t+1) &= x_{id}(t) + v_{id}(t), \end{aligned} \quad (2)$$

where  $c_1$  and  $c_2$  denotes the learning factor,  $\Lambda$  denotes the inertia factor, larger  $\Lambda$  means stronger global search ability and weaker local search ability, and smaller  $\Lambda$  means stronger local search ability and weaker global search ability. The particle swarm algorithm requires fewer parameters to be adjusted, is easy to implement, and has strong generality by using real numbers to solve [33]. At present, the particle swarm algorithm is widely used in pattern recognition, image processing, neural network training, decision scheduling, and other related industries.

**2.3. PSO-GRU.** The basic idea is to optimize the initial weights of GRU by using PSO, which makes the network converge faster and achieve better prediction. Figure 2 shows the detail design of the PSO-GRU model for regional economic forecasting.

The specific steps are described as follows:

Step 1: Initialize the GRU model and determine the model parameters.

Step 2: Process the data, and this paper adopts the maximum-minimum method to normalize the data, so that the range of the data after processing falls between [0, 1].

Step 3: Initialize the parameters of the particle swarm algorithm.

Step 4: Initialize the velocity and position of the particles.

Step 5: Determine the fitness function of the particles,

$$f(x_i) = \frac{1}{N} \sum_I (\tilde{y}_i^* - y_i^*), \quad (3)$$

where  $\tilde{y}_i^*$  and  $y_i^*$  denote the desired output and the actual output of the training set, respectively.

Step 6: Calculate the corresponding fitness  $fit_{x_i}$  of each particle  $X$ ; and compare the fits with the individual extremes  $P_{est}$ , if  $fit_{x_i} < P_{est}$ , then replace  $P_{est}$  with  $fit_{x_i}$  to complete the update of  $P_{est}$ .

Step 7: Compare the best fitness (individual extreme value)  $P_{est}$  of each particle with the global extreme value  $g_{est}$ , if  $P_{est} < g_{est}$ , then replace  $g_{est}$  with  $P_{est}$  to complete the update of  $g_{est}$ .

Step 8: Update the velocity and position of the particle itself. Calculate the fitness of the new particle and find the individual extreme value and global extreme value of the new particle here.

Step 9: After satisfying the termination condition of PSO algorithm (usually the maximum number of

iterations or the minimum fitness value), the optimal particles are input to the GRU model as their initialized weights and thresholds, and the PSO-GRU model is trained.

### 3. Results and Analysis

*3.1. Experimental Data and Settings.* Economic forecasts generally need to follow: the larger the amount of data the more accurate the results, the shorter the time the more accurate, the need to estimate in advance the possibility of, the forecasting method should be tested before use, and so on. Based on these principles, the prediction experiments in this paper are designed. The ultimate purpose of economic forecasting is to meet the needs of decision making and management, and the two major economic indicators, Gross Domestic Product (GDP) and Consumer Price Index (CPI), are selected as the forecasting targets. In order to ensure the accuracy as well as the credibility of the forecast results, we must first ensure the accuracy, reliability, and timeliness of the data. In order to ensure the accuracy and credibility of the forecast results, we must first ensure the accuracy, reliability, and timeliness of the data. The data used in this paper are all from the official website of the National Bureau of Statistics, which are released by the state and are true and reliable. Secondly, we need to standardize the data units, values, and scales to ensure the consistency of the data, and preprocess the collected data to ensure the smooth conduct of the experiments afterwards. In this paper, the experiments are normalized and preprocessed by using the standardized method of deviation for the economic forecasting data.

### 4. Numerical Results and Analysis

In order to quantitatively compare the forecasting performance of BP LSTM GUR PSO-GRU, we applied the mean absolute error (MAE), mean square error (MSE), and mean relative error to measure the forecasting accuracy, and the formulas of the above three indicators are defined as follows:

$$\begin{aligned} \text{MAE} &= \frac{1}{n} \sum_{i=1}^n |y_i - \hat{y}_i|, \\ \text{MSE} &= \frac{1}{n} \sum_{i=1}^n (y_i - \hat{y}_i)^2, \\ \text{RMSE} &= \sqrt{\frac{1}{n} \sum_{i=1}^n (y_i - \hat{y}_i)^2}. \end{aligned} \quad (4)$$

From Table 1 and Figure 3, we can see that the errors of the three methods are not large, and they can predict the consumer price index of Guangdong Province with a certain degree of accuracy, reflecting the pattern of changes in the price index. The PSO-GUR model has the best performance in terms of mean absolute error (MAE) and mean relative error, reflecting the better modeling accuracy of PSO-GUR. However, the LSTM and BP models perform better in the mean squared error (MSE), which is an indicator of the

TABLE 1: Detail of performance comparison of different method.

Method	MAE	MSE	RSME
BP	0.67	0.74	0.65
LSTM	0.52	0.69	0.56
GRU	0.47	0.45	0.52
PSO-GRU	0.41	0.35	0.38

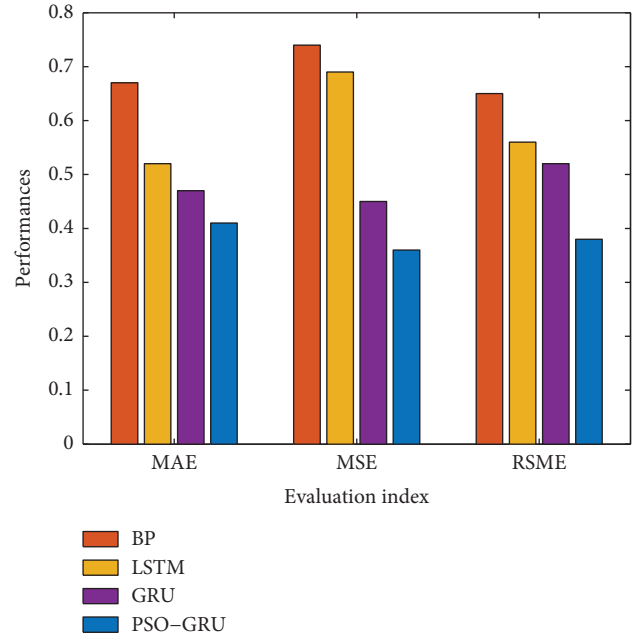


FIGURE 3: Performance comparison of different method.

volatility of the prediction error, which also reflects that the linear model like VAR is more difficult to capture the part of drastic changes, while the BP neural network is worse in all indicators. It indicates that PSO-GRU can tap the complex change patterns inherent in the data to improve the prediction accuracy and is a better nonlinear prediction method than BP neural network, while it can make up for the shortcomings of traditional linear time series models.

From Figure 4, the actual consumer price index in Guangdong Province showed a slight decline and then stabilized during the forecast period from June 2014 to February 2015, and the forecast results of PSO-GRU model could follow the downward trend of the consumer price index in Guangdong Province more closely in the first six months, which is consistent with the actual situation, while the forecasts of BP all showed the downward trend of the consumer price index in Guangdong Province in the first seven months. The former is good for the government to prevent inflation in time, while the latter may lead to the loss of timely control of possible inflation.

Figure 5 gives the error convergence curves of the PSO-GRU deep learning model and the BP neural network in the training and learning phase. In terms of convergence speed, PSO-GRU is faster than the BP, LSTM, and GRU model and does not show oscillation. This is mainly because the



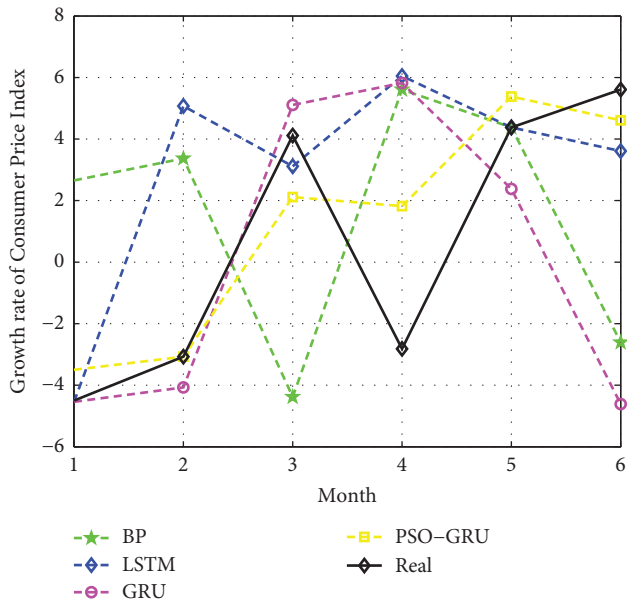


FIGURE 4: Performance comparison of different method on growth ratio of CPI.

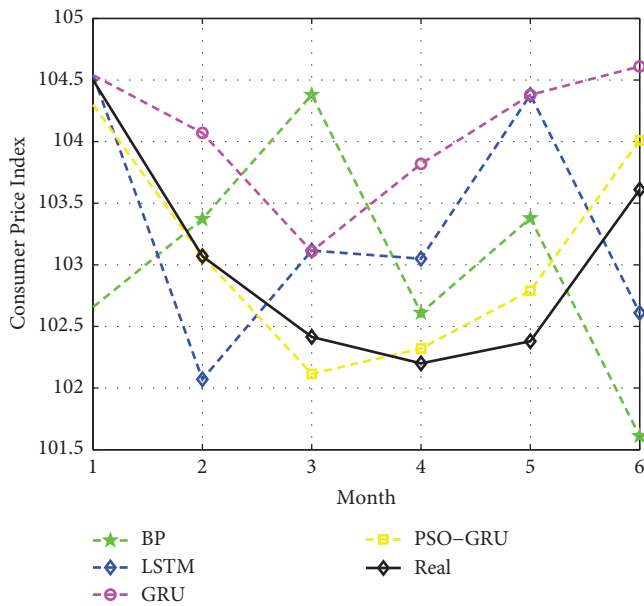


FIGURE 5: Performance comparison of different method on CPI.

pretraining learning method used by PSO-GRU can well provide a good initial value for the network; while the BP, LSTM, and GRU model use random parameters to initialize the network, thus its error curve has a higher starting point, longer convergence time, and may show oscillations, which is a reason for the poor performance of the final BP prediction.

The aforementioned experiments show that the PSO-GRU deep learning method can effectively forecast the consumer price index in Guangdong Province, and the objective indicators such as mean absolute error (MAE), mean square error (MSE), and mean relative error show that

the PSO-GRU method has higher forecasting accuracy compared with BP, LSTM, and GRU model. At the same time, PSO-GRU method has faster convergence speed and stronger generalization ability, especially when there are fewer labeled training samples, and it is a more superior economic forecasting modeling tool.

### 5. Conclusions

In response to the multivariate and nonlinear characteristics of macroeconomic forecasting, this paper proposes the application of artificial neural networks for forecasting. This paper introduces the recurrent neural network into the field of economic forecasting to solve the problems of the traditional BP network economic forecasting method. The experimental data are verified and the experimental results prove that the studied scheme based PSO-GRU improve the performance of economic forecasting.

### Data Availability

The data supporting the conclusion of the article are shown in relevant figures and tables in this article.

### Conflicts of Interest

The authors declare that there are no conflicts of interest regarding the publication of this article.

### References

- [1] Y. Li, H. Ma, L. Wang, S. Mao, and G. Wang, "Optimized content caching and user association for edge computing in densely deployed heterogeneous networks," *IEEE Transactions on Mobile Computing*, vol. 21, no. 6, pp. 2130–2142, 2022.
- [2] Z. Guo, K. Yu, Z. Lv, K. K. R. Choo, P. Shi, and J. J. P. C. Rodrigues, "Deep federated learning enhanced secure poi microservices for cyber-physical systems," *IEEE Wireless Communications*, vol. 29, no. 2, pp. 22–29, 2022.
- [3] X. Wang, M. Feckan, and J. R. Wang, "Forecasting economic growth of the group of seven via fractional-order gradient descent approach," *Axioms*, vol. 10, no. 4, p. 257, 2021.
- [4] J. Lv, C. Wang, W. Gao, and Q. Zhao, "An economic forecasting method based on the lightgbm-optimized LSTM and time-series model," *Computational Intelligence and Neuroscience*, vol. 2021, Article ID 8128879, 10 pages, 2021.
- [5] T. Seth and V. Chaudhary, "A predictive framework for multi-horizon financial crises forecasting using macro-economic data," in *Proceedings of the 2021 IEEE International Conference on Big Data (Big Data)*, pp. 1109–1118, IEEE, Orlando, FL, USA, December 2021.
- [6] A. Lunde and M. Torkar, "Including news data in forecasting macro economic performance of China," *Computational Management Science*, vol. 17, no. 4, pp. 585–611, 2020.
- [7] C. Wang, S. Xiong, and X. Chen, "Correlation situation forecasting of economic indicators based on partial least squares and kernel method regression model," in *Advances in Human Factors, Business Management and Leadership AHFE 2020 Advances in Intelligent Systems and Computing*, J. Kantola, S. Nazir, and V. Salminen, Eds., Springer, Cham, pp. 523–529, 2020.

- [8] Z. Guo, K. Yu, A. K. Bashir, D. Zhang, Y. D. Al-Otaibi, and M. Guizani, "Deep Information Fusion-Driven Poi Scheduling for mobile Social Networks," *IEEE Network*, pp. 1–7, 2022.
- [9] S. Xia, Z. Yao, Y. Li, and S. Mao, "Online distributed off-loading and computing resource management with energy harvesting for heterogeneous mec-enabled iot," *IEEE Transactions on Wireless Communications*, vol. 20, no. 10, pp. 6743–6757, 2021.
- [10] M. George and I. Nenov, "Towards an intelligent neural system for economic and business forecasting," in *Proceedings of the 2020 10th IEEE International Conference on Intelligent Systems, IS 2020*, pp. 340–344, IEEE, Varna, Bulgaria, August 2020.
- [11] A. J. López-Menéndez and R. Pérez-Suárez, "Acknowledging uncertainty in economic forecasting. some insight from confidence and industrial trend surveys," *Entropy*, vol. 21, no. 4, p. 413, 2019.
- [12] Z. Min and Q. Rui, "Data mining and economic forecasting in dw-based economical decision support system," *International Journal of Reasoning-Based Intelligent Systems*, vol. 11, no. 4, pp. 300–307, 2019.
- [13] M. Ahmadi, S. Jafarzadeh-Ghoushchi, R. Taghizadeh, and A. Sharifi, "Presentation of a new hybrid approach for forecasting economic growth using artificial intelligence approaches," *Neural Computing & Applications*, vol. 31, no. 12, pp. 8661–8680, 2019.
- [14] M. Qin and R. Zhu, "A Monte Carlo localization method based on differential evolution optimization applied into economic forecasting in mobile wireless sensor networks," *EURASIP Journal on Wireless Communications and Networking*, vol. 2018, no. 1, 32 pages, 2018.
- [15] S. H. Kim, G. Lee, and Y.-J. Shin, "Economical energy storage systems scheduling based on load forecasting using deep learning," in *Proceedings of the IEEE International Conference on Big Data and Smart Computing (BigComp)*, pp. 1–7, IEEE, Kyoto, Japan, March 2019.
- [16] X. Luo, "Construction of artificial neural network economic forecasting model based on the consideration of state transition diagram," *Neural Computing & Applications*, vol. 31, no. 12, pp. 8289–8296, 2019.
- [17] Y. Han, X. Sha, E. Grover-Silva, and P. Michiardi, "On the impact of socio-economic factors on power load forecasting," in *Proceedings of the 2014 IEEE International Conference on Big Data (Big Data)*, pp. 742–747, IEEE, Washington, DC, USA, October 2014.
- [18] Z. Li, L. Wang, and H. Lou, "Analysis and forecasting on the relationship between port logistics capacity and coastal marine economic growth based on PKNN in case of zhejiang province," in *Proceedings of the Eighth International Conference on Computational Intelligence and Security CIS*, pp. 247–251, IEEE, Guangzhou, China, November 2012.
- [19] N. Jin, F. Yang, Y. Mo et al., "Highly accurate energy consumption forecasting model based on parallel LSTM neural networks," *Advanced Engineering Informatics*, vol. 51, Article ID 101442, 2022.
- [20] T. Banerjee, S. Sinha, and P. Choudhury, "Long term and short term forecasting of horticultural produce based on the LSTM network model," *Applied Intelligence*, vol. 52, no. 8, pp. 9117–9147, 2022.
- [21] M. Karbasi, M. Jamei, M. Ali, A. Malik, and Z. M. Yaseen, "Forecasting weekly reference evapotranspiration using auto encoder decoder bidirectional LSTM model hybridized with a boruta-catboost input optimizer," *Computers and Electronics in Agriculture*, vol. 198, Article ID 107121, 2022.
- [22] P. Hoang Vuong, T. Tan, T. Khoi Mai, P. Hoang Uyen, and P. The Bao, "Stock-price forecasting based on xgboost and LSTM," *Computer Systems Science and Engineering*, vol. 40, no. 1, pp. 237–246, 2022.
- [23] C. Fan, Y. Li, L. Yi, L. Xiao, X. Qu, and Z. Ai, "Multi-objective LSTM ensemble model for household short-term load forecasting," *Memetic Computing*, vol. 14, no. 1, pp. 115–132, 2022.
- [24] T. Zhang and Ge Guo, "Graph attention LSTM: a spatio-temporal approach for traffic flow forecasting," *IEEE Intelligent Transportation Systems Magazine*, vol. 14, no. 2, pp. 190–196, 2022.
- [25] Y. Tang, F. Yu, W. Pedrycz, X. Yang, J. Wang, and S. Liu, "Building trend fuzzy granulation-based LSTM recurrent neural network for long-term time-series forecasting," *IEEE Transactions on Fuzzy Systems*, vol. 30, no. 6, pp. 1599–1613, 2022.
- [26] C. Shang, J. Gao, H. Liu, and F. Liu, "Short-term load forecasting based on PSO-KFCM daily load curve clustering and CNN-LSTM model," *IEEE Access*, vol. 9, pp. 50344–50357, 2021.
- [27] Z. Fang, D. L. Dowe, S. Peiris, and D. Rosadi, "Minimum message length in hybrid ARMA and LSTM model forecasting," *Entropy*, vol. 23, no. 12, p. 1601, 2021.
- [28] H. Du Nguyen, K. Tran, S. Thomassey, and M. Hamad, "Forecasting and anomaly detection approaches using LSTM and LSTM autoencoder techniques with the applications in supply chain management," *International Journal of Information Management*, vol. 57, Article ID 102282, 2021.
- [29] A. Vagale, L. Steina, and V. Vecins, "Time series forecasting of mobile robot motion sensors using LSTM networks," *Applied Computer Systems*, vol. 26, no. 2, pp. 150–157, 2021.
- [30] T. Xiong, J. He, H. Wang, X. Tang, Z. Shi, and Q. Zeng, "Contextual sa-attention convolutional LSTM for precipitation nowcasting: a spatiotemporal sequence forecasting view," *Ieee Journal of Selected Topics in Applied Earth Observations and Remote Sensing*, vol. 14, pp. 12479–12491, 2021.
- [31] Y. P. Zaychenko, H. Zaichenko, and G. Hamidov, "Investigation of recurrent networks LSTM in the problem of covid-19 forecasting," in *Proceedings of the IEEE 16th International Conference on Computer Sciences and Information Technologies, CSIT 2021*, pp. 9–12, IEEE, Lviv, Ukraine, September 2021.
- [32] H. Xu, Bo Xu, J. He, and J. Bi, "Deep transfer learning based on LSTM model in stock price forecasting," in *Proceedings of the ICCSE '21: 5th International Conference on Crowd Science and Engineering*, pp. 73–80, ACM, Jinan, China, October 2021.
- [33] S. F. Tekin, O. Karaahmetoglu, F. Ilhan, I. Balaban, and S. S. Kozat, "Spatio-temporal weather forecasting and attention mechanism on convolutional lstms," 2021, <https://arxiv.org/abs/2102.00696>.

## Research Article

# Application of Computer Vision in Intelligent Manufacturing under the Background of 5G Wireless Communication and Industry 4.0

Yan Li 

*School of Information and Telecommunication Engineering, Liaoning Equipment Manufacturing, Vocational and Technical College, Shenyang 110161, China*

Correspondence should be addressed to Yan Li; 18402335@masu.edu.cn

Received 2 August 2022; Revised 2 September 2022; Accepted 7 September 2022; Published 6 October 2022

Academic Editor: A. M. Bastos Pereira

Copyright © 2022 Yan Li. This is an open access article distributed under the Creative Commons Attribution License, which permits unrestricted use, distribution, and reproduction in any medium, provided the original work is properly cited.

With the development of 5G wireless communications and the arrival of Industry 4.0, computer vision has further penetrated the manufacturing sector. This paper makes a comprehensive study on the field of intelligent manufacturing. By constructing a model analysis method, the current situation of computer vision intelligent manufacturing under the background of 5G wireless communication and industry 4.0 is comprehensively analyzed. It is found that today's computer vision technology is developing rapidly, while the Industry 4.0 stage and 5G communication technology have helped the field of intelligent manufacturing. At the same time, the author deeply analyzes the characteristics of intelligent manufacturing enterprises supported by computer vision and finds that it has the problem of unbalanced distribution of enterprises. After that, the author demonstrates the application of computer vision re-intelligent manufacturing from multiple dimensions. The application of computational optimization methods provides more diverse and comprehensive algorithms for labor saving and resource utilization improvement. Computer vision technology drives and promotes the development of intelligent applications and promotes a more comprehensive development of intelligent manufacturing.

## 1. Introduction

The industrial 4.0 era means that products and services will be based on big data, Internet of things, and artificial intelligence technology, through the combination of software, hardware and environment, to produce new products and services, completely different from the traditional production mode of intelligent manufacturing mode. Industry 4.0 is an upgrade in the industrial 3.0 stage. Industry 3.0 refers to the rise of Internet of Things, big data, artificial intelligence and other technologies. Industry 4.0 is developed and applied on the basis of industry 3.0. Industry 4.0 brings opportunities for enterprise intelligent manufacturing. A prominent feature of Industry 4.0 is intelligent manufacturing. Big data, Internet of Things, artificial intelligence and other technologies are the technical support for the development of Industry 4.0. It is also the core driving force for the development of intelligent

manufacturing. The core of the Internet of things is to realize the interconnection of all things, through the connection of things to connect the information fortress between things, to realize the interconnection of all things. Big data has the ability to analyze massive amounts of data, analysis of massive amounts of data generated in the process of intelligent manufacturing. Artificial intelligence, which gives human thinking to machines, promotes the intelligent transformation of manufacturing industry. The intelligent production workshop and intelligent decision-making system constructed by the Internet of things, big data, artificial intelligence and other core technologies have greatly promoted the transformation and development of intelligent manufacturing industry. In the enterprise's specific production, parts assembly, disassembly sequence can be improved by intelligent algorithms production team efficiency. For example, Matt used genetic algorithms to implement an enterprise intelligent assembly sequencing method. There

are also many challenges in developing Industry 4.0. In the context of Industry 4.0, there may be challenges such as information leakage. But the opportunities of Industry 4.0 outweigh the challenges [1–3].

Haier is a pioneer in the development of intelligent manufacturing. It takes the lead in improving business models, introducing technologies such as the Internet of Things and artificial intelligence, and building a series of industrial models. Now, Haier is intelligent manufacturing practice has a certain development results. Its business model has changed from mass manufacturing to mass customization, building a smart life platform, and transforming foreign enterprises from producing product hardware to providing smart solutions; internally integrate user fragmentation requirements and achieve personalized customization through interconnected factories. Many of Haier's products are produced by supporting customized housing affairs. For example, TianPing Air Conditioning is produced through user creation. Traditional air conditioning is square, platinum air conditioning is round, structure like bird's nest-like. Users put forward ideas online, hoping that air conditioning can achieve such an effect, and ultimately this product has received a lot of support.

With the rise of 5G technology and the arrival of Industry 4.0, computer vision has become an important driving force for the development of intelligent manufacturing. In order to further promote the development of intelligent manufacturing, it is necessary to accurately analyze the role of computer vision in the field of intelligent manufacturing. In this paper, through the rise of China's technology in the era of Industry 4.0, such as the Internet of Things and artificial intelligence, the application framework of computer vision is built to promote the wide application of computer vision technology. Computer vision technology design is applied in various fields of intelligent manufacturing industry, covering computer computing, artificial intelligence signal processing, automatic design and autonomous learning, graphics and image processing and other fields. [4, 5]. Promoting the application of computer vision in the field of intelligent manufacturing can improve the quality and efficiency of manufacturing products and achieve steady growth in manufacturing output [6, 7].

Nowadays, the development of intelligent manufacturing not only pursues economic benefits, but also considers ecological benefits. Development is infinite, but our ecological environment is limited. A good business model not only to ensure the healthy development of enterprises, but also to enable enterprises to continue to develop. In the process of developing intelligent manufacturing in enterprises, green sustainability is a factor that cannot be ignored [8–10].

The purpose of this paper is to promote the development of enterprise intelligent manufacturing with the help of computer vision technology in the background of industry 4.0 and 5G communication. The purpose of this paper is closely related to the Internet of Things, artificial intelligence technology and 5G communication technology under the background of Industry 4.0. The Internet of Things makes things interconnected in intelligent manufacturing. Artificial

intelligence plays an important role in intelligent production and intelligent decision-making. 5G provides technical support for information communication in all aspects of intelligent manufacturing. This article carried out on the basis of previous studies, on the whole there are both breakthroughs and shortcomings. The research content of this paper is not deep enough, and the investigation is not enough. However, on the basis of previous studies on industrial 4.0 and 5G communication technology under the background of intelligent manufacturing theory sent support, trends, methods of analysis more thorough. The induction of the theory in this field is the novelty of this study.

## 2. Computer Vision Technology to Promote the Development of Intelligent Manufacturing

*2.1. Basic situation of computer vision technology.* With the widespread popularization of 5G wireless communication networks and the advent of the industrial 4.0 technology era, the widespread application and continuous prosperity of computer vision technology have also brought a new technical foundation. In the context of the continuous improvement of industrial productivity requirements, based on computer vision technology, productivity improves, improves the production level of various production departments, improves the efficiency of data collection processing, and greatly improves the intelligent level of machines [11]. Since the 1950s, computer vision technology has entered a new stage of development through the use of intelligent production in the field of intelligent production, which has entered a new stage of development and promoted the steady improvement of various productive forces. In the process of comprehensive research on production methods and development models, we found that the widespread promotion of computer vision technology has an important role in improving the efficiency, methods, and optimizing the utilization of resource utilization in the field of intelligent manufacturing [12]. At the same time, the extensive promotion of computer vision technology has brought new concepts of development [13, 14]. In Figure 1, the domestic computer vision application market share was investigated in 2021.

*2.2. New development prospects brought by the field of intelligent manufacturing.* With computer vision technology, the new development model brought by intelligent manufacturing has promoted the comprehensive innovation of computer vision technology in the field of industrial production [15]. With the continuous prominent concept and new theory, computers visual technology has achieved a new production and development model update in the process of integrating industrial production development technology. In different development processes, a new productive development has been promoted. In the 1980s and 1990s, computer vision technology promoted the comprehensive promotion of development in the field of intelligent manufacturing [16]. By integrating more comprehensive computer vision technology with network nerve

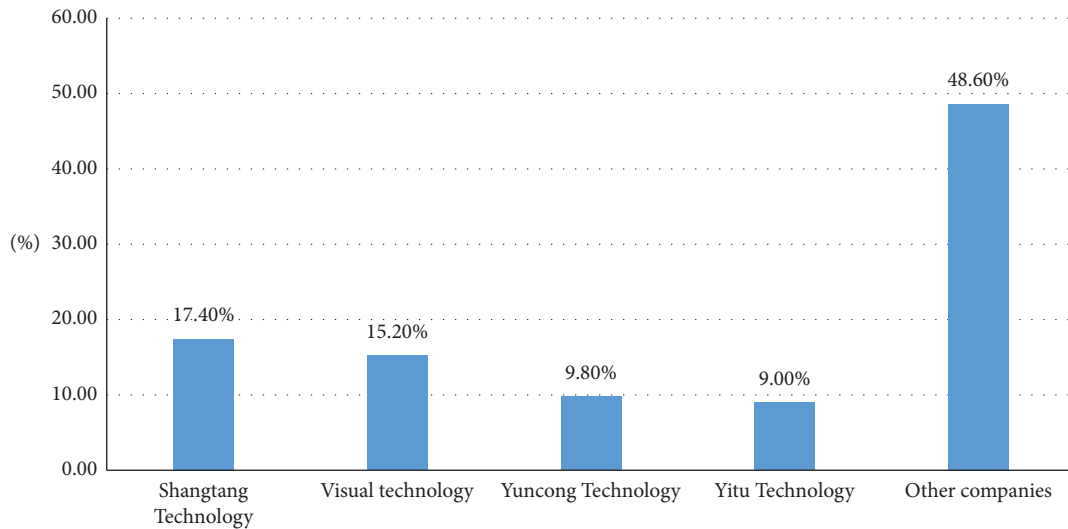


FIGURE 1: 2021 domestic computer vision application market share.

technology, it effectively promoted the new development of the field of intelligent manufacturing. With the development of the production technology and processes in the field of intelligent manufacturing, the production technology and processes have promoted the improvement of the efficiency of the entire process of intelligent manufacturing. In this process, computer vision technology has played a positive role in the optimization of the data collection process. At the same time, in the process of promoting the integration of computer vision technology and industrial production, the exposed problems, after intelligent identification and solution, make the development of the industrial industry more efficient and enter the era of new intelligent development [17, 18]. The development of the field of intelligent manufacturing has driven and promoted the improvement of productivity in the entire industrial field, greatly enhanced the utilization of resource utilization, and reduced pollution to the natural environment. It has taken a road of green, ecological, low-carbon, and sustainable development [19, 20].

Computer identification has brought great benefits to intelligent manufacturing, which can improve the production efficiency and production level of enterprise teams. For example, in the machine assembly process and quality inspection. Assembly is to realize the connection of mechanical parts or components according to the requirements of drawings, and combine mechanical parts or components into machines. Mechanical assembly is an important part of machine manufacturing and repair. The quality of assembly work plays a very important role in the efficiency of the machine, the duration of repair, the labor and cost of the work. Many companies use computer vision to track their machines and assembly operations in real time. For example, ZDT software produced by FANUC is a preventive maintenance software for capturing images from cameras installed on robots. These data are then processed to provide fault diagnosis and detect any potential problems. Quality inspection is a process of checking, measuring, measuring and testing one or more characteristics of products or

services according to standards or regulations through necessary and qualified inspection workers, measuring tools, instruments and equipment, and comparing the data or results of inspection with the requirements of standards or regulations to determine whether they meet the requirements. It is a quality basis for monitoring product manufacturing and judging whether product quality and service quality meet the standards and regulations. Content and function of quality inspection. Use computer vision to monitor packaging and product quality to reduce the generation of defective products. Improve the efficiency of enterprise production.

### 3. The Characteristics of the Development of Intelligent Manufacturing under Computer Vision Technology

*3.1. The degree of technology patented by the computer vision industry is high.* Throughout the world, in the field of computer vision technology, countries such as Germany and Japan are taken as examples. In the computer vision industry, during the survey of technological patent level, we found that the development of computer vision technology is relatively high in patent applications in countries and regions earlier, with a large number of patented technologies. In the process of using patented technology in other regions and countries, to a certain extent, it restricts the optimization of industrial assets in the country and region. Therefore, under the premise that my country's computer vision technology starts late, in order to better realize the extensive and far-reaching development of computer vision technology, it is necessary Innovation and development will achieve effective promotion and driving for industrial intelligence economy [21, 22]. In Figure 2, the development trend of China's computer vision industry in 2016-2021.

Refer to the specific data Wang Tiesheng' computer vision technology development and application [23].

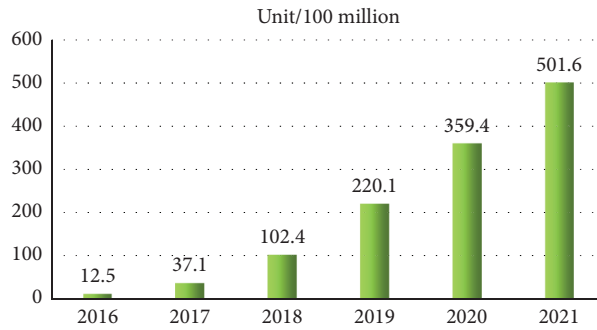


FIGURE 2: 2016-2021 China's market scale development trend.

At present, it can be seen from Figure 2 that computer vision has developed well in many fields. Although these manufacturing applications are different, the pattern of development of computer vision in various industries is the same. The specific mode is shown in Figure 3.

**3.2. Computer Vision Technology Promotes the Development of Intelligent Project Application.** In the process of computer vision technology, in the field of intelligent manufacturing, it effectively drives and promotes the new development of industrial productivity, promotes the continuous improvement of industrial productivity levels, and proposes a new development model for the development path of the 4.0 era of Industry 4.0. With the new development of intelligent productivity, 3D vision is newly applied to the era of Industry 4.0, so that more data collection is obtained, and more industrial production factors are organically integrated, and more industrial production factors are organized. Intelligent screening and analysis of a large amount of data, the accurate development direction and production development model are obtained to promote and drive the new development concept of Industry 4.0. In Figure 4, the proportion of development directions in the application field of artificial intelligence projects in computer vision design in 2021 [24, 25].

**3.3. Computer Vision Technology Promotes the Core Value of Industry.** In the process of computer vision technology, in the field of intelligent manufacturing, with the application of different fields and different stages of industrial production, it reflects the promotion and driving role of computer vision technology. During the application of computer vision technology to the mid-to-high-end industrial production market, it has been occupied by more developed countries such as Germany and Japan. In most developing countries led by our country, with the continuous innovation and drive of the core development concept of computer vision technology, it has promoted the continuous accumulation of the technical foundation during the entire production chain, realizing computer vision technology, and in intelligent manufacturing in intelligent manufacturing The widespread development and drive of the field have greatly improved production

efficiency, improved resource utilization, optimized the distribution of labor, and steadily improved the level of productivity. At the same time, the development of computer vision technology is promoted and the entire core value of the industrial chain has effectively improved. In Table 1, the angle comparison of human vision and computer vision is as follows [26, 27].

**3.4. Computer vision technology promotes the intelligent development of industry.** With the widespread development of computer vision technology, the advanced technologies of advanced machine vision manufacturing are integrated, which greatly improves the integration of technology and customer service quality. In different fields, in the process of extensive development, it provides more comprehensive and more efficient solutions for intelligent manufacturing. At the same time, the prosperity of 5G wireless communication networks allows computer vision technology to bring in major domestic industrial production areas. Effective industrial expansion. With the continuous development of computer vision technology, it has brought new investment opportunities to major industries, and core technology and limited resources have complemented the integrated development, promoting the process of computer vision technology, and promoting the widespread development of intelligent manufacturing fields. Among them, a broader and diverse development trend has brought about the improvement of the benefits of major enterprises and companies within the industry. At the same time, it has strongly replaced imported products, which has brought about the new computer vision technology innovation and innovation development [28, 29].

## 4. The Application of Computer Vision Technology in the Field of Intelligent Manufacturing

**4.1. Computer vision technology to promote the development of artificial intelligence technology.** In the process of the widespread development and continuous innovation of computer technology, it has effectively promoted and promoted the continuous application and expansion of artificial intelligence technology, and promoted and promoted all aspects of the field of industrial intelligence manufacturing. With more efficient technical means, the productivity of

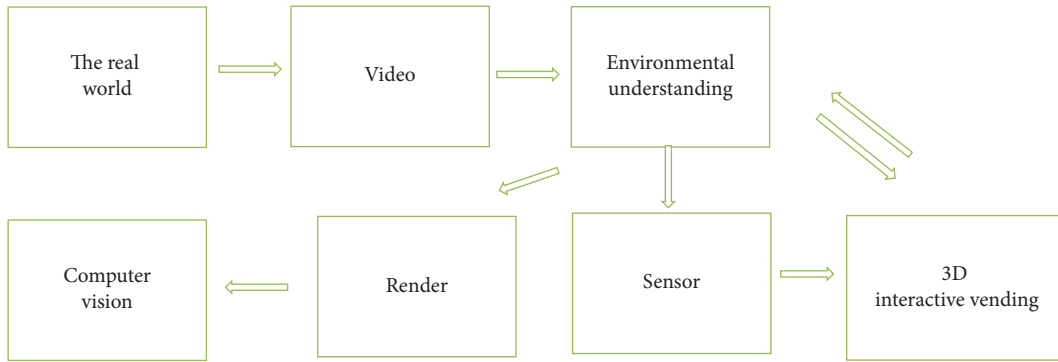


FIGURE 3: Application mode of computer vision in multiple manufacturing applications.

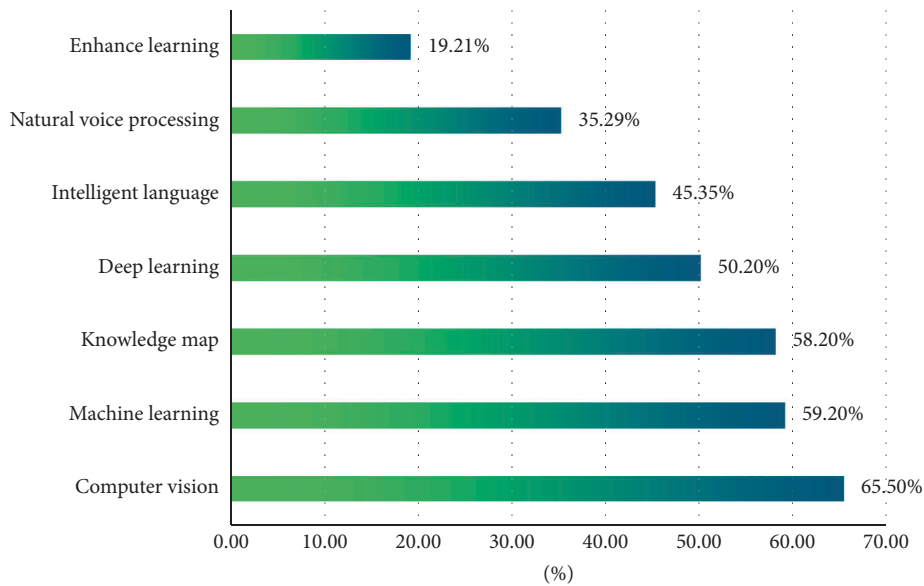


FIGURE 4: The development direction of the application field of artificial intelligence projects in computer vision design in 2021.

different industries in China has been improved, and the more comprehensive development of electronic products, clothing manufacturing, and services has been promoted. At the same time, computer vision technology has brought motivation to the development and update of artificial intelligence technology, enhanced more corporate benefits, and the development of the field of intelligent manufacturing is more comprehensive in the context of Industry 4.0.

In the field of driving and promoting industrial intelligent manufacturing, in the process of long-term construction and development, the production factor of modern factories is integrated and the purpose is to standardize production. The comprehensive and accurate manufacturing expansion in the field of mechanical manufacturing will effectively obtain resources information, and scientifically use natural resources to increase industrial output ratio. In the process of industrial 4.0, more efficient computer vision technology has been used to drive and promote the comprehensive improvement and development of the field of intelligent manufacturing. The new development concept is driven and promoted. In the process of industrial

production, the production efficiency is continuously optimized and production is improved to improve production. Effects make in the field of traditional mechanical manufacturing, through the application of intelligent manufacturing methods and methods, optimize the industrial production process and greatly improve production efficiency. Through the application of computer vision technology to the field of intelligent manufacturing, it greatly improves production efficiency and improves the work progress of various production lines. Informatization technology promotes productivity improvement, becomes the field of intelligent manufacturing, and has a more vivid development direction [30, 31].

The application of computer vision technology has driven and promoted the widespread development of the intelligent manufacturing industry in the context of Industry 4.0. Let the comprehensive visual system technology be applied to the field of intelligent manufacturing, and provides a clear development direction for industrial development and productivity improvement with more comprehensive development and clear development positioning. In the process of building a clearer smart

TABLE 1: The comparison between human vision and computer vision.

Number	Project	Artificial vision	Computer vision
1	Accuracy	The resolution is greater than 100 microns	Observe micron level
2	Speed of work	Speed less than 40m/s	Observation speed is high
3	Adaptability	Environmental adaptability is not strong	Strong adaptability to the environment
4	Objectivity	Data deviation	Data are more accurate
5	Repetitiveness	Fatigue cause errors	Strong sustainability
6	Reliability	Receive artificial emotional influence	Stable job
7	Work efficiency	Low efficiency	Efficient

manufacturing development goal, by improving the utilization of natural resources and technological innovation, effectively integrating and coordinated development, driving and promoting computer vision technology, solving the shortcomings of high efficiency in industrial costs, and lack of time consumption. The cost of labor is greatly reduced, so that modern intelligent manufacturing industrial technology is fully applied. Table 2 investigated the proportion of Chinese computer vision enterprises from 2017-2021.

#### 4.2. Computer vision technology drive and promote industry

**4.0 construction.** The new application of computer vision technology has driven and promoted the development and development of mechanical integration, so that the field of industrial production, innovative construction in intelligent manufacturing development, allowed industrial 4.0 construction and development, and entered a new stage of development. From the aspects of control and management of various industries and the control of various processes, injecting a new driving force into the innovation and development of computer vision technology, the optimization of various production processes in the process of focusing on the improvement of production efficiency has enabled major production processes, so that computer vision technology is made in computer vision technology Application development is more diverse. The efficiency of the intelligent manufacturing field has been greatly improved, and the opposite drives the continuous optimization of visual technology. In the process of innovation and development, due to the high efficiency of its visual technology and the great improvement of production efficiency, it has driven and promoted a new construction of the construction and development of industrial 4.0, and promoted and promoted Industry 4.0 with more comprehensive development methods and innovative development concepts. Construction and development. In the use of computer vision technology, many factories that promote development, through the use of computer vision technology, continuously optimize visual algorithms, and optimize and upgrade in the field of computer mathematics technology control. In Table 3, the proportion of financing in the global computer vision application segmentation in 2021.

**4.3. Optimization processing of computer visual technology algorithm.** During the development of computer vision technology, based on the continuous optimization of algorithms, the development of intelligent manufacturing is

TABLE 2: 2017-2021 The proportion of Chinese computer vision enterprises.

Number	Business field	Proportion
1	Industry	32.10%
2	Medical Treatment	15.10%
3	Smart City	11.10%
4	Retail	8.10%
5	Common Technology	7.30%
6	Security	4.80%
7	Public Security	5.10%
8	Government Affairs	2.50%
9	Finance	1.90%
10	Transportation	1.80%
11	Smart Home	1.70%
12	Office	1.50%
13	the Internet	1.60%
14	Energy	1.40%
15	Marketing	0.90%
16	Media	0.90%
17	Electricity	0.80%
18	Environmental Friendly	0.70%
19	Agriculture	0.50%
20	Judicial	0.20%

more diverse. By building a clearer development model, constantly optimize the algorithm, innovate the production process and production factors, fine control, and other methods to reduce labor costs Computer visual technology algorithms, in the process of optimization, promote and promote comprehensive efficiency improvement in the field of intelligent manufacturing. Through the effective detection and processing of production data during the production process, the intelligent algorithm is used to perform accurate process control, which greatly saves labor costs, replaces traditional production models with more efficient production methods, and is suitable for modern production requirements.

By constructing an optimization algorithm in the field of intelligent manufacturing, based on computer vision technology, the edge computing model of the production node is effectively optimized, and a more accurate target function is proposed:

$$P = f_{\text{exit}}(x; \xi), \quad (1)$$

where  $\xi$  is the optimization factor and  $x$  is the item to be optimized.  $f_{\text{exit}}$  is a special function  $P$  represents the objective function.



TABLE 3: 2021 Global Computer Visual Application Segmentation Fresh Performance.

Number	Segmentation	Financing situation/100 million yuan
1	Computer deep learning	27.8
2	Computer vision development	24.4
3	Smart robot	18.3
4	Intelligent gesture control	15.25
5	Voice input processing	14.25

The constructed function model is determined by various influencing factors in the industrial production process based on neural network analysis methods, and the judgment results are constructed as follows:

$$\bar{K} = \text{softmax}(P) = \frac{e^P}{\sum_{P \in C} e^P}, \quad (2)$$

where  $P$  represents the objective function,  $e$  is the natural logarithm, and soft max is a special function that takes the largest proportion of factors.

Based on the above-mentioned state judgment target function, the computing loss function of different production nodes during the production process is as follows:

$$D_n(\bar{K}, P, \xi) = \frac{1}{|C|} \sum_{c \in C} K \log \bar{K}, \quad (3)$$

where  $K$  represents different nodes, and  $C$  is a set of influence factors. Formula (3) is the optimization of the edge computing model of the production node. Formula (1) proposes the optimization objective function, and Formula (2) constructs the judgment result. (3) calculates the computational loss of different production nodes in the production process. The above three formulas can effectively optimize the edge computing model of production nodes.

Through the application of the above calculation and optimization method, the intelligent manufacturing of the application of computer vision technology has been greatly deepened. Through the optimization of algorithms, the entire matrix algorithm is optimized, because the application of different development stages and technical means is extremely great. It has improved production efficiency and provides more diverse and comprehensive algorithms for labor saving and resource utilization [32, 33].

**4.4. Wide integration of computer vision technology.** In the process of computer vision technology efficiently, the production and development departments need to conduct comprehensive investigations on the actual situation of industrial production efficiency, and give more comprehensive computer vision technology application data support. By constructing a clearer and comprehensive development process, for computer vision technology, and the application of intelligent manufacturing fields, build a more comprehensive development prospect. Due to the more comprehensive application development of computer vision technology in terms of image application processing, the application and integration of the two key technologies of image collection and image analysis and processing

through computer vision technology, so that in the intelligent manufacturing process, based on computer vision technology-based images Collect applications to effectively collect and summarize a large amount of data.

In the process of integrating the two key technologies of computer vision technology, on the one hand, we must pay attention to improving the speed, quality, and accuracy of image collection, supporting more accurate and efficient data collection technology as a support, and for computer vision technology to carry on the images. Treatment analysis and provide a solid data foundation. On the other hand, based on optimized algorithms, the intelligent manufacturing technology foundation obtained by computer vision technology, continuously optimizes the processing process during the processing and analysis of the image, effectively screening and organic integration of the image, and continuously optimize the data collection standards. With more efficient data processing methods, the entire production process is optimized to improve the overall efficiency of the production line. Through image processing software, the optimization processing of images and the screening of key parts, effectively promoting and driving the effective integration and long-term development of the two key areas in the two key areas of computer vision technology.

**4.5. The future development trend of computer vision technology.** Based on the background of 5G wireless communication networks and Industry 4.0, the development and application of computer vision technology has a clear direction of development. In the process of promoting and promoting the development of intelligent manufacturing, it has a new development trend. Using intelligent robots to integrate into the process of industrial production process, through optimized algorithm control, reasonable use of industrial production efficiency and production resources, to promote and promote the efficiency of intelligent manufacturing efficiency. With the continuous optimization of algorithms, in the process of computer vision technology in the future, it is mainly concentrated in the following two development aspects. First, in the process of optimizing the image, computer vision technology, based on more efficient and accurate computer vision algorithms, continuously optimize the algorithm, more accurate process control, and attach more importance to the maturity of technology application. Second, in the field of intelligent manufacturing, more efficient computer vision technologies are applied to intelligent manufacturing methods such as strong applicability, high work efficiency, and strong work stability in the

production process to carry out high-efficiency applications, improve the overall analysis processing speed of the system, and in intelligent manufacturing in intelligent manufacturing. In the context, the continuous optimization of production processes, improving the overall stability and safety of the production line, and eliminating the impact of major influencing factors.

## 5. Conclusion

Under the background of a more comprehensive development of 5G wireless communication networks and more comprehensive construction of industrial 4.0, computer vision technology, applied to the field of intelligent manufacturing, its more optimized algorithm and more accurate analysis and processing capabilities, for the development of intelligent manufacturing and the improvement of resource utilization has brought new development prospects. This article conducted a wide range of investigations in the development status of computer vision in the field of industrial 4.0 in the background of Industrial a wide range of development status of different levels of computer vision technology at home and abroad, and did a comprehensive research. The study build a more accurate and efficient computer vision technology algorithm model. Based on different development concepts and different production model conditions, effective technological innovations have been carried out to drive and promote long-term development of the field of intelligent manufacturing.

In the process of computer vision technology, it is applied to the field of intelligent manufacturing, because of the development of industrial production, the effective application of computer vision technology can greatly reduce production costs, improve the utilization of production factors, greatly saves labor costs, and for industrial productive forces. Improvement provides important technical guarantees. At the same time, the development of intelligent manufacturing has certain deficiencies and disadvantages. The optimization of computer vision technology and the fusion of technology are still the key areas of long-term attention and continuous innovation and development in major countries and regions in the future.

Studying the impact of computer vision on intelligent manufacturing in the context of 5G communications and Industry 4.0 can theoretically promote the development of China's manufacturing industry, improve manufacturing productivity, promote China's economic development, and accelerate China's goal of becoming a manufacturing power. In practice, through computer vision technology to achieve automatic appearance defect detection, parts assembly, etc., these have become the preferred solution for various enterprises, and have also achieved mature applications in various subdivisions. On the one hand, it greatly improves the efficiency of detection and production. On the other hand, it reduces the labor cost of enterprises and truly improves the productivity level of enterprises.

This article draws lessons from the lack of theoretical analysis of previous articles and analyzes the theoretical basis

of the article from multiple levels. However, this article also has the problems of insufficient research data and deep research.

This article is based on previous studies, coupled with its own innovations, such as the optimization of computer vision algorithm technology. The comprehensive theoretical summary in the field of intelligent manufacturing is also the highlight of the article. However, the research on innovation and green development concept is not deep enough. It is hoped that future research can develop towards green manufacturing and innovative manufacturing [34, 35].

## Data Availability

The data used to support the findings of this study are available from the corresponding author upon request.

## Conflicts of Interest

The authors declare that they have no conflicts of interests.

## References

- [1] A. K. Inkulu, M. V. A. Raju Bahubalendruni, A. Dara, and K. SankaranarayanaSamy, "Challenges and opportunities in human-robot collaboration context of Industry 4.0-a state of the art review," *Industrial Robot: The International Journal of Robotics Research and Application*, vol. 49, 2021.
- [2] A. Kumar Gulivindala, M. V. A. Raju Bahubalendruni, R. Chandrasekar, E. Ahmed, M. Haider Abidi, and A. Al-Ahmari, "Automated disassembly sequence prediction for industry 4.0 using enhanced genetic algorithm," *Computers, Materials & Continua*, vol. 69, no. 2, pp. 2531–2548, 2021.
- [3] M. V. A. R. Bahubalendruni and B. B. Biswal, "An intelligent approach towards optimal assembly sequence generation," *Proceedings of the Institution of Mechanical Engineers - Part C: Journal of Mechanical Engineering Science*, vol. 232, no. 4, pp. 531–541, 2018.
- [4] X. Yao, M. Liu, and J. Zhang, "Intelligent manufacturing in the perspective of artificial intelligence past life and future," *Computer integration manufacturing system*, vol. 25, no. 1, pp. 19–34, 2019.
- [5] P. Li, "Talk about the nature and true meaning of intelligent manufacturing," *Journal of China*, vol. 7, no. 8, pp. 05–30, 2019.
- [6] J. Zhou, "Steady for the direction of intelligent manufacturing to accelerate the construction of a manufacturing power," *China Aviation News*, vol. 3, no. 5, pp. 11–14, 2019.
- [7] Q. Gao and L. Ting, "Made in China 2025" research progress and evaluation," *Industrial Technology Economy*, vol. 37, no. 10, pp. 59–66, 2018.
- [8] U. Awan, A. Kraslawski, and J. Huiskonon, "Buyer-supplier relationship on social Sustainability: moderation analysis of cultural intelligence," *Cogent Business & Management*, vol. 5, no. 1, 2018.
- [9] U. Awan, "Impact of social supply chain practices on social sustainability performance in manufacturing firms," *International Journal of Innovation and Sustainable Development*, vol. 13, no. 2, p. 198, 2019.
- [10] M. Ikram, R. Sroufe, U. Awan, and N. Abid, "Enabling progress in developing economies: a novel hybrid decision-making model for green technology planning," *Sustainability*, vol. 14, no. 1, p. 258, 2021.

- [11] B. Liu, "A review of computer vision research," *Digital communication world*, no. 12, p. 97, 2019, [https://t.cnki.net/kcms/detail?v=fX7MPsm60QhoggylZhrCC\\_VjBlee97YxTb8Hb-cnVPyfS1jDouxmf8AIWn-DYaEuJqZbnBfCN6m3jAsyaInTRjxsX3WA8\\_FLkV3fPEYg2uG2umseiAv8vv3Qpmj\\_IW3I&uniplatform=NZKPT](https://t.cnki.net/kcms/detail?v=fX7MPsm60QhoggylZhrCC_VjBlee97YxTb8Hb-cnVPyfS1jDouxmf8AIWn-DYaEuJqZbnBfCN6m3jAsyaInTRjxsX3WA8_FLkV3fPEYg2uG2umseiAv8vv3Qpmj_IW3I&uniplatform=NZKPT).
- [12] X. Liu, "Computer vision technology enables five major industries," *Tech Daily*, no. 004, [https://t.cnki.net/kcms/detail?v=fX7MPsm60QjPV3pbaDLhRLVqVQlq8j3d9XUYO6D5aG1u\\_TpAxuzlr69Cj28OSxNMfk6XFpeoS-1WtFhDX9uoMgTpYLLBIm1SqU2tJbS4taZbLEVUxhMMBhLVESv-TcSk&uniplatform=NZKP](https://t.cnki.net/kcms/detail?v=fX7MPsm60QjPV3pbaDLhRLVqVQlq8j3d9XUYO6D5aG1u_TpAxuzlr69Cj28OSxNMfk6XFpeoS-1WtFhDX9uoMgTpYLLBIm1SqU2tJbS4taZbLEVUxhMMBhLVESv-TcSk&uniplatform=NZKP), 2022.
- [13] Y. Zhang, D. Zhang, and S. Ren, "Intelligent manufacturing and key technical research status and trend review," *Mechanical Science and Technology*, vol. 38, no. 3, pp. 329–338, 2019.
- [14] D. Wang and Y. S. Wang, "Lessons for the development of intelligent manufacturing and enlightenment of China," *Tax and economy*, vol. 8, no. 1, pp. 20–24, 2019.
- [15] "The 5th China conference on pattern recognition and computer vision," *Journal of Intelligent Systems*, vol. 17, no. 03, p. 575, 2022, <https://chn.oversea.cnki.net/KCMS/detail/detail.aspx?sfid=fn&QueryID=2&CurRec=1&recid=&FileName=ZNXT202203018&DbName=CJFDLAST2022&DbCode=CJFD&yx=&pr=&URLID=>.
- [16] X. Liu, "Five development trends in the field of computer vision in 2022," *Tech Daily*, 004, [https://t.cnki.net/kcms/detail?v=fX7MPsm60QjPV3pbaDLhRLVqVQlq8j3d9XUYO6D5aG1u\\_TpAxuzlr90oTYWU-FpDNeKmLdG71yNBs6Fn0mtdvPMaoza5btbcSd7CpiPG0ilxzZdOgc0iijFgiPqC5-bm&uniplatform=NZKPT](https://t.cnki.net/kcms/detail?v=fX7MPsm60QjPV3pbaDLhRLVqVQlq8j3d9XUYO6D5aG1u_TpAxuzlr90oTYWU-FpDNeKmLdG71yNBs6Fn0mtdvPMaoza5btbcSd7CpiPG0ilxzZdOgc0iijFgiPqC5-bm&uniplatform=NZKPT).
- [17] Z. S. Chen and W. Yang, "Application of artificial intelligence in computer vision and network," *Huadong Science and Technology*, no. 01, pp. 108–110, 2022, [https://t.cnki.net/kcms/detail?v=fX7MPsm60QhN0p4mPjpenKucGOyJVL3iyi\\_S1fE4zBnk\\_xCrDdw\\_neLqNeAdf49haBf6mFW94MgZHI6g-Qw1w2zYYFA98gpqUa0EKPANm3Ga5C5LZ\\_Hb911djMwY\\_W-q&uniplatform=NZKPT](https://t.cnki.net/kcms/detail?v=fX7MPsm60QhN0p4mPjpenKucGOyJVL3iyi_S1fE4zBnk_xCrDdw_neLqNeAdf49haBf6mFW94MgZHI6g-Qw1w2zYYFA98gpqUa0EKPANm3Ga5C5LZ_Hb911djMwY_W-q&uniplatform=NZKPT).
- [18] C. Huang, Yu-W. Chan, and N. Yen, *Data Processing Techniques and Applications for Cyber-Physical Systems (DPTA 2019)* vol. 1088, Springer, Singapore, 2020.
- [19] L. Li and L. J. love, "40 years of manufacturing: intelligent process and prospects," *China Soft Science*, vol. 8, no. 11, pp. 1–9, 2019.
- [20] T. Tang, T. Lin, and J. Wu, "Comprehensive realization of digitalization is the only way to intelligent manufacturing: interpretation of "Intelligent Manufacturing: digital Chemical Factory," *China Mechanical Engineering*, vol. 29, no. 3, pp. 366–377, 2018.
- [21] S. Ren, Y. Zhang, and B. Huang, "New pattern of lifecycle big-data-driven smart manufacturing service for complex product," *Journal of Mechanical Engineering*, vol. 54, no. 22, pp. 194–203, 2018.
- [22] Y. Lu, Q. Min, and F. Liu, "Summary of visualization classification of China's intelligent manufacturing research: scientific measurement analysis based on CNKI (2005-2018)," *Industrial Engineering & Management*, vol. 24, no. 4, pp. 14–22, 2019.
- [23] T. Wang, "Development and application of computer vision technology," *Information & Systems Engineering*, no. 04, pp. 63–66, 2022.
- [24] J. Zhang, J. Wang, and Y. Lu, "Big data-driven intelligent manufacturing," *China Mechanical Engineering*, vol. 30, no. 2, pp. 127–133, 2019.
- [25] L. Chen, "My country's intelligent manufacturing industry development model: based on the era of Industry 4.0," *Research on Technology, Economy and Management*, vol. 7, no. 3, pp. 109–113, 2018.
- [26] H. Chen, H. Chen, and X. Zhou, "Analysis of the literature of Chinese intelligent manufacturing research," *Intelligence science*, vol. 36, no. 11, pp. 122–125, 2018.
- [27] S. Yin, Y. Ren, and T. Liu, "Application of the application of machine vision in modern automobile manufacturing," *Journal of Optics*, vol. 38, no. 8, Article ID 0815001, 2018.
- [28] M. May 1st, H. Jia, and W. He, "Summary of machine visual testing on the surface defect of transparent parts," *Mechanical Science and Technology*, vol. 40, no. 1, pp. 116–124, 2021.
- [29] Q. Liu, F. Duan, and Y. Sang, "Summary of visual SLAM closed-loop detection methods in complex environments," *Robot*, vol. 41, no. 1, pp. 112–123, 2019.
- [30] Z. Hu, L. Qi, and Y. Luo, "V-SLAM's point cloud withdrawal algorithm improvement and mobile robot experiment," *Journal of Harbin University of Technology*, vol. 51, no. 1, pp. 170–177, 2019.
- [31] Y. Zhao and B. Zuo, "Research on the application of machine vision on fabric defect detection," *Computer engineering and application*, vol. 56, no. 2, pp. 11–17, 2020.
- [32] P. Zhang, Y. Song, and L. Zong, "3D target detection progress review," *Computer science*, vol. 47, no. 4, pp. 94–102, 2020.
- [33] W. Tan, F. Miao, and F. Duan, "Research and application of 3D laser plane measurement system based on machine vision," *Journal of Instrument and Instrument*, vol. 41, no. 1, pp. 241–249, 2020.
- [34] U. Awan, "Effects of buyer-supplier relationship on social performance improvement and innovation performance improvement," *International Journal of Applied Management Science*, vol. 11, no. 1, pp. 21–35, 2019.
- [35] S. Begum, M. Ashfaq, E. Xia, U. Awan, and R. Welford, "Does green transformational leadership lead to green innovation? The role of green thinking and creative process engagement," *Business Strategy and the Environment*, vol. 31, pp. 1–13, 2020.

## Retraction

# Retracted: Application of Data Warehouse Technology Based on Neural Network in Physical Education Quality Management

### Mathematical Problems in Engineering

Received 17 October 2023; Accepted 17 October 2023; Published 18 October 2023

Copyright © 2023 Mathematical Problems in Engineering. This is an open access article distributed under the Creative Commons Attribution License, which permits unrestricted use, distribution, and reproduction in any medium, provided the original work is properly cited.

This article has been retracted by Hindawi following an investigation undertaken by the publisher [1]. This investigation has uncovered evidence of one or more of the following indicators of systematic manipulation of the publication process:

- (1) Discrepancies in scope
- (2) Discrepancies in the description of the research reported
- (3) Discrepancies between the availability of data and the research described
- (4) Inappropriate citations
- (5) Incoherent, meaningless and/or irrelevant content included in the article
- (6) Peer-review manipulation

The presence of these indicators undermines our confidence in the integrity of the article's content and we cannot, therefore, vouch for its reliability. Please note that this notice is intended solely to alert readers that the content of this article is unreliable. We have not investigated whether authors were aware of or involved in the systematic manipulation of the publication process.

In addition, our investigation has also shown that one or more of the following human-subject reporting requirements has not been met in this article: ethical approval by an Institutional Review Board (IRB) committee or equivalent, patient/participant consent to participate, and/or agreement to publish patient/participant details (where relevant).

Wiley and Hindawi regrets that the usual quality checks did not identify these issues before publication and have since put additional measures in place to safeguard research integrity.

We wish to credit our own Research Integrity and Research Publishing teams and anonymous and named external researchers and research integrity experts for contributing to this investigation.

The corresponding author, as the representative of all authors, has been given the opportunity to register their agreement or disagreement to this retraction. We have kept a record of any response received.

### References

- [1] B. Zhao and Y. Liu, "Application of Data Warehouse Technology Based on Neural Network in Physical Education Quality Management," *Mathematical Problems in Engineering*, vol. 2022, Article ID 4456885, 10 pages, 2022.

## Research Article

# Application of Data Warehouse Technology Based on Neural Network in Physical Education Quality Management

Bo Zhao<sup>1,2</sup> and Yanjin Liu<sup>3</sup> 

<sup>1</sup>Chengdu Sport University, Chengdu, Sichuan 610041, China

<sup>2</sup>Sichuan Zhuoyi Dream Education Technology Co, Ltd., Chengdu, Sichuan 610000, China

<sup>3</sup>Sichuan International Education Development Research Center, Chengdu 611130, Sichuan, China

Correspondence should be addressed to Yanjin Liu; 021019@cdnu.edu.cn

Received 12 August 2022; Revised 11 September 2022; Accepted 15 September 2022; Published 28 September 2022

Academic Editor: Dinesh Kumar Saini

Copyright © 2022 Bo Zhao and Yanjin Liu. This is an open access article distributed under the Creative Commons Attribution License, which permits unrestricted use, distribution, and reproduction in any medium, provided the original work is properly cited.

Data warehouse technology has been created because of China's technological advancement and the increasing requirements of the educational sector. Physical assessments are treated as tests by many students. Institutions spend plenty of time every year through physical tests, yet the results are rarely shared with students. Teachers are impeded by the size and complexity of physical test data, finding it challenging to support experiments or judge individual students' development. Students have trouble following up and delivering test-based feedback after instruction. In recent years, various researchers have offered insightful advice on how to build multidimensional database structures for such trouble. However, quality requirements alone are not adequate to guarantee quality in reality. So, this paper presents a novel Hypertuned wide polynet convolutional neural network (HWPCNN) framework in the data warehouse technology to attain the greatest performance in physical education quality management. In this paper, we first apply HWPCNNs for physical education quality management to analyze the accuracy and recall of the model. It is no secret that HWPCNN is now one of the most widely used deep learning techniques. When it comes to managing the quality of physical education, the HWPCNN's local perception feature in the data warehouse technology allows it to achieve the best possible results. To validate the model's performance, it is compared to other models and then improved further to increase its accuracy. The physical education resources are gathered as a raw dataset for this inquiry. The raw dataset is cleaned using the Z-score approach to get it ready for further data processing. Then, a sparse matrix approach is employed to build a data cube, while the proposed method is used to index multidimensional databases. To demonstrate that our work is of the best quality in managing physical education, performance metrics of the suggested method are also evaluated and compared with other traditional methods.

## 1. Introduction

The new health-oriented Physical Education (PE) curriculum, which places more emphasis on health promotion and regular physical activity engagement than it does on athletic performance, presents a new challenge for physical education teachers. Specifically, the challenge lies in the fact that the new health-oriented PE curriculum. The health information of students has to be monitored during both practice and competition to build effective training routines and reduce the risk of accidents and illnesses. Large volumes of nonvolatile, summarized, and historical data may be stored,

managed, and analyzed using data warehousing (DW). Data warehouses are multidimensional repositories that collect students' physical data from a variety of systems into a single repository. The primary goal of DW is to help organizations have a better understanding of their performance and make better decisions. Data analytics (DAs), as well as online analytical processing (OLAP), are areas that examine the physical data in this database in cooperation with one another. Data analysis (DA) is the process of employing technical and statistical tools to analyze the physical data in the DWH to conclude and generating new knowledge from the data [1]. The "Extract, Transform and Load (ETL)" is a

critical building component of a DW since it extracts students' data from sources, fixes existing errors in the data integrates the data to meet the model of a target DW and loads it into a DW. For example, commercial and open-source models, relational and nonrelational databases, and technologies may all be used by the sources. The ETL procedure is the most time-consuming part of a data warehouse's development life cycle. ETL transformations may include one-to-one, many-to-one, and many-to-many mappings, as well as a variety of other mappings. This may result in inaccurate analytical findings as a consequence of faulty ETL implementations, which can be exacerbated by complicated transformations. The need of testing ETL procedures to guarantee reliable extraction and transmission of original data into storage systems cannot be overstated [2]. To support their judgments, educational staff members use a variety of tools and apps, including DSSs, mobile learning, and web-based tools like information extraction, which are all based on distinct techniques and approaches. This time around, the findings and inferences that may be taken from prior studies and in-depth analysis have more of an impact and are more legitimate than they were in the past. Online analytical findings are provided by the Educational DW, which is the best alternative for all educational leaders. Educational DW gives a broad overview of the student's performance and enables them to identify the roadblocks on their path to success. A large educational DW may be used to implement any strategy or technique that applies to a small one. Educational DW may successfully eliminate educational mistakes that impair academic decision-making [3].

Figure 1 depicts the holistic perspective of DW in education. Data Warehousing platforms traditionally used by organizations face many difficulties, including bottlenecks in the collection of students' physical data as well as the analysis techniques of that data. These bottlenecks are due to the increasing number of "information efficiency," "scalability," and "elasticity" that can only be obtained through parallel storage and processing. All data marts are loaded from the same DWH, therefore they all share the same consistent dimensional representation of data. Because it takes a bird's-eye view of the company, the top-down method lends itself well to change management. On the other hand, is advocated for when resources are limited, and data marts are built in stages. Strategic priorities gleaned from an information requirement analysis may guide the development and deployment of data marts. The goals of the organization, the structure of the company, the available funds, and the interdependencies across departments all have a significant bearing on the strategy that should be used while developing a DWH for an educational institution. A comparison of the two methods is shown schematically in Figure 1. The ETL procedure of the top-down method is shown in Figure 1; in this procedure, data is taken from both internal and external data sources. Afterward, operations like cleaning, scrubbing, and deduplication are carried out to alter these data sets. Clean data are then put into a centralized DWH before being partitioned into data marts for various business units [4]. Standard DWs have a stringent modeling approach, which further underscores the need for a "Big Data Warehouse

(BDW)." Despite this, the current state of BDW demonstrates the concept's youth, uncertainty, and lack of standard techniques for building BDWs [5]. Data is being gathered from all around the globe and stored in the massive data warehouse (DW). For operational processing and issue solving, DW divides data sets and programs into two distinct categories: data sets used for operational processing and those utilized for analysis. Historical layers may be included in the preaggregated and preintegrated data. When it comes to data warehouses, invariance and low redundancy are the most important characteristics. With today's DWs, management can make choices based on almost endless volumes of very accurate data, which helps firms avoid a variety of issues. Each significant corporation retains and deploys new DWs. The issue is that DWs are expected to become more expensive to build, support, and maintain. This research evaluates the application of DW technology based on a neural network in Physical Education Quality Management. The Contribution of the research work is depicted as follows:

- (i) This study selected a raw dataset of physical education materials from China university students
- (ii) The Z-score technique is used to clean the raw dataset in preparation for future data processing
- (iii) To construct the data cube, a sparse matrix is used
- (iv) To index multidimensional databases, Hypertuned wide polynet convolutional neural network (HWPCNN) is used

The other portion of this study is divided as follows: Section 2 depicts a literature work. Section 3 includes the suggested approach. Section 4 illustrates the result and discussion. Section 5 depicts the conclusion.

## 2. Literature Work

Wyant and Baek [6] explore variables that impact physical education instructors' acceptance of technology in teaching, detail how decision-making research may educate the technology acceptance processes, then give a guidance document to increase technology adoption among physical education teachers. Interactive virtual technology for college physical education that integrates the Internet of Things (IoT), a compute cluster, as well as a mobile application, is described by Ding et al. [7]. A 12-year-old girl was found to have many odontogenic keratocysts on her teeth [8]. Data properties and query statistics are taken into consideration in Tomashevskiy et al. [9], the scientific and practical challenge in establishing information technology for hybrid distributed databases [9]. Salaki and Ratnam [10] analysis in Higher Education shows the value of Agile Analytics in the creation of "Business Intelligence" and DW. According to Cigánek [11], an open DW uses data from a variety of sources. They explain the principles of data warehouses, as well as the reason for open data. Sutudja et al. [12] examined and construct a data warehouse for integrating multiple operational databases required to offer data on XYZ University's active students. According to Garg [13], digital approaches were used to connect physical objects and depict

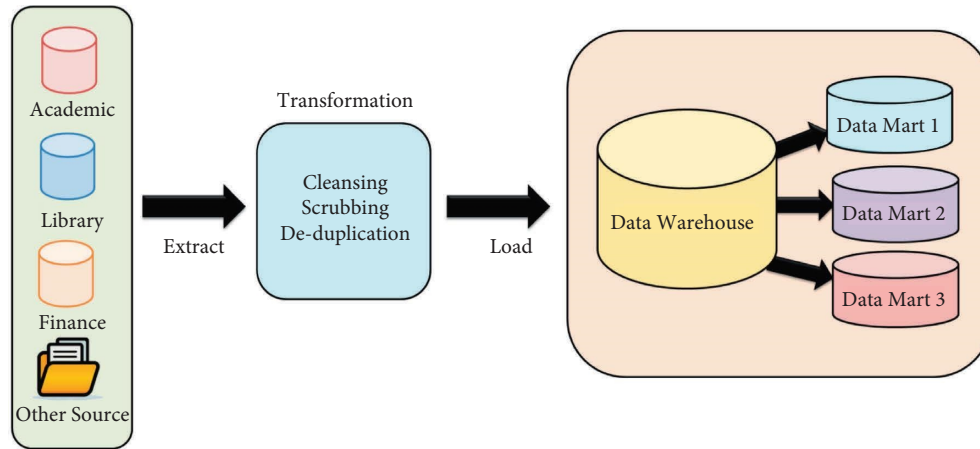


FIGURE 1: A holistic perspective on DW in education.

their current status. According to Sebaa et al. [14] and Ahmed and Ali [15], an overview of typical data warehouse research topics is presented as well as several noteworthy Hadoop-based data warehouses. Shahabzand and Afzal [16] examined how semantics may be used as a tool to connect data warehouses, NoSQL databases, and big data in a meaningful manner. The developments in data storage and processing evolved to manage large data but also pushed conventional, previously existing systems out of focus and created a divide between the old and the new. Garani et al. [17] described the data warehouse schema in a way that integrates temporal and geographical data in an all-encompassing data warehouse architecture. It is becoming more vital to integrate time- and space-based data. Li [18] present a hybrid network system for “business intelligence,” “analytics,” and “knowledge management” based on an educational DW and a service design repository that empowers the advancement of knowledge and the visualization and outline of dissimilar organizational components. Following “Satya Wacana Christian University (SWCU)” financial and educational data, according to Somya et al. [19], the SoBI will be used to integrate DW. According to Salihuan and Zayyanu [20], the development of a college sports training aid decision-making support system is based on the use of data warehouse and data analysis technology to realize various aspects such as university students’ controller is developed, innovative training methods used in university sports management, and combined User input to generate a sensible sports training program.

### 3. Proposed Methodology

When Devlin and Murphy (1988) came up with the idea of a “data warehouse (DW)” for storing corporate information, they sought a read-only database that would allow customers to look at and access the data for use in making choices. Later on, the term “subject-oriented,” “integrated,” “time-variant,” and “nonvolatile” were added to the definition of DW. Even if this data is summarized and detailed, each of these studies admits that since DW can physically separate information from operational databases, it offers a way for

real-time decision-making that is quicker than without DW. As a result of this recognition, DW has emerged as a key hub for decision support inside organizations. HWPCNNs are among the most popular deep learning methods. The data warehouse technology used by the HWPCNN permits it to provide optimal outcomes in the management of physical education quality. The model’s efficacy is established by comparison to benchmarks and it is then refined to achieve higher levels of precision. Figure 2 illustrates the suggested approach flow.

**3.1. Physical Education Dataset.** Second-year pupils at a university in central China that participated in the “Basketball Club” option of a mandatory PE program were the subjects in this data analysis. The instructor in charge of the club was a member of the faculty in the department of physical education and had been active in this club system for the past three years. An additional faculty member was assigned to teach novice players, while physical education majors aided with refereeing tasks to support them. This research did not gather any information from the support staff.

When they arrived for their first lesson, students were given a short report to complete, which allowed them to gather information about their prior basketball experience, their estimation of how good they are at the sport, and why they chose it. An overview of the data for these participants may be seen in Table 1.

**3.2. Data Preprocessing Using Z-Score Normalization.** In operations, each user’s data is sized individually. The quality of the original data may be affected if grouping is done using that data. An excellent technique to improve data accuracy is to convert all data to a single scale. To standardize all data, the Z score normalization procedure is used. The Z-score normalization formula may be found in the following equation:

$$Z = \frac{X - \mu}{\sigma} \quad (1)$$

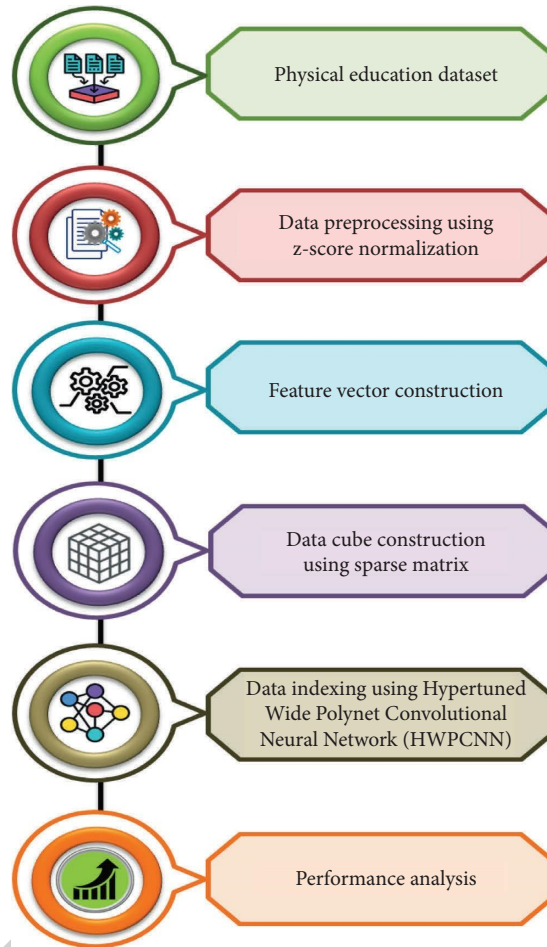


FIGURE 2: Flow of the suggested approach.

TABLE 1: Data for students [21].

Gender ( <i>n</i> )	Sport education		Individual practice	
	Female (47)	Male (55)	Female (21)	Male (29)
Age (%)	19.3	19.4	19.4	19.4
Experiences (%)	None (13)	None (11)	None (25)	None (15)
	Some (54)	Some (17)	Some (45)	Some (59)
	Regular (33)	Regular (71)	Regular (30)	Regular (26)
Skill (%)	Medium (26)	Medium (20)	Medium (16)	Medium (4)
	Entry level (64)	Entry level (34)	Entry level (47)	Entry level (83)
	Novice (10)	Novice (40)	Novice (37)	Novice (13)
Why basketball (%)	Learn (18)	Learn (15)	Learn (19)	Learn (12)
	Fitness (10)	Fitness (11)	Fitness (19)	Fitness (21)
	Love (13)	Love (0)	Love (0)	Love (0)
	Interest (59)	Interest (74)	Interest (63)	Interest (67)

In this example,  $Z$  is the data value's normal frequency.  $X$  stands for providing practical numbers of characters that have a special connection.  $\mu$  is the average of the functions of user operations that are comparable. There is a zero-to-one variation in  $Z$  score normalization's overall average.  $\sigma$  is a

variation of the distribution data warehouse concept. The average variance is calculated using the following equation:

$$\sigma = \sqrt{\left(\frac{\sum (X - \bar{X})}{g}\right)}. \quad (2)$$



Vendor operations quantities,  $X$ , make up the rest of the world's technical quantities. Overall, a variable's total score is calculated ( $X$ ). In all,  $g$  samples of physical data were collected from vendors for this study. Distributor distribution test data, standardized average, as well as frequency data, are utilized to calculate a  $Z$  score for a distributor distribution test dataset.

**3.3. Feature Vector Construction.** When using a self-organizing network, an input matrix is generated that contains the parameters specified by the dimensions. Input parameters are prepared by selecting dimension values. Key values are allocated numeric values based on the character reference table for each dimension. Key value parameters are defined by using this data. Self-organizing networks may use these parameters as input.

Self-organizing networks may use these parameters as input. Each time a winning neuron receives an input; its neighbors' weights are adjusted to reflect the new information. The final weights for each dimension of the self-organizing net are saved when training and testing are complete. Weights will be applied to indices at the time of data access to arrive at these results. The active neuron index numbers for each dimension are gathered. In other words, they are the values' indices. To avoid index values colliding, the self-organizing net is used, and the indices created during training are arranged in the same order as the dimension values. MOLAP cube creation will take into account each dimension's index number. This will also be the best option for storing things once we are not used.

**3.4. Data Cube Construction Using Sparse Matrix.** Analyze each data one by one in the fact database to acquire tuple-specific indexes. Then, put the fact values at those indexes. Due to the sparsity of multidimensional data cubes, index values for nonnegative cell entries are stored in sparse matrices. To store indexes of three-dimensional values, we need to define a sparse structure with three variables, and a fourth to store the matching values. One tuple is stored in a single instance of the sparse structure. The term "defined array" refers to a structural array that has a size that is equal to the number of records in a fact table. Fact tables are examined one by one, looking at each tuple and calculating the measured value for each dimension to put it into a sparse structure. Dimensional weight matrices are used to construct indexes for dimensional data. Each node in the self-organizing net is assigned a final weight value once the weight matrices for each dimension have been stored. We may use the multidimensional character reference server's numerical values of characters to generate an input vector that can be used to retrieve the index of any dimension value. A weight matrix of that dimension determines the Euclidean distance of this vector from each self-organizing network node. For each dimension, the cluster index number created is the index. In the sparse structure, each tuple's index value is computed and stored in the same place as the corresponding measure value. The sparse structure array may now hold the whole matrix. Table 2 depicts the data cube in the sparse matrix.

TABLE 2: Data cube in sparse matrix.

Physical education resources	Products	Year	Value
1	3	10	36596.23
1	3	8	19496.45
1	2	10	6803.54
1	2	9	571.40
1	2	8	11321.19
1	2	7	2669.1
1	2	6	2581.02
1	2	7	7723.14
1	1	6	15.29
1	1	5	12.15
1	1	4	7.16
1	1	3	5.05
1	1	2	0.0
1	1	1	8579.62

This design shows that each cube dimension corresponds to a tuple in the fact table. Each data row cube contains a single tuple, making it a sparse structure. All of the records in the fact table are represented by a single instance. There are several instances of the multidimensional array-based sparse data cube for each cell carrying the value of a tuple in the multidimensional array. As the number of the tuple's in a sparse structure rises, it will be easier to split the fact table contained in the sparse structures by taking each tuple in one instance of a sparse structure. All of the dimensions are represented in the data cube shown above. To store the whole data cube, you will need a lot of storage space. Many aggregates are recomputed by decision support systems to speed up aggregation queries. It is feasible to calculate aggregates along all conceivable group-bys in a data cube. Data cubes must be kept in front of group-bys for a fast data retrieval system.  $2^N - 1$  aggregate calculations are needed for an  $N$ -dimensional data cube. In the above case, there are three dimensions and one measure value so  $2^3 = 8$  group-bys are calculated as {Physical education resources, Products, Year}, {Physical education resources, Products}, {Physical education resources, Year}, {Products, Year}, {Physical education resources}, {Products}, {Year}, and all. The term "data cube" is used to describe a collection of group-bys. There are two formal routes to group-bys before sparse cube creation. A sparse structure may hold both the fact table and all the views of the fact dimensions. The enormous memory needed makes this approach prohibitively expensive. Second, the sparse data cube that was generated from the original fact table may be used for aggregation along dimensions, and the resulting group-bys will also be saved in the sparse structure. Any group-by will be computed by selecting the smallest of the previously computed group-bys as its parent. In the above-given data cube, the cardinalities of the dimensions are 100, 101, and 11 for Physical education resources, Products, and Year, respectively. The original data cube will be used for calculating group-bys {Physical education resources, Products}, {Physical education resources, Year}, and {Products, Year} from these group-bys the group-bys {Physical education resources}, {Products}, and {Year} are computed using {Physical education resources, Year}

and {Products, Year} as they are smallest parents for these aggregates or group-bys. Similarly, super aggregate all is calculated from parent group-by {Year}. These group-bys are used for and kept in sparse structures for aggregation queries are quick to obtain since they do not need data from the original data cube. In addition, less memory is needed to store these group-bys.

**3.5. Data Index Using Hyper Tuned Wide Polynet Convolutional Neural Networks Algorithm (HWPCNN).** A distinct index is created for each dimension when working with a multidimensional database. As a result of the clustering of the data, related data values are clustered together into various groups. The dimension's number of occurrences is not predetermined. Unsupervised learning makes clustering ideal for dimensional data indexing. In this research, for both classification and regression problems, hyper tuned wide polynet convolutional neural networks algorithm neural network technique is used. HWPCNN uses convolution layers to choose between accuracy and latency for parameter values, which is a simpler framework to understand and apply to real-world problems. The HWPCNN technique has a key advantage in that it minimizes the network size. A quantized configuration that analyses a common problem difficulty in depth via many abstraction layers seems to be the underlying structure of software. Modeling platforms use a common rectified linear unit (ReLU) to point across different abstraction levels. The dimensions and internal representation of each layer may be reduced by increasing resolution by  $w$ .

Residual layer with stride 1 and second decreasing layer with stride 2 in this design. There are three sublayers to the two primary layers: residual and shrinking. ReLu6 was used to construct a  $2 \times 2$  convolution as the first layer. Convolution is the next phase in the design process. Depth-Wise may benefit from a single convolutional layer for light filtering. None of the proposed architecture's three convolution layers have any nonlinearity. When it comes to output, the ReLu6 component plays a key role. ReLu6 enhances the model's unpredictability under low-precision settings. The number of output channels does not vary at any point for the whole of the sequence. During the training phase of contemporary architectural models, dropout and batch normalization are both used. These models employ a filter with a size of three by three. Because the activation component of ReLu6 has a residual component, batch processing is simplified by using this component.

$$Y = \{(y_1.a_1), (y_2.a_2), \dots, (y_n.a_n)\}. \quad (3)$$

If we have a feature vector map of size  $Y$ , we may refer to the input variable as  $l$  and the output variable as  $m$ . In other words,  $l$  represents the input and  $m$  represents the result. For the sake of the neural network's input patterns, the values of the data are represented as dimensional feature vectors. The following equation may be used to arrive at an estimate of the total amount of computational work required by the fundamental abstract layers of the design.

$$Y = \frac{1}{axz} \sum_{s=1}^a \sum_{w=1}^z \phi UN(s, w). \quad (4)$$

The probability of index multidimensional databases can be identified using the following equation:

$$J(\beta) = \frac{1}{N} \sum_{i=1}^n \text{classify}(h_{\beta}(x^{(i)}, y^{(i)}), \quad (5)$$

$$J(\beta) = \frac{1}{N} \sum_{i=1}^n \text{classify} \left( h_{\beta} \left( x^{(i)}, y^{(i)} + \frac{\lambda}{2N} \sum_{j=1}^n \beta_j^2 \right) \right).$$

In the same manner, anomalous feature estimators are used to numerically optimize the equation [6],

$$f(Y1) = y, \dots, y_n | a_1, \dots, a_n. \quad (6)$$

Then, the trust value of the data was calculated.

$$C_{tv} = (C_{n\_fea} \text{ dist corr}). \quad (7)$$

Here,  $C_{tv}$  denotes the data's trusted value. Use this kind of neural network architecture to group input patterns and the data values of each dimension are used as the clustering data set for indexing multidimensional databases based on the features of a specific data collection. Since the dimension's cardinality is unknown at all times, data are updated at a set interval in a data warehouse. It is expanding at an astronomical pace. An indexing system does not need any additional effort to add more data values. Consequently, a new indexing system must have this capability.

## 4. Result and Discussion

In this section, the results of applying data warehouse technology based on neural networks to the management of physical education quality are discussed. Eleven metrics are taken into consideration to examine the efficacy of our suggested HWPCNN technique as well as the implications of the proposed features. These metrics are as follows: "true positive rate", "false positive rate", "true negative rate", "false negative rate", "f1 score", "accuracy", "precision", "f1-score", "specificity", "MAE", and "ROC", "k-Means Clustering and Genetic Algorithm based Optimized Case-Based Reasoning Approach (kMC-GA based OCBRA)", "Backtracking Search Optimization Algorithm (BSOA)", "Modified Artificial Bee Colony algorithm (MABCA)", and "Manhattan Frequency k-Means (MFk-M)" algorithm are some of the existing methods that are compared to our proposed method. Four elements will be considered in this evaluation:

**True Positives ( $t_p$ ).** The actual and expected class values are both positive, which indicates that these values have been accurately recognized as positive

**True Negatives ( $t_n$ ).** These estimated negative values are genuine, which suggests that the typical class value is negligible and the projected class value is also nil

**False Positives ( $f_p$ ).** There is a discrepancy between the projected class and the real class

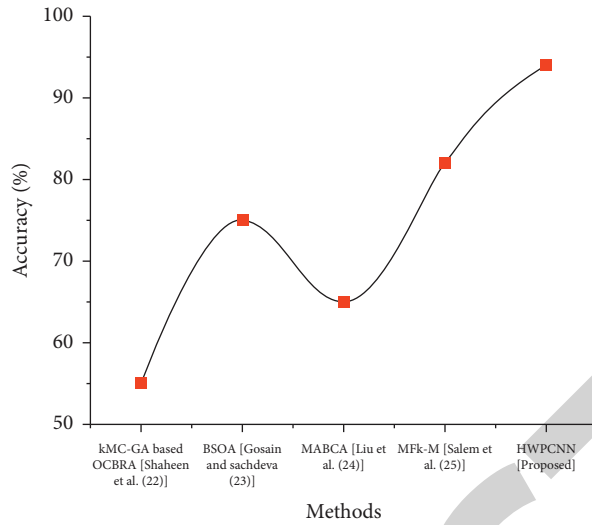


FIGURE 3: Comparison of the accuracy.

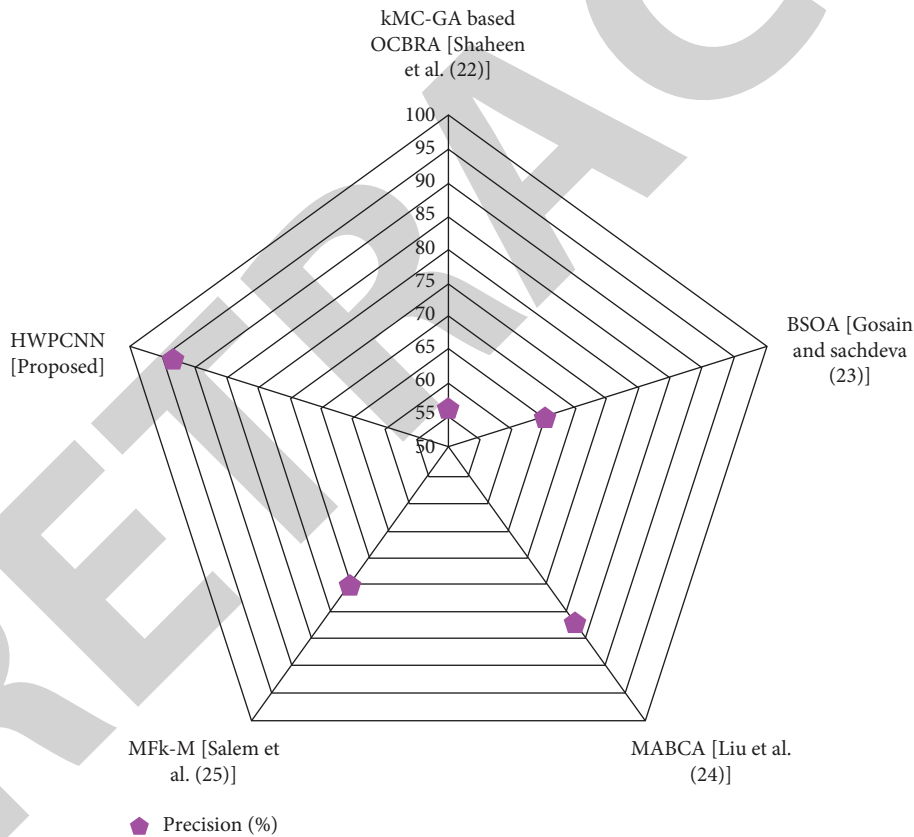


FIGURE 4: Comparison of the precision.

False Negatives ( $f_n$ ). Any time the real class matches the projected one, although the predicted one does not match

Accuracy, the metric that makes the most intuitive sense, is explained as the ratio of properly expected observations to the total of observations. The accuracy of the suggested method is compared to that of the method that is currently being used in Figure 3. The proposed method had a higher

average accuracy than the existing methods. Accuracy is calculated by using the following equation:

$$\text{Accuracy} = \frac{t_p + t_n}{t_p + t_n + f_p + f_n} \tag{8}$$

Precision is the ratio of correctly predicted observations to the total of all predicted positive observations. The precision of the suggested method is compared to that of the

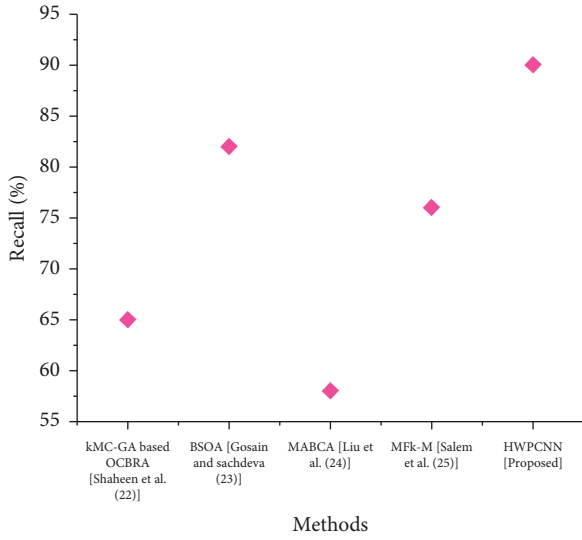


FIGURE 5: Comparison of the recall.

method that is currently being used in Figure 4. The proposed method had a higher precision than the existing methods. Accuracy is calculated by using the following formula:

$$\text{Precision} = \frac{t_p}{t_p + f_p}. \quad (9)$$

“Recall” refers to the fraction of correctly anticipated positive observations in a class. The recall of the suggested method is compared to that of the method that is currently being used in Figure 5. The figure clearly shows that the suggested method is superior to the conventional techniques in terms of recall. The recall is calculated by using the following formula:

$$\text{Recall} = \frac{t_p}{t_p + f_n}. \quad (10)$$

Precision and Recall are weighted together to get the F1 Score. The F1-score of the suggested method is compared to that of the method that is currently being used in Figure 6. The figure shows that the proposed method is higher than the conventional techniques in terms of the f1-score. F1-score is evaluated by using the following formula:

$$F1 - \text{score} = \frac{2 \times \text{precision} \times \text{recall}}{\text{precision} + \text{recall}}. \quad (11)$$

True negatives that are accurately anticipated by the mode are known as specificity. The specificity of the suggested method is compared to that of the method that is currently being used in Figure 7. The figure shows that the suggested method is better when compared to the traditional techniques in terms of specificity. Specificity is calculated by using the following formula:

$$\text{Specificity} = \frac{t_n}{t_n + f_p}. \quad (12)$$

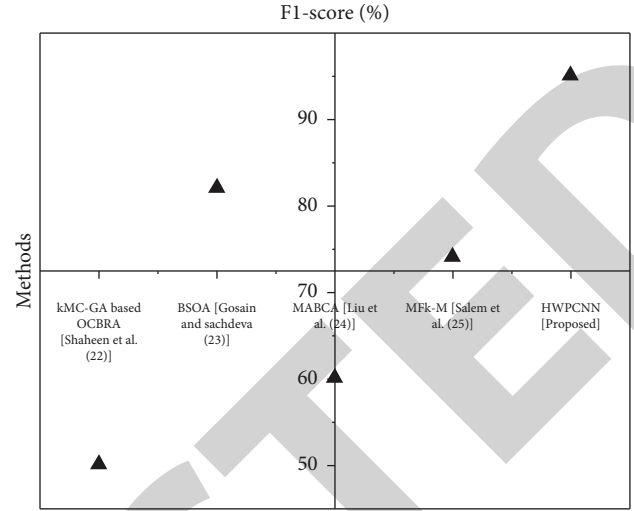


FIGURE 6: Comparison of the F1-score.

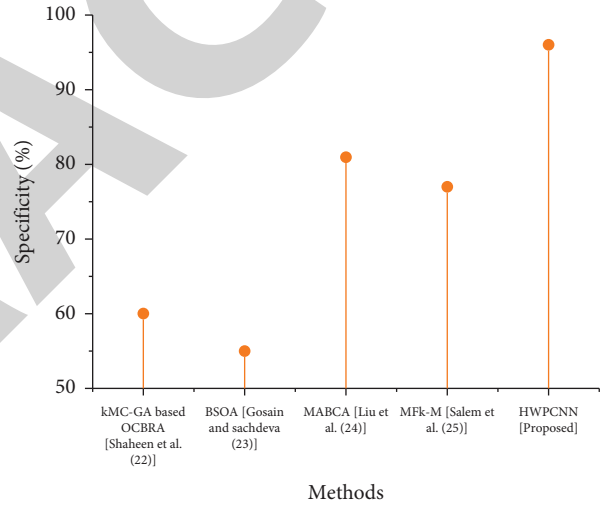


FIGURE 7: Comparison of the specificity.

A measure of the errors that occur between paired observations that both describe the same phenomena is called the mean absolute error (MAE). The MAE of the suggested method is compared to that of the method that is currently being used in Figure 8. The figure shows that the suggested method is lower when compared to the traditional techniques in terms of MAE. MAE is calculated by using the following formula:

$$\text{Mean Absolute Error} = \frac{\sum_{j=1}^m |x_j - y_j|}{m}, \quad (13)$$

where  $x_j$  denotes prediction,  $y_j$  denotes true value, and  $m$  denotes the total number of data points.

False positives (FPs) and true positives (TPs) are represented by the receiver operating characteristic (ROC). Because it accurately identifies all positive and negative instances, (0, 1) is the best classifier in the ROC plot. The ROC of the suggested method is compared to that of the

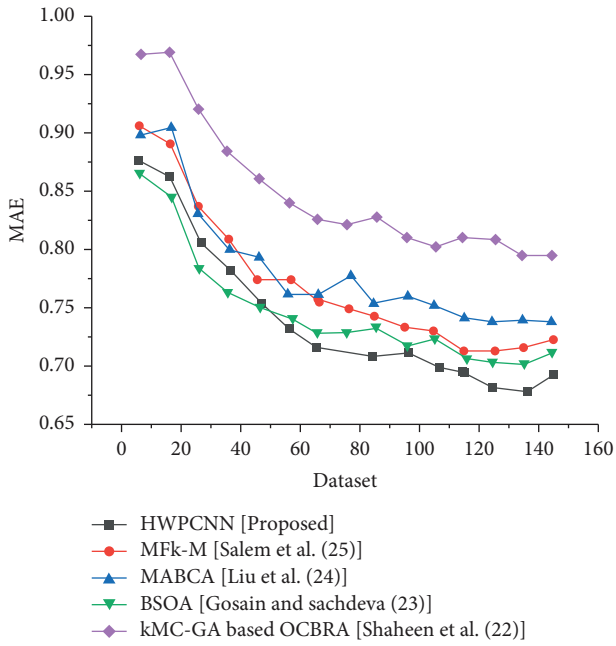


FIGURE 8: Mean absolute error.

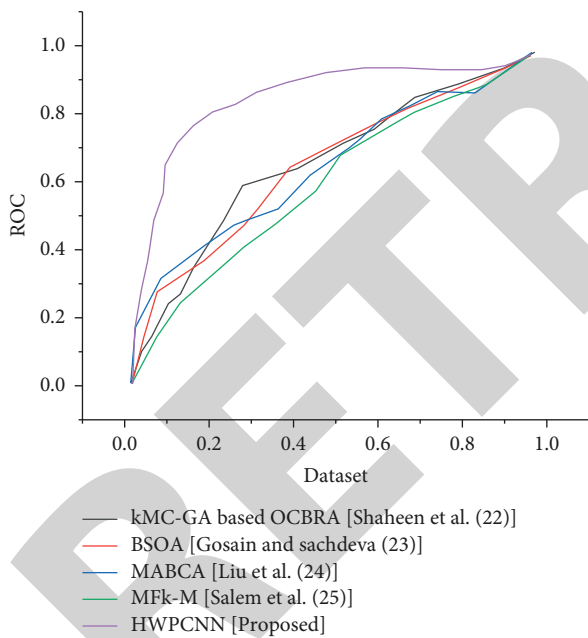


FIGURE 9: Receiver operating characteristic(ROC).

method that is currently being used in Figure 9. The figure shows that the suggested technique is far better when compared to the traditional techniques in terms of ROC.

### 5. Discussion

This study discovered that the deployment of data warehouse technology needs the support of top-quality management, as this is a prerequisite for a program to receive the essential Physical education resources for success. Figures 3–9 display the comparison of the suggested

approach with that of the existing method. The figure demonstrates that the suggested technique outperforms the existing methods because of the following shortcomings of existing methods. kMC-GA based OCBRA approach is expensive and hence it is difficult to implement, BSOA is easy to fall into local optimum, MABCA suffers from incorrect exploitation in addressing intricate issues, and MFk-M has the challenge in clustering data when clusters are of various sizes and densities. There is a need for improvement in the system’s resilience regarding indexing since there are situations in which creating the correct index of that key value is impossible if the value of the lost character is the highest in the character reference table. This limitation demands more research. Since only the final weight matrices from the conditioned neural network are maintained, the space requirements of the resulting indices are minimal. Final weight requires less space than hash tables. Implementation, Proposed Schema, Data Analysis, Efficiency, Effectiveness, Business Needs, and User Needs. Based on our research, we’ve discovered several key aspects of successful DWH initiatives and proposed a five-step process for creating your DWH for use in your endeavors. [22].

### 6. Conclusion

Decision-making in any corporation depends on the quality and management of data in physical education. Data quality and management challenges resulting from the physical education material source systems must be addressed by organizations. In addition, data quality and management are not only about identifying and correcting data quality problems. A DW and any other systems dealing with data gathering, storage, and analysis are also critical to the success of business operations. We proposed a novel HWPCNN approach to index multidimensional databases in PE quality management. Our proposed method achieves an accuracy of 94%, precision of 93%, recall of 90%, F1-score of 95%, and specificity of 96%. This study focused on only one China government department, and only at the head office level. There are numerous China government departments and most exist at national, provincial, regional, and local levels. Conducting future research into a data warehouse in physical education quality management and at only one level, that is, the national level, maybe neither a good representation of other government departments nor of other levels.

### Data Availability

The data used to support the findings of this study are available from the corresponding author upon request.

### Conflicts of Interest

The authors declare that there are no conflicts of interest.

### Acknowledgments

This work was supported by the Chengdu Sport University.

## *Retraction*

# **Retracted: Evaluation Method of Writing Fluency Based on Machine Learning Method**

### **Mathematical Problems in Engineering**

Received 26 September 2023; Accepted 26 September 2023; Published 27 September 2023

Copyright © 2023 Mathematical Problems in Engineering. This is an open access article distributed under the Creative Commons Attribution License, which permits unrestricted use, distribution, and reproduction in any medium, provided the original work is properly cited.

This article has been retracted by Hindawi following an investigation undertaken by the publisher [1]. This investigation has uncovered evidence of one or more of the following indicators of systematic manipulation of the publication process:

- (1) Discrepancies in scope
- (2) Discrepancies in the description of the research reported
- (3) Discrepancies between the availability of data and the research described
- (4) Inappropriate citations
- (5) Incoherent, meaningless and/or irrelevant content included in the article
- (6) Peer-review manipulation

The presence of these indicators undermines our confidence in the integrity of the article's content and we cannot, therefore, vouch for its reliability. Please note that this notice is intended solely to alert readers that the content of this article is unreliable. We have not investigated whether authors were aware of or involved in the systematic manipulation of the publication process.

Wiley and Hindawi regrets that the usual quality checks did not identify these issues before publication and have since put additional measures in place to safeguard research integrity.

We wish to credit our own Research Integrity and Research Publishing teams and anonymous and named external researchers and research integrity experts for contributing to this investigation.

The corresponding author, as the representative of all authors, has been given the opportunity to register their agreement or disagreement to this retraction. We have kept a record of any response received.

### **References**

- [1] S. Gao, "Evaluation Method of Writing Fluency Based on Machine Learning Method," *Mathematical Problems in Engineering*, vol. 2022, Article ID 1253614, 12 pages, 2022.

## Research Article

# Evaluation Method of Writing Fluency Based on Machine Learning Method

**Sheng Gao** 

Zhengzhou SIAS University, Zhengzhou 450000, Henan, China

Correspondence should be addressed to Sheng Gao; 11024@sias.edu.cn

Received 23 July 2022; Revised 24 August 2022; Accepted 29 August 2022; Published 17 September 2022

Academic Editor: Dinesh Kumar Saini

Copyright © 2022 Sheng Gao. This is an open access article distributed under the Creative Commons Attribution License, which permits unrestricted use, distribution, and reproduction in any medium, provided the original work is properly cited.

In light of society's rapid advancement, more and more people worldwide are placing importance on education. There are several domains in China where the importance of writing exceeds the importance of reading, listening, or speaking. It has been shown that many Chinese students commit grammar problems if they are writing an article. Several researchers attempted to determine students' writing talents in terms of amount and complexity, on the one side, and then also focused on identifying conclusions on the accuracy, the organization of ideas, and the barriers to fluent writing via qualitative data gathering approaches. This research uses a machine learning technique to measure students' writing fluency. Writing fluency capabilities can be predicted using a novel adaptive generative adversarial network-based deep support vector machine (AGAN-DSVM) technique. The trace-oriented approach can be used to examine the features like accuracy, syntactic complexity, and organization of ideas aspects. The prediction rate of lexical complexity and sentence complexity of our proposed method achieves 90 and 95%, respectively. Plots created with origin's graphing tool display the results of a comparison between the proposed approach and several other ways already in use. The proposed method is evaluated and compared using several different metrics, including the accuracy dimension, syntactic complexity dimension, organization of ideas dimension, distributions of the mistakes in the text, lexical complexity, sentence complexity, essay particularities, and comparison of accuracy, F1 score, and syntactic complexity.

## 1. Introduction

People throughout the world are paying more attention to education as society develops rapidly (de Wit and Altbach [1]). For an individual to attain fluency in English, they must master four language skills: hearing, speaking, reading, and writing (Abrejo et al. [2] and Mody and Bhoosreddy [3]). Writing, on the other hand, appears to be the most difficult and unappealing skill to master. Since it demands a lot of time and careful feedback, which is essential to the growth of writing, teachers find it the most difficult to teach (Altnmakas and Bayyurt [4]).

A well-expressed piece of art possesses a specific set of traits. Furthermore, their ideas are organized logically and cohesively, which includes proper grammar and spelling, punctuation, and syntax standards (Wang and Fan [5]). The author employs a wide range of complex phrase structures and language, all while keeping the text intelligible. It is not

difficult for someone with good writing skills to organize their material, and they do not waste a lot of time on the task of putting together coherent ideas. The more a person's writing ability increases, the better he or she can meet the needs of written expression (Mkandawire et al. [6]). As a result, writing is so highly valued in China that in some disciplines, it may even be more valuable than reading, listening, or even speaking.

To begin with, grammar is an inherent aspect of writing in the English language. Studies by Song [7] show that many Chinese students make grammatical errors when they write academic articles. For example, a sentence may have two verbs, the writers may not have understood what the pronoun "it" meant, or a sentence may be written without a subject. These types of errors can be seen in the writing of Chinese students of any grade level.

Figure 1 depicts a lesson plan for improving students' academic writing skills. According to the figure, teachers



FIGURE 1: Cycle of implementation of pedagogy to improve students' academic writing.

critiqued the students' opinion essay draughts, followed by a class discussion. They were asked to self-evaluate their work. Once they have done that, they will be asked to write a reflection journal entry in which they may share their thoughts on their performance, what they have learned, and their mistakes. This was followed by a class discussion in which the teacher addressed the points raised by the students. The pupils then worked in pairs to correct each other's work. They once again evaluate and provide feedback. Another reflective diary entry from each student provided the teacher with topics for a second whole-class discussion and explanation.

A clear focus will make our writing's goal more understandable and make it easier for readers to follow our logic. By structuring our body paragraphs, we make sure that both we and our readers maintain focus on and make connections with our thesis statement. A solid organizational structure enables us to express, evaluate, and make sense of our ideas. The notion represented in the main phrase is supported, explained, illustrated, or supported by evidence in the supporting sentences, which are also known as the paragraph's body. Additionally, elaboration provides more information to clarify what has already been presented. By mastering grammar, you will have the opportunity to choose your style nuances and make your writing more readable and understandable. Style affects the reader's perception of the material itself by serving as the container for the text's meaning. Chinese college graduates are increasing annually, and as English has become the de facto language of academia, they must be able to write in it for academic purposes (MacDonald [8] and Ahmed and Ali [9]). This study makes an effort to develop a system that is based on machine learning to analyze the writing fluency of students. This is necessary because manually evaluating students' writing fluency is a difficult task. The following are the contributions made by the study.

- (i) To predict the writing fluency capabilities, a novel adaptive generative adversarial network-based

deep support vector machine (GAN-DSVM) technique is used.

- (ii) The trace-oriented approach can be used to examine the features.

The remaining parts of the research were organized in the following way: the relevant works are illustrated in Section 2, the proposed technique is illustrated in Section 3, the findings and discussion are illustrated in Section 4, and the conclusion is illustrated in Section 5.

## 2. Literature Survey

The use of automated writing evaluation (AWE) in second language writing schools has become more popular in recent years. While the technology is focused on lower-level (LL) abilities, like grammar, instructors believe AWE may help by enabling them to focus more on higher-level (HL) writing skills like content and structure. This may have a favorable effect on student revisions. There is, however, a lack of data to back up these assertions, raising doubts about AWE's influence on classroom instruction. To test these claims, Link et al. [10] compared two second language writing courses allocated to either an AWE + teacher feedback or a teacher-only feedback condition. Geng and Razali [11] provide a comprehensive evaluation of the research into the usefulness of automated feedback. Analytical synthesis includes eleven publications published in the last five years that met the inclusion and exclusion criteria. Analysis of prior research gaps in automated feedback, such as lack of design for delayed post-tests, student writing performance, and students' writing techniques concerning the AWE program, is shown through a literature review matrix for synthesis. In China, "Automated Writing Evaluation (AWE)" has been extensively used in computer-assisted language acquisition. Research on what motivates students to utilize AWE is limited. To this goal, Garg et al. [12] and Li et al. [13] surveyed 245 Chinese college students and used their responses to evaluate several suggested hypotheses utilizing two external variables (i.e., computer self-efficacy and computer fear) added to the technology acceptance model (TAM). Perceived usefulness, attitude toward usage, and computer self-efficacy were shown to have a direct impact on learners' behavioral intention to use AWE, whereas perceived ease of use and computer self-efficacy had an indirect effect. Alobaid [14] and Shahabaz and Afzal [15] emphasize and use YouTube's online English learning materials as an example of a smart learning environment. This study hypothesizes that learners who utilize online language resources may improve their writing fluency over time. Salihuand and Zayyanu [16] and Zedelius et al. [17] explored whether human judgments of short story originality can be predicted by creativity metrics and linguistic analysis. College students (with and without creative writing expertise) composed short tales based on a prompt. The rubric assessments corresponded with existing creativity measures. Two computerized text analysis methods were used to examine the short tales' linguistic properties. Even though Frankenberg-Garcia points out that automated



writing assessment software has garnered a lot of attention in the CALL literature, there is a paucity of empirical research on predictive text and smart writing aids. To fill this knowledge vacuum, Dizon and Gayed [18] and Li [19] looked at the influence of Grammarly, an intelligent writing helper that uses predictive text technology to improve the quality of mobile writing produced by Japanese L2 English students in the USA. China's English-language colleges often use the AI-based writing assessment system. Using Juku "Automated Writing Evaluation (AWE)", Lu [20] found that AWE is effective in helping students with their English writing; both teachers and students have a positive attitude toward the use of Juku AWE in terms of immediate and clear feedback, time savings, and awakening interest in English writing.

To begin, a cross-sectional methodology looks at the variables of AWE adoption after a period that may have had some unavoidable and prospective effects on individual aspects of learners due to the long-term exposure to AWE. The longitudinal and comparative validity of results for the rapidly evolving context of AWE usage is still an open question. The research did not check for the moderating impacts of key variables like gender and other demographics. Students' preoccupation with correctness rather than flow in their writing was a significant obstacle. Therefore, students were reassured that making mistakes is not a "sign of inhibition" that must be eliminated, but rather a strategy for learning and an entirely normal part of picking up a second language. Learners, however, would be reminded of the need of achieving a happy medium between correctness and flow in both their formal and casual writing. The New Media Consortium's 2016 Horizon Report for Higher Education highlights the difficulty of customized learning, which includes the restriction of having to create learning environments that are flexible and responsive to unique learners in specific scenarios. Specifically, the issue of "one size fits all" arises when students are offered a choice between two or three episodes of the YouTube BBC language program as the focus of the next class; inevitably, a small number of students will choose the episode that the majority of their peers have chosen. When this happens, teachers will take note of the student's preferences and propose those subjects to other courses so that students have access to a wide range of information. Fortunately, the smart learning environment was able to assist with these difficulties, thanks to the many features and benefits that have since become standard in this kind of learning environment, as well as the proliferation of individualized learning opportunities. To investigate these issues, the present research develops an AGAN-DSVM.

### 3. Proposed Methodology

In this section, we will go into further detail on the machine learning technique to evaluate writing fluency. Figure 2 represents the suggested approach flow. Data collection tools were first used to acquire participant samples. After that, a normalization technique was used to preprocess the

acquired data. Trace-oriented feature analysis is used to examine the data's features. Then to estimate the writing fluency skills, a unique adaptive generative adversarial network-based deep support vector machine (AGAN-DSVM) approach is applied.

*3.1. Samples of Participants.* 74 first-year English majors from two courses at a local university in southwest China participated in this study, with only eight of them being male, which is typical for majors like English. Most of them had been studying English since junior high school for at least six years and were proficient in the language (Yang 2020). Participants had to produce an essay expressing their viewpoints.

*3.2. Data Collection Tools.* The qualitative and quantitative aspects of fluent writing were measured using both qualitative and quantitative data gathering methods. The data collection tools listed below were used to gather student writings and their data.

- (i) Writing Quantity Formula—A more objective metric for assessing writing output is the number of syllables written per minute, which may be calculated as an average of all words written in a given period.
- (ii) Language Accuracy Holistic Scale—Accuracy was evaluated using the "Language Accuracy Holistic Scale." From 0 to 9, there are ten possible outcomes on this scale. From 0 to 10, each category ranks the writer's use of spelling, punctuation, and grammar accuracy.
- (iii) Lexical Diversity Formula—Before figuring out lexical diversity, the total number of words and the number of different words were counted. In this study, unlike the others, polysemy was taken into account when figuring out how many different words there were. However, it was not taken into account when trying to figure out what kind of difference there would be when polysemy was taken into account and when it was not.

$$\text{Lexical diversity} = \frac{\text{Different no of words}}{\text{total no of words}} \times 100. \quad (1)$$

- (iv) Lexical Density Formula—Students' texts were counted, and their lexical density was calculated by subtracting the terms on this list from the total number of words in each text.

$$\text{Lexical density} = \frac{\text{No of content words}}{\text{total number of words}} \times 100. \quad (2)$$

- (v) Syntactic Complexity Scale—The method that the researcher used to determine the level of syntactic complexity involved looking at the grammatical structure of the sentence as well as the components that contributed to the sentence's meaning.

*3.3. Preprocessing Using Normalization.* A common preprocessing step in most data mining systems is data

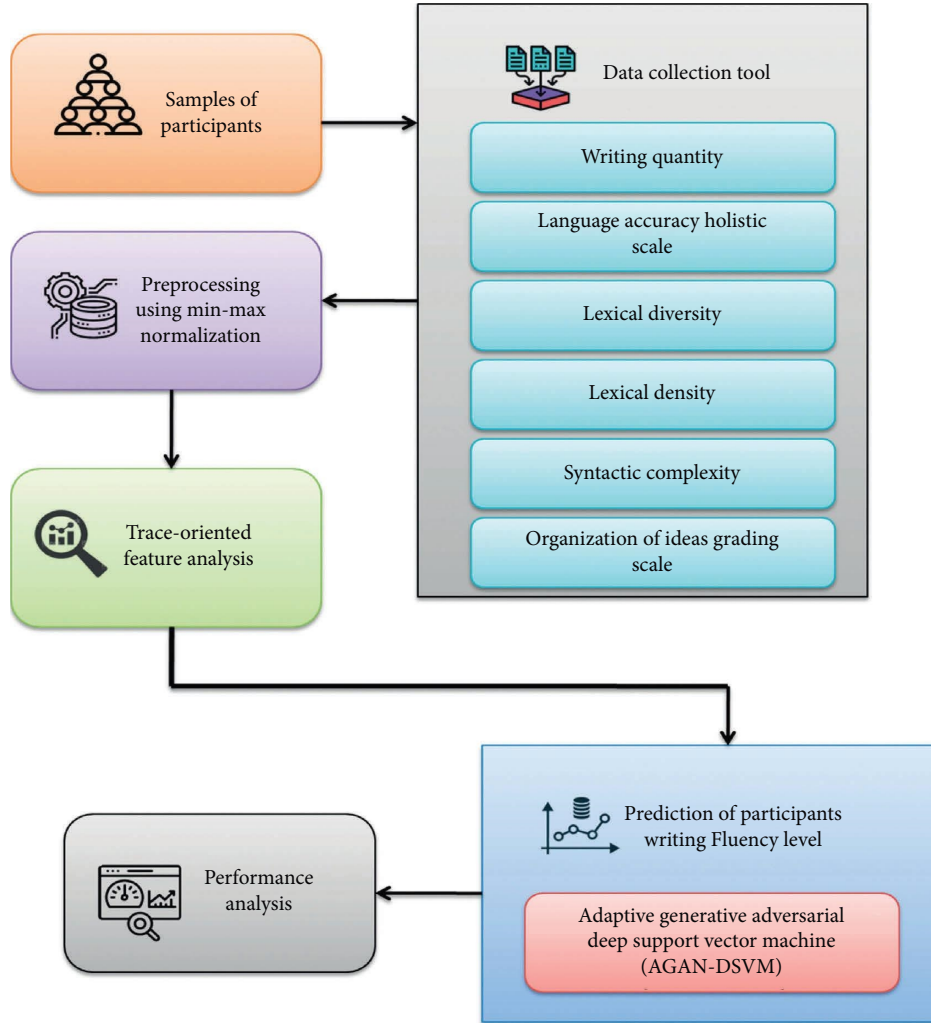


FIGURE 2: Flow diagram of the suggested approach.

normalization. When it comes to data cleansing, there are several methods at our disposal. We have chosen to employ z-score normalization because it is quick and easy.

**3.3.1. Z-Score Normalization.** By taking the mean and standard deviation of each feature throughout a training dataset and dividing it by the dataset's size, Z-score normalization, also known as zero-mean normalization, normalizes each input feature vector. Each attribute's average and standard deviation are calculated. The transformation is required, as mentioned in the general formula.

$$n' = \frac{(n - \mu)}{\sigma}. \quad (3)$$

The discussed attribute  $n$  has a mean of  $\mu$  and a standard deviation of  $\sigma$ . Every feature in the dataset is subjected to z-score normalization before training can commence. Once training data have been obtained, the standard deviation and mean of each feature should be stored for use as algorithm weights.

**3.4. Trace-Oriented Feature Analysis (TOFA).** TOFA is used to analyze the features of the student's writing after it has been preprocessed. Finding a suitable projection matrix  $U \in C^{o \times l}$  for linearly projecting  $t_b = U^Y Z_b \in C^l$ ,  $b = 1, 2, \dots, j$  to lower the text vector dimension from  $o$  to  $l$ , where  $l \ll o$  is the goal of the linear feature extraction (FE) issue. The optimal projection matrix  $U$  is obtained from a set of text data  $Z$  by maximizing an objective function  $N(U)$  under the restriction that  $U \in M_{va}$  where  $M_{va} = \{U \in C^{o \times l} | U^Y U = B\}$  is the solution space of the FE issue. The matrices  $B \in C^{l \times l}$  are identical in this case.  $M_{va}$  is a continuous solution space because  $W$  can be any real value. Any FE algorithm's objective function, denoted by  $N_{va}(U)$ , can be expressed as follows:

$$U^* = \arg \max_{U \in M_{va}} N_{va}(U). \quad (4)$$

PCA, MMC, and OCA are three of the most often used feature extraction techniques that can be evaluated using the optimization framework outlined in [4].

**3.4.1. Principal Component Analysis.** We can discover a  $p$ -dimensional subspace that has basic vector oriented in directions that have substantial variations with the use of PCA, which is an unsupervised FE technique. In this example, the covariance matrix of all the text documents is  $R = \sum_{b=1}^j (z_b - H)(z_b - H)^Y / j$ , where  $h = \sum_{b=1}^j z_b / j$  is the mean of the text documents. There are a few ways to express the PCA's objective function in terms of the matrix trace, such as  $N_{\text{LRE}}(U) = \text{yc}\{U^Y R U\}$  where  $\text{yc}\{R\} = \sum_{b=1}^j R_{bb}$ . Singular value decomposition (SVD), which has a time complexity, is the main source of PCA's computational burden. Thus, PCA's answer is

$$U^* = \arg \max_{U \in M_{va}} N_{\text{LRE}}(U). \quad (5)$$

**3.4.2. Maximum Margin Criterion.** The maximum margin criterion is a new supervised method that has been suggested. There may be  $s$  classes of data in the collection; the number of classes is given by the symbol  $z_b$  and  $j_n$ , which is equal to 1, 2, ..s, etc. The vector of the centroid for the next class is given by

$$h_n = \frac{\sum_{z_b \in s_n} z_b}{j_n}. \quad (6)$$

The objective function of MMC is similar to that of LDA in that it utilizes an inter-class scatter matrix

$$K_i = \sum_{b=1}^s \frac{j_b}{j} (h_b - h)(h_b - h)^Y, \quad (7)$$

and an intra-class scatter matrix.

$$K_u = \sum_{b=1}^s \frac{j_b}{j} z_b \in s_n^A \{(z_b - h_n)(z_b - h_n)^Y\}. \quad (8)$$

To maximize the distance between documents of various classes and the proximity of documents of a similar class in the low-dimensional space being projected, MMC employs many techniques. To solve MMC, the objective function is  $N_{\text{HHR}}(U) = \text{yc}\{U^Y (K_i - K_u)U\}$ , and hence the solution is

$$U^* = \arg \max_{U \in M_{va}} N_{\text{HHR}}(U). \quad (9)$$

**3.4.3. Orthogonal Centroid Algorithm.** The orthogonal centroid algorithm (OCA) is a supervised algorithm, too. A GC matrix decomposition test proved to be an excellent approach for text categorization problems. Large-scale data processing demands cannot be met by the efficiency of GC decomposition because of its time and space needs. Lemma 1 demonstrates that the OCA may be formulated in the optimization framework as well.

**Lemma 1.** *The following optimization issue is equivalent to solving OCA,*

$$U^* = \arg \max_{U \in M_{va}} N_{\text{DRE}}(U) = \arg \max_{U \in M_{va}} \text{yc}\{U^Y K_i U\}. \quad (10)$$

*It is clear from equations (6), (9), and (10) that the PCA, MMC, and OCA are all working toward the same goal, which is to maximize the trace of the various matrices. Because of this, we can refer to these linear feature extraction techniques as trace-oriented approaches.*

**3.5. Prediction of Participants' Writing Fluency Level.** The methods that AGAN-DSVM uses will be covered in this section of the article. First, the justification behind and the specifics of using AGAN as a strategy to create more data on the performance of training students are discussed. After that comes DSVM, which is the part of the algorithm that handles the prediction model for the student's performance.

### 3.5.1. Generation of Training Data by GAN.

Unsupervised and semi-supervised learning are two of the most common applications for GAN. The generator (GR) network creates synthetic data samples that seem like actual data, whereas the discriminator (DR) network uses both real and fake data samples to determine what is real and what is not to make accurate classifications. A Nash equilibrium is reached when both networks are working together. To communicate with the generating network, it must use a discriminator that can distinguish between actual and fraudulent data samples. Data generated by the GR are checked against the ground truth by the discriminator, which generates an error signal. The error signal is utilized to enhance the generator's ability to produce more high-quality fake data.

A generator or discriminator often employs a multi-layered network composed of layers that are either fully linked or convolutional. The generator and discriminator do not have to be perfectly invertible for this to work. The adaptive GAN proposed in this paper incorporates the best aspects of prior CGANs. It can be expressed as follows:

$$P_{\text{source}} = A[\log L(K = \text{real}|Z_{\text{real}})] \\ + A[\log L(K = \text{fake}|Z_{\text{fake}})],$$

$$P_{\text{class}} = A[\log L(R = e|Z_{\text{real}})] \\ + A[\log L(K = e|Z_{\text{fake}})],$$

$$B(e, Q(j, e)) = A_{z \sim Q(j, e)} [A_{e \sim L(\theta/z)} [\log G(e|z)]] + M(e). \quad (11)$$

This formulation's goal is to optimize  $P_{\text{source}} + P_{\text{class}} - \succ B(e, Q(j, e))$  for the discriminator and optimize  $P_{\text{class}} - P_{\text{source}} - \succ B(e, Q(j, e))$  for the generator. Both of these optimizations are intended to be carried out in the context of the  $Q(j, e)$  function. Keep in mind that  $\succ$  is the hyperparameter and that  $B(e, Q(j, e))$  is the representation of the information that lies between  $Q(j, e)$  and  $e$ . The architecture of the currently operational CGAN is shown in Figure 3(a). The term NS refers to the noise source, CR denotes the category or class, GR stands for generator,  $Y$  stands for actual data,  $Y'$  offers synthetic data, and  $A$  stands for added network.

According to the likelihood score,  $D$  can tell whether the incoming data coming from a GR dataset or a real

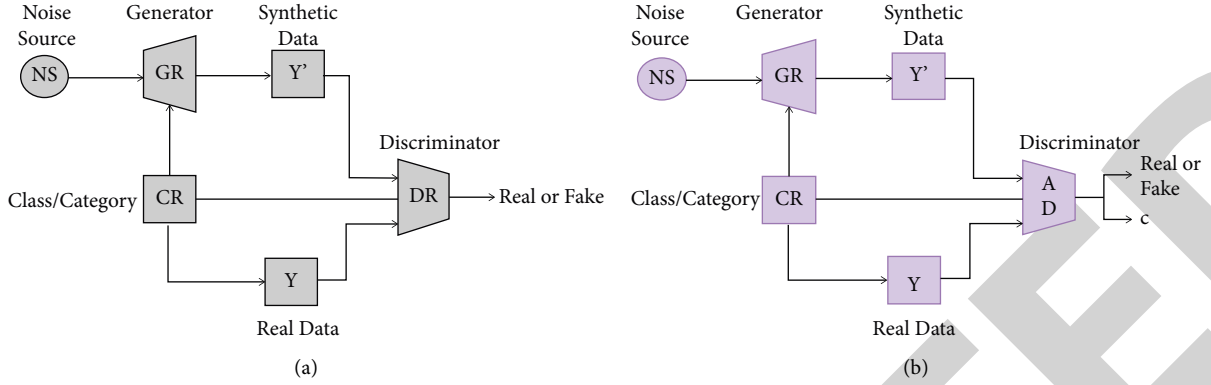


FIGURE 3: Architectural diagram of (a) existing CGAN and (b) proposed AGAN.

dataset. The GR and  $D$  networks are both conditional. By enhancing the data's diversity, it is possible to avoid bias in the generated data. The proposed AGAN is shown in Figure 3. AGAN has made three changes to the existing CGAN:

- (i) Added a class variable or conditional statement to  $D$ .
- (ii) Added a  $D$ -based extended network.
- (iii) Each sample of data was tagged with a unique name.

**3.5.2. Prediction of Students' Performance.** Deep SVM layers are used to build a model that predicts students' writing performance. Like a deep neural network model, the framework is composed of numerous hidden layers of SVM. SVM, on the other hand, has a more flexible architecture because of its kernel function estimate and can handle large-scale inputs. It is more effective with smaller datasets. Because of its robust regularization ability, the suggested SVM can avoid overfitting. Figure 4 depicts the architecture of deep SVM in its entirety. Depending on the training data, the number of hidden layers may vary. The number of hidden layers was reduced in this work by using the grid search strategy, which also minimizes the computational cost. The model's performance may suffer as a result of an increase in the number of layers.

Existing research in the SVM model often uses kernels such as radial basis, linear, sigmoid, and polynomial. Several studies have also employed custom kernels because of the low performance of these kernels for many applications. Mercer's theorem is used to create a customized kernel in this study. It is more accurate to use radial-based kernel functions, as illustrated in equations (12)–(15), which show linear, sigmoid, and polynomial kernels, respectively.

$$S_1(z_1, z_2) = (z_1, z_2), \quad (12)$$

$$S_2(z_1, z_2) = \exp\left(\frac{\|z_1 - z_2\|^2}{2\sigma}\right), \quad (13)$$

$$S_3(z_1, z_2) = (z_1, z_2 + R)^L, \quad (14)$$

```
sL = SVC(kernel = 'linear')
//sL denotes "svcLinear"
sP = SVC(kernel = 'poly', degree = 8)
//sP denotes "svc Poly"
sG = SVC(kernel = 'rbf')
//sG denotes "svcGaussian"
sS = SVC(kernel = 'sigmoid')
//sS denotes "svcSigmoid"
model = Sequential()
model.add(sL)
model.add(sP)
model.add(sG)
model.add(sS)
model.fit_generator(X_train, Y_train)
```

ALGORITHM 1: Deep SVM.

$$S_4(z_1, z_2) = \tanh(z_1, z_2 + R), \quad (15)$$

where  $k(x_1, x_2)$  is the kernel function,  $c$  is a real number, and  $p$  is a positive value. A heuristic approach has been used to learn numerous kernels. The  $M$ -heuristic is shown in equation (16) by examining the mean square error.

$$\mu_b = \frac{\sum_{b=b}^4 (H_b - H_n)}{\sum_{n=b}^4 \sum_{b=b}^4 (H_b - H_n)}. \quad (16)$$

It is important to note that the structure of the numerous kernels used in SVMs might differ from one layer to the next. There are two main reasons why the technique that was just described is preferable to those that were presented in the earlier research. In the first place, the complexity of AGAN is comparable to that of the existing GAN because it is built on the same techniques. Second, other DL models are not as complicated. To put the suggested method into action, Algorithm 1 provides an implementation of the proposed approach.

## 4. Results and Discussion

In the following part, the findings of an evaluation of the student's writing fluency using a machine learning algorithm

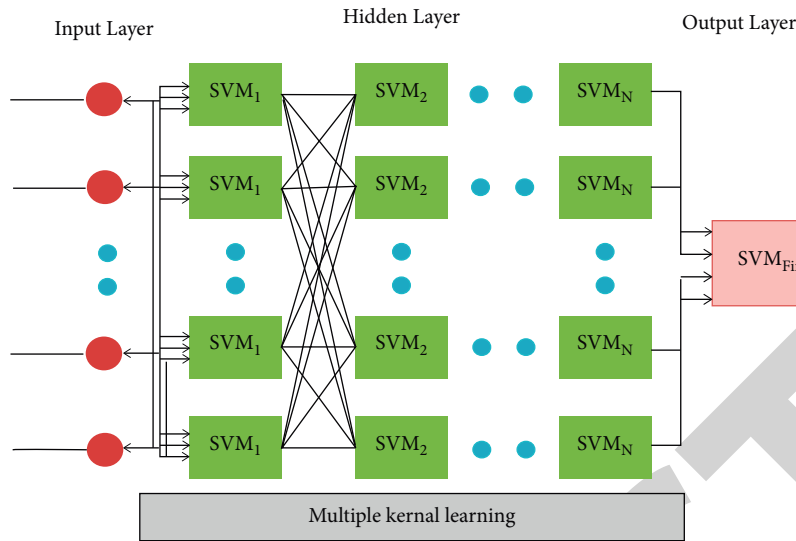


FIGURE 4: Architecture of proposed deep SVM.

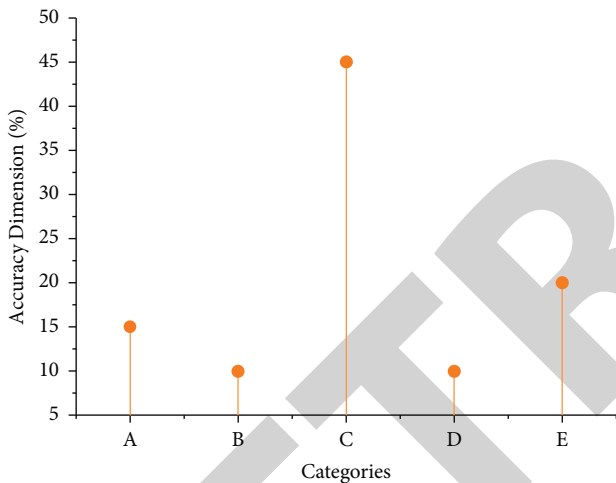


FIGURE 5: Fluent writing's accuracy dimension.

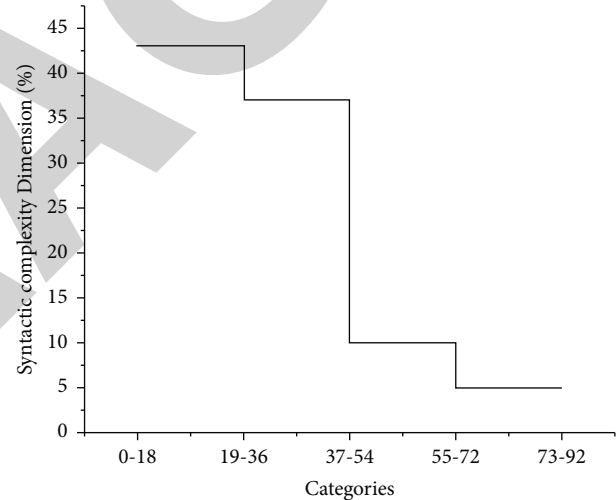


FIGURE 6: Syntactic complexity dimension.

are presented. The “scikit-learn library” and the “Natural Language Process Tool Kit (NLTK)” are used to implement the ML models. Our proposed method is compared with existing methods to prove the proposed method’s efficiency. Figure 5 depicts the accuracy dimension of fluent writing for the students that participated in the study. A indicates that the pupil did not produce a writing sequence that could be analyzed; B indicates that the reader understands obvious deficiencies in “words,” “spelling,” “punctuation,” or “grammar”; C indicates that the reader sees obvious deficiencies in the organization of words, and E suggests that the reader does not see any grammar errors. The majority of the students’ works were graded as belonging to the C category, as shown in the figure. The percentage of pupils whose texts were placed in category A was 15%, category B was 10%, category C was 45%, category D was 10%, and category E was 20%.

Figure 6 shows the fluent writing points earned by students in the syntactic complexity category. Figures from

this study show that 5% of students wrote an essay with a score of 0–18. Similarly, 5% of students had a text grade between 73 and 92. The majority of secondary school students wrote an essay with a point value ranging from 19 to 36.

Figure 7 depicts students’ fluent writing scores regarding the organization of ideas dimension. “A” suggests a weak link between ideas and the topic, “B” indicates a clear main idea, “C” indicates a strong relationship between ideas and the topic, and “D” indicates that ideas have not strayed too far from the topic, according to this figure. Over three-fifths of student texts (35%) fall into the B category.

To check the progress that the pupils had made in their writing ability, additional factors, such as sentence structure, which was denoted as “A,” sentence component, which was denoted as “B,” collocation, which was denoted as “C,” misuse of tense, which was denoted as “D,” misuse of different parts of speech, which was denoted as “E,” and misuse

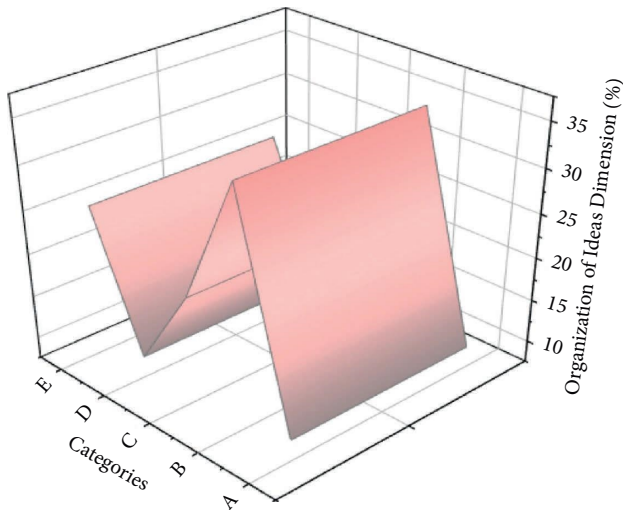


FIGURE 7: Organization of idea dimension.

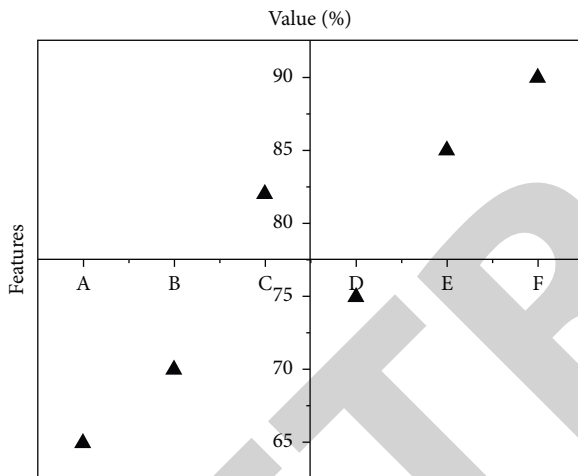


FIGURE 8: Distributions of the mistakes in text.

of spelling, which was denoted as “F,” were analyzed. The features of the errors in the text are illustrated in Figure 8. The figure shows that the majority of the students’ work falls within the “F” category.

Language complexity is defined as “the fraction of relatively unusual or advanced terms in the text that is being read by learners.” It can tell you how good your writing is and how formal it is. Figure 9 compares the lexical complexity prediction of the proposed method with existing methods. Proposed methods outperform existing methods.

The ratio of clauses to the total number of *T* units (*C/T*) was used to determine the sentence complexity. “An independent clause and all its dependent clauses” is the definition of a *T* unit. *C/T* was chosen because it has been proved to predict both syntactic and writing proficiency. Figure 10 illustrates how the proposed method’s sentence complexity prediction compares to other methods. Proposed methods outperform existing methods.

The *F1* score is evaluated by finding the harmonic mean of the recall and precision scores. The *F1* score of the

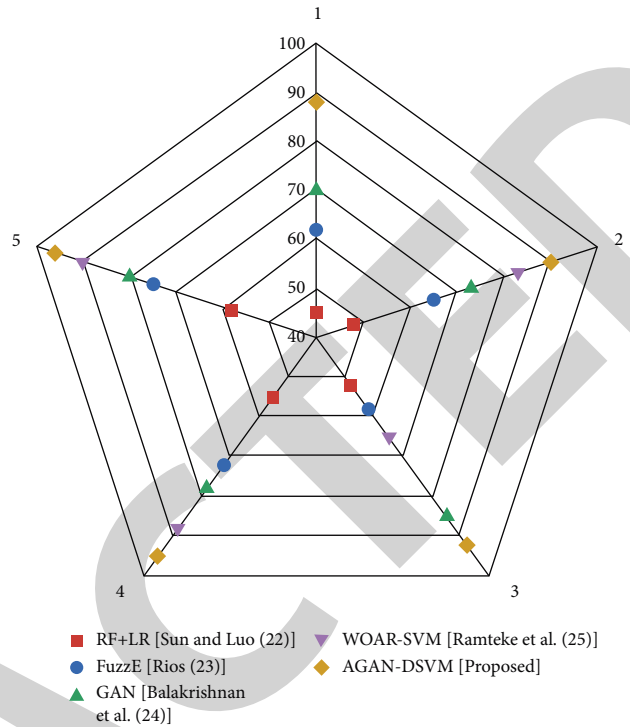


FIGURE 9: Lexical complexity.

suggested approach is compared to the *F1* score of the existing methods in Figure 11. It is abundantly evident that the suggested method is superior to the methods that are already in use. It is determined by applying the formula to the calculation.

$$F1 - score = \frac{2 \times precision \times recall}{precision + recall} \tag{17}$$

The relative level of difficulty of each portion of the essay is displayed in Figure 12, which may be found here. The letter “A” in the figure denotes the background information, the letter “B” indicates the primary contents, the letter “C” indicates the topic sentences, the letter “D” indicates the supporting thoughts, and the letter “E” indicates the concluding sentences, and the letter “F” indicates the main conclusion. The majority of pupils had the most trouble with items in the categories “B” and “F,” as shown in the figure.

Accuracy is a classifier’s predictions that match the true value of a label during the evaluation phase. It may also be expressed as a percentage of right assessments relative to the total number of exams. Figure 13 shows the comparison of accuracy for existing and proposed methodologies. When compared to the existing method, the proposed method has greater accuracy. RF + LR has a 55%, FuzzE has a 63%, GAN has a 74%, WOAR-SVM has a 85%, and the proposed AGAN-DSVM has 94% accuracy.

In this context, syntactic complexity refers to “the variety and sophistication of grammatical resources demonstrated in linguistic creation.” This means that syntactic complexity encompasses similar ideas like variety, diversity, and the level of linguistic fanciness. Figure 14 shows the comparison

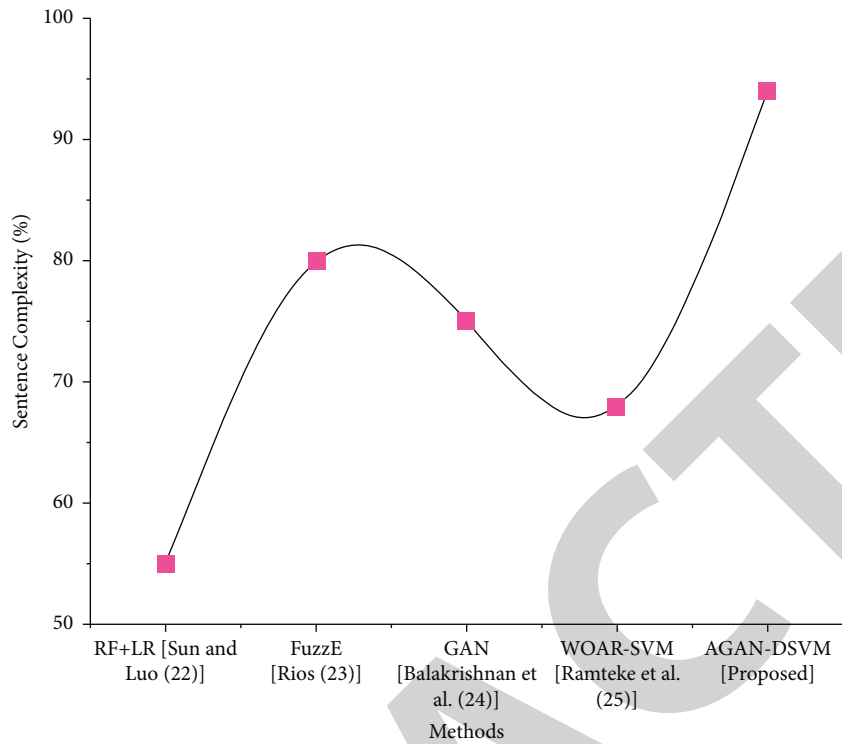


FIGURE 10: Sentence complexity.

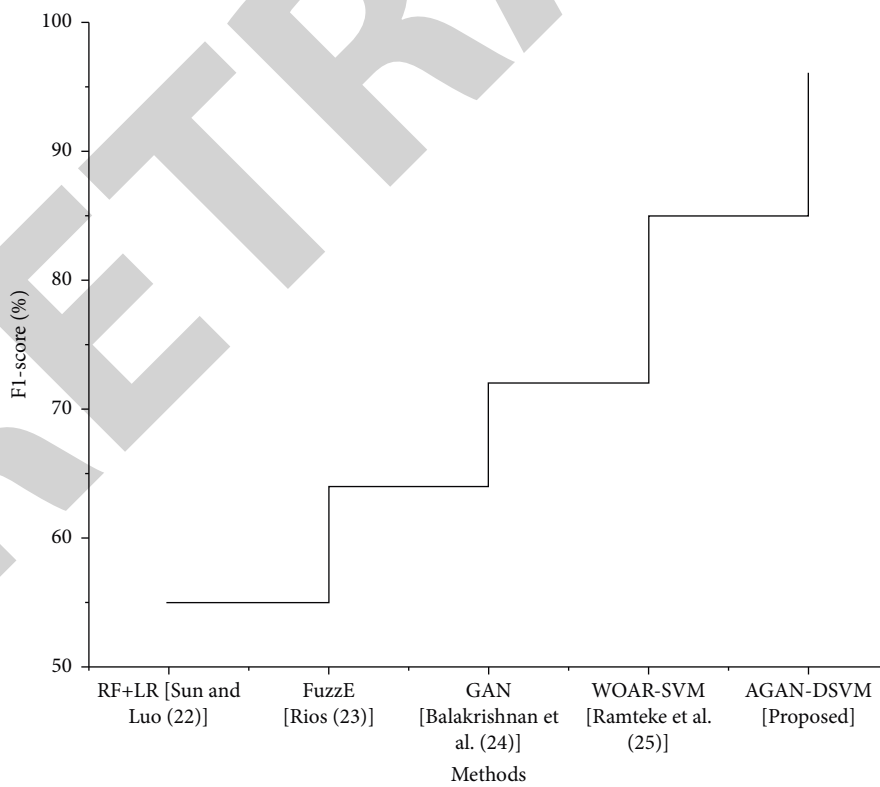


FIGURE 11: Comparison of F1-score.

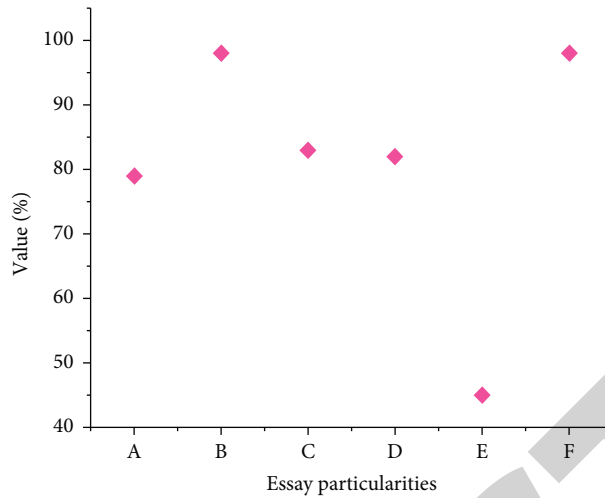


FIGURE 12: Essay particularities.

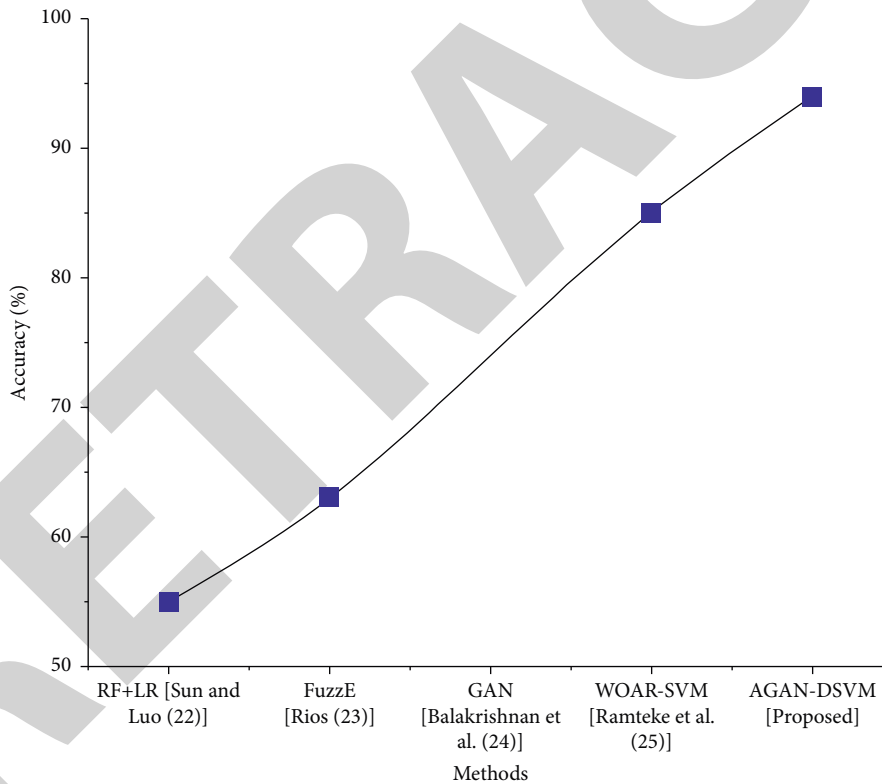


FIGURE 13: Comparison of accuracy for existing and proposed methods.

of syntactic complexity for existing and proposed methodologies. When compared to the existing method, the proposed method has lower syntactic complexity. RF + LR has a 91%, FuzzE has a 82%, GAN has a 74%, WOAR-SVM has a 66%, and the proposed AGAN-DSVM has 53% syntactic complexity.

Comparative analysis of the proposed technique with existing models is depicted in Figures 9–11. “Random forest + logistic regression (RF + LR),” “FuzzE,” “generative

adversarial network (GAN),” and “weighted one-against-rest support vector machine (WOAR-SVM)” are the existing methods employed in this research. Figures prove that the proposed strategy outperforms the existing methods, because of the shortcomings of the existing approach. The following is a list of the current approaches’ shortcomings. Predictions made using RF + LR, FuzzE, and GAN are ineffectual for real-time predictions, while WOAR-SVM does not work well with very large datasets.



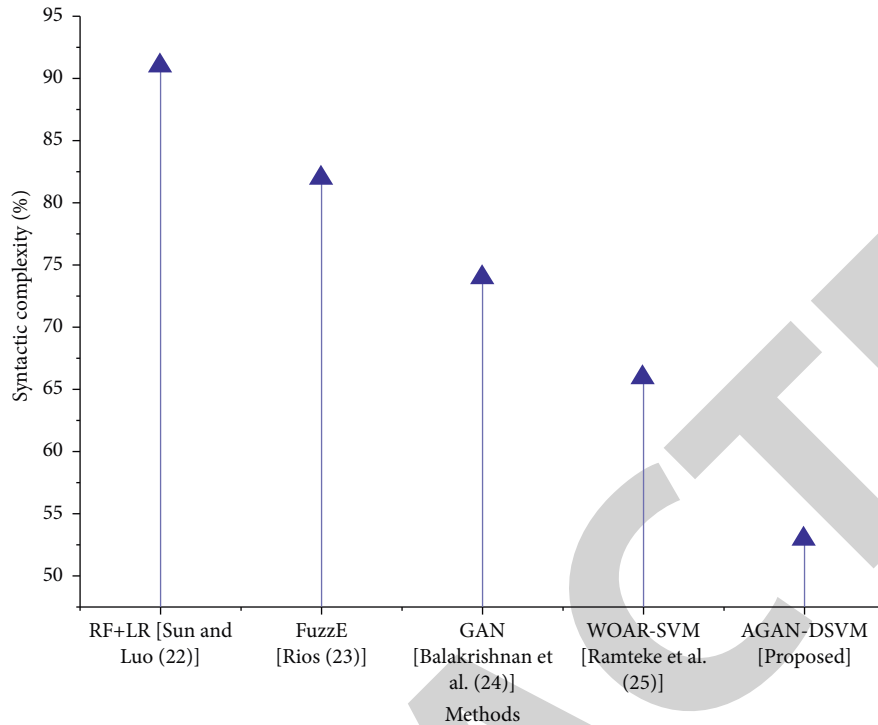


FIGURE 14: Comparison of syntactic complexity for existing and proposed methods.

## 5. Conclusion

To assess students' writing fluency, this study used a machine learning technique. A novel AGAN-DSVM technique can predict writing fluency. Examining the features is possible through the use of a trace-oriented technique. Numerous studies have found that students' inability to use punctuation correctly, their failure to follow spelling standards, their failure to construct structurally appropriate sentences, and their inability to choose the right words are the most common causes of errors in their writing. According to the findings of our study, the spelling mistakes made by students account for 90% of all faults found in their written work. Our suggested strategy can attain 90 and 95% accuracy for predicting lexical difficulty and sentence complexity, respectively. When taken together, these results show that writing composition is an essential field of inquiry for future research to focus on in Chinese students. Given the importance of writing to one's academic and professional success, researchers should continue their work in this field by expanding their focus to include a variety of additional abilities that might boost one's ability to write effectively.

## Data Availability

The data used to support the findings of this study can be obtained from the author upon request.

## Conflicts of Interest

The author declares that there are no conflicts of interest or personal relationships that could have appeared to influence the work reported in this paper.

## Acknowledgments

This work was supported by Zhengzhou Sias University.

## References

- [1] H. de Wit and P. G. Altbach, "Internationalization in higher education: global trends and recommendations for its future," *Policy Reviews in Higher Education*, vol. 5, no. 1, pp. 28–46, 2021.
- [2] B. Abrejo, S. Sartaj, and S. Memon, "English language teaching through communicative approach: a qualitative study of public sector colleges of Hyderabad, Sindh," *Advances in Language and Literary Studies*, vol. 10, no. 5, pp. 43–49, 2019.
- [3] R. N. Mody and A. R. Bhoosreddy, "Summer-Fall, Multiple odontogenic keratocysts: a case report," *Annals of Dentistry*, vol. 54, no. 1-2, pp. 41–43, 1995.
- [4] D. Altinmakas and Y. Bayyurt, "An exploratory study on factors influencing undergraduate students' academic writing practices in Turkey," *Journal of English for Academic Purposes*, vol. 37, pp. 88–103, 2019.
- [5] L. Wang and J. Fan, "The Establishment of a Descriptive Scheme for the Business English writing scale," in *Working towards a Proficiency Scale of Business English Writing: A Mixed-Methods Approach*, pp. 63–82, Springer, Singapore, 2021.
- [6] S. B. Mkandawire, "Literacy versus language: Exploring their Similarities and differences," *Journal of Lexicography and Terminology*, vol. 2, no. 1, pp. 37–56, 2018.
- [7] S. Song, "The influence on Chinese students' English writing caused by the difference of Chinese and Western Thinking model--to Analyse from the Perspective of Conceptual fluency," *Frontiers in Educational Research*, vol. 3, no. 4, 2020.

## Research Article

# Analysis of the Impact of Energy Factor Allocation Efficiency on Green Total Point Productivity from a Low-Carbon Perspective

Jiegang Sun 

*School of Economics and Management, Shanxi University, Taiyuan 030006, Shanxi, China*

Correspondence should be addressed to Jiegang Sun; 202113812008@email.sxu.edu.cn

Received 24 July 2022; Revised 25 August 2022; Accepted 29 August 2022; Published 16 September 2022

Academic Editor: Dinesh Kumar Saini

Copyright © 2022 Jiegang Sun. This is an open access article distributed under the Creative Commons Attribution License, which permits unrestricted use, distribution, and reproduction in any medium, provided the original work is properly cited.

The high consumption of energy resources but low utilization, low factor allocation, and unreasonable economic structure affect the sustainability of economic development. Based on the energy factor theory from a low-carbon perspective, this paper constructs an impact model of green total point productivity and conducts a detailed analysis of the resource mismatch in the energy industry. Under the premise of efficient resource allocation, the factor input of an enterprise is positively correlated with total point productivity. Second, the model adds environmental constraints, considers the undesired output of carbon dioxide, and considers the input of energy factors, and reduces the undesired output as much as possible while increasing the expected output. The model realizes the update estimation of each component of the stationary part of a class of nonstationary stochastic processes and can use the information at a certain time and its previous time in a cycle to forecast all subsequent times. In the simulation process, in order to make the results more objective and accurate, this paper calculates the index and its decomposition results under two conditions, and uses MaxDEA 6.0 professional software to measure the regional industry total point productivity index. The experimental results show that the effective factor of low-carbon data is 0.91, and the relative error is less than 3.11%, which meets the test threshold and effectively improves the robustness of the model.

## 1. Introduction

At present, some regions blindly follow the economic development concept of GDP (gross domestic product), which greatly reduces the quality and efficiency of regional economic development [1]. The resulting problems such as large consumption of energy resources but low utilization, low factor allocation, unreasonable economic structure, and serious ecosystem damage have affected the sustainability of regional economic development [2]. Nowadays, the traditional factor-driven economic growth mode is unsustainable. As another important engine driving economic growth, total point productivity has begun to become the main force of economic growth [3], and the contribution of factor accumulation and total point productivity to output growth. This change has become the main basis for judging the transformation of economic growth mode [4–6]. The main connotation of the transformation of regional economic development mode is the

transformation from factor accumulation-driven to total point productivity-driven [7].

The free flow of economic factors between regions, the diffusion of innovation, and the spillover of technology have strengthened the interregional economic development [8]. In terms of linkage, traditional theories regard different regions as closed economic entities [9–11], which cannot fully understand the impact mechanism of green productivity and the micromechanism of improving green productivity [12]. To ensure the healthy, green, and sustainable development of the national economy [13], focusing on the green economic development model, green total point productivity (GTFP) with energy and environmental constraints is added, which can reflect the comprehensive competitiveness of regional green economy and the essential connotation of green development [14].

Based on the theory of energy factors from a low-carbon perspective, this paper constructs an impact model of green total point productivity. Focusing on the main line of

regional GTFP, based on the theoretical basis of new economic geography and spatial measurement, this paper empirically studies the effect of interprovincial GTFP from the perspective of spatial spillover estimation and its influencing factors. First, the index was used to estimate the GTFP and its sources of 30 regions in the region, and the country was divided into different regions according to different spatial scale division standards, and the regional regions were analyzed and compared from the horizontal cross-sectional dimension and the vertical time dimension. Second, we use spatial statistical methods to test whether there is spatial autocorrelation and spatial dependence of GTFP in each region. During the survey period of the sample, the national GTFP showed an overall growth trend, showing obvious periodic characteristics. Among them, the contribution of green technology efficiency is 10.7%, while the contribution of green technology progress is 3.1%. Since the growth rate is greater than the reduction rate of green technology efficiency, the overall performance is the growth of green productivity.

## 2. Related Work

The research objects are the differences in TFP growth between regions and the characteristics of TFP growth in different industries [15]. Some scholars incorporate spatial factors into the research framework when studying regional economic growth [16]. Some algorithms search for the pitch period with the most predicted delay corresponding to the minimum value of the difference function within the frame. In the difference function, the change of the amplitude will cause the corresponding difference value at all time delay  $m$  to change synchronously, thus weakening the influence of the amplitude change on the peak value. Through scientific and technological investment, the establishment of a modern agricultural system will update the current industrial structure, realize the modern and intelligent development of the primary industry, improve the effective utilization of resources, increase the rationalization of the industrial structure, and drive the internal transformation of the economy in an all-round way.

From the traditional estimation method of TFP, it can be mainly referred to: the first category is the growth kernel algorithm. The residual calculated according to the neo-classical theory can be regarded as a component of a special formal function. Chen et al. [17] proposed it to describe the relationship between input and output, which became the earliest method to quantify and systematically study the relationship between productivity and economic growth. Hou et al. [18] introduced the time trend term into production function, which represents the changing level of efficiency, according to which the production function is used to estimate productivity growth. Zafar et al. [19] are the first to incorporate technological progress into the production function and separate the impact from per capita output growth, and this technological progress is called "Solo residual value." Wang and Feng [20] used translog production function to measure productivity from two levels

of sector and total. It is a very good precondition, but there are problems such as low energy utilization rate and relatively backward environmental protection technology in the development process, which leads to aggravation of energy depletion and deterioration of the ecological environment, and ultimately leads to negative growth of green productivity. However, when  $m$  takes a small value, that is, a small period, the function will have a zero value. For this reason, the cumulative average normalized difference function is used to replace the difference function in the subsequent improvement.

Some researchers have constructed an input-output model to study the effect of intermediate input mismatch on total point productivity. It shows that the progress of green technology, which represents technological innovation, has a significant "growth effect," while the "horizontal effect" of green technology efficiency, which represents the optimal allocation of resources, is obviously insufficient [21]. It is necessary to increase the introduction and investment of modern technology in agriculture, including its own technology innovation, replication innovation introduced, and new sales methods brought by various publicity channels and sales channels, help the sales development of agriculture, forestry, animal husbandry, and fishery. Scholars first used the model to examine the loss of productivity caused by the misallocation of intermediate inputs. When the distortion of intermediate products is considered, the room for improvement is 551%; when the distortion of intermediate products is ignored, the room for improvement is 61% [22]. It can be seen that when studying the efficiency loss of resource mismatch, it is necessary to consider the role of intermediate products [23]. This paper will introduce intermediate inputs on the basis of predecessors and analyze the efficiency loss caused by resource mismatch under the expanded theoretical framework [24].

## 3. Model Construction of the Impact of Energy Factor Allocation Efficiency on Green Total Point Productivity from a Low-Carbon Perspective

*3.1. Low-Carbon Vision Space.* Under the low-carbon vision space, "intensional resource mismatch" refers to the situation where the marginal output of factors is not equal in cross section. According to the basic theory, under the premise of efficient allocation of resources, if the production technology of enterprises is convex, then the marginal product of factors of all enterprises should be equal. When in an efficient allocation state, the marginal capital output (MPK) curves of the two firms should intersect at point A, so the amount of capital acquired by firm 1 is OA1, and the amount of capital acquired by firm 2 is OA2. The total output  $w(i, j)$  in the economy  $x(i)$  is the sum of the areas of the two curved trapezoids. However, due to some distortion  $I(i, j)$ , firm 2 only gets OE2 units of capital, while firm 1 gets OE1 units of capital  $e(i, j - 1)$ .

$$\sum_{i,j=1,2,\dots,n} w(s,t) - \frac{1}{n-s} w(t) = \frac{1-s}{w(x(s)-x(t))}, \quad (1)$$

$$I(i,j) - \sum e(i,i-1) - e(i,j-1) - 1 - i < 0.$$

In the formula, the capital-labor substitution elasticity is  $\text{var}(x, i) = 1/(1+P)$ ,  $x$  and  $P$  represent the technological progress parameter, the distribution coefficient, and the factor substitution elasticity parameter, respectively. The capital-labor elasticity of substitution is  $t = 1/(1-P)$ . When producers are in equilibrium, according to the necessary conditions of producer equilibrium  $\text{var}(x-1)$ , the following can be obtained. The parameterization method is mainly donated.

$$\sqrt{\frac{\text{var}(x, i) - \text{var}(x)}{\text{var}(x-1) - r(xi)}} > 1 - x,$$

$$\frac{q(s)q(t, t-1)}{d(s)d(s-1)} = \begin{cases} \frac{1}{d(s)}, & s \neq t, \\ \frac{1+dt}{ds}, & s = t. \end{cases} \quad (2)$$

The concept of environmental technical efficiency  $d(i)$  is closely linked to the production environment frontier. When the directional distance function value  $q(i)$  is 0, it means that the observation point is at the frontier of the production environment, and the environmental technical efficiency value  $d(i-1)$  is 1. The larger the value of environmental technical efficiency  $x(t, t-1)$ , the closer the observation point is to the frontier of the production environment; that is, for a given resource input, the greater the gap between the actual expected output and the maximum expected output  $dt/si$ , the actual undesired output and the minimum undesired output  $y(i)$ .

$$x(i) - \frac{x(t, t-1)}{s(t)-1} = -\frac{1}{(i+dt/si)},$$

$$y(i) - y(t) = \begin{cases} p(i)w(i) - w(n), \\ \exp(w(n) - w(i)). \end{cases} \quad (3)$$

The directional distance function is different under different model conditions. The calculation of each productivity index  $P(i)w(i)$  requires the solution using the mixed directional distance function and the input-output value in period  $t+l$ . In this paper, the sequential method is used to reduce the phenomenon of linearity  $w(x, y)$  and no misunderstanding when computing mixed directional distance functions.

$$\begin{cases} \sum c(w(u, y), y(u-t, y-t)) = 1, \\ \sum c(w(u, y) - u - 1) = 1, \end{cases} \quad (4)$$

$$y(i) = x(i = 1, 2, 3, \dots, n-1, n | t = 1 - n).$$

The research background of this paper points out that this paper expresses the transformation performance of regional economic development mode  $y(x-t, y-t)$  from the perspective of total point productivity, measuring the transformation performance of economic development mode is to measure total point productivity. Therefore, this article will discuss the measurement method based on total point productivity.

During the survey period of the sample in Figure 1, the spatial distribution pattern of GTFP in each region has significant fluctuation characteristics. According to the principle of statistical grouping, the GTFP data of each province in each year are divided into four grades, and the quartile map is drawn accordingly. At the same time, compared with the traditional analysis method, the method is real-time and recursive, and can perform real-time dynamic estimation and analysis of the energy monitoring network flow in the time domain. And it has the characteristics of high coincidence with the real control network traffic and small prediction error, which can achieve good tracking and prediction performance; at the same time, using the panel data of 36 industries, the calculation takes into account foreign capital and the environment. Compared with the traditional nonlinear prediction model, its complexity is lower and it is convenient for real-time prediction.

**3.2. Distribution of Energy Elements.** The energy factor is a consideration in data selection. The following is a brief description of the specific process of data processing. In general, data processing involves two aspects, one is to construct panel data, and the other is to deflate nominal indicators. When constructing the panel data, considering the problems of duplication and wrong entry of the enterprise code in the database, following Brandt's idea, we first use the enterprise code to identify the same enterprise, and then use the legal person name, registration information, start year, main products, etc. Indicators are further matched.

$$H(u, k) \in \text{least} \{u(1), u(2), u(3); x(k-1), x(k), \dots, x(n)\},$$

$$\frac{y(i, t)}{e^{(j=1-p) - w(i, 1)e(i) - v}} = x(i | t - n) - \frac{u(i)}{u(t)}. \quad (5)$$

The endogenous economic growth model shows that technological progress has an important impact on total point productivity, and human capital GFT  $(i, j)$ , which is closely related to technological progress, has an important impact  $\log(i-1)$ , which reflects an important variable in the technological content of economic growth. Therefore, when studying the input index of total point productivity  $ed(i)$ , it is necessary to consider the input of human capital, that is, to estimate its stock.

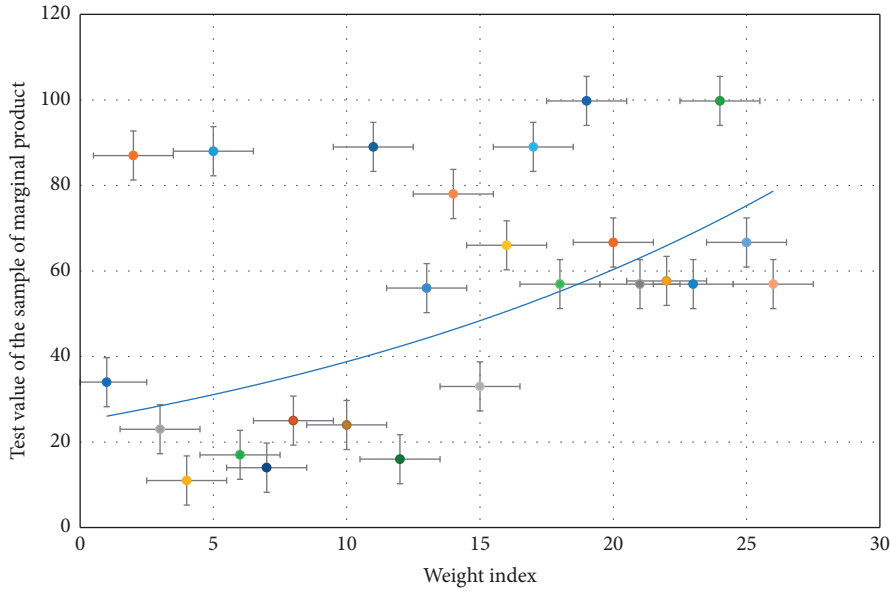


FIGURE 1: Sample inspection distribution of marginal product.

$$\log GFT(i, j) = \begin{cases} a + b \log \frac{ED(i)}{ed(i)}, \\ a - b \log \frac{ED(i-1)}{ed(i-1)}, \end{cases} \quad (6)$$

$$\frac{\alpha + \beta \log Es(i) - \log s(i)}{\log s(i-1)} \ll 1.$$

Since GDP is an added value, energy  $s(i)$  is generally not taken into account in traditional TFP calculations as an intermediate input. In recent years, some scholars have taken resource inputs such as energy into account in productivity calculations because they are assumed to be the main source of undesired output  $ec(i, i-1)$ . The energy input in this paper takes the energy consumption converted into standard coal as the energy input index  $COF(i-1, j)$ .

$$CF(x, i) - \frac{CC(i-1, j-1)}{COF(i-1, j)} \in C, \quad (7)$$

$$CO(x, y) = \sum \frac{ec(i, i-1) - ce(i, j-1)}{1 - ec(i, i-1) - ce(i, j-1)}.$$

The function shows that GTFP is a function of the above five variables. Due to the large value  $ce(i, j-1)$  selected in this paper, the logarithmic form can be used to better explain the degree of correlation between variables, and the heteroscedasticity caused by the data itself will also be to an extent. The explanatory relationship between the variables is changed, which makes the difference between variables become a percentage to explain the concept. This feature is also in line with the economic interpretation method at the macro level. When the data indicators are too large, the percentage change between the data is often used to find a certain relationship between them.

After the operation in Table 1, the matching success rate of this paper is 85.12%, which is almost the same as the result of Brandt. When deflating nominal indicators, this paper sets 2018 as the base period, deflates the gross industrial output value with the industrial ex-factory price index, and deflates the total industrial output with the consumer price index. The index deflates gross wages.

**3.3. Configuration Efficiency Calculation.** In order to study the changes in the allocation efficiency of each province and explore the source of the changes, this chapter calculates the Malmquist-Luenberger index of each province without considering environmental factors, considering one pollutant, and considering two pollutants simultaneously, and calculates its geometrical values. From the results in the above table, it can be seen that whether energy and environmental factors are considered or not directly affects the calculation results of the TFP index, which in turn affects the scientificity of the performance measurement of the transformation of the regional economic development mode. After the above processing, we have obtained 89135 records, and now, the basic statistical results are summarized. It can be seen that the standard deviation of capital input is the largest, which is 1.98, and the data fluctuation is the most obvious.

It can be clearly seen from Figure 2 that during the sample investigation period, the global Moran's I index showed an upward trend with the passage of time, indicating that the spatial dependence of GTFP in each region has gradually increased. In 2020, the order of efficiency loss from high to low is oil and gas extraction, and electricity. Among them, coal mining and selection industry have the lowest resource mismatch, at 21.96%, while oil and natural gas mining industry has the most serious resource mismatch, which is as high as 82.93%, which is 3.78 times that of the former. There are two ways to assemble a program from modules: one is to test each module separately, and then put all the modules together

TABLE 1: Distribution of energy elements.

Element node	Sample number	Variables range	Mean value	Covariance value	Mean square error
Level a	60	-0.29	0.66	0.74	0.06
Level b	46	1.01	0.32	0.34	0.07
Level c	52	1.52	0.01	0.09	0.85
Level d	25	-0.29	0.81	0.52	0.86
Level e	76	-0.97	0.48	0.44	0.02

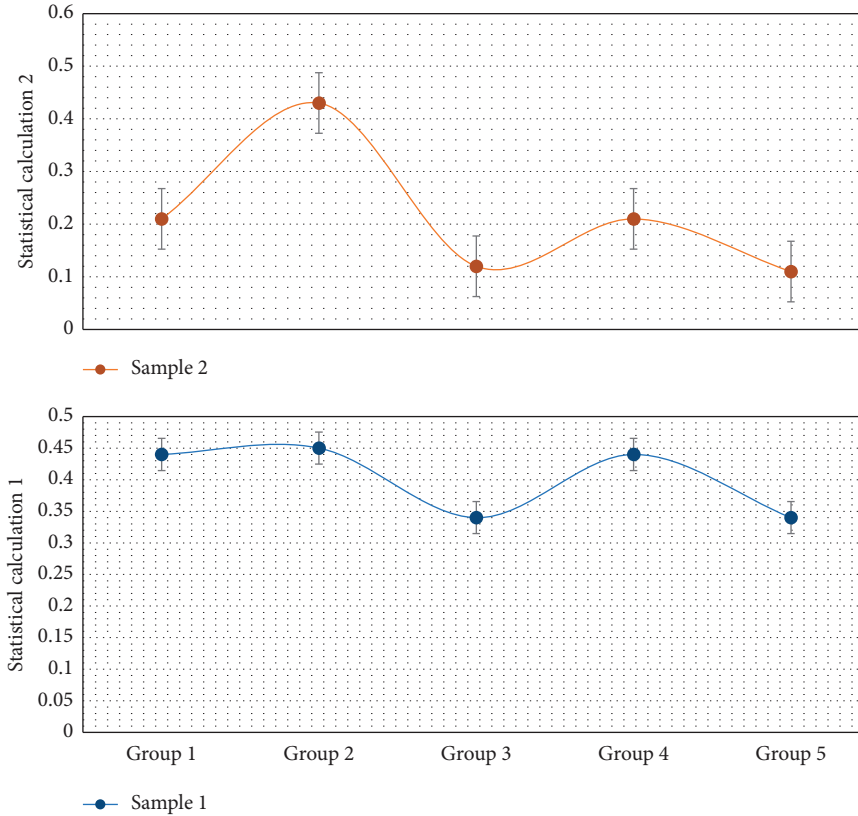


FIGURE 2: Statistical calculation of configuration efficiency.

according to the design requirements to form the desired program. This method is called a nonincremental test method; the next module to be tested is combined with those modules that have already been tested for testing. After the test is completed, the next module that should be tested is combined for testing. This method of adding one module at a time is called incremental testing. This approach actually does both unit testing and integration testing at the same time, and introduces the indicators involved in the green growth evaluation system under this theory into the influencing factor indicators of green total factor productivity.

**3.4. Green Total Factor Indicators.** The average growth rate of economic development mode transformation performance based on energy and environmental total point productivity is 0.1%, which is significantly lower than 2.7% without considering energy and environmental factors. This is mainly because the TFP value of most provinces in the region will be greatly reduced after considering energy and environmental

factors. The numerical value shows the characteristic of gradually decreasing in the east, middle, and west. The average milliliter values were 1.047, 1.003, and 0.985, respectively, and there were large differences in the transformation performance among regions. The growth trend of green productivity index in economically developed regions is obvious. When using the ML index to study regional environmental total point productivity, it is found that the “u”-shaped relationship between per capita GDP and TFP growth rate is similar. This conclusion also proves to a certain extent that green total point productivity supports the “environmental Kuznets curve” hypothesis; that is, if there is no policy intervention in the environment, a country’s overall energy efficiency and environmental quality level will first deteriorate and then improve along with economic growth.

It can be seen from Figure 3 that the elasticity of intermediate inputs is relatively large, all above 0.7, which indicates that the regional energy industry is highly dependent on intermediate inputs, and ignoring the impact of intermediate inputs will bring a large deviation to the

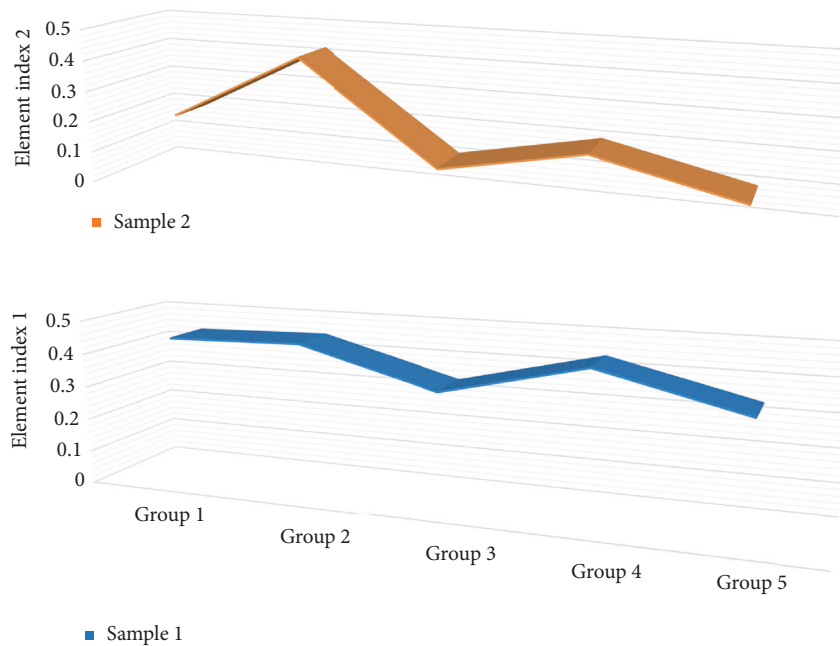


FIGURE 3: Distribution of green total factor indicators.

estimation of total point productivity. Multicollinearity is common in multiple regression linear models. It can be seen from the correlation coefficient between variables that there is a certain degree of collinearity between variables, but we are more concerned about the degree of multicollinearity. The test found that the value is 3.89, which is far less than the reasonable value of 10, indicating that the collinearity of the model is not serious, and the model has a greater impact after excluding an explanatory variable, so the existence of such collinearity can be accepted. At the same time, the estimation results of the fixed effect model are also given. It is not difficult to find that the labor elasticity under the improved method is lower than the estimation result of the fixed effect method, while the capital elasticity is relatively high, which indicates that the improved method is used. The results show that, except for the oil processing industry, the other three industries reject the null hypothesis of constant returns to scale, which prompts us in the subsequent theoretical model, and consider the situation of diminishing returns to scale.

#### 4. Model Application and Analysis of the Impact of Energy Factor Allocation Efficiency on Green Total Point Productivity from a Low-Carbon Perspective

**4.1. Data Processing of Energy Elements.** In order to compare the fitting effects between various models, the general econometric regression analysis can be carried out regional GTFP. The choice of mixed OLS (ordinary least squares) regression, fixed-effect panel regression and random-effects panel regression can be determined for the results of LM (Lagrange multiplier) test and Hausman test. The main purpose of the LM test is to choose between mixed OLS

regression and random effects. The statistic calculated using Statal 3.1 software is 1222.39, strongly rejecting the null hypothesis at the 1% significance level; therefore, between mixed regression and random effects, Figure 4 selects random effects. This approach is based on the same purpose of research on the connotation of green growth and green total factor productivity, that is, to achieve the sustainability of economic growth, so this approach has certain rationality.

There should be a significant correlation between the total point productivity of enterprises and factor input. It should be emphasized that the above conclusions are obtained under the premise of efficient allocation of resources. Therefore, by examining the correlation between factor input and the total point productivity of enterprises, we can infer the current situation of resource allocation in the energy industry. If the actual situation is consistent with the theory, we believe that the resource allocation efficiency of the energy industry is relatively high; on the contrary, if the actual situation is inconsistent with the theory, it can be judged that there is a serious distortion in the energy industry. The paper shows the correlation between capital input and total point productivity, which also shows similar characteristics. It can be seen from the previous analysis that the resource allocation of the energy industry has not reached the Pareto optimality, and the degree of resource mismatch is relatively deep.

**4.2. Selection of Configuration Efficiency Variables.** The above economic indicators are mainly obtained from the "Statistical Yearbook," which can reflect the real economic situation, and the data in the real economy often have a variety of influencing factors along with time, so in general, the data are often nonstationary, so this paper uses Stata software to analyze the nature of the data to prevent a large impact. In

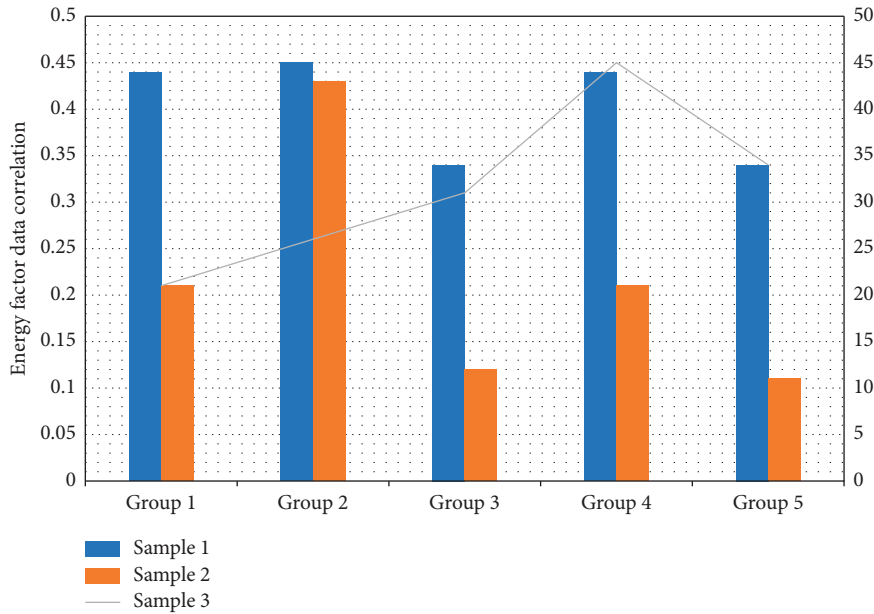


FIGURE 4: Correlation processing of energy factor data.

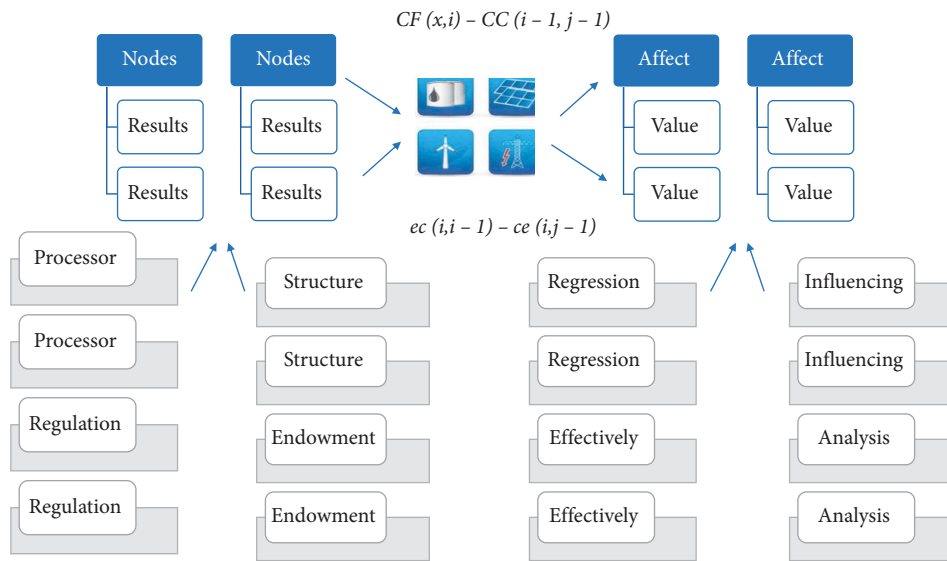


FIGURE 5: Process of configuring efficiency variables.

this paper, we use Stata software to perform unit root test, and use stationary\*, stationary\*\*, and stationary\*\*\* to indicate that they are stationary at the 10%, 5%, and 1% significant levels. The test results are shown below. The logical idea of the whole article is introduced in an orderly manner, indicating that the current economic growth is lagging behind, so it is extremely important to achieve green economic development and improve green total factor productivity.

The influencing factors of GTFP may have the problem that the model is set incorrectly. Therefore, next, the linkage effect of economic units in geographic space is introduced into the model, and the spatial panel econometric model is reconstructed to conduct empirical analysis on the

influencing factors of GTFP. Incremental testing is the opposite of nonincremental testing. It divides the program into small sections to construct and test, so that errors can be easily located and corrected after they occur, and the interface can be tested more thoroughly. Therefore, the incremental integration test method is adopted in the digital-based multimedia information management system. When testing, the mixed method is used for testing. The subsystem with write operation in this software structure uses the top-down method, and the subsystem with read operation in this software is organized and tested from the bottom up to the root node module.

In order to ensure that the system has good flexibility and easy expansion during use, the following design is



adopted in the design and development of the system in Figure 5: the system provides enough preset functions. Once new functions are added, we try not to program them, realize the expansion of functions, and add new functions through programming, as long as the interface can be used to expand and upgrade the system without modifying the existing functional modules; the sequence adjustment of each link of the process processing system is particularly flexible. In this multimedia information management system based on digital campus, according to the input, output conditions and logical structure of this system module, the test cases of white-box testing are the main, and the test cases of black-box testing are supplemented to identify unreasonable input or output in Table 2.

The authenticated user opens the browser, enters the system address, and enters the system login main interface. The user will initiate work orders, process work orders, and review work according to the permissions. The process administrator can also set process parameters, and the system administrator can also perform system management work such as system parameter setting, organizational adjustment, or system security work such as system backup. After logging in to the system, a user with relevant role permissions can select “Submit Work Order” and click “Create” to create a “Report Work Order.” That is, we assign a unique work order serial number to the “report work order,” and send a prompt message to the relevant processing personnel through the “message notification” module.

**4.3. Green TFP Simulation.** Therefore, the nonstationary economic variables are stabilized through differential processing, and the software running results are shown below, and the data after differential processing are stable. The  $P$ -values for LMLAG (lag test) and LMERR (error test) are 0.016 and 0.027, both of which passed the 5% significance level test, but LMLAG was more significant than LMERR. The  $P$ -values of LMLAG and R-LMERR were 0.006 and 0.403, respectively. R-LMLAG passed the 1% significance level test, while R-LMERR failed the statistical test. Therefore, the choice of SLM will be more in line with the model requirements, and the test shows that the model should use fixed effects for regression analysis. Based on the implementation method and whether to pay attention to the level of the internal structure of the software, it can be divided into three different types. Among them, white-box testing is to design test cases for the logical structure of the program and use logical coverage to measure the integrity of the test; black-box testing, also known as functional testing, is to test the internal structure of the program without knowing it.

Figure 6 uses the panel data from 2016 to 2020 and selects 9 indicators from 6 aspects as exogenous control variables. The vertical axis is set to a fixed maximum value of 1.1 and a fixed minimum value of 0.8, and the scale units are both 0.05. From the perspective of interprovincial green total point productivity, the regional distribution of green total point productivity index under the influence of comprehensive environmental factors shows a trend: the eastern provinces are the best, the central areas are also relatively

TABLE 2: Green total factor production algorithm.

Production algorithm codes	Green total factor information
#Include <iostream>	As of the system $a^2 + b^2$
#Include <math.h>	Program them $i - j$
#Include <time.h>	Following in the design
Int flavorsbox(flavors goods[]);	In order to $1 + i + j$
Int n, int cpu_num, int mem	Ensure that $\beta \log Es(i)$
Goods[], int n, int cpu_num	$\max(t, t - 1)$
Void distribution(flavors flavors[])	Try not to $CO(x, y)$
Psypsnum = flavorsbox(f, ecs.mem);	Design is adopted
Lavors, totalprenum, ecs.cpu	$i - 1 - x$ has good flexibility
Flavorsbox(flavors, totalprenum,	The system and easy $t(i - 1)$
Psypsnum = 56, 128);	Once new functions are added
Int flavorsbox(flavors, int mem)//	Preset functions $x(t)$

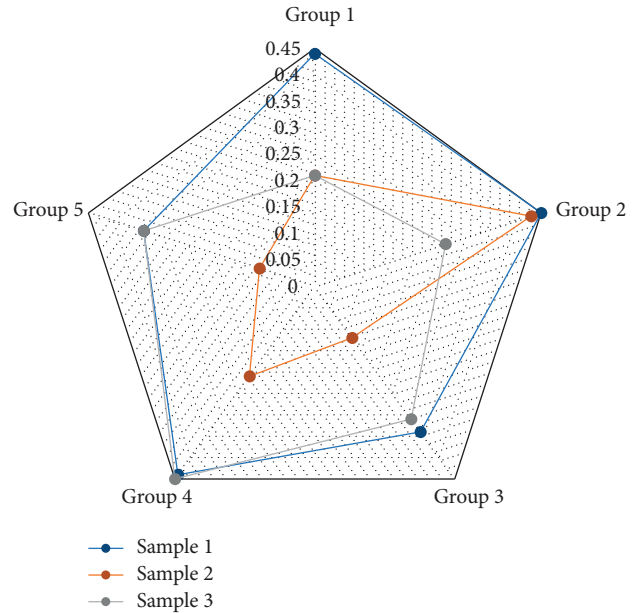


FIGURE 6: Fixed-effects simulation test results.

good, and the western provinces are the worst. This may be because the central and western provinces have developed some traditional heavy industries such as coal, iron, and steel and chemical industries, which have caused some environmental pollution effects and urgently need to transform into green industries. The second chapter mainly introduces the theoretical basis and research review. Mainly based on the research of relevant domestic and foreign experts and scholars, drawing on the research content and ideas of well-known literature summarizes the current measurement methods and influencing factors of green total factor productivity, and obtains the mechanism and mechanism, which provides a theoretical basis for the entire article.

**4.4. Example of Application and Analysis.** The economic activities between them have significant spatial autocorrelation, which means that a region achieves positive growth of GTFP, which will drive the GTFP improvement of adjacent

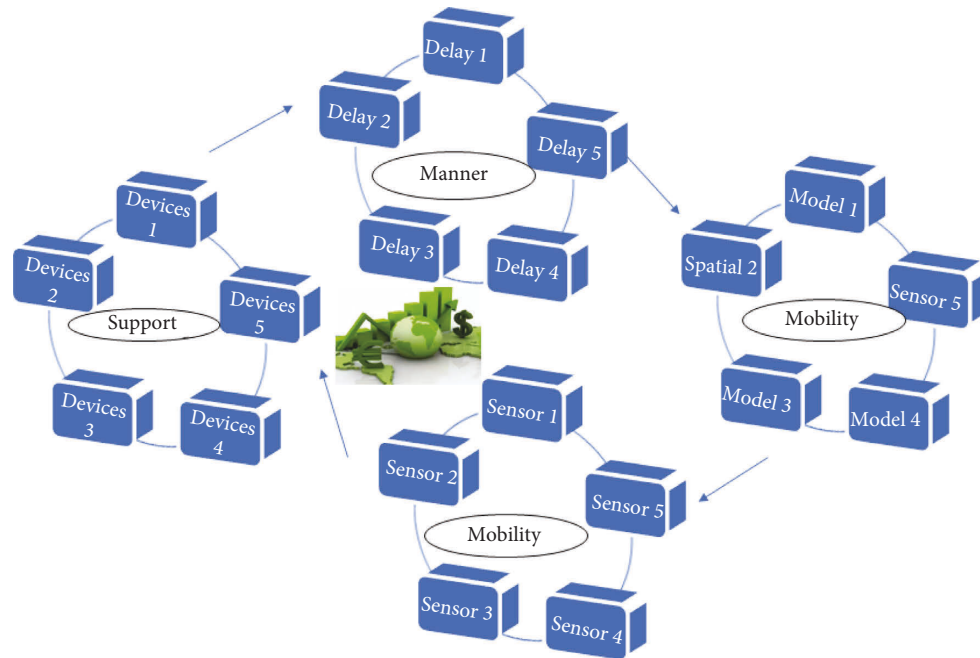


FIGURE 7: General metering topology for spatial factors.

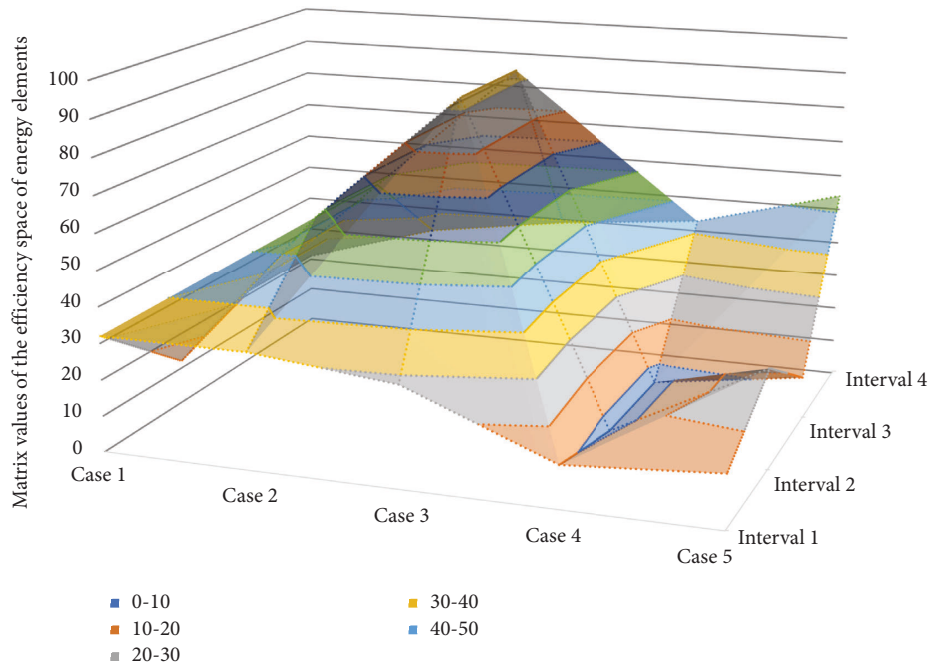


FIGURE 8: The allocation efficiency space matrix of energy elements.

regions through the “trickle-down effect” radiation. In the actual development of software, the software testing stage is of great significance, which can well test the software functions. By testing the software, the final review of software requirements analysis, design specifications, and coding can be well achieved to ensure that the software design is consistent with the requirements. The idea of linear programming is to construct a standard production frontier

by setting decision-making units and then use the degree of deviation of the selected research decision-making units from the relative frontier to judge the effectiveness.

When the spatial econometric model in Figure 7 uses the geographic distance spatial matrix and the comprehensive spatial weighting matrix of economic scale and geographic distance, the estimated results of the robustness test are basically consistent with the empirical research results. The

biggest difference lies in the estimated coefficients of some variables, and the spatial autocorrelation estimation coefficient and its significance level have been reduced or improved to different degrees. In order to further test the robustness of the model estimation results, the geographic distance spatial weight matrix and the economic scale and geographic distance re-examine the above empirical research results.

The chapter mainly introduces the empirical analysis of its specific influencing factors, which is also the core part of this article. With the support of data, building a model, and using appropriate indicators, a detailed analysis of the effects of different influencing factors is carried out, so as to provide the supporting role of quantitative research for the article, and echo the conclusions and suggestions in the following paragraphs. For the indicator, it represents the upgrading of the technical level, which will lead to the expansion of production efficiency, and is related to the possibility of production. If the value is greater than 1, it indicates that the technology has been upgraded and improved, while the value is less than 1, indicating that the technology is backward and needs to be improved.

Before performing differential GMM estimation on the model in Figure 8, Sargan and Arellano tests were performed first. The regression results show that  $a = 36.07975$ ,  $t$  value is 32.5, and  $P$  value is 0.006, indicating that the coal-dominated energy structure has a hindering effect on the growth of total point productivity after considering environmental constraints. When its value is greater than 1, it means that the factor has improved and productivity has improved; when its value is less than 1, it means that GTFP has decreased compared with the previous year, and productivity has declined. For the factor, it represents the comprehensive economic and social benefits.

The cointegration test is used to analyze the relationship between variables. The degree of correlation and the rationality of the model also need to be judged by the cointegration test to a certain extent, especially when the trend effect of the time series data itself is significant, the original model is often constructed reasonably through the cointegration test, we test the residual sequence to determine whether there is a co-integration relationship between variables. The explained variable green total point productivity and the core explanatory variable are both at the 1% significant level, rejecting the null hypothesis that there is a unit root, and other control variables at 1%, 5%, and 1%.

## 5. Conclusion

This paper constructs an impact model of green total point productivity, based on the concept of total point productivity index of energy and environmental factors, and discusses the feasibility of using energy and environmental total point productivity to represent the transformation performance of regional economic development. Second, it introduces the method of total point productivity and the measurement method of the transformation performance of the regional economic development mode in this paper. Considering the continuity and availability of data, this

paper selects the balance of loans from 21 major energy conservation and environmental protection projects multiplied by the proportion of the balance of institutions in different regions as a positive indicator. There is a certain influence between the performance of the expected results and the explanatory variables, and the core of the contrast between them can be divided into positive and negative influences. During the survey period of the sample, the national GTFP showed an overall growth trend, showing obvious periodic characteristics, with a rate of 2.4%. Among them, the contribution of green technology efficiency is 0.7%, while the contribution of green technology progress is 3.1%. Since the growth rate is greater than the reduction of green technology efficiency, the overall performance is the growth of green productivity. Among them, it is extremely important to pay attention to the development of the ecological environment. Ecological and economic symbiosis and complementary, coordinated development is the only way to achieve economic sustainability in the future. Finally, according to the results of this paper, combined with the problems existing in the current economic transformation process in the region, a series of targeted policy recommendations are put forward, in order to make valuable contributions to the development of regional green economy.

## Data Availability

The data used to support the findings of this study can be obtained from the corresponding author upon request.

## Conflicts of Interest

The author declares that there are no conflicts of interest or personal relationships that could have appeared to influence the work reported in this paper.

## Acknowledgments

This work was supported by Shanxi University.

## References

- [1] S. Zhong, J. Li, and X. Guo, "Analysis on the green total factor productivity of pig breeding in China: evidence from a meta-frontier approach," *PLoS One*, vol. 17, no. 6, Article ID e0270549, 2022.
- [2] B. Lin and M. Xu, "Exploring the green total factor productivity of China's metallurgical industry under carbon tax: a perspective on factor substitution," *Journal of Cleaner Production*, vol. 233, pp. 1322–1333, 2019.
- [3] D. Yu, X. Li, J. Yu, and H. Li, "The impact of the spatial agglomeration of foreign direct investment on green total factor productivity of Chinese cities," *Journal of Environmental Management*, vol. 290, Article ID 112666, 2021.
- [4] Y. Jiang, H. Wang, and Z. Liu, "The impact of the free trade zone on green total factor productivity — evidence from the shanghai pilot free trade zone," *Energy Policy*, vol. 148, Article ID 112000, 2021.
- [5] H. Chen, W. Guo, X. Feng et al., "The impact of low-carbon city pilot policy on the total factor productivity of listed

- enterprises in China,” *Resources, Conservation and Recycling*, vol. 169, Article ID 105457, 2021.
- [6] H. Wang, H. Cui, and Q. Zhao, “Effect of green technology innovation on green total factor productivity in China: evidence from spatial durbin model analysis,” *Journal of Cleaner Production*, vol. 288, Article ID 125624, 2021.
- [7] Y. Feng, X. Wang, Z. Liang, S. Hu, Y. Xie, and G. Wu, “Effects of emission trading system on green total factor productivity in China: empirical evidence from a quasi-natural experiment,” *Journal of Cleaner Production*, vol. 294, Article ID 126262, 2021.
- [8] M. Wang, M. Xu, and S. Ma, “The effect of the spatial heterogeneity of human capital structure on regional green total factor productivity,” *Structural Change and Economic Dynamics*, vol. 59, pp. 427–441, 2021.
- [9] C. C. Lee and C. C. Lee, “How does green finance affect green total point productivity? Evidence from China[.],” *Energy Economics*, vol. 107, Article ID 105863, 2022.
- [10] B. Lin and Z. Chen, “Does factor market distortion inhibit the green total point productivity in China?” *Journal of Cleaner Production*, vol. 197, pp. 25–33, 2018.
- [11] S. Qiu, Z. Wang, and S. Liu, “The policy outcomes of low-carbon city construction on urban green development: evidence from a quasi-natural experiment conducted in China,” *Sustainable Cities and Society*, vol. 66, Article ID 102699, 2021.
- [12] X. Cao, M. Deng, and H. Li, “How does e-commerce city pilot improve green total point productivity? Evidence from 230 cities in China,” *Journal of Environmental Management*, vol. 289, Article ID 112520, 2021.
- [13] J. Cheng, J. Yi, S. Dai, and Y. Xiong, “Can low-carbon city construction facilitate green growth? Evidence from China’s pilot low-carbon city initiative,” *Journal of Cleaner Production*, vol. 231, pp. 1158–1170, 2019.
- [14] X. Xiang, G. Yang, and H. Sun, “The impact of the digital economy on low-carbon, inclusive growth: promoting or restraining,” *Sustainability*, vol. 14, no. 12, p. 7187, 2022.
- [15] X. Shi and L. Li, “Green total factor productivity and its decomposition of Chinese manufacturing based on the MML index:2003–2015,” *Journal of Cleaner Production*, vol. 222, pp. 998–1008, 2019.
- [16] G. Li, D. Gao, and Y. Li, “Dynamic environmental regulation threshold effect of technical progress on green total factor energy efficiency: evidence from China,” *Environmental Science and Pollution Research*, vol. 29, no. 6, pp. 8804–8815, 2022.
- [17] C. Chen, Q. Lan, M. Gao, and Y. Sun, “Green total factor productivity growth and its determinants in China’s industrial economy,” *Sustainability*, vol. 10, no. 4, p. 1052, 2018.
- [18] B. Hou, B. Wang, M. Du, and N. Zhang, “Does the SO2 emissions trading scheme encourage green total point productivity? An empirical assessment on China’s cities,” *Environmental Science and Pollution Research*, vol. 27, no. 6, pp. 6375–6388, 2020.
- [19] S. Z. Zafar, Q. Zhilin, H. Malik et al., “Spatial spillover effects of technological innovation on total factor energy efficiency: taking government environment regulations into account for three continents,” *Business Process Management Journal*, 2021.
- [20] M. Wang and C. Feng, “Regional total-factor productivity and environmental governance efficiency of China’s industrial sectors: a two-stage network-based super DEA approach,” *Journal of Cleaner Production*, vol. 273, Article ID 123110, 2020.
- [21] C. Feng, J. B. Huang, and M. Wang, “Analysis of green total-factor productivity in China’s regional metal industry: a meta-frontier approach,” *Resources Policy*, vol. 58, pp. 219–229, 2018.
- [22] H. Jiang, P. Jiang, D. Wang, and J. Wu, “Can smart city construction facilitate green total point productivity? A quasi-natural experiment based on China’s pilot smart city,” *Sustainable Cities and Society*, vol. 69, Article ID 102809, 2021.
- [23] T. Li, D. Han, Y. Ding, and Z. Shi, “How does the development of the internet affect green total point productivity? Evidence from China,” *IEEE Access*, vol. 8, Article ID 216477, 2020.
- [24] C. Liu, Z. Zhou, Q. Liu, R. Xie, and X. Zeng, “Can a low-carbon development path achieve win-win development: evidence from China’s low-carbon pilot policy,” *Mitigation and Adaptation Strategies for Global Change*, vol. 25, no. 7, pp. 1199–1219, 2020.

## Research Article

# Normality Test for Influence Function of Mining Surface Subsidence Based on Network Observation Station

Pengyu Li,<sup>1</sup> Zhenqi Hu ,<sup>1,2</sup> Yaokun Fu,<sup>1</sup> Gensheng Li,<sup>3</sup> Jiaxin Guo,<sup>1</sup> and Dongzhu Yuan<sup>1</sup>

<sup>1</sup>*Institute of Land Reclamation and Ecological Restoration, China University of Mining and Technology (Beijing), Beijing 100083, China*

<sup>2</sup>*School of Environment Science and Spatial Informatics, China University of Mining and Technology, Xuzhou 221116, China*

<sup>3</sup>*School of Public Policy and Management, China University of Mining and Technology, Xuzhou 221116, China*

Correspondence should be addressed to Zhenqi Hu; [huzq@cumtb.edu.cn](mailto:huzq@cumtb.edu.cn)

Received 5 June 2022; Revised 3 August 2022; Accepted 9 August 2022; Published 5 September 2022

Academic Editor: Punit Gupta

Copyright © 2022 Pengyu Li et al. This is an open access article distributed under the Creative Commons Attribution License, which permits unrestricted use, distribution, and reproduction in any medium, provided the original work is properly cited.

Coal is the primary energy source in China, while underground mining is the mainstream way of coal mining. By triggering surface movement and deformation, underground mining can cause damage to arable land, buildings, roads, and so on, which is detrimental to the ecological environment in the mining area. In order to assess the severity of damage caused by this to the ground buildings and ecological environment in the mining area, it is necessary to predict mining-induced surface subsidence before the mining activities are carried out. Currently, the most used prediction method is the Probability Integral Method. It is based on probabilistic theory to mathematically demonstrate that the surface downwelling caused by underground extraction conforms to normal distribution. However, there is a lack of validation with measured subsidence basin data. Since the 1960s, China has been paying increased attention to the study of mining subsidence. However, there are still few network stations built across China to monitor subsidence basin. Herein, SPSS software is applied to re-analyze these valuable historical data. By analyzing the observation results and comparing them with the calculation results as obtained by using the probability integral method, it can be found out that the surface subsidence in the center of the subsidence basin conforms to normal distribution, not the subsidence at the edge of the subsidence basin. Therefore, it is inevitable for errors to occur at the edge of the subsidence basin when the normal distribution function is used as the mining influence function to calculate the surface subsidence. This conclusion is expected to provide practical reference for the prediction of surface subsidence in coal mines, and this experience can be extended to the mining of other solid minerals.

## 1. Introduction

Although China has been putting much efforts into the development and utilization of renewable energy [1, 2], coal remains the dominant source of energy [3]. In 2020, the national raw coal production in China amounted to 3.9 billion tons, accounting for 47.3% of the world's total, to which underground mining contributed as high as 85%. Nowadays, China has the highest proportion of coal production and underground mining in the world [4–6]. In order to evaluate the severity of damage caused by mining to ground buildings and ecological environment in the mining area, it is necessary to assess the risk of surface movement and deformation before mining gets underway. So far, the

research on surface subsidence in coal mines has been conducted for more than 100 years [7]. There are a wide variety of empirical function models proposed in plenty of studies for specific geological and mining conditions based on the data collected by linear observation stations, such as negative exponential function, hyperbolic function, trigonometric function, etc. [8–11]. In the 1950s, Knothe proposed a mining influence function that conformed to normal distribution according to the observation data [12, 13] by treating the surface movement process caused by mining as a random process, Litwiniszyn put forward the random medium theory, arguing that the mining influence function followed normal distribution as well [14]; In 1965, Liu Baochen and Liao Guohua adopted the probability theory to

mathematically demonstrate that the mining influence function conformed to normal distribution, which led to the Probability Integral Method [15–22]. Among the three calculation methods as mentioned above, the Knothe influence function method assumes that the mining influence function conforms to normal distribution based on the observation data. Differently, Litwiniyszyn and Liu Baochen reached their conclusion through the simplified mathematical processing in an ideal state. Despite being based on different assumptions, these three calculation methods lead to the same conclusion, which making people default that the mining influence function obeys the normal distribution. However, there is still a lack of requisite test data.

As the Chinese government attaches increasing significance to addressing the environmental damage caused by surface subsidence [23, 24], it is essential for coal mine productions to comply with national laws and regulations. On the one hand, it is necessary to reduce the surface subsidence caused by mining. On the other hand, it is necessary to take remedial actions in those areas where surface subsidence have occurred. At the same time, in order to reduce the cost of damage compensation incurred by mining for buildings, it is necessary to accurately calculate and evaluate the surface subsidence occurring coal mines. To achieve this purpose, it is essential to evaluate the mining impact function, and to verify the rationality of using the normal distribution as the mining influence function.

To establish whether the subsidence occurring outside the main section of the settlement basin conforms to normal distribution, it is necessary to obtain the measured data for the entire network of observation stations in the basin. In China, surface movement observation did not start until the early 1960s. Up to now, there have been many linear surface movement observation stations built in the mining areas. However, there are still as few as two networks of observation stations built for the Pingdingshan and Chailli coal mines [25]. In this paper, the historical data collected by Chailli coal mine network observation station are reanalyzed in an advanced way to explore the distribution law of mining influence function. According to the research results, a significant calculation error will arise from the practice of taking the normal distribution as the mining influence function at the edge of the subsidence basin. This result will influence the judgment on mining subsidence basin boundary, which affects production safety, land damage, and building damage compensation. The results of this study provide a practical reference for the prediction of surface subsidence in coal mining areas, which can be extended to the mining of other solid minerals.

## 2. Study Area

The study area is located in Xigang Town, Tengzhou City, which is about 22 km away from the city center of Tengzhou, and its location is shown in Figure 1. In terms of climate, the study area shows the characteristics of temperate arid to monsoon continental climate, with an annual average temperature of 13.6°C. The annual precipitation reaches about 793.0 mm, and the average annual evaporation stands

at 1791.7 mm [26, 27]. Geographically, the study area features a lakeside alluvial plain with flat terrain, highly developed road network and dense population. The terrain declines slowly from the northeast to the southwest. Ground elevation decreases from +43.73 m to +35.30 m, with a slope of about 1‰. The soil texture in the area is dominated by clay loam and loam, the sandy clay ratio is moderate, the permeability is high, the soil quality is excellent, the level of soil fertility is satisfactory, and the production capacity is high.

*2.1. General Situation of Working Face.* The strike length of working face 331 is 540 m, and the inclined length is 136 m. Strike longwall comprehensive mechanized coal mining is adopted for the working face, and the full caving method is applied for roof management. On average, the ground elevation is about +40.0 m, and the mining depth is 132 m. The first-time mining was conducted in July, 1973, and the last-time mining took place in October, 1976. According to the histogram analysis of a borehole near the working face, the overlying strata is 132 m deep on average. The quaternary system results from the interactive deposition of the clay layer and sandstone layer, with a thickness of 71 m. Besides, the sandstone layer is 30 m and the mudstone layer is 31 m in thickness. The overlying strata show a medium hardness in the comprehensive lithology. The coal seam is simple in structure and stability in occurrence, with an average thickness of 1.8 m and an average dip angle of 4°. The false roof is 2–7 m mudstone, and the coal seam floor is grayish black sandy mudstone, 9–14 m. Figure 2 shows the comprehensive histogram of the overlying strata.

*2.2. Layout of Observation Stations.* In general, there are two types of surface movement observation stations: linear observation station and network observation station [25]. At present, linear observation stations are most commonly seen in China. Usually, the observation line of linear observation station is comprised of strike line and inclination line, which are perpendicular to each other. In some cases, it is possible to set only one or half observation line. For example, the strike length of the working face is too large, the workload of setting the full strike observation line is high, and the observation time is long. In this case, a common practice is to set half of the strike observation line. In another example, one side of the dip direction is affected by the mining of the adjacent working face, which means only half of the dip observation line can be set. The observation line setting scheme depends on the exact purpose of observation and on-site conditions in the setting area. Its selection is based on the practicalities and principle of obtaining as much reliable data as possible. The layout of several different linear observation stations is shown in Figure 3(a).

In the network observation station, the observation points are arranged into a network, so as to monitor the whole area, half area or quarter area of surface movement and deformation, as shown in Figure 3(b). The layout of surface movement network observation stations is treated as the control network for monitoring the whole subsidence

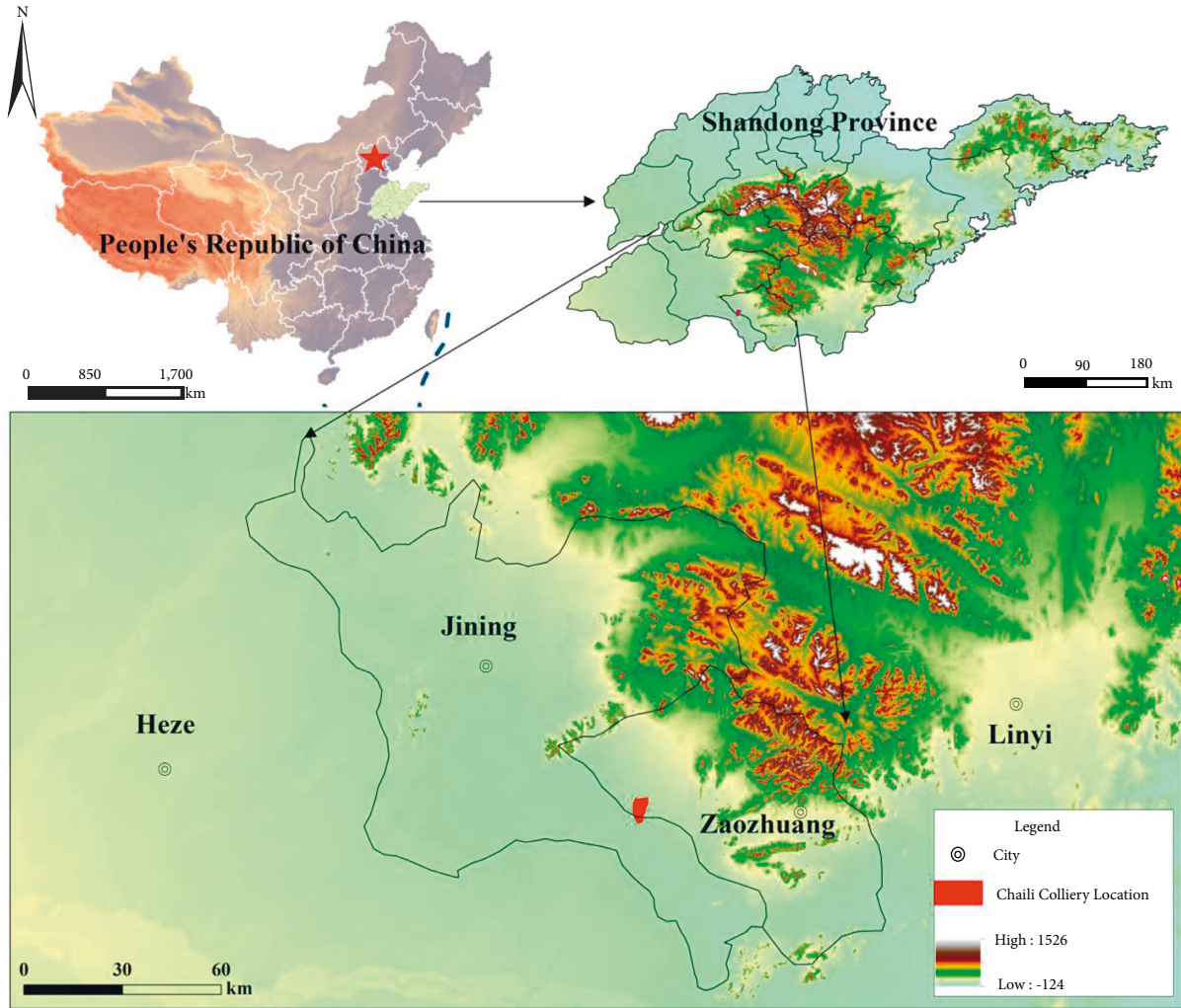


FIGURE 1: Location of the Chaili colliery.

basin to fully show the movement and deformation law of the whole surface movement basin.

The network observation station involved in this study was established on June 15, 1973. After 4 years of observation, the final data of surface subsidence observation were collected. Figure 4 shows the layout of observation station network and embedding of point markers. There are 146 points in total, the distance between two observation stations is 15 m, and there are 20 observation lines, of which 7 are in the strike direction and 13 are in the inclination direction.

After all the points of the observation station are marked, dig pits and bury point markers, which are made of concrete. The top surface of the point mark is sized 250\*250 mm, the height is 1000 mm, the mark center is 520 mm iron bar, and the top is engraved with a cross. Theodolite is used to indicate the direction of the observation line at the time of burying stake, and a steel ruler is used to mark the position on the observation line. After all points are buried, the point number is red painted on the top surface of the stake.

The altitude is measured at the observation stations by using precision leveling instruments and a total of 18

leveling measurements. Also, data processing is carried out through the subsidence calculation formula. The formula used to calculate subsidence for point  $n$  during the  $m$ th time observation is expressed as

$$W_n = H_{n0} - H_{nm}, \quad (1)$$

where  $W_n$  represents the subsidence value of point  $n$ .  $H_{n0}, H_{nm}$  refer to the altitudes at the first and the  $m$ -th observation, respectively.

The final subsidence values at each point for the net observation lines are listed in Table 1.

### 3. Results

**3.1. Test Results of the Normal Subsidence of the Observation Line.** The commonly used normal test methods can be divided into three categories in general [28]. The first one is graphical representation, which is examined mainly using probability plots (P-P plots) and quantile plots (Q-Q plots). The second one is the kurtosis-skewness joint test. Kurtosis indicates how flattened or steep the top of the frequency

Lithology	Layer Thickness (m)	Layer Depth (m)	Columnar
Clay	5.20	5.20	
Fine-grained sandstone	1.60	6.80	
Clay	2.40	9.20	
Siltstone	1.00	10.20	
Clay	4.80	15.00	
Sandy mudstone	1.40	16.40	
Clay	5.50	21.90	
Medium grained sandstone	1.40	23.30	
Clay	1.60	24.90	
Fine-grained sandstone	0.90	25.80	
Clay	2.80	28.60	
Core-grained sandstone	5.40	34.00	
Clay	1.60	35.60	
Sandy mudstone	2.60	38.20	
Clay	3.20	41.40	
Fine-grained sandstone	4.10	45.50	
Clay	6.90	52.40	
Core-grained sandstone	2.00	54.40	
Clay	4.20	58.60	
Sandy mudstone	0.80	59.40	
Clay	8.50	67.90	
Gravel	3.10	71.00	
Sand shale	31.00	102.00	
Siltstone	30.00	132.00	
Coal	1.80		
Siltstone	0.40		
Core-grained sandstone	14.20		

FIGURE 2: Comprehensive histogram of overburden of 331 working face.

distribution curve is for the test sample, and skewness is used to indicate the degree to which a distribution deviates from symmetry. The last one is the Kolmogorov Smirnov test (K-S normality test). The latter two are more reliable than graphical representation. Therefore, the kurtosis-skewness joint test and K-S normality test are adopted in this study to verify the normality of surface subsidence with the assistance of SPSS software.

3.1.1. Kurtosis-Skewness Normality Test. The kurtosis and skewness coefficient values of the data are used to determine whether the samples conform to normal distribution or not. If the absolute values of kurtosis coefficient  $Z_K$  and skewness coefficient  $Z_S$  fall below 1.96 simultaneously, the distribution of sample data is considered to conform to normal distribution. If either or both the absolute values of  $Z_K$  or  $Z_S$  exceed 1.96, the sample data are considered not to conform to normal distribution [29]. The formulas used to calculate  $Z_K$  and  $Z_S$  are expressed as follows:

$$Z_K = \frac{K - 0}{S_K}, Z_S = \frac{S - 0}{S_S}. \tag{2}$$

Where  $S_K$  and  $S_S$  represent standard error for kurtosis coefficient and skewness coefficient, respectively.

Table 2 depicts the calculation results obtained from the normality test on the subsidence kurtosis and the skewness of the observation lines in the inclination direction. It is found out that the absolute kurtosis coefficient and skewness coefficient values are less than 1.96 during 12 observation lines, the sedimentation profiles of which conform to normal distribution. However, the absolute values of kurtosis coefficient and skewness coefficient of the A13-G13 observation line exceed 1.96, which means the subsidence of this observation line does not follow normal distribution.

Table 3 presents the calculation results obtained from the normality test on the subsidence kurtosis and the skewness of the strike parallel observation lines. The absolute values of the kurtosis coefficient and the skewness coefficient of the seven strike parallel observation lines fall below 1.96, which suggests that the subsidence distribution of the strike parallel observation lines conforms to normal distribution.

3.1.2. K-S Normal Test. The rationale of the K-S normality test is described as follows. To calculate the theoretical cumulative probability value  $F(x)$  of the sample data, it is assumed that normal distribution is followed. Then, the actual cumulative probability value  $S(x)$  of the sample is calculated. The D-value  $D(x)$  between them is calculated as follows:

$$D = \max(|S(x_i) - F(x_i)|). \tag{3}$$

$D$  must be corrected into

$$D = \max(\max(|S(x_i) - F(x_i)|), \max(|S(x_{i-1}) - F(x_{i-1})|)). \tag{4}$$

SPSS software is directly applicable to calculate the probability value ( $p$ -value). As for whether the sample value conforms to the normal distribution, it is determined by whether the significance level is exceeded (0.05 in general) [30]. If the probability value falls below 0.05, it is considered that the test sample does not conform to normal distribution. If the value reaches above 0.05, the test sample is considered to conform to normal distribution.

Table 4 lists the results of normality test conducted on the inclination parallel observation lines. It can be seen clearly from the table that there are 12 observation lines



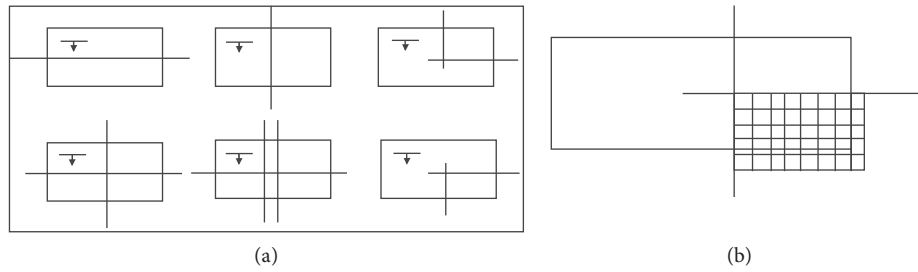


FIGURE 3: Diagrammatic sketch of linear and network observation stations. (a) are linear observation stations, Observation lines are the main section observation line; (b) is a network observation station.

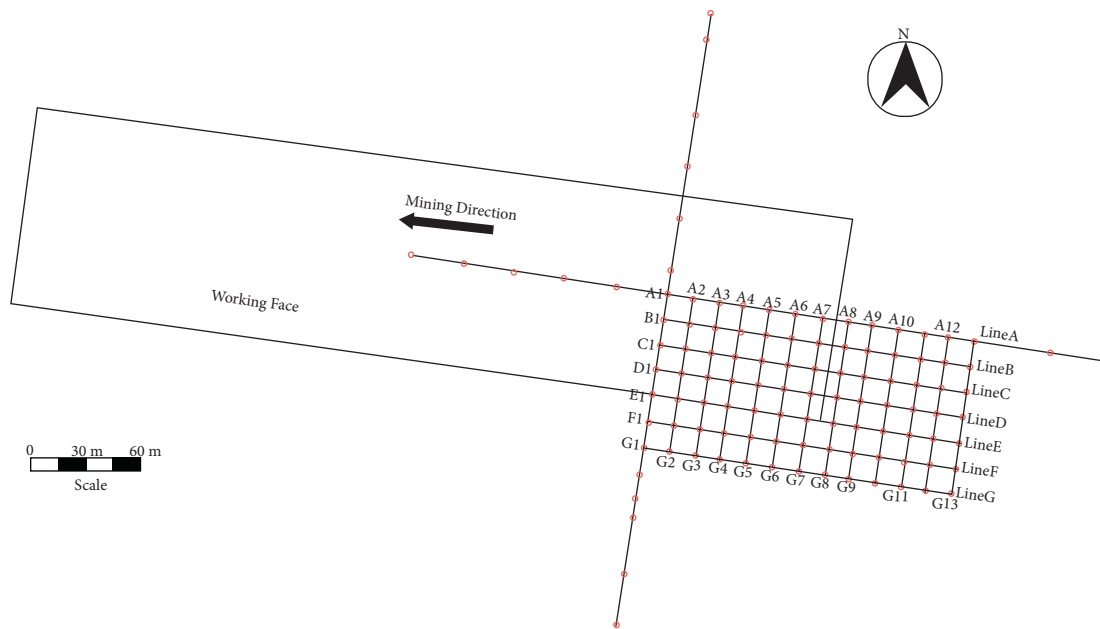


FIGURE 4: Layout of the network of observation stations.

TABLE 1: Final subsidence value of network observation station.

Subsidence value/mm	Line A	Line B	Line C	Line D	Line E	Line F	Line G
Line A1–G1	-1318.00	-1263.00	-1087.00	-713.00	-366.00	-162.00	-78.00
Line A2–G2	-1265.28	-1326.15	-1065.26	-698.74	-355.02	-160.38	-70.98
Line A3–G3	-1225.74	-1212.48	-1054.39	-698.74	-338.34	-184.68	-68.64
Line A4–G4	-1212.56	-1199.85	-1054.39	-698.74	-344.04	-163.62	-62.40
Line A5–G5	-1146.66	-1136.7	-967.43	-641.70	-286.47	-118.26	-53.04
Line A6–G6	-948.96	-896.73	-739.16	-456.32	-208.62	-86.33	-45.24
Line A7–G7	-553.56	-505.20	-391.32	-235.29	-139.08	-58.32	-22.62
Line A8–G8	-276.78	-239.97	-195.66	-114.08	-62.22	-43.74	-16.27
Line A9–G9	-92.26	-88.41	-76.09	-49.91	-36.60	-30.78	-14.04
Line A10–G10	-52.72	-50.52	-40.33	-28.52	-22.37	-19.44	-13.66
Line A11–G11	-26.36	-23.73	-21.74	-18.23	-14.64	-13.28	-10.14
Line A12–G12	-13.18	-12.63	-10.22	-14.26	-12.43	-11.34	-8.37
Line A13–G13	-11.23	-9.88	-21.74	-12.67	-10.47	-9.76	-10.14

with a greater  $p$ -value than 0.05. That is to say, the subsidence of 12 inclination direction observation lines conforms to normal distribution. Only the  $p$ -value of the Line A13-G13 is less than 0.05, which suggests that the subsidence of this observation line does not follow normal distribution.

Table 5 shows the results of normality test on the strike parallel observation lines. Since the  $p$ -value of the strike parallel observation lines are significantly higher than 0.05, it is judged that the subsidence distribution of each observation line parallel to the strike of the main section conforms to normal distribution.

TABLE 2: Results of the kurtosis-skewness normality test of the observation lines in the inclination direction.

Observation lines	N	Normal parameter		K	S <sub>K</sub>	Z <sub>K</sub>	S	S <sub>S</sub>	S <sub>K</sub>
		Mean value	Standard deviation						
LineA1-G1	7	-712.429	522.116	0.036	0.794	0.045	-2.171	1.587	1.368
LineA2-G2	7	-705.973	524.506	0.003	0.794	0.005	-2.139	1.587	1.348
Line A3-G3	7	-683.287	492.890	0.075	0.794	0.094	-2.216	1.587	-1.396
Line A4-G4	7	-676.514	492.484	0.101	0.794	0.127	-2.214	1.587	-1.395
Line A5-G5	7	-621.466	474.331	0.056	0.794	0.071	-2.247	1.587	-1.416
Line A6-G6	7	-479.050	387.682	-0.073	0.794	-0.092	-2.180	1.587	-1.374
Line A7-G7	7	-272.199	213.994	-0.211	0.794	-0.266	-1.905	1.587	-1.200
Line A8-G8	7	-135.531	102.435	-0.282	0.794	-0.355	-1.872	1.587	-1.180
Line A9-G9	7	-53.821	32.265	-0.003	0.794	-0.004	-2.020	1.587	-1.273
Line A10-G10	7	-32.509	15.486	-0.286	0.794	-0.360	-1.813	1.587	-1.142
Line A11-G11	7	-18.303	5.937	-0.004	0.794	-0.005	-1.464	1.587	-0.922
Line A12-G12	7	-11.776	1.980	0.732	0.794	0.922	0.166	1.587	0.105
Line A13-G13	7	-12.270	4.296	-2.365	0.794	-2.979	5.767	1.587	3.634

TABLE 3: Results of the kurtosis-skewness normality test of the observation lines in the strike direction.

Observation lines	N	Normal parameter		K	S <sub>K</sub>	Z <sub>K</sub>	S	S <sub>S</sub>	S <sub>K</sub>
		Mean value	Standard deviation						
Line I	13	-626.407	564.244	-0.065	0.616	-0.106	-2.097	1.191	-1.761
Line A	13	-612.712	562.983	-0.115	0.616	-0.187	-2.081	1.191	-1.748
Line B	13	-517.287	478.136	-0.142	0.616	-0.231	-2.100	1.191	-1.7638
Line C	13	-336.938	314.855	-0.190	0.616	-0.308	-2.091	1.191	-1.7568
Line D	13	-168.946	150.802	-0.224	0.616	-0.364	-1.965	1.191	-1.6508
Line E	13	-81.687	67.439	-0.390	0.616	-0.634	-1.684	1.191	-1.414
Line F	13	-36.426	27.040	-0.384	0.616	-0.623	-1.781	1.191	-1.495

TABLE 4: Results of the K-S normality test of each line in the inclination direction.

Observation lines	N	Normal parameter		Statistic	p
		Mean	Standard deviation		
Line A1-G1	7	-712.429	522.116	0.508	0.959
Line A2-G2	7	-705.973	524.506	0.481	0.975
Line A3-G3	7	-683.287	492.890	0.537	0.936
Line A4-G4	7	-676.514	492.484	0.548	0.925
Line A5-G5	7	-621.466	474.331	0.518	0.951
Line A6-G6	7	-479.050	387.682	0.492	0.969
Line A7-G7	7	-272.199	213.994	0.428	0.993
Line A8-G8	7	-135.531	102.435	0.507	0.960
Line A9-G9	7	-53.821	32.265	0.486	0.972
Line A10-G10	7	-32.509	15.486	0.458	0.985
Line A11-G11	7	-18.303	5.937	0.423	0.994
Line A12-G12	7	-11.776	1.980	0.532	0.940
Line A13-G13	7	-12.270	4.296	0.847	0.047

There is consistence shown in the conclusions between the normal test of the kurtosis-skewness and the K-S normal test. Among the 20 observation lines tested, only observation line A13-G13, which is the farthest away from the subsidence basin center, does not conform to normal distribution. However, the subsidence of the other strike and inclination parallel observation lines conforms to normal distribution, i.e., the subsidence in the surface of the mining area conforms to normal distribution overall.

3.2. Calculation Error of the Surface Subsidence at Any Point. Based on the Knothe influence function method [13], Figure 5 is built to show the working face and the calculation coordinate system of the horizontal coal seam, where  $l$  represents the calculation length of the trend;  $L$  indicates the calculation width of the tendency; and  $A(x, y)$  denotes any point on the surface.

Since the probable directions of  $x$  and  $y$  are independent of each other, the subsidence at  $A(x, y)$  is expressed as follows:

$$\begin{aligned}
 W(x, y)_A &= W_{\max} \iint_F f(x, y) dF \\
 &= W_{\max} \iint_F f(x) f(y) dx dy,
 \end{aligned} \tag{5}$$

$$f(x) = \frac{1}{r} e^{-\frac{x^2}{r^2}},$$

$$f(y) = \frac{1}{r} e^{-\frac{y^2}{r^2}},$$

where  $W_{\max}$  represents the maximum surface subsidence;  $r$  indicates the main mining influence radius;  $f(x)$ ,  $f(y)$  denotes the Knothe influence function, which follows a  $N(0, \sigma^2)$  distribution, and  $\sigma = r/\sqrt{2\pi}$ .

$O$  represents the coordinate origin in Figure 5, so that the subsidence at  $A(x, y)$  is expressed as follows:

TABLE 5: Results of the K-S normality tests of each observation line in the strike direction.

Observation lines	N	Normal parameter		Statistic	p
		Mean value	Standard deviation		
Line I	13	-626.407	564.244	0.767	0.599
Line A	13	-612.712	562.983	0.753	0.623
Line B	13	-517.287	478.136	0.762	0.607
Line C	13	-336.938	314.855	0.800	0.543
Line D	13	-168.946	150.802	0.800	0.544
Line E	13	-81.687	67.439	0.671	0.759
Line F	13	-36.426	27.040	0.842	0.477

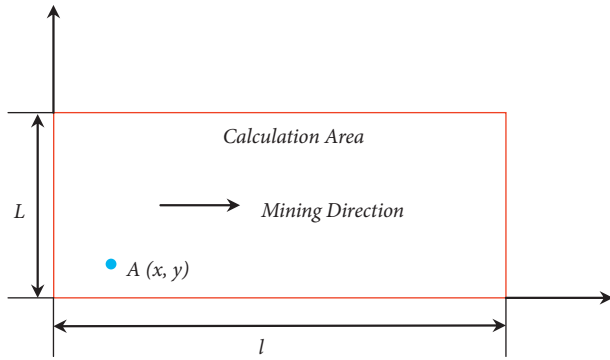


FIGURE 5: Calculation coordinate system.

$$\begin{aligned}
 W(x, y)_A &= \frac{W_{\max}}{r^2} \int_{-x}^{l-x} e^{-\pi \left(\frac{x}{r}\right)^2} dx \int_{-y}^{l-y} e^{-\pi \left(\frac{y}{r}\right)^2} dy \\
 &= W_{\max} \times \frac{1}{2} \left\{ \left[ \operatorname{erf} \left( \sqrt{\pi} \frac{x}{r} \right) + 1 \right] \right. \\
 &\quad \left. - \left[ \operatorname{erf} \left( \sqrt{\pi} \frac{x-l}{r} \right) + 1 \right] \right\} \times \frac{1}{2} \left\{ \left[ \operatorname{erf} \left( \sqrt{\pi} \frac{y}{r} \right) + 1 \right] \right. \\
 &\quad \left. - \left[ \operatorname{erf} \left( \sqrt{\pi} \frac{y-L}{r} \right) + 1 \right] \right\} \\
 &= W_{\max} C_{(x)} C_{(y)},
 \end{aligned} \quad (6)$$

where  $C_{(x)}$ ,  $C_{(y)}$  refer to the subsidence distribution coefficients of the trend and tendency, respectively.

The working face is a rectangular mining area, the mining length along the strike is  $l = 540m$ , the mining width along the strike is  $L = 136m$ , and the main influence radius of the mining is  $r = 98m$ . The coordinate system is established with the lower left corner of the mining area as the coordinate origin as of the coordinate system (Figure 5): The maximum settlement value of the main section is measured to be  $W_0 = 1318mm$ .

**3.2.1. Prediction Error of the Distribution of the Surface Settlement along the Inclined Observation Lines.** According to the observation data, the settlement coefficient is determined as  $q = 0.73$ , the tangent of the main influence angle is determined as  $\tan \beta = 2.2$ , and the subsidence at any point on the surface is calculated using (6). Figure 6 shows all

the predicted and measured values of the inclination parallel observation lines. It can be found out that the predictions of each observation line in the inclined direction deviate clearly from the actual subsidence curve, with similarity shown only around the maximum subsidence values.

The Root Mean Square Error (RMSE) [31] and the Percent Relative Error (PRE) [32] are adopted to examine how subsidence is accurately and reliably predicted by using the formula for each observation line at any point in the surface. As a numerical measure of prediction accuracy, RMSE refers to the square root of the sum of the squares of the difference between predicted and measured values and the ratio of the number of observations  $n$ . A smaller RMSE value indicates a higher accuracy of prediction [33]. The PRE is advantageous in reflecting the reliability of the predicted formula, with a lower absolute value of PRE indicating a greater reliability.

$$RMSE = \pm \sqrt{\frac{\sum [\Delta\Delta]}{n}} \quad (7)$$

$$PRE = \Delta/L' \times 100\%,$$

where  $\Delta$  is the true error between predicted and measured values and  $L'$  is the measured value.

Table 6 shows the calculation of the RMSE and PRE between the predicted value and the measured value of the surface subsidence along the inclination parallel observation lines. In general, the RMSE of the predicted values of the subsidence for observation lines is high in the inclined direction. However, according to the PRE, the prediction accuracy of the inclined direction observation lines shows a gradual trend of increasing from the center of the subsidence basin to the edge.

**3.2.2. Prediction Error of the Distribution of the Surface Subsidence along the Strike Parallel Observation Lines.** Figure 7 shows the comparison between the predicted and measured values of all the strike parallel observation lines. It can be discovered that the predictions of observation lines A and B at the center of the subsidence basin are relatively close to the measured subsidence curves, despite a significant difference in the observation line subsidence curves toward the edge of the basin.

Table 7 shows the measured and predicted distribution of the surface subsidence along the strike parallel observation lines as well as the RMSE and PRE. To be specific, RMSE is predicted to be the minimum for the A-line subsidence toward the main section. When shifting away from the center line of the subsidence basin, the RMSE for the other observations increases first and then decreases. However, judging from the PRE, the prediction accuracy of the strike line reaches the highest in the center of the basin and it increases gradually when moving away from the center of the subsidence basin.

According to the comparison in subsidence prediction and RMSE between the actual measurement data and the

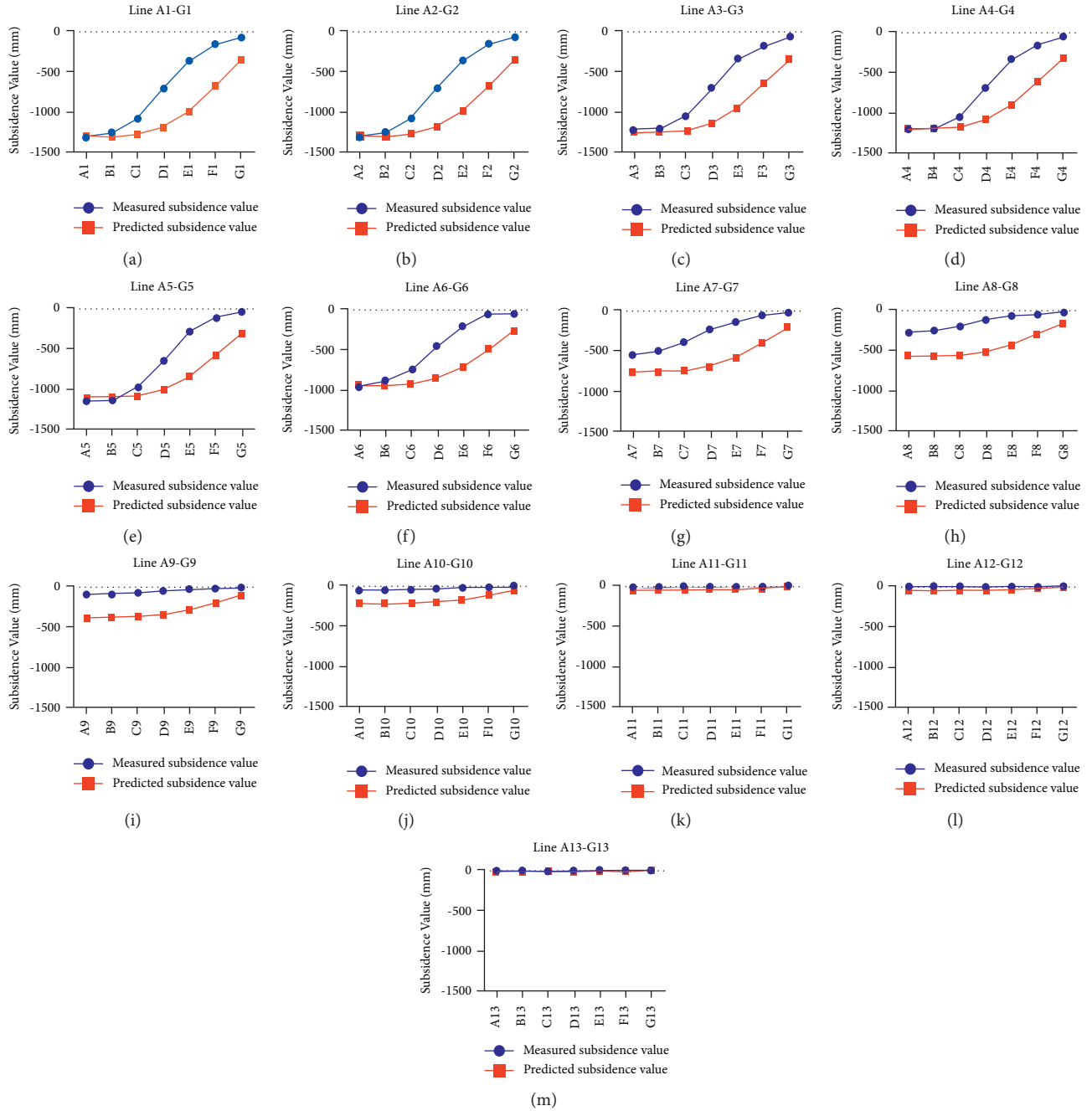


FIGURE 6: The measured and predicted distribution of the surface subsidence along the inclination parallel lines.

TABLE 6: Predicted errors of each line in the inclined direction.

Observation lines	Measured mean value/mm	RMSE of predicted/(mm)	PRE%
Line A1-G1	-712.43	380.34	43.26
Line A2-G2	-705.97	380.71	43.94
Line A3-G3	-673.48	363.14	44.00
Line A4-G4	-676.51	333.54	38.74
Line A5-G5	-621.47	320.15	41.74
Line A6-G6	-479.05	314.97	53.71
Line A7-G7	-272.20	335.76	117.67
Line A8-G8	-135.53	315.56	224.74
Line A9-G9	-53.82	254.37	452.33
Line A10-G10	-32.51	149.32	436.30
Line A11-G11	-18.30	28.95	147.53
Line A12-G12	-11.78	40.40	317.56
Line A13-G13	-12.27	8.27	60.00

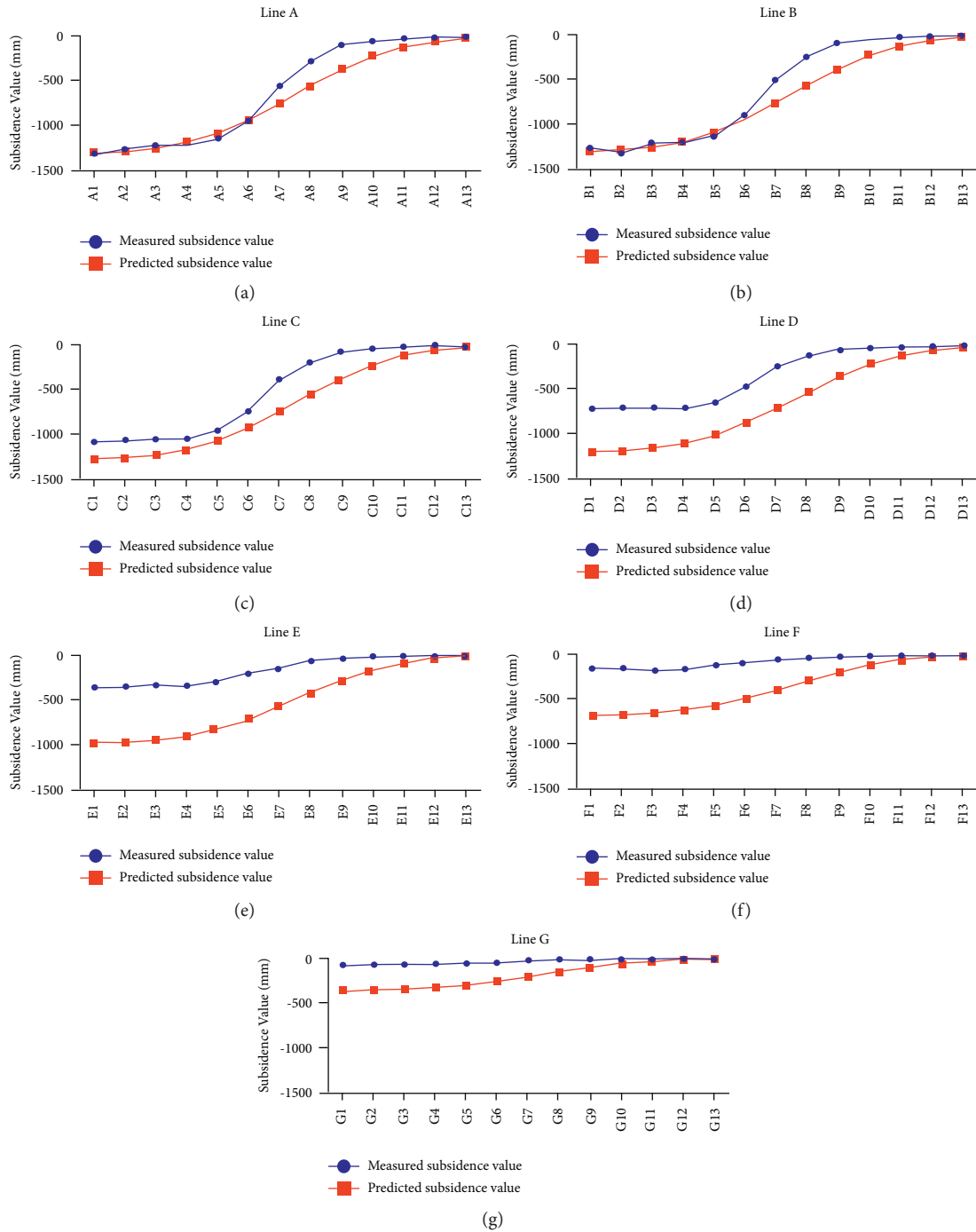


FIGURE 7: The measured and predicted distribution of the surface subsidence along the strike parallel observation lines.

TABLE 7: Predicted relative errors of each line in the strike direction.

Observation line	Measured mean value (mm)	RMSE of predicted (mm)	PRE%
Line A	-626.41	139.55	15.37
Line B	-612.71	153.46	17.72
Line C	-517.29	207.28	34.58
Line D	-336.94	354.16	92.78
Line E	-168.95	436.50	219.78
Line F	-81.69	346.23	353.46
Line G	-36.43	192.14	436.92

prediction result for each observation line, it can be known that the subsidence prediction formula at any point on the surface has lower RMSE and higher prediction accuracy in the central part of the subsidence basin. In the region which is more distant from the center of the subsidence basin, however, the RMSE of the predicted values is larger and the level of prediction accuracy is lower.

## 4. Discussion and Conclusion

*4.1. Discussion.* At present, most of the research focuses on linear observation stations, analyzing only the law of subsidence for the main section of the subsidence basin. Consequently, there is little research on the law of subsidence in other areas of the subsidence basin. In this study, the historical subsidence monitoring data of the network observation station is reanalyzed. According to the research results, the subsidence in the central area of the subsidence basin conforms to normal distribution law, not that on the edge of the subsidence basin. Such a deviation is related to the exact ground structure. The mining depth of the working face in the study area is 132 m, but the thickness of the Quaternary loose layer in the overlying strata is 71 m, which is relatively large. To some extent, this will contribute to the occurrence of surface subsidence [34–36].

As a highly complex mechanical and spatiotemporal process, the surface subsidence caused by mining is attributed to many factors, which in turn affects the distribution law of subsidence. According to the superposition principle of mining influence, mining surface subsidence can be regarded as the superposition of multiple independent unit mining, with each unit mining having limited impact on the overall subsidence. Therefore, the stratum subsidence caused by underground coal seam mining basically conforms to normal distribution. Therefore, it is universally reasonable to apply the normal distribution function as the mining surface subsidence influence function [37, 38].

Due to the exact geological conditions of mining, which affects how surface subsidence develops, the surface subsidence may not fully conform to normal distribution. Therefore, it is necessary to evaluate the geological mining conditions in the first place when the probability integral method based on the normal distribution is adopted. Under exceptional geological conditions, such as the stratum that contains thick topsoil or thick and hard, it is necessary to modify the model parameters of the probability integral method, or introduce other distribution functions and probability integral method into the construction of a combined model for the improvement of prediction accuracy.

## 5. Conclusion

In this paper, the field measurement data of the network observation station are analyzed through statistical methods, so as to explore the law of subsidence in the whole subsidence basin. Furthermore, the following conclusions are drawn.

- (1) By conducting Kurtosis–Skewness normality test and K–S normality test, the subsidence data of each

observation line of network observation are analyzed. On this basis, it is concluded that the surface subsidence caused by coal mining usually conforms to normal distribution, rather than the subsidence of observation line A13–G13 at the edge of subsidence basin. Besides, the subsidence of all other observation lines conforms to normal distribution.

- (2) The prediction equation intended for the calculation of surface settlement at any point is used to predict the settlement along the observation lines of the observation station network. According to the calculation results, the relative error is the least significant for the equation used to predict the surface settlement at any point through the probability integral method. In the strike direction, the PRE is 15.37% for the settlement prediction of the observation line *a*, and the PRE reaches the maximum of 436.92% for the observation line *f*. As the observation line shifts away from the center of the sinking basin, the PRE increases progressively. In the tilt direction, there is a small PRE of the four observation lines A1–G1 to A5–G5 close to the center of the basin, reaching about 40%, which indicates high reliability. Then, as the observation line shifts away from the center of the basin, it gradually increases, with the PRE of the observation line A9–G9 reaching a maximum of 452.33%. Judging from the change of PRE in the comprehensive strike and tilt direction, PRE gradually increases from the center of the basin to the edge of the basin. That is to say, the reliability of probability integral method in predicting the subsidence at any point on the surface diminishes gradually from the center of the basin to the edge of the basin.
- (3) When the surface subsidence prediction method is adopted that is based on normal distribution as the mining influence function, it is necessary to take into account the particularity of geological mining conditions and the possibility of prediction deviation. Due to the limited observation data involved, it is necessary to further explore the law of surface subsidence under extraordinary geological mining conditions.

## Data Availability

Data will be available on request.

## Conflicts of Interest

The authors declare that they have no conflicts of interest.

## Acknowledgments

This research was supported by the National Natural Science Foundation of China (Grant no. 41771542) and the National Public Welfare Industry Research Project (Grant No. 200911015–3). All of the financial support provided is gratefully acknowledged.

## References

- [1] J. Li, S. Chen, Y. Wu et al., "How to make better use of intermittent and variable energy? A review of wind and photovoltaic power consumption in China," *Renewable and Sustainable Energy Reviews*, vol. 137, no. 2020, p. 110626, 2021.
- [2] X. Ruhang, S. Zixin, T. Qingfeng, and Y. Zhuangzhuang, "The cost and marketability of renewable energy after power market reform in China: a review," *Journal of Cleaner Production*, vol. 204, pp. 409–424, 2018.
- [3] Z. Jia and B. Lin, "How to achieve the first step of the carbon-neutrality 2060 target in China: the coal substitution perspective," *Energy*, vol. 233, p. 121179, 2021.
- [4] G. Li, Z. Hu, P. Li, D. Yuan, W. Wang, and K. Yang, "The optimal framework and model to balance underground coal mining and cropland protection in Jining, eastern China," *Resources Policy*, vol. 74, no. April, p. 102307, 2021.
- [5] J. Wang, S. S. Peng, and Y. Li, "State-of-the-art in underground coal mining and automation technology in the United States," *Journal of China Coal Society*, vol. 46, no. 1, pp. 36–45, 2021.
- [6] G. Li, Z. Hu, P. Li et al., "Innovation for sustainable mining: integrated planning of underground coal mining and mine reclamation," *Journal of Cleaner Production*, vol. 351, no. 2021, p. 131522, 2022.
- [7] G. A. H. Die, *Theorie der Bodensenkungen in Kohlengebieten mit besonderer Berücksichtigung der Eisenbahnsenkungen des Ostrau-Karwiner Steinkohlenrevieres*, Springer-Verlag, Berlin, 1913.
- [8] J. Yue, M. Rafal, P. Li, X. Yuan, S. Anton, and Y. Jiang, "Summary and development of mining subsidence theory," *Mental Mine*, vol. 520, pp. 1–7, 2019.
- [9] Y. Jiang, R. Misa, K. Tajduś, A. Sroka, and Y. Jiang, "A new prediction model of surface subsidence with Cauchy distribution in the coal mine of thick topsoil condition," *Archives of Mining Sciences*, vol. 65, no. 1, pp. 147–158, 2020.
- [10] L. Yucheng and D. Huayang, "Hyperbolic function model for predicting the main section surface deformation curve due to approximate horizontal coal seam underground longwall mining," *Journal of China University of Mining and Technology*, vol. 48, no. 3, pp. 676–681, 2019.
- [11] K. Tajduś, A. Sroka, R. Misa, A. Tajduś, and S. Meyer, "Surface deformations caused by the convergence of large underground gas storage facilities," *Energies*, vol. 14, no. 2, p. 402, 2021.
- [12] A. Sroka, S. Knothe, K. Tajduś, and R. Misa, "Point movement trace vs. The range of mining exploitation effects in the rock mass," *Archives of Mining Sciences*, vol. 60, no. 4, pp. 921–929, 2015.
- [13] A. Sroka, R. Misa, and K. Tajduś, "Determination of the horizontal deformation factor for mineral and fluidized deposits exploitation," *Acta Geodynamica et Geomaterialia*, vol. 15, no. 1, pp. 23–26, 2017.
- [14] J. Litwiniszyn, *Stochastic Methods in Mechanics of Granular Bodies*, Springer, Wien, 1974.
- [15] B. Liu and G. Liao, *Basic Law of Surface Movement in Coal Mines*, China Industrial Press, Beijing, China, 1965.
- [16] X. Tan, B. Song, H. Bo, Y. Li, M. Wang, and G. Lu, "Extraction of irregularly shaped coal mining area induced ground subsidence prediction based on probability integral method," *Applied Sciences*, vol. 10, no. 18, pp. 6623–6640, 2020.
- [17] P. Li, D. Peng, Z. Tan, and K. Deng, "Study of probability integration method parameter inversion by the genetic algorithm," *International Journal of Mining Science and Technology*, vol. 27, no. 6, pp. 1073–1079, 2017.
- [18] G. Wang, P. Li, Q. Wu, X. Cui, and Z. Tan, "Numerical simulation of mining-induced damage in adjacent tunnels based on FLAC3D," *Advances in Civil Engineering*, vol. 2021, pp. 1–21, 2021.
- [19] P. Li, L. Yan, and D. Yao, "Study of tunnel damage caused by underground mining deformation: calculation, analysis, and reinforcement," *Advances in Civil Engineering*, vol. 2019, pp. 1–18, 2019.
- [20] H. Li, B. Zhao, G. Guo, J. Zha, and J. Bi, "The influence of an abandoned goaf on surface subsidence in an adjacent working coal face: a prediction method," *Bulletin of Engineering Geology and the Environment*, vol. 77, no. 1, pp. 305–315, 2018.
- [21] Y. Fu, J. Shang, Z. Hu et al., "Ground fracture development and surface fracture evolution in n00 method shallowly buried thick coal seam mining in an arid windy and sandy area: a case study of the ningtiaota mine (China)," *Energies*, vol. 14, pp. 7712–22, 2021.
- [22] Y. Yuan, H. Li, H. Zhang, Y. Zhang, and X. Zhang, "Improving reliability of prediction results of mine surface subsidence of northern pei county for reusing land resources," *Applied Sciences*, vol. 10, no. 23, pp. 8385–8397, 2020.
- [23] P. Li, W. Zhu, and Z. Xie, "Diverse and divergent influences of phenology on herbaceous aboveground biomass across the Tibetan Plateau alpine grasslands," *Ecological Indicators*, vol. 121, p. 107036, 2021.
- [24] G. Li, "Optimal layout of underground coal mining with ground development or protection: a case study of Jining, China," *Resources Policy*, March, vol. 76, , p. 102639, 2022.
- [25] K. Deng, Z. Tan, Y. Jiang, H. Dai, Y. Shi, and L. Xu, *Deformation Monitoring and Subsidence Engineering*, China University of Mining and Technology Press, Xuzhou, China, 2014.
- [26] W. Zhang, D. Zhang, D. Qi, Z. He, and X. Duan, "A mechanical analysis of support instability risk along the strike of coalface in thick coal seam with large dip angle: a case study," *Earth Sciences Research Journal*, vol. 25, no. 1, pp. 101–108, 2021.
- [27] W. Zhang, J. Guo, K. Xie et al., "Comprehensive technical support for safe mining in ultra-close coal seams: a case study," *Energy Exploration & Exploitation*, vol. 39, no. 4, pp. 1195–1214, 2021.
- [28] W. Yang and T. Zhang, *Introduction and Application of SPSS Statistical Analysis*, Tsinghua University Press, Beijing, China, 2022.
- [29] W. Jijun, R. Guoyu, K. Xiaoyan, and W. Fang, "Normality analysis of the monthly and annual precipitation in henan province," *Climatic and Environmental Research (in Chinese)*, vol. 15, no. 4, pp. 522–528, 2010.
- [30] S. R. Naganna and P. C. Deka, "Variability of streambed hydraulic conductivity in an intermittent stream reach regulated by Vented Dams: a case study," *Journal of Hydrology*, March, vol. 562, , pp. 477–491, 2018.
- [31] T. Chai and R. R. Draxler, "Root mean square error (RMSE) or mean absolute error (MAE)? -Arguments against avoiding RMSE in the literature," *Geoscientific Model Development*, vol. 7, no. 3, pp. 1247–1250, 2014.
- [32] M. Wiberg, W. J. Van Der Linden, and A. A. Von Davier, "Local observed-score kernel equating," *Journal of Educational Measurement*, vol. 51, no. 1, pp. 57–74, 2014.
- [33] D. S. K. Karunasingha, "Root mean square error or mean absolute error? Use their ratio as well," *Information Sciences*, vol. 585, pp. 609–629, 2022.

- [34] Z. Dawei, W. Kan, B. Zhihui et al., "Formation and development mechanism of ground crack caused by coal mining: effects of overlying key strata," *Bulletin of Engineering Geology and the Environment*, vol. 78, no. 2, pp. 1025–1044, 2019.
- [35] D. Zhou, K. Wu, X. Miao, and L. Li, "Combined prediction model for mining subsidence in coal mining areas covered with thick alluvial soil layer," *Bulletin of Engineering Geology and the Environment*, vol. 77, no. 1, pp. 283–304, 2018.
- [36] J. Ma, D. Yin, N. Jiang, S. Wang, and D. Yao, "Application of a superposition model to evaluate surface asymmetric settlement in a mining area with thick bedrock and thin loose layer," *Journal of Cleaner Production*, vol. 314, no. June, p. 128075, 2021.
- [37] S. Ju, S. Shiqian, and P. Chenyi, *Probability Theory and Mathematical Statistics*, Higher Education Press, Beijing, 4th Edition, 2008.
- [38] C. Xiru, *Probability Theory and Mathematical Statistics*, China University of science and Technology Press, Hefei, 2009.



## Research Article

# Modeling and Optimizing Based on OTCPN in Multi-Tier Shuttle Warehousing System

Huishuang Zhu,<sup>1</sup> Meng Wang<sup>1,2</sup> ,<sup>2</sup> and Huaijin Gao<sup>2</sup>

<sup>1</sup>School of Machinery and Automation, Weifang University, Weifang 261061, Shandong, China

<sup>2</sup>School of Mathematics and Information Science, Weifang University, Weifang 261061, Shandong, China

Correspondence should be addressed to Meng Wang; [wm0206@wfu.edu.cn](mailto:wm0206@wfu.edu.cn)

Received 11 July 2022; Revised 1 August 2022; Accepted 5 August 2022; Published 29 August 2022

Academic Editor: Dinesh Kumar Saini

Copyright © 2022 Huishuang Zhu et al. This is an open access article distributed under the Creative Commons Attribution License, which permits unrestricted use, distribution, and reproduction in any medium, provided the original work is properly cited.

This paper models the multi-tier shuttle warehousing system and optimizes the system structure and control strategy. This kind of system is a discrete event dynamic system because it only takes place at discrete time points, while previous warehousing system models. We propose the object-oriented timed colored Petri net to model it, to improve the accuracy of the model and avoid the problem of status explosion in the process of Petri net modeling. We propose two control strategy optimization methods: one is to balance the task assignment, and the other is to change the return time point of the buffer status information. The results of numerical experiments show that consideration of both optimization strategies can reduce the total picking time by 40% ~ 62%. Additionally, we analyze the influence of the buffer capacity. The results show that the buffer capacity can reduce the total picking time, and enough amount of buffer capacity has the same effect as control strategy optimization.

## 1. Introduction

Multi-tier shuttle warehouse system (MSWS) is a new automatic warehouse system to store and retrieve items stored on totes. MSWS belongs to the tier-captive autonomous vehicle-based storage and retrieval system (AVS/RS) with the tier-captive shuttles; i.e., the shuttles are captive to its dedicated tier to provide quick horizontal tote movement. Moreover, the vertical tote movement is provided by the lifter located at the beginning of the aisle. Therefore, considering high-density storage and flexibility, MSWS has been adopted by more and more logistics distribution centers. Figure 1 presents the components of MSWS. A single-deep, double-side storage rack is used to store totes. The shuttles run along the aisles to transfer the totes and only hold one tote at once. The lifters, which also hold one tote once time, are dedicated to one aisle that is divided into input lifter and output lifter. The input/output point (I/O point) is located at the first tier and combined by several roller conveyors to join the I/O lifter and transportation loop. The workstations are located along the

periphery of the transportation loop and divided into input workstations and output workstations.

MSWS is controlled by the order management system. The order management system receives orders from customers and suppliers and extracts effective information to create storage and retrieval tasks. Orders occur only at discrete time points; therefore, the MSWS conforms to a discrete event dynamic system (DEDS). Common theoretical research methods for DEDS are as follows: formal language and automata, Markov chain, queuing theory, and Petri net. There are some studies through queuing theory to the model system. Marchet et al. [1] used the open queuing network (OQN) to model the tier-captive AVS/RS and evaluate the system performance. Zou et al. [2] modeled the tier-captive AVS/RS as a fork-join queuing network (FJQN) and compared the parallel and sequential processing policy. Wang et al. [3] provided the OQN to study the storage assignment optimization. Tappia et al. [4] developed the semi-open queuing network (SOQN) to study the effect of storage system technology on order throughput times and the effect of the picking station input buffer size on order picking

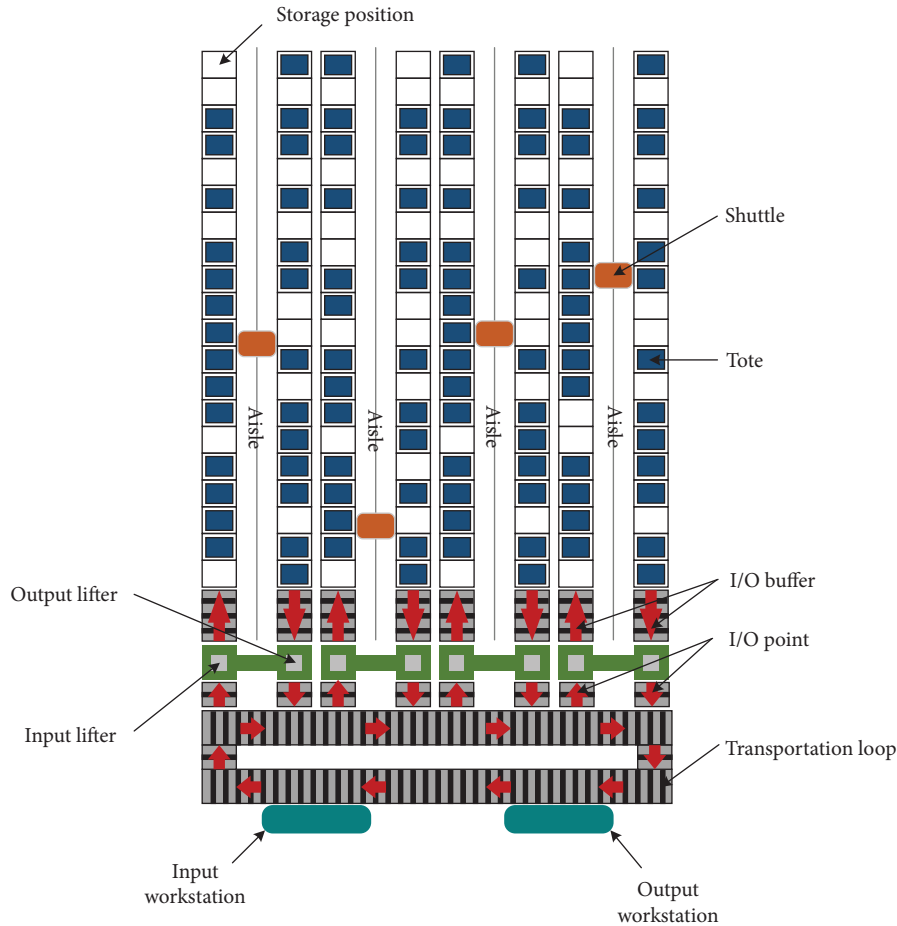


FIGURE 1: Top view of MSWS.

performance. Wu et al. [5] used the OQN to model the shuttle-based storage and retrieval system (SBS/RS) and compare the SBS/RS with the robotic order fulfillment system (ROFS) in terms of cost and system throughput. Different from the above, Lerher et al. [6, 7] proposed the travel time model to evaluate the system performance with single- and double-deep storage position. Ning et al. [8] studied the optimal solution of the tier-captive AVS/RS through an efficient simulation model. Borovinšek et al. [9] proposed a multi-objective solution including the minimization of the average cycle time of transactions, energy consumption, and total investment cost for designing the tier-captive AVS/RS. Ekren et al. [10] proposed discrete time Markov chain (DTMC) to estimate the mean and variance of travel time of AVS/RS, as well as the mean amount of energy consumption and energy regeneration per transaction for a predefined SBS/RS.

Petri net can describe the system structure visually and presents the parallel, synchronization, conflict relationship of the system. However, to the best of the knowledge, there are few studies to model the MSWS through Petri net. Qiqiang and Ran [11] and Yindi et al. [12] proposed the Petri net to model the sorting system, but the operation process of the equipment is not reflected. Tian et al. [13] studied the automated storage and retrieval system (AS/RS) which is similar to the MSWS. They developed the hierarchical colored Petri nets

and used the CPN tools to optimize the scheduling strategy. However, ordinary Petri nets are difficult to describe the operation process of complex discrete event systems. Therefore, high-level Petri nets combine object-oriented theory and give time and type constraints to make complex discrete event systems easier to understand [14]. Consequently, this paper develops the object-oriented timed colored Petri net (OTCPN) to model the MSWS and illustrates the operation process of each component. Via numerical examples and sensitivity analysis, we find that the MSWS performance is sensitive to the I/O buffer capacity and task scheduling level.

The remainder of this paper is as follows: Section 2 briefly describes the MSWS and presents the retrieval and storage transaction flow. Section 3 presents the OTCPN concept and the MSWS models. Section 4 describes the control strategy optimization method. Section 5 analyzes the optimization effect by numerical experiments. Section 6 summarizes the results, the contributions, and directions for future research.

## 2. MSWS Description

MSWS consists of six subsystems: the shuttle system, the input lifter system, the output lifter, the input workstation, the output workstation, and the order management system. As Figure 2 illustrates, the MSWS can execute both storage

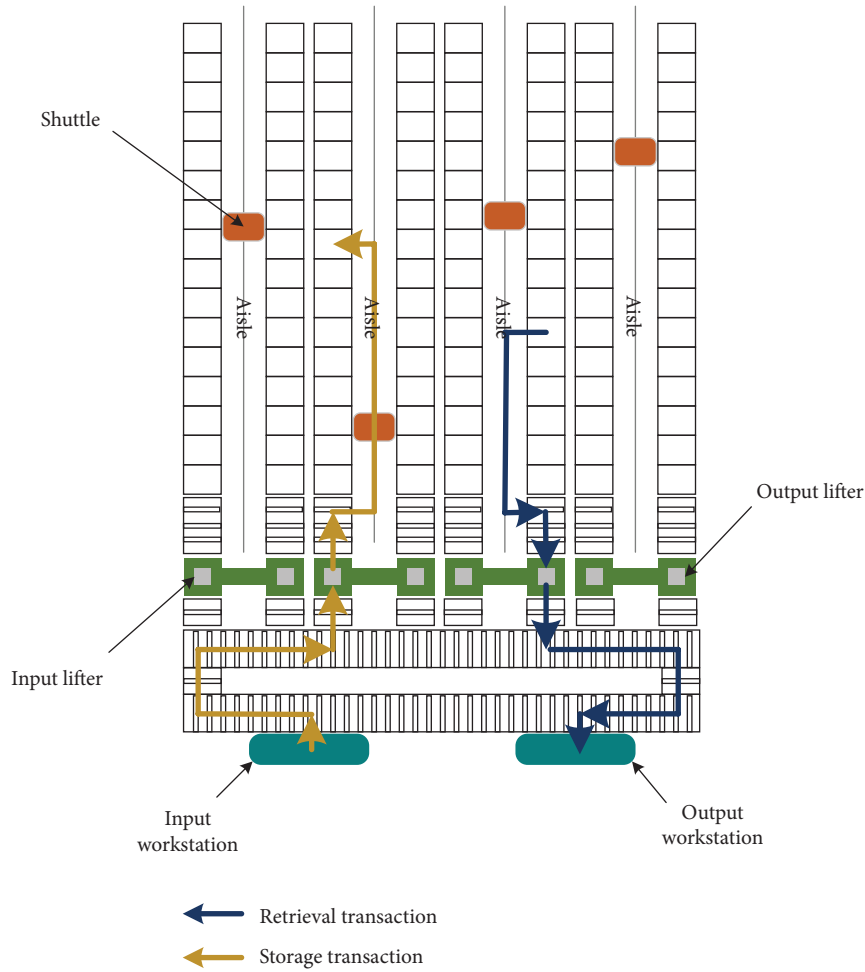


FIGURE 2: Description of the operation process in the MSWS.

and retrieval transactions concurrently. The storage transaction is initiated by the totes at the input workstation. The operators complete the packing and send the storage information to the order management system. Then, the transportation loop moves the totes to the input point. Simultaneously, the order management system sends the information to the lifter.

Subsequently, the lifter picks up the totes and drops them at the input buffer of the destination tier. Finally, the shuttle of the designated tier travels from its dwell point to the input buffer and picks up the totes. The storage transaction is completed when the totes are transferred to the destination storage position by the shuttle. Similarly, the retrieval transaction starts when the order management system sends this retrieval information to shuttles. Then, the shuttle transports the totes from their storage position to the output buffer. Then, the lifter reaches the destination tier, picks up this tote, and transfers it to the output point located at the first tier. The tote is released and conveyed to the output workstation by the transportation loop. At last, the operator picks the items from the tote according to the order.

As mentioned previously, the lifter provides vertical transaction from tier to tier, while the shuttle undertakes the horizontal transaction at the destination tier. Under the

parallel processing of transactions in the MSWS, the I/O buffer become the one factor to determine the status of the shuttles and the lifters. Namely, the input lifter is unavailable for one tier if the input buffer is occupied in this tier. Similarly, the shuttle is unavailable because the output buffer is occupied. Moreover, the shuttles and the lifters follow the first-come-first-serve (FCFS) service and point-of-service-completion (POSC) dwell point policy.

### 3. OTCPN Modeling for MSWS

**3.1. OTCPN Concept.** A basic Petri net (PN) model can be represented by a directed bipartite graph, which includes two types of nodes: places and transitions. Places  $P = \{p_i\}_m$  are represented by circles and used to describe the resources and job status. Transactions  $T = \{t_j\}_n$  are represented by blocks and used to describe the events and processes. These two types of nodes are linked by arrowed arcs, e.g., from the places to the transitions or from the transitions to the places, but the arc cannot connect two nodes of the same types.

The basic PN model can describe parallelism, synchronization, conflict, and causality, but it is very difficult to describe a system with high complexity only by using the basic PN model. Considering the complexity and hierarchy

of the MSWS, the object-oriented timed colored Petri net (OTCPN) combines the object Petri net (OPN), timed Petri net (TPN), and colored Petri net (CPN) to evaluate systems' performance and optimize scheduling [15].

*Definition 1.* An object-oriented timed colored Petri net is a tuple:  $OTCPN = (OP, OT, C, E^t, I, O, N, M_0)$ , where:

- (1)  $OP = P \cup IMP \cup OMP$ ,  $OP$  is the set of places and composed of three types of finite nonempty places.  $P$  is the set of common places within the object subnet, which is used to represent the tasks and devices status in MSWS.  $IMP$  is the set of information input place between object subnets, and  $OMP$  is the set of information output place between object subnets.
- (2)  $OT = T \cup G$ ,  $OT$  is the set of transitions and composed of  $T$  and  $G$ .  $T$  is the set of common transitions within the object subnet, which is used to represent the processing of tasks in MSWS.  $G$  is the set of condition transitions between object subnet, which determines the direction of information transfer based on the properties and status of the object.
- (3)  $C$  is the set of multiple colors.  $C(P)$  represents the set of all types of colors that belongs to the token in the places  $P$ , and  $C(T)$  represents the set of all types of colors that appears on the transitions  $T$ . In MSWS, the color set  $Task = \{0, 1, \dots, T\}$  represents the shuttles, and the color set  $Type = \{0, 1\}$  represents the task type. Therefore,  $TypeTask$  is defined as the Cartesian product of  $Type$  and  $Task$  to represent the tasks assigned to each device.
- (4)  $E^t$  introduces the concept of time stamps so that the places  $P$  and the transitions  $T$  have time variables. In a TCPN, it represents the firing of the transitions  $T$  which takes a certain time duration and is represented as "@+time value" [16].
- (5)  $I(OP, OT) = I(P, T) \cup I(OMP, G)$ ,  $I(P, T)$  is the input function from the places  $P$  to the transitions  $T$  and represented by the colored directed arcs from  $P$  to  $T$ :  $C(P) \times C(T) \rightarrow N$ ,  $N = 0, 1, 2, \dots$ .  $I(OMP, G)$  is the input function from the information output places  $OMP$  to the condition transitions  $G$  and represented by the colored directed arcs from  $OMP$  to  $G$ :  $C(OMP) \times C(G) \rightarrow N$ ,  $N = 0, 1, 2, \dots$ .
- (6)  $O(OT, OP) = O(T, P) \cup O(G, IMP)$ ,  $O(T, P)$  is the output function from the transitions  $T$  to the places  $P$  and represented by the colored directed arcs from  $T$  to  $P$ :  $C(T) \times C(P) \rightarrow N$ ,  $N = 0, 1, 2, \dots$ .  $O(G, IMP)$  is the output function from the conditions transitions  $G$  to the information input places  $IMP$  and represented by the colored directed arcs from  $G$  to  $IMP$ :  $C(G) \times C(IMP) \rightarrow N$ ,  $N = 0, 1, 2, \dots$ .
- (7)  $N$  is the finite sets of all objects in the system.
- (8)  $M_0$  is the initial marking function.

**3.2. MSWS Model.** Figure 3 presents the input workstation model.  $IMP11$  means the storage tasks and items are ready.

$P11$  means the input workstation is idle.  $P12$  means the operator is idle.  $P13$  means the information is correct.  $P14$  means the totes and items are ready to transport.  $T11$  means the operator checks item information. The duration of this process is "operation\_time."  $T12$  means the operator binds items and totes.  $T13$  means the operator puts the totes on the transportation loop.  $OMP11$  means the operation is completed.

Figure 4 presents the order assignment system model.  $IMP21$  means all types of tasks are in the task pool.  $IMP22$  means there is an idle storage position.  $IMP23$  means the order management system receives the storage tasks.  $P21$  means the totes get the storage position.  $P22$  means the storage task is ready.  $P23$  means the retrieval task is ready.

$T21$  means the system assigns the storage position.  $P23$  means the retrieval task is ready.  $T21$  means the system assigns the storage position.  $T23$  means the system selects the storage tasks with the condition of  $ty = 0$ .  $T24$  means the system releases the storage tasks.  $T25$  means the system selects the retrieval tasks with the condition of  $ty = 1$ .  $T26$  means the system releases the retrieval tasks.  $OMP21$  means the storage task assignment is completed.  $OMP22$  means the retrieval task assignment is completed.

Figure 5 presents the input lifter model.  $IMP31$  means the input lifter receives the storage tasks.  $IMP32$  means there are enough input buffers to use.  $P31$  means the input lifter is ready to load the totes.  $P32$  means the input lifter is ready to transport the totes.  $P33$  means the input lifter is ready to unload the totes.  $P34$  means the input lifter is idle.  $T31$  means the input lifter travels to the first tier.  $T32$  means the input lifter loads the totes.  $T33$  means the input lifter transports the totes to the destination tier.  $T34$  means the input lifter unloads the totes. The condition of  $t = b$  represents there is one buffer to hold the totes.  $OMP31$  means the input lifter completes the storage task. The duration of  $T31, T33$  is "operation\_time" and calculated with considering the acceleration/deceleration of the lifter [5].

Figure 6 presents the shuttle model.  $IMP41$  means the shuttle receives the storage tasks.  $IMP42$  means the shuttle receives the retrieval tasks.  $IMP43$  means there are enough output buffers to use.  $P41, P42$ , and  $P45$  mean the shuttle is ready to transport the totes.  $P43$  and  $P46$  mean the shuttle is ready to unload the totes.  $P44$  means the shuttle is ready to load the totes.  $P47$  means the shuttle is idle.  $T41$  means the shuttle travels to the input buffer.  $T42$  and  $T46$  mean the shuttle loads the totes.  $T43$  means the shuttle transports the totes to the destination storage position.  $T44$  and  $T48$  mean the shuttle unloads the totes.  $T45$  means the shuttle travels to the destination storage position.  $T47$  means the shuttle transports the totes to the output buffer.  $OMP41$  means the output buffer is idle.  $OMP42$  means the shuttle completes the retrieval task.  $OMP43$  means the shuttle completes the storage task. The duration of  $T41, T43, T45, T47$  is "operation\_time" and calculated with considering the acceleration/deceleration of the shuttle.

Figure 7 presents the output lifter model.  $IMP51$  means the output lifter receives the retrieval tasks.  $P51$  means the output lifter is ready to load the totes.  $P52$  means the output lifter is ready to transport the totes.  $P53$  means the output

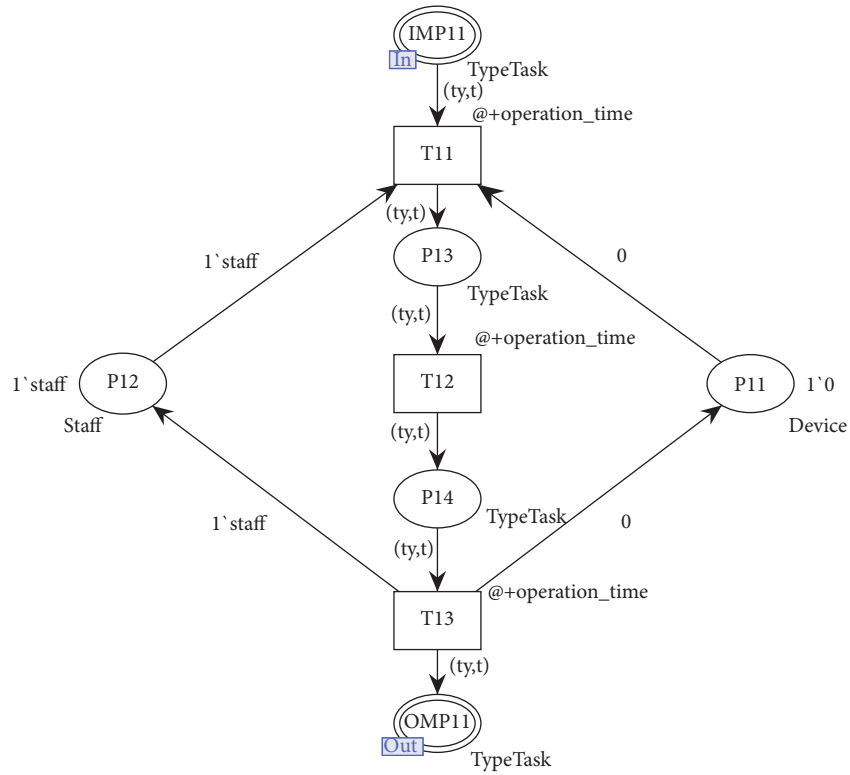


FIGURE 3: Input workstation model.

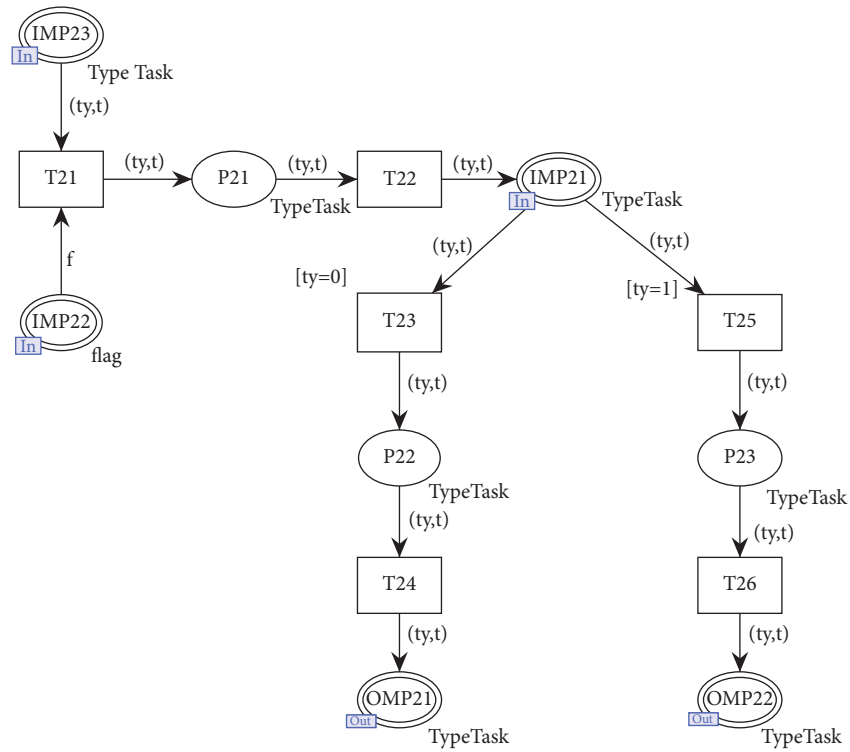


FIGURE 4: Order management system model.

lifter is ready to unload the totes.  $P54$  means the output lifter is idle.  $T51$  means the output lifter travels to the destination tier.  $T52$  means the output lifter loads the totes.  $T53$  means

the output lifter transports the totes to the first tier.  $T54$  means the output lifter unloads the totes.  $OMP51$  means the output buffer is idle.  $OMP52$  means the output lifter

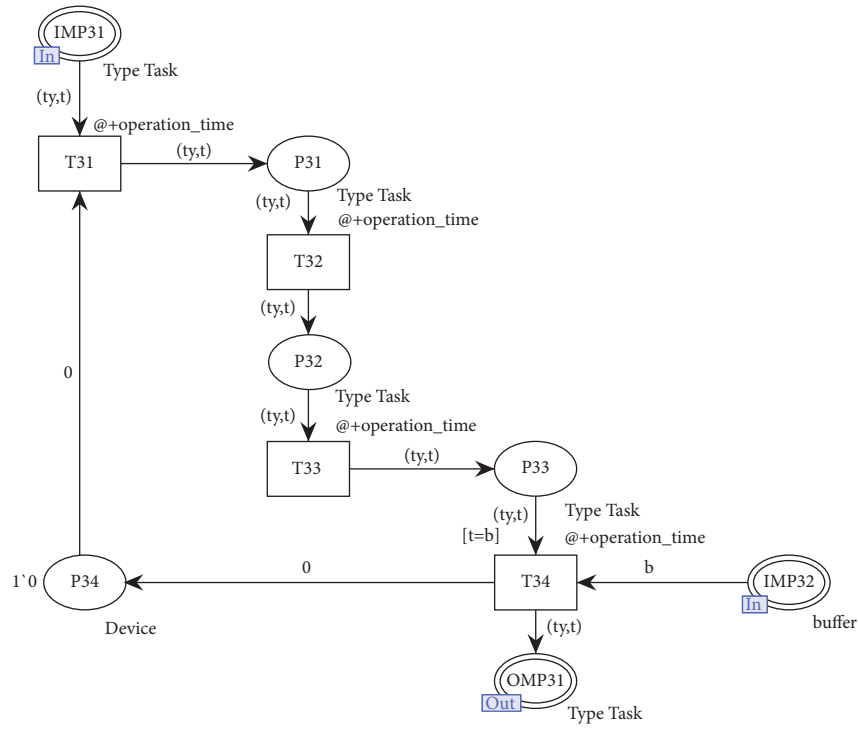


FIGURE 5: Input lifter model.

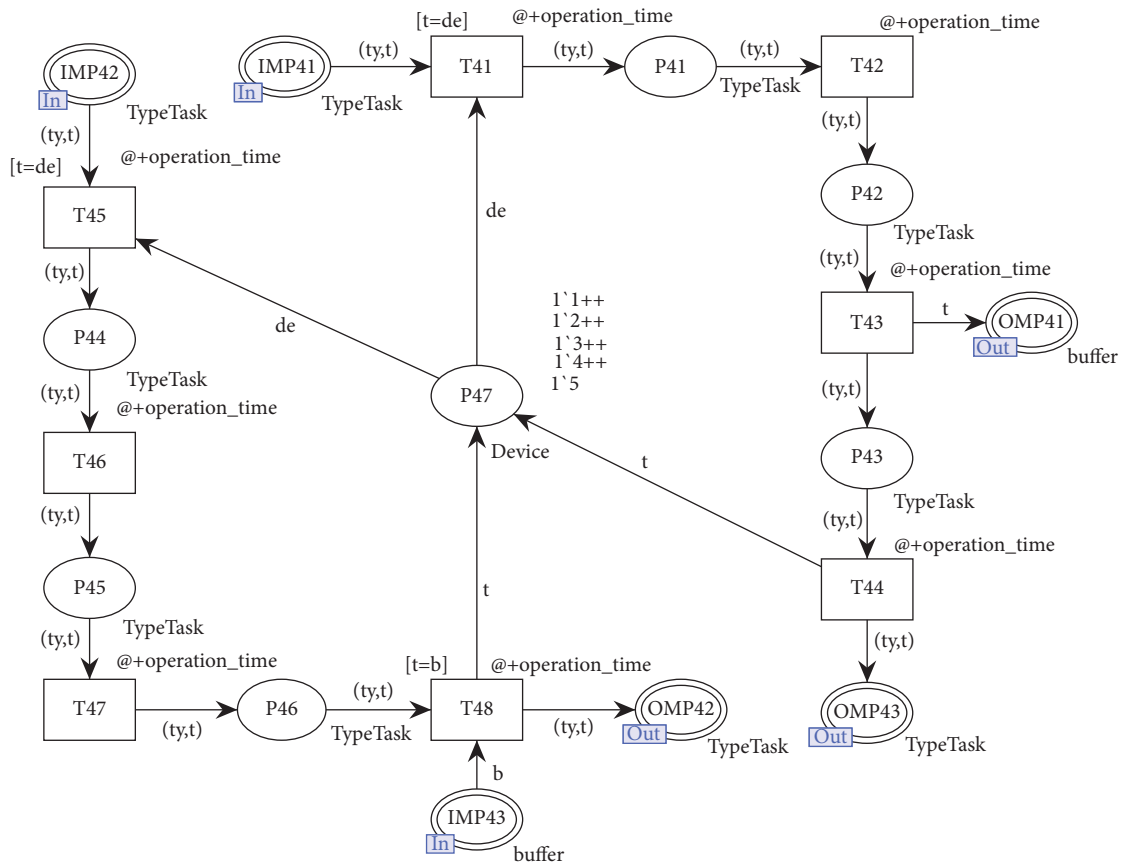


FIGURE 6: Shuttle model.

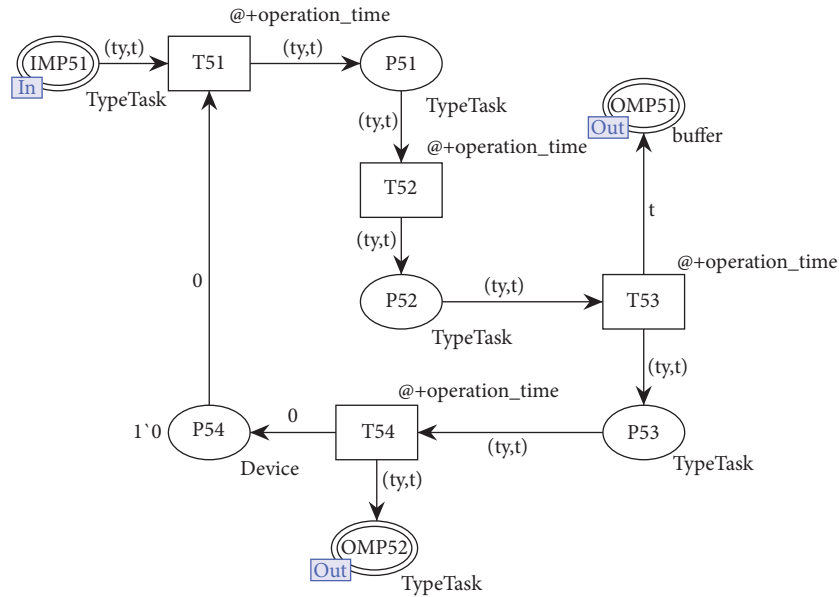


FIGURE 7: Output lifter model.

completes the retrieval task. The duration of  $T_{51}, T_{53}$  is “operation\_time” and calculated with considering the acceleration/deceleration of the lifter.

Figure 8 presents the output workstation model.  $IMP_{61}$  means the output workstation receives the retrieval task.  $P_{61}$  means the operator is idle.  $P_{62}$  means the input workstation is idle.  $P_{63}$  means the information is correct.  $T_{61}$  means the operator checks item information.  $T_{62}$  means the operator picks the items by orders.  $OMP_{61}$  means the operation is completed.

Figure 9 presents the MSWS model.  $G_{12}$  means the input workstation transmits storage task information to the order management system.  $G_{23}$  means the order management system transmits storage task information to the input lifter.  $G_{24}$  means the order management system transmits retrieval task information to the shuttle.  $G_{34}$  means the input lifter transmits storage task information to the shuttle.  $G_{43}$  means the shuttle transmits the input buffer information to the input lifter.  $G_{45}$  means the shuttle transmits the retrieval task information to the output lifter and the storage position information to the order management system.  $G_{54}$  means the output lifter transmits the output buffer information to the shuttle.  $G_{56}$  means the output lifter transmits the retrieval task information to the output workstation.

#### 4. Scheduling Strategy Optimization

MSWS is a discrete event system with multiple devices (e.g., shuttles, I/O lifters, and I/O workstations) working in coordination and parallel. The most direct way to improve the system efficiency is to increase the number of devices or operating speed, i.e., to increase the throughputs per unit time. However, this will greatly increase equipment investment costs, or it may not be possible due to the mechanical and electrical structural constraints. Therefore, without changing the number and

performance of the equipment, and without increasing the cost, scheduling strategy optimization is the better choice to increase the parallel working time of equipment and reduce the total time of order picking. This study considers the task balance strategy as the task assignment optimization (TA-opt); i.e., the order management system evenly allocates storage tasks and retrieval tasks according to the number of shuttles and lifters. Through TA-opt, we can increase the parallel operation rate of tasks and reduce the total picking time.

Through the OTCPN analysis, the lifters and the shuttles are occupied by one task for too long time. Therefore, this paper proposes an information scheduling optimization (IS-opt) to reduce the occupied time of the equipment. From the input lifter model (see Figure 5), there are no tokens in the place of  $P_{34}$  if  $IMP_{32}$  has no matched tokens; i.e., if there is no free position in the input buffer of one tier, the input lifter will always be occupied and cannot fulfill other storage tasks. This is bound to increase the total time of storage tasks. Therefore, the IS-opt of the input lifter is as shown in Figure 10:  $IMP_{32}$ , which means there are enough input buffers to use, is changed to one of the enabling conditions. That means the input lifter needs to check whether there is enough free position in the input buffer of the destination tier before starting the storage tasks.

Also in the shuttle model (see Figure 6), the  $IMP_{43}$ , as one of the conditions for releasing the shuttles, increases the time occupied by the shuttles. For this reason, the shuttles cannot fulfill other storage tasks. Therefore, the optimization strategy is to let  $IMP_{43}$  as one of the enabling conditions for  $T_{45}$  as shown in Figure 11; i.e., when the shuttles fulfill the retrieval tasks, it needs to check whether there is enough free position in the output buffer. If no, it needs to suspend the current task and execute other tasks that meet the execution conditions first.

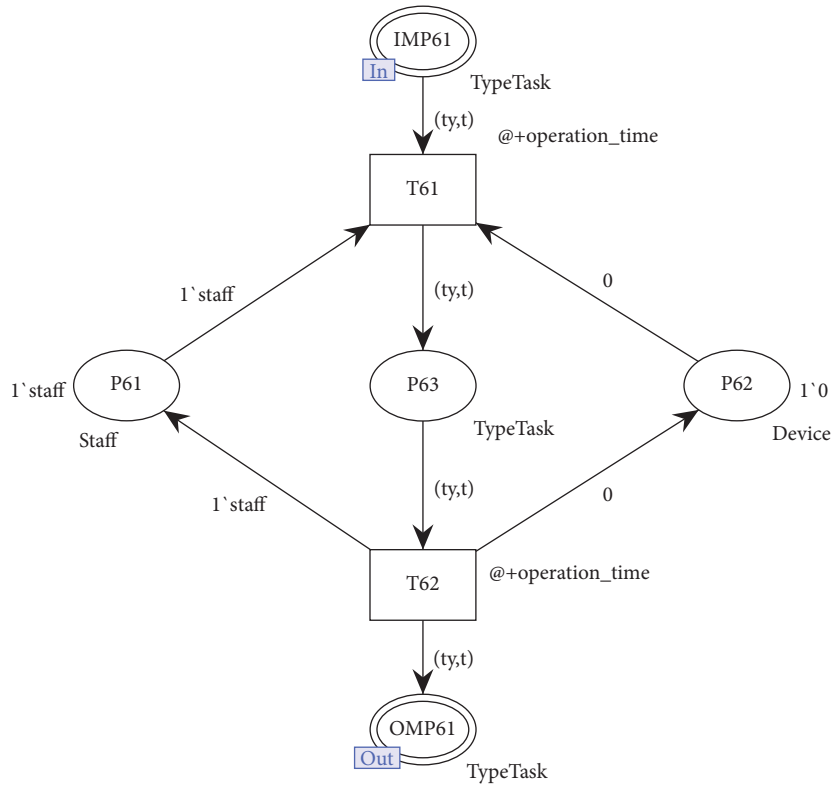


FIGURE 8: Output workstation model.

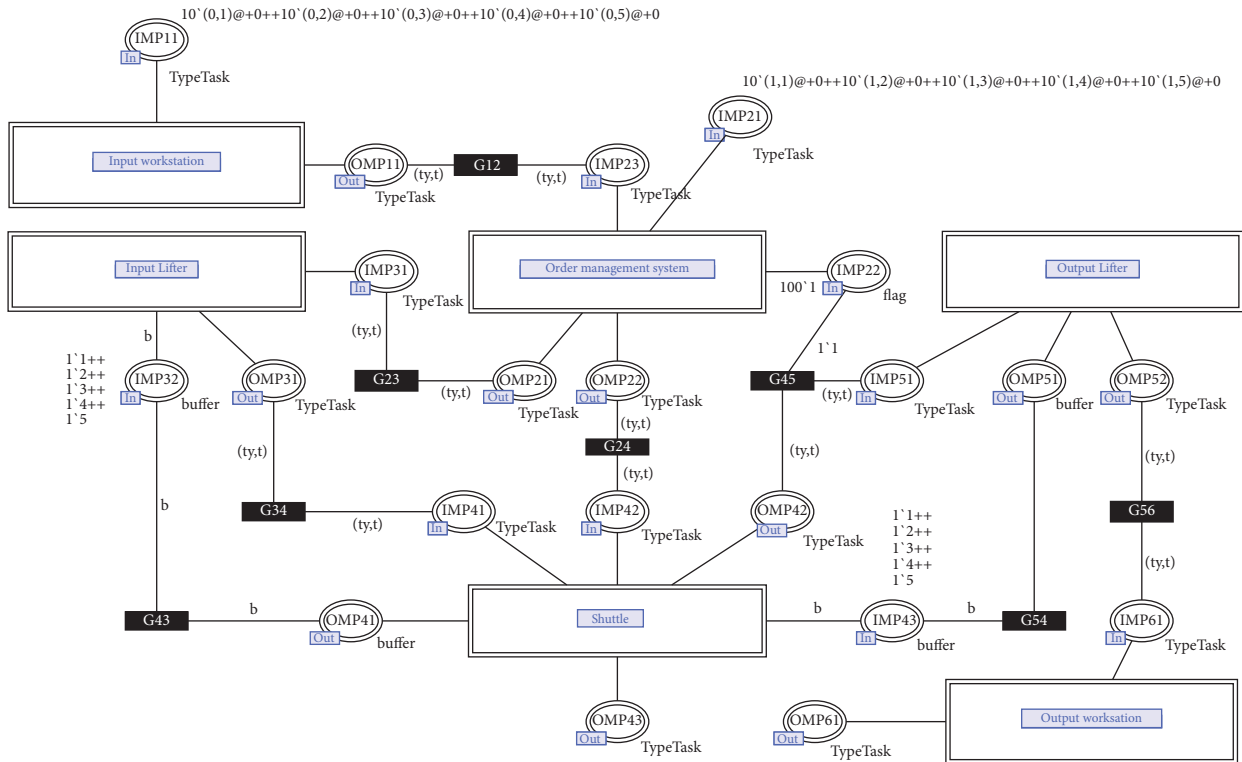


FIGURE 9: The OTCPN model of MSWS.



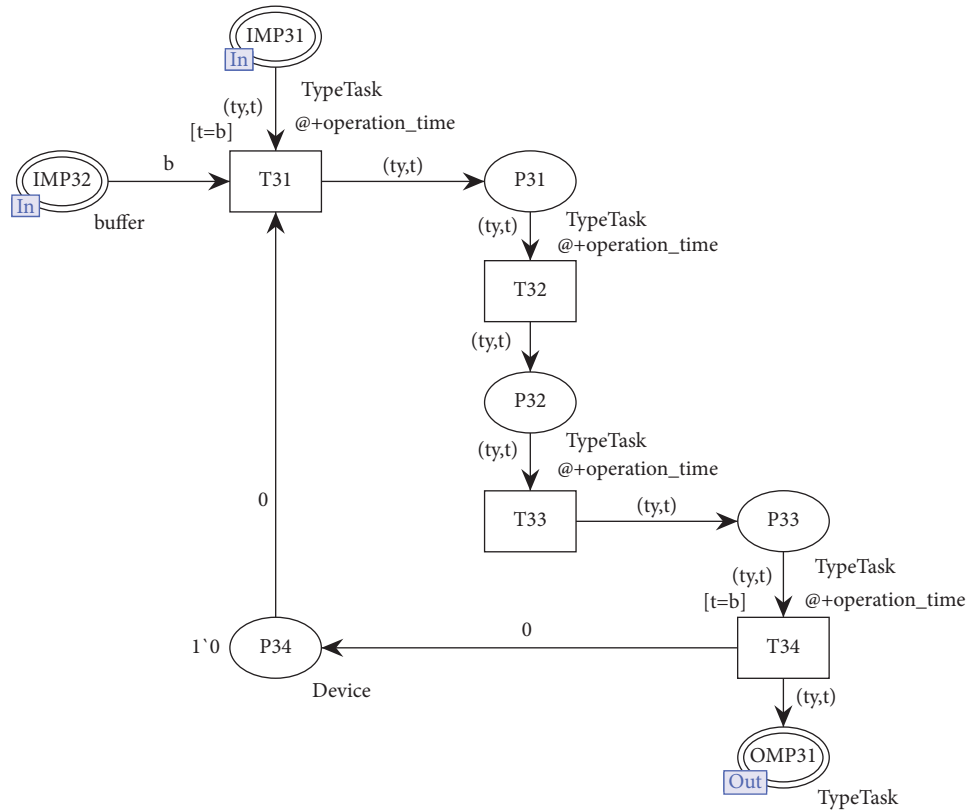


FIGURE 10: IS-opt for the input lifter.

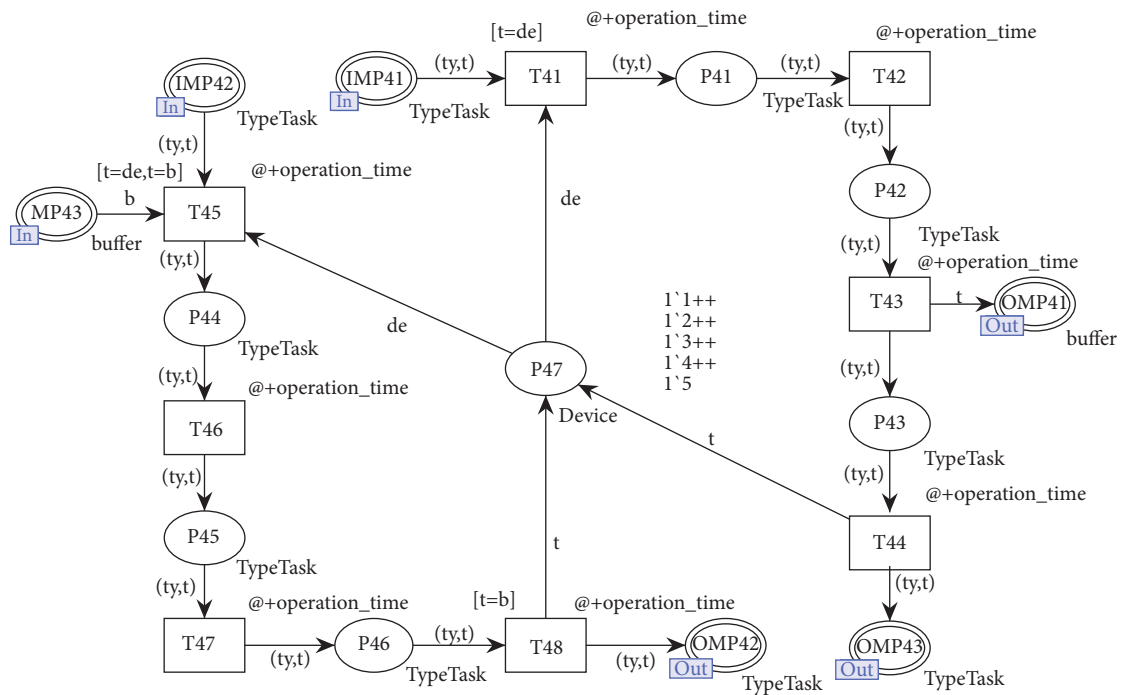


FIGURE 11: IS-opt for the shuttle.

TABLE 1: Parameters of the MSWS.

Parameters	Notation	Value
Width of a unit storage position	$W_s$	0.5 m
Depth of a unit storage position	$D_s$	0.7 m
Height of a unit storage position	$H_s$	0.5 m
Maximum velocity of shuttles	$v_s$	2 m/s
Maximum velocity of lifters	$v_l$	3 m/s
Acceleration/deceleration rate of shuttles	$a_l$	1 m/s <sup>2</sup>
Acceleration/deceleration rate of lifters	$a_l$	3 m/s <sup>2</sup>
Fixed time required for the shuttle, lifter to load or unload the tote	$t_l$	2 s
Fixed time required for the I/O workstation operation	$t_w$	15 s

TABLE 2: Comparison of the total picking time ( $T_{\text{total}}$ ) under TA-opt and IS-opt.

Tier	Column	NO-opt	TA-opt	IS-opt	TA-opt + IS-opt
T = 5	C = 30	926.19	637.17	688.44	<b>430.65</b>
	C = 60	1228.55	763.98	750.64	<b>461.70</b>
	C = 90	1492.35	882.27	904.25	<b>554.35</b>
	C = 120	1697.25	999.66	954.70	<b>632.75</b>
	C = 150	1967.31	1169.38	1085.70	<b>734.92</b>
T = 7	C = 30	1024.11	939.88	711.30	<b>586.41</b>
	C = 60	1073.26	1015.20	823.15	<b>594.49</b>
	C = 90	1300.96	1185.26	974.34	<b>635.53</b>
	C = 120	1441.50	1272.07	1111.62	<b>684.82</b>
	C = 150	1603.75	1372.90	1279.63	<b>774.12</b>
T = 9	C = 30	1309.25	1235.46	755.76	<b>748.65</b>
	C = 60	1385.67	1336.51	789.61	<b>754.27</b>
	C = 90	1520.07	1478.24	879.46	<b>777.04</b>
	C = 120	1721.10	1585.83	1023.06	<b>808.86</b>
	C = 150	1891.16	1664.27	1149.85	<b>855.72</b>
T = 11	C = 30	1528.06	1438.08	911.52	<b>905.52</b>
	C = 60	1852.00	1721.46	963.75	<b>915.17</b>
	C = 90	1976.43	1873.07	1077.20	<b>922.79</b>
	C = 120	2234.68	2027.14	1244.16	<b>940.08</b>
	C = 150	2280.20	2018.44	1422.51	<b>990.49</b>
T = 13	C = 30	2003.48	1817.92	1192.24	<b>1067.31</b>
	C = 60	2237.61	2145.90	1327.79	<b>1075.82</b>
	C = 90	2514.35	2176.27	1480.56	<b>1074.65</b>
	C = 120	2612.89	2289.99	1631.91	<b>1097.09</b>
	C = 150	2825.74	2530.31	1863.11	<b>1103.45</b>
T = 15	C = 30	2234.74	2081.13	1225.99	<b>1129.87</b>
	C = 60	2391.40	2062.92	1265.52	<b>1232.53</b>
	C = 90	2642.82	2450.26	1250.27	<b>1249.27</b>
	C = 120	2897.73	2660.22	1353.61	<b>1239.08</b>
	C = 150	2998.06	2944.18	1470.10	<b>1266.13</b>

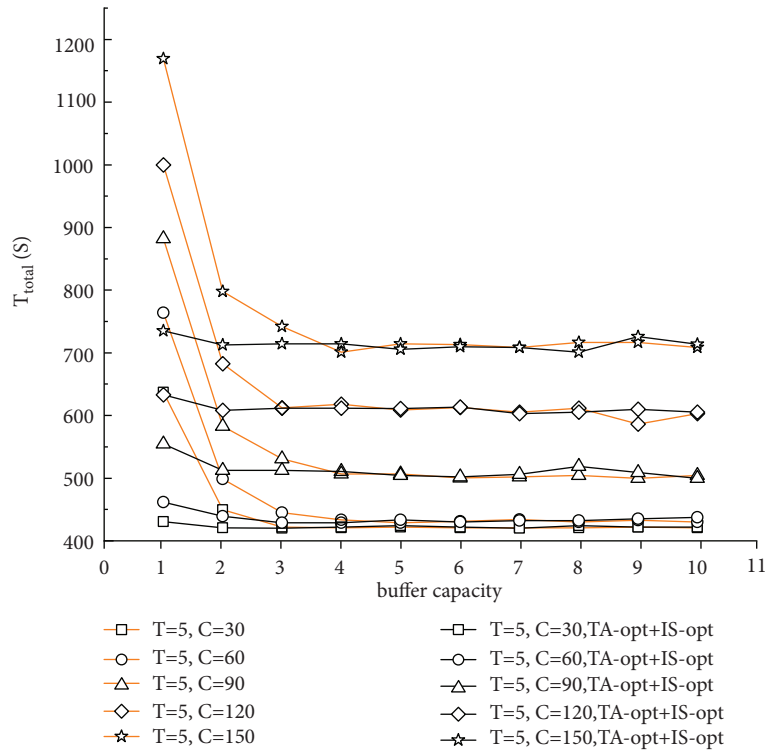
## 5. Numerical Experiments

*5.1. Simulation of MSWS.* We develop numerical experiments based on OTCPN models and consider one aisle with  $T$  tier in MSWS. The parameters of MSWS come from Table 1, and this data source is the actual device parameters of a device supplier.

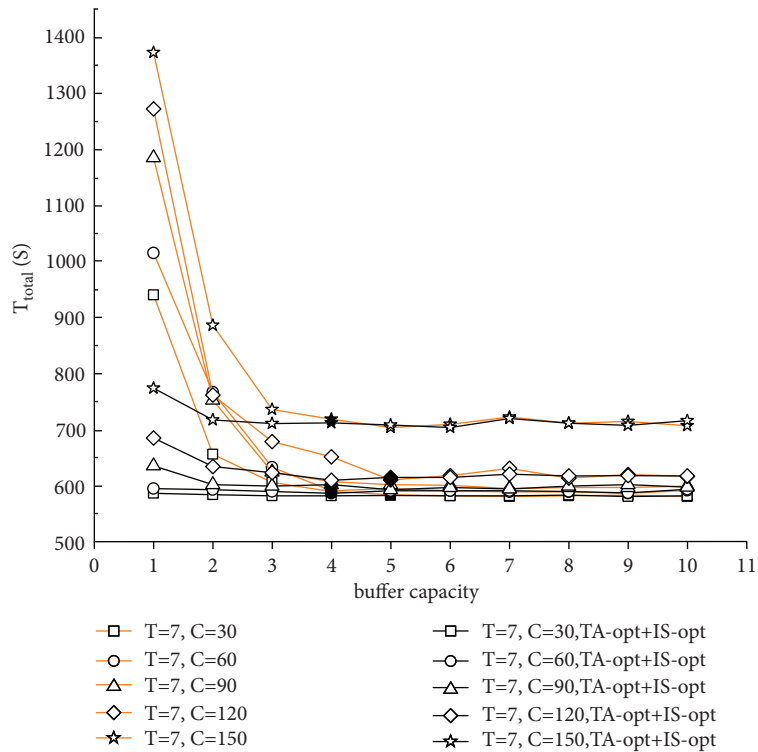
*5.2. Comparison of TA-Opt and IS-Opt.* This experiment is to verify the optimization effect of TA-opt and IS-opt. Therefore, the I/O buffer is set to 1 to eliminate the effect of buffer capacity. 120 scenarios are used to verify the optimization based on the variation of the number of tiers ( $T$ )

and the number of columns ( $C$ ). In order to eliminate the bias, the experiment was repeated 50 times. The average value of the total operation time ( $T_{\text{total}}$ ) is used.

Table 2 shows the result of total picking time  $T_{\text{total}}$ . The NO-opt column as the baselines without TA-opt and IS-opt demonstrates the superiority of the optimization. The TA-opt column shows the results with task assignment optimization, and the IS-opt column shows the results with information scheduling optimization. The result shows that the optimization efficiency of TA-opt is 1.8% ~ 40%, and IS-opt can improve 20% ~ 53%. The total picking time can be reduced by 40% ~ 62% when the TA-opt and IS-opt are used simultaneously.

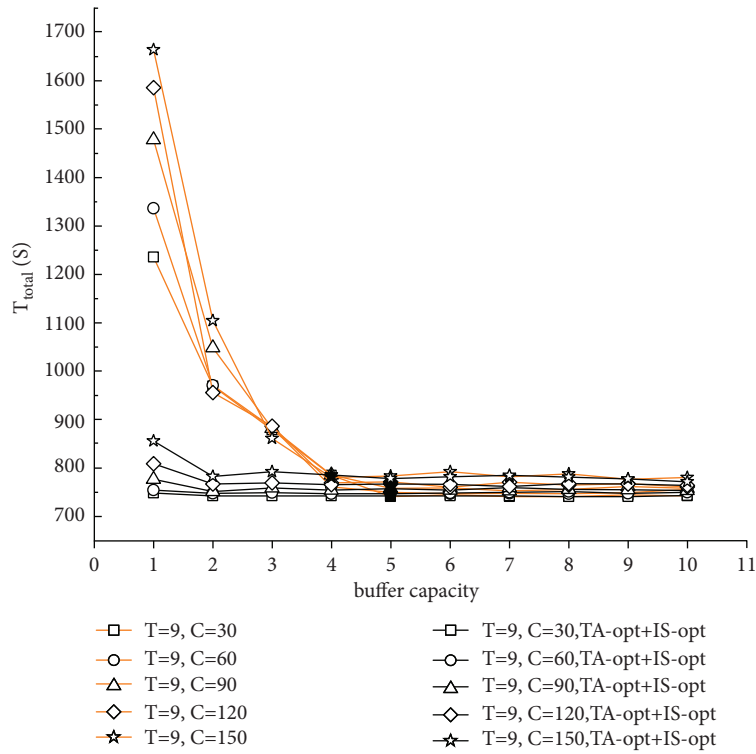


(a)

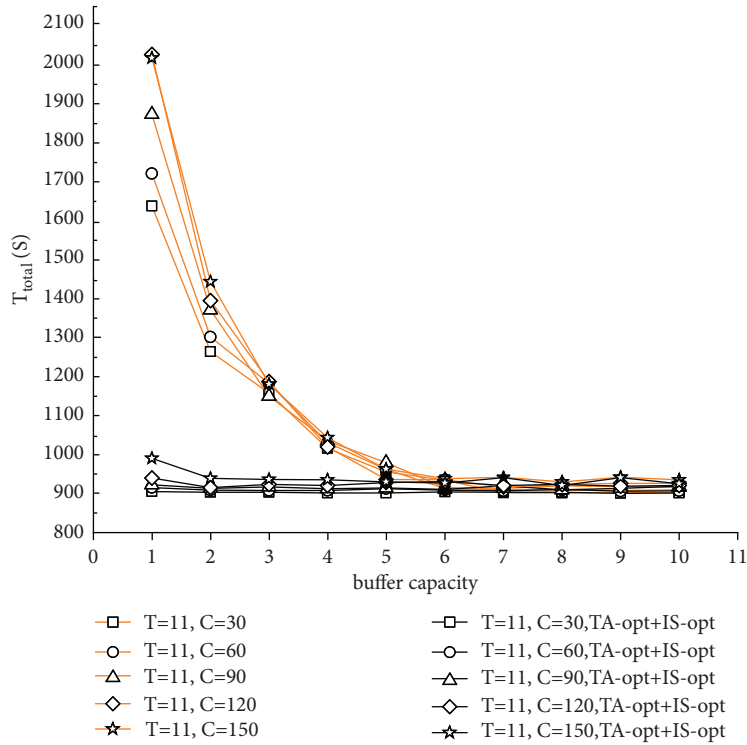


(b)

FIGURE 12: Continued.



(c)



(d)

FIGURE 12: Continued.

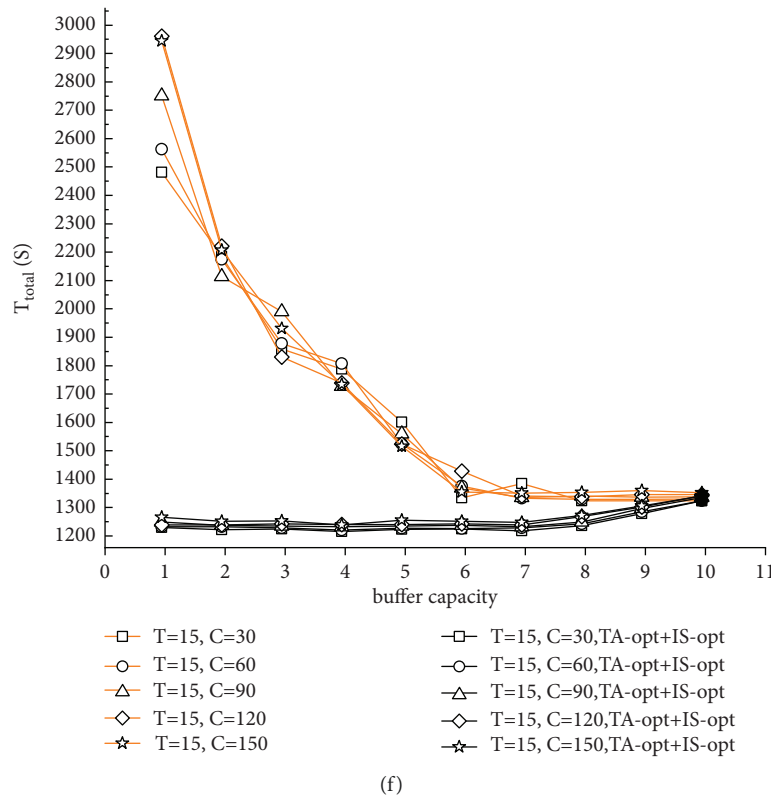
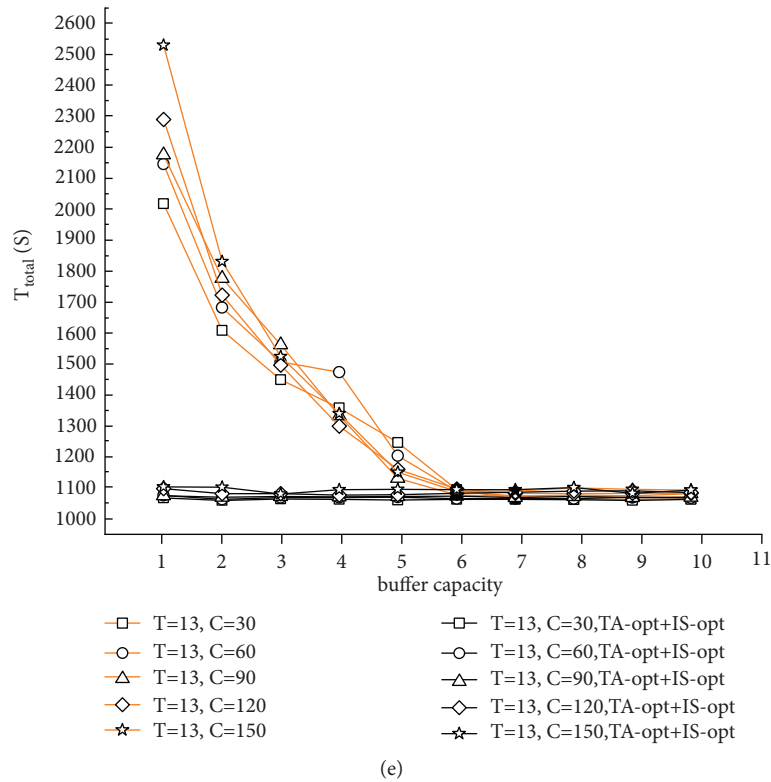


FIGURE 12: Comparison of the total picking time ( $T_{total}$ ) with the buffer capacity. (a)  $T = 5$ . (b)  $T = 7$ . (c)  $T = 9$ . (d)  $T = 11$ . (e)  $T = 13$ . (f)  $T = 15$ .

5.3. Analyzing the Buffer Capacity with TA-Opt and IS-Opt. This experiment is to verify the effect of buffer capacity with TA-opt and IS-opt. Therefore, the I/O buffer is set to 1 to 10. There are 600 scenarios with the variation of the number of

tiers ( $T$ ), the number of columns ( $C$ ), and the buffer capacity. In order to eliminate the bias, the experiment was repeated 50 times. The average value of the total operation time ( $T_{total}$ ) is used.

The result is shown in Figure 12. It is obvious that the total operation time can be reduced by expanding the buffer capacity. However, for a low rack system, the optimization effect is low or even almost loses the optimization ability, when the buffer capacity increases to a certain amount. For example, as is shown in Figure 12(a), the data show that  $T_{\text{total}}$  does not change significantly. When buffer capacity is greater than 4, that is because 4 capacities are enough to balance the efficiency of the lifters and the shuttles. On the other hand, Figure 12 shows that the optimization effect of TA-opt and IS-opt is greater with small buffer capacity, while the optimization effect of TA-opt and IS-opt is not obvious with large buffer capacity. Moreover, the expansion of buffer capacity has no obvious effect on the optimization of TA-opt and IS-opt.

## 6. Conclusion

This paper models the multi-tier shuttle warehouse system (MSWS) with tier-captive shuttles in which the shuttles can only serve the dedicated tier and process the horizontal movement of the totes. We proposed the object-oriented timed colored Petri net (OTCPN) to model the MSWS, and it reduces the modeling difficulty and complexity and provides a reference for other complex warehouse system modeling.

We build the OTCPN simulation model and analyze the influence of system structure and control strategy. Therefore, we carry out numerical experiments to evaluate the total picking time with the task assignment, the information schedule, and the buffer capacity. The result shows that the task assignment with the task balance strategy (TA-opt) can reduce the total picking time, and the improvement is 1.8% ~ 40%. The information schedule (IS-opt) means checking the buffer capacity before releasing the task, so that it reduces the device occupancy time. The improvement in total picking time is 20% ~ 53%. Considering both TA-opt and IS-opt, the total picking time can be reduced by 40% ~ 62%.

For the system structure, we analyze the I/O buffer capacity. The result shows that expanding the buffer capacity can reduce the total picking time. However, an unlimited increase in buffer capacity does not result in significant optimizations. The appropriate capacity of buffers to balance the efficiency of the lifters and shuttles can reduce the total picking time. Moreover, the result shows the buffer capacity has no obvious effect on the optimization of TA-opt and IS-opt.

In future work, it is interesting to model other warehouse systems with OTCPN. We can also study the deterministic relationship between buffer capacity and different system sizes in different warehouse systems to guide system planning and design.

## Data Availability

The data used to support the findings of this study are available from the corresponding author upon request.

## Conflicts of Interest

The authors declare that they have no conflicts of interest or personal relationships that could have appeared to influence the work reported in this paper.

## Acknowledgments

This work was supported by Shandong Provincial Natural Science Foundation (ZR2019MA022).

## References

- [1] G. Marchet, M. Melacini, S. Perotti, and E. Tappia, "Analytical model to estimate performances of autonomous vehicle storage and retrieval systems for product totes," *International Journal of Production Research*, vol. 50, no. 24, pp. 7134–7148, 2012.
- [2] B. Zou, X. Xu, Y. Yale Gong, and R. De Koster, "Modeling parallel movement of lifts and vehicles in tier-captive vehicle-based warehousing systems," *European Journal of Operational Research*, vol. 254, no. 1, pp. 51–67, 2016.
- [3] Y. Wang, S. Mou, and Y. Wu, "Storage assignment optimization in a multi-tier shuttle warehousing system," *Chinese Journal of Mechanical Engineering*, vol. 29, no. 2, pp. 421–429, 2016.
- [4] E. Tappia, D. Roy, M. Melacini, and R. De Koster, "Integrated storage-order picking systems: technology, performance models, and design insights," *European Journal of Operational Research*, vol. 274, no. 3, pp. 947–965, 2019.
- [5] Y. Wu, C. Zhou, W. Ma, and X. T. R. Kong, "Modelling and design for a shuttle-based storage and retrieval system," *International Journal of Production Research*, vol. 58, no. 16, pp. 4808–4828, 2020.
- [6] T. Lerher, B. Y. Ekren, G. Dukic, and B. Rosi, "Travel time model for shuttle-based storage and retrieval systems," *International Journal of Advanced Manufacturing Technology*, vol. 78, no. 9–12, pp. 1705–1725, 2015.
- [7] T. Lerher, "Travel time model for double-deep shuttle-based storage and retrieval systems," *International Journal of Production Research*, vol. 54, no. 9, pp. 2519–2540, 2016.
- [8] Z. Ning, L. Lei, Z. Saipeng, and G. Lodewijks, "An efficient simulation model for rack design in multi-elevator shuttle-based storage and retrieval system," *Simulation Modelling Practice and Theory*, vol. 67, pp. 100–116, 2016.
- [9] M. Borovinšek, B. Y. Ekren, A. Burinskienė, and T. Lerher, "MULTI-OBJECTIVE optimisation model of shuttle-based storage and retrieval system," *Transport*, vol. 32, no. 2, pp. 120–137, 2016.
- [10] B. Y. Ekren, A. Akpunar, Z. Sari, and T. Lerher, "A tool for time, variance and energy related performance estimations in a shuttle-based storage and retrieval system," *Applied Mathematical Modelling*, vol. 63, pp. 109–127, 2018.
- [11] L. Qiqiang and D. Ran, "Modeling of sorting system based on controlled and extended time petri net," *COMPUTER SIMULATION*, vol. 18, no. 5, pp. 62–66, 2001.
- [12] H. Yindi, Z. Yinquan, S. Mingxi, and W. Chunfeng, "Modeling & simulation of the picking system based on petri-net," *LOGISTICS TECHNOLOGY*, vol. 3, pp. 78–81, 2006.
- [13] G. Tian, Z. Pan, T. Wei, L. Xiaolei, and L. Fei, "Research on the scheduling problems of the warehousing system based on hierarchical colored petri nets," *Chinese Journal of Mechanical Engineering*, vol. 41, no. 04, pp. 148–153, 2005.

- [14] Y. Chongyi, *Principle and Application of Petri Nets*, Publishing House of Electronics Industry, Bei Jing, 2005.
- [15] J. Kurt, *Coloured Petri Nets: Basic Concepts, Analysis Methods and Practical Use*, Publishing House of Electronics Industry, New York, 1995.
- [16] O. T. Baruwa and M. A. Piera, "A coloured Petri net-based hybrid heuristic search approach to simultaneous scheduling of machines and automated guided vehicles," *International Journal of Production Research*, vol. 54, no. 16, pp. 4773–4792, 2016.

## Research Article

# Fuzzy Analysis of SVIRS Disease System with Holling Type-II Saturated Incidence Rate and Saturated Treatment

Hu Zhang,<sup>1</sup> V. Madhusudanan ,<sup>2</sup> B. S. N. Murthy,<sup>3</sup> M. N. Srinivas,<sup>4</sup>  
and Biruk Ambachew Adugna <sup>5</sup>

<sup>1</sup>School of Management Science and Engineering, Anhui University of Finance and Economics, Bengbu 233030, China

<sup>2</sup>Department of Mathematics, S.A. Engineering College, Chennai 600077, Tamil Nadu, India

<sup>3</sup>Department of Mathematics, Aditya College of Engineering and Technology, Surampalem, Andhra Pradesh, India

<sup>4</sup>Department of Mathematics, School of Advanced Sciences, Vellore Institute of Technology, Vellore 632014, Tamil Nadu, India

<sup>5</sup>Department of Computer Science, Ambo University, Ambo, Ethiopia

Correspondence should be addressed to V. Madhusudanan; mvmsmaths@gmail.com and Biruk Ambachew Adugna; biruk.ambachew@ambou.edu.et

Received 1 May 2022; Revised 25 May 2022; Accepted 13 June 2022; Published 29 August 2022

Academic Editor: Punit Gupta

Copyright © 2022 Hu Zhang et al. This is an open access article distributed under the Creative Commons Attribution License, which permits unrestricted use, distribution, and reproduction in any medium, provided the original work is properly cited.

This article presents a fuzzy SVIRS disease system with Holling type-II saturated incidence rate and saturated treatment, in which all parameters related to population dynamics have been considered as fuzzy numbers. Then, the existence condition and permanence of the SVIRS model have been discussed and we derived disease-free and endemic equilibrium points of the proposed fuzzy system. The local stability conditions of the fuzzy system around these equilibrium points using Routh–Hurwitz criteria are discussed. We also verified global stability around the interior steady state using Lozinskii measure. Computer simulations are provided to understand the dynamics of the proposed system. Parameter analysis is carried out with the help of computer simulation. Fuzzy provides better solution for any disease modeling in many ways like disease detection and transmission, different stages of disease, risk analysis (through parameter analysis), and optimal recovery solutions. Earlier literature acts as background to startup this disease modeling and optimal solutions provided by fuzzy logic is one of the motivational key element behind this fuzzy SVIRS model with Holling type-II and its analysis by both analytical and computer simulation.

## 1. Introduction

Epidemiology, which studies the stealing and determinants of contamination hazard in individual communities, is sometimes referred to as the nucleus discipline of community wellbeing. Mathematical epidemic models aid in the understanding of infectious disease transmission and spread, the recognition of factors leading the transmission procedure in order to discover flourishing organize tactics, and the evaluation of observation strategies and interference procedures. Kermack and McKendrick [1] systematically introduced deterministic models for communicable diseases. In their concept, three epidemiological classes are regarded the fundamental aspects describing infectious diseases [2]: the vulnerable group  $S(t)$ , the infective class  $I(t)$  [3], and the recovered class  $R(t)$  [4]. In order to better

recognize the process of communicable disease transmission [5], some authors have investigated several types of epidemic systems by taking into account dissimilar compartment models such as SI [6], SIS [7], SIR [8], SIRS [9], SEIR [10], SVEIR [11], and others [12].

In recent years, controlling infectious diseases has become a more difficult task [13]. Vaccination is one approach for controlling infectious diseases [14]. Vaccination is an important component of health treatments aiming at avoiding the spread of transferable diseases because of its wellbeing and rate efficiency [15]. Certainly, high vaccination rates have resulted in dramatic reductions or even eradication of various vaccine-preventable transferable diseases, as seen in the case of smallpox [16]. Nonetheless, one of the most important aspects of vaccination is its level of safety, both in terms of its capacity to prevent sickness and



the longevity of the generated immunity. Some vaccines, such as measles [17], are quite successful, whereas others, such as varicella, are not [18]. Due to medical circumstances, as well as the variation and progress of communicable diseases, the efficacy and levels of fortification offered by a vaccine may gradually reduce with time since the flu virus [19] can evolve quickly. Last year's influenza vaccine is improbable to protect people from this year's viral strains. The measles syndrome [20], which is protected by the measles-mumps-rubella vaccine, does not change substantially from time to time, representative that it is just as probable to defend people now as it was 10 years ago. A quantity of vaccines reduces the risk of infection [21], but they do not prevent the disease from forming and spreading in someone who has been vaccinated [22]. Although these flawed vaccines may not completely avoid contagion [23], they may reduce the likelihood of infection or the severity of infection, hence reducing the burden of infectious disease [24]. Many researchers in the mathematical epidemiology literature have looked at epidemic models with poor immunization [25].

The incidence rate plays an imperative function in determining the dynamics of epidemic models in mathematical modeling of communicable diseases. Kermack and Mckendrick proposed the prevalence rate in its traditional mass action version in 1927. The interaction term in this incidence rate is a linearly rising function of the numeral of infective, which is not optimal for large inhabitants. Anupama et al. [26] postulated a nonlinear prevalence rate for various psychological impacts as a result of this. Anupama et al. were motivated by behavioural changes: during periods of high frequency the apparent threat of disease might become quite high, leading to drastic changes in people's behaviour and, as a result, lowering the real risk of infection. Only a few authors have emphasised the importance of nonlinear frequency rates in the study of infectious disease spread dynamics [27]: Anderson and May [28], Wei and Chen [29], Zhang et al. [30], Li et al. [31], Kumar [32, 33], and Goel [34, 35]. A nonlinear incidence rate SIR model was proposed by Zhou and Fan [36]. At this frequency rate, the quantity of effective interactions between infective and susceptible individuals may oversupply due to an overpopulation of infective individuals. Despite the fact that the dynamics of SIR or SIS diseases models with the saturated incidence rate have been extensively studied in the literature [37], few investigations on the saturated treatment function, even in SEIR epidemic models, have been published [38]. In this article, we will investigate the SEIR model with the saturated incidence rate and saturated treatment function in order to better understand the effects of these points on the spread of infectious diseases [39]. We believe that virus-infected hosts are unable to infect other hosts during the incubation period, and that recovered people and vaccinated-treated people have established eternal resistance and are no longer susceptible to infection [36].

In recent literature, disease models with fuzzy analysis are trending and inspiring many scientists; likewise, we also studied disease models with risk analysis using fuzzy logic, which is the motivation for our work also [40]. Literature on

disease modeling with fuzzy system is also little less in number, so we proposed the fuzzy SVIRS disease system with Holling type-II functional response. The current model is studied under fuzzy system and studied analytically and numerically using mathematical and computer software tools, respectively [41]. This work focused on parameter analysis also to analyze all parameters numerically to identify, which parameter influences and effects the system strongly [42]. The current work focused on the fuzzy system for the SVIRS disease model with Holling type-II functional response. All disease models are driven from the basic disease model SIR and SIER [43]. These models are very basic in nature. To capture disease detection, disease transmission, and risk analysis, we need to study the model with little complex constraints which may be interactions (like functional responses) which are complex in nature [44]. To serve an optimal solution for disease detection, disease transmission and its stages and recovery status and its stages can be achieved greatly by fuzzy systems. The fuzzy system works greatly when the scenario is complex in nature, uncertainty in scenario, and vague data are involved.

The parameters used to mathematically express biological events are typically assumed to be accurate. Researchers have only made a few attempts to include environmental uncertainty into their research. The application of diverse mathematical approaches and concepts aids in the better understanding of biological and physical processes. In biological modeling, interval parameters or fuzzy parameters should be employed more frequently than recent attempts due to the realistic scenario. The fuzzy set theory, proposed by Zadeh [40], can be used to account for uncertainty in biological data. The application of fuzzy logic and fuzzy sets in biological systems offers a lot of potential, but there are not many of them. Reference [45] has several examples of fuzzy mathematics applications. Angalaeswari et al. describe some epidemic models that take into account parameter uncertainty and population heterogeneity [45]. We investigated a fuzzy SVIRS diseases system with Holling type-II incidence rate and saturated therapy based on the motivation of [30–36, 46], in which all parameters linked to population dynamics were considered as fuzzy numbers. The current work is definitely different previous works in view of parameter analysis, which says the control parameters for disease transmission and recovery greatly. Fuzzy analysis definitely added strength to the current work which shapes it as a novel innovative and informative study. Certainly, this work can contribute qualitative information and notable conclusions to the literature.

## 2. Preliminaries of Fuzzy Analysis

A fuzzy set is a collection of things in which there is no clear distinction between those that belong to the group and those that do not. We will go over some basic notations for fuzzy sets in this section [46]. We recommend Natrayan [47] and Klir and Yuan [48] for further information on fuzzy sets.

*Definition 1.*  $\zeta$ -cut of a fuzzy number: a nonempty set  $P$ , a fuzzy set in  $P$  is a map  $f: P \rightarrow [0, 1]$ . A  $\zeta$ -cut of a fuzzy number  $\tilde{f}$  in  $P$  is denoted by  $f_\zeta = [f_l(\zeta), f_u(\zeta)]$ , where

$f_l(\zeta)$  and  $f_u(\zeta)$  are the lower and upper bounds of the closed interval in that order and is defined as the following fuzzy set [49]:

$$f_\zeta = \left\{ \frac{P}{\Xi_{\tilde{f}}} (p) \geq \zeta, p \in P \right\} \text{ where } \zeta \in [0, 1]. \quad (1)$$

Figure 1 shows the  $\zeta$ -cut of a triangular fuzzy number. Figure 2 shows the triangular fuzzy number.

**Definition 2.** Triangular fuzzy number.

A triangular fuzzy number is a continuous membership function  $\Xi_{\tilde{f}}(p): P \rightarrow [0, 1]$  and is denoted by  $\tilde{f}$ .

**Definition 3.** Utility function method.

The utility function is defined as the weighted sum of the objectives:

$$U = \sum_{k=1}^n \sigma_k f_k, \sigma_k \geq 0, \quad (2)$$

where  $\sigma_k$  is a scalar that represents the relative importance of the objectives  $f_k$  and subject to the condition  $\sum_{k=1}^n \sigma_k = 1$ .

### 3. Fuzzy Model

Let  $\tilde{S}(t)$ ,  $\tilde{V}(t)$ ,  $\tilde{I}(t)$ , and  $\tilde{R}(t)$  denote the population densities of fuzzy susceptible, vaccinated, infected, and recovered human in the environment at time  $t$ , respectively. By using the concept on the fuzzy initial value problem [1] and differentials of fuzzy functions [2] and considering a set of fuzzy differential equations regarding the following SVIRS model [50], Table 1 shows the physical description of the symbols. Figure 3 shows the schematic diagram of the SVIRS fuzzy model.

$$\begin{cases} D\tilde{S} = \tilde{\Delta} - \tilde{\Omega}S - \frac{\tilde{\alpha}SI}{1 + \tilde{\beta}I} - \tilde{\gamma}S = \tilde{\phi}R, \\ D\tilde{V} = \tilde{\Omega}S - \frac{\tilde{\chi}SI}{1 + \tilde{\beta}I} - \tilde{\gamma}V, \\ D\tilde{I} = \frac{\tilde{\alpha}SI}{1 + \tilde{\beta}I} + \frac{\tilde{\chi}SI}{1 + \tilde{\beta}I} - (\tilde{\gamma} + \tilde{\eta} + \tilde{\psi})I - \frac{\tilde{m}I}{1 + \tilde{n}I}, \\ D\tilde{R} = \tilde{\psi}I + \frac{\tilde{m}I}{1 + \tilde{n}I} - \tilde{\phi}R - \tilde{\gamma}R, \end{cases} \quad (3)$$

where  $D \equiv d/dt$ .

Let the solution of the fuzzy system (1) can be defined as  $[D\tilde{Z}]_\sigma = [(DZ)_l^\sigma, (DZ)_u^\sigma]$ , then the deterministic system of the fuzzy model (1) is given by

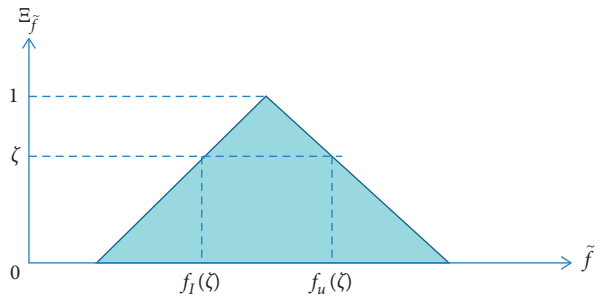


FIGURE 1:  $\zeta$ -cut of a triangular fuzzy number.

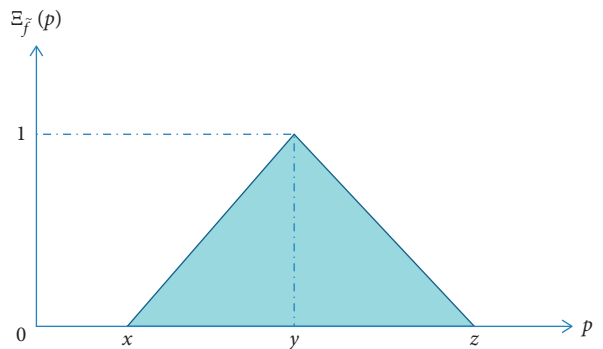


FIGURE 2: Triangular fuzzy number.

$$\begin{cases} [DS]_l^\sigma = [\Delta_l]^\sigma - [(\delta_u)^\sigma + (\gamma_u)^\sigma]S - \frac{(\alpha_u)^\sigma SI}{1 + (\beta_l)^\sigma I} + [\phi_l]^\sigma, \\ [DS]_u^\sigma = [\Delta_u]^\sigma - [(\delta_l)^\sigma + (\gamma_l)^\sigma]S - \frac{(\alpha_l)^\sigma SI}{1 + (\beta_u)^\sigma I} + [\phi_u]^\sigma, \\ [DV]_l^\sigma = [\delta_l]^\sigma S - \frac{(\chi_u)^\sigma VI}{1 + (\beta_l)^\sigma I} - (\gamma_u)^\sigma V, \\ [DV]_u^\sigma = [\delta_u]^\sigma S - \frac{(\chi_l)^\sigma VI}{1 + (\beta_u)^\sigma I} - (\gamma_l)^\sigma V, \\ [DI]_l^\sigma = \frac{(\alpha_l)^\sigma SI}{1 + (\beta_u)^\sigma I} + \frac{(\chi_l)^\sigma VI}{1 + (\beta_u)^\sigma I} \\ \quad - [(\gamma_u)^\sigma + (\eta_u)^\sigma + (\psi_u)^\sigma]I - \frac{(m_u)^\sigma I}{1 + (b_l)^\sigma I}, \\ [DI]_u^\sigma = \frac{(\alpha_u)^\sigma SI}{1 + (\beta_l)^\sigma I} + \frac{(\chi_u)^\sigma VI}{1 + (\beta_l)^\sigma I} \\ \quad - [(\gamma_l)^\sigma + (\eta_l)^\sigma + (\psi_l)^\sigma]I - \frac{(m_l)^\sigma I}{1 + (b_u)^\sigma I}, \\ [DR]_l^\sigma = (\psi_l)^\sigma I + \frac{(m_l)^\sigma I}{1 + (n_u)^\sigma I} - [(\phi_u)^\sigma + (\gamma_u)^\sigma]R, \\ [DR]_u^\sigma = (\psi_u)^\sigma I + \frac{(m_u)^\sigma I}{1 + (n_l)^\sigma I} - [(\phi_l)^\sigma + (\gamma_l)^\sigma]R. \end{cases} \quad (4)$$

TABLE 1: Physical description of the symbols.

Fuzzy parameters	Description of the symbols
$\tilde{\Delta}$	The recruitment rate of susceptible
$\tilde{\alpha}$	The vigor of infection
$\tilde{\beta}$	The reticence actions taken by the infected
$\tilde{\chi}$	The rate at which vaccinated persons become infected
$\tilde{\Omega}$	The transmission rate from susceptible individuals to vaccinated ones
$\tilde{\phi}$	The transmission rate from recovered individuals to susceptible ones
$\tilde{\psi}$	The transmission rate from infected individuals to recovered ones
$\tilde{\gamma}$	The natural fatality rate of all the individuals
$\tilde{\eta}$	The death rate due to disease
$\tilde{m}$	The treatment rate
$\tilde{n}$	The rate of limitation in medical resource

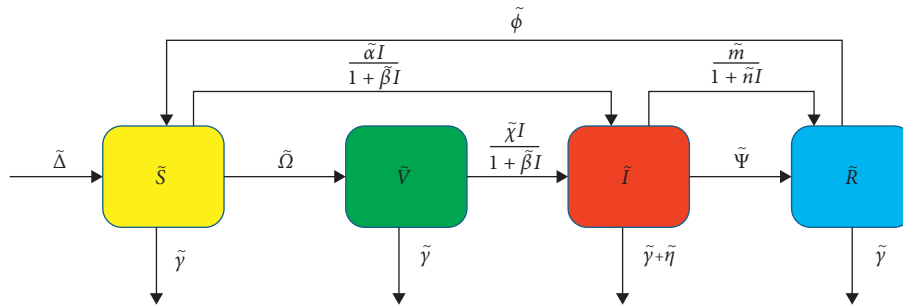


FIGURE 3: A schematic diagram of the SVIRS fuzzy model.

The above system of differential equations can be solved using the UFM principle as follows [51]:

$$\begin{cases} DS = \sigma_1 [DS]_l^\sigma + \sigma_2 [DS]_u^\sigma, \\ DV = \sigma_1 [DS]_l^\sigma + \sigma_2 [DS]_u^\sigma, \\ DI = \sigma_1 [DS]_l^\sigma + \sigma_2 [DS]_u^\sigma, \\ DR = \sigma_1 [DS]_l^\sigma + \sigma_2 [DS]_u^\sigma, \end{cases} \quad (5)$$

where  $\sigma_1$  and  $\sigma_2$  are two weight functions such that  $\sigma_1 + \sigma_2 = 1$  and  $\sigma_1 + \sigma_2 \geq 0$ ; then, (5) can be written as

$$\begin{cases} DS = u_{11} - u_{12}SI - u_{13}S + u_{14}R, \\ DV = u_{21}S - u_{22}VI - u_{23}V, \\ DI = u_{31}SI - u_{32}VI - u_{13}I + u_{34}I, \\ DR = u_{41}I - u_{42}I - u_{43}R, \end{cases} \quad (6)$$

where

$$\begin{aligned} u_{11} &= \sigma_1 (\Delta_l)^\sigma + \sigma_2 (\Delta_u)^\sigma; u_{12} = \sigma_1 \frac{(\alpha_u)^\sigma}{1 + (\beta_u)^\sigma I} + \sigma_2 \frac{(\alpha_l)^\sigma}{1 + (\beta_l)^\sigma I}; u_{14} = \sigma_1 (\phi_l)^\sigma + \sigma_2 (\phi_u)^\sigma, \\ u_{13} &= \sigma_1 [(\delta_u)^\sigma + (\gamma_u)^\sigma] + \sigma_2 [(\delta_l)^\sigma + (\gamma_l)^\sigma]; u_{21} = \sigma_1 (\delta_l)^\sigma + \sigma_2 (\delta_u)^\sigma, \\ u_{22} &= \sigma_1 \frac{(\chi_u)^\sigma}{1 + (\beta_u)^\sigma} + \sigma_2 \frac{(\chi_l)^\sigma}{1 + (\beta_l)^\sigma}; u_{23} = \sigma_2 (\gamma_u)^\sigma + \sigma_2 (\gamma_l)^\sigma; u_{31} = \sigma_1 \frac{(\alpha_l)^\sigma}{1 + (\beta_u)^\sigma} + \sigma_2 \frac{(\alpha_u)^\sigma}{1 + (\beta_l)^\sigma}, \\ u_{32} &= \sigma_1 \frac{(\chi_u)^\sigma}{1 + (\beta_u)^\sigma} + \sigma_2 \frac{(\chi_l)^\sigma}{1 + (\beta_l)^\sigma}; u_{34} = \sigma_1 \frac{(m_u)^\sigma}{1 + (n_l)^\sigma I} + \sigma_2 \frac{(m_l)^\sigma}{1 + (n_u)^\sigma I}, \\ u_{33} &= \sigma_1 [(\gamma_u)^\sigma + (\eta_u)^\sigma + (\psi_u)^\sigma] + \sigma_2 [(\gamma_l)^\sigma + (\eta_l)^\sigma + (\psi_l)^\sigma]; u_{41} = \sigma_1 (\psi_l)^\sigma + \sigma_2 (\psi_u)^\sigma, \\ u_{22} &= \sigma_1 \frac{(m_l)^\sigma}{1 + (n_u)^\sigma} + \sigma_2 \frac{(m_u)^\sigma}{1 + (n_l)^\sigma}; u_{43} = \sigma_1 (\phi_u)^\sigma + \sigma_2 (\phi_l)^\sigma; u_{44} = \sigma_1 (\gamma_u)^\sigma + \sigma_2 (\gamma_l)^\sigma. \end{aligned} \quad (7)$$

### 4. Positivity and Boundedness of the SVIRS Fuzzy Model

In this section, all solutions of the proposed system (3) have been bounded [52]. First, we use Lemma 1 to verify the positivity of system (3).

**Lemma 1.** *If  $u_{13} - u_{21} > 0, u_{43} - u_{14} > 0, u_{34} - u_{33} - u_{41} - u_{42} > 0, u_{31} - u_{12} > 0, u_{32} - u_{22} > 0$  provided that  $(\delta_l)^\sigma + (\gamma_l)^\sigma > (\delta_u)^\sigma, (\phi_l)^\sigma > (\phi_u)^\sigma, (m_l)^\sigma/1 + (n_u)^\sigma + (\gamma_l)^\sigma + (\eta_l)^\sigma + (\phi_l)^\sigma > (\phi_u)^\sigma + (m_u)^\sigma/1 + (n_l)^\sigma, (\alpha_u)^\sigma/1 + (\beta_l)^\sigma > (\delta_u)^\sigma$ , then the solutions  $S(t), V(t), I(t)$ , and  $R(t)$  of system (3) are positives.*

*Proof.* Consider

$$\begin{cases} u_{13} - u_{21} = \sigma_1 [(\delta_u)^\sigma + (\gamma_u)^\sigma] + \sigma_2 [(\delta_l)^\sigma + (\gamma_l)^\sigma] \\ -\sigma_1 (\delta_l)^\sigma - \sigma_2 (\delta_u)^\sigma \\ = \sigma_1 \{2(\delta_u)^\sigma + (\gamma_u)^\sigma - 2(\delta_l)^\sigma + (\gamma_l)^\sigma\} \\ + (\delta_l)^\sigma + (\gamma_l)^\sigma - \sigma_2 (\delta_u)^\sigma. \end{cases} \quad (8)$$

Now,  $\sigma_1 = 0$ , we have  $u_{31} - u_{21} = (\delta_l)^\sigma + (\gamma_l)^\sigma - (\delta_u)^\sigma$ ; then,  $u_{13} - u_{21}$  will be positive for  $\sigma_1 = 0$  if

$$(\delta_l)^\sigma + (\gamma_l)^\sigma > (\delta_u)^\sigma. \quad (9)$$

Therefore, from equation (8), it is obtained that

$$\frac{d}{d\sigma_1} (u_{13} - u_{21}) = \{2(\delta_u)^\sigma + (\gamma_u)^\sigma - 2(\delta_l)^\sigma + (\gamma_l)^\sigma\} > 0, \quad (10)$$

$$\forall \sigma_1 \in [0, 1].$$

So,  $u_{13} - u_{21}$  is an increasing function with respect to  $\sigma_1$ , and it will be positive if condition (9) holds. In the similar way, it can be proved that  $u_{43} - u_{14}, u_{33} + u_{34} - u_{41} - u_{42}$  is an increasing function with respect to  $\sigma_1$ , and it will be positive if the condition  $(\phi_l)^\sigma > (\phi_u)^\sigma + (\psi_l)^\sigma > (m_l)^\sigma/1 + (n_u)^\sigma + (\gamma_l)^\sigma + (\eta_l)^\sigma + (\psi_l)^\sigma > (\psi_u)^\sigma + (m_u)^\sigma/1 + (n_l)^\sigma, (\alpha_u)^\sigma/1 + (\beta_l)^\sigma > (\delta_u)^\sigma, (\chi_u)^\sigma/1 + (\beta_l)^\sigma > (\chi_l)^\sigma/1 + (\beta_u)^\sigma$  holds.  $\square$

**Theorem 1.** *All solutions of system (3) are bounded in the region  $R_+^4$  provided that*

$$\begin{aligned} u_{31} > u_{12}, u_{32} > u_{22}, \\ \mu = \min\{u_{23}, u_{13} - u_{21}, u_{43} - u_{14}, u_{33} + u_{34} - u_{41} - u_{42}\}. \end{aligned} \quad (11)$$

*Proof.* Let us define a function  $G = S + V + I + R$ .

Now, by separating and simplifying with regard to time  $t$ , we have

$$\begin{aligned} DG &= DS + DV + DI + DR, \\ \begin{cases} DG = u_{11} - u_{23}V + (u_{21} - u_{13})S \\ + (u_{41} + u_{42} - u_{34} - u_{33})I \\ + (u_{14} - u_{43})R + (u_{31} - u_{12})SI \\ + (u_{32} - u_{22})VI. \end{cases} \end{aligned} \quad (12)$$

For a positive real number  $\mu$ ,

$$\begin{aligned} DG + \mu G &= u_{11} + [\mu - u_{23}]V + [\mu - (u_{13} - u_{21})]S \\ &+ [\mu - (u_{34} + u_{33} - u_{41} - u_{42})]I \\ &+ [\mu - (u_{43} - u_{14})]R \\ &+ (u_{31} - u_{21})SI + (u_{32} - u_{22})VI. \end{aligned} \quad (13)$$

Now, according to Lemma 1, if  $\mu = \min\{u_{23}, u_{13} - u_{21}, u_{43} - u_{14}, u_{34} + u_{33} - u_{41} - u_{42}\}$ , then the above equation becomes  $DG + \mu G \leq u_{11}$ . Solving this, we get  $G \leq u_{11}/\mu + ke^{-\mu t}$ . As  $t \rightarrow \infty$ , we have  $G \leq u_{11}/\mu$ . So, it can show  $S(t) \leq u_{11}/\mu, V(t) \leq u_{11}/\mu, I(t) \leq u_{11}/\mu, R(t) \leq u_{11}/\mu$ . This establishes that the system's solution is bounded.

The solutions of system (3) are bounded in the region  $R_+^4$  provided that  $a_{31} > a_{12}, a_{32} > a_{22}$  and  $\mu = \min\{u_{23}, u_{13} - u_{21}, u_{43} - u_{14}, u_{33} + u_{34} - u_{41} - u_{42}\} \sigma_1 = 0$ .  $\square$

### 5. Existence and Stability Analysis

In this section, we look at the presence and stability of the fuzzy system's nonnegative equilibrium point (3). In a fuzzy system (3), there are two nonnegative equilibrium points. The following are the existence and stability conditions for them [53]:

(i) Disease free equilibrium point  $P_1(S^0, 0, 0, 0) = (u_{11}/u_{13}, 0, 0, 0)$

(ii) Endemic equilibrium point  $P_2(S^*, V^*, I^*, R^*)$

Here,  $S^* = u_{11}u_{43} + u_{14}u_{11} + u_{14}u_{42}/u_{43}u_{13} + u_{43}u_{12}I^*$ ,  $V^* = u_{21}u_{11}u_{43} + u_{21}u_{14}u_{41} + u_{21}u_{14}u_{42}/u_{43}u_{12}u_{22}I^* + u_{43}u_{13}u_{22}I^* + u_{43}u_{12}u_{23}I^* + u_{43}u_{13}u_{23}$ ,

$$R^* = \frac{u_{41} + u_{42}I^*}{u_{43}}, \quad (14)$$

$$\Gamma_1 I^{*2} + \Gamma_2 I^* + \Gamma_3 = 0,$$

where

$$\begin{aligned} \Gamma_1 &= u_{12}u_{22}u_{33}u_{43} + u_{12}u_{22}u_{34}u_{43}, \\ \Gamma_2 &= u_{13}u_{22}u_{33}u_{43} + u_{13}u_{22}u_{34}u_{43} + u_{12}u_{23}u_{33}u_{43} \\ &+ u_{12}u_{23}u_{34}u_{43} - u_{11}u_{22}u_{31}u_{43} \\ &- u_{22}u_{31}u_{14}u_{41} - u_{14}u_{22}u_{31}u_{42}, \\ \Gamma_3 &= u_{13}u_{23}u_{33}u_{43} + u_{13}u_{23}u_{34}u_{43} - u_{11}u_{31}u_{23}u_{43} \\ &- u_{14}u_{31}u_{23}u_{41} - u_{14}u_{31}u_{23}u_{42} - u_{11}u_{21}u_{32}u_{43} \\ &- u_{14}u_{21}u_{32}u_{41} - u_{14}u_{21}u_{32}u_{42}. \end{aligned} \quad (15)$$

**Theorem 2.** *Fuzzy system (3) is locally asymptotically stable at disease free equilibrium point  $P_1(S^0, 0, 0, 0)$  if  $u_{13}^2 - u_{11}u_{13} > 0$  and  $u_{13}u_{44} - u_{11}u_{31} > 0$ ; otherwise, it is unstable.*

*Proof.* The characteristic equation of the fuzzy system (3) at disease free equilibrium point  $P_1(S^0, 0, 0, 0)$  is

$$\lambda^4 + \sum_1 \lambda^3 + \sum_2 \lambda^2 + \sum_3 \lambda + \sum_4 = 0, \quad (16)$$

where

$$\begin{aligned} \sum_1 &= u_{13} + u_{23} + u_{33} + u_{43} + u_{44} - u_{31}S^0, \\ \sum_2 &= u_{13}u_{43} + u_{13}u_{33} + u_{13}u_{44} + u_{23}u_{43} + u_{23}u_{33} \\ &\quad + u_{23}u_{44} + u_{13}u_{23} - u_{31}u_{13}S^0 - u_{23}u_{31}S^0, \\ \sum_3 &= u_{13}u_{33}u_{43} + u_{13}u_{43}u_{44} + u_{23}u_{33}u_{43} + u_{23}u_{43}u_{44} \quad (17) \\ &\quad + u_{23}u_{43}u_{13} + u_{23}u_{33}u_{13} + u_{23}u_{13}u_{44} \\ &\quad - u_{23}u_{31}u_{43}S^0 - u_{23}u_{31}u_{13}S^0, \\ \sum_4 &= u_{13}u_{33} + u_{13}u_{44} - u_{31}u_{13}S^0. \end{aligned}$$

The required and sufficient requirements for local stability of a disease-free equilibrium point  $p_1(S^0, 0, 0, 0)$

according to Routh–Hurwitz criteria if  $\sum_1 > 0$ ,  $\sum_3 > 0$ ,  $\sum_4 > 0$ ,  $\sum_3(\sum_1 \sum_2 - \sum_3) > \sum_1 \sum_4$ , and  $\sum_4(\sum_1 \sum_2 \sum_3 - \sum_1^2 \sum_4 - \sum_3^2) > 0$ . It is evident that  $u_{13}^2 - u_{11}u_{13} > 0$  and  $u_{13}u_{44} - u_{11}u_{31} > 0$ .  $\square$

**Theorem 3.** Fuzzy system (3) is locally asymptotically stable at endemic equilibrium point  $p_2(S^*, V^*, I^*, R^*)$  if  $S^* < \max\{u_{13}/u_{31}, u_{33}/u_{31}\}$ ,  $V^* < \max\{u_{23}/u_{32}, u_{34}/u_{32}\}$ ,  $u_{33} - u_{31} > 0$ ,  $u_{22} - u_{12} > 0$ ,  $u_{12}u_{23}u_{33} > u_{14}u_{31}(u_{41} + u_{42})$ ,  $u_{12}u_{23}u_{33}u_{43} > u_{14}u_{22}u_{31}(u_{41} + u_{42})$ ; otherwise, it is unstable [54].

*Proof.* The characteristic equation of fuzzy system (3) at the endemic equilibrium point  $p_2(S^*, V^*, I^*, R^*)$  is

$$\lambda^4 + \Theta_1 \lambda^3 + \Theta_2 \lambda^2 + \Theta_3 \lambda + \Theta_4 = 0, \quad (18)$$

where

$$\begin{aligned} \Theta_1 &= u_{13} + u_{23} + u_{33} + u_{34} + u_{43} + u_{12}I^* + u_{22}I^* - u_{31}S^* - u_{32}V^*, \\ \Theta_2 &= u_{13}u_{23} + u_{13}u_{33} + u_{13}u_{34} + u_{23}u_{43} + u_{23}u_{34} \\ &\quad + u_{23}u_{43} + u_{33}u_{43} + u_{34}u_{43} + u_{12}u_{23}I^* + u_{12}u_{33}I^* \\ &\quad + u_{12}u_{34}I^* + u_{12}u_{43}I^* + u_{13}u_{22}I^* + u_{22}u_{33}I^* \\ &\quad + u_{22}u_{34}I^* + u_{22}u_{43}I^* - u_{13}u_{31}S^* - u_{23}u_{31}S^* \\ &\quad - u_{31}u_{43}S^* - u_{13}u_{32}V^* - u_{23}u_{32}V^* \\ &\quad - u_{32}u_{43}V^*I^* - u_{22}u_{31}S^*I^*, \\ \Theta_3 &= u_{13}u_{23}u_{33} + u_{13}u_{23}u_{34} + u_{13}u_{23}u_{43} + u_{13}u_{33}u_{43} + u_{13}u_{43}u_{34} \\ &\quad + u_{33}u_{23}u_{43} + u_{43}u_{23}u_{34} - u_{31}u_{14}u_{42}I^* - u_{14}u_{31}u_{41}I^* \\ &\quad + u_{22}u_{34}u_{43}I^* + u_{22}u_{33}u_{43}I^* + u_{13}u_{22}u_{43}I^* + u_{13}u_{22}u_{34}I^* \\ &\quad + u_{13}u_{33}u_{22}I^* + u_{22}u_{34}u_{43}I^* + u_{22}u_{33}u_{43}I^* + u_{13}u_{22}u_{43}I^* \\ &\quad + u_{13}u_{22}u_{34}I^* + u_{13}u_{33}u_{22}I^* + u_{13}u_{33}u_{22}I^* + u_{12}u_{34}u_{43}I^* \\ &\quad + u_{12}u_{33}u_{43}I^* + u_{12}u_{23}u_{33}I^* - u_{31}u_{23}u_{43}S^* - u_{23}u_{43}u_{32}V^* \\ &\quad + u_{22}u_{34}u_{43}I^* - u_{13}u_{23}u_{31}S^* - u_{13}u_{23}u_{32}V^* - u_{13}u_{31}u_{43}S^* \\ &\quad - u_{13}u_{43}u_{32}V^* + u_{12}u_{22}u_{34}I^{*2} + u_{12}u_{22}u_{43}I^{*2} - u_{12}u_{23}u_{32}V^*I^* \\ &\quad - u_{12}u_{31}u_{43}S^*I^* - u_{31}u_{22}u_{43}S^*I^* + u_{12}u_{23}u_{32}VI^{*2} + u_{21}u_{12}u_{32}S^*I^* \\ &\quad + u_{12}u_{22}u_{33}S^*I^{*2} + u_{12}u_{31}u_{43}S^*I^* - u_{12}u_{22}u_{31}S^*I^{*2}, \\ \Theta_4 &= u_{13}u_{23}u_{33}u_{43} + u_{13}u_{23}u_{33}u_{43} + u_{13}u_{23}u_{34}u_{43} + u_{12}u_{23}u_{34}u_{43}I^* \\ &\quad - u_{14}u_{23}u_{31}u_{41}I^* - u_{14}u_{23}u_{31}u_{42}I^* + u_{13}u_{22}u_{33}u_{43}I^* + u_{13}u_{22}u_{34}u_{43}I^* \\ &\quad - u_{14}u_{21}u_{32}u_{41}I^* - u_{14}u_{23}u_{32}u_{42}I^* - u_{13}u_{23}u_{31}u_{43}S^* - u_{13}u_{23}u_{32}u_{43}V^* \\ &\quad + u_{13}u_{23}u_{33}u_{43}I^* - u_{13}u_{23}u_{31}u_{43}S^* - u_{13}u_{23}u_{32}u_{43}V^* + u_{12}u_{22}u_{32}u_{43}V^*I^{*2} \\ &\quad - u_{13}u_{22}u_{31}u_{43}S^*I^* - u_{12}u_{23}u_{32}u_{43}V^*I^* + u_{12}u_{22}u_{33}u_{43}I^{*2} + u_{12}u_{32}u_{22}u_{43}V^*I^{*2} \\ &\quad + u_{12}u_{22}u_{34}u_{43}I^{*2} + u_{12}u_{21}u_{32}u_{43}S^*I^* - u_{14}u_{22}u_{31}u_{41}I^{*2} - u_{14}u_{22}u_{31}u_{42}I^{*2}. \end{aligned} \quad (19)$$

The required and sufficient requirements for local stability of a disease-free equilibrium point  $p_1(S^0, 0, 0, 0)$  according to the Routh–Hurwitz criteria if  $\Theta_1 > 0$ ,  $\Theta_3 > 0$ ,

$\Theta_4 > 0$ ,  $\Theta_3(\Theta_1\Theta_2 - \Theta_3) > \Theta_1^2\Theta_4$  and  $\Theta_4(\Theta_1\Theta_2\Theta_3 - \Theta_1^2\Theta_4 - \Theta_3^2) > 0$ .

It is evident that

$$S^* < \text{MAX} \left\{ \frac{u_{13}}{u_{31}}, \frac{u_{33}}{u_{31}} \right\}, V^* < \text{MAX} \left\{ \frac{u_{23}}{u_{32}}, \frac{u_{34}}{u_{32}} \right\},$$

$$u_{33} - u_{31} > 0, u_{22} - u_{12} > 0, \tag{20}$$

$$u_{12}u_{23}u_{33} > u_{14}u_{31}(u_{41} + u_{42}),$$

$$u_{12}u_{23}u_{33} > u_{14}u_{31}(u_{41} + u_{42}). \quad \square$$

**Theorem 4.** Fuzzy system (3) is globally asymptotically stable at the endemic equilibrium point  $p_2(S^*, V^*, I^*, R^*)$ . If  $\aleph_1 > 0$ , where

$$\aleph_1 = u_{31}\aleph + u_{32}\aleph - u_{33} - u_{34} + \min \left[ \begin{aligned} & \{u_{12}\aleph - u_{13} - u_{22}\aleph - u_{23} - \max\{u_{22}\aleph, u_{12}\aleph\}\}, -u_{21} - u_{31}\aleph \\ & + \min\{u_{22}\aleph + u_{23}, -u_{32}, \aleph(u_{22} - u_{32}) + u_{33} + u_{34}\} \end{aligned} \right]. \tag{21}$$

*Proof.* Let us consider the subsystem of fuzzy system (3):

$$\begin{cases} DS = u_{11} - u_{12}SI - u_{13}S + u_{14}R, \\ DV = u_{21}S - u_{22}VI - u_{23}V, \\ DI = u_{31}SI + u_{33}VI - u_{33}I - u_{34}I. \end{cases} \tag{22}$$

Let N be the variation matrix of the system (8) is

$$N = \begin{bmatrix} -u_{12}I^* - u_{13} & 0 & -u_{12}S^* \\ u_{21} & -u_{22}I^* - u_{23} & -u_{22}V^* \\ u_{13}I^* & u_{32} & u_{31}S^* + u_{32}V^* - u_{33} - u_{34} \end{bmatrix}. \tag{23}$$

Let  $N^{[2]}$  be the second additive compound matrix of N, we have

$$N = \begin{bmatrix} -u_{12}I^* - u_{13} - u_{22}I^* - u_{23} & -u_{22}V^* & -u_{12}S^* \\ u_{32} & -u_{22}I^* - u_{23}u_{31}S^* + u_{32}V^* - u_{33} - u_{34} & 0 \\ u_{13}I^* & u_{21} & -u_{22}I^* - u_{23}u_{31}S^* + u_{32}V^* - u_{33} - u_{34} \end{bmatrix}. \tag{24}$$

Let us consider the function  $\prod_x = \partial \prod / \partial x = \text{diag}(S/I - SI/I^2, S/I - SI/I^2, S/I - SI/I^2)$ .

Thus, we have  $\prod_x \prod^{-1} = \text{diag}(S/I - SI/I, S/S - I/I^2, S/I - I/I)$  and  $\prod N^{[2]} \prod^{-1} = N^{[2]}$ , so that

$$\Xi = \prod_x \prod + \prod N^{[2]} \prod^{-1} = \begin{bmatrix} \Xi_{11} & \Xi_{12} \\ \Xi_{21} & \Xi_{22} \end{bmatrix}, \tag{25}$$

where  $\Xi_{11} = S/S - I/I - u_{12}I^* - u_{13} - u_{22}I^* - u_{23}$ ;  $\Xi_{12} = [-u_{22}V^* u_{12}S^*]$ ;  $\Xi_{21} = [u_{21}u_{13}I^*]^T$ .

$$\Xi_{22} = \begin{bmatrix} \frac{S}{S} - \frac{I}{I} - u_{22}I^* - u_{23} - u_{22}V^* \\ u_{32}\frac{S}{S} - \frac{I}{I} + u_{31}S^* - u_{32}V^* - u_{33} - u_{34} \end{bmatrix}. \tag{26}$$

We considered  $\mathfrak{R}$  as the Lozinskii measure by Martin [7] with respect to the norm defined in three-dimensional space  $\|(x, y, z)\| = \max\{|x|, |y| + |z|\}$ , where  $(x, y, z)$  is any vector in  $R^3$ . Hence,  $\mathfrak{R}\{P\} \leq \sup\{P_i, P_1\}$ , where  $P_i = \mathfrak{R}\{\Xi_{ii}\} + |\Xi_{ij}|$  for  $i = 1, 2$  and  $i \neq j$  and  $\mathfrak{R}_1$  denotes the Lozinskii measure with

respect to the  $\Gamma_1$  vector norm. The Lozinskii measure for the matrix  $\Xi$  is given by

$$\mathfrak{R}_1(\Xi_{11}) = \frac{S}{S} - \frac{I}{I} - u_{12}I^* - u_{13} - u_{22}I^* - u_{23}; |\Xi_{12}| = \max\{u_{22}V^*, u_{12}S^*\} \tag{27}$$

$$\Xi_{21} = [u_{21}u_{13}I^*]^T; \mathfrak{R}_1(\Xi_{22}) = \frac{S}{S} - \frac{I}{I} - \text{MIN}\{u_{22}I^* + u_{23}, V^*(u_{22} - u_{32}) + u_{33} + u_{34}\}.$$

Here,  $P_1 = \mathfrak{R}_1(\Xi_{11}) + |\Xi_{12}| = S/S - I/I - u_{12}I^* - u_{13} - u_{22}I^* - u_{23} + \text{MAX}\{u_{22}V^* + u_{12}S^*\}$  and

$$P_2 = \mathfrak{R}_1(\Xi_{22}) + |\Xi_{21}| = \frac{S}{S} - \frac{I}{I} - u_{21}I^* - \min\{u_{22}I^* + u_{23}, -u_{32}, V(u_{22} - u_{32}) + u_{33} + u_{34}\}. \tag{28}$$

Thus, we have  $I/I = u_{31}S + u_{32}V - u_{33} - u_{34}$ , so that

$$\mathfrak{R}_1(\Xi) \leq \frac{S}{S} - u_{31}\aleph - u_{32}\aleph + u_{34} - \min \left[ \begin{aligned} & \{u_{12}\aleph - u_{13} - u_{22}\aleph - u_{23} - \max\{u_{22}\aleph, u_{12}\aleph\}\}, -u_{21} - u_{31}\aleph \\ & + \min\{u_{22}\aleph + u_{12}, -u_{32}, \aleph(u_{22} - u_{32}) + u_{33} + u_{34}\} \end{aligned} \right]. \tag{29}$$

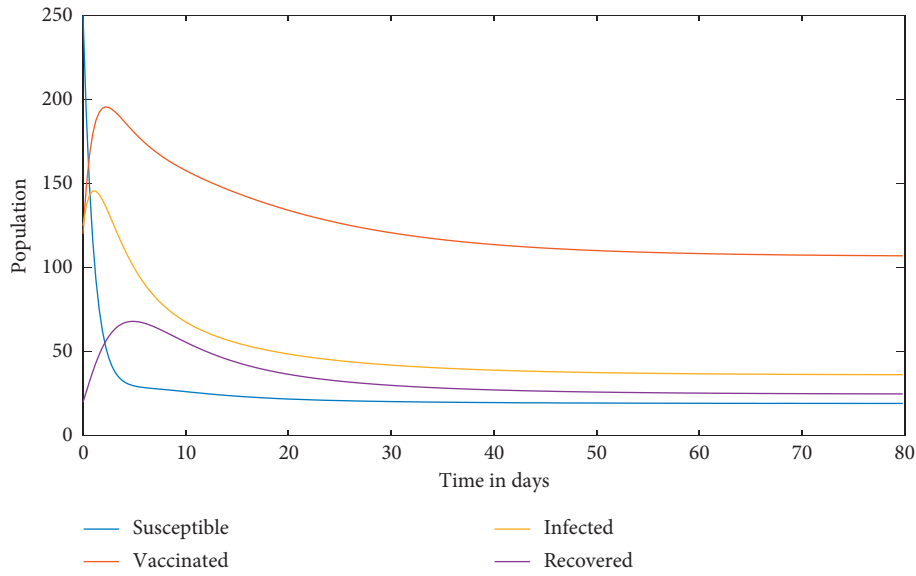


FIGURE 4: Solution curves of the SVIRS disease system with the attributes in Example 1.

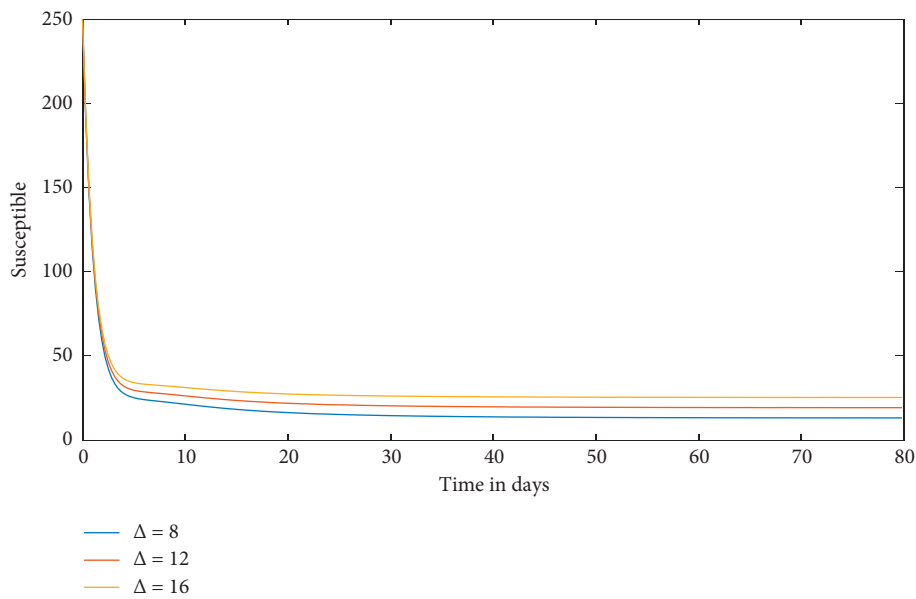


FIGURE 5: Time series evaluation of susceptible population for the recruitment rates  $(\Delta) = 8, 12, 16$ .

Since  $\mathfrak{N} = \min\{\inf S^*(t), \inf V^*(t), \inf I^*(t)\}$ , and hence  $\mathfrak{R}_1\{\Xi\} \leq S/S - \mathfrak{N}_1$ , where

$$\mathfrak{N}_1 = u_{31}\mathfrak{N} + u_{32}\mathfrak{N} - u_{33} - u_{34} + \min \left[ \begin{aligned} & \{u_{12}\mathfrak{N} - u_{13} - u_{22}\mathfrak{N} - u_{23} - \max\{u_{22}\mathfrak{N}, u_{12}\mathfrak{N}\}\}, -u_{21} - u_{31}\mathfrak{N} \\ & + \min\{u_{22}\mathfrak{N} + u_{23}, -u_{23}, \mathfrak{N}(u_{22} - u_{32}) + u_{33} + u_{34}\} \end{aligned} \right]. \tag{30}$$

Now, integrating  $\mathfrak{R}_1\{\Xi\}$  w.r.t  $t$  on both sides between the limits 0 to  $t$  and on letting  $t \rightarrow \infty$ , we obtain  $\int_0^t \mathfrak{R}(\Xi)dt = \log S(t)/S(0) - \mathfrak{N}t \Rightarrow \lim_{t \rightarrow \infty} \sup \sup 1/t \int_0^t \mathfrak{R}_1$

$(\Xi)dt < -\mathfrak{N}_1$ , if  $\mathfrak{N}_1 > 0$ . Therefore, the interior equilibrium point  $p_2(S^*, V^*, I^*, R^*)$  will be globally asymptotically stable.  $\square$

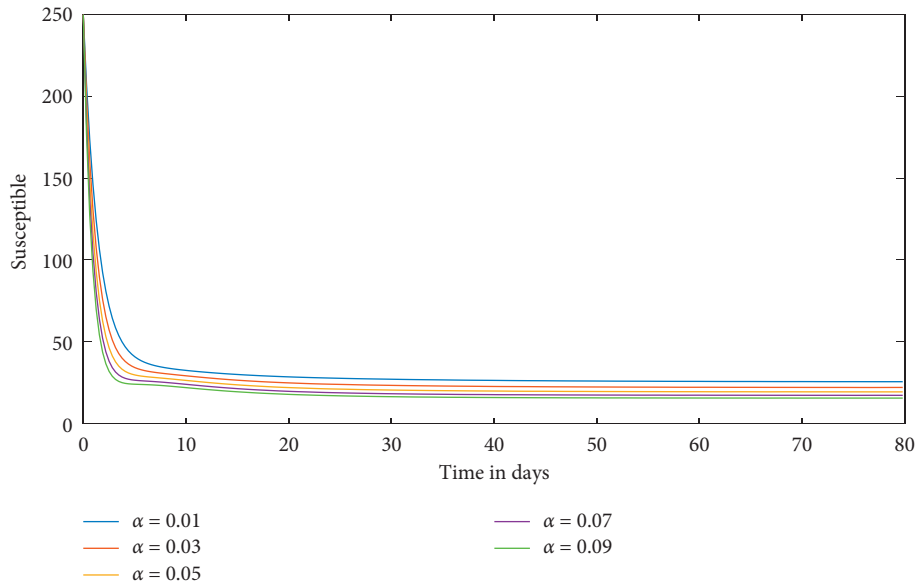


FIGURE 6: Time series evaluation of susceptible population for  $\alpha = 0.01; 0.03; 0.05; 0.07; 0.09$ .

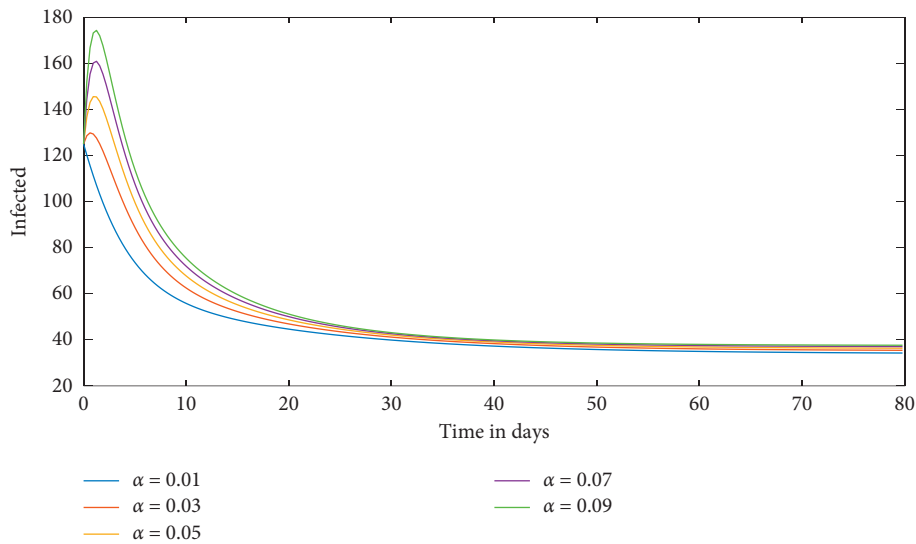


FIGURE 7: Time series evaluation of infected population for  $\alpha = 0.01; 0.03; 0.05; 0.07; 0.09$ .

### 6. Numerical Simulation

In this numerical section, the dynamical behavior of the fuzzy SVIRS system is investigated.

*Example 1.* The case of endemic equilibrium is illustrated for the following numerical data.

$$\begin{aligned} \tilde{\Delta} &= [6, 15]; \tilde{\alpha} = [0.01, 0.09]; \tilde{\beta} = [0.01, 0.3]; \tilde{\chi} = [0.005, 0.02]; \tilde{\Omega} = [0.3, 0.6]; \tilde{\Phi} = [0.1, 0.5]; \\ \tilde{\Psi} &= [0.1, 0.6]; \tilde{\gamma} = [0.05, 0.15]; \tilde{\eta} = [0.01, 0.03]; \tilde{m} = [1, 8]; \tilde{n} = [1, 12]. \end{aligned} \tag{31}$$

Figure 4 shows solution curves of the SVIRS disease system with the attributes in Example 1. Figure 5 shows time series evaluation of susceptible population for the recruitment rates  $(\Delta) = 8, 12, 16$ . Figure 6 shows time series evaluation of susceptible population for  $\alpha = 0.01; 0.03;$

$0.05; 0.07; 0.09$ . Figure 7 shows time series evaluation of infected population for  $\chi = 0.007, 0.009, 0.01, 0.02, 0.03$ .

Figure 8 shows time series evaluation of susceptible population for  $\beta = 0.05; 0.10; 0.15; 0.20; 0.25$ . Figure 9 shows time series evaluation of vaccinated population for



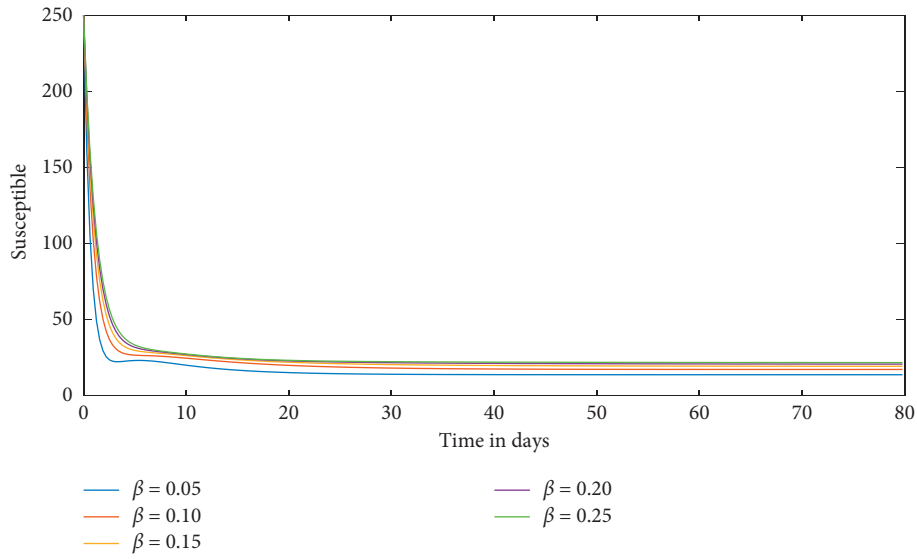


FIGURE 8: Time series evaluation of susceptible population for  $\beta = 0.05; 0.10; 0.15; 0.20; 0.25$ .

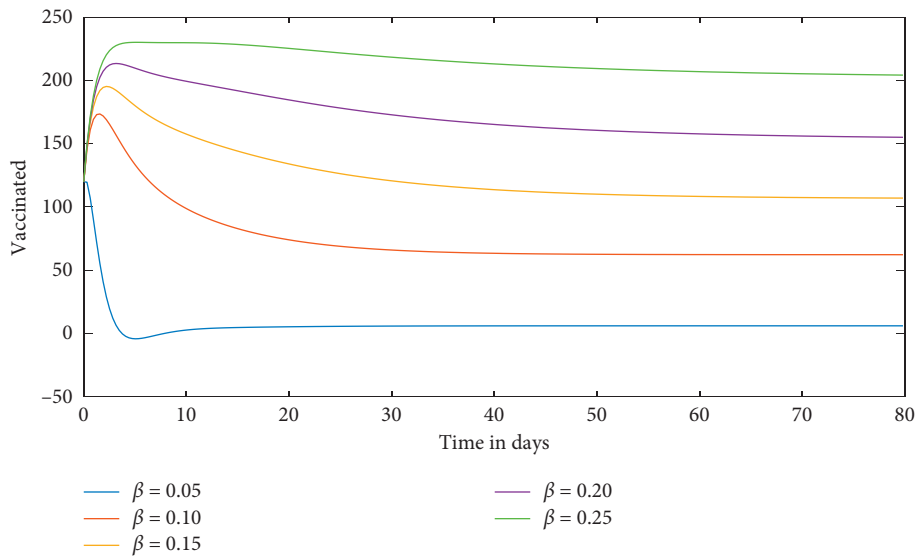


FIGURE 9: Time series evaluation of vaccinated population for  $\beta = 0.05; 0.10; 0.15; 0.20; 0.25$ .

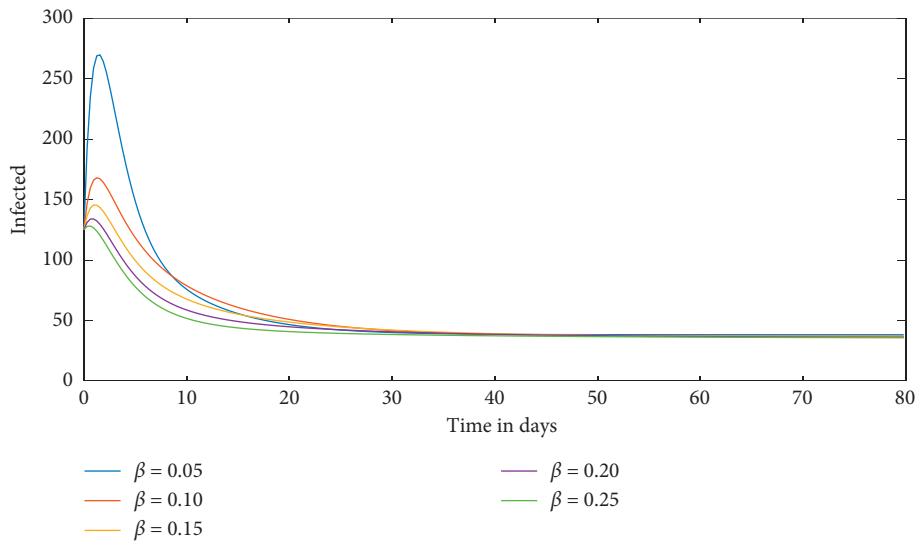


FIGURE 10: Time series evaluation of infected population for  $\beta = 0.05; 0.10; 0.15; 0.20; 0.25$ .

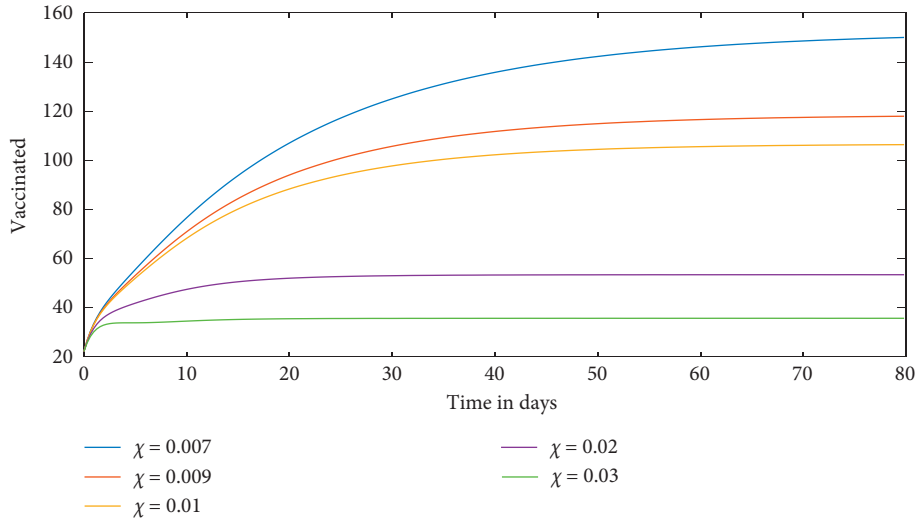


FIGURE 11: Time series evaluation of vaccinated population for  $\chi = 0.007, 0.009, 0.01, 0.02, 0.03$ .

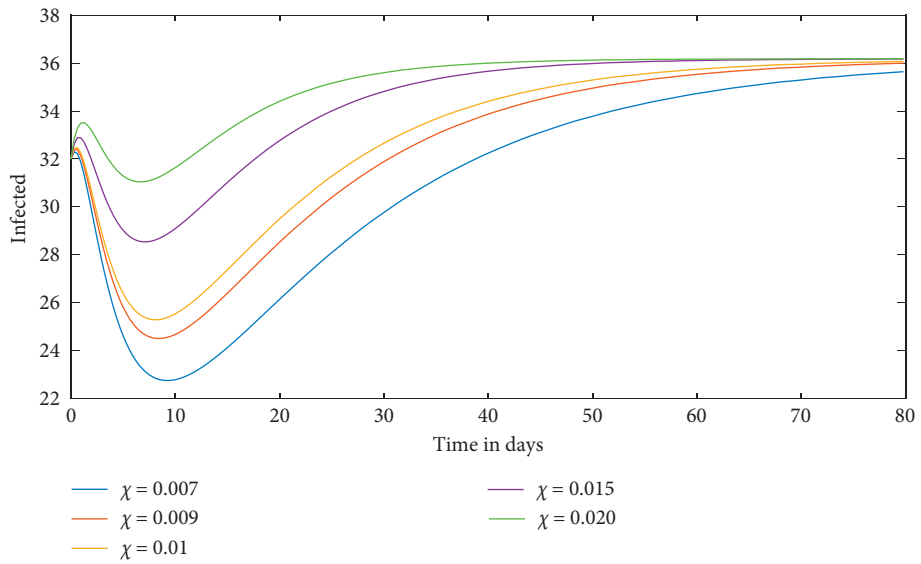


FIGURE 12: Time series evaluation of infected population for  $\chi = 0.007, 0.009, 0.01, 0.02, 0.03$ .

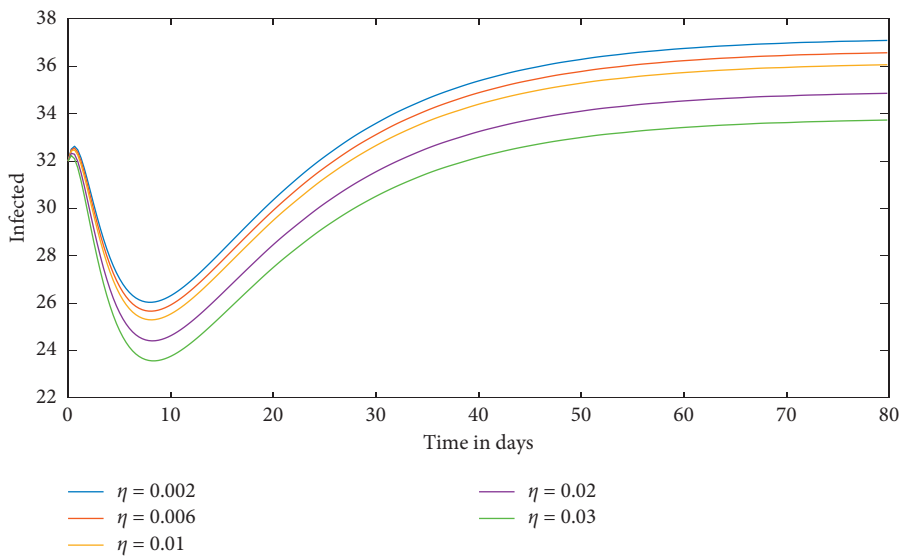


FIGURE 13: Time series evaluation of infected population for  $\eta = 0.002, 0.006, 0.01, 0.02, 0.03$ .



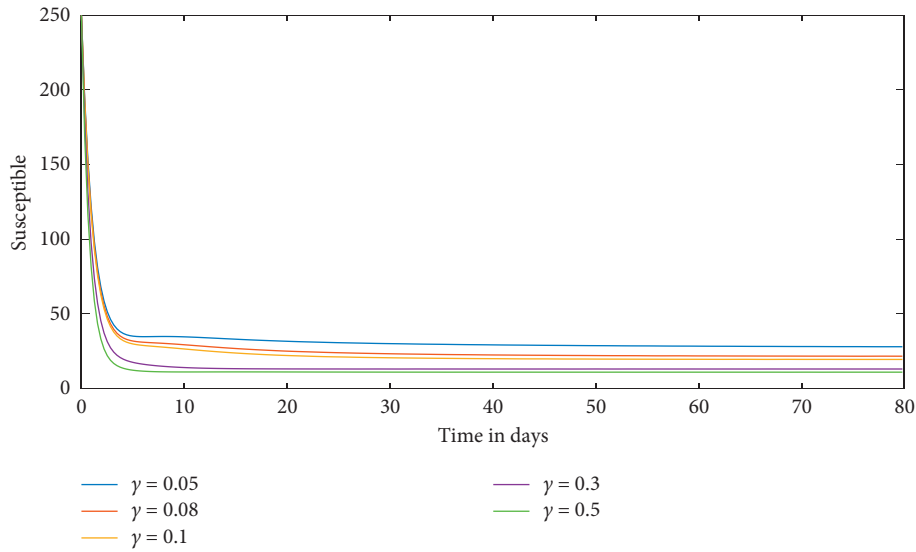


FIGURE 17: Time series evaluation of susceptible population for  $\gamma = 0.05; 0.08; 0.1; 0.3; 0.5$ .

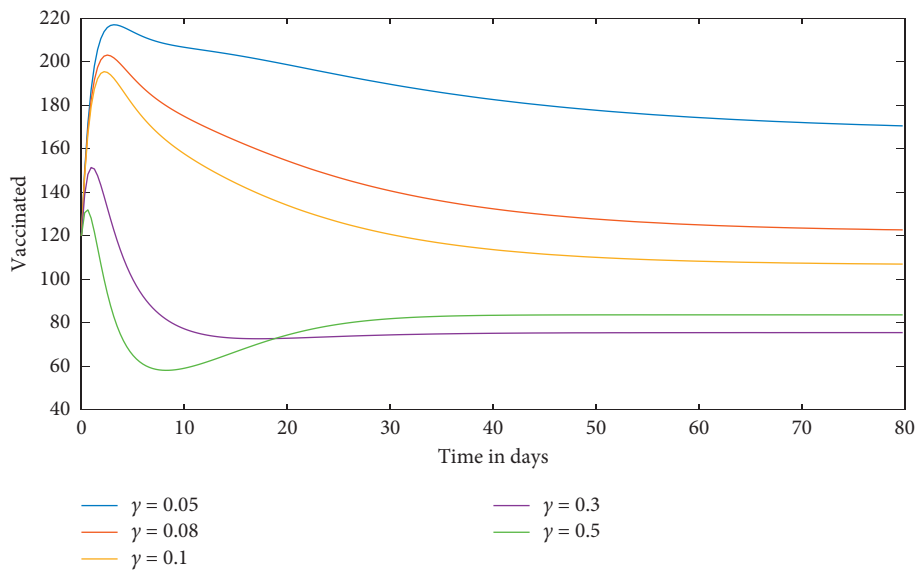


FIGURE 18: Time series evaluation of vaccinated population for  $\gamma = 0.05; 0.08; 0.1; 0.3; 0.5$ .

$\beta = 0.05; 0.10; 0.15; 0.20; 0.25$ . Figure 10 shows time series evaluation of infected population for  $\beta = 0.05; 0.10; 0.15; 0.20; 0.25$ . Figure 11 shows time series evaluation of vaccinated population for  $\chi = 0.007, 0.009, 0.01, 0.02, 0.03$ . Figure 12 shows time series evaluation of infected population  $\chi = 0.007, 0.009, 0.01, 0.02, 0.03$ . Figure 13 shows time series evaluation of infected population for  $\eta = 0.002, 0.006, 0.01, 0.02, 0.03$ .

Figure 14 shows time series evaluation of recovered population for  $\psi = 0.10, 0.15, 0.20, 0.25, 0.30$ . Figure 15 shows time series evaluation of susceptible population for  $\Omega = 0.3, 0.5, 0.7$ . Figure 16 shows time series evaluation of vaccinated population for  $\Omega = 0.3, 0.5, 0.7$ . Figure 17 shows time series evaluation of susceptible population for  $\gamma = 0.05; 0.08; 0.1; 0.3; 0.5$ .

Figure 18 shows time series evaluation of vaccinated population for  $\gamma = 0.05; 0.08; 0.1; 0.3; 0.5$ . Figure 19 shows time series evaluation of infected population for  $\gamma = 0.05; 0.08; 0.1; 0.3; 0.5$ . Figure 20 shows time series evaluation of recovered population for  $\gamma = 0.05; 0.08; 0.1; 0.3; 0.5$ .

Figure 21 shows time series evaluation of susceptible population for  $\phi = 0.04; 0.08; 0.2; 0.4; 0.6$ . Figure 22 shows time series evaluation of vaccinated population for  $\phi = 0.04; 0.08; 0.2; 0.4; 0.6$ . Figure 23 shows time series evaluation of recovered population  $\phi = 0.04; 0.08; 0.2; 0.4; 0.6$ . Figure 24 shows time series evaluation of infected population for  $m = 0.5, 3.5, 6.5, 9.5, 12.5$ . Figure 25 shows time series evaluation of Recovered population for  $m = 0.5, 3.5, 6.5, 9.5, 12.5$ . Figure 26 shows time series

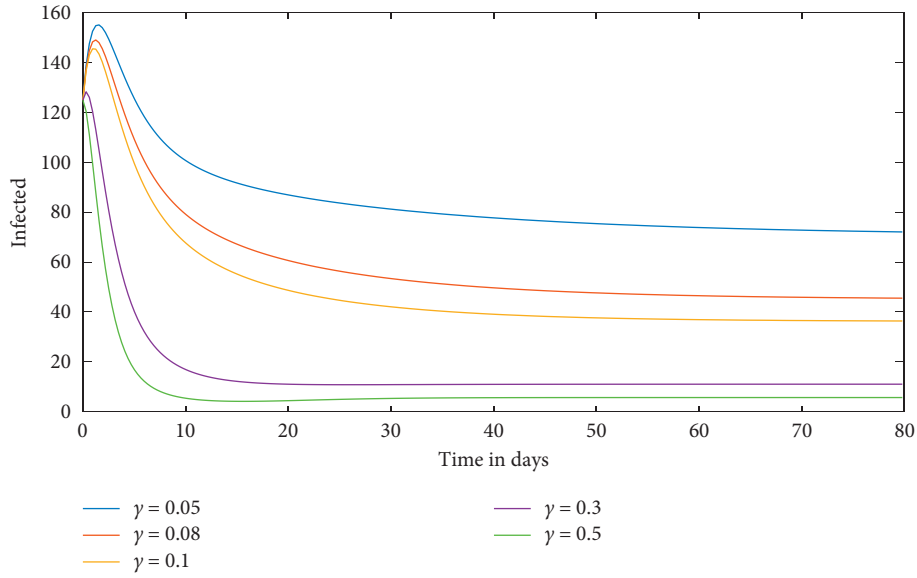


FIGURE 19: Time series evaluation of infected population for  $\gamma = 0.05; 0.08; 0.1; 0.3; 0.5$ .

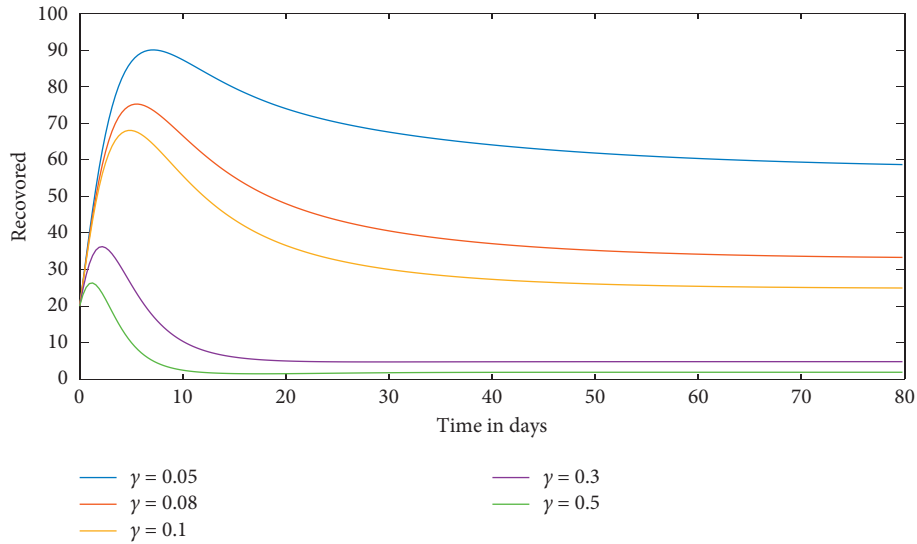


FIGURE 20: Time series evaluation of recovered population for  $\gamma = 0.05; 0.08; 0.1; 0.3; 0.5$ .

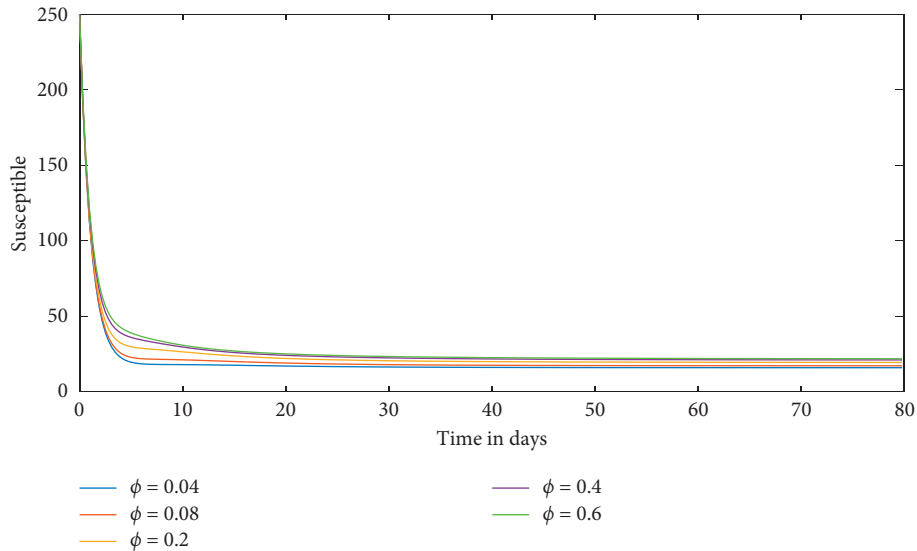


FIGURE 21: Time series evaluation of susceptible population for  $\phi = 0.04; 0.08; 0.2; 0.4; 0.6$ .

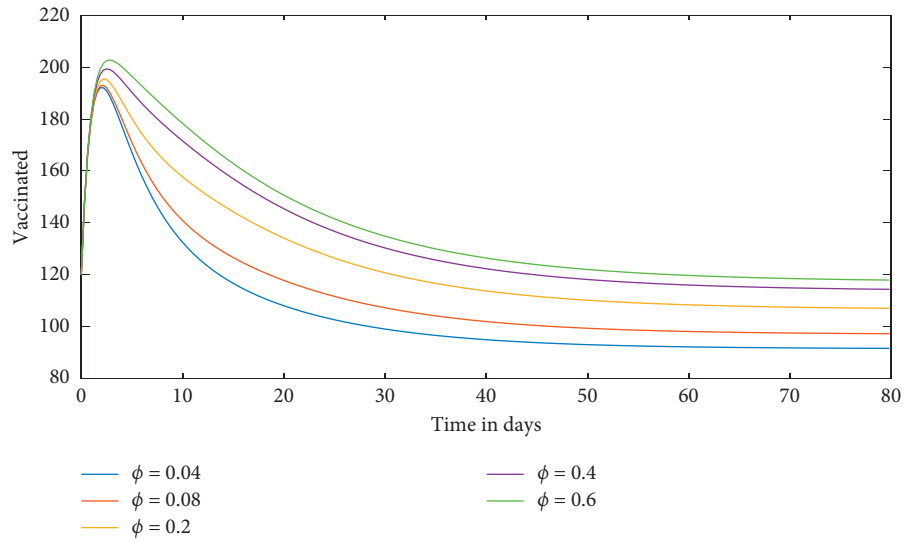


FIGURE 22: Time series evaluation of vaccinated population for  $\phi = 0.04; 0.08; 0.2; 0.4; 0.6$ .

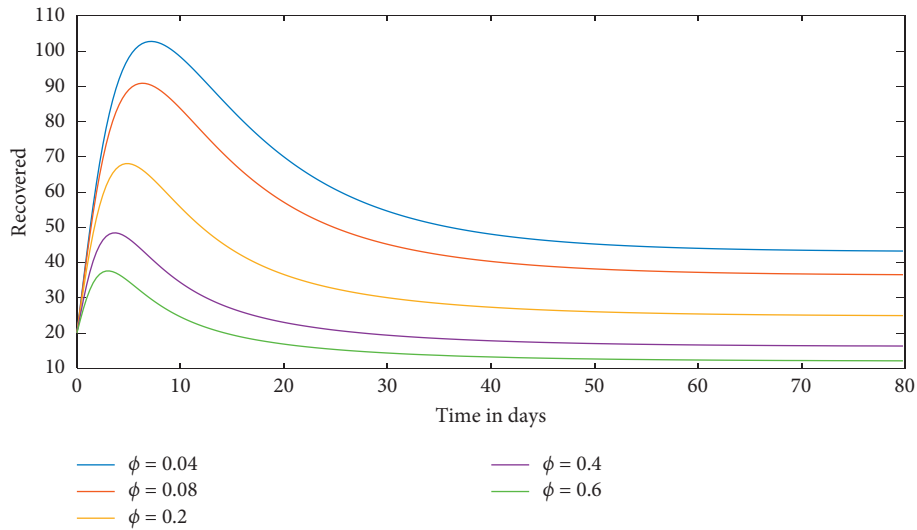


FIGURE 23: Time series evaluation of recovered population for  $\phi = 0.04; 0.08; 0.2; 0.4; 0.6$ .

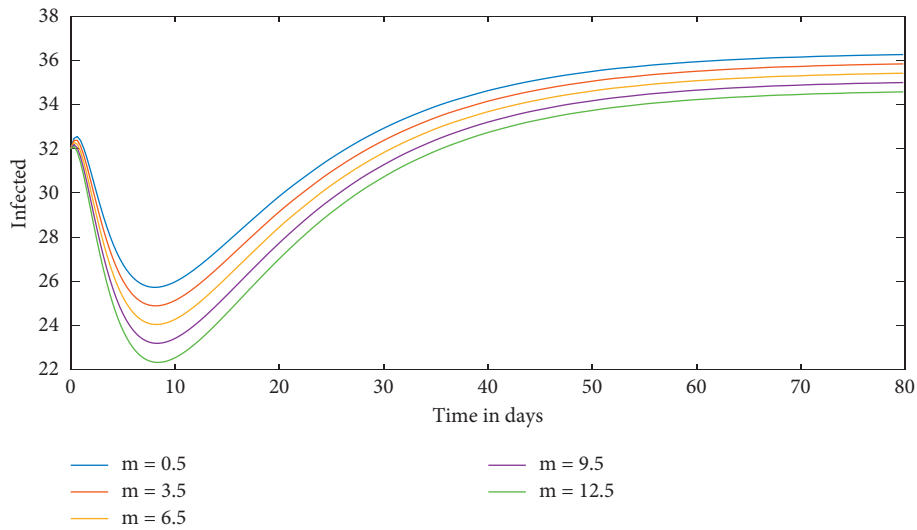


FIGURE 24: Time series evaluation of infected population for  $m = 0.5, 3.5, 6.5, 9.5, 12.5$ .

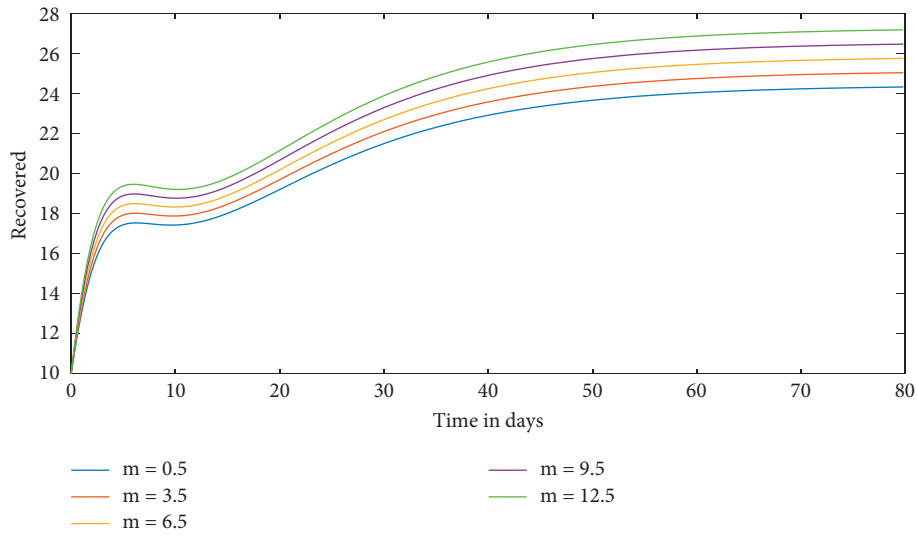


FIGURE 25: Time series evaluation of recovered population for  $m = 0.5, 3.5, 6.5, 9.5, 12.5$ .

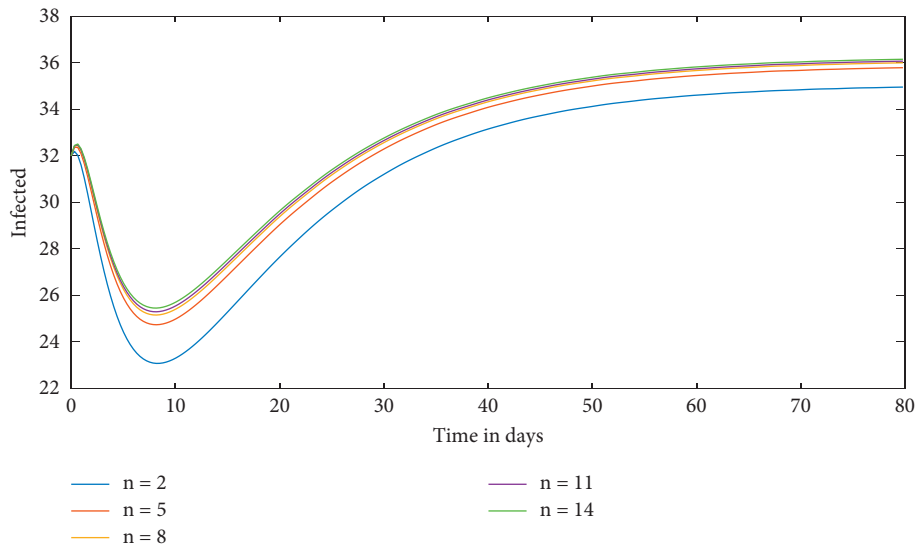


FIGURE 26: Time series evaluation of recovered population for  $n = 2, 5, 8, 10, 14$ .

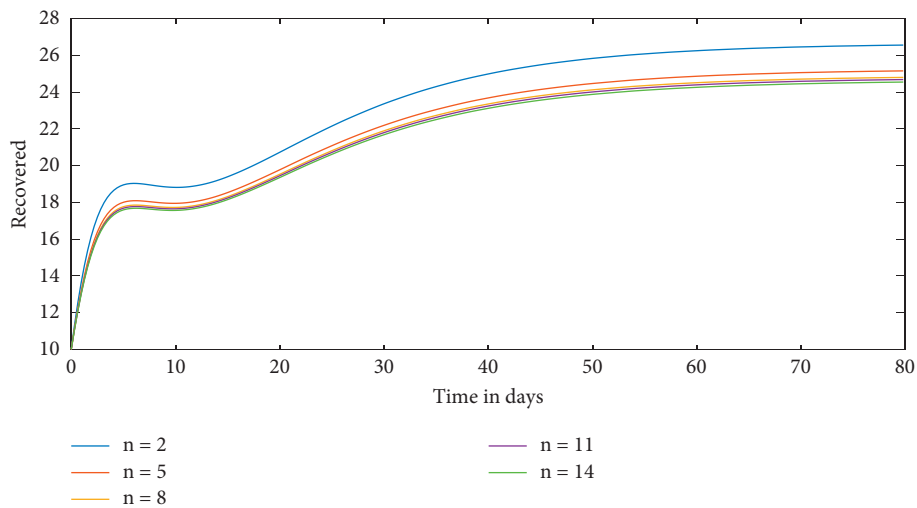


FIGURE 27: Time series evaluation of recovered population for  $n = 2, 5, 8, 10, 14$ .

evaluation of recovered population for  $n = 2, 5, 8, 10, 14$ . Figure 27 shows time series evaluation of recovered population for  $n = 2, 5, 8, 10, 14$ .

## 7. Conclusions and Remarks

In this study, we provide a fuzzy SVIRS epidemic model with a Holling type-II incidence rate and saturating treatment, in which all population dynamics parameters are handled as fuzzy integers. The SVIRS model's existence and durability were next investigated, and the disease-free and endemic equilibrium points of the proposed fuzzy system were computed. The Routh–Hurwitz criteria are used to talk about the fuzzy system's local stability conditions around these equilibrium locations. Using the Lozinskii metric, global stability surrounding the internal steady state was also verified. To further understand the dynamics of the suggested model, numerical simulations are provided. The following interpretations are based on the numerical simulations of Section 6:

- (i) Figure 4 shows how the population of solution curves (population) changes over time.
- (ii) Figure 5 depicts how vulnerable populations change over time at various recruitment rates.
- (iii) Figures 6 and 7 show the variations in susceptible and infected populations respectively for various levels of infection force.
- (iv) Figures 8, 9, and 10 show how sensitive, vaccinated populations behave over time in days for various inhibitory tactics implemented by the infected. Also, as the sick person's inhibitory measures become more effective, the number of vulnerable and vaccinated people grows. However, as seen in Figure 10, the number of infection individuals is decreasing as the population grows.
- (v) The number of people who have been vaccinated has decreased as the values of  $\chi$  have risen (Figure 11), whereas the number of people who have been infected has increased (Figure 12).
- (vi) When the death rate from disease ( $\eta$ ) rises, the number of sick people decreases (Figure 13).
- (vii) Figure 14 illustrates that the number of recovered individuals grows as the transmission rate from infected persons to recovered individuals ( $\psi$ ) increases.
- (viii) When the transmission rate from susceptible to vaccinated ( $\Omega$ ) is growing, the number of susceptible and vaccinated persons is falling and increasing, respectively (Figures 15 and 16).
- (ix) The number of vulnerable (Figure 17), vaccinated (Figure 18), infected (Figure 19), and recovered (Figure 20) persons decreases as the natural death rate ( $\gamma$ ) rises.
- (x) The number of susceptible (Figure 21) and vaccinated (Figure 22) individuals increases when the transmission rate from recovered individuals to susceptible ( $\phi$ ) increases, while the number of recovered individuals (Figure 23) decreases.
- (xi) When the treatment rate ( $m$ ) rises, the number of infected people (Figure 24) falls while the number of recovered people (Figure 25) rises.
- (xii) In addition, whenever the rate of medical resource scarcity ( $m$ ) rises, the number of infected (Figure 26) and recovered (Figure 27) individuals rises and falls, respectively.
- (xiii) All parameters play major role in the proposed fuzzy SVIRS, which means the current system can be treated as one of the better solutions for any type of disease models. Previous works focused on stability analysis analytically and numerically, and some are focused on delay dynamics. Delay-induced mathematical model and its analysis also greatly helps us in detecting disease controlling parameters and to detect parameters which allows us to reduce disease transmission.
- (xiv) The current work is mainly focused on deterministic (without randomness) approach both analytically and numerically. We can extend this model to capture rich dynamics of system (stochastic model) under noise (randomness, environmental factors around us) by both analytically (using Fourier transform tool) and numerically (using MATLAB software tool). We can extend this model to study the spatio-temporal analysis by constructing a diffusive model using partial differential equations. These can be considered as one of our future projects [51].

## Data Availability

The data used to support the findings of this study are included within the article. Should further data or information be required, these are available from the corresponding author upon request.

## Conflicts of Interest

The authors declare that there are no conflicts of interest regarding the publication of this paper.

## Authors' Contributions

All authors have worked equally. The authors agreed on the used mathematical models, while the first author suggested that the concept of fuzzy parameters should be used to extend the model. The second and third author presented the positivity and boundedness of the system and discussed the stability analysis of the model. The third author presented the numerical simulations of the proposed model.

## Acknowledgments

The authors thank Anhui University of Finance and Economics, Bengbu, China, for providing support to complete this research work.



## References

- [1] W. O. Kermack and A. G. McKendrick, "A contribution to the mathematical theory of epidemics," *Proc R Soc Lond Ser A*, vol. 115, no. 7, pp. 700–721, 1927.
- [2] S. Kaliappan, M. D. Raj Kamal, D. S. Mohanamurugan, and D. P. K. Nagarajan, "Analysis of an innovative connecting rod by using finite element method," *Taga Journal of Graphic Technology*, vol. 2018, pp. 1147–1152, 2018.
- [3] D. Mukherjee, "Stability analysis of an S-I epidemic model with time delay," *Mathematical and Computer Modelling*, vol. 24, no. 9, pp. 63–68, 1996.
- [4] K. Nagarajan, A. Rajagopalan, S. Angalaeswari, L. Natrayan, and W. D. Mammo, "Combined economic emission dispatch of microgrid with the incorporation of renewable energy sources using improved mayfly optimization algorithm," *Computational Intelligence and Neuroscience*, vol. 2022, Article ID 6461690, 22 pages, 2022.
- [5] A. d'Onofrio, P. Manfredi, and E. Salinelli, "Vaccinating behaviour, information, and the dynamics of SIR vaccine preventable diseases," *Theoretical Population Biology*, vol. 71, no. 3, pp. 301–317, 2007.
- [6] B. Buonomo, A. d'Onofrio, and D. Lacitignola, "Global stability of an SIR epidemic model with information dependent vaccination," *Mathematical Biosciences*, vol. 216, no. 1, pp. 9–16, 2008.
- [7] R. H. Martin, "Logarithmic norms and projections applied to linear differential systems," *Journal of Mathematical Analysis and Applications*, vol. 45, no. 2, pp. 432–454, 1974.
- [8] K. Goel, "Stability behavior of a nonlinear mathematical epidemic transmission model with time delay," *Nonlinear Dynamics*, vol. 98, no. 2, pp. 1501–1518, 2019.
- [9] A. Kumar and K. Goel, "A deterministic time-delayed SIR epidemic model: mathematical modeling and analysis," *Theory in Biosciences*, vol. 139, no. 1, pp. 67–76, 2019.
- [10] A. S. Kaliappan, S. Mohanamurugan and P. K. Nagarajan, Numerical investigation of sinusoidal and trapezoidal piston profiles for an IC engine," *Journal of Applied Fluid Mechanics*, vol. 13, no. 1, pp. 287–298, 2020.
- [11] A. Kumar, "Stability of a delayed SIR epidemic model by introducing two explicit treatment classes along with nonlinear incidence rate and Holling type treatment," *Computational and Applied Mathematics*, vol. 38, no. 3, p. 130, 2019.
- [12] D. K. Jain, S. K. S. Tyagi, S. Neelakandan, M. Prakash, and L. Natrayan, "Metaheuristic optimization-based resource allocation technique for cybertwin-driven 6G on IoE environment," *IEEE Transactions on Industrial Informatics*, vol. 18, no. 7, pp. 4884–4892, 2022.
- [13] B. Dubey, A. Patra, P. K. Srivastava, and U. S. Dubey, "Modeling and analysis of an SEIR model with different types of nonlinear treatment rates," *Journal of Biological Systems*, vol. 21, no. 03, Article ID 1350023, 2013.
- [14] S. Tipsri and W. Chinviriyasit, "Stability analysis of SEIR model with saturated incidence and time delay," *International Journal of Applied Physics and Mathematics*, vol. 4, no. 1, pp. 42–45, 2014.
- [15] A. B. Gumel, C. C. McCluskey, and J. Watmough, "An SVEIR model for assessing potential impact of an imperfect anti-sars vaccine," *Mathematical Biosciences and Engineering*, vol. 3, no. 3, pp. 485–512, 2006.
- [16] K. R. Vaishali, S. R. Rammohan, L. Natrayan, D. Usha, and V. R. Niveditha, "Guided container selection for data streaming through neural learning in cloud," *International Journal of System Assurance Engineering and Management*, vol. 16, pp. 1–7, 2021.
- [17] A. Darshan, N. Girdhar, R. Bhojwani et al., "Energy audit of a residential building to reduce energy cost and carbon footprint for sustainable development with renewable energy sources," *Advances in Civil Engineering*, vol. 2022, pp. 1–10, Article ID 4400874, 2022.
- [18] P. Asha, L. Natrayan, B. Geetha et al., "IoT enabled environmental toxicology for air pollution monitoring using AI techniques," *Environmental Research*, vol. 205, Article ID 112574, 2022.
- [19] S. S. Sundaram, N. H. Basker, and L. Natrayan, "Smart clothes with bio-sensors for ECG monitoring," *International Journal of Innovative Technology and Exploring Engineering*, vol. 8, no. 4, pp. 298–301, 2019.
- [20] F. Brauer, "Backward bifurcations in simple vaccination models," *Journal of Mathematical Analysis and Applications*, vol. 298, no. 2, pp. 418–431, 2004.
- [21] C. N. Podder and A. B. Gumel, "Qualitative dynamics of a vaccination model for HSV-2," *IMA Journal of Applied Mathematics*, vol. 75, no. 1, pp. 75–107, 2010.
- [22] O. Sharomi, C. N. Podder, A. B. Gumel, S. M. Mahmud, and E. Rubinstein, "Modelling the transmission dynamics and control of the Novel 2009 swine influenza (H1N1) pandemic," *Bulletin of Mathematical Biology*, vol. 73, no. 3, pp. 515–548, 2011.
- [23] A. B. Gumel, "Causes of backward bifurcations in some epidemiological models," *Journal of Mathematical Analysis and Applications*, vol. 395, no. 1, pp. 355–365, 2012.
- [24] M. Safan and F. A. Rihan, "Mathematical analysis of an SIS model with imperfect vaccination and backward bifurcation," *Mathematics and Computers in Simulation*, vol. 96, pp. 195–206, 2014.
- [25] A. d'Onofrio and P. Manfredi, "Bistable endemic states in a susceptible-infectious-susceptible model with behavior-dependent vaccination," in *Proceedings of the Mathematical and Statistical Modeling for Emerging and Re-emerging Infectious Diseases*, G. Chowell and J. Hyman, Eds., Springer, Cham, pp. 341–354, July 2016.
- [26] C. S. S. Anupama, L. Natrayan, E. Laxmi Lydia et al., "Deep learning with backtracking search optimization based skin lesion diagnosis model," *Computers, Materials & Continua*, vol. 70, no. 1, pp. 1297–1313, 2021.
- [27] A. d'Onofrio and P. Manfredi, "Information-related changes in contact patterns may trigger oscillations in the endemic prevalence of infectious diseases," *Journal of Theoretical Biology*, vol. 256, no. 3, pp. 473–478, 2009.
- [28] R. M. Anderson and R. M. May, "Regulation and stability of host-parasite population. Interactions: I. Regulatory processes," *Journal of Animal Ecology*, vol. 47, no. 1, pp. 219–267, 1978.
- [29] C. Wei and L. Chen, "A delayed epidemic model with pulse vaccination," *DiscretDyn Nat Soc*, vol. 2008, Article ID 746951, 12 pages, 2008.
- [30] J. Z. Zhang, Z. Jin, Q. X. Liu, and Z. Y. Zhang, "Analysis of a delayed SIR model with nonlinear incidence rate," *DiscretDyn Nat Soc*, vol. 2008, Article ID 636153, 12 pages, 2008.
- [31] X. Z. Li, W. S. Li, and M. Ghosh, "Stability and bifurcation of an SIR epidemic model with nonlinear incidence and treatment," *Applied Mathematics and Computation*, vol. 210, no. 1, pp. 141–150, 2009.
- [32] A. Kumar, "Stability of a time delayed SIR epidemic model along with nonlinear incidence rate and Holling type-II

- treatment rate,” *International Journal of Computational Methods*, vol. 15, no. 06, Article ID 1850055, 2018.
- [33] A. Kumar, “Dynamical model of epidemic along with time delay; Holling type II incidence rate and Monod-Haldane type treatment rate,” *Differ EquDynSyst*, vol. 27, no. 1–3, pp. 299–312, 2018.
- [34] A. Kumar, “Mathematical analysis of a delayed epidemic model with nonlinear incidence and treatment rates,” *Journal of Engineering Mathematics*, vol. 115, no. 1, pp. 1–20, 2019.
- [35] K. Goel, “A mathematical and numerical study of a SIR epidemic model with time delay, nonlinear incidence and treatment rates,” *Theory in Biosciences*, vol. 138, no. 2, pp. 203–213, 2019.
- [36] L. Zhou and M. Fan, “Dynamics of an SIR epidemic model with limited medical resources revisited,” *Nonlinear Analysis: Real World Applications*, vol. 13, no. 1, pp. 312–324, 2012.
- [37] M. Yang and F. Sun, “Global stability of SIR models with nonlinear Incidence and discontinuous treatment,” *The Electronic Journal of Differential Equations*, vol. 2015, no. 304, pp. 1–8, 2015.
- [38] K. Goel and A. Kumar, “A deterministic time-delayed SVIRS epidemic model with incidences and saturated treatment,” *Journal of Engineering Mathematics*, vol. 121, no. 1, pp. 19–38, 2020.
- [39] X. B. Liu and L. J. Yang, “Stability analysis of an SEIQV epidemic model with saturated incidence rate,” *Nonlinear Analysis: Real World Applications*, vol. 13, no. 6, pp. 2671–2679, 2012.
- [40] S. Magesh, V. R. Niveditha, P. S. Rajakumar, and L. Natrayan, “Pervasive computing in the context of COVID-19 prediction with AI-based algorithms,” *International Journal of Pervasive Computing and Communications*, vol. 16, no. 5, pp. 477–487, 2020.
- [41] O. A. Arqub, A. Elajou, S. Momani, and N. Shawagfeh, “Analytical Solutions of fuzzy initial value problem by HAM,” *Appl.Math.Inform.Sci*, vol. 7, pp. 1903–1919, 2013.
- [42] O. A. Arqub, “series solution of a fuzzy differential equation under strongly generalized differentiability,” *J.Adv.Re-s.Appl.Math*, vol. 5, pp. 31–52, 2013.
- [43] P. K. Mondal, S. Jana, P. Haldar, and T. K. Kar, “Dynamical behavior of an epidemic model in a fuzzy transmission,” *Int.J.Unc.Fuzz.Knowl.BasedSyst*.vol. 23, no. 05, pp. 651–665, 2015.
- [44] D. Nagarajan, M. Lathamaheswari, S. Broumi, and J. Kavikumar, “A new perspective on traffic control management using triangular interval type-2 fuzzy sets and interval neutrosophic sets,” *Operations Research Perspectives*, vol. 6, Article ID 100099, 2019.
- [45] A. sendrayaperumal, S. Mahapatra, S. S. Parida et al., “Energy auditing for efficient planning and implementation in commercial and residential buildings,” *Advances in Civil Engineering*, vol. 2021, Article ID 1908568, 10 pages, 2021.
- [46] L. C. Barros, M. Leite, and R. Bassanezi, “The SI epidemiological models with a fuzzy transmission parameter,” *Computers & Mathematics with Applications*, vol. 45, no. 10–11, pp. 1619–1628, 2003.
- [47] L. P. Natrayan, “Sakthi shunmuga sundaram. J. Elumalai. Analyzing the Uterine physiological with MMG Signals using SVM,” *International journal of Pharmaceutical research*, vol. 11, no. 2, pp. 165–170, 2019.
- [48] G. J. Klir and B. Yuan, “Fuzzy sets and fuzzy logic: theory and applications. Possibility Theory versus Probab,” *Theory*, vol. 32, no. 2, pp. 207–208, 1996.
- [49] S. Adak and S. Jana, “Dynamical behavior of an epidemic model with fuzzy transmission and fuzzy treatment control,” *J. Appl. Math. Comput*.vol. 68, no. 3, pp. 1929–1948, 2021.
- [50] S. K. Nandi, S. Jana, M. Manadal, and T. K. Kar, “Analysis of a fuzzy epidemic model with saturated treatment and disease transmission,” *International Journal of Biomathematics*, vol. 11, no. 01, Article ID 1850002, 2018.
- [51] Y. T. Mangongo, J. D. K. Bukweli, and J. D. B. Kampempe, “Fuzzy global stability analysis of the dynamics of malaria with fuzzy transmission and recovery rates,” *American Journal of Operations Research*, vol. 11, no. 06, pp. 257–282, 2021.
- [52] M. K. Sharma, N. Dhiman, N. Vandana, and V. N. Mishra, “Mediative fuzzy logic mathematical model: a contradictory management prediction in COVID-19 pandemic,” *Applied Soft Computing*, vol. 105, Article ID 107285, 2021.
- [53] N. Lefevr, A. Kanavos, V. C. Gerogiannis, L. Iliadis, and P. Pintelas, “Employing fuzzy logic to analyze the structure of complex biological and epidemic spreading models,” *Mathematics*, vol. 9, p. 977, 2021.
- [54] J. Zhang, J. Jia, and X. Song, “Analysis of an SEIR epidemic model with saturated incidence and saturated treatment function,” *The Scientific World Journal*, vol. 2014, Article ID 910421, 11 pages, 2014.

## Research Article

# A Digital Assessment Method for Multisource Influence Factors on Corrosion Characteristics in the Karst Areas

Zhanfei Gu <sup>1,2,3</sup> and Zhikui Liu <sup>1,3</sup>

<sup>1</sup>College of Civil Engineering and Architecture, Guilin University of Technology, Guilin, Guangxi 541004, China

<sup>2</sup>College of Civil Engineering and Architecture, Zhengzhou University of Aeronautics, Zhengzhou, Henan 450046, China

<sup>3</sup>Technical Innovation Center of Mine Geological Environmental Restoration Engineering in Southern Area, Nanning, Guangxi 530029, China

Correspondence should be addressed to Zhikui Liu; 1998009@glut.edu.cn

Received 11 June 2022; Revised 9 July 2022; Accepted 13 July 2022; Published 25 August 2022

Academic Editor: Punit Gupta

Copyright © 2022 Zhanfei Gu and Zhikui Liu. This is an open access article distributed under the Creative Commons Attribution License, which permits unrestricted use, distribution, and reproduction in any medium, provided the original work is properly cited.

Taking dolomite and limestone in Guilin and Liuzhou regions in the north of Guangxi Province as research objects, this paper analyzed their mineral composition and chemical composition and proposed a digital assessment method for multi-source factors on corrosion characteristics in the Karst areas. Specifically, the chemical corrosion test, the corrosion test under the chemical-temperature actions, and the corrosion test under the action of vibration load are carried out from the digital view, respectively. Four aspects can be found in digital assessment results. Firstly, the dolomite in northern Guangxi mainly has a fine crystalline texture and a massive structure with low content of acid-insoluble matters, while limestone mainly has a powder crystalline texture and a massive structure with high content of acid-insoluble matters, and the purity of both dolomite and limestone are very high. Secondly, the difference of corrosion between dolomite and limestone mainly depends on the ratio of CaO/MgO in their chemical composition and the content of silica and acid insoluble matters. Thirdly, the corrosion rates of pure dolomite and pure limestone are basically the same under the same external conditions. Finally, temperature and vibration load have a relatively large influence on the corrosion rates of dolomite and limestone, and the corrosion rates of dolomite and limestone increase with the increase of temperature, but the influence of vibration load on the corrosion rate is more significant than temperature. This research can provide theoretical basis and technical support for large-scale engineering construction and prevention of karst geologic disasters in karst stone mountainous areas in northern Guangxi.

## 1. Introduction

In carbonate rock areas, due to the differences in mineral composition and chemical composition of rock mass, the differences in internal structure and pore characteristics, and the influence of external conditions such as groundwater occurrence, temperature, and vibration load, dolomite and limestone distributed in these areas have differential corruptions. The differential corruptions often destroy the integrity of the rock mass, affect the mechanical properties and stability of the rock mass, and have a great impact on the safety of buildings and constructs attached to it. China's

karst landforms are widely distributed with a large area, and mainly distributed in Guangxi, Guizhou, and eastern Yunnan. It is one of the largest karst areas in the world, with large continuous limestones and dolomites distributed. With the continuous reinforcement of China's economic strength and the continuous advancement of the development strategy in Southwest China, the strategic planning of "Silk Road Economic Belt" and "twenty-first Century Maritime Silk Road," urban railway transits, underground utility tunnels, and other infrastructure constructions have achieved unprecedented development, and numerous large-scale infrastructures such as high-speed railways and

highways have been started in Southwest China one after another. Due to the complexity of geological structure in Southwest China, engineering geological problems have appeared in most projects, among which karst geologic disasters are overriding. The wide range of karst distribution has seriously hindered the development of transportation infrastructure in Southwest China. Therefore, it is of great engineering practical significance to profoundly study the structural characteristics and differential corrosions of the limestone and dolomite.

The research on karst geologic disasters is mainly divided into two categories: theoretical research on corrosion mechanisms and research on karst detection methods. The corrosion test of carbonate rocks is an important content of theoretical research. Scholars in the past have done a lot of experiments on the corrosion characteristics of carbonate rocks, and have achieved many results. Liu et al. [1] used the two-scale continuous medium model to simulate the dissolution reaction process and predict the optimal injection rate during acidification treatment of carbonate rocks and put forward a general numerical method to simulate structured and unstructured reaction flow problems. Zhao et al. [2, 3] proposed a new alternative method for theoretically dealing with the evolution process of chemical dissolution surface in water-saturated porous rocks when propagating in a chemical system. In this method, porosity, pore fluid velocity, and acid concentration were taken as independent variables so that the problem of water-rock interaction could be solved by numerical methods and algorithms. Liu et al. [4] studied the infiltration and corrosion change process of carbonate rocks under different dynamic water pressure conditions, and the results showed that the infiltration and corrosion along the internal pores of rocks had an important influence on corrosion rate. Liu [5] and Gu [6] analyzed the characteristics of carbonate rocks from macro- and micro-perspectives, focusing on the investigation of the influence of differential weathering of limestones and dolomites on the causes of avalanche, stone peaks, and rocky desertification. She et al. [7] studied the morphology of carbonate rocks after corrosion by scanning electron microscope (SEM), and found that although the mineral composition and content of carbonate rocks have a certain influence on their corrosion, the types and connectivity of pores formed after the corrosion are more closely related to the formation of favorable carbonate rock reservoirs. Wei et al. [8, 9] studied the corrosion of rocks containing dolomitic limestone and dolomitic limestones from different corrosion time scales. Under the same pH value and the same corrosion time, the corrosion rate of dolomitic limestones is higher than that of rocks containing dolomitic limestone. Zhang et al. [10] revealed that the rock microstructure plays a controlling role in the corrosion rate, and the corrosion rates of dolomites with different structures are as follows: mesocrystalline to fine crystalline dolomites > fine crystalline to powder crystalline dolomites > powder crystalline to micritic dolomites; the specific surface area is related to the total corrosion amount, but independent of the corrosion rate per unit surface area. The corrosion starts from intergranular and intercrystalline pores, structural

microfractures, and cleavage, and gradually expanded to make pores and fissures connected with each other. The abovementioned pieces of research on corrosion investigated the corrosion characteristics of limestones and dolomites from the aspect of the water-rock interaction mechanism with the consideration of the influence of lithology, the characteristics of acidic solution and microorganisms, etc., which provides a theoretical basis and practical reference for the research of this project. On the basis of the above research results, taking the action factors of temperature and vibration load into account can further confirm and improve the above research conclusions and would be more in line with the actual situation, so it has certain feasibility and important significance.

Temperature is one of the important factors affecting the mechanical properties of rocks. Rock is composed of solid mineral particles and tiny gaps between the particles. The solid mineral particles and the channel networks formed by gaps between the mineral particles are often filled with fluid media. When changes in the environment of such porous media of rocks occur, the water presenting in the pores and fissures inside the rocks will undergo a phase change, leading to changes in the physical and mechanical properties of the rocks. These changes are not only related to their physical structure but also affected by the existing water, temperature, and stress state in the rocks. A lot of research have been done on this influence at home and abroad. She et al. [11] found that with the increase in temperature, the dissolution amount of carbonate rocks showed the pattern of slow decline-slow rise-rapid decline, of which 80–100°C is a favorable temperature. Nomeli et al. [12] used a kinetic model extended based on the standard Arrhenius equation to study the corrosion rate of calcite in the temperature range of 50–100°C and the pressure up to 600 bar and determined the functional relationship between calcite dissolution and temperature, pressure, and salinity. Eliwa et al. [13] studied the thermodynamics and kinetics of the dissolution process of carbonate rocks. Mutlutuk et al. [13] found that the change in temperature can destroy the rock integrity through repeated cyclic freeze-thaw experiments, and the more times and higher frequency of freeze-thaw cycles are undergone, the greater the loss of rock integrity occurs, and the more obvious the characteristics of damage and destruction is. Ding et al. [14] took the limestone from Longmen Grottoes in Luoyang as the research object and carried out mechanical tests under the action of different hydrochemical solutions and freeze-thaw coupling with the consideration of the influence of the erosion of limestone seepage solution and freeze-thaw damage in winter. Yang et al. [15] used diamond anvil cell (DAC) technology to conduct corrosion experiments and concluded that with the increase in stratum temperature and pressure, limestone exhibits obvious cementation (sediment), and dolomite is not more easily corroded than limestone under the conditions of acidic stratum fluid with a high temperature and high pressure. Temperature is an important factor that affects the dynamic mechanical properties of rocks and the internal structure of rocks will

be damaged due to temperature changes. After undergoing temperature changes, the strength and deformation of rocks have great changes, which will have a great impact on engineering structures.

Under the action of vibration load and stress, the primary pores, crack propagation, and fracture of carbonate rocks will change the permeability, and the carbonate rocks show different characteristics in different stress-strain stages. Xie et al. [16] studied the ground vibration under the coupling action of earthquake and high-speed trains. The coupling of the two will increase the dynamic displacement of the ground. When the speed of the train is greater than a certain critical value, the coupling effect is significant. Vital et al. [17] studied the hydrodynamic problems in the concretion and dissolution processes of carbonate rocks in the southeast Buenos Aires Province, Argentina, and pointed out the influence of mineral particle size on hydrochemistry and the relationship between mineral structure changes and hydrodynamic pressure in the process of dissolution. Ma et al. [18] carried out tests on seepage characteristics of fissuring rock masses under different confining pressures. The groundwater transported in rock cracks is affected by the width of cracks and their interconnection, and is also strictly controlled by the geometric shape and confining pressure conditions required by water flow. Ishibashi et al. [19] discussed the seepage evolution of cracks in carbonate rocks caused by mechanical stress and nonequilibrium chemistry (pH value). According to the combination of constraint stress and liquid pH, pore spaces of cracks are either open (permeability increases) or closed (permeability decreases). Sheng et al. [20] through designing experiments under different working conditions and with the condition of changing osmotic pressure and chemical solutions, acquired the change of fissure permeability under the action of stress, and theoretically described the permeability characteristics of rock mass fissures under the seepage-stress-chemical coupling action, and further revealed the mechanism of the seepage-stress-chemical coupling action. Chen et al. [21] reviewed the research status of thermal, water, and mechanical properties of rock masses under low temperature and freeze-thaw cycle conditions, and put forward to establish a water-heat coupling model of rock masses with phase transition at low temperature and a turbulence model of tunnel airflow field by considering the influence of air temperature and humidity by the means of field monitoring, a large number of indoor freeze-thaw tests, and uniaxial and triaxial compression tests. Chen [22, 23] reviewed the impact of vibration caused by train operation on the foundation based on the field test data.

To sum up, there are many kinds of research focusing on the corrosion of dolomite and limestone under the action of chemistry, temperature, and vibration load, but the existing chemical corrosions and researches in karst areas mainly focus on limestone-dominated areas or areas with miscellaneous lithology, so the study on corrosion in areas with dolomite-dominated lithology needs to be further strengthened. Scientific problems such as differential corrosion characteristics of rocks and identification of influencing factors in dolomite and limestone development areas have not been completely solved. Therefore, it is of great

theoretical and practical significance to systematically carry out tests to determine the structural characteristics and differential corrosions of limestone and dolomite and explore the influencing mechanism of differences between dolomite and limestone in karst geologic disasters.

## 2. Test Samples

*2.1. Collection and Analysis of the Test Samples.* Several limestone and dolomite samples were collected from large-scale construction sites such as highways, main roads, and urban railway transits in the Guilin and Liuzhou regions in the north of Guangxi. After returning to the laboratory, the representative samples were selected and analyzed for the minerals and structural characteristics of the rocks with an optical microscope, so as to roughly obtain the mineral composition, structural characteristics, and name of the samples. The specific test results are shown in Table 1.

*2.2. Description of Characteristics of the Test Samples.* In the process of mineral and rock identification, it is difficult to accurately judge the mineral and rock only by naked eyes and simple tools for some fine-grained, micro-grained, aphanitic, or vitreous rocks; so it is necessary to triturate the 0.03 mm thick rock or mineral slices and identify with the aid of an optical microscope. The transmission polarizing microscope is used for the identification of transparent minerals, while the reflection polarizing microscope is used for the identification of opaque minerals. The test samples shown in Table 1 are photographed with an optical microscope and further described in details below.

*2.2.1. Test sample No. 1.* The rock has a fine crystalline texture. The rock is composed of 0.06–0.25 mm dolomite. The dolomite is in irregular particles with a poor automorphic degree, and the particles are closely embedded into aggregates (Figure 1). The dolomite is not colored with the alizarin red staining. The rock contains 2% calcite, 97% dolomite, and < 1% others.

*2.2.2. Test sample No. 2.* The rock has a fine crystalline texture. The rock is mainly composed of 0.03–0.06 mm calcite and a small amount of carbonaceous and siliceous minerals (Figure 2). The rock contains 85% calcite, 8% carbonaceous mineral, and 7% siliceous mineral. The calcite is colored with the alizarin red staining, and its content is about 85%. The rock minerals are slightly oriented.

*2.2.3. Test sample No. 3.* The rock has a fine crystalline texture. The rock is composed of 0.06–0.25 mm dolomite. The dolomite is in irregular particles with poor automorphic degree (rhombus is found locally). The particles are closely embedded into aggregates (Figure 3). The dolomite is not colored with the alizarin red staining. The rock contains 98% dolomite and 2% calcite.

TABLE 1: Mineral composition and structural characteristics of the test samples.

Sample no.	Macroscopic observation	Mineral composition	Structure construction	Name
1	The rock is in gray-white color, with a fine crystalline texture and massive structure. It bubbles slightly when dropping cold diluted HCl solution. It is mainly composed of carbonate minerals.	Dolomite: 97%; calcite: 2%; others: 1%	Fine crystalline texture, massive structure	Fine-grained dolomite
2	The rock is in dark black color, with a powder crystalline texture and massive structure. The rock is so hard that a knife cannot strike on it. The rock is in dark black, but it does not pollute the hands. It bubbles strongly when dropping cold diluted HCl solution. It is mainly composed of carbonate minerals, carbonaceous matter, and siliceous matter.	Calcite: 85%; carbonaceous matter: 8%; siliceous matter: 7%	Powder crystalline texture, massive structure	Carbonaceous siliceous limestone
3	The rock is in gray-white color, with a fine crystalline texture and massive structure. It bubbles slightly when dropping cold diluted HCl solution. It is mainly composed of carbonate minerals.	Dolomite: 98%; calcite: 2%	Fine crystalline texture, massive structure	Fine-grained dolomite
4	The rock is in gray color, with an argillaceous texture and massive structure. The knife can strike on it. The rock powder has a slippery feeling. It is mainly composed of mud. It is in lamina and lamellation configuration. The minerals have a slightly oriented arrangement, but not obvious. A thin layer of pyrite is found in the hand specimen, which is granular aggregates and concentratedly distributed locally.	Dolomite: 98%; calcite: 2%.	Argillaceous texture, massive structure	Pyrite-bearing and sand-bearing mudstone
5	The rock is in gray color, with a powder crystalline to mesocrystalline texture and massive structure. It bubbles strongly when dropping cold diluted HCl solution. It is mainly composed of carbonate minerals. It fragments in a later stage, with broken cracks in lattices interspersed.	Calcite: 98%; dolomite: 1%; others: 1%	Powder crystalline to mesocrystalline texture, massive structure	Mesocrystalline limestone
6	The rock is in gray-white color, with a fine crystalline texture and massive structure. It bubbles slightly when dropping cold diluted HCl solution. It is mainly composed of carbonate minerals.	Dolomite: 97%; calcite: 2%; others: 1%	Fine crystalline texture, massive structure	Fine-grained dolomite
7	The rock is in dark gray color, with a mesocrystalline texture and massive structure. It bubbles weakly when dropping cold diluted HCl solution. It is mainly composed of carbonate minerals. The rock is broken, with broken cracks interspersed.	Dolomite: 98%; calcite: 2%	Mesocrystalline texture, massive structure	Mesocrystalline dolomite
8	The rock is in black color, with a microcrystalline to powder crystalline texture and massive structure. It bubbles slightly when dropping cold diluted HCl solution. It is mainly composed of carbonate minerals and carbonaceous matter.	Dolomite: 40%; calcite: 55%; carbonaceous matter: 5%	Microcrystalline to powder crystalline texture, massive structure.	Carbonaceous dolomite

2.2.4. *Test sample No. 4.* The rock has an argillaceous texture. The rock is mainly composed of clay minerals, a small amount of quartz sand, and a small amount of granular pyrite. The rock contains about 90% clay minerals, about 5% quartz sand, and

about 5% pyrite, with quartz sand and pyrite scattered (Figure 4). Sandy grains vary from 0.05 to 0.20 mm and are mostly sub-round. Pyrite is opaque (Figure 5), with a size of 0.02–0.04 mm. Minerals are in an oriented arrangement, but not obvious.

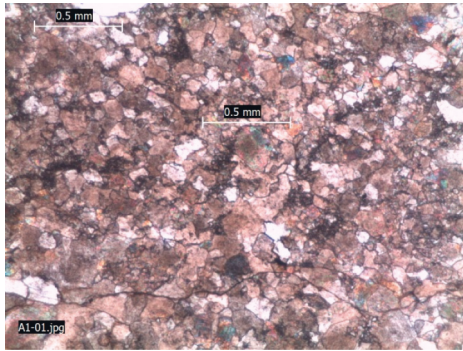


FIGURE 1: Fine-grained dolomite.

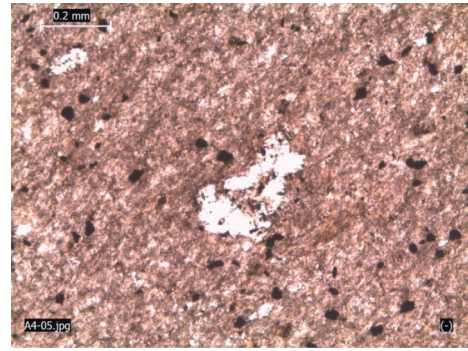


FIGURE 5: Pyrite and sand-bearing mudstone.

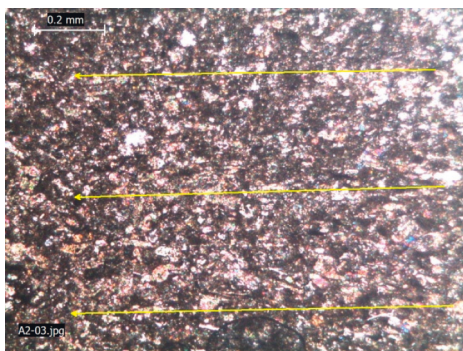


FIGURE 2: Carbonaceous siliceous limestone.

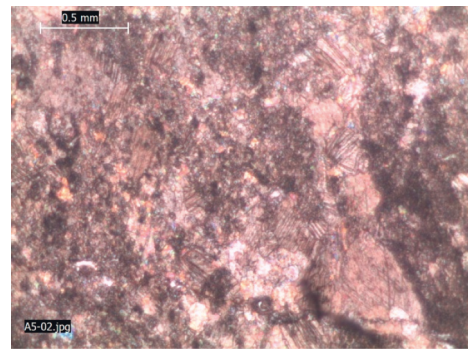


FIGURE 6: Mesocrystalline limestone.



FIGURE 3: Fine-grained dolomite.

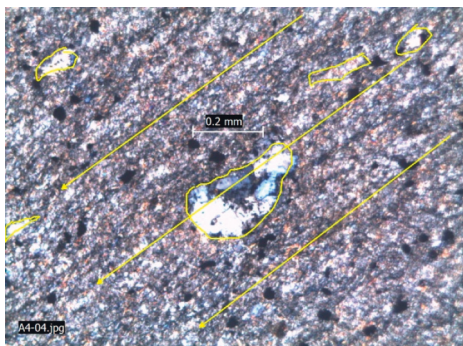


FIGURE 4: Pyrite and sand-bearing mudstone.

2.2.5. *Test sample No. 5.* The rock has a powder crystalline to the mesocrystalline texture (Figure 6). The rock is mainly composed of 0.03–0.50 mm calcite minerals. The calcite is irregularly granular, in rhombohedron, rhombic cleavage, high-grade white interference color, and 0.03–0.50 mm in size, of which over 80% is in the range of 0.25–0.50 mm. The calcite is red and the dolomite is not colored when the rock is dyed with alizarin red. The rock contains 98% calcite, 1% dolomite, and < 1% other organic matters. In the later stage, the broken cracks are interspersed and filled with calcite (Figure 7).

2.2.6. *Test sample No. 6.* The rock has a fine crystalline texture. The rock is composed of 0.05–0.25 mm dolomite, of which more than 95% is in the range of 0.06–0.25 mm. The dolomite is in irregular particles with a poor automorphic degree. The particles are closely embedded into aggregates (Figure 8). The dolomite is not colored with the alizarin red staining. The rock contains 2%, 97% dolomite, and < 1% others. In the later stage, the cracks are filled with calcite.

2.2.7. *Test sample No. 7.* The rock has a fine crystalline and mesocrystalline texture. The rock is mainly composed of 0.05–0.50 mm dolomite minerals (Figures 9 and 10), of which 15% is in the range of 0.05–0.25 mm and 85% is in the range of 0.25–0.50 mm. Only the calcite filled in the cracks is colored with the alizarin red staining, with a content of about 2% (Figure 10). The remaining is mainly dolomite with a content of about 98%.

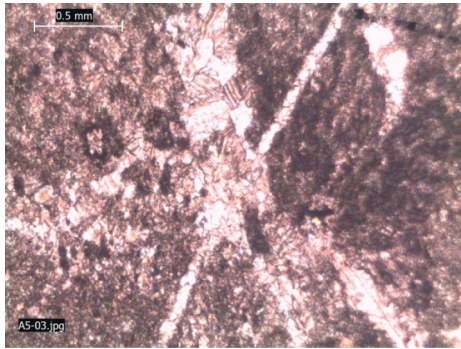


FIGURE 7: Mesocrystalline limestone.

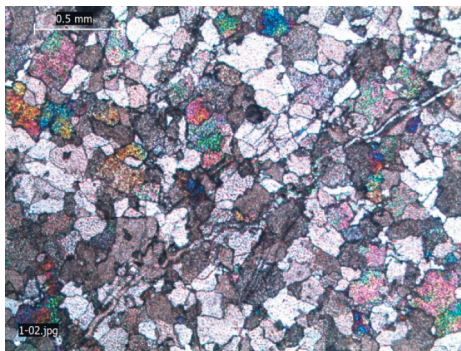


FIGURE 8: Fine-grained dolomite.

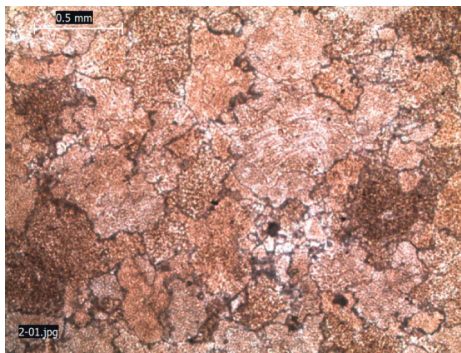


FIGURE 9: Mesocrystalline dolomite.

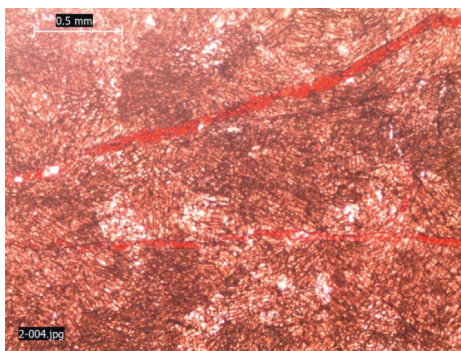


FIGURE 10: Mesocrystalline dolomite.

2.2.8. *Test sample No. 8.* The rock has a microcrystalline to powder crystalline texture and is mainly composed of dolomite, calcite, and opaque carbonaceous mineral. The mineral particle size is mainly between 0.005 and 0.10 mm, of which more than 70% is in the range of 0.03–0.06 mm. The rock is dyed with alizarin red and contains about 40% calcite, about 55% dolomite, and 5% carbonaceous mineral and others (Figures 11 and 12). The calcite is irregularly granular, with high-grade white interference color, and is evenly distributed in the rock. The dolomite is irregularly granular, with a particle size of 0.05–0.10 mm.

2.3. *Chemical Composition Analysis of the Test Samples.* As shown in Table 1, the above description that the test samples taken in the experiments are mainly crystalline dolomites and limestones with high purity (except for test sample no. 4). The test samples with good appearance and characters other than test sample no. 4 were select, and detected for the amounts of CaO, MgO, CO<sub>2</sub>, SiO<sub>2</sub>, acid insoluble matter, and loss on ignition by using the high-frequency infrared sulfur-carbon analyzer and X-ray fluorescence spectrometer, respectively. The specific test results are shown in Table 2. Then the ratio of CaO/MgO was calculated to judge the purity of dolomite and limestone [24, 25]. Among them, dolomite and limestone with high purity were selected, and then the subsequent corrosion tests were carried out.

### 3. Corrosion Tests

The corrosion (corrodibility) of water is an internal factor of water-rock interaction, and the mobilization property and chemical characteristics of water will inevitably affect the characteristics of action of water on carbonate rocks. The main acidic fluids of dolomite and limestone corrosion in the actual field environment are the aqueous solutions of CO<sub>2</sub>, organic acids, and H<sub>2</sub>S. However, in the indoor simulation tests, the acidity of the carbonic acid solution is weak, and its reaction with limestone and dolomite is slow under static conditions. When calcium chloride or solution containing calcium ions is added to the aqueous solution of organic acids, insoluble calcium salt precipitate can be formed. H<sub>2</sub>S gas is toxic. In acidic solutions commonly used in laboratories, SO<sub>4</sub><sup>2-</sup> in sulfuric acid solution will react with the corroded Ca<sup>2+</sup> and Mg<sup>2+</sup> to generate slightly soluble substances and insoluble substances, which will affect the determination of Ca<sup>2+</sup> and Mg<sup>2+</sup>. At the same time, due to the fairly long reaction process between the ions in groundwater and the minerals in rocks in nature, it is difficult to obtain ideal test results under limited time and conditions, so hydrochloric acid solution at pH 3.0 was specially prepared for the indoor accelerated corrosion tests.

3.1. *Comparison of the Static Corrosion Test Results between Dolomite and Limestone under the Same Conditions.* All the devices used in this experiment are self-designed, and the experimental devices mainly include a thermostat, vibration equipment, pH measuring instrument, measuring



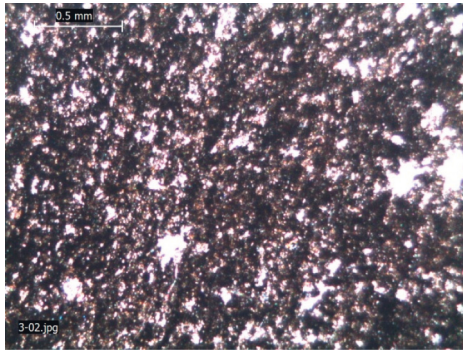


FIGURE 11: Carbonaceous dolomite.

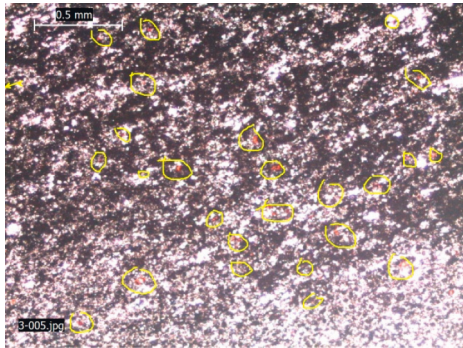


FIGURE 12: Carbonaceous dolomite.

equipment for  $\text{Ca}^{2+}$  and  $\text{Mg}^{2+}$ , and related chemicals and reagents, etc. The thermostat and temperature controller can keep the experimental environment at a stable temperature all the time and reduce the influence caused by the external environment. A constant speed stirrer is mounted at the bottom of the thermostat, which makes the solution flow through the rotation at a constant speed, thus simulating the outdoor hydrodynamic conditions.

In order to reduce the discreteness of the test samples, the rock samples taken for the experiment were made into cylindrical slices, and the pulsed ultrasonic penetration method was used to detect and screen the samples, from which the rock samples with similar wave velocities were selected. The specific experimental steps are as follows:

- (i) Measuring the diameter and height of the rock samples by vernier caliper and weighing the rock samples (Table 3), and calculating the parameters such as surface area, volume, and density;
- (ii) Washing the test samples with distilled water, drying them in an oven, cooling them in a dryer to room temperature and weighing;
- (iii) Adding 5 L hydrochloric acid solution at pH 3.0 into a clean beaker, and adding the rock samples successively;
- (iv) Standing at room temperature, removing the corroded liquid every 2 hours, and measuring the concentration of calcium and magnesium ions in the solution by ethylene diamine tetraacetic acid (EDTA) solution titration method;

- (v) Determine the pH of the remaining solution, and calculate the corrosion amount of the rock samples. In order to eliminate the influence of surface area differences of the rock samples, the results of this experiment are expressed by the corrosion amount per unit of surface area.

As shown in Figure 13, the corrosion rates of dolomite and limestone are basically the same under static conditions, and the corrosion amount per unit surface area for dolomite is 0.341 mg (average value), which is slightly larger than that of limestone (0.328 mg). And there is little difference between them for a long time.

**3.2. Comparison of Dolomite Test Results under Different Conditions.** Temperature is one of the important factors affecting the mechanical properties of rocks. Rock is composed of solid mineral particles and tiny gaps between the mineral particles. The solid mineral particles and the channel networks formed by the gaps between the mineral particles are often filled with fluid media. When the environment of such porous media of the rock changes, the water existing in the pores and fissures inside the rock would undergo a phase change, which leads to changes in the physical and mechanical properties of the rock. These changes are not only related to the physical structure but also affected by the existing water, temperature, and stress state of the rock. At the same time, under the action of vibration load and stress, the primary pores, crack propagation, and fracture of dolomite and limestone cause the permeability to change, and then the dolomite and limestone exhibit different characteristics in different stress-strain stages. In order to study the influence of temperature and vibration load on the corruptions of dolomite and limestone, a group of dolomite and limestone were specially selected (the specifications and size of the samples are shown in Table 4), and the corrosion tests were carried out at different temperatures ( $0^{\circ}\text{C}$  and  $40^{\circ}\text{C}$ ) and vibration conditions. The corrosion results of the selected samples under different conditions are shown in Table 4 and Figure 14. Vibration conditions: The authors fixed a crossbar on the upper part of the Electric Sieve Shaker (the vibration amplitude is 10 mm, and the number of shocks is about 150 times/min.), and then use a thin cotton thread to tie the rock sample to one end of the crossbar. The sample is shaken every half an hour for 2 to 3 minutes.

As shown in Figure 14, the corrosion rate of dolomite is the lowest at  $0^{\circ}\text{C}$ , and is increased at  $40^{\circ}\text{C}$ , but the difference is not significant. However, the corrosion rate and amount of dolomite are increased significantly under the vibration condition, and the corrosion rate under the vibration condition is about 1.75 times of the corrosion rate at  $0^{\circ}\text{C}$ . The results indicate that vibration load has a more significant effect on the corrosion rate of dolomite than temperature.

As shown in Figure 15, the corrosion rate of limestone is the lowest at  $0^{\circ}\text{C}$ , the corrosion amount is increased at  $40^{\circ}\text{C}$ , and the variation amplitude of limestone is larger than that of dolomite. At the same time, the corrosion rate and amount of limestone under the vibration load are also increased significantly, and the corrosion rate under the

TABLE 2: List of chemical composition analysis of dolomite and limestone test samples.

Sample no.	Field naming	Chemical composition of dolomite and limestone samples (%)						
		CaO	MgO	SiO <sub>2</sub>	Loss	Acid insoluble matter	CO <sub>2</sub>	CaO/MgO
1	Dolomite	36.07	16.78	0.27	45.96	0.48	45.13	2.15
2	Limestone	36.20	3.25	15.17	33.29	23.74	31.57	11.13
3	Limestone	50.32	4.51	0.64	43.10	1.31	42.71	11.16
4	Limestone	53.65	0.39	0.90	42.79	1.72	42.52	137.56
5	Limestone	20.38	2.55	32.03	22.15	53.08	18.21	7.98
6	Dolomite	32.14	20.27	0.24	46.15	0.31	45.76	1.59
7	Dolomite	32.14	20.27	1.18	46.05	2.68	45.65	1.59
8	Dolomite	32.07	19.95	1.32	45.93	2.60	45.34	1.61
9	Limestone	29.91	2.74	26.93	28.00	37.72	26.01	10.90

TABLE 3: List of parameters and corrosion results of limestone and dolomite test samples.

Sample no.	Lithology	Weight g	Diameter mm	Height mm	Surface area mm <sup>2</sup>	Volume mm <sup>3</sup>	Density g/cm <sup>3</sup>	Corrosion amount mg	Corrosion amount per unit area, mg/mm <sup>2</sup>
1-14	Dolomite	120.81	68.87	12.21	10087.07	45461.68	2.66	3583.01	0.355
3-6	Dolomite	115.27	69.25	11.54	10038.35	43442.52	2.65	3473.27	0.327
2-10	Limestone	127.23	70.58	12.69	10633.39	49624.32	2.56	3293.24	0.328

vibration load is about 1.88 times of the corrosion rate at 0°C. The results demonstrate that the corrosion rate of limestone is highly sensitive to both temperature and vibration load.

#### 4. Analysis and Discussion of the Test Results

The corrosion of erosive aqueous solution is an internal factor of water-rock interaction, and the mobilization property and chemical characteristics of water affect the characteristics of action of erosive aqueous solution on dolomite and limestone. With the progress of water-rock interaction, the change of internal structure and pore characteristics of rock would inevitably lead to the unceasing change of groundwater seepage field. At the same time, the hydrochemical property in the rock mass also changes correspondingly, which is mainly reflected in the coupling process of the chemical field, temperature field, and stress field of water-rock interaction.

The dolomite (from Liuzhou area) selected in this study has a CaO/MgO ratio of less than 2.2, an acid insoluble content between 0.31% and 0.68%, and a SiO<sub>2</sub> content between 0.24% and 1.32%, so it belongs to pure dolomite. The selected limestone (from the Guilin area) has a CaO/MgO ratio of greater than 10, the contents of acid insoluble matter and SiO<sub>2</sub> are generally higher, and the purity is slightly lower. In pure carbonate rocks, the corrosion rate of calcite is generally higher than that of dolomite, and the corrosion rate increases with the increase of calcite content and decrease with the increase of dolomite content. In the impure carbonate rocks, due to the increase of acid insoluble matters and SiO<sub>2</sub> content, the amount of physical damage is increased, which inhibits the relationship between the corrosion rate and the calcite and dolomite content. Similarly, the structure of rock also has a certain influence on the corrosion rate. Generally speaking, the smaller the grain size, the larger the specific surface area, and the

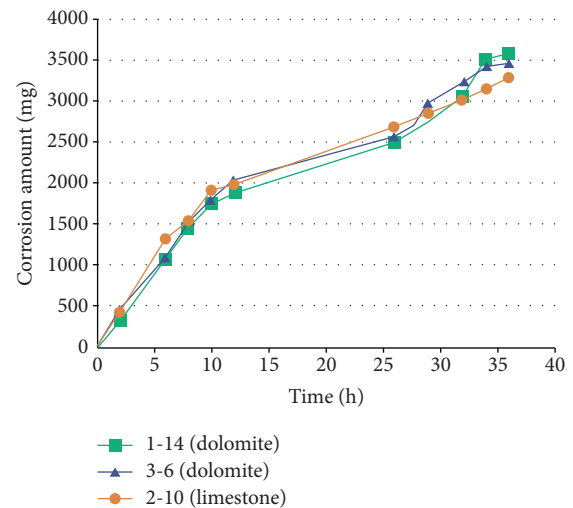


FIGURE 13: Comparison of corrosion test results of dolomite and limestone under the same conditions.

faster the corrosion rate. Therefore, in this study, the corrosion rates of dolomite and limestone are basically the same under the same conditions. However, under the influence of different temperatures and vibration loads, the corrosion rates of dolomite and limestone are somewhat different.

Temperature is one of the important factors affecting the properties of dolomite and limestone. In fact, the corrosion process of dolomite and limestone is a process in which ions in the lattice of carbonate minerals leave their original positions and transfer into water under the influence of electric charge and thermodynamic conditions of the polar molecules in the erosive water. In the surface environment, this process involves a three-phase complex system of gas, liquid, and solid, and their chemical reactions are influenced

TABLE 4: List of parameters and corrosion results of limestone and dolomite samples.

Sample no.	Lithology	Weight g	Diameter Mm	Height mm	Surface area mm <sup>2</sup>	Volume mm <sup>3</sup>	Density g/cm <sup>3</sup>	Corrosion amount mg	Corrosion amount per unit area, mg/mm <sup>2</sup>
4-7	Limestone	119.45	68.50	12.26	10003.84	45158.68	2.65	2246.13	0.225
4-14		118.14	68.68	12.01	9995.619	44470.63	2.66	3749.75	0.375
4-6		118.17	68.47	12.15	9972.58	44714.32	2.64	4216.24	0.423
1-10		121.90	67.88	12.69	9938.867	45900.24	2.66	2652.67	0.267
1-12	Dolomite	122.08	68.79	12.35	10096.95	45876.18	2.66	2916.88	0.287
1-11		124.48	68.74	12.71	10161.92	47144.85	2.64	4604.62	0.456

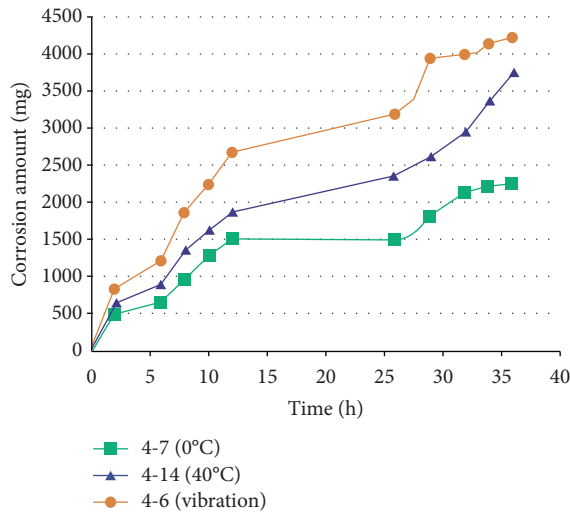


FIGURE 14: Comparison of the corrosion test results of dolomite under different conditions.

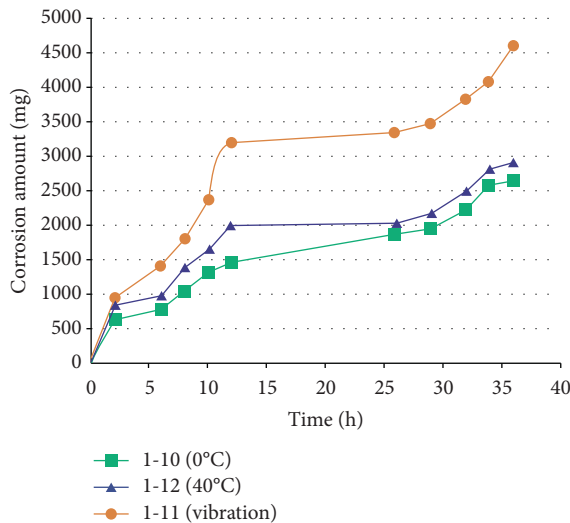


FIGURE 15: Comparison of the corrosion test results of limestone under different conditions.

by many factors such as pH, temperature, hydrodynamic conditions, specific surface area of minerals, genesis structure of minerals, and external vibration load conditions. In northern Guangxi, the solar radiation is intense, the average sunshine time is long, and the rock surface heats up quickly

and cools down slowly, which has a significant heating effect. Rock surface and Earth surface temperature can reflect the water-heat exchange process of Earth surface, which has a certain influence on the corrosion rate of carbonate rocks. In northern Guangxi, the corrosion amount per unit surface area is 0.267 mg/mm<sup>2</sup> for dolomite, and 0.225 mg/mm<sup>2</sup> for limestone at 0°C. The corrosion amount per unit surface area is 0.287 mg/mm<sup>2</sup> for dolomite, and 0.375 mg/mm<sup>2</sup> for limestone at 40°C. The corrosion rate of both dolomite and limestone increases with the increase of the experimental temperature, and the increasing amplitude for limestone is larger than that for dolomite. This is possible because the dolomite has more pores on the surface, mostly has stratification structures, and is easy to form corrosion films and pores on the surface, while the limestone has fine mineral particles (microcrystalline to powder crystalline), has compact structures, and is more conducive to the surface corrosion with the increase of temperature.

Corrosion includes chemical dissolution and mechanical damage, and vibration load is one of the causes of mechanical damage. With the rapid development of the economy and society and the adjustment of national strategy, more and more high-speed railways and highways need to pass through the karst areas in northern Guangxi. In the process of construction and operation, the influence of vibration loads such as vehicles (especially high-speed trains and urban railway transits) is more conducive to increasing the corrosion rate of dolomite and limestone, especially obvious in the districts with better hydrodynamic conditions. The vibration of the train can increase the deformation of the rock mass, especially the deformation of the rock mass with cracks or connected pores. In addition, vibration loads will aggravate the degree of chemical corrosion of water on the rocks, and the coupling of mechanical destruction and chemical corrosion will lead to the generation of secondary minerals and secondary pores in the rocks, which will accelerate the rate of corrosion reaction. The corrosion rate of dolomite in northern Guangxi is increased significantly under the vibration load conditions, which is about 1.75 times that at 0°C. The corrosion rate of limestone also increased significantly, which is about 1.88 times of that at 0°C. Under the action of vibration load, physical disintegration is dominant in the corrosion process of dolomite, and the rock fragments provided by physical disintegration are more conducive to chemical corrosion. In addition, the uniform intercrystalline pores in dolomite are beneficial to the overall corrosion. However, the distribution of fissuring gaps is

extremely uneven when the limestone is stressed, and thus the limestone is easy to form rock cracks and cave systems, which are characterized by obvious differential corrosion.

## 5. Conclusions

- (1) The dolomite in northern Guangxi mainly has a fine crystalline texture and massive structure, and the ratio of CaO/MgO is generally less than 2.2. The dolomite has high purity. The limestone mainly has a powder crystalline texture and massive structure. The ratio of CaO/MgO is generally greater than 10, and the highest ratio can reach about 140. The limestone also has high purity. The content of acid-insoluble matter is low in dolomite but is high in limestone due to the high content of carbonaceous matter.
- (2) The corrosion of dolomite and limestone mainly depends on the chemical composition of rocks, the structure of rocks and minerals, the ratio of different mineral components, seepage conditions, and other factors. The difference in corrosion between dolomite and limestone mainly depends on the ratio of CaO/MgO in their chemical composition, and only when the acid insoluble matter exceeds 10% will the corrosion amount be substantially affected.
- (3) Under the same external conditions, the corrosion rates of the pure dolomite and the pure limestone are basically the same. The corrosion amount per unit surface area is 0.341 mg for dolomite, and 0.328 mg for limestone. The corrosion amount per unit surface area of dolomite is slightly larger than that of limestone.
- (4) The corrosion rates of dolomite and limestone are largely influenced by temperature and vibration load. The corrosion rates of dolomite and limestone are low at 0°C and are increased with the increase of temperature, but the influence of vibration load on corrosion rate is more significant than temperature.
- (5) The influence of chemicals, temperature, and other factors on the dissolution of limestone and dolomite were analyzed based on the experiment. The introduction of vibration conditions is a major feature of this paper. The results can provide technical support for the construction, operation, and maintenance of high-speed railways in the karst rocky area of Southwest China. However, due to the limitations of indoor test conditions, the simulated test may be different from the situation. The authors will simulate the actual situation more realistically in future studies [16].

## Data Availability

The research data of the paper can be obtained from Zhanfei Gu by e-mail.

## Disclosure

A preprint has previously been published [6], and the link is <https://www.researchsquare.com/article/rs-942174/v1.pdf>.

## Conflicts of Interest

The authors have no conflict of interest to disclose.

## Authors' Contributions

Zhanfei Gu was responsible for original writing, methodology, and visualization. Zhikui Liu was responsible for supervision and funding.

## Acknowledgments

This research was funded by the National Natural Science Foundation of China (Grant no. 41867039), the Foundation of Technical Innovation Center of Mine Geological Environmental Restoration Engineering in Southern Area (Grant no. CXZX 120201002), project funded by Guangxi Key Laboratory of Geotechnical Engineering (20-Y-XT-03), Key R&D and Promotion Projects in Henan Province (Grant no. 222102320177), and project funded by Key Scientific Research Projects of Colleges and Universities in Henan Province (Grant no. 22A560019).

## References

- [1] P. Liu, G. D. Couples, J. Yao, Z. Huang, W. Song, and J. Ma, "A general method for simulating reactive dissolution in carbonate rocks with arbitrary geometry," *Computational Geosciences*, vol. 22, no. 5, pp. 1187–1201, 2018.
- [2] C. b. Zhao, B. Hobbs, and A. Ord, "Effects of different numerical algorithms on simulation of chemical dissolution-front instability in fluid-saturated porous rocks," *Journal of Central South University*, vol. 25, no. 8, pp. 1966–1975, 2018.
- [3] C. Zhao, H. Bruce, and O. Alison, "A New Alternative Approach for Investigating Acidization Dissolution Front Propagation in Fluid-Saturated Carbonate Rocks," *Science China Technological Sciences*, vol. 8, pp. 1–14, 2017.
- [4] Q. Liu, Y. Lu, and F. Zhang, "Laboratory simulation experiment on dissolution of limestone under hydrodynamic pressure," *Carbonates and Evaporites*, vol. 28, no. 1-2, pp. 3–11, 2013.
- [5] Q. Liu, Z. Gu, Y. Lu, and Z. Liu, "The experimental study of dolomite dissolution and pore characteristics in shibing, guizhou," *Acta Geoscientia Sinica*, vol. 36, no. 4, pp. 413–418, 2015.
- [6] Z. Gu and Z. Liu, *Experimental study on the structural features and corrosion characteristics of dolomite and limestone in the karst stone mountainous areas in northern Guangxi*, Guangxi, 2022.
- [7] M. She, J. F. Shou, A. J. Shen, Y. Zhu, and X. P. Zheng, "Experimental simulation of dissolution for carbonate rocks in organic acid under the conditions from epigenesis to deep burial environments," *Geochimica*, vol. 43, no. 5, pp. 276–286, 2014.
- [8] X. H. Wei, T. T. Ma, J. Wang, and H. Z. Ye, "The simulation study of the effect of liquid with different pH values on corrosion for limestone," *Journal of Foshan University (Social Science Edition)*, vol. 31, no. 2, pp. 17–22, 2013.

- [9] Z. Guo, Y. Shen, S. Wan, W. Shang, and K. Yu, "Hybrid intelligence-driven medical image recognition for remote patient diagnosis in internet of medical things," *IEEE Journal of Biomedical and Health Informatics*, vol. 1, 2021.
- [10] L. X. Zhang, Q. H. Zhao, X. B. Hu, and Z. H. A. O. Xing, "Laboratory dissolution test on dolomite and its micro-dissolution mechanism," *Journal of Engineering Geology*, vol. 20, no. 4, pp. 576–584, 2012.
- [11] M. She, Y. M. Jiang, A. P. Hu, and A. Raoof, "The progress and application of dissolution simulation of carbonate rock," *Marine Origin Petroleum Geology*, vol. 25, no. 1, pp. 12–21, 2020.
- [12] M. A. Nomeli and A. Riaz, "Effect of CO<sub>2</sub> solubility on dissolution rate of calcite in saline aquifers for temperature range of 50–100 °C and pressures up to 600 bar: alterations of fractures geometry in carbonate rocks by CO<sub>2</sub> acidified brines," *Environmental Earth Sciences*, vol. 76, no. 9, p. 352, 2017.
- [13] A. A. Eliwa and A. Atef, "Kinetics and thermodynamics of carbonate dissolution process of uranium from abu-zeniema wet crude uranium concentrates," *Journal of Radioanalytical and Nuclear Chemistry*, vol. 312, no. 1, pp. 1–11, 2017.
- [14] M. Mutlutürk, R. Altindag, and G. Türk, "A decay function model for the integrity loss of rock when subjected to recurrent cycles of freezing–thawing and heating–cooling," *International Journal of Rock Mechanics and Mining Sciences*, vol. 41, no. 2, pp. 237–244, 2004.
- [15] W. X. Ding, T. Xu, and H. Wang, "Experimental study of mechanical property of limestone under coupled chemical solution and freezing–thawing process," *Yanshilixue Yu Gongcheng Xuebao/chinese Journal of Rock Mechanics & Engineering*, vol. 34, no. 5, pp. 979–985, 2015.
- [16] W. Xie, GY. Gao, J. Song, and Y. Wang, "Ground vibration analysis under combined seismic and high-speed train loads," *Underground Space*, vol. 7, no. 3, pp. 363–379, 2021.
- [17] M. Vital, D. E. Martínez, N. Borrelli, and S. Quiroga, "Kinetics of dissolution processes in loess-like sediments and carbonate concretions in the southeast of the province of Buenos Aires, Argentina," *Environmental Earth Sciences*, vol. 75, no. 17, p. 1231, 2016.
- [18] D. Ma, X. X. Miao, Z. Q. Chen, and X. B. Mao, "Experimental investigation of seepage properties of fractured rocks under different confining pressures," *Rock Mechanics and Rock Engineering*, vol. 46, no. 5, pp. 1135–1144, 2013.
- [19] T. Ishibashi, T. P. McGuire, N. Watanabe, N. Tsuchiya, and D. Elsworth, "Permeability evolution in carbonate fractures: competing roles of confining stress and fluid ph," *Water Resources Research*, vol. 49, no. 5, pp. 2828–2842, 2013.
- [20] J. Sheng, L. Fengbin, D. Yao, Q. Huang, H. Song, and M. Zhan, "Experimental study of seepage properties in rocks fracture under coupled hydro-mechanochemical process," *Chinese Journal of Rock Mechanics and Engineering*, vol. 31, no. 5, pp. 1016–1025, 2012.
- [21] W. Chen, X. Tan, Y. Hongdan, K. Yuan, and L. Shuca, "Advance and review on thermo-hydro-mechanical characteristics of rock mass under condition of low temperature and freeze-thaw cycles," *Yanshilixue Yu Gongcheng Xuebao/Chinese Journal of Rock Mechanics and Engineering*, vol. 30, no. 7, pp. 1318–1336, 2011.
- [22] G. Chen, "Ground vibration analysis induced by high-speed train based on in-situ data," *Yanshilixue Yu Gongcheng Xuebao/Chinese Journal of Rock Mechanics and Engineering*, vol. 34, no. 3, pp. 601–611, 2015.
- [23] Y. He, L. Nie, T. Guo, K. Kaur, M. M. Hassan, and K. Yu, "A NOMA-enabled framework for relay deployment and network optimization in double-layer airborne access VANETs," *IEEE Transactions on Intelligent Transportation Systems*, vol. 2021, Article ID 3139888, 15 pages, 2022.
- [24] Y. M. Zhu, *Sedimentary Rocks*, pp. 182–183, Petroleum industry publishing house, Beijing, 2008.
- [25] Y. Peng, A. Jolfaei, and K. Yu, "A novel real-time deterministic scheduling mechanism in industrial cyber-physical systems for energy internet," *IEEE Transactions on Industrial Informatics*, vol. 18, no. 8, pp. 5670–5680, 2022.

## Research Article

# A Novel Architecture for Diabetes Patients' Prediction Using K-Means Clustering and SVM

Nitin Arora <sup>1</sup>, Anupam Singh <sup>2</sup>, Mustafa Zuhaer Nayef Al-Dabagh <sup>3</sup>,  
and Sumit Kumar Maitra <sup>4</sup>

<sup>1</sup>Electronics & Computer Discipline, Indian Institute of Technology, Roorkee, India

<sup>2</sup>School of Computer Science, University of Petroleum and Energy Studies, Dehradun, India

<sup>3</sup>Department of Computer Science, Knowledge University, Erbil 44001, Iraq

<sup>4</sup>Department of Electrical and Computer Science, Wachemo University, Hosaena, Ethiopia

Correspondence should be addressed to Sumit Kumar Maitra; [sumitmaitra@wcu.edu.et](mailto:sumitmaitra@wcu.edu.et)

Received 10 June 2022; Accepted 22 July 2022; Published 24 August 2022

Academic Editor: Punit Gupta

Copyright © 2022 Nitin Arora et al. This is an open access article distributed under the Creative Commons Attribution License, which permits unrestricted use, distribution, and reproduction in any medium, provided the original work is properly cited.

Diabetes is one of the alarming issues in today's era. It is a chronic disease that may cause many health-related problems. It is a group of syndrome that results in too much sugar in the blood. Diabetes's chronic hyperglycemia has been linked to long-term damage, organ breakdown, and organ failure, notably in the eyes, kidneys, nerves, heart, and veins. Machine learning has quickly advanced, and it is now used in many facets of medical health. The goal of this research is to create a model with the highest level of accuracy that can predict a patient's chance of developing diabetes. This paper proposes a novel architecture for predicting diabetes patients using the K-means clustering technique and support vector machine (SVM). The features extracted from K-means are then classified using an SVM classifier. A publicly available dataset, namely, the Pima Indians Diabetes Database, is tested using this approach. Accuracy of 98.7% is noted on the used dataset. On this dataset, the combined method performs better than the conventional SVM-based classification. This paper also compared the accuracy, precision, recall, and F1-score of the different machine learning techniques for classifying diabetes patients.

## 1. Introduction

Various forms of diabetes exist. In type 1, pancreatic insulin stops producing hormones. This hormone helps digest carbohydrates, fats, and proteins. In type 2 diabetes, cells associated with the digestive system cannot process insulin. Over time, the production of insulin in the body stops. Because of this, various internal organs start to become useless, which causes death. Type 3 diabetes is associated with pregnancy, in which a woman's blood sugar level increases [1–4]. A person cannot do anything special in advance for type 1 rescue. In type 2, nutritious food, regular exercise, and weight control are the best measures in prevention, and they can prevent 90% of diabetes [5, 6]. In 2014, in the clinic examination of 4.21 crore citizens, diabetes was found in 31 lakhs, i.e., about 7.75% of people. Awareness about diabetes is still low. 40% of affected citizens are unable

to take proper care of themselves. They are not able to control their sugar level either. Half of them have never got an eye test done, even though they are at entire risk of retinopathy.

*1.1. Motivation.* According to the WHO, 7.30 million adults in India are in the grip of diabetes. 10.7 to 14.2% of the population is diabetic in cities, while 3 to 6.8% in villages. According to the central government, a quarter of India's 4.25 crore diabetes patients are in India. As per the National Family Health Survey-4, the number of diabetes patients in the country doubled in the year 2007 compared to 2007. 3.5% of women and 3.5% of men aged 35 to 49 have diabetes. Diabetes is present in 9.7% of Indians over 80, while the same is present in 13.1% of people aged 60 to 69 and 13.2 in 70 to 79. After aging, the condition has reduced because the

patient is not survived. Among those who are left and are living for 60 years or even beyond, diabetes is about 36% or say one-third compared to people in the age group of 60 to 79. Heart disease, stroke, kidney disease, and blindness are also becoming a significant threat to health due to the increasing incidence of diabetes in the new generation [7–9].

**1.2. Main Contributions.** The contributions of this manuscript are as follows:

- (i) This paper proposed a novel architecture to diagnose diabetes based on some parameters early.
- (ii) This paper used  $K$ -means clustering combined with an SVM algorithm to classify the data.
- (iii) For experiment purposes, the Pima Indians Diabetes Database is used. In the Pima Indians Diabetes Database, there are 668 female patients' data. 80% of these data are used to train machine and 20% to test the machine on the proposed architecture.

Sections break apart the remaining text of the paper: Section 2 describes the related work and compares the work done by all the researchers on the Pima Indians Diabetes Database using different techniques. Section 3 outlines the suggested approach. This section briefly describes our architecture and uses algorithms to improve the accuracy of predicting diabetes. Section 4 contains the experimental evaluation and results. This section briefly describes the used dataset with all the measured parameters. Section 5 of the paper puts it to a conclusion.

## 2. Related Work

Diabetes prediction using the Pima Indians Diabetes Database is a topic of interest among researchers during the last few decades. This section highlighted some of the methods used by the research to predict diabetes using the Pima Indians Diabetes Database and the accuracy achieved.

AlJarullah [10] has used the decision tree algorithm to predict type II diabetes. The data preprocessing part and the second diabetes prediction are completed in the first phase using the decision tree algorithm. The maximum accuracy achieved in this paper is 78.17%. Anand et al. [11] used higher-order neural network (HONN) combined with principal component analysis (PCA) to predict type II diabetes. In this paper, the authors used PCA to handle the missing data and also to scale the data in the same range of values. The maximum accuracy achieved in this paper is 89.47%. Banerjee et al. [12] used neural network, an evolutionary algorithm-based approach for predicting diabetes. This paper also compares the neural network model with other models. The maximum accuracy achieved in this paper is 93.5%. Barale and Shirke [13] used the  $K$ -means clustering algorithm combined with an artificial neural network (ANN) and  $K$ -means combined with logistic regression classifiers to predict diabetes. The maximum accuracy achieved in this paper is 98%. In order to uncover hidden patterns in the dataset, the  $K$ -means clustering technique is applied.

Chikh et al. [14] used the modified artificial immune recognition system (AIRS). In this, they used the fuzzy  $K$ -nearest neighbor algorithm to diagnose diabetes. The maximum accuracy achieved in this paper is 89.1%. Choubey and Paul [15] used the GA combined with multilayer perceptron neural network method for diagnosing diabetes. In the first phase, the genetic algorithm (GA) is used for feature selection, and in the second, diabetes classification is completed using multilayer perceptron neural network. The maximum accuracy achieved in this paper is 79.13%. Christobel and Sivaprakasam [16] used class-wise  $K$ -nearest neighbor (CkNN) to classify the diabetes dataset. In the first phase, data preprocessing is done, and the mean value is substituted in place of missing values. In the second phase of diabetes, classification is completed using modified KNN. The maximum accuracy achieved in this paper is 78.16%.

Deperlioglu and Utku [17] used a multilayer feedforward NN structure trained by the Bayesian regularization algorithm and the mean square error function. The maximum accuracy achieved in this paper is 95.5%. In this study, the ANN was trained ten times. Gandhi and Prajapathi [18] used F-score,  $K$ -means clustering, Z-score normalization, and SVM. In the first phase, data preprocessing is done using F-score and  $K$ -means. In the second phase, diabetes classification is completed using SVM. The maximum accuracy achieved in this paper is 98%. Ganji and Abadeh [19] used ant colony optimization (ACO) to predict diabetes. The maximum accuracy achieved in this paper is 84.24%—using an ant colony-based classification method, a set of fuzzy rules for diabetic illness diagnosis may be extracted. Hayashi and Yukita [20] used Re-RX with J48 graft, combined with sampling selection techniques for predicting diabetes. As a “white-box” model, the recursive-rule extraction (Re-RX) method delivers extremely accurate categorization. The maximum accuracy achieved in this paper is 83.83%. Huang and Lu [21] used information gain (IG) along with DNN for the prediction of diabetes. The maximum accuracy achieved in this paper is 90.16%. Iyer et al. [22] used the J48 decision tree algorithm and naïve Bayes algorithm for the classification dataset and achieved an accuracy of 76.9% and 79.5%, respectively. Kahramanli and Allahverdhi [23] used an ANN and fuzzy NN to classify diabetes datasets. The maximum accuracy achieved in this paper is 86.8%.

Karatsiolis and Schizas [24] used a SVM with an RBF kernel and a SVM with a polynomial kernel to classify the diabetes dataset. First, the dataset was divided into two subsets. Then, one of the subsets, SVM with an RBF kernel, is applied, and on the other subset, SVM with a polynomial kernel is used. The maximum accuracy achieved in this paper is 82.2% and 81%, respectively. Karegowda et al. [25] used  $K$ -means clustering along with GA and CFS for the classification of the diabetes dataset. Classification accuracy of 96.68% is achieved in three phases. The  $K$ -means clustering algorithm is applied in the first phase to identify and eliminate incorrectly classified instances. In the second phase, a GA and correlation-based feature selection (CFS) are applied to extract relevant features. Finally, in the third phase, classification is done using  $K$ -nearest neighbor (KNN) algorithm. Karegowda et al. [26] used  $K$ -means

clustering combined with decision tree C4.5 to classify the diabetes dataset. In the first phase, K-means clustering is used to eliminate incorrect instances. In the second phase, the decision tree algorithm C4.5 is used to classify the data. The maximum accuracy achieved in this paper is 93.33%. Karegowda et al. [27] used a GA and back propagation network (BPN) to classify the data. The maximum accuracy achieved in this paper is 77.7%. Kayaer and Yildirim [28] used the GRNN to classify the data and achieved an accuracy of 80.21%.

Kumar Das et al. [29] used random forest and gradient boosting classifiers to classify diabetes datasets and achieved an accuracy of 90%. Initially, data preprocessing is done, and then the classifier is applied to classify the data. Senthil Kumar et al. [30] used covering-based rough set classification for the dataset classification. This is a pattern-based approach. Maximum accuracy of 79.34% is achieved using this procedure. Kumari and Chitra [31] used SVM with RBF kernel to classify the data and achieved an accuracy of 75.5%. Nirmala Devi et al. [32] used amalgam KNN to classify the data and achieved an accuracy of 97.4%. This amalgam of KNN consists of K-means with KNN. K-means algorithm is used to identify missing values. Missing values are replaced by the mean and median in this algorithm. Patil et al. [33] used K-means clustering combined with decision tree C4.5 and achieved an accuracy of 92.38% to classify the dataset. Polat [34] used fuzzy C-means combined with SVM and KNN and weighting methods (FCMAW) and achieved an accuracy of 91.41 and 84.38, respectively. Polat et al. [35] used GDA and least square support vector and achieved an accuracy of 82.05% to classify the data. Rado et al. [36] used random forest combined with recursive feature elimination, and the accuracy achieved was 73%. Raghavendra et al. [37] used a neural network model with a backward elimination feature selection method and made the accuracy of 84.52% to classify the dataset. Rajni and Amandeep [38] achieved a classification accuracy of 72.9% by using the RB-Bayes algorithm. In this, the mean is used to handle the missing values. Ramana and Boddu [39] used the naïve Bayes classification algorithm, and the accuracy achieved was 76.34%. Balajiet al. [40] used a deep NN restricted Boltzmann machine, and 80.9% accuracy was achieved.

Vaishali et al. [41] used Goldberg's GA combined with a multi-objective evolutionary fuzzy classifier to classify the type 2 diabetes dataset. In the first stage, essential features are extracted using Goldberg's GA. In the second stage, the multi-objective evolutionary fuzzy classifier is applied, and an accuracy of 83.04% is achieved using this method. Vosoulipour et al. [42] used NN and ANFIS structures and achieved an accuracy of 81.3%. Wong and Lease [43] used Cartesian genetic programming and achieved an accuracy of 80.5%. Wu et al. [44] used an improved K-means algorithm and the logistic regression algorithm for the dataset classification and achieved an accuracy of 95.42%. Zolfaghari [45] used SVM combined with NN and achieved an accuracy of 88.04%, and Bano and Khan [46] used K-NN and achieved an accuracy of 82.29% to classify the dataset.

An automated model for diagnosing diabetes was reported by Lakhvaniet al. [47] utilizing a three-layered artificial neural network (ANN). For neuron activation, the authors employed a logistic activation function, and they trained the model using the quasi-Newton approach. Through the use of the Pima Indian Diabetes Dataset, Patil and Ingle [48] offered a comparative analysis of different ML classification algorithms with diabetes prediction. For statistical modeling and accuracy verification, authors employed KNN, LR, which is based on the regression problem, naive Bayes probabilistic classifier, SVM with both linear and nonlinear kernel, and decision tree with RF classifier. 80.20 percent accuracy is the highest possible. LDA and GA were employed for feature selection by Alharan et al. [49] to increase the classification accuracy for diabetes. The approach has a maximum accuracy of 90.89 percent. Sivaranjani et al. [50] presented a model for diabetes categorization using SVM and RF techniques. PCA is also used to reduce the number of dimensions, with maximum accuracy rates of 83 and 81.4 percent, respectively.

In all the techniques used by the researchers, the main challenge is to improve the accuracy of the system for early diagnosis of diabetes. To overcome this problem, this paper suggested a fusion technique in two phases. In the first phase, data preprocessing is done using K-means, and in the second phase, diabetes classification is completed using SVM to achieve the maximum accuracy. Techniques used by different researchers and achieved accuracy are summarized in Table 1.

### 3. Proposed Methodology

This section describes the proposed Pima diabetes patient classification model using K-means clustering and SVM. Figure 1 presents an overview of the suggested model. The proposed model first created the clusters using the K-means clustering and then used the SVM for the classification.

**3.1. K-Means Clustering Algorithm.** K-Means algorithm is used to cluster the dataset into different classes. K-Means works for multi-dimensional data. For two-dimensional data, the example is shown in Figure 2.

The following steps are used in the K-means clustering algorithm [51]:

- (1) Choose the  $K$  number of clusters.
- (2) Choose at random  $k$  points. These  $k$  points will be the centroids of the  $k$  clusters. It is not necessarily that these  $k$  points are from dataset. Any  $k$  points can be selected.
- (3) Assign each data point to the nearest centroid, and the resulting  $k$  cluster will be formed. The Euclidian distance is used to calculate distance.
- (4) Determine and set each cluster's new centroid.
- (5) Change the centroid that corresponds to each data point. If there was a reassignment, proceed to step 4, otherwise, end.



TABLE 1: Comparative study of existing approaches used by the researchers and accuracy achieved.

Sr. no.	Method used	Accuracy (%)	Reference
1	Decision tree	78.17	[10]
2	Higher-order NN with PCS	89.47	[11]
3	NN	93.5	[12]
4	Classifier using the K-means algorithm with logistic regression	98	[13]
5	Fuzzy K-nearest neighbors	89.1	[14]
6	GA combined with multilayer perceptron neural network	79.13	[15]
7	Class-wise K-nearest neighbor (CkNN)	78.16	[16]
8	Multilayer feedforward neural network	95.5	[17]
9	F-score, K-means clustering along with Z-score normalization and SVM	98	[18]
10	Ant colony optimization (ACO)	84.24	[19]
11	Re-RX with J48 graft, combined with sampling selection techniques	83.83	[20]
12	Information gain (IG) along with deep NN	90.26	[21]
13	Decision tree and naïve Bayes	76.9 and 79.5 respectively	[22]
14	ANN and FNN	86.8	[23]
15	SVM with an RBF kernel and with a polynomial kernel	82.2	[24]
16	K-means clustering along with GA and CFS	96.68	[25]
17	K-means clustering combined with decision tree C4.5	93.33	[26]
18	GA and back propagation network (BPN)	77.7	[27]
19	General regression neural network (GRNN)	80.21	[28]
20	Random forest and gradient boosting classifiers	90	[29]
21	Covering-based rough set	79.34	[30]
22	SVM (with RBF kernel)	75.5	[31]
23	Amalgam KNN	97.4	[32]
24	K-means clustering combined with decision tree C4.5	92.38	[33]
25	Fuzzy C-means combined with SVM and KNN and weighting methods (FCMAW)	91.41 and 84.38, respectively	[34]
26	GDA and least square support vector	82.05	[35]
27	Random forest combined with recursive feature elimination	73	[36]
28	Neural network model with backward elimination feature selection method	84.52	[37]
29	RB-Bayes	72.9	[38]
30	Naïve Bayes	76.3	[39]
31	Deep neural network restricted Boltzmann machine	80.9	[40]
32	Goldberg's GA combined with multi-objective evolutionary fuzzy classifier	83.04	[41]
33	Neural network and ANFIS structures	81.3	[42]
34	Cartesian genetic programming	80.5	[43]
35	Improved the K-means and the logistic regression	95.42	[44]
36	SVM combined with neural network	88.04	[45]
37	KNN	82.29	[46]

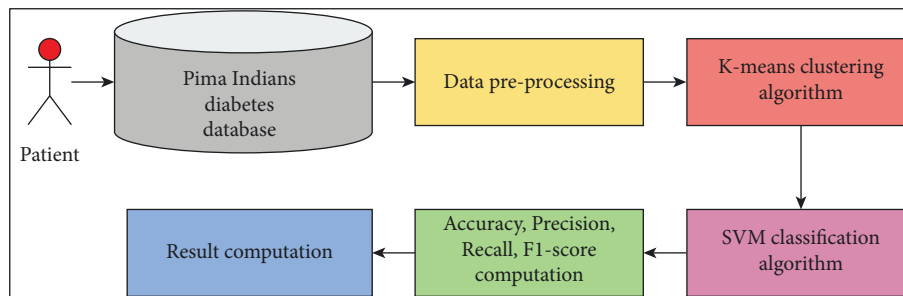


FIGURE 1: The suggested Pima diabetic patient classification model utilizing K-means clustering and SVM.

The number of clusters (in step 1) is computed using the elbow method. For the used dataset, the number of clusters is 5.

**3.2. SVM Classification Algorithm.** SVM was developed nationally in the 1960s and later found in the 1990s. SVM is very popular in machine learning because SVM is a

robust algorithm. SVM is very different from other machine learning algorithms. SVM is about finding the best decision boundary that helps to separate the dataset into different classes. SVM separates the types through the maximum margin boundary between support vectors. For the best boundary, the sum of the distances of the boundary line from support vectors should be maximum. This boundary line is known as the maximum

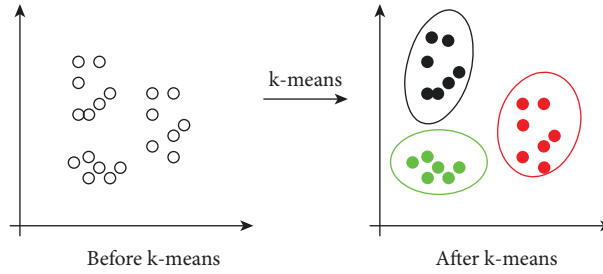


FIGURE 2: Data space before and after applying K-means clustering algorithm.

margin hyperplane or maximum margin classifier. The support vector classification (SVC) class is used to implement SVM. In SVC, there are many parameters. In this model, we used the linear kernel for linear classification [52].

#### 4. Experimental Evaluation and Results

The specifics of the dataset utilized in this investigation are presented in this section. Results are calculated using various categorization algorithms and suggested methods. The details are as follows.

**4.1. Dataset Description.** This paper used a publicly available dataset, namely, Pima Indians Diabetes Dataset [53]. This dataset contains the data of a total of 668 female patients with eight independent parameters, namely, pregnancies, glucose, blood pressure (BP), skin thickness (ST), insulin, BMI, diabetes pedigree function and age, and one dependent parameter, outcome [53]. The first five records of the dataset are presented in Table 2.

All the parameters of the used dataset are as follows:

- (i) Pregnancies: This parameter represents the number of times pregnant.
- (ii) Glucose: During an oral glucose tolerance test, plasma glucose concentration exceeded 2 hours.
- (iii) Blood Pressure: Diastolic heart rate (mm Hg).
- (iv) Skin Thickness: This parameter represents the triceps skinfold thickness (mm).
- (v) Insulin: This parameter expresses the 2-hour serum insulin ( $\mu\text{U/ml}$ ).
- (vi) BMI: This parameter describes the body mass index (weight in  $\text{kg}/\text{height in } m^2$ ).
- (vii) Diabetes Pedigree Function (DPF): DPF is a function that scores the likelihood of diabetes based on family history.
- (viii) Age: This parameter represents the age of the person (in years).
- (ix) Outcome: This parameter represents the class variable. 0 means nondiabetic, and 1 means diabetic.

**4.2. Performance Measure.** All the approaches are compared using accuracy, precision, recall, and F1-score for performance measures. Accuracy, precision, recall, and F1-score are computed using (1)–(4) [54]. The confusion matrix is plotted for calculating all the performance measure parameters. The generated confusion matrix of the proposed method is shown in Figure 3.

The used performance measurement parameters are for confusion matrix (Table 3) with two classes (binary classification).

- (i) Accuracy: The proportion of correct classification (true positive and true negative) from the overall number of cases.

$$\text{Accuracy} = \frac{TP + TN}{TP + TN + FP + FN} \quad (1)$$

- (ii) Precision: The percentage of instances that were correctly classified as positive (true positive) when they were expected to be positive.

$$\text{Precision } (P) = \frac{TP}{TP + FP} \quad (2)$$

- (iii) Recall: The percentage of correctly classifying positive instances as positive (true positive).

$$\text{Recall } (R) = \frac{TP}{TP + FN} \quad (3)$$

- (iv) F1-score: The balance between precision and recall is shown by the F1-score.

$$F1 - \text{score} = \frac{2 \times P \times R}{P + R} \quad (4)$$

**4.3. Experimental Results.** The discussion presented in Table 4 shows the result of the proposed approach to the Pima Indians Diabetes Dataset. The accuracy of 98.7% is recorded using the proposed method, whereas the accuracy of 82.46% is recorded using only the SVM classification algorithm. An improvement of 19.69% is achieved on the Pima Indians Diabetes Dataset.

The comparison of the various classification methods, namely, decision tree, random forest, kernel SVM, naive Bayes, KNN, logistic regression, SVM, and the proposed approach based with respect to accuracy, precision, recall, and F1-score, is shown in Figures 4–7.

TABLE 2: First five records in the Pima Indians Diabetes Dataset.

Sr. no.	Pregnancies	Glucose	BP	ST	Insulin	BMI	DPF	Age	Outcome
0	6	148	72	35	0	33.6	0.627	50	1
1	1	85	66	29	0	26.6	0.351	31	0
2	8	183	64	0	0	23.3	0.672	32	1
3	1	89	66	23	94	28.1	0.167	21	0
4	0	137	40	35	168	43.1	2.288	33	1

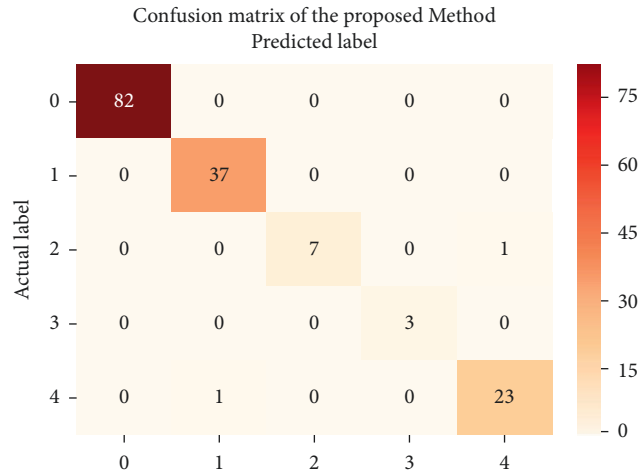


FIGURE 3: Confusion matrix of the proposed method.

TABLE 3: Confusion matrix for two classes.

Actual class	Predicted class	
	Negative	Positive
Negative	TN	FP
Positive	FN	TP

TN: true negative, TP: true positive, FP: false positive, FN: false negative.

TABLE 4: Performance evaluation of several classification methods.

Method used	Accuracy	Precision	Recall	F1-score
Decision tree	70.77	67	69	67.5
Random forest	78.57	75	72.5	73.5
Kernel SVM	79.22	76	72.5	74
Naive Bayes	79.22	75.5	74.5	74.5
KNN	79.87	76.5	75.5	75.5
Logistic regression	82.46	80	77	78
SVM	82.46	80	77	78
<b>Proposed approach</b>	<b>98.7</b>	<b>98.6</b>	<b>96.8</b>	<b>97.5</b>

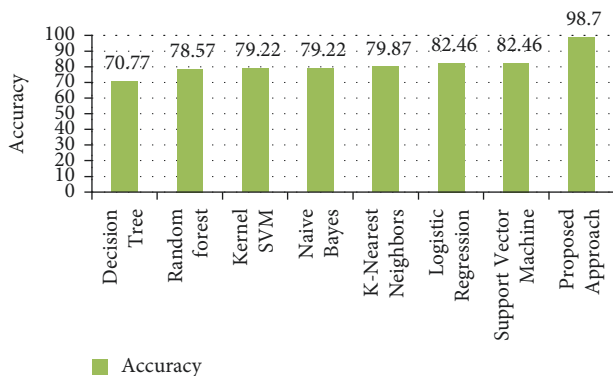


FIGURE 4: Accuracy using different classification approaches.

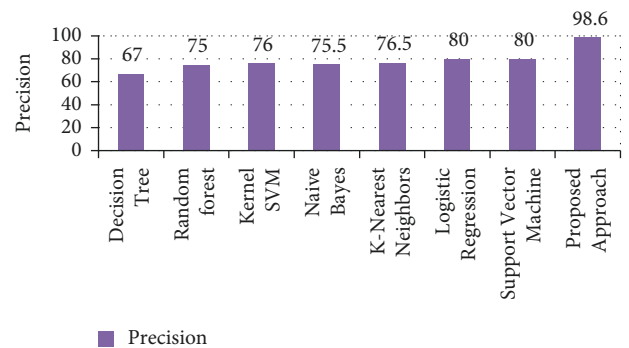


FIGURE 5: Precision using different classification approaches.

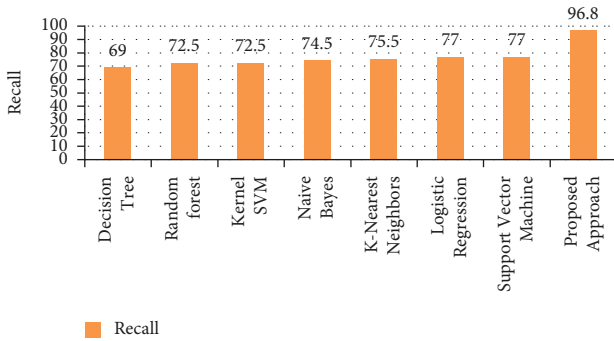


FIGURE 6: Recall using different classification approaches.

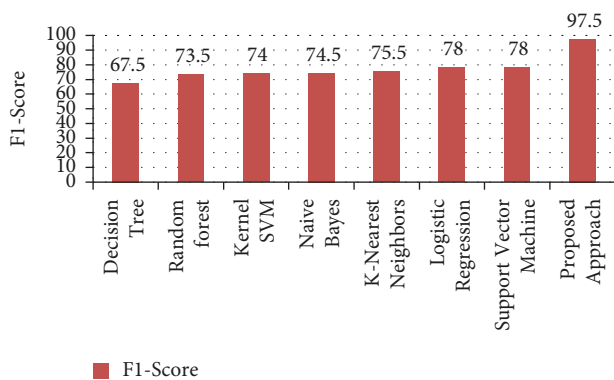


FIGURE 7: F1-score using different classification approaches.

The accuracy, precision, recall, and F1-score of the proposed method are 98.7%, 98.6%, 96.8%, and 97.5%, respectively.

## 5. Conclusion and Future Scope

This study suggested a brand-new architecture for diabetes patient categorization using K-means clustering and SVM. The clusters of the database are designed using a K-means clustering method. The predictions are then computed based on the created clusters considered as features for categorization using SVM. The Pima Indians Diabetes Database is used to verify the approach's resilience against a publicly accessible dataset. The Pima Indians Diabetes Database has 668 female patients' data. 80% of these data are used to train machine and 20% to test the machine on the proposed architecture, with a maximum accuracy of 98.7%. By obtaining more reliable characteristics from the database, the classification rates may rise in the future. Additionally, combining techniques like decision fusion of several classifiers might help the classification process.

## Data Availability

The data used to support the findings of this study are available from the corresponding author upon request.

## Conflicts of Interest

The authors declare that they have no conflicts of interest.

## References

- [1] J. Spranger, A. Kroke, M. Möhlig et al., "Adiponectin and protection against type 2 diabetes mellitus," *The Lancet*, vol. 361, no. 9353, pp. 226–228, 2003.
- [2] B. B. Lowell and G. I. Shulman, "Mitochondrial dysfunction and type 2 diabetes," *Science*, vol. 307, no. 5708, pp. 384–387, 2005.
- [3] R. S. Lindsay, T. Funahashi, R. L. Hanson et al., "Adiponectin and development of type 2 diabetes in the Pima Indian population," *The Lancet*, vol. 360, no. 9326, pp. 57–58, 2002.
- [4] M. E. Miller, R. P. Byington, D. C. Goff Jr et al., "Effects of intensive glucose lowering in type 2 diabetes," *New England Journal of Medicine*, vol. 358, no. 24, pp. 2545–2559, 2008.
- [5] G. Klöppel, M. Löhr, K. Habich, M. Oberholzer, and P. U. Heitz, "Islet pathology and the pathogenesis of type 1 and type 2 diabetes mellitus revisited," *Pathology & Immunopathology Research*, vol. 4, no. 2, pp. 110–125, 1985.
- [6] B. Zinman, C. Wanner, J. M. Lachin et al., "Empagliflozin, cardiovascular outcomes, and mortality in type 2 diabetes," *New England Journal of Medicine*, vol. 373, no. 22, pp. 2117–2128, 2015.
- [7] American Diabetes Association, "Diagnosis and classification of diabetes mellitus," *Diabetes Care*, vol. 32, no. Suppl 1, pp. S62–S67, 2009, <https://www.ncbi.nlm.nih.gov/pmc/articles/PMC2613584/>.
- [8] Health Information, "Diabetes in older people," *Health Information*, <https://www.nia.nih.gov/health/diabetes-older-people>, 2020.
- [9] An overview of diabetes types and treatments, "An overview of diabetes types and treatments," *RECALL OF METFORMIN EXTENDED RELEASE*, <https://www.medicalnewstoday.com/articles/323627.php>, 2020.
- [10] A. A. Al Jarullah, "Decision tree discovery for the diagnosis of type II diabetes," in *Proceedings of the 2011 International conference on innovations in information technology*, pp. 303–307, IEEE, 2011, April.
- [11] R. Anand, V. P. S. Kirar, and K. Burse, "K-fold cross-validation and classification accuracy of PIMA Indian diabetes data set using higher-order neural networks and PCA," *International Journal of Soft Computing and Engineering*, vol. 2, no. 6, pp. 2231–2307, 2013.
- [12] C. Banerjee, S. Paul, and M. Ghoshal, "An evolutionary algorithm based parameter estimation using pima Indians diabetes dataset," *International Journal on Recent and Innovation Trends in Computing and Communication*, vol. 5, no. 6, pp. 374–377, 2017.
- [13] M. S. Barale and D. T. Shirke, "Cascaded modeling for PIMA Indian diabetes data," *International Journal of Computer Application*, vol. 139, no. 11, pp. 1–4, 2016.
- [14] M. A. Chikh, M. Saidi, and N. Settouti, "Diagnosis of diabetes diseases using an artificial immune recognition system2 (AIRS2) with fuzzy k-nearest neighbor," *Journal of Medical Systems*, vol. 36, no. 5, pp. 2721–2729, 2012.
- [15] D. K. Choubey and S. Paul, "GA\_MLP NN: a hybrid intelligent system for diabetes disease diagnosis," *International Journal of Intelligent Systems and Applications*, vol. 8, no. 1, pp. 49–59, 2016.

- [16] Y. A. Christobel and P. Sivaprakasam, "A New Classwise k Nearest Neighbor (CKNN) method for the classification of diabetes dataset," *International Journal of Engineering and Advanced Technology*, vol. 2, no. 3, pp. 396–200, 2013.
- [17] O. Deperlioglu and K. O. S. E. Utku, "Diabetes determination using retraining neural network," in *Proceedings of the 2018 International Conference on Artificial Intelligence and Data Processing (IDAP)*, pp. 1–5, IEEE, 2018, September.
- [18] K. K. Gandhi and N. B. Prajapati, "Diabetes prediction using feature selection and classification," *International journal of advance Engineering and Research Development*, vol. 1, no. 05, 2014.
- [19] M. F. Ganji and M. S. Abadeh, "A fuzzy classification system based on Ant Colony Optimization for diabetes disease diagnosis," *Expert Systems with Applications*, vol. 38, no. 12, pp. 14650–14659, 2011.
- [20] Y. Hayashi and S. Yukita, "Rule extraction using Recursive-Rule extraction algorithm with J48graft combined with sampling selection techniques for the diagnosis of type 2 diabetes mellitus in the Pima Indian dataset," *Informatics in Medicine Unlocked*, vol. 2, pp. 92–104, 2016.
- [21] L. Huang and C. Lu, "Intelligent diagnosis of diabetes based on information Gain and deep neural network," in *Proceedings of the 2018 5th IEEE International Conference on Cloud Computing and Intelligence Systems (CCIS)*, pp. 493–496, IEEE, 2018, November.
- [22] A. Iyer, S. Jeyalatha, and R. Sumbaly, *Diagnosis of Diabetes Using Classification Mining Techniques*, <http://arXiv.org/abs/1502.03774>, 2015.
- [23] H. Kahramanli and N. Allahverdi, "Design of a hybrid system for the diabetes and heart diseases," *Expert Systems with Applications*, vol. 35, no. 1-2, pp. 82–89, 2008.
- [24] S. Karatsiolis and C. N. Schizas, "Region-based support vector machine algorithm for medical diagnosis on the pima Indian diabetes dataset," in *Proceedings of the 2012 IEEE 12th International Conference on Bioinformatics & Bioengineering (BIBE)*, pp. 139–144, IEEE, 2012, November.
- [25] A. G. Karegowda, M. A. Jayaram, and A. S. Manjunath, "Cascading k-means clustering and k-nearest neighbor classifier for categorization of diabetic patients," *International Journal of Engineering and Advanced Technology*, vol. 1, no. 3, pp. 147–151, 2012.
- [26] A. G. Karegowda, V. Punya, M. A. Jayaram, and A. S. Manjunath, "Rule-based classification for diabetic patients using cascaded k-means and decision tree C4. 5," *International Journal of Computer Application*, vol. 45, no. 12, pp. 45–50, 2012.
- [27] A. G. Karegowda, A. S. Manjunath, and M. A. Jayaram, "Application of genetic Algorithm optimized neural network connection weights for medical diagnosis of Pima Indians diabetes," *International Journal of Soft Computing*, vol. 2, no. 2, pp. 15–23, 2011.
- [28] K. Kayaer and T. Yildirim, "Medical diagnosis on Pima Indian diabetes using general regression neural networks," in *Proceedings of the international conference on artificial neural networks and neural information processing (ICANN/ICONIP)*, vol. 181, p. 184p. 184, 2003, June.
- [29] S. Kumar Das, A. Kumar Mishra, and P. Roy, "Automatic diabetes prediction using tree-based ensemble learners," *International Journal of Computational Intelligence & IoT*, vol. 2, no. 2, 2019.
- [30] S. Senthil Kumar, H. Hannah Inbarani, A. T. Azar, and K. Polat, "Covering-based rough set classification system," *Neural Computing & Applications*, vol. 28, no. 10, pp. 2879–2888, 2017.
- [31] V. A. Kumari and R. Chitra, "Classification of diabetes disease using a support vector machine," *International Journal of Engineering Research in Africa*, vol. 3, no. 2, pp. 1797–1801, 2013.
- [32] M. NirmalaDevi, S. A. alias Balamurugan, and U. V. Swathi, "An amalgam KNN to predict diabetes mellitus," in *Proceedings of the 2013 IEEE International Conference ON Emerging Trends in Computing, Communication, and Nanotechnology (ICECCN)*, pp. 691–695, IEEE, 2013, March.
- [33] B. M. Patil, R. C. Joshi, and D. Toshniwal, "Hybrid prediction model for type-2 diabetic patients," *Expert Systems with Applications*, vol. 37, no. 12, pp. 8102–8108, 2010.
- [34] K. Polat, "Intelligent recognition of diabetes disease via FCM based attribute weighting," *International Journal of Computer and Information Engineering*, vol. 10, no. 4, pp. 783–787, 2016.
- [35] K. Polat, S. Güneş, and A. Arslan, "A cascade learning system for classification of diabetes disease: generalized discriminant analysis and least square support vector machine," *Expert Systems with Applications*, vol. 34, no. 1, pp. 482–487, 2008.
- [36] O. Rado, N. Ali, H. M. Sani, A. Idris, and D. Neagu, "Performance analysis of feature selection methods for classification of healthcare datasets," in *Proceedings of the Intelligent Computing-Proceedings of the Computing Conference*, pp. 929–938, Springer, Cham, 2019, July.
- [37] S. Raghavendra, S. Kumar, and B. K. Raghavendra, "Evaluating the performance of neural network using feature selection methods on pima INDIAN diabetes dataset," *Journal of emerging technologies and innovative research*, 2018.
- [38] R. Rajni and A. Amandeep, "RB-Bayes algorithm for the prediction of diabetic in Pima Indian dataset," *International Journal of Electrical and Computer Engineering*, vol. 9, no. 6, p. 4866, 2019.
- [39] B. V. Ramana and R. S. K. Boddu, "Performance comparison of classification algorithms on medical datasets," in *Proceedings of the 2019 IEEE 9th Annual Computing and Communication Workshop and Conference (CCWC)*, pp. 0140–0145, IEEE, 2019, January.
- [40] H. Balaji, N. Iyengar, R. D. Caytiles, and R. D. Caytiles, "Optimal predictive analytics of Pima diabetics using deep learning," *International Journal of Database Theory and Application*, vol. 10, no. 9, pp. 47–62, 2017.
- [41] R. Vaishali, R. Sasikala, S. Ramasubbareddy, S. Remya, and S. Nalluri, "Genetic algorithm-based feature selection and MOE Fuzzy classification algorithm on Pima Indians Diabetes dataset," in *Proceedings of the 2017 International Conference on Computing Networking and Informatics (ICCNI)*, pp. 1–5, IEEE, 2017, October.
- [42] A. Vosoulipour, M. Teshnehlab, and H. A. Moghadam, "Classification of diabetes mellitus dataset based-on artificial neural networks and ANFIS," in *Proceedings of the 4th Kuala Lumpur International Conference on Biomedical Engineering 2008 Berlin, Heidelberg*, pp. 27–30, Springer, 2008.
- [43] W. K. Wong and B. A. Lease, "Spherical bounding classifier using CGP generated transforms," in *Proceedings of the IOP Conference Series: Materials Science and Engineering*, vol. 495, no. No. 1, p. 012016p. 012016, 2019, April.
- [44] H. Wu, S. Yang, Z. Huang, J. He, and X. Wang, "Type 2 diabetes mellitus prediction model based on data mining," *Informatics in Medicine Unlocked*, vol. 10, pp. 100–107, 2018.
- [45] R. Zolfaghari, "Diagnosis of diabetes in female population of Pima Indian heritage with an ensemble of bp neural network

- and SVM,” *Int. J. Comput. Eng. Manag.*, vol. 15, pp. 2230–7893, 2012.
- [46] S. Bano and M. N. A. Khan, “A framework to improve diabetes prediction using k-NN and SVM,” *International Journal of Computer Science and Information Security*, vol. 14, no. 11, p. 450, 2016.
- [47] K. Lakhwani, S. Bhargava, K. K. Hiran, M. M. Bundele, and D. Somwanshi, “Prediction of the onset of diabetes using artificial neural network and pima indians diabetes dataset,” in *Proceedings of the 2020 5th IEEE International Conference on Recent Advances and Innovations in Engineering (ICRAIE)*, pp. 1–6, IEEE, 2020, December.
- [48] V. Patil and D. R. Ingle, “Comparative analysis of different ML classification algorithms with diabetes prediction through Pima Indian diabetics dataset,” in *Proceedings of the 2021 International Conference on Intelligent Technologies (CONIT)*, pp. 1–9, IEEE, 2021, June.
- [49] A. F. Alharan, Z. M. Algelal, N. S. Ali, and N. Al-Garaawi, “Improving classification performance for diabetes with linear discriminant analysis and genetic algorithm,” in *Proceedings of the 2021 Palestinian International Conference on Information and Communication Technology (PICICT)*, pp. 38–44, IEEE, 2021, September.
- [50] S. Sivaranjani, S. Ananya, J. Aravinth, and R. Karthika, “Diabetes prediction using machine learning algorithms with feature selection and dimensionality reduction,” in *Proceedings of the 2021 7th International Conference on Advanced Computing and Communication Systems (ICACCS)*, vol. 1, pp. 141–146, IEEE, 2021, March.
- [51] J. A. Hartigan and M. A. Wong, “Algorithm AS 136: a k-means clustering algorithm,” *Applied Statistics*, vol. 28, no. 1, p. 100, 1979.
- [52] R. Ranjan, A. Singh, A. Rizvi, and T. Srivastava, “Classification of chest diseases using convolutional neural network,” in *Proceedings of First International Conference on Computing, Communications, and Cyber-Security (IC4S 2019). Lecture Notes in Networks and Systems*, P. Singh, W. Pawłowski, S. Tanwar, N. Kumar, J. Rodrigues, and M. Obaidat, Eds., vol. 121, Singapore, Springer, 2020.
- [53] J. W. Smith and J. E. Everhart, “Predict the onset of diabetes based on diagnostic measures,” *Pima Indians Diabetes Database*, <https://www.kaggle.com/uciml/pima-indians-diabetes-database/download>, 1988.
- [54] T. N. Do, P. Lenca, S. Lallich, and N. K. Pham, “Classifying very-high-dimensional data with random forests of oblique decision trees,” in *Advances in Knowledge Discovery and Management*, pp. 39–55, Springer, Berlin, Heidelberg, 2010.

## Research Article

# Research on Vehicle-Mounted Electromagnetic Ejection Remote Fire Extinguishing System

Xing Wang,<sup>1</sup> Yadong Li,<sup>2</sup> Zhenrui Shi,<sup>3</sup> Baoshan Cao,<sup>4</sup> Yanjie Cao,<sup>4</sup> Hui Zhao,<sup>3</sup> and Xun Gong<sup>3</sup> 

<sup>1</sup>*Xi'an University of Architecture and Technology, Xi'an, China*

<sup>2</sup>*School of Materials Science and Engineering, Dalian University of Technology, Dalian, China*

<sup>3</sup>*School of Materials Science and Engineering, Shenyang Ligong University, Shenyang, China*

<sup>4</sup>*Liaoning Shunda Machinery Manufacturing (Group) Co., Ltd., Huludao, China*

Correspondence should be addressed to Xun Gong; [gongxun83@aliyun.com](mailto:gongxun83@aliyun.com)

Received 15 June 2022; Accepted 27 July 2022; Published 23 August 2022

Academic Editor: Punit Gupta

Copyright © 2022 Xing Wang et al. This is an open access article distributed under the Creative Commons Attribution License, which permits unrestricted use, distribution, and reproduction in any medium, provided the original work is properly cited.

This article first introduces the characteristics and disadvantages of traditional remote fire extinguishing technology and proposes a remote fire extinguishing system based on electromagnetic ejection. Based on the finite element analysis method and the grid matrix method, a seven-segment electromagnetic launcher model is designed. As the initial energy source, the capacitor can accelerate a 10 kg fire extinguishing bomb to 113 m/s with a range of 2 km. The results show that the electromagnetic catapult designed in this study can meet the needs of fire extinguishing bombs. This paper also designs the overall structure of the vehicle electromagnetic catapult remote fire extinguishing system, discusses its role in the field of firefighting, and prospects the future work.

## 1. Introduction

The traditional long-range fire extinguishing techniques are shoulder-fired, air-propelled, air-dropped, artillery, and rocket-propelled. The shoulder-mounted type generally means that firefighters carry water guns and fire extinguishers and other fire extinguishing equipment into the fire scene. The water gun is connected to the fire truck through a hose. After the firefighters enter the fire site, the water in the fire truck is pumped to the fire site by a water pump, and the water gun is sprayed to extinguish the fire. The original fire extinguishing technology can only extinguish low-altitude and short-distance fires but does not perform well on long-distance and ultrahigh fires. Therefore, various fire extinguishing bombs for long distance fires have been developed at home and abroad. Fire extinguishing bombs are launched into the fire site by fire extinguishing guns, aircraft, etc., and detonate at the right time to disperse the fire extinguishing agent in the bomb to the fire site for extinguishment. Compared with fire extinguishing equipment such as cloud

ladders, fire extinguishing bombs are more mobile, and the fire extinguishing height can reach hundreds of meters, without being affected by the surrounding environment.

*1.1. The Research Status.* Hungarian engineers invented a fire extinguishing bomb with a large caliber, long-range, large capacity, and continuous firing [1]. In 2001, Russia refitted the BTR-80 vehicle into a fire extinguishing vehicle, the model is GAZ-5903, which can continuously launch 22 fire extinguishing bombs with a range of 50 ~ 300 m and can extinguish three types of explosive dangerous goods A, B, and C fire. The fire extinguishing vehicle adopts the military fire control system with a high level of automation [2]. In 2005, Italy developed an air fire cannon with strong mobility and a maximum firing range of up to 200 m, but it could not fire continuously and the fire extinguishing efficiency was low [3]. Germany has developed a fire extinguishing missile, which can carry 500 kg of foam fire extinguishing agent and spray continuously for 20 ~ 30 s. The fire extinguishing

missile can fly at high speed and low altitude and can fly directly to the accident site. After spraying, it can automatically fly back to the scheduled recovery location. After recovery, the fire extinguishing agent can be refilled and reused.

In 2006, Qingguo proposed a PJ120 type pneumatic fire extinguishing gun with a weight of 32.4 kg, a range of 180 m, a vertical height of 100 m, and a maximum range of impact point dispersion radius of  $\leq 6.5$  m. The diameter of the fire extinguishing bomb is 120 mm, the weight of the fire extinguishing bomb is 4.6 kg, the mass of extinguishing agent is 3 kg, and the maximum fire extinguishing area is  $9 \text{ m}^2$ . In 2010, the 710 Research Institute of China Shipbuilding Industry Corporation developed the “CMH-1 Remote Intelligent Forest Fire Extinguishing System,” with a maximum range of 600 m; it is a single bomb which can spread an area of not less than  $100 \text{ m}^2$  with a salvo fire extinguishing range not less than  $1000 \text{ m}^2$ ; the fire extinguishing bomb has a net weight of 17 kg and adopts Doppler-fixed height, where timing and impact fuzes and is filled with a self-developed high-efficiency liquid water glue fire extinguishing agent. It is suitable for extinguishing large-scale fires in forests and grasslands. In 2011, Nanjing University of Science and Technology proposed a 105 mm vehicle-mounted multitube fire extinguishing gun device, which uses the mortar firing method to shoot fire extinguishing shells at high speed with a chamber pressure of 20 MPa, a projectile’s initial velocity of 125 m/s, a projectile weight of 7495 g, and a range of 2 km. The width of the device is 1825 mm, and the load weight is 1820 kg [4]. In 2014, Harbin Engineering University developed a pneumatic fire extinguishing gun, which uses aerodynamic force without gunpowder to launch fire extinguishing bombs. A single gas cylinder is 50 L with  $4 \text{ rounds}/\text{min}^{-1}$ , and has an exit speed of 93.1 m/s [5]. In 2015, the 206 Institute of Aerospace Science and Industry Corporation developed the projectile type dry powder fire truck for high-rise buildings.” The firing height range is 100 ~ 300 m, the maximum elevation angle is  $70^\circ$ , and the firing distance is 1 km. There are 24 combined fire extinguishing bombs on the launching module, and each bomb is equipped with 3.6 kg of ultrafine efficient fire extinguishing agent, and one fire extinguishing bomb can cover  $60 \text{ m}^3$  of space. In 2016, North University of China carried out kinematics and dynamics simulation analysis on fire extinguishing projectile launched by an air cannon. The mass of fire extinguishing projectile is 5 kg, the diameter of projectile body is 120 mm, and the total length is 1150 mm [6].

At present, the most widely used in the field of fire fighting is the China Aerospace Science and Industry Corporation multipipe fire-fighting system for high-rise buildings developed by the Second Institute of Fire Control. Fire-fighting bombs are fired in the form of rockets into the walls of high-rise buildings or the interior, which are equipped with gunpowder at the end and detonating device at the head. The fire-extinguishing operation is carried out by blasting the fire-extinguishing bomb in the fire field. Fire extinguishing operations are carried out by blasting fire bombs. 24 fire bombs are integrated in the single vehicle, and the fire extinguishing

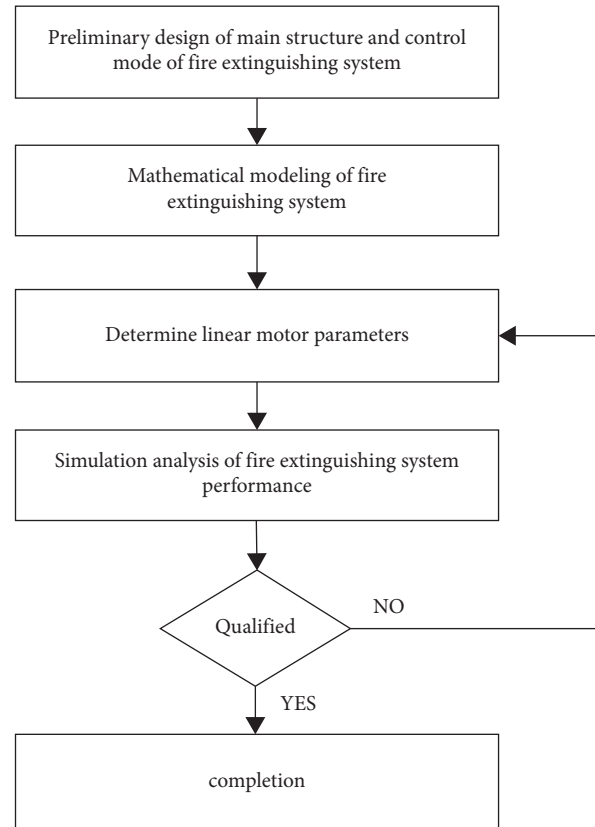


FIGURE 1: Research technology route.

height is 300 meters. The disadvantage is that the muzzle velocity of fire bombs cannot be regulated, and the safety of firing with gunpowder is not easy to guarantee.

**1.2. Problems Existing in the Fire Extinguishing System.** In recent years, the remote fire extinguishing system has made great progress, and the fire extinguishing distance, height, and coverage area have all been improved. However, the traditional remote fire extinguishing system has its natural limitations, which are manifested in the following aspects:

- (1) *High Cost of Construction and Poor Continuity.* The carrier cost of airborne long-range fire extinguishing technology based on UAV and aircraft is too high, which results in its failure to be fully popularized. In addition, limited by the size of the carrier, the quantity of fire extinguishing agents that can be carried at one time is less than that carried by land equipment, so its continuous fire extinguishing performance is poor.
- (2) *Insufficient Range.* With the increasing pace of urbanization, the number of super high-rise buildings is increasing, which is also an important scene of fire. In order to ensure the safety of firefighters, the range of remote fire extinguishing technology should be further increased. If the range is increased, the air pressure will be increased, which will increase the



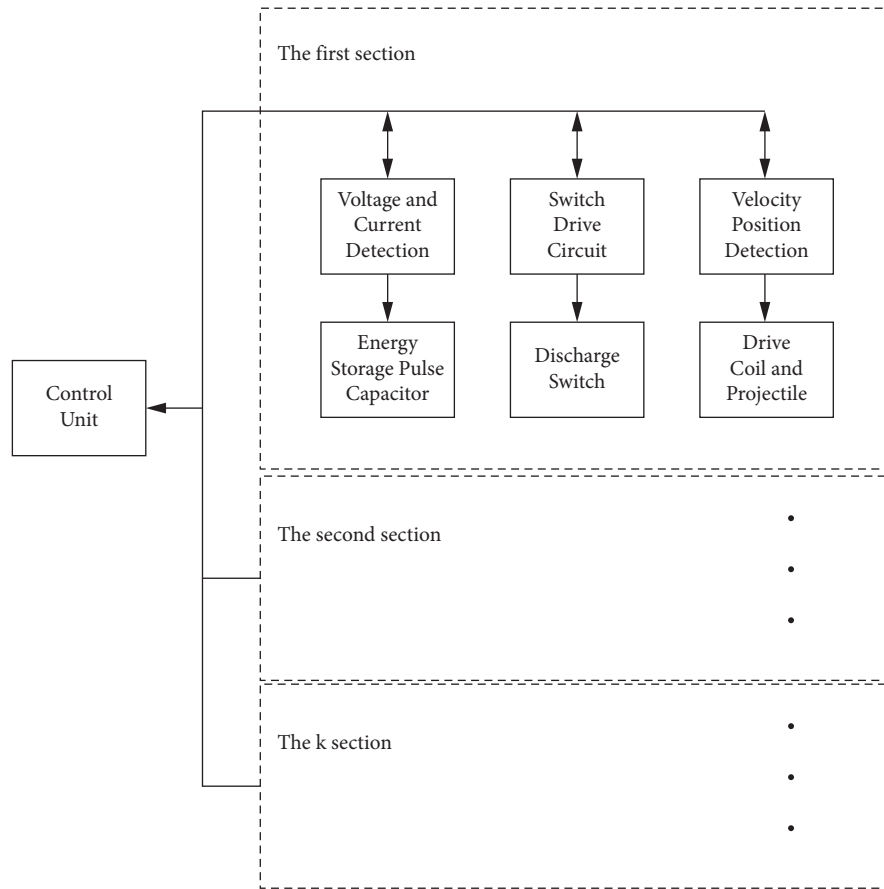


FIGURE 2: Engineering principles of the electromagnetic launch system.

weight of the launcher and reduce the flexibility and mobility of the air thrust equipment.

- (3) *Large Potential Safety Hazard of Explosive Devices.* The rocket-propelled long-range fire extinguishing system relies on gunpowder to be propelled. As the gunpowder is a kind of explosive product, it is strictly controlled. The purchase of gunpowder requires the approval of relevant departments, and there are strict requirements for storage, so the rocket-propelled fire extinguishing system cannot be commercialized. Its use is strictly restricted, cannot be close to the dangerous and explosive petrochemical products, and also cannot be close to the fire scene; otherwise, it is easy to become the source of fire. Artillery and rocket-propelled versions require increased gunpowder, but residual gunpowder can cause a secondary fire.

*1.3. Technical Route.* This research adopts the research route as shown in Figure 1 [7]. Through the design of the main structure and control module of the electromagnetic ejection system, the mathematical model is constructed to determine the parameters, and the simulation is conducted to test the simulation effect.

## 2. Electromagnetic Ejection Remote Fire Extinguishing Technology

*2.1. Electromagnetic Ejection Technology.* Aiming at the problems of remote fire extinguishing technology mentioned above, this paper proposes a remote fire extinguishing technology based on vehicle electromagnetic launch. Electromagnetic emission technology is a revolution of the launch mode after the launch of mechanical energy and chemical energy. It uses electromagnetic force (energy) to propel the object to a high speed or ultrahigh speed launch technology. By transforming the electromagnetic energy into the instantaneous kinetic energy required by the launch load, it can accelerate the load from grams to dozens of tons of high speed in a short distance and break the speed and energy limit of the traditional launch mode, which is the inevitable part of the future launch mode [8]. Electromagnetic coil propulsion occurs with the primary application of strong pulse current, forming secondary synchronous or asynchronous electromagnetic traveling wave and the projectile induced by the eddy current interaction to achieve the projectile acceleration. Electromagnetic catapult by electromagnetic propulsion has the advantages of long range, high launch frequency, strong persistence, and ability to realize cold launch, low operating cost, and easy operation and maintenance.

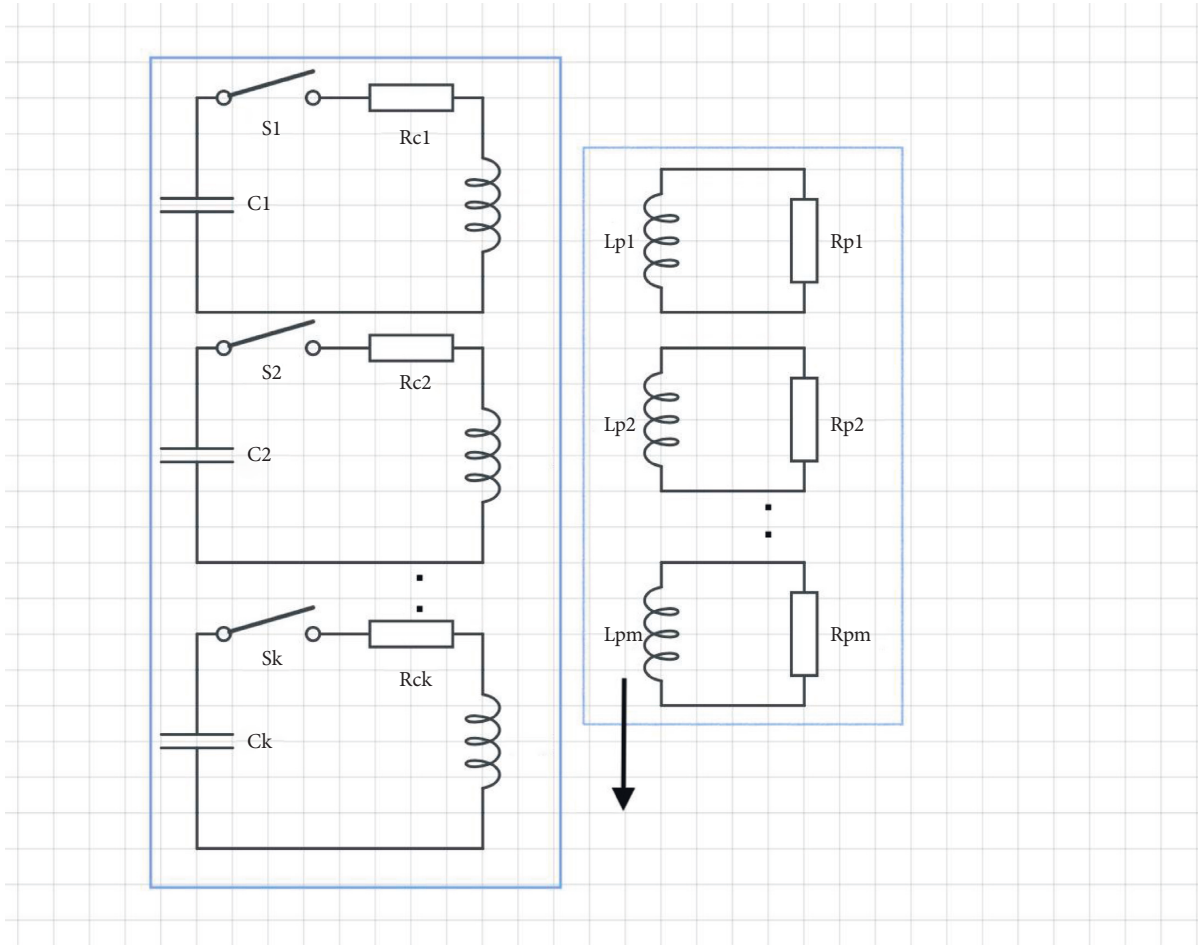


FIGURE 3: Lumped parameter model of the transmitter.

TABLE 1: Notations.

Symbol	Definition
$\mathbf{I}$	The column vector of coil current and armature wire current
$\mathbf{R}$	The diagonal matrix of coil resistance and armature current wire resistance
$\mathbf{L}$	The diagonal matrix of current wire inductance and coil inductance
$\mathbf{M}$	Mutual inductance between coils current wires and between coils and current wires
$\mathbf{C}$	The capacitance value vector of the capacitor
$\mathbf{V}_c$	The terminal voltage vector of the capacitor
$\mathbf{X}$	The speed of motion of the armature
$\mathbf{Y}$	The position of the armature
$\mathbf{M}$	The quality of the armature

The Sandia Laboratories in the United States is one of the first laboratories in the world to study electromagnetic catapult [9]. As early as 2007, Sandia Laboratories carried out research on the electromagnetic gun project, using a synchronous coaxial coil launcher, and 45 coils were synchronized to form a 3.7-meter-long gun barrel with a caliber of 120 mm, and the 18 kg M934 mortar simulation projectile was pushed to the exit speed of 424 m/s. In China, the Institute of Electrical Engineering of Chinese Academy of Sciences has also carried out related research, and developed

a 4-segment coil transmitter that can launch objects with a mass of 5 kg to 500 m/s [10]. It can be seen that electromagnetic ejection technology has been studied deeply and can be applied in the field of remote fire suppression.

Electromagnetic catapult technology has rich application scenarios. In military, it is used as an ultrahigh speed kinetic energy weapon [11] for strategic defense and tactics. In the aerospace field, it can be used for ground-to-air directional launch rockets and pure payloads, and in space, it is used to promote spacecraft to carry out orbit transfer in the field of

transportation, using the principle of electromagnetic launch electromagnetic train, using the original railway track, and its cost is only 1/4 of that of the magnetic levitation train. In industries, it can be used to make electromagnetic pumping unit so as to improve pumping efficiency and reduce cost. In addition, electromagnetic force can launch ultrahigh speed projectiles, so it can be used as a means and tool for high-pressure physics experiments and controlled nuclear fusion research.

### 2.2. Principle and Modeling of Electromagnetic Ejection.

At present, there are two main methods to study coil gun: circuit model analysis method and finite element method [12]. In this study, finite element analysis and the grid matrix method were used. Due to the skin effect, the induced current distribution on the electrical pivot section is not uniform. If the armature is divided into  $m$  concentric rings, then when the axial cross-sectional area of the ring is small enough, the induced current can be considered to be evenly distributed on the cross section; that is,  $m$  loops are used to make it equivalent to the original armature. We can assume that the excitation coils have a total of  $k$  stages.

Figure 2 shows the basic process of electromagnetic ejection. Figure 3 is the equivalent circuit model.

The excitation current is transient in the firing process of the coil gun, and the lumped parameter model of each coil can be established with the parameters of resistance, self-induction, mutual induction, inductance gradient, etc. Finally, the lumped parameter model can be summed up as the initial value problem of the nonlinear variable coefficient ordinary differential equation. The primary notations used in this paper are listed in Table 1 [15–20].

The ordinary differential equation can be established by the grid matrix method:

$$(\mathbf{R} + \mathbf{M}) \frac{d\mathbf{I}}{dt} \mathbf{V}_c - \mathbf{R}\mathbf{I} - \mathbf{v} \frac{d\mathbf{M}\mathbf{I}}{dt}. \quad (1)$$

The relation between capacitor voltage and excitation current is

$$\mathbf{C} \frac{d\mathbf{V}_c}{dt} - \mathbf{I}d. \quad (2)$$

The motion governing equation of the coil emitter system is

$$m \frac{dv}{dt} = \sum \sum_{I_p} \mathbf{I}_p \frac{pd}{dx}, \quad (3)$$

$$\frac{dx}{dt} = v. \quad (4)$$

**2.3. Simulation and Experiment of Electromagnetic Coil Propulsion.** In this study, a seven-section electromagnetic coil ejection device is designed. Each segment consists of six coils, and each coil is wound by solid copper wire. The diameter of the emitter is 120 mm, and the total length is 1 m. The structure of the ejection device is shown in Figure 4 [13].

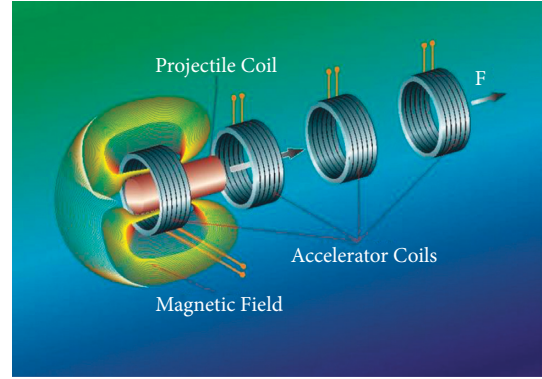


FIGURE 4: Technical principle of electromagnetic coil transmitter.

This research adopts the simulation program [14] of the process, as shown in Figure 5, the first input system parameters, and the calculation system matrix. The input system parameters include the drive coil geometry, projectile geometric parameters, material parameters of the driving coil and projectile, the drive coil on the number of segments and its connection mode, each power supply parameters, calculation of system parameters including the self-inductance, mutual inductance, resistance, and the fragmentation of the projectile self-inductance, mutual inductance and resistance. Then, according to the different connection modes of the drive coils, the parallel or series calculation models are selected to calculate the trigger delay between phases. Then, by solving the differential equations, the voltage, current, displacement, velocity, acceleration, and the temperature rise of the projectile and the driving coil are obtained. Then, judge whether to leave the coil or not [21–25]. If so, calculate the energy error of this section, average temperature rise, kinetic energy conversion efficiency, etc. If not, the time step is increased, and the variables of the differential equation are recalculated. When leaving the coil of this stage, judge whether to leave the final coil. If leaving, output results and the process will be terminated. If not, increase the number of segments of the driving coil, take the projector current, displacement, and time variables as the system parameters input of the next segment of the driving coil, and start the process again [26–30].

Figures 6 ~ 7 show the simulation and experimental results of the three-phase capacitor current. The black line represents the three-phase capacitor results, the red dotted line represents the mesh matrix, and the blue line represents the simulation results of the finite element method. The picture shows the velocity and force of the projectile as it passes through the 7-stage electromagnetic coil emitter.

It can be seen from the figure that the initial velocity of the projectile in the first to seventh stages is 13 m/s, 42 m/s, 84 m/s, 104 m/s, 112 m/s, 112 m/s, and 113 m/s, respectively. The maximum axial force of the projectile in the third stage is 47 kN. Compared with the results of finite element analysis, the mesh matrix, and the actual test, it can be found that the simulation results fit well with the experimental results.

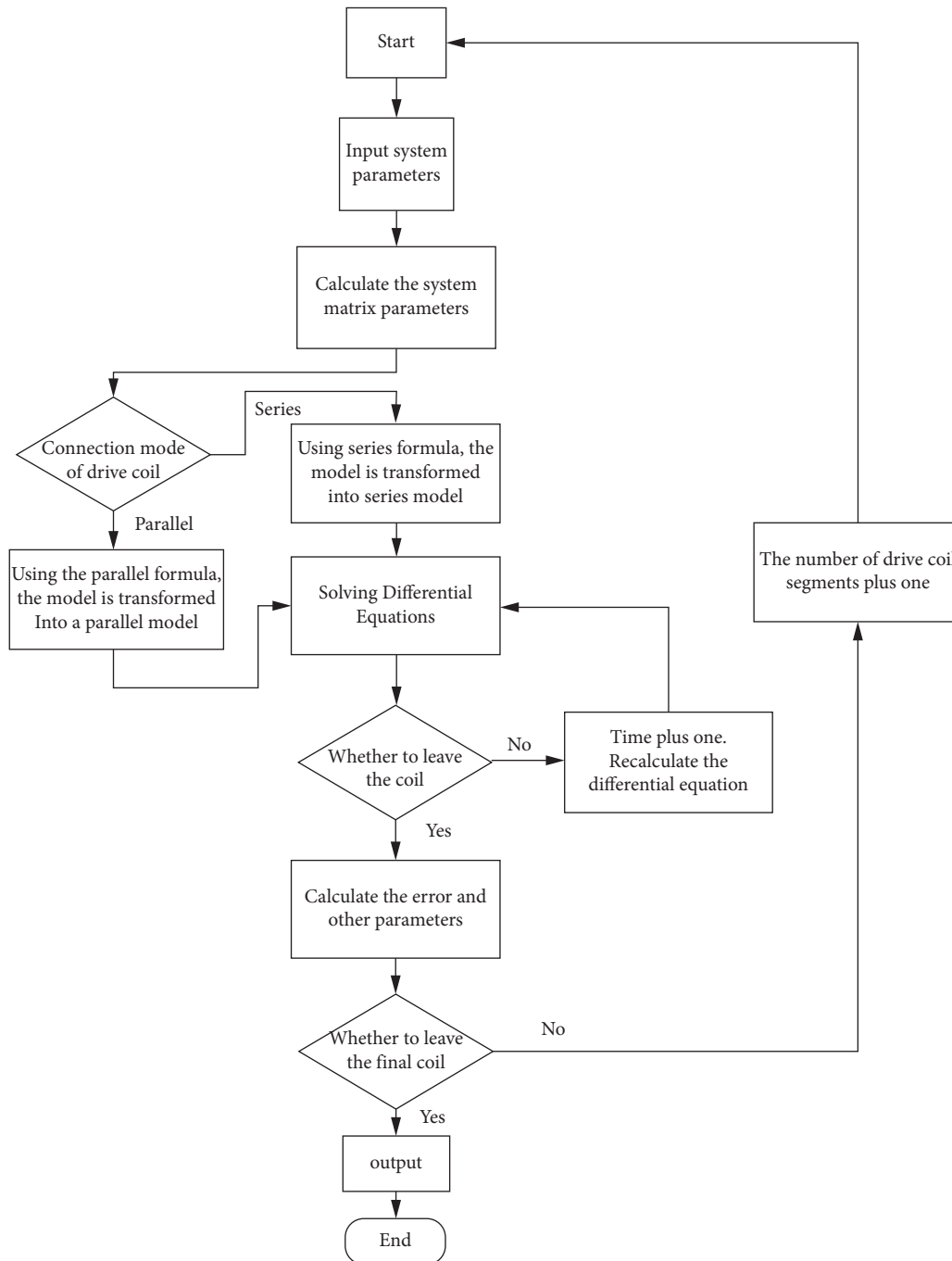


FIGURE 5: Flow chart of the simulation experiment.

### 3. Vehicle-Mounted Electromagnetic Catapult Extinguishing System

Based on the above simulation results of electromagnetic ejection and existing firefighting technology, we propose a vehicle-mounted firefighting system based on electromagnetic ejection [30, 31]. The overall structure is shown in Figure 8:

The whole system consists of five parts: vehicle body, launching power supply, electromagnetic propulsion device, projectile body loading device, and diesel generator. The

operating principle of the remote fire extinguishing system is shown in the figure below. Considering the power consumption problem in areas with insufficient power, the diesel generator is used as the secondary power supply and connected to the charging module to supply energy to the system. The charging module is connected to the energy storage capacitor, and the capacitor is charged after the charging module is charged. The laser rangefinder sends the position signal to the discharge control module, and the central controller controls the capacitor discharge to complete the emission as the driving coil function [32, 33].

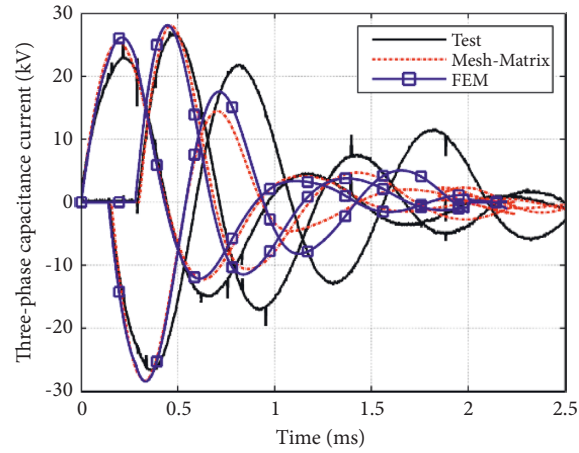


FIGURE 6: Simulation and experimental results of capacitive three-phase current.

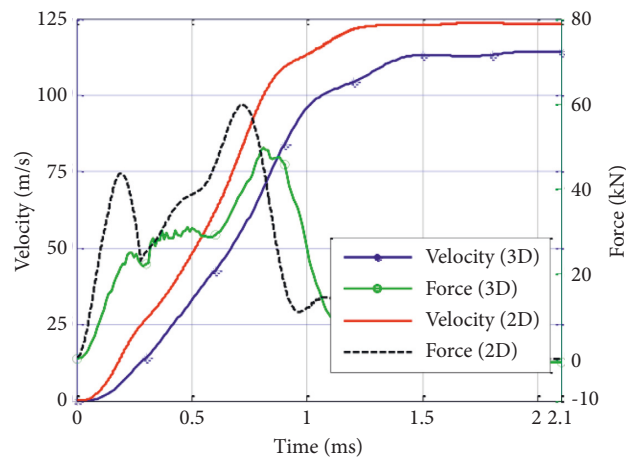


FIGURE 7: Variation of velocity and thrust of the fire extinguishing projectile.

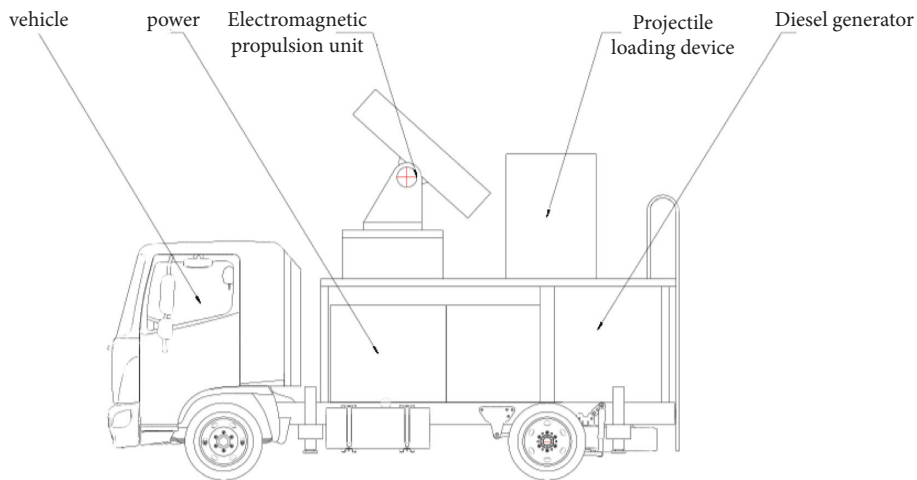


FIGURE 8: Overall structure of vehicle-mounted electromagnetic catapult remote fire extinguishing system.

The system has the following characteristics:

- (1) Vehicle-mounted electromagnetic coil launch technology, long-distance throwing efficient special fire bombs
- (2) To ensure the safety of operators, with high fire extinguishing efficiency, low operating cost, and easy operation and maintenance
- (3) No relevant products in the field of fire protection promote the development of fire protection equipment

The electromagnetic catapult on-board fire extinguishing system proposed in this study has the following advantages compared with the aforementioned on-board multipipe fire extinguishing system:

- (1) The equipment is small in size and can pass through narrow streets, which is conducive to quick rescue
- (2) Electromagnetic propulsion can launch heavier shells and has flexible distance adjustment, and the fire extinguishing effect is more obvious
- (3) It can realize joint control with the UAV system, dynamically collect fire site information, formulate flexible fire extinguishing plan, realize unmanned fire site operation, and ensure the life safety of front-line firefighters

## 4. Summary and Prospect

**4.1. Summary.** In view of the severe fire situation facing the world at present, this paper analyzes the characteristics and existing problems of the traditional remote fire extinguishing technology and puts forward the scheme of using an electromagnetic catapult to the launch fire extinguishing projectile. The seven-stage catapult is adopted, which can shoot at 2 km with the 10 kg fire extinguishing projectile, and the exit speed can reach 113 m/s to meet the demand of remote fire extinguishing. Finally, this study also designed the overall structure of the vehicle-type fire extinguishing system, which can not only be used for firefighting of dangerous chemicals, toxic, explosive, high voltage, and other fires but also be used for firefighting and rescue of high-rise buildings, effectively reducing fire and rescue casualties.

**4.2. Discussion.** At present, the research on fire cannon is not sufficient in the academic circle, but the fire bombs used are mostly fired under the action of gunpowder or high-pressure gas, which limits the weight of the fire extinguishing agent carried and the effect of fire extinguishing. On the basis of summarizing the current research achievements of electromagnetic ejection, this paper studies the vehicle electromagnetic ejection fire extinguishing system, which is a new type of firefighting equipment. The vehicle-mounted electromagnetic ejection fire extinguishing system is driven by electric power. Through the action of electromagnetic force, the fire extinguishing projectile can advance rapidly in the gun barrel and finally launch. Compared with other fire guns, the vehicle electromagnetic catapult fire extinguishing system uses

electromagnetic propulsion, and it can fire more heavy fire bomb, so the fire extinguishing effect will be more obvious.

**4.3. Summary.** Compared with other fire guns, the vehicle-mounted electromagnetic catapult fire extinguishing system has many incomparable advantages, but it is still in the preliminary research stage, and there are many problems to be solved:

- (1) Structural design and optimization of vehicle-mounted electromagnetic ejection system
- (2) Thrust fluctuation problem
- (3) Heating during launch, etc.

Further research is needed on these issues in the future.

## Data Availability

All data generated or analyzed during this study are included in this article.

## Disclosure

Xing Wang, Yadong Li, and Zhenrui Shi are cofirst authors.

## Conflicts of Interest

The authors declare no conflicts of interest.









## References

- [1] F. Levinton, "The motional Stark effect: Overview and future development (invited)," *Review of Scientific Instruments*, vol. 70, no. 1, pp. 810–814, 1999.
- [2] Y. He, "BTR-80 armored transport vehicle and GAZ-5903 firefighting train," *Weapon Knowledge*, vol. 9, p. 39, 2001.
- [3] C. Konrad, R. Braddy, and M. Martinez, "Joint actinide shock physics experimental research (jasper) facility overview Tech. rep. Bechtel Nevada Corporation (US)," in *Proceedings of the 52nd Meeting of the Aeroballistic Range Association Québec City, Québec, Canada, September 2001*.
- [4] H. Qingguo, *Analysis and research on the Fire Control System of a Multi Barrel Vehicle Mounted Fire Monitor*, Ph.D. thesis, Nanjing University of Science and Technology, Nanjing, 2011.
- [5] L. Gang, *Study on Pneumatic Launching Fire Extinguishing Gun for High Buildings*, Ph.D. thesis, Harbin Engineering University, Harbin, 2012.
- [6] Z. Haohe, *Zhongbei*, University, 2017.
- [7] Bo Qiu, *Research and Simulation of Electromagnetic Catapult forest Fire gun[D]*, Chinese Academy of Forestry, 2009.
- [8] M. Weiming and L. Junyong, "Electromagnetic emission technology," *Journal of National University of Defense Technology*, vol. 38, pp. 1–5, 2016.
- [9] R. Kaye, B. Turman, M. Aubuchon et al., "Induction coilgun for em mortar," in *Proceedings of the 2007 16th IEEE International Pulsed Power Conference*, pp. 1810–1813, IEEE, Albuquerque, NM, USA, June 2007.
- [10] B. D. Skurdal and R. L. Gaigler, "Multimission electromagnetic launcher," *IEEE Transactions on Magnetics*, vol. 45, no. 1, pp. 458–461, 2009.

- [11] Z. Su, Bo Zhang, W. Guo, X. Liu, and W. Qu, "A review of electromagnetic launch technology used in UAV[J]," *Journal of gun launch and control*, no. 01, pp. 93–96, 2011.
- [12] A. Keshtkar, L. Gharib, and M. Abbasi, "Comparison between conventional railgun and two-turn railgun by 3d-fem," in *Proceedings of the 2012 16th International Symposium on Electromagnetic Launch Technology*, pp. 1–5, IEEE, Beijing, China, May 2012.
- [13] X. Li, H. S. Wang, S. Z. Chen, and J. H. Liu, "Design and test of a five-section linear induction coil launcher," in *Proceedings of the 2015 IEEE International Conference on Applied Superconductivity and Electromagnetic Devices (ASEMD)*, pp. 422–424, IEEE, Shanghai, China, November 2015.
- [14] L. F. Shampine and M. W. Reichelt, "The MATLAB ODE suite," *SIAM Journal on Scientific Computing*, vol. 18, no. 1, pp. 1–22, 1997.
- [15] D. G. Elliott, "Mesh-matrix analysis method for electromagnetic launchers," *IEEE Transactions on Magnetics*, vol. 25, no. 1, pp. 164–169, 1989.
- [16] J. He, Z. Zabar, E. Levi, and L. Birenbaum, "Transient performance of linear induction launchers fed by generators and by capacitor banks," *IEEE Transactions on Magnetics*, vol. 27, no. 1, pp. 585–590, 1991.
- [17] Z. Zabar, X. Lu, J. He et al., "Test results for three prototype models of a linear induction launcher," *IEEE Transactions on Magnetics*, vol. 27, no. 1, pp. 558–562, 1991.
- [18] R. Haghmaram and A. Shoulaie, "Literature review of theory and technology of air-core tubular linear induction motors [electromagnetic launcher applications]," in *Proceedings of the 39th International Universities Power Engineering Conference*, pp. 517–522, IEEE, Bristol, UK, September 2004.
- [19] H. Xie, H.-Y. Yang, J. Yu et al., "Research progress on advanced rail materials for electromagnetic railgun technology," *Defence Technology*, vol. 17, no. 2, pp. 429–439, 2021.
- [20] X. Cai, S. Tan, and J. Lu, "Research on active arc-ignition technology as a possible residual-energy-release strategy in electromagnetic rail launch[J]," *Plasma Science and Technology*, vol. 23, no. 08, pp. 187–194, 2021.
- [21] M. He, X. L. Li, Q. W. Wang, Q. Wang, Z. Y. Liu, and C. J. Wang, "Influence Factors analysis of Fe-C Alloy Blocking Layer in the electromagnetic induction-controlled automated Steel Teeming technology," *Acta Metallurgica Sinica*, vol. 33, no. 5, pp. 671–678, 2020.
- [22] P. Li, J. Zhou, and J. Xiao, "Research progress of On-line Monitoring technology for electromagnetic environment of power Transmission and Transformation projects[J]," *Meteorological and Environmental Research*, vol. 10, no. 06, pp. 67–71, 2019.
- [23] G. Bai and X. Ma, "Research of Anti electromagnetic Interference technology for PMSM driving system[C]," in *Proceedings of the 2010 3rd International Conference on Computer and Electrical Engineering*, pp. 226–230, IACSIT Press, Singapore, 2012.
- [24] Z. Cao and Y. Zuo, "Electromagnetic riveting technique and its applications," *Chinese Journal of Aeronautics*, vol. 33, no. 1, pp. 5–15, 2020.
- [25] L. Wei, Z. Cao, and R. Wu, "Research and development of electromagnetic ejection system for high-rise building fire extinguishers [J]," *Fire Science and Technology*, vol. 40, no. 4, pp. 519–523, 2021.
- [26] S. Liu, Bo Qiu, and Y. Pang, "Research on electromagnetic ejection forest fire monitor [J]," *Journal of Beijing Forestry University*, vol. 32, no. 01, pp. 108–113, 2010.
- [27] Li Gao, H. Zhang, and Y. Sun, "Design and implementation of a fully automatic electromagnetic ejection system[J]," *Journal of Huangshan University*, vol. 23, no. 05, pp. 19–23, 2021.
- [28] K. Zhao, H. Xiang, and L. Sun, "Structural design and dynamic ejection performance of electromagnetic catapult [J]," *Journal of Ordnance Equipment Engineering*, vol. 40, no. 7, pp. 70–75, 2019.
- [29] X. Wang and J. Wu, "Mengqingfu Design of a continuous electromagnetic ejection system for UAV [J]," *Fire and command and control*, vol. 46, no. 4, pp. 141–146+151, 2021.
- [30] Y. Zhang, M. Xiong, and M. Dong, "Research on fire fighting system of electromagnetic ejection fire extinguisher [J]," *Intense laser and particle beam*, vol. 32, no. 2, pp. 127–132, 2020.
- [31] D. Li, W. Ma, and H. Tian, "A brief discussion on the electromagnetic compatibility (EMC) of fire brigade equipment in China[J]," *Proceedings of 2012 China Fire Protection Association Annual Conference on Science and Technology*, pp. 75–80, 2012.
- [32] H. Yang, P. Yang, and R. Liu, "Double coil coupled multistage electromagnetic acceleration ejection system [J]," *New technology of electrical energy*, vol. 39, no. 2, pp. 40–45, 2020.
- [33] Z. He, C. Deng, and Y. Yan, "Absolute angle detection of fire monitor based on Hall rotation sensor [J]," *Fire Science and Technology*, vol. 40, no. 8, pp. 1213–1216, 2021.

## Research Article

# Nonisolated DC to DC Converters for High-Voltage Gain Applications Using the MPPT Approach

**C. Subba Rami Reddy** <sup>1</sup>, **Bharath Kumar Narukullapati** <sup>2</sup>, **M. Uma Maheswara Rao** <sup>2</sup>,  
**Sangu Ravindra** <sup>3</sup>, **P. M. Venkatesh** <sup>2</sup>, **T. Ch. Anil Kumar** <sup>4</sup>, **B. Mouli Chandra** <sup>5</sup>,  
**and Afework Aemro Berhanu** <sup>6</sup>

<sup>1</sup>Department of Electrical and Electronics Engineering, B. V. Raju Institute of Technology, Vishnupur 502313, India

<sup>2</sup>Department of Electrical and Electronics Engineering, Vignan's Foundation for Science Technology and Research, Guntur 522213, India

<sup>3</sup>Department of Electrical and Electronics Engineering, VVIT, Nambur, Guntur, Andhra Pradesh, India

<sup>4</sup>Department of Mechanical Engineering, Vignan's Foundation for Science Technology and Research, Guntur 522213, India

<sup>5</sup>Department of Electrical and Electronics Engineering, QIS College of Engineering & Technology, Ongole 523272, India

<sup>6</sup>Department of Environmental Engineering, College of Biological and Chemical Engineering, Addis Ababa Science and Technology University, Addis Ababa, Ethiopia

Correspondence should be addressed to Afework Aemro Berhanu; [afework.aemro@aastu.edu.et](mailto:afework.aemro@aastu.edu.et)

Received 25 May 2022; Revised 25 June 2022; Accepted 18 July 2022; Published 22 August 2022

Academic Editor: Punit Gupta

Copyright © 2022 C. Subba Rami Reddy et al. This is an open access article distributed under the Creative Commons Attribution License, which permits unrestricted use, distribution, and reproduction in any medium, provided the original work is properly cited.

It is proved and examined in this research paper that the perturb and observe (P and O) technique for isolating the photovoltaic array (PVA) from the power structure may be used to isolate the PV array from the power structure. A single specified voltage setup can remove the maximum power from a PV cell because of the nonlinear properties of the PV cell's output. As a result, in PVA, the maximum power point tracking (MPPT) algorithm is utilized to increase the yield control range by increasing the maximum power point. In this study, the MPPT computations are carried out with the assistance of a DC-DC boost converter for usage in applications needing high voltage gain at a variety of sun-positioned irradiances and cell temperatures, as demonstrated in the literature.

## 1. Introduction

The incorporation of renewable energy sources such as solar photovoltaics and fuel cells has increased the popularity of DC microgrids [1]. Beyond their original use in renewable energy conversion, high-gain dc-dc converters have found widespread adoption in a variety of other fields, including battery backup systems for uninterrupted power supplies, and high-intensity discharge lamp ballasts for automobile headlamps, electric tractions, and even some medical equipment [2–4]. Since high-frequency transformers may be configured to support any required turns ratio, isolated DC-DC converters and coupled inductor type converters using these devices can deliver significant voltage gain [5]. Electricity generated from renewable sources can be used to

power outlying locations when combined with the grid. Increased availability of grid-connected PV systems can be attributed to the development of DC-DC converter topologies and inverter control methods. Power feed efficiency is highly dependent on the DC-DC converter stage being properly selected and operating at peak efficiency [6]. When connecting the dc microgrid, high-efficiency high-gain DC-DC converters are required because of the low output voltage of these dc power generators. When it comes to photovoltaics, it is best known as a process for generating electric power by converting solar-generated energy into electrical energy through the photovoltaic effect [7]. PV cells generate direct current as the electrical source from light, which can be used to power DC equipment or to recharge a battery, depending on their orientation [8]. Initially,



photovoltaics were used to control satellites and other rockets in the vicinity; however, today, the vast majority of photovoltaic modules [9, 10] are used for cross-sectional related applications with the assistance of power electronic converters and to generate enormous amounts of energy, which was the original rationale for their use. The typical yield of a PV module is determined by the daylight-based irradiance and the air temperature, and the yield voltage of a PV module is determined by the relationship between PV modules. It is critical to demonstrate and reauthorize for maximum power point tracking (MPPT) [11] of PV array applications because PV modules have nonlinear characteristics, and the yield is dependent on solar radiation [12]. Various MPPT procedures have been used in the past, but the bother and watch (P&O) calculation is the most widely recognized and ideal for use by industry because of its straightforwardness and ease of execution [13]. As a result, this calculation continues to be the most widely used [14].

In order to make use of the P&O calculation, the controller changes voltage if the deliberate power is more prominent or less prominent than the previous estimation of intensity [15]. The controller makes alterations in a similar manner until there is no greater increment or decrement in power [16]. Figure 1 depicts the block diagram of a PVA structure that makes use of a boost converter [17].

## 2. PV Panel

An electronic device that converts solar power into electrical power is known as a photovoltaic cell. The power rating of a solar-powered [18] board is determined by the size of the PV board and the arrangement of modules within the board; as a result, the voltage rating and current evaluations change, while the power rating remains constant. Because a single PV panel may not be able to generate the necessary amount of power, we connect multiple panels in series or parallel to meet our needs. Series association of PV board increment voltage rating in a series arrangement and parallel association of PV board increment current rating in a parallel arrangement is done [19]. The electrical equivalent of the PV panel is shown in Figure 2.

The I-V characteristics of the PV module are depicted in Figure 3 at a cell temperature of 25°C. A PV cell's output current can be determined by applying KCL and given in the following equation:

$$I_{pv} = I_{sc} - I_D - I_{sh}, \quad (1)$$

where  $I_{pv}$  = PV module current,  $I_{sc}$  = photo current (or) solar cell current,  $I_D$  = diode current, and  $I_{sh}$  = shunt current.

The current-voltage attributes condition of a PV module is depicted as given in the following equation:

$$I_{pv} = N_p I_{ph} - I_{rs} \left( e^{\left( \frac{q(V_{pv} + (R_s I_{pv}))}{(N_s AKT)} \right)} - 1 \right) - \frac{V_{pv} + I_{pv} R_{rs}}{R_{sh}}, \quad (2)$$

where  $q$  = electron charge ( $1.602 * 10^{-19}$ C),  $N_s$  = number of sun-based cells related in plan in series,  $N_p$  = number of

daylight-based cells related in parallel,  $I_{rs}$  = reverse saturation current,  $T$  = total temperature,  $K$  = Boltzmann constant ( $1.38 * 10^{-23}$  J/K).

Also,

$$I_{ph} = I_{sc} + \frac{K_i (T - 298)G}{100},$$

$$I_0 = I_{rs} \left[ \frac{T}{T_r} \right]^3 \left( e^{\left( \frac{qV_{oc}}{(N_s AKT)} \right)} \left[ \left( \frac{1}{T_r} \right) - \left( \frac{1}{T} \right) \right] \right), \quad (3)$$

where  $I_{sc}$  = short out current of PV module at standard test states of 25°C and 1000 W/m<sup>2</sup>,  $K_i$  = temperature coefficient of short out current,  $G$  = the sun-based lights. The turnaround immersion current of the PV module is given in the following equation:

$$I_{rs} = \frac{I_{sc}}{\left( e^{\left( \frac{qV_{oc}}{(nN_s KT)} \right)} - 1 \right)}, \quad (4)$$

where  $n$  = the dreamer factor of the diode = 1.3  $V_{oc}$  = open circuit voltage. The current through the shunt resistor of the above PV module is given in the following equation:

$$I_{sh} = \frac{V_{pv} + I_{pv} R_{rs}}{R_{sh}}. \quad (5)$$

The most common photovoltaic system applications are on rooftops and in buildings, and they include concentrator photovoltaic systems, photovoltaic thermal hybrid solar collectors, rural electrification systems, standalone systems, spacecraft applications, specialty power systems, and specialty lighting systems [20].

## 3. DC-DC Boost Converter

The boost converter is a converter that has an output voltage that is higher than the source voltage. Boost converters are used in data conversion [21]. It is additionally referred to as a step-up converter. Whenever the feedback regulation is functioning properly, the control loop keeps the output voltage where it needs to be, and the converter operates at a duty cycle below the critical level [22]. However, when the feedback loop is saturated by excessive load current, inadequate input power [23], or an increase in the resistance of the converter switches, the output voltage drops below the desired value [24]. When the controller's duty cycle goes above a certain threshold, the conversion gain goes negative [25]. The gain polarity inversion and excessive inductor current can be prevented by fixing the duty-cycle limit [26].

A regular DC-DC converter circuit is depicted in Figure 4.

It is a switching converter that operates by intermittently opening and closing a power electronic switch, as described above. DC voltage source, inductor  $L$ , controlled semiconductor switch ( $S$ ), diode ( $D$ ), capacitor ( $C$ ), and load containment ( $R$ ) are the components of the boost converter. MOSFETs, IGBTs, and BJTs are the semiconductor switches

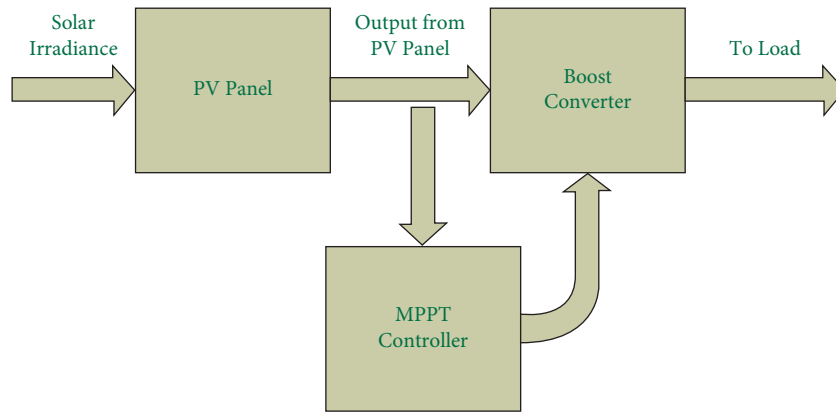


FIGURE 1: Block diagram of the boost converter with the MPPT controller.

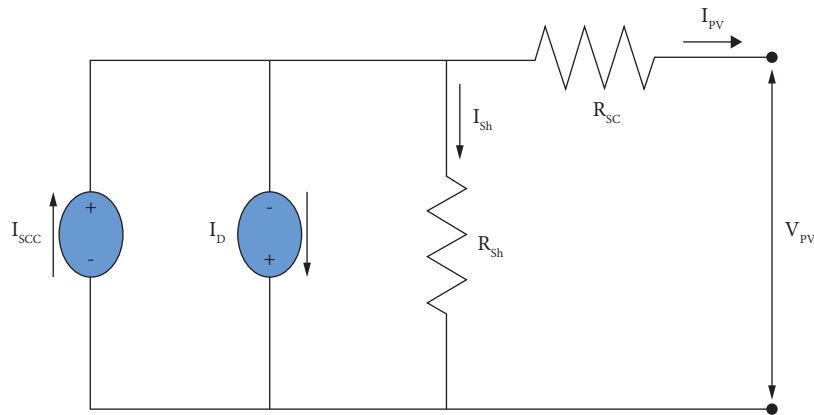


FIGURE 2: The electrical equivalent of the PV panel.

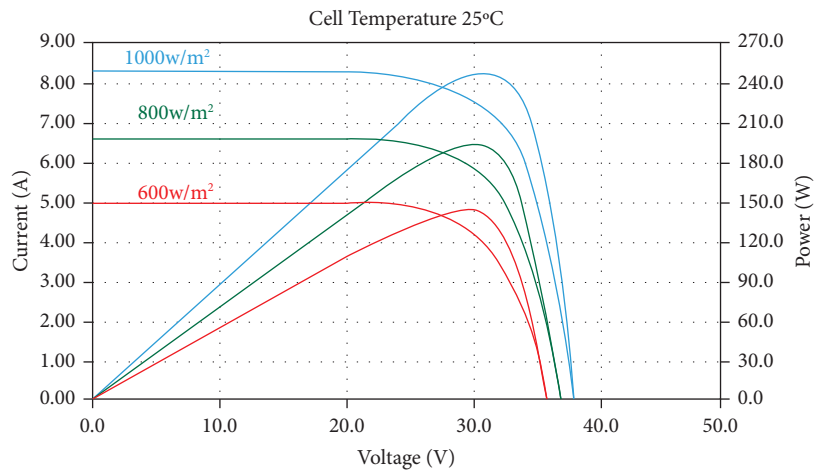


FIGURE 3: I-V and P-V characteristics of the PV module.

that are used in this converter. MOSFET is utilized due to the fact that it is a voltage-controlled device, and its switching frequency is higher. It also requires little current, which has a high switching rate and operates in the mill amperes per second range. There are two modes of operation available in this converter.

### 3.1. Methods of Activity

3.1.1. Mode-1. When switch  $S$  is turned off, diode  $D$  is turned unevenly, to be precise. The inductor is connected in series with the source and charges up, causing the inductor current to expand. Because of the inductor's high voltage, it

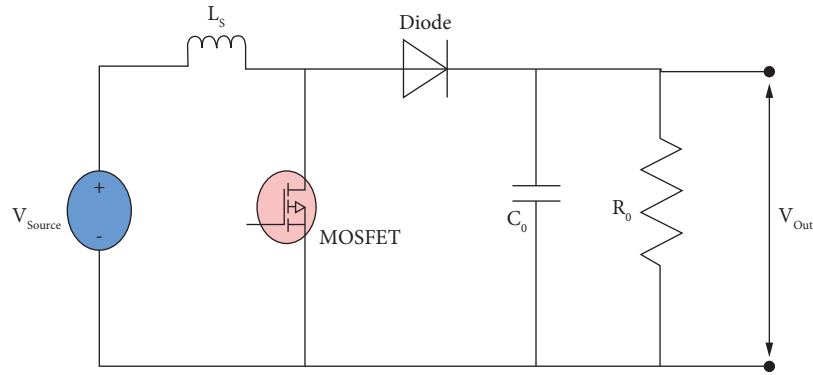


FIGURE 4: Conventional DC-DC boost converter.

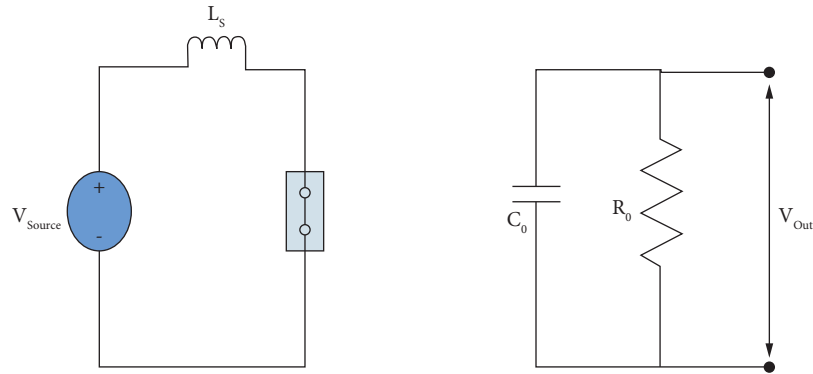


FIGURE 5: Conventional DC-DC boost converter in ON-state (switch shunt).

is comparable to the data voltage. The on-state circuit diagram of the converter is shown in Figure 5.

$$V_{\text{source}} = L \frac{di_L}{dt}, \quad (6)$$

$$\Delta i_{L_{\text{opened}}} = \frac{DTV_{\text{source}}}{L}.$$

**3.1.2. Mode-2.** As soon as switch  $S$  is activated, diode  $D$  is in the forward uneven state. The current flows towards the stack, causing the regard to escape the inductor's and information's centrality in the circuit. The circuit diagram of a typical DC-DC support converter is shown in Figure 6 when the turn is opened in the OFF state.

$$V_L = V_{\text{source}} - V_{\text{out}},$$

$$\Delta i_{L_{\text{closed}}} = (V_{\text{source}} - V_{\text{out}}) \frac{(1-D)T}{L}, \quad (7)$$

$$V_{\text{source}} - V_{\text{out}} = L \frac{di_L}{dt}.$$

In steady-state operation,

$$\Delta i_{L_{\text{opened}}} + \Delta i_{L_{\text{closed}}} = 0. \quad (8)$$

The yield voltage condition of the lift converter is

$$V_{\text{source}}T_{\text{ON}} + (V_{\text{source}} - V_{\text{out}})T_{\text{OFF}} = 0,$$

$$V_{\text{source}}T_{\text{ON}} + V_{\text{source}}T_{\text{OFF}} = V_{\text{out}}T_{\text{OFF}},$$

$$V_{\text{source}}(T_{\text{ON}} + T_{\text{OFF}}) = V_{\text{out}}T_{\text{OFF}}, \quad (9)$$

$$\frac{V_{\text{out}}}{V_{\text{source}}} = \frac{T_{\text{ON}} + T_{\text{OFF}}}{T_{\text{OFF}}}$$

$$= \frac{T_S}{T_{\text{OFF}}} = \frac{1}{(1-D)}.$$

The output current equation of the boost converter can be deduced from the equation shown in Figure 7. During the off-time, it provides the output circuit. During on-time, the inductor-free wheels on the source side result in no current being delivered to the load during on-time.

$$V_{\text{source}}T_{\text{OFF}} = V_{\text{out}}T_s,$$

$$\frac{T_S}{T_{\text{OFF}}} = \frac{1}{(1-D)},$$

$$V_{\text{out}} = V_{\text{source}}(1-D), \quad (10)$$

$$V_{\text{source}}T_s = V_{\text{out}}T_0,$$

$$V_{\text{source}}I_L = \frac{[(V_{\text{source}}/(1-D))]^2}{R}.$$

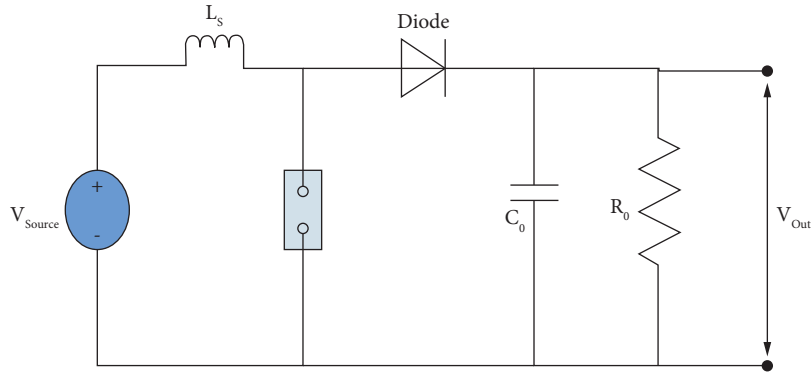


FIGURE 6: Conventional DC-DC boost converter in OFF-state (switch opened).

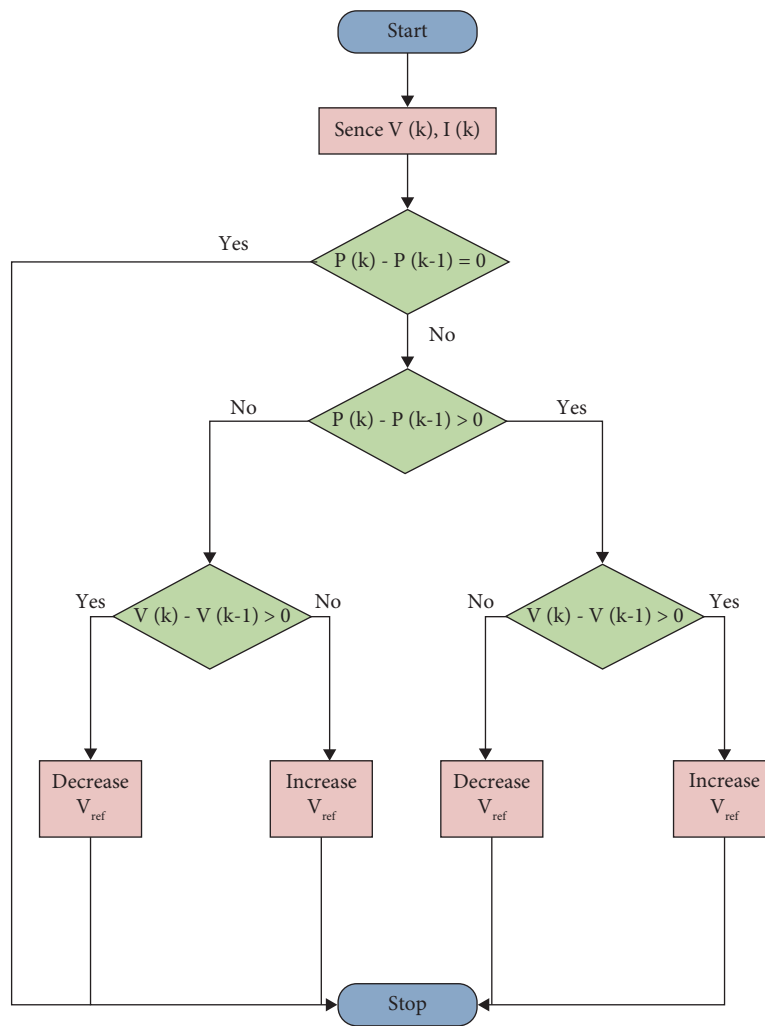


FIGURE 7: Flow chart of perturbation and observation.

From the above condition, we can discover normal inductor current as given in the following equation:

$$I_L = \frac{V_{source}}{R(1-D)^2}. \quad (11)$$

The most extreme inductor current can be composed as given in the following equation:

$$I_{Lmax} = I_L - \frac{\Delta I_L}{2} = \frac{V_{source}}{R(1-D)^2} - \frac{V_{source}}{DT2L}. \quad (12)$$

The base estimation of the inductance and the base estimation of the capacitor for the predictable current mode can be formed using the equations given in the previous section equation.

$$I_{L\min} \geq 0, \quad (13)$$

$$L_{\min} = \frac{D(1-D)^2 R}{2}.$$

The swell factor and the base estimation of capacitor for nonstop current mode can be formed as shown in the following equation:

$$\Delta Q = \frac{V_{\text{out}} DT}{R} = C \Delta V_{\text{out}}, \quad (14)$$

$$\Delta V_{\text{out}} = \frac{V_{\text{out}} DT}{RC} = \frac{V_{\text{out}} D}{RCf}, \quad (15)$$

$$r = \frac{\Delta V_{\text{out}}}{V_{\text{out}}}, \quad (16)$$

$$C_{\min} = \frac{V_{\text{out}} D}{\Delta V_{\text{out}} Rf}. \quad (17)$$

#### 4. MPPT Controller

Estimates of MPPT (maximum power point tracking) are integrated into a charge controller and used for evacuating the majority of extraordinary open power structure PV modules under explicit conditions. This maximum power point tracking technique adjusts the boost converter duty cycle step size based on the input conditions of the system. This procedure begins by calculating the differential value of the instantaneous radiation, photovoltaic voltage and current, and load power. This technique maximises the duty cycle during constant radiation conditions, allowing the MPPT algorithm to track more quickly [27]. There is a transitory period of oscillations with the irradiance change. Because of these extraneous variations in weather, it is necessary that everything gradually converges on the MPP. The voltage at which a PV module can produce the maximum amount of power is referred to as the maximum power point. MPPT (maximum power point tracking) is a technique used in PV board charge controllers to track the maximum power point, known as a maximum power point technique (MPPT), and an electronic DC-DC converter is a device that improves the match between a solar-powered showcase (PV sheets) and a battery bank or a power-generation structure. No, the MPPT is not a mechanical after structure that physically moves the modules in order to make their point even more authentic at the sun [28]. MPPT is a completely electronic/modernized system that is responsible for the electrical operation of the module. The majority of today's MPPT charge controllers are approximately 93–95 percent effective in the transformation; however, the very best MPPT charge controllers can be up to 97–99 percent effective. Duty-cycle control works by

comparing the power output of a PV module (determined by multiplying its voltage by its current) to its output from a prior cycle. The duty is controlled so that the maximum power point is maintained, and this is determined by comparing the current sample value of the voltage to the prior value in the same manner as before. To determine the optimal power point tracking methodology, the duty cycle is compared to the power and voltage [29].

P&O calculation, gradual conductance, and other calculations are performed by the MPPT controller [30]. The first of these calculations is performed by the P&O calculation.

In order to make use of the correlation between PV module voltage and power output, the P&O technique is employed. By adjusting the voltage in the direction of increasing the power, the maximum power point can be tracked by observing the resulting change in power. In order to determine the link between the power output and the voltage input of a solar cell, the incremental conductance method makes use of the slope of the power-voltage (P-V) curve. Maximum power is reached at a voltage of zero, with the voltage increasing when the slope is positive and decreasing when the slope is negative [31].

Within the scope of this work, we presented how the P&O method can be utilised. Because of its simplicity and ease of implementation, the perturb and observe (P&O) approach is extensively employed as an MPPT algorithm for PV system applications [32]. The method introduces disturbances to the duty cycle by either increasing or reducing it by a constant duty step size and then monitors the effects on the PV system's output power [33]. If the change in output power is more than zero, the operating point has shifted closer to the maximum power point (MPP) [34], and the duty cycle will continue to be perturbed in the same direction [35]. The cycle will continue until the maximum physiological state (MPS) is reached and maintained [36]. Unfortunately, the steady-state operating point of this algorithm oscillates about the MPP. This causes a minor drop in PV efficiency. Reducing the duty cycle dampens the steady-state oscillation but slows down the dynamic response. Therefore, the duty cycle must be properly adjusted to achieve a balance between the two [37]. The P&O calculation graph is illustrated in Figure 7.

##### 4.1. Drawbacks

- (1) If the voltage is far away from the MPP, the P&O technique is only moderately effective in locating the MPP [29]
- (2) Small (and fixed) gradual changes are used in the P&O strategy to produce a large transient following time “ $t$ ” is defined as the amount of time it takes an MPPT calculation to reach within 95 percent of the most extreme normal power available at MPP

#### 5. Simulation Results

The simulation diagram of a PV board is shown in Figures 8 and 9. The I-V traits and P-V attributes of the PV board are plotted and shown in Figures 10 and 11, respectively.

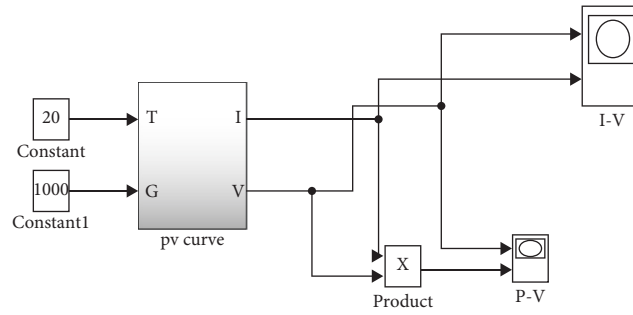


FIGURE 8: Simulation diagram of the PV board.

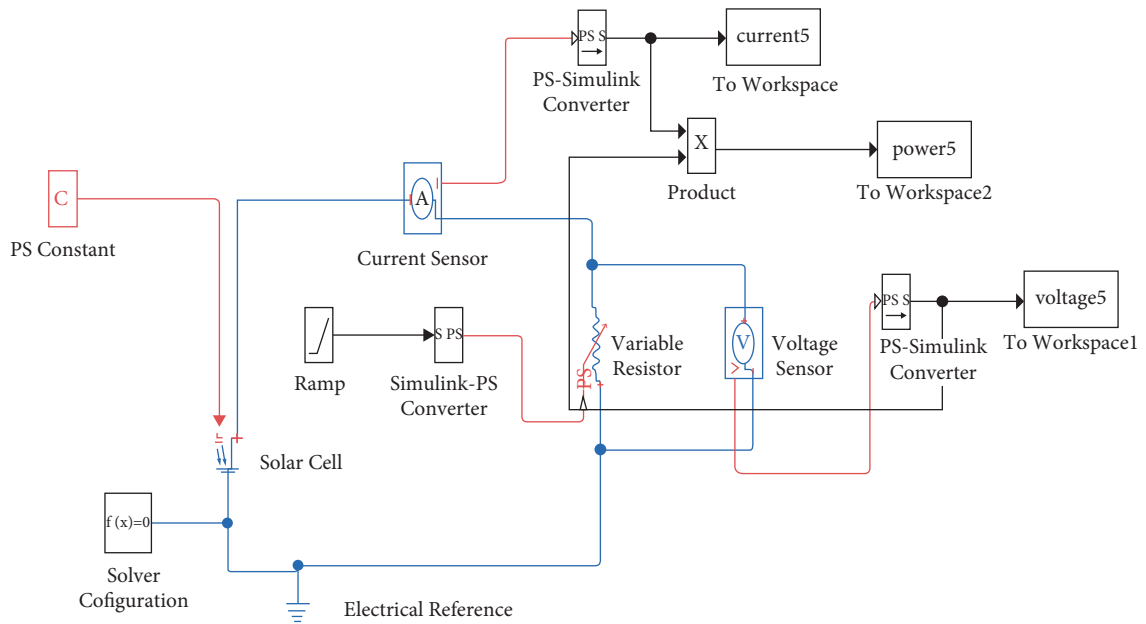


FIGURE 9: Schematic representation of a simulation used to determine solar cell characteristics.

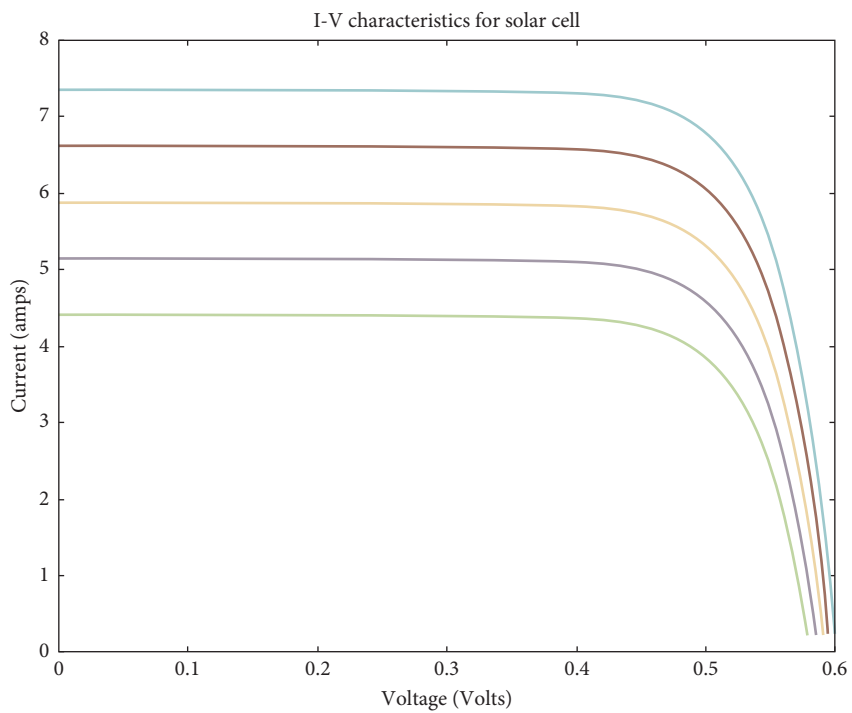


FIGURE 10: I-V traits of the PV board.

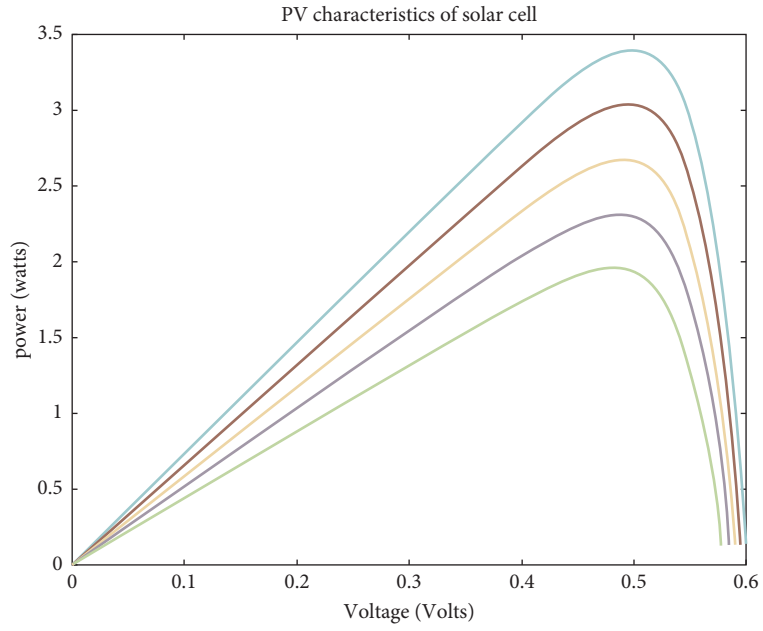


FIGURE 11: P-V attributes of the PV board.

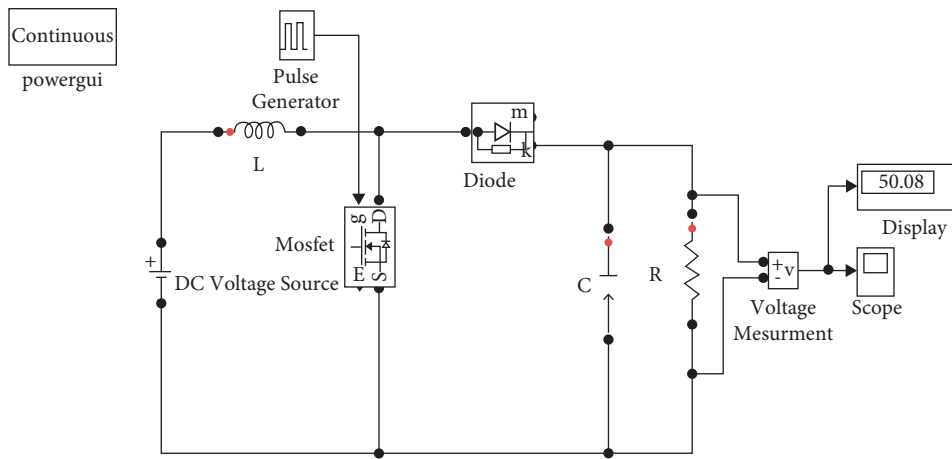


FIGURE 12: Simulation diagram of the typical boost converter.

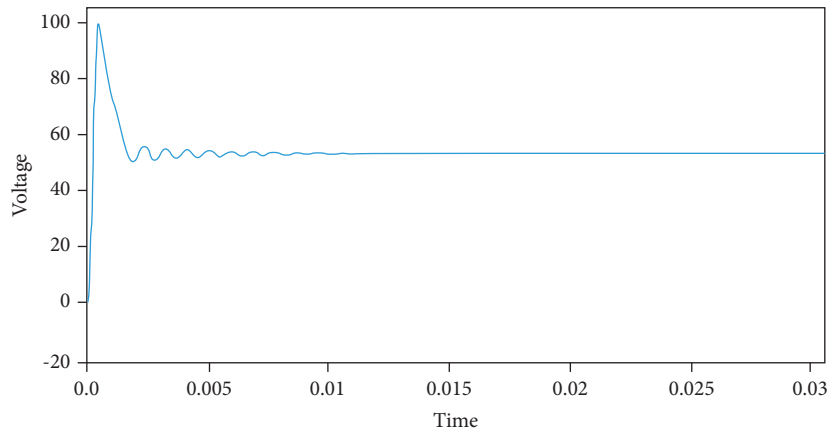


FIGURE 13: After-effect of the boost converter.

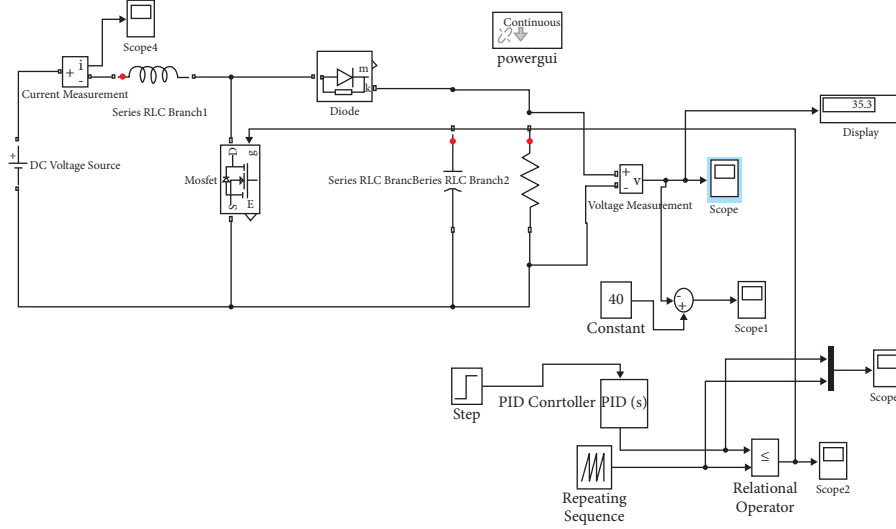


FIGURE 14: Simulation diagram of the boost converter.

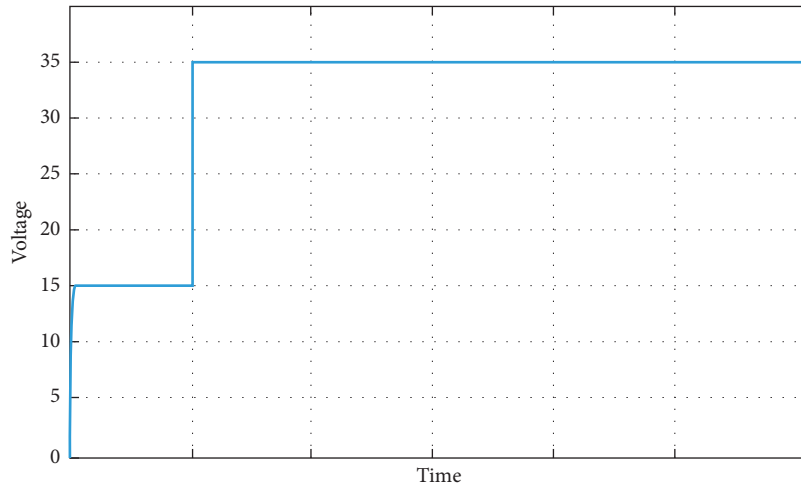


FIGURE 15: Converter voltage waveform.

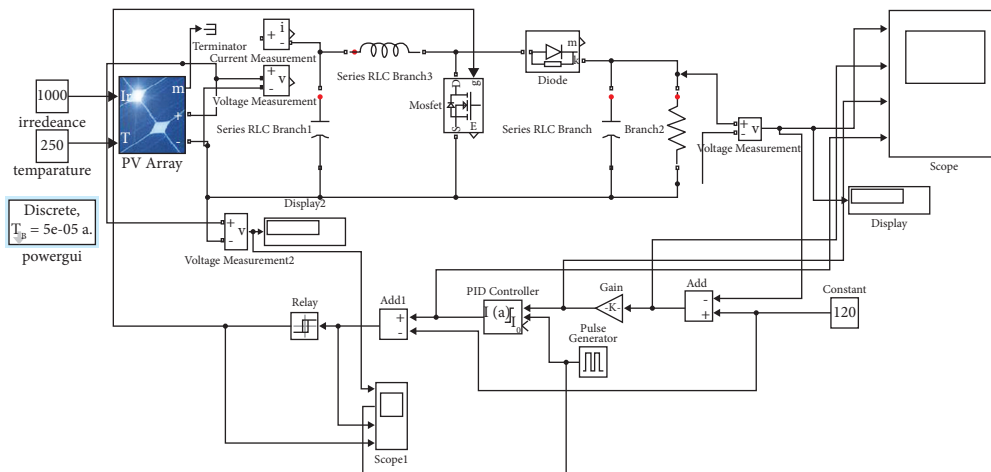


FIGURE 16: Simulation diagram of PV with the boost converter.



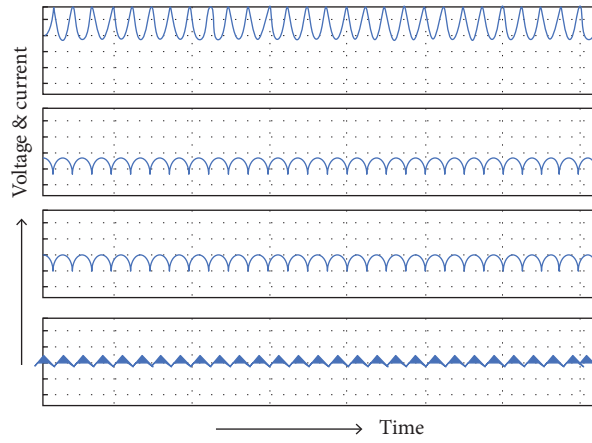


FIGURE 17: Output voltage and current waveforms of PV with the boost converter.

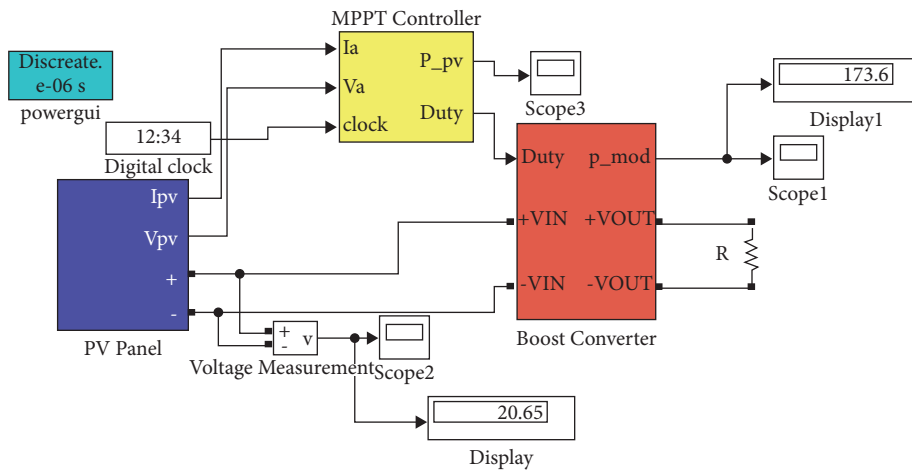


FIGURE 18: Simulation diagram of solar MPPT with the boost converter.

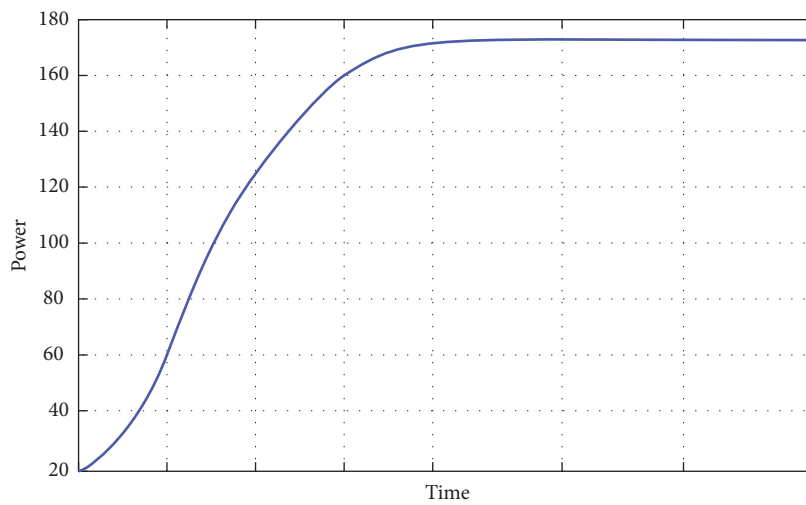


FIGURE 19: Power curve of solar MPPT with the boost converter.

The simulation diagrams of the boost converter are shown in Figures 12 and 13. The voltage waveform of the after-effect of the boost converter and converter voltage waveform are shown in Figures 14 and 15, respectively.

The simulation diagram of the PV module with the boost converter is designed and illustrated in Figure 16, and the associated output voltage and current waveforms of PV with the boost converter are shown in Figure 17.

The simulation diagram of solar MPPT with boost converter is designed and illustrated in Figure 18, and the power waveform of solar MPPT with boost converter is shown in Figure 18. Power curve of solar MPPT with boost converter is shown in Figure 19.

## 6. Conclusion and Future Works

In this article, the P&O algorithm is used to track the maximum power point and is given as input to the DC-DC converters which are operating at a high duty cycle ratio. The converter considered here will function properly at a high duty cycle to prevent the excessive inductor current. Due to the ease with which it can be implemented and due to its top-level viability, the perturb and observe MPPT system is used in our methodology. As an alternative, a modified P&O MPPT algorithm can be designed to stabilize the output voltage under rapid radiation change conditions and varied load conditions in our future works, which is especially useful for small or domestic PV systems.

## Data Availability

The data used to support the findings of this study are included within the article. Should further data or information be required, these are available from the corresponding author upon request.

## Conflicts of Interest

The authors declare that there are no conflicts of interest regarding the publication of this paper.

## Acknowledgments

The authors thank Addis Ababa Science and Technology University for providing characterization support to complete this research work.

## References

- [1] M. Lakshmi and S. Hemamalini, "Nonisolated high gain DC-DC converter for DC microgrids," *IEEE Transactions on Industrial Electronics*, vol. 65, no. 2, pp. 1205–1212, 2018.
- [2] B. Bryant and M. K. Kazmierczuk, "Voltage-loop power-stage transfer functions with MOSFET delay for boost PWM converter operating in CCM," *IEEE Transactions on Industrial Electronics*, vol. 54, no. 1, pp. 347–353, 2007.
- [3] X. Wu, J. Zhang, X. Ye, and Z. Qian, "Analysis and derivations for a family ZVS converter based on a new active clamp ZVS cell," *IEEE Transactions on Industrial Electronics*, vol. 55, no. 2, pp. 773–781, 2008.
- [4] F. L. Tofoli, D. D. C. Pereira, W. Josias de Paula, and D. D. S. Oliveira Júnior, "Survey on non-isolated high-voltage step-up dc-dc topologies based on the boost converter," *IET Power Electronics*, vol. 8, no. 10, pp. 2044–2057, 2015.
- [5] M.-K. Nguyen, T.-D. Duong, Y.-C. Lim, and Y.-J. Kim, "Isolated boost DC-DC converter with three switches," *IEEE Transactions on Power Electronics*, vol. 33, no. 2, pp. 1389–1398, 2018.
- [6] B. Sri Revathi and M. Prabhakar, "Non isolated high gain DC-DC converter topologies for PV applications - a comprehensive review," *Renewable and Sustainable Energy Reviews*, vol. 66, pp. 920–933, 2016.
- [7] H. F. Abdul Wahab and H. Sanusi, "Simulink Model of Direct torque control of induction machine," *American Journal of Applied Sciences*, vol. 5, no. 8, pp. 1083–1090, 2008.
- [8] C. L. Toh, N. R. N. Idris, and A. H. M. Yatim, "Torque ripple reduction in direct torque control of induction motor drives," power engineering conference, Bangi, Malaysia, December 2003.
- [9] Y. Hayashi, Y. Matsugaki, and T. Ninomiya, "Design consideration for high step-up nonisolated multicellular dc-dc converter for PV micro converters," *Journal of Engineering*, vol. 2018, Article ID 5098083, 16 pages, 2018.
- [10] K. Mohan Reddy and A. Naveen Reddy, "Solar PV array fed four switch buck-boost converter for LHB coach," *International Journal of Control Theory and Applications*, vol. 9, no. 29, pp. 249–255, 2016.
- [11] A. Naveen Reddy, "Performance and improvement of induction motor by using multilevel," *Inverter International Journal of Control Theory and Applications*, vol. 9, no. 10, pp. 4211–4219, 2016.
- [12] P. V. S. Sobhan, M. Subba Rao, N. Bharath Kumar, and A. Sriharibabu, "Design of fuzzy logic based photovoltaic fed battery charging system," *Journal of Green Engineering (JGE)*, vol. 9, no. 2, pp. 270–281, 2019.
- [13] F. M. Shahir and E. Babaei, "Application of high voltage gain DC-DC converter in photovoltaic system with energy storage," in *Proceedings of the 2017 8th Power Electronics, Drive Systems & Technologies Conference (PEDSTC)*, pp. 265–269, IEEE, Mashhad, Iran, February 2017.
- [14] H. Shayeghi, S. Pourjafar, S. Majid Hashemzadeh, and F. Sedaghati, "Presenting of the magnetic coupling-based transformer-less high step-up DC-DC converter for renewable energy applications," *International Transactions on Electrical Energy Systems*, vol. 2022, Article ID 3141119, 15 pages, 2022.
- [15] V. R. Teja, S. Srinivas, and M. K. Mishra, "A three port high gain non-isolated DC-DC converter for photovoltaic applications," in *Proceedings of the 2016 IEEE International Conference on Industrial Technology (ICIT)*, pp. 251–256, IEEE, Taipei, Taiwan, March 2016.
- [16] M. H. Taghvaei, M. A. M. Radzi, S. M. Moosavain, H. Hizam, and M. Hamiruce Marhaban, "A current and future study on non-isolated DC-DC converters for photovoltaic applications," *Renewable and Sustainable Energy Reviews*, vol. 17, pp. 216–227, 2013.
- [17] C. Balakishan, N. Sandeep, and M. V. Aware, "Design and implementation of three-level DC-DC converter with golden section search based MPPT for the photovoltaic applications," *Advances in Power Electronics*, vol. 2015, Article ID 587197, 9 pages, 2015.
- [18] S. Thangavelu and P. Umapathy, "Design of new high step-up DC-DC converter topology for solar PV applications,"

- International Journal of Photoenergy*, vol. 2021, Article ID 7833628, 11 pages, 2021.
- [19] P. K. Maroti, S. Padmanaban, F. Blaabjerg, L. Martirano, and P. Siano, "A novel multilevel high gain modified SEPIC DC-to-DC converter for high voltage/low current renewable energy applications," in *Proceedings of the 2018 IEEE 12th International Conference on Compatibility, Power Electronics and Power Engineering (CPE-POWERENG 2018)*, pp. 1–6, IEEE, Doha, Qatar, April 2018.
- [20] C. Muranda, E. Ozsoy, S. Padmanaban, M. S. Bhaskar, V. Fedák, and V. K. Ramachandaramurthy, "Modified SEPIC DC-to-DC boost converter with high output-gain configuration for renewable applications," in *Proceedings of the 2017 IEEE Conference on Energy Conversion (CENCON)*, pp. 317–322, IEEE, Kuala Lumpur, Malaysia, October 2017.
- [21] K. Nagarajan, A. Rajagopalan, S. Angalaeswari, L. Natrayan, and W. D. Mammo, "Combined economic emission dispatch of microgrid with the incorporation of renewable energy sources using improved mayfly optimization algorithm," *Computational Intelligence and Neuroscience*, vol. 2022, Article ID 6461690, 22 pages, 2022.
- [22] S. Mahapatra, S. S. Parida, K. Surana, P. Balamurugan, L. Natrayan, and P. Paramasivam, "Energy auditing for efficient planning and implementation in commercial and residential buildings," *Advances in Civil Engineering*, vol. 2021, Article ID 1908568, 10 pages, 2021.
- [23] G. Kanimozhi, L. Natrayan, S. Angalaeswari, and P. Paramasivam, "An effective charger for plug-in hybrid electric vehicles (PHEV) with an enhanced PFC rectifier and ZVS-ZCS DC/DC high-frequency converter," *Journal of Advanced Transportation*, vol. 2022, Article ID 7840102, 14 pages, 2022.
- [24] L. Natrayan, P. S. S. Sundaram, and J. Elumalai, "Analyzing the Uterine physiological with MMG Signals using SVM," *International journal of pharmaceutical research*, vol. 11, no. 2, pp. 165–170, 2019.
- [25] S. S. Sundaram, N. H. Basker, and L. Natrayan, "Smart clothes with bio-sensors for ECG monitoring," *International Journal of Innovative Technology and Exploring Engineering*, vol. 8, no. 4, pp. 298–301, 2019.
- [26] V. Michal, "Dynamic duty-cycle limitation of the boost DC/DC converter allowing maximal output power operations," in *Proceedings of the 2016 International Conference on Applied Electronics (AE)*, pp. 177–182, IEEE, Pilsen, Czech Republic, September 2016.
- [27] K. Javed, H. Ashfaq, and R. Singh, "An improved MPPT algorithm to minimize transient and steady state oscillation conditions for small SPV systems," *International Journal of Renewable Energy Development*, vol. 7, no. 3, pp. 191–197, 2018.
- [28] A. Abusorrah and M. M. Al-Hindawi, Y. Al-Turki, K. Mandal, D. Giaouris, S. Banerjee, S. Voutetakis, S. Papadopoulou, "Stability of a boost converter fed from photovoltaic source," *Solar Energy*, vol. 98, pp. 458–471, 2013.
- [29] E. Ozsoy, S. Padmanaban, V. Fedak, C. Muranda, and M. Cernet, "Modified SEPIC DC-to-DC converter 2/(1-k) output gain configuration for renewable power energy and high voltage applications," in *Proceedings of the 2018 IEEE 18th International Power Electronics and Motion Control Conference (PEMC)*, pp. 145–149, IEEE, Budapest, Hungary, August 2018.
- [30] P. Sanjeevikumar, G. Grandi, P. W. Wheeler, F. Blaabjerg, and J. Loncarski, "A simple MPPT algorithm for novel PV power generation system by high output voltage DC-DC boost converter," in *Proceedings of the 2015 IEEE 24th International Symposium on Industrial Electronics (ISIE)*, pp. 214–220, IEEE, Buzios, Brazil, June 2015.
- [31] J. C. Kim, J. H. Huh, and J. S. Ko, "Optimization design and test bed of fuzzy control rule base for PV system MPPT in micro grid," *Sustainability*, vol. 12, no. 9, p. 3763, 2020.
- [32] P. Asha, L. Natrayan, B. T. Geetha, J. R. Beulah, R. Sumathy, G. Varalakshmi, S. Neelakandan, "IoT enabled environmental toxicology for air pollution monitoring using AI techniques," *Environmental Research*, vol. 205, Article ID 112574, 2022.
- [33] S. Magesh, V. R. Niveditha, P. S. Rajakumar, and L. Natrayan, "Pervasive computing in the context of COVID-19 prediction with AI-based algorithms," *International Journal of Pervasive Computing and Communications*, vol. 16, no. 5, pp. 477–487, 2020.
- [34] K. R. Vaishali, S. R. Rammohan, L. Natrayan, D. Usha, and V. R. Niveditha, "Guided container selection for data streaming through neural learning in cloud," *International Journal of System Assurance Engineering and Management*, vol. 16, pp. 1–7, 2021.
- [35] C. S. S. Anupama, L. Natrayan, E. Laxmi Lydia et al., "Deep learning with backtracking search optimization-based skin lesion diagnosis model," *Computers, Materials & Continua*, vol. 70, no. 1, pp. 1297–1313, 2021.
- [36] D. K. Jain, S. K. S. Tyagi, S. Neelakandan, M. Prakash, and L. Natrayan, "Metaheuristic optimization-based resource allocation technique for cybertwin-driven 6G on IoE environment," *IEEE Transactions on Industrial Informatics*, vol. 18, no. 7, pp. 4884–4892, 2021.
- [37] J. Lee, J. Jo, and H. Cha, "MPPT performance comparison between duty-cycle control and current control for photovoltaic power conditioning system," in *Proceedings of the 2018 21st International Conference on Electrical Machines and Systems (ICEMS)*, pp. 1036–1040, Jeju, Korea (South), October 2018.

## Research Article

# An Epidemic Patch-Enabled Delayed Model for Virus Propagation: Towards Evaluating Bifurcation and White Noise

Zhigang Liu,<sup>1</sup> V. Madhusudanan ,<sup>2</sup> M. N. Srinivas,<sup>3</sup> ChukwuNonso H. Nwokoye,<sup>4</sup> and Tadele Degefa Geleto <sup>5</sup>

<sup>1</sup>School of Control Technology, Wuxi Institute of Technology, Wuxi 214121, China

<sup>2</sup>Department of Mathematics, S.A. Engineering College, Chennai 600077, Tamil Nadu, India

<sup>3</sup>Department of Mathematics, School of Advanced Sciences, Vellore Institute of Technology, Vellore 632014, Tamil Nadu, India

<sup>4</sup>Open Studies Unit, Nigeria Correctional Service, Awka, Nigeria

<sup>5</sup>Department of Computer Science, Ambo University, Ambo, Ethiopia

Correspondence should be addressed to V. Madhusudanan; madhusudhanan@saec.ac.in and Tadele Degefa Geleto; tadele.degefa@ambou.edu.et

Received 26 May 2022; Revised 12 July 2022; Accepted 19 July 2022; Published 17 August 2022

Academic Editor: Punit Gupta

Copyright © 2022 Zhigang Liu et al. This is an open access article distributed under the Creative Commons Attribution License, which permits unrestricted use, distribution, and reproduction in any medium, provided the original work is properly cited.

The massive disruptions caused by malware, such as a virus in computer networks and other aspects of information and communication technology, have generated attention, making it a hot research topic. While antivirus and firewalls can be effective, there is also a need to understand the spread patterns of viral infection using epidemic models to curb its incidences. Many previous research attempts have produced analytical models for computer viruses under various infectiousness situations. As a result, we suggested the SLBS model, which considers infection latency and transient immunity in patched nodes. Under certain conditions, the local stability of all equilibrium points is investigated. By setting the delay parameter, we established the occurrence of a Hopf bifurcation (HB) as it crossed a crucial point by several analyses. We also used the centre manifold theorem and normal form theory to examine the attributes of the HB. While the former was used to study the time delay and direction of Hopf bifurcation, the latter was used to investigate external noise and its intensities. Finally, numerical simulations two dimensional and three-dimensional graphs were used to depict the perturbations of the model, thus bolstering the essentiality of the study.

## 1. Introduction

The Internet and computer networks have greatly facilitated human effort, education, and living since the rising notoriety of computers [1] and the fast evolution of information communication technology. In light of this, new cyber threats are arising as their actors' techniques are always advancing to retain or increase their prominence in the threat ecosystem through exploiting vulnerabilities [2]. Be it for individuals, organizations or critical national infrastructure, black hat hackers target zero-day issues in certain situations, but more likely, they target freshly fixed flaws and "unpatched systems" [3].

Due to the increasing growth of communication networks and their applications, virus transmission has become

one of the topics of interest in computing research [4]. Besides worms and trojans [5], the virus is one way through which malicious attacks can arise in a computer network. In a networked system, whenever the computers are contaminated with viruses, the regular resident applications may lose the ability to function properly, corrupt saved files, or cause the loss of essential data on those machines. Subsequently, through the infected computers, the virus infection is transmitted to other computers through several means, which include able storage media (CD, USB, and flash drives) and e-mail attachments [6].

To curb viral spread incidences and safeguard computer networks against viruses, antimalicious programmes, firewalls, and patches are used to filter out all infections that remain in personal devices including personal laptops and

other detachable storage media [7]. Cybersecurity solutions largely aim to prevent harmful malware from entering and operating on computer systems [8]. Other ways include integrating audits, performing updates to security infrastructure [9], and modelling threats. Mathematical models have been developed to grasp the spread of malicious programs fully. These models are based on intriguing parallels between virtual viruses and their biological counterparts; wherein numerous phenomena are represented [2, 6, 7].

The basic inspiration for constructing the model is motivational research on mathematical modelling for Wireless Sensor Networks. Disease modelling is trending in the latest research works, particularly e-epidemic models are attractive and interesting, leading to our current proposed model with delay and stochastic dynamics. Some qualitative literature on delay models and stochastic models. In any Disease model, whether epidemic or e-epidemic, the delay is a key attribute to changing the system dynamics in terms of stability; environmental noise (stochastic) is also one of the key attributes which play a major role in the system dynamics. Motivational research works on delay and stochastic dynamics in various systems.

Therefore, in this paper, we propose the deterministic susceptible ( $S$ ), latent ( $L$ ), breaking out ( $B$ ), and patched ( $P$ ) model and a modification to include stochasticity in the form of noise, alongside delay and bifurcation. This paper is organized as follows: Section 2 contains the related literature; Section 3 presents the mathematical model; Section 4 contains the delay analysis, and Section 5 contains the directions of Hopf bifurcation and stability of the periodic solutions. Section 6 contains the SLBP model with noise; Section 7 contains the numerical simulations.

## 2. Related Literature

A sophisticated virus's primary purpose is to damage more computer systems; to achieve that purpose, the malware would attempt to infiltrate as many computers without being detected. For purposes of infection modelling Yang and Yang [10], two typical stages of a virus are the latent ( $L$ ) and breaking out ( $B$ ) stages. While the former signifies the entry period, when the virus inhabits the host, the latter represents the time the infection starts causing harm to the host computer. Here, models representing virus propagation in computers and their networks using this SLB format are reviewed.

Yang et al. [11] employed the SLB model internal computers and derived the reproduction number, equilibria, and stability of points. Yang et al. [12] modelled the spread of computer viruses in the complex World-Wide-Web using the SLB model. They discovered that a greater heterogeneity and a scale-free graph with smaller power-law exponents promote virus growth. Representing recovered computers in separate compartments and reinfection, Yang et al. [13] derived the global stability of the susceptible-latent-breaking-out-recovered-susceptible (SLBRS) model. Zhang et al. [14] employed the SLBRS model to represent virus dissemination

but used the time delay of antivirus cleaning as a bifurcating parameter. Due to the ubiquity of the mass action infection rate, Yang and Yang [15] adopted a nonlinear type of incidence for virus growth using the SLB model.

Contrary to homogenous mixing, prevalent in most models, Yang et al. [16] used the SLB model to represent a scenario where distinct nodes have varied infectious, exploding, and remedial rates. The SLBR model was used by Zhang [17] to model both storage media and internal/external computers. Zhang and Bi [18] investigated the existence and properties of Hopf bifurcation using the SLB model. Zhang and Wang [19] considered isolation of contaminated hosts and thus developed the susceptible-latent-breaking out-quarantined-recovered (SLBQR) model, which was later used to investigate Hopf bifurcation. Zhang [20] applied the SLB model for multilayer computer subnetworks. Similarly, Zhao and Bi [21] used the SLBQR to model virus spread with two-time delays and the existence of Hopf bifurcation. Another delayed version of the SLBS model was developed by Zhang et al. [22] and after studying its stability analyses. Because most models only represent horizontal transmission (HT), Zhu et al. [23] utilized the SLBR model to represent both HT and vertical transmission of viruses in a computer network.

More SLB models were observed in the following studies; [24, 25]. Other models which have been used to represent virus propagation in computers alongside detachable storage, external computers, and age structure using the susceptible-infected-countermeasure (SIC) model [7], strongly protected susceptible-weakly protected susceptible-infective-external (SWIE) model [6] and susceptible-infected-recovered (SIR) model [2]. A critical evaluation of the above-given models shows that besides considering the deterministic SLB model with their delay analysis, this work presents its SLB's stochastic version, wherein the impact of white noise is studied. Our model also includes the patch ( $P$ ) compartment that prevents the inundation [26] of the computer network as a result of virus infestation. The following sections contain the proposed models and further analysis.

## 3. Mathematical Model

In this part, a patch-enabled SLBP model is developed to capture the dynamics of virus and patch transmission. Computers are divided into two groups for virus propagation offline and online: internal computers linked to the Internet (World Wide Web) and external computers not connected to the world wide web. The host computers are called nodes for the sake of simplicity. All internal nodes are connected to the world wide web and divided into four categories, namely, susceptible nodes without virus ( $S$ ), latently infected ( $L$ ), breaking out infected ( $B$ ), and nodes that have received patches ( $P$ ) at the time  $t$ . In the latent state, the virus infection is inactive. Therefore,  $S(t) + L(t) + B(t) + P(t) \equiv 1$ . We suggested the following conditions alongside the mathematical model based on the inspiration:

- (A1) When an external node connects to the world wide web, it becomes vulnerable. At rate  $\delta$ , nodes are added to or withdrawn from the network.
- (A2) Both infected nodes ( $L$ ,  $B$ ) can potentially infect susceptible nodes. Infection rates from  $L$  and  $B$  to  $S$  nodes are  $\beta_1$  and  $\beta_2$ , respectively. It is assumed that the incidence function is of the mass-action type.
- (A3) With a rate of  $\alpha$ , the  $L$  node becomes  $B$ .
- (A4) Remediation of  $L$  nodes occurs at rate  $\gamma_2$  and then becomes vulnerable.
- (A5) The patched node will become invalid due to the development of new viruses. As a result, it loses immunity at a rate of  $\gamma_1$ .
- (A6) Patches are acquired at a rate of  $\beta P$  by nodes  $S$ ,  $L$ , or  $B$ .

$$\begin{aligned} S'(t) &= \delta - (\beta_1 L + \beta_2 B)S - \beta SP + \gamma_1 P + \gamma_2 L - \delta S, \\ L'(t) &= (\beta_1 L + \beta_2 B)S - \beta LP - \gamma_2 L - \alpha L - \delta L, \\ B'(t) &= \alpha L - \beta B(t - \tau)P - \delta B, \\ P'(t) &= \beta(S + L)P - \beta B(t - \tau)P - \gamma_1 P - \delta P, \end{aligned} \quad (1)$$

With the initial conditions

$$S(0) \geq 0, L(0) \geq 0, B(0) \geq 0, P(0) \geq 0. \quad (2)$$

By direct computation, the system equation (1) has a unique positive equilibrium point  $E_*$  ( $S^*$ ,  $L^*$ ,  $B^*$ ,  $P^*$ ) in which

$$\begin{aligned} S^* &= \frac{\beta + \alpha + \gamma_2 - \gamma_1}{\beta_1 + \beta_2 \alpha / \beta - \gamma_1}, \\ L^* &= \frac{\beta - \gamma_1}{\beta - \gamma_1 + \alpha} \left( \frac{\gamma_1 + \delta}{\beta} - S^* \right), \\ B^* &= \frac{\alpha}{\beta - \gamma_1 + \alpha} \left( \frac{\gamma_1 + \delta}{\beta} - S^* \right), \\ P^* &= \frac{\beta - \gamma_1 + \alpha}{\beta}. \end{aligned} \quad (3)$$

#### 4. Delay Analysis

The linear system of equation (1) about endemic equilibrium point  $E_*$  ( $S^*$ ,  $L^*$ ,  $B^*$ ,  $P^*$ ) is given by the following equations:

$$S'(t) = a_{11}S(t) + a_{12}L(t) + a_{13}B(t) + a_{14}P(t), \quad (4)$$

$$L'(t) = a_{21}S(t) + a_{22}L(t) + a_{23}B(t) + a_{24}P(t), \quad (5)$$

$$B'(t) = a_{32}L(t) + a_{33}B(t) + a_{34}P(t) + b_{31}B(t - \tau), \quad (6)$$

$$P'(t) = a_{41}S(t) + a_{42}L(t) + a_{44}P(t) + b_{41}B(t - \tau), \quad (7)$$

where

$$\begin{aligned} a_{11} &= -\beta_1 L^* - \beta_2 B^* - \beta P^* - \delta; a_{12} = \gamma_2 - \beta_1 S^*; a_{13} = -\beta_2 S^*; a_{14} = \gamma_1 - \beta S^*, \\ a_{21} &= \beta_1 L^* + \beta_2 B^*, a_{22} = \beta_1 S^* - \beta P^* - \gamma_2 - \alpha - \delta; a_{23} = \beta_2 S^*; a_{24} = -\beta L^*, \\ a_{32} &= \alpha; a_{33} = -\delta, a_{34} = b^*; b_{31} = -\beta P^*, \\ a_{41} &= \beta P^*; a_{42} = \beta P^*, a_{44} = \beta S^* + \beta L^* - \gamma_1 - \delta; b_{41} = \beta P^*. \end{aligned} \quad (8)$$

Then, the associated characteristic equation is

$$\begin{aligned} \lambda^4 + A_1 \lambda^3 + A_2 \lambda^2 + A_3 \lambda + A_4 \\ + (B_1 \lambda^3 + B_2 \lambda^2 + B_3 \lambda + B_4) e^{-\lambda \tau} = 0, \end{aligned} \quad (9)$$

where

$$\begin{aligned} A_1 &= -(a_{11} + a_{22} + a_{33} + a_{44}), \\ A_2 &= a_{11}a_{22} + a_{11}a_{33} + a_{11}a_{44} + a_{22}a_{33} + a_{22}a_{44} + a_{33}a_{44} + a_{23}a_{32} + a_{42}a_{24} - a_{21}a_{12}; \\ A_3 &= a_{23}a_{34}a_{42} + a_{33}a_{44}a_{24} + a_{11}a_{23}a_{32} + a_{42}a_{24}a_{11} + a_{14}a_{34}a_{41} + a_{13}a_{21}a_{32} + a_{13}a_{34}a_{41} + a_{33}a_{21}a_{12} + a_{12}a_{21}a_{44} \\ &\quad - a_{11}a_{22}a_{33} - a_{11}a_{33}a_{44} - a_{11}a_{22}a_{44} - a_{14}a_{21}a_{32}, \\ A_4 &= a_{11}a_{22}a_{33}a_{44} + a_{14}a_{21}a_{44}a_{32} + a_{14}a_{34}a_{42}a_{21} + a_{14}a_{23}a_{32}a_{41} + a_{22}a_{34}a_{44}a_{41} - a_{23}a_{32}a_{11}a_{44} \\ &\quad - a_{23}a_{34}a_{11}a_{42} - a_{11}a_{33}a_{24}a_{42} - a_{13}a_{32}a_{21}a_{44} - a_{34}a_{21}a_{13}a_{42} - a_{13}a_{34}a_{22}a_{41} - a_{24}a_{32}a_{13}a_{41}, \\ B_1 &= -b_{11}; \\ B_2 &= b_{11}(a_{22} + a_{44}) - a_{34}b_{12}; \\ B_3 &= a_{22}a_{34}b_{12} + a_{24}a_{32}b_{12} + a_{42}a_{24}b_{11} + a_{12}a_{21}b_{11} - a_{11}a_{22}b_{11} - a_{11}a_{44}b_{11} + a_{34}a_{11}b_{12} - a_{22}a_{44}b_{11}, \\ B_4 &= a_{11}a_{22}(b_{11}a_{44} - b_{12}a_{34}) + a_{21}a_{12}(b_{11}a_{44} - b_{31}a_{34}) - a_{11}a_{24}(b_{12}a_{32} + b_{11}a_{42}). \end{aligned} \quad (10)$$

Put  $\tau = 0$  in equation (8), we get the following equation:

$$\lambda^4 + (A_1 + B_1)\lambda^3 + (A_2 + B_2)\lambda^2 + (A_3 + B_3)\lambda + (A_4 + B_4) = 0. \quad (11)$$

From equation (9),

$$A_1 + B_1 = (\beta_1 L^* + \beta_2 B^* + \beta P^* + \delta) + (\beta_1 S^* - \beta P^* - \gamma_2 - \alpha - \delta) + (-\delta) + (\beta S^* + \beta L^* - \gamma_1 - \delta) + \beta P^* > 0. \quad (12)$$

By using Routh–Hurwitz criteria, sufficient conditions for all roots of equation (11) to be negative real parts are given in the following form:

$$D_2 = \begin{vmatrix} A_1 + B_1 & 1 \\ A_2 + B_2 & A_3 + B_3 \end{vmatrix}, \quad (13)$$

$$D_3 = \begin{vmatrix} A_1 + B_1 & 1 & 0 \\ A_3 + B_3 & A_2 + B_2 & A_1 + B_1 \\ 0 & A_4 + B_4 & A_3 + B_3 \end{vmatrix}, \quad (14)$$

$$D_4 = \begin{vmatrix} A_1 + B_1 & 1 & 0 & 0 \\ A_3 + B_3 & A_2 + B_2 & A_1 + B_1 & 1 \\ 0 & A_4 + B_4 & A_3 + B_3 & A_2 + B_2 \\ 0 & 0 & 0 & A_4 + B_4 \end{vmatrix}. \quad (15)$$

This, if conditions equations (11), (13)–(15) hold,  $E_*$  is locally asymptotically stable in the absence of delay.

For  $\tau > 0$ , Put  $\lambda = i\omega$  in equation (8) we have the following equation:

$$\begin{aligned} &(\omega^4 - iA_1\omega^3 - A_2\omega^2 + iA_3\omega + A_4) \\ &+ (-iB_1\omega^3 - B_2\omega^2 + iB_3\omega + B_4)(\cos \omega\tau - i \sin \omega\tau) = 0. \end{aligned} \quad (16)$$

Equating real and imaginary parts we have the following equation:

$$(B_3\omega - B_1\omega^3)\sin \omega\tau + (B_4 - B_2\omega^2)\cos \omega\tau = (A_2\omega^2 - \omega^4 - A_4), \quad (17)$$

$$(B_3\omega - B_1\omega^3)\cos \omega\tau - (B_4 - B_2\omega^2)\sin \omega\tau = (A_1\omega^3 - A_3\omega) \quad (18)$$

Squaring and Adding equations (17) and (18) we get the following equation:

$$\omega^8 + C_1\omega^6 + C_2\omega^4 + C_3\omega^2 + C_4 = 0, \quad (19)$$

where

$$\begin{aligned} C_1 &= A_4^2 - B_4^2, \\ C_2 &= A_3^2 - 2A_4A_2 - B_3^2 + 2B_2B_4, \\ C_3 &= A_2^2 - 2A_3A_1 - B_2^2 + 2B_3B_1 + 2A_4, \\ C_4 &= A_4^2 - B_4^2. \end{aligned} \quad (20)$$

Now, by assuming  $\omega^2 = u$  then the equation (19) becomes

$$u^4 + C_1u^3 + C_2u^2 + C_3u + C_4 = 0. \quad (21)$$

The function is defined as follows:

$$f(u) = u^4 + C_1u^3 + C_2u^2 + C_3u + C_4 = 0. \quad (22)$$

clearly  $\lim_{u \rightarrow \infty} f(u) = \infty$ . Thus, if  $C_4 < 0$ , then equation (22) has at least one positive root.

Solving from equations (17) and (18), we get the following equation:

$$\cos \omega\tau = \frac{Q_1\omega^6 + Q_2\omega^4 + Q_3\omega^2 + Q_4}{Q_5\omega^6 + Q_6\omega^4 + Q_7\omega^2 + Q_8}, \quad (23)$$

where

$$\begin{aligned} Q_1 &= B_2 - A_1B_1, Q_2 = A_3B_1 + A_1B_3 + A_2B_2 - B_4; Q_3 = A_4B_2 + A_2B_4 - A_3B_3; \\ Q_5 &= -A_4B_4; Q_6 = B_1^2; Q_7 = B_2^2 - 2B_1B_3; Q_8 = B_4^2 \\ Q_{10} &= B_5^2. \end{aligned} \quad (24)$$

So, corresponding to  $\lambda = i\omega_0$ , there exists

$$\tau_{0n} = \frac{1}{\omega_0} \cos^{-1} \left[ \frac{Q_1\omega^6 + Q_2\omega^4 + Q_3\omega^2 + Q_4}{Q_5\omega^6 + Q_6\omega^4 + Q_7\omega^2 + Q_8} \right] + \frac{2n\pi}{\omega_0} \text{ where } n = 0, 1, 2, \dots \tag{25}$$

Differentiate equation (8) with respect to  $\tau$ , we have the following equation:

$$\left( \frac{d\lambda}{d\tau} \right)^{-1} = \frac{4\lambda^3 + 3A_1\lambda^2 + 2A_2\lambda + A_3}{\lambda(\lambda^4 + A_1\lambda^3 + A_2\lambda^2 + A_3\lambda + A_4)} + \frac{3B_1\lambda^2 + 2B_2\lambda + B_3}{\lambda(B_1\lambda^3 + B_2\lambda^2 + B_3\lambda + B_4)}. \tag{26}$$

Thus,  $\text{Re}(d\lambda/d\tau)^{-1} = f(v_*)/B_1\omega_0^6 + (B_2^2 - 2B_3B_1)\omega_0^4 + (B_3^2 - 2B_4B_2)\omega_0^2 + B_4^2$  where  $E_* = \omega_0^2$  and  $f(v) = v^4 + C_1v^3 + C_2v^2 + C_3v + C_4$ .

Thus, if the condition  $f'(v_*) \neq 0$  and  $\text{Re}(d\lambda/d\tau)^{-1} \neq 0$ , therefore the transversality conditions hold and hence Hopf bifurcation occurs at  $\tau = \tau_0$

**Theorem 1.** *If  $E_*$  exists with the condition equations (13)–(15) and  $u = \omega^2$  be a positive root of equation (19) then there exists  $\tau = \tau_0$  such that*

- (i)  $E_*$  is locally asymptotically stable for  $0 \leq \tau < \tau_0$
- (ii)  $E_*$  is unstable for  $\tau > \tau_0$
- (iii) The system equation (1) undergoes Hopf bifurcation around  $E_*$  at  $\tau = \tau_0$ , where

$$\tau_{0n} = \frac{1}{\omega_0} \cos^{-1} \left[ \frac{Q_1\omega^6 + Q_2\omega^4 + Q_3\omega^2 + Q_4}{Q_5\omega^6 + Q_6\omega^4 + Q_7\omega^2 + Q_8} \right] + \frac{2n\pi}{\omega_0} \text{ where } n = 0, 1, 2, \dots \tag{27}$$

### 5. Hopf Bifurcation and the Periodic Solution's Stability

Using the theories of normal form and centre manifold [27] of the system, we explore stability and Hopf bifurcation's direction.

**Theorem 2.** *If  $\mu_H > 0$  then the Hopf bifurcation is supercritical otherwise it is subcritical. Here, sign determines the direction of the Hopf bifurcation.*

$$\mu_H = \frac{\text{Re}\{Z(0)\}}{\text{Re}\{\lambda^1(\tau_0)\}}. \tag{28}$$

If  $\Omega_p > 0$  then the bifurcated periodic solutions are stable otherwise it is unstable. Here, the sign of  $\Omega_p$  determines the stability of the bifurcated periodic solutions.

$$\Omega_p = 2\text{Re}\{Z(0)\}. \tag{29}$$

If  $\Theta_I > 0$  then the period of the bifurcated solutions increases otherwise it decreases. Here, the sign of  $\Theta_I$  determines the period of the bifurcated periodic solutions.

$$\Theta_I = -\frac{\text{Im}\{Z(0)\} + \mu_H \text{Im}\{\lambda^1(\tau_0)\}}{\tau_0 \omega_0},$$

$$Z(0) = \frac{i}{2\tau_0 \omega_0} \left\{ Z_{11}Z_{20} - 2|Z_{11}|^2 - \frac{|Z_{02}|^2}{3} \right\} + \frac{Z_{21}}{2} \tag{30}$$

$$W_1(t) = S(t) - S^*, W_2(t) = L(t) - L^*, W_3(t) = B(t) - B^*, W_4 = P(t) - P^*.$$

*Proof.* Let  $W_1(t) = S(t) - S^*, W_2(t) = L(t) - L^*, W_3(t) = B(t) - B^*, W_4 = P(t) - P^*$  and normalize the delay with  $t = t/\tau$ . Let  $\tau = \tau_0 + \xi, \xi \in R$ , then  $\xi = 0$  is the Hopf-bifurcation

value of system equation (2) and system equation (2) can be transformed into a functional differential equation in  $C = C([-1, 0], R^4)$  as follows:



$$\dot{W}(t) = L_\xi(W_t) + G(\xi, W_t), \quad (31)$$

where  $W(t) = (W_1(t), W_2(t), W_3(t), W_4(t))^T \in C = C([-1, 0], R^4)$  and  $L_\xi: C \rightarrow R^4$  and  $G: R^4 \times C \rightarrow R^4$  are given, respectively, by the following equation:

$$L_\xi Y = (\tau_0 + \xi)[\Lambda_{\max} Y(0) + \Pi_{\max} Y(-1)],$$

$$G(\xi, Y) = \begin{bmatrix} -Y_1(0)\{\beta_1 Y_2(0) + \beta_2 Y_3(0)\} \\ Y_1(0)\{\beta_1 Y_2(0) + \beta_2 Y_3(0)\} \\ 0 \\ 0 \end{bmatrix},$$

$$\text{With } \Lambda = \begin{bmatrix} m_1 & m_2 & m_3 & m_4 \\ m_5 & m_6 & m_7 & m_8 \\ 0 & m_9 & m_{10} & 0 \\ m_{11} & m_{12} & 0 & m_{13} \end{bmatrix} \text{ and } \Pi = \begin{bmatrix} 0 & 0 & 0 & 0 \\ 0 & 0 & 0 & 0 \\ 0 & 0 & \pi_1 & 0 \\ 0 & 0 & \pi_2 & 0 \end{bmatrix}. \quad (32)$$

where

$$\begin{aligned} m_1 &= -(\beta_1 L^* + \beta_2 B^*) - \beta P^* - \delta; m_2 \\ &= -\beta_1 S^* + \gamma_2; m_3 = -\beta_2 S^*; m_4 = -\beta S^* + \gamma_1, \\ m_5 &= \beta_1 L^* + \beta_2 B^*; m_6 = \beta_1 S^* - \beta_2 P^* - \gamma_2 - \alpha - \delta; m_7 \\ &= \beta_2 S^*; m_8 = -\beta L^*; m_9 = \alpha; m_{10} = -\delta, \\ m_{10} &= -\delta; m_{11} = \beta P^*; m_{12} = \beta P^*; m_{13} \\ &= \beta S^* + \beta L^* - \gamma_1 - \delta; \pi_1 = -\beta P^*; \pi_2 = \beta P^*. \end{aligned} \quad (33)$$

By the Riesz representation theorem, there exists a function  $\eta(\theta, \xi)$  of bounded variation for  $\theta \in [-1, 0]$  such that

$$L_\xi Y = \int_{-1}^0 d\eta(\theta, \xi) Y(\theta) \text{ for } Y \in C. \quad (34)$$

In fact, we choose

$$\eta(\theta, \xi) = (\tau_0 + \xi)(\Lambda_{\max} \delta(\theta) + \Pi_{\max} \delta(\theta + 1)). \quad (35)$$

where  $\delta(\theta)$  is the dirac delta function. For  $Y \in C([-1, 0], R^4)$ , define

$$J(\xi)Y(\theta) = \begin{cases} \frac{dY(\theta)}{d\theta}, & -1 \leq \theta < 0, \\ \int_{-1}^0 d\eta(\theta, \xi) Y(\theta) = L_\xi Y, & \theta = 0, \end{cases} \quad (36)$$

$$K(\xi)Y(\theta) = \begin{cases} 0, & -1 \leq \theta < 0, \\ G(\xi, Y), & \theta = 0. \end{cases}$$

The system equation (1) is equivalent to

$$\dot{u}(t) = J(\xi)u_t + K(\xi)u_t. \quad (37)$$

For  $\varphi \in C^1([0, 1], (R^4)^*)$ , the adjoint operator  $J^*$  of  $J(0)$  is defined as follows:

$$J^*(\xi)\varphi(\mu) = \begin{cases} \frac{d\varphi(\mu)}{d\mu}, & 0 < \mu \leq 1, \\ \int_{-1}^0 d\eta(\sigma, 0)\varphi(-\sigma), & \mu = 0. \end{cases} \quad (38)$$

Next, we define the bilinear inner form for  $A$  and  $A^*$ .

$$\langle \varphi(\mu), Y(\theta) \rangle = \bar{\varphi}(0)Y(0) - \int_{\theta=-1}^0 \int_{\xi=0}^{\theta} \bar{\varphi}^T(\xi - \theta) d\eta(\theta) Y(\xi) d\xi, \quad (39)$$

where  $\eta(\theta) = \eta(\theta, 0)$ .

Let  $q(\theta) = (1, q_2, q_3, q_4)^T e^{i\tau_0 W_0 \theta}$  be the eigen vector of  $J(0)$  corresponding to  $i\tau_0 W_0$  and  $q^*(S) = V(1, q_2^*, q_3^*, q_4^*) e^{i\tau_0 W_0 S}$  be the eigen vector of  $J^*(0)$  corresponding to  $-i\tau_0 W_0$  respectively. Based on the definition of  $J(0)$  and  $J^*(0)$  one can obtain the following equation:

$$\begin{aligned} q_2 &= \frac{(m_5 + m_8 q_4)(m_{10} + \pi_1 e^{-i\tau_0 \omega_0} - i\omega_0)}{m_7 m_9 + (i\omega_0 - m_6)(m_{10} + \pi_1 e^{-i\tau_0 \omega_0} - i\omega_0)}; q_3 = \frac{m_9 q_2}{m_{10} + \pi_1 e^{-i\tau_0 \omega_0} - i\omega_0}; \\ q_4 &= \frac{1}{m_4} \left[ \frac{i\omega_0 - m_1 - m_2 q_2 - m_3 q_3}{m_4} \right]; q_2^* = -\frac{(m_9 q_3^* + m_{12} q_4^* + m_2)}{m_6 + i\omega_0}; q_3^* = -\frac{(m_3 + m_7 q_2^* + m_2 e^{i\tau_0 \omega_0} q_4^*)}{m_{10} + \pi_1 e^{i\tau_0 \omega_0} + i\omega_0}; \\ q_4^* &= \frac{m_4 m_5 - m_8 (m_1 + i\omega_0)}{m_8 m_{11} - (m_{13} + i\omega_0) m_5}. \end{aligned} \quad (40)$$

From equation (5), we have  $\bar{q} = [1 + q_2 \bar{q}_2^* + q_3 \bar{q}_3^* + q_4 \bar{q}_4^* + \tau_0 e^{-i\tau_0 \omega_0} q_2 (\pi_1 \bar{q}_2^* + \pi_2 \bar{q}_3^*)]^{-1}$  such that  $\langle q^*, q \rangle = 1$  and  $\langle q^*, \bar{q} \rangle = 0$ .

According to the algorithms in [27] and a similar computation process to that in [2], we can obtain the following expressions:

$$\begin{aligned}
 Z_{20} &= 2\tau_0\bar{q}(q_4^* - 1)(\beta_1q_2 + \beta_2q_3); \\
 Z_{11} &= 2\tau_0\bar{q}(q_4^* - 1)(\beta_1(q_2 + \bar{q}_2) + \beta_2(q_3 + \bar{q}_3)); \\
 Z_{02} &= 2\tau_0\bar{q}(\bar{q}_4^* - 1)(\beta_1\bar{q}_2 + \beta_2\bar{q}_3); \\
 Z_{21} &= \tau_0\bar{q}(\bar{q}_4^* - 1) \left\{ \begin{aligned} &(\beta_1\bar{q}_2 + \beta_2\bar{q}_3)w_{20}^{(1)}(0) + 2(\beta_1q_2 + \beta_2q_3)w_{11}^{(1)}(0) + \\ &\beta_1(w_{20}^{(2)}(0) + 2w_{11}^{(2)}(0)) + \beta_2(w_{20}^{(3)}(0) + 2w_{11}^{(3)}(0)) \end{aligned} \right\};
 \end{aligned}
 \tag{41}$$

with

$$\begin{aligned}
 w_{20}(\theta) &= \frac{i\mu_{20}}{\omega_0\tau_0}q(\theta) + i\frac{\bar{\mu}_{02}}{3\omega_0\tau_0}\bar{q}(\theta) + E_1e^{2i\omega_0\tau_0\theta}, \\
 w_{11}(\theta) &= -i\frac{\mu_{11}}{\omega_0\tau_0}q(\theta) + i\frac{\bar{\mu}_{11}}{\omega_0\tau_0}\bar{q}(\theta) + E_2,
 \end{aligned}
 \tag{42}$$

where  $E_1$  and  $E_2$  can be obtained by the following two equations:

$$\begin{aligned}
 E_1 &= \begin{bmatrix} 2i\omega_0 - m_1 & -m_2 & -m_3 & m_4 \\ -m_5 & 2i\omega_0 - m_6 & -m_7 & -m_8 \\ 0 & -m_9 & 2i\omega_0 - m_{10} - \pi_1e^{-2i\tau_0\omega_0} & 0 \\ -m_{11} & -m_{12} & -\pi_2e^{-2i\tau_0\omega_0} & 0 \end{bmatrix}^{-1} \begin{bmatrix} (\beta_1 + \beta_2)q_3 \\ (\beta_1 + \beta_2)\bar{q}_3 \\ 0 \\ 0 \end{bmatrix}, \\
 E_2 &= \begin{bmatrix} m_1 & m_2 & m_3 & m_4 \\ m_5 & m_6 & m_7 & m_8 \\ 0 & m_9 & m_{10} + \pi_1 & 0 \\ m_{11} & -m_{12} & \pi_2 & m_{13} \end{bmatrix}^{-1} \begin{bmatrix} -(\beta_1 + \beta_2)(q_3 + \bar{q}_3) \\ (\beta_1 + \beta_2)(q_3 + \bar{q}_3) \\ 0 \\ 0 \end{bmatrix}.
 \end{aligned}
 \tag{43}$$

Then, we can obtain the following equation:

$$\begin{aligned}
 Z(0) &= \frac{i}{2\tau_0\omega_0} \left\{ Z_{11}Z_{20} - 2|Z_{11}|^2 - \frac{|Z_{02}|^2}{3} \right\} + \frac{Z_{21}}{2}, \\
 \mu_H &= -\frac{\text{Re}\{Z(0)\}}{\text{Re}\{\lambda^1(\tau_0)\}}, \\
 \Omega_p &= 2\text{Re}\{Z(0)\}; \\
 \Theta_I &= -\frac{\text{Im}\{Z(0)\} + \mu_H\text{Im}\{\lambda^1(\tau_0)\}}{\tau_0\omega_0}.
 \end{aligned}
 \tag{44}$$

Thus, we can obtain the results described in theorem (2). The proof is completed.  $\square$

### 6. The SLBP Model with Noise

In this section, we considered a SLBP stochastic epidemic model, which includes four compartments i.e., susceptible, latent, breaking out, and patched with the mass action

incidence rate. Specifically, we are investigating the effect of Gaussian white noise on the model (without delay) proposed by Zhang and Upadhyay [27] for various low, medium, and high intensities. The schematic representation of the proposed model is as follows.

The following system of nonlinear differential equations with noise describes the dynamics of the proposed model:

$$\begin{aligned}
 S'(t) &= \mu - (\beta_1L + \beta_2B)S - \beta\text{SP} + \gamma_1P + \gamma_2L - \delta S + \alpha_1\xi_1(t), \\
 L'(t) &= (\beta_1L + \beta_2B)S - \beta\text{LP} - \gamma_2L - \alpha L - \delta L + \alpha_2\xi_2(t), \\
 B'(t) &= \alpha L - \beta\text{BP} - \delta B + \alpha_3\xi_3(t), \\
 P'(t) &= \beta(S + L + B)P - \gamma_1P - \delta P + \alpha_4\xi_4(t).
 \end{aligned}
 \tag{45}$$

where  $S(t)$ ,  $L(t)$ ,  $B(t)$ , and  $P(t)$  represent nodes of susceptible, latent, breaking out, and patch at time  $t$ , respectively. In this analysis, we emphasis on the dynamics of the model about the interior equilibrium point  $D_*(S^*, L^*, B^*, P^*)$  only according to the method introduced by Nisbet and Gurney [28] and Carletti [29].

$$\text{Let } S(t) = u_1(t) + S^*; L(t) = u_2(t) + V^*; B(t) = u_3(t) + B^*; P(t) = u_4(t) + P^*.
 \tag{46}$$

And, by focusing solely on the effects of linear stochastic perturbations As a result, the model (47)-(50) is reduced to the linear system shown as follows:

$$u_1'(t) = (-\beta S^*)u_1 + (-\beta S^*)u_3 + (-\beta S^*)u_4 + \alpha_1 \xi_1(t), \quad (47)$$

$$u_2'(t) = (\beta_1 V^*)u_1(t) + (\beta V^*)u_4(t) + \alpha_2 \xi_2(t), \quad (48)$$

$$u_3'(t) = (-\beta B^*)u_4(t) + \alpha_3 \xi_3(t), \quad (49)$$

$$u_4' = (\beta P^*)u_1(t) + (\beta P^*)u_2(t) + (\beta P^*)u_3(t) + \alpha_4 \xi_4(t). \quad (50)$$

Taking the Fourier transform of equations (47)–(50) we get the following equation:

$$\alpha_1 \tilde{\xi}_1(\omega) = (i\omega + \beta_1 S^*)\tilde{u}_1(\omega) + (\beta_2 S^*)\tilde{u}_3(\omega) + (\beta S^*)\tilde{u}_4(\omega), \quad (51)$$

$$\alpha_2 \tilde{\xi}_2(\omega) = -(\beta V^*)\tilde{u}_1(\omega) + (i\omega)\tilde{u}_2(\omega) + (-\beta V^*)\tilde{u}_4(\omega), \quad (52)$$

$$\alpha_3 \tilde{\xi}_3(\omega) = (i\omega)\tilde{u}_3(\omega) + (\beta B^*)\tilde{u}_4(\omega), \quad (53)$$

$$\alpha_4 \tilde{\xi}_4(\omega) = (-\beta P^*)\tilde{u}_1(\omega) + (-\beta P^*)\tilde{u}_2(\omega) + (-\beta P^*)\tilde{u}_3(\omega) + (-\beta P^*)\tilde{u}_4(\omega). \quad (54)$$

Equations (51) and (54) have a matrix form as follows:

$$M(\omega)\tilde{u}(\omega) = \tilde{\psi}(\omega), \quad (55)$$

$$\text{where, } M(\omega) = \begin{pmatrix} A_1 & B_1 & C_1 & D_1 \\ A_2 & B_2 & C_2 & D_2 \\ A_3 & B_3 & C_3 & D_3 \\ A_4 & B_4 & C_4 & D_4 \end{pmatrix};$$

$$\tilde{u}(\omega) = [\tilde{u}_1(\omega), \tilde{u}_2(\omega), \tilde{u}_3(\omega), \tilde{u}_4(\omega)]^T,$$

$$\tilde{\xi}(\omega) = [\alpha_1 \tilde{\xi}_1(\omega), \alpha_2 \tilde{\xi}_2(\omega), \alpha_3 \tilde{\xi}_3(\omega), \alpha_4 \tilde{\xi}_4(\omega)]^T,$$

$$A_1 = i\omega + \beta_1 S^*; B_1 = 0; C_1 = \beta_2 S^*; D_1 = \beta S^*; \quad (56)$$

$$A_2 = -\beta_1 V^*; B_2 = i\omega; C_2 = 0; D_2 = -\beta V^*;$$

$$A_3 = 0; B_3 = 0; C_3 = i\omega; D_3 = \beta B^*;$$

$$A_4 = -\beta P^*; B_4 = -\beta P^*; C_4 = -\beta P^*; D_4 = -\beta P^*.$$

Alternatively, equation (55) can be written as follows:

$$\tilde{u}(\omega) = [M(\omega)]^{-1}\tilde{\xi}(\omega), \quad (57)$$

$$\text{Let } [M(\omega)]^{-1} = K(\omega), \quad (58)$$

$$\text{where } K(\omega) = \frac{a \, dj[M(\omega)]}{|M(\omega)|}. \quad (59)$$

If the function's  $Y(t)$  mean value is zero, the fluctuation intensity (variance) of its components in frequency intervals  $[\omega, \omega + d\omega]$  is  $S_Y(\omega)d\omega$ , where  $S_Y(\omega)$  is the spectral density  $Y$  and is defined as follows:

$$S_Y(\omega) = \lim_{T \rightarrow +\infty} \frac{|Y(\omega)|^2}{T}. \quad (60)$$

The auto covariance function is the inverse transform of  $S_Y(\omega)$  if  $Y$  has a zero mean value.

$$C_Y(\tau) = \frac{1}{2\pi} \int_{-\infty}^{\infty} S_Y(\omega) e^{i\omega\tau} d\omega. \quad (61)$$

And, the variance of the corresponding fluctuations in  $Y(t)$  is given by the following equation:

$$\sigma_Y^2 = C_Y(0) = \frac{1}{2\pi} \int_{-\infty}^{\infty} S_Y(\omega) d\omega. \quad (62)$$

The normalised auto covariance function is the auto correlation function.

$$P_Y(\tau) = \frac{C_Y(\tau)}{C_Y(0)}. \quad (63)$$

For a Gaussian white noise process, it is

$$S_{\xi_i, \xi_j}(\omega) = \lim_{T \rightarrow \infty} \left[ \frac{E[\tilde{\xi}_i(\omega), \tilde{\xi}_j(\omega)]}{T} \right] \\ = \lim_{T \rightarrow \infty} \frac{1}{T} \int_{-\tilde{T}/2}^{\tilde{T}/2} \int_{-\tilde{T}/2}^{\tilde{T}/2} \\ \cdot E[\xi_i(t), \xi_j(t')] e^{-i\omega(t-t')} dt dt' = \delta_{ij}. \quad (64)$$

The components of equation (57)'s solutions are as follows:

$$\tilde{u}_i(\omega) = \sum_{j=1}^4 K_{ij}(\omega) \tilde{\xi}_j(\omega); \quad i = 1, 2, 3, 4. \quad (65)$$

The range of  $u_i$ ,  $i = 1, 2, 3, 4$  is provided by the following equation:

$$S_{u_i}(\omega) = \sum_{j=1}^4 \alpha_j |K_{ij}(\omega)|^2; \quad i = 1, 2, 3, 4. \quad (66)$$

Hence the intensities of fluctuations in the variable  $u_i$ ,  $i = 1, 2, 3, 4$  are given.

As a result, the intensities of the variable's  $u_i$ ,  $i = 1, 2, 3, 4$  fluctuations are given by the following equation:

$$\sigma_{u_i}^2 = \frac{1}{2\pi} \sum_{j=1}^4 \int_{-\infty}^{\infty} \alpha_j |K_{ij}(\omega)|^2 d\omega; \quad i = 1, 2, 3, 4. \quad (67)$$

In other words, the variances of  $u_i$ ,  $i = 1, 2, 3, 4$  are calculated as follows:

$$\begin{aligned} \sigma_{u_1}^2 &= \frac{1}{2\pi} \left\{ \int_{-\infty}^{\infty} \alpha_1 \left| \frac{A_{11}(\omega)}{|M(\omega)|} \right|^2 d\omega + \int_{-\infty}^{\infty} \alpha_2 \left| \frac{A_{12}(\omega)}{|M(\omega)|} \right|^2 d\omega + \int_{-\infty}^{\infty} \alpha_3 \left| \frac{A_{13}(\omega)}{|M(\omega)|} \right|^2 d\omega + \int_{-\infty}^{\infty} \alpha_4 \left| \frac{A_{14}(\omega)}{|M(\omega)|} \right|^2 d\omega \right\}, \\ \sigma_{u_2}^2 &= \frac{1}{2\pi} \left\{ \int_{-\infty}^{\infty} \alpha_1 \left| \frac{B_{11}(\omega)}{|M(\omega)|} \right|^2 d\omega + \int_{-\infty}^{\infty} \alpha_2 \left| \frac{B_{12}(\omega)}{|M(\omega)|} \right|^2 d\omega + \int_{-\infty}^{\infty} \alpha_3 \left| \frac{B_{13}(\omega)}{|M(\omega)|} \right|^2 d\omega + \int_{-\infty}^{\infty} \alpha_4 \left| \frac{B_{14}(\omega)}{|M(\omega)|} \right|^2 d\omega \right\}, \\ \sigma_{u_3}^2 &= \frac{1}{2\pi} \left\{ \int_{-\infty}^{\infty} \alpha_1 \left| \frac{C_{11}(\omega)}{|M(\omega)|} \right|^2 d\omega + \int_{-\infty}^{\infty} \alpha_2 \left| \frac{C_{12}(\omega)}{|M(\omega)|} \right|^2 d\omega + \int_{-\infty}^{\infty} \alpha_3 \left| \frac{C_{13}(\omega)}{|M(\omega)|} \right|^2 d\omega + \int_{-\infty}^{\infty} \alpha_4 \left| \frac{C_{14}(\omega)}{|M(\omega)|} \right|^2 d\omega \right\}, \\ \sigma_{u_4}^2 &= \frac{1}{2\pi} \left\{ \int_{-\infty}^{\infty} \alpha_1 \left| \frac{D_{11}(\omega)}{|M(\omega)|} \right|^2 d\omega + \int_{-\infty}^{\infty} \alpha_2 \left| \frac{D_{12}(\omega)}{|M(\omega)|} \right|^2 d\omega + \int_{-\infty}^{\infty} \alpha_3 \left| \frac{D_{13}(\omega)}{|M(\omega)|} \right|^2 d\omega + \int_{-\infty}^{\infty} \alpha_4 \left| \frac{D_{14}(\omega)}{|M(\omega)|} \right|^2 d\omega \right\}. \end{aligned} \quad (68)$$

Here,  $M(\omega) = R(\omega) + iI(\omega)$ , where  $R(\omega)$  is the real part of  $M(\omega)$  and  $I(\omega)$  is the an imaginary part of  $M(\omega)$ ,  $|M(\omega)|^2 =$

$[R(\omega)]^2 + [I(\omega)]^2$  where  $R(\omega) = \omega^4 - \omega^2\beta^2P^*B^* - \omega^2\beta^2P^*V^* - \beta^3\beta_2V^*P^*S^*B^* - \omega^2\beta^2P^*S^*$ .

$$\begin{aligned} A_{11} &= B_2C_3D_4 - B_2C_4D_3 - B_4C_3D_2; A_{12} = B_4C_3D_1 - B_4C_1D_3; \\ A_{13} &= B_2C_4D_1 - B_2C_1D_4 + B_4C_1D_2; A_{14} = B_2C_1D_3 - B_2C_3D_1; \\ B_{11} &= A_2C_4D_3 - A_2C_3D_4 + A_4C_3D_2; B_{12} = A_1C_3D_4 - A_1C_4D_3 + A_4C_1D_3 - A_4C_3D_1; \\ B_{13} &= A_1C_4D_2 + A_2C_1D_4 - A_2C_4D_1 - A_4C_1D_2; B_{14} = A_2C_3D_1 - A_2C_1D_3 - A_1C_3D_2; \\ C_{11} &= A_4B_2D_3 - A_2B_4D_3; C_{12} = A_1B_4D_3; C_{13} = A_1B_2D_4 - A_1B_4D_2 + A_2B_4D_1 - A_4B_2D_1; C_{14} = -A_1B_2D_3; \\ C_{12} &= A_1B_4D_3; C_{13} = A_1B_2D_4 - A_1B_4D_2 + A_2B_4D_1 - A_4B_2D_1; C_{14} = -A_1B_2D_3; \\ D_{11} &= A_2B_4C_3 - A_4B_2C_3; D_{12} = -A_1B_4C_3; D_{13} = A_4B_2C_1 - A_2B_4C_1 - A_1B_2C_4; \\ D_{14} &= A_1B_2C_3; \end{aligned} \quad (69)$$

We can derive the following from these numbers and equation (68):

$$\begin{aligned} \sigma_{u_1}^2 &= \frac{1}{2\pi} \int_{-\infty}^{\infty} \frac{1}{[R(\omega)]^2 + [I(\omega)]^2} [\alpha_1 (A_{11})^2 + \alpha_2 (A_{12})^2 + \alpha_3 (A_{13})^2 + \alpha_4 (A_{14})^2] d\omega, \\ \sigma_{u_2}^2 &= \frac{1}{2\pi} \int_{-\infty}^{\infty} \frac{1}{[R(\omega)]^2 + [I(\omega)]^2} [\alpha_1 (B_{11})^2 + \alpha_2 (B_{12})^2 + \alpha_3 (B_{13})^2 + \alpha_4 (B_{14})^2] d\omega, \\ \sigma_{u_3}^2 &= \frac{1}{2\pi} \int_{-\infty}^{\infty} \frac{1}{[R(\omega)]^2 + [I(\omega)]^2} [\alpha_1 (C_{11})^2 + \alpha_2 (C_{12})^2 + \alpha_3 (C_{13})^2 + \alpha_4 (C_{14})^2] d\omega, \\ \sigma_{u_4}^2 &= \frac{1}{2\pi} \int_{-\infty}^{\infty} \frac{1}{[R(\omega)]^2 + [I(\omega)]^2} [\alpha_1 D_{11}^2 + \alpha_2 D_{12}^2 + \alpha_3 D_{13}^2 + \alpha_4 D_{14}^2] d\omega. \end{aligned} \quad (70)$$

If we are interested in the system dynamics of equations (47)–(50) with either  $\alpha_1 = 0$  (or)  $\alpha_2 = 0$  (or)  $\alpha_3 = 0$  (or)  $\alpha_4 = 0$ , then the population variances are as follows.

If  $\alpha_1 = \alpha_2 = \alpha_3 = 0$  then

$$\begin{aligned}\sigma_{u_1}^2 &= \frac{1}{2\pi} \int_{-\infty}^{\infty} \frac{1}{[R(\omega)]^2 + [I(\omega)]^2} [\alpha_4 (A_{14})^2] d\omega, \\ \sigma_{u_2}^2 &= \frac{1}{2\pi} \int_{-\infty}^{\infty} \frac{1}{[R(\omega)]^2 + [I(\omega)]^2} [\alpha_4 (B_{14})^2] d\omega, \\ \sigma_{u_3}^2 &= \frac{1}{2\pi} \int_{-\infty}^{\infty} \frac{1}{[R(\omega)]^2 + [I(\omega)]^2} [\alpha_4 (C_{14})^2] d\omega, \\ \sigma_{u_4}^2 &= \frac{1}{2\pi} \int_{-\infty}^{\infty} \frac{1}{[R(\omega)]^2 + [I(\omega)]^2} [\alpha_4 D_{14}^2] d\omega.\end{aligned}\tag{71}$$

If  $\alpha_1 = \alpha_3 = \alpha_4 = 0$  then,

$$\begin{aligned}\sigma_{u_1}^2 &= \frac{1}{2\pi} \int_{-\infty}^{\infty} \frac{1}{[R(\omega)]^2 + [I(\omega)]^2} [\alpha_2 (A_{12})^2] d\omega, \\ \sigma_{u_2}^2 &= \frac{1}{2\pi} \int_{-\infty}^{\infty} \frac{1}{[R(\omega)]^2 + [I(\omega)]^2} [\alpha_2 (B_{12})^2] d\omega, \\ \sigma_{u_3}^2 &= \frac{1}{2\pi} \int_{-\infty}^{\infty} \frac{1}{[R(\omega)]^2 + [I(\omega)]^2} [\alpha_2 (C_{12})^2] d\omega, \\ \sigma_{u_4}^2 &= \frac{1}{2\pi} \int_{-\infty}^{\infty} \frac{1}{[R(\omega)]^2 + [I(\omega)]^2} [\alpha_2 D_{12}^2] d\omega.\end{aligned}\tag{72}$$

If  $\alpha_1 = \alpha_2 = \alpha_4 = 0$  then,

$$\begin{aligned}\sigma_{u_1}^2 &= \frac{1}{2\pi} \int_{-\infty}^{\infty} \frac{1}{[R(\omega)]^2 + [I(\omega)]^2} [\alpha_3 A_{13}^2] d\omega, \\ \sigma_{u_2}^2 &= \frac{1}{2\pi} \int_{-\infty}^{\infty} \frac{1}{[R(\omega)]^2 + [I(\omega)]^2} [\alpha_3 B_{13}^2] d\omega, \\ \sigma_{u_3}^2 &= \frac{1}{2\pi} \int_{-\infty}^{\infty} \frac{1}{[R(\omega)]^2 + [I(\omega)]^2} [\alpha_3 C_{13}^2] d\omega, \\ \sigma_{u_4}^2 &= \frac{1}{2\pi} \int_{-\infty}^{\infty} \frac{1}{[R(\omega)]^2 + [I(\omega)]^2} [\alpha_3 D_{13}^2] d\omega.\end{aligned}\tag{73}$$

If  $\alpha_2 = \alpha_3 = \alpha_4 = 0$  then,

$$\begin{aligned}\sigma_{u_1}^2 &= \frac{1}{2\pi} \int_{-\infty}^{\infty} \frac{1}{[R(\omega)]^2 + [I(\omega)]^2} [\alpha_1 A_{11}^2] d\omega, \\ \sigma_{u_2}^2 &= \frac{1}{2\pi} \int_{-\infty}^{\infty} \frac{1}{[R(\omega)]^2 + [I(\omega)]^2} [\alpha_1 B_{11}^2] d\omega, \\ \sigma_{u_3}^2 &= \frac{1}{2\pi} \int_{-\infty}^{\infty} \frac{1}{[R(\omega)]^2 + [I(\omega)]^2} [\alpha_1 C_{11}^2] d\omega, \\ \sigma_{u_4}^2 &= \frac{1}{2\pi} \int_{-\infty}^{\infty} \frac{1}{[R(\omega)]^2 + [I(\omega)]^2} [\alpha_1 D_{11}^2] d\omega.\end{aligned}\tag{74}$$

Thus, for modest levels of mean square fluctuations, population variances imply nodes stability, whereas larger values of variances suggest nodes instability.

## 7. Numerical Simulations

In this section, we present a Numerical Simulation to validate of our analytical findings in this paper with help of Matlab software [30].

For the parameters,  $\lambda = 4, \beta_1 = 0.02, \beta_2 = 0.01, \beta = 0.02, \gamma_1 = 0.3, \gamma_2 = 0.1, \delta = 0.4, \alpha = 0.1$ .

In the case of the absence of delay, the endemic equilibrium point  $E_* E_*$  (19.6227, 0.5138, 1.9337, 16.1464) is locally asymptotically stable, and corresponding time series is shown in Figure 1 [31].

In the presence of delay, for the value of  $\tau = 30.50 < 40.50$ , the endemic equilibrium point is  $E_*$  (19.6227, 0.5138, 1.9337, 16.1464) locally asymptotically stable and the dynamical behavior of the time series as shown in Figure 2 [32].

Furthermore, we increase the delay value the system equation (1) undergoes a Hopf-Bifurcation at the endemic equilibrium [33] point  $E_*$  (19.6227, 0.5138, 1.9337, 16.1464) and a family of bifurcating periodic solutions at  $\tau = 35.650 = \tau^*$ . Bifurcation from  $E_*$  (19.6227, 0.5138, 1.9337, 16.1464) which can be shown using the corresponding time series for this case in Figure 3.

Finally, if  $\tau = 40.50 > \tau^*$ , the system losses its stability and becomes unstable, then the corresponding time series as shown in Figure 4 [34].

Also, the phase portrait of S-L-P with  $\tau = 30.50 < \tau^*$  and  $\tau = 40.50 > \tau^*$  as shown in Figures 5 and 6.

Also, the phase portrait of S-B-L with [35],  $\tau = 30.50 < \tau^*$  and  $\tau = 40.50 > \tau^*$  as shown in Figures 7 and 8.

**7.1. Numerical Observations.** If there is no delay, the endemic equilibrium  $E_*$  is really  $E_*$  (19.6227, 0.5138, 1.9337, 16.1464) is locally asymptotically stable and the corresponding time series is shown in Figure 1. Figure 9 represents the time series evaluation of nodes for the values of example 1 in the presence of stochastic parameters [36]. At the values of noise intensities  $\alpha_1 = 0.01; \alpha_2 = 0.02; \alpha_3 = 0.01; \alpha_4 = 0.02$  time series evaluation of four nodes, which are S(t), L(t), B(t), and P(t) are captured in Figure 9 [37]. At these low noise values, the proposed system (SLBP) is also less affected and clearly shown as less fluctuating [38]. Figure 10 represents the time series evaluation of nodes for the values of example 1 in the presence of stochastic parameters [39]. At the values of noise intensities  $\alpha_1 = 0.04; \alpha_2 = 0.05; \alpha_3 = 0.04; \alpha_4 = 0.05$  time series evaluation of four nodes, which are S(t), L(t), B(t), and P(t) are captured in Figure 10 [40].

At these low noise values, the proposed system (SLBP) is also a little less affected and clearly shown as a little less fluctuating [41]. Figure 11 represents the time series evaluation of nodes for the values of example 1 in the presence of stochastic parameters. At the values of noise intensities,  $\alpha_1 = 0.1; \alpha_2 = 0.2; \alpha_3 = 0.1; \alpha_4 = 0.2$  time series evaluation of four

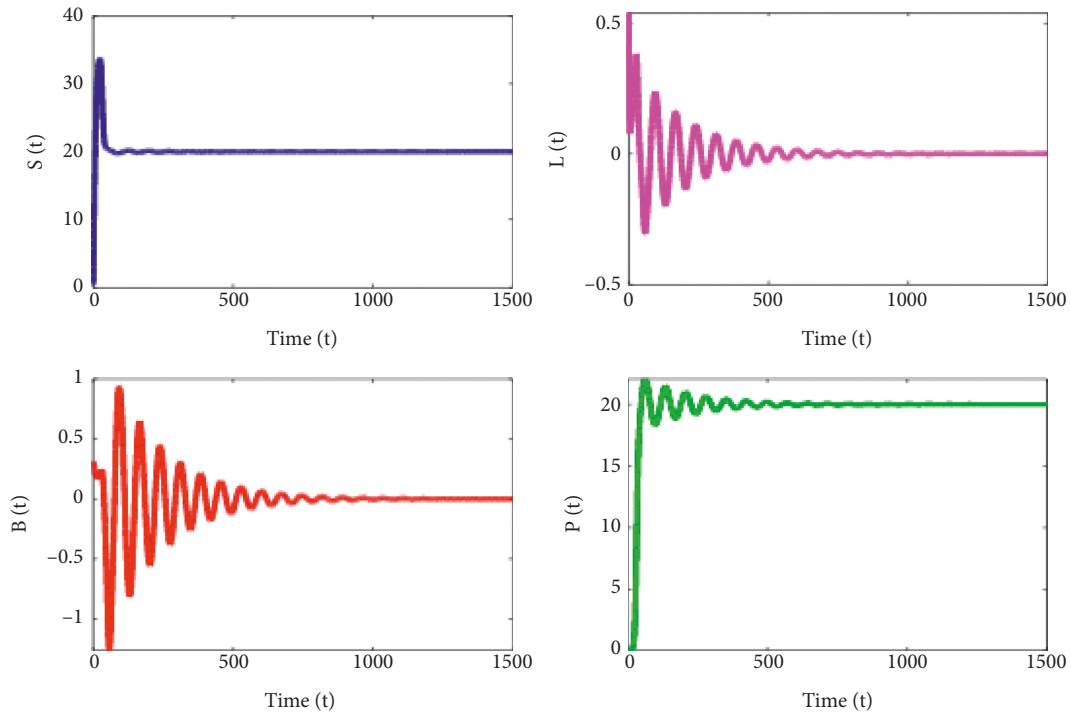


FIGURE 1: Time history of  $S$ ,  $L$ ,  $B$ , and  $P$  computers with the attributes mentioned in Section 7, in presence of delay.

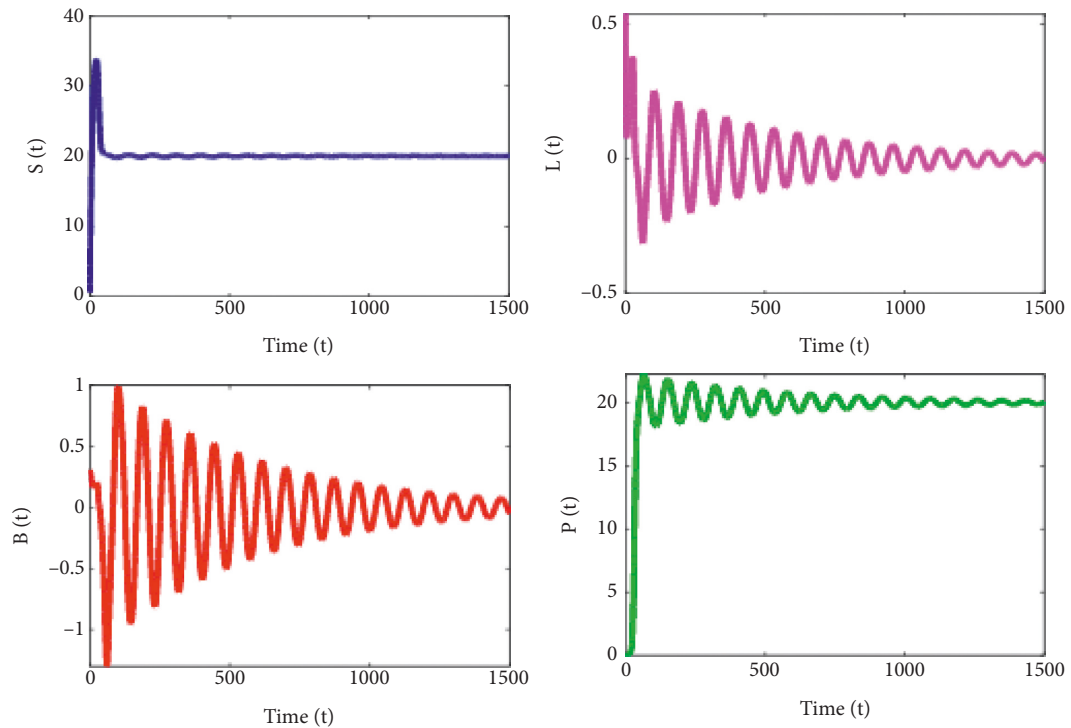


FIGURE 2: Time history of  $S$ ,  $L$ ,  $B$ , and  $P$  computers with the attributes mentioned in Section 7, with  $\tau = 30.50$ .

nodes [42], which are  $S(t)$ ,  $L(t)$ ,  $B(t)$ , and  $P(t)$  are captured in Figure 11. At these values of noise, the proposed system (SLBP) is affected remarkably [43] and clearly notable fluctuations in the projections as  $P(t)$  increases and  $S(t)$  is started decreasing. Both  $P(t)$  and  $B(t)$  are affected and

fluctuates more rapidly when compared with  $S(t)$  and  $L(t)$  [44]. Figures 11(a)–11(d) are the Phase portrait plot for the nodes  $S(t)$ ,  $L(t)$ ,  $B(t)$ , and  $P(t)$  with various combinations. Figure 11(a) represents the phase portrait plot for the nodes  $S(t)$ ,  $L(t)$ , and  $B(t)$  with the values of Example 1 along with

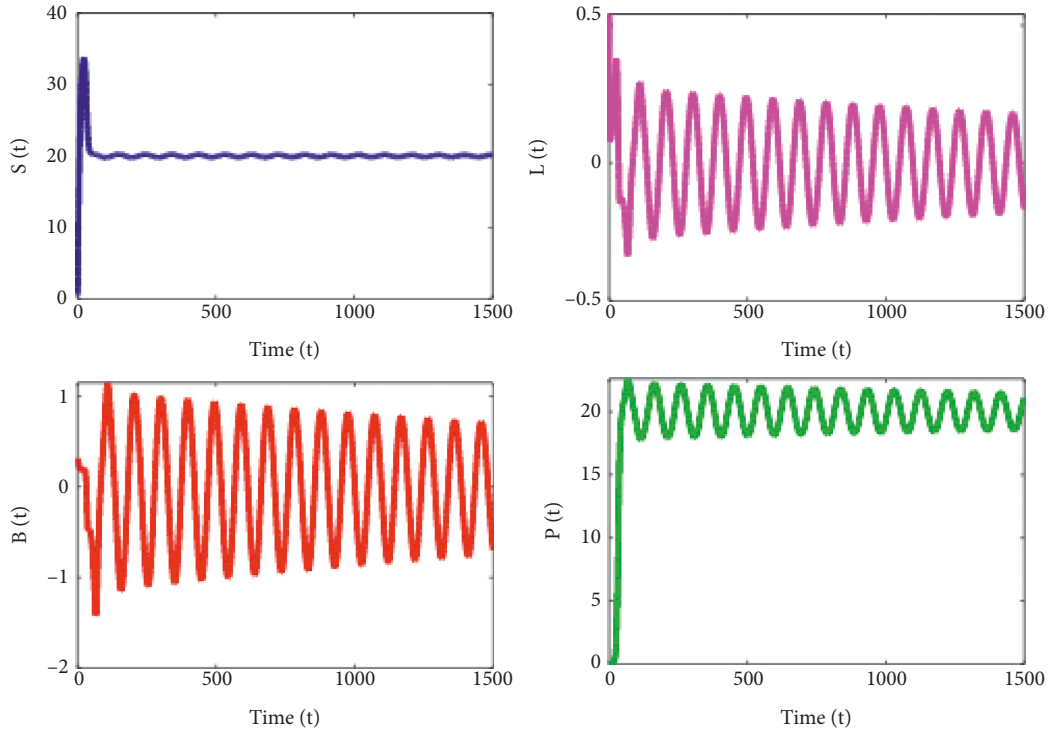


FIGURE 3: Time history of  $S$ ,  $L$ ,  $B$ , and  $P$  computers with the attributes mentioned in Section 7, with  $\tau = 35.650 = \tau'$ .

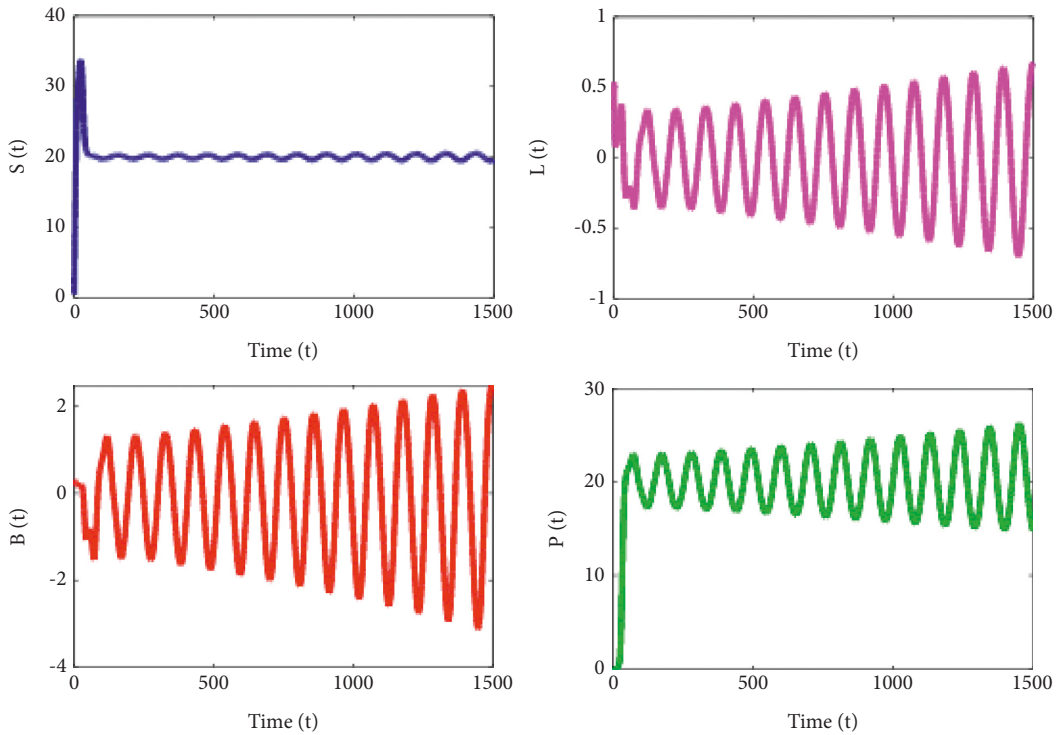


FIGURE 4: Time history of  $S$ ,  $L$ ,  $B$ , and  $P$  computers with the attributes mentioned in Section 7, with  $\tau = 40.05 > \tau'$ .

noise intensities 0.1, 0.2, 0.1, and 0.2 for  $S(t)$ ,  $L(t)$ ,  $B(t)$ , and  $P(t)$ . Figure 11(b) represents the phase portrait plot for the nodes  $L(t)$ ,  $B(t)$ , and  $P(t)$  with the values of Example -1 along with noise intensities 0.1, 0.2, 0.1, and 0.2 for  $S(t)$ ,  $L(t)$ ,  $B(t)$

and  $P(t)$  [45]. Figure 11(c) represents the phase portrait plot for the nodes  $S(t)$ ,  $L(t)$ , and  $P(t)$  with the values of Example -1 along with noise intensities 0.1, 0.2, 0.1, and 0.2 for  $S(t)$ ,  $L(t)$ ,  $B(t)$ , and  $P(t)$ . Figure 11(d) represents the phase portrait

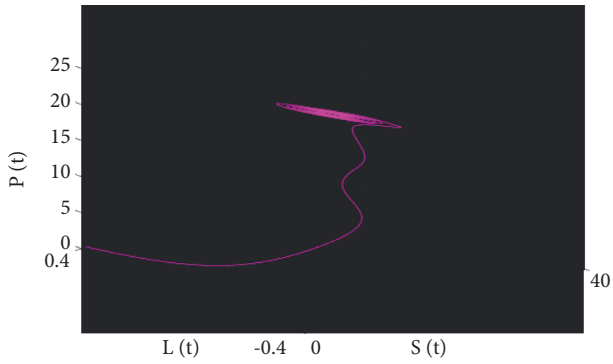


FIGURE 5: Dynamical behaviour of the system equation (1) projection  $S$ - $L$ - $P$  with  $\tau = 30.05 < \tau'$ .

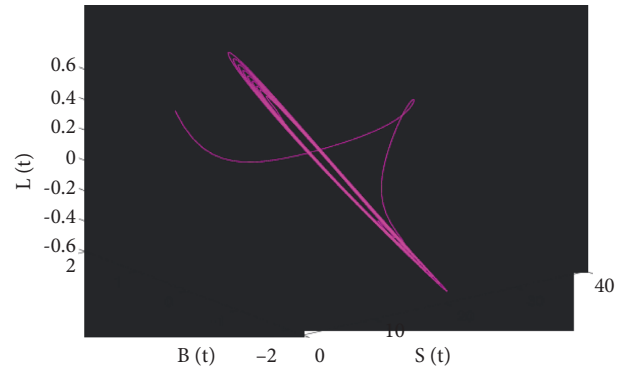


FIGURE 8: Dynamical behaviour of the system equation (1) projection  $S$ - $B$ - $L$  with  $\tau = 40.50 > \tau'$ .

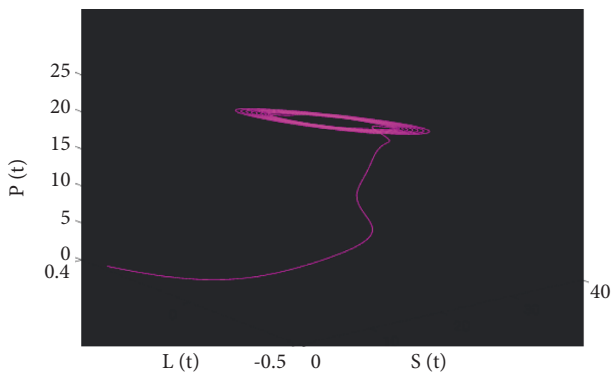


FIGURE 6: Dynamical behaviour of the system equation (1) projection  $S$ - $L$ - $P$  with  $\tau = 40.05 > \tau'$ .

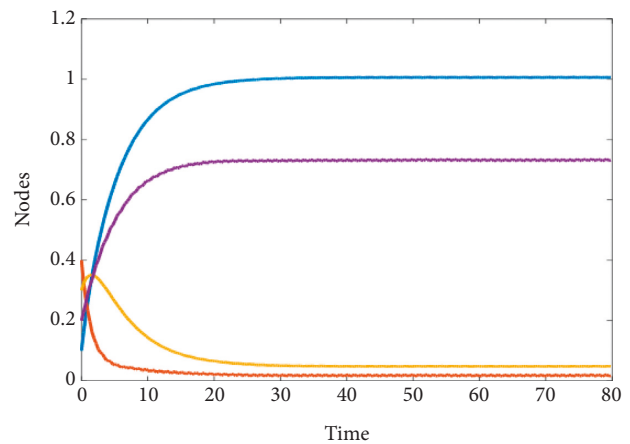


FIGURE 9: Representing time series evaluation of nodes for the values of the attributes of example 1 with noise intensities.  $a_1 = 0.01; a_2 = 0.02; a_3 = 0.01; a_4 = 0.02$ .

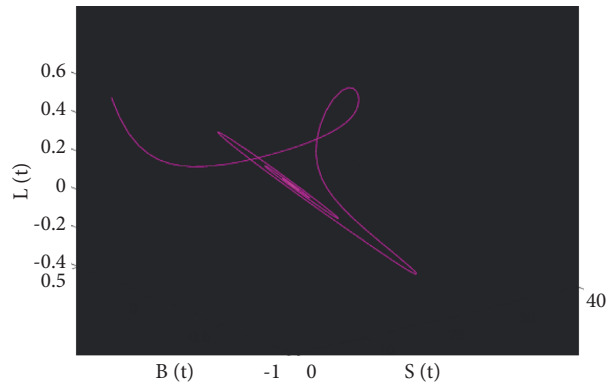


FIGURE 7: Dynamical behaviour of the system equation (1) projection  $S$ - $B$ - $L$  with  $\tau = 25.16 < \tau'$ .

plot for the nodes  $S(t)$ ,  $B(t)$ , and  $P(t)$  with the values of Example -1 along with noise intensities 0.1, 0.2, 0.1, and 0.2 for  $S(t)$ ,  $L(t)$ ,  $B(t)$ , and  $P(t)$ . Figures 11(a), 11(b), and 11(d) show that noise intensity greatly affects the system. Figure 11(c) shows that noise intensity is not affecting much the system [46].

Figure 12 represents the time series evaluation of nodes for the values of example 1 in the presence of stochastic parameters. The values of noise intensities/time series evaluation of four nodes, which are  $S(t)$ ,  $L(t)$ ,  $B(t)$ , and  $P(t)$ , is captured in Figure 12. At these values of noise, the

proposed system (SLBP) is affected remarkably and notable fluctuations in the projections as  $P(t)$  is increased and  $S(t)$  is started decreasing. Both  $P(t)$  and  $B(t)$  affected greatly and fluctuated more rapidly when compared with  $S(t)$  and  $L(t)$ . Figure 13 represents the time series evaluation of nodes for the values of example 1 in the presence of stochastic parameters. At the values of noise intensities  $\alpha_1 = 4; \alpha_2 = 5; \alpha_3 = 4; \alpha_4 = 5$  time series evaluation of four nodes, which are  $S(t)$ ,  $L(t)$ ,  $B(t)$ , and  $P(t)$  are captured in Figure 13. At these values of noise, the proposed system (SLBP) is affected greatly, and oscillatory fluctuations in the projections as  $P(t)$  increases and  $S(t)$  decreases, and  $S(t)$  moves very close to  $B(t)$  and  $L(t)$ . Both  $P(t)$ , and  $B(t)$  affected greatly and fluctuates more rapidly when compared with  $S(t)$ ,  $L(t)$ .

Figures 13(a)–13(d) are the Phase portrait plot for the nodes  $S(t)$ ,  $L(t)$ ,  $B(t)$ , and  $P(t)$  with various combinations. Figure 13(a) represents the phase portrait plot for the nodes  $S(t)$ ,  $L(t)$ , and  $B(t)$  with the values of Example -1 along with noise intensities 10, 20, 10, and 20 for  $S(t)$ ,  $L(t)$ ,  $B(t)$ , and  $P(t)$ . Figure 13(b) represents the phase portrait plot for the



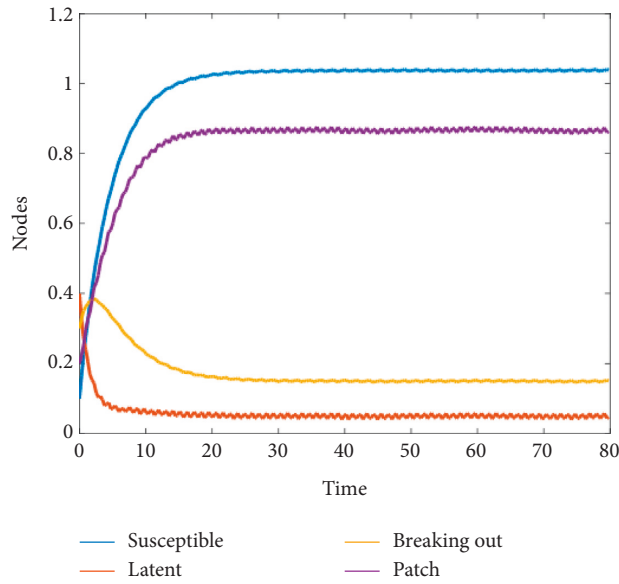
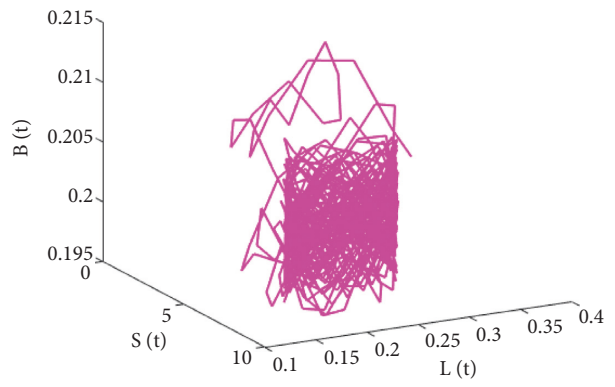
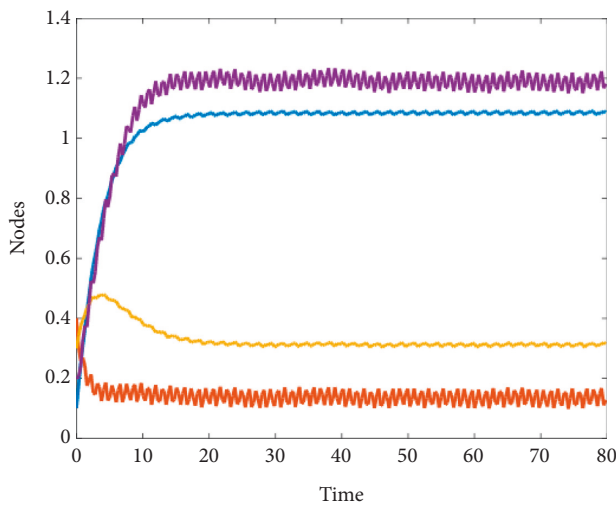
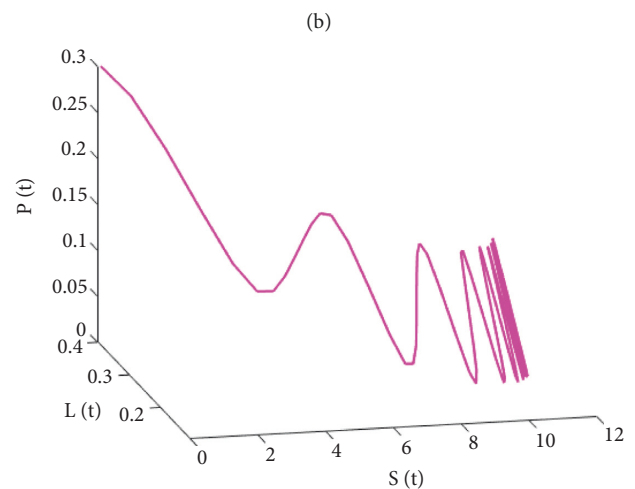
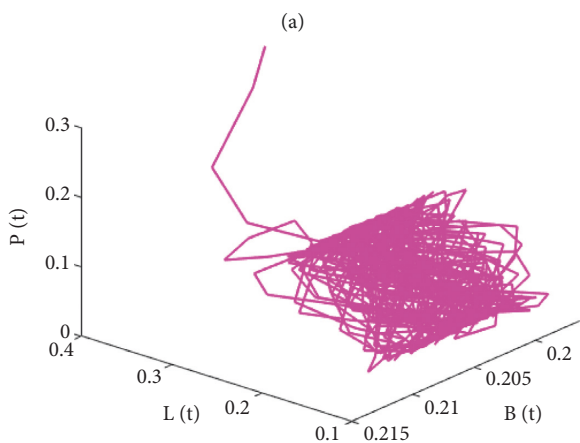


FIGURE 10: Showing time series evaluation of nodes for the values of the attributes of example 1 with noise intensities  $a_1 = 0.04; a_2 = 0.05; a_3 = 0.04; a_4 = 0.05$ .



(a) Susceptible Breaking out  
Latent Patch



(c)

(d)

FIGURE 11: Continued.

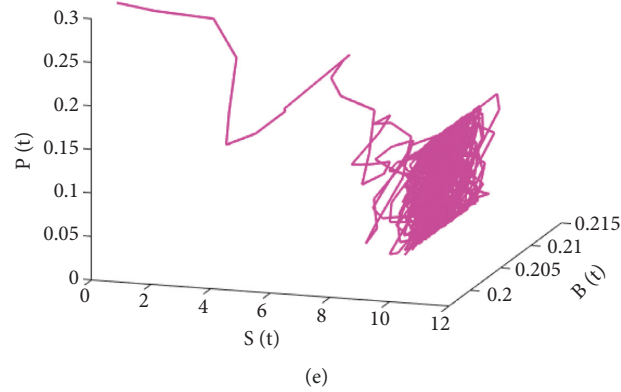


FIGURE 11: (a) Representing time series evaluation of nodes for the values of the attributes of example 1 with noise intensities  $a_1 = 0.1; a_2 = 0.2; a_3 = 0.1; a_4 = 0.2$ . (b) Representing the phase portrait diagram of the nodes  $S(t), L(t)$ , and  $B(t)$ . (c) Representing the phase portrait diagram of the nodes  $L(t), B(t)$ , and  $P(t)$ . (d) Representing the phase portrait diagram of the nodes  $S(t), L(t)$  and  $P(t)$ . (e) Representing the phase portrait diagram of the nodes  $S(t), B(t)$ , and  $P(t)$ .

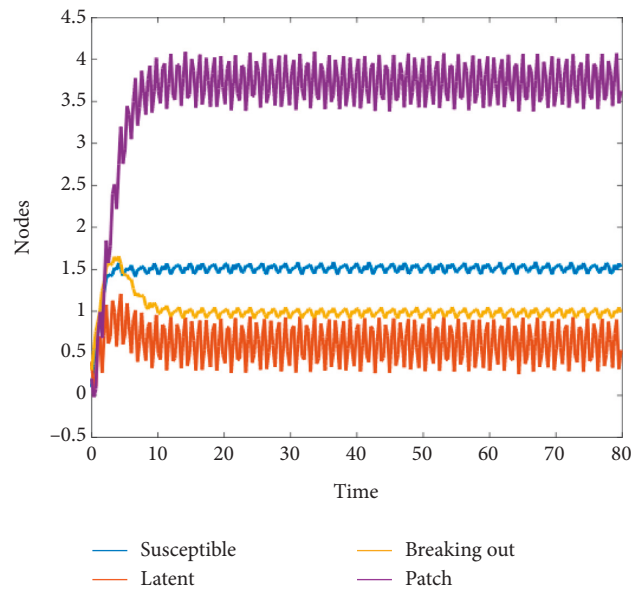


FIGURE 12: Representing time series evaluation of nodes for the values of the attributes of example 1 with noise intensities.

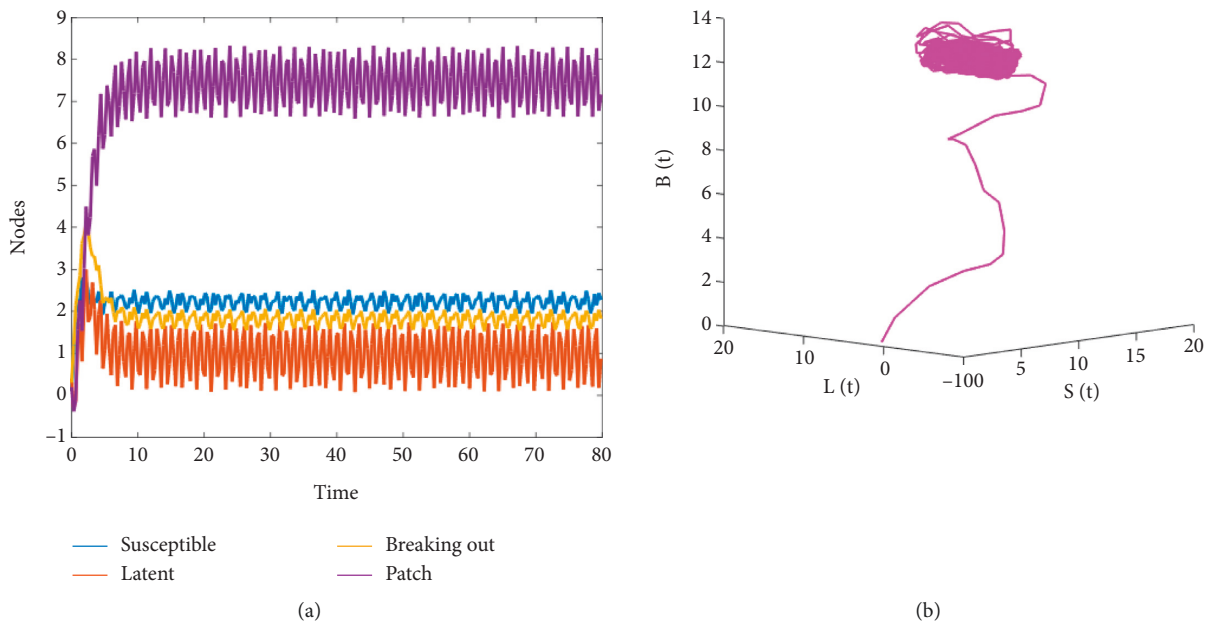


FIGURE 13: Continued.

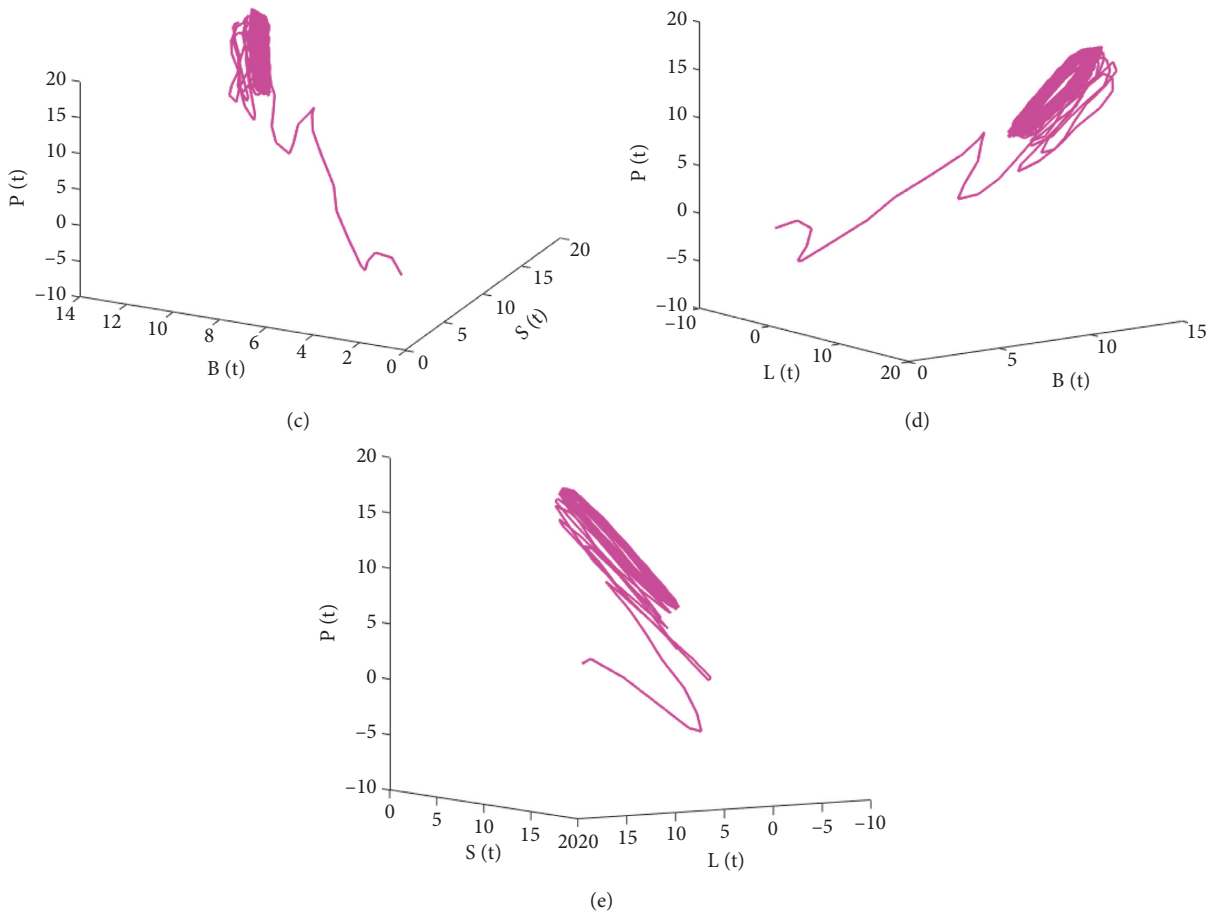


FIGURE 13: (a) Representing time series evaluation of nodes for the values of the attributes of example 1 with noise intensities. (b) Representing the phase portrait diagram of the nodes  $S(t)$ ,  $L(t)$ , and  $B(t)$ . (c) Representing the phase portrait diagram of the nodes  $S(t)$ ,  $B(t)$ , and  $P(t)$ . (d) Representing the phase portrait diagram of the nodes  $L(t)$ ,  $B(t)$ , and  $P(t)$ . (e) Representing the phase portrait diagram of the nodes  $S(t)$ ,  $L(t)$ , and  $P(t)$ .

nodes  $S(t)$ ,  $B(t)$ , and  $P(t)$  with the values of Example -1 along with noise intensities 10, 20, 10, and 20 for  $S(t)$ ,  $L(t)$ ,  $B(t)$ , and  $P(t)$ . Figure 13(c) represents the phase portrait plot for the nodes  $L(t)$ ,  $B(t)$ , and  $P(t)$  with the values of Example -1 along with noise intensities 10, 20, 10, and 20 for  $S(t)$ ,  $L(t)$ ,  $B(t)$ , and  $P(t)$ .

Figure 13(d) represents the phase portrait plot for the nodes  $S(t)$ ,  $L(t)$ , and  $P(t)$  with the values of Example -1 along with noise intensities 10, 20, 10, and 20 for  $S(t)$ ,  $L(t)$ ,  $B(t)$ , and  $P(t)$ . Figure 14 represents the time series evaluation of nodes for the values of example 1 in the presence of stochastic parameters. The values of noise intensities/time series evaluation of four nodes, which are  $S(t)$ ,  $L(t)$ ,  $B(t)$ , and  $P(t)$ , is captured in Figure 14. The proposed system (SLBP) is affected greatly by these noise values. Rapid fluctuations in the projections as  $P(t)$  increases and  $S(t)$  decreases, and all three projections of  $S(t)$ ,  $B(t)$ , and  $L(t)$  emerge; all  $P(t)$ ,  $S(t)$ ,  $B(t)$ , and  $L(t)$  is affected greatly and fluctuates more rapidly and oscillatory.

Figures 15 and 16 are time-series plots (deterministic graphs) of nodes for the values of Example-I in the absence of noise. Figures clearly show that the system attains stability

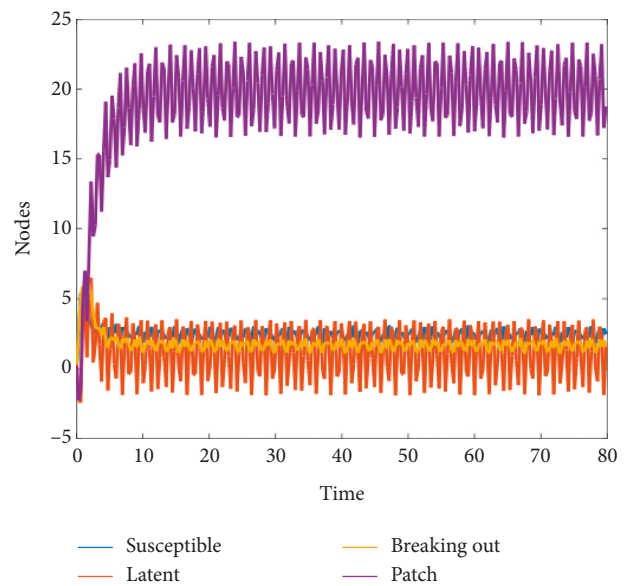


FIGURE 14: Representing time series evaluation of nodes for the values of the attributes of example 1 with noise intensities.

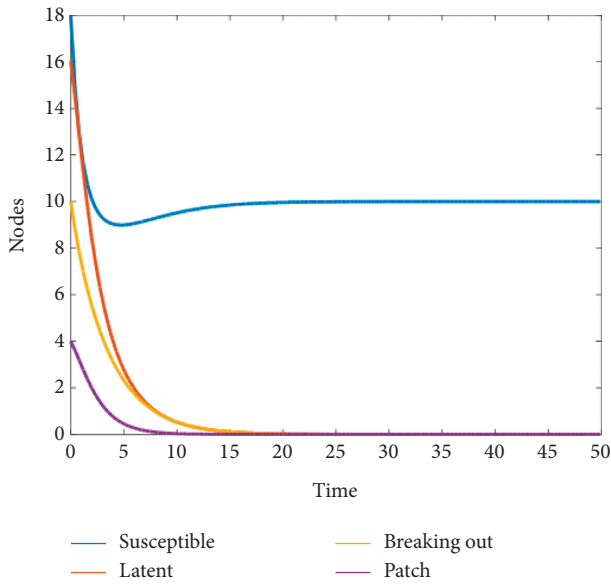


FIGURE 15: Representing the time series plot (deterministic graph) for the nodes  $S(t)$ ,  $L(t)$ ,  $B(t)$ , and  $P(t)$  for the values of example-I.

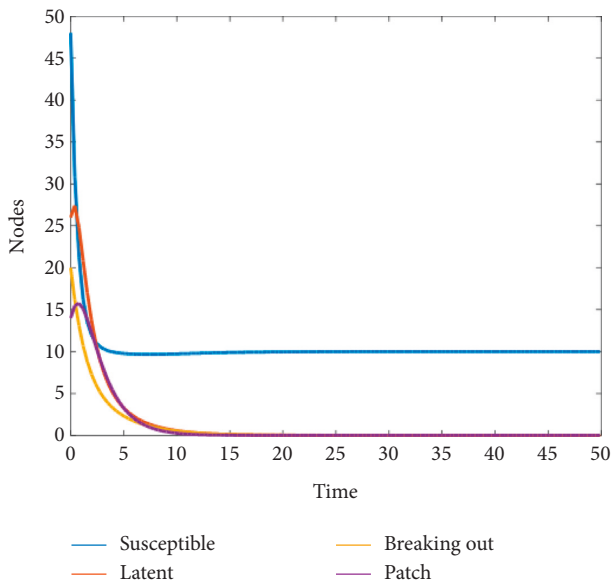


FIGURE 16: Representing the time series plot (deterministic graph) for the nodes  $S(t)$ ,  $L(t)$ ,  $B(t)$ , and  $P(t)$  for the values of example-I.

in a very short span in the absence of stochastic parameters in the proposed system. Whereas Figures 9–14 clearly show that noise affects the system SLBP greatly and the figures exhibit the disturbances in the form of oscillatory behaviour for various noise intensity values. The system is highly oscillatory at higher values of the noise intensity, which is captured by computer simulations, particularly from Figures 10–14.

### 8. Conclusions

We proposed a four compartmental model for understanding the complexity and exploitation created by virus

and their impacts on networks. With this aim, we proposed an SLBS model consisting of  $S(t)$ ,  $L(t)$ ,  $B(t)$ , and  $P(t)$ . Under certain conditions, the local stability of all equilibrium points is investigated. The delay parameter was set, and we established the occurrence of a Hopf bifurcation as it crossed a crucial point by both analytical and numerical analysis. We also used the centre manifold theorem and normal form theory to investigate the properties of the Hopf bifurcation. We performed numerical simulation tests under various scenarios with appropriate sample values to support the theoretical findings.

Furthermore, this article investigates the prospects of infected node eradication and patched node persistence in a computer network. The proposed model exhibits rich dynamics for various studies like delay and Hopf bifurcation analysis. This model exhibits effective rich dynamics in the presence of delay particularly after reaching a certain value as  $\tau = 30.50$ . It is very clearly shown in the numerical findings that the system bifurcates and exhibits its dynamics at  $\tau = 30.650 = \tau^*$ . Phase portrait figures are drawn for various combinations under different delay parameter values, which are clearly presented the delay dynamics of the system. Delay dynamics exhibited by the system by both ways, analytically and numerically are captured and presented greatly.

We also focussed on the impact of additive white noise in the proposed system. We introduced noise intensities as stochastic parameters to the system and studied the stochastic model by linearizing the model using the perturbation technique and applying Fourier Transform. By finding out the noise intensities under certain constraints, the system should attain its steadiness as per the values of distinct noise parameters. Analytical results are checked with numerical simulations with appropriate example values. Notable numerical observations are discussed based on the various noise intensity values. The proposed model exhibits rich dynamics for various intensity values numerically and analytically, which is captured in stochastic analysis.

*Future Scope:* we can go for more deterministic graphs with parameter variations in terms of Sensitivity analysis is one of the approaches which allows to study and draw some interesting results. We can reconstruct this model in partial differential equations, including diffusive parameters, to catch the spatiotemporal dynamics more innovatively.

### Data Availability

The data used to support the findings of this study are included within the article.

### Conflicts of Interest

The authors declare that there are no conflicts of interest regarding the publication of this paper.

### Acknowledgments

The authors gave thanks to the Wuxi Institute of Technology, Wuxi for providing support to complete this research work.

## References

- [1] J. Wakefield, "Ecologic studies revisited," *Annual Review of Public Health*, vol. 29, no. 1, pp. 75–90, 2008.
- [2] H. Cao, S. Wang, D. Yan, H. Tan, and H. Xu, "The dynamical analysis of computer viruses model with age structure and delay," *Discrete Dynamics in Nature and Society*, vol. 2021, no. 1, 13 pages, Article ID 5538438, 2021.
- [3] Z. Zhang, Y. Wang, and L. Guerrini, "Bifurcation analysis of a delayed worm propagation model with saturated incidence," *Advances in Mathematical Physics*, vol. 2018, Article ID 7619074, 9 pages, 2018.
- [4] Z. Zhang and L. Song, "Dynamics of a delayed worm propagation model with quarantine," *Advances in Difference Equations*, vol. 2017, no. 1, pp. 155–168, 2017.
- [5] C. Nwokoye, I. Umeh, and O. Ositanwosu, *Characterization of Heterogeneous Malware Contagions In Wireless Sensor Networks: A Case Of Uniform Random Distribution*, vol. 154, Springer Nature, Lecture Notes in Networks and Systems: ICT Analysis and Applications Networks, pp. 813–821, 2020.
- [6] W. S. Bahashwan and S. M. Al-Tuwairqi, "Modeling the effect of external computers and removable devices on a computer network with heterogeneous immunity," *International Journal of Differential Equations*, vol. 2021, Article ID 6694098, 13 pages, 2021.
- [7] X. Zhang and Y. Li, "Modelling and analysis of propagation behavior of computer viruses with nonlinear countermeasure probability and infected removable storage media," *Discrete Dynamics in Nature and Society*, vol. 2020, Article ID 8814319, 7 pages, 2020.
- [8] N. D. K. Reddy Chukka, A. Arivumangai, S. Kumar et al., "Environmental impact and carbon footprint assessment of sustainable buildings: an experimental investigation," *Adsorption Science and Technology*, vol. 2022, Article ID 8130180, 8 pages, 2022.
- [9] D. Veeman, D. Duraisami, G. J. Surendhar, L. Natrayan, B. Stalin, and Ramaswamy, "Systematic review on nine hallmarks of neurodegenerative disease," *Indian Journal of Biochemistry & Biophysics*, vol. 59, no. 3, pp. 249–257, 2022.
- [10] X. Yang and L. X. Yang, "Towards the epidemiological modeling of computer viruses," *Discrete Dynamics in Nature and Society*, vol. 2012, Article ID 259671, 11 pages, 2012.
- [11] L. X. Yang, X. Yang, L. Wen, and J. Liu, "A novel computer virus propagation model and its dynamics," *International Journal of Computer Mathematics*, vol. 89, no. 17, pp. 2307–2314, 2012.
- [12] L. X. Yang, X. Yang, J. Liu, Q. Zhu, and C. Gan, "Epidemics of computer viruses: a complex-network approach," *Applied Mathematics and Computation*, vol. 219, no. 16, pp. 8705–8717, 2013.
- [13] X. Yang, B. Liu, and C. Gan, "Global stability of an epidemic model of computer virus," *Abstract and Applied Analysis*, vol. 2014, Article ID 456320, 5 pages, 2014.
- [14] Z. Zhang, Y. Wang, and M. Ferrara, "Stability and hopf bifurcation for a delayed computer virus model with antidote in vulnerable system," *Journal of Control Science and Engineering*, vol. 2017, no. 1, 9 pages, Article ID 9360430, 2017.
- [15] L. X. Yang and X. Yang, "The impact of nonlinear infection rate on the spread of computer virus," *Nonlinear Dynamics*, vol. 82, no. 1–2, pp. 85–95, 2015.
- [16] L. X. Yang, M. Draief, and X. Yang, "The impact of the network topology on the viral prevalence: a node-based approach," *PLoS One*, vol. 10, no. 7, Article ID e0134507, 15 pages, 2015.
- [17] X. Zhang, "Modeling the spread of computer viruses under the effects of infected external computers and removable storage media," *International Journal of Security and Its Applications*, vol. 10, no. 3, pp. 419–428, 2016.
- [18] Z. Zhang and D. Bi, "Dynamical analysis of a computer virus propagation model with delay and infectivity in latent period," *Discrete Dynamics in Nature and Society*, vol. 2016, Article ID 3067872, 9 pages, 2016.
- [19] Z. Zhang and Y. Wang, "Qualitative analysis for a delayed epidemic model with latent and breaking-out over the Internet," *Advances in Difference Equations*, vol. 2017, no. 1, pp. 31–13, 2017.
- [20] C. Zhang, "Global behavior of a computer virus propagation model on multilayer networks," *Security and Communication Networks*, vol. 2018, Article ID 2153195, 9 pages, 2018.
- [21] T. Zhao and D. Bi, "Hopf bifurcation analysis for an epidemic model over the Internet with two delays," *Advances in Difference Equations*, vol. 2018, p. 97, 2018.
- [22] Z. Zhang, S. Kumari, and R. K. Upadhyay, "A delayed e-epidemic SLBS model for computer virus," *Advances in Difference Equations*, vol. 2019, p. 414, 2019.
- [23] Q. Zhu, P. Xiang, X. Luo, and C. Gan, "Dynamical behavior of hybrid propagation of computer viruses," *Security and Communication Networks*, Article ID 2576685, 15 pages, 2022.
- [24] Z. Zhang, R. K. Upadhyay, D. Bi, and R. Wei, "Stability and hopf bifurcation of a delayed epidemic model of computer virus with impact of antivirus software," *Discrete Dynamics in Nature and Society*, vol. 2018, Article ID 8239823, 18 pages, 2018.
- [25] K. S. Behal, S. Gakkhar, and T. Srivastava, "Dynamics of virus-patch model with latent effect," *International Journal of Computer Mathematics*, vol. 99, no. 9, pp. 1754–1769, 2022, –16.
- [26] C. H. Nwokoye and V. Madhusudanan, "Epidemic models of malicious-code propagation and control in wireless sensor networks: an indepth review," *Wireless Personal Communications*, vol. 125, no. 2, pp. 1827–1856, 2022.
- [27] Z. Zhang and R. K. Upadhyay, "Dynamical analysis for a deterministic SVIRS epidemic model with Holling type II incidence rate and multiple delays," *Results in Physics*, vol. 24, Article ID 104181, 2021.
- [28] R. M. Nisbet and W. S. Gurney, *Modelling Fluctuating Populations*, John Wiley, New York, 1982.
- [29] M. Carletti, "Numerical simulation of a Campbell-like stochastic delay model for bacteriophage infection," *Mathematical Medicine and Biology: A Journal of the IMA*, vol. 23, no. 4, pp. 297–310, 2006.
- [30] G. Kanimozhi, L. Natrayan, S. Angalaeswari, and P. Paramasivam, "An effective charger for plug-in hybrid electric vehicles (PHEV) with an enhanced PFC rectifier and ZVS-ZCS DC/DC high-frequency converter," *Journal of Advanced Transportation*, vol. 2022, Article ID 7840102, 14 pages, 2022.
- [31] A. sendrayaperumal, S. Mahapatra, S. S. Parida et al., "Energy auditing for efficient planning and implementation in commercial and residential buildings," *Advances in Civil Engineering*, vol. 2021, Article ID 1908568, 10 pages, 2021.
- [32] S. S. Sundaram, N. Hari Basker, and L. Natrayan, "Smart clothes with bio-sensors for ECG monitoring," *International Journal of Innovative Technology and Exploring Engineering*, vol. 8, no. 4, pp. 298–301, 2019.
- [33] V. Balaji, S. Kaliappan, D. M. Madhuvanesan et al., "Combustion analysis of biodiesel-powered propeller engine for least environmental concerns in aviation industry," *Aircraft*

- Engineering & Aerospace Technology*, vol. 94, no. 5, pp. 760–769, 2022.
- [34] Anupama, L. Natrayan, E. Laxmi Lydia et al., “Deep learning with backtracking search optimization-based skin lesion diagnosis model,” *Computers, Materials & Continua*, vol. 70, no. 1, pp. 1297–1313, 2021.
- [35] K. R. Vaishali, S. R. Rammohan, L. Natrayan, D. Usha, and V. R. Niveditha, “Guided container selection for data streaming through neural learning in cloud,” *International Journal of System Assurance Engineering and Management*, vol. 16, pp. 1–7, 2021.
- [36] L. P. Natrayan, P. Sakthi Shunmuga Sundaram, and J. Elumalai, “Analyzing the Uterine physiological with MMG Signals using SVM,” *International journal of pharmaceutical research*, vol. 11, no. 2, pp. 165–170, 2019.
- [37] K. Seeniappan, B. Venkatesan, and N. N. Krishnan, “A comparative assessment of performance and emission characteristics of a DI diesel engine fuelled with ternary blends of two higher alcohols with lemongrass oil biodiesel and diesel fuel,” *Energy & Environment*, vol. 13, Article ID 0958305X2110513, 2021.
- [38] S. Magesh, V. R. Niveditha, P. S. Rajakumar, S. Radha RamMohan, and L. Natrayan, “Pervasive computing in the context of COVID-19 prediction with AI-based algorithms,” *International Journal of Pervasive Computing and Communications*, vol. 16, no. 5, pp. 477–487, 2020.
- [39] D. K. Jain, S. K. S. Tyagi, S. Neelakandan, M. Prakash, and L. Natrayan, “Metaheuristic optimization-based resource allocation technique for cybertwin-driven 6G on IoE environment,” *IEEE Transactions on Industrial Informatics*, vol. 18, no. 7, pp. 4884–4892, 2022.
- [40] S. Kaliappan, M. D. Raj Kamal, S. Mohanamurugan, and P. K. Nagarajan, “Analysis of an innovative connecting rod by using finite element method,” *Taga Journal Of Graphic Technology*, vol. 14, pp. 1147–1152, 2018.
- [41] K. Nagarajan, A. Rajagopalan, S. Angalaeswari, L. Natrayan, and W. D. Mammo, “Combined economic emission dispatch of microgrid with the incorporation of renewable energy sources using improved mayfly optimization algorithm,” *Computational Intelligence and Neuroscience*, vol. 2022, Article ID 6461690, 22 pages, 2022.
- [42] P. Asha, L. Natrayan, B. T. Geetha et al., “IoT enabled environmental toxicology for air pollution monitoring using AI techniques,” *Environmental research*, vol. 205, Article ID 112574, 2022.
- [43] A. S. Kaliappan, S. Mohanamurugan and P. K. Nagarajan, Numerical investigation of sinusoidal and trapezoidal piston profiles for an IC engine,” *Journal of Applied Fluid Mechanics*, vol. 13, no. 1, pp. 287–298, 2020.
- [44] C. H. Nwokoye, V. Madhusudanan, M. N. Srinivas, and N. N. Mbeledogu, “Modeling time delay, external noise and multiple malware infections in wireless sensor networks,” *Egyptian Informatics Journal*, vol. 23, no. 2, pp. 303–314, 2022.
- [45] H. Zhang, V. Madhusudanan, R. Geetha, M. N. Srinivas, and C. H. Nwokoye, “Dynamic analysis of the e-SITR model for remote wireless sensor networks with noise and sokol-howell functional response,” *Results in Physics*, vol. 38, Article ID 105643, 2022.
- [46] L. Zhu, H. Zhao, and X. Wang, “Bifurcation analysis of a delay reaction diffusion malware propagation model with feedback control,” *Communications in Nonlinear Science and Numerical Simulation*, vol. 22, no. 1-3, pp. 747–768, 2015.

## Research Article

# Parameter Calibration of Sediment Transport Capacity Formula of the Third Entrance of Xinqiman Reservoir in Tarim River Based on CCHE2D Model

Yixin Geng, Yujian Li , Liang Mao, and Peng An

College of Hydraulic and Civil Engineering, Xinjiang Agricultural University, Urumqi, Xinjiang 830052, China

Correspondence should be addressed to Yujian Li; yujianli@xjau.edu.cn

Received 10 May 2022; Accepted 6 July 2022; Published 2 August 2022

Academic Editor: Dinesh Kumar Saini

Copyright © 2022 Yixin Geng et al. This is an open access article distributed under the Creative Commons Attribution License, which permits unrestricted use, distribution, and reproduction in any medium, provided the original work is properly cited.

In this study, sediment transport at the third entrance of the Xinqiman Reservoir in the Tarim River was simulated using the CCHE2D model. The flow conditions, the suspended sediment concentration of each grain size, and the boundary grain size of the wash load in the reach were determined. Regressions between the suspended sediment concentration,  $S$ , and flow condition,  $U^3/gH$ , and flow-sediment factor,  $U^3/R\omega$ , were developed, which strongly adhered to the power law and Zhang Ruijin's formula for the sediment transport capacity. The parameters in Zhang Ruijin's formula for the target reach were determined. Under the defined flow and sediment conditions, sediment particles  $\geq 0.091$  mm and particles  $\leq 0.061$  can be regarded as the bed material and wash loads, respectively. Using multivariate linear regression, the sediment transport capacity coefficient ( $k_0$ ) and exponent ( $m$ ) were determined to be 0.0197 and 0.928, respectively. These results can serve as an important theoretical reference for the calculation of sediment transport at the third entrance of the Xinqiman Reservoir in the Tarim River.

## 1. Introduction

Sediment transport capacity is the amount of sediment that can be discharged through the reach under certain flow and sediment conditions [1]. Currently, Zhang Ruijin's formula for sediment transport capacity [2] is widely used in China for rivers with low sediment discharge ( $<10$  kg/m<sup>3</sup>).

$$S^* = K \left( \frac{U^3}{g\omega R} \right)^m = k_0 \left( \frac{U^3}{R\omega} \right)^m, \quad (1)$$

where  $S^*$  is the sediment transport capacity (kg/m<sup>3</sup>);  $U$  is the average flow velocity in the cross section (m/s);  $R$  is the hydraulic radius (m), which can be substituted by the average water depth  $H$  (m) for wide and shallow natural rivers;  $\omega$  is the sediment settling velocity (m/s);  $g$  is the gravitational acceleration (m/s<sup>2</sup>); and  $k_0$  and  $m$  are the sediment transport coefficient and sediment transport exponent, respectively, which adhere to  $k_0 = K/g^m$ .

In (1), the key to accurately calculating the sediment transport capacity is to determine the values of coefficient  $k_0$

and exponent  $m$ . Such parameters have been calibrated by many researchers using measurement data from the middle and lower reaches of the Yangtze and Yellow rivers. One example is the study by a sediment transport research group at the Wuhan Institute of Hydraulic and Electrical Engineering. By analyzing the measurement data, the parameters suitable for the upper and lower reaches of the Yangtze River were identified as follows:  $K = 0.061$ ,  $m = 1.54$ , and  $K = 0.036$ ,  $m = 1.54$ , whereas the parameters suitable for the Yellow River were identified as  $K = 0.22$  and  $m = 0.76$  [3, 4]. Chunhang et al. [5] utilized the hydrological and sediment data from the Tarim River.

The Alar station, which is located at the entrance section of the primary stream of the Tarim River, enabled the calibration of the sediment transport capacity parameters of the Alar reach, and the obtained results were  $k_0 = 0.02$  and  $m = 0.92$  [5, 6].

The third entrance of the Xinqiman Reservoir is located in the lower section of the upper reaches of the Tarim River, which is a typical wandering reach with a relatively straight river body intertwined with wide and shallow sandbars [7].

To improve the adaptability of Zhang Ruijin's formula for sediment transport capacity, the parameters of the formula were adjusted according to the actual flow and sediment conditions in the reach. Based on this analysis, the current study uses the CCHE2D model to perform a numerical simulation of sediment transport at the third entrance of the Xinqiman Reservoir of the Tarim River and determines the parameters in the Zhang Ruijin's sediment transport capacity (1). The research aims to provide an important theoretical reference for the calculation of sediment transport at the third entrance of the Xinqiman Reservoir of the Tarim River.

## 2. Fundamental Equations of the CCHE2D Model

The CCHE2D model was developed by the National Center for Computational Hydroscience and Engineering (NCCHE), USA. The model can simulate the dynamic interaction processes of flow and sediment transport in rivers, lakes, estuaries, and coastal waters. The equations used in this study for the numerical simulations are discussed in subsequent sections.

**2.1. Governing Equations.** CCHE2D is based on finite element methods and adopts the following two-dimensional equations to solve shallow-water problems:

### 2.1.1. Continuity Equation

$$\frac{\partial h}{\partial t} + \frac{\partial(hU)}{\partial x} + \frac{\partial(hV)}{\partial y} = 0, \quad (2)$$

where  $x$  and  $y$  are the Cartesian coordinates in the horizontal plane,  $h$  is the water depth (m), and  $U$  and  $V$  are the depth-averaged flow velocity components in the  $x$ - and  $y$ -directions, respectively (m/s).

### 2.1.2. Momentum Equations

$$\begin{aligned} & \frac{\partial(hU)}{\partial t} + \frac{\partial(hUU)}{\partial x} + \frac{\partial(hUV)}{\partial y} \\ &= -gh \frac{\partial z_s}{\partial x} + \frac{1}{\rho} \frac{\partial(hT_{xx})}{\partial x} + \frac{1}{\rho} \frac{\partial(hT_{xy})}{\partial y} \\ & \quad + \frac{\partial D_{xx}}{\partial x} + \frac{\partial D_{xy}}{\partial y} + \frac{1}{\rho} (\tau_{sx} - \tau_{bx}) + f_c hV, \\ & \frac{\partial(hV)}{\partial t} + \frac{\partial(hUV)}{\partial x} + \frac{\partial(hVV)}{\partial y} \\ &= -gh \frac{\partial z_s}{\partial y} + \frac{1}{\rho} \frac{\partial(hT_{yx})}{\partial x} + \frac{1}{\rho} \frac{\partial(hT_{yy})}{\partial y} \\ & \quad + \frac{\partial D_{yx}}{\partial x} + \frac{\partial D_{yy}}{\partial y} + \frac{1}{\rho} (\tau_{sy} - \tau_{by}) + f_c hU, \end{aligned} \quad (3)$$

where  $Z_s$  is the water surface elevation (m);  $g$  is the gravitational acceleration ( $\text{m/s}^2$ );  $T_{xx}$ ,  $T_{xy}$ ,  $T_{yx}$ , and  $T_{yy}$  are the depth-averaged turbulence Reynold stresses ( $\text{N/m}^2$ );  $D_{xx}$ ,  $D_{xy}$ ,  $D_{yx}$ , and  $D_{yy}$  are the discrete terms to compensate for the nonuniformity of velocity and the influence of secondary flow;  $\rho$  is the density of water ( $\text{kg/m}^3$ );  $\tau_{bx}$  and  $\tau_{by}$  are the shear stresses on the bed surface ( $\text{N/m}^2$ );  $\tau_{sx}$  and  $\tau_{sy}$  are the shear stresses on the flow surface ( $\text{N/m}^2$ ); and  $f_c$  is the Coriolis coefficient.

**2.2. Two-Dimensional  $k$ - $\varepsilon$  Model.** In this model, the equations for the turbulent kinetic energy  $k$  ( $k = 0.5\overline{u'_i u'_i}$ ) and the rate of dissipation of turbulent kinetic energy  $\varepsilon$  ( $\varepsilon = \mu_t \overline{\partial u'_i / \partial x_j \partial u'_i / \partial x_j}$ ) are presented correspondingly. The average equations of the vertical lines of  $k$  and  $\varepsilon$  are

$$\begin{aligned} & \frac{\partial k}{\partial t} + u \frac{\partial k}{\partial x} + v \frac{\partial k}{\partial y} - \frac{\partial}{\partial x} \left( \frac{v_t}{\sigma_k} - \frac{\partial k}{\partial x} \right) - \frac{\partial}{\partial y} \left( \frac{v_t}{\sigma_k} - \frac{\partial k}{\partial y} \right) \\ &= P - \varepsilon + P_{kV}, \\ & \frac{\partial \varepsilon}{\partial t} + u \frac{\partial \varepsilon}{\partial x} + v \frac{\partial \varepsilon}{\partial y} - \frac{\partial}{\partial x} \left( \frac{v_t}{\sigma_\varepsilon} - \frac{\partial \varepsilon}{\partial x} \right) - \frac{\partial}{\partial y} \left( \frac{v_t}{\sigma_\varepsilon} - \frac{\partial \varepsilon}{\partial y} \right) \\ &= c_{1\varepsilon} \frac{\varepsilon}{k} P - c_{2\varepsilon} \frac{\varepsilon^2}{k} + P_{\varepsilon V}, \end{aligned} \quad (4)$$

where  $P$  is the pressure (Pa);  $c_f$  is the friction coefficient; and the empirical constants are  $c_{1\varepsilon} = 1.45$ ,  $c_{2\varepsilon} = 1.90$ ,  $\sigma_k = 1.0$ , and  $\sigma_\varepsilon = 1.3$ .

**2.3. Sediment Transport Equation.** The sediment model adopted by the CCHE2D numerical simulation software primarily comprised suspended load. The transport equation for the suspended load is as follows:

$$\begin{aligned} & \frac{\partial(hC_k)}{\partial t} + \frac{\partial(UhC_k)}{\partial x} + \frac{\partial(VhC_k)}{\partial y} \\ &= \frac{\partial}{\partial x} \left( \varepsilon_s h \frac{\partial C_k}{\partial x} \right) + \frac{\partial}{\partial y} \left( \varepsilon_s h \frac{\partial C_k}{\partial y} \right) + \frac{\partial S_x}{\partial x} \\ & \quad + \frac{\partial S_y}{\partial y} + \alpha \omega_{sk} (C_{*k} - C_k), \end{aligned} \quad (5)$$

where  $C_k$  is the depth-averaged concentration of the suspended load ( $\text{kg/m}^3$ );  $C_{*k}$  is the capacity or depth-averaged concentration of the suspended load in the equilibrium state of sediment transport ( $\text{kg/m}^3$ );  $\varepsilon_s$  is the turbulent diffusion coefficient of the sediment, which is determined by  $\varepsilon_s = vt/\sigma_s$ , in which  $\sigma_s$  is the turbulent Schmidt number, ranging between 0.5 and 1.0;  $\omega_{sk}$  is the settling velocity of the sediment (m/s);  $\alpha$  is the nonequilibrium adaptation coefficient; and  $k = 1, 2, \dots, N$ .

## 3. Experiments Using Numerical Simulation

**3.1. The Flume Model.** Experiments with the flume model were performed at the Key Laboratory of Water Conservancy Engineering Safety and Water Disaster Prevention of



TABLE 1: Scales of the flume model.

Type of scale	Value of scale
Horizontal scale	$\lambda_L = 250$
Vertical scale	$\lambda_H = 25$
Velocity scale	$\lambda_V = \lambda_H^{1/2} = 5$
Roughness scale	$\lambda_n = \lambda_H^{7/6} / (\lambda_V \lambda_L^{1/2}) = 0.541$
Time scale of flow movement	$\lambda_t = \lambda_L / \lambda_V = 50$
Flow scale	$\lambda_Q = \lambda_L \lambda_H \lambda_V = 31250$
Sediment settling velocity scale	$\lambda_w = \lambda_V (\lambda_H / \lambda_L)^{3/4} = 0.889$
Sediment starting velocity scale	$\lambda_{V_0} = \lambda_V = 5$
Sediment transport capacity scale	$\lambda_{S_*} = \lambda_k \lambda_{\gamma_s} / \lambda_{(\gamma_s - \gamma) / \gamma} = 1.6$
Sediment concentration scale	$\lambda_s = \lambda_{s_*} = 1.6$
Sediment grain diameter scale	$\lambda_d = \lambda_H^{1/2} \lambda_V^{1/2} \lambda_L^{-1/4} \lambda_{(\gamma_s - \gamma) / \gamma}^{-1/4} = 0.775$



FIGURE 1: Front view of the flume model.

Xinjiang, Xinjiang Agricultural University. The flume model was built using the third entrance section of the Xinqiman Reservoir of the Tarim River as its prototype. The scales of the model are listed in Table 1. The flume model exhibited a wide and shallow geometry of length 8.0 m, maximum width 1.33 m, height 0.2 m, and slope  $i = 1/4000$  [8] (Figure 1). This simulation considers many conditions, such as geometric similarity, gravity similarity, resistance similarity, sediment sedimentation similarity, sediment suspension similarity, sediment start-up similarity, riverbed abundant deformation time similarity, and density current movement occurrence condition similarity, to ensure that the model is basically consistent with the actual river channel and make the simulation results more accurate.

**3.2. Numerical Simulation.** First, the topographic data file of the flume model in Figure 1 was imported into CCHE-MESH. Subsequently, a boundary was defined to perform elevation interpolation. Finally, the model was meshed with quadrilateral grids; the maximum number of longitudinal grid lines,  $I_{\max}$ , was set to 180, the maximum number of horizontal grid lines,  $J_{\max}$ , was set to 600, and the RL (with smooth function-1) orthogonal meshes were used to improve the distribution of regional mesh quality and density, as well as to optimize the overall mesh quality. The layout of the numerical model and the meshes is shown in Figure 2.

### 3.3. Configuration of Initial Conditions

**3.3.1. Flow Conditions.** According to the statistics of floods discharged at the Xinqiman Hydrological Station in the primary stream of the Tarim River between the years 1956–2012, the floods are categorized into the following groups by their occurrences: once in 100 years, once in 50 years, once in 20 years, once in 10 years, and once in 5 years, with flow discharges of 1890 m<sup>3</sup>/s, 1770 m<sup>3</sup>/s, 1600 m<sup>3</sup>/s, 1450 m<sup>3</sup>/s, and 1280 m<sup>3</sup>/s [9], respectively. After the flow scale conversion, the flow discharges for the simulation of these cases were 0.06048 m<sup>3</sup>/s, 0.05664 m<sup>3</sup>/s, 0.0512 m<sup>3</sup>/s, 0.0464 m<sup>3</sup>/s, and 0.04096 m<sup>3</sup>/s, respectively.

**3.3.2. Sediment Discharge Conditions.** According to the statistics of Xinqiman Hydrological Station of the Tarim River, the annual average sediment discharge ranges between 2.32 and 5 kg/m<sup>3</sup>, the maximum average sediment discharge in the cross section ranges between 8.84 and 12.7 kg/m<sup>3</sup> [9]. Therefore, the sediment discharge conditions for the simulation were chosen as integer values from 2 to 10 kg/m<sup>3</sup>.

**3.3.3. Roughness Conditions.** The comprehensive roughness coefficient is an important parameter in the mathematical modelling of fluid flow [10]. A comprehensive dimensionless number reflects the influence on flow resistance. The rougher the boundary surface, the greater the roughness; the smoother the boundary surface, the smaller the roughness. The authors of this study calibrated the comprehensive roughness coefficient of the third entrance of the Xinqiman Reservoir of the Tarim River by using the CCHE2D model. The consistency between the simulated and measured flow surface profiles was compared, considering the standard deviation, correlation coefficient, and root mean square error. Consequently, the comprehensive roughness coefficient of the flume model that yielded the minimum error was 0.018. According to the model-scale conversion, the comprehensive roughness coefficient of the original reach was 0.01 [11]. Therefore, 0.018 was selected as the comprehensive roughness coefficient for the numerical simulations in this study.

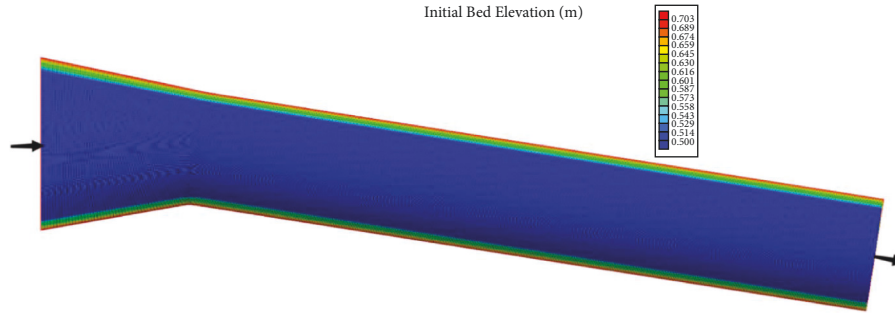


FIGURE 2: Layout of the numerical model and meshes.

TABLE 2: Statistics of suspended load gradation of Alar station (2001).

Grain size (mm)	0.002	0.004	0.008	0.016	0.031	0.062	0.125	0.25	0.5	1
Cumulative gradation (%)	7	13.4	25.2	39.4	56.8	76.8	92.8	98.1	99.6	100
Grouping gradation (%)	7	6.4	11.8	14.2	17.4	20	16	5.3	1.5	0.4

TABLE 3: Statistics of suspended load gradation used in numerical simulation.

Grain size (mm)	0.006	0.02	0.035	0.042	0.061	0.091	0.11	0.131	0.16	0.193
Cumulative gradation (%)	6.8	13.8	24.7	31.6	51.2	75.6	86.5	94.1	98.6	100
Grouping gradation (%)	6.8	7.0	10.9	6.9	19.6	24.4	10.9	7.6	4.5	1.4

**3.3.4. Suspended Load Gradation.** The gradation of the suspended load is one of the key factors affecting sediment movement, which has a direct impact on sediment transport capacity. Chaoqing et al. [9] collected four groups of suspended loads graded from measurements of the Alar station in the flood season of 2001 and considered the average as the representative gradation of the average suspended load of the original inlet section in the flood season (Table 2) [9].

Based on the scheme presented in Table 2, the gradation of the suspended load required for this study was developed. Considering the test conditions and other factors, the median grain size of the modeled sediment was 0.06 mm, and the median grain size of the original sediment was 0.047 mm [9]. The final suspended load gradations used in the numerical simulation in this study are listed in Table 3. The grain size distribution curves of both the modeled sediment and original sediment are presented in Figure 3.

From Figure 3, it can be seen that the gradation curve of the modeled sediment is similar to that of the original sediment. Therefore, the gradation of the modeled sediment can be representatively used in this study.

### 3.3.5. Settling Velocity of Modelling Sediment in Static Water.

The settling velocity of particles is given by Stokes equation as follows:

$$\omega = \frac{1}{18} \frac{\gamma_s - \gamma}{\gamma} \frac{gd^2}{\nu}, \quad (6)$$

where  $\omega$  is the settling velocity (m/s),  $\gamma_s$  is the weight density of the sediment ( $N/m^3$ ),  $\gamma$  is the weight density of water ( $N/m^3$ ), and  $\nu$  is the kinematic viscosity coefficient ( $m^2/s$ ).

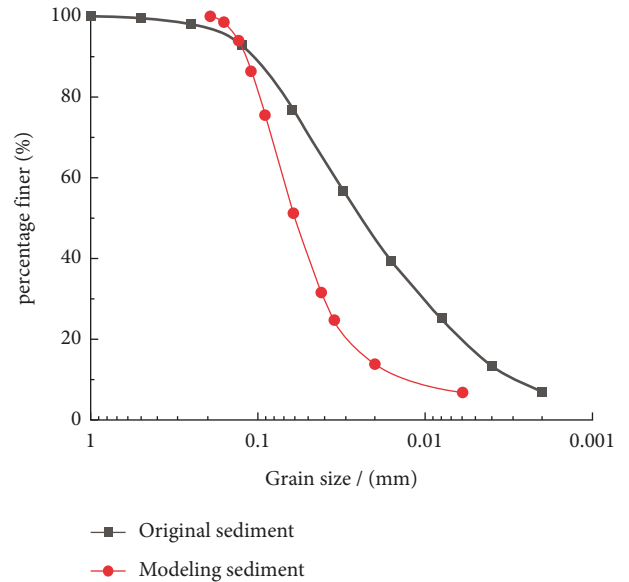


FIGURE 3: Grain size distribution curves of suspended load.

From (8), the theoretical settling velocity was calculated to be 0.00252 m/s. The measurement of the settling velocity in static water performed by Zhou (2015) concluded that the modeled sediment  $d_{50}$  of 0.06 mm exhibited a settling velocity of 0.0025 m/s [8], which is considerably close to the calculated value. Therefore, the calculated settling velocity of 0.00252 m/s can be representatively used in this study.

TABLE 4: Statistics of bed sediment gradation used in numerical simulation.

Grain size (mm)	0.005	0.01	0.025	0.05	0.1	0.25
Cumulative gradation (%)	2.0	3.5	15.0	50	98	100
Grouping gradation (%)	2.0	1.5	11.5	35	48	2

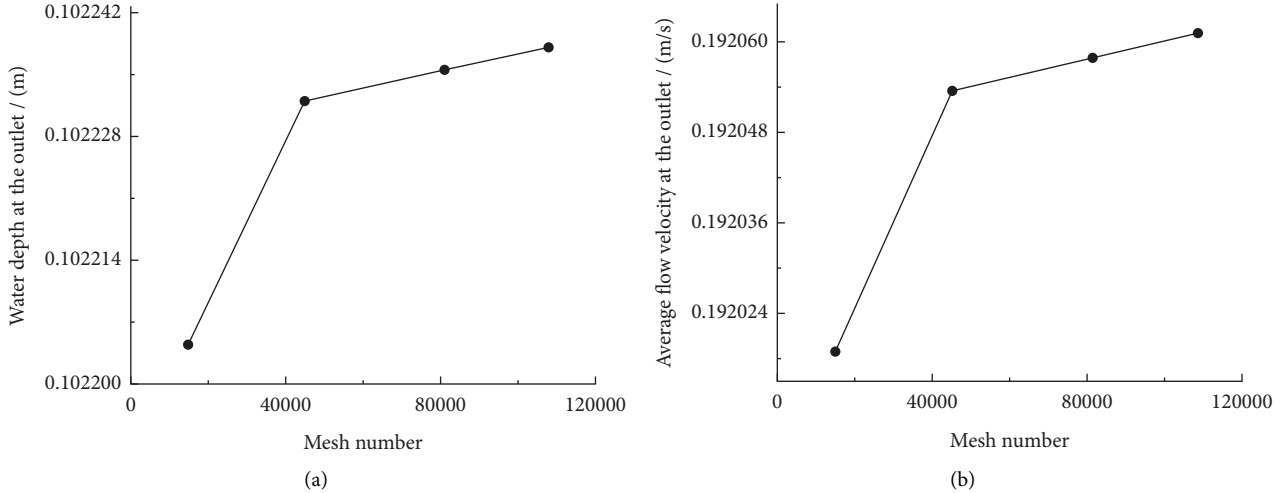


FIGURE 4: Simulation results under different mesh numbers: (a) water depth at the outlet; (b) average flow velocity at the outlet.

3.3.6. *Gradation of Bed Sediment.* Based on the gradation of the surface bed sediment collected by Chaoqing et al. [9] on the left bank of Xinqiman and the primary stream of the Tarim River, the gradation of the bed sediment in the numerical simulation is shown in Table 4.

3.4. *Verification of the Independency on Meshing.* At the simulated flow discharge of  $0.0512 \text{ m}^3/\text{s}$ , steady flow simulations were performed with four different configurations of mesh numbers: 15000, 45000, 81000, and 108000. The dependencies of both the water depth and average flow velocity at the outlet on the number of meshes were verified, and the results are shown in Figure 4.

As illustrated in Figure 4, with the increase in mesh number, both the water depth and average flow velocity at the outlet tended to plateau. Considering the computational capability with respect to ensuring accuracy, grid 4 was used in the simulations of this study.

3.5. *Verification of the Model.* Chunhong et al. [5] determined the relationship between the average water depth  $H$  and flow discharge  $Q$  as  $H = 0.3192Q^{0.2336}$ , through a large number of measurements obtained at the Xinqiman section of the Tarim River. To verify the accuracy and reliability of the model designed to simulate the third entrance of the Xinqiman Reservoir of the Tarim River, steady flow simulations were performed under the five different discharges discussed in Section 3.3.1. Through this, the simulation results of the water depth at the outlet section were extracted. The results from the numerical simulation were then compared with those calculated using the relationship between the water depth  $H$  and flow discharge  $Q$ , derived by

Chunhong et al. [5]. The details of these comparisons are presented in Table 5.

Table 5 shows that the deviation between the numerical simulation and calculation was between 0.05295 and 0.06168 m. As defined in the Technical Regulations for Flow and Sediment Simulation of Inland Waterways and Ports [12], the allowable deviation of the modelling water level in plain regions is  $\pm 0.5$  m. The deviation of this simulation is a little larger than the standard one, which can basically meet the requirements of this study. In summary, the computation method, boundary conditions, and initial conditions selected for the model are equitable, and the CCHE2D model can appropriately simulate the scenario of this study.

## 4. Distinction of Bed-Material Load and Wash Load

4.1. *Classification of Bed-Material Load and Wash Load.* In the classical theory of river dynamics, the coarse particles which are constantly exchanged with the sediment on the riverbed are often called “bed-material load,” whereas the fine particles which basically remain suspended and do not exchange with the sediment on the riverbed, are called “wash load”. Einstein was one of the earliest scholars to propose the concepts of wash load and bed-material load. Through a flume test with approximately constant flow, the sediment discharged from the upstream was modified, and the sediment transport downstream was studied. The transport of the sediment with a grain size  $>0.1$  mm was identified to be constant, whereas that of sediment  $<0.06$  mm varied with the sediment discharge. Thus, Ning [13] introduced the concepts of wash load and bed-material load [13]. According to the method summarized by Huai et al. [14] for the distinction between the two loads,

TABLE 5: Average water depth under different flow conditions.

Flow discharge $Q$ ( $\text{m}^3/\text{s}$ )	Average water depth $H$ (m)		
	Numerical simulation	Calculation	Water depth deviation
0.04096	0.08964	0.15132	0.06168
0.04640	0.09655	0.15580	0.05925
0.05120	0.10226	0.15942	0.05716
0.05664	0.10848	0.16323	0.05475
0.06048	0.11280	0.16575	0.05295

0.06 mm or 0.0625 mm is usually considered as the boundary grain size of the wash load. For sediment particles larger than the boundary grain size, the transport volume becomes irrelevant to the upstream sediment discharge and is always maintained approximately at a certain average value; therefore, it is categorized as a bed-material load. In contrast, for sediment particles smaller than the boundary grain size, its transport volume changes according to the sediment discharge, which makes it the wash load [14].

Therefore, in this study, under the condition of different sediment discharges, sediment transport was simulated utilizing the CCHE2D model, and the suspended sediment concentration of each grain size at the outlet section was extracted from the simulation results. For increasing sediment discharge from upstream, the sediment that was always maintained approximately at a certain average concentration was classified as bed-material load. The sediment whose concentration increased with the volume of sediment discharged from the upstream was classified as wash load [15].

**4.2. Results and Analysis.** The suspended sediment concentration for each grain size at the outlet section under different sediment discharges is shown in Figure 5.

As shown in Figure 5, for sediment particles of grain size 0.193 mm, the suspended sediment concentration at the outlet section always remained  $0.0118 \text{ kg/m}^3$ , approximately, despite the increase in sediment discharge. Similar results were observed for sediments of 0.160, 0.131, and 0.110 mm, with constant suspended sediment concentrations of 0.0512, 0.1304, and  $0.2851 \text{ kg/m}^3$ , respectively. As these suspended sediment concentrations were independent of the sediment discharged, the sediments of these grain sizes could be grouped into bed-material load.

For the sediment of grain size 0.091 mm, the suspended sediment concentration at the outlet section changed simultaneously with the sediment discharge, whereas the latter was smaller than  $5 \text{ kg/m}^3$ . When the sediment discharge was above the threshold of  $5 \text{ kg/m}^3$ , the suspended sediment concentration at the outlet section was stable at approximately  $1.049 \text{ kg/m}^3$ . Provided that the average maximum sediment discharge in the Xinqiman reach of the Tarim River was from  $8.84$  to  $12.7 \text{ kg/m}^3$ , the sediment of grain size 0.091 mm used in this study could be categorized as bed-material load.

For sediment of grain sizes 0.006, 0.020, 0.035, 0.042, and 0.061 mm, the suspended sediment concentrations at the outlet section increased with increasing sediment discharge. Therefore, under the conditions of this study, these sediment dimensions were grouped into wash load.

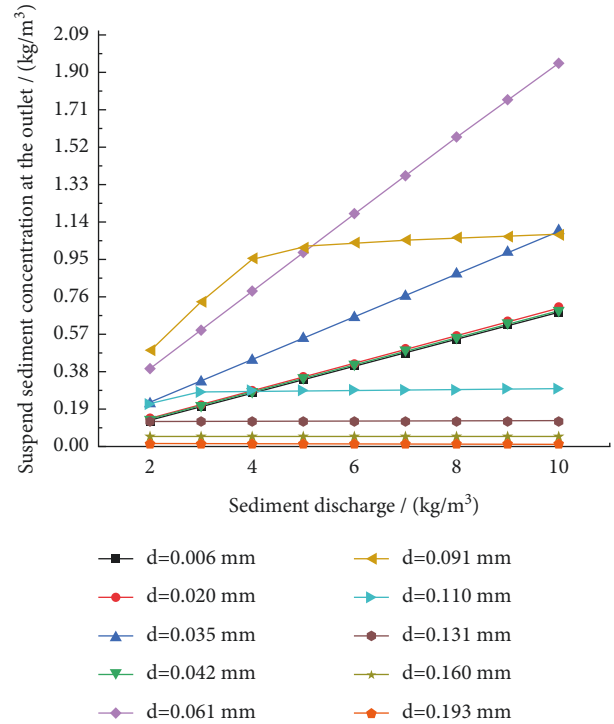


FIGURE 5: Concentration of each grain size at the outlet section under different sediment discharge.

To summarize, under the flow and sediment conditions of this study, sediment of grain size  $\geq 0.091$  mm was classified as bed-material load, whereas sediment of grain size  $\leq 0.061$  mm was classified as wash load. This classification of bed-material load and wash load agrees with the analyses by Einstein and Qian Ning.

## 5. Parameter Calibration in Zhang Ruijin's Formula of Sediment Transport

**5.1. Methods.** In this study, under different flow and sediment conditions, the CCHE2D model was used to simulate the sediment transport at the third entrance of the Xinqiman Reservoir of the Tarim River. In the simulation results, the flow conditions such as bed sediment concentration,  $S$ , cross-sectional average water depth, and average flow velocity were extracted, and the flow-sediment factor,  $U^3/R\omega$ , was calculated, in which the hydraulic radius,  $R$ , could be replaced by the average water depth,  $H$ , in natural rivers that are wide and shallow. Relevant data of the original reach were obtained through model-scale conversion. Thus, the

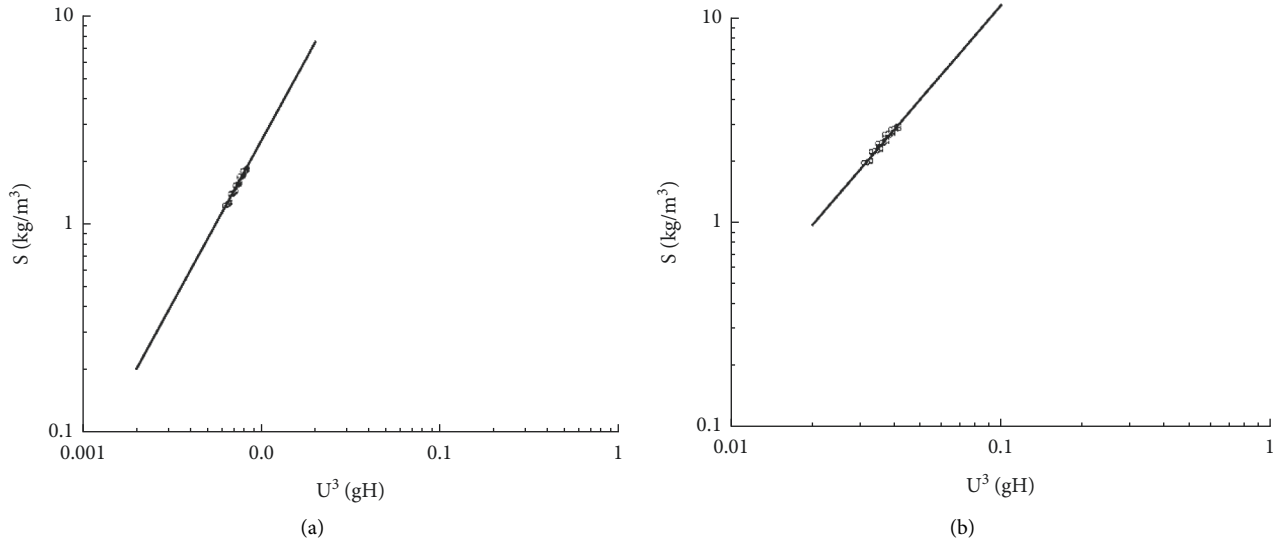


FIGURE 6: Regression between suspended sediment concentration,  $S$ , and flow conditions,  $U^3/gH$ , for the (a) numerical model and (b) original reach.

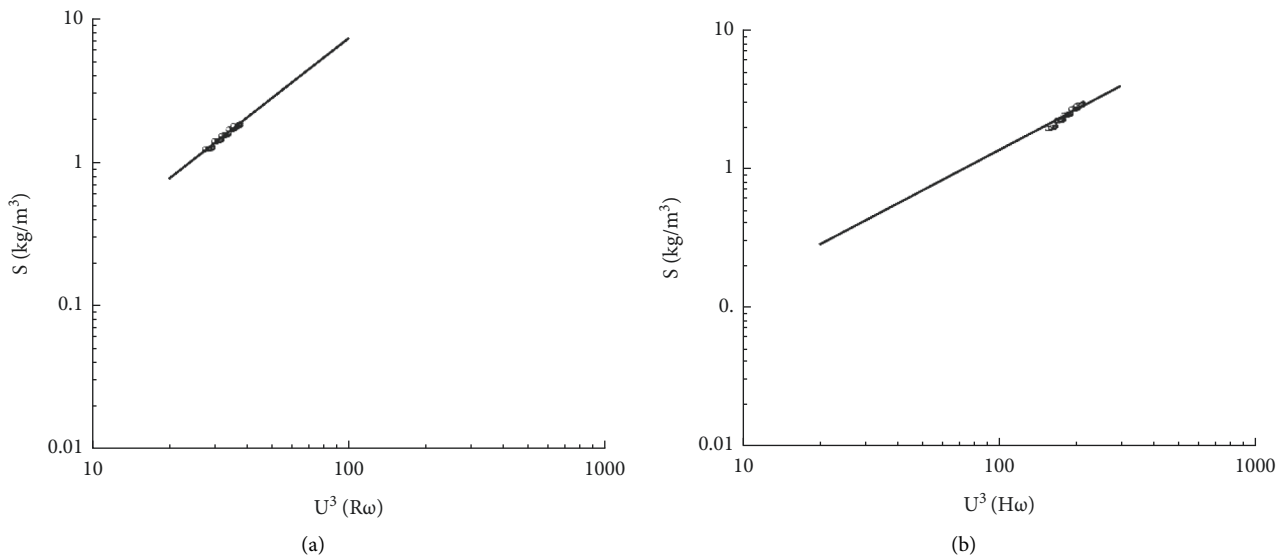


FIGURE 7: Regression between suspended sediment concentration and flow-sediment factor for the (a) numerical model and (b) original reach.

parameters in Zhang’s sediment transport formula were calibrated for this reach.

**5.2. Results and Analysis.** A multivariate linear regression method was adopted to fit the numerical model and original reach. Figure 6 displays the regression between the suspended sediment concentration,  $S$ , and the flow condition,  $U^3/gH$ .

Consequently, the regression equation relating  $S$  and  $U^3/gH$  for the numerical model was determined to be  $y = 3536.26x^{1.574}$ ,  $R^2 = 0.961$ ; for the original reach, the relationship was determined to be  $y = 410.02.95x^{1.55}$ ,  $R^2 = 0.950$ . It can be concluded that the suspended sediment concentration and flow condition adhered significantly through the power law, which complies with (1).

The multivariate linear regression method was also used to fit the relationship between  $S$  and the flow-sediment factor,  $U^3/R\omega$ , to determine the coefficient  $k_0$  and exponent  $m$  in (1) for the third entrance of the Xinqiman Reservoir of the Tarim River. The relationship between  $S$  and  $U^3/R\omega$  for the numerical model and the original reach are shown in Figure 7.

Consequently, the regression equation defining the relationship between  $S$  and  $U^3/R\omega$  for the numerical model was determined to be  $y = 0.012x^{1.4}$ ,  $R^2 = 0.961$ ; for the original reach, the relationship was determined to be  $y = 0.0197x^{0.928}$ ,  $R^2 = 0.854$ . Therefore, the sediment transport capacity coefficient,  $k_0$ , in (1) for the original reach was 0.0197 and the exponent,  $m$ , was 0.928. Consequently, the sediment transport capacity formular for the third entrance of the

Xinqiman Reservoir of the Tarim River could be drawn as follows:

$$S^* = 0.0197 \left( \frac{U^3}{H\omega} \right)^{0.928} = 0.164 \left( \frac{U^3}{g\omega H} \right)^{0.928}, \quad (7)$$

where  $S^*$  is the sediment transport capacity ( $\text{kg}/\text{m}^3$ ),  $U$  is the average flow velocity in the cross section ( $\text{m}/\text{s}$ ),  $H$  is the average water depth ( $\text{m}$ ), and  $\omega$  is the sediment settling velocity ( $\text{m}/\text{s}$ ).

**5.3. Theoretical Verification.** In general, the sediment transport capacity coefficient,  $k_0$ , ranges between 0.01 and 0.05. The range of  $k_0$  for the mainstream of the Tarim River is 0.015–0.023 [9]. Thus, the  $k_0$  values obtained in this study considerably agree with the theoretical ranges.

The semiempirical estimation of  $k_0$  proposed by Changqing et al. [9] is as follows:

$$k_0 = \frac{\rho_s \rho_0 B_r}{(\rho_s - \rho_0) C^2}, \quad (8)$$

where  $\rho_s$  is the sediment density ( $\text{kg}/\text{m}^3$ ),  $\rho_0$  is the water density ( $\text{kg}/\text{m}^3$ ),  $B_r$  is the kinematic parameter of suspended sediment, which is set to 0.01, based on Bagnold's research on laboratory-measured data, and  $C$  is the Chézy coefficient. The calculated  $k_0$  from equation (8) was 0.012, which is similar to the result obtained in this study. Therefore, it is reasonable to conclude that  $k_0 = 0.0197$  can be representatively used to study the sediment transport capacity in the target reach.

## 6. Conclusions

In this study, the CCHE2D model was used to simulate the sediment transport at the third entrance of Xinqiman Reservoir in the Tarim River, and the parameters in Zhang Ruijin's formula of sediment transport capacity were determined under different flow and sediment conditions.

The primary conclusions of this study are as follows:

- (1) Under the flow and sediment conditions of this study, sediment of grain size  $\geq 0.091$  mm can be considered as bed-material load, whereas sediment of grain size  $\leq 0.061$  mm can be considered as wash load.
- (2) There is a good power-law relationship between the suspended sediment concentration,  $S$ , and the flow condition,  $U^3/gH$ , at the third entrance of the Xinqiman Reservoir of the Tarim River, which is consistent with the law of Zhang Ruijin's formula for sediment transport capacity.
- (3) Using multivariate linear regression, the relationship between suspended sediment concentration,  $S$ , and flow-sediment factor,  $U^3/H\omega$ , at the third entrance of the Xinqiman Reservoir of the Tarim River was fitted, and the parameters in Zhang Ruijin's formula for sediment transport capacity were determined as  $k_0 = 0.0197$  and  $m = 0.928$ .

## Data Availability

The datasets used and/or analysed during the current study are available from the corresponding author on reasonable request.

## Disclosure

The sponsors had no role in the design, execution, interpretation, or writing of the study.

## Conflicts of Interest

The authors declare no conflicts of interest.

## Acknowledgments

This study was supported by the National Natural Science Foundation of China (51469032) and the Research project of Key Laboratory of Water Conservancy Engineering Safety and Water Disaster Prevention of Xinjiang (ZDSYS-YJS-2021-02).

## References

- [1] Q. Ning and W. Zhaohui, *Sediment Dynamics*, Science Press, Beijing, China, 1983.
- [2] Z. Ruijin, *River Sediment Dynamics, Ver. 2*, China Water & Power Press, Beijing, China, 1998.
- [3] Y. Ming, "A study on the sediment transport capacity of the middle and lower reaches of the Yangtze River as well as a discussion on the general energy-balance pattern in flows carrying sediments (primarily suspended loads)," *Journal of Sedimentary Research*, vol. 2, pp. 54–73, 1959.
- [4] Y. Ming, "A study on the sediment transport capacity of the middle and lower reaches of the Yangtze River as well as a discussion on the general energy-balance pattern in flows carrying sediments (primarily suspended loads) (continued)," *Journal of Sedimentary Research*, vol. 3, pp. 59–72, 1959.
- [5] J. Han, H. Cheng, Y. Shi, L. Wang, Y. Song, and W. Zhang, "Connectivity analysis and application of fracture cave carbonate reservoir in Tazhong," *Science Technology and Engineering*, vol. 16, no. 5, pp. 147–152, 2016.
- [6] G. Qingchao, L. Qin, Z. Yujiang, and D. Anjun, "Mathematical modeling of sediment transport and bed variation in the Main Stem Tarim River," *Journal of Sedimentary Research*, vol. 3, pp. 1–7, 2015.
- [7] L. Yujian, S. Kebin, and A. Ceng, "Pattern and characteristic analysis of the mainstream of the Tarim River," *Yellow River*, vol. 33, no. 6, pp. 17–19, 2011.
- [8] Z. Qingqing, *Experimental Study on Effect of Sediment Promoting and Flow Retarding and Main Influencing Factors of Permeable Hydraulic Flashboard spur dike*, Xinjiang Agricultural University, Ürümqi, China, 2015.
- [9] J. Wei, H. Cheng, B. Fan, Z. Tan, L. Tao, and L. Ma, "Research and practice of one opening-one closing productivity testing technology for deep water high permeability gas wells in South China Sea," *Fresenius Environmental Bulletin*, vol. 29, no. 10, pp. 9438–9445, 2020.
- [10] D. Anjun, G. Qingchao, and C. Jianguo, "Study on the roughness in sediment-laden flows," *Journal of Sedimentary Research*, vol. 5, pp. 24–29, 2007.

- [11] Y. LiLi, Y. GengGeng, and L. MaoMao, "Calibration method for Manning's roughness coefficient for a river flume model," *Water Supply*, vol. 20, no. 8, pp. 3597–3603, 2020.
- [12] R Tianjin, "Research Institute for Water Transport Engineering, the Ministry of Transport of the People's Republic of China. Technical Specification For Simulating Flows And Sediments In Inland Waterways And Harbors," China Communications Press, Beijing, China, JTS/T 231-4-2018, 2018.
- [13] Q. Ning, "On the concepts of "bed-material load" and "wash load" Institute of hydraulic research," *Journal of Hydraulic Engineering*, vol. 1, pp. 29–45, 1957.
- [14] C. . Huai, Z. Lijun, W. Jianzhong, and F. Hongxia, "Review on division criteria between bed material load and wash load," *Journal of Sedimentary Research*, vol. 4, pp. 74–80, 2016.
- [15] C. Zhang and H. Tang, "Advances in water resources & hydraulic engineering," in *Proceedings of the 16th IAHR-APD Congress and 3rd Symposium of IAHR-ISHS*, 2009.

## Review Article

# Influence of Urban Atmospheric Ecological Environment on the Development of Outdoor Sports

Linqiang Xu <sup>1</sup> and Gia Lyu <sup>2</sup>

<sup>1</sup>*School of International Culture and Tourism, Zhejiang University City College, Hangzhou 310000, China*

<sup>2</sup>*Department of Computer Science, Saigon University, Ho Chi Minh City 700000, Vietnam*

Correspondence should be addressed to Gia Lyu; [lyugia@sg.edu.vn](mailto:lyugia@sg.edu.vn)

Received 11 May 2022; Accepted 16 June 2022; Published 31 July 2022

Academic Editor: Punit Gupta

Copyright © 2022 Linqiang Xu and Gia Lyu. This is an open access article distributed under the Creative Commons Attribution License, which permits unrestricted use, distribution, and reproduction in any medium, provided the original work is properly cited.

In recent years, the process of urbanization in China has developed rapidly. However, many problems have also appeared, such as a rapid population increase, resource shortage, and deterioration of the ecological environment. The deterioration of the ecological environment has led to increased air pollution and noise pollution, threatening human health, and hindering outdoor sports. This paper takes a certain city outdoor sports venue as the research object and studies the influence of the urban atmospheric ecological environment on the development of outdoor sports through the method of questionnaire survey and mathematical statistics. The results show that the city's air quality index in 2019 was "excellent" and "good" for a total of 240 days, the greening rate reached 35%, the noise decibels were between 38 dB and 67 dB, and the ecological environment was good. According to statistics, 5.8% of students, 24.23% of middle-aged people, and 37.24% of elderly people in the city who engaged in outdoor sports often experience physical discomfort. After launching outdoor sports in this atmospheric ecological environment, 49.84% of students, 44.59% of office workers, and 39.65% of elderly people feel that their body and mind have improved. A good urban ecological environment can improve the physical and mental health of outdoor sports personnel. Through outdoor sports, the physical and mental health of all sports groups in the ecological environment has been improved. According to the location of this study, the subjects generally said that in the good atmospheric ecological environment of the city, outdoor sports improved physical and mental health.

## 1. Introduction

Air pollution refers to the atmospheric state where the content of some substances in the air environment reaches a harmful level, which leads to ecological damage and affects people's health and safety. Air environmental pollution brings serious harm to the normal activities and life of human beings [1]. The human body is exposed to the polluted air environment to inhale pollutants and cause diseases. As the concentration of pollutants in the air environment rises to a certain level, it will directly affect the earth's water resources and food. The human body inhales the heavy metal diseases in the polluted air, which brings serious harm to the human life and health [2]. With people's enthusiasm for outdoor sports, outdoor sports in an air-polluted environment will inevitably

inhale more pollutants under accelerated breathing, causing pollutants to enter the human body with respiration and be transported with the blood, leading to respiratory diseases, lung cancer, capillary diseases, and other chronic diseases [3].

According to investigations and studies, the content of air pollution particles such as aromatic compounds in each cubic meter of air rises by 10 micrograms, and the long-term lung cancer mortality rate rises by 8%. Long-term outdoor sports in the polluted air will dilute the air by lung function. Diffusion and purification ability are weakened, affecting health [4]. Therefore, studying the impact of air pollution on outdoor sports people and formulating corresponding defensive measures are of great significance to ensure physical health and safety and reduce the harm of air pollution to outdoor sportsmen [5].



Air is the distributed atmosphere on the surface of the earth. Air provides people with a source of oxygen to breathe. It is also an important component of the earth's environment. Air is the foundation for all living substances to survive [6, 7]. However, with the continuous advancement of the current industrial process, the development of the chemical industry and the increase in dust storms and automobile exhaust emissions have caused serious damage to the air environment and further deterioration of air quality. Air pollution has seriously affected the safety of human life and brought serious harm to human health and dietary health. Smoke and fine particles in the air can cause bronchitis, lung cancer, and various chronic diseases [8]. The polluted air environment can easily lead to the destruction of the ozone layer, resulting in acid rain and PM2.5 substances, which will damage the earth's water sources and ecological substances, thereby seriously affecting the safety of the earth's survival. Air environmental pollution refers to the factors that come from man-made and natural factors. With the increase in the quantity, concentration, and retention time of pollutants discharged into the air, the dilution, diffusion, and purification ability of the atmosphere in the air environment is weakened, which leads to the deterioration of air quality [9, 10]. The substances in the air environment exceed the indicators that human health can withstand.

Pollutants in the air environment are mainly composed of aerosol state pollutants, particulate matter, sulfur-containing compounds, nitrogen-containing compounds, and carbon compounds [11, 12]. Depending on the source of emissions, pollutants will cause primary pollution and secondary pollution, which will undergo chemical reactions or photochemical reactions that form compounds such as  $H_2S$ ,  $CO_2$ ,  $CO$ , and  $HF$ , and the oxygen compounds in the atmosphere will also form carbon monoxide, carbon dioxide, sulfur dioxide, and organic compounds [13]. These compounds are suspended in liquid droplets or solid particles through hydration. The increase in total suspended particulate (TSP) matter and the increase in inhalable particles. The hydrocarbons, oxygen-containing organic compounds, sulfur oxides, and lead compounds in the air have become the main components of air pollution. According to the nature of the pollution, the air pollutants are divided into two types: oxidizing and reducing [14].

The pollution sources of the air environment are mainly divided into two aspects: human and natural factors. The composition of air pollution sources includes human factors and natural factors. Natural factors include forest fires, volcanoes, sand, dust, etc., which will produce  $CO$ ,  $CO_2$ ,  $SO_2$ , and  $NO_2$ . HC and other combustion materials, natural wind, and sand will cause dust, smoke droplets, fog, dust, floating dust, suspended matter, and other pollutants to float in the air [15, 16]. The pollution of the air environment caused by human factors includes fuel combustion, emissions from industrial production, emissions from transportation, emissions from agricultural activities, etc. Among them, the pollution caused by fuel combustion is mainly due to industrial production. The burning of coal in industrial production will produce carbon monoxide, carbon dioxide,

sulfur dioxide, and other substances, which can cause great pollution to natural air, water bodies, and soil [17].

Emissions during transportation mainly come from the exhaust emissions of automobiles and the emissions of ships and airplanes. With the increase of automobiles, automobile exhaust emissions seriously pollute the environment. Nitrogen oxides, hydrocarbons, and oxygen-containing organic compounds in the exhaust are inhaled by the human body, which can cause cerebral infarctions, tuberculosis, and other respiratory diseases [18]. Therefore, it is necessary to control automobile exhaust emissions and achieve energy saving and emission reduction. Agricultural emissions mainly refer to air pollution caused by burning straws, pesticides and dust, and other particulate matter, which mainly produce carbon, oxygen compounds, and hydrogen-combined hydrocarbons, and other pollutants and produce colorless and pungent odor gases such as sulfur dioxide [19]. These pollutants can damage the lungs of the human body and cause harm to outdoor sports people. This paper conducts a questionnaire survey on several outdoor sports venues in a city to understand the impact of the urban atmospheric ecological environment on the development of outdoor sports.

## 2. Materials and Methods

*2.1. Research Object.* The selected locations of the article research are outdoor sports venues in three squares and four parks in a certain city and investigate and study the crowds who carry out outdoor sports in these places. 400 men and 400 women were selected for the study, a total of 800 persons, aged 20–75 years. The study objects included school students, individuals, and retired persons [20].

### 2.2. Research Method

*2.2.1. Questionnaire Survey.* We collect relevant questionnaire survey data and design survey questionnaires according to needs. A questionnaire survey was conducted among 800 citizens who are engaged in outdoor sports activities in various ecological environments of the city.

*(1) Test the Validity and Reliability of the Questionnaire.* We invite an expert team including 6 professors and 10 associate professors to review the content of the questionnaire item by item and check whether the content of the questionnaire fits the subject and whether the survey information provided is accurate. The questionnaire proposes amendments, which will be reviewed by the expert team after the amendments and will be issued after passing the questionnaire survey. Retesting the reliability of the questionnaire: the method used in the reliability test of the questionnaire is the retest method. In August 2019, 800 questionnaires were distributed at 7 locations among the research subjects. The distribution method was random. After collecting the questionnaires, the questions were counted, and related questions were modified and debugged. After one month, the questionnaires were redistributed randomly, measured again, and finally determined.

(2) *Questionnaire Indicators.* The indicators set by the survey questionnaire include outdoor sports items, outdoor sports methods, outdoor sports goals, outdoor sports frequency, outdoor sports duration, time distribution, etc.

(3) *Distributed Questionnaires and Return Questionnaires.* The article survey questionnaire was distributed using random sampling method. 800 outdoor sports athletes were randomly selected from the research target sites to conduct a survey. A total of 800 questionnaires were distributed in this survey. The distribution and collection results are shown in Table 1.

A total of 800 questionnaires were distributed, and 761 questionnaires were returned. All of the questionnaires were valid. The average recovery rate was 95%. 400 male and 400 female subjects were randomly selected, aged 20–75 years, with an average age of 48 years.

(4) *Questionnaire Distribution Quality and Recycling Quality.* Because the questionnaire survey method has a strong randomness, it can guarantee that the respondents will not have specificity. Before randomly distributing the questionnaires, the staff who distributed the questionnaires

were trained on the content of the questionnaire to ensure the professionalism of the staff.

2.2.2. *Mathematical Statistics.* We organized the questionnaires collected by the questionnaire survey method, used the SPSS26.0 to count and analyze the data, and obtained the required data. In order to study the impact of the city’s urban ecological environment on outdoor sports, mathematical statistics combined with RS and GIS technologies were used to calculate the city’s ecological environment indicators. Using the Landsat TM’s image data in 2019, the bands are combined into 4, 3, and 2, using the polynomial model geometric error correction. The urban ecological environment data comes from the provincial water resources announcement and the municipal environmental statistics annual report.

(1) *Vegetation Cover Index.* The various types of land in the city account for the proportion of the total urban land area. The types of land include construction land, forest land, fields, grassland, and unused land. The vegetation coverage index formula is as follows:

$$X = \frac{\text{Aveg}(0.38 \times F + 0.34 \times G + 0.19 \times P + 0.07 \times B + 0.02 \times M)}{Q}, \quad (1)$$

where  $X$  represents the vegetation coverage index;  $F$  and  $G$  represent forest land and grassland area, respectively;  $P$  and  $B$  represent field area and construction land, respectively;  $M$  represents unused land;  $Q$  represents the total area of the urban area; and Aveg represents the normalization coefficient of  $X$ , which is set as 588.37 in this study.

The urban ecological environment quality index can quantitatively express the city’s ecological environment quality. The following formula shows the urban ecological environment quality index expression:

$$YA_t = \frac{\sum_{i=1}^n HJ_i \times D_i}{Q}, \quad (2)$$

where  $n$  represents the number of land types,  $YA_t$  and  $D_i$ , respectively, represent the ecological environment quality index and the weight of the  $i$ -th land ecological environment index; and  $HJ_i$  represents the area of the  $i$ -th land type in the urban area during the  $t$  study period.

(2) *Measurement of Urban Air Pollution Degree and Urban Noise.* The elements that cause air pollution and noise pollution in the urban ecological environment are mainly automobile exhaust emissions, factory emissions, traffic noise, industrial imaging, and life noise.

(3) *Urban Air Pollution Detection.* The particle detector produced in the United Kingdom: DustMate smoke detector is used to detect the air pollution in 7 areas of the research

object (3 squares and 4 public parks), and the accuracy of the instrument is  $0.01 \mu\text{g m}^{-3}$ .

(4) *Urban Noise Measurement.* AWA6218 noise monitor was used to monitor the noise pollution in 7 areas (3 squares and 4 parks) of the research object, and the accuracy of the instrument was 0.01 dB(A).

### 3. Results

Using the article method to count the air quality index of the city, there are 6 levels from “excellent” to “severe pollution,” corresponding to each color and level. When the weather forecast is broadcast, the impact of different air quality indexes on human health is measured. Table 2 shows the air quality index for the whole year of 2019. The number of days with an air quality index of “excellent” in the whole year is 114 days, accounting for 31.23% of the total pollution in the year. This air quality index is the most suitable for outdoor sports. The number of days when the air quality index is “good” is 126 days, accounting for 34.52% of the total annual pollution. This air quality index is more suitable for outdoor sports. When the air quality index is at the “pollution” level, it is no longer suitable for children, the elderly, and people with special diseases to carry out outdoor sports. It can be seen from Table 2 that the city did not experience “severe pollution” and “severe pollution” in mid-2019. The number of days with “light pollution” and “moderate pollution” was 98 days and 22 days, respectively, accounting for 26.84% and

TABLE 1: Distribution and recycling statistics.

Place	Distributed quantity (part)	Recycled amount (part)	Recovery rate (%)
A square	140	132	94.29
B square	120	115	95.83
C square	100	96	96.00
A park	120	113	94.17
B park	120	116	96.67
C park	100	95	95.00
D park	100	94	94.00

TABLE 2: Air quality status.

Air quality factor	Excellent	Good	Light pollution	Moderately pollution	Heavy pollution	Serious pollution
Series	1	2	3	4	5	6
Index	0-50	51-100	101-150	151-200	201-300	>300
Days	114	126	98	22	5	0
Annual total pollution (%)	31.23	34.52	26.85	6.03	1.37	0.00

6.02% of the total pollution in the year. On the whole, the number of days suitable for outdoor sports in the city is about 240 days. After analysis, it can be seen that the urban ecological environment has a greater impact on the development of outdoor sports, and only a good air quality index can be beneficial to the development of outdoor sports.

The city has a large area of forest resources. According to statistics, the city's urban greening rate has reached 35%. The greening of parks and squares is the point, the street greening is the line, and the woodland greening is the surface, making the entire urban ecological environment present a point-to-face greening scale. Over the years, the city has always implemented the sustainable development route, increased ecological environmental protection, strengthened pollution control, increased vegetation area, advocated outdoor sports, and encouraged the public to actively participate in it. The level of vegetation and greening in public places such as parks and squares has improved, and more and more citizens are actively participating in outdoor sports. Therefore, it can be seen that the greening level of the urban ecological environment will also affect the development of outdoor sports. A good urban ecological environment can attract more people to participate in outdoor sports.

As a part of the urban ecological environment, noise pollution also has a huge impact on the urban ecological environment. Figure 1 shows the average value of traffic noise in 2019.

Figure 1 shows the annual average value of traffic noise in the seven research object places monitored by this method. Three squares are open spaces, and the traffic noise is relatively close to the road, so the traffic noise decibels are between 54 and 67 dB. The four parks are semiencllosed spaces and are far away from the road, so the noise decibels are low, and the noise decibels are between 38 and 43 dB. According to the noise evaluation standard, they are all Grade I, which is at a relatively good level, indicating that the seven places studied in the article have good ecological environments and are suitable for outdoor sports.

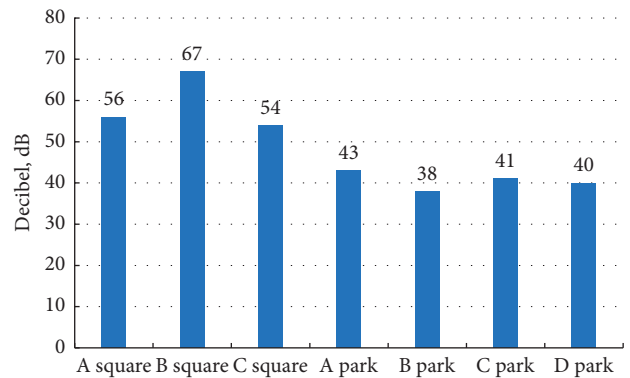


FIGURE 1: Average value of traffic noise.

Based on the abovementioned air quality status, vegetation coverage index, and average traffic noise results, the ecological environment changes in the city are evaluated. The evaluation results are presented in the form of scores. The evaluation standards are as follows: 0-60 points (the ecological environment level is poor), 60-75 points (the ecological environment level is normal), 75-85 points (the ecological environment level is good), and 85-100 points (eco-environmental grade is excellent). Table 3 shows the assessment results of changes in the city's ecological environment.

The urban ecological environment directly affects the physical health of outdoor sports personnel. The article method is used to count the physical conditions of different age groups after outdoor sports in the urban ecological environment. It can be seen from the results that after the article method statistics, outdoor athletes of different age groups reflect different physical conditions when they exercise outdoors in the ecological environment (Figure 2). The probability of the student group feeling regular physical discomfort is very low, 5.8% of students have physical discomfort, and 37.32% of students have no physical discomfort at all. 24.23% of middle-aged (24-55 years old) outdoor sports personnel often have physical

TABLE 3: Assessment results of changes in atmospheric ecological environment.

Area	A square	B square	C square	A park	B park	C park	D park
Ecological environment score	79	82	83	88	91	96	90
Evaluation results	Good	Good	Good	Excellent	Excellent	Excellent	Excellent

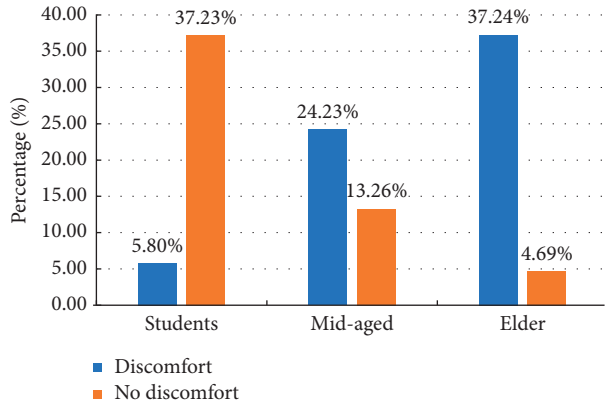


FIGURE 2: Responses to physical conditions of different groups of people.

discomfort, and 13.26% have no physical discomfort at all. 37.24% of the elderly are often unwell, and only 4.69% of the elderly have no physical discomfort at all. Generally speaking, the elderly people carry out outdoor sports in the city's ecological environment, and their health is affected by environmental pollution, traffic noise, and other factors. However, students and middle-aged people have higher physical fitness such as immunity and are less affected by the ecological environment, so the body does not have much impact. It can be seen that the urban ecological environment has a great influence on the development of outdoor sports, and outdoor athletes with poor physical fitness are more seriously affected by the urban ecological environment.

We use the article method to count the physical and mental perception of outdoor athletes after exercising in the ecological environment for a period of time. It can be seen from the statistical results (Figure 3) that 49.84% of students said that physical and mental health of outdoor sports activities in the city's ecological environment have changed, and only 0.86% of students said that no physical and psychological changes have occurred after they carried out outdoor sports activities in the city's ecological environment. 44.59% of middle-aged people said that carrying out outdoor sports activities in the city's ecological environment can change their physical and mental health, and 12.34% of middle-aged people said that there has been no change in their physical and mental health. 39.65% of the elderly said that physical and mental health of outdoor sports activities in the city's ecological environment has been improved, and 10.25% of the elderly believe that no changes have occurred. Generally speaking, the physical and mental health of all sports groups in the ecological environment by carrying out outdoor sports has improved. According to the statistics of the article, the research

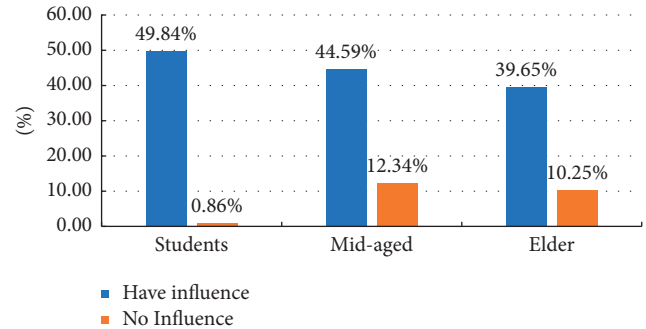


FIGURE 3: Whether the atmospheric ecological environment affects physical and mental health.

subjects generally stated that in the city's atmospheric ecological environment, outdoor sports have generally improved physical and mental health. It shows that the urban ecological environment has an important influence on the development of outdoor sports.

#### 4. Conclusions

- (1) In this paper, questionnaire survey and mathematical statistics are used to integrate the two methods. Taking three squares and four park outdoor sports venues in a city as the research sites, 400 men and 400 women, a total of 800 people, aged 20–75 years, were selected. This paper analyzes the impact of outdoor sports development on urban atmospheric ecological environment through questionnaire survey.
- (2) The results show that the average value of noise and other factors affects the development of outdoor sports to varying degrees. Urban air quality has a physiological impact on outdoor sports people. A good urban ecological environment can bring good development to outdoor sports.
- (3) The results of this study show that the number of days of air reaching the standard in the city is 240 days, accounting for 65.8% of the whole year; According to the noise evaluation standard, the noise of the seven locations in this study is level I, which is at a good level. People of different ages have different physical perception characteristics of air quality. The elderly are more sensitive to outdoor urban environment. The higher the quality of urban environment, the more conducive to people's health.

#### Data Availability

The figures and tables used to support the findings of this study are included in the article.

## Conflicts of Interest

The authors declare that they have no conflicts of interest.

## Acknowledgments

The authors would like to show sincere thanks to those technicians who have contributed to this research.

## References

- [1] N. Kumar, A. Chu, and A. Foster, "An empirical relationship between PM<sub>2.5</sub> and aerosol optical depth in Delhi Metropolitan," *Atmospheric Environment*, vol. 41, no. 21, pp. 4492–4503, 2007.
- [2] F. S. Silva, J. Cristale, P. A. André, P. H. N. Saldiva, and M. R. R. Marchi, "PM<sub>2.5</sub> and PM<sub>10</sub>: the influence of sugarcane burning on potential cancer risk," *Atmospheric Environment*, vol. 44, no. 39, pp. 5133–5138, 2010.
- [3] H. Biglari, S. Geravandi, M. J. Mohammadi et al., "Relationship between air particulate matter & meteorological parameters," *Fresenius Environmental Bulletin*, vol. 26, no. 6, pp. 4047–4056, 2017.
- [4] I. I. Ozyigit, B. E. Yaln, I. Dogan, G. Demir, and C. Yarci, "Determining element accumulations in Turkish red pine used as a bioindicator for revealing of existing pollution on both sides of Bosphorus in Istanbul," *Fresenius Environmental Bulletin*, vol. 29, no. 7, pp. 4963–4972, 2020.
- [5] M. Tuzen, "Determination of some metals in honey samples for monitoring environmental pollution," *Fresenius Environmental Bulletin*, vol. 11, no. 7, pp. 366–370, 2002.
- [6] M. C. Mckean, M. Leech, P. C. Lambert, C. Hewitt, S. Myint, and M. Silverman, "A model of viral wheeze in nonasthmatic adults: symptoms and physiology," *European Respiratory Journal*, vol. 18, no. 1, pp. 23–32, 2001.
- [7] X. Liu and F. Yu, "The effect of air pollution on the expression of serum IL-6 and TNF- $\alpha$  in exercise crowd," *Journal of Guangzhou Sport University*, vol. 26, no. 6, pp. 72–74, 2006.
- [8] H. Kim, D. Lee, H. M. Choi, and J. Park, "Joint cooling does not hinder athletic performance during high-intensity intermittent exercise," *International Journal of Sports Medicine*, vol. 37, no. 8, pp. 641–646, 2016.
- [9] S. S. Park, J. M. Ko, and S. Y. Cho, "Investigation of possible sources of water-soluble organic carbon particles observed with an online monitoring system," *Atmospheric Environment*, vol. 45, no. 19, pp. 3257–3266, 2011.
- [10] Y. Liu and R. M. Harrison, "Properties of coarse particles in the atmosphere of the United Kingdom," *Atmospheric Environment*, vol. 45, no. 19, pp. 3267–3276, 2011.
- [11] R. D. Magomet and N. A. Mironenkova, "The impact of anthropogenic activities on the indicators of environmental pollution," *Biosciences Biotechnology Research Asia*, vol. 12, no. 1, pp. 7–14, 2015.
- [12] K. Ebisu and M. L. Bell, "Airborne PM<sub>2.5</sub> Chemical components and low birth weight in the northeastern and mid-atlantic regions of the United States," *Environmental Health Perspectives*, vol. 120, no. 12, pp. 1746–1752, 2012.
- [13] S. Zoras, A. G. Triantafyllou, and V. Evagelopoulos, "Modelling of PM<sub>2.5</sub> episodes in four cities of northwestern Greece," *Fresenius Environmental Bulletin*, vol. 15, no. 4, pp. 306–313, 2006.
- [14] B. D. Jimenez-Velez, A. Gioda, U. Perez, and Z. Rosa, "Particulate matter (PM<sub>10</sub> and PM<sub>2.5</sub>) from different areas of Puerto Rico," *Fresenius Environmental Bulletin*, vol. 16, no. 8, pp. 861–868, 2007.
- [15] X. S. Luo, Z. Zhao, Y. Chen, X. Ge, and D. Zhang, "Effects of emission control and meteorological parameters on urban air quality showed by the 2014 Youth Olympic Games in China," *Fresenius Environmental Bulletin*, vol. 26, no. 7, pp. 4798–4807, 2017.
- [16] P. Louie, J. G. Watson, J. C. Chow, A. Chen, D. Sin, and A. Lau, "Seasonal characteristics and regional transport of PM<sub>2.5</sub> in Hong Kong," *Atmospheric Environment*, vol. 39, no. 9, pp. 1695–1710, 2005.
- [17] C. C. Daigle, D. C. Chalupa, F. R. Gibb et al., "Ultrafine particle deposition in humans during rest and exercise," *Inhalation Toxicology*, vol. 15, no. 6, pp. 539–552, 2003.
- [18] I. Mordukhovich, J. Lepeule, B. A. Coull, D. Sparrow, P. Vokonas, and J. Schwartz, "The effect of oxidative stress polymorphisms on the association between long-term black carbon exposure and lung function among elderly men," *Thorax*, vol. 70, no. 2, pp. 133–137, 2015.
- [19] L. Shao, Z. Shi, and Q. Huang, "Research on inhalable particulate matter in Urban atmospheric environment," *Environmental Protection*, vol. 23, no. 1, pp. 24–26, 2000.
- [20] G. T. Proias, P. T. Nastos, and A. G. Paliatsos, "PM<sub>10</sub> concentrations in the urban area of Volos, Greece," *Fresenius Environmental Bulletin*, vol. 11, no. 8, pp. 499–504, 2002.

## Research Article

# Granger Causality Analysis of Foreign Trade in Cement Products and Ecological Impact in China

**Chen Feng** 

*Henan Institute of Economics and Trade, Zhengzhou, Henan 450000, China*

Correspondence should be addressed to Chen Feng; 19407129@masu.edu.cn

Received 23 May 2022; Accepted 16 June 2022; Published 8 July 2022

Academic Editor: Punit Gupta

Copyright © 2022 Chen Feng. This is an open access article distributed under the Creative Commons Attribution License, which permits unrestricted use, distribution, and reproduction in any medium, provided the original work is properly cited.

This paper presents an in-depth study and analysis of the impact of foreign trade on cement products and the ecological environment in China through Granger causality analysis. Based on the theoretical basis of foreign trade, ecological environment, and the relationship between them, a general equilibrium model is used to empirically analyze the “three effects” of foreign trade in Chinese cement products on the ecological environment, and the effects of import and export trade on ecological environment and the net effects are calculated, respectively. Then, based on the data of domestic and foreign cement product production and trade, the purpose, scope, and environmental impact factors of the ecological impact of foreign trade of Chinese cement products were determined by the life cycle assessment method, and the inventory analysis was carried out in phases based on the six aspects of nonrenewable resource depletion, global warming, photochemical ozone generation, acidification, eutrophication, and human health damage. The results were characterized and standardized, and the hierarchical analysis method was used to weight the evaluation of each environmental impact type, and finally, the resource consumption coefficient and environmental impact load index values and corresponding ratios were determined based on the green product evaluation method. This paper establishes an index system for the ecological and environmental impacts of foreign trade of cement products, which is a guide for the ecological and environmental impacts of foreign trade of other products in China. The results of the study on the ecological and environmental impacts of foreign trade of Chinese cement products also have important practical significance for the formulation of regulations and standards related to the cement industry, the adjustment of the import and export structure of cement products, and the improvement of production equipment and processes.

## 1. Introduction

Amid economic globalization and fierce market competition, human material civilization has developed rapidly, yet this has also increased the pressure on the healthy development of resources and the environment. While the wave of the industrial revolution pushes the development of productivity, it also brings different degrees of environmental pollution problems. While pursuing material life civilization, human beings must pay attention to the traditional industrial model as a kind of over-consumption and predatory development, which makes the quality of resources and environment deteriorate continuously [1]. Humankind began to reflect on whether the path of economic development was not accompanied by the

deteriorating quality of the environment. People realize that it is unscientific to pursue economic growth unilaterally without considering resources and the environment, so how to promote the coordinated development of economic growth and energy conservation and environmental protection has become an issue of keen concern [2]. At present, China’s economic growth has entered a new normal stage, with the growth rate shifting from high to medium-high, but this does not mean that China is no longer concerned about the speed of economic growth, but rather focuses on the quality of development. China is now in the ranks of middle-income countries, but this is accompanied by problems such as the widening gap between the rich and the poor and serious environmental pollution. To prevent China from falling into the middle-income trap, it is crucial to

coordinate economic development with environmental protection and slow down the growth rate, which not only can optimize the product structure, but also can effectively promote China into the ranks of high-income countries [3]. In the new normal stage, economic development is changing from focusing on speed to improving quality, which will inevitably slow down the speed, but improve the quality of economic development to gain more benefits, which will help China's economy achieve sustainable development overall. The change of China's economic growth model has also driven China's economic development from investment-driven to innovation-driven, improving the ability of science and technology innovation, which can improve productivity and has a significant positive effect on the management of environmental pollution and resource conservation [4]. In the context of the new economic normal, this paper studies the interaction between China's export trade and environmental issues and makes a point of policy suggestion to realize the coordinated development of cement products trade development and environmental governance.

In recent years, with the widespread concern of global warming and the increasing pressure on the global ecological environment, scholars from various countries have put forward new terms such as circular economy, environmentally coherent design, and eco-friendly materials, and extensive research has been conducted on the ecological and environmental issues such as implied energy and implied ecological footprint. This provides an alternative way to study the relationship between traditional foreign trade and the ecological environment, that is, from the perspective of final consumption, the analysis of implied carbon and implied pollution in trade import and export products reveals the impact of foreign trade on the environment and thus verifies whether there is pollution transfer and other problems [5]. Therefore, for the current situation of foreign trade in the cement industry of "two highs and one capital," the impact on the ecological environment can be evaluated qualitatively and quantitatively by using methods such as life cycle assessment (LCA). It is important to analyze the environmental impact of cement foreign trade, formulate relevant policies, adjust its import, and export structure, and improve the process.

China is currently facing a slowdown in economic growth, weak profitability in the real economy and declining prices of industrially manufactured goods, and double-digit economic growth has become outdated. In the context of the new normal, supply-side reform is an inevitable choice. The slowdown in China's economic growth is not a lack of demand, but a change in domestic demand, but the supply side cannot meet the current changes in the demand side, so adjustments should be made on the supply side to make the product structure more optimal to meet the people's growing needs. At present, profits in industries such as steel and cement have fallen sharply, and some industries are even experiencing losses. Overcapacity has become a roadblock on the road to China's economic transformation. The oversupply of low and medium value-added products and undersupply of high value-added products has led to an

asymmetry between supply and demand, so it is imperative to promote supply-side reform, which requires the Chinese government to actively adjust the export structure and foreign trade growth, eliminate a certain percentage of zombie enterprises with backward capacity, and vigorously support green and clean industries. The economic development has produced environmental problems such as air pollution, serious waste of water resources, and soil erosion, which seriously restrict China to achieve sustainable development. This paper mainly focuses on a descriptive statistical analysis of China's export trade and environmental pollution, effect analysis of export trade and environmental pollution and environmental regulation, and empirical analysis of the interaction between China's export trade and environmental problems. Combined with the above argumentation results, this paper proposes some countermeasures to promote the coordinated development of China's export trade and environment, which is helpful to promote the implementation. It also provides some reference for the coordinated development of export trade and environmental issues in China under the new situation, and has some theoretical significance as well as practical significance.

## 2. Methods and Materials

*2.1. Current Status of Research.* Differences in environmental regulations are an important reason for industrial spatial reconfiguration, if the more stringent level of environmental regulations in the home country will increase the operating costs of enterprises and thus prompt them to move out of the country, the differences in environmental regulations bring about the repositioning of enterprise location choice is to verify the pollution paradise hypothesis [6]. There are three main approaches to study this issue: first, to examine the impact of foreign investment due to differences in environmental regulations in different regions of the host country; second, to examine the impact of foreign investment due to differences in environmental regulations in different industries in the host country; and third, to examine the impact of foreign investment due to differences in environmental regulations in the home and host countries [7–9].

Eco-efficiency has the following three connotations: Firstly, eco-efficiency considers both the economic and environmental goals of a business. From a business perspective, it requires the provision of win-win with economic benefits and environmental benefits [10]. Secondly, the input and lower cost to create higher quality products, to achieve the enterprise district city economy to provide integration into the sustainable development of eco-efficiency will be sustainable development as the enterprise's own goals, to provide an opportunity for the enterprise or regional economy to integrate into the process of sustainable development, industrial enterprises to generate ideas about the environment at the same time to reduce the environmental impact to a minimum, from the guarantee [11]. Thirdly, eco-efficiency requires enterprises to produce high-quality products while reducing environmental impact to a

minimum, from the raw materials of the product to the entire process of production and sales, WBCSD points out that the implementation of ecological three heart elements of enterprises to reduce the environment within the limits of self-sustainability [12]. According to the World Business Council for Sustainable Development (WBCSD), there are seven basic principles to be met by enterprises in implementing efficiency: firstly, the intensity of raw material consumption for products and services should be reduced; secondly, the intensity of energy consumption for products and services should be reduced; thirdly, the emission of toxic substances should be reduced; fourth, the recyclability of raw materials should be increased; fifth, the use of renewable resources should be maximized; sixth, the durability of products should be continuously improved; and seventh, the use of products should be increased, and the service intensity of the product should be enhanced gradually. From these seven elements, we can realize the reduction of resource consumption and the gradual reduction of environmental impact, and finally realize the eco-efficiency goal of improving product quality and service [13–15].

To sum up, scholars at home and abroad have mainly studied the relationship between export trade and environmental pollution from the three aspects. In this paper, we have combed through the relevant literature on foreign trade and environmental issues, and we can see that in terms of theory, scholars at home and abroad have established the general equilibrium analysis theory and the theory of environmental effects of export trade, etc. In terms of empirical evidence, some scholars have adopted the CGE model, some have established panel data, and some have adopted the input-output approach. However, due to the different ideas and perspectives of each scholar, and the different statistical caliber of data, various conclusions are obtained. It can be found that most scholars only study the single influence relationship between export trade and environmental problems, and few scholars study the influence of the environment on the export trade. Based on previous studies, this paper conducts effect analysis and empirical analysis on the interaction between export trade and environmental problems based on the VAR model, draws conclusions, and puts forward some policy recommendations based on the analysis results.

## 2.2. Granger Causality Analysis of Foreign Trade in Cement Products and Eco-Environmental Design in China

### 2.2.1. Granger Causality Analysis Model Analysis.

By analyzing the current situation of China's foreign trade in cement products and the current situation of China's ecological impact, it can be assumed that there is a causal relationship between China's foreign trade in cement products and the ecological impact [16]. To determine whether there is a causal relationship between the two, and if so, which side is the cause and which side is the effect, the Granger causality test is used to analyze this paper. Granger causality is defined as the variance that depends on the best least squares prediction using all the information at some

time point in the past. A prerequisite for Granger causality test is that the time series must be stable, otherwise false regression may occur. Granger causality test assumes that the information about each variable of  $x$  and  $y$  is included in their time series, and its regression model is shown in the following equations.

$$y_t = \sum_{i=1}^q a_i x_{t-i} - \sum_{j=1}^q \beta_j x_{t-j}, \quad (1)$$

$$x_t = \sum_{i=1}^q \lambda_i y_{t-i} - \sum_{j=1}^q \delta_j y_{t-j}. \quad (2)$$

The hypothesis was tested using the postmortem test, i.e.,

$$F = \frac{(RSS_R + RSS_U) * q}{RSS_U / (n - k)}. \quad (3)$$

It invites the number of parameters to be estimated in the unconstrained regression of the distribution with and degrees of freedom. The null hypothesis is rejected if the value calculated at the selected significant level exceeds the critical value. By doing the regression of  $Xt$  with and without the lagged term through equation (3), respectively, the sum of squared residuals is

$$RSS_1 = \sum_{i,t=1}^n (X_{t-i} + X_{t+i}). \quad (4)$$

Linear causality test is not able to determine whether the variables have nonlinear causality, considering the nonlinear model:

$$X_t = \beta_i x_{t-1} X X_{t-i} - \varepsilon_i. \quad (5)$$

In this paper, we examine whether there is a causal relationship between the export and import trade of cement products and the ecological environment in China, respectively. Among them, the causal relationship between export trade of cement products and ecological environment is selected to test the export trade volume of our enclosed cement products from 2016 to 2020 and the data of cement industry emissions of wastewater,  $SO_2$ , dust, soot, solid waste and coal, and electricity consumption; since the pollutant emissions generated during the production of imported cement products are in the producing countries, and the foreign data of cement industry pollutant emissions are difficult to obtain. In this paper, domestic pollutant emission data are used instead to approximate whether there is a causal relationship between the import trade of cement products and the ecological environment, and the data are obtained from the China Statistical Yearbook and EPS Global Statistical Platform in previous years. Granger causality test can be performed for any two variables using Eviews 6.0, and considering both the serial correlation of the test model and the red pool information criterion (AIC), it is found that the lagged 4th order test model does not have 1st order autocorrelation, and the AIC value is small, so the test results at 5% significance level, as shown in Figure 1.



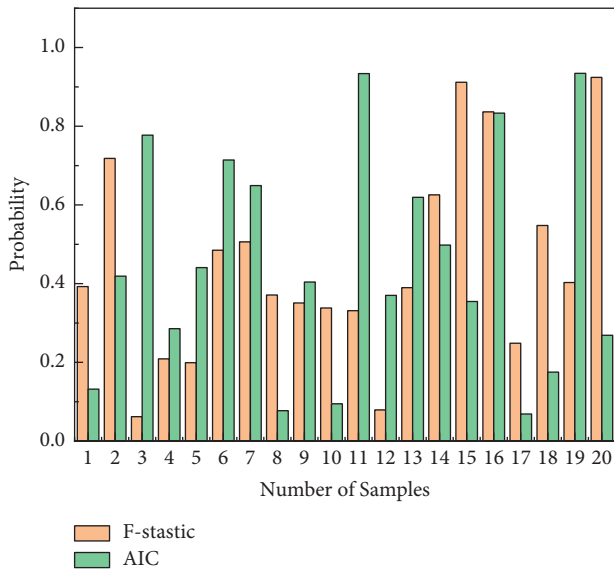


FIGURE 1: Granger causality test results.

where EX denotes the export trade volume of Chinese cement products by year, IM denotes the import trade volume of Chinese cement products by year, WW denotes the wastewater emission of the Chinese cement industry by year,  $SO_2$  denotes the  $SO_2$  emission of the Chinese cement industry by year, SMOKE denotes the soot emission of Chinese cement industry by year, DUST denotes the dust emission of Chinese cement industry by year, SW denotes the solid waste emission of Chinese cement industry by year, COAL indicates the coal consumption of Chinese cement industry by year, and  $E$  indicates the electricity consumption of Chinese cement industry by year.

As can be seen from Figure 2, at the 5% significance level, the lag length is within 3. The export trade of Chinese cement products is the cause of wastewater,  $SO_2$ , dust, and solid waste emissions, not the cause of soot emissions, while none of the pollutant emissions is the cause of export trade, and the export trade of Chinese cement products and coal and electricity consumption are causal; on the other hand, the import trade of our cement products is the cause of wastewater,  $SO_2$ , dust, and solid waste emissions, not the cause of soot emissions, while none of the pollutant emissions is the cause of export trade. And the electricity consumption in the producing countries is the cause of import trade of Chinese cement products, and vice versa, and there is no causal relationship between import trade and coal consumption in the producing countries [17]. This result could indicate that the import and export trade of Chinese cement products is the cause of ecological impacts, while changes in the ecological environment may not affect the import and export trade of cement products. This result may be because labor, capital, and resources play a decisive role in the production process of cement products, while the relative influence of the ecological environment is limited, which is particularly evident in the causal relationship between the export trade of Chinese cement products and the ecological environment. The development of the Chinese cement industry lacks a market for effective trading of

energy, resource use, and pollution externalities, which largely limits the role of ecology in influencing its foreign trade.

The current situation and problems of China's ecological environment are introduced, the overview of China's cement industry and the current situation of foreign trade of cement products are briefly explained, and the role of China's cement industry in influencing the ecological environment is investigated. The Granger causality test model is used to test whether there is a causal relationship between the foreign trade of Chinese cement products and the ecological environment, and it is concluded that: the export trade of Chinese cement products is the cause of wastewater,  $SO_2$ , dust, and solid waste emissions, not the cause of soot emissions, while none of the pollutant emissions is the cause of export trade, and the export trade of Chinese cement products. On the other hand, the import trade of Chinese cement products is the cause of wastewater,  $SO_2$ , dust and solid waste emissions in the producing countries, not the cause of soot emissions, and none of the pollutant emissions in the producing countries is the cause of the import trade, and the electricity consumption in the producing countries is the cause of the import trade of Chinese cement products, otherwise, there is no causal relationship between the import trade and coal consumption in the producing countries [18].

Due to the influence of environmental regulations, multinational enterprises are happy to invest and build factories in China, especially at the beginning of the reform and opening because of the forced economic development, China does not pay enough attention to the environment and is pollution-intensive industries have room to survive. The environmental endowment of any country is certain, but the government can choose how many environmental resources to use, so it is also possible to play political games, even if the resource endowment is the same, it will be different because of the amount of use, so the national environmental regulations reflect the number of resources used. If China implements more lenient environmental regulations, then environmental factors are relatively abundant, while if developed countries implement more stringent environmental regulations, then environmental factors are relatively scarce. As mentioned above, the implementation of more stringent environmental regulations in the home country means adding additional production costs, investing more resources to control pollution emissions, or bearing fines for violating pollution limits, such additional expenses for enterprises means losing their competitive advantage, then multinational enterprises will re-strategize the global layout to adjust production costs. Therefore, to reduce production costs, more production projects will be moved to China, where environmental regulations are lax, and then China becomes a pollution haven for developed countries. Therefore, this paper analyzes the pollution paradise hypothesis theory through the cost-benefit model.

The industrial distribution of foreign investment is not only in the polluting industries, with the change of China's investment policy, there are also some high-tech industries new pollution, regardless of which industries, but the

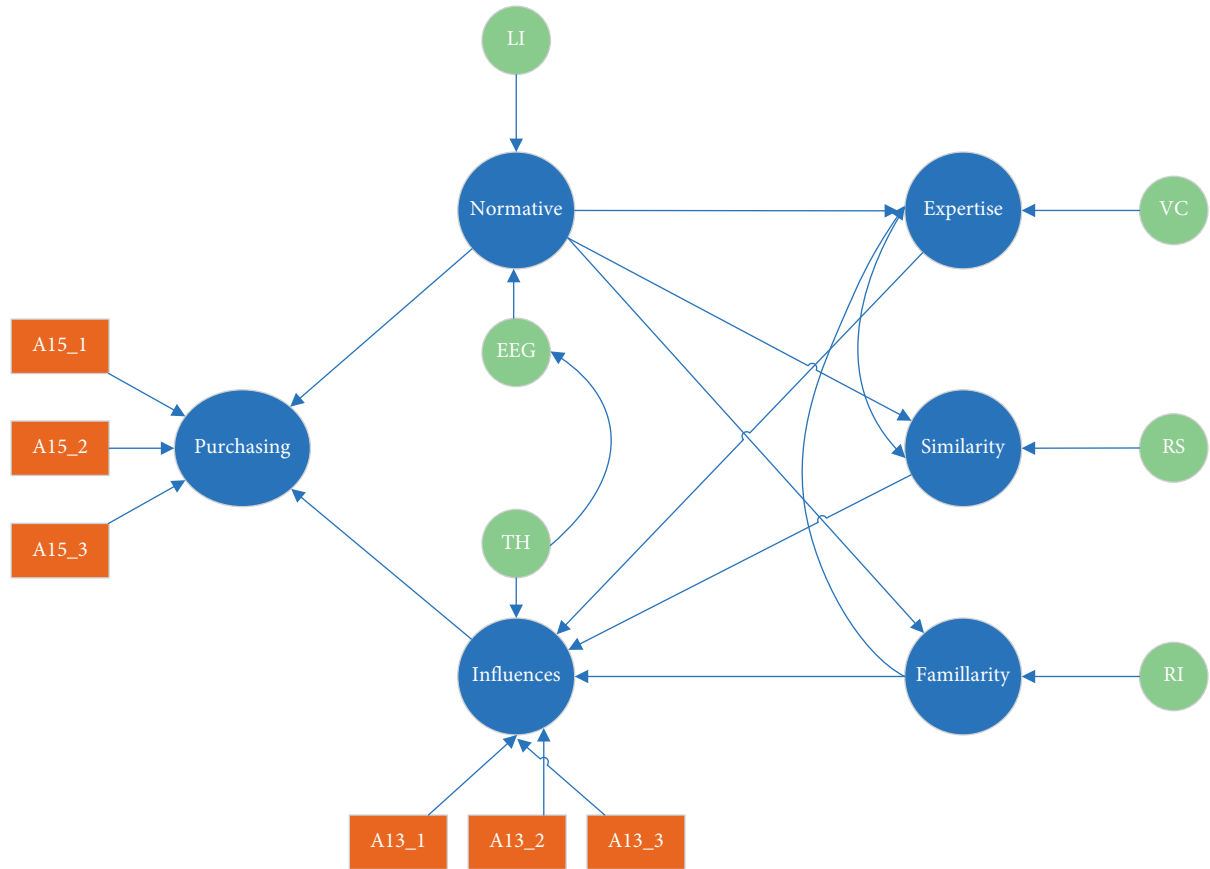


FIGURE 2: Granger causality analysis model.

important thing is also that China to undertake the link, even if it is a polluting industry, if China is only responsible for the design of R&D or late sales planning and other links, then the environmental impact is very different.

2.2.2. *Analysis of Foreign Trade and Ecological Environment of Cement Products in China.* Cement production is characterized by seasonality and regional differences, etc. Considering the integrity, repeatability, representativeness, and timeliness of data in life cycle evaluation, the time boundary is defined as one year as one life cycle of cement foreign trade. The research content is spatially uncertain and the spatial boundary is blurred. Considering the differences in cement industry activities, legislative requirements, and consumption habits in different countries and regions, this paper divides the life cycle of foreign trade of cement products into two parts, one for the import of cement products and the other for the export of cement products. In these two parts of the study, to make the research findings general and to simplify the calculation, “import dummy countries” and “export dummy countries” are set up, respectively, and the data related to the main import and export countries of cement in China are analyzed comprehensively from 2016 to 2020. The main import and export countries (regions) of Chinese cement products and the corresponding import and export volume data in 2020. Cement products have a complete life cycle starting from the

extraction of raw materials, through production, use, and finally disposal, but the use and disposal stages of cement are a long process with little geographical variation in its environmental impact, and given that the main study of this paper is the life cycle of cement foreign trade, the scope of this study is defined as the extraction of raw materials, the ecological impact of production, processing, and transportation of finished cement products, and the environmental impact of cement use and disposal [19]. The impact of cement use and disposal is not included in the scope of this study.

The functional unit determines the scale for comparing products and thus allows the standardization of inputs and outputs of a product system, so the functional unit must be clearly defined and measurable. In this paper, considering the production efficiency, service life, and quality standard of cement, P.O.42.5 cement with high LT production and wide application is selected as a functional unit. This functional unit can express the serviceability of cement and is comparable with international cement products, so it is appropriate to be applied in the study of foreign trade. Based on the determination of the functional unit, the composition of the baseline flow needs to be determined for characterizing the inputs and outputs of the system. The system boundary is shown in Figure 3.

The cement industry not only consumes huge amounts of energy and resources but also seriously pollutes the environment. The cement production process inevitably

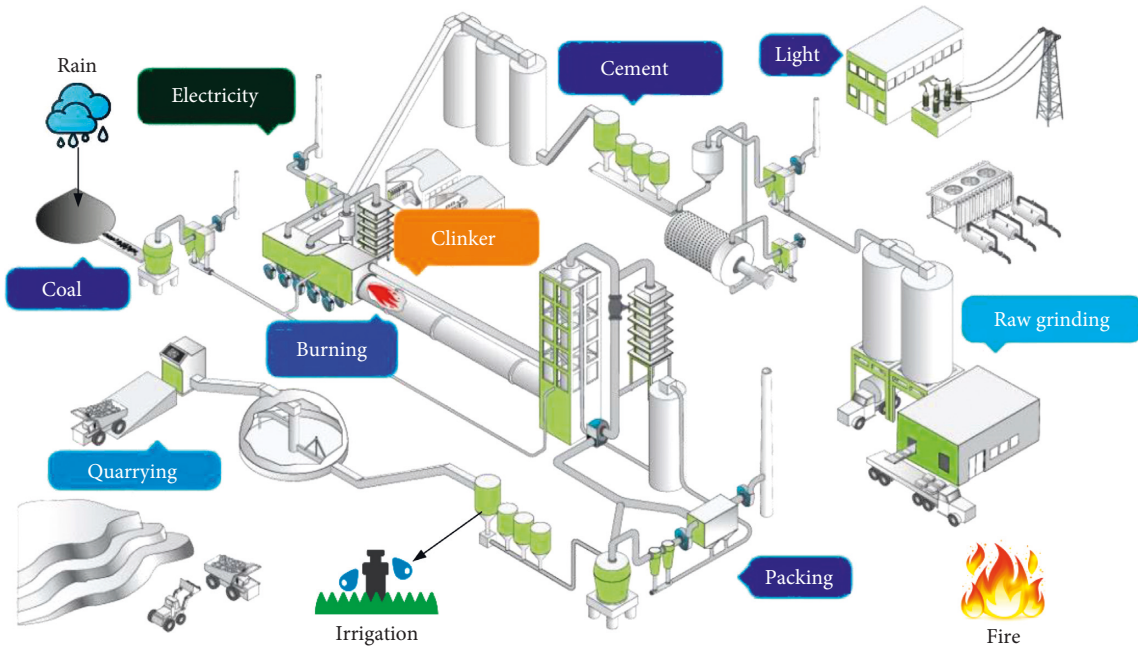


FIGURE 3: System boundary.

consumes energy and resources and emits pollutants such as waste gas and dust. This requires the identification of the main environmental impact factors of the cement industry. Currently, the main pollutants in the cement industry are soot and dust, which are characterized by large emissions and many emission points,  $\text{CO}_2$ , and  $\text{NO}_x$ , which are also the main pollutants in the cement industry. The new dry cement process does not produce industrial wastewater directly, but mainly cooling water for equipment, which can be recycled. The cement industry not only produces and discharges less solid waste but also can conditionally use coal gangue, slag, and fly ash as alternative raw materials and fuels. According to this analysis, the environmental impact factors of this study are dust,  $\text{CO}_2$ ,  $\text{SO}_2$ , and  $\text{NO}_x$ .

Inventory analysis is the process of collecting qualitative or definitive input and output data from a production system and quantifying the data by performing calculations. It includes the process of collecting and calculating data to quantify the inputs and outputs of a product system. The inputs and outputs mainly include the use of resources and emissions to air, water, and land associated with the system, which can be interpreted according to the purpose and scope of the evaluation based on the above data quality requirements and are also used as input components for the LCA. It is usually divided into four stages: determining the functional units, describing the internal processes of the system, collecting data, and processing data. It is necessary to collect data to be included in the inventory for each unit process within the system boundary, including both qualitative and quantitative. The process of collecting data varies depending on the unit process and its purpose and scope. The following is an analysis of the ecological impact inventory for each stage in the life cycle of cement products sub-export and import.

The system shown in Figure 4 is separated from the system boundary that surrounds it, and the system

environment outside the boundary is both the source and sink of all inputs to the system and all outputs. To describe the specific processes of the model and the types of data associated with them, process flow diagrams are drawn, as shown in Figure 4.

Raw material extraction stage, using Di Xianghua calculated by China's resources and energy production of life-cycle emissions data to calculate pollution emissions data [20]. In the stage of raw material transportation and energy and resource production, the pollutant emission data of China's common process is used to calculate by multiplying the corresponding raw material and energy consumption, and the list of the main raw material and energy consumption of import and export cement products with the transportation method and the basic data of pollutant emission of common process. In the production stage of cement products, the data of dust emission is calculated by the ratio of the data after dust removal treatment and dust removal efficiency; the emission data of  $\text{SO}_2$  and  $\text{NO}_x$  are obtained from monitoring data; the emission of  $\text{CO}_2$  is usually not monitored, so the emission of  $\text{CO}_2$  is calculated by the empirical formula. The import and export of cement products in China are mainly through waterways, and the ecological impact of import and export of cement products per unit function can be calculated from the pollutant emission data of waterways.

External managers decide certain requirements of the design according to the market situation (product performance requirements, environmental policy requirements, market price requirements, etc.), and then internal design managers put forward the conceptual framework of the design according to the external requirements combined with their actual situation and development purposes, and then hand over to the designers to complete the detailed technical process design. The whole process is regulated and

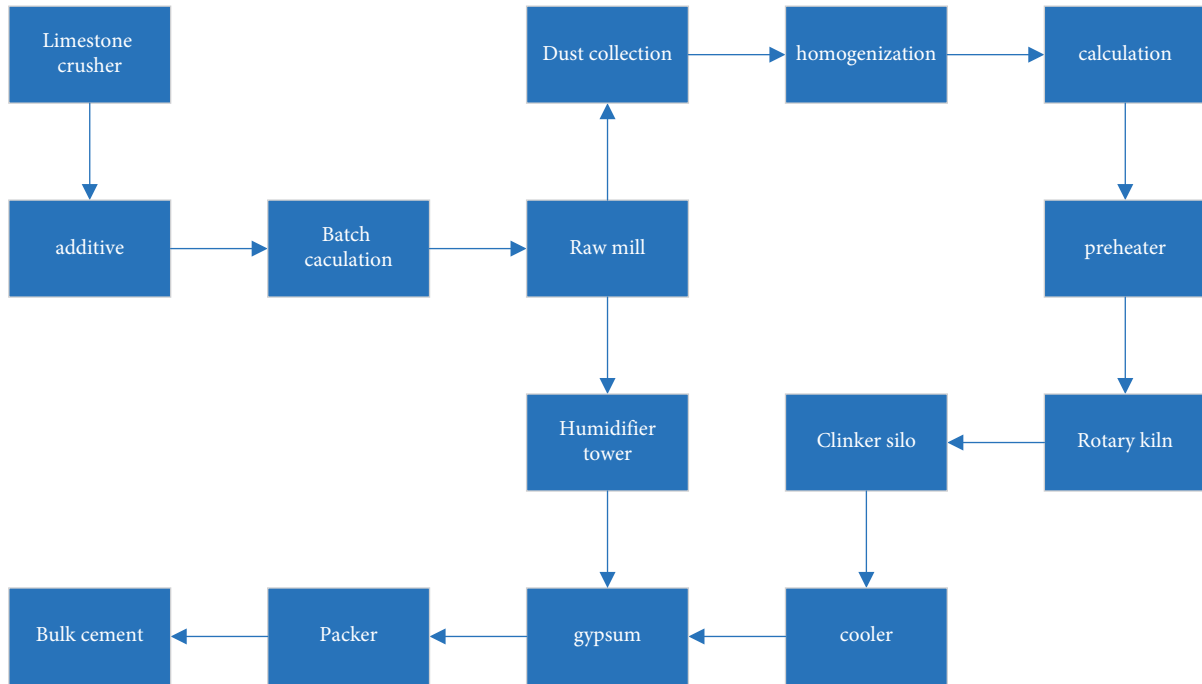


FIGURE 4: Cement production flow chart.

coordinated by the three parties, and the final design plan is decided by the external managers after several mutual feedbacks. The research and development design of environmental materials is the issue of environmental design of materials. It takes the strategy of sustainable development of the material industry as the starting point and takes into consideration the environmental compatibility, economy, and functionality of the material during the whole life cycle from the design stage of the material, and balances each other, to make its comprehensive performance index reach the standard of environmental material.

### 3. Results

**3.1. Multivariate Nonlinear Granger Causality Test Results.** To verify the feasibility of the data sharpening method, we first investigate from bivariate data, two sets of data are selected for simulation,  $\eta$  values are taken at equal spacing on  $[-1, 1]$ ,  $\varepsilon$  is the number of  $n$  randomly generated from a normal distribution with mean 0 and variance 1,  $y = \sin 4\pi - \varepsilon$ ,  $n = 300$ , these two sets of data have a nonlinear causal relationship, first use Leave-one-out cross-validation (Leave-one-out), to obtain the optimal bandwidth, the bandwidth graph is shown in Figure 5. Leave-one-out means that only one item in the original sample is used as verification data, while the rest is left as training data. This step continues until each sample is treated as validation data.

The optimal bandwidth  $h = 0.04$  is obtained from the bandwidth graph, and then the data is sharpened using the Nadaraya–Watson estimation-based data sharpening method to obtain the sharpened graph. From the sharpened data graph, we can see that the estimated red dashed line based on the Nadaraya–Watson estimation method is

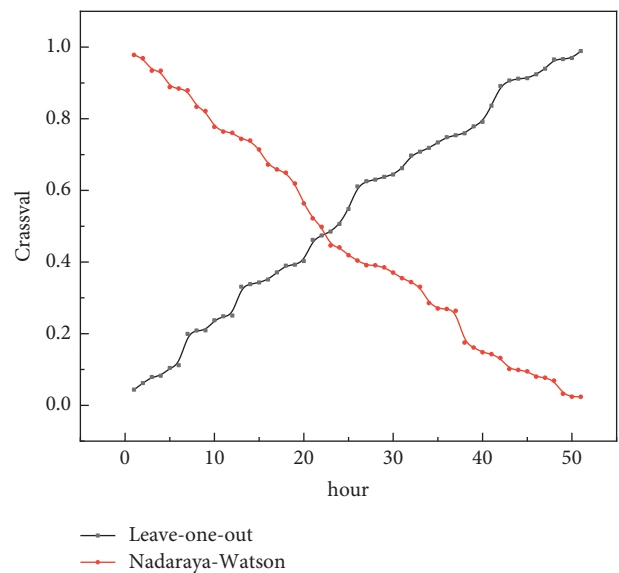


FIGURE 5: Cross-validation bandwidth map.

different from the original data, and the first and third wave peaks are lower than the original data after sharpening. Therefore, we can use the data sharpening method to reduce the model error and obtain more accurate results (Figure 6).

The residuals of the bivariate and eight-variate data filtered with the VAR model are then examined using the nonlinear NKTN causality test. Finally, the residuals are tested with the symmetric GARCH-BEKK model and APARCH model after filtering the volatility data to obtain the unidirectional and bidirectional causality of RMB exchange rate changes. It is found that the causal relationship between the variables decreases with the filtering method, indicating that there is a causal relationship between the

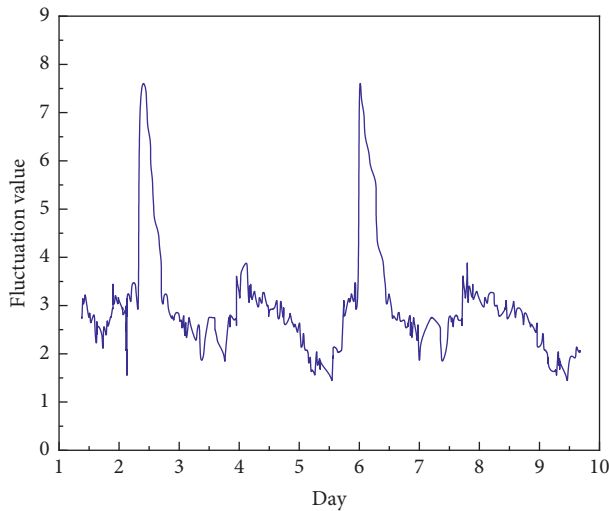


FIGURE 6: Data sharpening graph.

residuals and volatility. To reduce the error in the multivariate causality test, we use the data sharpening method, which is to obtain new data by acting on the data with a high-dimensional kernel function. In this paper, we propose the approximate test statistic QNKTN and its limiting distribution based on the research method in Diks and Wolski [21] and the data sharpening method. The nonlinear QNKTN causality test yields nonlinear causality not detected by the nonlinear NKTN causality test, which validates the feasibility of the QNKTN statistic and its limiting distribution, and illustrates that the data sharpening method enhances the performance of the multivariate causality test.

The numerical simulations and empirical analyses in this paper verify the feasibility of data sharpening methods for multivariate nonlinear Granger causality tests, and the performance of nonlinear QNKTN causality tests is enhanced by data sharpening. We can use the data sharpening method to effectively reduce the bias of multivariate nonlinear Granger causality test, and we also need to further investigate the application of the data sharpening method in nonlinear Granger causality test for multidimensional data such as 3D and 4D data. For the linear Granger causality test, we compare the study of linear Granger causality with the study of nonlinear Granger causality. The bivariate and eight-variate tests of linear causality are applied to the raw data of RMB exchange rate changes using the linear Granger causality test. The linear relationship is then filtered by the VAR model on the raw data and the residuals are subjected to the linear Granger causality test to obtain the causal factors. Finally, the residuals were filtered by symmetric GARCH-BEKK model and APARCH model to examine the change in causality after filtering volatility, and the relationship and causes of exchange rate changes were studied from multiple methods and perspectives to obtain the most direct linear causality between variables.

**3.2. Impact Evaluation Results.** Since the results of such an analysis alone do not give an overall picture of the ecological coherence of each situation, standardization of the various

ecological impacts is also required. The purpose of standardizing the parameter results is to better recognize the relative magnitude of each parameter result in the product system under study. This step is the process of calculating the results of the type parameter calculations by dividing them with the very quasi-values. After standardization, the ranking of the equivalent values caused by each ecological impact category of cement product foreign trade is  $GWP > ADP > AP > NP > POCP > HT$ , which indicates that the global warming effect is the largest among the ecological impacts caused by cement product foreign trade, followed by the nonrenewable resource consumption and effects. Comparing the eco-environmental impacts of import and export of cement products, the total eco-environmental impact equivalent value of an exported unit of cement products is 16.41% more than that of imported, among which ADP is 3.22% more; GWP is 23.51% more; POCP is 9.98% less; AP is 3.35% less; NP is 11.33% less; HT is 42.88% more.

The relative index of ecological impact can be expressed in terms of the ratio of the number of ecological impact equivalents to the total number of ecological impact equivalents corresponding to the entire study area. According to the formula of the relative index of eco-environmental impact, the characteristic knot of the eco-environmental impact of each functional unit of cement product foreign trade can be standardized, and the results are shown in Figure 7.

After the standardization of ecological impacts, it is necessary to determine the weight coefficients of each ecological impact, and then obtain the specific environmental impact values. The standardized ecological impact types can be theoretically summed up by unifying the scale and reference standard, and thus the overall ecological coordination can be quantitatively analyzed. Given the different importance of each ecological impact type, the relative weights of each ecological impact type should be determined. The weighted evaluation uses value-based coefficients to convert the index values of each ecological impact type and then combines the parameter results. Since there is no fixed method to determine the weighting factors because it is not very mature yet, the common methods include the expert method, hierarchical analysis, and linear regression equation method. In this paper, the combination of hierarchical analysis and expert method is used to determine the weights. The principle of the abbreviated method of hierarchical analysis is based on experimental data and expert opinion to determine the relative importance of each ecological impact type, then, with the help of matrix operations to derive the relative weight coefficients of each ecological impact type, and finally, the weighted sum to determine the total ecological impact index. Based on the comprehensive analysis of existing cement environmental compatibility evaluation reports and relevant public publications, and combined with expert opinions, the importance scales of cement production eco-environmental impact types are determined in this paper. The relative importance scale used in this paper is shown in Figure 8.

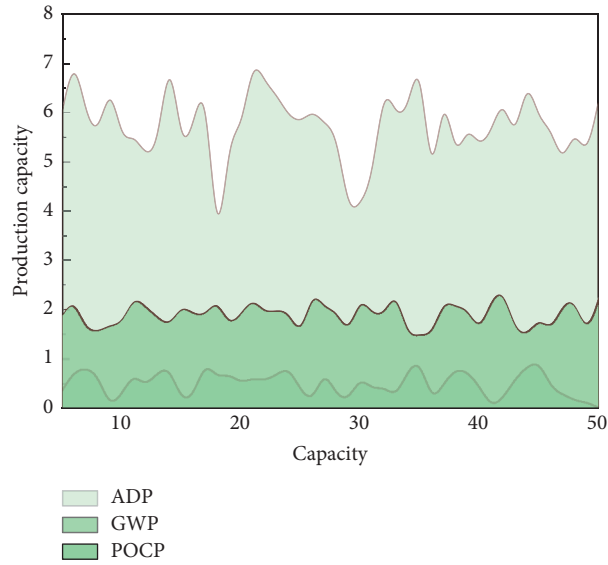


FIGURE 7: Ecological and environmental impact equivalents of foreign trade in cement products.

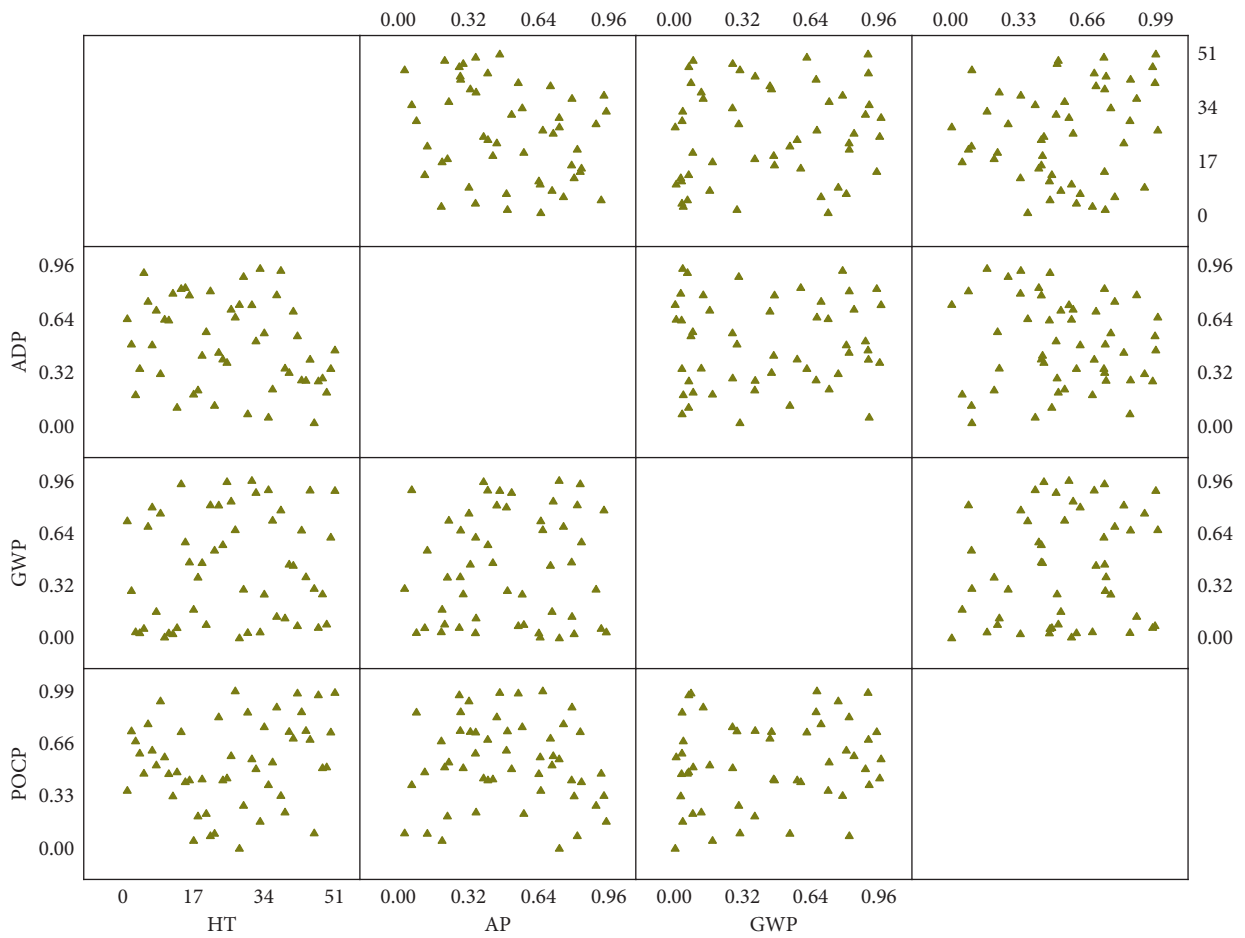


FIGURE 8: Ecological impact type desirability scale.

The sum of the impact ratios of ADP and GWP both exceed 96%. This indicates that the impact on nonrenewable resource depletion and global warming is still the largest among the ecological impacts of foreign trade in cement

products, followed by acidification, with little impact on photochemical ozone formation, eutrophication, and human health damage. From Figure 8, it can also be concluded that the total eco-environmental impact equivalent value of

exported cement products per unit function is 16.00% more than that of imported ones, including 10.31% more ADP; 23.50% more GWP; 10.16% less POCP; 3.33% less AP; 11.43% less NP; and 60.00% more HT. Due to the high solid waste recycling rate of imported cement products, not only the amount of limestone is saved, but also the raw mill output is increased, the crushing and grinding of limestone are greatly reduced, and the consumption of electricity and coal is correspondingly reduced, which makes the consumption of nonrenewable resources decrease. In addition, the reduction of limestone consumption leads to further reduction of CO generated by calcium carbonate decomposition, and thus the impact on the country is also reduced.

In addition, according to the model of the AGP method, ADP corresponds to the resource consumption coefficient, and GWP, POCP, APNP, and HT corresponds to the environmental impact load. The resource consumption coefficient of imported trade is 23.626 and the environmental impact load is 24.581, accounting for 49.01% and 50.99% of the total ecological impact of imported trade, respectively; the total resource consumption coefficient of foreign trade is 49.689 and the total environmental impact load is 54.439, accounting for 47.72% and 52.28% of the total ecological impact index, respectively.

#### 4. Conclusion

- (1) The scale effect and technology effect of import and export trade of Chinese cement products have negative effects on the ecological environment, while the structure effect has positive effects on the ecological environment; the trade openness of the export trade has negative effects on the ecological environment, while the import trade discusses the effects of mode effect, technology effect, and trade openness on the ecological environment of foreign trade of products, and concludes that the scale effect, technology effect, and trade openness have negative effects on the ecological environment.
- (2) It is concluded that the scale effect, technology effect, and trade openness harm the ecological environment, while the structural effect on the ecological environment cannot be determined because of the difference in the effect on different pollutant emissions. According to the model of AGP method, the resource consumption coefficient of export trade of Chinese cement products is 26.063 and the environmental impact load is 29.858, accounting for 46.61% and 53.39% of the total ecological impact of export trade, respectively; the resource consumption coefficient of import trade is 23.626 and the environmental impact load is 24.581, accounting for 49.01% and 50.99% of the total ecological impact of import trade, respectively.
- (3) LCA can provide a more complete overview of the interaction between product life cycle and ecological environment, thus promoting a comprehensive and correct understanding of the ecological impact

caused by the product life cycle. LCA can provide a more complete overview of the interaction between product life cycle and ecological environment, and thus promote a comprehensive and correct understanding of the ecological impact caused by product life cycle, and provide a judgment basis for finding ways to improve the ecological environment and for product and technology selection. In addition, LCA as a systematic method and tool overcomes the limitations and stages of traditional methods for analyzing the problems and is a very important guide for improving the overall ecological environment quality.

#### Data Availability

The figures used to support the findings of this study are included within the article.

#### Conflicts of Interest

The authors declare that they have no conflicts of interest.

#### Acknowledgments

The authors would like to show sincere thanks to the technicians who have contributed to this research.

#### References

- [1] A. K. Seth, A. B. Barrett, and L. Barnett, "Granger causality analysis in neuroscience and neuroimaging," *Journal of Neuroscience*, vol. 35, no. 8, pp. 3293–3297, 2015.
- [2] Z. Rong, K. Ma, D. Gang, and S. Chen, "Study on the short-term and long-term Granger causality relationship between China's domestic and imported timber prices," *Journal of Forest Research*, vol. 24, no. 2, pp. 1–6, 2019.
- [3] J. Huo and Y. Tao, "An empirical study of the impact of China's foreign trade on the ecological environment," *Ekoloji*, vol. 27, no. 106, pp. 945–950, 2018.
- [4] M. Matthews and J. D. Reynolds, "Ecological impact of crayfish plague in Ireland," *Hydrobiologia*, vol. 234, no. 1, pp. 1–6, 1992.
- [5] A. Arfa, M. Benderradji, and D. Alatu, "Statistics on forest fire and analysis of their economic impact in Algeria between 1985 and 2006," *New Medicine*, vol. 8, no. 1, pp. 46–51, 2009.
- [6] M. Eichler and V. Didelez, "On Granger causality and the effect of interventions in time series," *Lifetime Data Analysis*, vol. 16, no. 1, pp. 3–32, 2010.
- [7] J. G. Tamba, D. Njomo, T. Limanond, and B. Ntsafack, "Causality analysis of diesel consumption and economic growth in Cameroon," *Energy Policy*, vol. 45, no. 2, pp. 567–575, 2012.
- [8] U. Triacca, A. Attanasio, and A. Pasini, "Anthropogenic global warming hypothesis: testing its robustness by Granger causality analysis," *Environmetrics*, vol. 24, no. 4, pp. 260–268, 2013.
- [9] Z. Yi, L. Qiang, X. Wen, W. Cai, and G. J. Wang, "Granger causality reveals a dominant role of memory circuit in chronic opioid dependence," *Addiction Biology*, vol. 22, no. 4, pp. 1068–1080, 2017.

- [10] G. Deshpande, S. Laconte, G. A. James, S. Peltier, and X. Hu, "Multivariate Granger causality analysis of fMRI data," *Human Brain Mapping*, vol. 30, no. 4, pp. 1361–1373, 2010.
- [11] S. Ghosh, "Electricity supply, employment and real GDP in India: evidence from cointegration and Granger-causality tests," *Energy Policy*, vol. 37, no. 8, pp. 2926–2929, 2009.
- [12] H. Hassaballa, "Testing for Granger causality between energy use and foreign direct investment inflows in developing countries," *Renewable and Sustainable Energy Reviews*, vol. 31, no. 2, pp. 417–426, 2014.
- [13] G. D. Salvucci, J. A. Saleem, and R. Kaufmann, "Investigating soil moisture feedbacks on precipitation with tests of Granger causality," *Advances in Water Resources*, vol. 25, no. 8/12, pp. 1305–1312, 2002.
- [14] F. S. Matias, L. L. Gollo, P. V. Carelli, S. L. Bressler, M. Copelli, and C. R. Mirasso, "Modeling positive granger causality and negative phase lag between cortical areas," *NeuroImage*, vol. 99, no. 10, pp. 411–418, 2014.
- [15] T. Eichner and R. Pethig, "EU-type carbon emissions trade and the distributional impact of overlapping emissions taxes," *Journal of Regulatory Economics*, vol. 37, no. 3, pp. 287–315, 2010.
- [16] H. Y. Yang, "Carbon emissions control and trade liberalization: coordinated approaches to Taiwan's trade and tax policy," *Energy Policy*, vol. 29, no. 9, pp. 725–734, 2001.
- [17] S. K. Yazdi and B. Shakouri, "The impact of energy consumption, income, trade, urbanization and financial development on carbon emissions in Iran," *Advances in Environmental Biology*, vol. 8, no. 5, pp. 1293–1300, 2014.
- [18] Z. Wang, Y. Li, H. Cai, Y. Yang, and B. Wang, "Regional difference and drivers in China's carbon emissions embodied in internal trade," *Energy Economics*, vol. 83, pp. 217–228, 2019.
- [19] E. Tzimas, A. Mercier, C. C. Cormos, and S. D. Petevs, "Trade-off in emissions of acid gas pollutants and of carbon dioxide in fossil fuel power plants with carbon capture," *Energy Policy*, vol. 35, no. 8, pp. 3991–3998, 2007.
- [20] Y. Li and C. N. Hewitt, "The effect of trade between China and the UK on national and global carbon dioxide emissions," *Energy Policy*, vol. 36, no. 6, pp. 1907–1914, 2008.
- [21] C. Diks and M. Wolski, "Nonlinear granger causality (NGC)-guidelines for multivariate analysis," *Journal of Applied Econometrics*, vol. 2016, pp. 1333–1351, 2008.



## Research Article

# Prediction of Fault Occurrences in Smart City Water Distribution System Using Time-Series Forecasting Algorithm

**Maheswari Chenniappan** <sup>1</sup>, **Divya Gnanavel** <sup>2</sup>, **Kavi Priya Gunasekaran** <sup>2</sup>,  
**R.R. Rajalakshmi** <sup>3</sup>, **A.S Ramya** <sup>4</sup>, **Albert Alexander Stonier** <sup>5</sup>, **Geno Peter** <sup>6</sup>,  
**and Vivekananda Ganji** <sup>7</sup>

<sup>1</sup>Department of Mechatronics Engineering, Kongu Engineering College, Perundurai, India

<sup>2</sup>Department of Information Technology, Hindusthan College of Engineering and Technology, Coimbatore, India

<sup>3</sup>Department of Computer Science Engineering, Kongu Engineering College, Perundurai, India

<sup>4</sup>Department of Civil Engineering, Sanskrithi School of Engineering, Puttaparthi, India

<sup>5</sup>Department of Electrical and Electronics Engineering, Kongu Engineering College, Perundurai, India

<sup>6</sup>CRISD, School of Electrical and Technology, University of Technology Sarawak, Sibu, Malaysia

<sup>7</sup>Department of Electrical and Computer Engineering, Debre Tabor University, Debra Tabor, Ethiopia

Correspondence should be addressed to Vivekananda Ganji; [drvivek@bhu.edu.et](mailto:drvivek@bhu.edu.et)

Received 24 February 2022; Revised 11 April 2022; Accepted 11 June 2022; Published 5 July 2022

Academic Editor: Punit Gupta

Copyright © 2022 Maheswari Chenniappan et al. This is an open access article distributed under the Creative Commons Attribution License, which permits unrestricted use, distribution, and reproduction in any medium, provided the original work is properly cited.

The proposed research work is focused on forecasting the future requirements of water supply based on the current requirement of water and also identifying the possibility of occurrences of cracks and leaks using the ARIMA (autoregressive integrated moving average) model. The experiments were conducted using real-time experimental hardware. The pressure data obtained and their  $p$ -value is less than 0.05, which represents the stability of the data in the ARIMA model. The forecasted pressure data range between 0.451379 N/m<sup>2</sup> and 2.022273 N/m<sup>2</sup>. The frequency of the forecasted pressure ranges between 1.706869 N/m<sup>2</sup> and 3.065836 N/m<sup>2</sup> (maximum peak) and -0.81046 N/m<sup>2</sup> and 1.042164 N/m<sup>2</sup> (minimum peak). Forecasted data of pressure at damaged condition lie between 2.880788 N/m<sup>2</sup> and 3.29797 N/m<sup>2</sup> and frequency ranges between 4.866227 N/m<sup>2</sup> and 5.664348 N/m<sup>2</sup>. Similarly, future forecasted data of water requirement for the next 1 year range between 614.6292 (liters/week) and 620.0099 (liters/week), the frequency of the forecast value with maximum ranging from 617.0086 (liters/week) to 628.5465 (liters/week), and the minimum peaks ranging from 611.0967 (liters/week) to 612.2914 (liters/week). The above data are for a single water distribution pipeline.

## 1. Introduction

Water pipelines face significant problems as a result of chemical leaks, fires, and deformations such as particle accumulation, corrosion, and cracks caused by a variety of factors. The above leads to serious consequences, as the distribution of clean water is one of the major objectives and the whole world depends on it. Hopkins states that the water supply framework today comprises of foundation that gathers, oversees, stores, and conveys water from water sources to shoppers. Because of the absence of new common water sources and an inexorably developing populace, inventive water assets the executive's approaches are required.

[1] Water conveyance frameworks are right now confronting various significant difficulties, including maturing foundation, the interest for consumable water, protecting consumable water quality, debased foundation because of framework failures, ecological concerns, and rising energy costs [2]. Another significant issue facing water utilities is spillage; when it is not noticed long ago, most endeavors address this issue happened after a break or hole had happened. [3, 4] Many researchers studied on the mean-shift algorithm with Gaussian's profile and made applications in the tracking system for better performance in the field of tracking objects. [5, 6] Monica et al. brief that the breaks and holes were fundamentally brought about by enormous varieties in pipe

pressure inside a water conveyance framework [7, 8]. This proposed research is related to [9–12] oil pipeline transportation monitoring using a machine learning algorithm, which is the base work to carry out the present research. What's more, subsequently, in this task, research has been led to recognize the issues that might be happening in the water circulation frameworks ahead of time utilizing time arrangement estimation calculation. The ARIMA model is used for predicting the future based on the past history of variations in datasets. However, it cannot be used to predict highly uncertain long predictions [13]. Jianbin Huang et al. clarify that the time arrangement anticipation is the way toward fitting models to chronicled information and afterward utilizing those models to foresee future perceptions. [14] In the initial step, past perceptions are accumulated and dissected to make a numerical model that catches the arrangement of hidden information-age measures. The model has been utilized to conjecture future occasions in the subsequent stage. This technique is particularly helpful when there is no sufficient logical model accessible. [15, 16] There are various kinds of time-series forecasting broadly utilized. [17] A study used an integrated genetic algorithm (GA), an algorithm which is used for forecasting monthly electrical energy consumption. [18] A detailed review study has been carried out by the authors [19] about the different forecasting models. Among them, the ANN models, support-vector machine models, and ARIMA models were mostly preferable. The present research work uses the ARIMA model for anticipating the future requirements of the water management system. This examination of the line breaks and harms is used to screen the gas or oil pipelines that regularly get harmed and dirty the climate. [20–22] Ling Yang et al. state that the anticipation should be possible by utilizing the both occasional and nonoccasional ARIMA models. [23]. Time arrangements are utilized in the assortment of fields, including numerical money, fabricating, occasion information, IoT information, and some other space of applied science and designing that require worldly estimations. [24–26] As the quickest developing fragment of the information-based industry, time arrangement DBMS will bear witness to the business' developing requirement for time arrangement determination. [27, 28]. Stormwater and drainage management system with an IoT module was developed by the researchers to predict the drainage using machine learning algorithms. The results show that a well-trained algorithm can predict the drainage situations. Hence, the proposed research work is focused on using a time series-based ARIMA model explored through the R studio software, which is one of the widely used platforms for stock predictions. The detailed mathematical study and the results are provided in the subsequent sections to ensure the prediction accuracy.

## 2. Methodology

*2.1. Experimental Hardware for Water Distribution System.* The real-time data are collected from the experimental hardware for the water distribution system, which consists of various components' process tank, reservoir tank, I/P converter, pressure control valve, gate valve, manual hand

valve drain valve, pressure gauge, flow control valve, orifice flow meter, etc., [29] as shown in Figure 1. The experimental hardware comprises three different water control loops from the reservoir to the distribution station for measuring pressure, flow, and level in the water distribution system [30]. Pressure, flow, and level are measured using sensors, and their corresponding data will be monitored using a master control engineering station [31, 32]. The control mechanism involves two-layer control, namely, operator work station and engineering station. The former one has the highest control capability than the second one.

The output of the transmitters is fed as input to the input/output hub module, which is interfaced with the field control station. The process flow diagram for the experimental setup is shown in Figure 2. The flowing water in the setup shown in Figure 2 is discussed as follows [33, 34]. The water is sucked from the water reservoir and is fed into the process level tank with the use of a pump and transmitted to the pipeline system. Different setups for level recording, flow recording, and pressure recording are made to record the real-time data from the water distribution system [35, 36] as shown in Figures 3, 4, and 5. The water distribution system is pilot scaled and used for real-time data monitoring based on pressure and flow sensors' feedback.

The data are obtained in the form of graphs and datasets by using the front end of HMI [37] as shown in Figures 4 and 6. The water is again drained into the water reservoir after the recordings are made, and the total system is shut down. Auto-tuning PID controller is used in the experimental hardware, and it is used for flow and pressure control [38, 39].

*2.1.1. The ARIMA Model for the Future Prediction.* The autoregressive integrated moving average (ARIMA) model is used for future predicted time-series values based on current pressure and flow data in the water distribution system. The ARMA model and ARIMA models have many similarities. However, the general autoregressive model estimates predictions using previous values of the dependent variable [40, 41]. The ARIMA uses the linear regression model, which uses lags as predictors. The ARIMA model uses a forecasting equation based on the time-series regression equation, and it is represented as follows:

Predicted value  $M$  = weighted sum of recent values of  $M$  + weighted sum of recent values of the errors.

The time-series forecasting functional equation is constructed as follows [33, 34]. First, let the predicted value  $M$  indicates  $n$ , which is the  $n$ th difference of  $M$ , and it can be represented as follows:

$$\begin{aligned} \text{When, } n = 0: M_t &= M_t, \\ \text{When, } n = 1: M_t &= M_t - M_{t-1}. \end{aligned} \quad (1)$$

When  $n = 2$ ,

$$\begin{aligned} M_t &= (M_t - M_{t-1}) - (M_{t-1} - M_{t-2}) \\ &= M_t - 2M_{t-1} + M_{t-2}. \end{aligned} \quad (2)$$

From equation (2), it is pointed out that, when  $n = 2$ , it gives a discrete version of the analog second derivative value.



FIGURE 1: Experimental hardware for water distribution system.

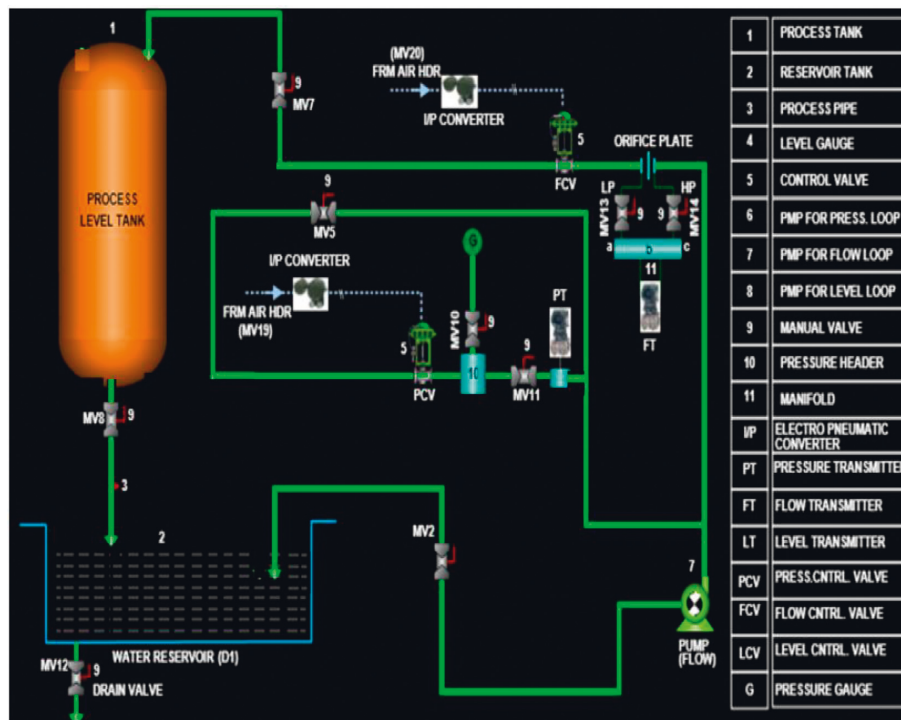


FIGURE 2: Process flow diagram for the experimental setup.

It represents the local acceleration of the time-series forecasting values instead of a normal trend.

Hence, for the future predicted value  $M$ , the forecasting formula is represented as follows:

$$M_t = \mu + \phi_1 M_{t-1} + \dots + \phi_p M_{t-p} - \theta_1 e_{t-1} - \dots - \theta_q e_{t-q}, \quad (3)$$

where  $\theta$  is the moving average parameter,  $M$  is the predicted value, and  $e$  is the error terms sampled with zero mean. Equation (3) can be rewritten and represented as the autoregressive model equation as follows:

$$\left(1 - \sum_{i=1}^p \alpha_i L^i\right) M_t = \left(1 + \sum_{i=1}^q \theta_i L^i\right) e_t, \quad (4)$$

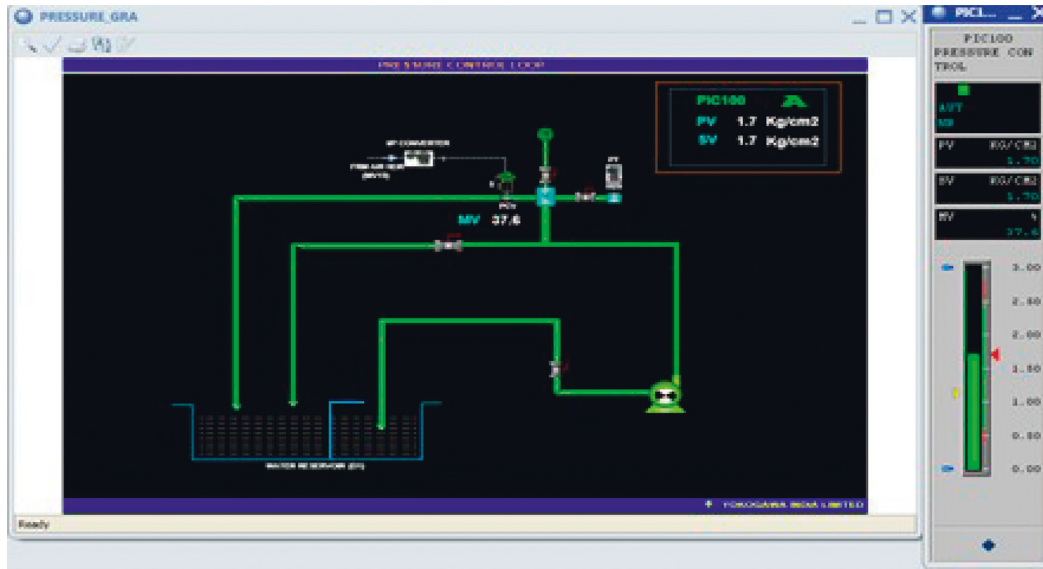


FIGURE 3: Pressure control loop for water distribution system.

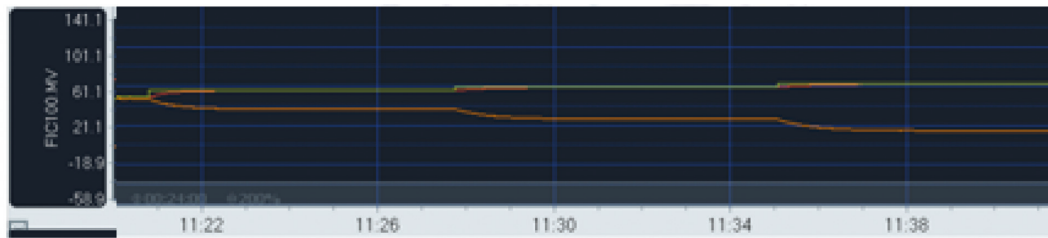


FIGURE 4: Front-end HMI for pressure data recording.

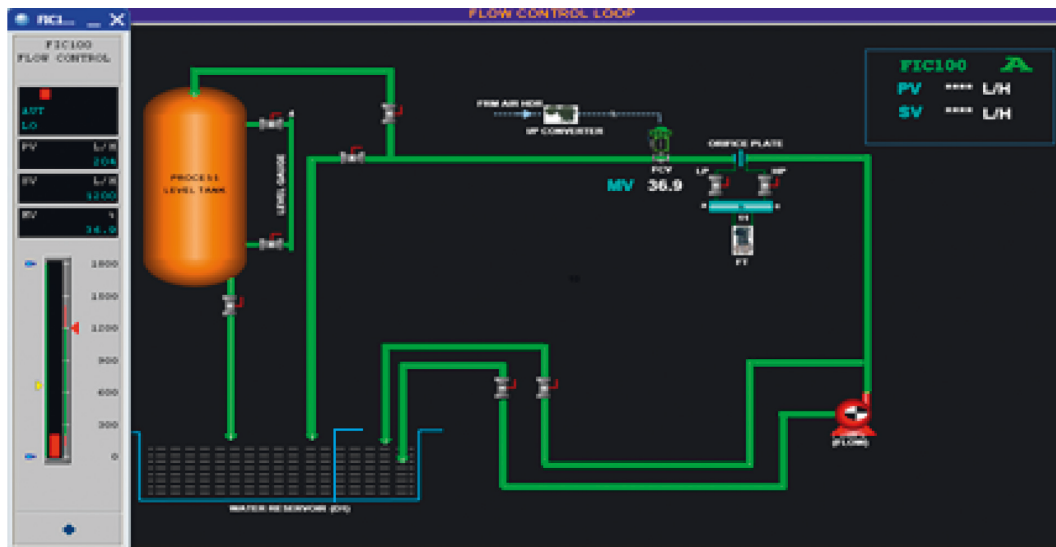


FIGURE 5: Flow control loop for water distribution system.

where  $L$  represents the lag operator, and  $\alpha$  represents the parameters of all autoregressive part as mentioned in equation (3). An ordinary least squares called as OLS is used to for predicting the slope coefficients in the ARIMA model. The unit test root method is used for this purpose. From

equation (4),  $(1 - \sum_{i=1}^p \alpha_i L^i)$  is involved with the unit root  $1 - L_i$  with the multiple factor  $U$  as follows:

$$\left(1 - \sum_{i=1}^p \alpha_i L^i\right) = \left(1 - \sum_{i=1}^{p-u} \alpha_i L^i\right) (1 - L)^u. \quad (5)$$

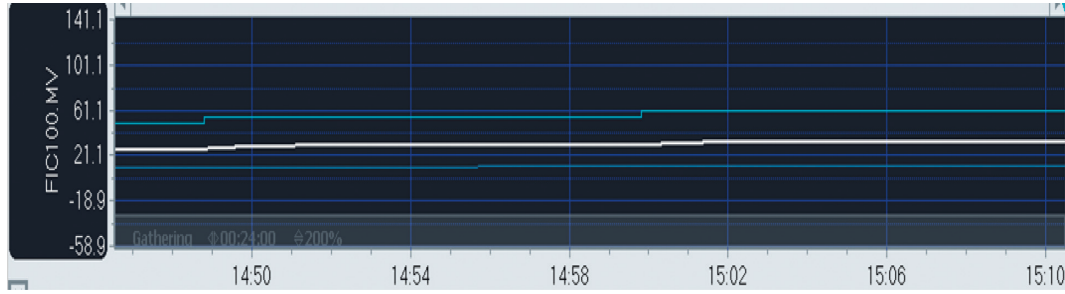


FIGURE 6: Front-end HMI for flow data recording.

The ARIMA  $(p, u, q)$  process is represented, and then, equation (4) can be rewritten based on equation (5) as follows:

$$\begin{aligned} \left(1 - \sum_{i=1}^p \alpha_i L^i\right) (1-L)^u M_t \\ = \left(1 + \sum_{i=1}^q \theta_i L^i\right) e_t. \end{aligned} \quad (6)$$

From equation (5), the generalized ARIMA equation is defined by the following term, ARIMA  $(P, Q+1)$  process with “ $u$ ” roots.

$$\begin{aligned} \left(1 - \sum_{i=1}^p \varphi_i L^i\right) (1-L)^u M_t \\ = \delta + \left(1 - \sum_{i=1}^q \theta_i L^i\right) e_t. \end{aligned} \quad (7)$$

The following steps are involved in data processing using the ARIMA model for future prediction using R software functions.

- (i) The dataset values obtained are first imported to the environment part in R studio software and then tested for class. The class should be in a time-series format to predict and forecast future data.
- (ii) The dataset is then converted to .ts from .xlsx format and checked for autocorrelation function—`acf()`, partial autocorrelation function—`pacf()`, augmented Dickey-Fuller test `adf.test()` to check the significant stationarity of the time-series dataset values.
- (iii) The time-series dataset values are partially or completely converted into a simple or fully formed statistical model by using the ARIMA model, and the  $p$ -value is checked for the newly formed model to check the sustainability of the formed statistical model. The  $p$ -value should be less than alpha 0.05 to conclude that the model is statistically significant [9, 10].
- (iv) `acf()`, `pacf()`, and `ADF.test()` functions are used to check the newly formed ARIMA model to check the significant nature of the framed model.

- (v) The responses with the forecasted value are obtained from the R studio, and the predicted data are collected from the execution of the comments in the console part of the R studio.

### 3. Results

In order to predict the future needs in supplying water through a pipeline, historical output data of the water pipeline system have been regularly taken. With the help of experimental hardware, a certain amount of data has been periodically collected and those data can be used as datasets for future prediction of water requirements. Those pressure datasets and flow datasets are going to play a vital role in future predictions and forecasting [11, 12].

#### 3.1. Forecasting the Possibility of Occurrence of Cracks and Leaks Based on Pressure Datasets

**3.1.1. Input Time-Series Data Graph.** The input dataset values obtained from the Excel by controlling the pressure control valve attached to the pipeline over equal intervals of time for three different conditions, namely, normal, crack, and damaged, which are fed to the R studio, are plotted and shown in Figure 7.

**3.1.2. Forecasting Process-Normal Condition.** The input dataset values of normal condition are imported through the SCADA system to the R studio. The plot of the values associated with the pressure at normal condition is shown in Figure 8. The input dataset values of pressure at the normal condition are fed to the R studio; as the forecasting process requires statistical data, the R studio converts the input data into a time-series data with the time-series function and the plot of the time-series dataset values associated with the pressure at the normal condition with respect to the time [42].

The stability and sustainability of the time-series data of pressure at normal condition are checked, and the results of `acf()` and `pacf()` plots are shown in Figure 9.

Figure 10 shows that the data are not within the range of expectations of the stability, so here comes the necessity of making the data into an ARIMA model to obtain statistically stable data. The ARIMA model is built for prediction; the

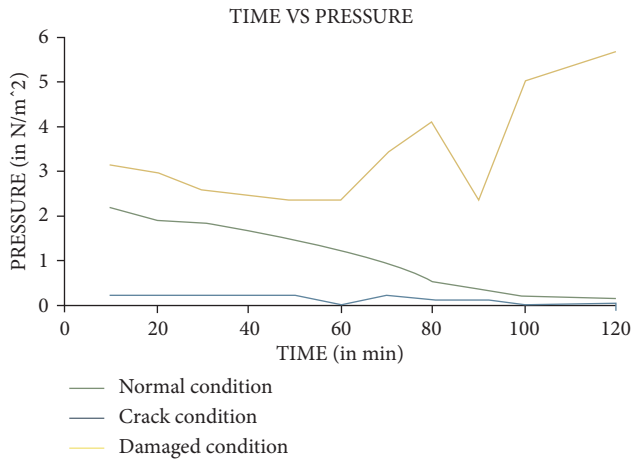


FIGURE 7: Input time-series data graph obtained from Excel.

stability and sustainability of the ARIMA model of the pressure residuals at normal condition are checked; and the results of  $acf()$  and  $pacf()$  plots are shown in Figure 10.

Figure 11 shows that the data are within the range of expectations of the stability, and the  $p$ -value is less than 0.05, which represents the stability of the data in the ARIMA model of pressure at normal condition over a period of time, which can be used for forecasting. The lag value represents the lead time period over which the average of moving values obtained from the preceding data values remains to be same for the same lead time period in the succeeding data. The predicted value of the ARIMA model of pressure forecast at damaged condition is plotted on the graph as shown in Figure 11.

Figure 11 represents the future forecasted data of pressure at normal condition for the next 1 hour where the blue line represents the average of the forecast value, which ranges with a minimum peak of  $0.451379 \text{ N/m}^2$  and  $2.022273 \text{ N/m}^2$  as the maximum peak. The shaded region represents the frequency of the forecast value with maximum peaks ranging from  $1.706869 \text{ N/m}^2$  to  $3.065836 \text{ N/m}^2$  and the minimum peaks ranging from  $-0.81046 \text{ N/m}^2$  to  $1.042164 \text{ N/m}^2$ . The average of the forecast value reduces in its frequency as the pressure from the pressure control valve is reduced over equal intervals of time, and it is assumed to be constant when the pressure from the pressure control valve remains constant. The predicted time-series data are based on the pressure data collected with very less frequency say 125 minutes of cumulative data. In case if the frequency is high, say a month or early data the prediction accuracy will be more.

**3.1.3. Forecasting Process-Crack Condition.** The input dataset values of the crack condition are fed to the R studio, and the plot of the values associated with the pressure at the crack condition is shown in Figure 12.

The input dataset values of pressure at the normal condition in the pipe are fed to the R studio; as the forecasting process requires statistical data, the R studio converts the input data into a time-series data with the time-series

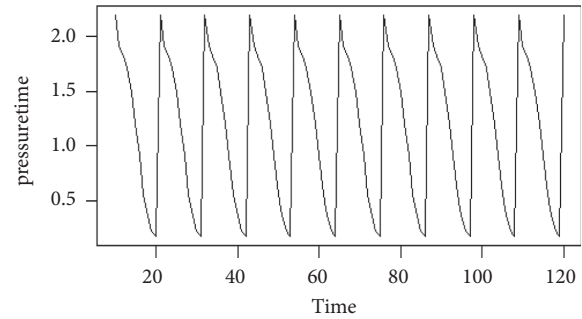


FIGURE 8: Input time-series plot.

function and the plot of the time-series dataset values associated with the pressure at the normal condition with respect to the time that is shown in Figure 13.

The stability and sustainability of the time-series data of pressure at crack condition are checked, and the results of  $acf()$  and  $pacf()$  plots are shown in Figure 14.

Figure 14 shows that the data are not within the range of expectations of the stability, so here comes the necessity of making the data into an ARIMA model to obtain statistically stable data. The ARIMA model is built for prediction; the stability and sustainability of the ARIMA model of the pressure residuals at crack condition are checked; and the results of  $acf()$  and  $pacf()$  plots are shown in Figure 15.

Figure 15 shows that the data are within the range of expectations of the stability, and the  $p$ -value is less than 0.05, which represents the stability of the data in the ARIMA model of pressure at crack condition over a period of time, which can be used for forecasting. The lag value represents the lead time period over which the average of moving values obtained from the preceding data values remains to be same for the same lead time period in the succeeding data. The predicted value of the ARIMA model of pressure forecast at crack condition is plotted on the graph as shown in Figure 16.

Figure 16 represents the future forecasted data of pressure at crack condition for the next 1 hour where the blue line represents the average of the forecast value remains same as  $0.144865 \text{ N/m}^2$  as the pressure remains the same at the crack region without any rise or fall in pressure irrespective of the change in pressure made by the pressure control valve. The minimum peak of the forecast value remains at  $-0.02742 \text{ N/m}^2$ , and the maximum peak of the forecast value remains at  $0.317153 \text{ N/m}^2$ . This infers that the pressure remains unchanged over a period of time till the crack is sealed in the pipeline. The estimated value seems like constant with respect to time, since less frequency pressure data are taken for the forecasting analysis. The dataset's quantitative expansion improves prediction accuracy.

**3.1.4. Forecasting Process-Damaged Condition.** The input dataset values of normal condition are fed to the R studio, and the plot of the values associated with the pressure at normal condition is shown in Figure 17.

The input dataset values of pressure at the normal condition in the pipe are fed to the R studio; as the

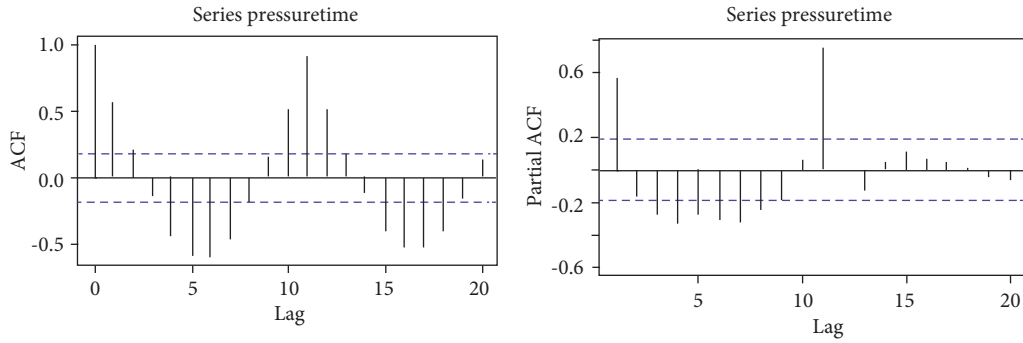


FIGURE 9: Checking stability of the data.

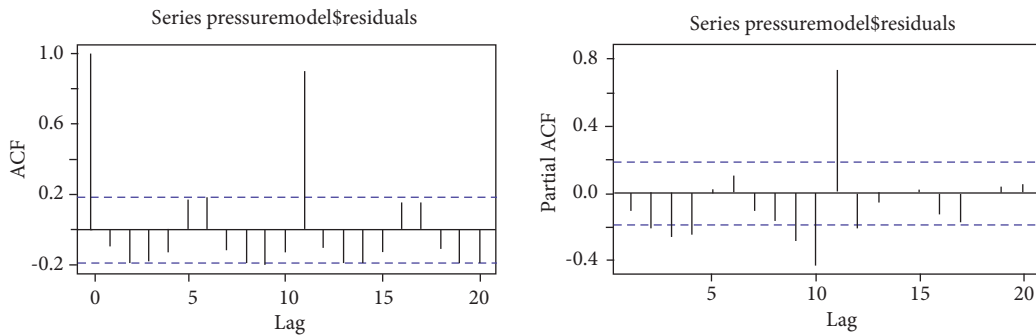


FIGURE 10: Checking of the ARIMA model data (stable).

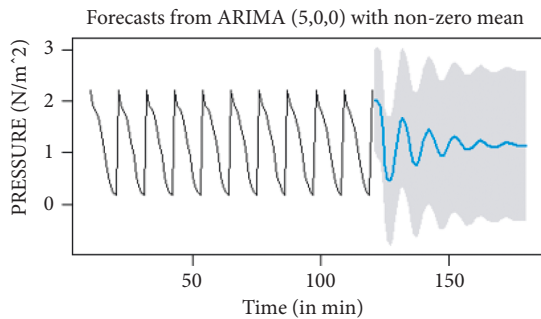


FIGURE 11: Forecast time-series data graph from R studio.

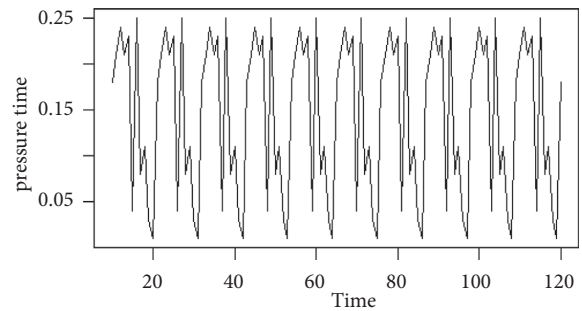


FIGURE 13: Input time-series plot.

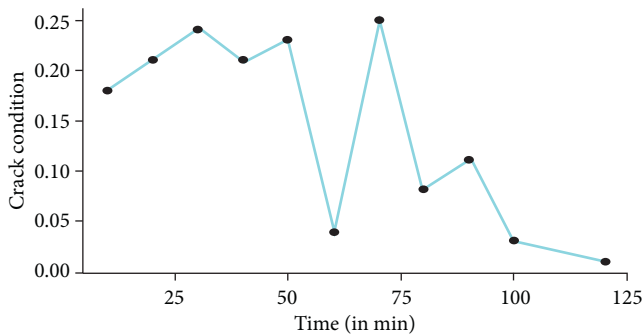


FIGURE 12: Input dataset value.

forecasting process requires a statistical data, the R studio converts the input data into a time-series data with the time-series function and the plot of the time-series dataset values

associated with the pressure at the normal condition with respect to the time that is shown in Figure 18.

The stability and sustainability of the time-series data of pressure at damaged condition are checked, and the results of `acf()` and `pacf()` plots are shown in Figure 19.

Figure 19 shows that the data are not within the range of expectations of the stability, so here comes the necessity of making the data into an ARIMA model to obtain statistically stable data. The ARIMA model is built for prediction; the stability and sustainability of the ARIMA model of the pressure residuals at damaged condition are checked, and the results of `acf()` and `pacf()` plots are shown in Figure 20.

Figure 20 shows that the data are within the range of expectations of the stability, and the  $p$ -value is less than 0.05, which represents the stability of the data in the ARIMA model of pressure at damaged condition over a period of time, which

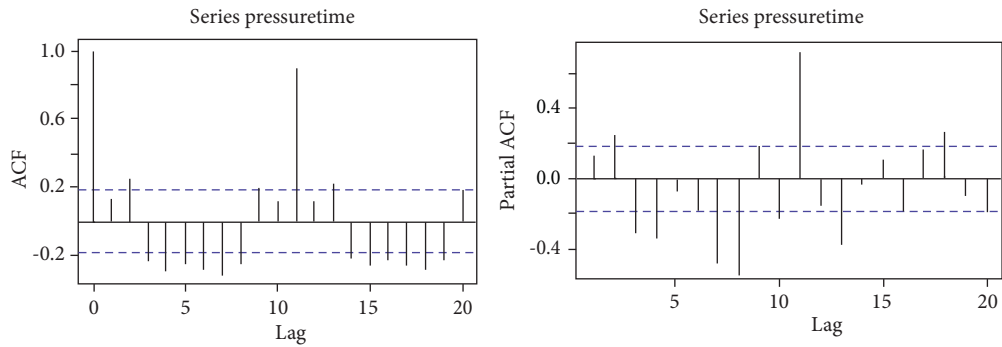


FIGURE 14: Checking stability of the data.

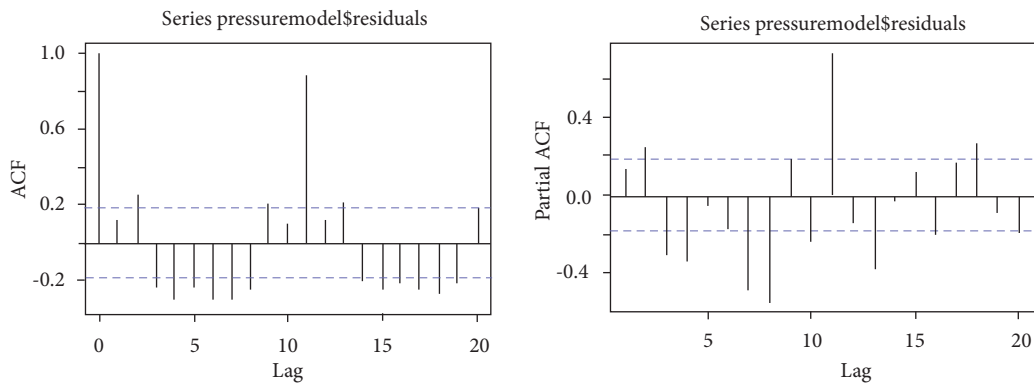


FIGURE 15: Checking of the ARIMA model data (stable).

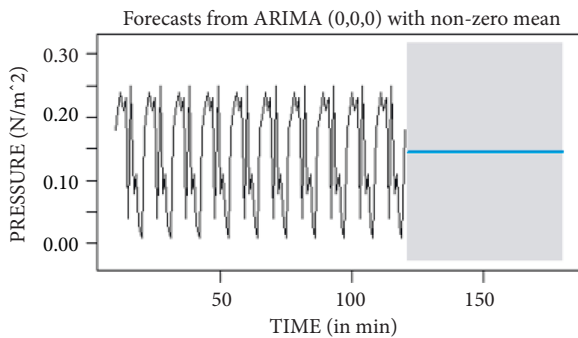


FIGURE 16: Forecast time-series data graph from R studio.

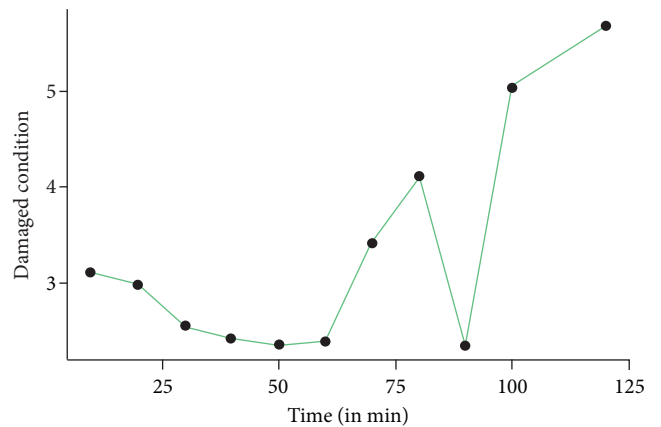


FIGURE 17: Input dataset value.

can be used for forecasting. The lag value represents the lead time period over which the average of moving values obtained from the preceding data values remains to be same for the same lead time period in the succeeding data. The predicted value of the ARIMA model of pressure forecast at damaged condition is plotted on the graph as shown in Figure 21.

Figure 21 represents the future forecasted data of pressure at damaged condition for the next 1 hour where the blue line represents the average of the forecast value, which increases from the minimum peak of  $2.880788 \text{ N/m}^2$  to the maximum peak of  $3.29797 \text{ N/m}^2$  and becomes constant. The shaded region represents the frequency of the forecast value with maximum peaks ranging from  $4.866227 \text{ N/m}^2$  to  $5.664348 \text{ N/m}^2$ .

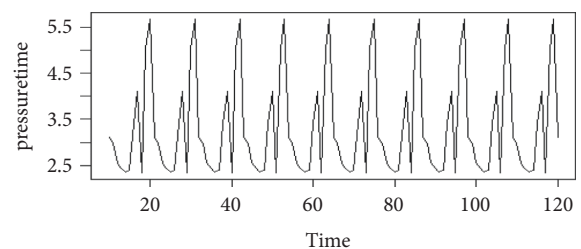


FIGURE 18: Input time-series plot.



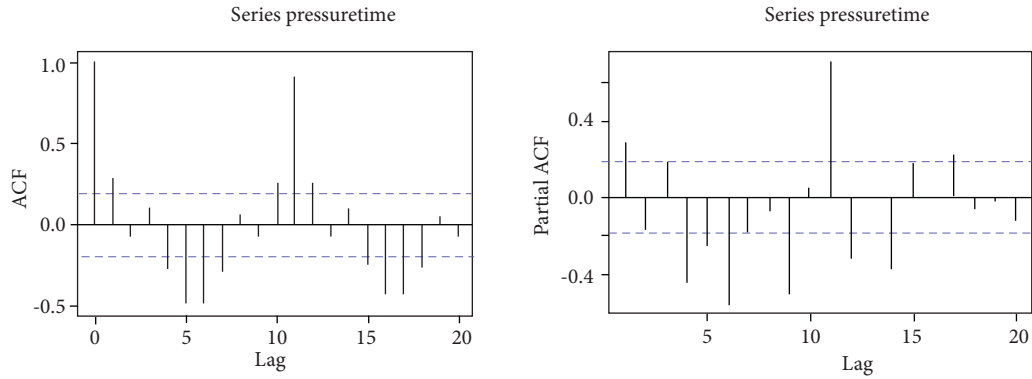


FIGURE 19: Checking stability of the data.

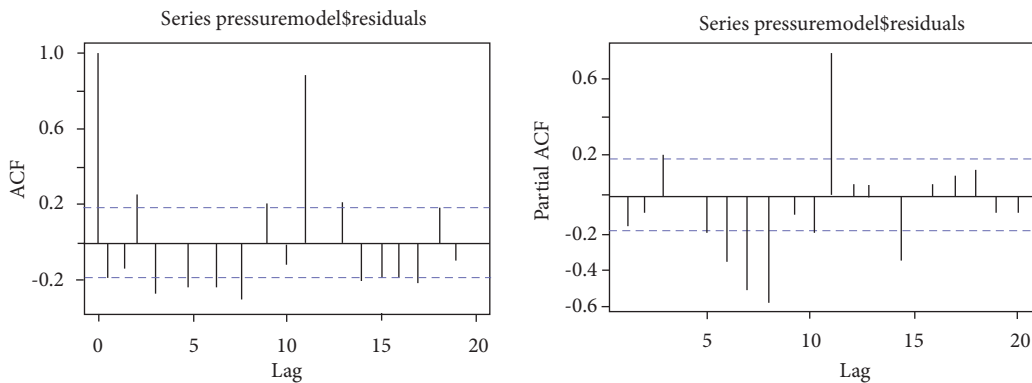


FIGURE 20: Checking of the ARIMA model data (stable).

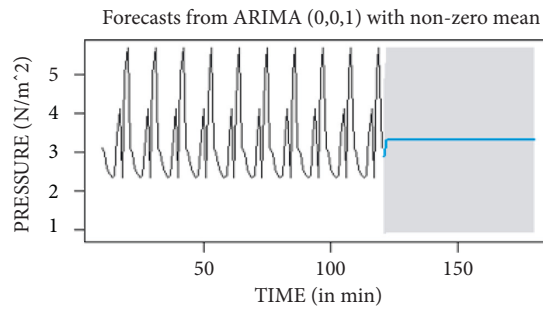


FIGURE 21: Forecast time-series data graph from R studio.

$m^2$  and the minimum peaks ranging from  $0.895349 N/m^2$  to  $0.931593 N/m^2$ . The constant average value of the forecast infers that the pressure remains unchanged over a period of time till the damaged pipeline is replaced with a new pipeline.

### 3.2. Flow Forecasting

3.2.1. *Input Time-Series Data Graph.* The input dataset values obtained from Excel by monitoring the flow over a pipeline on a weekly basis, which are fed to the R studio, are plotted and shown in Figure 22.

3.2.2. *Forecasting Process.* The input dataset values of flow in the pipe are fed to the R studio; as the forecasting process

requires a statistical data; the R studio converts the input data into a time-series data with the time-series function; and the plot of the time-series dataset values associated with the flow with respect to the time that is shown in Figure 23.

The stability and sustainability of the time-series data of flow are checked, and the results of `acf()` and `pacf()` plots are shown in Figure 24. The data are not within the range of expectations of the stability, so here comes the necessity of making the data into an ARIMA model to obtain statistically stable data.

Figure 24 shows that the data are not within the range of expectations of the stability, so here comes the necessity of making the data into an ARIMA model to obtain statistically stable data. The ARIMA model is built for prediction; the

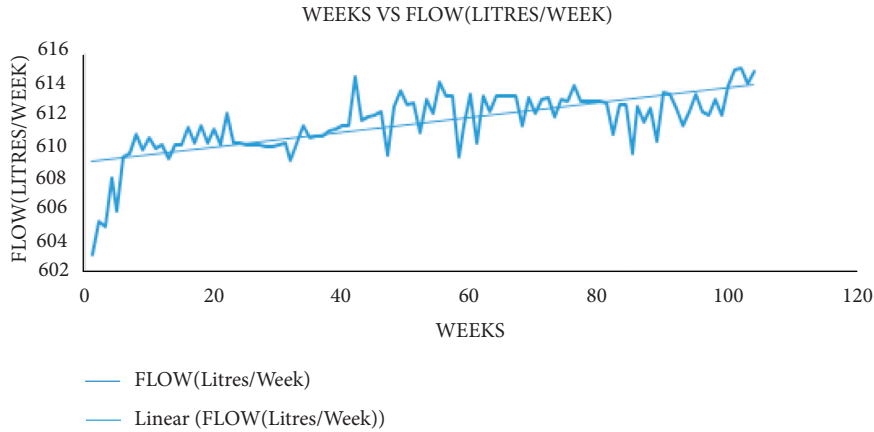


FIGURE 22: Input dataset value graph.

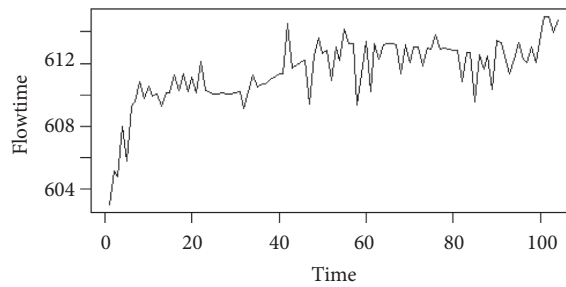


FIGURE 23: Input time-series plot.

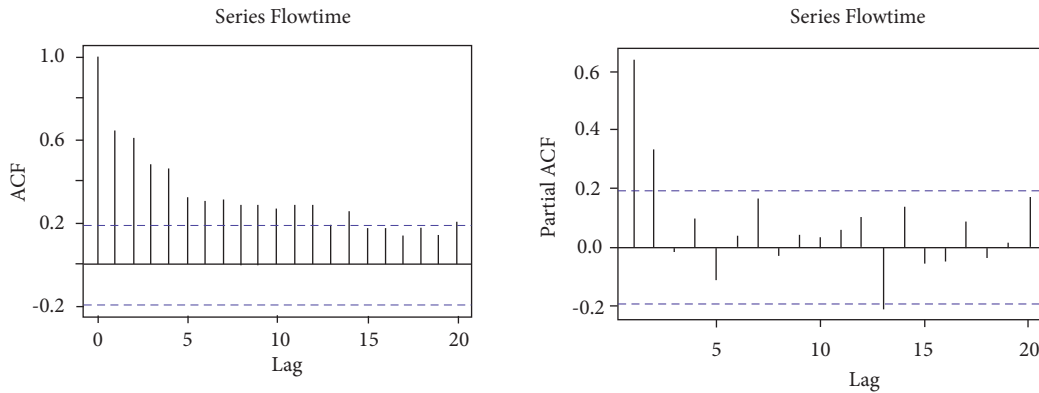


FIGURE 24: Checking stability of the data.

stability and sustainability of the ARIMA model of the flow residuals are checked, and the results of `acf()` and `pacf()` plots are shown in Figure 25.

Figure 25 shows that the data are within the range of expectations of the stability, and the  $p$ -value is less than 0.05, which represents the stability of the data in the ARIMA model of flow over a period of time, which can be used for forecasting. The lag value represents the lead time period over which the average of moving values obtained from the preceding data values remains to be same for the same lead time period in the succeeding data. The predicted value of the ARIMA model of flow forecast is plotted on the graph as shown in Figure 26.

Figure 26 represents the future forecasted data of water requirement for the next 1 year where the blue line represents the average of the forecast value, which increases from the minimum peak of 614.6292 (liters/week) to the maximum peak of 620.0099 (liters/week) and becomes constant. The shaded region represents the frequency of the forecast value with maximum peaks ranging from 617.0086 (liters/week) to 628.5465 (liters/week) and the minimum peaks ranging from 611.0967 (liters/week) to 612.2914 (liters/week). This infers that the requirement of water quantity in the next year increases as represented by the average of the forecast data.

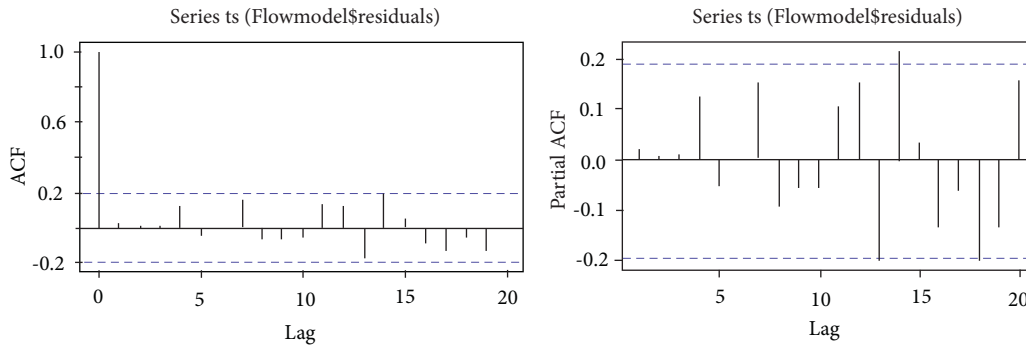


FIGURE 25: Checking of the ARIMA model data (stable).

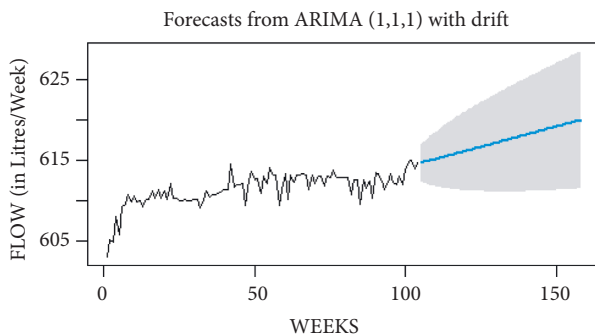


FIGURE 26: Forecast time-series data graph from R studio.

## 4. Conclusions

The identification of the crack, pressure difference, leakages, and blockages with the help of abnormal pressure rise or drop in the municipal water distribution system was analyzed [43, 44]. On the other side, the water flow in the pipeline was monitored and prediction for the future requirements was made by analyzing its present utilization of the flow datasets obtained from the preceding two years. With the help of the time-series forecasting algorithm, the collection of datasets for the flow periodically was made [45, 46]. Those datasets have been used as a source of input to the R studio under the time-series forecasting algorithm. The flow rate datasets of the past two years were recorded, and the datasets are analyzed on the time-series forecasting algorithm. As an output of the algorithm, the need for the next year was predicted and figured out in the form of a graph. This provides a strategy for forecasting the needs for the upcoming year. The stability of the statistical data was confirmed by using the  $p$ -value (less than 0.05) provided by the ARIMA model of data for both pressures and flow datasets. The future prediction of the pressure concerning the flow in damaged conditions would range between 2.880788 and 3.29797 N/m<sup>2</sup>. The future prediction of the pressure concerning flow in normal conditions would range between 0.451379 and 2.022273 N/m<sup>2</sup>. The future prediction of the pressure concerning flow in crack condition would remain unchanged but lower than the normal condition. The future prediction of the flow requirement would range between 614.6292 and 620.0099 liters/week. Furthermore, future studies may be incorporated based

on the smart pig for the identification of fault and data transmission in oil pipelines.

## Data Availability

The required data can be obtained from the corresponding author upon request.

## Conflicts of Interest

The authors declare that they have no conflicts of interest.

## Acknowledgments

Editing and writing were carried out at the Debre Tabor University, Ethiopia.

## References

- [1] A. Terkawi and N. Innab, "Major impacts of key reinstallation attack on internet of things system," in *Proceedings of the 2018 21st Saudi Computer Society National Computer Conference (NCC)*, pp. 1–6, Riyadh, Saudi Arabia, April 2018.
- [2] H. M. Ramos, A. McNabola, P. A. López-Jiménez, and M. Pérez-Sánchez, "Smart water management towards future water sustainable networks," *Water*, vol. 12, no. 1, p. 58, 2019.
- [3] X. Wei, L. Zhang, H.-Q. Yang, L. Zhang, and Y.-P. Yao, "Machine Learning for Pore-Water Pressure Time-Series Prediction: Application of Recurrent Neural Networks," *Geoscience Frontiers*, vol. 12, no. 1, pp. 453–467, 2021.
- [4] K. G. Liakos, P. Busato, D. Moshou, S. Pearson, and D. Bochtis, "Machine learning in agriculture: a review," *Sensors*, vol. 18, no. 8, Article ID 2674, 2018.
- [5] N. Y. K. Phan and H. T. Nguyen, "Inflammatory bowel disease classification improvement with metagenomic data binning using mean-shift clustering," in *Communications in Computer and Information Science (CCIS)*, T. K. Dang, J. Küng, M. Takizawa, and T. M. Chung, Eds., FDSE 2020, Springer, Singapore, pp. 294–308, 2020.
- [6] G. Liu, Ya Zhang, W.-J. Knibbe et al., "Potential impacts of changing supply-water quality on drinking water distribution," *International Journal on ELSEVIER*, vol. 116, 2020.
- [7] M. M. Giraldo-González and J. P. Rodríguez, "Comparison of statistical and machine learning models for pipe failure modeling in water distribution networks," *Water*, vol. 12, no. 4, 2020, <https://www.mdpi.com/about/journals>.
- [8] Q. Fang, J. Zhang, C. Xie, and Y. Yang, "Detection of multiple leakage points in water distribution networks based on

- convolutional neural networks,” *Water Supply*, vol. 19, no. 8, pp. 2231–2239, 2019.
- [9] N. A. Kumar, G. Shyni, G. Peter, A. A. Stonier, and V. Ganji, “Architecture of network-on-chip (NoC) for secure data routing using 4-H function of improved TACIT security algorithm,” *Wireless Communications and Mobile Computing*, vol. 2022, pp. 1–9, Article ID 4737569, 2022.
- [10] E. B. Priyanka, S. Thangavel, V. Madhuvishal, S. Tharun, K. V. Raagul, and C. S. S. Krishnan, “Application of integrated IoT framework to water pipeline transportation system in smart cities,” *Intelligence in Big Data Technologies—Beyond the Hype*, Springer, pp. 571–579, Singapore.
- [11] G. Peter, J. Livin, and A. Sherine, “Hybrid optimization algorithm based optimal resource allocation for cooperative cognitive radio network,” *Array*, vol. 12, Article ID 100093, 2021.
- [12] E. B. Priyanka, C. Maheswari, S. Thangavel, and M. P. BalaBala, “Integrating IoT with LQR-PID controller for online surveillance and control of flow and pressure in fluid transportation system,” *Journal of Industrial Information Integration*, vol. 17, Article ID 100127, 2020.
- [13] J. S. Armstrong, *Long-range Forecasting: From crystal ball to Computer*, John Wiley & Sons, NJ, USA, 1978.
- [14] S. Wambura, J. Huang, and H. Li, “Long-range forecasting in feature-evolving data streams,” *Knowledge-Based Systems*, vol. 206, 2020.
- [15] S. Mehran Jafari, A. Reza Zahiri, O. Bozorg Hadad, and M. M. R. Tabari, “A hybrid of six soft models based on ANFIS for pipe failure rate forecasting and uncertainty analysis: a case study of gorgan city water distribution network, methodologies and application,” *Soft Computing-A Fusion of Foundations, Methodologies and Applications*, vol. 25, no. 11, pp. 7459–7478, 2021.
- [16] J. Wang, F. Zhou, L. Zhang et al., “Experimental study of wax deposition pattern concerning deep condensate gas in Bozi block of Tarim Oilfield and its application,” *Thermochimica Acta*, vol. 671, pp. 1–9, 2019.
- [17] M. Monteiro and M. Costa, “A time series model comparison for monitoring and forecasting water quality variables,” *Hydrology*, vol. 5, no. 3, p. 37, 2018.
- [18] J. F. Joe and T. V. Raja, “Enhanced robustness for digital images using geometric attack simulation,” *Procedia Engineering*, vol. 38, pp. 2672–2678, 2012, <https://doi.org/10.1016/j.proeng.2012.06.314>.
- [19] J. Liu, S. Wang, N. Wei, Xi Chen, H. Xie, and J. Wang, “Natural gas consumption forecasting: a discussion on forecasting history and future challenges,” *Journal of Natural Gas Science and Engineering*, vol. 90, Article ID 103930, 2021.
- [20] A. O. Adejo, A. J. Onumanyi, J. M. Anyanya, and S. O. Oyewobi, “Oil and gas process monitoring through wireless sensor networks: a survey,” *Journal of Applied Sciences*, vol. 6, pp. 5660–5568, 2013.
- [21] G. Dundulis, A. Grybenas, R. Karalevicius, and V. Makarevicius, “Static analytical and experimental research of energy analysis to safeguard the oil transportation system,” *Energy analysis statistics*, vol. 67, pp. 239–248, 2018.
- [22] P. Hopkins, “The structural integrity of oil and gas transmission pipelines,” *Computer Structural Integrity*, vol. 1, pp. 87–123, 2018.
- [23] Y. Chen, L. Song, Y. Liu, L. Yang, and D. Li, “A review of the artificial neural network models for water quality prediction,” *Applied Sciences*, vol. 10, no. 17, p. 5776, 2020.
- [24] D. P. Abreu, K. VelasquezVelasquez, M. CuradoCurado, and E. MonteiroMonteiro, “A resilient Internet of Things architecture for smart cities,” *Annals of Telecommunications*, vol. 72, no. 1–2, pp. 19–30, 2017.
- [25] M. A. Khan and K. Salah, “IoT security: review, blockchain solutions, and open challenges,” *Future Generation Computer Systems*, vol. 82, pp. 395–411, 2018.
- [26] M. Kim, “A quality model for evaluating IoT applications,” *International Journal of Computer and Electrical Engineering*, vol. 8, no. 1, pp. 66–76, 2016.
- [27] O. Novo, “Blockchain meets IoT: an architecture for scalable access management in IoT,” *IEEE Internet of Things Journal*, vol. 5, no. 2, pp. 1184–1195, 2018.
- [28] S. Susan Jacob and Dr. R. Vijayakumar, “Sentiment analysis over twitter bigdata using modified meanshift clustering,” vol. 7, no. 15, pp. 5835–5841, 2020.
- [29] G. Bin Iderus and S. Bin Iderus, “Design of enhanced energy meter using GSM prepaid system and protective relays,” *Materials Today Proceedings*, vol. 39, pp. 582–589, 2021.
- [30] R. Ranjbarzadeh and B. Saadi, “Automated liver and tumor segmentation based on concave and convex points using fuzzy c-means and mean shift clustering,” *Measurement*, vol. 150, Article ID 107086, 2020.
- [31] D. V. Brower and N. Prescott, “Real-time subsea monitoring and control smart field solutions,” *Subsea Rio 2018 Conference*, vol. 3, pp. 3413–3462, 2018.
- [32] J. Najafi, A. Peiravi, A. Anvari-Moghaddam, and J. M. Guerrero, “An efficient interactive framework for improving resilience of power-water distribution systems with multiple privately-owned microgrids,” *International Journal of Electrical Power & Energy Systems*, vol. 116, Article ID 105550, 2020.
- [33] J. D. Hamilton, *Time Series Analysis*, Princeton University Press, NJ, USA, 1994.
- [34] M. Khashei and M. Bijari, “A novel hybridization of artificial neural networks and ARIMA models for time series forecasting,” *Applied Soft Computing*, vol. 11, no. 2, pp. 2664–2675, 2011.
- [35] V. A. O. P. da Silva, R. C. de Freitas, P. R. de Oliveira et al., “Microfluidic paper-based device integrated with smartphone for point-of-use colorimetric monitoring of water quality index,” *Measurement*, vol. 164, Article ID 108085, 2020.
- [36] T. M. P. Junaidi, A. Surtono, G. A. Puazi, S. W. Suciyan, I. Firdaus, and L. Rumiyan, “Measurement of physical parameters of water quality in real-time based on arduino,” *Journal of Physics: Conference Series*, vol. 1751, no. 1, Article ID 012067, 2021.
- [37] R. I. Pereira, I. M. Dupont, P. C. Carvalho, and S. C. Jucá, “IoT embedded Linux system based on Raspberry Pi applied to real-time cloud monitoring of a decentralized photovoltaic plant,” *Measurement*, vol. 114, pp. 286–297, 2018.
- [38] E. B. Priyanka, C. Maheswari, and B. Meenakshipriya, “Parameter monitoring and control during petrol transportation using PLC based PID controller,” *Journal of Applied Research and Technology*, vol. 14, no. 2, pp. 125–131, 2016.
- [39] G. Sherine and A. Sherine, “Induced over voltage test on transformers using enhanced Z-source inverter based circuit,” *Journal of Electrical Engineering*, vol. 68, no. 5, pp. 378–383, Sep. 2017.
- [40] S. Bhoumik, S. Chatterjee, A. Sarkar, A. Kumar, and F. J. John Joseph, “Covid 19 prediction from X ray images using fully connected convolutional neural network,” in *Proceedings of the CSBio '20: Proceedings of the Eleventh International Conference on Computational Systems-Biology and Bioinformatics*, pp. 106–107, ACM, Bangkok Thailand, November 2020.

- [41] G. Petris, C. Patrizia, and P. Sonia, *Dynamic Linear Models with R*, Springer Science & Business Media, Germany, 2009.
- [42] K. L. Keung, C. K. M. Lee, K. K. H. Yeung, and C. K. Yeung, "Smart city application and analysis: real-time urban drainage monitoring by IoT sensors: a case study of Hong Kong," in *Proceedings of the 2018 IEEE International Conference on Industrial Engineering and Engineering Management (IEEM)*, pp. 521–525, Bangkok, Thailand, December 2018.
- [43] Z. Jia, Z. Wang, W. Sun, and Z. Li, "Pipeline leakage localization based on distributed FBG hoop strain measurements and support vector machine," *Optik*, vol. 176, pp. 1–13, 2019.
- [44] J. Shen, Z. Gui, S. Ji, J. Shen, H. Tan, and Y. Tang, "Cloud-aided lightweight certificateless authentication protocol with anonymity for wireless body area networks," *Journal of Network and Computer Applications*, vol. 106, pp. 117–123, 2018.
- [45] A. Y. Scanlon, B. R. Scanlon, "How can Big Data and machine learning benefit environment and water management: a survey of methods, applications, and future directions," *Environmental Research Letters*, vol. 14, no. 7, p. 073001, 2019.
- [46] G. Manogaran, R. Varatharajan, D. Lopez, P. M. Kumar, R. Sundarasekar, and C. Thota, "A new architecture of Internet of Things and big data ecosystem for secured smart healthcare monitoring and alerting system," *Future Generation Computer Systems*, vol. 82, pp. 375–387, 2018.

## Research Article

# A Decision-Making Model for Selection of the Suitable FDM Machine Using Fuzzy TOPSIS

S. Raja and A. John Rajan 

*School of Mechanical Engineering, Vellore Institute of Technology, Vellore, Tamil Nadu 632014, India*

Correspondence should be addressed to A. John Rajan; [ajohnrajan@gmail.com](mailto:ajohnrajan@gmail.com)

Received 19 April 2022; Revised 16 May 2022; Accepted 21 May 2022; Published 30 June 2022

Academic Editor: Punit Gupta

Copyright © 2022 S. Raja and A. John Rajan. This is an open access article distributed under the Creative Commons Attribution License, which permits unrestricted use, distribution, and reproduction in any medium, provided the original work is properly cited.

Additive manufacturing (AM) or 3D printing has been playing a very important role in the manufacturing sector in recent decades. The AM basic process is meant to produce an object layer by layer and has many advantages that include the occurrence of only minimal production waste during production and easy manufacture of even the most geometrically complex materials. However, there are many challenging decision-making situations in the production of AM for its users, for example, the build chamber, material specification, technology types, and application requirements. This includes the choice of the best AM machine (AMM) from many AMM with slightly different features that are identical on the market, especially on a real-time basis. This research explored ways that AMM is to be selected using multi-criteria decision-making (MCDM) on a real-time basis. This includes the use of the MCDM fuzzy Technique for Order of Preference by Similarity to Ideal Solution (TOPSIS) to help select the most suitable fusion deposition modeling (FDM) for an Indian nongovernment organization (NGO) from nine different machines based on contemporary. Practice in this research paper, an Indian NGO is considered as a decision-maker in the choice of the best FDM machine based on nine common criteria because an NGO has prescribed nine different FDM machines and the NGO needs the help for the purchase of the suitable FDM to produce different fields of prototypes. The outcome of this research is to recommend a suitable FDM machine from the nine similar to slightly different features of FDM machines by the suggestion of the field experts (AM machine users). The contribution of this research is not only to enable the purchase of the suitable AM machine but also to reveal the various contemporary FDM machines and the general criteria to be considered in choosing them.

## 1. Introduction

Conventional manufacturing (CM) or subtractive manufacturing methods have been used in the manufacturing industry for the past several years. Alternatively, for the past 3.5 decades, AM has been one of the leading technologies in the manufacturing sector, wherever the product is converted from digital format to standard triangle language (STL) file and can be easily produced a product directly layer by layer [1–3]. According to a previous research report, AM is found in the manufacturing industry under many names. This AM production method has been divided into seven types based on the report of the American Society for Testing and Materials (ASTM), and the previous literature on each method has its own unique features. These

seven methods are stereolithography, material jetting, material extrusion, binder jetting, powder bed fusion, sheet lamination, and direct energy deposition [4]. What researchers consider to be the hallmark of AM is such simplicity that helps the production of products with accuracy, freedom in design, low inventory, low lead time, and very rigorous production design [5–8]. Many of the challenges in AM are related to product quality, mechanical property, supply chain-related requirements, shrinkage, printing underutilization, etc. [9–12]. Choice of the suitable AM machine, in particular, is also a challenge. This is due to the continuous increase in the number of machinery suppliers and in the number of machinery with slightly different features, which makes the selection of suitable machine challenging. AM executes its shares in a number of key

sectors. The Wohlers 2021 report also reveals that 3D printing sales increased by 7.5% compared with previous years [13–16].

The aim of this research paper was to present a method that aid the selection of a suitable FDM 3D printers machine in many real-time markets for the production of prototypes of various fields required for a nongovernment organization (NGO), taking into account nine 3D printing-based criteria for the selection of a suitable FDM machine for a particular NGO from the nine FDM machines in the current market. The main purpose of this research paper was to calculate the criteria weight of the nine FDM machines using the MCDA technique called fuzzy TOPSIS and ultimately give ranking based on priority value and help the decision-maker in easy selection of the most suitable machine. Experts in the field were given questions online for the calculation of criteria weight using the fuzzy TOPSIS method. The first part of this research paper describes the AM and MCDM or MCDA using a literature survey, and TOPSIS technique can be used especially in complex decision-making challenges, a component that has traditionally been used in operation research to assist decision-makers. The other parts of this research paper include detailed problem identification, research methodology, result and discussion, and conclusion.

## 2. Literature Survey

*2.1. 3D Printing or Additive Manufacturing.* 3D printing technology is capable of creating an object with very little waste during production reducing the quantity of raw materials needed for production. The use of 3D printing has been on the rise in various fields in recent decades, according to a research report [6]. The most important reason for this is the ability of 3D printing to produce very complex objects very easily and with options also provided for selecting modes of action in 3D printing. However, some of the problems that researchers consider in 3D printing are high prototype costs, high material cost, unavailability of material, and some real-time experiments that make it difficult [17–19]. At the same time, 3D printing results in shorter prototype production time and lower production costs compared with CM [20]. The 3D printing technology industry has less design flow, design dependence, and design aspects compared with CM [21]. Ramola et al. [22] have conducted research on 3D printing process selection in the field of health care. It includes instructions for creating customized healthcare products with the help of 3D printing. Following this, Kokotsaki et al. [23] found a methodology for selecting AM processes in the spare parts and a new manufacturing industry. The authors have discovered a methodology to reduce production failures and increase productivity by a systematic review of the best AM criteria. Rashid [24] and Petrovic et al. [25] have provided a study on 3D printing, in that authors have explored the basic explanations of 3D printing in the best way. The authors have also narrated the demerits relating to business opportunity and process selection tool in AM. Drizo and Pegna have the market dominance of 3D printing technology in

many fields, from shown manufacturing to medicine, cosmetics, defense, etc., in the third industrial revolution [26].

Pham and Gault have explained the main advantages of 3D printing by comparing it with several techniques. 3D printing reduces the time in manufacturing an item and taking it to market [27]. Bak [28] has recorded rapid prototype (RP) that leads to mass customized production without tools. Rao and Padmanaban [29] used a matrix approach and graph theory for the selection of 3D printing processes. It is possible to estimate the selected index by assigning ranks using quantitative and qualitative data as selection parameters. Following this, Xu and Wong explored a model 3D printing process selection. They made a comparison between process parameters such as build time, build cost, surface roughness, and benchmark parts [30]. Masood and Soo used the rule-based expectation system for solving 3D printing education process selections [31]. Previous researchers have similarly used the TOPSIS method for the selection of 3D printing processes. The criteria including elongation prototype cost, build material, and build time were considered [32].

In 3D printing, Kim and Oh [33] recorded low material wastage compared with accuracy, material properties, speed, material cost, and roughness in the quantitative comparison method. Groth et al. and Ramalingam who are known for their investigation of orthodontistry application have published a report that reports the abilities of 3D printing to improve accuracy and reduce material wastage [34, 35]. Touelf et al. Gay et al. and Vlasea et al. found that significant property orientation can be identified by manufacturing mechanical properties in 3D printing [36–38]. In recent years, multi-criteria decision analysis (MCDA) methods have played an important role in solving any problem in decision-making. MCDA also plays an important role in the most complex selection situations [17]. The following section describes the MCDA objective, need, and technique with the help of a research paper by previous researchers on multiple disciplines and MCDA applications.

*2.2. Multi-Criteria Decision Analysis (MCDA).* The method of selecting the right and suitable homogeneous alternative from more than one based on the decision-maker's wishes is called MCDA [39]. The basis of the MCDA system helps rank all the alternatives using any one of the MCDA methods, taking into account some common criteria from the alternatives and selecting the appropriate alternative for the decision-maker [40, 41]. The basic steps of MCDA include the choice of the best alternative using criteria and alternatives according to the decision-maker's opinion [42].

This MCDA has been used in many fields in recent decades and plays an important role in operational research. According to previous researchers, MCDA has several techniques, namely analytical hierarchy process (AHP), Technique for Order of Preference by Similarity to Ideal Solution (TOPSIS), Preference Ranking Organization Method for Enrichment of Evaluations (PROMTHEE), and Decision Making Trial and Evaluation Laboratory (DEMATEL) [43]. Previous researchers have used many

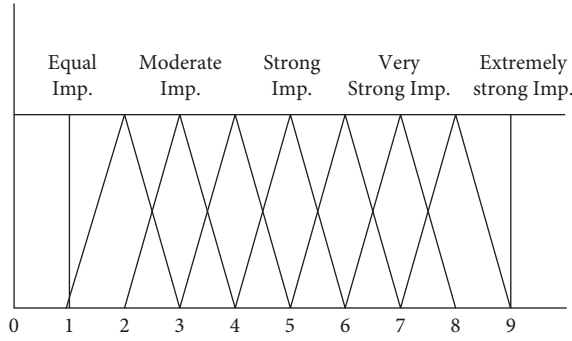


FIGURE 1: Triangular membership function.

MCDA methods in many fields. For example, the lot process selection has been done by the AHP-MCDA method [44]. Researchers in the agile manufacturing sector generally use fuzzy techniques with TOPSIS, AHP, and DEMATEL for selection [45].

MCDA also plays a key role in supply chain management (SCM) [46], management science system engineering sustainability [47, 48], product development evaluation, strategic management, and planning [49]. MCDA is also used in fuzzy TOPSIS and failure mode effect analysis (FMEA) in risk evaluation processes [50]. Fuzzy TOPSIS plays an important role in facility layout planning [51], and each of these MCDA methods has its own uniqueness [52]. The FTOPSIS method used in recent years has been used in this research paper. The fuzzy TOPSIS method is unique in finding the FNIS and FPIS for selected decision-making problems, which differ from other MCDA methods [53]. This method helps solve innovative problems in comparison with the other methods using the case study technique. Further detailed descriptions of the FTOPSIS method can be found below with the help of the researchers' research paper.

**2.3. Fuzzy TOPSIS.** The basis of fuzzy TOPSIS has in finding the best alternative to the longest geometric distance from the negative ideal solution and the shortest geometric distance from the positive ideal solution [54]. Fuzzy TOPSIS also helps in the selection of the best alternative by finding out how close the selected alternative is to the desired solution [55]. The fuzzy TOPSIS method is used in this research paper as follows.

**Step 1. Fundamental concept**

The linguistic term is used in this study, which is the first step in the measurement of alternatives and criteria. The linguistic terms are then converted to the fuzzification mode as a triangular membership function. The fuzzification method is one of the parts of a fuzzy term. Membership functions can be of many types, for example, in terms of shape trapezoidal, which is detailed under bell-shaped. The triangle membership function has been used in this research paper. Fuzzy value is usually denoted by the symbol ( $\mu^{\check{A}}$ ). The further triangle membership function is shown in Figure 1.

$$\mu^{\check{A}}(X) = \check{A}. \tag{1}$$

The lower, middle, and upper fuzzy numbers in the triangle membership functions have been obtained from formula (1).

The Saaty scale used in the AHP system is referred to as the relative of alternative. This Saaty scale is generally used only as a crisp value. Hence, the decimal value is incalculable. For example, a decimal value like 3.5 cannot be calculated when a decision-maker has to make a choice between moderate and intermediate values and strong values on the Saaty scale given below [19, 56]. A fuzzy number is calculated for solving this problem based on the triangular membership function as shown in Table 1.

The five linguistic terms shown in Table 2 have been used in this research paper. The fuzzy numbers described above the same triangular membership function-based are also used here.

More than one integrated decision-making systematic group decision-making has been used in this research paper. Then, the common decision matrix for alternatives and criteria is created through the use of linguistic term and then the equivalent fuzzy value is modified as shown in Table 2.

**Step 2. Combined decision matrix**

The group decision matrix queues conversion into a decision matrix using the formula given below for the achievement of the purpose of this research paper.

$$\begin{aligned} X_{ij} &= (a_{ij} \cdot b_{ij} \cdot c_{ij}), \\ a_{ij} &= \frac{\min}{k} \{a_{ij} \cdot k\}, \\ b_{ij} &= \frac{1}{K} \sum_{k=1}^k b_{ij}, \\ c_{ij} &= \frac{\max}{k} \{c_{ij} \cdot k\}. \end{aligned} \tag{2}$$

The terms of the formula are detailed in Section 4.3 (refer step 2).

**Step 3. Weightage with single decision matrix**

Here, the criteria weightage is meant to change the weightage value from a single decision matrix to fuzzy numbers from the linguistic term (refer Table 2).

**Step 4. Compute normalized decision matrix**

The following two steps are required in this step.

- (i) Identify the beneficial criteria
- (ii) Identify the nonbeneficial criteria or cost criteria

**Step 5. Find the beneficial criteria and cost criteria**

The beneficial and cost criteria are found by the use of formula given below and a detailed explanation of the formula terms that follow in Section 4.3 (refer step 5).



TABLE 1: Triangular membership function values for AHP Saaty scale [56].

Saaty parameters	Saaty scale	Fuzzy values based on triangular membership function
Equal importance	1	1, 1, 1
Moderate importance	3	2, 3, 4
Strong importance	5	4, 5, 6
Very strong importance	7	6, 7, 8
Extremely strong importance	9	9, 9, 9
Intermediate importance	2	1, 2, 3
	4	3, 4, 5
	6	5, 6, 7
	8	7, 8, 9

TABLE 2: Linguistic terms and fuzzy number.

Linguistic terms	Linguistic scales	Fuzzy values based on triangular membership function
Very low (VL)	1	1, 1, 3
Low (L)	2	1, 3, 5
Average (A)	3	3, 5, 7
High (H)	4	5, 7, 9
Very high (VH)	5	7, 9, 9

$$r_{ij} = \left[ \frac{a_{ij}}{c^*}, \frac{b_{ij}}{c^*}, \frac{c_{ij}}{c^*} \right]. \quad (3)$$

$C^* = \max\{c_{ij}\}$  beneficial criteria

$$r_{ij} = \left[ \frac{a_j}{c_{ij}}, \frac{a_j}{b_{ij}}, \frac{a_j}{a_{ij}} \right]. \quad (4)$$

$a_j = \min\{a_{ij}\}$  cost criteria

Step 6. Compute the weighted normalized fuzzy decision matrix

The weighted normalized fuzzy decision matrix has been obtained by the use of formula (1) and a detail of the below-mentioned formula in Section 4.3.

$$V_{ij} = r_{ij} \times W_j$$

$$\begin{aligned} A_1 \times A_2 &= (a_1, b_1, c_1) \times (a_2, b_2, c_2) \times (a_3, b_3, c_3) \\ &= (a_1 \times a_2, b_1 \times b_2, c_1 \times c_2). \end{aligned} \quad (5)$$

Step 7. Compute the fuzzy positive ideal solution (FPIS) and fuzzy negative ideal solution (FNIS)

The fuzzy positive ideal solution (FPIS) and fuzzy negative ideal solution (FNIS) have been obtained by the use of the formula given below and a detail of the below-mentioned formula in a later section.

$$\begin{aligned} A^* &= (V_1, V_2, \dots, V_n^*), & V &= \max\{V_{ij}\} \\ A^{*} &= (V_1, V_2, \dots, V_n^*), & V &= \min\{V_{ij}\}. \end{aligned} \quad (6)$$

Step 8. Compute the distance from each alternative to the FPIS and to the FNIS

The distances from each alternative to the FPIS and to the FNIS have been obtained by the use of the formula given below and a detail of the below-mentioned formula in the section that follows.

$$d(\dot{x}, \dot{y}) = \text{sq} \sqrt{\left( \frac{1}{3} [(a_1 - a_2) \wedge 2 + (b_1 - b_2) \wedge 2 + (c_1 - c_2) \wedge 2] \right)}. \quad (7)$$

Step 9. Find  $d_i^*$  and  $d_i^-$

The total distances from each alternative to the FPIS and to the FNIS have been obtained by the use of the formula given below and a detail of the below-mentioned formula in a later section.

$$\begin{aligned} d_i^* &= \sum_{j=1}^n d(V_{ij}, V_j), \\ d_i &= \sum_{j=1}^n d(V_{ij}, V_j). \end{aligned} \quad (8)$$

Step 10. Compute the closeness coefficient ( $CC_i$ ) for each alternative and give the ranking based on  $CC_i$

The final step of fuzzy TOPSIS method, closeness coefficient ( $CC_i$ ), for each alternative has been obtained by the use of the below formula and the ranking based on higher  $CC_i$  for getting the first rank, while other alternatives help obtain simultaneous ranks into details of the below-mentioned formula in a later section.

$$CC_i = \frac{d_i^-}{d_i^- + d_i^*}. \quad (9)$$

### 3. Problem Description

Earlier researchers have provided a detailed description of the use of AM in many fields and the many optimizations used in the production method. One of these research studies deals with help to a customer in the choice of selection of the right and most suitable FDM machine from a contemporary basis using the technique of choice.

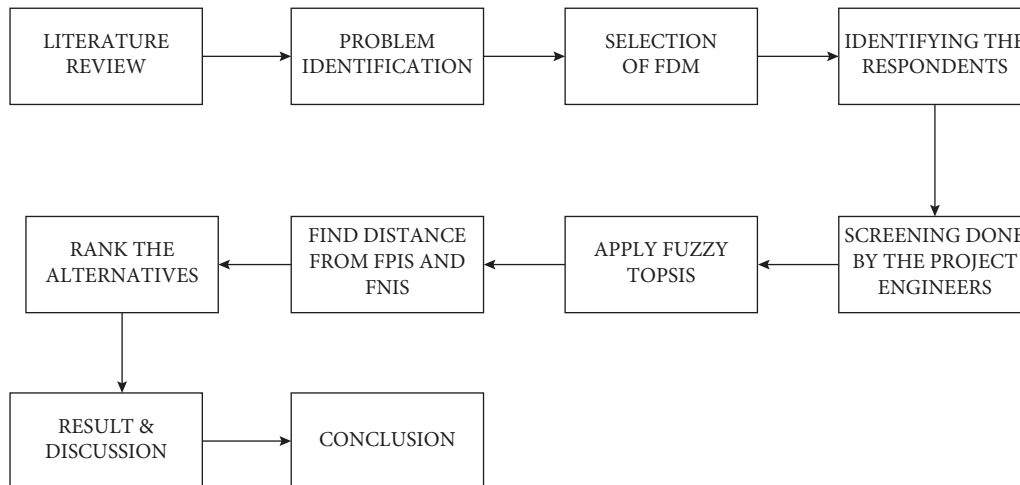


FIGURE 2: Research flow of the paper.

According to previous researchers, 3D printing technology is used in many fields, but AM has seven types with their own unique characteristics. Although there are many advantages to 3D printing technology, manufacturers often avoid this method due to its production cost being slightly higher than that of the conventional manufacturing method. The price of a commodity includes the costs of those relating to the machine used in production and items used in manufacturing and profits. The choice of the right production machine by optimization enables a slight reduction in the cost of production. The purpose of this research paper was therefore to enable the NGO (respondent) to select the best production FDM with the help of an optimization tools with nine criteria such as price, build, and volume.

#### 4. Research Methodology

The purpose of this research paper was to enable the selection of a specific NGO (respondent) of the most suitable FDM with the help of the multi-criteria decision-making (MCDM) technique. The 9 criteria in this research study and the nine alternatives suggested by the NGO (respondent) help selection of the best and most suitable alternative using the fuzzy TOPSIS MCDA method. The basic objective is to select an optimal and suitable FDM, and the criteria including price (C1), build volume (C2), extruder type (C3), printing speed (C4), operating temperature (C5), filament material (C6), tolerance (C7), environmental factor (C8), and safety of the machine (C9) are considered. Also, recommended FDM alternatives by NGO (respondent) include Make 3D Pratham 6.0 (A1), Cube Pro Duo (A2), Make 3D Pratham 5.0 (A3), Global Pramaan 310 HT (A4), Belity 3 Max (A5), Botzlab Drona (A6), Make 3D Pratham 3.0 (A7), 3Idea Max 300 (A8), and 3Idea Creativity (A9) in the choice of the best and the most suitable machine from the present. Figure 2 illustrates the overall research flow of this study.

Moreover, the objective of this research was determined and work began. The first step was to identify common and important criteria from NGO (respondent) recommended FDMs through the papers of previous literary researchers.

Then, FPIS and FNIS were calculated using the Fuzzy TOPSIS MCDA method and ranked for alternatives.

*4.1. Selection Process.* Despite the presence of various additive manufacturing machines (AMMs) in the market, it is very important for the manufacturers to choose the optimal manufacturing machine. This research paper assists the NGO (respondent) in the selection of suitable FDM needed to produce the prototype from nine different FDMs based on the present. The reasons for selecting the 9 machines specified by the NGO (respondent) have been confirmed by the literature. This is due to the reduction in the cost of manufactured product as the most important goal to be done through the selection of the high and most suitable FDM machine for NGO (respondent). In the Indian automobile market, Maruti Suzuki has retained its number one position in the area of sales service through service centers setup in all cities. Considering the most problematic among the customers is the repairs to the goods purchased after the sale and the required raw material with focus by Maruti Suzuki [57].

In the opinion of previous literary researchers also, the most important factors in the selection of a machine include the spare part production, the raw material, and the after-sales service of the machine [2, 3]. Therefore, nine FDM machines recommended by NGO (respondent) are used as alternatives in this research paper due to the presence of all these factors in NGO (respondent) recommended machines.

*4.2. Screening Process.* The screening process has been further enhanced by the field experts (AM machine users) dealing in to the objective of this research question about criteria and alternatives asked and resolved through a Google Form. Here with 46 project managers, 70 research scholars, 22 professors, 3 college students, and 31 other AM industry experts participated in this research as respondents, experts in the field were asked questions about alternatives and criteria, such as the very low (VL), low (L), average (A), high (H), and very high (VH) linguistic term, from one to

five points. This screening process was carried out with the help of available data and the project engineer of the NGO (respondent). The nine alternatives and their overall specific features are shown in Figure 3. Table 3 shows some more criteria and alternatives. The group decision matrix was designed with three maximum points for each alternative. The selection of the respondents (AM machine users) of the maximum value of the criteria was used as the criteria weights in this research paper. Based on this, the following fuzzy TOPSIS method has been designed, and their ranking from the decision matrix helps to achieve the objective of this research paper. Table 3 represents a comparison of alternatives A and B and NGO (respondent) prescribed alternatives. Tables 4 and 5 represent the field expert (AM machine users) weightage for the criteria and alternatives. In this research, a total of 172 respondents (AM machine users) were involved in different locations and working positions. Figure 3 shows the working area of the respondent (AM machine users) as shown as follows.

Figure 3 shows the different geolocation of the respondents (AM machine users) that include 71.5% of respondents (AM machine users) from India, 7% of respondents (AM machine users) from the USA, and the remaining respondents (AM machine users) chosen from China and other countries.

Figure 4 shows the working areas of respondents (AM machine users), and it represents 51.7% from research institute and 26.7% from industry, 12.2% from entrepreneurs, and the remaining were from AM-based work.

Figure 5 shows the designation of respondent (AM machine users) and the data already detailed above.

This research expresses the data of respondents (AM machine users) who experienced the particular brands and FDM process in their institutional or industries. Figure 6 shows all the respondents (AM machine users) holding the AMM with a proper background in the field of additive manufacture. Figure 6 shows 100 percent of respondent (AM machine users) institutes or industries holding additive manufacturing machines. Figure 7 expresses the raw material used by the respondents (AM machine users) in their working institution or industry.

Figure 7 shows the raw material used mostly by the respondents (AM machine users) that include plastic/polymer (PA, ABS, PLA, PEEK, etc.) and metals (Ti, SS, bronze, brass, gold, etc.).

Tables 4 and 5 data are taken from Figures 8 and 9 as shown as follows.

Criteria weight in Figure 8 shows the questions to the respondents (AM machine users) for calculating the criteria weight. The maximum values of respondent (AM machine users) answers were taken as criteria weights as shown in Table 4. Figure 9 represents the question to the respondents (AM machine users) for forming the decision matrix by the answers of respondent (AM machine users) about the alternatives. Figure 8(a) shows the most respondents (AM machine users) according to 4 points for criteria 1 as mentioned in Table 4 as criteria 1 (C1) equals 4 as criteria weight by the respondent (AM machine users) points. Figures 8(b)–8(i) show the most respondents (AM machine

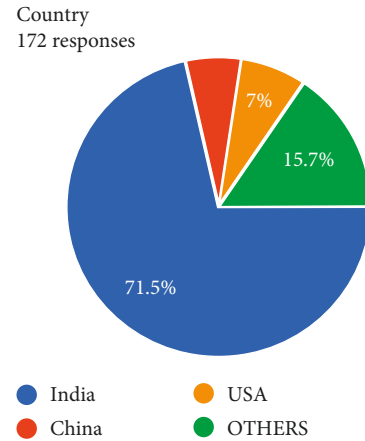


FIGURE 3: Location of respondents (AM machine users).

users) according to 5, 2, 3, 3, 4, 1, 4, and 5 points for C2 to C9 criteria weight. Similarly, all the criteria weight values have been taken from Figure 8 and it is mentioned in Table 4.

Table 5 indicates the alternatives and alternative weight used by the respondent (AM machine users) point. For example, Figure 9(a) shows the question and answers relating to the alternative one (A1). Here, in A1, most of the respondents (AM machines users) were seen according to four points and secondly gave 5 points and thirdly gave 3 points. For group decision matrix purpose, the top 3 points are taken into account to solve the novel problem. Then, it is mentioned in Table 5 and the rest of the alternative values are taken in the same manner.

#### 4.3. Evaluation by Fuzzy TOPSIS

##### Step 1

The evaluation process started with the group decision matrixes such as decision-maker I, decision-maker II, and decision-maker III. As per Table 4 data, the 3 highest points given by the respondent (AM machine users) to alternatives were taken as decision-maker I, decision-maker II, and decision-maker III. Thus, the group decision matrixes are shown in Tables 6(A)–6(C). This decision-making table was formed by the use of information of response provided by the respondents (AM machine users) as per Tables 4 and 5; it initially takes linguistic terms as per Table 2 followed by the linguistic terms replaced by the fuzzy number as these Tables 6(D)–6(F) represented. The fuzzy numbers are formed by the triangular matrix with the help of analytical hierarchy process Saaty scale. This was explained in Section 2.3.

##### Step 2

The combined decision matrix for calculating purpose was formed from the group decision matrix. The combined decision matrix is shown in Table 6(G). The combined decision matrix was obtained by the use of the formula given as follows:

$$X_{ij} = (a_{ij} \cdot b_{ij} \cdot c_{ij}), \quad (10)$$



TABLE 4: Criteria and criteria weight by respondent points.

Criteria	Criteria weight by respondent points
C1	4
C2	5
C3	2
C4	3
C5	3
C6	4
C7	1
C8	4
C9	5

TABLE 5: Alternatives and alternative weight by respondent (AM machine users).

Alternatives	Alternative weight by respondent (AM machine users) points
A1	4, 5, 3
A2	4, 5, 3
A3	3, 4, 2
A4	4, 3, 2
A5	3, 2, 1
A6	5, 4, 3
A7	3, 4, 2
A8	4, 3, 2
A9	2, 3, 1

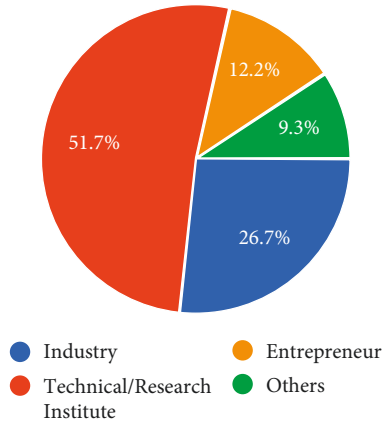
Working Area  
172 responses

FIGURE 4: Working area.

where  $X_{ij}$  = value in each cell.  $i$  = number of row and  $j$  = number of column (refer Tables 6(D)–6(F) with 6(G)).  $(a_{ij}, b_{ij}, c_{ij})$  represents each cell fuzzy number as Tables 6(D)–6(F).

An example of the combined decision matrix as shown in Table 6(G) first shells is solved below. Let first shell values of Tables 6(D)–6(F) be 3, 5, and 7 in decision-maker I, 5, 7, and 9 in decision-maker II, and 1, 3, and 5 in decision-maker III.

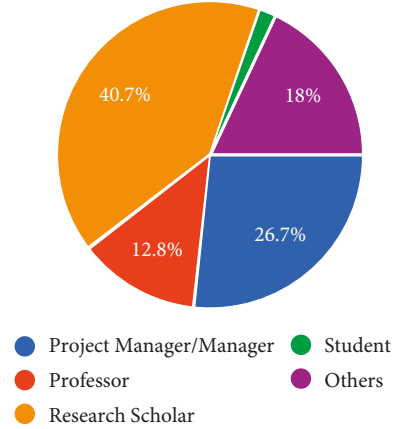
Designation  
172 responses

FIGURE 5: Designation of respondent (AM machine users).

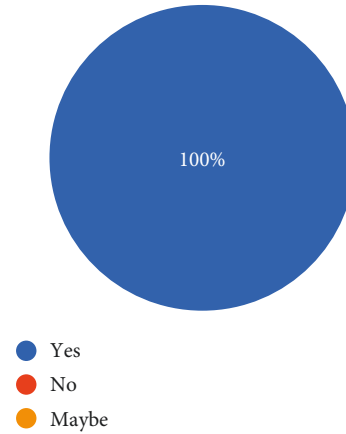
Did your institution or industry have additive manufacturing?  
172 responses

FIGURE 6: Ensuring the respondents (AM machine users) on field of additive manufacturing.

Here  $a_{11} = 3, 5, 1,$

$b_{11} = 5, 7, 3,$

$c_{11} = 7, 9, 5:$   $k$  – number of decision maker,

$$a_{ij} = \frac{\min}{k} \{a_{ijk}\},$$

$$a_{ij} = \min(3, 5, 1) = 1,$$

$$b_{ij} = \frac{1}{K} \sum_{k=1}^k b_{ijk},$$

$$b_{ij} = \frac{1}{3} (5, 7, 3) = 5,$$

$$c_{ij} = \frac{\max}{k} \{c_{ijk}\},$$

$$c_{ij} = \max(7, 9, 5) = 9.$$

(11)

Which type of raw materials required for your industry/institute?  
172 responses

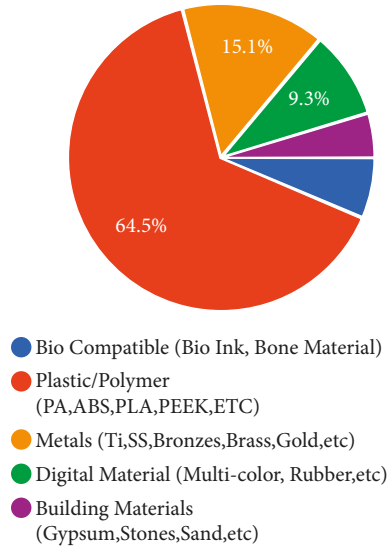


FIGURE 7: Raw materials used by respondent (AM machine users) industry/institute.

Hence, in the decision matrix Table 6(G) first shells were obtained (1, 5, and 9) and the rest of the terms were obtained in a similar manner.

Step 3

In the third step, Table 6(H) was formed with the help of respondent (AM machine users) response (refer Table 4) for the criteria weight and the term in the linguistic term. Then, Table 6(I) was formed by the replacement of the linguistic terms with fuzzy number as per Table 2.

Step 4

Table 6(J) is a normalized fuzzy decision matrix, and before finding this, the criteria are identified in two categories namely cost criteria or nonbeneficial criteria and beneficial criteria. In this research paper, the beneficial criteria are build volume, extruder type, printing speed, operating temperature, filament material, tolerance, environmental factors, and the safety of machine. The nonbeneficial criteria or cost criteria are only the price of the machine in our novel problem.

Step 5

Table 6(J) normalized fuzzy decision matrix is obtained by the following formula.

$$r_{ij} = \left[ \frac{a_{ij}}{c^*}, \frac{b_{ij}}{c^*}, \frac{c_{ij}}{c^*} \right]. \tag{12}$$

$C^* = \max\{c_{ij}\}$  beneficial criteria

$$r_{ij} = \left[ \frac{a_j}{c_{ij}}, \frac{a_j}{b_{ij}}, \frac{a_j}{a_{ij}} \right]. \tag{13}$$

$a_j^* = \min\{a_{ij}\}$  cost criteria

Let Table 6(I) cost criteria be only price and the rest be beneficial criteria.

Here,  $C^* = \max\{c_{ij}\}$  beneficial criteria, and it is the maximum value of “C” component in all individual alternatives.

Then,  $a_j^* = \min\{a_{ij}\}$  cost criteria, and it is the minimum value of “a” component in all individual alternatives.

Note: in the normalized decision matrix, ( $a_j^*$ ) in cost criteria section, “c” component is taken in the first place in denominator and “a” component is taken in the last row of denominator (refer Table 6(J)).

Finally, each value of beneficial criteria was divided by  $c^*$  and with the above note each value of cost criteria was divided by  $a_j^*$ .

Step 6

The criteria weight on Table 6(J) was multiplied on each component with each component as below. For example, “a” component was multiplied by “a” component. Similar to Table 6 (J), the rest of the criteria weight and alternatives were determined. Finally, Table 6(K) weighted normalized fuzzy decision matrix was obtained by the use of the formula given as follows.

$$V_{ij} = r_{ij} \times W_j$$

$$A_1 \times A_2 = (a_1, b_1, c_1) \times (a_2, b_2, c_2) \times (a_3, b_3, c_3) \tag{14}$$

$$= (a_1 \times a_2, b_1 \times b_2, c_1 \times c_2),$$

where  $V_{ij}$  = fuzzy decision matrix,  $r_{ij}$  = row and column of each alternative, and  $w_j$  = weightage of each column.

Step 7

The next step was to find the fuzzy positive ideal solution (FPIS) and fuzzy negative ideal solution (FNIS) using the formula given as follows:

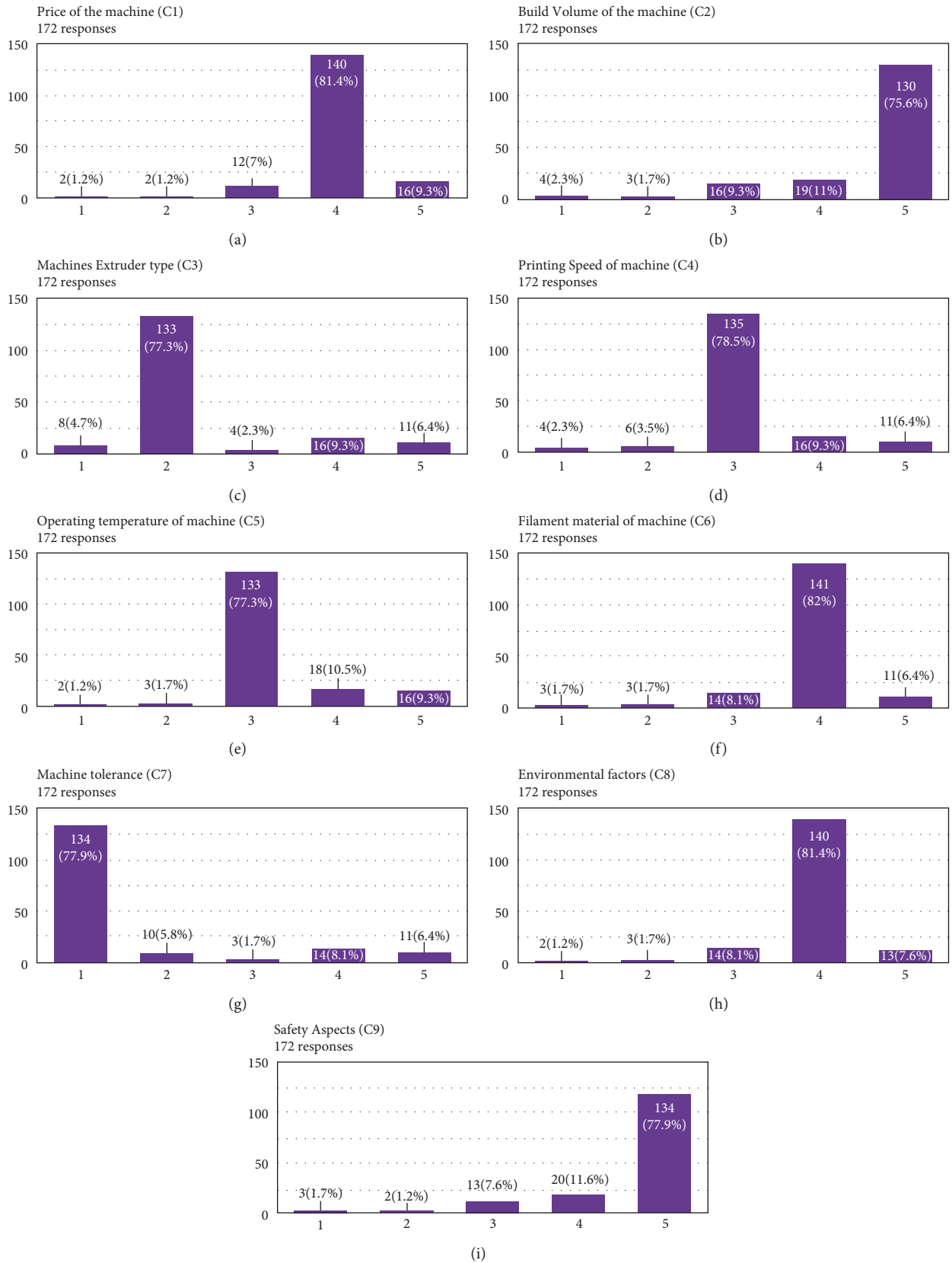
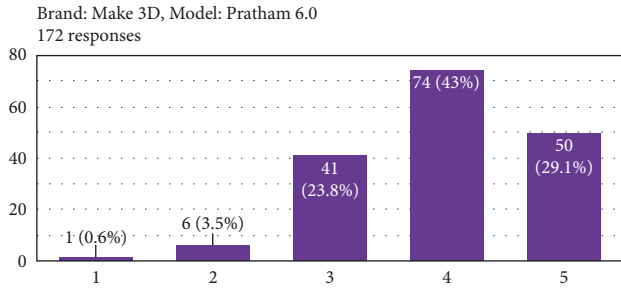
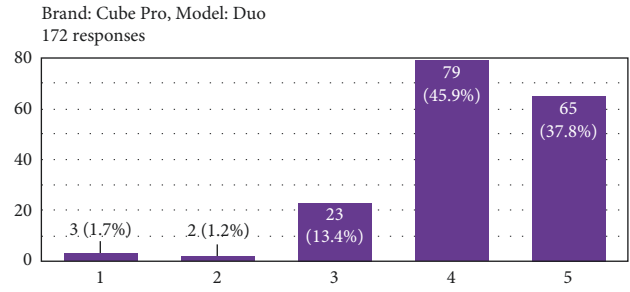


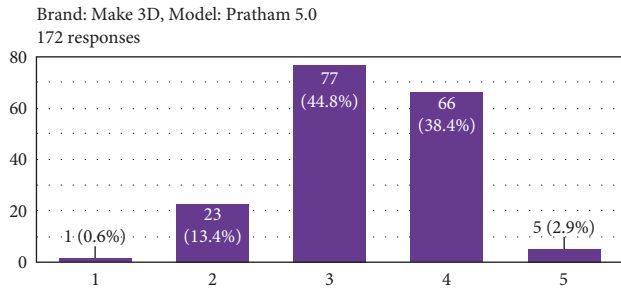
FIGURE 8: Criteria weights by respondents (AM machine users) (refer Table 4). (Figures 8(a)–8(i) show the response from field experts (AM machine users) about the criteria of selected AM machines, and it is considered as criteria weight).



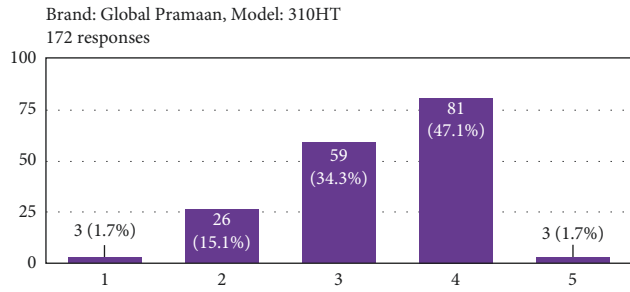
(a)



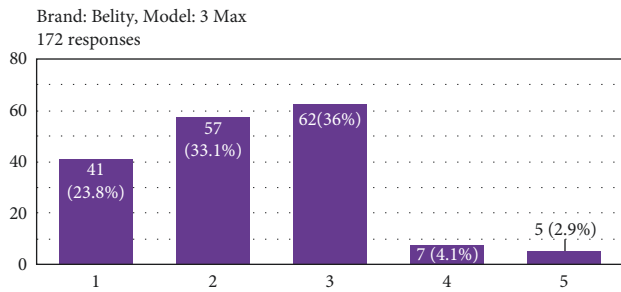
(b)



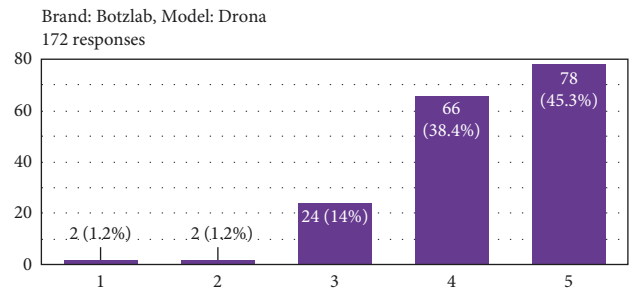
(c)



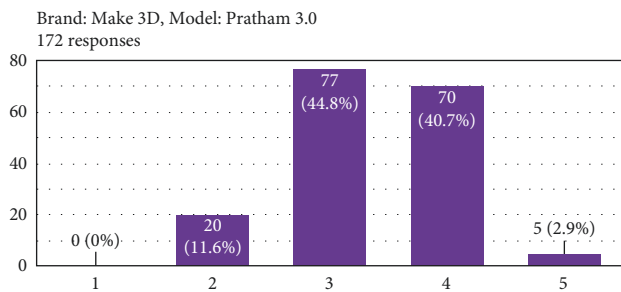
(d)



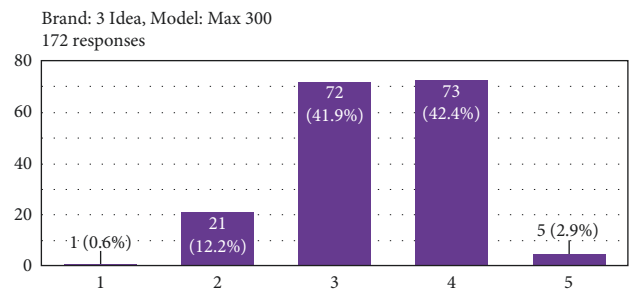
(e)



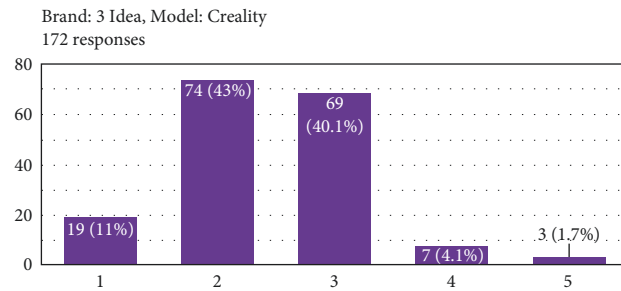
(f)



(g)



(h)



(i)

FIGURE 9: Alternative weights by respondents (AM machine users). (Figures 9(a)–9(i) show the response from field experts (AM machine users) about the alternatives (selected AM machines), and it is considered as alternative weight (refer Table 5)).



$$\begin{aligned} A^* &= (V_1, V_2, \dots, V_n^*), & V &= \max\{V_{ij3}\} \\ A^{-*} &= (V_1, V_2, \dots, V_n^*), & V &= \min\{V_{ij3}\}. \end{aligned} \quad (15)$$

Here,  $v_{ij3}$  = fuzzy number of “c” component,  $A^*$  = fuzzy positive ideal solution (FPIS), and  $A^{-*}$  = fuzzy negative ideal solution (FNIS).

The fuzzy positive ideal solution of  $A^*$  was found by the maximum value of “c” components and the fuzzy negative ideal solution of  $A^-$  was found by the minimum value of “a” component in the weighted normalized fuzzy decision matrix Table 6(K) in each alternative.

#### Step 8

The distance from each alternative to the FPIS and to the FNIS was obtained by the use of formula given below from the weighted normalized fuzzy decision matrix Table 6(K).

$$d(x, y) = \text{sq} \sqrt{\left(\frac{1}{3} [(a_1 - a_2)^2 + (b_1 - b_2)^2 + (c_1 - c_2)^2]\right)}, \quad (16)$$

where  $a_1$ ,  $b_1$ , and  $c_1$  are solved fuzzy numbers of weighted normalized fuzzy decision matrix, and  $a_2$ ,  $b_2$ , and  $c_2$  are  $A^*$  fuzzy numbers solved in the previous steps.

Similarly, the weighted normalized fuzzy decision matrix Table 6(K) is solved with the same above formula, but  $a_2$ ,  $b_2$ , and  $c_2$  are  $A^-$  fuzzy numbers solved in the previous steps. Finally, the single values were obtained for each alternative and it is known as distance values.

#### Step 9

The distance ( $d^*$ ) for the positive ideal solution was obtained from the  $A^*$  term of previous steps, and the distance ( $d^-$ ) for the negative ideal solution was obtained from  $A^-$ .

$$\begin{aligned} d_i^* &= \sum_{j=1}^n d(V_{ij}, V_j^*), \\ d_i^- &= \sum_{j=1}^n d(V_{ij}, V_j^-). \end{aligned} \quad (17)$$

Thus, the values are summed with their each row as final  $d^*$  and  $d^-$  for each alternative. Then, it is shown in Table 6(L).

#### Step 10

final step of the coefficient of closeness ( $CC_i$ ) was found by the below formula and the final ranking is given to the alternatives based on the  $CC_i$  values. More value alternatives obtained the first rank, and others obtained higher rank. The ranking is shown in Table 6(L).

$$CC_i = \frac{d_i^-}{d_i^- + d_i^*}. \quad (18)$$

## 5. Result and Discussion

The most important objective of this research is also to highlight the many modern 3D printing technologies in the manufacturing market and increase the usability of additive manufacturing. The novelty of this research is that the fuzzy TOPSIS system helps the selection of an FDM machine that is necessary and suitable for NGO (respondent) from several slightly different FDM machines seen as identical. For this purpose, FPIS and FNIS were identified through the creation of a decision matrix with the help of 172 additive manufacturing industry experts (AM machine users) for the selection of the right and appropriate FDM machine from the FDM machines currently on the market recommended to the NGO. Further criteria and alternatives based on MCDA were first identified using the research papers. Also highlighted were the 9 criteria and 9 alternatives used in this research. The 9 criteria used are price, build volume, extruder type, printing speed, operating temperature, filament material, tolerance, environmental factor, and safety. Also used as 9 alternatives were Make 3D Pratham 6.0, Cube Pro Duo, Make 3D Pratham 5.0, Global Pramaan 310 HT, Belity 3 Max, Botzlab Drona, Make 3D Pratham 3.0, 3Idea Max 300, and 3Idea Creality. The views of previous literary researchers have been presented in detail in part 2 in three sections. It explains the use of AM, many methods, the advantages, the challenges, etc., the MCDA methods, and the fuzzy TOPSIS method and its steps. Then, the novel problem of this research paper has been mentioned. This research flows through the research methodology, and the details of the experts (AM machine users) involved in the research are outlined. It explains the basic data required for use in the fuzzy TOPSIS method. Finally, Table 6(L) is gradually diagnosed using fuzzy TOPSIS. Wherever alternative 2 (A2) takes the first place, alternatives 1, 3, 4, and 8 take the second place, alternative 9 takes the third place, and alternatives 5 and 7 take the fourth place (refer Table 6(L)). It is therefore recommended that the Cube Pro Duo AM machine is the most optimal. The purpose of this research was to help future researchers in finding the most useful and various features of 3D printing.

## 6. Conclusion

The 3D printing system incorporates many innovative technologies with many machines on the market every day coming with the same slightly different features. Choice of the right machine from these machines in the market is one of the most challenging choices for the customers. In this research, with the help of experts (AM machine users) in the field, the authors have identified the optimum among the nine machines recommended for the specific NGO (respondent) using the MCDA systemic fuzzy TOPSIS based on the most important criteria. This entire research was carried out with the help of field experts (AM machine users) by the online mode on a qualitative survey via Google Forms. All the machines referred to in this study have been used or explored by industry experts (AM machine users). 172 field expert (AM machine users) responses about the selected

criteria and alternatives play a major role to find the most optimum FDM machine for the NGO (respondent). From the final result obtained, alternative 2 Cube Pro Duo FDM machine selected for NGO (respondent) is a better choice compared with other alternatives with 9 criteria. This study was conducted for NGO (respondent) to produce prototypes in the fields of medicine and construction. The prototypes will be made with any materials most of the time, and with FDM technology, the biodegradable polymers are used as raw material (filament). This decision is subject to changes when other machines or criteria or applications are used. Similarly, only machines specific to the NGO (respondent) have been used in this study. Finally, testing this study using other MCDA methods will be a novelty for future researchers.

### Data Availability

The data that support the findings of this study are available on request from the corresponding author (John Rajan A). The data are not publicly available due to privacy concerns.

### Additional Points

(i) Selection of AM machine in the real-time basis. (ii) Machine selection problem using fuzzy TOPSIS. (iii) Current 3D printing technology.

### Conflicts of Interest

The authors declare that there are no financial interests/personal relationships, which may be considered as potential conflicts of interest.

### Acknowledgments

The authors wish to thank VIT University for the consent encouragement and motivation in publishing this article; the laboratory in charge and technician of Additive Manufacturing (DIGI-MAN) Laboratory, VIT Vellore, for the facility provided to carry out this research work; and Mr. R Educational Services (NGO) for giving opportunities.

### Supplementary Materials

Numerical evaluation by fuzzy TOPSIS method. (*Supplementary Materials*)

### References

- [1] M. Sugavaneswarn, "A multi-criteria decision making method for vapor smoothening fused deposition modelling part," *Rapid Prototyping Journal*, vol. 28, 2021.
- [2] K. Ransikarbum and P. Khamhong, "Integrated fuzzy analytic hierarchy process and technique for order of preference by similarity to ideal solution for additive manufacturing printer selection," *Journal of Materials Engineering and Performance*, vol. 30, 2021.
- [3] M. Palanisamy, A. Pugalendhi, and R. Ranganathan, "Selection of suitable additive manufacturing machine and materials through best-worst method (BWM)," *International Journal of Advanced Manufacturing Technology*, vol. 107, no. 5–6, pp. 2345–2362, 2020.
- [4] Astm, *Standard Terminology for Additive Manufacturing Technologies*, ASTM International, West Conshohocken, PA, 2012.
- [5] M. Ancau and C. Caizar, "The computation of Pareto-optimal set in multi-criteria optimization of rapid prototyping processes," *Computers & Industrial Engineering*, vol. 58, pp. 696–708, 2010.
- [6] J. Y. Han, "A study on the prototype modeling method using 3D printing," *J. Packag Culture Design Res.* vol. 34, pp. 97–109, 2013.
- [7] M. K. Thompson, G. Moroni, T. Vaneker et al., "Design for Additive Manufacturing: Trends, Opportunities, Considerations, and Constraints," *CIRP Annals-Manufacturing Technology*, vol. 65, 2016.
- [8] S. Ha, K. Ransikarbum, H. Han, D. Kwon, H. Kim, and N. Kim, "A dimensional compensation algorithm for vertical bending deformation of 3D printed parts in selective laser sintering," *Rapid Prototyping Journal*, vol. 24, no. 6, pp. 955–963, 2018.
- [9] K. Ransikarbum, S. Ha, J. Ma, and N. Kim, "Multi-objective optimization analysis for part-to-Printer assignment in a network of 3D fused deposition modeling," *Journal of Manufacturing Systems*, vol. 43, pp. 35–46, 2017.
- [10] K. Ransikarbum, C. Yingviwatanapong, R. Leksomboon, T. Wajanavisit, and N. Bijaphala, "Additive manufacturing-based healthcare 3D model for education: literature review and A feasibility study," in *Proceedings of the 2019 Research, Invention, and Innovation Congress (RI2C)*, pp. 1–6, IEEE, Bangkok, Thailand, December, 2019.
- [11] K. Ransikarbum, R. Pitakaso, and N. Kim, "A decision-support model for additive manufacturing scheduling using an integrative analytic hierarchy process and multi-objective optimization," *Applied Sciences*, vol. 10, no. 15, p. 5159, 2020.
- [12] K. Nyembwe, D. de Beer, K. van der Walt, S. Bhero, and K. Katuku, "Comparison of Additive Manufacturing Processes for Rapid Casting for Tooling Application Using the Analytic Hierarchy Process (AHP)," in *Proceedings of the Computers and Industrial Engineering*, p. 42, Cape Town, South Africa, July, 2012.
- [13] K. Ransikarbum and S. J. Mason, "Multiple-objective analysis of integrated relief supply and network restoration in humanitarian logistics operations," *International Journal of Production Research*, vol. 54, no. 1, pp. 49–68, 2016.
- [14] K. Ransikarbum and S. J. Mason, "Goal programming-based post-disaster decision making for integrated relief distribution and early-stage network restoration," *International Journal of Production Economics*, vol. 182, pp. 324–341, 2016.
- [15] C. Puchongkawarin and K. Ransikarbum, "An integrative decision support system for improving tourism logistics and public transportation in Thailand," *Tourism Planning & Development*, vol. 18, pp. 1–16, 2020.
- [16] T. Wohlers, "Wohlers Report 2021 Inc," 2021.
- [17] B. Ceballos, M. T. Lamata, and D. A. Pelta, "A comparative analysis of multi-criteria decision-making methods," *Progress in Artificial Intelligence*, vol. 5, no. 4, pp. 315–322, 2016.
- [18] F. T. S. Chan and N. Kumar, "Global supplier development considering risk factors using fuzzy extended AHP-based approach," *Omega*, vol. 35, no. 4, pp. 417–431, 2007.
- [19] Y. Wang, R. Blache, and X. Xu, "Selection of additive manufacturing processes," *Rapid Prototyping Journal*, vol. 23, no. 2, pp. 434–447, 2017.

- [20] S. Zaroni, M. Ashourpour, A. Bacchetti, M. Zanardini, and M. Perona, "Supply chain implications of additive manufacturing: a holistic synopsis through a collection of case studies," *International Journal of Advanced Manufacturing Technology*, vol. 102, no. 9–12, pp. 3325–3340, 2019.
- [21] H. Bikas, P. Stavropoulos, and G. Chrystolouris, "Additive manufacturing methods and modeling approaches: a critical review," *International Journal of Advanced Manufacturing Technology*, vol. 83, no. 1–4, pp. 389–405, 2016.
- [22] M. Ramola, V. Yadav, and R. Jain, "On the adoption of additive manufacturing in healthcare: a literature review," *Journal of Manufacturing Technology Management*, vol. 30, no. 1, pp. 48–69, 2019.
- [23] D. Kokotsaki, V. Menzies, and A. Wiggins, "Durham research online woodlands," *Critical Studies on Security*, vol. 2, no. 2, pp. 210–222, 2014.
- [24] A. Rashid, "Additive manufacturing technologies," in *CIRP Encyclopedia of Production Engineering* Springer, New York, NY, USA, 2019.
- [25] V. Petrovic, J. Vicente Haro Gonzalez, O. Jordá Ferrando, J. Delgado Gordillo, J. Ramón Blasco Puchades, and L. Portolés Griñan, "Additive layered manufacturing: sectors of industrial application shown through case studies," *International Journal of Production Research*, vol. 49, no. 4, pp. 1061–1079, 2011.
- [26] A. Drizo and J. Pegna, "Environmental impacts of rapid prototyping: an overview of research to date," *Rapid Prototyping Journal*, vol. 12, no. 2, pp. 64–71, 2006.
- [27] D. T. Pham and R. S. Gault, "A comparison of rapid prototyping technologies," *International Journal of Machine Tools and Manufacture*, vol. 38, no. 10–11, pp. 1257–1287, 1998.
- [28] D. Bak, "Rapid prototyping or rapid production? 3D printing processes move industry towards the latter," *Assembly Automation*, vol. 23, no. 4, pp. 340–345, 2003.
- [29] R. V. Rao and K. K. Padmanabhan, "Rapid prototyping process selection using graph theory and matrix approach," *Journal of Materials Processing Technology*, vol. 194, no. 1–3, pp. 81–88, 2007.
- [30] F. Xu, Y. S. Wong, and H. T. Loh, "Toward generic models for comparative evaluation and process selection in rapid prototyping and manufacturing," *Journal of Manufacturing Systems*, vol. 19, no. 5, pp. 283–296, 2001.
- [31] S. H. Masood and A. Soo, "A rule based expert system for rapid prototyping system selection," *Robotics and Computer-Integrated Manufacturing*, vol. 18, no. 3–4, pp. 267–274, 2002.
- [32] H. S. Byun and K. H. Lee, "A decision support system for the selection of a rapid prototyping process using the modified TOPSIS method," *International Journal of Advanced Manufacturing Technology*, vol. 26, no. 11–12, pp. 1338–1347, 2005.
- [33] G. D. Kim and Y. T. Oh, "A benchmark study on rapid prototyping processes and machines: quantitative comparisons of mechanical properties, accuracy, roughness, speed, and material cost," *Proceedings of the Institution of Mechanical Engineers - Part B: Journal of Engineering Manufacture*, vol. 222, no. 2, pp. 201–215, 2008.
- [34] P. Jones, *Three-Dimensional Printing Technology*, 2020.
- [35] S. Ramalingam, "Fuzzy interval-valued multi criteria based decision making for ranking features in multi-modal 3D face recognition," *Fuzzy Sets and Systems*, vol. 337, pp. 25–51, 2018.
- [36] M. Taufik and P. K. Jain, "Role of build orientation in layered manufacturing: a review," *International Journal of Manufacturing Technology and Management*, vol. 27, no. 1–3, pp. 47–73, 2013.
- [37] P. Gay, D. Blanco, F. Pelayo, A. Noriega, and P. Fernández, "Analysis of factors influencing the mechanical properties of flat PolyJet manufactured parts," *Procedia Engineering*, vol. 132, pp. 70–77, 2015.
- [38] M. Vlasea, R. Pilliar, and E. Toyserkani, "Control of structural and mechanical properties in bioceramic bone substitutes via additive manufacturing layer stacking orientation," *Additive Manufacturing*, vol. 6, pp. 30–38, 2015.
- [39] R. K. Gavade, *Multi-Criteria Decision Making: An overview of different selection problems and methods*, vol. 5, no. 4, pp. 5643–5646, 2014.
- [40] F. E. Boran, S. Genç, M. Kurt, and D. Akay, "A multi-criteria intuitionistic fuzzy group decision making for supplier selection with TOPSIS method," *Expert Systems with Applications*, vol. 36, no. 8, Article ID 11363, 2009.
- [41] S. PrasannaVenkatesan and M. Goh, "Multi-objective supplier selection and order allocation under disruption risk," *Transportation Research Part E: Logistics and Transportation Review*, vol. 95, pp. 124–142, 2016.
- [42] W. Ho, "Review on Supplier Selection. Iii," 2018, <http://hdl.handle.net/11343/118668>.
- [43] L. F. C. S. Durão, M. M. Carvalho, S. Takey, P. A. Cauchick-Miguel, and E. Zancul, "Internet of Things process selection: AHP selection method," *International Journal of Advanced Manufacturing Technology*, vol. 99, no. 9–12, pp. 2623–2634, 2018.
- [44] A. Kumar, B. Sah, A. R. Singh et al., "A review of multi criteria decision making (MCDM) towards sustainable renewable energy development," *Renewable and Sustainable Energy Reviews*, vol. 69, no. November, pp. 596–609, 2017.
- [45] Z.-J. Wang, "A note on "A group decision making model based on a generalized ordered weighted geometric average operator with interval preference matrices"," *Fuzzy Sets and Systems*, vol. 341, pp. 145–153, 2018.
- [46] S. Vinodh, T. S. Sai Balagi, and A. Patil, "A hybrid MCDM approach for agile concept selection using fuzzy DEMATEL, fuzzy ANP and fuzzy TOPSIS," *International Journal of Advanced Manufacturing Technology*, vol. 83, no. 9–12, pp. 1979–1987, 2016.
- [47] R. Ranganathan, "Prioritized fsn analysis of inventory management in private and hospital pharmacy followed by questionnaire," *International Research Journal of Pharmacy*, vol. 7, no. 12, pp. 104–113, 2017.
- [48] A. Amindoust, S. Ahmed, A. Saghafinia, and A. Bahreininejad, "Sustainable supplier selection: a ranking model based on fuzzy inference system," *Applied Soft Computing*, vol. 12, no. 6, pp. 1668–1677, 2012.
- [49] A. Mardani, A. Jusoh, K. Md Nor, Z. Khalifah, N. Zakwan, and A. Valipour, "Multiple criteria decision-making techniques and their applications - a review of the literature from 2000 to 2014," *Economic Research-Ekonomska Istraživanja*, vol. 28, no. 1, pp. 516–571, 2015.
- [50] J. Sarkis and S. Talluri, "A model for strategic supplier selection," *Journal of Supply Chain Management*, vol. 38, no. 4, pp. 18–28, 2002.
- [51] J. Rezaei, J. Wang, and L. Tavasszy, "Linking supplier development to supplier segmentation using Best Worst Method," *Expert Systems with Applications*, vol. 42, no. 23, pp. 9152–9164, 2015.
- [52] R. Muvunzi, K. Mpofu, and I. Daniyan, "An evaluation model for selecting part candidates for additive manufacturing in the transport sector," *Metals*, vol. 11, no. 5, 2021.

- [53] B. Vahdani, M. Salimi, and M. Charkhchian, "A new FMEA method by integrating fuzzy belief structure and TOPSIS to improve risk evaluation process," *International Journal of Advanced Manufacturing Technology*, vol. 77, no. 1–4, pp. 357–368, 2015.
- [54] P. Sharma and S. Singhal, "Implementation of fuzzy TOPSIS methodology in selection of procedural approach for facility layout planning," *International Journal of Advanced Manufacturing Technology*, vol. 88, no. 5–8, pp. 1485–1493, 2017.
- [55] M. B. Anand, "Application of Fuzzy AHP – TOPSIS for ranking Additive manufacturing process for micro-fabrication," *Rapid Prototyping Journal*, vol. 24, 2016.
- [56] S. NÄdÄban, S. Dzitac, and I. Dzitac, "Fuzzy TOPSIS: a general view," *Procedia Computer Science*, vol. 91, no. Itqm, pp. 823–831, 2016.
- [57] J. Fitria, D. dan, and E. Sudaryati, "International journal of research in commerce and management studies," *International Journal of Research in Commerce and Management Studies*, vol. 2, no. 04, pp. 74–89, 2020.

## Research Article

# Visual Object Tracking Based on Adaptive Background-Awareness and Spatial Constraint

Keqi Fan <sup>1</sup>, Qianqian Yu,<sup>1</sup> Yiyang Wang,<sup>1</sup> Deng Chen <sup>1,2,3</sup> and Yuhui Zheng<sup>1</sup>

<sup>1</sup>Engineering Research Center of Digital Forensics, Ministry of Education, Nanjing University of Information Science and Technology, Nanjing 210044, China

<sup>2</sup>Zhejiang Academy of Science and Technology Information, 33 Huanchengxi Rd, Hangzhou 310006, China

<sup>3</sup>Key Laboratory of Open Data Zhejiang Province, Zhejiang, China

Correspondence should be addressed to Deng Chen; chen0571@zjinfo.gov.cn

Received 21 March 2022; Revised 13 April 2022; Accepted 18 April 2022; Published 29 June 2022

Academic Editor: Punit Gupta

Copyright © 2022 Keqi Fan et al. This is an open access article distributed under the Creative Commons Attribution License, which permits unrestricted use, distribution, and reproduction in any medium, provided the original work is properly cited.

The correlation filter method is effective in visual tracking tasks, whereas it suffers from the boundary effect and filter degradation in complex situations, which can result in suboptimal performance. Aiming at the solving above problem, this study proposes an object tracking method with a discriminant correlation filter, which combines an adaptive background perception and a spatial dynamic constraint. In this method, an adaptive background-awareness strategy is used to filter the background information trained by the interference filter to improve the discriminability between the object and the background. In addition, the spatial regularization term is introduced, and the dynamic change of the real filter and the predefined spatial constraint template is used to optimize filter learning to enhance the spatial information capture ability of the filter model. Experiments on the OTB100, VOT2018, and TrackingNet standard datasets demonstrate that our method achieves favorable accuracy and success rates. Compared with the current popular correlation filter methods, the proposed method can still maintain stable tracking performance with a scene scale variation, complex background, motion blur, and fast motion.

## 1. Introduction

As one of the popular research fields of computer vision, the main task of visual tracking is to obtain cues, such as the scale and position of the target of interest in every frame of the video by designing tracking models and algorithms to gain the object movement trajectory and acquire object tracking. With the expeditious development of computer vision technology, object tracking algorithms have made remarkable progress and have been widely used in traffic monitoring, video surveillance, security check systems, and other application fields [1]. It should be noted that object tracking methods often face the challenges of multiple adverse factors, such as illumination variation, background clutters, and occlusion in real applications. Therefore, designing a robust tracker in complex background environments is a pendent challenge.

Currently, mainstream object tracking methods can be coarsely divided into deep learning (DL)-based [2] methods and correlation filter (CF)-based [3] methods. The former achieves tracking by connecting multilayer neural networks, training large-scale datasets, and extracting deep features rich in semantic information for training and optimizing tracking models. Representative DL trackers include C-COT [4], ECO [5], MDNet [6], CREST [7], CFCF [8], and DeepSRDCF [9]. With the increasing complexity of deep neural network models, the large computational overhead and model size limit the application of DL-based tracking methods on mobile devices, such as drones, unmanned boats, and smart cars. In contrast, CF-based tracking methods are relatively simple and interpretable. The concept of CF originated in the field of signal processing to describe the correlation between signals. In the field of vision tracking, this CF-based method uses the minimum mean square error results of the ideal filter

template and the real image samples to train a filter model that acts on the search area of the image samples of subsequent frames, while filtering the maximum output response as the object position of the current frame. The CF-based method uses a fast Fourier transform (FFT) to convert the convolution calculation into a less complex dot product operation, which greatly improves the tracking efficiency of the algorithm. CF-related research work is still receiving much attention from scholars.

Generally, CF-based methods can be further divided into generative correlation filters (GCF) and discriminative correlation filters (DCF). The GCF learns online and establishes a generative model to characterize the appearance of the object and then predicts the object location by searching for the region with the most similar features to the model. The representative methods include optical flow estimation [10, 11], Kalman filter [12], MeanShift [13], Kernel Particle Filter [14], etc. The DCF regards the tracking task as a classification problem. It distinguishes the object and background regions by training filters to obtain the object position as the tracking result. Relevant representative methods include MOSSE [15], CSK [16], KCF [17], SRDCF [18], BACF [19], CACF [20], and ASRCF [21]. Compared with DCF's better robustness and higher computational efficiency in complex scenes, this GCF often ignores background region information and only uses object area information for modeling. Therefore, modern GCF's performance is often poor for diverse object scenes. As a result, this work focuses on the DCF method.

It is well known that DCF often causes boundary effects [22]. The reason is that the cyclic sampling method does not remove boundary samples, which makes the tracker produce an overfitting learning phenomenon, resulting in a decrease in the discriminative power of the model. In response to the above problems, background-aware correlation filter (BACF) introduces a clipping matrix to filter the boundary samples of the cyclic sampling set. Although BACF can effectively suppress the background information interference outside the object frame, it ignores the surrounding background information inside the object frame, and the model is still affected by the background interference to some extent, which affects the discriminability of the filter. Subsequently, spatially regularized correlation filters (SRDCF) construct a spatial regularization term to improve the spatial representability of the filter for boundary region features. It is regrettable that the linear space regularization term makes the filter difficult to adapt to the image content. When there is interference, such as scale variation and video scene variation in the background, the background information is easily included in the tracking frame, which affects the object discriminability of the filter model, causing the tracking object to drift and the tracking performance to drop substantially.

Motivated by the abovementioned discussions, we propose a method based on adaptive background awareness and spatial dynamic constraint correlation filters (BSCF) in this work. The major contributions are summarized as follows:

- (i) A new adaptive background perception is introduced, which makes full use of the background

information of the surrounding area of the object. This strategy can punish the nonobject area more accurately and greatly improve the classification and discriminability of the filter model.

- (ii) The proposed spatial dynamic constraints are added to the filter to enhance its adaptive learnability, so the filter is restricted more pertinently, thus effectively resolving the problem of boundary distortion and further improving its robustness to object tracking in complex scenes.
- (iii) Experimental results on the OTB100, VOT2018, and TrackingNet benchmark datasets validate the performance advantages of BSCF in the object motion scene; especially under the conditions of scene scale variation and complex background conditions, compared with popular methods, the proposed method performs better.

The remaining sections of this study are arranged as follows: Section 2 summarizes the traditional CF method, the spatial regularization CF method, and the background-aware CF method. Section 3 describes the method in detail. Section 4 presents the experimental analysis and the comparison of various mainstream tracking methods; the benchmark scoring dataset and evaluation metrics are briefly described. Section 5 summarizes the full text.

## 2. Preliminaries

*2.1. Traditional CF Methods.* Henriques et al. proposed a circulant structure of tracking-by-detection with kernels (CSK) [16] using the intensive sampling method of the cycle matrix by modeling the translation around the object to obtain random negative samples to expand the amount of samples and then to improve the training effect of CSK filter model. This proposed method clinched the matter of sample redundancy result in the original sparse sampling and achieves accurate and stable real-time tracking.

The objective function of the traditional CF method is written specifically in the form as follows:

$$\min_w \|A_0 w - y\|_2^2 + \lambda_1 \|w\|_2^2, \quad (1)$$

where  $w$  represents the filter,  $A_0$  is the cyclic matrix obtained after the cyclic sampling of the initial sample  $a_0$ ,  $y$  is the ideal Gaussian response and the vectorized regression object for the image, and  $\lambda_1$  is the regularization coefficient. The regular term in equation (1) is used to penalize over-deformed samples after cyclic sampling and prevent the filter from learning overfitting.

We optimize the above objective function with a closed solution, which is the global optimal filter coefficient. The specific calculation formula is as follows:

$$\hat{w} = \frac{\hat{a}_0^* \odot \hat{y}}{\hat{a}_0^* \odot \hat{a}_0 + \lambda_1}, \quad (2)$$

where  $\hat{a}_0$ ,  $\hat{w}$ ,  $\hat{y}$  are the Fourier transform results of initial sample  $a_0$ , filter  $w$ , and regression object  $y$ , respectively. \*

represents the conjugate operation and  $\odot$  denotes the dot product operation of vector.

**2.2. The Spatial Regularization CF Method.** To solve the boundary effect problem of traditional correlation filtering methods caused by cyclic sampling, Danelljan et al. proposed spatially regularized correlation filter (SRDCF) [18]. The method imposes spatial regularization constraints on the negative Gaussian shape distribution on the filter template, punishing the background region away from the object, thus reducing the boundary region filter response value and making the filter focus on the object central region. SRDCF can effectively improve the proportion of real object samples and better reduce the boundary effect. The objective function of the spatial regularized filter is exactly as follows:

$$\min_w \sum_{i=1}^k \left\| \sum_{l=1}^d x_i * w^l - y \right\|_2^2 + \lambda_1 \sum_{l=1}^d \left\| \omega \odot w^l \right\|_2^2, \quad (3)$$

where  $X = (x_1, x_2, \dots, x_k)$  is the image sample data,  $w$  is the filter template, the upper corner mark  $l$  represents the spatial feature channel, and  $\omega$  is the spatial regular penalty matrix with a negative Gaussian shape distribution, which is used to adjust the regular parameters of the object sample and the boundary sample. By penalizing the boundary samples, the filter pays more attention to the objective information.

It should be emphasized that the addition of the spatial regularization term destroys the closed solution structure of the relevant filtering framework, and equation (3) usually adopts the Gaussian–Sidel optimization filter solution using the iteration method, which greatly affects the tracking speed. Furthermore, the SRDCF uses a fixed space weight matrix, and the constraint term cannot be adaptively updated with the object, which affects the robustness of the filter model.

**2.3. The Background-Aware CF Method.** To solve the boundary effect problem inherent in traditional methods and reduce the large time consumption of the spatial regularization object tracking algorithm, Mueller et al. proposed the context-aware correlation filter (CACF) to increase the constraint on context background information based on the CF framework [20]. The CACF takes the object as a positive sample and the context background block as a negative sample, which are used together for filter training to improve the number and quality of the samples. The objective function of the proposed method can be specifically expressed as follows:

$$\min_w \left( \left\| A_0 w - y \right\|_2^2 + \lambda_1 \left\| w \right\|_2^2 + \lambda_2 \sum_{i=1}^k \left\| A_i w \right\|_2^2 \right), \quad (4)$$

where  $A_i$  ( $A_i \in R^{n \times n}$ ,  $w \in R^{n \times n}$ ) is the cycle matrix of the background information  $a_i$  of the object sample.  $\lambda_2$  is the regularization coefficient, and the response strength of the filter to the object and the background information is adjusted to ensure that the response value of the object area of the sample is much higher than that of the background area; the penalty for the context information is realized.

Contextual background information can assist in filter training, substantially improving the tracking effect. The CACF only collects the context information of the objective neighborhood, ignores the spatial constraints on the filter, and does not consider the object boundary samples, affecting the accuracy of the filter model tracking.

### 3. Proposed Method

This section first describes the BSCF tracking model, focusing on filter model construction. Then, the sampling strategy of the adaptive background perception is expounded, and the model optimization solution process is introduced in detail. Finally, the specific implementation steps of the tracking algorithm are given.

**3.1. BSCF Model.** To improve the spatial adaptive learnability of the filter and enhance the model robustness against the complex background, we propose the BSCF model. The specific objective functions are as follows:

$$\min_w \left\| A_0 w - y \right\|_2^2 + \lambda_1 \sum_{k=1}^n \left\| M_k w \right\|_2^2 + \lambda_2 \left\| w \right\|_2^2 + \lambda_3 \left\| w - w^r \right\|_2^2, \quad (5)$$

where  $\lambda_3$  represents the regularization parameter and  $M_k$  is the circular matrix of the maximum background response samples.  $w^r$  represents the filter spatial reference template initialized to a Gaussian shape distribution. The template  $w^r$  changes with the object movement, allowing the filter to learn more accurate spatial weights.  $\lambda_1 \sum_{k=1}^n \left\| M_k w \right\|_2^2$  is an adaptive background sensing term, which collects negative samples of background interference information around the object and adds them to filter model training. To upgrade the filter's capability to distinguish the object from the background information,  $\lambda_3 \left\| w - w^r \right\|_2^2$  is a spatial dynamic constraint term. It introduces the filter space prior information as a predefined space template and dynamically updates the filter according to the change in the predefined space template, improving its robustness. Figure 1 illustrates the BSCF model framework.

Specifically, the proposed BSCF filter adopts an adaptive background-aware sampling strategy to obtain background sample information around the object, and the information is sampled from regions with higher filter response values around the object. We denote the response calculation result of objective sample and the filter in the current frame as matrix  $R$ , and the local maximum in the response result graph is  $R_l$ . Then, the latter  $R_l$  is able to be calculated by the formula as follows:

$$R_l = \text{imregionalmax}(R) (l = 1, 2, 3, \dots), \quad (6)$$

The background-aware negative sample  $M_k$  is taken from the three sublargest values  $R_1, R_2,$  and  $R_3$  in  $R_l$  are next to the maximum response value of the object center. Figure 2 shows the schematic diagram of background sampling. If these background negative samples next to the objective filter response value are not distinguished, they are easily

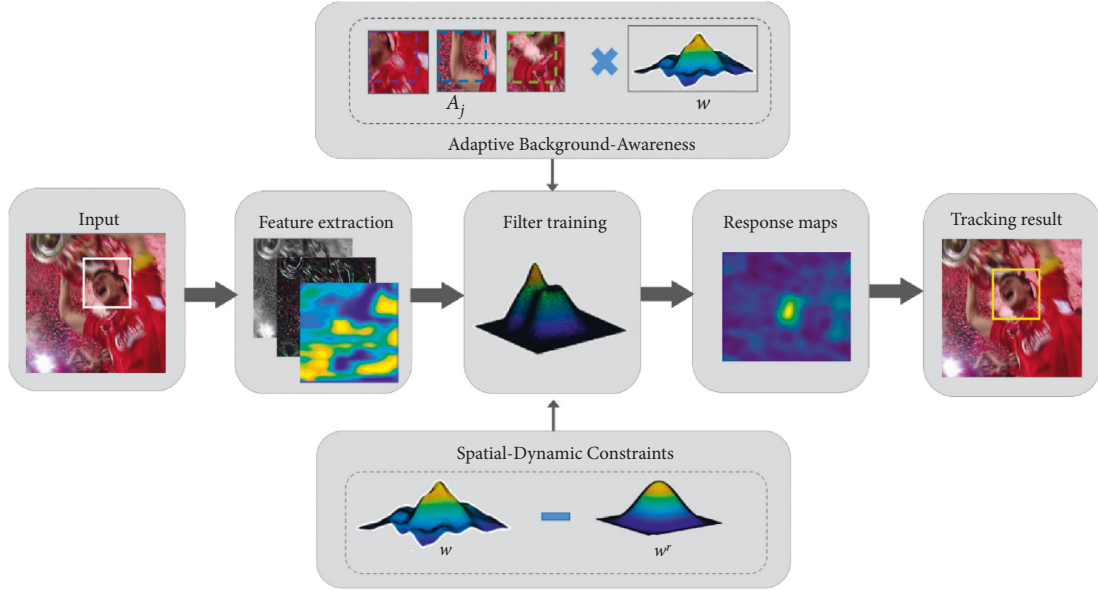


FIGURE 1: The tracking framework diagram of our BSCF model.

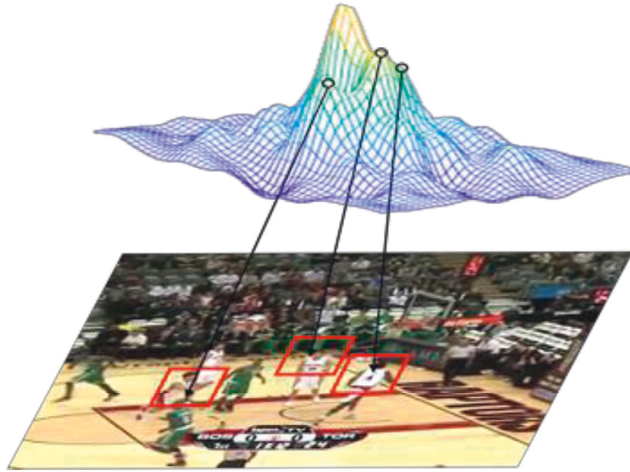


FIGURE 2: The adaptive background-sensing sampling strategy for the proposed BSCF model.

regarded as objective samples by the filter. As a result, object samples  $A_i$  and background-aware samples  $M_k$  are distinguished by adaptive weighted strategies, which are then used for filter training.

In contrast to traditional filters, the proposed BSCF introduces background sample information into the filter training process. The comparison with the traditional filter training results is shown in Figure 3.

**3.2. Optimization.** The proposed BSCF model objective function is a convex function with a globally optimal closed solution. The filter wants the response value to be high at the object sample and near zero at the remaining background samples. As a result, the object sample cycle matrix  $A_0$  and the background-aware sample cycle matrix  $M_k$  in equation (5) can be merged into a cycle matrix  $H$  to represent the sample characteristics. At the same time, the response matrix

$y$  in equation (5) is converted into  $\bar{y}$ . To maintain the corresponding constraints of the filter on the object and background samples, the object samples are made close to the ideal regression object  $y$ , and the background negative samples are close to 0. Accordingly, equation (5) is rewritten as follows:

$$f_p(w, H) = \|Hw - \bar{y}\|_2^2 + \lambda_2 \|w\|_2^2 + \lambda_3 \|w - w^r\|_2^2, \quad (7)$$

where  $H = [A_0, \sqrt{\lambda_1} M_1, \dots, \sqrt{\lambda_1} M_n]^T$  and  $\bar{y} = [y, 0, \dots, 0]^T$ . By setting the partial derivative of  $w$  in equation (7) to 0, the closed solution of the filter is obtained:

$$w = (H^T H + \lambda_1 I)^{-1} \cdot (H^T \bar{y} - \lambda_3 w^r), \quad (8)$$

where  $H^T$  is the transpose of matrix  $H$ . Given that the circulant matrix is able to express as the diagonalized form of



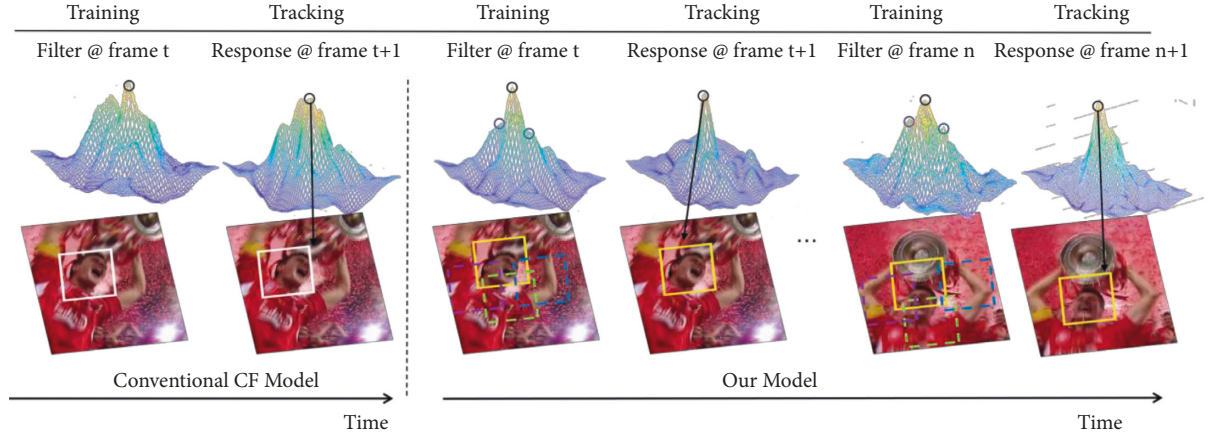


FIGURE 3: The proposed BSCF visualization comparison with traditional CF trackers.

the Fourier transform matrix. Therefore, the circulant matrices  $H$  and  $H^T$  in equation (8) are expressed as follows:

$$\begin{aligned} H &= F \text{diag}(\hat{h}) F^H, \\ H^T &= F \text{diag}(\hat{h}^*) F^H, \end{aligned} \quad (9)$$

where  $h = (h_1, h_2, \dots, h_n)$  denotes the group of row vectors that constitute the circulant matrix.  $F$  expresses the Fourier transform matrix.  $\hat{h}$  means the Fourier transform of  $h$ .  $h^*$  indicates the conjugate vector of  $h$ .  $F^H$  is the conjugate matrix of  $F$ . According to equation (9), equation (8) can be simplified as follows:

$$w = \left[ F \text{diag} \left( \hat{h}_0 \odot \hat{h}_0^* + \lambda_1 \sum_{k=1}^n \hat{h}_k \odot \hat{h}_k^* + \lambda_2 \right) F^H \right]^{-1} \left[ F \text{diag}(\hat{h}_0^*) F^H \hat{y} - \lambda_3 w^r \right], \quad (10)$$

where  $I$  is a cyclic identity matrix whose Fourier transform result is expressed as a real number 0.

According to the characteristic that the simplification of the cyclic inverse matrix is equivalent to the inversion of its eigenvalues, equation (10) is further rewritten as follows:

$$w = \left[ F \text{diag} \left( \frac{1}{\hat{h}_0^* \odot \hat{h}_0 + \lambda_1 \sum_{k=1}^n \hat{h}_k^* \odot \hat{h}_k + \lambda_2} \right) F^H \right] \left[ F \text{diag}(\hat{h}_0^*) F^H \hat{y} - \lambda_3 w^r \right]. \quad (11)$$

According to the diagonalization property of the circulant matrix,  $F \text{diag}(\hat{x}) F^H = G[F^{-1}(x)]$ . For the digestion

and simplification of equation (11), we can obtain the formula as follows:

$$w = G \left[ F^{-1} \left( \frac{\hat{h}_0^*}{\hat{h}_0^* \odot \hat{h}_0 + \lambda_1 \sum_{k=1}^n \hat{h}_k^* \odot \hat{h}_k + \lambda_2} \right) \right] \hat{y} - G \left[ F^{-1} \left( \frac{1}{\hat{h}_0^* \odot \hat{h}_0 + \lambda_1 \sum_{i=1}^n \hat{h}_k^* \odot \hat{h}_k + \lambda_2} \right) \right] \lambda_3 w^r. \quad (12)$$

Furthermore, according to the circular matrix convolution theorem, we obtain the optimal solution of the filter  $\hat{w}$  by converting equation (12) into the Fourier domain, specifically as follows:

$$\hat{w} = \frac{\hat{h}_0^* \odot \hat{y} - \lambda_3 \hat{w}^r}{\hat{h}_0^* \odot \hat{h}_0 + \lambda_1 \sum_{k=1}^n \hat{h}_k^* \odot \hat{h}_k + \lambda_2}. \quad (13)$$

The specific implementation steps of BSCF tracker are demonstrated, as shown in Algorithm 1.

## 4. Experiments

**4.1. Evaluation Data and Settings.** To verify the effectiveness and the feasibility of the proposed BSCF, we evaluate it with state-of-the-art methods on three standard tracking

benchmarks, that is, OTB100 [23], VOT2018 [24], and TrackingNet [25]. The proposed BSCF tracker is implemented in MATLAB 2017b. Intel I9-9900X4.50 GHz processor is used for filter training and testing, and an NVIDIA GTX 2080ti GPU is used for acceleration. We set the regularization parameter factor  $\lambda_1 = 1$ ,  $\lambda_2 = 0.0001$ , and  $\lambda_3 = 10$  and use the standard filter update rule with learning rate  $Y = 0.015$ . The search box size is set to padding = 4. All parameters remain fixed in all experiments below.

The specific attribute information of the benchmark datasets used in this study is as follows: the OTB100 dataset consists of 100 sequences that can comprehensively evaluate the overall performance of the method. It covers a series of sequence attributes, which represent challenging aspects in visual tracking, such as occlusion (OCC), illumination variation (IV), scale variation (SV), deformation (DEF), fast motion (FM), background clutters (BC), and motion blur (MB). The VOT2018 dataset consists of 60 sequences, which are designed to evaluate the short-term tracking performance of a single object in complex scenes. The test sequence covers the influencing factors, such as camera motion, illumination variation, scale variation, and motion variation. It is the authoritative measurement data at present. The TrackingNet dataset is the first dataset dedicated to the field of visual object tracking, where there are more than 30,000 videos, including 27 object categories. The number of videos and labels is larger than other tracking datasets. The test sequence includes a series of influencing factors, such as background interference, camera motion, fast motion, occlusion, and scale variation. The broad and diverse object audience of the TrackingNet ensures the validity of the assessment.

**4.2. Experimental Results and Analysis.** The experimental results and analysis are carried out from the following three datasets: OTB100, VOT2018, and TrackingNet.

**4.2.1. Evaluation on OTB100.** The tracker effects are compared and analyzed on the OTB100 benchmark scoring dataset, and two standard evaluation methods under the one-pass evaluation (OPE) method are used as the quantitative evaluation criteria, namely, precision plots and success plots.

The precision plots show the percentage of video frames, where the distance between the center point of the tracker's predicted object (bounding box) and the artificially labeled object (ground truth) is less than a given threshold, and the threshold is set to 20 pixels in the experiment. The calculation formula of precision is expressed as follows:

$$\text{Precision}(T, P) = \left( \sum_{i=1}^n |T_i - P_i|^2 \right)^{1/2}, \quad (14)$$

where  $i$  is the object dimension,  $T_i$  is the center point coordinate of the ground truth, and  $P_i$  is the center point coordinate of the object position predicted by the tracker.

The success plots show the percentage of successful frames in all frames, where the definition of successful

frames is that the overlap rate between the tracker's predicted object and the real object frame is greater than the set threshold, which is set to 0.5 here. The formula for calculating the success is given as follows:

$$\text{Success}(T, P) = \frac{R_T \cap R_P}{R_T \cup R_P}, \quad (15)$$

where  $R_T$  is the area of the ground truth,  $R_P$  is the area of bounding box predicted by the tracking method, and  $\cap$  and  $\cup$  respectively represent the intersection and union of two regions.

The proposed BSCF is compared with nine mainstream CF methods, including ASRCF [21], ECO [5], C-COT [4], TADT [26], DeepSRDCF [9], BACF [19], SRDCF [18], STAPLE [27], and KCF [17]. The precision and the success rate are used as the quantitative evaluation metrics for the experiments. Figures 4–6 show the experimental results.

Figure 4 illustrates the precision and the success plot results on the OTB100 dataset. Our BSCF method achieves the great performance with a relatively excellent precision accuracy of 91.4% and a finest success rate score of 69.5%. Compared with the baseline methods, SRDCF and BACF, the accuracy is improved by 15.8% and 12%, and the success rate is improved by 16.2% and 13%, respectively. Compared with the similar improved method, ASRCF, the proposed BSCF has improved in terms of success rate. Overall, the proposed BSCF method has comparable performance compared with the existing outstanding tracker, the ASRCF.

Furthermore, to estimate the tracking results of BSCF on different visual scenes, we evaluate the proposed BSCF trackers using 8 attributes and report their success plots on OTB100 benchmark, as shown in Figure 5. These scene attributes include scale variation (SV), background clutters (BC), illumination variation (IV), deformation (DEF), motion blur (MB), fast motion (FM), in-plane rotation (IPR), and out-of-plane rotation (OPR). The results show that our BSCF tracker achieves the highest success rate. The proposed BSCF can better handle these challenges, especially for scale variation and background clutters.

Combined with Figures 4 and 5, the BSCF exhibits excellent tracking performance in the experimental results. This proves that on the basis of the traditional CF method, adding adaptive background perception terms and spatial dynamic constraints, the tracker can learn more sample information and conduct training to ensure that for complex scenes and scene scale variation, the background information is not affected. Capture is more sensitive, greatly improving the quantity and quality of object samples. Therefore, the success rate and accuracy of the proposed BSCF have been improved, and it has excellent performance results for different complex scenes, does not involve deep features, and only uses traditional handcrafted features.

Figure 6 demonstrates the visualization performance of the trackers on different scene sequences of OTB100 dataset. We select four challenging video sequences for qualitative analysis of specific scenes with scene scale variation, background clutters, motion blur, and fast motion.

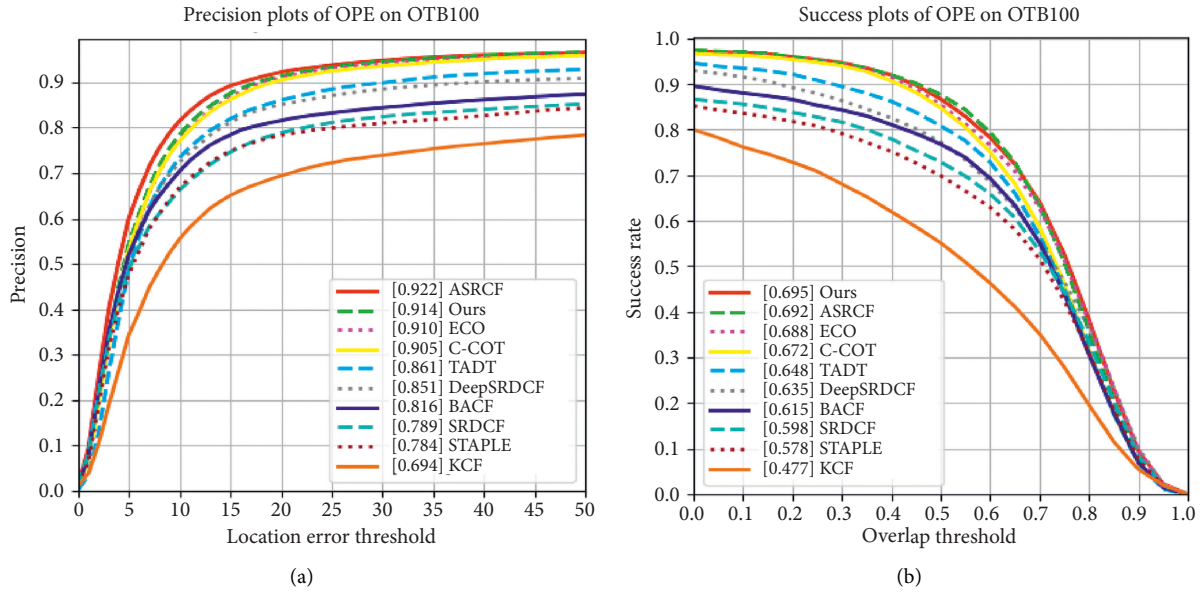


FIGURE 4: The experimental results on OTB100. This figure shows the precision and the success plots compare the proposed BSCF with other state-of-the-art trackers in terms of the OPE protocol.

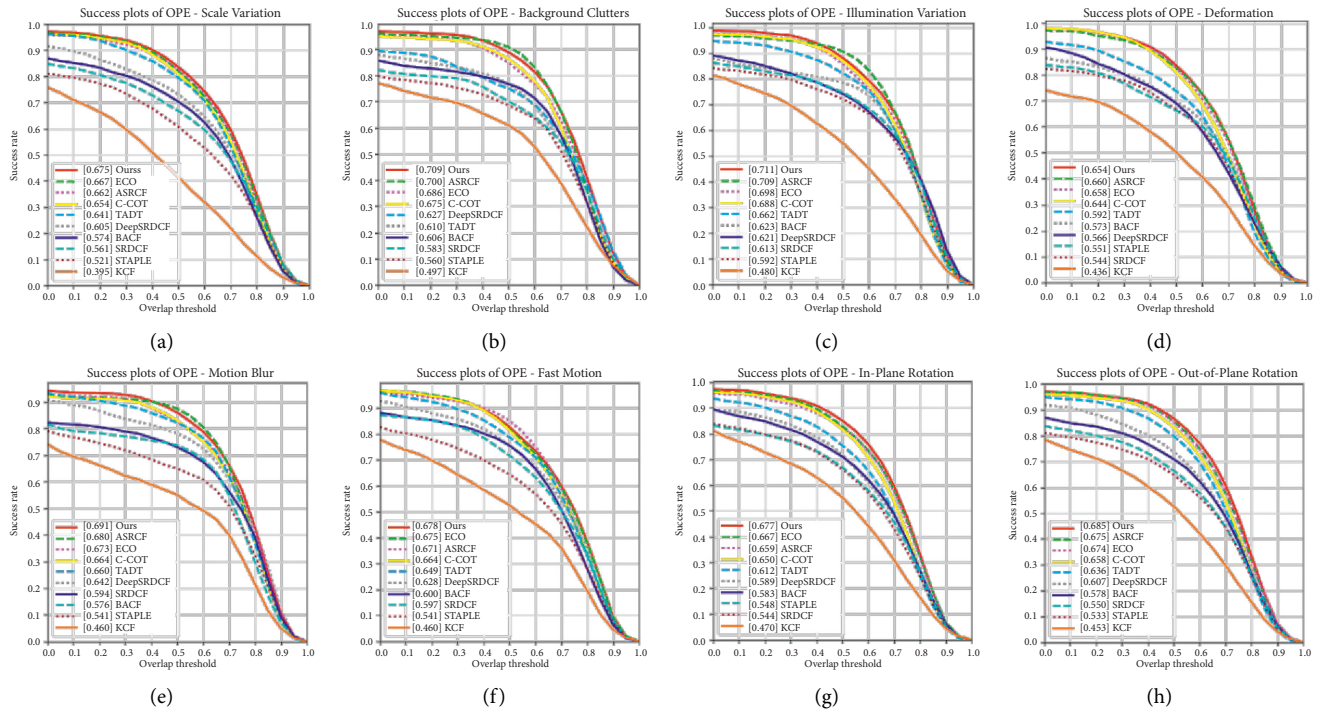


FIGURE 5: The performance of our BSCF and other state-of-the-art methods is evaluated on the OTB100 benchmark according to 8 challenging attributes. The reported attributes include (a) scale variation, (b) background clutters, (c) illumination variation, (d) deformation, (e) motion blur, (f) fast motion, (g) in-plane rotation, and (h) out-of-plane rotation.

In the Bird1 and Couple video sequences, most tracking methods are able to achieve stable tracking when the object does not undergo scene scale variation and deformation. During the strong scene variation from 186th to the 368th frame of the Bird1 sequence, all comparison methods deviated to different degrees. BACF, ECO, and C-COT methods even lost the object at the beginning, which greatly affected

the subsequent real-time tracking performance of the tracker, while the proposed BSCF maintained good tracking performance. In the Couple sequence, the proposed BSCF is still able to maintain high tracking accuracy along with the substantial variation of pedestrian movement scenes.

We add the attribute challenges of fast motion, motion blur, and occlusion to the sequence with scale variation and



FIGURE 6: Illustration of qualitative experimental results on challenging sequences including Bird1, Couple, DragonBaby, and Matrix. The color bounding boxes are the corresponding results of our BSCF tracker, SRDCF, C-COT, BACF, ECO, ASRCF, and KCF, respectively.

deformation. The performance of each tracking method is shown in Figures 5(c) and 5(d). We employ the DragonBaby and Matrix videos sequence as examples. When fast motion and motion blur occur in frame 42 of the DragonBaby sequence, the object is lost except for ECO, KCF, and the proposed BSCF. Until the 83rd to the 107th frame, when the object has fast motion and scale variation, the ECO and the BSCF achieve stable tracking throughout the process, while the C-COT and the KCF methods cannot be adaptive to the variation of the object appearance. In the Matrix sequence, when the scene changes in frame 78, the object moves rapidly, and even the appearance of the object changes; only the proposed BSCF method is able to accurately focus on the object. Even though the 82nd frame motion blur is more serious, other methods are more likely to lose track and drift or maintain a short return after deviation, and the BSCF can always maintain the sensitivity of capturing the object.

The BSCF has better adaptability to the scale variation of the object scene and the other background information variation due to variation in motion conditions.

**4.2.2. Evaluation on VOT2018.** The evaluation metrics of the VOT2018 benchmark scoring dataset adopt the expected average overlap (EAO), robustness (R), and accuracy (A). The EAO is obtained by calculating the average of the overlap of the predicted box and the actual object box per frame and then dividing it by the number of videos for that frame. The bigger the EAO value is, the more excellent the tracking performance. Robustness evaluates the stability of the tracker tracking the objective. It is measured by the number of times the tracking method has missed the object. The bigger the robustness value is, the less excellent the

tracker stability. The accuracy is measured by the intersection ratio between the predicted box and the real object box. The larger the accuracy value is, the more excellent the tracking effect.

Table 1 lists the evaluation results of the proposed BSCF and other 10 mainstream tracking methods on VOT2018. The specific methods include ATOM [28], BACF[19], C-COT [4], ECO [5], KCF[17], MDNet [6], SiamRPN++ [29], SRDCF [18], STAPLE [27], and STRCF [30].

Our BSCF achieves optimal results in terms of accuracy, outperforming other algorithms, including the CF-based and DL-based algorithms. The proposed BSCF scores 0.397 in the EAO indicator, which surpasses the mainstream methods of the CF-based in general, and is second only to the DL SiamRPN++ and ATOM tracking methods. In terms of robustness, the proposed BSCF is second only to the first place, with a score of 0.03. It basically achieves robust tracking. Compared with the traditional CF tracking methods, the proposed BSCF enhances the robustness of the tracker, while ensuring the accuracy and algorithm stability. It achieves an effective improvement of the CF-based methods.

**4.2.3. Evaluation on TrackingNet.** The TrackingNet benchmark dataset uses success, precision, and normalized precision as evaluation metrics. The two former evaluation indicators are consistent with the definition standards of the OTB100 dataset, and the normalized accuracy can better avoid the influence of the image scale and the object frame size on accuracy measurement. Table 2 lists the comparison of the experimental results between BSCF and 9 top-performing trackers on TrackingNet. These specific methods are

**Input:** Image sample  $x_i$ , filter model  $w$ , filter spatial reference template  $w^r$ , object box position and scale information.

**Output:** The scale and the position information of the target in each frame, the updated filter model  $\hat{w}$ , and the updated appearance model.

(1) **initialization:**

The filter space reference template  $w^r$  as a Gaussian shape distribution.

(2) : **repeat**

(3) : Extract the image sample  $x_i$  of the frame  $i$  to form a sample matrix  $A_i$ ;

(4) : Extract the background information samples  $\max_{R_l} (l = 1, 2, 3)$  by using equation (6);

(5) : The background information samples form a matrix  $M_k (k \in [1, n])$ ;

(6) : Solve the filter model  $w$  of the current frame according to equation (5);

(7) : Obtain the model peak response of the filter  $w$  representing the object location;

(8) : Obtain the position and scale information of the tracking object;

(9) : According to equation (13), the filter model parameter  $\hat{w}$  is obtained;

(10) : Update filter model  $w$  and filter space template  $w^r$ .

(11) : **end**

(12) : **until** End of the video sequence of frame  $n$ ;

ALGORITHM 1: BSCF Tracker.

TABLE 1: Evaluation of 11 advanced trackers on VOT2018 by the means of EAO, robustness, and accuracy. The top three results are shown in red, blue, and green, respectively.

	EAO	R	A
ATOM [28]	0.401	0.204	0.590
BACF [19]	0.169	0.674	0.511
C-COT [4]	0.267	0.494	0.318
ECO [5]	0.280	0.276	0.483
KCF [17]	0.295	1.35	0.54
MDNet [6]	0.383	1.12	0.55
SiamRPN++ [29]	0.414	0.234	0.600
SRDCF [18]	0.308	0.74	0.42
STAPLE [27]	0.179	0.665	0.524
STRCF [30]	0.152	0.679	0.483
Ours	0.398	0.211	0.623

TABLE 2: Evaluation of 11 advanced trackers on TrackingNet by the means of success, precision, and normalized precision. The top three results are shown in red, blue, and green, respectively.

	Success	Precision	Normalized precision
ATOM [28]	0.703	0.648	0.771
BACF [19]	0.523	0.461	0.580
DiMP [31]	0.723	0.633	0.785
ECO [5]	0.554	0.492	0.618
KCF [17]	0.447	0.419	0.546
MAML [32]	0.757	0.672	0.822
SRDCF [18]	0.521	0.455	0.573
SiamRPN++ [29]	0.733	0.694	0.800
STAPLECA [20]	0.529	0.468	0.605
Ours	0.752	0.667	0.831

ATOM [28], BACF [19], DiMP [31], ECO [5], KCF [17], MAML [32], SRDCF [18], SiamRPN++ [29], and STAPLECA [20].

Compared with the CF method, the proposed BSCF shows a significant gain on TrackingNet. Compared with the tracking method using the deep network as the backbone network, the performance of the BSCF tracker proposed in this study still has room for improvement. Although the

proposed BSCF is on par with SiamRPN++, DiMP, and ATOM, there is still a certain gap with the MAML.

## 5. Conclusion

In this work, we develop an adaptive background-aware and spatially dynamically constrained CF tracking model. Adaptive background-aware constraints and dynamic space constraints are introduced into the framework of the original tracking model to screen negative samples of background information around the object. This avoids the problem of filter degradation due to dynamic changes in the object. Thus, the background awareness and the interference discriminability of the tracker are effectively improved. This method is applied to object tracking on three challenging aerial object tracking benchmarks. Compared with the current mainstream CF-based and DL-based trackers, we exhibit the competitive performance of our BSCF method. The accuracy and success rate are greatly improved under eight tracking challenges, including scale variation, background clutters, illumination variation, and motion blur. The proposed BSCF can better meet the object tracking requirements of complex scenes and achieve efficient tracking.

## Data Availability

The data used to support the findings of this study are available from the author upon request. For details, please contact via e-mail: 20201220013@nuist.edu.cn.

## Conflicts of Interest

The authors declare that they have no conflicts of interest.

## Acknowledgments

This research was supported in part by Zhejiang Provincial Science and Technology Program in China under grant no. 2022C01083, in part by the Natural Science Foundation of

Jiangsu Province under grant no. BK20211539, in part by the National Natural Science Foundation of China under grant nos. U20B2065, 61972206, 62011540407, and J2124006, in part by the 15th Six Talent Peaks Project in Jiangsu Province under grant no. RJFW-015, in part by the Qing Lan Project, and in part by the PAPD Fund.

## References

- [1] C. Fu, J. Ye, J. Xu, and Y. F. He, "Disruptor-aware interval-based response inconsistency for correlation filters in real-time aerial tracking," *IEEE Transactions on Geoscience and Remote Sensing*, vol. 59, no. 8, pp. 6301–6313, 2021.
- [2] L. Jiao, D. Wang, Y. Bai, and P. F. Chen, "Deep learning in visual tracking: a review," *IEEE Transactions on Neural Networks and Learning Systems*, pp. 1–20, 2021.
- [3] S. Du and S. Wang, "An overview of correlation-filter-based object tracking," *IEEE Transactions on Computational Social Systems*, vol. 9, 2021.
- [4] M. Danelljan, A. Robinson, and F. Shahbaz Khan, "Beyond correlation filters: learning continuous convolution operators for visual tracking," in *Proceedings of the Computer Vision - ECCV 2016, European conference on computer vision*, pp. 472–488, Amsterdam, the Netherlands, September 2016.
- [5] M. Danelljan, G. Bhat, F. S. Khan, and M. Felsberg, "Eco: efficient convolution operators for tracking," in *Proceedings of the 2017 IEEE Conference on Computer Vision and Pattern Recognition (CVPR)*, pp. 6638–6646, Honolulu, HI, USA, July 2017.
- [6] Z. Zhang, Y. Xie, F. Xing, and M. L. McGough, "Mdnnet: a semantically and visually interpretable medical image diagnosis network," in *Proceedings of the 2017 IEEE Conference on Computer Vision and Pattern Recognition (CVPR)*, pp. 6428–6436, Honolulu, HI, USA, July 2017.
- [7] Y. Song, C. Ma, L. Gong, J. Zhang, R. Lau, and M.-H. Yang, "Crest: convolutional residual learning for visual tracking," in *Proceedings of the 2017 IEEE International Conference on Computer Vision (ICCV)*, pp. 2555–2564, Venice, Italy, October 2017.
- [8] E. Gundogdu and A. A. Alatan, "Good features to correlate for visual tracking," *IEEE Transactions on Image Processing*, vol. 27, no. 5, pp. 2526–2540, 2018.
- [9] M. Danelljan, G. Hager, F. S. Khan, and M. Felsberg, "Convolutional features for correlation filter based visual tracking," in *Proceedings of the 2015 IEEE International Conference on Computer Vision Workshop (ICCVW)*, pp. 58–66, Santiago, Chile, December 2015.
- [10] D. Sun, S. Roth, and M. J. Black, "Secrets of optical flow estimation and their principles," in *Proceedings of the 2010 IEEE Computer Society Conference on Computer Vision and Pattern Recognition*, pp. 2432–2439, Francisco, CA, USA, June 2010.
- [11] L. Li Xu, J. Jiaya Jia, and Y. Matsushita, "Motion detail preserving optical flow estimation," *IEEE Transactions on Pattern Analysis and Machine Intelligence*, vol. 34, no. 9, pp. 1744–1757, 2012.
- [12] Y. T. Chan, A. G. C. Hu, and J. B. Plant, "A Kalman filter based tracking scheme with input estimation," *IEEE Transactions on Aerospace and Electronic Systems*, vol. AES-15, no. 2, pp. 237–244, 1979.
- [13] D. Comaniciu, V. Ramesh, and P. Meer, "Real-time tracking of non-rigid objects using mean shift," *proceedings IEEE conference on computer vision and pattern recognition, CVPR 2000 (Cat. No. PR00662)*, vol. 2, pp. 142–149, 2000.
- [14] C. Cheng Chang and R. Ansari, "Kernel particle filter for visual tracking," *IEEE Signal Processing Letters*, vol. 12, no. 3, pp. 242–245, 2005.
- [15] D. S. Bolme, J. R. Beveridge, B. A. Draper, and Y. M. Lui, "Visual object tracking using adaptive correlation filters," in *Proceedings of the 2010 IEEE Computer Society Conference on Computer Vision and Pattern Recognition*, pp. 2544–2550, Francisco, CA, USA, June 2010.
- [16] J. F. Henriques, R. Caseiro, P. Martins, and J. Batista, "Exploiting the Circulant Structure of Tracking-By-Detection with Kernels," *Computer Vision - ECCV 2012*, vol. 7575, pp. 702–715, 2012.
- [17] J. F. Henriques, R. Caseiro, P. Martins, and J. Batista, "High-speed tracking with kernelized correlation filters," *IEEE Transactions on Pattern Analysis and Machine Intelligence*, vol. 37, no. 3, pp. 583–596, 2015.
- [18] M. Danelljan, G. Hager, F. S. Khan, and M. Felsberg, "Learning spatially regularized correlation filters for visual tracking," in *Proceedings of the 2015 IEEE International Conference on Computer Vision (ICCV)*, pp. 4310–4318, Santiago, Chile, December 2015.
- [19] H. K. Galoogahi, A. Fagg, and S. Lucey, "Learning background-aware correlation filters for visual tracking," in *Proceedings of the 2017 IEEE International Conference on Computer Vision (ICCV)*, pp. 1135–1143, Venice, Italy, October 2017.
- [20] M. Mueller, N. Smith, and B. Ghanem, "Context-aware correlation filter tracking," in *Proceedings of the IEEE Conference on Computer Vision and Pattern Recognition*, pp. 1396–1404, Honolulu, HI, USA, July 2017.
- [21] K. Dai, D. Wang, H. Lu, and C. J. Sun, "Visual tracking via adaptive spatially-regularized correlation filters," in *Proceedings of the 2019 IEEE/CVF Conference on Computer Vision and Pattern Recognition (CVPR)*, pp. 4670–4679, Beach, CA, USA, June 2019.
- [22] H. K. Galoogahi, T. Sim, and S. Lucey, "Correlation filters with limited boundaries," in *Proceedings of the 2015 IEEE Conference on Computer Vision and Pattern Recognition*, pp. 4630–4638, Boston, MA, USA, June 2015.
- [23] Y. Wu, J. Lim, and M. H. Yang, "Online Object Tracking: A Benchmark," in *Proceedings of the IEEE Conference on Computer Vision and Pattern Recognition*, pp. 2411–2418, Portland, OR, USA, June 2013.
- [24] M. Kristan, A. Leonardis, J. Matas et al., "The sixth visual object tracking vot2018 challenge results," in *Proceedings of the European Conference on Computer Vision (ECCV) Workshops, 11129*, Munich, Germany, September 2018.
- [25] M. Müller, A. Bibi, S. Giancola, and S. B. Alsubaihi, "Trackingnet: a large-scale dataset and benchmark for object tracking in the wild," in *Proceedings of the Computer Vision - ECCV 2018, 11205*, pp. 310–327, Munich, Germany, September 2018.
- [26] X. Li, C. Ma, B. Wu, Z. He, and M.-H. Yang, "Target-aware deep tracking," in *Proceedings of the 2019 IEEE/CVF Conference on Computer Vision and Pattern Recognition (CVPR)*, pp. 1369–1378, Long Beach, CA, USA, June 2019.
- [27] L. Bertinetto, J. Valmadre, S. Golodetz, O. Miksik, and H. S. T. Philip, "Staple: complementary learners for real-time tracking," in *Proceedings of the IEEE Conference on Computer Vision and Pattern Recognition*, pp. 1401–1409, Las Vegas, NV, USA, June 2016.
- [28] M. Danelljan, G. Bhat, F. S. Khan, and M. Felsberg, "Atom: accurate tracking by overlap maximization," in *Proceedings of the 2019 IEEE/CVF Conference on Computer Vision and*

- Pattern Recognition (CVPR)*, pp. 4660–4669, Long Beach, CA, USA, June 2019.
- [29] B. Li, W. Wu, Q. Wang, and F. J. J. Zhang, “Siamrpn++: evolution of siamese visual tracking with very deep networks,” in *Proceedings of the 2019 IEEE/CVF Conference on Computer Vision and Pattern Recognition (CVPR)*, pp. 4282–4291, Long Beach, CA, USA, June 2019.
- [30] F. Li, C. Tian, W. Zuo, and L. M.-H. Zhang, “Learning spatial-temporal regularized correlation filters for visual tracking,” in *Proceedings of the 2018 IEEE/CVF Conference on Computer Vision and Pattern Recognition*, pp. 4904–4913, Salt Lake City, UT, USA, June 2018.
- [31] G. Bhat, M. Danelljan, L. V. Gool, and T Radu, “Learning discriminative model prediction for tracking,” in *Proceedings of the IEEE/CVF Conference on Computer Vision and Pattern Recognition*, pp. 6181–6190, Seoul, Korea (South), October 2019.
- [32] G. Wang, C. Luo, X. Sun, Z Xiong, and W Zeng, “Tracking by instance detection: a meta-learning approach,” in *Proceedings of the IEEE/CVF Conference on Computer Vision and Pattern Recognition*, pp. 6288–6297, Seattle, WA, USA, June 2020.

## Research Article

# A Comparative Study on Detection of Malware and Benign on the Internet Using Machine Learning Classifiers

J. Pavithra  and S. Selvakumara Samy 

*Department of Computational Intelligence, SRM Institute of Science and Technology, Kattankulathur, India*

Correspondence should be addressed to S. Selvakumara Samy; [kumaraselva67@gmail.com](mailto:kumaraselva67@gmail.com)

Received 28 April 2022; Revised 27 May 2022; Accepted 2 June 2022; Published 27 June 2022

Academic Editor: Punit Gupta

Copyright © 2022 J. Pavithra and S. Selvakumara Samy. This is an open access article distributed under the Creative Commons Attribution License, which permits unrestricted use, distribution, and reproduction in any medium, provided the original work is properly cited.

The exponential growth in network usage has opened the way for people who use the Internet to be exploited. A phishing attack is the most effective way to obtain sensitive information about a target individual without their knowledge over the Internet. Phishing detection has an increased false-positive rate and is inaccurate. The motivation behind the research is to analyze and classify the applications among malware or benign with less time complexity. The main purpose is to find the algorithm which provides better accuracy for detecting the adware. The comparative analysis was made with three machine learning classifiers to find a better one. Random forest, SVM, and naïve Bayes were selected because of the better results obtained in previous research papers. Using a confusion matrix, the classifier methods were evaluated for accuracy, precision, recall, and F-measure with positive rates of both true and false. This research indicates that there are a number of classifiers that, if accurately detected, offer better reliable phishing detection outcomes. Random forest has proven to be an effective classifier with 0.9947 accuracy and a 0.017 false-positive rate. In this study, the comparative analysis reveals that the best ML classifiers have a lesser prediction accuracy for spoofing threat identification, implying that nonphishing programmers can use the best ML classifiers to evaluate the attributes of spoofing threat recognition and classification.

## 1. Introduction

Advertising is used to advertise, promote, and sell a product, a service. Marketing strategies have quickly moved to digital advertising as the Internet and recently developed Smartphones have grown in popularity, and this trend shows no indications of retarding. When you visit a website or use a mobile application, you will see digital advertisements [1, 2]. However, a wide spectrum of fraudulent activity has an impact on the process of placing advertisements on mobile networks and the Internet. Adware is software which extends above and beyond the appropriate marketing used within freeware as well as shareware. Adware is often distinct software launched at the same time as shareware or perhaps another equivalent application [2]. Even if the user does not run the apparently needed software, the adware will usually assist to enhance marketing [3]. With a greater

portion of the global market share, Android has become the most popular mobile operating system. And over a billion Android smartphones have been purchased of which Google Play alone estimates 65 billion app downloads. The quantity of malware exploits the security of consumer gadgets considerably in terms of the tremendous rise of smart gadgets and accessible software devices. Mobile phones are commonly applied in several areas of human existence, especially economic, commercial, societal, professional, and academic endeavours. Because of these factors, smartphones are now more valuable than merely for making calls, but also for making a sustainable economic and traditional career [4]. Smartphones can also be used to obtain appropriate web services such as online ticketing, shopping, and web-based platforms. There are various options designed for various mobile software functionalities. With the rising deployment of digital devices for bank transfers, the



sudden growth in malware attacks is becoming highly complicated, inflicting personal and financial output changes to individuals, requiring the development of efficient and reliable methods to identify this malware [5, 6]. The focus of secure communications is on methodologies for protecting devices from harmful data and programs. The following are the three security-related properties to consider while securing data:

- (i) Confidentiality: it concerns with prohibiting illegal users from accessing data stored on a device.
- (ii) Integrity: it enables online facts or data modification, i.e., data cannot be changed by intruders.
- (iii) Availability: it restricts data retention or collection. The registered user is able to access and use the software and services.

Classification approaches were used to model and analyze the actions of Android users in order to distinguish between malware and benign apps. Analysis of the active or passive characteristics of apps is used to make classification choices. The integrity of the features, such as how particular they are, has a big impact on the prediction performance of a classifier. Android-based classification technologies are far from optimal in terms of accuracy. With the isolated static characteristics, the state-of-the-art classification yields a false-negative (FN) result rate. Data- and control-flow studies are used to extract these characteristics. Programs with hybrid features have a higher FN rate. While retaining a suitable FN and FP rate, most adaptive classification techniques produce increased false-positive (FP) rates. The false-positive rate [7, 8] shows the probability of benign apps that are incorrectly labelled as malicious. The main aim of this study is to analyze the legitimate keywords, classify the malware, benign adware, and find algorithms with better accuracy.

## 2. Related Work

Classification techniques are extensively used since they have shown they can acquire from samples and then work effectively with manual input to examine a variety of adware concerns over time. Attacks against automated algorithms, on the other hand, are conceivable because an intruder can alter inputs in order to force the algorithm to get the desired result. The researchers looked into a supervised learning method for detecting Android adware based on static and complex data [1]. The manifest file was used to gather static features, while the network trace was used to collect dynamic characteristics. By addressing these parameters, each adware sample was then grouped into a specific family after being identified as adware or benign. The researchers used neural models, random forests, AdaBoost, and SVM, among other machine learning techniques. The binary detection challenge was shown to be more difficult than the multiclass adware classification problem [2].

LagoDroid [6] is a development tool that takes a malicious payload as input and a destination category as output and then changes the feature samples to classify it as adhering with the category while keeping the sample's core concepts.

Despite Google's efforts to restrict the spread of Android malware in its official store, the app store, then the problem persists.

In Android apps, dynamic and static analytics are prominent approaches for detecting harmful apps. Despite the fact that both analyzing methodologies have strengths and drawbacks, a unique fusion malware detection analysis called mad4a was presented to reveal certain undiscovered components of Android malware by combining the benefits of these two techniques (dynamic and static) [9]. Over the last few years [10], Android operating systems are becoming increasingly popular, and the platform has made a name for itself in both mobile and Internet of Things (IoT) platforms.

However, it has become the target of malicious apps, and this demand has evolved with more security difficulties [11]. MalDozer, an automated Android malware analysis and family attribution framework that depends on orders of classification using deep learning classifiers, was suggested in [12–16]. An Android malware detection system (APK Auditor) is based on permissions that employ static analysis to analyze and classify Android applications as benign or malicious. MalDozer extracts and learns the malicious and benign behaviours from the actual sample to identify malware from the raw sequence of the app's API requests, which is presented in [17]. It may be used as a detector not just on servers, but also on smartphones and Edge computing. To protect the systems and users' security and privacy, the authors in [18] built a system that might facilitate both the analysis and removal of harmful apps. This was done by looking at the different permissions requested by an app after installation. Clustering and classification algorithms are used in this investigation. The aim of the system was to identify and eliminate malware from users' Android mobile devices. Many applications hide individual activities by encrypting them and transmitting sensitive data across the network. Because of the flexibility and transparency of Android operating systems, new surface attacks are being created every day. The author addresses the detection of two malware attacks: intent-based hijacking and authenticated session hijacking. In order to detect these two virus problems, the honey pot approach was applied. Multiple apps and their connections only with honey pot were updated and tested using a virtual machine or perhaps an Internet browser to get the desired outcome. It must be believed that runtime methodologies, rather than traditional machine learning methods, can detect hijacked malware with great precision. Mobile attackers are creating a big number of harmful apps, especially for Android because it is the most widely used mobile operating system, by changing existing apps, which often results in malware being organized into families. Applications of the same family will act in a similar manner, gathering data and transferring them to a

remote server controlled by the attacker. A deep learning method can discriminate between benign and malicious Android applications. This APK analyzer is made up of three parts:

- (i) A signature database is used to hold information about applications and analysis results that have been extracted.
- (ii) An Android client for granting application analysis requests from end-users.
- (iii) A central server that oversees the whole analysis process and communicates both with the data repository and the Smartphone app.

Many applications were gathered in order to analyze, evaluate, and construct the system. The result shows that APK analyzer can locate and highlight the majority of well-known malware. Malware detection in Android was designed to prevent malicious software from being installed on the victim's device by detecting unusual boot sequences. It assists in the identification of malware designed for the Android operating system. There was a proposal for a sequence of pattern recognition procedures with the processing levels, as follows:

- (i) Analyzing
- (ii) Reviewing
- (iii) Making a decision

In the initial stage, the infected app runs in a secure and protected domain to retrieve a series of system calls. It generates the measurements required for decision-making during the analysis step. To begin, the Wilcoxon signed-rank test and the global alignment technique were used to compare the similarity of legal and malignant network call patterns and then determine whether the differences between samples and shared activity are substantial [19]. In [20], the authors established a convolution neural network-based technique that was applied to the probability of system calls using dynamic analysis. A dynamic analysis methodology, unlike existing machine learning-based malware detection identification methodologies [16], authorized user trust guarantees in malware detection that are unaffected by data bias and hold for both malware and legitimate classes independently. The output based on empirical evidence accuracy, usefulness, and objectivity is demonstrated using the curved prediction technique in combination with the random forest classifier.

A machine learning-based malware defensive model for IoT environment is presented in, which uses two different approaches in the selection of adversarial samples and by computing distance from cluster centres and probability values, the method performs classification. Towards identifying the abuse in crypto mining generated by malwares, an efficient approach is presented in [20]. The method finds a set of network flow which is relevant and able to classify a set of flow generated by crypto mining. The method works according to the network flow and finds malicious flow generated.

The Android particular intent explicit and implicit features have produced a faster and more effective outcome than the Android permission function for identifying assaults [21]. In comparison to other well-known and explored qualities such as authorization, the intent is a semantic-based feature capable of storing malware's intents. This has been used as a backdoor to access numerous transmissions in the Android framework. This interaction is frequently driven by an intent messaging object on the Android platform, which is a late runtime legally enforceable communicating object.

### 3. Methodology

There are three steps were involved to carry over the research: Dataset Preparation, Machine learning techniques are used in a variety of situations, and their performance is evaluated. In Figure 1, the architecture framework contains the preprocessed dataset and it should be loaded at first. In the feature selection, 80 features were taken for analysis. Among the 80 features, adware-related features are selected for the classification. 70% of data is taken for training and 30% is for testing. The model was run with the help of selected three machine learning classifiers. The test results will be evaluated, and a comparison will be made for analyzing a better algorithm based on higher accuracy. Then, the false-positive and true-positive rates will be calculated by a confusion matrix.

*3.1. Dataset Preparation.* The dataset collection consists of APK samples compensate the (Adware-A). In 631956 samples from the Android malware adware, the dataset employed 80 characteristics of various variable kinds. For raw analysis of data, the dataset is transformed to .csv format (a machine learning-compatible format). The dataset contains 80% samples for training and 20% samples for testing the applications, and the public raw dataset was taken for the reference to compare the results [22–24].

*3.2. Application of Algorithm.* Among several algorithms, many researchers suggested and attained higher accuracy results in these three algorithms such as random forest, naïve Bayes, and SVM were applied in this study to properly categorize the dataset, as well as a 5, 10, and 70% for splitting cross-validation. The results of extensive testing on multiple datasets, with diverse learning processes, led to the selection of 10, 5, and 70 cross-validations, However, 10-fold has shown to be the ideal amount of folds for obtaining the most accurate measurement. A specified number of folds is chosen for cross-validation, as well as the data are arbitrarily segmented into 10 parts, and each of which roughly reflects the class in the same ratio as in the entire dataset. Before being applied to the remaining set, the constructivist approach is trained on the remaining nine-tenths of each partition. As a result, the learning method is repeated ten times across different training sets. Eventually, the total percentage of the 10 error predictions was

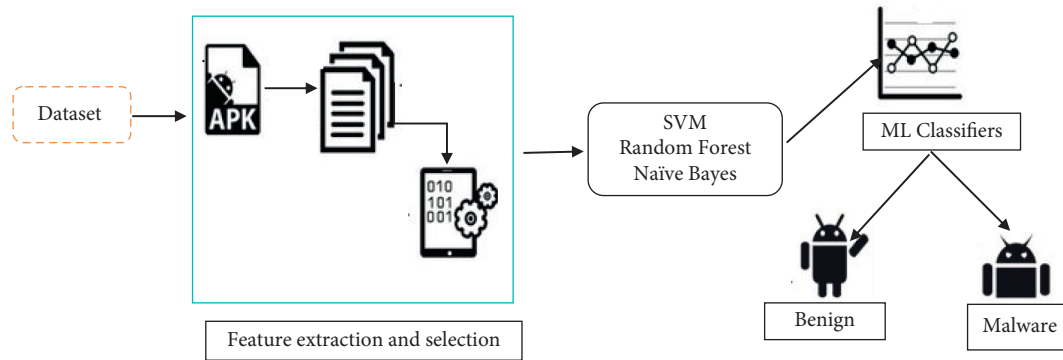


FIGURE 1: Architecture framework.

combined together to provide an overall error estimate, and the 5-fold and 2-fold error estimates were calculated in the same way. For comparison, the dataset had also been analyzed using a proportion, which allows you to test a specific percentage of the data; in this example, a 70% split was employed.

**3.3. Feature Extraction.** In order to set up an efficient Android adware categorization, it is recommended to acquire resilient and most relevant elements such as user permissions, user-specific, flow, count features and receiver's information, intent filters, process name, and files underneath analysis software. All of the above features are retrieved through reverse-engineering, which breaks down the feature APK into simple code, which is then modified and transformed back into an APK file. A simple APK disassembler is used to reverse engineer the apps.

All activities, services, broadcast receivers, and content providers are included in the app's components. Basic properties, including the name of the Kotlin or Java class, must be defined for each component. It can also declare capabilities like which device configurations it can support and intent filters that describe how the component can be launched. The name also serves as the application ID, which must be unique globally in order for your app to be published on Google Play. The build tools, however, override the package name at the conclusion of the build process by leveraging the `applicationId` field from the build Gradle file (used by Android Studio projects). This will not be an issue as long as the package name in the manifest matches the `applicationId` in the build file. If these two values differ, see how to configure the application ID to learn about the differences between "package name" and "application ID."

Features including constant strings from binaries, permissions, carriers, transmitters, intent filters, and process names were extracted from Android `manifest.xml` files by reverse-engineering the Android platform. After reverse-engineering an app, constant strings actually take the binaries of Android apps that exist in a folder. Attackers can take advantage of a device by reversing the application and altering the persistent strings [25–27]. After obtaining the

source code of an application through reverse-engineering, hackers alter constant strings, repackage the application, and submit it to play stores. Adware attackers can modify the constant string, for example, [`constant-string v1, "Rooted Device"`] and [`constant-string v1, "Device Not Rooted"`]. Then, in parallel, by altering constant strings in Android applications, they can launch several attacks. Android provides significant advantages to reverse engineer that iOS does not. Because Android is open source, you can examine its source code at the Android Open Source Project (AOSP) and update the operating system and its standard tools in any way you wish. Even on normal retail devices, activating developer mode and side loading programs can be done without jumping through too many hoops. Here, Algorithm 1, extracts the data from the input dataset and performs the PCA analysis, checks with the threshold value, and performs the ranking process based on the mean value. There are a variety of conveniences to make your life easier, from the strong tools that come with the SDK to the large range of available reverse-engineering tools.

Every Android app has a single `manifest.xml` file that requests all user permissions. Users will not be able to install the app until they accept all of the permissions that have been requested. Keywords (manifest feature) are taken from applications in addition to constant strings. As stated in Table 1, a list of keywords is produced for this purpose based on information from current malware and legitimate applications. Table 1 contains keywords gathered from malicious `manifest.xml` files of Android applications. The keywords were gathered to assist in the detection of dangerous software. In the `manifest.xml` file, each term in Table 1 has a specific function, such as "Read SMS," which reads sent and received messages from an Android phone user. In Android malicious apps, the terms Read MSG, Send MSG, Duration, and a few more listed in Table 1 were commonly used. We have extracted all the existed keywords frequently in manifest files of malicious software by analyzing harmful applications. The keyword structure is compared to genuine and malicious `manifest.xml` files once the keywords have been extracted. Here, the RRT represents the Rapidly exploring random trees, flowpkts denotes flow packets, and avgpkts denotes average packets.

- (i) Steps: Input  $\rightarrow$  Dataset (Malware and benign)
- (ii) **Output.** Feature extraction (Ranked Features)
- (iii) Extraction  $\rightarrow$  Through PCA (Mean and threshold value based on 100 features)  
 $\rightarrow$  Classes.dex  $\rightarrow$  android manifest.xml (A XML jar)  $\rightarrow$  output extraction If
- (iv) Extraction  $E =$  extracted features
- (v) Apply  $\rightarrow$  bakenal tool - .smalicious files, API functions and permissions
- (vi) THEN
- (vii) Vectorization - matrix values split together
- (viii) Feature vector  $\in$  feature extracte values  $\forall$  columns,
- (ix) Extracted features ----through vector (6features (Ranking based on threshold PCA))
- (x) Features ranked (for classification)
- (xi) END

ALGORITHM 1: Feature Extraction.

TABLE 1: Android application keyword.

List of keywords taken as features				
Permissions	Count	Section-flow	Intent-filter (action)	General specific
Read_MSG	std_fpctl	Total_fhlen	downUpRatio	bAvgBytesPerBulk
Send_MSG	std_bpctl	total_bhlen	fAvgSegmentSize	bAvgPacketsPerBulk
Duration	total_fiat	fPktsPerSecond	fHeaderBytes	bAvgBulkRate
total_f packets	Fpsh_ cnt	bPktsPerSecond	fAvgPacketsPerBulk	bAvgSegmentSize
max_fpctl	bpsh_cnt	flowPktsPerSecond	fAvgPacketsPerBulk	RRT_samples_clnt
max_bpctl	furg_cnt	flowBytesPerSecond	fAvgBulkRate	Act_data_pkt_forward
Mean_ fpctl	Min_ fpctl	—	avgPacket size	—
mean_bpctl	Max_ fpctl	—	—	—

The process of supervised classification is to classify benign and malware applications in the dataset. As a result, analyzing all malicious application manifest.xml files in our data set can create a data structure. The full keyword list used in this classification is shown in Table 1. As Table 1 describes, the keywords over previously developed classification were the improved ones.

**3.4. Classification of Malware and Benign.** Before extracting features from adware and benign apps, a data repository of applications and Android systems was gathered. Binaries files and manifest.xml files were among the features extracted. Here, Algorithm 2 provides the experimental details about the algorithm analysis based on the feature ranks and classifies the APK whether it is benign or malware. In Algorithm 2, Fn refers to the features, and A is variable which is assigned for the algorithms. Keywords include intent filters (action), broadcast receivers, senders, permissions, and process names. Whereas constant strings, application programming interface calls, and system calls are made with built-in binaries. Constant strings from both benign and malicious applications were collected at random. Android manifest.xml files of applications from Android were collected for analyzing malware samples in the case of keywords (manifest features).

**3.5. Evaluation Metrics.** The following evaluation metric refers to the performance metrics:

$$\text{Accuracy} = \frac{\text{TP} + \text{TN}}{\text{TP} + \text{TF} + \text{TN} + \text{FN}} \quad (1)$$

For random forest, the accuracy rate is 0.9947.

Equation (1) denotes that true positive (TP) refers to the number of right malware classification predictions, whereas false negative (FN) refers to the number of incorrectly classified malware occurrences in the set. TPR stands for recall and sensitivity, among other things:

$$\text{Precision} = \frac{\text{TP}}{\text{TP} + \text{FP}} \quad (2)$$

Equation (2) refers that the precision score and false positive (FP) are the number of misclassified predictions of benign apps:

$$\text{F - Measure} = \frac{2 * \text{Precision}}{\text{precision} + \text{Recall}} \quad (3)$$

Equation (3) indicates that the entire dataset was subjected to a 5,10-fold cross-validation, and 70-percentage split into training data. For the performance analysis, comparing the score of parameters such as accuracy, precision, recall, and F-measure were employed, as summarized in the result.

(i) Steps: (ii) <b>Input:</b> 1. Features (F1,F2,F3....Fn) (2) Algorithms: A (SVM, Naive Bayes, random forest) (iii) <b>Output</b> Classification of.apk (benign or malware) (iv) Begin (v) Extract the F1- Fn features (vi) Select data points →features (ranked) (vii) Apply on algorithms (here referred SVM, Naive Bayes, random forest) (viii) For $i = 1$ to $n$ do// $i$ represents the features. (ix) If the rank $r$ in $F_n$ (equal or max similarity) (x) Then (xi) Classify →malware or benign (xii) Else (xiii) Repeat the rank similarity (xiv) Check $\forall$ .APK (xv) Apply on Time Complexity (xvi) Find the suitable algorithm based on Time Complexity. (xvii) END
--

ALGORITHM 2: Classification of APK.

TABLE 2: Comparison of techniques for the parameters.

Techniques	Precision	F-measure	Recall
SVM	0.871	0.817	0.833
Random forest	<b>0.9947</b>	0.993	0.99
Naïve Bayes	0.784	0.718	0.789

## 4. Result Analysis

The dataset was reduced from 631956 individuals and 80 attributes to 3799 individuals and 60 attributes, which were employed in the study using a 70% split, and 5- and 10-fold cross-validation. This table shows the precision, accuracy, and reliability of the results. Table 2 depicts the outcomes in terms of accuracy, precision, recall, and F-measure. The obtained datasets of both bloatware and whiteware are used in experiments.

**4.1. Precision, F-Measure, and Recall.** Precision refers to the percentage of important recollected instances, whereas recall refers to the percentage of important recollected instances. Precision and recall are both dependent on a thorough understanding of and assessment of significance. Discussing the accuracy and recall scores in Figure 2 explains the results with one measure are compared to a specified level on the other measure, or the two measures are combined into one. Because both precision and recall are required to be higher, a high F-measure is necessary, and random forest has the greatest precision value of 0.994.

Here, different parameters such as precision, F-measure, and recall with the three algorithms explain the detection accuracy which is obtained on the experimental results. Figure 2 compares the algorithms for precision parameter which shows that the random forest classifier has better results. When compared with F-measure, the same

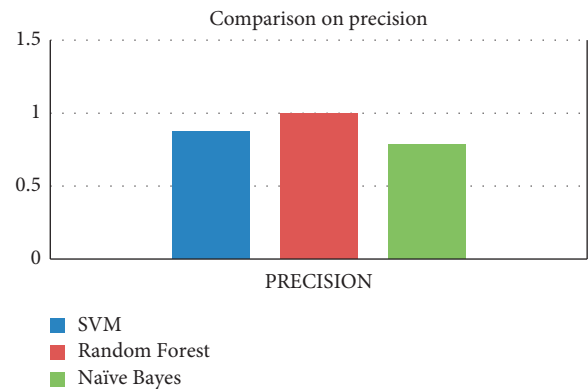


FIGURE 2: Comparison on precision.

random forest has provided the higher results shown in Figures 3 and 4.

**4.2. Accuracy.** Accuracy is a metric that indicates how accurate a prediction is. It does not take positives and negatives into account separately.

The other performance measurements are used in addition to accuracy that is mentioned in Figure 5. Random forest has a value of 0.9947, SVM has a value of 0.9625, and naive Bayes has a value of 0.9412 in this study.

**4.3. Time Complexity.** Time complexity measures the value of time taken for classification of various algorithms based on the given samples. It has been measured as follows:

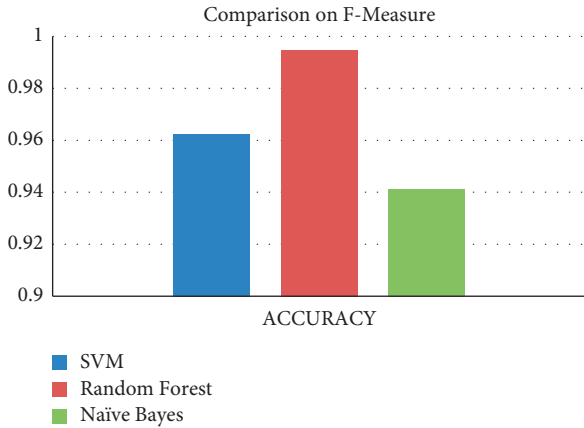


FIGURE 3: Comparison of F-measure.

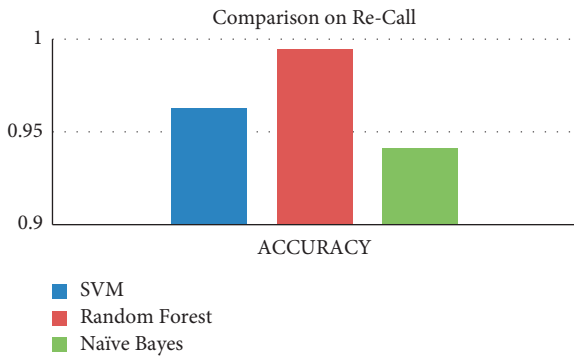


FIGURE 4: Comparison of recall.

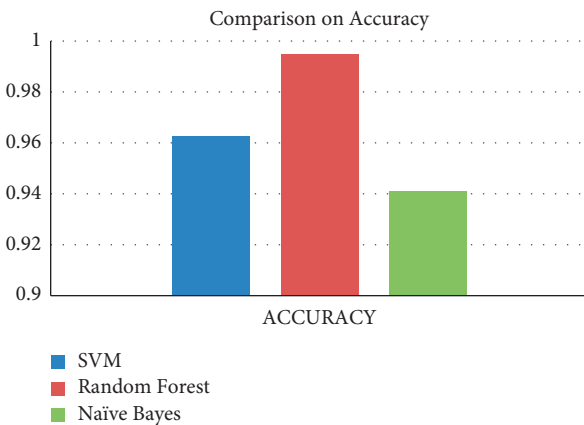


FIGURE 5: Comparison of accuracy.

TimeComplexity

$$= \frac{\text{TotalTimeTakenforMalwareClassification}}{\text{TotalNumberofTestssamplesubmitted}} \quad (4)$$

With reference to equation (4), the analysis is performed by considering different number of techniques and features and the time taken for prediction. The processing time for

TABLE 3: Time complexity for the 631956 samples.

Techniques	Time complexity
631956 samples	
SVM	1 min
Random forest	94 seconds
Naïve Bayes	1 minute 20 seconds

each technique has been mentioned in Table 3. In each case, it compares the results with the existing approaches.

### 5. Conclusion

Using a machine learning classification approach, this paper developed an efficient and reliable adware classification. Variations in parameters and their impact on classification accuracy have been investigated. Random forest outperformed other classification algorithms out of three (3) distinct classification methods utilized in an experiment on an adware dataset with two test choices. According to the obtained results, random forest performed exceptionally well for adware classification with an accuracy of 0.9947, outperforming other well-known classification algorithms such as naive Bayes and SVM. On the larger dataset, the time complexity for the random forest is very less when compared to other techniques. It shows that it analyzes and classifies the application whether it is malicious or benign. As a result, it is recommended that more experiments should be conducted on a larger number of adware datasets from various sources, with future research focusing on new methodologies that will be applied to a larger number of classification algorithms for adware dataset analysis. Experiments show that the strategy outperforms other similar strategies. The next aim is to work on additional variation features in parallel to improve classification accuracy and eliminate false positives.

### 6. Future Work

Malware has a long history of posing a severe security danger to computers. The rapid development of antidetection technology has limited the capability of traditional detection approaches based on static and dynamic analysis. However, due to viral differences, feature extraction is difficult, making traditional neural network applications inefficient. Extended versions of PCA and XGBoost were used to perform the extraction and classification process. The results are projected to improve in accuracy in the future.

### Data Availability

The data that support the findings of this study are available on request from the corresponding author. The data are not publicly available due to privacy concerns.

### Conflicts of Interest

The authors declare that they have no conflicts of interest.

## References

- [1] S. Suresh, F. Di Troia, K. Potika, and M. Stamp, "An analysis of Android adware," *Journal of Computer Virology and Hacking Techniques*, vol. 15, no. 3, pp. 147–160, 2019.
- [2] S. Yilmaz and S. Zavrak, "Adware: a review," *International Journal of Computer Science and Information Technologies*, vol. 6, no. 6, pp. 5599–5604, 2015.
- [3] L. A. Freeman and A. Urbaczewski, "Why do people hate spyware?" *Communications of the ACM*, vol. 48, no. 8, pp. 50–53, 2005.
- [4] S. Shefali, R. Jolivot, and W. Choensawat, "Android malware classification based on mobile security framework," *IAENG International Journal of Computer Science*, vol. 45, no. 4, pp. 514–522, 2018.
- [5] A. Altaher and O. Mohammed, "Intelligent hybrid approach for Android malware detection based on permissions and API calls," *International Journal of Advanced Computer Science and Applications*, vol. 8, no. 6, pp. 60–67, 2017.
- [6] J. Y. Ndagi and J. K. Alhassan, "Machine Learning Classification Algorithms for Adware in Android Devices: A Comparative Evaluation and Analysis," in *Proceedings of the In2019 15th International Conference on Electronics, Computer and Computation (ICECCO)*, pp. 1–6, IEEE, Abuja, Nigeria, March 2019.
- [7] S. Yerima, "Android Malware Dataset for Machine Learning 2 figshare. Dataset," 2018.
- [8] M. Alazab, R. Layton, S. Venkataraman, and P. Watters, "Malware detection based on structural and behavioral features of API calls," 2010.
- [9] K. Vijayan, G. Ramprabu, S. Selvakumara Samy, and M. Rajeswari, "Cascading model in underwater wireless sensors using routing policy for state transitions," *Microprocessors and Microsystems*, vol. 79, Article ID 103298, 2020.
- [10] A. T. Kabakus, T. Abdullah, and I. AlperDogru, "An in-depth analysis of Android malware using hybrid techniques," *Digital Investigation*, vol. 24, pp. 25–33, 2018.
- [11] F. Tchakounte, *A Malware Detection System for Android*, Universität Bremen, Bremen, Germany, PhD diss, 2015.
- [12] C. Arun, S. Karthick, S. Selvakumarasamy, and S. Joseph James, "Car parking location tracking, routing and occupancy monitoring system using cloud infrastructure," *Materials Today Proceedings*, 2021.
- [13] K. O. Elish, D. D. Y. XiaokuiShu, B. G. Ryder, X. Jiang, and X. Jiang, "Profiling user-trigger dependence for Android malware detection," *Computers & Security*, vol. 49, pp. 255–273, 2015.
- [14] O. Mirzaei, J. de Fuentes, J. Tapiador, and L. Gonzalez-Manzano, "AndrODet: an adaptive Android obfuscation detector," *Future Generation Computer Systems*, vol. 90, pp. 240–261, 2019.
- [15] M. Rhode, P. Burnap, and K. Jones, "Early-stage malware prediction using recurrent neural networks," *Computers & Security*, vol. 77, pp. 578–594, 2018.
- [16] K. A. Talha, D. I. Alper, and C. Aydin, "APK Auditor: permission-based Android malware detection system," *Digital Investigation*, vol. 13, pp. 1–14, 2015.
- [17] R. Ahuja, V. Maheshwari, R. A. AbihaKazmi, A. Gupta, R. Arora, and A. Gupta, "Malicious apps identification in android devices using machine learning algorithms," *International Journal of Sensors, Wireless Communications & Control*, vol. 10, no. 4, pp. 559–569, 2020.
- [18] A. A. Ali and A. S. H. Abdul-Qawy, "Static analysis of malware in android-based platforms: a progress study," *International Journal of Computing and Digital Systems*, vol. 10, pp. 321–331, 2021.
- [19] V. G. Shankar and G. Somani, "Anti-Hijack: runtime detection of malware initiated hijacking in android," *Procedia Computer Science*, vol. 78, pp. 587–594, 2016.
- [20] F. Martinelli, F. Marulli, and F. Mercaldo, "Evaluating convolutional neural network for effective mobile malware detection," *Procedia Computer Science*, vol. 112, pp. 2372–2381, 2017.
- [21] M. Almseidin, S. K. MaenAlzubi, and A. Mouhammd, "Evaluation of machine learning algorithms for intrusion detection system," in *Proceedings of the InIEEE 15th International Symposium On Intelligent Systems And Informatics (SISY)*, pp. 000277–000282, IEEE, Subotica, Serbia, October 2017.
- [22] K. Raman, "Selecting features to classify malware," 2012.
- [23] M. Al-Kasassbeh, S. Mohammed, M. Alauthman, and A. Almomani, "Feature selection using a machine learning to classify a malware," in *Handbook of Computer Networks and Cyber Security*, pp. 889–904, Springer, Berlin, Germany, 2020.
- [24] A. Altyeb, A. Almomani, M. Anbar, and S. Ramadass, "Malware detection based on evolving clustering method for classification," *Scientific Research and Essays*, vol. 7, no. 22, pp. 2031–2036, 2020.
- [25] A. Feizollah, R. S. NorBadrulAnuar, R. Salleh, W. Ainuddin, and A. W. A. Wahab, "A review on feature selection in mobile malware detection," *Digital Investigation*, vol. 13, pp. 22–37, 2015.
- [26] W. Z. ZarniAung, "Permission-based android malware detection," *International Journal of Scientific & Technology Research*, vol. 2, no. 3, pp. 228–234, 2013.
- [27] S. SelvakumaraSamy, V. Sivakumar, T. Sood, and Y. S. Negi, "Intelligent web-history based on a hybrid clustering algorithm for future-internet systems," in *Artificial Intelligence and Evolutionary Computations in Engineering Systems*, pp. 571–581, Springer, Berlin, Germany, 2020.

## Research Article

# A Threshold Segmentation Algorithm for Sculpture Images Based on Sparse Decomposition

Zhao Yang<sup>1</sup> and Jixin Wan <sup>2</sup>

<sup>1</sup>School of Fine Arts and Design, Yangzhou University, Yangzhou 225009, Jiangsu, China

<sup>2</sup>Xiamen Academy of Arts and Design, Fuzhou University, Xiamen 361021, Fujian, China

Correspondence should be addressed to Jixin Wan; [t04303@fzu.edu.cn](mailto:t04303@fzu.edu.cn)

Received 14 March 2022; Accepted 3 June 2022; Published 23 June 2022

Academic Editor: Punit Gupta

Copyright © 2022 Zhao Yang and Jixin Wan. This is an open access article distributed under the Creative Commons Attribution License, which permits unrestricted use, distribution, and reproduction in any medium, provided the original work is properly cited.

Aiming at the problem of low efficiency and insufficient accuracy of threshold solution in multithreshold sculpture image segmentation, this paper proposes a threshold segmentation algorithm for sculpture images based on sparse decomposition. In this paper, sparse decomposition is introduced to optimize the model to reduce the impact of local noise on segmentation accuracy, and an energy functional based on pixel coconstraint is built to make up for the defect that pixels cannot retain local details. At the same time, the weighted sum of elite solution sets is used to determine Neighborhood centers increase communication between groups. Experiments show that compared with other algorithms, the above method has significant advantages in convergence efficiency and accuracy.

## 1. Introduction

The influence of images on sculpture is first and foremost a result of the shift in the manner in which art is disseminated. Public sculptures in the classical period are always placed in the heart of a city square or in front of significant buildings in order to hold the most prominent position in a city and emphasize the crucial function that sculptures play in a society. For people living throughout the classical period, these public locations where sculptures could be found were the best public places in which they could use word of mouth as a means of communication in order to gain information, spread knowledge, and investigate the truth. Because of the necessities of the colossal setting, classical sculpture allows the work to get attention and spread throughout the world. Over time, the rise of modern industrial society has eroded the monumentality and public visibility that sculpture formerly possessed. While at the same time, the growth of science and technology resulted in modern architecture bursting out with an unparalleled amount of energy. Because the interior space now has more possibilities and a greater variety of changes, modern architecture has progressively

taken over the traditional role of sculpture from volume to space, and has emerged as a key player in the development of urban public space. While the public's awareness of sculpture is waning, the likelihood of it being propagated and displayed in public spaces is becoming increasingly remote as time goes on.

More sculpture works are being presented in galleries, art galleries, and museums, and they are being spread through albums as a result of the blooming of modernist art and the changing of art ecology. They have an impact on the entire public on a broad scale. When the world entered the postindustrial age in the second half of the twentieth century, electronic media soon displaced text media as the major mode of information dissemination and rose to become the most influential mode of communication. These days, the rapid arrival of the Internet era has been swiftly characterized as an era of world images, in which the world has been transformed into images. People's primary source of knowledge and understanding of the world has shifted from written words to visual images. In the invasion and transformation of art discourse, the features of image distribution have been increasingly important in recent years.



The sculpture as a three-dimensional art form must make adjustments and new alterations to some notions and principles that have been established since the classical period in order to get access to today's popular communication by absorbing some visual experience of images.

Image segmentation (IS) is a fundamental and difficult scientific issue to understand. As a critical link in the image processing chain, the accuracy of picture target extraction and recognition, as well as the effectiveness of future work, are all influenced by the quality of segmentation performed. Because of its simplicity and efficacy, threshold segmentation is commonly employed in picture segmentation [1–8]. IS is a technique for dividing an image into several sections, each having a distinct meaning, in order to retrieve the portion of interest for further investigation. One of the most important methods in IS, the ACM model, has been widely applied in CV, PR, target tracking, and a variety of other applications. In recent years, with the advancement of NN, the combination of deep learning and active contour models has become increasingly popular for solving complicated segmentation and recognition challenges in medical pictures. Deep learning and active contour models are being used by some researchers to autonomously segment the left ventricle from magnetic resonance imaging data. It is possible to separate active contour models into two types: active contour models based on global information and active contour models based on local information [9–14].

3D feature extraction and automatic reconstruction of sparse image sequences using 3D feature reconstruction and sparse scattered point structure reorganization methods are becoming more common as 3D image processing technology advances. These methods can improve the automatic resolution and feature recognition capabilities of sparse image sequences as 3D feature reconstruction and sparsely scattered point structure reorganization methods become more common. In this paper, we investigate the 3D reconstruction method of the sparse image sequence, and we combine the adaptive feature reconstruction (AFR) of image and the point cloud data analysis method in order to realize the AFR of the sparse image sequence and improve the automatic recognition and detection ability of sparse images. Research in related image processing technology is extremely important in the disciplines of medical image processing, artificial intelligence recognition, and remote detection, among other applications [15–24].

It is more robust to picture segmentation results with big disparities in foreground and background gray levels when the CV model is used, but it is more sensitive to high noise when the CV model is used. Value filtering and Gaussian filtering are used to regularize the level set technique. To punish the level set function as a binary function, the level set function is first transformed into a Gaussian smoothing kernel and then regularized. This method combines the advantages of the CV model with the characteristics of local and global segmentation to provide a powerful tool for data analysis [25–30]. The SPF function is created to drive the contour evolution, which enhances the model's resistance to noise by increasing the number of iterations. The model, on the other hand, is sensitive to the position of the beginning

contour, and it is simple to slip into the local optimum early, failing to catch the remote target during the evolution of the active contour during its evolution. Other researchers have proposed a saliency-driven top-down level set model of the region edge as a solution to this problem. Incorporating the saliency feature map and color gray level to produce energy functional, this model, which is based on the CV model, increases the extraction of the model from complex backdrops. As a result of the model's reliance on saliency maps, it is sensitive to changes in visual noise and intensity, among other things [31–38].

As a result, the level set IS model's segmentation results are not accurate enough and are sensitive to the beginning contour position and noise, and the threshold solution efficiency and accuracy in multithreshold sculpture IS are both low. It is proposed in this paper that a threshold segmentation technique for sculpture images based on sparse decomposition be used to segment sculpture photos. It is necessary to first introduce the pixel extraction picture block information in order to develop a symbolic pressure function in order to prevent the contour from becoming stuck in its local optimum during the evolution phase. To compensate for the fact that superpixels are incapable of preserving local features, a new energy functional based on pixel coconstraints is developed. Additionally, this document introduces, for the purpose of optimizing the model, a sparse decomposition method which is applied to limit the impact of local noise on segmentation accuracy.

## 2. Visualization of Sculpture

*2.1. The Reason for the Change.* One of the most prevalent problems facing conventional visual art in modern times is that a single professional knowledge base cannot keep up with the rapid development of modern society, which has seen everything from printing to video to interactive media in the last several decades. An increase in this kind of development is sufficient evidence that the nature of art culture is shifting from verbal to visual culture. It is more important for the public that the sculptural culture be aesthetically pleasing to the eye rather than just providing traditional visual stimulation. Sculpture, when viewed through the eyes of someone who is accustomed to seeing images, can appear dull due to the monotonous colors used in its creation. As a result, space art that has lost its visual experience will be unable to convey its original appeal. In this setting, the sculpture will move in a direction of visualization that is extremely distinct from the typical orientation of the discipline.

*2.2. Performance of Transformation.* Rodin's prognosis is now a reality, and sculpture has undergone profound transformations in the setting of visual culture as a result. The French scholar Baudrillard once divided cultural history since the Renaissance into three stages based on changes in the symbolic representation system: the first stage was the classical cultural period, during which imitation served as the primary paradigm and which lasted from the Renaissance to

the Industrial Revolution; the second stage was the modern cultural period, during which imitation served as the primary paradigm and which lasted from the Renaissance to the Industrial Revolution; the third stage was the postmodern cultural period, which lasted from the Renaissance to the Industrial Revolution. The recreation of natural phenomena was during the Industrial Revolution that the second stage emerged, which was characterized by a production-oriented mindset. These days, symbols are not only restricted to the imitation of reality but also possess a certain degree of autonomy in their own right. The third stage is referred to as digital control and is the current dominant paradigm in the simulacrum stage, and symbols have complete autonomy, manufacturing, and replicating according to their own logic in order to create virtual reality. The third stage, sometimes known as the visual culture stage, is concerned with the cultural context of the current artist's creation.

Visual culture can be defined as the representation of culture in visual form. There are no restrictions on how it can be used in the sphere of visual art. Visual phenomena have spread to every sphere of social life, encompassing everything from prints, television images, and mobile phone interfaces to architectural styles and urban visual images, among other things. The characteristics of this era are as follows: the dominant mode of understanding the world is not through direct touch with the real world but rather through indirect interaction with the real world through watching and experiencing images. According to Heidegger, in essence, the world image does not refer to a vision of the world but rather to the world as it is comprehended as an image by the individual.

*2.2.1. Color Realization of Sculpture.* Many contemporary sculpture artists place a strong emphasis on the use of color in their work. Because traditional sculpture is regarded as the art of mixing material and space, a single hue can usually be used to better showcase the texture of the sculpture material in order to attract the attention of onlookers. As a result, when it comes to creating, color is not the most important consideration for artists. Since the beginning of the Renaissance, sculptures built by artists have been painted only on a few occasions, despite the fact that there has been a creative way of painting sculptures since ancient times. A single form of color expression was substituted for the use of multiple colors in sculpture at that time, in order to better portray the spiritual appeal of classicism and put the audience in a state of concentration. However, the rationale behind this aesthetic style does not allow it to match the visual aesthetic standards of the contemporary public. Once the artist has painted the sculpture with a variety of colors, the texture of the sculptural material itself no longer has the expressiveness of the past. If you look at modern sculpture's link between fishing and form, in particular, the shape of the sculpture is frequently exhibited with vivid colors in order to provide sufficient preparations for the ultimate color presentation. As a result, when we look at photographs of these sculptures, we have no way of knowing if the photographer is photographing a sculpture or a painting.

*2.2.2. Image Expression of Sculpture.* The trend of "imagination" can be seen in sculptural works created in the context of current people's visual culture. The usage of images as inspiration for artists to produce sculptures can be said to be a given, and images are also closely associated with the materials that are used in the construction of artistic sculptures. A sculpture is first and foremost an artistic creation based on a certain image. A sculpture, from a specific point of view, is a three-dimensional representation of an idea in three dimensions. In traditional sculpture creation, artists are frequently inspired by the real world; some of these inspirations are objects found in nature, while others are the hands of humans. Crafts, for example, the sculptural artist Rodin is preoccupied with the human body, and the artist Henry is obsessed with the many forms of coastal pebbles, all of which might express a specific relationship between the sculptural artist and the world in which they live. As a result of this shift in aesthetic perceptions, sculpting artists are no longer able to draw the resources needed for production from their surroundings and are instead turning to various pictures recognized by the general public to obtain those resources needed for creation. That is to say, when artists create sculptures, they frequently draw inspiration from cultures in the developing world and transform flat pictures into three-dimensional artistic forms of expression. Wang Du, a sculptor who lives in France, is a good example of this. The artist transforms a specific image seen in magazines and newspapers into a three-dimensional creative sculpture with the use of digital technology. The prominent sculpture artist Xu Hongfei was influenced by the Guangzhou Daily and developed a series of sculpture works with the motivation of creating "Lovely Soldier," which had a significant impact on the area of art.

*2.2.3. The Presentation Method of Sculpture.* In the world of contemporary art, the sculpture is seen as a notion that is extremely open to interpretation. For example, the iconic piece "Spiral Breakwater" by artist Robert Smith, as well as artist Heizer's book "Double Negative," are both considered works of art. Because of different limits in terms of space and time, some ordinary audiences are unable to access the world of sculpture art at all; additionally, because these works of art are on a monumental scale, even those audiences who are present at the sculpture site are unable to use a typical camera. The piece can only be seen in its whole if viewed from a specific angle, and only through an image captured from that specific angle can you appreciate its complete face. As a result, the works generated by these writers are frequently offered to the public through contemporary means such as photographs and videos. Therefore, the image is vital in the understanding of sculptures and is crucial and decisive in the process of distributing the art form, according to this point of view.

### 3. Method

First of all, this paper introduces the traditional segmentation method, CV model, LIF model, and SBGFRSL method. The energy function of the CV model is

$$E^{cv}(\alpha, a_1, a_2) = \sum_{i=1}^2 \lambda_i \int e_i(x) ds, \quad (1)$$

where  $\lambda_i$  is the weight index,  $a_1$  and  $a_2$  are the average pixel intensity values inside and outside the curve, and  $e_1(x)$  and  $e_2(x)$  are

$$e_1^{cv}(x) = |I - a_1|^2 H(\alpha), \quad (2)$$

$$e_2^{cv}(x) = |I - a_2|^2 (1 - H(\alpha)), \quad (3)$$

where  $H(\alpha)$  is the Heaviside function.

The energy function of the LIF model is

$$E^{lif}(\alpha) = \frac{1}{2} \int_{\Omega} |I(x) - I^{lif}(x)|^2 dx, \quad (4)$$

where  $x \in \Omega$  and the local image fitting formula is

$$I^{lif} = b_1 H_{\varepsilon}(\alpha) + b_2 (1 - H_{\varepsilon}(\alpha)), \quad (5)$$

where

$$b_1 = \text{average}(I \in \{x \in \Omega | \alpha(x) < 0\} \cap W_k(x)), \quad (6)$$

$$b_2 = \text{average}(I \in \{x \in \Omega | \alpha(x) > 0\} \cap W_k(x)). \quad (7)$$

The symbolic pressure function of SGBFRLS is

$$spf(I(x)) = \frac{I(x) - (a_1 + a_2/2)}{\max(I(x) - (a_1 + a_2/2))}. \quad (8)$$

The evolution equation of SGBFRLS is

$$\begin{aligned} \frac{\partial \alpha_p}{\partial t} = spf(I(x)) \times \left( \text{div} \left( \frac{\nabla \alpha_p}{|\nabla \alpha_p|} \right) + \beta \right) \\ + \nabla spf(I(x)) \times \nabla \alpha. \end{aligned} \quad (9)$$

ACM based on global information can handle images with simple intensity information well, but ACM based on local information may be used to extract targets from complicated scenes with more image details, and both methods are effective. As a result, integrating image local information with ACM-based global information can increase the segmentation ability of ACM-based global information.

Next, we introduce the OTSU segmentation method. OTSU can help us determine the threshold. The probability  $p_i$  that a pixel appears in the image is

$$p_i = \frac{f_i}{M \times N} \quad (10)$$

$$\sum_{i=0}^{L-1} p_i = 1$$

Set the threshold combination as  $[t_1, t_2, \dots, t_k]$  to divide the image into  $K + 1$  regions. Then, the proportion  $w_i$  and average gray level  $u_i$  of each area are

$$\left\{ \begin{array}{l} w_0 = \sum_{i=0}^{t_1-1} p_i, w_1 = \sum_{i=t_2}^{t_2-1} p_i \\ \vdots \\ w_k = \sum_{i=t_k}^{L-1} p_i \end{array} \right. \quad (11)$$

$$\left\{ \begin{array}{l} u_0 = \sum_{i=0}^{t_1-1} \frac{i p_i}{w_0}, u_1 = \sum_{i=t_2}^{t_2-1} \frac{i p_i}{w_1} \\ \vdots \\ u_k = \sum_{i=t_k}^{L-1} \frac{i p_i}{w_k} \end{array} \right. \quad (12)$$

Let  $u_t$  be the average gray level of the image; then, the interclass variance is expressed as

$$\sigma_B^2(t_1, t_2, \dots, t_k) = \sum_{i=0}^k w_i \times (u_j - u_t)^2. \quad (13)$$

$$u_t = \sum_{i=0}^{L-1} i p_i. \quad (14)$$

ACM only evaluates the global information of the image throughout the process of contour evolution, which makes it simple to fall into local optimum and to be affected by noise in the process of contour evolution. However, introducing local image information into ACM on the basis of global information requires a significant amount of iterative time. The superpixel algorithm is a widely used image pre-processing algorithm that divides an image into several visually meaningful and spatially disjoint regions while retaining the effective information of the image for more in-depth image analysis. It divides an image into several visually meaningful and spatially disjoint regions while retaining the effective information of the image for more in-depth image analysis. It performs an analysis while at the same time preserving the boundary information of the target in the image. Given that superpixels retain the image's nonglobal information, the use of superpixels in the segmentation process can reduce the influence of local grayscale differences on contour evolution, improve the segmentation accuracy of the image, and reduce the amount of computation required to accelerate the evolution of contours in the image. Simple linear iterative clustering is one of the most extensively used superpixel segmentation methods currently available, owing to its quick running time and ability to maintain ideal outlines in the image. Calculating the pixel gray difference between pixels and centroids is accomplished through the usage of the metric function. In addition to distance difference, a clustering operation is conducted on pixels, and a small number of superpixels is utilized to describe picture attributes in place of a large number of

pixels, therefore reducing the complexity of image processing.

We further introduce superpixels, and the pressure function in this paper is

$$spf(I_{\text{our}}(x)) = \frac{I_{\text{our}}(x) - (a_1 + a_2/2)}{\max(I_{\text{our}}(x) - (a_1 + a_2/2))}, \quad (15)$$

$$I_{\text{our}}(x) = \sum_{l=1}^K \text{Average}(I_l). \quad (16)$$

Although superpixels keep the regional information of an image and can make greater use of the link between distant pixels, relying solely on superpixel features to preserve picture details would result in a loss of image details. As a result, when the superpixel is undersegmented, it is possible that the target contour will not be accurately retrieved. We present an IS approach based on pixel/superpixel cooperative constraints in this study in order to compensate for the flaw that a single superpixel is incapable of preserving local features. Sparse constraints are included in the model in order to reduce the influence of oversegmentation and local noise on contour evolution, and the evolution equations are provided in equations (17) and (18) to illustrate how this is accomplished.

$$\frac{\partial \alpha_p}{\partial t} = spf(I(x)) \times \left( \text{div} \left( \frac{\nabla \alpha_p}{|\nabla \alpha_p|} \right) + \beta \right) + \nabla spf(I(x)) \times \nabla \alpha_p, \quad (17)$$

$$\begin{aligned} \frac{\partial \alpha_{\text{sup}}}{\partial t} &= \omega \times spf(I_{\text{sup}}(x)) \times \left( \text{div} \left( \frac{\nabla \alpha_{\text{sup}}}{|\nabla \alpha_{\text{sup}}|} \right) + \beta \right) \\ &+ \nabla spf(I_{\text{sup}}(x)) \times \nabla \alpha_{\text{sup}} \\ &+ \mu \times \frac{(\partial \alpha_p / \partial t) - \min(\partial \alpha_p / \partial t)}{\max(\partial \alpha_p / \partial t) - \min(\partial \alpha_p / \partial t)}. \end{aligned} \quad (18)$$

Equations (17) and (18) can be simplified to

$$\frac{\partial \alpha_p}{\partial t} = spf(I(x)) \cdot |\nabla \alpha_p|, \quad (19)$$

$$\begin{aligned} \frac{\partial \alpha_{\text{sup}}}{\partial t} &= \omega \cdot spf(I_{\text{sup}}(x)) \cdot |\nabla \alpha_p| + \mu \\ &\times \frac{(\partial \alpha_p / \partial t) - \min(\partial \alpha_p / \partial t)}{\max(\partial \alpha_p / \partial t) - \min(\partial \alpha_p / \partial t)}. \end{aligned} \quad (20)$$

Furthermore, this paper introduces a sparse decomposition method to solve the scaled coordinates.

$$x_{k+1} = x_k + \gamma R_e x_k, \quad (21)$$

$$x_{k+1} = x_k + \zeta R_a x_k, \quad (22)$$

where  $R_a$  is a sparse random diagonal matrix with nonzero values from a standard normal distribution.

Using the local mean noise reduction approach, the collected original three-dimensional sculpture point sparse image is isolated from noise. The feature points' thresholds



FIGURE 1: Original image cloud feature sampling.

are then set, and the noise separation processing is carried out in accordance with the threshold judgment result. The feature point set that has been formed is as follows:

$$\begin{pmatrix} x & y & z \\ 0 & 0 & 0 \end{pmatrix} = \begin{pmatrix} (H + \tau \cdot I) & P \\ P^T & O \end{pmatrix} \begin{pmatrix} \gamma & \theta & \omega \\ a & b & c \end{pmatrix}. \quad (23)$$

#### 4. Sculpture Image Threshold Segmentation (SITS)

The simulation experiment analysis is carried out in this research in order to evaluate the performance of the threshold segmentation algorithm of a sculptured picture based on sparse decomposition in terms of performance. For the experiment, the MATLAB simulation tool is used to design the experiment, and Visual Studio 2020 is used to create the image processing software platform for the 3D reconstruction of sparsely scattered points. The pixels collected for sparse images of sculpture points are 20 million, the number of connection points of feature lines is 500, and the feature resolution is  $640 \times 400$ , the interference noise is Gaussian noise, and the intensity is  $-12$  dB. The original point cloud feature sample is achieved as illustrated in Figure 1 using the simulation parameter settings described above.

Using the sampled image in Figure 2 as input, the detection result is shown in Figure 1. The three-dimensional point cloud feature of the sculpture point sparse image is detected and shown in Figure 3.

The gradient operation method is used to decompose the feature detected in Figure 3 as the input of the threshold segmentation of the sculpture point image, and the information enhancement and fusion filtering of the sparse image of the sculpture point are realized, and the image is reconstructed, and the reconstructed output is obtained as shown in Figure 4.

JS and Dice coefficients are employed in order to study and evaluate the segmentation quality of the suggested SITS model. This allows us to validate the effectiveness of our strategy.

The JS and DICE values for the four approaches are depicted in Figures 5 and 6, respectively. It can be observed



FIGURE 2: Edge profile feature.

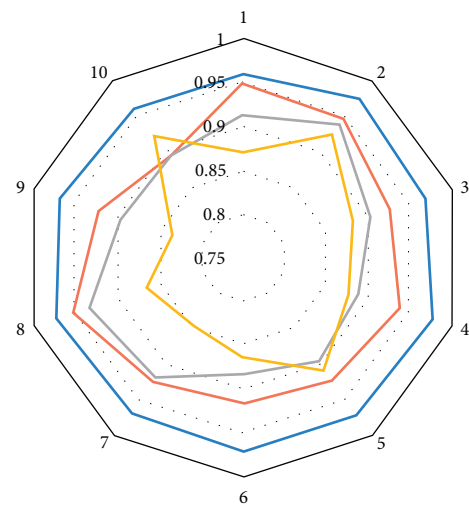


FIGURE 3: Sparse scattered point features.



FIGURE 4: Sculpture image reconstruction output.

in Figures 5 and 6 that CV and LIF are susceptible to strong noise and weak boundaries; their average JS values are 0.845 and 0.869, and their average DICE values are 0.848 and 0.788, respectively, indicating that they are susceptible to strong noise and weak boundaries. The SBGFRLS model is



— SITS  
— CV  
— SBGFRLS LIF  
— Comparison of JS value.

FIGURE 5: Comparison of JS value.

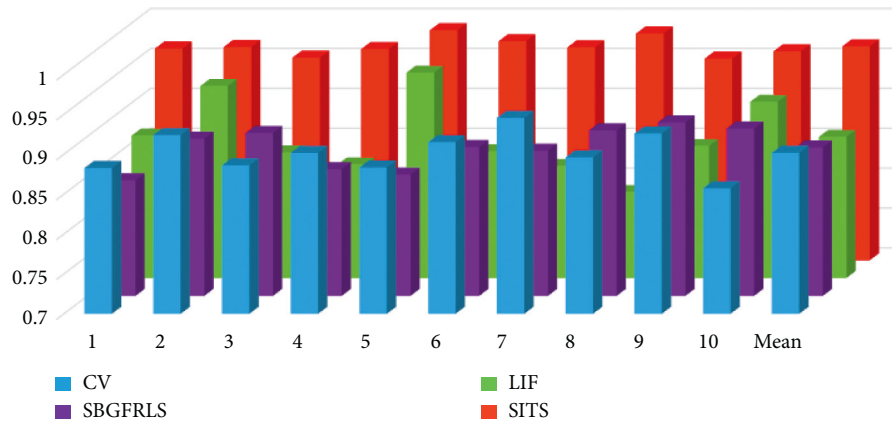


FIGURE 6: Comparison of DICE value.

unable to capture pixels at the extreme end of the spectrum. As a result of this, the relationship between them is susceptible to falling into a local maximum, with an average JS value of 0.715 in the experiment.

## 5. Conclusion

In order to address the issue that the segmentation results of the sculpture IS model are not accurate enough and are sensitive to the initial contour position and noise, this paper proposes a threshold segmentation algorithm for sculpture images based on sparse decomposition. This algorithm realizes the adaptive structural reorganization of sparse image sequences and improves the automatic processing of sparse images by reducing the sensitivity to the initial contour position and noise with the ability to identify and notice potential dangers. In order to address the issue of sluggish evolution of the active contour model based on nonglobal information, the model makes use of superpixel blocks to accelerate the evolution of the active contour model. The findings of this study demonstrate that the method described in this paper requires less prior knowledge for sculptural picture segmentation, and that both the JC and DICE indicators perform much better than traditional comparison methods.

## Data Availability

The data used to support the findings of this study are available from the corresponding author upon request.

## Conflicts of Interest

The authors declare that they have no conflicts of interest.

## Acknowledgments

The paper was supported by the project source: Research on the Improvement path of the quality of urban humanistic landscape from the perspective of public cultural service and fund project: supported by the Humanities and Social Sciences Foundation of Yangzhou University, Project No.: 26.

## References

- [1] Y. Xue, X. Guo, and X. Cao, "Motion saliency detection using low-rank and sparse decomposition," in *Proceedings of the 2012 IEEE international conference on acoustics, speech and signal processing (ICASSP)*, pp. 1485–1488, IEEE, Kyoto, Japan, March 2012.
- [2] X. Shen and Y. Wu, "A unified approach to salient object detection via low rank matrix recovery," in *Proceedings of the 2012 IEEE Conference on Computer Vision and Pattern Recognition*, pp. 853–860, IEEE, Providence, RI, USA, June 2012.
- [3] H. Mohimani, M. Babaie-Zadeh, and C. Jutten, "A fast approach for overcomplete sparse decomposition based on smoothed  $\ell_0$  norm," *IEEE Transactions on Signal Processing*, vol. 57, no. 1, pp. 289–301, 2008.
- [4] C. Shi, Y. Cheng, J. Wang, Y. Wang, K. Mori, and S. Tamura, "Low-rank and sparse decomposition based shape model and probabilistic atlas for automatic pathological organ segmentation," *Medical Image Analysis*, vol. 38, pp. 30–49, 2017.
- [5] H. Peng, B. Li, H. Ling et al., "Salient object detection via structured matrix decomposition," *IEEE Transactions on Pattern Analysis and Machine Intelligence*, vol. 39, no. 4, pp. 818–832, 2016.
- [6] M. D. Collins, J. Xu, L. Grady et al., "Random walks based multi-image segmentation: quasiconvexity results and gpu-based solutions," in *Proceedings of the 2012 IEEE Conference on Computer Vision and Pattern Recognition*, pp. 1656–1663, IEEE, Providence, RI, USA, June 2012.
- [7] J. Pont-Tuset, P. Arbelaez, and J. T. Barron, "Multiscale combinatorial grouping for image segmentation and object proposal generation," *IEEE Transactions on Pattern Analysis and Machine Intelligence*, vol. 39, no. 1, pp. 128–140, 2016.
- [8] R. Xia, Y. Pan, and L. Du, "Robust multi-view spectral clustering via low-rank and sparse decomposition," *Proceedings of the AAAI Conference on Artificial Intelligence*, vol. 28, no. 1, 2014.
- [9] J.-L. Starck, M. Elad, and D. L. Donoho, "Image decomposition via the combination of sparse representations and a variational approach," *IEEE Transactions on Image Processing*, vol. 14, no. 10, pp. 1570–1582, 2005.
- [10] B. Trémouliéac, N. Dikaios, and D. Atkinson, "Dynamic MR image reconstruction–separation from undersampled ( $\ell_1$ ,  $\ell_2$ )-Space via low-rank plus sparse prior," *IEEE Transactions on Medical Imaging*, vol. 33, no. 8, pp. 1689–1701, 2014.

- [11] I. Ramirez, P. Sprechmann, and G. Sapiro, "Classification and clustering via dictionary learning with structured incoherence and shared features," in *Proceedings of the 2010 IEEE Computer Society Conference on Computer Vision and Pattern Recognition*, pp. 3501–3508, IEEE, San Francisco, CA, USA, June 2010.
- [12] J. Funke, F. Tschopp, and W. Grisaitis, "Large scale image segmentation with structured loss based deep learning for connectome reconstruction," *IEEE Transactions on Pattern Analysis and Machine Intelligence*, vol. 41, no. 7, pp. 1669–1680, 2018.
- [13] F. Sultana, A. Sufian, and P. Dutta, "Evolution of image segmentation using deep convolutional neural network: a survey," *Knowledge-Based Systems*, vol. 201-202, Article ID 106062, 2020.
- [14] M. Elad and M. Aharon, "Image denoising via sparse and redundant representations over learned dictionaries," *IEEE Transactions on Image Processing*, vol. 15, no. 12, pp. 3736–3745, 2006.
- [15] E. Imani, M. Javidi, and H.-R. Pourreza, "Improvement of retinal blood vessel detection using morphological component analysis," *Computer Methods and Programs in Biomedicine*, vol. 118, no. 3, pp. 263–279, 2015.
- [16] W. Sun, C. Liu, J. Li, Y. M. Lai, and W. Li, "Low-rank and sparse matrix decomposition-based anomaly detection for hyperspectral imagery," *Journal of Applied Remote Sensing*, vol. 8, no. 1, Article ID 083641, 2014.
- [17] W. Hu, Y. Yang, and W. Zhang, "Moving object detection using tensor-based low-rank and saliently fused-sparse decomposition[J]," *IEEE Transactions on Image Processing*, vol. 26, no. 2, pp. 724–737, 2016.
- [18] J. Mairal, F. Bach, and J. Ponce, "Online dictionary learning for sparse coding," in *Proceedings of the 26th annual international conference on machine learning*, pp. 689–696, Montreal, Quebec, Canada, June 2009.
- [19] W. Weisheng Dong, L. Lei Zhang, G. Guangming Shi, and fnm Xiaolin Wu, "Image deblurring and super-resolution by adaptive sparse domain selection and adaptive regularization," *IEEE Transactions on Image Processing*, vol. 20, no. 7, pp. 1838–1857, 2011.
- [20] X. Fu, Z. J. Zha, and F. Wu, "Jpeg artifacts reduction via deep convolutional sparse coding," in *Proceedings of the IEEE/CVF International Conference on Computer Vision*, pp. 2501–2510, Seoul, Korea, October 2019.
- [21] D. Liu, Z. Wang, B. Wen, J. Yang, W. Han, and T. S. Huang, "Robust single image super-resolution via deep networks with sparse prior," *IEEE Transactions on Image Processing*, vol. 25, no. 7, pp. 3194–3207, 2016.
- [22] R. A. Borsoi, T. Imbiriba, and J. C. M. Bermudez, "A fast multiscale spatial regularization for sparse hyperspectral unmixing," *IEEE Geoscience and Remote Sensing Letters*, vol. 16, no. 4, pp. 598–602, 2018.
- [23] X. Pan, L. Li, H. Yang et al., "Accurate segmentation of nuclei in pathological images via sparse reconstruction and deep convolutional networks," *Neurocomputing*, vol. 229, pp. 88–99, 2017.
- [24] Z. Huang, X. Wang, and J. Wang, "Weakly-supervised semantic segmentation network with deep seeded region growing," in *Proceedings of the IEEE conference on computer vision and pattern recognition*, pp. 7014–7023, IEEE, Lake City, UT, USA, June 2018.
- [25] X. Yu, T. Liu, and X. Wang, "On compressing deep models by low rank and sparse decomposition," in *Proceedings of the IEEE Conference on Computer Vision and Pattern Recognition*, pp. 7370–7379, IEEE, Honolulu, HI, USA, July 2017.
- [26] H. Zhu, F. Meng, J. Cai, and S. Lu, "Beyond pixels: a comprehensive survey from bottom-up to semantic image segmentation and cosegmentation," *Journal of Visual Communication and Image Representation*, vol. 34, pp. 12–27, 2016.
- [27] C. Yan, Z. Li, Y. Zhang, Y. Liu, X. Ji, and Y. Zhang, "Depth image denoising using nuclear norm and learning graph model," *ACM Transactions on Multimedia Computing, Communications, and Applications*, vol. 16, no. 4, pp. 1–17, 2020.
- [28] L. Hou, D. Samaras, and T. M. Kurc, "Patch-based convolutional neural network for whole slide tissue image classification," in *Proceedings of the IEEE conference on computer vision and pattern recognition*, pp. 2424–2433, IEEE, Honolulu, HI, USA, October 2016.
- [29] S. Javed, A. Mahmood, T. Bouwmans, and S. K. Jung, "Background-foreground modeling based on spatiotemporal sparse subspace clustering," *IEEE Transactions on Image Processing*, vol. 26, no. 12, pp. 5840–5854, 2017.
- [30] A. Heshmati, M. Gholami, and A. Rashno, "Scheme for unsupervised colour-texture image segmentation using neutrosophic set and non-subsampled contourlet transform," *IET Image Processing*, vol. 10, no. 6, pp. 464–473, 2016.
- [31] Y. Qian and M. Ye, "Hyperspectral imagery restoration using nonlocal spectral-spatial structured sparse representation with noise estimation," *Journal of Selected Topics in Applied Earth Observations and Remote Sensing*, vol. 6, no. 2, pp. 499–515, 2012.
- [32] C. Scharfenberger, A. Wong, and K. Fergani, "Statistical textural distinctiveness for salient region detection in natural images," in *Proceedings of the IEEE conference on computer vision and pattern recognition*, pp. 979–986, IEEE, Portland, OR, USA, June 2013.
- [33] K. K. Maninis, J. Pont-Tuset, and P. Arbeláez, "Convolutional oriented boundaries: from image segmentation to high-level tasks," *IEEE Transactions on Pattern Analysis and Machine Intelligence*, vol. 40, no. 4, pp. 819–833, 2017.
- [34] Z. Wang, D. Liu, and J. Yang, "Deep networks for image super-resolution with sparse prior," in *Proceedings of the IEEE international conference on computer vision*, pp. 370–378, IEEE, Santiago, Chile, December 2015.
- [35] W. Ren, J. Tian, and Z. Han, "Video desnowing and deraining based on matrix decomposition," in *Proceedings of the IEEE Conference on Computer Vision and Pattern Recognition*, pp. 4210–4219, IEEE, Honolulu, HI, USA, July 2017.
- [36] L. Shao, R. Yan, and X. Li, "From heuristic optimization to dictionary learning: a review and comprehensive comparison of image denoising algorithms," *IEEE Transactions on Cybernetics*, vol. 44, no. 7, pp. 1001–1013, 2013.
- [37] T. Blaschke, C. Burnett, and A. Pekkarinen, "Image segmentation methods for object-based analysis and classification," *Remote Sensing Image Analysis: Including the Spatial Domain*, Springer, Dordrecht, pp. 211–236, 2004.
- [38] L. Garcia Ugarriza, E. Saber, S. R. Vantaram, V. Amuso, M. Shaw, and R. Bhaskar, "Automatic image segmentation by dynamic region growth and multiresolution merging," *IEEE Transactions on Image Processing*, vol. 18, no. 10, pp. 2275–2288, 2009.

## Research Article

# Discriminating the Pneumonia-Positive Images from COVID-19-Positive Images Using an Integrated Convolutional Neural Network

Vetrithangam D <sup>1</sup>, V. Indira,<sup>2</sup> Syed Umar <sup>3</sup>, Bhaskar Pant,<sup>4</sup> Mayank Kumar Goyal <sup>5</sup>,  
and Arunadevi B <sup>6</sup>

<sup>1</sup>Department of Computer Science and Engineering, Chandigarh University, Mohali, Punjab, India

<sup>2</sup>Department of Mathematics, Indira Gandhi College of Arts and Science, Kathirkamam, Puducherry, India

<sup>3</sup>Department of Computer Science & Engineering, Wollega University, Oromiya, Nekemte, Ethiopia

<sup>4</sup>Department of Computer Science and Engineering, Graphic Era Deemed to Be University Bell Road Clement Town, Dehradun 248002, Uttarakhand, India

<sup>5</sup>Department of Computer Science & Engineering, School of Engineering and Technology Sharda University, Greater Noida, India

<sup>6</sup>Department of Electronics and Communication Engineering, Dr. N.G.P Institute of Technology, Coimbatore, Tamilnadu, India

Correspondence should be addressed to Vetrithangam D; [vetrigold@gmail.com](mailto:vetrigold@gmail.com) and Syed Umar; [syedumar@wollegauniversity.edu.et](mailto:syedumar@wollegauniversity.edu.et)

Received 13 April 2022; Revised 15 May 2022; Accepted 25 May 2022; Published 17 June 2022

Academic Editor: Dinesh Kumar Saini

Copyright © 2022 Vetrithangam D et al. This is an open access article distributed under the Creative Commons Attribution License, which permits unrestricted use, distribution, and reproduction in any medium, provided the original work is properly cited.

One of the most pressing issues in the current COVID-19 pandemic is the early detection and diagnosis of COVID-19, as well as the precise separation of non-COVID-19 cases at the lowest possible cost and during the disease's early stages. Deep learning-based models have the potential to provide an accurate and efficient approach for the identification and diagnosis of COVID-19, with considerable increases in sensitivity, specificity, and accuracy when used in the processing of modalities. COVID-19 illness is difficult to detect and recognize since it is comparable to pneumonia. The main objective of this study is to distinguish between COVID-19-positive images and pneumonia-positive images. We have proposed an integrated convolutional neural network focused on discriminating against COVID-19-infected patients and pneumonia patients. Preprocessing is done on the image datasets. The novelty of this research work is to differentiate the COVID-19 images from the pneumonia images. It will help the medical experts in the decision-making. In order to train the model, the image is given directly as input to integrated convolutional neural network architecture; after training the model, the system is integrated with three different kinds of datasets: COVID-19 image dataset, RSNA pneumonia dataset, and a new dataset created from COVID-19 image dataset. The attainment of the system is evaluated by calculating the measures of sensitivity, specificity, precision, and accuracy, and this system produces the accuracy values of 94.04%, 97.2%, and 97.5% for the above datasets, respectively.

## 1. Introduction

Coronavirus pandemic was brought about by the stringent acute respiratory syndrome coronavirus (SARS-CoV-2) and has quickly spread over the world. Because of the virus's sneaky infectious nature and a lack of vaccinations or effective therapies, early diagnosis is critical in preventing further transmission and controlling it within current healthcare institutions. The most dangerous sickness

induced by COVID-19 is pneumonia, which affects the lungs. High fever, dyspnea, cough, and runny nose are some of the symptoms of the condition [1]. Chest X-ray imaging analysis for abnormalities is the most common way to diagnose these situations. X-radiation, often known as X-ray, is a type of electromagnetic radiation that absorbs radiation. As a COVID-19 innovative diagnostic approach, X-ray imaging has a number of advantages over conventional testing procedures [2]. The low cost, wide accessibility of



X-ray imaging, noninvasiveness, reduced time consumption, and equipment accessibility are only a few of the advantages [3]. In light of the current global healthcare crisis, imaging of X-ray may be the best choice for a mass, simple, and active diagnosis technique in a generic situation such as COVID-19. Image-based medical diagnostics can save a lot of time when it comes to detecting COVID-19, which can help to limit and prevent the spread of the virus. The major forms of pictures that can play a big role in defeating COVID-19 are CXR and CT [4]. The convolutional layer, which acts on a localized area rather than all over, is used in the first portion of CNN. It pulls distinctions from raw input and turns that layer into the one before it. The pooling layer then takes what is learned from the preceding layer and reduces the process's complexity. The completely linked layer executes the features learned from all preceding layers in the second half, resulting in the intended classified outputs [5].

## 2. Related Works

Deep learning explicitly in clinical images depends on the determination. Models of deep learning achieved conspicuously on PC objective issues connected with the clinical image examination. The ANNs beat other customary models and strategies for image investigation. Because of the exceptionally encouraging outcomes given by CNNs in the clinical image examination and order, they are speculated to be the obvious norm in this area. CNN has been utilized for an assortment of classifying tasks connected with clinical findings. For example, lung sickness identification of malaria sick in images of slender blood smears, bosom malignant growth identification, remote endoscopy images, and interstitial lung contamination CAD depends on the determination in radiography of chest analysis of skin disease by order and programmed conclusion of different chest illnesses utilizing chest X-beam image characterization. Various scientists are locked in with the experimentation and examination exercises connected with the finding, treatment, and management of COVID-19. One more huge review has provided details regarding the X-beam dataset, including X-ray images having a place with normal COVID-19 patients, pneumonia patients, and individuals with no sickness [6]. The review utilizes the best in CNN structures for the automated, accurate identification of COVID-19 patients. Move learning has accomplished exactness about 97.82% in the identification of COVID-19 [7]. This review and one more recent and significant review have led to the approval and versatility of transfer, deform, and compose, type deep-based CNN for COVID-19 identification utilizing chest X-beam picture arrangement [8]. In the current review, 18 shape features were separated. Then, at that point, the shape highlights, descriptors of the two-layered size, and the state of the ROI were incorporated. The shape features are free of the gray level force circulation in the ROI; in this way, they are just determined on the noninferred images. In the local force distinction features, different elements, including hecticness, coarseness, intricacy, contrast, and surface strength, were registered [9].

Investigating the gathering of tests determined to have COVID-19, the stamped superpixels are somewhat more centered on the chest and body area rather than the checked superpixels in the examples with practically no analyzed pathology. Here, shoulders, neck, and hands are set apart with a huge size of patches. Moreover, when the images pairwise COVID-19 are analyzed with the ordinary images, we can see that areas of positive superpixels in COVID-19 images are generally sheltering similar situations as the negative superpixels in other characterized images [10]. In the clinical field, the CNN method and deep learning are the first rates at images that are utilized to make clinical pictures, not just for making and, furthermore, for grouping and recognizing the images. The convolution neural networks are used for image characterization and recognition [11]. CNNs play out the best exact for the pneumonia recognition with X-ray images taken from the part of the chest. The outcomes show more than 95% of exactness. Not just pneumonia, the CNN plays out the very good accuracy for the identification of pneumonia disease with X-ray images taken from the part of the chest. The outcomes show more than 95% of accuracy [12].

## 3. Existing Methodologies

*3.1. Convolutional Neural Networks (CNNs).* The CNNs are influenced by the perceptible arrangement of the individual mind. The thought of bringing up the rear CNNs, consequently, is to make the PCs fit for review of the world as people see it. In this direction, CNNs can be utilized in the domains of image acknowledgment and investigation, image arrangement, and regular language handling [13]. CNN is a kind of deep-seated neural organization, which consists of the pooling, convolutional, and nonlinear actuation layers. The convolutional layer, regarded as a fundamental layer of a convolutional NN, plays out the activity called "convolution" that provides the name for CNN. Kernels available in the layer of convolution are exercised on the input layer [14]. The convolutional layers' results are interinvolved as an insight map. In this review, the ReLU has been utilized in the function of activation amidst a convolutional layer that is useful to expand the nonlinearity in the provided input image because the images are generally nonlinear in general [15]. Accordingly, CNN in connection with ReLU in the present situation is simpler and quicker. Because the score of ReLU is zero for generally bad information sources, it tends to be constituted as just  $Z_{max}(0, I)$ . Here, the capacity infers that the result  $z$  is 0 for generally regrettable and positive-remaining parts of the steady [16].

*3.2. Deep Convolutional Neural Networks (DCNNs).* Normally, deep convolutional neural organizations (DCNNs) perform better in a more prominent database than in a more modest dataset [17]. Transfer learning (TL) is valuable in systems like CNN with a generally restricted assortment of information. In this review, we have attempted the assignment of characterization of pictures of chest X-beams into one of the following 3 classes: COVID-

19-positive, viral pneumonia, or typical [5, 18]. The constructed CNNs were tested using databases such as MNIST and CIFAR-10 to see how well they performed. The test results were 99.467% and 91.167%, respectively. These findings are similar to those of other CNNs that have been tested for accuracy. As a result, it was established that the constructed CNN not only has fewer parameters than existing CNNs but also performs well in tests [19].

**3.3. KNN Classifier.** The contribution to the model that classifies is a bunch of images of 2 groups: COVID-19 and ordinary cases. The equal FrMEMs are exercised on multicenter CPUs to derive the highlights of the image. At that instant, an optimization-based algorithm is utilized in view of element extraction. At long last, a KNN method was prepared and assessed. The consequences of the suggested COVID-19 X-beam characterization, image-oriented strategy contrasted and other famous MH procedures that are employed as FS; the particular methods incorporate sine cosine calculation SCA, grey wolf improvement GWO, whale streamlining calculation WOA, and Harris hawks' analyzer HHO [20]. These calculations are utilized in this correlation since they set them up for their presentation in various appliances like worldwide improvement and element determination techniques [21]. They have enumerated images from the SIRM and created the COVID-19 database. This dataset comprises 219 numbers of COVID-19-positive images and 1341 numbers of negative COVID-19 images. For two datasets, the images derived from the COVID-19 image dataset were gathered from a person aged between 40 and 84, representing the two sexes. The information encompasses 216 numbers of COVID-19-positive and 1675 COVID-19 negative [22]. The KNN-based method is used to conclude whether a provided chest X-beam image is a COVID-19 or typical case. The suggested technique was assessed on a number of distinctive datasets. Contrasting with an effective CNN design, the MobileNet model and the presented strategy accomplished practically identical execution on the exactness, review, and accuracy of assessment measurements with the least number of features [23].

**3.4. FCN- and MMD-Based Domain Adaptation Module.** It comprises a backbone network, an arrangement descent, and a division descent. Compared to FCN, our model has a helper grouping descent. The task grouping descent is intended for the two tasks: one type is to empower our method to achieve both grouping classification and division tasks for the mechanised disease estimation and COVID-19 determination. Another part is to work with the utilization of MMD-oriented strategies for the area's transformation. The backbone-oriented network is answerable for separating deep highlights by playing out the spatial and convolution pooling procedures on CXRs and DRRs. The extricated deep highlights are then taken care of in the order of descent and division descent independently. In the characterization part, we embrace an extremely straightforward construction with a worldwide normal pooling layer and a completely convolution-oriented layer. In this framework, an off-the-rack

MMD-based space transformation method is taken on. LMMD can quantify the error of neighborhood circulations by thinking about the connections of the applicable subdomains. By limiting the loss of LMMD while the preparation of deep models, the dispersions of significant subdomains inside a similar class in the fountain area and function space are moved closer. Just as the LMMD strategy is suggested with regards to protest acknowledgment and digit arrangement undertakings, we use it to the order of descent straight by adjusting the deep elements from layers of GAP. The impact of element arrangement can be engendered on the division part, verifiably through the contribution of the layer GAP [1, 24].

**3.5. COVID-19-GATNet Architecture.** There are two potential ways of improving the expressive force of the CNN model. One is to expand the number of layers to make it more profound, the other is to increment the quantity of layers to make it more profound, and the third is to build the quantity of convex channels to make it progressively wide. The work process of this review starts with an assortment of essential datasets that encompass 2 image groups: one group of images had a place with the chest X-ray of COVID-19 affirmed cases and another group of images had a place with individuals with pneumonia infection. The concerned clinical experts investigated the dataset and eliminated a portion of the X-beam images that were not satisfactory as far as quality and indicative boundaries. Henceforth, the produced dataset was exceptionally perfect, as every X-beam image was of good quality, just as clear as far as huge demonstrative boundaries as per their expertise [13]. In DenseNet, each layer in the organization is straightforwardly layered to understand the reuse of associated features. As the quantity of layers expands, the organization progressively adds the new element data produced by each layer to the current worldwide element data. The Coronavirus GATNet adds numerous arrangements of autonomous consideration instruments by adding a diagram consideration layer. After that, the element extraction has done, so that the multihead consideration system can act as the conveyance of various pertinent elements between the focal hub and neighbour hubs. Hubs in a similar area dole out various loads, which can grow the model scale and make the model learning capacity all the more impressive. By consolidating the strong element extraction ability of DenseNet and the consideration system, the fundamental construction of the COVID-19-GAT model is acquired [25].

## 4. Dataset and Preprocessing

**4.1. Dataset.** Table 1 lists the dataset used for the proposed neural network systems. Our system considers three types of image datasets taken from open sources: the first image dataset is the COVID-19 image dataset, which includes 584 numbers of COVID-19 images and 1760 numbers of normal images among a total number of 2344 images [26]. The RSNA pneumonia dataset consists of 500 numbers of pneumonia images and 1600 numbers of normal images

TABLE 1: Dataset used for the proposed neural network systems.

S. no.	Dataset	COVID-19 images	Pneumonia images	Normal images	Total images
1	COVID-19 image dataset	584		1760	2344
2	RSNA pneumonia dataset		500	1600	2100
3	Newly created dataset	484		1400	1884

among a total number of 2100 images. The third dataset is created by taking the data from the COVID-19 image dataset and the RSNA pneumonia dataset; the newly created dataset contains 484 numbers of both COVID-19-positive and pneumonia-positive images, as well as 1400 normal images among a total number of 1884 images [27]. The pneumonia dataset named RSNA is comprised of images from NIH (NI of Health) and marked by the Radiological Society of North America alongside the Thoracic Radiology Society. The objective of this dataset was to foster an AI classifier equipped to recognize control and pneumonia images, so it was delivered in the competition of Kaggle in the year 2018. It comprises 26684 pictures, of which 20672 are control and 6012 are pneumonia pictures. However, in this study, just 2100 pictures are considered for performance assessment. Choosing X-ray images for analysis is helpful because they are cheaper, faster, and more common [28].

*4.2. Dataset Preprocessing.* Pneumonia positive cases and discriminating pneumonia from the COVID-19 positive case images have been used to stabilize the dataset to enhance the attainment of the suggested CNN models in identifying COVID-19 cases. The data preprocessing includes the accompanying tilt correction, removing noises, cropping images, and padding. The tilt correction is significant since the model can perceive all of the data in the same orientation when it is trained. Directly addressing the tilt in big datasets is time consuming and costly. As a result, an automatic tilt correction technique in preprocessing before training is required. In the wake of applying these preprocessing steps to information, we see that model accuracy has expanded altogether [29]. During preprocessing, eliminating noises is a vital stage since the information is improved on later in the execution, so we can see it all the more obviously. In this way, the model can be prepared well. Tilt correction is the arrangement of the chest X-ray in a proposed manner. At the point when tilt is experienced by chest X-ray pictures, it might bring about misalignment for clinical applications. It is significant in the data that when we train the model, it can see the entire information through a similar arrangement. Physically correcting the tilt for huge scope of information is tedious and costly. In this manner, there is a requirement for a programmed method of performing tilt correction in preprocessing [30]. Cropping the image is expected to put the chest X-ray image in the middle and dispose of pointless pieces of chest X-ray. Likewise, some may be put in various areas inside the image. By cropping the image and adding cushions, we will ensure practically every one of the images is in the same area inside the general images itself.

## 5. The Proposed Methodology

This proposed method will diagnose and classify different kinds of diseases. A convolutional neural network is trained. The modules include dataset creation, dataset preprocessing, and building convolutional neural networks. The convolutional neural network was chosen because it automatically discovers significant features without the need for human intervention. From two datasets, a new dataset was randomly created; they are COVID-19 chest X-ray image dataset, pneumonia dataset, and a dataset that is downloaded from Kaggle. This dataset contains two types of images: one is pneumonia-positive image and another one is pneumonia negative image. Pneumonia negative images are considered as COVID-19 negative images. A convolutional neural network is trained with pneumonia negative images, COVID-19-positive images, and pneumonia-positive images. This method is developed using Python, TensorFlow, and Keras, which combines a variety of methods and models to allow users to build deep neural networks for applications like image recognition and classification. The complete path of the COVID-19-positive image dataset is set and trained. OpenCV is used to read the images. In the first phase, COVID-19 negative and COVID-19-positive images are trained. The main intention of this work is to distinguish between pneumonia-positive images and COVID-19-positive images [31]. Three different kinds of datasets are considered for training and testing. After preprocessing, the image datasets are trained. Figure 1 shows the proposed architecture for an integrated convolutional neural network.

The size of the image can be changed, and in turn, the image can be changed to gray color. In this modified convolutional neural network architecture, the image is given directly as input. We have a parallel 2D convolutional layer of  $128@3 \times 3$ ,  $128@5 \times 5$ , and  $128@7 \times 7$ . In order to create a parallel convolutional layer, the kernel size is defined as 3, 5, and 7. All three layers are appended into a single layer. The second layer is the concatenation layer, which is created by concatenating all the convolutional layers. Then, we have a general layer of convolution  $64@3 \times 3$ , where 64 kernels are available, and another layer with  $32@3 \times 3$ , where 32 kernels are available. The data coming from the 2D convolutional layers are given as input into the flatten layer, the dense layer (128), and the dense layer (64). To construct a single lengthy feature vector, we flatten the output of the convolutional layers. It is also linked to the final classification model. Finally, the output layer, which had two neurons, produces two results: one is COVID-19-positive and the other one is pneumonia-positive. Specifically, two neurons, COVID-19-positive and pneumonia-positive, are produced as the output. This metadata.csv file contains the

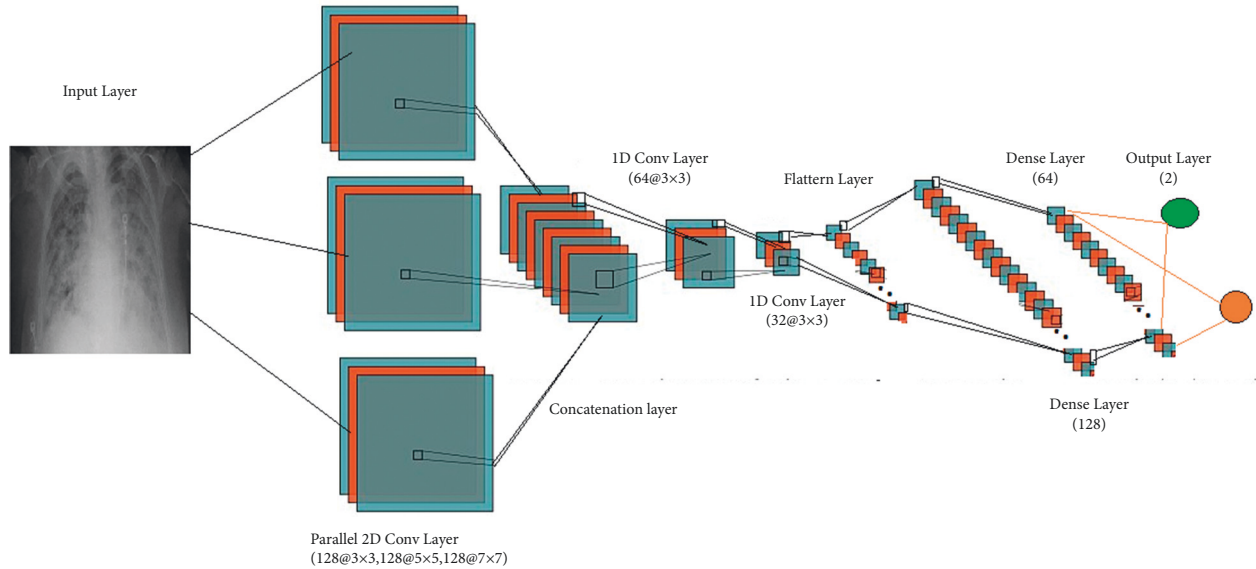


FIGURE 1: The proposed architecture for an integrated convolutional neural network.

image file name, disease name, patient age, and other details also. The metadata.csv file is read and it filters the COVID-19 images from the image dataset. Softmax is used as the activation of the output. In this implementation, we have used 85% of the data for training purposes and 15% of the data for testing purposes. In our system, a modified and integrated convolutional neural network is utilized for diagnosing and segregating the chest X-ray images. The first convolutional layer will process the dataset with different diseases and produce output as a result of the output layer. The output layer produces two outputs as a result. The first result category is an image with disease (positive) and the second category is an image without the disease (negative).

### 6. Results and Discussion

Following the dataset’s preprocessing, it was comprised of a total of 2344 X-ray images. The dataset was isolated into two different subsets. The training dataset is comprised of 584 COVID-19 X-ray images and 1760 normal X-ray images, leading to a total of 2344 X-ray images trained using the integrated convolutional neural network. This new CNN was tested using the testing dataset, which similarly contained 285 chest X-ray images. Figure 2 shows the confusion matrix of the ICNN on the COVID-19 image dataset.

As a first test, our integrated convolutional neural network is trained with the abovementioned number of chest X-ray images and tested using the test dataset with 285 images taken from the RSNA pneumonia dataset. This model produced the results of 258 numbers of true positives, 10 numbers of true negatives, 9 numbers of false negatives, and 8 numbers of false positives among the 285 images of test data and sensitivity of 96.60%, specificity of 55.60%, precision of 96.90%, and accuracy of 96.81% were calculated and other measures such as negative predictive value, false-positive rate, false discovery rate, F1 score, and Matthews correlation coefficient are listed in Table 2.

Total: 285	True Positive	True Negative
Predicted Positive	TP :258	FP:8
Predicted Negative	FN:9	TN:10

FIGURE 2: Confusion matrix of the ICNN on COVID-19 image dataset.

As a second test, our integrated convolutional neural network is trained using the training dataset with 500 chest X-ray images and tested using the test dataset with 500 images taken from the RSNA pneumonia dataset. Figure 3 shows the confusion matrix of the ICNN on the RSNA pneumonia dataset.

This model produced the results of 451 numbers of true positives, 35 numbers of true negatives, 10 numbers of false negatives, and 4 numbers of false positives among the 500 images of test data. Sensitivity was 99.12%, specificity was 77.78%, precision was 97.83%, and accuracy was 97.2%. Other measures such as negative predictive value, false discovery rate, F1 score, false-positive rate, and Matthews correlation coefficient are listed in Table 3. Finally, our integrated convolutional neural network is trained using the training dataset with 484 chest X-ray images and tested utilizing the test dataset with 200 images taken from the RSNA pneumonia dataset. Figure 4 shows the confusion matrix of the ICNN on the newly created dataset.

This model produced the results of 158 numbers of true positives, 37 numbers of true negatives, 3 numbers of false negatives, and 2 numbers of false positives among the 200 images of test data, a sensitivity of 98.14%, specificity of 94.87%, precision of 98.75%, and accuracy of 97.5% are

TABLE 2: Performance measures of the ICNN for the COVID-19 image dataset.

Measure	Sensitivity	Specificity	Precision	NPV	FPR	FDR	FNR	Accuracy	F1 score	MCC
Value	96.60	55.60	96.90	52.60	44.44	3.01	3.37	94.04	96.81	50.89

Total: 500	True Positive	True Negative
Predicted Positive	451	10
Predicted Negative	4	35

FIGURE 3: Confusion matrix of the ICNN on RSNA pneumonia dataset.

TABLE 3: Performance measures of the ICNN for the RSNA pneumonia dataset.

Measure	Sensitivity	Specificity	Precision	NPV	FPR	FDR	FNR	Accuracy	F1 score	MCC
Value	99.12	77.78	97.83	89.74	22.22	2.17	0.88	97.2	98.47	82.06

Total: 200	True Positive	True Negative
Predicted Positive	158	2
Predicted Negative	3	37

FIGURE 4: Confusion matrix of the ICNN on the newly created dataset.

TABLE 4: Performance measures of the ICNN for the newly created dataset from COVID-19 dataset and pneumonia dataset.

Measure	Sensitivity	Specificity	Precision	NPV	FPR	FDR	FNR	Accuracy	F1 score	MCC
Value	98.14	94.87	98.75	92.5	5.13	1.25	1.86	97.5	98.44	92.13

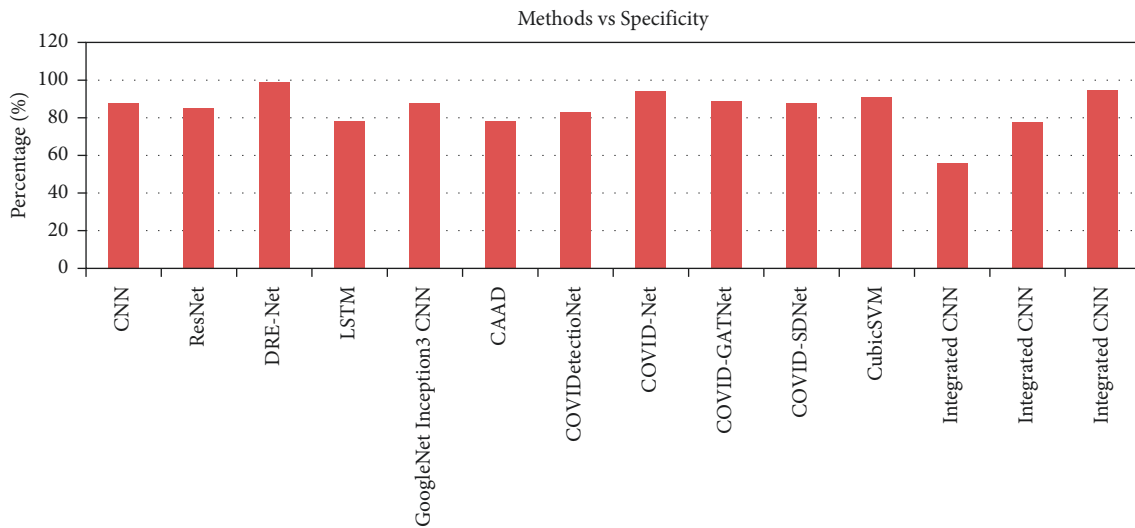


FIGURE 5: Comparison of specificity performance measures based on different methods.

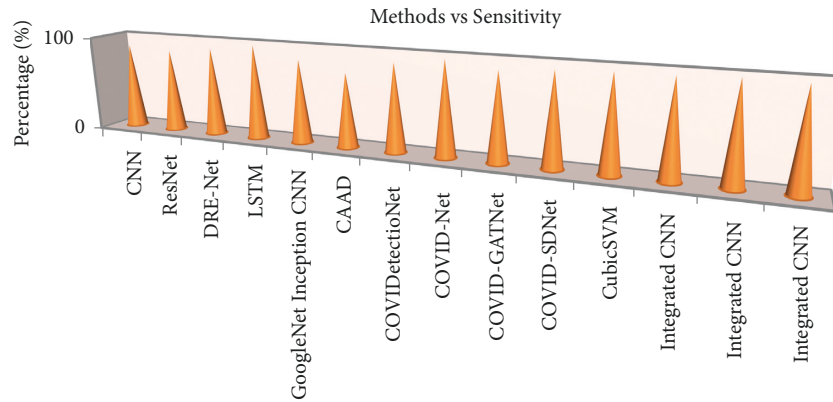


FIGURE 6: Comparison of sensitivity performance measures based on different methods.

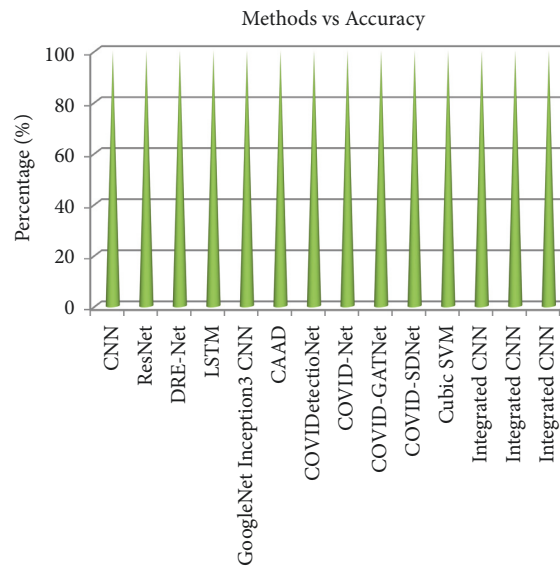


FIGURE 7: Comparison of accuracy performance measures based on different methods.

calculated, and other measures such as false-positive rate, negative predictive value, false discovery rate, F1 score, and Matthews correlation coefficient are listed in Table 4. Our proposed system has produced a value of 98.14% of the sensitivity based on the newly created dataset when comparing sensitivity and specificity.

The specificity performance measure is compared with all the existing methods used in the previous work. We have used three different kinds of datasets for testing our newly developed model. Our system produced good results based on the newly created dataset rather than the RSNA pneumonia dataset, and it produced a difference value of 17.09% of the specificity. Figure 5 shows the comparison of specific performance measures based on different methods and specificity measures for the datasets 1, 2, and 3 are plotted; here, our third dataset was created from both the COVID-19 image dataset and produced good results.

The sensitivity performance measure is compared with all the existing methods used in the previous work. We have used three different kinds of datasets for testing our newly developed model. Figure 6 shows the comparison of

sensitivity performance measures based on different methods and sensitivity measures for the datasets 1, 2, and 3 are plotted; here, our second dataset derived from the RSNA pneumonia dataset and the RSNA pneumonia dataset produced good results.

The accuracy of our developed system is compared with all the existing methods used in the previous work. We have used three different kinds of datasets for testing our newly developed model. Our proposed system has produced a value of 98.14% of the sensitivity based on the newly created dataset when comparing sensitivity and accuracy. Figure 7 shows the comparison of accuracy performance measures based on different methods and accuracy measures for the datasets 1, 2, and 3 are plotted; here, our third dataset is derived from the RSNA pneumonia dataset, and the RSNA pneumonia dataset produced good accuracy.

## 7. Conclusions

Patients with pneumonia symptoms are more likely to have COVID-19 viral pneumonia than bacterial pneumonia

acquired in the environment. It is difficult to tell whether pneumonia is caused by the COVID-19 virus or by bacteria. It is impossible to deliver the optimal treatment to individuals with lung infections without a firm diagnosis of the condition. We have developed an integrated convolutional neural network; this will identify the COVID-19-positive images in the COVID-19 image dataset by separating them from normal images. Pneumonia-positive images are identified from the RSNA pneumonia dataset by separating them from normal images. The COVID-19 images are diagnosed and identified from pneumonia-positive images from the dataset, which is newly created by taking the images from both the COVID-19 image dataset and the RSNA pneumonia dataset. The model is tested with three different kinds of image datasets with 285,500 and 200 numbers of images. The results of the experiments revealed that our new model ICNN achieves good accuracy, specificity, and F1-score values. In the future, the system will be tested with a large image dataset.

## Data Availability

The data used to support the findings of this study are included within the article. Should further data or information be required, these are available from the corresponding author upon request.

## Conflicts of Interest

The authors declare that there are no conflicts of interest.

## Acknowledgments

The authors thank Chandigarh University, Punjab, for providing characterization support to complete this research work.

## References

- [1] C. Zhou, J. Song, S. Zhou, Z. Zhang, and J. Xing, "COVID-19 detection based on image regrouping and ResNet-SVM using chest X-ray images," *IEEE Access*, vol. 9, pp. 81902–81912, 2021.
- [2] S. Angalaeswari, K. Jamuna, K. Mohana sundaram, L. Natrayan, L. Ramesh, and K. Ramaswamy, "Power-sharing analysis of hybrid microgrid using iterative learning controller (ILC) considering source and load variation," *Mathematical Problems in Engineering*, vol. 2022, Article ID 7403691, 6 pages, 2022.
- [3] J. Zhang, Y. Xie, G. Pang et al., "Viral pneumonia screening on chest X-rays using confidence-aware anomaly detection," *IEEE Transactions on Medical Imaging*, vol. 40, no. 3, pp. 879–890, 2021.
- [4] M. A. Kamel, M. Abdelshafy, M. Abdulrazek, O. Abouelkhir, A. Fawzy, and A. T. Sahlol, "Efficient classification approach based on COVID-19 CT images analysis with deep features," *2021 International Conference on Computing, Communication, and Intelligent Systems (ICCCIS)*, vol. 99, pp. 459–464, 2021.
- [5] M. M. R. Khan, S. Sakib, M. d. A. B. Siddique et al., "Automatic detection of COVID-19 disease in chest X-ray images using deep neural networks," in *Proceedings of the 2020 IEEE 8th R10 Humanitarian Technology Conference (R10-HTC)*, pp. 7–12, Kuching, Malaysia, 2020–December.
- [6] G. M. Varghese, R. John, A. Manesh, R. Karthik, and O. C. Abraham, "Clinical management of COVID-19," *The Indian journal of medical research*, vol. 151, no. 5, p. 401, 2020.
- [7] T. Tuncer, F. Ozyurt, S. Dogan, and A. Subasi, "A novel Covid-19 and pneumonia classification method based on F-transform," *Chemometrics and Intelligent Laboratory Systems*, vol. 210, p. 104256, October 2021.
- [8] S. Ying, S. Zheng, L. Li et al., "Deep learning enables accurate diagnosis of novel coronavirus (COVID-19) with CT images," *IEEE/ACM Transactions on Computational Biology and Bioinformatics*, vol. 18, no. 6, p. 1, 2020.
- [9] A. sendrayaperumal, S. Mahapatra, S. S. Parida et al., "Energy auditing for efficient planning and implementation in commercial and residential buildings," *Advances in Civil Engineering*, vol. 2021, pp. 1–10, 2021.
- [10] G. Vrbancic, S. Pecnik, and V. Podgorelec, "Identification of COVID-19 X-ray images using CNN with optimized tuning of transfer learning," *2020 International Conference on Innovations in Intelligent SysTems and Applications (INISTA)*, vol. 92, 2020.
- [11] X. Xu, X. Jiang, C. Ma et al., "A deep learning system to screen novel coronavirus disease 2019 pneumonia," *Engineering*, vol. 6, no. 10, pp. 1122–1129, 2020.
- [12] P. Mahesh, Y. G. Prathyusha, B. Sahithi, and S. Nagendram, "Covid-19 detection from chest X-ray using convolution neural networks," *Journal of Physics: Conference Series*, vol. 1804, no. 1, p. 012197, 2021.
- [13] K. R. Vaishali, S. R. Rammohan, N. L, N. V.R, and D. Usha, "Guided container selection for data streaming through neural learning in cloud," *International Journal of System Assurance Engineering and Management*, vol. 16, pp. 1–7, 2021.
- [14] S. Tabik, A. Gomez-Rios, J. L. M. Rodriguez et al., "COVIDGR dataset and COVID-SDNet methodology for predicting COVID-19 based on chest X-ray images," *IEEE Journal of Biomedical and Health Informatics*, vol. 24, no. 12, pp. 3595–3605, 2020.
- [15] A. Joshi, M. S. Khan, S. Soomro, A. Niaz, B. S. Han, and K. N. Choi, "SRIS: saliency-based region detection and image segmentation of COVID-19 infected cases," *IEEE Access*, vol. 8, pp. 190487–190503, 2020.
- [16] M. Turkoglu, "COVIDetectioNet: COVID-19 diagnosis system based on X-ray images using features selected from pre-learned deep features ensemble," *Applied Intelligence*, vol. 51, no. 3, pp. 1213–1226, 2021.
- [17] C. S. Anupama, L. Natrayan, E. Laxmi Lydia et al., "Deep learning with backtracking search optimization based skin lesion diagnosis model," *Computers, Materials & Continua*, vol. 70, no. 1, pp. 1297–1313, 2021.
- [18] M. J. Hasan, M. S. Alom, and M. S. Ali, "Deep learning based detection and segmentation of COVID-19 & pneumonia on chest X-ray image," *2021 International Conference on Information and Communication Technology for Sustainable Development (ICICT4SD)*, vol. 100, pp. 210–214, 2021.
- [19] S. S. Sundaram, "Smart clothes with bio-sensors for ECG monitoring," *International Journal of Innovative Technology and Exploring Engineering*, vol. 8, no. 4, pp. 298–301, 2019.
- [20] M. Al Mehedi Hasan, J. Shin, and F. Parvin, "Deep transfer learning based detection of COVID-19 from chest X-ray images," *2021 11th International Conference on Biomedical Engineering and Technology*, vol. 99, pp. 64–70, 2021.

- [21] J. Skibinska, R. Burget, A. Channa, N. Popescu, and Y. Koucheryavy, "COVID-19 diagnosis at early stage based on smartwatches and machine learning techniques," *IEEE Access*, vol. 9, pp. 119476–119491, 2021.
- [22] V. K. Gupta, A. Gupta, D. Kumar, and A. Sardana, "Prediction of COVID-19 confirmed, death, and cured cases in India using random forest model," *Big Data Mining and Analytics*, vol. 4, no. 2, pp. 116–123, 2021.
- [23] P. Asha, L. Natrayan, B. T. Geetha et al., "IoT enabled environmental toxicology for air pollution monitoring using AI techniques," *Environmental Research*, vol. 205, p. 112574, 2022.
- [24] M. A. Elaziz, K. M. Hosny, A. Salah, M. M. Darwish, S. Lu, and A. T. Sahlol, "New machine learning method for image-based diagnosis of COVID-19," *PLoS One*, vol. 15, no. 6, p. e0235187, 2020.
- [25] P. Zhang, Y. Zhong, Y. Deng, X. Tang, and X. Li, "Drr4covid: learning automated COVID-19 infection segmentation from digitally reconstructed radiographs," *IEEE Access*, vol. 8, pp. 207736–207757, 2020.
- [26] L. P. Natrayan, "Sakthi shunmuga sundaram. J. Elumalai. Analyzing the Uterine physiological with MMG Signals using SVM," *International journal of Pharmaceutical research*, vol. 11, no. 2, pp. 165–170, 2019.
- [27] H. Nasiri and S. A. Alavi, "A novel framework based on deep learning and ANOVA feature selection method for diagnosis of COVID-19 cases from chest X-ray Images," *Computational Intelligence and Neuroscience*, vol. 2022, pp. 1–20, December 2019, <http://arxiv.org/abs/2110.06340>.
- [28] A. Darshan, N. Girdhar, R. Bhojwani et al., "Energy audit of a residential building to reduce energy cost and carbon footprint for sustainable development with renewable energy sources," *Advances in Civil Engineering*, vol. 2022, pp. 1–10, 2022.
- [29] K. Nagarajan, A. Rajagopalan, S. Angalaeswari, L. Natrayan, and W. D. Mammo, "Combined economic emission dispatch of microgrid with the incorporation of renewable energy sources using improved mayfly optimization algorithm," *Computational Intelligence and Neuroscience*, vol. 2022, pp. 1–22, 2022.
- [30] D. K. Jain, S. K. S. Tyagi, S. Neelakandan, M. Prakash, and L. Natrayan, "Metaheuristic optimization-based resource allocation technique for cybertwin-driven 6G on IoE environment," *IEEE Transactions on Industrial Informatics*, vol. 18, no. 7, pp. 4884–4892, 2022.
- [31] M. S. N. V.R, R. P.S., R. R. M. S, and N. L, "Pervasive computing in the context of COVID-19 prediction with AI-based algorithms," *International Journal of Pervasive Computing and Communications*, vol. 16, no. 5, pp. 477–487, 2020.



## Research Article

# Psychological Mechanism and Exercise Intervention of College Students' Problematic Internet Use Based on IoT Technology

Zhiqiang Chen <sup>1,2</sup> and Pu Sun<sup>1</sup>

<sup>1</sup>College of Physical Education and Sports, Beijing Normal University, Beijing 100875, China

<sup>2</sup>Department of Physical Education, Xinjiang University, Urumqi 830046, Xinjiang, China

Correspondence should be addressed to Zhiqiang Chen; 201731070008@mail.bnu.edu.cn

Received 21 April 2022; Revised 26 May 2022; Accepted 30 May 2022; Published 15 June 2022

Academic Editor: Punit Gupta

Copyright © 2022 Zhiqiang Chen and Pu Sun. This is an open access article distributed under the Creative Commons Attribution License, which permits unrestricted use, distribution, and reproduction in any medium, provided the original work is properly cited.

Dangerous Internet use alludes to unreasonable utilization of the Internet that unfavorably influences individual emotional well-being, relational correspondence, social transformation, social turn of events, learning, and work. This paper aims to study how to analyze and study the psychological mechanism and exercise intervention of problematic Internet use based on the Internet of Things technology, and describe it. It addresses the question of problematic web usage, and this question is based on IoT technology. This paper then elaborates on the concept of data mining and related algorithms. It designs and analyzes the psychological mechanism and exercise intervention of college students' problematic Internet use. The experimental results showed that in the incidence of Internet addiction, gender, grade, family economic environment, and single-parent family will be affected. Moderate-intensity (50%–80% VO<sub>2</sub> max) aerobic and anaerobic exercise for more than 30 minutes per year has a positive effect on college students' Internet addiction.

## 1. Introduction

As a new type of science and technology, the Internet of Things technology is a new technological form. It uses a new type of detection technology to realize the expansion from virtual space to real physical space through the Internet. The new development and utilization of Internet of Things advancement has step by step changed people's creation, life, and perspective. It narrows the distance between people and people and things, and greatly improves the efficiency of labor production. The Internet of Things built by the third wave of the world's information industry after the computer and the Internet. As we all know, modern students are the population with the highest Internet penetration rate. Among the hundreds of millions of Internet users in China, university users top the list. At the same time, more and more students have the problem of indulging in the virtual world of the Internet. The number of Chinese students with Internet addiction has exceeded 300,000 of which 40,000 are severely Internet

addicts. Internet addiction among college students has caused a series of mental health problems, ideological and behavioral problems, and even serious social problems. This not only hinders the development and success of students but also affects the long-term development of the entire country and society. Their basic psychological needs are inherent and necessary psychological needs of the body.

Problematic Internet use (PIU) refers to excessive Internet use that has adverse effects on an individual's mental health, interpersonal communication, social adaptation, study, and work. In 2018, the 42nd report released by the China Internet Network Information Center showed that among Chinese netizens in 2018, by age, the 20–29 age groups had the highest proportion of netizens. According to occupational classification, school students account for 24.8%, which is the largest percentage of the total population. In China, students seem to be a huge group of Internet users. Therefore, the problem of college students' use of the Internet has attracted much attention.

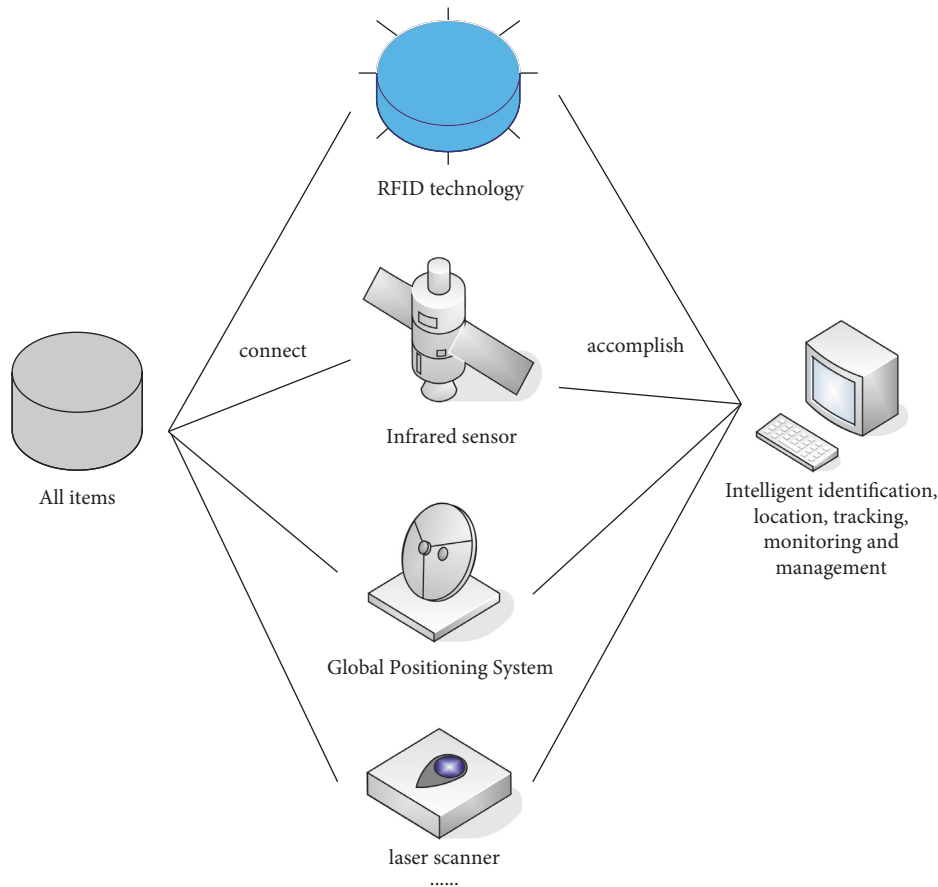


FIGURE 1: Conceptual diagram of the original meaning of the Internet of Things.

The innovation of this paper (1) combines the Internet of Things technology with the use of problem networks, and introduces the theory and related methods of data mining in detail. (2) In the face of the psychological mechanism of college students, it analyzes the related factors of Internet addiction. This paper concludes that gender, grade, family economic environment, and single-parent family are all affected in the incidence of Internet addiction.

## 2. Related Work

With the continuous development of the Internet and the popularity of smartphones, students usually spend a lot of time using the Internet, and the phenomenon of problems with Internet use is still cause for concern. Gómez et al. characterized the demographics and rates of participation in online risky experiences among Spanish secondary school students and screened for problematic Internet use [1]. Ilesanmi et al. investigated examples of Web use (PIU) and the predominance of PIU previously and during the COVID-19 lockdown, as well as the causes, impacts, and expected alleviations of PIU during lockdown [2]. Rosenkranz et al. analyzed the habit-forming capability of 8 unique Internet applications to separate male and female clients. He researched various relationships being referred to among Internet gamers and generalized Internet users [3]. Rooij et al. observationally investigated the choice of

renouncing a bound together way to deal with address risky “Web use” by dividing ideas into more unambiguous application-level measures [4]. Canan et al. planned to research the conceivable relationship between the proportion of center and ring fingers and Internet habit, and whether this relationship is connected with impulsivity [5]. The essential goal of Laconi et al. was to research the connection between dangerous Internet use and online time, online movement, and psychopathology by considering diverse and distinctions in sexual orientation [6]. Li et al. planned to analyze the intervening job of a sleeping disorder on the relationship between risky Web use, including Web compulsion and online long range informal communication habit, and young adult wretchedness [7]. The point of Peker et al. was to inspect the interceding job of life fulfillment and imperativeness in the connection between young people’s anxiety toward coronavirus and hazardous Web use [8]. However, their study did not explore this psychological mechanism and did not intervene in the study subjects.

## 3. Methods Based on IoT Technology

### 3.1. IoT and IoT Technology

**3.1.1. Definition of the Internet of Things.** The so-called Internet of Things, as can be seen from its name, refers to the “Internet of things connected with things” [9]. This concept

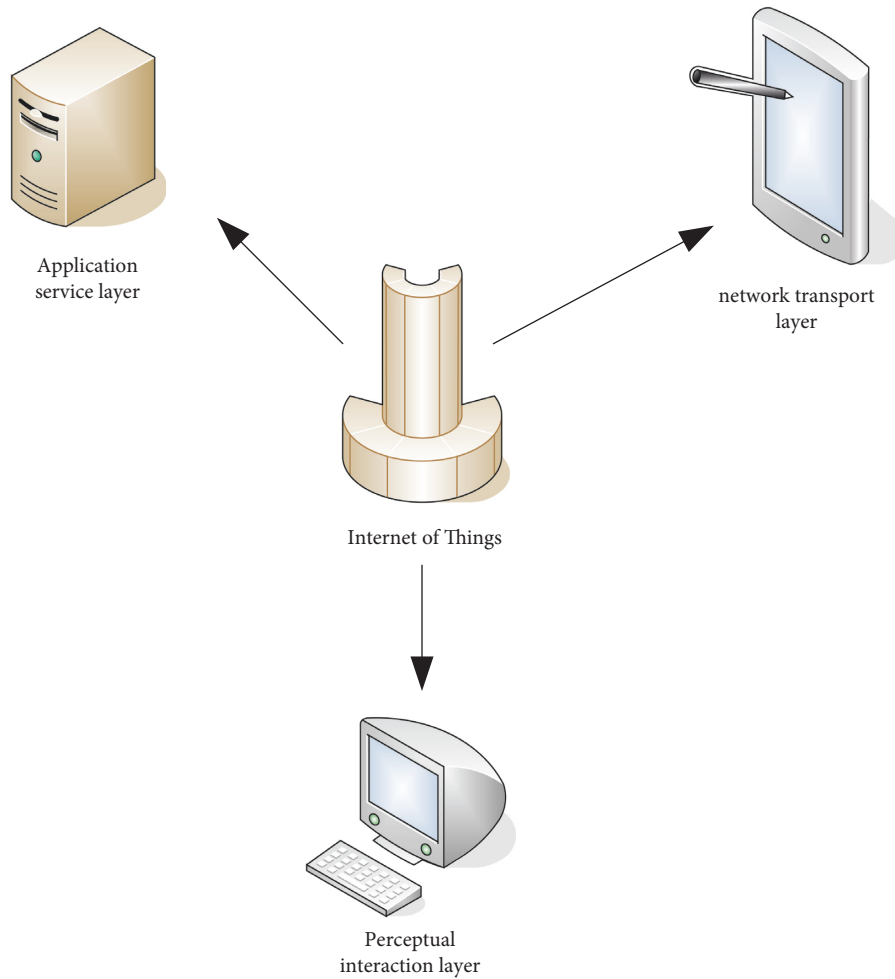


FIGURE 2: IoT composition system.

was proposed by the MIT Research Center in 1999, and its original meaning is shown in Figure 1.

So far, there is still no unified international standard for the definition of the Internet of Things. The author's more recognized definition of the Internet of Things is a network that realizes the comprehensive interconnection of people and people, people and things, and things and things for the purpose of perception. Its prominent feature is to obtain various information of the physical world through various perception methods. It combines the Internet, mobile communication network, etc. for information transmission and interaction, and uses intelligent computing technology to analyze and process information, thereby improving people's perception of the material world and realizing intelligent decision making and control.

**3.1.2. Internet of Things Technology.** The Internet of Things is a typical new field of cross-application of information technology and sensing technology. It is a huge and complex integrated information system [10]. The Internet of Things is a system composed of three main technical levels, as shown in Figure 2.

The perception layer is mainly used to collect various data. Without it, there is no information about the characteristic data of objects on the Web. Only when the perception layer technology meets the requirements, the entire Internet of Things can operate normally.

Embedded identification technology can enable the "things" in the Internet of Things to have certain intelligent data communication capabilities. The embedded technology in the Internet of Things is to add a chip to the object and integrate the chip system and the software system through the corresponding software. This enables data communication between objects and the outside world. Most of the items in the Internet of Things use embedded technology to make all things have the level of intelligent communication, and connect these intelligent items with the network [11, 12].

The network layer mainly completes functions such as long-distance transmission of information. It includes the Internet, telecommunication networks, satellite networks, radio, television, and television networks.

The application layer is mainly to process data and complete the work of service discovery and service presentation. It realizes information storage, analysis, mining, etc., and ultimately provides users with various information services and applications. It involves the computational

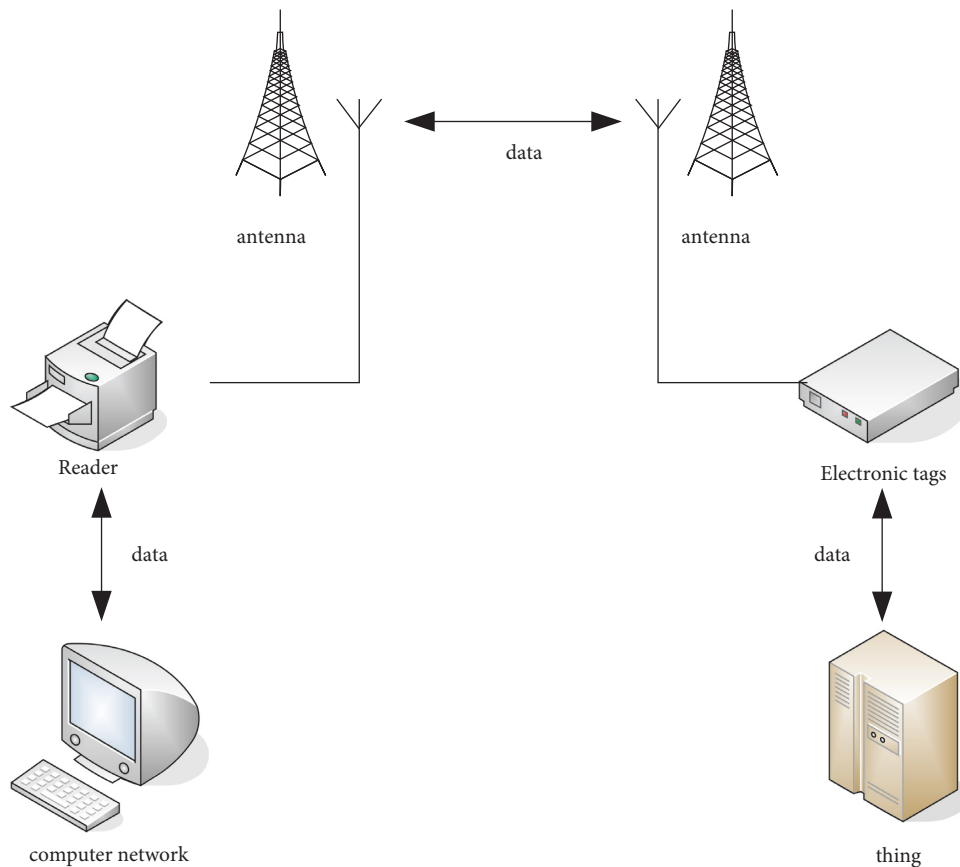


FIGURE 3: Components of an RFID system.

processing of large amounts of data in the application layer. The development of cloud computing technology has greatly improved the information processing capabilities of the Internet of Things. It enables IoT technology to design different solutions according to the needs of different users [13].

**3.2. Key Technologies of the Internet of Things.** IoT technology mainly includes intelligent perception and marking technology, network and communication technology, computing, and service push technology. Perception and marking technologies include RFID, QR codes, and sensors. Network and communication technologies include Ethernet, 3G, Bluetooth, and WIFI. Computing and service technologies include data mining and data push [14, 15].

**3.2.1. RFID Technology.** RFID is radio frequency identification, which also known as electronic tag. RFID is a noncontact automatic identification technology that transmits data through radio waves. It uses radio signals to read and write data and identify specific targets. RFID appeared in the 1990s. It is considered to be the most widely used best and most important technology in the field of automatic identification. The composition of RFID systems varies according to their applications and functions. But in general, it basically includes three parts: electronic tag, reader, and

antenna [16]. The electronic label is attached to the object and contains a data storage area, which stores the marking information of the object. The reader/writer is used to write specific marking information into the memory of the electronic tag or read the marking information of the item from the storage area of the electronic tag, and exchange data with the electronic tag. The antenna is used to transmit and receive radio frequency signals to complete the data exchange between the electronic tag and the reader. The organization of the RFID framework is displayed in Figure 3.

Antenna used in conjunction with electronic tags and readers to transmit radio frequency signals between electronic tags and readers. Electronic labels, including coupling elements and chips, have a unique electronic code. Object-related information is stored in the encoding to identify the target object. Reader is a device that reads or writes tag information. Computer network is a RFID system that generally contains multiple readers. The reader should read the electronic tags of multiple objects and process the data. And it requires high real-time performance, so the data processing task is handed over to the computer network to complete.

**3.2.2. Sensor Technology.** In daily life, people use their senses to perceive information from the outside world. But the natural world is colorful and complex, and it is not enough to perceive information such as high temperature, radio

waves, speed, and electromagnetic radiation only by your own senses. Therefore, in order to perceive more information that people cannot perceive, sensors emerge as the times require. A sensor is a device that senses certain information and converts it into other forms of signals according to certain rules. Sensors can perceive information that humans cannot. They are extensions of the human sense organs. They are an important way to obtain various types of information and the primary link of automatic control [17].

(1) *Composition.* A sensor is a monitoring device that detects a test object. It converts it into an electrical signal or other desired signal form according to specific rules. The measured information can be various physical quantities, biomass, chemical quantities, or state quantities. The converted signal can be used for storage, display, recording, and inspection. Sensors convert the collected signals from one to another. This form is easy to identify and has certain information processing and conversion capabilities. The four components of the sensor are shown in Figure 4.

The sensitive element directly senses the element to be measured and generates a certain amount of the measured object. The conversion element converts the quantity output by the sensitive software into an electrical signal and does not directly perceive the measured object. The conversion circuit further converts the electrical signal output by the conversion element for easy recording, identification, and storage.

(2) *Classification.* There are a wide variety of sensors and a rich variety. The principles are different, and there are many classification methods. It is shown in Figure 5.

(3) *Wireless Sensor Network.* Wireless sensor network is composed of many sensor nodes, all of which are deployed in a monitoring area to form a multihop self-organizing network through wireless communication. The number of these sensor nodes is very large, the size is small, and they exist within a fixed range, which can be used to sense the information in the monitoring area and spread it out through wireless communication.

A wireless sensor network includes sensor nodes, sink nodes, and management nodes. Its structure is shown in Figure 6. Many sensor nodes are deployed in a certain area, and these sensor nodes form a network in a self-organizing manner. A sensor node collects data and transmits it to adjacent sensor nodes and then reaches the sink node. It is transmitted by the sink node to the management node, and the management node processes it and transmits it to the user.

3.2.3. *Data Mining.* The modern world is a data-based world with unlimited data sources. Very large datasets are stored in a central data warehouse. In recent years, methods for discovering new knowledge from raw data have exploded in order to extract valuable information from these giant datasets. Data mining methods and their applications have been widely studied [18, 19].

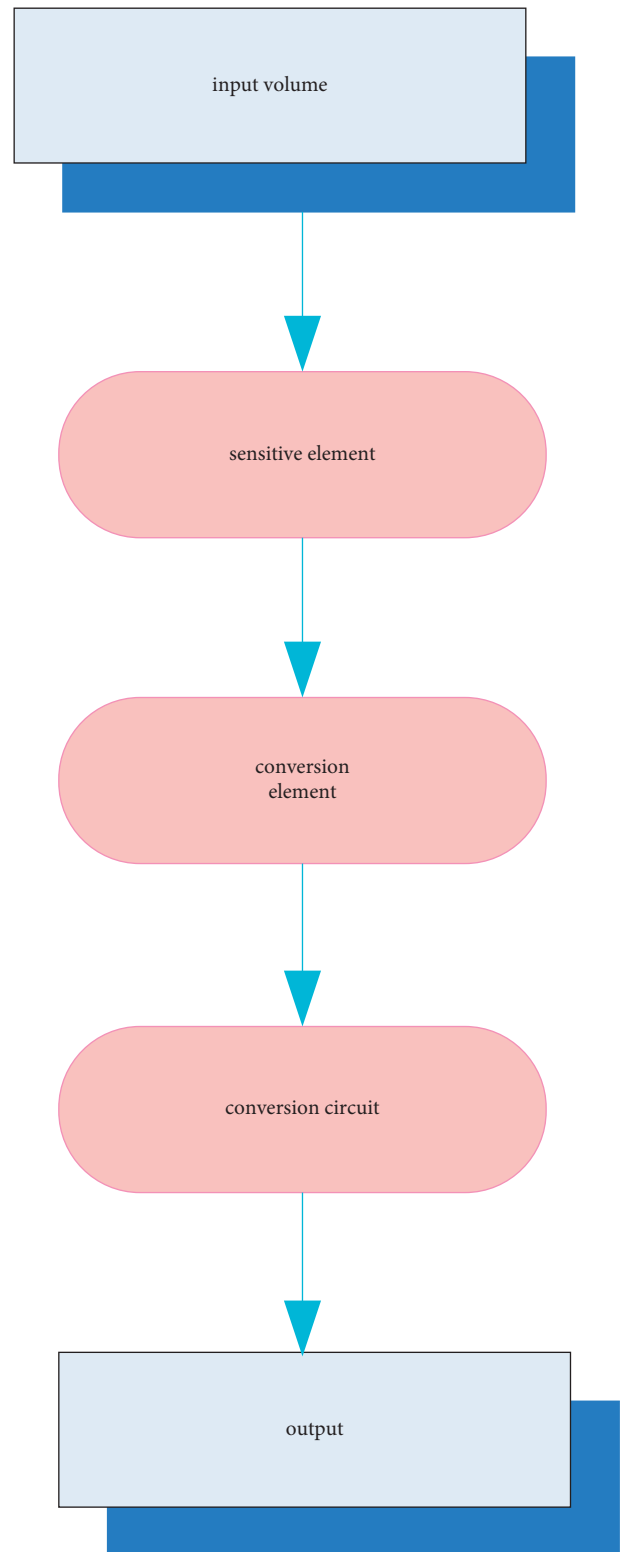


FIGURE 4: Composition of the sensor.

(1) *Association Analysis Method.* Association analysis method is a method of mining associated knowledge or information by discovering valuable attributes or association rules between items in a data warehouse. Its task is to reduce a large amount of incomprehensible, disordered data to a

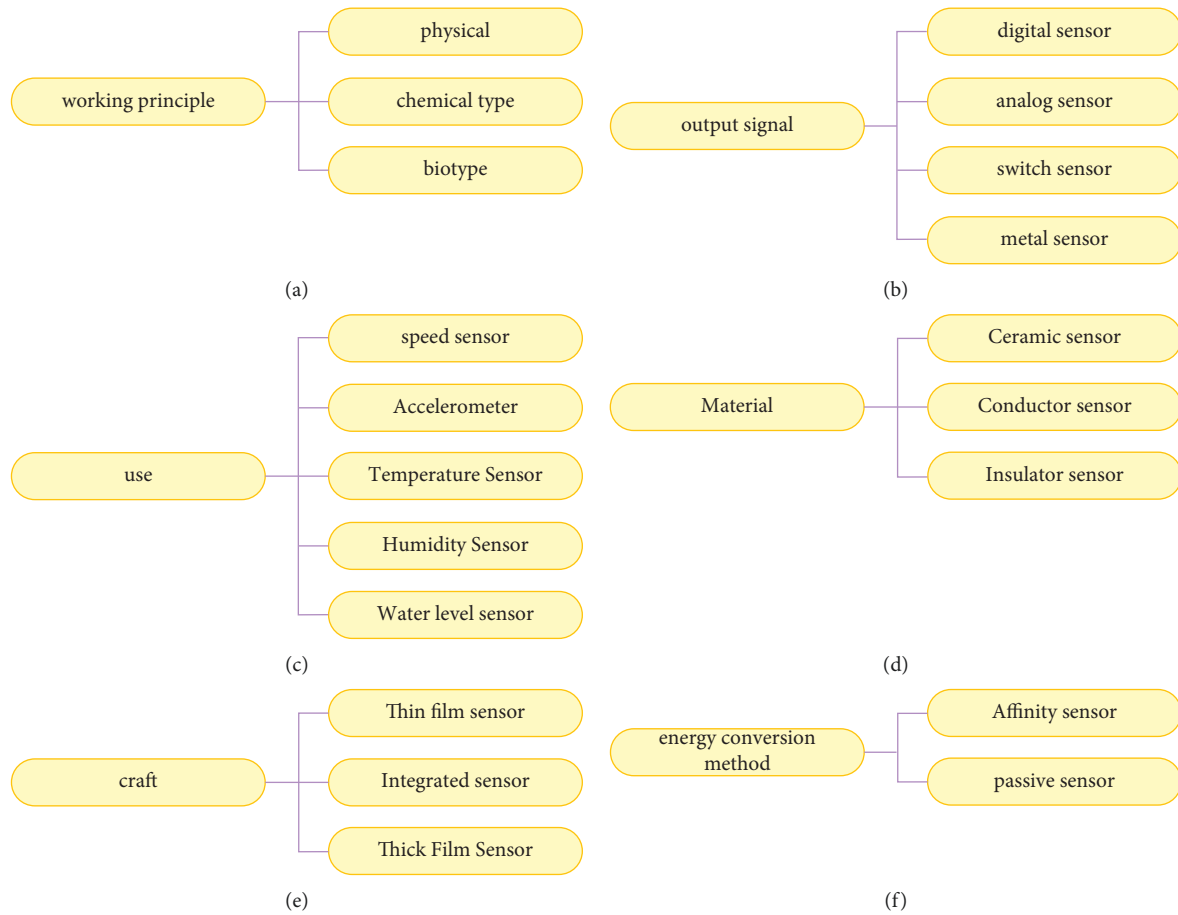


FIGURE 5: Classification of sensors.

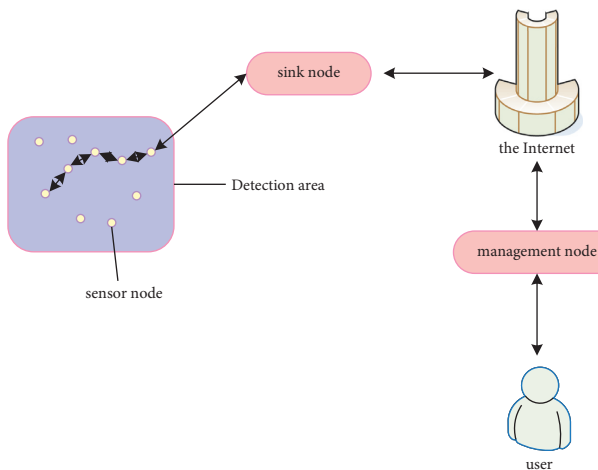


FIGURE 6: Wireless sensor network structure.

small amount of static data or information that is easy to observe and understand. The most classic example of the application of associative knowledge discovery in the business domain is shopping basket analysis. According to different classification standards, it has different

classification methods. And the algorithm it implements is not unique, as shown in Table 1.

The core of the Apriori algorithm is a recursive algorithm based on the idea of two-stage frequency sets, which belongs to single-dimensional, single-layer, and Boolean association rules. In order to improve the algorithm performance of Apriori algorithm, some researchers proposed an FP-growth algorithm based on FP tree to generate frequent itemsets.

(2) *Classification Method*. In the knowledge model of data mining, classification is a more important model. The classification analysis method is also a very necessary and effective analysis method. Among the classification tools of data mining, the function of decision tree sorting is more comprehensive. The main idea is to highlight the test data and sort it correctly [20]. Decision tree learning belongs to recursive learning, which generally adopts a top-down approach. From the root node, the attribute values are compared to determine how to branch downward. Then, the comparison of attribute values is continued at each internal node of the decision tree, and according to the judgment of attribute values, branches are constructed step by step downward, and finally, a conclusion is obtained at the leaf nodes of the tree. Each path is a conjunction rule, and all paths together constitute the entire decision tree. The

TABLE 1: Classification of association rules and comparison of implementation algorithms.

Classification criteria	Classification	Algorithm	Analyze
Level of abstraction	Single-level association rules and generalized association rules		Apriori algorithm is an algorithm for mining frequent itemsets of Boolean association rules, which belongs to single-dimensional and single-layer association rules; FP-growth algorithm is about an order of magnitude faster than Apriori algorithm; and Eclat algorithm adds the idea of inversion
Data dimension	Single-dimensional association rules and multidimensional association rules	Apriori algorithm, FP-growth algorithm, and Eclat algorithm	
The type of value handled	Boolean association rules and quantity association rules		

TABLE 2: Comparison of decision tree algorithms.

Decision tree algorithm	Analysis of algorithms	Use analytics
KNN method	The $K$ -nearest neighbor method is only related to a very small number of adjacent samples in the category decision, which can better avoid the problem of sample imbalance, but the amount of calculation is large.	It is suitable for the sample set to be divided with more overlapping or overlapping class domains.
Bayes method	A pattern classification method with known prior probabilities and class conditional probabilities. It is necessary to obtain the probability distribution of the category population and the probability distribution function (or density function) of various samples	The samples are required to be independent of each other, and the samples are large enough
Reverse KNN method	It can reduce the computational complexity of KNN algorithm and improve the efficiency of classification	It is suitable for automatic classification of the class domain with a relatively large sample size. If the sample size is small, it is easy to cause misclassification.
ID3 algorithm, C4.5, C5.0, and CART (classification regression tree)	Using divide and conquer strategy, ID3 algorithm is the representative of each algorithm, and other algorithms are improved based on its principle, and use information gain to find the attribute field with the most information in the database to establish the node of the decision tree.	It has the characteristics of simple description and fast classification speed, and is suitable for large-scale data processing.

decision tree algorithm is relatively mature, and its comparative analysis is shown in Table 2.

(3) *Neural Network Classification Learning*. As shown in Figure 7, it assumes that the input layer of the BP network has an input signal  $I$ , and the hidden layer consists of  $J$  neurons. Finally, there are  $K$  signals at the output level. The input of the neuron is denoted by  $v$ , and the output is denoted by  $u$ . The thresholds of neurons introduced into the hidden layer and output layer are  $x_0 = -1$  and  $y_0 = -1$ , respectively. It inputs vector  $X_k = (X_1, X_2, \dots, X_i, \dots, X_n)^D$ , and then, the output vector of the hidden layer corresponding to any training sample  $X_k = (X_1, X_2, \dots, X_i, \dots, X_n)^D$  is  $Y = (y_1, y_2, \dots, y_i, \dots, y_m)^D$ . The actual output is  $Q = (q_1, q_2, \dots, q_k, \dots, q_l)^D$ , while the expected output is  $p = (p_1, p_2, \dots, p_k, \dots, p_l)^D$ . The weight  $w_{ii}$  from the input layer to the hidden layer is the weight  $w_{ik}$  from the hidden layer to the output layer, and  $d$  is the number of repetitions of the learning process.

When  $X_k$  is used as an input sample to operate through the output layer, it can be obtained as follows:

For the hidden layer, there are

$$v_j^J = \sum_{i=0}^A w_{ij}^A x_{ni} \quad j = 1, 2, \dots, J, \quad (1)$$

$$u_j^J = f\left(\sum_{i=0}^I w_{ij}^I x_{ni}\right) \quad j = 1, 2, \dots, J.$$

For the output layer, there are

$$v_k^K = \sum_{j=0}^J w_{jk}^J x_j^J \quad k = 1, 2, \dots, K, \quad (2)$$

$$u_k^K = f\left(\sum_{j=0}^J w_{jk}^J x_j^J\right) \quad k = 1, 2, \dots, K.$$

From the above four equations, it can be obtained as follows:

$$y_{nk} = u_k^K = f(v_k^K) = f\left(\sum_{j=0}^J w_{jk}^J x_j^J\right) \quad k = 1, 2, \dots, K. \quad (3)$$

The above is the basic framework of the three-layer BP neural network.

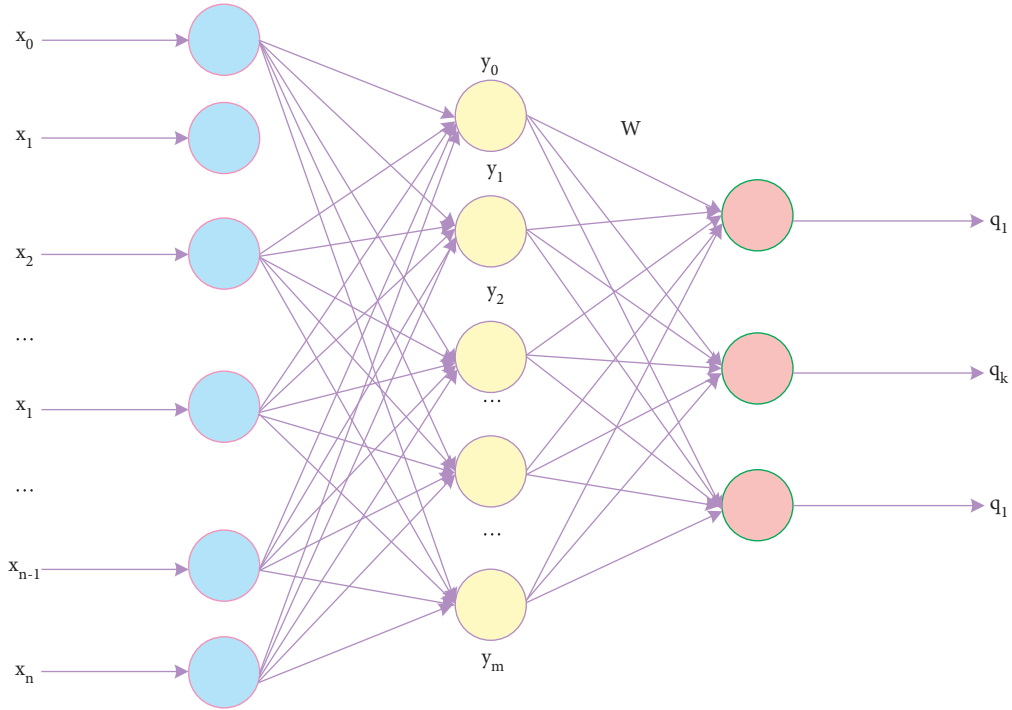


FIGURE 7: Three-layer BP network structure diagram.

The sum of error energies  $\theta$  results from the unequal relationship between the expected and actual outputs obtained during network operation

$$\theta(d) = \frac{1}{2} \sum_{k=1}^K (p_{nk} - q_{nk})^2. \quad (4)$$

It sets  $\theta_{nk}(d)$  to be the error signal obtained through the output layer during forward propagation

$$\theta_{nk}(d) = p_{nk}(d) - q_{nk}(d). \quad (5)$$

It propagates the error signal from the output stage to the input stage during the back-propagation of the error signal. It performs hierarchical adjustments to the network and modifies the network weights.

In order to gradually reduce the error, it must be corrected in the direction of the negative gradient of the weights. It was found that the weight correction amount  $\Delta w_{jk}$  is proportional to the negative tilt direction of the error, namely

$$\begin{aligned} \Delta w_{jk} &\propto -\frac{\Re \theta(d)}{\Re w_{jk}}, \\ \Delta w_{jk} &\propto -\frac{\Re \theta(d)}{\Re w_{ij}}. \end{aligned} \quad (6)$$

Because differentiable functions are transitive, it is obtained as follows:

$$\frac{\Re \theta(d)}{\Re w_{jk}} = \frac{\Re \theta(d)}{\Re \theta_{nk}(d)} \cdot \frac{\Re \theta_{nk}(d)}{\Re y_{nk}(d)} \cdot \frac{\Re y_{nk}(d)}{\Re v_k^K(d)} \cdot \frac{\Re v_k^K(d)}{\Re w_{jk}(d)}. \quad (7)$$

In

$$\frac{\Re E(d)}{\Re w_{jk}(d)} = \vartheta_{nk}(d),$$

$$\frac{\Re \vartheta_{nk}(d)}{\Re y_{nk}(d)} = \vartheta_{nk}(d),$$

$$\frac{\Re y_{nk}(d)}{\Re v_k^K(d)} = g'(v_k^K(d)),$$

$$\frac{\Re v_k^K(d)}{\Re w_{jk}(d)} = u_j^j.$$

(8)

Then

$$\frac{\Re \theta(d)}{\Re w_{jk}(d)} = -\vartheta_{nk}(d) \cdot g'(v_k^K(d)) \cdot u_j^j,$$

$$\eta_k^K = -\frac{\Re \theta(d)}{\Re v_k^K(d)}$$

$$= -\frac{\Re \theta(d)}{\Re u_k^K(d)} \cdot \frac{\Re v_k^K(d)}{\Re v_k^K(d)}$$

$$= g'(v_k^K(d))_{nk}(d).$$

(9)

So, there are

$$\vartheta_k^K = y_{nk}(d)(1 - y_{nk}(d)) \cdot \vartheta_{nk}(d)$$

$$= -y_{nk}(d)(1 - y_{nk}(d)) \cdot \vartheta_{nk}(p_{nk}(d) - q_{nk}(d)).$$

(10)



The correction of  $w_{jk}$  is

$$\begin{aligned} w_{jk} &= -\mu \frac{\aleph\theta(d)}{\aleph w_{jk}} \\ &= \mu \left( \frac{\aleph E(d)}{\aleph v_k^K(d)} \right) \cdot \frac{\aleph v_k^K(d)}{\aleph w_{jk}} \\ &= \mu \vartheta_k^K(d) \cdot u_k^K(d). \end{aligned} \quad (11)$$

In the next iteration, the weight of any node from hidden layer  $J$  to output plane  $K$  is

$$w_{jk}(d+1) = w_{jk}(d) + \Delta w_{jk}(d). \quad (12)$$

The weight correction value from the input layer to the hidden layer is similar to the above adjustment method, as follows:

$$\begin{aligned} \frac{\aleph\theta(d)}{\aleph w_{ij}(d)} &= \frac{\aleph\theta(d)}{\aleph v_j^J(d)} \cdot \frac{\aleph v_j^J(d)}{\aleph w_{ij}(d)} \\ &= \frac{\aleph\theta(d)}{\aleph v_j^J(d)} \cdot x_{ni}(d). \end{aligned} \quad (13)$$

It sets the local gradient

$$\begin{aligned} \eta_j^J &= \frac{\aleph\theta(d)}{\aleph v_j^J(d)} \\ &= \frac{\aleph\theta(d)}{\aleph u_j^J(d)} \cdot \frac{\aleph v_j^J(d)}{\aleph v_j^J(d)}. \end{aligned} \quad (14)$$

In

$$\frac{\aleph u_j^J(d)}{\aleph v_j^J(d)} = g'(v_j^J(d)). \quad (15)$$

For

$$\theta(k) = \frac{1}{2} \sum_{k=1}^K \vartheta_{nk}^2(d). \quad (16)$$

So

$$\begin{aligned} \frac{\aleph\theta(d)}{\aleph u_j^J(d)} &= \sum_{k=1}^K \vartheta_{nk}(d) \cdot \frac{\aleph\vartheta_{nk}(d)}{\aleph u_b^B(d)} \\ &= \sum_{k=1}^K \vartheta_{nk}(d) \cdot \frac{\aleph\vartheta_{nk}(d)}{\aleph u_k^K(d)}(d) \cdot \frac{\aleph u_k^K(d)}{\aleph u_j^J(d)}. \end{aligned} \quad (17)$$

**3.3. Problematic Internet Use.** The definition of problem Internet use has evolved from Internet addiction to pathological Internet use and problem Internet use. While the definitions and nomenclature of such behaviors are not identical, the definition of such behaviors includes behaviors that are most typically problematic with Internet use. Under

TABLE 3: Age, gender, and professional distribution of the tested.

Group	Grade		Profession		Total
	Male	Female	Science	Liberal arts	
Freshman	118	136	134	120	254
Sophomore	124	152	167	109	276
Junior year	112	140	155	97	252
Senior year	132	86	143	75	218
Group	486	514	599	401	1000

the influence of nonaddictive substances, people use the Internet excessively. Internet addiction can cause people to sit in front of a computer or use a cell phone for long periods of time. This behavior can lead to decreased vision, shoulder and back muscle strain, disturbed sleep rhythms, decreased appetite, indigestion, and decreased immune function. Although they did not swallow any addictive substances, the problem netizens lived in poor living conditions due to excessive Internet addiction. For example, their lives are not healthy. Some people may spend a lot of time on the Internet and indulge in Internet fantasies. This can lead to a reduction in their social activities in real life and cause some people to experience problems such as carelessness at work and study. On the other hand, problematic Internet users face some emotional problems such as depression and anxiety. Individuals may experience symptoms such as insomnia and irritability. Therefore, it is very important to study the psychological factors that influence individuals' problem behaviors when using the Internet.

## 4. Psychological Mechanism and Exercise Intervention Experiment of College Students' Problematic Internet Use

### 4.1. Questionnaire Survey on Internet Addiction among College Students

**4.1.1. Research Objects.** The subjects of the study were college students in a university, and a total of 1000 questionnaires were distributed. Because it is an on-site investigation, the effective rate is 100%. There were 486 boys and 514 girls. The distribution of grades and genders is shown in Table 3.

**4.1.2. Statistical Tools.** SPSS13.0 is used for data analysis and processing,  $t$ -test, variance analysis and  $\chi^2$  test, correlation analysis, regression analysis, etc.

### 4.2. Questionnaire Survey Results

**4.2.1. Analysis of Gender, Grade, and Major Differences.** Among the college students, there is a significant correlation between gender and Internet addiction (as shown in Figure 8(a)) ( $\chi^2 = 21.20$ ,  $P < 0.001$ ). The probability of male college students in the survey sample is 10.29% (50 people), and the probability of female college students is 3.89% (20 people). Male college students are significantly more than female college students, indicating that boys are more prone

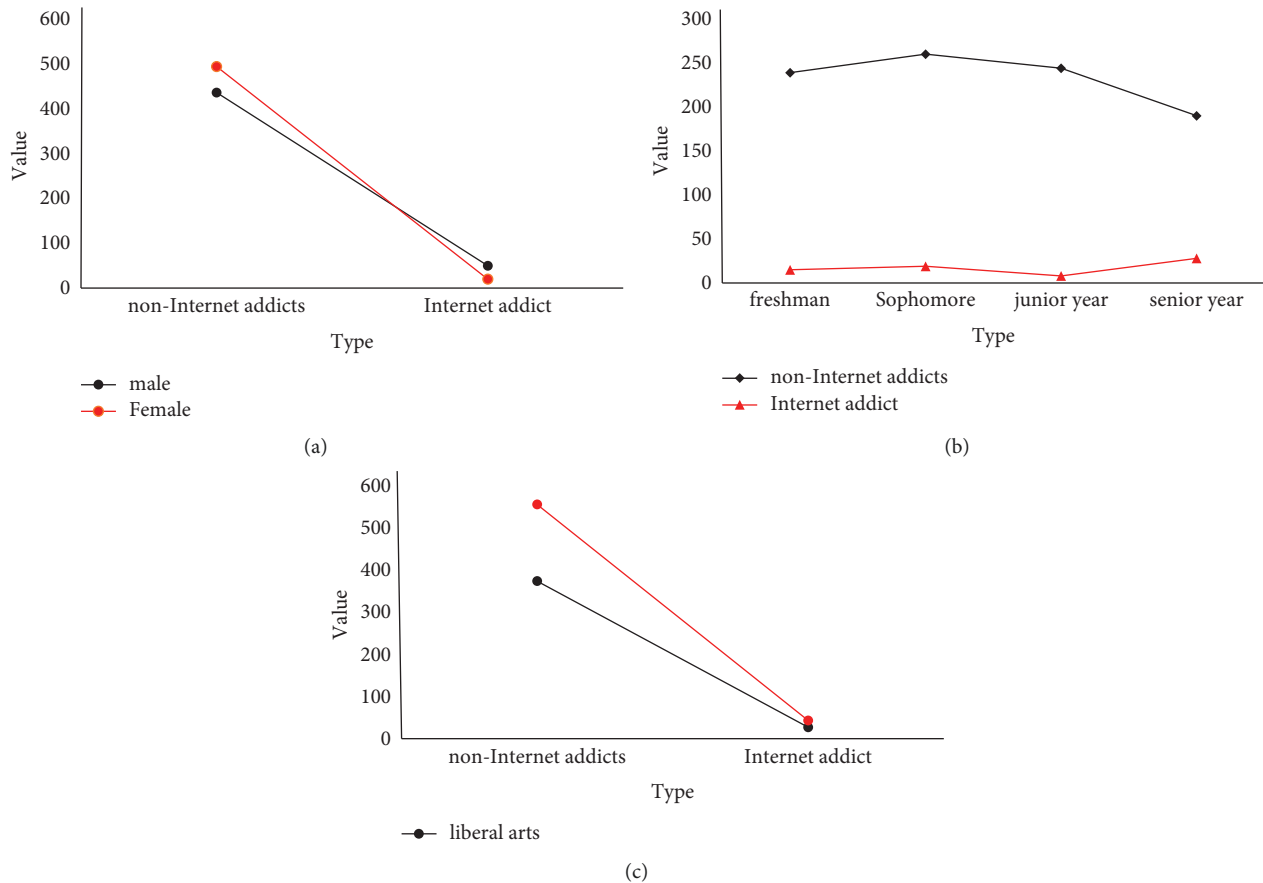


FIGURE 8: Comparison of gender, grade, and major differences. (a) Comparison of differences in the incidence of Internet addiction among college students of different genders. (b) Comparison of differences in the incidence of Internet addiction among college students of different ages. (c) Comparison of differences in the incidence of Internet addiction among college students with different majors.

to Internet addiction problems. The analysis of the degree of addiction of students with Internet addiction showed that the average score of boys was higher than that of girls, reaching a significant level ( $t = 3.35$ ,  $P < 0.05$ ).

Among college students, there was a significant correlation between grade and Internet addiction in the research on the probability of occurrence of Internet addiction (as shown in Figure 8(b)) ( $\chi^2 = 27.30$ ,  $P < 0.001$ ). The detection rate of freshmen was 5.90% (15 people), 6.88% (19 people), 3.17% (8 people) in the third grade, and 12.84% (28 people) in the fourth grade. There is a trend of significantly higher addiction rates in graduating grades. In the degree of Internet addiction, with the increase of grade, the degree of addiction also deepened, but it did not reach a significant level ( $F = 1.50$ ,  $P > 0.05$ ).

Among the college students, in the research on the probability of occurrence of Internet addiction, there was a significant uncorrelation between major and Internet addiction (as shown in Figure 8(c)) ( $\chi^2 = 0.81$ ,  $P > 0.05$ ). The detection rate of science students was 7.18% (43 people), and the detection rate of liberal arts students was 6.73% (27 people). The incidence rate of science students was higher than that of liberal arts students, but it did not reach a significant level. Taking major as a variable, the degree of Internet addiction of college students was analyzed. The

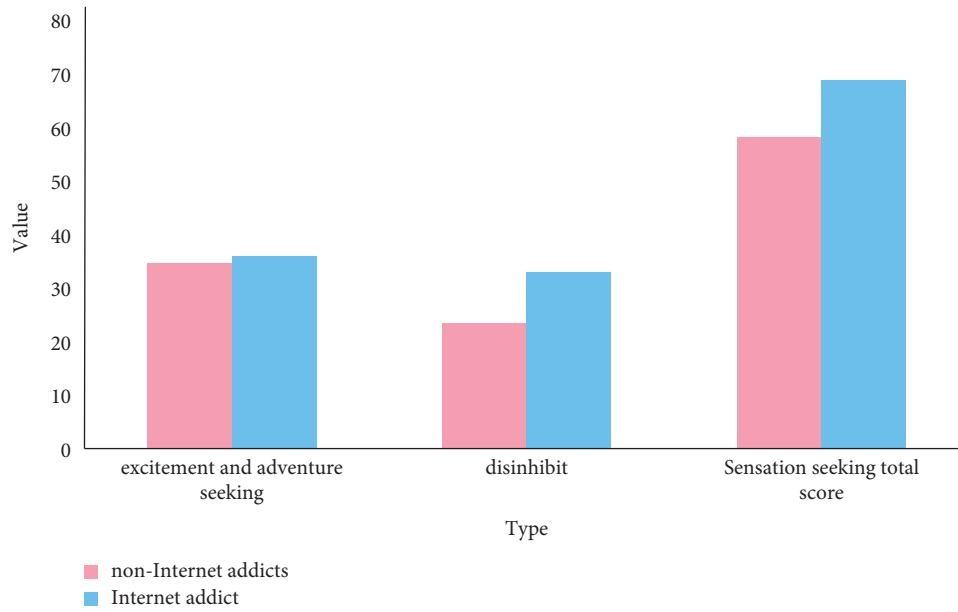
degree of addiction of science students was significantly higher than that of liberal arts students, and the difference between the average levels reached a significant level ( $t = 5.41$ ,  $P < 0.05$ ).

**4.2.2. Analysis of Family Differences.** In the college student population, there is a significant correlation between family economic environment and Internet addiction in the research on the probability of occurrence of Internet addiction (as shown in Table 4 for details,  $\chi^2 = 10.10$ ,  $P < 0.05$ ). The probability of occurrence of household annual income of less than 3,000 yuan is 7.87% (17 people), the probability of occurrence of economic income between 3,000 and 10,000 is 11.17% (23 people), and the probability of occurrence of 10,000–30,000 yuan is 3.09% (12 people), and the detection rate of more than 30,000 people was 9.47% (18 people). Children from upper-middle-income families have the lowest addiction rate, and children from high-income families have the highest Internet addiction rate.

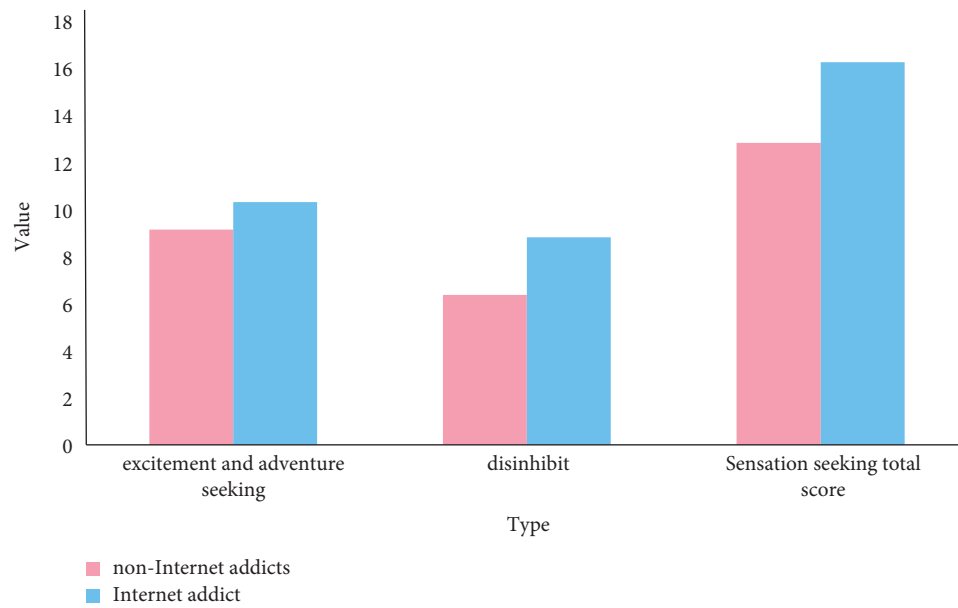
Among the college students, the probability of occurrence of Internet addiction was studied, whether there was a significant relationship between single-parent families and Internet addiction (as shown in Table 4) ( $\chi^2 = 19.28$ ,  $P < 0.001$ ). The detection rate of Internet addiction among

TABLE 4: Comparison of differences in the incidence of Internet addiction among college students affected by family factors.

Research variables	Classification	Non-Internet addicts (%)	Internet addicts (%)	Total	$\chi^2$	$P$
Annual household income (yuan)	Less than 3000	199 (92.13%)	17 (7.87%)	216	10.10	0.015
	3,000 to 10,000	183 (88.83%)	23 (11.17%)	206		
	10,000 to 30,000	376 (96.91%)	12 (3.09%)	388		
	More than 30,000	172 (90.53%)	18 (9.47%)	190		
Single-parent family	Yes	63 (80.77%)	15 (19.23%)	78	19.28	0.02
	No	871 (94.06%)	55 (5.94%)	926		



(a)



(b)

FIGURE 9: Differences in sensory seeking between the two groups. (a) Mean differences in sensory seeking between the two groups. (b) Differences in sensory seeking SD between the two groups.

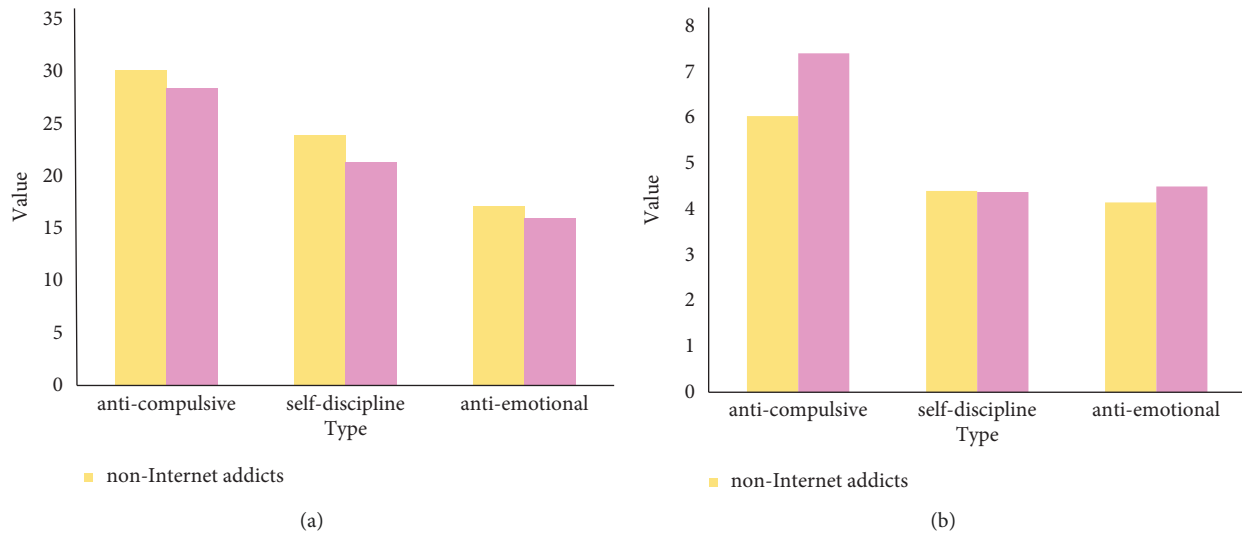


FIGURE 10: Difference test of self-control between the two groups. (a) Mean differences in self-control between the two groups. (b) SD difference between the two groups in self-control.

students from single-parent families was 19.23% (15 people), and the incidence of Internet addiction among non-single-parent college students was 5.94% (55 people), indicating that students from single-parent families were more prone to Internet addiction problems.

**4.2.3. Difference Tests between Two Groups in Different Dimensions.** The tactile inquiry contrast test between the Internet habit bunch and the nonenslavement bunch is displayed in Figure 9. The disinhibition score and complete score of tactile looking for in the Internet dependence bunch were essentially higher than those in the non-Internet enslavement bunch ( $t = 13.10$ ,  $t = 7.31$ ,  $P < 0.001$ ); there was no tremendous contrast between the scores of fervor and experience looking for between the Internet habit bunch and the nonfixation bunch ( $t = 1.12$ ,  $P > 0.05$ ).

The difference test of self-control between the two groups is shown in Figure 10. The anticompulsion, self-discipline, anti-emotional scores, and total scores of self-control in the Internet addiction group were significantly lower than those in the non-Internet addiction group ( $t = -2.49$ ,  $t = -5.02$ ,  $t = -2.74$ ,  $P < 0.001$ ).

**4.3. Exercise Intervention for College Students with Internet Addiction.** The use of sports to intervene in Internet addiction should specifically analyze the specific causes of Internet addiction among addicted students, and select corresponding exercise programs. The intensity, time, frequency, and other exercise prescriptions should be determined according to the specific reasons. College students are willing to look online for their interpersonal and self-actualization needs. Basketball can improve the negative reactions and psychological state of netizens. Badminton is accompanied by an increase in blood flow and oxygen intake, which has a good effect on the central nervous system, stimuli, and nervous system, resulting in positive and

antidepressant effects in the mood of Internet-addicted students. Depending on the cause of the addiction, individuals performed alternative exercise three times a week for 0.5 to 2 hours each. For those who are addicted to the Internet due to lack of communication with others, we organize regular, collaborative team sports; for those who are not confident, we organize sports for athletes whose learning is challenging; timed sports or competitions were organized for athletes who could not control their time; those who were bored were assigned a more interesting exercise program for 18 weeks.

The results show that exercise intervention has a good effect on correcting students' Internet addiction, but it is better to choose an appropriate exercise program according to the specific cause of the addiction. Regardless of the cause of Internet addiction, the stimulation of the human body by intermittent high-intensity exercise will immediately stimulate the practitioner's right brain and enter into a pleasant atmosphere. At the same time, increased blood flow and oxygen intake during exercise stimulate the central nervous system, thereby promoting the formation of positive emotions and expectations in Internet addicts. Exercise can strengthen achievement incentives, correct psychological barriers, improve physical and mental health, and achieve the purpose of getting rid of Internet addiction.

The current sports intervention research on Internet addiction students mainly uses aerobic sports badminton, basketball, and volleyball (including games, training, and competitions). The target heart rate is maintained at 130~150 minutes/minute, 40~60 minutes/time, 3 times a week, plus 55%~65% of the maximum force, 8~12 times per set. According to the strength training cycle of different functional equipment, a total of 3 groups, each 30~40 minutes, exercise twice a week for Internet addiction students prescribed intervention research. The results showed that the Internet addiction among college students improved in all aspects, and the body composition indicators of the

intervention subjects also changed. Therefore, exercise prescription has a good effect on college students who rely on the Internet to get rid of Internet addiction and obtain a reasonable body composition. On this basis, high-intensity intermittent exercise was used 3 times a week for 8 weeks to intervene students with Internet addiction. Each workout consists of a 10-minute warm-up, 30 minutes of high-intensity intervals, and a 10-minute cooldown. Among them, high-intensity interval training consists of 10 cycles, and each cycle includes 1 minute of corridor high-intensity exercise and 2 minutes of interval exercise. Operation on the runway requires an operating speed of 7.5 to 9.3 km/h and an inclination of 10%. The results show that high-intensity interval exercise intervention has a good effect on the withdrawal of Internet addiction among college students.

## 5. Discussion

First of all, through the study of relevant knowledge points in literature works, this paper has initially mastered the basic knowledge related to problematic Internet use and analyzed how to research the psychological mechanism and exercise intervention of college students' problem Internet addiction based on the Internet of Things technology. It expounds the technical concepts and algorithms of the Internet of Things, studies sensor technology, explores data mining, and analyzes the applicability of exercise intervention in the psychological mechanism of college students' problematic Internet use through experiments.

The development of the Internet has changed the way people receive information and understand the world. The advent of smartphones has brought great changes to people's way of life. The way people use the Internet has also shifted from computers to mobile devices, a feature of multiple access. With the increasingly rich network functions and the increasing convenience of the network, the psychological characteristics of network users have also undergone corresponding changes.

Through experimental analysis, this paper shows that moderate-intensity (50%~80%  $\text{VO}_2$  max) aerobic and anaerobic exercise, more than 30 minutes each time, has a positive corrective effect on Internet addiction symptoms. It is better to select appropriate intervention studies. Internet addiction exercise programs for different reasons are more effective, but there are few studies on this aspect. Therefore, future research should further select intervention objects to achieve multiplier effect with half the effort.

## 6. Conclusions

The problem of Internet addiction among college students has long appeared and has shown a rapid development momentum and bad influence, which has aroused extensive attention from all walks of life. Different scholars have discussed the causes of college students' Internet game addiction from various disciplinary perspectives, and a large number of attempts have emerged for the prevention and treatment of college students' Internet addiction, and the main results are concentrated in the fields of medicine and

psychology. A large number of Internet addiction treatment centers have sprung up like mushrooms after a spring rain, and they are making a lot of money. From a medical perspective, it is believed that the treatment of Internet addiction must be drug therapy or even physical therapy such as electric shock; from the perspective of psychology, Internet addiction is considered to be a mental disease, and psychological counseling is advocated to solve it. In fact, Internet addiction of college students is a complex social problem, which is caused by a combination of factors.

## Data Availability

Data will be available on request.

## Conflicts of Interest

The authors declare that they have no conflicts of interest.

## References

- [1] P. Gómez, S. K. Harris, C. Barreiro, M. Isorna, and A. Rial, "Profiles of Internet use and parental involvement, and rates of online risks and problematic Internet use among Spanish adolescents," *Computers in Human Behavior*, vol. 75, pp. 826–833, 2017.
- [2] O. S. Ilesanmi, P. O. Akosile, A. A. Afolabi, and V. O. Ukwenya, "Handling distrust on risk communication in Nigeria: a strategy to strengthening the COVID-19 outbreak response," *Disaster Medicine and Public Health Preparedness*, vol. 27, no. 1, pp. 1–22, 2021.
- [3] T. Rosenkranz, K. W. Müller, M. Dreier, M. E. Beutel, and K. Wölfling, "Addictive potential of internet applications and differential correlates of problematic use in internet Gamers versus generalized internet users in a representative sample of adolescents," *European Addiction Research*, vol. 23, no. 3, pp. 148–156, 2017.
- [4] A. Rooij, C. J. Ferguson, D. Mheen, and T. M. Schoenmakers, "Time to abandon Internet Addiction? Predicting problematic internet, game, and social media use from psychosocial well-being and application use," *Clinical Neuropsychiatry*, vol. 14, no. 1, pp. 113–121, 2017.
- [5] F. Canan, S. Karaca, M. Düzgün et al., "The relationship between second-to-fourth digit (2D:4D) ratios and problematic and pathological Internet use among Turkish university students," *Journal of Behavioral Addictions*, vol. 6, no. 1, pp. 30–41, 2017.
- [6] S. Laconi, K. Kaliszewska-Czeremska, A. Gnisci et al., "Cross-cultural study of problematic internet use in nine European countries," *Computers in Human Behavior*, vol. 84, pp. 430–440, 2018.
- [7] J.-B. Li, J. T. F. Lau, P. K. H. Mo et al., "Insomnia partially mediated the association between problematic Internet use and depression among secondary school students in China," *Journal of Behavioral Addictions*, vol. 6, no. 4, pp. 554–563, 2017.
- [8] A. Peker, S. Cengiz, and M. Nebioğlu Yıldız, "The mediation relationship between life satisfaction and subjective vitality fear of COVID-19 and problematic internet use (tur)," *Journal of Clinical Psychiatry*, vol. 24, no. 2, pp. 199–206, 2021.
- [9] I. Reiner, A. N. Tibubos, J. Hardt, K Müller, K Wölfling, and M. E Beutel, "Peer attachment, specific patterns of internet use and problematic internet use in male and female adolescents,"

- European Child & Adolescent Psychiatry*, vol. 26, no. 10, pp. 1257–1268, 2017.
- [10] T. Marci, C. Marino, C. Sacchi, X. Lan, and M. M. Spada, “Problematic Internet Use in early adolescence: the role of attachment and negative beliefs about worry,” *Journal of Behavioral Addictions*, vol. 10, no. 1, pp. 194–200, 2021.
- [11] S. A. Khalil, H. Kamal, and H. Elkholy, “The prevalence of problematic internet use among a sample of Egyptian adolescents and its psychiatric comorbidities,” *International Journal of Social Psychiatry*, vol. 68, no. 2, pp. 294–300, 2022.
- [12] M. Boniel-Nissim and H. Sasson, “Bullying victimization and poor relationships with parents as risk factors of problematic internet use in adolescence,” *Computers in Human Behavior*, vol. 88, pp. 176–183, 2018.
- [13] H. Alheneidi, L. Alsumait, D. Alsumait, and A. P. Smith, “Loneliness and problematic internet use during COVID-19 lock-down[J],” *Behavioral Science*, vol. 11, no. 5, pp. 1–11, 2021.
- [14] C. Buzzai, P. Filippello, S. Costa, V. Amato, and L. Sorrenti, “Problematic internet use and academic achievement: a focus on interpersonal behaviours and academic engagement,” *Social Psychology of Education*, vol. 24, no. 1, pp. 95–118, 2021.
- [15] S. Feijóo, M. Foody, J. O’Higgins Norman, R. Pichel, and A. Rial, “Cyberbullies, the cyberbullied, and problematic internet use: some reasonable similarities,” *Psicothema*, vol. 33, no. 2, pp. 198–205, 2021.
- [16] H. Morioka, O. Itani, Y. Osaki et al., “The association between alcohol use and problematic internet use: a large-scale nationwide cross-sectional study of adolescents in Japan,” *Journal of Epidemiology*, vol. 27, no. 3, pp. 107–111, 2017.
- [17] S. Park and Y. Lee, “Associations of body weight perception and weight control behaviors with problematic internet use among Korean adolescents,” *Psychiatry Research*, vol. 251, pp. 275–280, 2017.
- [18] S. Laconi, M. Vigouroux, C. Lafuente, and H. Chabrol, “Problematic internet use, psychopathology, personality, defense and coping,” *Computers in Human Behavior*, vol. 73, no. Aug, pp. 47–54, 2017.
- [19] Y. Natanael, “Analisis rasch model Indonesia problematic internet use scale (IPIUS),” *Persona:Jurnal Psikologi Indonesia*, vol. 10, no. 1, pp. 167–186, 2021.
- [20] B. Koronczai, G. Kökönyei, R. Urbán et al., “Confirmation of the Chinese version of the problematic internet use questionnaire short form (PIUQ-SF),” *International Journal of Mental Health and Addiction*, vol. 15, no. 1, pp. 191–197, 2017.

## Research Article

# Fault Diagnosis Using Data Fusion with Ensemble Deep Learning Technique in IIoT

**S. Venkatasubramanian,<sup>1</sup> S. Raja,<sup>2</sup> V. Sumanth,<sup>3</sup> Jaiprakash Narain Dwivedi ,<sup>4</sup>  
J. Sathiaparkavi,<sup>5</sup> Santanu Modak,<sup>6</sup> and Mandefro Legesse Kejela <sup>7</sup>**

<sup>1</sup>Department of Computer Science Engineering, Saranathan College of Engineering, Trichy 620012, Tamilnadu, India

<sup>2</sup>School of Mechanical Engineering, Vellore Institute of Technology, Vellore 632004, Tamilnadu, India

<sup>3</sup>Department of Computer Science Engineering, Presidency University, Bengaluru 560064, Karnataka, India

<sup>4</sup>Department of Electronics & Communication Engineering, Lingayas Vidyapeeth, Faridbad 121002, India

<sup>5</sup>Department of Computer Science Engineering, Saranathan College of Engineering, Trichy 620012, Tamilnadu, India

<sup>6</sup>Department of Computer Science, Asutosh College, West Bengal 700026, India

<sup>7</sup>Department of Computer Science Engineering, Ambo University, Ambo, Ethiopia

Correspondence should be addressed to Mandefro Legesse Kejela; [mandefro.legesse@ambou.edu.et](mailto:mandefro.legesse@ambou.edu.et)

Received 18 April 2022; Accepted 28 May 2022; Published 14 June 2022

Academic Editor: Punit Gupta

Copyright © 2022 S. Venkatasubramanian et al. This is an open access article distributed under the Creative Commons Attribution License, which permits unrestricted use, distribution, and reproduction in any medium, provided the original work is properly cited.

Detecting the breakdown of industrial IoT devices is a major challenge. Despite these challenges, real-time sensor data from the industrial internet of things (IIoT) present several advantages, such as the ability to monitor and respond to events in real time. Sensor statistics from the IIoT can be processed, fused with other data sources, and used for rapid decision-making. The study also discusses how to manage denoising, missing data imputation, and outlier discovery using preprocessing. After that, data fusion techniques like the direct fusion technique are used to combine the cleaned sensor data. Fault detection in the IIoT can be accomplished by using a variety of deep learning models such as PropensityNet, deep neural network (DNN), and convolution neural networks-long short term memory network (CNS-LSTM). According to various outcomes, the suggested model is tested with Case Western Reserve University (CWRU) data. The results suggest that the method is viable and has a good level of accuracy and efficiency.

## 1. Introduction

Connected gadgets are commonplace in the IoT, a computing paradigm that relies on ubiquitous Internet connectivity. These smart things can sense their surroundings, transmit, and analyze the data they collect from the environment and then return relevant details to their surroundings in a form that can be understood by humans. M2M technologies with applications in the automation industry make up a subset of the IIoT, which is a subset of the IoT. Improved production efficiency and long-term viability are two key benefits of the IIoT's [1, 2] introduction to the industry. For Industry 4.0, which is enabled by the integration of cloud technologies and cyber systems, a wide

range of sensors are being installed around the industrial operational situation and tackled. Proactive maintenance and a reduction in unplanned downtime can be achieved by the use of [3–7] data analysis technologies.

If some measures are missing owing to network or hardware subjects in the IIoT, then we must have a working mechanism in place. The problem of value imputation becomes crucial when sensor data contain many missing values. High-frequency data collection results in large gaps between data points, and all measurements taken during that period are lost if the network goes down. When data are missing [8], it could be because of a sensor failure or a network failure, or because hackers have removed data with malicious intent while it is being collected, processed, stored,

or sent. Filling in the missing values is a related research challenge that must be addressed to ensure that the imputed values are as close as feasible to the genuine values to analyze the data. The data collected are so diverse that to deal with missing data in IoT systems, the methodologies created must be able to provide a high level of confidence for various applications and endure the expanding deployments in the IoT (and IIoT) space. Additionally, real-time IoT application requirements require light-weight solutions [9].

Only data imputation, anomaly detection, and fault classification have been documented in the literature so far. Because each strategy may be maximized individually in this study, we can increase the monitoring system's overall performance by integrating all three techniques. There are three primary objectives for sensor networks in the IIoT, one being extracting relevant information for decision making [10, 11].

In the raw sensor data provided by IIoT sensors, there are a lot of unnecessary and uncleaned data. Consequently, to get any meaningful information from the cleaned IoT sensor data, the raw sensor data must be cleaned [12, 13]. A constrained IoT sensor network can also lead to high computational expenses and overuse of resources because of the vast amount of unwanted and worthless data [14–16].

## 2. Related Works

For chiller malfunction detection systems, Srinivasan et al. [15] showed the rank of understandable AI (XAI). One-dimensional convolutional neural networks (CNNs) were created by Li et al. [16] for defect identification in HVAC systems. Other M&E service systems have data-driven FDD approaches proposed in addition to the interpretability research for HVAC systems. Defect detection in sewerage systems was pioneered by Kumar et al. [17]. For picture object detection, the deep learning assembly trusts the CNN. In comparison to other machine learning (ML) techniques, the image processing skill employing the CNN is more understandable by experts. Gonzalez-Jimenez et al. [18] evaluated the existing fault diagnosis methods for electrical energies and re-examined the general process utilizing ML practices for electric drive fault detection. The lack of specific events in each electric drive is a major shortcoming of the data-driven FDD technique [18].

A microgrid's energy management system was studied by Marquez et al. [19], who used a fault detection and reconfiguration process. A reconfiguration block received fault information through acquiring residuals. Microgrid fault detection is all discussed in Morato et al. [20]. For early wind turbine breakdown detection, Ruiming et al. [21] proposed combining SCADA data and a dynamic network marker. Radial basis functions with two input parameters were used by Hussain et al. [22] to detect faults in solar systems [22]. Most solar energy applications are concerned with fault discovery in solar systems rather than fault diagnosis in solar power facilities. To better anticipate solar hot water system performance under various weather circumstances [23, 24], multiple deep learning models have been

constructed to look for deviations between predictions and observations.

A significant advantage over prior approaches is the ability to isolate problems with the collectors' optical efficiency, flow rate, and thermal losses. In contrast to optical efficiency problems, which are caused by dirty or externally imposed collectors, deteriorating, breaking down, corroding, or otherwise degrading, problems with flow rate are caused by a loop that is out of balance, relative to the rest of the plant [25]. Assuming, as is the case in most real plants, that the only flow meter for the whole system is situated at the pump, and that thermal losses are caused by dirt, wear, insulation failures, and pipe breakage. However, the temperature reduction could be caused by an incorrect reading of the loop flow rate or by a broken pipe. Since the treatment for each case is different, it is important to know where the problem is to fix it quickly. Since a flow meter replacement is costly, it should only be done when there is confidence that this is the faulty component.

## 3. Proposed System

Consistently or in response to an external incident, IIoT sensors generate data. The other phase involves the collection, aggregation, analysis, and visualization of data generated by sensor nodes. This information is subsequently translated into a form that can be communicated as a response to an external stimulus. Data from IIoT sensors have the following notable properties:

**Technical constraints:** the sensor's small size imposes limitations on the sensor's computer power, storage capacity, and memory. Consequently, sensor data may be lost or incorrect information may be obtained if these devices are attacked or fail to operate.

**Real-time processing:** in future, the sensor network will be able to execute increasingly complicated networking activities and perform real-time data transformations from raw sensor data.

**Scalability:** the sensor network in the real world is made up of a variety of sensors and actuators. As the number of sensors and actuators continues to expand, the need for scalable sensor networks that can handle the increasing volume of data expands too.

**Data representation:** sensor data are often stored in the form of a tiny tuple containing structured information. Sensor data can be represented in a variety of ways, including Boolean, binary, featured, continuous, and numeric.

**Heterogeneity:** there is a wide range of data from IIoT sensors from rigorously formatted datasets to real-time information systems.

**3.1. Denoising.** IIoT networks create a lot of sensor data, which need to be analyzed and used for real-time decision-making. Sensor data have a wide range of features, including high velocities, large volumes, and a wide range of dynamic



values and type values. They pollute and complicate decision-making in real time, as the sensor data are being collected and analyzed. Unwanted changes and modifications to the signal's original vectors are caused by noise, an uncorrelated signal component. To process and utilize the unusable data, resources are wasted because of the noise characteristic. It is possible to accurately characterize the signal using wavelet transform methods and to solve the problem of signal estimation using these methods. By reducing the signal's noise, the wavelet transformation keeps the original signal coefficients intact. This is accomplished through the use of a thresholding approach that is optimized for low-coefficient noise signals. To analyze and synthesize continuous-time signal energy, wavelet transformation is widely used.

To express the signal energy, we can use  $e(t), t - R$ .

$$|e|^2 = \int_{-\infty}^{\infty} |e(t)|^2 dt < \infty. \quad (1)$$

In (1), it must be within the squared search space L2 for the signal energy  $e(t)$  to satisfy the requirement (R). Analysis of discrete-time signal energy can also be done using the wavelet transformation.

**3.2. Missing Data Imputation.** When dealing with missing data, imputation is a necessary preprocessing step [26]. Various sectors and fields such as smart cities, healthcare, GPS, and smart transportation rely heavily on data generated by the internet of things (IoT). Algorithms for analyzing IIoT data typically presume that the data are completed before beginning their analysis. IoT data that are partial or missing can give unreliable results because of the data analytics conducted on that data. For the IIoT, an estimation of the missing value is required. As a first step, three things must be done. Identifying the cause of missing data is a critical first step. This is a result of poor network connectivity and defective sensor systems as well as environmental conditions and synchronization challenges. Data that are entirely missing at random (MCAR) are the most common sort of missing data, which is also the most difficult to find (NMAR). The next step is to look at the patterns of data that are missing. A random missing pattern is RMP and a monotonous missing pattern is AMP. As the last step, they create an IIoT for the missing datasets.

**3.3. Data Outlier Detection.** Sensor nodes in the IIoT sensor network are extensively dispersed and diverse. Note that, in a real-world physical context, such a design leads to significant sensor node failure and danger owing to a variety of outside influences. As a result, the IIoT sensor network's original data are vulnerable to manipulation, leading to data outliers [27]. Data outliers must be identified before data analysis or decision-making may take place.

Voting mechanism: an aberrant sensor node can be recognized in this manner through the comparison of its readings with those of neighboring sensors. According to Shahraki et al. [28], using a Poisson distribution to generate data in sensor network applications is the norm. Outliers for

short-term, nonperiodic, and inconsequential variations in data patterns are generated in the IoT sensor network's data sets. Outliers in the IoT sensor network data with a Poisson distribution can be easily identified using the standard deviation and boxplot. The data generated by the failing sensor node and its nearby neighbors are also assessed using Euclidean distances in a distributed context. The data from this node is considered an outlier if the estimated variation exceeds a predetermined threshold. This approach, with its simplicity and convenience of use, relies heavily on the proximity of the sensor nodes to each other. The sparse network also has low precision.

**3.4. Data Fusion.** It is required to integrate or fuse data from several sensors to increase the accuracy of various applications. Sifting data from multiple sensors into an accurate, reliable, and trustworthy representation of the dynamic system's state is known as sensor fusion. This approximation is more accurate than using the sensors one at a time. Sensor fusion aims to lower the system's cost, complexity, and the number of parts while also improving the system's sensing precision and confidence. It is a multifaceted approach.

System states can include acceleration and distance from sensors or mathematical models. In addition to increasing the quality of data, the fusion of sensors can also boost the dependability, measure unmeasured states, and expand the coverage area.

Using this method, all sensors are connected and used to classify each other. A data-level fusion occurs at this point. When all of the sensors' data is combined, data features can be retrieved. Objects with sensors can be identified using these data properties. When numerous sensors' association identities are jointly proclaimed, this technique of direct fusion is also known as joint identity declaration. Equations (2)–(5) show the formal design of the direct fusion process.

$$O: S_i \longrightarrow S_j \forall j \neq i \in \{1, 2, 3, \dots, n\}, \quad (2)$$

$$P: f_{f_e} \left( f_{d_f} (f_A(O)) \right), \quad (3)$$

$$ID_{\text{data\_extraction}}(S_i) = g(p), \quad (4)$$

$$Q: JID_{\text{declaration}}(S_i). \quad (5)$$

The feature extraction result is subjected to the identity declaration function ( $g$ ) in order to identify the specific sensor data (P). Finally, the function JID declaration ( $\cdot$ ) and the result Q are the outcomes of joint identification in the direct fusion strategy.

**3.5. Fault Classification Using Proposed Model.** An ensemble deep learning model for fault diagnosis uses these fused datasets as input.

**3.5.1. Deep Neural Network (DNN).** Artificial neural networks (ANNs) are a class of techniques that use stacks of layers to build a DNN model. Supervised learning can be

used as unsupervised learning [29] as well. Weights in DNN models are stored in hidden layers. They are constantly being recalibrated during the training as they process new information. Finding more accurate patterns is why the weights are adjusted. The researcher does not need to indicate any patterns in advance for a DNN to learn. A subfield of machine learning known as “representation learning” (sometimes known as “feature learning”) underpins deep learning techniques [30]. In contrast to machine learning algorithms, which need the researcher to manually select features before they can be employed, these approaches automatically select features.

There are four completely connected layers in the DNN architecture depicted in Table 1. According to [31], deep learning models are constructed by combining layers that are compatible and allow for effective data manipulations. Deep learning models can only take and produce outputs of a specific shape, which means that each layer of a model is limited to receiving and producing input tensors of one specific shape. According to [31], there is no need to be concerned about the connecting layers’ suitability because they are created to match the geometry of the incoming layer. Tensor dimensions that are returned by a layer are known as its output shape. Table 1 demonstrates that the first hidden layer of DNN will return a tensor with dimensions of  $n = 1$  (None, 64). The output form of this first hidden layer is (None, 64), and it has 64 neurons/units. The output shape from the first layer is automatically inferred as the input shape for the second layer. For a variable batch size, a dynamic dimension of a batch called a “mini-batch” (None) is utilized, allowing the user to specify any batch size for the deep neural network. Except for the most extreme circumstances, it is unnecessary to fix the first dimension of None at this time. During the fit or prediction phase, the batch size is determined.

To avoid models from overfitting, the dropout layers after the dense layers are utilized [32]. To stabilize the learning process and dramatically minimize training epochs, the design leverages batch normalization. The DNN learning process includes two important steps. The first stage is that the input layer delivers the raw data for the training data’s forward propagation phase. As a second stage, the erroneous signal must be retransmitted. Neurons in the hidden layers process the data provided to the output layers to generate output data. Nonlinear functions are used to transfer the output data to the next layer. Activation functions refer to these nonlinear functions. The logistic function, the hyperbolic tangent, and the rectified linear unit ReLU are all examples of activation functions. An input signal from a DNN node is transformed into an output signal by these devices. This study employs the ReLU activation function, which significantly decreases training time and provides faster computation and convergence [33]. In deep learning, ReLU outperforms the sigmoid and tanh activation functions in terms of performance and generalization. DNN’s final layer for multiclass models is a softmax layer, which keeps track of the probabilities associated with each class. The definition of the softmax layer used for K-class classification is as follows [34]:

TABLE 1: The architecture of DNN.

Type of layer	Number of parameters	Output shape
Dropout	0	(None, 32)
Dense	528	(None, 16)
Dense	768	(None, 64)
Dropout	0	(None, 64)
Dense	2080	(None, 32)
Batch normalization	64	(None, 16)
Dense	17	(None, 1)

$$f(x_i) = \frac{\exp(x_i)}{\sum_j \exp(x_j) \forall j \in \{1, \dots, K\}} \quad (6)$$

The  $f(x_i)$  softmax function generates an output ranging from 0 to 1, with a probability total of 1. For binary classification, we will use a sigmoid function as the final layer to generate probabilities ranging from zero to one. Each new/test unit’s propensity score is calculated using these probabilities.

**3.5.2. PropensityNet.** According to [35], the PropensityNet (PN) is a deep neural network capable of predicting propensity scores. Table 2 shows that PN has five dense layers, which means they are all connected. To tackle a binary classification problem, PropensityNet uses Adadelta [36] as an optimizer and binary cross-entropy as an error measure. As the final layer, a sigmoid function is employed to provide probabilities ranging from 0 to 1. For each new/test unit, these probabilities serve as a measure of its propensity score. PropensityNet was built using Keras with a Tensorflow backend in R [37].

**3.5.3. CNN-LSTM.** To learn long-term dependencies, long short-term memory networks (LSTMs) [38] have typically been used (subnets). Recurrent neural networks are an example of this type of network (RNNs). For nontemporal/sequential data, we employ a hybrid model that blends CNN and LSTM models. As a result, we check to see if the hybrid model can be tweaked to predict the probability of class membership (propensity scores). If we want to get probabilities (propensity scores) between zero and one, we will have to utilize a sigmoid function as the last layer. Li et al. [39] provide a thorough explanation of CNN-LSTM. Table 3 shows the hybrid CNN-LSTM model’s design.

## 4. Results and Discussion

**4.1. Simulation Environment.** Ubuntu 18.04, 32 GB of RAM, and an Intel i7-8700K CPU type powered our test PC. Ensemble deep learning models were developed mostly on the Python programming language.

**4.2. CWRU Dataset Introduction.** Multiple accelerometers were placed around the bearing motor to collect vibration data in various operating conditions, resulting in the CWRU dataset from Case Western Reserve University Laboratory.

TABLE 2: The architecture of PN.

Type of layer	Number of parameters	Output shape
Dropout	0	(None, 32)
Dense	1056	(None, 32)
Dropout	0	(None, 32)
Dense	1056	(None, 32)
Dropout	0	(None, 32)
Dense	512	(None, 32)
Dropout	0	(None, 32)
Dense	1056	(None, 32)
Dense	33	(None, 1)

TABLE 3: The architecture of CNN-LSTM.

Type of layer	Number of parameters	Output shape
Conv1D	2080	(None, 15, 32)
Conv1D	4160	(None, 15, 64)
Maxpooling1D	0	(None, 15, 64)
Flatten	0	(None, 480)
Maxpooling1D	0	(None, 15, 32)
Dropout	0	(None, 15, 32)
LSTM	8320	(None, 15, 32)
Conv1D	128	(None, 15, 64)
Maxpooling1D	0	(None, 15, 64)
Dense	61568	(None, 128)
Dropout	0	(None, 128)
Dense	129	(None, 1)

In the CWRU dataset, the electric spark destroyed the bearing motor, replicating actual bearing failures. The inner raceway, the rolling element, and the outside raceway of the bearing driving end or fan end all had different fault locations. Various forms of fault could be represented by the bearing rolling element's four available diameters. Each of the four load types and four speeds of the bearing motor represented a different issue in the bearing motor. For the bearing motor depicted in Figure 1, see [39].

Experimental data were drawn from a subset of the CWRU dataset. Conditions for gathering normal state data included the motor load value of 1 horsepower and 1772 rpm speed value. It was determined that the frequency was 12000 samples per second and the diameter was 0.007 inches. The drive end had faults in three places: the rolling raceway, the outer raceway, and the inner raceway.

**4.3. Evaluation Metrics.** There are many ways to evaluate the performance of a suggested approach for fault diagnostics. The Confusion Matrix, which is a two-dimensional matrix that provides information about the actual and predicted classes, serves as the basis for all evaluation criteria.

The right predictions are signified by the confusion matrix's diagonal members, while the incorrect guesses are represented by the confusion matrix's nondiagonal members. Confusion matrix attributes are depicted in Table 4.

Aside from that, recent research has employed a variety of evaluation metrics.

**Precision:** all samples projected as faults divided by the correct number of faults is represented by this ratio.

$$\text{Precision} = \frac{TP}{TP + FP} \quad (7)$$

**Recall:** all samples accurately categorized as Faults are divided by the total number of samples that are in fact faults to get this ratio. Detection rate is another name for it.

$$\text{Recall} = \text{detection rate} = \frac{TP}{TP + FN} \quad (8)$$

**False alarm rate:** also known as the false positive rate, it is the proportion of fault samples that are found to be normal.

$$\text{False alarm rate} = \frac{FP}{FP + TN} \quad (9)$$

**True negative rate:** as a percentage of all samples that are categorized as normal, it is known as a normality index.

$$\text{True negative rate} = \frac{TN}{TN + FP} \quad (10)$$

**Accuracy:** it is a measure of how many cases were correctly categorized out of all the ones that were found. When a dataset is balanced, the detection accuracy metric can be used as a helpful performance measure.

$$\text{Accuracy} = \frac{TP + TN}{TP + TN + FP + FN} \quad (11)$$

**F-measure:** to put it another way, it is the arithmetic mean of precision and recall combined. Accuracy may be evaluated by looking at both the system's precision and recall, which is what this technique is all about.

$$F - \text{measure} = 2 \left( \frac{\text{precision} \times \text{recall}}{\text{precision} + \text{recall}} \right) \quad (12)$$

**4.4. Performance Evaluation of the Proposed Model.** Here, the performance of the proposed ensemble model is tested with two different training sets and testing sets. Initially, 50% of training data and 50% of testing data are considered for validation, which is shown in Table 5 and Figure 2 presents the comparative analysis of the proposed model with different techniques in terms of accuracy for different data ratios.

In the analysis of accuracy, CNN, DNN, and CNN-LSTM achieved 92%, LSTM and RNN achieved nearly 85%, PropensityNet achieved 93%, and the proposed model achieved 94.32%. The single classifiers achieved less performance, but when it is in ensemble state, they achieved better performance. The reason is that training data are accurate and the prediction of faults on each technique is accurate and it is finalized effectively. However, the accuracy of performance and recall is low even for the proposed ensemble model (i.e., 93.24% of recall) and this is because only 50% of data is trained and tested with the remaining 50% of data. In addition, some data are missed while training the model. But, in the analysis of precision, all techniques achieved nearly 88% to 90% and achieved nearly 92% to 96% of F-score. The next set of experiments is carried out by considering 75% of training data and 25% of testing data, which is shown in Table 6.

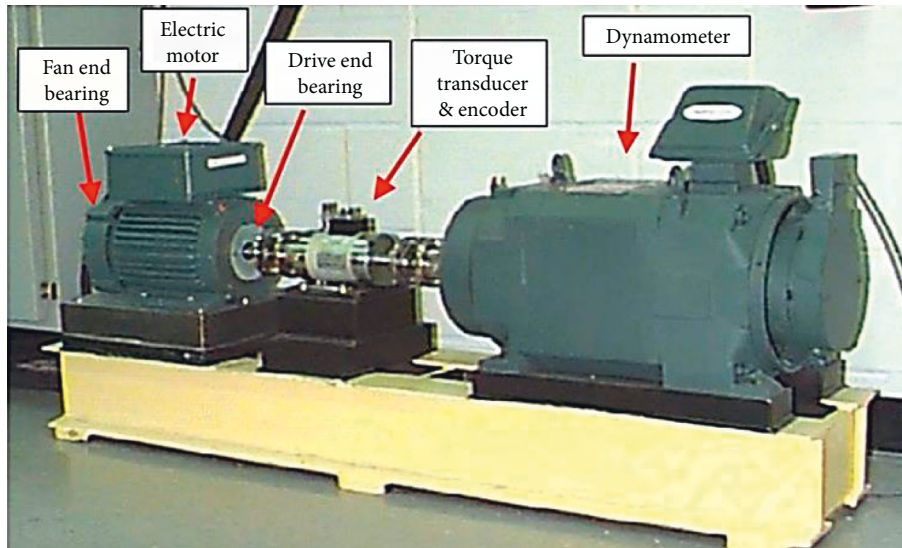


FIGURE 1: Bearing motor setup to generate CWRU dataset.

TABLE 4: Confusion matrix.

		Predicted class	
		Fault	Normal
Actual class	Normal	False positive	True negative
	Fault	True positive	False negative

TABLE 5: Comparative analysis of 50%–50% on the proposed model with various existing algorithms.

Algorithm	Accuracy	Precision	Recall	F-score
RNN	81.10	89.41	75.91	86.72
LSTM	87.70	89.41	85.21	91.82
CNN	92.50	89.82	90.98	95.27
DNN	92.50	87.63	91.38	95.18
CNN-LSTM	92.70	88.90	91.93	95.32
PropensityNet	93.27	87.91	92.47	95.63
Proposed ensemble	94.32	90.95	93.24	96.02

TABLE 6: Comparative analysis of 75%–25% on the proposed model with various existing algorithms.

Algorithm	Accuracy	Precision	Recall	F-score
RNN	85.71	84.32	85.93	83.45
LSTM	92.10	92.43	92.15	91.68
CNN	92.46	93.48	92.44	91.81
DNN	89.52	90.21	89.54	89.03
CNN-LSTM	94.53	96.61	92.52	92.24
PropensityNet	94.16	96.17	92.32	92.10
Proposed ensemble	95.62	98.32	94.62	94.53

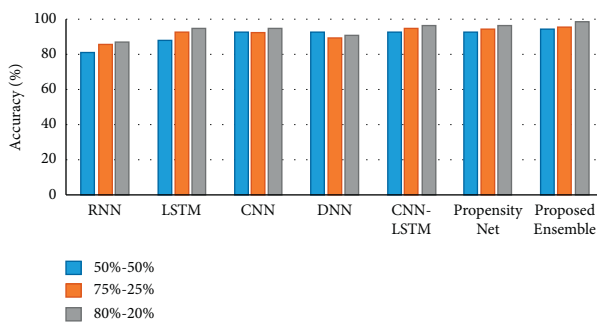


FIGURE 2: Graphical representation of the proposed model in terms of accuracy for different training and testing data ratios.

When the training data is increased, the performance of the models is increased; for instance, the proposed ensemble model achieved 95.62% of accuracy, 98.32% of precision,

94.62% of recall, and 94.53% of F-score. When compared with all techniques, RNN achieved low performance, i.e., 85.71% of accuracy, 84.32% of precision, 85.93% of recall, and 83.45% of F-score. The reason for poor performance is that RNN takes a long time to train the network and it is inefficient to handle the missing data. Moreover, the raw data are fused by direct fusion techniques, and then it is used for identifying the faults in machines. All proposed single classifiers such as DNN, CNN-LSTM, and PropensityNet achieved nearly 94% of accuracy, 96% of precision, 92% of recall, and an F-score. LSTM and CNN models achieved 92% of accuracy, 93% of precision, 92% of recall, and 91% of F-score. The training set is increased to 80% and testing data is set at 20%, which is shown in Table 7.

Most of the techniques' recall and F-score are nearly the same; for instance, RNN achieved 81%, LSTM achieved 88%, CNN achieved 92%, DNN achieved 92%, CNN-LSTM achieved 91%, PropensityNet achieved 92%, and the proposed ensemble model achieved 93%. The accuracy of all techniques is increased, when compared with the first set of experiments. That is, the proposed model achieved 98.84% of accuracy, CNN-LSTM and PropensityNet achieved 96%, and LSTM and CNN achieved 94% of accuracy. The DNN has 93.45% of precision, CNN-LSTM achieved 97.85% of precision, PropensityNet achieved 98.23% of precision, and the ensemble model achieved 99.23% of precision.

TABLE 7: Comparative analysis of 80%–20% on the proposed model with various existing algorithms.

Algorithm	Accuracy	Precision	Recall	F-score
RNN	87.35	78.21	81.10	81.11
LSTM	94.82	89.33	87.70	88.64
CNN	94.62	88.82	92.50	89.02
DNN	90.76	93.45	92.50	87.39
CNN-LSTM	96.63	97.85	92.70	90.33
PropensityNet	96.12	98.23	93.27	91.02
Proposed ensemble	98.84	99.23	94.32	92.91

## 5. Conclusion

As artificial intelligence technology continues to advance, it is now possible to foresee mechanical failures based on the IIoT. Sensor data fusion knowledge relies on big data processing and analysis. Models and methods for sensing data fusion in defect detection and prediction were examined in this research. The direct fusion model is provided here in terms of fusion models. To train and retrieve the original data, the relevant ensemble methods based on deep learning can be immediately implemented. Data preprocessing is not usually necessary, but the learning curve was steep and the machine performance needs were high. Because of this, the preprocessing stage includes missing data, outlier detection, and data imputation. Results from the trials demonstrate that the suggested ensemble model achieved 94% accuracy on 50%–50% of data, 95.6% accuracy on 75% to 25% of data, and 98% accuracy on 80%–20% of data, where the single DL models achieved approximately 96% accuracy on 80%–20% data.

## 6. Limitation and Future Scope

The following are the obstacles and difficulties encountered in the context of fusing sensory data, based on the current development state of fusion models:

- (1) Fusion models are not all the same: there is no one-size-fits-all model for mechanical defect diagnosis and prediction in the field. A large number of current fusion models are based on a certain type of device. Developing a common framework for identifying mechanical equipment failures in the future would be advantageous.
- (2) Uncertainty in the original data: during the data gathering process, a lot of noise is present in the actual data obtained since environmental elements cannot be controlled. Data fusion and feature extraction are often incorrect if the unique data are used directly. It is therefore vital to select a suitable data preprocessing approach instead of techniques utilized in this study when raw data are given. A set of preprocessing methods for diverse sensors used in fault analysis and prediction for mechanical gear will be beneficial in the future development process.
- (3) Long running time: finding appropriate hyper parameters requires a lot of running time when using fusion methods based on deep learning. Overfitting can also occur. Fusion techniques typically necessitate feature extraction by hand, which adds time to the computation time. Research into the feature and decision-level fused algorithms are the focus of the majority of fusion algorithms. There are very few data fusion algorithms. As a result, it will be necessary to continue working on data fusion algorithms in the future.

## Data Availability

The data that support the findings of this study are available on request from the corresponding author. The data are not publicly available due to privacy concerns.

## Conflicts of Interest

The authors declare that they have no conflicts of interests.

## References

- [1] E. Sisinni, A. Saifullah, S. Han, U. Jennehag, and M. Gidlund, "Industrial Internet of things: challenges, opportunities, and directions," *IEEE Internet of Things Journal*, vol. 14, 2018.
- [2] Ericsson, "Cellular networks for massive IoT," 2020, <https://www.ericsson.com/assets/local/publications/whitepapers/wp%20iot.pdf>.
- [3] Y. Liu, T. Dillon, W. Yu, W. Rahayu, and F. Mostafa, "Missing value imputation for industrial iot sensor data with large gaps," *IEEE Internet of Things Journal*, vol. 7, no. 8, pp. 6855–6867, 2020.
- [4] F. Civerchia, S. Bocchino, C. Salvadori, E. Rossi, L. Maggiani, and M. Petracca, "Industrial internet of things monitoring solution for advanced predictive maintenance applications," *Journal of Industrial Information Integration*, vol. 7, pp. 4–12, 2017.
- [5] J. Wan, S. Tang, D. Li et al., "A manufacturing big data solution for active preventive maintenance," *IEEE Transactions on Industrial Informatics*, vol. 13, no. 4, pp. 2039–2047, 2017.
- [6] B. Cheng, J. Zhang, G. P. Hancke, S. Karnouskos, and A. W. Colombo, "Industrial cyberphysical systems: realizing cloud-based big data infrastructures," *IEEE Industrial Electronics Magazine*, vol. 12, no. 1, pp. 25–35, 2018.
- [7] W. Yu, T. Dillon, F. Mostafa, W. Rahayu, and Y. Liu, "A global manufacturing big data ecosystem for fault detection in predictive maintenance," *IEEE Transactions on Industrial Informatics*, vol. 16, no. 1, pp. 183–192, 2020.
- [8] P. Nardelli, C. Papadias, C. Kalas et al., "Framework for the identification of rare events via machine learning and iot networks," in *Proceedings of the 2019 16th International Symposium on Wireless Communication Systems (ISWCS)*, pp. 656–660, IEEE, Oulu, Finland, August, 2019.
- [9] A. Gonzalez-Vidal, P. Rathore, A. Rao, J. Mendoza-Bernal, M. Palaniswami, and A. Skarmeta-Gomez, "Missing data imputation with bayesian maximum entropy for internet of things applications," *IEEE Internet of Things Journal*, vol. 8, 2020.
- [10] X. Deng, P. Jiang, X. Peng, and C. Mi, "An intelligent outlier detection method with one class support tucker machine and genetic algorithm toward big sensor data in internet of things," *IEEE Transactions on Industrial Electronics*, vol. 66, no. 6, pp. 4672–4683, 2019.

- [11] S. Sanyal and P. Zhang, "Improving quality of data: IoT data aggregation using device to device communications," *IEEE Access*, vol. 6, Article ID 67830, 2018.
- [12] D. B. Rubin, "Inference and missing data," *Biometrika*, vol. 63, no. 3, pp. 581–592, 1976.
- [13] Y. Dong and C.-Y. J. Peng, "Principled missing data methods for researchers," *SpringerPlus*, vol. 2, no. 1, p. 222, 2013.
- [14] C. Cunqing Hua and T.-S. P. Yum, "Optimal routing and data aggregation for maximizing lifetime of wireless sensor networks," *IEEE/ACM Transactions on Networking*, vol. 16, no. 4, pp. 892–903, 2008.
- [15] S. Srinivasan, P. Arjunan, B. Jin, A. L. Sangiovanni-Vincentelli, Z. Sultan, and K. Poolla, "Explainable AI for chiller fault-detection systems: gaining human trust," *Computer*, vol. 54, no. 10, pp. 60–68, 2021.
- [16] G. Li, Q. Yao, and C. Fan, "An explainable one-dimensional convolutional neural networks based fault diagnosis method for building heating, ventilation and air conditioning systems," *Building and Environment*, vol. 203, Article ID 108057, 2021.
- [17] S. S. Kumar, D. Abraham, and M. Rosenthal, "Leveraging visualization techniques to develop improved deep neural network architecture for sewer defect identification," in *Construction Research Congress 2020: Infrastructure Systems and Sustainability*, pp. 827–835, American Society of Civil Engineers, Reston, VA, USA, 2020.
- [18] D. Gonzalez-Jimenez, J. del-Olmo, J. Poza, F. Garramiola, and P. Madina, "Data-driven fault diagnosis for electric drives: a review," *Sensors*, vol. 21, no. 12, p. 4024, 2021.
- [19] J. J. Marquez, A. Zafra-Cabeza, C. Bordons, and M. A. Ridao, "A fault detection and reconfiguration approach for mpc-based energy management in an experimental microgrid," *Control Engineering Practice*, vol. 107, Article ID 104695, 2021.
- [20] M. M. Morato, P. R. C. Mendes, and J. E. Normey-Rico, "Dealing with energy-generation faults to improve the resilience of microgrids: a survey," in *Proceedings of the 2019 IEEE PES Innovative Smart Grid Technologies Conference - Latin America*, p. 1e6, September, 2019.
- [21] F. Ruiming, W. Minling, G. xinhua, S. Rongyan, and S. Pengfei, "Identifying early defects of wind turbine based on scada data and dynamical network marker," *Renewable Energy*, vol. 154, pp. 625–635, 2020.
- [22] M. Hussain, M. Dhimish, S. Titarenko, and P. Mather, "Artificial neural network based photovoltaic fault detection algorithm integrating two bi-directional input parameters," *Renewable Energy*, vol. 155, pp. 1272–1292, 2020.
- [23] C. Correa-Jullian, J. M. Cardemil, E. L. Droguett, and M. Behzad, "Assessment of deep learning algorithms for fault diagnosis in solar thermal systems," in *ISES Solar World Congress*, 2019.
- [24] C. Correa-Jullian, J. M. Cardemil, E. López Droguett, and M. Behzad, "Assessment of deep learning techniques for prognosis of solar thermal systems," *Renewable Energy*, vol. 145, pp. 2178–2191, 2020.
- [25] A. J. Gallego, M. Macías, F. d. de Castilla, and E. F. Camacho, "Mathematical modeling of the Mojave solar plants," *Energies*, vol. 12, no. 21, p. 4197, 2019.
- [26] X. Yan, W. Xiong, L. Hu, F. Wang, and K. Zhao, "Missing value imputation based on Gaussian mixture model for the internet of things," *Mathematical Problems in Engineering*, vol. 2015, pp. 1–8, 2015.
- [27] A. A. Al-khatib, B. Mohammed, and K. Abdelmajid, "A survey on outlier detection in internet of things big data," in *Big Data-Enabled Internet of Things*, pp. 265–272, IET, London, UK, 2020.
- [28] A. Shahraki, Ø. Haugen, and Ø. Haugen, "An outlier detection method to improve gathered datasets for network behavior analysis in IoT," *Journal of Communications*, vol. 14, pp. 455–462, 2019.
- [29] A. Sivaram, L. Das, and V. Venkatasubramanian, "Hidden representations in deep neural networks: Part 1. Classification problems," *Computers & Chemical Engineering*, vol. 134, Article ID 106669, 2020.
- [30] Y. Bengio, A. Courville, and P. Vincent, "Representation learning: a review and new perspectives," *IEEE Transactions on Pattern Analysis and Machine Intelligence*, vol. 35, no. 8, pp. 1798–1828, 2013.
- [31] F. Chollet, *Deep Learning with Python*, Simon & Schuster, New York, NY, USA, 2021.
- [32] N. Srivastava, G. Hinton, A. Krizhevsky, I. Sutskever, and R. Salakhutdinov, "Dropout: a simple way to prevent neural networks from overfitting," *Journal of Machine Learning Research*, vol. 15, no. 1, 2014.
- [33] C. Nwankpa, W. Ijomah, A. Gachagan, and S. Marshall, "Activation Functions: Comparison of Trends in Practice and Research for Deep Learning," 2018, <https://arxiv.org/abs/1811.03378>.
- [34] V. Ramachandra, "Deep Learning for Causal Inference," 2018, <https://arxiv.org/abs/1803.00149>.
- [35] M. D. Zeiler, "ADADELTA: An Adaptive Learning Rate Method," 2012, <https://arxiv.org/abs/1212.5701>.
- [36] F. Chollet and J. Allaire, "R interface to Keras," 2017, <https://github.com/rstudio/keras>.
- [37] S. Hochreiter and J. Schmidhuber, "Long short-term memory," *Neural Computation*, vol. 9, no. 8, pp. 1735–1780, 1997.
- [38] A. Whata and C. Chimedza, "Deep learning for SARS COV-2 genome sequences," *IEEE Access*, vol. 9, Article ID 59597, 2021.
- [39] S. Li, G. Liu, X. Tang, J. Lu, and J. Hu, "An ensemble deep convolutional neural network model with improved D-S evidence fusion for bearing fault diagnosis," *Sensors*, vol. 17, no. 8, p. 1729, 2017.

## *Retraction*

# **Retracted: Research on Mobile Ideological and Political Teaching in Universities Based on the Android Platform**

### **Mathematical Problems in Engineering**

Received 26 September 2023; Accepted 26 September 2023; Published 27 September 2023

Copyright © 2023 Mathematical Problems in Engineering. This is an open access article distributed under the Creative Commons Attribution License, which permits unrestricted use, distribution, and reproduction in any medium, provided the original work is properly cited.

This article has been retracted by Hindawi following an investigation undertaken by the publisher [1]. This investigation has uncovered evidence of one or more of the following indicators of systematic manipulation of the publication process:

- (1) Discrepancies in scope
- (2) Discrepancies in the description of the research reported
- (3) Discrepancies between the availability of data and the research described
- (4) Inappropriate citations
- (5) Incoherent, meaningless and/or irrelevant content included in the article
- (6) Peer-review manipulation

The presence of these indicators undermines our confidence in the integrity of the article's content and we cannot, therefore, vouch for its reliability. Please note that this notice is intended solely to alert readers that the content of this article is unreliable. We have not investigated whether authors were aware of or involved in the systematic manipulation of the publication process.

Wiley and Hindawi regrets that the usual quality checks did not identify these issues before publication and have since put additional measures in place to safeguard research integrity.

We wish to credit our own Research Integrity and Research Publishing teams and anonymous and named external researchers and research integrity experts for contributing to this investigation.

The corresponding author, as the representative of all authors, has been given the opportunity to register their agreement or disagreement to this retraction. We have kept a record of any response received.

### **References**

- [1] J. Chen and Y. Guan, "Research on Mobile Ideological and Political Teaching in Universities Based on the Android Platform," *Mathematical Problems in Engineering*, vol. 2022, Article ID 1214684, 8 pages, 2022.

## Research Article

# Research on Mobile Ideological and Political Teaching in Universities Based on the Android Platform

Jinxin Chen <sup>1</sup> and Yuanyuan Guan<sup>2</sup>

<sup>1</sup>Wuhan Technology and Business University, Wuhan 430065, China

<sup>2</sup>Wuchang Institute of Technology, Wuhan 430065, China

Correspondence should be addressed to Jinxin Chen; [chenjinxin@wtbu.edu.cn](mailto:chenjinxin@wtbu.edu.cn)

Received 1 March 2022; Revised 20 March 2022; Accepted 22 March 2022; Published 10 June 2022

Academic Editor: Punit Gupta

Copyright © 2022 Jinxin Chen and Yuanyuan Guan. This is an open access article distributed under the Creative Commons Attribution License, which permits unrestricted use, distribution, and reproduction in any medium, provided the original work is properly cited.

The traditional ideological and political teaching is very old-fashioned, the teaching content is very fixed, and the teaching methods are very old. Based on the analysis of the problems existing in the traditional teaching mode, this study proposes a cloud service architecture plan with cloud, network, and terminal as the core design ideas, clarifies the goals and problems to be solved, and then conducts functional requirements analysis. In the system design stage, the whole system is firstly designed as a whole, and then the business process in the teaching system is analyzed, the redundant business in the business process is found, and the process is reorganized. The mobile learning system based on the Android platform meets the existing teaching needs and can be expanded to a certain extent. It can achieve good results in teaching application and make certain contributions to the construction of educational informatization, improving learning efficiency and enhancing students' autonomous learning ability.

## 1. Introduction

On the university campus, the intelligent terminal has become their best partner when the college students finish their classroom study. On the negative side, various intelligent terminals emerge endlessly, especially some entertainment software that fascinates young college students and consumes a lot of time and energy. How to make college students better receive education in the era of more and more advanced intelligent terminals? Given this, the concept of mobile teaching based on mobile learning arises at the historic moment.

The concept of mobile teaching was first proposed abroad as a form of mobile learning. On the one hand, mobile teaching and mobile learning are just different subjects. The same system is a learning platform for students and a teaching system for teachers. On the other hand, mobile teaching is a more advanced concept based on the concept of mobile learning, which adds more interactive functions and personalized learning settings. Mobile teaching takes the client as the carrier, allowing students to use the client for learning. In this process, teaching activities

between teachers and students are increasingly reflected [1]. In addition, as early as 2014, according to the data released by Strategy Analytics, Android and iOS together accounted for nearly 96% of the global smartphone market, out of which iOS accounted for 12.3% market share, while Android accounted for 83.6% market share, still maintaining its dominant position [2]. The increasing purchase rate of Domestic Android phones among college students, as well as the high market share of Android phones in recent years, are important and practical reasons why this study chose to develop a mobile teaching auxiliary system for ideological and political courses based on Android.

At present, the domestic research on mobile teaching is relatively backward compared with foreign countries. There is no professional research team in China to study the theory and practice of mobile learning, and there are few academic research teams formed by educational institutions in the real sense [3]. The existing domestic research on mobile learning systems is mainly initiated by some M-learning providers, and their purpose is mainly to make profits in the market [4].

There are more than 20,000 tablet and mobile phone software and hardware developers in China, and more than 2



million Apple and Android system developers. OEM and ODM are also very easy and convenient, and the technology applications are mature, which provides a very rich solution for the development of cloud, network, and terminal applications of university teaching in the future [5].

Mobile learning is based on digital learning, further combined with the mobile Internet technology and computer technology. The feature of being able to learn anytime, anywhere will bring new experience to learners, and change from the traditional learning mode with teachers as the main body to the learning mode with students' autonomous learning as the main body, so as to improve students' learning initiative and enthusiasm. The mobile learning mode should be regarded as the main learning mode in the future. However, mobile learning, as a new learning model, still has some problems [6]. This study analyzes and summarizes the research status at home and abroad and draws the following conclusions:

- (1) In the current research, the feasibility of mobile education has been fully demonstrated, which can bring changes to the teaching model. The research focus is mainly on the feasibility of mobile education, resource development, short message service, WAP site construction, and other four aspects.
- (2) In the current research, there is not much discussion on the user needs of the mobile learning system, what functions should be implemented, and what standards the system should abide by. The research on how to realize mobile teaching and how to implement it in colleges and universities is especially lacking, and the technical standards are not unanimous.
- (3) In recent years, new technologies have constantly emerged in the field of communication and IT, which provide support for mobile learning platforms. At the same time, with the emergence of smartphones and tablet computers, the demand for mobile teaching platforms is also increasing.
- (4) Although the mobile learning system at home and abroad have carried out extensive research and got rapid development, because of the complexity of the mobile learning platform, how to realize the communication and resource sharing between different platforms such as also the need for in-depth analysis, so the research of mobile learning platform at present is still in the stage of development. However, with the rise of mobile e-commerce and the development of Android programming technology, mobile teaching platforms based on Android technology will have a broad prospect.

## 2. Related Work

*2.1. Research Status.* As a new learning mode, mobile teaching is a successful application of mobile communication technology, mobile computing technology, and mobile Internet technology in the field of education, and its

application results have attracted worldwide attention [7]. In recent years, a lot of research has been carried out on the application of mobile teaching abroad, including technical support, system architecture platform, the realization of learning materials, etc.

At present, the foreign application research of mobile teaching platforms is mainly concentrated in some developed countries. Since 2000, the object, method, and technology of mobile teaching have been deeply discussed in Europe, and the feasibility of the application of mobile teaching platform in practical teaching has been analyzed from a practical point of view, and more than 30 projects have been launched to study the mobile teaching platform [8]. Many universities have successively established their educational sites based on WAP, such as Griffith University and the University of Minnesota in the United States, and the University of Edmonton in Canada, etc. [9].

On this basis, The University of Birmingham has also carried out the HandLeR project, which is based on the development direction of future education and according to the needs of learners, and also plans to develop a mobile learning resource suitable for different ages and different learning needs. In the current research results, the study tool developed by this project is suitable for 9–11 years old children, and its actual experimental effect is very good [10].

China only put forward the concept of mobile teaching and mobile learning in 2001. In 2001, Peking University undertook the research and development of the Mobile Teaching Theory and Practice project of the Ministry of Education and established the first mobile teaching laboratory in China. During the four years from January 2002 to December 2005, Peking University developed three different versions of the mobile learning platform. Among them, a mobile teaching platform was mainly realized by a short message, which was mainly used for teaching information sharing on mobile networks and the Internet.

The Ministry of Education has been doing mobile education research at Peking University, Tsinghua University, Beijing Normal University, and other universities since 2002. In 2008, Beijing Normal University hosted the 5th International Conference on The Application of Wireless Mobile Technology in Education (WMUTE2008), which marked the start of China's mobile education and learning research in accordance with international norms [11]. According to the findings, the research is primarily focused on the feasibility of mobile education, resource development, short message service, WAP site design, and the other four factors. However, there is a distinct paucity of studies on how to achieve mobile teaching and how to put it into practice at colleges and universities [12].

Shanghai TV University has also carried out the practice of mobile learning, carrying out the "mobile Campus" plan, in which 80,000 students have used mobile phones to study. The mobile learning plan mainly carries out two parts of the function, with real-time notification and teaching guidance, to ensure the communication between teachers and students. In 2009, Beijing Normal University's Institute of Modern Education Technology developed the application mode and method of mobile teaching system in discipline

teaching from the perspectives of classroom teaching mode and extracurricular mobile learning, as well as researching the application mode of mobile teaching system. The value and application of mobile teaching platforms in teaching are thoroughly validated by the analysis, as is the wide prospect of mobile teaching platform application [13].

**2.2. Overall Functional Module Design.** Based on the demand analysis of the mobile teaching system and fully considering the characteristics of mobile teaching, teachers, and students to facilitate the daily teaching and learning as the goal, the set mobile teaching system was composed of two components, the client and server and the server category includes user management, resources management, and announcement to inform management function module. [14–16], The client mainly reports functional modules such as course management, resource management, group discussion, and viewing news bulletins. The functional modules of the system are shown in Figure 1.

After the server is started, the client can interact with the server. The server responds to the request of the client and sends the required data to the client. In addition, another important function of the server is to provide an interface for the administrator to maintain the background data. The functions of the server are described as follows:

- (1) User management function: after logging in to the server, the administrator can add, query, delete, and modify user information to maintain user information.
- (2) Resource category management function: the administrator can add, delete and modify resource categories. At the same time, the administrator can maintain resource categories in the system.
- (3) Announcement and notice management function: the administrator is responsible for the input and maintenance of announcement information to ensure the accuracy of the announcement and notice. The system automatically clears expired bulletins.

### 3. Android-Based Mobile Teaching Auxiliary System Design

It offers a big quantity of instructional materials and encourages users to contribute to them. Users can utilize the mobile teaching support client to learn with teachers' recommendations, and the system also proposes learning resources based on its recommendation algorithm when faced with a large database.

In the learning recommendation module, students are recommended to choose a variety of course materials. First, there is a rolling recommendation system page on the home page, which is a recommendation display for learning activities. Then the following drop-down list shows teachers' recommendations and recommendations made by the system using its recommendation algorithm.

This system is the recommendation system interface, the display of video course masters forum, website links,

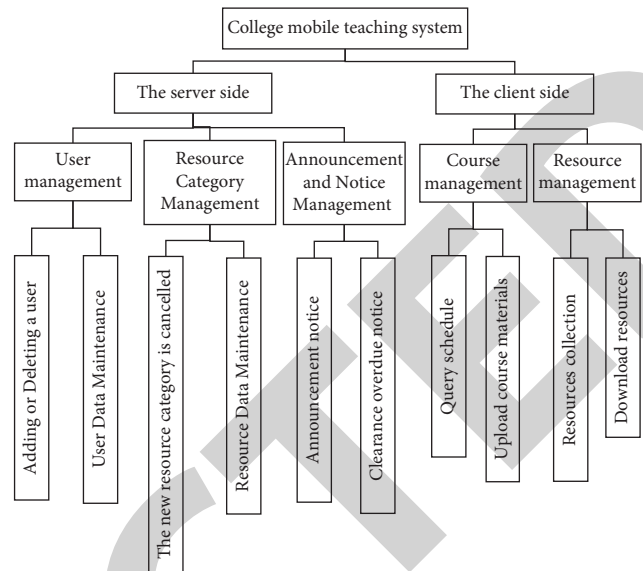


FIGURE 1: Functional module diagram of mobile teaching system in colleges and universities.

reference materials, current affairs and politics, current affairs, teacher recommendations, and other materials. However, for personalized recommendations, recommendation algorithms will be used to train preferences for specific users. Users' preferences are considered to be their preferences for certain items. For example, a student likes to watch current political news, so politics is a potential preference of the same student. So we can use the user's preference model to judge the user and recommend specific learning materials for the former user. However, for a specific user, his preference in the current time stage is different from his learning preference in the future, and the user's interest will shift with the transfer of his concern. So in the current system function range, the user's preference extraction is very important.

In the playback view module of the ideological and political class teaching view, we use the conversion between the two interfaces. First of all, the system will give feedback on a list of videos according to the search or recommendation module of the system. For these video materials, we designed VideoLitActivity to operate the page. After clicking, we entered the course video module and used PlayerActivity to play the course view. Of course, the real-time interaction with the server is still set up as adapter class, designed course introduction, course catalog, course evaluation, and bullet-screen view class insertion, such as the Video class, as well as the HttpContants class, Basebean class, and MyHttpClient class. The class design of part of the course viewing module is shown in Figure 2.

The data type returned by the interaction with the server is represented by the BaseBean class. The server side must have an accessible interface class. We use HttpConstants and Use the MyHttpClient class as the access data library class. The classes that control the login user interface are represented by the LoginActivity class, and the RegisterActivity class shows the classes that control the registration mode. The login and registration classes are inherited

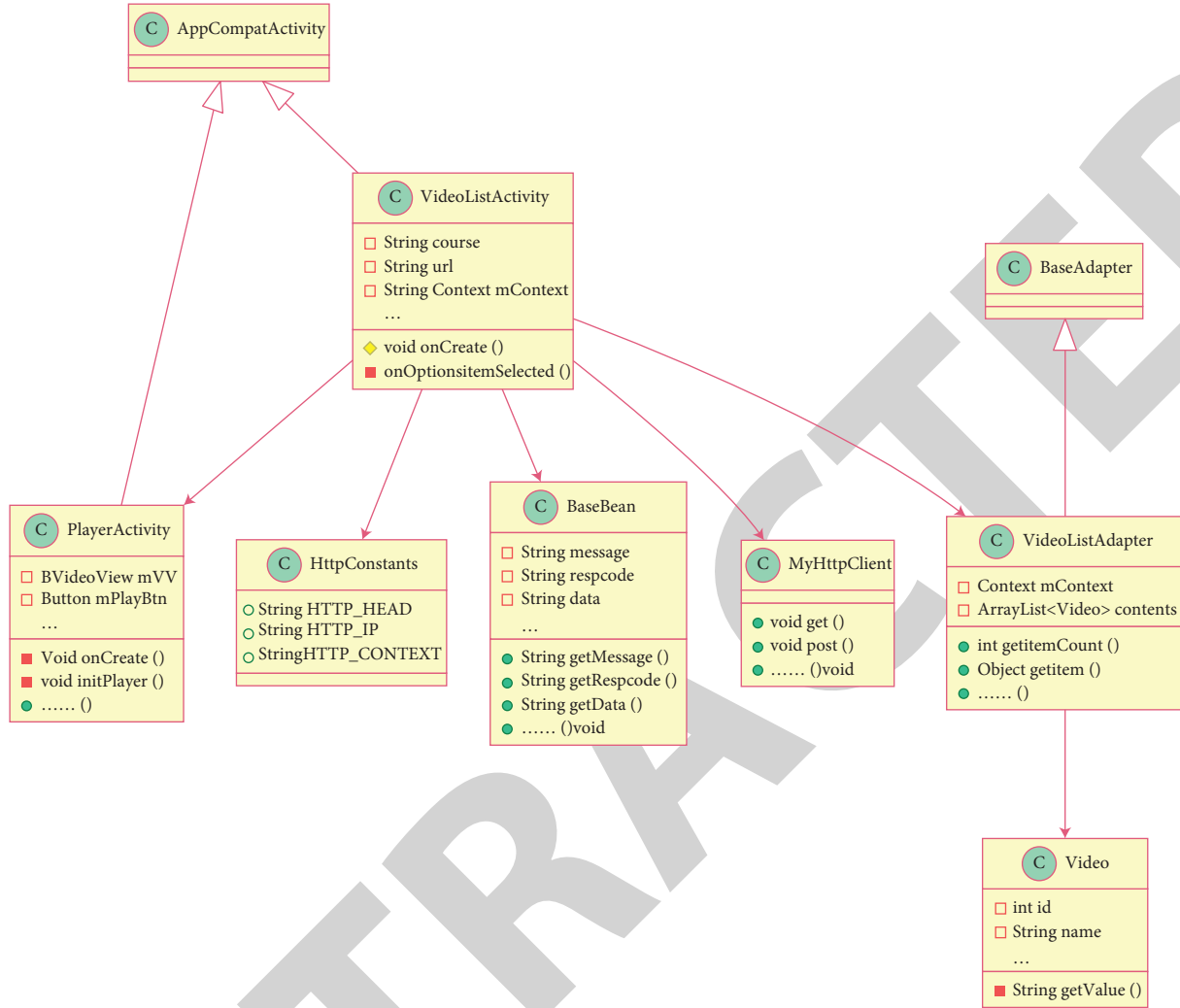


FIGURE 2: Class diagram of the course view module part classes.

CompatActivity classes. The class diagram for login registration is shown in Figure 3.

The recommendation algorithm based on the bipartite graph model is used in our mobile teaching auxiliary system of ideological and political courses. This system assumes a total of  $U$  users and  $V$  courses. If a single user  $U$  has selected course  $V$ , then there will be a relational edge between users  $U$  and  $V$  in the graph model.

Let the score of user  $U_i$  and  $U_j$  in  $n$ -dimensional term space be expressed as vector  $R_{U_i}$  respectively, then the similarity between user  $U_i$  and user  $U_j$  is  $\text{sim}(U_i, U_j)$ :

$$\text{sim}(U_i, U_j) = \frac{R_{U_i} \cdot R_{U_j}}{\|R_{U_i}\| * \|R_{U_j}\|}, \quad (1)$$

where  $U_i, U_j$  represents different customer groups. Table 1 is taken as an example (assuming a total of 5 active users) to illustrate the calculation method of similarity among users. The number 0 in Table 1 means that user  $U_i$  has not watched this video, and the number 1 means that user  $U_j$  has watched this video.

Assuming  $S_i$  is the set of all videos watched by user  $U_i$ , the similarity between user  $U_i$  and user  $U_j$  can be defined as follows:

$$\text{sim}(U_i, U_j) = \frac{|S_i \cap S_j|}{|S_i \cup S_j|} \quad (2)$$

The similarity of user  $U_1$  and user  $U_2$ , user  $U_3$ , user 4, and user 5 can be calculated according to formula (2):

$$\begin{aligned} \text{sim}(U_1, U_2) &= \frac{|S_1 \cap S_2|}{|S_1 \cup S_2|} = 0.6, \\ \text{sim}(U_1, U_3) &= \frac{|S_1 \cap S_3|}{|S_1 \cup S_3|} = 0.6, \\ \text{sim}(U_1, U_4) &= \frac{|S_1 \cap S_4|}{|S_1 \cup S_4|} = 0.4, \\ \text{sim}(U_1, U_5) &= \frac{|S_1 \cap S_5|}{|S_1 \cup S_5|} = 0.5. \end{aligned} \quad (3)$$

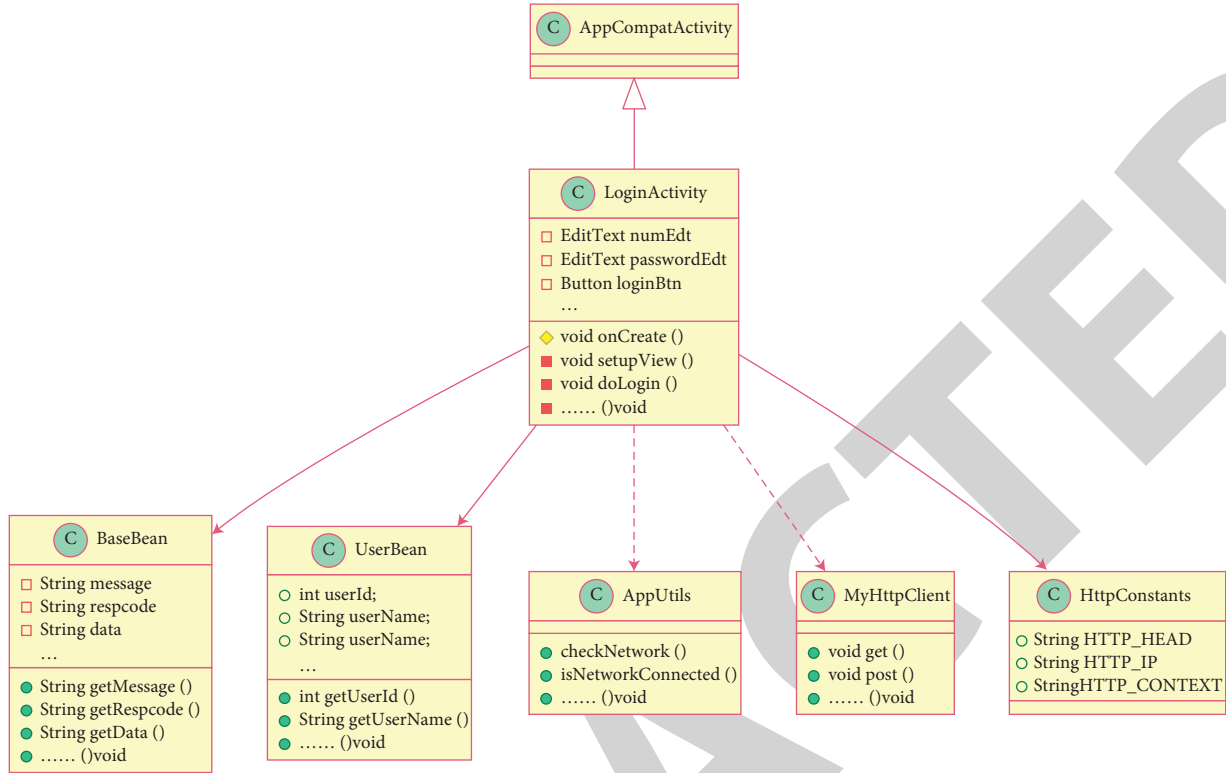


FIGURE 3: My account module part class diagram.

TABLE 1: Video viewing record of representative users.

User	Video 1 mmc1	Video 2 mmc2	Video 3 mmc3	Video 4 mmc4	Video 5 mmc5
U1	1	0	1	1	1
U2	0	1	1	1	1
U3	1	0	1	1	0
U4	0	1	1	0	1
U5	0	1	0	1	0

If the threshold  $Q=0.5$  is set, the neighbors of the user include user1 and user5. In addition, if there is no watch record user, the user’s basic information can be used as the basis for calculating the similarity, the calculation methods similar to the users have to watch record, just change Table 1 of the video to use each of the different users’ information characteristics (such as log in number, grade, class, professional) to replace, if a particular information feature the same assignment 1, assignment 0 otherwise if you can calculate the similarity and find out the neighbor users.

The main principle of fuzzy clustering for users of teaching resources is to cluster users through user description files, that is, the level of users’ interest in the target teaching resources. User’s interest degree description can be expressed in the vector space model and clustering is used to choose representative users as the clustering centers, according to the calculation for the current user, and the similarity clustering center is used to dynamically adjust the clustering center continuously, until it meets the preset threshold, eventually to produce target teaching resources fuzzy clustering of users. The calculation formula of similarity is as follows:

$$\text{sim}(w, v) = \frac{\sum_{k=1}^n (\mu_k(w) - \bar{\mu}(w)) * \mu_k(v) - \bar{\mu}(v)}{\sqrt{\sum_{k=1}^n (\mu_k(w) - \bar{\mu}(w))^2} * \sqrt{\sum_{k=1}^n (\mu_k(v) - \bar{\mu}(v))^2}} \quad (4)$$

After the user fuzzy clustering center is determined,  $N$  users in the cluster where the user to be recommended are selected according to the similarity, and the prediction of the target teaching resource  $R$  by the user to be recommended is completed according to the interest degree of the  $N$  nearest users in the target teaching resource. The calculation formula is as follows:

$$S(w, v) = \overline{SA}_w + \frac{\sum_{v=1}^n \text{sim}(w, v) * (SA_{v,r} - \overline{SA})}{\sum_{v=1}^n \text{sim}(w, v)} \quad (5)$$

$\text{Sim}(w, v)$  represents the similarity between user  $w$  and its nearest neighbor user  $v$ .

The selection of interest degree is defined as suppose  $U$  is the set of all URLs in the website session,  $H$  is the set of all browsing subpaths,  $k(k=L, 2, \dots, n)$  The selection interest of various choices is formula (6) as follows:

$$P_A = \frac{A_k}{((\sum_{i=1}^n A_i)/n)} \quad (6)$$

The degree of interest in access time is defined as follows: U is the set of all URLs of website sessions, H is the set of all subpaths of browsing, and the first  $m$  bits of them are the same;  $m + L$  bits have N different choices;  $T_i$  represents the sum of access time for users to enter the next page through the  $i$ th choice, where  $k(1(k=L, 2, \dots, n))$ . The interest degree of access time selected is formula (7), which is as follows:

$$P_T = \frac{T_k}{((\sum_{i=1}^n T_i)/n)} \quad (7)$$

Considering the choice interest and access time interest comprehensively, the path interest is composed of choice interest and access time interest, and formula (8) is as follows:

$$P = \alpha \times P_A + \beta \times P_T, \quad (8)$$

where  $a+b=1$ , and  $b$  is the adjustment coefficient. By setting the size of  $a$  and  $b$ , the role of  $P_A$  and  $P_T$  in calculating path interest can be changed. The algorithm uses path interest degree to represent user interest degree for calculation and recommendation.

#### 4. Experimental Results and Analysis

The experimental data set is based on the basic education and teaching resource database of Lianyungang Educational Center to validate the effectiveness and quality of the recommendation approach provided in this article. The resources cover nearly 10 TB capacity of all subjects in primary and secondary schools, with more than 9,000 registered users and more than 1,000 daily visits. Through sorting, 31,000 evaluation data of 300 users' interest in 1600 teaching resources were collected, and the sparsity level of the data set was  $1-31000/(300 * 1600) = 0.9354$ . The value is an integer from 0 to 5. The higher the value is, the higher the user's interest in the teaching resource is.

The average absolute deviation MAE (MAE) is used to assess the recommendation method's prediction accuracy. The average absolute deviation (MAE) between the actual and projected value of resource consumers' interest in resources is the average absolute deviation. The lower the MAE, the more accurate the advised prediction. If the data set for the anticipated value of users' interest in teaching resources is  $\{P_1, P_2, \dots, P_n\}$  and the data set for the actual value is  $\{q_1, q_2, \dots, q_n\}$ , then

$$MAE = \sum_{i=1}^n \frac{|p_i - q_i|}{n} \quad (9)$$

The number of nearest neighbors of the target user of instructional resources increases from 20 to 50 during the trial, with a step size of 5. The MAE of the standard collaborative filtering recommendation method and the fuzzy cluster-based recommendation approach suggested in this study are calculated and compared in Figure 4, and the experimental results are shown.

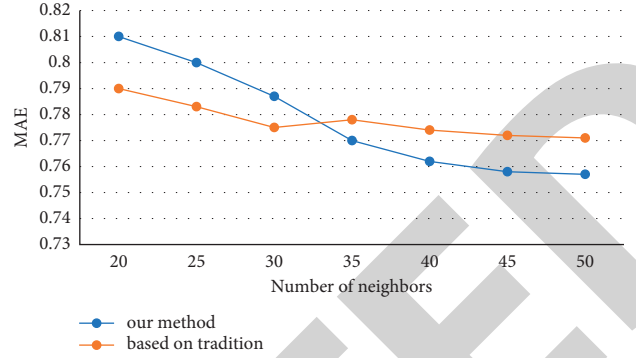


FIGURE 4: Experimental results.

From the experimental results in Figure 4, it can be seen that compared with the traditional collaborative filtering recommendation method, the recommendation method based on fuzzy clustering has a smaller MAE value, indicating that the accuracy and quality of the teaching resource recommendation predictions are better than the simulation results of the method in this study. The rate of descent is faster and more realistic. This is because the traditional collaborative filtering recommendation algorithm searches the nearest neighbor of the target user in all user Spaces, while the fuzzy clustering-based recommendation algorithm searches in the user space after clustering, so the accuracy of recommendation is greatly improved. Moreover, with the increase in the number of neighbors of target users recently, the larger their MAE difference value is, indicating that the recommendation prediction accuracy and quality advantage of the fuzzy clustering-based recommendation method is more obvious. In addition, by further enlarging the experimental data set, it is found that the recommendation method based on fuzzy clustering takes into account the similarity of clustering users' interests in the relevant teaching resource set and reduces the search scope of the nearest neighbor of the target user. The sparsity, cold start, and real-time recommendation speed of the traditional collaborative filtering recommendation method can also be greatly improved.

The experiment was divided according to the proportion of the training set and the test set from 0.1 to 0.9, and then MAE values of the three collaborative filtering methods were calculated respectively. Each MAE value was obtained by conducting at least ten experiments, and then the average value was calculated. The experimental results of the three recommendation algorithms are shown in Figure 5.

According to the experimental results, the MAE value of the dual clustering recommendation algorithm is the smallest, indicating the highest recommendation accuracy. Therefore, the dual clustering recommendation algorithm designed in this topic has obvious advantages and application significance.

The number of users for the collection and test of this recommendation system is limited, and there is a small amount of traffic and data collection at ordinary times, so there is a large problem of sparsity. Table 2 shows part of the user project score matrix data after algorithm processing. In

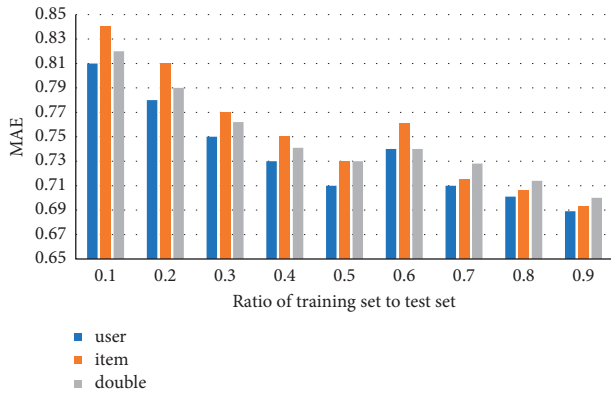


FIGURE 5: MAE experimental result diagram of the recommendation algorithm.

TABLE 2: The user project score matrix after partial processing.

	1	2	3	4	5	6	7	8	9
1	2.322	2.223	2.655	3.522	2.968	2.657	2.672	2.235	2.553
2	2.22	2.295	2.672	2.273	2.735	2.265	2.582	3.852	2.872
3	3.672	2.562	3.728	2.367	5.829	2.729	2.27	2.389	2.728
4	2.289	2.283	2.293	2.293	2.928	2.983	3.872	2.282	2.23
5	2.27	2.29	2.572	2.282	2.222	2.293	2.283	2.982	2.872
6	2.375	2.985	2.738	2.265	3.872	2.972	2.752	2.852	2.822
7	2.552	2.578	2.62	2.265	2.325	3.992	2.256	3.223	2.822
8	3.652	2.563	2.762	2.592	2.952	2.73	2.825	3.995	2.553

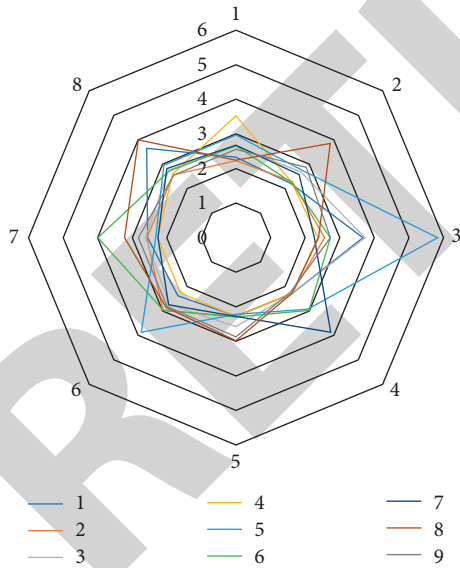


FIGURE 6: Shows the user project score matrix after partial processing.

addition, we display the scoring matrix through the radar chart, as shown in Figure 6, so that we can more intuitively observe the distribution of scoring at all levels.

Therefore, the MAE value calculated through the experiment is generally large, with the maximum MAE value of 0.94 and the minimum MAE value of 0.82 when the  $K$  value is 14, as shown in Figure 7.

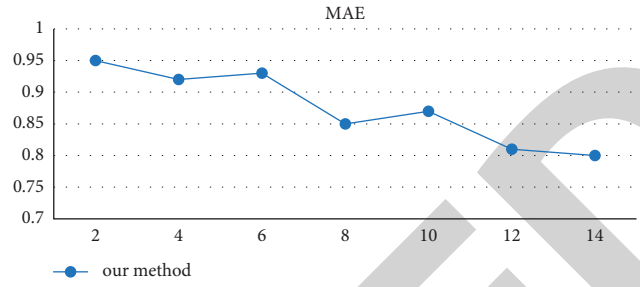


FIGURE 7: MAE distribution.

According to the recommendation results, MAE still shows a downward trend when the number of neighbors increases step by step, but the value of the whole foot is still too large. The recommendation effect will be more obvious only when the number of neighbors is larger.

### 5. Conclusion

This study investigates the current status of ideological and political teaching and proposes to develop an Android-based mobile teaching assistance system for ideological and political courses in colleges and universities based on on-demand analysis. On the basis of in-depth demand analysis, four functional modules are introduced: home page module, all courses module, course view module, and my account module. These modules are mainly to meet the functional requirements of the Android-based mobile teaching assistance system for ideological and political courses in colleges and universities. Since the role of the mobile teaching assistance system for ideological and political courses is mainly carried out remotely, there is a certain gap in the guidance of professors to students. In response to this demand, the system implements the recommendation system function, improves the integrity of the tutor's recommendation, and also provides personalized recommendation. This creates a breakthrough for some limitations of ideological and political education, and to a certain extent reflects the value-leading characteristics of ideological and political courses. Although the system has achieved the needs of its functional goals, in the face of the rapid development of international and domestic technology, the growing desire of college students for new and better learning methods, and the ever-changing impact of mobile learning, the function of the system is highly imperfect. The mobile teaching auxiliary platform for ideological and political courses in colleges and universities is a platform for integrating the wonderful teaching of famous teachers of ideological and political courses in colleges and universities, and the online live course module should be expanded. At the same time, the mobile teaching assistance system should follow the route of open participation and interactive communication, and further reflect the characteristics and styles of public participation, advancing with the times, and integrating into the life of information-based ideological and political theory courses.

## Research Article

# CRUN-Based Leaf Disease Segmentation and Morphological-Based Stage Identification

J. Sujithra <sup>1</sup> and M. Ferni Ukrit <sup>2</sup>

<sup>1</sup>Research Scholar School of Computing, SRM Institute of Science and Technology, Chennai-603203, Tamilnadu, India

<sup>2</sup>School of Computing, SRM Institute of Science and Technology, Chennai 603203, Tamilnadu, India

Correspondence should be addressed to M. Ferni Ukrit; ferniukm25@gmail.com

Received 19 April 2022; Revised 16 May 2022; Accepted 20 May 2022; Published 10 June 2022

Academic Editor: Punit Gupta

Copyright © 2022 J. Sujithra and M. Ferni Ukrit. This is an open access article distributed under the Creative Commons Attribution License, which permits unrestricted use, distribution, and reproduction in any medium, provided the original work is properly cited.

Natural growth is eliminated by the process of globalization in today's globe owing to the development of technology and landscapes. The majority of today's youngsters, as well as our seniors, lack an appropriate understanding of natural species such as plant names, tree names, and medicinal plants. This is attributed to technological advancements and a decline in gardening interest. To close this gap, horticulture may employ technology that aids in the improvement of plant understanding and growth. This method is implemented in the existing system for diagnosing leaf diseases using image processing and machine learning techniques. In the existing process, the classification of leaf disease is performed using image processing steps, such as pre-processing, segmentation, feature extraction, feature reduction, and classification. Even though it utilizes multiple processing steps and region-based classification, it identifies only the type of disease. In this paper, a combined approach of regional-based convolutional neural networks and U-Net (CRUN) is proposed for segmenting the leaf diseases from the augmented leaf dataset. Then, the segmented images are subjected to a morphological process to identify the level of disease in the leaf. This identification helps to identify the leaf's nature and suggests a process to reduce the disease's spread to other leaves through the proper use of fertilizers. The proposed method is applied to real-time images of sugarcane leaf diseases, such as bacterial blight and red rot, and banana leaf diseases, such as yellow and black sigatoka. This method is also applied to public sugarcane and banana leaf datasets from the Kaggle website. The proposed CRUN algorithm effectively segments the disease region. The morphological process helps to identify the disease level and protect the plant from further spread of disease. As a result, the proposed CRUN and morphological tests are most effective for automating leaf disease detection and prevention.

## 1. Introduction

Technology has advanced in every industry in today's society. The user's cell phone aids them in acquiring access to the objects around them. Researchers have developed an easy-to-use method for analyzing leaf diseases using image processing technology. This might be included as mobile apps in the future. To diagnose leaf disease, a combination of deep learning and morphological processes is proposed in this work. The next sections go through some of the more current ways of identifying leaf diseases.

A segmentation-based alfalfa leaf disease classification was proposed in [1]. Here, they utilized the K-nearest

neighbor (KNN) based ranking algorithm called Relief was used for the feature selection process. Then, the selected features were classified with the help of a support vector machine (SVM) with an accuracy of eighty percent. A manual region of interest-based leaf disease classification was proposed in [2]. Here, they resized the original image into 256 rows and columns. For that, the leaf disease region was segmented manually, and then convolutional neural networks were used for the classification process.

A specialized classification process for soy leaf disease was proposed in [3]. Here, they performed segmentation and feature extraction on soy leaf that was collected at various height levels from 1 to 16 m with desired intervals. The SVM and KNN were used for the classification of the extracted

characteristics from different soy leaves. In particular, this approach produced good results in foliar diseases.

An image transformation based on cucumber leaf diseases classification was proposed in [4]. Here, they utilized LAB colour space for segmentation and feature extraction instead of the regular RGB colour space. Traditional algorithms such as k-means clustering were used for segmentation, and then the segmented images were subjected to singular value decomposition-based feature reduction in order to reduce the textural features. Then, the classification was performed using an SVM classifier.

A deep learning CNN algorithm was proposed in [5] for rice leaf disease classification. They achieved accuracy above ninety-five percent with the help of a 10-fold cross-validation technique. A survey paper was analyzed for leaf stress analysis using multiband images. The term multiband image is the hyperspectral image and the technique used for the analysis was also discussed in [6].

A segmentation-based leaf diseases classification was proposed in [7]. The traditional algorithms such as simple iterative clustering were used for segmentation, and those segmented images were subjected for feature extraction to obtain colour- and texture-related features. Then, the classification was performed by using an SVM classifier.

In the above articles, either traditional feature reduction like ranking algorithms, cross-validation, and singular value decomposition or principal component analysis were used. These approaches were based on the manual threshold or feature selection approach. A new approach called the automated approach for feature selection uses metaheuristic algorithms by solving the fitness functions in recent years.

Based on this metaheuristic approach, in [8] a bacterial foraging algorithm was used for selecting the optimal characteristics for fungal leaf disease classification. Here, the reduced characteristics were classified using a neural network with radial basis activation function. In [9], we also utilized the CNN for classification, but they have performed their classification on pretrained apple leaves of four diseases, and it enhanced the accuracy of the former Alexnet by ten percent. Most researchers in recent years utilized the CNN deep learning algorithm for leaf disease classification [10].

The paper is organized in the following manner. Section 2 highlights the recent works on leaf diseases. Sections 3 and 4 describe the proposed method and then discuss the results. Finally, the paper summarized the proposed method advantages in Section 5, and Section 6 proposed the future work.

## 2. Literature Survey

The authors in [11] investigated numerous parameters for the categorization of soy leaf diseases. The results revealed that images were taken at 1 m and 2 m, as well as colour and texture, features using convolutional neural networks, performed better in detecting foliar illnesses in soybean leaves than prior SVM and KNN classification.

The article from [12] enhanced the convolutional neural network for predicting crop diseases. It improved the feature set by including squeezing and excitement. As a result, it obtained 91 percent accuracy. However, because it does not

compare any multiclass categorization, its result is ineffective.

The authors in [13] surveyed the importance of leaves in plant disease detection and explored the various methodologies and attributes utilized in crop diagnosis of diseases. Dhingra et al. [14] suggested a novel approach for classifying leaf diseases. The technique is based on colour, shape, and the histogram.

For plant leaf disease classification, an optimized and nine-layer CNN by [15]. It attained an accuracy of 96.11 percent. By supplementing the dataset in six different ways and tweaking the batch size, epoch, and iteration, the efficiency is increased.

A deep learning strategy to classify soybean plant disease [16]. It encompasses the sixteen disease classes in the soy crop and has an accuracy of 98.14 percent. However, it was built specifically for a single leaf to complete this categorization. Chen et al. [17] used a combination of approaches to enhance tomato leaf disease detection. Despite using various methodologies, it only obtained eighty-nine percent accuracy for tomato leaf diseases. The artificial bee colony technique was employed by researchers to determine the best threshold for segmenting the leaf areas.

A basic technique for groundnut leaf disease categorization was discussed in [18]. Along with the late blight spot, it was able to categorise five main leaf diseases. Altogether, it classified these disorders with 97.11 percent accuracy. CNN was used to extract features and an SVM was used to identify pathogens in rice crops [19].

The olive leaf disease classification uses the transfer learning principle in a convolutional neural network [20]. The best results were achieved with ADAM and SGD optimization in VGG-16 and 19 CNN. However, various leaves necessitate a lengthy processing period.

For segmentation, U-Net is utilized [21] to exclude complicated backgrounds in terms of reducing the effect of complex backgrounds on identification results.

Few other networks handle segmentation better. U-Net++ [22, 23] connected the encoder and decoder via densely layered skip connections. It is more effective than U-Net, but its massive intermediate convolutions are expensive.

In [24], DIResUNet uses modified ResUNet blocks and inception modules with a dense and global spatial pyramid pooling (DGSP) block, structurally similar to UNets but providing higher extraction performance and good generalization ability for multiclass semantic segmentation of HRRS pictures.

Most deep convolutional neural networks were used to identify and classify plant diseases based on their probability values. Pixel-level segmentation quantifies plant disease severity, which helps calculate pesticide dosage. In [25], the authors have presented deep learning to detect and measure grey mould illness in strawberry plants.

In the existing process, the classification of leaf diseases is performed using image processing steps such as pre-processing, segmentation, feature extraction, feature reduction, and classification. Even though it utilizes multiple processing steps to fine-tune the layers in neural networks



[26] or region-based classification or deep learning algorithms, it identifies only the type of disease.

The use of deep learning networks in phytopathology is on the rise due to the abundance of labelled leaf images and computationally efficient hardware [27–30]. Several open-source datasets exist. However, most were collected in a lab with a similar background and light illumination. Field conditions are opposite. A cluttered background, occlusion, and uneven illumination all influence image quality. It is one of the key reasons for poor model performance, trained on controlled environment images and assessed on-field images.

Hence, the proposed model is used for segmenting leaf diseases from the augmented leaf dataset. Then, the segmented images were subjected to a morphological process to identify the level of disease in these leaves. This identification helps to identify the leaf's nature and suggests a process to reduce the disease's spread to other leaves through the proper use of fertilizers.

### 3. Proposed Method

In this paper, a combination of deep learning and morphological processing is proposed to identify leaf disease stages and preventative actions in banana and sugarcane leaves. Figure 1 depicts the steps of the proposed method in a graphical format.

The following steps are a short description of the CRUN-morphological-based leaf disease level identification.

- (1) The input dataset comprises both real-time and public datasets of banana and sugarcane leaves.
- (2) Both datasets are subjected to a filtering process using a median filter. Here, the filtering process is carried out on the colour space transformed image.
- (3) The preprocessed and raw images are subjected to scaling, rotation, shifting, noise addition, and mirror-image formation to produce a new training dataset using the augmentation process for enhancing the deep learning-based segmentation process.
- (4) The augmented images are subjected to the diseased part segmentation in the leaf using the CRUN approach.
- (5) Here, in CRUN, first, the region-based convolution neural network is performed to segment the leaf foreground and background image.
- (6) The U-Net is used to segment the diseased part from the leaves.
- (7) Using this CRUN approach, the diseased part of the leaf was extracted.
- (8) After the extraction of the diseased part, morphological operation is applied to the region to extract the exact diseased region.
- (9) Finally, the bwarea parameter is used to estimate the diseased part.

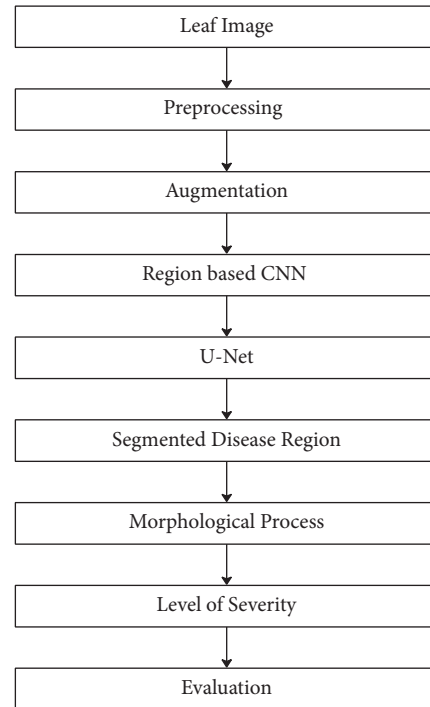


FIGURE 1: CRUN-morphological-based leaf disease classification flow chart.

- (10) The differences between the original and diseased part pixel values are calculated.
- (11) The level of disease was estimated using the difference value.
- (12) The CRUN performance is evaluated in terms of classification performance metrics.

**3.1. Preprocessing.** In this approach, three image preprocessing steps are performed on the input images before the augmentation process. The three preprocessing steps are as follows:

- (i) Image resizing: both datasets have different image sizes and it takes higher computational time for the larger size. To overcome this problem, the images are resized to 2.66 inches in height and width for further processing. This resizing operation on the image is the first preprocessing step in this approach.
- (ii) Image conversion: in this step, the resized image is subjected to the colour channel transformation process. Here, the image is from three input RGB channels to a single grey channel using

$$I_{GC} = (0.3 * I_R) + (0.59 * I_G) + (0.11 * I_B). \quad (1)$$

The subscripts in the above equation denote the channel and the term  $I$  denotes the corresponding pixel values.

- (iii) Filtering: this is the final step in the preprocessing of the proposed method. Here, the output image from the image conversion process is subjected to filtering to remove any artefacts that arise during the above preprocessing steps.

Here, the median filtering is carried out using the steps in [31] with  $3 \times 3$  as the window length. The steps in the median filter are described in the following example.

- (1) The greyscale image pixel value is shown in Figure 2.
- (2) Arrange the pixel values in ascending order that comes under  $3 \times 3$  window length 121, 122, 124, 125, 131, 144, 151, 152, and 163.
- (3) Calculate the median value for the step 2 output. Replace the first-pixel value in step 2 with this median value.
- (4) Repeat steps 2 and 3 for the complete image and the whole dataset.

By using the filtered greyscale value thrice, the RGB filtered image is formed. With these three processes, the basic augmentation process was carried out on input images.

**3.2. Extended Dataset Using Augmentation Process.** In literal meaning, the term augmentation refers to an increase in size. Here, the dataset is increased by performing the following actions as in Table 1.

Using this process, the input images in the dataset are increased along with the preprocessed and original images.

**3.3. Region-Based Convolutional Neural Network (RCNN).** In this step, the regions in the image like the leaf (foreground) and background parts like black or white colour and other regions of the leaf image are segmented using RCNN.

The layers in the RCNN structure are similar to the layers Alexnet, as shown in Figure 3.

Similar to Alexnet, RCNN also has an input layer, convolution layer, and max-pooling layer. However, it has a bounding box and an SVM output as final layers in RCNN instead of the softmax and is fully connected, as shown in Figure 4. The greatest advantage of RCNN is that all network layers can be upgraded during training. Caching requires no disc space. In addition, it provides high detection quality.

Using this bounding box, the leaf images are segmented to detect the leaf and diseased regions from the whole image. The bounding box indicates the different regions like foreground, leaf, background colour, and colour variation in the image. Then, this bounding box output is subjected to U-Net for the final segmentation of the diseased region.

**3.4. Diseased Region Extraction Using U-Net.** The foreground and colour variation regions from RCNN outputs are subjected to U-Net for the final diseased region classification process. Even though the RCNN and U-Net's objective is to segment the diseased region, this architecture does not utilize these two softmax and fully connected layers in their architecture.

121	122	151	147
124	125	131	134
144	152	163	142

FIGURE 2: Sample pixel value of an image.

TABLE 1: Augmentation techniques.

Technique	Value
Scaling	0.5
Rotation	$20^\circ$
Noise	Salt and pepper noise
Reflection	50%
Translational	+50 and -50 for both $x$ and $y$ axes

As per the [32] process, U-Net segments the diseased region from the bounded region outputs.

The name U-Net comes from its architectural shape because the architecture is in the form of a U-shape with more number convolution and max-pooling layers, as shown in Figure 5. Based on the medical image segmentation properties of U-Net, this is used for identifying the diseased region from the bounding box RCNN output. For both RCNN and U-Net, the image size is kept as [256 256].

Even though the RCNN and U-Net's objective is to segment the diseased region, this architecture does not utilize these two softmax and fully connected layers in their architecture. Instead of these layers, it highly utilizes the convolution and max-pooling layers.

- (1) The phrase up refers to upsampling the image by ratio 2
- (2) The word down refers to downsampling the pixel values by ratio 2
- (3) The name conv3 refers to performing convolution in all trio image channels using the [128 128] convolution filter
- (4) The term concatenate refers to the act of copying the preceding outcome and combining it with the present state
- (5) The phrase max-pool refers to the process of normalizing the previous stage results

By using the method described above, the picture is first downsampled before being convoluted with a convolution layer. The convoluted outputs are then upsampled, and convolution filtering is used to partition the images into healthy and unhealthy regions. To segment the diseased region in the leaf, the aforementioned U-Net architecture approach is used for both the enhanced and original datasets.

**3.5. Evaluation.** CRUN performances are evaluated using the traditional classification performance metrics as in Table 2.

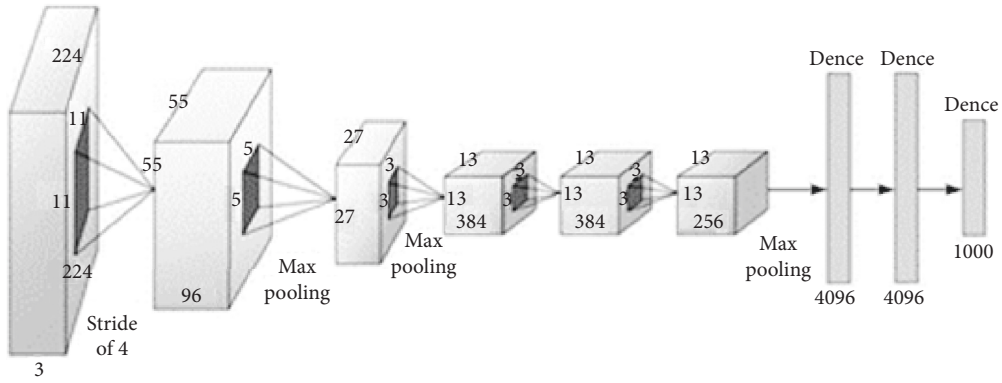


FIGURE 3: Alexnet architecture.

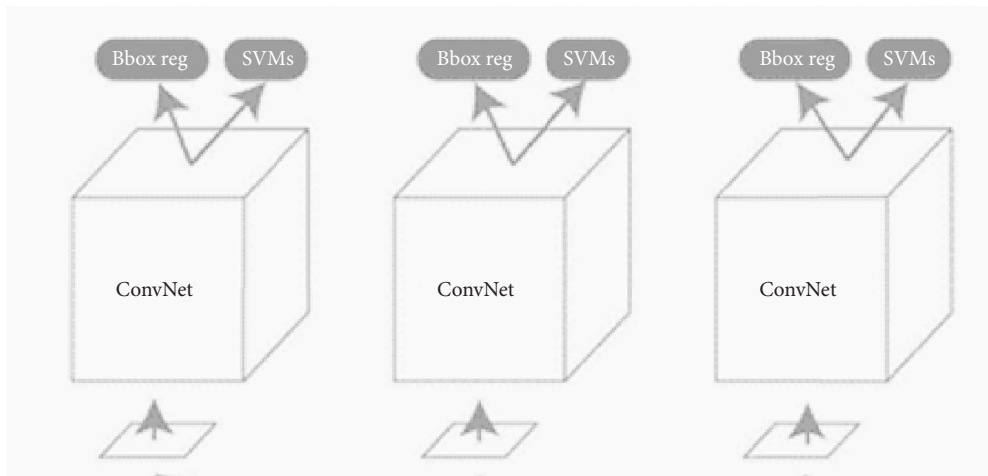


FIGURE 4: Final layers of RCNN.

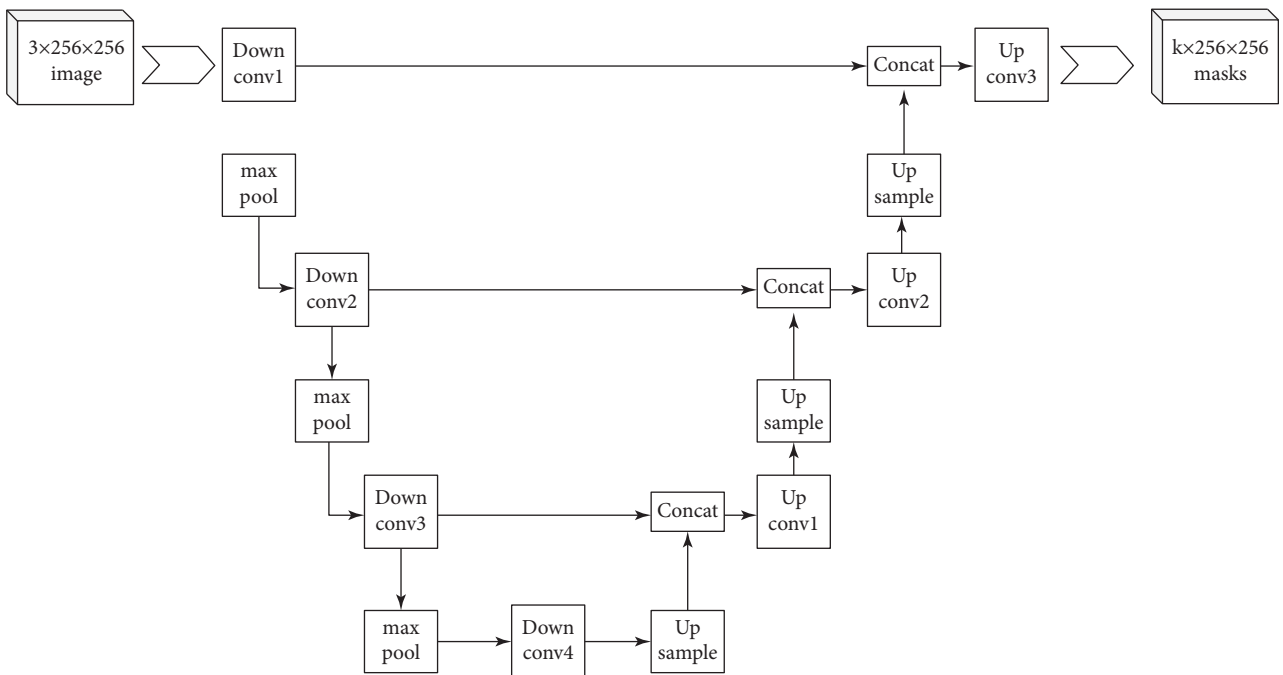


FIGURE 5: Architecture diagram of U-Net.

TABLE 2: CRUN evaluation metrics (CRUN-EM).

CRUN-EM	Equation	Purpose
Accuracy	No. of classes identified correctly/total images	Total CRUN assessment in identifying healthy and unhealthy regions
Sensitivity	No. of Unhealthy images identified/total unhealthy images	CRUN assessment in detecting the diseased region
Specificity	No. of healthy images identified/total healthy images	CRUN assessment in detecting the healthy region

3.6. *Morphological Processing.* After segmenting the diseased region, the morphological process like top hat and bottom hat transformation is performed on the segmented region to extract the exact diseased region. For both the transformations, the structural element disk is used with size 12. The overall morphological process formula for extracting the leaf region is represented in

$$I_M = \text{open}(\text{bot hat}(I_{\text{unet}})). \quad (2)$$

Here,  $I_M$  denotes the morphological output from the difference of the top and bottom hat of U-Net output image  $I_{U\text{-net}}$ . The sample operation of the proposed morphological operation is shown in Figure 6.

From the morphological output area, the area covered by black and white pixels was measured using bwarea properties. With this information, the identification of disease levels in the leaf region is performed as per Table 3.

At these levels, the leaves in mild and moderate regions can be protected from proper fertilizers to prevent the disease from spreading in the crop. The fertilizer in Table 4 is chosen based on the corresponding deficiency of nutrition in the plant.

## 4. Experimental Results and Discussion

In this, the proposed CRUN-based morphological for disease identification in leaves was implemented using MATLAB R2021a under a Windows 10 environment.

In this paper, both the real and public databases are used for the analysis. But in both the databases, the sugarcane and banana leaves are used for the analysis.

4.1. *Real-Time Dataset.* The real-time dataset is collected using a Nikon D5300 camera. The conditions for capturing the images which the camera should automatically adjust the flashlight and there is no bias correction to the images. The image resolution is set as 96 dpi for 5.3-inch height and 5.3-inch width.

Using these conditions, three major categories of banana and sugarcane leaf images are captured. The three major categories of banana leaves are healthy (HB), yellow sigatoka (YS), and black sigatoka (BS). In sugarcane, the three major categories are healthy (HS), bacterial blight (BB), and red rot (RR). Table 5 gives the image count in each category in the real-time dataset.

In banana leaves, it has 3510 images from all three categories. Similarly, sugarcane has 3126 images from all three categories.

4.2. *Public Dataset.* In this, both the banana and sugarcane leaf datasets are taken from the Kaggle website [33, 34].

In bananas, it has three major categories: healthy (HB), Pestalotiopsis leaf blight (PLB), sigatoka (S), and cordana (CB) disease. In sugarcane, the three major categories are healthy (HS), bacterial blight (BB), and red rot (RR). Table 6 gives the image count in each category in the public dataset.

Totally, banana leaves have 935 images from all three categories. Similarly, sugarcane leaves has 300 images from all three categories. Both these dataset images were subjected to preprocessing and segmentation, for extracting the diseased region from the leaf. The parameters used for evaluating the performance of the proposed model are listed in Table 7.

The sample input images for the real-time and public banana dataset are shown in Figure 7.

Similarly, the sample sugarcane leaf image from the dataset is shown in Figure 8.

The sample preprocessed greyscale output for the unhealthy leaves is shown in Figure 9.

The preprocessed images are subjected to augmentation and then subjected to CRUN architecture to segment the diseased region from the leaf.

Using the architecture in Figure 10, the leaves get segmented and the segmented diseased region using CRUN is shown in Figure 11.

Using Table 2, the CRUN performance is evaluated for banana and sugarcane. The results are tabulated from Tables 8–10.

Tables 8 to 10 prove that the proposed CRUN is the best for segmenting the diseased region, and the pictorial representations of the comparative results are shown in Figures 12–14. Then, the segmented image is subjected to the morphological process on the cropped image using the bounding box as in Figures 15.

Then, the cropped image is subjected to morphological operation with a disk element size of 12 and followed by a binarization process to estimate the level of disease. The corresponding output is shown in Figure 16.

The white region indicates the diseased part and the black region indicates the healthy part. Then, the area

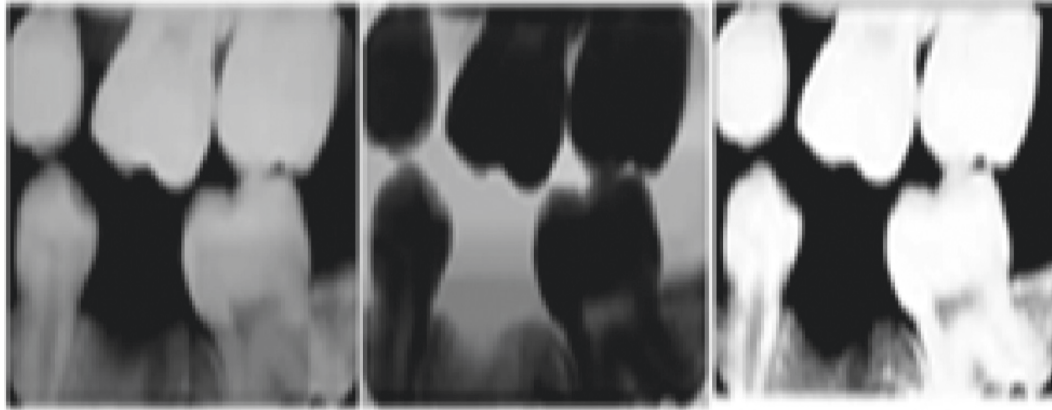


FIGURE 6: Sample images of proposed morphological operation (G) fertilizer suggestion.

TABLE 3: Diseased level identification.

Pixel range	Diseased level
Black area > white area	Mild
Black area < white area	Lethal
White area = black area	Severe
White area > black area/2	Moderate

TABLE 4: Fertilizers for preventing the spreading of disease.

Leaf	Disease	Deficiency	Fertilizer
Banana	S and CB	Potassium and phosphorus	50 g Di-ammonium phosphate or 300 g super phosphate is added to each dug and followed by watering
	PLB	Nitrogen	A small trench should be dug and 100 g of urea applied per plant, followed by watering.
Sugarcane	RR	Potassium	At fortnight interval, spray twice, 1% of potassium chloride 4 kg of ammonium sulphate - 24% S for an acre
	BB	Sulphur	

TABLE 5: Real-time dataset image counts.

Leaf	Category	Image counts
Banana	HB	1330
	YS	1020
	BS	1160
Sugarcane	HS	1064
	BB	1050
	RR	1012

TABLE 6: Public dataset image counts.

Leaf	Category	Image counts
Banana	HB	89
	PLB	133
	S	433
	CB	120
Sugarcane	HS	100
	BB	100
	RR	100

covered by black and white pixels was estimated for analyzing the level of disease. Based on their level, the actions in Table 4 will be taken.

Therefore, the proposed approach is suitable for predicting the level of disease and the corresponding fertilizers can be used.

TABLE 7: Parameters used for evaluating the performance of the proposed model.

Parameters	Values
Total number of images	7711
Crop varieties	Sugarcane and banana
Datasets	Real-time and Kaggle datasets
Total epoch	50
Performance metrics considered	Accuracy, specificity, and sensitivity
Proposed model	CRUN model






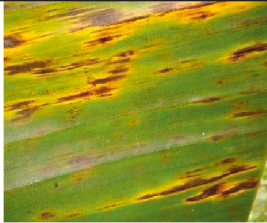
Real Time dataset-Banana		Public Dataset-Banana	
Type	Image	Type	Image
HB		HB	
YS		CB	
BS		S	

FIGURE 7: Banana leaf sample images.




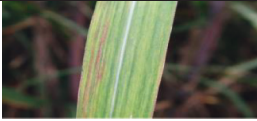


Real Time Dataset-Sugarcane		Public dataset-Sugarcane	
Type	Image	Type	Image
HS		HS	
BB		BB	
RR		RR	

FIGURE 8: Sugarcane leaf sample images.

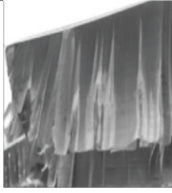
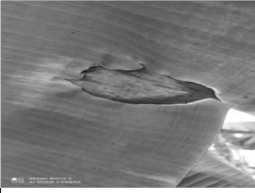
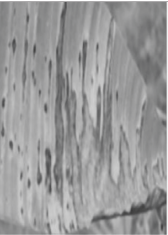

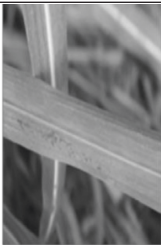
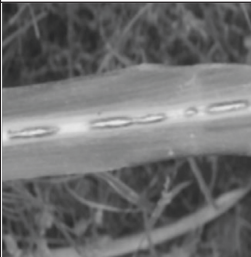
Leaf	Diseases type	Image	Diseases type	Image
Banana	YS		CD	
	BS		PLB	
Sugarcane	BB		RR	

FIGURE 9: Preprocessed output.

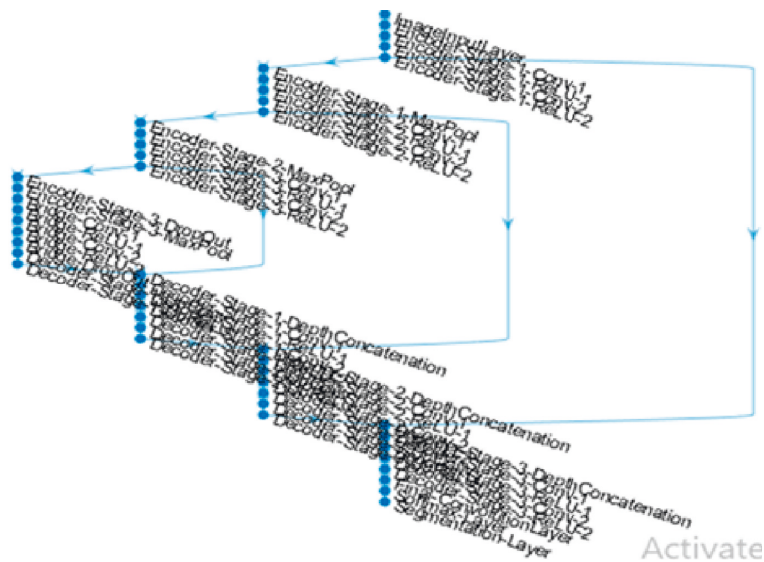


FIGURE 10: U-Net structure in CRUN.



FIGURE 11: Segmented disease region.

TABLE 8: CRUN evaluation for banana leaf.

Metric/method	Accuracy (%)	Sensitivity (%)	Specificity (%)
Histogram-based for banana	95.1	96.2	94.3
U-Net based on banana	96.2	97.3	96.4
H + U-Net for banana	98.4	98.8	97.5
Proposed CRUN-MP for real-time banana	98.9	99.1	98.6
Proposed CRUN-MP for Kaggle time banana	99	99.2	99.3

TABLE 9: CRUN evaluation for sugarcane.

Metric/method	Accuracy (%)	Sensitivity (%)	Specificity (%)
Histogram-based for sugarcane	94.1	95.3	93.2
U-Net based on sugarcane	95.3	96.4	94.3
H + U-Net for sugarcane	98.5	98.0	97.8
Proposed CRUN-MP for real-time sugarcane	98.9	99.1	98.6
Proposed CRUN-MP for Kaggle sugarcane	99	99.2	99.3

TABLE 10: CRUN evaluation for multiclass leaves.

Metric/method	Accuracy (%)	Sensitivity (%)	Specificity (%)
Histogram-based for real-time data	93.6	95.2	92.7
U-Net based on real-time data	94.6	95.5	93.3
H + U-Net for real-time data	97.6	96.5	96.2
Proposed CRUN-MP for real-time dataset	98.4	98.2	98.6
Proposed CRUN-MP for Kaggle dataset	99.2	99.1	99.3

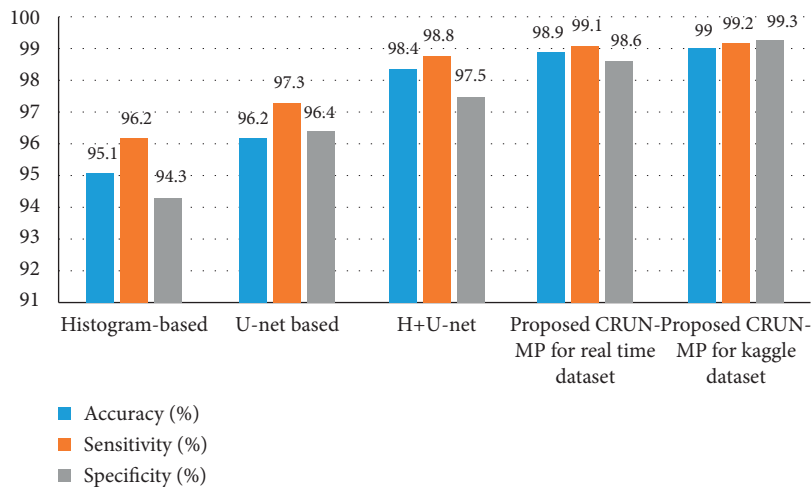


FIGURE 12: CRUN evaluation for banana dataset.



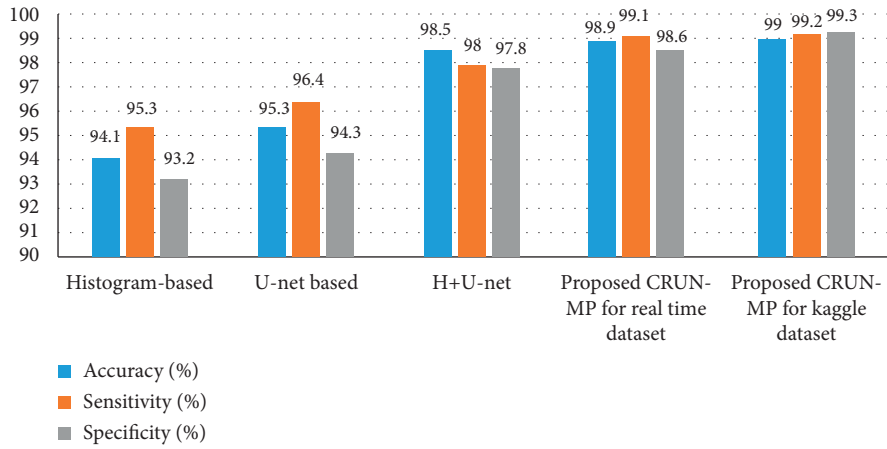


FIGURE 13: CRUN evaluation for sugarcane dataset.

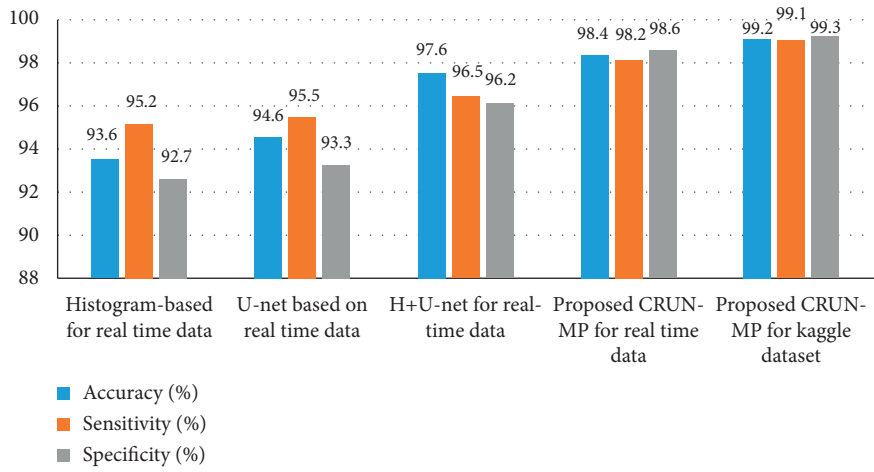


FIGURE 14: CRUN evaluation for multiclass.



FIGURE 15: Cropped disease region.



FIGURE 16: The output of the morphological operation.

## 5. Conclusion

In this paper, the proposed CRUN approach is used for identifying the segmentation of diseased parts in the leaf. The proposed morphological operation is best for identifying the level of disease in the leaf. Finally, the area estimation on the pixels helps to identify the severity level of the leaf and performs the necessary action on the diseased region. Therefore, the proposed CRUN-based morphological approach is suitable for predicting the level of disease and the usage of fertilizers.

## 6. Future Works

In future, the proposed method can be further enhanced by using the improved morphological process.

## Data Availability

The data can be shared by the authors J. Sujithra and M. Ferni Ukrit, if it is requested. The data are not publicly available due to privacy concerns.

## Consent

Not applicable as no human or animal sample was involved in this study.

## Conflicts of Interest

The authors declare that they have no conflicts of interest.

## References

- [1] F. Qin, D. Liu, B. Sun, L. Ruan, Z. Ma, and H. Wang, "Identification of alfalfa leaf diseases using image recognition technology," *PLoS One*, vol. 11, no. 12, Article ID e0168274, 2016.
- [2] S. Sladojevic, M. Arsenovic, A. Anderla, D. Culibrk, and D. Stefanovic, "Deep neural networks based recognition of plant diseases by leaf image classification," *Computational Intelligence and Neuroscience*, vol. 2016, Article ID 3289801, 11 pages, 2016.
- [3] N. A. D. S. Belete, D. A. Guimaraes, and H. Pistori, "Identification of soybean foliar diseases using unmanned aerial vehicle images," *IEEE Geoscience and Remote Sensing Letters*, vol. 14, no. 12, pp. 2190–2194, 2017.
- [4] S. Zhang, X. Wu, Z. You, and L. Zhang, "Leaf image based cucumber disease recognition using sparse representation classification," *Computers and Electronics in Agriculture*, vol. 134, pp. 135–141, 2017.
- [5] Y. Lu, S. Yi, N. Zeng, Y. Liu, and Y. Zhang, "Identification of rice diseases using deep convolutional neural networks," *Neurocomputing*, vol. 267, pp. 378–384, 2017.
- [6] A. Lowe, N. Harrison, and A. P. French, "Hyperspectral image analysis techniques for the detection and classification of the early onset of plant disease and stress," *Plant Methods*, vol. 13, no. 1, pp. 80–12, 2017.
- [7] Y. Sun, Z. Jiang, L. Zhang, W. Dong, and Y. Rao, "SLIC\_SVM based leaf diseases saliency map extraction of tea plant," *Computers and Electronics in Agriculture*, vol. 157, pp. 102–109, 2019.
- [8] S. S. Chouhan, A. Kaul, U. P. Singh, and S. Jain, "Bacterial foraging optimization based radial basis function neural network (BRBFNN) for identification and classification of plant leaf diseases: an automatic approach towards plant pathology," *IEEE Access*, vol. 6, pp. 8852–8863, 2018.
- [9] B. Liu, Y. Zhang, D. He, and Y. Li, "Identification of apple leaf diseases based on deep convolutional neural networks," *Symmetry*, vol. 10, no. 1, p. 11, 2017.
- [10] X. Chao, G. Sun, H. Zhao, M. Li, and D. He, "Identification of apple tree leaf diseases based on deep learning models," *Symmetry*, vol. 12, no. 7, p. 1065, 2020.
- [11] E. C. Tetila, B. B. Machado, G. K. Menezes et al., "Automatic recognition of soybean leaf diseases using UAV images and deep convolutional neural networks," *IEEE Geoscience and Remote Sensing Letters*, vol. 17, no. 5, pp. 903–907, 2020.
- [12] J. Hang, D. Zhang, P. Chen, J. Zhang, and B. Wang, "Classification of plant leaf diseases based on improved convolutional neural network," *Sensors*, vol. 19, no. 19, p. 4161, 2019.
- [13] S. Kaur, S. Pandey, and S. Goel, "Plants disease identification and classification through leaf images: a survey," *Archives of Computational Methods in Engineering*, vol. 26, no. 2, pp. 507–530, 2019.
- [14] G. Dhingra, V. Kumar, and H. D. Joshi, "A novel computer vision based neutrosophic approach for leaf disease identification and classification," *Measurement*, vol. 135, pp. 782–794, 2019.
- [15] A. P. Goel, "Identification of plant leaf diseases using a nine-layer deep convolutional neural network," *Computers & Electrical Engineering*, vol. 76, pp. 323–338, 2019.
- [16] A. Karlekar and A. Seal, "SoyNet: soybean leaf diseases classification," *Computers and Electronics in Agriculture*, vol. 172, Article ID 105342, 2020.
- [17] X. Chen, G. Zhou, A. Chen, J. Yi, W. Zhang, and Y. Hu, "Identification of tomato leaf diseases based on combination of ABCK-BWTR and B-ARNet," *Computers and Electronics in Agriculture*, vol. 178, Article ID 105730, 2020.
- [18] K. Suganya Devi, P. Srinivasan, and S. Bandhopadhyay, "H2K - a robust and optimum approach for detection and classification of groundnut leaf diseases," *Computers and Electronics in Agriculture*, vol. 178, Article ID 105749, 2020.
- [19] F. Jiang, Y. Lu, Y. Chen, D. Cai, and G. Li, "Image recognition of four rice leaf diseases based on deep learning and support vector machine," *Computers and Electronics in Agriculture*, vol. 179, Article ID 105824, 2020.
- [20] S. Uguz and N. Uysal, "Classification of olive leaf diseases using deep convolutional neural networks," *Neural Computing & Applications*, vol. 33, no. 9, pp. 4133–4149, 2021.
- [21] G. Hu and M. Fang, "Using a multi-convolutional neural network to automatically identify small-sample tea leaf diseases," *Sustainable Computing: Informatics and Systems*, vol. 35, Article ID 100696, 2022.
- [22] D. G. Lowe, "Distinctive image features from scale-invariant keypoints," *International Journal of Computer Vision*, vol. 60, no. 2, pp. 91–110, 2004.
- [23] S. M. M. Kahaki, M. Jan Nordin, A. H. Ashtari, and S. J. Zahra, "Deformation invariant image matching based on dissimilarity of spatial features," *Neurocomputing*, vol. 175, pp. 1009–1018, 2016.
- [24] S. Lal, J. Nalini, C. S. Reddy, and F. Dell'Acqua, "DIResUNet: Architecture for Multiclass Semantic Segmentation of High Resolution Remote Sensing Imagery Data," *Applied Intelligence*, pp. 1–21, 2022.
- [25] A. Bhujel, F. Khan, J. K. Basak et al., "Detection of gray mold disease and its severity on strawberry using deep learning

- networks,” *Journal of Plant Diseases and Protection*, vol. 129, pp. 1–14, 2022.
- [26] M. Turkoglu, B. Yanikoğlu, and D. Hanbay, “PlantDiseaseNet: convolutional neural network ensemble for plant disease and pest detection,” *Signal, Image and Video Processing*, vol. 16, no. 2, pp. 301–309, 2022.
- [27] M. Brahimi, M. Arsenovic, S. Laraba, and S. Sladojevic, *Deep Learning for Plant Diseases: Detection and Saliency Map Visualisation Deep Learning for Plant Diseases: Detection and Saliency Map Visualization*, Springer, Cham, The Capital Region of Denmark, 2018.
- [28] J. Chen, J. Chen, D. Zhang, Y. Sun, and Y. A. Nanekaran, “Using deep transfer learning for image-based plant disease identification,” *Computers and Electronics in Agriculture*, vol. 173, Article ID 105393, 2020.
- [29] K. P. Ferentinis, “Deep learning models for plant disease detection and diagnosis,” *Computers and Electronics in Agriculture*, vol. 145, pp. 311–318, 2018.
- [30] S. P. Mohanty, D. P. Hughes, and M. Salathé, “Using deep learning for image-based plant disease detection,” *Frontiers of Plant Science*, vol. 7, p. 1419, 2016.
- [31] P. M. Narendra, “A separable median filter for image noise smoothing,” *IEEE Transactions on Pattern Analysis and Machine Intelligence*, vol. PAMI-3, no. 1, pp. 20–29, 1981.
- [32] A. G. Smith, J. Petersen, R. Selvan, and C. R. Rasmussen, “Segmentation of roots in soil with U-Net,” *Plant Methods*, vol. 16, no. 1, pp. 13–15, 2020.
- [33] <https://www.kaggle.com/kaiesalmahmud/banana-leaf-dataset>.
- [34] <https://www.kaggle.com/prabhakaransoundar/sugarcane-disease-dataset>.

## Research Article

# Research on Dance Teaching Based on Motion Capture System

**Yuan Peng** 

*Art Education Center, Hangzhou Dianzi University, Hangzhou, Zhejiang 310008, China*

Correspondence should be addressed to Yuan Peng; pengyuan@hdu.edu.cn

Received 1 March 2022; Revised 19 March 2022; Accepted 22 March 2022; Published 10 May 2022

Academic Editor: Punit Gupta

Copyright © 2022 Yuan Peng. This is an open access article distributed under the Creative Commons Attribution License, which permits unrestricted use, distribution, and reproduction in any medium, provided the original work is properly cited.

Ethnic dance is a part of minority culture and an important chapter of intangible cultural heritage. Because the art of dance does not exist in a certain physical form in a certain environment, it is difficult to record and preserve dance. In traditional recording work, dancers' dance movements are mostly recorded through text, photos, videos, etc. However, these methods can only record and preserve dance movements in a two-dimensional manner from a limited number of angles and cannot achieve accurate and comprehensive record protection of dance poses. Moreover, data preserved by traditional methods can only be simply copied and transferred, and cannot be exploited, developed, or innovated. Therefore, motion capture technology can be applied to the protection of ethnic dance art, and motion capture technology can be used to obtain 3D gestures of ethnic minority dance spaces, restore and optimize digital movements, such as establishing a national dance art movement technology database, and combine the protection of the original ecological cultural atmosphere. It can accurately and comprehensively preserve the essence of ethnic minority dance art and provide effective reference for many ethnic minority dances with ethnic characteristics, digital protection of sports, and the future.

## 1. Introduction

With the development of modern society, the living space of minority dance cultural heritage is increasingly impacted by industrial civilization and economic globalization. Country of ethnic dance cultural heritage protection has gaining more attention; how to better protect ethnic minority dance, rescue, and mining cultural heritage and how to apply information technology to the minority cultural heritage protection, rescue, and mining have become a cultural and information technology in the research of a hot topic. Based on the dance characteristics of ethnic minorities, this article uses computer motion capture technology to carry out three-dimensional digital protection of dance posture of ethnic minorities, combining the original ecological and cultural atmosphere of ethnic dances and the advantages of other protection methods. Under the grammar category, dance movements of people folk dancing to the action of a virtual character library-oriented production process are analyzed emphatically and its corresponding relation is discussed based on the motion style under the emotion model identification theory, put forward based on the

characteristics of action unit properties and associated constraints to implement action cohesion method and define the method in the application of descriptive system framework.

Minority dancing is an essential aspect of the intangible cultural heritage of the United States. However, due to the change of cultural-ecological environment, some excellent Chinese folk performing arts are on the verge of extinction and extinction. It is urgent to protect and inherit them scientifically and effectively through different means. Although the traditional methods of photographing, recording, and video recording are convenient for collection and production, they cannot record the body movements of dancers in detail, let alone carry out scientific analysis and research on them, and apply them to choreography and creation. Therefore, in view of the lack of two-dimensional recording technology of text, photos, and videos, starting from the characteristics of dance, we use my country's motion capture technology to carry out all-round three-dimensional digital minority dance protection, protect minority dance, and provide a digital platform for future film and television programs [1–3]. It expands the scope of

intangible cultural heritage protection and has far-reaching implications for the preservation and scientific advancement of national culture.

Although studies on the protection of individual dances using motion capture technology have been conducted [4, 5], no unified and standardized technical process has been established, and the norms of 3D digitalization of ethnic dances have significant guiding value in promoting the protection of 3D digitalization of dances. As a result, this article examines the technique flow of 3D digital dance protection based on motion capture technology and provides guidance for swing dance collecting. At the same time, it provides a specific application example of motion capture data animation [6].

Motion capture technology can be used to digitize folk dance in three dimensions. Capturing three-dimensional data might be as basic as collecting the spatial position of bodily components, or as complicated as recording the intricate movement of facial expressions.

The research innovations of the article are as follows:

- (1) Applies motion capture technology to the protection of ethnic dance art
- (2) Uses motion capture technology to obtain 3D poses of ethnic minority dance spaces and optimize digital motion restoration
- (3) Establishes a national dance art movement technology database, and combines the original ecological cultural atmosphere and other protection models to accurately and comprehensively preserve the essence of ethnic minority dance art

## 2. Related Work

*2.1. Motion Capture Technology.* In Japan, to preserve the cultural heritage of dance, Atsushi, Institute of Industrial Science, University of Tokyo, Japan, Nakazawa1, et al. captured dance movements through motion capture system, decomposed dance movements into some original movement components, generated new dance movements through computer analysis and artificial intelligence technology, and then performed these dance movements through dance robots. In addition, Wayne Siegel and Jens Jacobsen2 of the Danish School of Electroacoustic Music studied interactive dance, in which dancers' dance movements can control performance movements of other devices, such as lights, music, images, and other devices [7].

In addition, the high inspection standard and Li Chao 4 studied the application of computer motion capture technology to our country carry on the omnidirectional three-dimensional digital minority dance protection; establish the minority dance database; save each dance art essence; protect the minority dance for the future research, movie, and TV programs; and restore precision digital platform [8].

In recent years, during the national "Eleventh Five-Year Plan" period, the development of cultural industry planning has been accelerated, and various domestic cultural and creative industries have begun to attach great importance to motion capture technology in high-tech enterprises,

universities, scientific research institutions, and art institutions and have purchased motion capture technology for their own research and development. In the research of motion capture system, especially in the past two years, it has developed very rapidly [9]. In addition, relevant scientific research institutions have established their motion captures laboratories, such as the digital Media Experimental Teaching Center of Century College of Beijing University of Posts and Telecommunications, Motion capture Laboratory of Beijing Practical Technology School, and Software Science of Huazhong University of Science and Technology [10].

Early Disney animation productions were the first to use motion capture technology. Motion capture technology has evolved and become more commonly employed in virtual reality, game design, motion simulation, and other sectors as science and technology have progressed. Motion capture technology is the measurement of an object's motion in 3D space using sensor equipment, recording the object's motion in the form of images, and then analyzing and processing the image data using computer technology to acquire the object's spatial coordinates [11].

This article uses an optical motion capture system. In the system, there are seven digital cameras, each with a different perspective, placed on the edge of the performance area. Dancers are required to wear tight clothing, and 29 "Marker" points are affixed to key parts of the body. The Marker points correspond to the system frame structure of the motion capture system, which can be identified by computer technology. Each camera at the performance was equipped with the body movements of the dancers corresponding to the reflective markers, and the images were formed during the shooting process [12].

*2.2. Animation Generation of 3D Data by Dance Motion Capture Technology.* Through the national dance, 3D data capture technology can form several national dance databases for minority dance choreography and interactive games provide more image data, in promoting China's animation production level and at the same time can effectively enhance national dance moves of feeling, use animation image table to show national dance art, and make the dance effect more vivid. The realization process of 3D digitization of folk dance is based on motion capture technology [13]. This flow chart intuitively reflects the process of realizing 3D digitalization of ethnic dance by using motion capture technology. By binding the motion capture data of ethnic dance to the data of good role mode, the generation of animated characters can be realized as required, and then the 3D digitalization of ethnic dance can be realized.

- (1) The establishment of dancer character models. Taking the Tujia wave dance as an example, in the process of three-dimensional digitalization of dance, it is necessary to capture the wave movements of dancers. Through modeling software, the role model is established in 3D Studio Max according to the actual body proportion of dancers. At the same time, the data of the task model are restored according to

the dance costumes of Tujia nationality, and then the 3D data are bound with the data of the character model so that the dance can be restored [14].

- (2) Bone binding of the human body model. When the motion capture system captures the motion track of dancers, it is realized through the determination of spatial data points. Therefore, to obtain more and more detailed data, it is necessary to bind 3D data according to the dancer's body proportion and skeletal system. The movement data can be captured by binding the dancer's skeleton. It should be noted that during bone binding, the influence of weight should be paid attention to, that is to say, the bone may have different influences on different limb parts of the character model. Only when the strength of these key points is appropriate, can the movements of the character model be smooth and natural [15].
- (3) Motion capture 3D data animation implementation. In order to achieve good recording result, general requirements focus on dance performers performing in the area of rules and the use of multiple cameras at the same time to record performers from different perspectives of different body movements and to deal with the data; the data are then mapped to the 3D character models. At this time, we can use the movement sequence to generate a series of animation and then match with the corresponding music, and we can use the computer to show the dance performance from various angles in an all-round way [16].

**2.3. Acquisition of Three-Dimensional Dance Data.** Obtaining national dance with motion capture technology, 3D data may be utilized to create minority dances, dance database action choreography, and interactive games [17–20]. Figure 1 depicts the entire process of 3D character animation generation, from the gathering of 3D movement data for folk dance through the generation of character animation.

### 3. Human Motion Pose Analysis Based on Feature Vector Matching

The process of tracking, collecting, obtaining, and evaluating human body posture features in order to get relevant motion posture parameters is known as motion posture analysis. The system in this paper can decompose the movements they perform in detail, each dance in detail; this parameter helps us to quantitatively analyze the gestures and provides a good help for the dance training to be more scientific and intelligent. A method of human body motion pose analysis based on the similarity matching concept of the feature plane was presented to better evaluate the motion state of dance artists. The method transformed a standard Euclidean distance computation based on several identification points into a calculation based on a feature vector and the angle of the feature plane. To calculate the difference and correlation of motion, the identification points of 21 critical positions are simplified into seven feature planes in this study. This

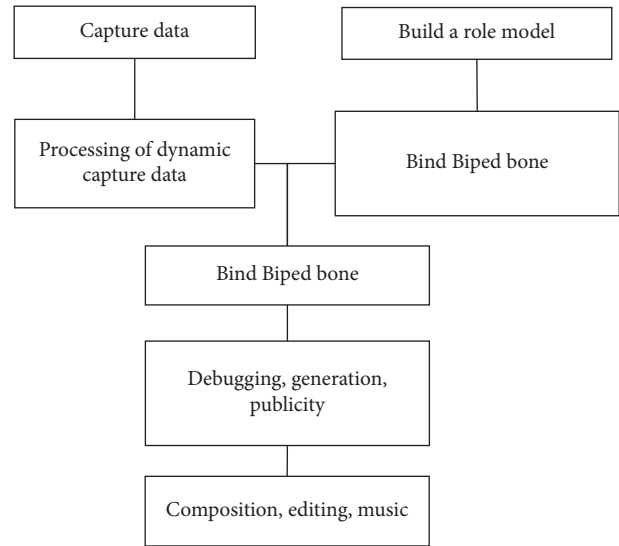


FIGURE 1: Animation generation flow chart based on motion capture data.

method can swiftly and efficiently assess human body motion posture through verification, and it may be applied to dance instruction to increase dance teaching efficiency.

The purpose of human pose similarity matching is to determine the degree of similarity or difference in stance between distinct human bodies. The classic Euclidean distance measurement is currently the most widely used method. The following are the approaches for calculating Euclidean distance in traditional 3D model similarity matching:

$$D = \sqrt{(x_1 - x_2)^2 + (y_1 - y_2)^2}, \quad (1)$$

$$D = \sqrt{(x_1 - x_2)^2 + (y_1 - y_2)^2 + (z_1 - z_2)^2},$$

where  $x_1 = (x_{11}, x_{12}, x_{13}, \dots, x_{1n})$ ,  $x_2 = (x_{21}, x_{22}, x_{23}, \dots, x_{2n})$  is the  $n$ -dimensional data. A calculating formula based on Euclidean distance can be used to calculate the difference between each two identification points. The standard action is compared to the track of the action to be examined at the same mark point.

The trajectories of two moving targets are compared using the classic Euclidean distance direct comparison method. The related distance difference value is gathered throughout the comparison process of each action sequence, and the data matching degree is calculated using the predefined threshold value. As a result, traditional approaches are limited by the rigid requirements for moving objects, which not only degrade computer performance but also lack universality.

The similarity function utilized in this article is cosine. This approach can determine not only the direction difference between vectors, but also the angle similarity and difference. The following is the method of calculation:

$$\text{similarity}(V_i, V_j) = \frac{v_i \times v_j}{\sqrt{(v_i)^2} \times \sqrt{(v_j)^2}} \quad (2)$$

Cosine similarity, as opposed to Euclidean distance, can better depict the difference in direction between two vectors. As a result, the difference in feature vector direction can be determined, and the calculation error caused by different target positions in Euclidean distance may be avoided. The dance movement to be assessed is compatible with the standard movement if the estimated cosine value is within the range of [0,1] and close to 1. If the value is close to 0, the difference between the dance movement being assessed and the standard movement is too great.

$$\theta_{(i,j)} = \arccos(\text{similarity}(V_i, V_j)). \quad (3)$$

The effective range of motion  $Q(i, j)$  between the feature vectors ranges from  $[Q_{\min}, Q_{\max}]$  can distinguish the standard of dance motion range.

The percentage of the human body is certain due to individual differences in the human body, such as the presence of height, weight, arm length, and other concerns. As a result, angle similarity must be used to determine whether the limbs' motion amplitude adheres to the norm. The following is the method of calculation:

$$\text{Corr}(\theta_{(i,j)}) = 1 - \left( \frac{\arccos(\text{similarity}(V_i, V_j))}{\pi} \right). \quad (4)$$

The results are shown in Table 1.

Calculate the weights of the joints. The value of  $A$  will influence the motion similarity evaluation result. The weight WI of these joints can be computed as follows:

$$\omega_i = \frac{S_i \cdot \alpha}{\sum_{j=1}^m S_j}. \quad (5)$$

The remaining weight is bisected by the rest joints, and the weight calculation formula is as follows:

$$\omega_i = \begin{cases} \frac{S_i \cdot \alpha}{\sum_{j=1}^m S_j} \\ \frac{(T - m)}{(1 - \alpha)} \end{cases}, \quad i = 1, 2, \dots, T. \quad (6)$$

Let  $p_r^i$  and  $q_r^i$  be the quaternion representations of the  $i$ th joint direction data of  $P$  and  $Q$ , respectively. The joint weight WI of  $Q$  can be calculated according to formula (1), and  $p_r$  and  $q_r$  distance can be obtained for any two frames. The measurement method is as follows

$$\text{dist}(p_r, q_r) = \sum_{i=1}^T \frac{\omega_i + \omega'_i}{2} d(p_r^i, q_r^i). \quad (7)$$

Specific experimental methods are referenced. An array MapFrame is created and kept track of the unique mapping relationship between all frame of reference action sequences  $P$  and  $Q$ . The common path is traversed and the mapping relationship in MapFrame is saved.  $P$  and  $Q$  are simulated using the multidimensional action features collected in the previous phase, and the distance of 2 is calculated and averaged to yield  $\text{Dist}(P, Q)$ .

TABLE 1: Correlation parameters of left arm gesture.

Subjects	Sim ( $V_i, V_{\text{stana}}$ )	Corr (Q1)	Corr (g)
Standard object	0.7053	0.8923	0.99
Object under test	0.4585	0.9802	0.8951

$$\text{Dist}(P, Q) = \frac{\sum_{r=1}^R \text{dist}(Kp_r, Kq_r)}{R}. \quad (8)$$

Similarity evaluation is obtained after normalization according to formula (4).

$$\text{Similarity}(P, Q) = \frac{1}{\text{Dist}(P, Q) + 1}. \quad (9)$$

Because the bulk of square dance aficionados are middle-aged and older, they rely heavily on trainers to learn new routines. To some extent, this challenge can be overcome by utilizing a motion sensor to gather motion and evaluating it using a motion similarity evaluation algorithm. The topic data of the sports coach following the motion sensation need to be highly followed and real time in the real-time motion evaluation system, and a relatively accurate evaluation system is the technical assurance to promote the application of rural public culture.

When the pedestrian is walking, it will produce a large torque to the acceleration sensor, that is, the acceleration of human movement. When the accelerometer is used to estimate the attitude direction, we assume that only the gravitational field affects the accelerometer. Therefore, in the "waking state," this premise hypothesis does not exist. We do not use an accelerometer and gyroscope for filtering and fusion and can only use the angular rate integral measured by the gyroscope sensor alone. Therefore, the estimation of attitude direction can be divided into two parts. When the pedestrian is in the "standing state," since the accelerometer is mainly affected by gravity, it can be obtained by combining the characteristics of accelerometer and gyroscope sensors with the method of gradient descent complementary filtering, as shown in the following formula:

$${}^b_g q_{opt,t} = {}^b_g q_{opt,t-1} + {}^b_g q_{opt,t-1}^* \Delta t. \quad (10)$$

When the pedestrian is in the "waking state," as the accelerometer is also affected by other torques of the foot, the continuous use of the accelerometer to estimate the direction will produce a large error. Therefore, in the "waking state," only the integration of the gyroscope is used to obtain the attitude angle, as shown in the following formula:

$${}^b_g q_{w,t} = {}^b_g q_{w,t-1} + {}^b_g q_{w,t-1}^* \otimes {}^b w_{t-1} \Delta t. \quad (11)$$

To calculate the angular rate error of the gyroscope at rest:

$$w_{err} = \frac{1}{N \Delta t} \sum_{i=0}^N ({}^b w_i) \Delta t = \frac{1}{N} \sum_{i=0}^N ({}^b w_i). \quad (12)$$

To correct the zero drift error of the gyroscope:

$$w = \begin{cases} 0, & t_i = t_{\text{sup}} \dots t_{\text{end}}, \\ w - w_{\text{err}}, & t_i = t_{\text{end}} \dots t_{\text{wend}}, \end{cases} \quad (13)$$

where  $w_{\text{err}}$  represents the drift error of the gyroscope sampled in the “standing state.” Since the movement between stride lengths is short, about 1-2s, it can be assumed that the drift error at this time can be approximated as the drift error of the next state, and the motion attitude angle at the next moment is shown as follows:

$${}^b_g q_{w,t} = {}^b_g q_{w,t-1} + \frac{1}{2} a_g^{b*} q_{w,t-1} \otimes {}^b (w_{t-1} - w_{\text{err}}) \Delta t. \quad (14)$$

The estimation of the track pedestrian motion is calculated, and the acceleration data to get the speed are integrated, and the acceleration data to get the speed are integrated. When integrating again to get the coordinates, it is necessary to transform the acceleration A from the carrier coordinate system B to the geographic coordinate system G, so that the velocity and position obtained are the coordinates and positions in the geographic coordinate system. According to the calculation rules of quaternions,

$${}^g_b q = {}^b_g q^*. \quad (15)$$

According to formula (15), the transformation from carrier coordinate B system to geographic coordinate G system can be obtained. In this way, according to the value  $b$  measured by the acceleration sensor in carrier coordinate B system, the value under geographic coordinate G system can be obtained after four-element transformation, as shown in the following formula:

$${}^g a = {}^g_b q \otimes {}^b a \otimes {}^g_b q^*. \quad (16)$$

#### 4. Experimental Results and Analysis

The experimental objects are randomly picked college students with dance foundations, and the produced movement database has 18 sets of dance movement fragments, each set of dance movement containing roughly 1200 frames. The subjects were asked to emulate the dance teacher’s standard movements and do equivalent dance moves while using an optical motion capture technology to retrieve movement characteristics of the subjects’ left arm joints. The concluding motions of the left arm of a single dance movement (within 0–10 s) were chosen for experimental comparison with the conventional movements. The disparities between the primary motion changes of the object to be examined and the standard movements are compared using a local motion sequence taken in real time as an example. The experimental results are shown in Figure 2.

Figure 2 shows the time sequence diagram of the parameters related to the movement of the left arm. It can be seen from the figure that the rocking effect of the left arm is recorded in this article in a more targeted manner. The learning of the two groups of students was confirmed

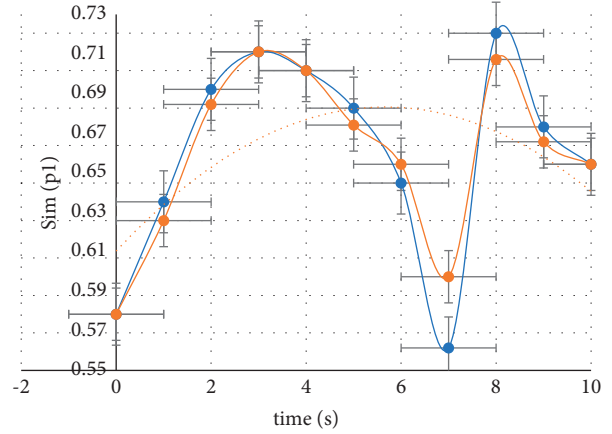


FIGURE 2: Timing sequence diagram of left arm motion correlation parameters.

through evaluation after all of the teaching hours were completed. The range, strength, coherence, and standardization of the two groups of students’ calisthenics motions were rated by the college PE teacher, and the data were analyzed using SPSS19.0. Table 2 displays the test results.

The correlation coefficient error is computed by utilizing the phase-to-phase error method as follows:

$$\Delta \text{corr}_i = \frac{|\text{corr}_i - \text{corr}_j|}{\text{corr}_i} \% \quad (17)$$

According to the above formula, the relative error is calculated to show the deviation degree of dance movements of each object to be tested compared with standard movements. The calculation results are shown in Table 3 and Figure 3.

The two sets of data are directly compared using the traditional 3D model’s similarity comparison method based on Euclidean distance. The pose analysis results are frequently not accurate enough for dancing motions with considerable motion amplitude. When the person being tested is different in height, fat, and thinness, as well as human body proportions, as shown in Figure 4, errors in the model’s displacement will occur. The spatial displacement deviation is frequently too large when the movement position of the person to be measured is not specified.

To verify the superiority of dividing and considering actions separately according to human body structure, we also implemented human actions as a whole on CityU and HDM05 datasets. The experimental results are shown in the figure below. Recognition accuracy is shown in Figure 5.

The classification performance of the somatic-based scheme was better than that of the somatic-based scheme in both datasets, especially in the HDM05 dataset. This is because the HDM05 dataset covers basic everyday actions, such as running and jumping, which can lead to greater intra-class differences.



TABLE 2: Comparison of experimental results.

Group	Movement range	Strength of action	Action continuity	Normative action
Regular group	73.6 ± 6.4	79.6 ± 7.6	73.4 ± 7.9	77.4 ± 6.5
The experimental group	73.3 ± 6.7	73.7 ± 5.3	73.3 ± 3.6	76.3 ± 4.6
Significant <i>P</i>	0.033	0.067	0.063	0.040

*P* represents the significance of the experimental effect, where  $P < 0.005$  is generally taken as significant. According to the experimental results, students who learn by motion capture have a better grasp of dance movements than those who learn by routine.

TABLE 3: Relative error of main motion pose of the object to be tested/%.

Order	Sim ( $V, V_{stand}$ )	Corr ( $V_{Larm}, V_{LFarm}$ )	Corr ( $V_{LFarm}, V_{stand}$ )
0 ~1 s	2.52	0.92	0.22
1~2 s	0.65	0.2	0.99
2~3 s	0.05	0.22	0.25
3~4 s	0.22	0.65	0.24
4~5 s	0.25	22.54	0.02
5~6 s	2.42	0.22	0.02
6~7 s	5.65	0.95	0.25
7~8 s	0.82	0.02	0.99
8~9 s	2.02	0.99	0.29
9~10 s	0.25	0.4	0.58

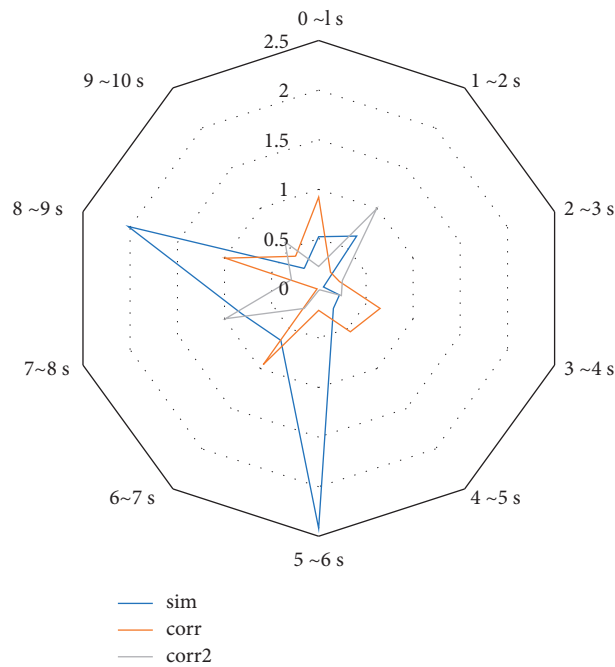


FIGURE 3: Relative error of main motion pose of the object to be tested.

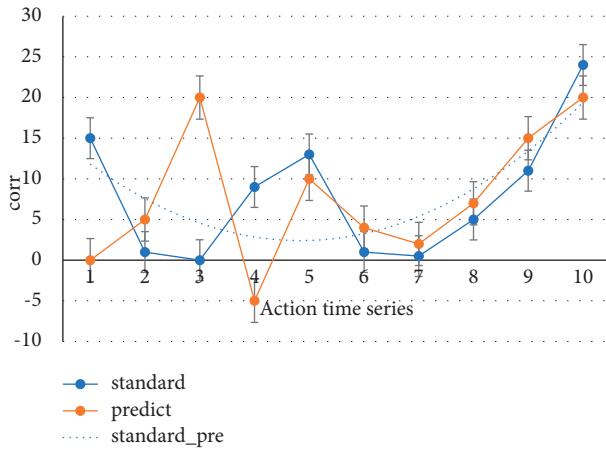


FIGURE 4: Wheelbase deviation of single feature point x.

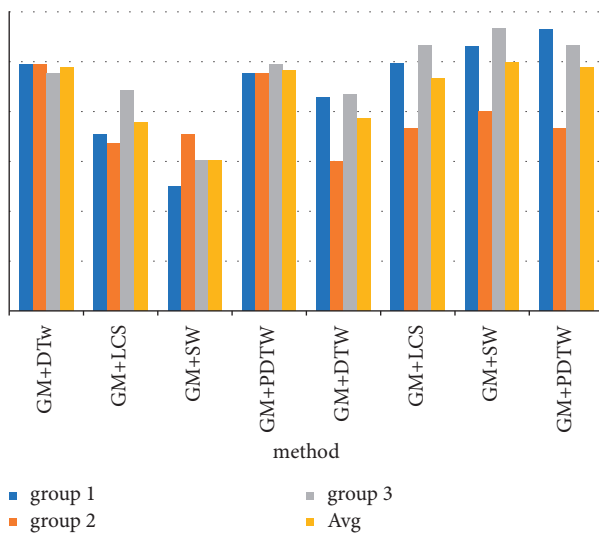


FIGURE 5: Recognition accuracy.

## 5. Conclusion

This research focuses on how motion capture technology can be used to achieve 3D digitalization of folk dance. Because traditional methods cannot accurately reproduce the original dance posture, reappear the elegant demeanor of art, copy the manufacturing cycle quickly, and low cost, the application of motion capture technology can effectively resolve the problems of incomplete records and provide more analysis data for modern dance choreography. Using photos and videos of traditional methods, this article gets the image data that are incomplete or inaccurately maintained the lack of dance art, explores the application of computer motion capture technology to carry on the omnidirectional 3D digital Chinese national dance protection methods, and shows animation as an example of how to apply the national dance of 3D data. Cultural protection and resource integration of folk dance can play a positive guiding role in the research and application of modern digital means to carry out dance art and, at the same time, promote the combination of culture and technology.

## Data Availability

The data used to support the findings of this study are available from the corresponding author upon request.

## Conflicts of Interest

The author declares that there are no conflicts of interest.

## References

- [1] G. Johansson, "Visual perception of biological motion and a model for its analysis," *Perception & Psychophysics*, vol. 14, no. 2, pp. 201–211, 1973.
- [2] D. P. Noonan, P. Mountney, D. S. Elson, A. Darzi, and G. Z. Yang, "A stereoscopic fibroscope for camera motion and 3D depth recovery during minimally invasive surgery," in *Proceedings of the 2009 IEEE International Conference on Robotics and Automation (ICRA)*, pp. 12–17, Kobe, Japan, May 2009.
- [3] T. W. Calvert, J. Chapman, and A. Patla, "Aspects of the kinematic simulation of human movement," *IEEE Computer Graphics and Applications*, vol. 2, no. 9, pp. 41–50, 1982.
- [4] Z. Chen and H. J. Lee, "Knowledge-guided visual perception of 3D human gait from a single image sequence," *IEEE Transactions on Systems Man and Cybernetics*, vol. 22, no. 2, pp. 336–342, 2015.
- [5] A. G. Bharatkumar, K. E. Daigle, M. G. Pandy, Q. Cai, and J. K. Aggarwal, "Lower limb kinematics of human walking with the medial axis transformation," in *Proceedings of the IEEE Workshop on Motion of Non-rigid and Articulated Objects*, pp. 70–76, Austin, TX, USA, November 1994.
- [6] J. Myers, S. Lephart, Y.-S. Tsai, T. Sell, J. Smoliga, and J. Jolly, "The role of upper torso and pelvis rotation in driving performance during the golf swing," *Journal of Sports Sciences*, vol. 26, no. 2, pp. 181–188, 2008.
- [7] K. Evans, S. A. Horan, R. J. Neal, R. S. Barrett, and P. M. Mills, "Repeatability of three-dimensional thorax and pelvis kinematics in the golf swing measured using a field-based motion capture system," *Sports Biomechanics*, vol. 11, no. 12, pp. 262–272, 2012.
- [8] S. O. H. Madgwick, "An efficient orientation filter for inertial and inertial/magnetic sensor arrays," *Department of Mechanical Engineering, University of Bristol*, vol. 109, pp. 8–36, 2010.
- [9] R. Mahony, T. Hamel, and J. M. Pflimlin, "Nonlinear complementary filters on the special orthogonal group," *Automatic Control, IEEE Transactions on*, vol. 53, no. 10, pp. 1203–1218, 2008.
- [10] E. Foxlin, "Inertial head-tracker sensor fusion by a complementary separate-bias kalman filter," in *Proceedings of the Virtual Reality Annual International Symposium the IEEE*, pp. 185–194, Santa Clara, CA, USA, April 1996.
- [11] J. L. Marins, X. Yun, E. R. Bachmann, R. B. McGhee, and M. J. Zyda, "An extended kalman filter for quaternion-based orientation estimation using marg sensors," in *Proceedings of the IEEE/RSJ International Conference on Intelligent Robots and Systems, 2001*, IEEE, Maui, HI, USA, November 2001.
- [12] A. M. Sabatini, "Quaternion-based extended kalman filter for determining orientation by inertial and magnetic sensing," *IEEE Transactions on Biomedical Engineering*, vol. 53, no. 7, pp. 1346–1356, 2006.

- [13] G. Johansson, "Spatio-temporal differentiation and integration in visual motion perception," *Psychological Research*, vol. 38, no. 4, pp. 379–393, 1976.
- [14] R. A. Claris, Y. H. Pua, K. Fortin et al., "Validity of the Microsoft Kinect for assessment of postural control," *Gait & Posture*, vol. 36, no. 3, pp. 372–377, 2012.
- [15] S. Choppin and J. Wheat, "The potential of the Microsoft Kinect in sports analysis and biomechanics[]," *Sports Technology*, vol. 6, no. 2, pp. 37–41, 2013.
- [16] M. Yuslimura, H. Murasato, T. Kai, and A. Ct, "Analysis of Japanese dance movements using motion capture system," *Systems and Computers in Japan*, vol. 37, no. 1, pp. 71–82, 2006.
- [17] T. Shiratori, A. Nakazawa, and K. Ikeuchi, "Dancing-to-Music character animation," *Computer Graphics Forum*, vol. 25, no. 3, pp. 449–458, 2006.
- [18] J. Kim, H. Fonad, J. Sibert, and J. K. Hahn, "Perceptually motivated automatic dance motion generation for music," *Computer Animations and Virtual Worlds*, vol. 20, no. 2-3, pp. 375–384, 2009.
- [19] G. Alankus, A. Bayazit, and O. Bayazit, "Automated motion synthesis for dancing characters," *Computer Animations and Virtual Worlds*, vol. 16, no. 3-4, pp. 259–271, 2005.
- [20] D. Sauer, Y. Yang, "Music-driven character animation," *ACM Transactions on Multimedia Computing, Communications, and Applications*, vol. 5, no. 4, p. 27, 2009.
- [21] G. Qian, F. Guo, T. Ingalls, L. Olson, J. James, and T. Rikakis, "A gesture-driven multimodal interactive dance system,"- vol. 3, pp. 1579–1582, in *Proceedings of the IEEE International Conference on Multimedia and Expo (ICME)*, vol. 3, pp. 1579–1582, IEEE, Taiwan, China, June 2004.

## Research Article

# Research on College English Teaching Evaluation Based on Neural Network

**Yuanyuan Zhao** 

*Hebei Polytechnic Institute, Shijiazhuang 050091, China*

Correspondence should be addressed to Yuanyuan Zhao; 1864300145@e.gzhu.edu.cn

Received 3 March 2022; Revised 2 April 2022; Accepted 6 April 2022; Published 7 May 2022

Academic Editor: Punit Gupta

Copyright © 2022 Yuanyuan Zhao. This is an open access article distributed under the Creative Commons Attribution License, which permits unrestricted use, distribution, and reproduction in any medium, provided the original work is properly cited.

Aiming at the difficulty in adapting the traditional English teaching evaluation model to the new situation of current education development, a research on college English teaching evaluation based on neural network is proposed. The thesis proposes that based on the neural network, from the perspective of teachers and students, while creating a positive and harmonious learning atmosphere, a college English teaching environment with interactive mechanism is established, and a teaching mode of English interactive mechanism is constructed in it. To obtain a better neural network model, to establish the performance evaluation index of college English teaching, to calculate the weight of the performance evaluation index of English teaching, and to realize the evaluation of college English teaching based on neural network, the experimental results show that the use of this method can significantly improve students' English scores, and the method has high approximation accuracy.

## 1. Introduction

English is a language communication tool. It transmits the information of social politics, economy, culture, and other aspects. It has become an important part of a country's comprehensive national strength. Doing well in English teaching is related to the country's international image, international influence, and international discourse [1]. Cultivate a large number of high-quality engineering and technical talents with strong innovation ability and adapt to the needs of economic and social development, international communication, and international competitiveness [2], which further highlights the importance of English Teaching [3]. In recent years, college English teaching has made great progress [4], but it still cannot meet the market demand for high-level talents, including high-quality skilled talents [5]. On the one hand, social transformation and upgrading requires a large number of highly skilled talents. On the other hand, the technical talents trained by universities are difficult to meet the needs of the society. In order to improve the training quality of college English majors, it is necessary to strengthen the reform of teaching evaluation. As a part of college education, the significance of college English teaching evaluation is highlighted.

As an important part of teaching, teaching evaluation guides various teaching activities to a great extent and is an effective way and method to solve the problems existing in teaching. Relevant scholars have carried out many studies on this. Xie [6] puts forward author evaluation in English Academic Writing Teaching from the perspective of methodology. This study summarizes the main research directions of author evaluation in English Academic Writing Teaching in the past two decades and the main methods used in the field of Applied Linguistics and discusses the advantages and disadvantages of methodological methods in revealing problems. According to the applied analytical framework, four document chains are determined: position chain, metadiscourse chain, evaluation chain, and voice chain. Then, it identifies and discusses the advantages and disadvantages of corpus-based research methods, in-depth text research methods, and ethnographic research methods in exploring the evaluation significance in English academic writing. Lei [7] proposes to consider cross-cultural communicative competence and formulates the evaluation list of teaching materials for English Majors in China. With people's increasing interest in cross-cultural communicative competence in language teaching, how to evaluate the attribute of cross-cultural communicative competence in English

teaching materials has become a matter of great concern. From the reference and expert research, this study finds out the evaluation criteria of ICC attribute in English Majors' textbooks and constructs a checklist to evaluate ICC attribute in Chinese English Majors' textbooks. Although the above research has made some progress, there are still some limitations in the research of college English teaching evaluation. Therefore, this study puts forward the research of college English teaching evaluation based on neural network and uses neural network to evaluate teaching quality, which has a good evaluation effect. Through experimental verification, the effectiveness conclusion is drawn. Improve the quality and efficiency of college English teaching evaluation, and then improve the quality of college English teaching as a whole.

## 2. College English Teaching Evaluation Based on Neural Network

**2.1. Neural Network.** Neural network is a multilayer feed-forward network trained according to error backpropagation algorithm. It is one of the most widely used teaching evaluation network models. Neural network is based on function approximation theory. It is a feedforward neural network with strong global optimization ability. It is widely used in the field of college English teaching evaluation. It is composed of forward propagation of teaching evaluation information and reverse propagation of error. The structure is three layers, namely, input layer, hidden layer, and output layer. The specific structure is shown in Figure 1.

In Figure 1, the function of input layer neurons is to receive and propagate input signals. The hidden layer is the internal information processing layer of college English teaching evaluation. The hidden layer structure is set according to the change needs of input signals. If it is a single hidden layer BP neural network [8], the signal is directly transmitted to the output layer for forward propagation. If it is a multihidden layer BP neural network, the last hidden layer propagates the signal to the output layer for forward propagation. The output layer outputs the processing signals of the first two layers [9]. When there is a large deviation between the output value of college English teaching evaluation information and the expected output value, it returns to the process of error backpropagation. The output error updates the weight of each layer by gradient descent and propagates inversely to the hidden layer and the input layer. In the neural network, the three-layer neural network has two weight vectors, in which the weights of the input layer and the hidden layer are static weights, the weights between the output layer and the hidden layer are dynamic weights, and the activation function of the hidden layer is radial basis function. Therefore, the output of the output layer is the weighted sum of the input data after activating the function through the hidden layer. The radial basis function and dynamic weight are the key of RBF neural network. The expression of radial basis function is

$$R(m) = \frac{\|r_n - v_b\|}{y(n)}, \quad (1)$$

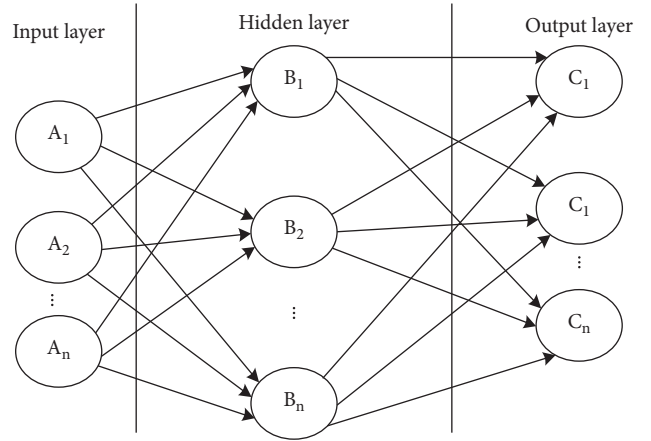


FIGURE 1: Structure of neural network.

where  $\|r_n - v_b\|$  represents the norm of  $r_n - v_b$  [10],  $r_n$  represents the sample data input by the input layer,  $v_b$  represents the center of the radial basis function, and  $y(n)$  represents the width of the radial basis function. After determining the network weight and radial basis function parameters, the output of the neural network can be expressed as

$$Y(j) = \frac{\|r_n - v_b\|}{y(n)} \times \sum_{i=1}^m q_i, \quad (2)$$

where  $q_i$  represents the weight between the hidden layer and the output. According to the solution process of neural network, the network optimization process is to continuously update the dynamic weight and the center and width of radial basis function according to the training data until the whole neural network realizes the required nonlinear function approximation [11, 12].

**2.2. Establishing Interactive Mechanism and College English Teaching Environment.** When applying neural network [13], we should first establish a new interactive college English teaching environment for students. The interactive mechanism teaching model is not confined to the classroom, but can adopt mobile interaction, human-computer interaction, and other forms at any time and place to promote the interaction between teachers and students. This shows the importance of the establishment of interactive mechanism college English teaching environment.

College English classroom teaching environment is mainly divided into two aspects: material environment and spiritual environment. Among them, the material environment mainly includes classrooms and teaching equipment. The spiritual environment usually refers to the classroom atmosphere and the tension of schoolwork. In the process of teaching tasks carried out by teachers and students centered on teaching objectives, the learning atmosphere generated in the process of this activity is the psychological state of students and teachers in the process of this activity. When the atmosphere between teachers and students is active, the communication between teachers and

students is smooth and pleasant. When one of the teachers and students is unhappy, the communication of poor students is astringent and inefficient. Therefore, to create a positive and good learning environment, we need to establish an interactive mechanism based on a harmonious and stable relationship between teachers and students. The process of college English teaching environment is shown in Figure 2.

When using the interactive mechanism to carry out English teaching, it is necessary to have the interactive mechanism, as shown in Figure 2, and the establishment process of college English teaching environment. Teachers need to seriously understand students' emotions, understand students' needs, regard students as an independent individual, actively integrate into students, and have equal communication, exploration, and discussion with students. And in the process of college English teaching, students are not judged by their achievements, and they are biased against students. In this process, students will actively cooperate with teachers and interact with teachers to achieve the due interactive teaching in English classroom, and the most key is the way of communication with students. Therefore, when there are differences between teachers and students, teachers should avoid being too dominant, but should become a listener, understand what they think from the perspective of students, and look for the significance of students' behavior, so as to regulate students' behavior in a more suitable way, guide students to see more ideas, and learn to think selectively, and in this process, teachers should also give students more encouragement and let students show themselves.

In the interactive mechanism college English teaching environment [14], teachers need to choose situational dialogue that can best mobilize students' interest and enthusiasm according to the characteristics of students in this class, so as to open the interactive door of this class and let students compete to speak. When teachers communicate with students kindly and peacefully, the content of communication is still what students are interested in, which will promote students to have more language output. Therefore, in the process of establishing the teaching environment, as the leader of the teaching task, teachers should create an equal and harmonious teaching atmosphere as much as possible so that students can become the main unit of the teaching task, and teachers should act as organizers and participants in teaching activities, so as to establish a good interactive environment for college English teaching [15–17].

*2.3. Construction of Interactive Mechanism Teaching Mode.* Using interactive mechanism to carry out English teaching needs to reconstruct the English interactive mechanism teaching mode. The four-fold interactive mode designed for this purpose is shown in Figure 3.

From the interactive mechanism teaching mode shown in Figure 3, it can be seen that the four reinteractive modes are interrelated so that students can have knowledge construction experience between different interactive modes. In the process of college English teaching, we can establish

application scenarios to improve students' enthusiasm, regulate and guide students' learning in this process, and promote students' good interaction with teachers [18, 19]. In the interactive mechanism teaching mode, there are four interaction modes between students, teachers, and teaching materials and web learning resources, between students, teachers, and students, inside and outside the classroom, and between students, teachers, and synchronous or asynchronous media. The interaction types include content, interpersonal, time and space, and media [20–22].

When using interactive mechanism in English teaching, teachers must understand students' ideas, accurately interpret students' behaviors, and provide students with flexible goals of interest according to students' ideas and behaviors, and let students have exploration interest, so as to make them actively participate in teaching activities. Teachers help teachers with English teaching by means of modern information technology and content interaction. When using modern information technology teaching methods, teachers need to design and develop high-quality web learning resources according to their many years of teaching experience, students' ideas and behavior, textbook content, curriculum progress, and so on. The content interaction process between students, teachers, teaching materials, and web learning resources is shown in Figure 4.

In the interactive mode of college English teaching content, as shown in Figure 4, it is necessary to take learning resources as the starting point and generate circular interaction between teachers and students through operational interaction. Teachers constantly guide students to learn, in an auxiliary position, so that students are in a leading position in learning. Teachers' feedback on the teaching evaluation of this course consists of teachers' teaching regulation and evaluation of students and students' information interaction with teachers. Through content interaction, students can constantly improve and enrich their knowledge structure.

Only by forming interpersonal interaction between students, teachers and students, and teachers and teachers can we better carry out college English teaching. From the above content interactive teaching mode, it can be seen that the teacher-student interaction generated by teachers' guiding students is the most basic form of interaction in the teaching process, but this form of interaction is difficult to achieve the maximum teaching efficiency. Therefore, the interpersonal interaction mode is designed in the interactive mechanism teaching mode shown in Figure 4 to form a two-way interaction process between teachers and students. On the basis of content interaction, let students use communication tools to feed back their needs for teachers' teaching and their opinions on teachers' English classroom to teachers, and then, teachers provide learning support services for students according to students' feedback, so as to form a two-way teacher-student interaction process and establish a new interactive mechanism college English teaching environment that directly affects the relationship between teachers and students [23, 24].

In addition to the above, teachers should also take the initiative to provide students with relevant support services

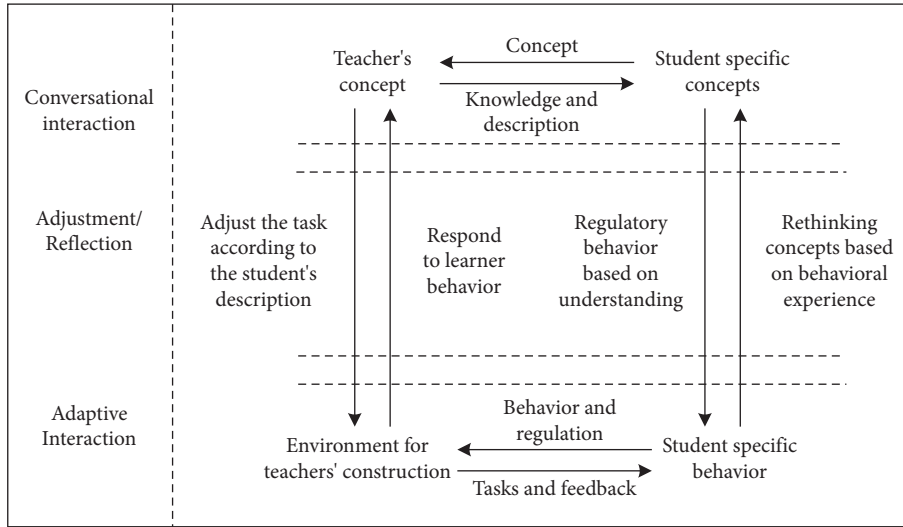


FIGURE 2: The process of establishing an interactive college English teaching environment.

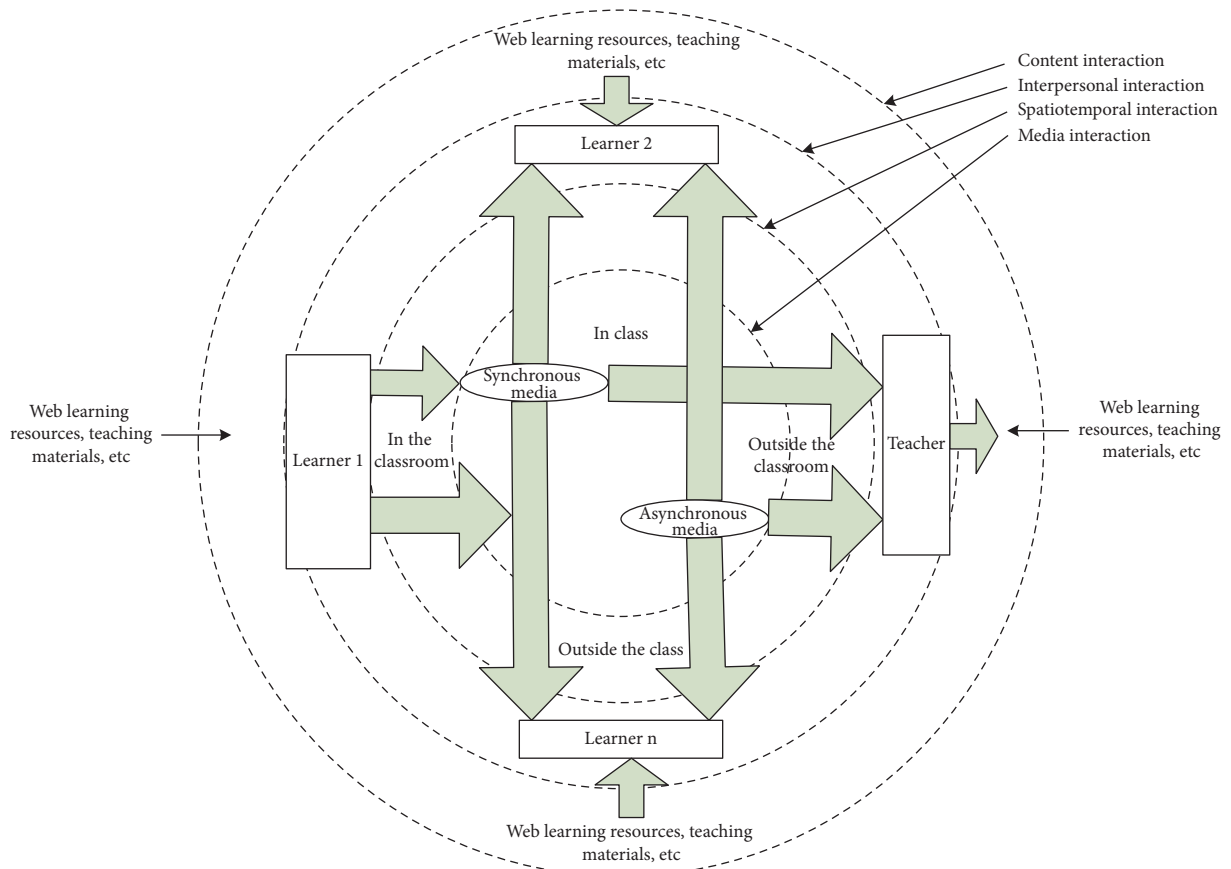


FIGURE 3: Interactive mechanism teaching mode.

not only learning support but also emotional support, so as to help students better overcome difficulties. This process can also enable teachers to grasp students' learning situation in time, find the shortcomings in the process of English teaching, and then adjust teaching strategies in time [25]. The college English teaching mode in the neural network environment is shown in Figure 5.

As can be seen from Figure 5, the essence of college English teaching mode is to introduce neural network into college English teaching, optimize the teaching process, and emphasize the combination of autonomous learning and classroom teaching. The teaching content includes listening, speaking, reading, writing, and translation, which can be organized separately or integrated. Students can get help,

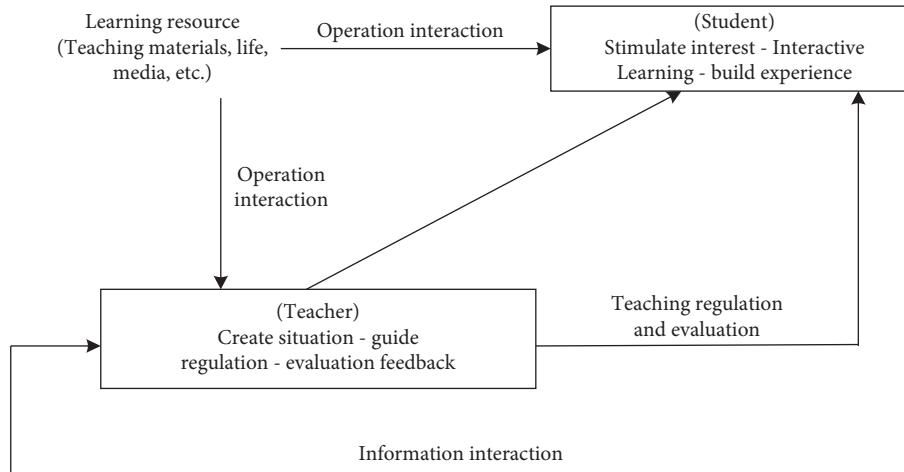


FIGURE 4: Interaction mode of college English teaching content.

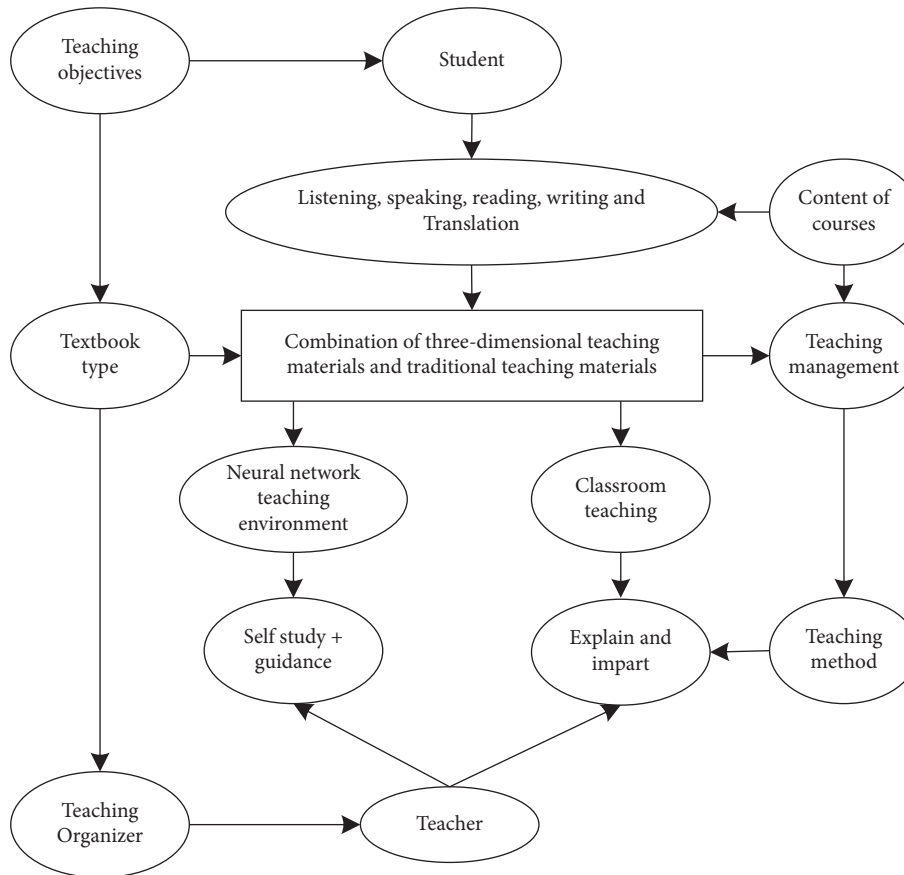


FIGURE 5: Schematic diagram of college English teaching mode under neural network environment.

encouragement, and criticism from their classmates in the process of learning, that is, student-student interaction. Let students test their learning effect through communication. Teacher-teacher interaction is the improvement of teaching resources, course content understanding, teaching methods, and so on. Through this form, teachers can clarify their own teaching level and professional skills, so as to selectively improve and better teach students English learning.

In the process of learning, the interaction mode of students is space-time interaction because they are not limited by time and space. In Figure 4, spatiotemporal interaction means that no matter where you are, you can complete information exchange with teachers in time. Teachers can use the current network to guide students to complete English learning. Under the time-space interaction, students can also flexibly arrange learning time and



complete teaching tasks according to the tasks assigned by teachers.

In the process of task completion, when students have problems that are difficult to solve, they can also seek the help of teachers through the current interactive mechanism to get teachers' suggestions, so as to improve learning efficiency. Therefore, in language teaching, teachers should make full use of the space-time interaction characteristics of the interaction mechanism, make full use of extracurricular time, and draw local materials according to the actual conditions so that students can consolidate their English knowledge at any time.

Media interaction is the necessary intermediary for the two-way interaction between teachers and students in the interaction mechanism. In the current Internet environment, the media interaction workers often used by people include WeChat, QQ, e-mail, and blog, which can become the media interaction forms used by teachers when teaching English. Teachers can use these media interactive tools to design interactive English teaching situations so that students can use various interactive tools to discuss each other. Teachers can also join the discussion team of students, provide students with new ideas, comment on students' views and problems, put forward their own opinions, and guide students to find a new direction. This form of media interaction has the advantages of low cost and real time. The media interaction process is shown in Figure 6.

In the media interaction mode shown in Figure 6, media interaction is divided into synchronous interaction and asynchronous interaction. Synchronous interaction is a time consistent interaction mode, such as classroom and simultaneous online chat. Asynchronous interaction is an interactive mode with inconsistent time, such as after-school homework.

### 3. Realize College English Teaching Evaluation Based on Neural Network

**3.1. Determine the Performance Evaluation Indicators of College English Teaching.** Based on the above research, the principles for determining college English teaching evaluation indicators are put forward, and the college English teaching performance evaluation indicators are determined, as shown in Table 1.

**3.2. Calculate the Weight of English Teaching Performance Evaluation Indicators.** According to the evaluation indexes designed above, after setting the index weight, the judgment matrix is established. It is assumed that the  $u$  evaluation index contains  $n$  items in total. If both item  $x$  and item  $y$  belong to  $n$ , the judgment matrix  $J_Z$  can be expressed as

$$J_Z = (a_{xy})_{n \times n}, \quad (3)$$

where  $a_{xy}$  represents the importance of different items, and the scale of judgment matrix is shown in Table 2.

According to the scale determined in Table 2, it can be determined that the pairwise comparison judgment matrix  $A$  has the properties of  $a_{xy} > 0$ ,  $a_{xy} = 1/a_{yx}$ ,  $a_{xy} = 1$ , etc. At

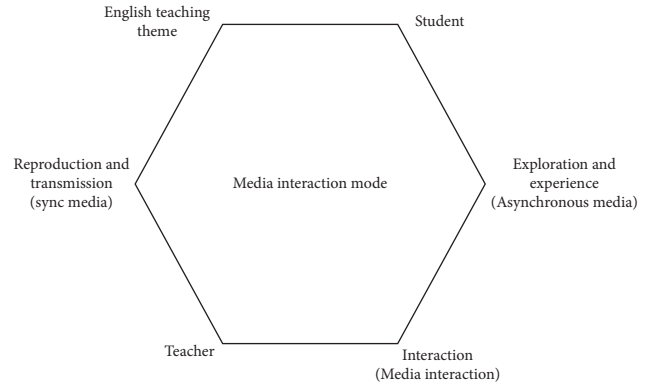


FIGURE 6: Media interaction mode.

this time, the weight of English teaching performance evaluation index can be calculated according to formula (4). That is, in the pairwise comparison judgment matrix  $J_Z$ ,  $n$  elements are calculated through judgment; then,

$$W_i = \frac{1}{n} \sum_{j=1}^n \frac{a_{xy}}{\sum_{k=1}^n a_{kj}}, \quad i = 1, 2, \dots, n, \quad (4)$$

where  $W_i$  represents the weight vector of English teaching performance evaluation index and  $k$  is an element in the English teaching performance evaluation index  $u$  determined. Formula (4) is to normalize the elements in the pairwise comparison judgment matrix  $J_Z$  and add the normalized  $J_Z$  levels to obtain the added vector. At this time, divide this vector by the number of elements  $n$  of the evaluation index  $u$  to obtain the weight vector  $\omega$  of the English teaching performance evaluation index. At this time, to get the weight vector, we also need to conduct consistency test to determine the objectivity of the weight calculation of the evaluation index and the accuracy of English teaching performance evaluation. Therefore, if the consistency index is  $C$  and the maximum eigenvalue of matrix  $J_Z$  is  $\lambda_{\max}$ , there are

$$C = \frac{\lambda_{\max} - n}{n - 1}. \quad (5)$$

At this time, in the calculated consistency index  $C$ , there is an average value  $R$ , that is, the average random consistency index  $R$ . The consistency of weight calculation results can be determined according to the data proportion  $C.R.$ ; then,

$$C.R. = \frac{C}{R}. \quad (6)$$

According to the calculation result of equation (6), when  $C.R. < 0.1$ , matrix  $J_Z$  meets the consistency requirements. When  $C.R. \geq 0.1$ , matrix  $J_Z$  must modify the matrix value again and change the English teaching performance evaluation indicators determined in Table 1.

**3.3. Evaluation of College English Teaching Performance.** According to the index weight obtained from formula (4), the English teaching performance evaluation indexes determined in Table 1 are sorted according to the index weight

TABLE 1: Teaching performance evaluation indicators.

Primary index	Secondary index	Tertiary index	Standard
Classroom culture A	Teacher-student relationship A1	Listen to a11	Give students more opportunities to speak Promote, encourage, and appreciate students by asking questions and suggestions
		Support A12	
Interactive A22	Learning atmosphere A2	Organization A21	Reasonable arrangement of time
		Good interaction and cooperation	
Course structure B	Question B1	Assessment reflection B11	Arrange self-summarizing thinking activities Group report
		AC display B12	
	Question B2	Design scheme B22 Evaluation scheme B21	Make plans through communication and investigation Generate, compare, and evaluate schemes
Question B3	Ask questions B31	Design questions to stimulate students' interest	
	Defining question B32	Let students learn to judge problems	
Course content C	Project characteristics C1	Authenticity C11	It has practical significance Give students specific task requirements Learn to use a variety of new technologies to achieve their goals
		Result clarity C12	
		Chimeric new technology C13	
Course content D	Organization association and application D1	Task ambiguity C14	No restriction on students' task process The knowledge learned is applied in practice Acquisition degree of relevant knowledge after class
		Application D12	
		Knowledge understanding D13	
Creativity D22	Learning orientation D2	Cooperation D21	Cooperate in the form of study groups
		Follow the development of students' thinking and cultivate creativity	

TABLE 2: Proportional scale.

Element comparison	Meaning	Scale
Comparison of element $x$ and element $y$	As important as	1
Comparison of element $x$ and element $y$	Element $x$ is more important	3
Comparison of element $x$ and element $y$	Element $x$ is obviously important	5
Comparison of element $x$ and element $y$	Element $y$ is very important	7
Comparison of element $x$ and element $y$	Element $y$ is particularly important	9
—	Judge the above adjacent intermediate values	2,4,6,8
When the importance ratio of element $x$ to element $y$ is $a_{xy}$	Element $x$ and element $y$ importance results $a_{xy} = 1/a_{yx}$	Reciprocal

level. At this time, the evaluation grade of English teaching performance evaluation index can be determined and the evaluation grading matrix  $H_e$  can be established:

$$H_e = \begin{bmatrix} h_{11} & h_{12} & \cdots & h_{1\theta} \\ \vdots & \cdots & \ddots & \vdots \\ h_{\theta 1} & h_{\theta 2} & \cdots & h_{\theta\theta} \end{bmatrix}, \quad (7)$$

where  $h$  represents the element level and  $\theta$  represents the comment. At this time, set the English teaching performance evaluation index set as  $u = \{u_1, u_2, \dots, u_j, \dots, u_n\}$ , and according to the evaluation grading matrix  $H_e$  in formula (7), the determined English teaching performance evaluation index comment  $\theta$  is

$$\theta = \{h_1, h_2, h_3, h_4, h_5\}, \quad (8)$$

where  $h_1$  represents good,  $h_2$  represents good,  $h_3$  represents average,  $h_4$  represents poor, and  $h_5$  represents poor. According to formula (8), college English teaching performance can be evaluated. The evaluation index system is the basis of English teaching quality evaluation. A scientific and reasonable index system is a powerful guarantee to ensure the performance of college English teaching quality evaluation. At present, there are many principles in the index system of evaluating teaching quality, such as the index construction based on teaching content and the index construction based on students' achievement. For the evaluation of English teaching quality, a specific evaluation index system is constructed, and the structure is shown in Table 3.

The evaluation process of college English teaching based on neural network is as follows:

TABLE 3: Evaluation index system.

Project	Evaluation index system
Teacher quality	Clear educational objectives
	Solid professional knowledge
	Teaching and explanation level
Teaching attitude	Coaching patient and positive
	Serious teaching
	Rigorous attitude
Content of courses	The conceptual theory is accurate
	Full content
	Practice
	Depth of expertise
Teaching method	Good at inspiration
	Diverse ways
	Pay attention to personality
	Stimulate innovation consciousness
Teaching effectiveness	Improve learning interest
	Knowledge understanding and mastery
	Problem solving ability
	Comprehensive quality

Step 1: build an evaluation index system and collect relevant data of teaching quality evaluation

Step 2: standardize the data and generate the correlation coefficient matrix of the evaluation index

Step 3: based on the interactive mode of college English teaching content, the evaluation indexes of English teaching quality are selected to remove redundant indexes and realize feature dimensionality reduction

Step 4: use neural network to evaluate the teaching quality and output the evaluation results, so as to realize the college English teaching evaluation based on neural network

#### 4. Experimental Analysis

In order to verify the effect of this study on the evaluation of college English teaching based on neural network, experimental analysis is carried out, and the methods of [6] and [7] are compared with the methods of this study, mainly comparing the English teaching effects of these three methods. Taking the freshmen of a school as the experimental object, 10 freshmen were randomly selected. The methods of this study and [6] and [7] were used for evaluation. During the experiment, the independent sample test method is used to require the compared subjects to be independent of each other, and there is no pairing relationship.

The English scores of 30 freshmen in the school before the implementation of the research and analysis and after the application of different methods are shown in Table 4:

It can be seen from Table 4 that, after the evaluation of college English teaching based on neural network, the students' English performance has been significantly improved compared with that before the evaluation. The students' scores have also improved by the methods of [6] and [7], but the improvement is not obvious. This method is

TABLE 4: Comparison of grades of senior one students.

Serial number	Prestudy results/scores	Paper method/scores	[6] method/scores	[7] method/scores
1	75	91	78	79
2	76	92	80	78
3	74	90	71	74
4	75	89	73	74
5	72	89	78	73
6	71	90	79	79
7	75	91	78	80
8	72	92	80	78
9	73	92	80	80
10	71	91	81	81

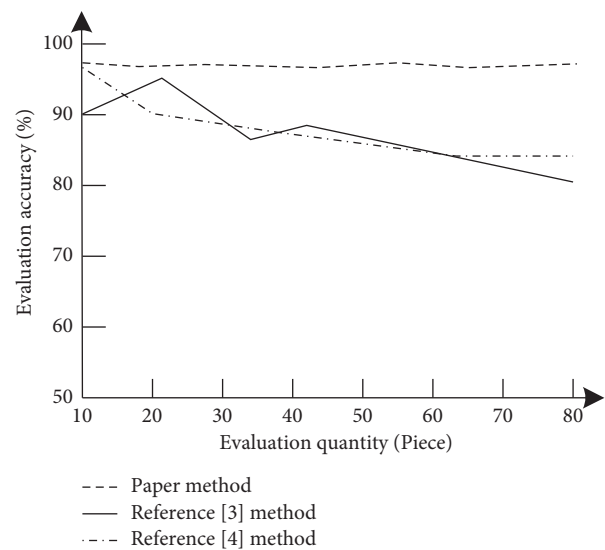


FIGURE 7: Evaluation accuracy curves of different methods.

used to evaluate the English teaching quality. The teaching quality evaluation accuracy of the test object data in the evaluation process is shown in Figure 7:

As can be seen from Figure 7, the simulation results of different models are also different. The method in this study has a good practical effect. The accuracy rate of college English teaching quality evaluation based on neural network is higher than 95%, and the evaluation accuracy rate of this method is always outperforms [6] and [7]. The test results show that, in the 80 test samples, the evaluation accuracy of [6] and [7] methods both show a downward trend to varying degrees, and the change trend of this method is relatively stable, indicating that the method has a higher performance approximate accuracy.

#### 5. Conclusion

College English teaching quality evaluation is an important measure to improve teaching quality. This study constructs a college English teaching quality evaluation based on neural network. This method screens the evaluation indicators, determines the college English teaching performance evaluation indicators, and realizes the high accuracy evaluation

of college English teaching quality. The test results verify that the application of this method can improve students' English performance. The research content provides a new method for the evaluation of college English teaching quality.

The construction of college English teaching evaluation system needs to establish a humanized evaluation concept based on the emotional demands of teachers and students, pay attention to the sustainable development of evaluation objects and the process of pursuing progress, absorb diversified evaluation subjects such as students and teachers, and adopt formative evaluation, diagnostic evaluation, summary evaluation, qualitative evaluation, and quantitative evaluation. Diversified evaluation methods such as self-evaluation need to evaluate the evaluation objects such as teaching content, teaching methods, teaching means, teaching resources, and teaching attitude, so as to improve the level of English language knowledge and skills and non-English language knowledge and skills of the evaluation objects, improve the reliability and validity of college English teaching evaluation, and improve the quality of college English teaching. This can be further studied in the future.

### Data Availability

The data used to support the findings of this study are available from the corresponding author upon request.

### Conflicts of Interest

The author declares that he has no conflicts of interest.

### References

- [1] R. Munirah and R. Refnaldi, "An evaluation of assessment designed by English language education student teachers during teaching practice," *Journal of English Language Teaching*, vol. 9, no. 1, pp. 1–10, 2020.
- [2] C. L. Yang, L. I. Li, H. G. Jia, X. Z. Zhang, and Y. Yu, "Establishment mechanism and procedure of training objectives of talent based on OBE," *Polymer Bulletin*, vol. 12, pp. 74–77, 2019.
- [3] T. Al-Habsi, S. Al-Busaidi, and A. Al-Issa, "Integrating technology in English language teaching through a community of practice in the Sultanate of Oman: implications for policy implementation," *Educational Research for Policy and Practice*, vol. 21, no. 1, pp. 1–10, 2021.
- [4] M. S. Yadav and M. K. Yadav, "Role of the transformational generative grammar and other language learning theories in English language teaching," *SSRN Electronic Journal*, vol. 2, no. 1, pp. 142–153, 2020.
- [5] H. A. Öztürk, "My quest for negotiating meaning. Reflections on my dilemmas about practices of English language teaching in public school context in Turkey," *Technium Social Sciences Journal*, vol. 7, no. 1, pp. 36–48, 2020.
- [6] J. Xie, "A review of research on authorial evaluation in English academic writing: a methodological perspective," *Journal of English for Academic Purposes*, vol. 47, no. 1, 100892, 2020.
- [7] W. K. Lei, "Developing an evaluation checklist for English majors' textbooks in China: focus on intercultural communicative competence," *Arab World English Journal*, vol. 11, no. 9, pp. 92–116, 2020.
- [8] Y. Zhao, S. Dong, F. Jiang, and A. Incecik, "Mooring tension prediction based on BP neural network for semi-submersible platform," *Ocean Engineering*, vol. 223, no. (4), 108714, 2021.
- [9] J. M. Zhang, Q. Shu, and Y. X. Yang, "Simulation of the low-complexity smart antenna target signal receiving design," *Computer Simulation*, vol. 36, no. 5, pp. 202–207, 2019.
- [10] Y. Yılmaz, "Computers and mathematics with applications schauder bases and approximation property in fuzzy normed spaces," *Computers & Mathematics with Applications*, vol. 59, no. 6, pp. 1957–1964, 2019.
- [11] M. Muoz-Guillermo, "Revisiting the business cycle model with cubic nonlinear investment function-Science Direct," *Chaos, Solitons & Fractals*, vol. 142, no. 1, 110510, 2020.
- [12] M. Lehmann, C. Wittpahl, H. B. Zakour, and A. Braun, "Resolution and accuracy of nonlinear regression of point spread function with artificial neural networks," *Optical Engineering*, vol. 58, no. (4), pp. 045101.1–045101.9, 2019.
- [13] R. S. Özbey, Ç. Muzaffer, A. Burak, and Ç. Tolga, "A transfer-learning approach for accelerated MRI using deep neural networks," *Magnetic Resonance in Medicine*, vol. 84, no. 2, pp. 663–685, 2020.
- [14] R. J. Pearson, "Clickers versus pickers: comparing two audience response systems in a smartphone-free teaching environment," *Journal of Chemical Education*, vol. 97, no. 8, pp. 2342–2346, 2020.
- [15] C. Pei, F. Jiang, and M. Li, "Fusing appearance and motion information for action recognition on depth sequences," *Journal of Intelligent and Fuzzy Systems*, vol. 40, no. 3, pp. 4287–4299, 2021.
- [16] X. Li and H. Zheng, "Target detection algorithm for dance moving images based on sensor and motion capture data," *Microprocessors and Microsystems*, vol. 81, no. 2, 103743, 2020.
- [17] D. Zhang, L. He, Z. Tu, S. Zhang, F. Han, and B. Yang, "Learning motion representation for real-time spatio-temporal action localization," *Pattern Recognition*, vol. 103, no. 1, 107312, 2020.
- [18] H. Xu, Q. Tian, Z. Wang, and J. Wu, "A joint evaluation of different dimensionality reduction techniques, fusion and learning methods for action recognition," *Neurocomputing*, vol. 214, no. 3, pp. 329–339, 2016.
- [19] I. Ajili, M. Malle, and J.-Y. Didier, "Human motions and emotions recognition inspired by LMA qualities," *The Visual Computer*, vol. 35, no. 10, pp. 1411–1426, 2019.
- [20] G. Mohebbi Tafreshi, M. Nakhaei, and R. Lak, "Evaluation of accuracy of hybrid model of gene expression planning-fuzzy logic in estimation of land subsidence risk," *Journal of Geosciences*, vol. 31, no. 1, pp. 163–172, 2021.
- [21] W. Lo, S. N. Purnomo, B. G. Dewanto, D. Sarah, and S. Sumiyanto, "Integration of numerical models and InSAR techniques to assess land subsidence due to excessive groundwater abstraction in the coastal and lowland regions of Semarang city," *Water*, vol. 14, no. 2, p. 201, 2022.
- [22] L. Gao, Y. Zhou, K. Guo, Y. Huang, and X. Zhu, "Determining the weights of influencing factors of construction lands with a neural network algorithm: a case study based on Ya'an City," *Earth Science India*, vol. 14, no. 4, pp. 1973–1985, 2021.

- [23] J. Y. Li and L. Wang, "Mining subsidence monitoring model based on BPM-EKTF and TLS and its application in building mining damage assessment," *Environmental Earth Sciences*, vol. 80, no. 11, pp. 1–18, 2021.
- [24] G. Gao, L. H. San, and Y. Zhu, "Flood inundation analysis in Penang island (Malaysia) based on InSAR maps of land subsidence and local sea level scenarios," *Water*, vol. 13, no. 11, 2021.
- [25] Z. Qian, A. Fl, and A. Ygwb, "CJC-net: a cyclical training method with joint loss and Co-teaching strategy net for deep learning under noisy labels[J]," *Information Sciences*, vol. 579, no. 10, pp. 186–198, 2021.

## *Retraction*

# **Retracted: Quality Assessment Method of Information Model Reform of Higher Mathematics Education Based on Big Data**

### **Mathematical Problems in Engineering**

Received 1 August 2023; Accepted 1 August 2023; Published 2 August 2023

Copyright © 2023 Mathematical Problems in Engineering. This is an open access article distributed under the Creative Commons Attribution License, which permits unrestricted use, distribution, and reproduction in any medium, provided the original work is properly cited.

This article has been retracted by Hindawi following an investigation undertaken by the publisher [1]. This investigation has uncovered evidence of one or more of the following indicators of systematic manipulation of the publication process:

- (1) Discrepancies in scope
- (2) Discrepancies in the description of the research reported
- (3) Discrepancies between the availability of data and the research described
- (4) Inappropriate citations
- (5) Incoherent, meaningless and/or irrelevant content included in the article
- (6) Peer-review manipulation

The presence of these indicators undermines our confidence in the integrity of the article's content and we cannot, therefore, vouch for its reliability. Please note that this notice is intended solely to alert readers that the content of this article is unreliable. We have not investigated whether authors were aware of or involved in the systematic manipulation of the publication process.

Wiley and Hindawi regrets that the usual quality checks did not identify these issues before publication and have since put additional measures in place to safeguard research integrity.

We wish to credit our own Research Integrity and Research Publishing teams and anonymous and named external researchers and research integrity experts for contributing to this investigation.

The corresponding author, as the representative of all authors, has been given the opportunity to register their agreement or disagreement to this retraction. We have kept a record of any response received.

### **References**

- [1] J. Li, J. Xue, and H. Fu, "Quality Assessment Method of Information Model Reform of Higher Mathematics Education Based on Big Data," *Mathematical Problems in Engineering*, vol. 2022, Article ID 5932902, 8 pages, 2022.

## Research Article

# Quality Assessment Method of Information Model Reform of Higher Mathematics Education Based on Big Data

Jiao Li, Jiao Xue , and Hongjuan Fu

Hebei Geology School, Huaxin College, Shijiazhuang 050200, Hebei, China

Correspondence should be addressed to Jiao Xue; 18409500@masu.edu.cn

Received 10 March 2022; Revised 5 April 2022; Accepted 8 April 2022; Published 30 April 2022

Academic Editor: Punit Gupta

Copyright © 2022 Jiao Li et al. This is an open access article distributed under the Creative Commons Attribution License, which permits unrestricted use, distribution, and reproduction in any medium, provided the original work is properly cited.

The quality of higher mathematics teaching in colleges and universities is related to a variety of influencing factors, and the changing laws are very complex, which makes the current model unable to accurately evaluate the quality of higher mathematics teaching in colleges and universities. In order to solve the deficiencies in the current teaching quality evaluation process in colleges and universities and improve the correct rate of college teaching quality evaluation, a quality evaluation method based on big data is proposed, which reforms the information model of college teaching quality evaluation. The literature related to mathematics teaching quality evaluation is researched and analyzed, and the influencing factors of higher mathematics teaching quality evaluation in colleges and universities are established. Then, collect the data of the influencing factors of higher mathematics teaching quality in colleges and universities, and establish a learning sample of college teaching quality evaluation through the star rating of the teaching quality of colleges and universities by experts. Finally, the neural network and decision tree of big data technology are introduced to train the learning samples to form an evaluation model of higher mathematics teaching quality in colleges and universities. The results show that our method can achieve high accuracy.

## 1. Introduction

When it comes to the new period, the development and advancement of the times are inextricably linked to reform and innovation, and the development of education is even more closely linked to reform and innovation as the subject of our day [1–3]. Continually strive to deepen education reform and innovation, fundamentally activate the innovation of graduate education in the era of big data, and build an effective system for developing high-caliber talent. Nowadays, with the advent of the big data era, there is an increasing demand for the quality of undergraduate graduates, with particular emphasis on the mathematical quality of talents [4–8]. Higher educators are confronted with a number of challenges as a result of these developments, and higher education must be reformatted as soon as possible to suit the needs of mass education and the new period of society for talents. At the same time, the teaching methods and content of higher mathematics are being reformed, and preliminary achievements have been accomplished to a

certain extent. All universities provide an advanced mathematics course as a required public basic course in engineering, which is one of the learning instruments that must be mastered before moving on to a more advanced level of study. Among its objectives are the development of students' abilities to analyze and solve problems, and the development of students' accurate logical thinking processes and talents. In practice, if our approaches are not adequate, it is possible that students may become bored with this course, and we will be unable to achieve the aim of teaching and students will be unable to reach their learning objectives [9, 10].

Increasingly evident in the quality of college education, higher mathematics teaching quality is becoming more and more apparent with the increasing number of college students. As such, higher mathematics teaching quality has become an indicator to measure the effectiveness of teaching as well as the evaluation of talents [11, 12]. Many universities have come to the conclusion that improving the quality of higher mathematics education is a good idea these days. Because of the large number of disciplines available at a

university, as well as some crossover across disciplines and a wide range of flexible and diverse teaching methods, evaluating the quality of teaching may be a complicated and difficult task [13–18].

At the moment, higher mathematics teaching quality assessment can be divided into two branches: one branch is based on qualitative analysis of higher mathematics teaching quality assessment methods, and the other branch is based on quantitative analysis of higher mathematics teaching quality assessment methods [19, 20]. Expert systems, association rules, and other qualitative analysis techniques are the most common. They just have a general understanding of the higher mathematics teaching quality, and they only look at the overall trend of change. It is difficult for qualitative analysis methods to describe the quality in a fine way because some quantitative factors are included as well as non-quantitative factors in the teaching quality assessment system [21], and the practical application value is low and only provides guiding significance [22]. One of the branches is quantitative analysis-based methods of higher education teaching quality assessment, which can be further subdivided into the following subcategories: traditional statistical methods of higher education mathematics teaching quality assessment and machine learning algorithms of higher education teaching quality assessment [23]. Traditional statistics, which primarily consists of linear regression and gray theory, can only describe the simple and linear statistical relationship between factors and quality, and as a result, the accuracy of higher mathematics teaching quality assessment does not meet the necessary standards [23, 24]. Machine learning algorithms encompass a variety of techniques such as BP neural networks, extreme learning machines, decision trees, and others. Based on modern statistical theory, they belong to the category of data mining and obtain better results in higher education teaching quality assessment in practical applications [25–31]. The parameter optimization problem of the BP neural network and the structure determination problem of the limit learning machine are not effectively solved, and the outcomes of the college teaching quality assessment are negatively impacted as a result of this [32, 33].

With the goal of improving the accuracy of higher mathematics college teaching quality assessment, the quality assessment method of higher mathematics education information model reform based on big data is designed with the goal of improving the accuracy of higher mathematics college teaching quality assessment and analyzes the superiority of higher mathematics teaching quality. The findings of this article demonstrate that the method provided in this study for assessing higher mathematics teaching quality has a substantially smaller error than the existing standard methods used in the field.

## 2. Related Work

*2.1. Mobilize Students' Enthusiasm.* Students are the focus of the entire teaching activity, while teachers, who constitute the primary body of the activity, are responsible for imparting knowledge to students.

First and foremost, the first impression a person has of another person is quite significant, and this is also true in the teaching process. The first impression that students get of the teacher will have a direct impact on their interest in the course. This, however, is a test of the overall quality of the teacher's performance. The first session in higher mathematics is extremely crucial in helping pupils accept and enjoy higher mathematics in the future. In the first class, the teacher can explain himself or herself, as well as his or her academic background, research interests. He or she should describe his or her academic background, research interests, and how mathematical knowledge is applied in contemporary high technology and what the prerequisites are for talents in the age of big data. Funny and witty words should be used throughout the document. To begin with, obviously, it allows for the development of students' knowledge about mathematics, including what new successes have been accomplished and what difficulties remain unanswered in the course of their academic careers. The opposite is also true: it can help to stimulate their interest in and inventiveness in learning advanced mathematics, which will have a greater impact than simply beginning to teach the topic the moment that the bell rings.

Second, it is critical to introduce students to the history of higher mathematics and to explain how higher mathematics has progressed from its inception and development to its current state of theoretical maturity. This entails, of course, explaining to students how university life differs from secondary school life and that university is a place where they may enhance their learning ability and creativity, as well as a transition from youth to maturity, all of which are important points to emphasize. We must inform students of the purpose for why they have come to college and help them develop a strategy for their four years of college. What we need to be clear about is why we need to study mathematics and what role it plays in the university curriculum and, even more importantly, in their future employment. Only when students have a clear comprehension of the significance of this subject as well as an emotional awareness of the teacher will they be able to use their initiative more effectively in future classroom instruction.

Moreover, the classroom teaching process should not be cluttered with duck-filled teaching approaches, which will soon cause pupils to despise mathematics, become bored, and rebel against it, as has happened in the past. They nap in class, hang out, and even play games on their cell phones while in class. The introduction of the history of an important mathematical problem to students at an appropriate time, interspersed with anecdotes about a famous mathematician, can help them achieve better learning states. This not only helps to liven up the classroom atmosphere, but also motivates students to learn. Students can have a basic comprehension of what they would be learning in this manner, which can help increase students' interest in learning.

Furthermore, teachers should not limit their mathematics instruction to classroom practice alone, but should make full use of the time they have outside of class to communicate with students, to understand their learning



methods and living habits, to provide them with specific guidance and advice, and to make students feel that you care about them and like them. Freshmen, in particular, having recently graduated from high school, have left their comfortable hometown, have separated from their parents, and have experienced some liberation, but have also experienced some discomfort. We need to show them that we care about them and that we are willing to assist them through this difficult time. Students will respect and adore their teachers from the bottom of their hearts if they receive this level of care and attention. As a result, they will be interested in the subject matter you are teaching and will work hard to master it. Teachers should assist students in responding to queries and resolving problems in a timely fashion. Their students can benefit from using the time before class to correct mistakes in homework and the time between classes and evening study to assist them in answering questions. This will allow them to overcome any challenges they may be having with advanced mathematics learning in a timely manner and thereby increase their enthusiasm for learning.

Finally, when it comes to abstract mathematical information, we may integrate modern teaching methods, such as multimedia instruction, to give pupils a more intuitive sense of what they are learning. It is preferable to develop a step-by-step derivation of the more dull knowledge and to explain the analysis process to make it more intelligible when dealing with more boring knowledge. For example, when it comes to memorizing the Taylor formula, pupils believe that it is a burden to have to do so. In this regard, we must first inform students about the origins of Taylor's formula as well as the applications of the formula. Finally, we can employ multimedia teaching to allow students to experience the Taylor formula approximation of a function, where the degree of approximation changes as the order of the derivative increases. During the process of learning mathematics, it is critical to communicate to children that mathematics is not just for subsequent professional classes but also for everyday life.

Mathematics is required in every aspect of our existence, and we cannot function well without it. Rather than being common information, the principles of many seemingly ordinary things are mathematical knowledge, and many of them are advanced mathematical knowledge, which cultivates students' enthusiasm in discovering and investigating. This also stimulates pupils' desire to learn and investigate new things.

*2.2. Initiating Student Initiative.* After pupils have been inspired to learn, they should be guided to take the initiative in their own learning. In addition to enhancing students' self-learning abilities and their daring to demonstrate themselves, this paradigm of transpersonal learning is extremely good for improving students' self-confidence. It is possible for students to demonstrate their self-learning abilities by explaining their thinking processes to themselves. It is also possible for students to demonstrate their information retention and understanding by explaining their thinking processes to themselves and applying them flexibly. Students will think about difficulties in a more extensive and comprehensive manner if they are given the

opportunity to stand at the podium and lecture. This technique helps students improve their abilities to study and collaborate with others. In this method, providing students with frequent opportunities to learn and exercise can substantially drive them to learn and take the initiative, thus making the abstract advanced mathematics classroom more engaging. Higher mathematics has traits such as being abstract, monotonous, densely packed with calculating procedures, logical, and so on. Students must synthesize appropriate methods and skills under the supervision of professors in order to better grasp, master, and apply what they have studied. This will help them master what they have learned and achieve integration. As a means of ensuring that students master the material they have learned and attain competence, educators must assist them in mastering the learning methods and skills so that they may better understand and apply the teaching materials of higher mathematics.

Second, when students first encounter advanced mathematics, they are frequently perplexed and do not understand why they should be studying mathematics in college, let alone whether it will be relevant in their future professional courses. Teachers should differentiate their assistance for students based on their majors at this time so that they can comprehend the function of higher mathematics in their respective majors and make it obvious that higher mathematics is the most fundamental information and tool for their respective majors. Only when they recognize the importance of advanced mathematics as a key to unlocking the doors to their respective fields of study will they take the initiative to learn it.

The final point to mention is that rather of merely presenting students with an overwhelming number of topics, we should direct them to review and summarize their work. Students should be allowed to sort out, summarize, and summarize their knowledge in accordance with the rule of human memory forgetting in order to ensure that they retain the information points correctly and absorb them entirely. Students can become familiar with the face of mathematics concerns and professional courses in the relevant type of problems if all chapters are combined and made simple to use, allowing them to gain mastery of all chapters. When you are juggling a lot of studying with an active college life, how do you find the time to review and summarize your work? These skills are especially important for first-year college students. When it comes to good advice, students in the first year can greatly benefit from it. It can not only inform them about the importance of cultivating good study habits and mastering good study methods, but can also greatly relieve them of all kinds of discomfort and unpreparedness when they first arrive at the university, as well as assist them in dealing with the pressure of future examinations, thereby increasing their motivation and initiative as they progress through the process of learning advanced mathematics.

### 3. Method

The first step toward a more accurate evaluation of the information mode reform of higher mathematics education

TABLE 1: Influencing factors of reform quality assessment.

Influencing factors for teachers	Influencing factors for students
Number of class suspensions	Reasonableness of course content
Number of class transfer	How good the classroom atmosphere is
Number of postponed classes	Relevance of the course content
Number of early class dismissals	The organization of the lecture
Number of substitute classes	Teaching skills
Number of assignments corrected	Teacher responsibility

is to identify and study some of the characteristics that influence the quality assessment of the reform.

As stated in Table 1, the influencing elements impacting the reform are mostly offered from two perspectives: that of the teachers themselves and those of the pupils.

BP neural network includes input layer, output layer, and hidden layer, and the output is as follows:

$$O_i^{(1)} = x(i), \quad i = 1, 2, \dots, n, \quad (1)$$

where  $x_i$  is the input. The input and output of hidden layer are as follows:

$$\begin{aligned} \text{net}_i^{(2)}(k) &= \sum_{j=1}^m w_{ij}^{(2)} O_j^{(1)}(k), \\ O_j^{(2)}(k) &= f[\text{net}_i^{(2)}(k)], \end{aligned} \quad (2)$$

where  $w_{ij}^{(2)}$  denotes layer weight coefficients,  $f[\cdot]$  is the mapping function.

The input and output of output layer are as follows:

$$\begin{aligned} \text{net}_i^{(3)}(k) &= \sum_{j=1}^m w_{ij}^{(3)} O_j^{(2)}(k), \\ O_j^{(3)}(k) &= f[\text{net}_i^{(3)}(k)]. \end{aligned} \quad (3)$$

The error function between  $O_p(k+1)$  and  $O'_p(k+1)$  is

$$\text{error} = \frac{[O_p(k+1) - O'_p(k+1)]^2}{2}. \quad (4)$$

The sum of error is

$$\text{sum error} = \sum_{p=1}^P \frac{[O_p(k+1) - O'_p(k+1)]^2}{2}. \quad (5)$$

The update equation of  $w_{ij}^{(2)}$  and  $w_{ij}^{(3)}$  is as follows:

$$\begin{aligned} w_{ij}^{(2)} &= \alpha w_{ij}^{(2)}(k-1) + \beta \frac{\partial(\text{sum error})}{\partial w_{ij}^{(2)}(k)}, \\ w_{ij}^{(3)} &= \alpha w_{ij}^{(3)}(k-1) + \beta \frac{\partial(\text{sum error})}{\partial w_{ij}^{(3)}(k)}, \end{aligned} \quad (6)$$

where  $\beta$  is learn rate, and  $\alpha$  is weight.

The core structure of the decision tree (DS) is shown in Figure 1.

Figure 1 presents the structure of DS, which introduces the detailed flow of the internal organization algorithm of the decision tree algorithm.

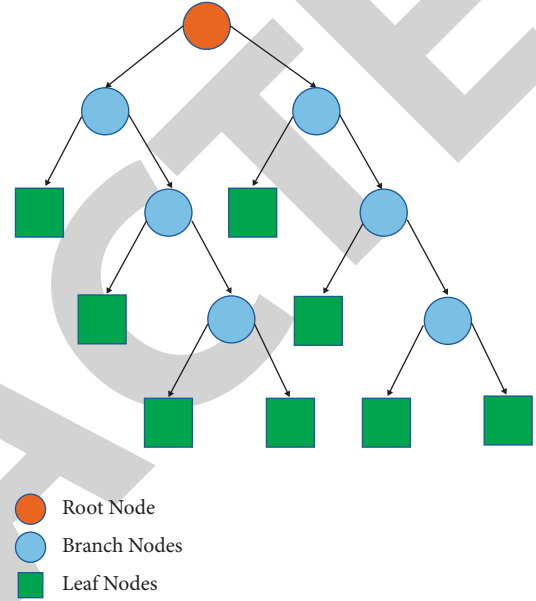


FIGURE 1: The structure of DS.

TABLE 2: Quality evaluation data.

University number	Number of teachers
1	15
2	15
3	15
4	12
5	8
6	10
7	12
8	14

The expected entropy is calculated as follows:

$$I(s_1, s_2, \dots, s_m) = - \sum_{i=1}^m \frac{s_i}{s} \log_2 \frac{s_i}{s}, \quad (7)$$

where  $s_i$  is the number of samples belonging to  $C_i$ . The expectation of attribute  $A$  for  $S$  division is

$$E(A) = \sum_{j=1}^m \frac{s_{1j} + s_{2j} + \dots + s_{mj}}{s} I(s_{1j} + s_{2j} + \dots + s_{mj}). \quad (8)$$

Then, we have

$$I(s_{1j} + s_{2j} + \dots + s_{mj}) = - \sum_{i=1}^m \frac{s_{ij}}{s_j} \log_2 \frac{s_{ij}}{s_j}. \quad (9)$$

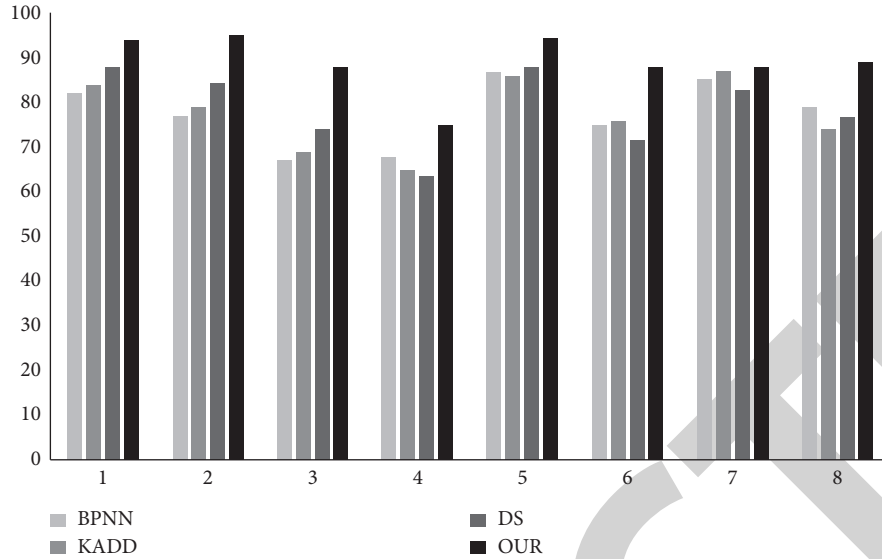


FIGURE 2: The precision curves of different methods.

And the expected entropy gain is

$$\text{Gain}(A) = I(s_1, s_2, \dots, s_m) - E(A). \quad (10)$$

We also have

$$\text{Gain}(A) = \frac{\text{Gain}(A)}{\text{splitinfo}(s)}, \quad (11)$$

where  $\text{splitinfo}(s) = \sum_{i=1}^m (s_i/|s|) \times \log_2(s_i/s)$ .

Using big data, the quality evaluation approach for higher mathematics education information model change may be broken down into the following steps:

- (1) Gather data in accordance with the influencing elements of higher mathematics teaching quality assessment listed in Table 1, and then initialize the data in order to generate samples for evaluation
- (2) Determine the corresponding grade values in accordance with the relevant influencing elements through the use of professionals
- (3) Determine the first incremental values of all indicators to generate DS using the results of step 3
- (4) Create categorization rules with the help of DS
- (5) According to the classification rules, the samples that have been labeled are filtered
- (6) Determine the structure of the neural network according to the influencing factors
- (7) Input the samples classified by DS for the first time and train the network until the training error meets the preset range

#### 4. Experiment Result

A comparison of the BPNN, the KADD model of literature [15], and the DS model was conducted on the same platform in order to determine the advantages of using the method of quality assessment of the information model reform of

higher mathematics education based on big data to analyze the advantages of the information model reform of higher mathematics education based on big data. A total of eight institutions were chosen as the research subject, and the number of professors selected in each university is displayed in Table 2. The corresponding values of the influencing factors were also collected, but they are not listed here owing to space constraints on the page layout.

To evaluate the quality of information model reform in higher mathematics education for teachers in eight universities (Table 2), four models were used, and the accuracy of quality assessment in higher mathematics education in each university was counted, with the resulting results depicted in Figure 2.

Because this cross-model combines BPNN and DS and introduces parameter adaptive optimization algorithm, it is able to overcome some problems in the current assessment process and effectively improve the assessment effect. As can be seen, the average value of higher mathematics education information model reform quality assessment method based on big data is significantly higher than the average value of BPNN, KADD, and DS models.

Because of the growing volume of data, this work improves the efficiency of the quality assessment method by analyzing and statistically estimating the modeling time of each model. The results are illustrated in Figure 3.

It can be shown in Figure 3 that the mean value of modeling practice time for the model used in this work is 22.4 milliseconds, which is in line with earlier findings. As a consequence of the results of the comparison, we can conclude that the high performance of the model presented in this study can raise the efficiency with which higher mathematics education institutions can reform their quality evaluation of the information model by increasing its efficiency.

Because of this, seven additional university courses were selected in order to further illustrate how effective the method presented in this paper is; the evaluation metrics

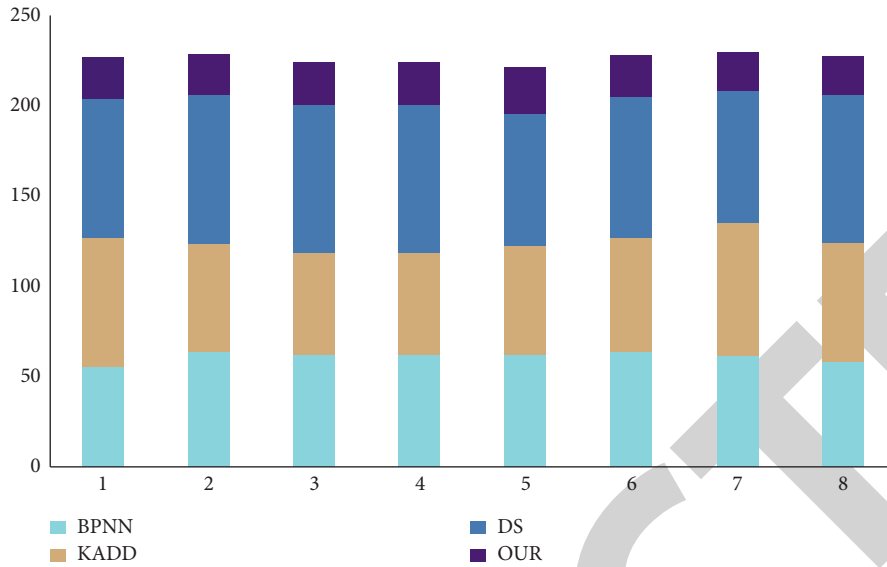


FIGURE 3: Comparison of the efficiency of different methods.

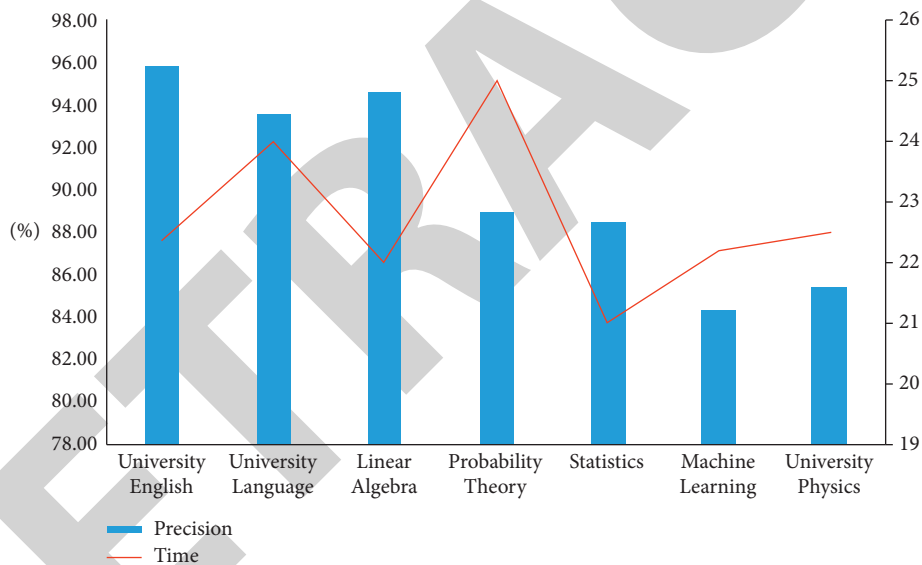


FIGURE 4: Generalization analysis of the algorithm in this paper.

used were modeling practice and modeling accuracy, as illustrated in Figure 4, which demonstrates how the algorithm presented in this paper has a high modeling accuracy while also having a short modeling time.

It can be seen that the accuracy rate of our proposed method can reach more than 94% and the modeling time is maintained at about 23 ms in three courses: college English, college language, and linear algebra. The modeling time for the probability theory course is higher, which is only 25 ms, and the shortest modeling time is 21.25 ms for the statistics course.

### 5. Conclusion

The quality of higher mathematics teaching reform in colleges and universities is related to a variety of influencing

factors. How to effectively combine these factors to carry out teaching reform has become a current research focus. In order to obtain better reform quality evaluation results, a big data-based reform quality evaluation method for higher mathematics education informatization model was proposed by introducing big data technology. First, the method is to study and analyze the current literature on the quality evaluation of higher mathematics teaching in colleges and universities, and establish the influencing factors of the quality evaluation. Then, the data of quality influencing factors are collected, combined with BPNN and DC methods, to construct the most adequate reform quality evaluation model. The results show that the model in this paper is a high precision and efficient quality evaluation model of higher mathematics teaching reform, which has a very wide range of application value.

## Data Availability

The data used to support the findings of this study are available from the corresponding author upon request.

## Conflicts of Interest

The authors declare that they have no conflicts of interest.

## References

- [1] H. Li, "A teaching quality evaluation model based on a wavelet neural network improved by particle swarm optimization," *Cybernetics and Information Technologies*, vol. 14, no. 3, pp. 110–120, 2014.
- [2] C.-L. Chang and C.-H. Chen, "Applying decision tree and neural network to increase quality of dermatologic diagnosis," *Expert Systems with Applications*, vol. 36, no. 2, pp. 4035–4041, 2009.
- [3] C.-J. Du and D.-W. Sun, "Learning techniques used in computer vision for food quality evaluation: a review," *Journal of Food Engineering*, vol. 72, no. 1, pp. 39–55, 2006.
- [4] P. Prasetyawan, I. Ahmad, R. I. Borman et al., "Classification of the period undergraduate study using back-propagation neural network," in *Proceedings of the 2018 International Conference on Applied Engineering (ICAE)*, pp. 1–5, IEEE, Batam, Indonesia, 3–4 Oct. 2018.
- [5] G. Geetharamani and A. P. Arun Pandian, "Identification of plant leaf diseases using a nine-layer deep convolutional neural network," *Computers & Electrical Engineering*, vol. 76, pp. 323–338, 2019.
- [6] N. Goel and P. Sehgal, "Fuzzy classification of pre-harvest tomatoes for ripeness estimation - an approach based on automatic rule learning using decision tree," *Applied Soft Computing*, vol. 36, pp. 45–56, 2015.
- [7] X. Wang, C. Zhou, and X. Xu, "Application of C4.5 decision tree for scholarship evaluations," *Procedia Computer Science*, vol. 151, pp. 179–184, 2019.
- [8] Y. Yang, "Quality evaluation method of a mathematics teaching model reform based on an improved genetic algorithm," *Scientific Programming*, vol. 2021, Article ID 6395349, 10 pages, 2021.
- [9] D. Pan, S. Wang, C. Jin et al., "Research on student achievement prediction based on BP neural network method," in *Proceedings of the International Conference of Artificial Intelligence, Medical Engineering, Education*, pp. 293–302, Springer, Moscow, Russia, October 2020.
- [10] D. Pan, S. Wang, Z. Li et al., "A neural network featured system for learning performance of students," in *Proceedings of the International Conference of Artificial Intelligence, Medical Engineering, Education*, pp. 399–408, Springer, Moscow, Russia, October 2020.
- [11] M. Yaghini, M. M. Khoshraftar, and M. Seydabadi, "Railway passenger train delay prediction via neural network model," *Journal of Advanced Transportation*, vol. 47, no. 3, pp. 355–368, 2013.
- [12] M. O. Asanbe, A. O. Osofisan, and W. F. William, "Teachers' performance evaluation in higher educational institution using data mining technique," *International Journals of Applied Information System (IJ AIS) Volume*, vol. 10, pp. 10–15, 2016.
- [13] S. Fong, Y. W. Si, and R. P. Biuk-Aghai, "Applying a hybrid model of neural network and decision tree classifier for predicting university admission," in *Proceedings of the 2009 7th International Conference on Information, Communications and Signal Processing (ICICS)*, pp. 1–5, IEEE, Macau, China, 8–10 Dec 2009.
- [14] D. Tien Bui, B. Pradhan, O. Lofman et al., "Landslide susceptibility assessment in vietnam using support vector machines, decision tree, and Naive Bayes Models," *Mathematical Problems in Engineering*, vol. 2012, 2012.
- [15] E. A. Amrieh, T. Hamtini, and I. Aljarah, "Preprocessing and analyzing educational data set using X-API for improving student's performance," in *Proceedings of the 2015 IEEE Jordan Conference on Applied Electrical Engineering and Computing Technologies (AEECT)*, pp. 1–5, IEEE, Amman, Jordan, 3–5 Nov. 2015.
- [16] G. K. F. Tso and K. K. W. Yau, "Predicting electricity energy consumption: a comparison of regression analysis, decision tree and neural networks," *Energy*, vol. 32, no. 9, pp. 1761–1768, 2007.
- [17] A. Li, K. Liu, K. Li, and Z. Ge, "Application of data mining in the colleges' in-class teaching quality evaluation system," *Journal of Computers*, vol. 10, no. 3, pp. 166–175, 2015.
- [18] J. Chen, J. Feng, X. Sun et al., "MOOC dropout prediction using a hybrid algorithm based on decision tree and extreme learning machine," *Mathematical Problems in Engineering*, vol. 2019, Article ID 8404653, 11 pages, 2019.
- [19] J. Dou, A. P. Yunus, D. Tien Bui et al., "Assessment of advanced random forest and decision tree algorithms for modeling rainfall-induced landslide susceptibility in the Izu-Oshima Volcanic Island, Japan," *The Science of the Total Environment*, vol. 662, pp. 332–346, 2019.
- [20] M. Biswal and P. K. Dash, "Detection and characterization of multiple power quality disturbances with a fast S-transform and decision tree based classifier," *Digital Signal Processing*, vol. 23, no. 4, pp. 1071–1083, 2013.
- [21] H. Duan, Z. Deng, F. Deng et al., "Assessment of groundwater potential based on multicriteria decision making model and decision tree algorithms," *Mathematical Problems in Engineering*, vol. 2016, Article ID 2064575, 11 pages, 2016.
- [22] A. Abu Saa, M. Al-Emran, and K. Shaalan, "Factors affecting students' performance in higher education: a systematic review of predictive data mining techniques," *Technology, Knowledge and Learning*, vol. 24, no. 4, pp. 567–598, 2019.
- [23] D. Kabakchieva, "Student performance prediction by using data mining classification algorithms," *International journal of computer science and management research*, vol. 1, no. 4, pp. 686–690, 2012.
- [24] J. Soni, U. Ansari, D. Sharma, and S. Soni, "Predictive data mining for medical diagnosis: an overview of heart disease prediction," *International Journal of Computer Application*, vol. 17, no. 8, pp. 43–48, 2011.
- [25] B. Pradhan, "A comparative study on the predictive ability of the decision tree, support vector machine and neuro-fuzzy models in landslide susceptibility mapping using GIS," *Computers & Geosciences*, vol. 51, pp. 350–365, 2013.
- [26] L. Qiao, "Teaching quality evaluation of ideological and political courses in colleges and universities based on machine learning," *Journal of Mathematics*, vol. 2022, 2022.
- [27] H. Chen, A. Chen, L. Xu et al., "A deep learning CNN architecture applied in smart near-infrared analysis of water pollution for agricultural irrigation resources," *Agricultural Water Management*, vol. 240, Article ID 106303, 2020.
- [28] S. Khokhar, A. A. Mohd Zin, A. P. Memon, and A. S. Mokhtar, "A new optimal feature selection algorithm for classification of power quality disturbances using discrete

## Research Article

# A Traffic Scheduling Method Based on SDN

**Li Wang** 

*China Oil & Gas Pipeline Network Corporation, Beijing 312000, China*

Correspondence should be addressed to Li Wang; [b20160502106@stu.ccsu.edu.cn](mailto:b20160502106@stu.ccsu.edu.cn)

Received 23 February 2022; Revised 21 March 2022; Accepted 1 April 2022; Published 30 April 2022

Academic Editor: Dinesh Kumar Saini

Copyright © 2022 Li Wang. This is an open access article distributed under the Creative Commons Attribution License, which permits unrestricted use, distribution, and reproduction in any medium, provided the original work is properly cited.

The rise of big data has brought severe challenges to data storage, which also means that computing resources and storage resources have become centralized. In the past, business data could end up after being processed locally or at the secondary node. Now, all data must be uploaded to each data center for unified processing. Data collection also requires users to access data center services and then send them back, which undoubtedly increases the pressure on the backbone network. This also means that the annual private line cost of the enterprise will increase with the growth of network traffic. Large enterprises often use multiple lines between network nodes to improve link utilization and network reliability. However, in most cases, the line utilization of the backup line is usually low, because the traditional routing algorithm forwards according to the optimal path. Load sharing or traffic scheduling is achieved by adjusting interface cost values or BGP parameters. In large networks, it often affects the entire body. Each adjustment requires detailed planning and validation. At the same time, due to the diversity of applications, different applications have different business characteristics. If the network can distinguish different applications, sense network conditions, and adjust the QoS and traffic paths of applications as needed, the link utilization of leased lines and the network quality of applications will be significantly improved. SDN separates the control plane from the data plane and intelligently controls the network forwarding policy through the global controller, which improves the flexibility and security of the network. Based on the traditional large-scale enterprise WAN architecture, this paper proposes a complete traffic scheduling solution based on SDN to achieve secure, controllable, and flexible scheduling of enterprise WAN network resources.

## 1. Introduction

With the rapid development of cloud computing, big data, mobile applications, and the Internet of things, the traffic on the WAN will also increase explosively, and the expenditure of enterprises on dedicated line fees will also rise sharply. However, the enterprise's dedicated line links often have low average utilization but high peak utilization, and the enterprise's redundant links cannot be effectively utilized. According to the prediction of authoritative institutions, the future traffic will continue to grow at a faster rate than expected. In order to cope with such growth, it is very expensive for enterprises to upgrade the bandwidth of leased lines and build and use free optical cables. Enterprises also hope to effectively control the bandwidth cost caused by the increase in bandwidth demand.

With the rapid growth of network traffic, some problems in the enterprise network are gradually exposed: at present, many enterprise networks are often unable to achieve comprehensive visualization, making the network business slow and unable to locate quickly; enterprises spend a lot of money on the improvement of dedicated line bandwidth, but in many cases, the service quality is still not improved. Therefore, enterprises urgently need to solve the problems in the existing network through the transformation of the network and technological innovation.

In terms of network visualization, the traditional network monitoring scheme is often realized through SNMP [1], which has complex configuration, low sampling frequency, and few monitoring indicators. The collected monitoring data are often only an auxiliary means to troubleshoot and solve problems and cannot be used as the basis for network optimization. Therefore, enterprises need

to use some new monitoring technologies, such as bgp-ls to realize the automatic drawing of network topology [2], telemetry to realize the second push of equipment performance indicators, and network probe to realize the accurate analysis of traffic [3]. Through a large number of monitoring data and analyzing the performance indicators of each service, the intelligent scheduling of network traffic is realized.

In terms of network traffic scheduling, traditional network engineers often realize service traffic scheduling by manually configuring MPLS-TE [4]. Its configuration is complex and error-prone. With the increase of enterprise network scale, its configuration often leads the whole body, which has high requirements for network engineers. Google's B4 pioneered the use of SDN to realize the service traffic scheduling between global data centers, which greatly improved the bandwidth utilization of its submarine optical cable and reduced the annual cost of the link cost [5]. At present, large enterprises are also facing this situation. If enterprises can use SDN technology to centrally control network business traffic, ensure important business operation, and improve bandwidth utilization, it will greatly reduce the leased line rental cost of enterprises.

This paper is divided into four parts. Section 1 introduces the overall scheme of SDN traffic scheduling. Section 2 introduces the design and implementation of the scheduling algorithm. Section 3 tests and verifies the scheduling algorithm. Section 4 is the summary and prospect.

The overall solution is mainly divided into three parts, including network visualization, traffic scheduling, and configuration distribution. The purpose of network visualization is to obtain the data and indicators of the whole network and provide a basic data source for the calculation of traffic scheduling. Traffic scheduling refers to the algorithms used in Google B4 [6] network (KSP algorithm, greedy algorithm, maximum, and minimum fair value algorithm [7]). According to the collected network indicators, application priority, network topology, and other information, each application is allocated its bandwidth, path, and priority globally and fairly [6]. The configuration distribution module generates the corresponding configuration according to the final traffic scheduling result and distributes it to the network device.

Network visualization mainly includes two parts: network topology visualization and network traffic visualization. Network topology visualization solves the problem of constructing the adjacency relationship between network nodes and links, and network traffic visualization solves the problem of network traffic data collection, analysis, and visualization.

At present, the most mainstream solution for network topology visualization is to obtain network topology information through BGP-LS (border gateway protocol link state). By extending the two attributes of address family and routing of BGP protocol, it carries the information of topology nodes, link information, and routing information of each node in the network through three attributes: node, link, and routing prefix [8]. At the same time, it also supports cross-domain network topology generation. The controller

only needs to establish a BGP-LS session with one device in each domain to draw the network topology information of the whole network.

There are traditional NetFlow schemes for network traffic visualization, port images combined with network probe schemes, and some technical schemes produced by various manufacturers to cooperate with their own controllers, such as IFIT. Because NetFlow appeared earlier, most network devices support this function. It can realize the monitoring based on the network quintuple. Because NetFlow relies on the device for network traffic analysis, when the traffic flow in the network is large, it has a high-performance loss to the device. Therefore, in many cases, it will reduce the loss of equipment performance by reducing its sampling rate, which leads to the inaccurate traffic data obtained by using NetFlow [9]. The solution provided by the manufacturer is like IFIT. Its essence is to sample and analyze network traffic data similar to NetFlow. Compared with NetFlow, it has the advantage that end-to-end traffic analysis can be realized through whole network deployment. The advantage of port mirroring combined with network probe is that it has little impact on the performance of network equipment and because it is full traffic collection and analysis, the collected traffic data are more accurate [10].

Traffic scheduling is mainly divided into two parts, including path calculation and path and bandwidth allocation. The purpose of path calculation is to create a traffic path in advance for the scheduling algorithm. Path and QoS allocation is to allocate the path and bandwidth for each application flow according to the maximum and minimum fair value algorithm according to the network path, link bandwidth, application priority, and required bandwidth, so as to achieve the global optimal effect.

The algorithm can calculate the  $K$  optimal paths without loops from a starting point to an end point. Generally speaking, the bandwidth of the enterprise's dedicated line link is much smaller than that used by the intranet line. Therefore, when using this algorithm, we only need to reduce the cost value of the high bandwidth link and increase the cost value of the low bandwidth link, plus the appropriate number of paths, we can generate a path covering all low bandwidth links.

Assuming that the number of nodes in the network topology is  $n$  and the node has  $m$  deviation points, in the  $k$ th iteration, we need  $1/2 \sum_{i=1}^m (N-i)^2 = 1/6qN^3$  insert operation and  $\sum_{k=1}^m (N-k)^2 = 1/3qN^3$  comparison operation, where  $0 < q \leq 1$ . Hence, the insertion operation to be performed by the whole algorithm is  $1/6qKN^3$ , the comparison operation is  $1/3qKN^3$ , and the additional space required is  $N^2 + KN$ .

Application path and bandwidth allocation: this paper uses the minimum and maximum fair value algorithm [11] to calculate the application path and bandwidth allocation. The implementation of specific scheduling and fair allocation algorithm is introduced in detail in Section 2.

The configuration distribution module mainly completes two things, including determining the content of configuration distribution and determining the protocol of configuration distribution. The content of configuration

TABLE 1: Time required for CLI script and NETCONF to complete a certain number of configurations.

	CLI (s)	NETCONF (s)
100	5.389	0.636
200	11.326	0.738
500	27.654	1.356
1000	56.276	2.153

distribution needs to be determined according to the actual situation of the current network. In networks that only support MPLS, path switching can be realized by MPLS-TE combined with PBR or CBTs. In networks supporting segment routing [12], application flow scheduling can be realized through SR-TE, SR policy combined with CBTs or PBTS. At present, only NETCONF [13] and CLI can be used to configure distribution. Compared with CLI, NETCONF has great advantages in distribution efficiency, configuration consistency, and development efficiency, but not all devices can support NETCONF protocol, and its device versatility is poor. Table 1 compares the CLI and NETCONF distribution efficiency. If the enterprise's ingress node cannot support the NETCONF protocol, the upper SDN controller needs to design a perfect distribution process when developing relevant modules to ensure the success of distribution and the rollback after distribution failure. Time required for CLI script and NETCONF to complete a certain number of configurations is shown in Table 1.

## 2. Design and Implementation of the Scheduling Algorithm

With the expansion of enterprise scale, there are many kinds of applications in the network, and the application characteristics of each application are also very different. Some applications are sensitive to delay and packet loss but do not require high bandwidth; some applications are sensitive to delay and packet loss but require high bandwidth; some applications have high requirements for delay, packet loss, and bandwidth. Therefore, if each application is divided into a policy, the number is very large, and it is difficult for network devices to schedule each application. In IP packet designing, the first three bits of the TOS field are used as IP priority. The larger the number from 0 to 7, the higher the importance of the service. Later, in order to identify more service types, a new definition of TOS was made in RFC 2474 [14], taking the first six bits as DSCP and reserving the last two bits, so that 0 ~ 63 service types can be represented. Since the priority field in the MPLS tag only contains 3 bits, it is consistent with the TOS field, and generally, 6 and 7 in the TOS are reserved for basic protocols such as routing protocols. Therefore, this paper implements scheduling according to six types of applications from 0 to 5.

Path calculation: in this paper, Yen algorithm [11] is used to calculate the path. The detailed algorithm flow is shown in Figure 1.

Time required for CLI script and NETCONF to complete a certain number of configurations is shown in Table 1.

Different enterprise nodes access various applications to form hundreds of application flow groups (FGs). Each FG contains source address, destination address, priority, path, bandwidth, and other QoS information. At the same time, there are multiple paths from one site to another. These paths are divided into a tunnel group (TG). Different application classes have different priority and bandwidth requirements. The fair value  $f_s$  (fair share) is obtained by priority according to the required bandwidth. The bandwidth function of each application can be obtained by taking the fair value  $s$  as the horizontal axis and the bandwidth  $B$  as

the vertical axis  $B(S) = \begin{cases} W \times S, 0 \leq S \leq B_{\max}/W \\ B_{\max}, S > B_{\max}/W \end{cases}$ , as shown

in Figure 2(a) The slope shown by each line is the weight  $W$  applied. For an application stream group FG, which contains several application streams, its bandwidth function is  $B_{\text{sum}}(S) = \sum_{k=1}^n B_k(S)$ ; we can use the linear superposition of each application stream bandwidth function to represent  $B$ .  $K(s)$  represents the bandwidth function of the  $k$ th application stream. As shown in Figure 2(b), the bandwidth function diagram of the final FG is composed of a group of broken lines.

If the bandwidth and path allocated by each FG are calculated by linear programming, it takes a long time and has no good scalability. Therefore, this paper calculates the final result by greedy algorithm combined with dichotomy.

The fair algorithm process and pseudocode are as follows:

- (1) Since the number of application streams covered at the branch node is small, bandwidth allocation for the bottle-neck link is given priority at the branch node. During allocation, all cases are enumerated by permutation and combination. The initial value of minfs is 0 and maxfs is the maximum fair value in the application flow group FG. Curfs represent the currently allocated fair value, which is initially set to maxfs. The pseudocode is as follows:

```

if (allocate_end (maxFS)==true) {
    curFS=maxFS;
}else{
    curFS=(maxFS+midFS)/2;
}
while (maxFS-curFS>=0.01) {
    if(allocate_end(curFS)==true){
        midFS=curFS;
        curFS=(maxFS+minFS)/2;
        save(); //save the end path info
    }else{
        maxFS=curFS;
        curFS=(maxFS+minFS)/2;
    }
}

```

- (2) The bandwidth of the bottleneck link at the core/convergence is allocated. The calculation results in the first step are sorted according to the allocated



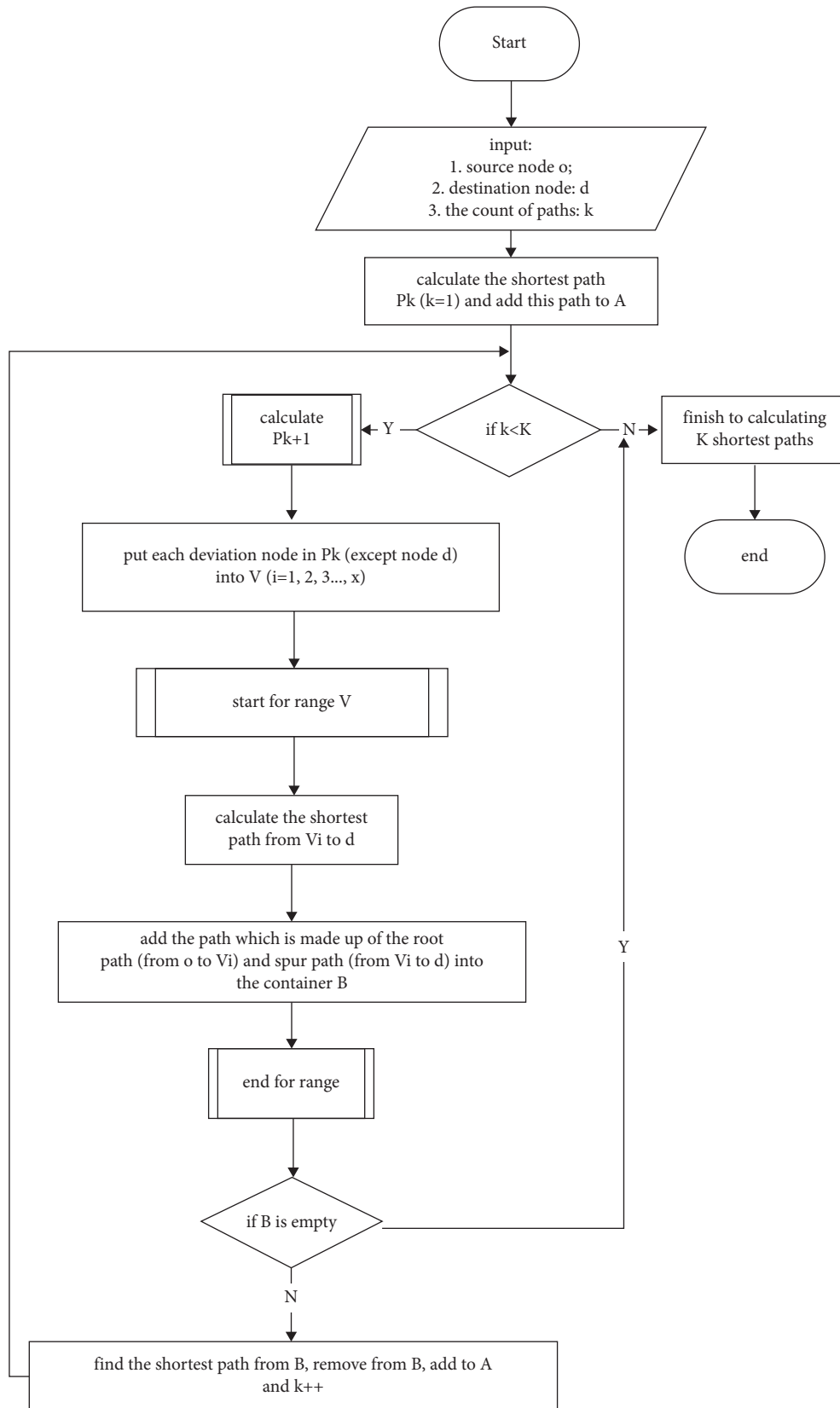


FIGURE 1: Implementation flow chart of Yen algorithm.

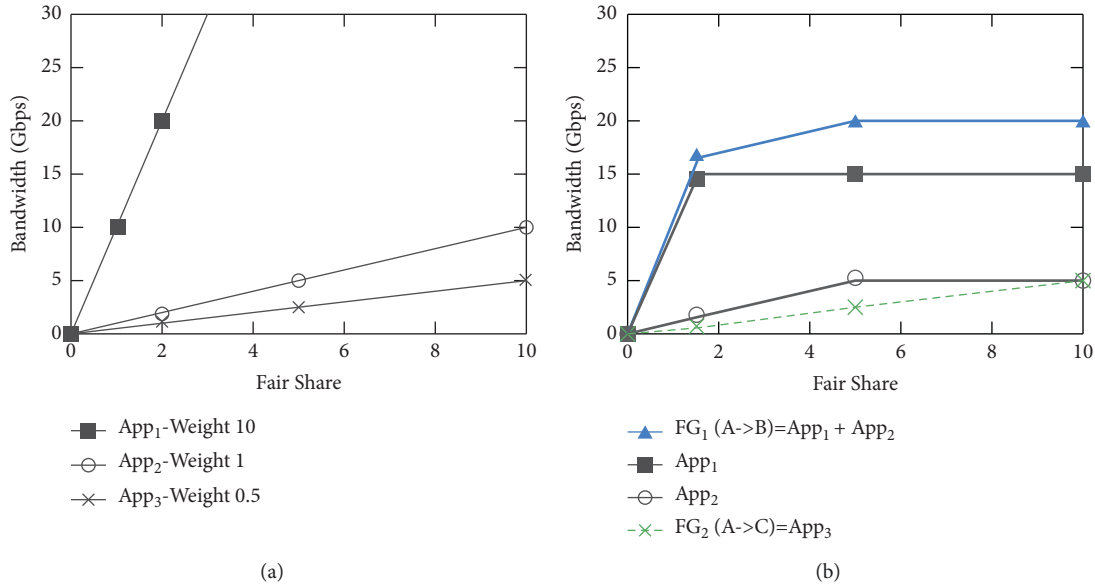


FIGURE 2: Bandwidth allocation function of the application stream group FG: (a) per-application and (b) FG-level composition.

bandwidth from large to small and then allocated to the links with large remaining bandwidth in all bottleneck lines. The exhaustive algorithm in the first step is not used here, mainly because the number of application streams at the core/aggregation link is relatively correct and the complexity of the exhaustive algorithm is high. Although the greedy algorithm used here is not the global optimal solution, its algorithm complexity is low and its error will decrease with the increase in the number of application streams. The maximum fair value  $\max_{fs}$  is the maximum current fair value in all application streams (calculated in step 1), the minimum fair value  $\min_{fs}$  is 0, the current fair value  $\text{cur}_{fs}$ ,  $\text{flow\_size}$  is the number of all application streams,  $\text{cur}_{bw}[i]$  is the current bandwidth of the  $i$ th application stream, and  $\text{priority}[i]$  is the priority of application stream  $i$ . The pseudocode is as follows:

```

if (allocate_begin (maxFS)==true) {
    curFS=maxFS;
}else {
    curFS=(maxFS+midFS)/2;
}
while (maxFS-curFS>=0.01) {
    if(allocate_begin(curFS)==true){
        midFS=curFS;
        curFS=(maxFS+minFS)/2;
        save(); //save the start path info
    }else{
        maxFS=curFS;
        curFS=(maxFS+minFS)/2;
    }
}
//calculate the result|
for(i=0;i<flow_size;i++){
    curBW[i]=min{curFS*priority[i],curBW[i]};
}

```

(3) The final path of the application flow is the path containing the bottleneck lines stored in steps 1 and 2.

### 3. Test and Result Analysis

This paper constructs a network topology, as shown in Figure 3: node  $E$  and node  $f$  are branch 1, nodes  $g$  and  $H$  are branch 2, and nodes  $I$  and  $j$  are branch 3. The link bandwidth is shown in the figure. Application flows are classified into five application classes. The path of flow1 is fixed as the optimal path, and flow5 is other nonimportant services. Its required bandwidth is the maximum bottleneck bandwidth value; that is, when meeting the bandwidth requirements of other important services, the remaining bandwidth can be allocated to this kind of applications.

The path from node  $a$  to each branch node is shown in Table 2. It can be seen that the path completely covers the bottleneck line.

By adjusting the required bandwidth in different scenarios, check whether the bandwidth is consistent with the expected bandwidth.

It can be seen from Table 3 that when the link bandwidth is greater than the required bandwidth of all application streams, when the link bandwidth is sufficient, the required bandwidth of each application stream will be met as much as possible.

Table 4 shows the results calculated by a fair algorithm when the link bandwidth is insufficient after adjusting the required bandwidth of high priority applications. It can be seen that the bandwidth requirements of high priority applications are guaranteed first, while the bandwidth of low priority applications can be allocated better when the link bandwidth is sufficient, and the bandwidth of bottleneck links can be fully used to improve the overall link utilization.

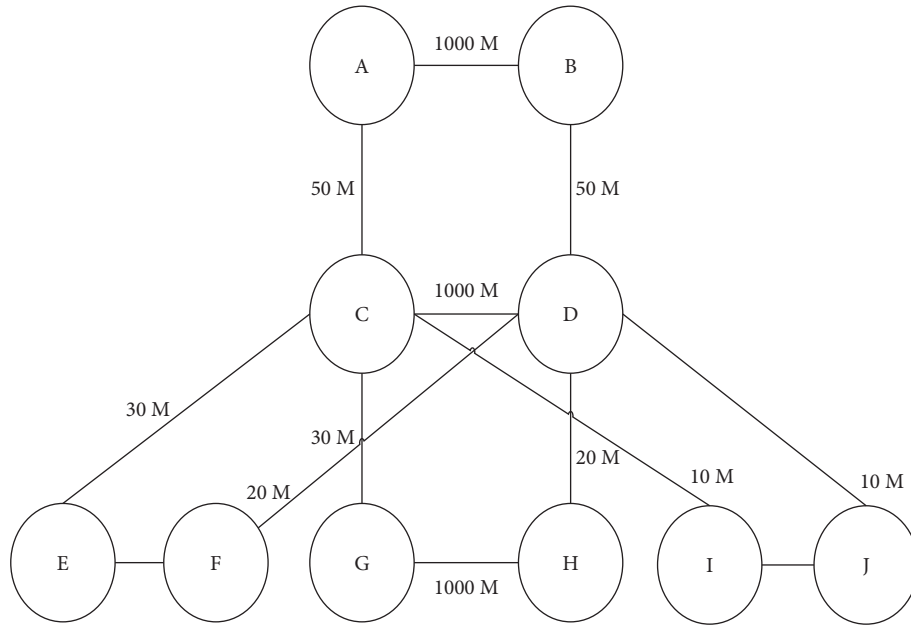


FIGURE 3: Example of network topology.

TABLE 2: All paths from node a to branch node.

Path name	Path detail
ETP1-path1	A -> c -> e
ETP1-path2	A -> c -> d -> f -> e
ETP1-path3	A -> b -> d -> c -> e
ETP1-path4	A -> b -> d -> f -> e
ETP2-path1	A -> c -> g
ETP2-path2	A -> c -> d -> h -> g
ETP2-path3	A -> b -> d -> c -> g
ETP2-path4	A -> b -> d -> h -> g
ETP3-path1	A -> c -> i
ETP3-path2	A -> c -> d -> j -> i
ETP3-path3	A -> b -> d -> c -> i
ETP3-path4	A -> b -> d -> j -> i

TABLE 3: Algorithm results when bandwidth demand is lower than link bandwidth.

Flow name	Calculated bandwidth (kbps)	Demand bandwidth (kbps)	Calculated path	Priority
ETP1_Flow1	4000	4000	ETP1-path1	6
ETP1_Flow2	8000	8000	ETP1-path4	5
ETP1_Flow3	8000	8000	ETP1-path3	4
ETP1_Flow4	2000	2000	ETP1-path3	3
ETP1_Flow5	20000	30000	ETP1-path2	1
ETP2_Flow1	4000	4000	ETP2-path1	6
ETP2_Flow2	4000	4000	ETP2-path4	5
ETP2_Flow3	8000	8000	ETP2-path4	4
ETP2_Flow4	2000	2000	ETP2-path3	3
ETP2_Flow5	20000	30000	ETP2-path1	1
ETP3_Flow1	4000	4000	ETP3-path1	6
ETP3_Flow2	4000	4000	ETP3-path1	5
ETP3_Flow3	2000	2000	ETP3-path1	4
ETP3_Flow4	2000	2000	ETP3-path4	3
ETP3_Flow5	8000	30000	ETP3-path4	1

TABLE 4: Algorithm calculation results after increasing the bandwidth required by high priority applications.

Flow name	Calculated bandwidth (kbps)	Demand bandwidth (kbps)	Calculated path	Priority
ETP1_Flow1	4000	4000	ETP1-path1	6
ETP1_Flow2	10000	10000	ETP1-path2	5
ETP1_Flow3	10000	10000	ETP1-path4	4
ETP1_Flow4	10000	10000	ETP1-path3	3
ETP1_Flow5	5750	30000	ETP1-path2	1
ETP2_Flow1	4000	4000	ETP2-path1	6
ETP2_Flow2	10000	10000	ETP2-path2	5
ETP2_Flow3	10000	10000	ETP2-path3	4
ETP2_Flow4	10000	10000	ETP2-path4	3
ETP2_Flow5	5750	30000	ETP2-path1	1
ETP3_Flow1	4000	4000	ETP3-path1	6
ETP3_Flow2	6000	10000	ETP3-path1	5
ETP3_Flow3	5000	10000	ETP3-path2	4
ETP3_Flow4	3750	10000	ETP3-path4	3
ETP3_Flow5	1250	30000	ETP3-path2	1

TABLE 5: The result of the etp2\_ calculation of the boosting algorithm.

Flow name	Calculated bandwidth (kbps)	Demand bandwidth (kbps)	Calculated path	Priority
ETP1_Flow1	4000	4000	ETP1-path1	6
ETP1_Flow2	10000	10000	ETP1-path1	5
ETP1_Flow3	10000	10000	ETP1-path4	4
ETP1_Flow4	9666	10000	ETP1-path4	3
ETP1_Flow5	3222	30000	ETP1-path1	1
ETP2_Flow1	4000	4000	ETP2-path1	6
ETP2_Flow2	16111	20000	ETP2-path2	5
ETP2_Flow3	10000	10000	ETP2-path3	4
ETP2_Flow4	9666	10000	ETP2-path3	3
ETP2_Flow5	3222	30000	ETP2-path2	1

TABLE 5: Continued.

Flow name	Calculated bandwidth (kbps)	Demand bandwidth (kbps)	Calculated path	Priority
ETP3_Flow1	4000	4000	ETP3-path1	6
ETP3_Flow2	6000	10000	ETP3-path3	5
ETP3_Flow3	5000	10000	ETP3-path2	4
ETP3_Flow4	3750	10000	ETP3-path4	3
ETP3_Flow5	1250	30000	ETP3-path4	1

Table 5 increases the required bandwidth of enterprise 2 application stream 2 compared with Table 4. From the calculation results, it can be seen that the allocated bandwidth of application flow under the same conditions of enterprise 1 and enterprise 2 is consistent, which shows the global fairness of the algorithm.

#### 4. Conclusions and Outlook

Based on the actual network situation of the current enterprise network, this paper introduces a complete solution for SDN service traffic scheduling, including network visualization, traffic scheduling, and configuration distribution. The rationality and correctness of the scheduling algorithm are verified by tests. The research content of this paper is more based on the status quo of the enterprise network to achieve business traffic scheduling. However, with the emergence of new technologies and the upgrading of enterprise equipment, enterprises can also achieve intelligent scheduling of business traffic in a more convenient and intelligent way, improve the bandwidth utilization of private lines, reduce private line costs, and improve operational efficiency. The method to improve the accuracy of network indicators, the ubiquity of scheduling algorithms, and the efficiency of configuration distribution are also the key directions of future research and practice and ultimately realize the complete integration of services and networks. The dynamic scheduling and universality of future data in the research of this paper are one of the key tasks of future research.

#### Data Availability

The data used to support the findings of this study are available from the corresponding author upon request.

#### Conflicts of Interest

The author declares that there are no conflicts of interest.

#### References

- [1] L. M. Surhone, M. T. Tennoe, and S. F. Henssonow, *Simple Network Management Protocol*, Springer, Berlin Heidelberg, 2006.
- [2] F. Chen and B. Xiaoxue, "SDN network topology generation system based on bgp-ls protocol [J]," *Network new media technology*, vol. 5, no. 1, pp. 21–26, 2020.
- [3] S. Dong, H. Mo, and J. Hu, "Probe based network condition monitoring technology," *Communication technology*, vol. 52, no. 4, pp. 908–911, 2019.
- [4] F. L. . Faucheur, "Requirements for support of differentiated services-aware MPLS traffic engineering," *British Journal of Plastic Surgery*, vol. 2, 2003.
- [5] T. Yuan, *Research on Node Migration and Optimization Method for SDN Transition [D]*, Beijing University of Posts and telecommunications, Beijing, China, 2018.
- [6] S. Jain, A. Kumar, S. Mandal et al., "B4: experience with a globally-deployed software defined WAN," in *Proceedings of the ACM SIGCOMM 2013 conference on SIGCOMM. ACM*, pp. 3–14, Hongkong China, August 2013.
- [7] E. Danna, A. Hassidim, and H. Kaplan, "Upward max min fairness," in *Proceedings of the INFOCOM, 2012 Proceedings IEEE*, pp. 837–845, IEEE, USA, March 2012.
- [8] I. Seremet and S. Causevic, "An analysis of reconvergence delay when using BGP-LS/PCEP as southbound protocols [C]," in *Proceedings of the 2019 42nd International Convention on Information and Communication Technology, Electronics and Microelectronics, MIPRO*, Opatija, Croatia, May 2019.
- [9] H. Sun, "Optimization model of Internet traffic collection based on NetFlow," *Data communication*, vol. 4, no. 6, pp. 11–12, 2019.
- [10] W. Jiahui, *Research and implementation of network traffic analysis*, North China Electric Power University (Beijing), Beijing, China, 2018.
- [11] J. Y. Yen, "An algorithm for finding shortest routes from all source nodes to a given destination in general networks," *Quarterly of Applied Mathematics*, vol. 27, no. 4, pp. 526–530, 1970.
- [12] G. Trimponias, Y. Xiao, H. Xu, X. Xu, and Y. Geng, *Centrality-based Middlepoint Selection for Traffic Engineering with Segment Routing*, USA, 2017.
- [13] R. Enns, M. Bjorklund, and J. Schoenwaelder, *Network Configuration Protocol (NETCONF)*, USA, 2011.
- [14] K. Nichols, *Definition of the Differentiated Services Field (DS Field) in the IPv4 and IPv6 Headers. RFC-2474*, USA, 1998.

## Research Article

# Evaluation Model of Sports Culture Industry Competitiveness Based on Fuzzy Analysis Algorithm

Guoqiang Sun <sup>1</sup>, Xinxin Zhang,<sup>2</sup> and Yu Lin<sup>1</sup>

<sup>1</sup>Jining Medical University, Jining, Shandong Province 272067, China

<sup>2</sup>Hainan Normal University, Haikou, Hainan Province 571158, China

Correspondence should be addressed to Guoqiang Sun; [sunguoqiang@mail.jnmc.edu.cn](mailto:sunguoqiang@mail.jnmc.edu.cn)

Received 15 March 2022; Revised 8 April 2022; Accepted 12 April 2022; Published 28 April 2022

Academic Editor: Punit Gupta

Copyright © 2022 Guoqiang Sun et al. This is an open access article distributed under the Creative Commons Attribution License, which permits unrestricted use, distribution, and reproduction in any medium, provided the original work is properly cited.

Since reform and opening, our country's sports and cultural industries have grown from nothing. Due to the complexity of the evaluation factors and methods used to determine the competitiveness of the sports cultural industry, this paper establishes a seven-dimensional sports cultural industry competition based on the integration and development of the sports tourism industry and national culture, drawing on the theory and methods used to determine the tourism industry's competitiveness. Based on a fuzzy analysis algorithm, we developed a system for evaluating strength and a model for evaluating the competitiveness of the sports culture industry. According to the results of the evaluation of the competitiveness of the sports culture industry in numerous regions of China, the evaluation method proposed in this paper is superior to the traditional evaluation method and has contributed to the development of China's sports culture industry.

## 1. Introduction

Sport industry must invest in high-quality development to fulfill its mission in the new millennium. It is also the most important means by which the sports industry can overcome the pressures of reality. The Central Economic Work Conference in December 2017 stated that creating and improving the institutional environment is necessary to promote high-quality development. As shown above, the indicator system promotes high-quality development of the sports business [1–6]. However, the sports sector in our nation is now in the early stages of high-quality development, and a somewhat systematic theoretical system has not yet been established, in addition to a temporary lack of an indicator system and a mechanism for performance evaluation. The development of a high-quality development index evaluation system for the sports industry is an important method to standardize the goals and processes of high-quality development in the sports industry in the new era, according to relevant scholars; designing index standards realistically and carrying out static and dynamic monitoring in a timely and feasible manner is an important

way to promote the development of the sports industry. A critical component of the industry is high-quality development process. A mechanism analysis—indicator system construction—exponential model design—empirical test approach is followed as a result, guided by high-quality development theory and based on this information [7–9]. An empirical test is conducted in Shanghai to evaluate the index system and index model of high-quality development in the sports industry in this new era, with the goal of improving the institutional environment for high-quality development in the sports industry in general and for high-quality development in particular [10, 11].

This theory states that a product's competitive advantage is not in serving the market's basic functions, but in fulfilling unique core functions that other products cannot fulfill. In plain English, this means you have advantages over others, such as technical, managerial, market, and other competitive advantages. The concept of core competitiveness emerged in the 1990s. It once sparked the imaginations of countless businesses seeking growth and expansion [12, 13]. Core competitiveness is now one of the most powerful tools a country or a nation can use to achieve

prosperity. After more than 40 years of reform and opening, our country's sports business has grown significantly. However, it is still in its infancy, with a small industrial scale and low level of development. Due to a lack of global competitiveness, the industrial structure must be optimized and updated. Let us face it: our country's sports industry clearly lacks core competitiveness in the face of fierce international sports industry competition, and it clearly does not reflect our overall economic progress [14, 15]. Enhancing the core competitiveness of the sector is therefore critical to the long-term development of the sports industry in our country and its involvement in worldwide competition.

Recent years have seen a resurgence in the discussion over the integration and development of the sports business and the tourism industry. Sports tourism is a new tourist product that is on its way to become the primary tourism product in the future. A growing sports tourism industry can help to increase the level of market consumption while also creating jobs and encouraging the growth of nontrade foreign exchange earnings in the region. In recent years, sports fever has progressively gained popularity as a phenomenon [16–18]. The quick development of the sports sector has aided in the development of the sports tourism business as a result of this rapid development. The sports tourism sector brings together the benefits of both sports and tourism, and as a result, sports tourism has emerged as the most important trend in the growth of the modern tourism industry [19, 20]. Due to the expansion of the sports sector, the influence of sports stars and sporting events has constantly expanded, particularly with the conducting of large-scale international sporting events, which has garnered widespread public interest and created a significant commercial potential. Sports tourism is a new cross-industry phenomenon characterized by dual characteristics that have emerged as a result of the merging of the tourist and sports industries. In this way, visitors can take part in sports tournaments, visit sporting sites, and participate in a wide range of fitness and sports activities, as well as entertainment and adventure activities, while on the road [21–29].

Shopping for sports memorabilia is just one example of a collection of actions. A well-developed sports tourism business may breathe fresh life into a city, allowing more people to get to know and understand themselves better, allowing them to take the initiative in urban competition and win the first opportunity they are presented with [30–32].

As a result, in light of the foregoing, this study provides a model for evaluating the competitiveness of the sports and cultural industries that are based on a fuzzy analytic algorithm, as well as a seven-dimensional sports and cultural industry competitiveness evaluation index system. This research assesses the competitiveness of the sports culture industry in a number of different Chinese locations. Based on the findings of this study, the assessment method provided in this paper outperforms the old evaluation approach and has made significant contributions to the growth of China's sport and cultural industries in general.

## 2. Background

### 2.1. Current Situation

*2.1.1. History of China Sports Industry.* Historically, China's sports industry was viewed as a national welfare initiative rather than an industry in the traditional economic sense. In the absence of a market system, state-owned sports goods producers had to compete with one another. There is no competition between them and no linkage between upstream and downstream connected firms in the sense of an industrial chain. As a result, the sports industry in our country has not really developed since the reform and opening. During the last 40 years of reform and opening, my country's economic structure has changed significantly. The most important task is to move from a planned to a market economy, gradually increase private sector participation in the economy, and create a market competitive system that is fair and free. People's demand for sports consumption is increasing, resulting in a rapid increase in the number and scale of sports product manufacturers, and the links between enterprises are becoming increasingly crisscrossed, forming the prototype of the industrial network. In the 1980s, China's sports industry began to take shape, and by the 1990s, it had mostly industrialized. It also spawned sports business rules, sports competition, sports betting, and athletics as we know it today. Tourism and related industries have grown significantly during this time period.

China has established a sports industry system with a wide range of categories, as planned by the State Sports General Administration. However, the structure is not logical and the development is not uniform. As a result, China's sports industry remains highly competitive globally. It is young, but it has the inherent ability to compete globally and maturely into a strong organization over time. Here are the reasons: First, China has the world's largest sports consumption market, which has enormous potential to support the Chinese sports sector's rapid expansion. Second, China has made the most progress in competitive sports. As a result of early state investment in competitive sports, China's sports industrialization has a strong foundation in terms of talent, sports infrastructure, and market influence. The Chinese sports culture is inclusive. For forty years of reform and opening, foreign sports and well-known brands have made their way to China, where they have thrived. On the surface, this type of inclusion appears to facilitate foreign product entry into the Chinese market. In the long run, it may help our country's sports industry innovate and grow, allowing it to expand abroad and enter the global sports industry market and take up residence somewhere. In the context of cultural tolerance, there has always been an introduction, digestion, invention, and renewal process. Fourth, the 19th National Congress of the Communist Party of China defined the path to socialism with Chinese characteristics, ensuring the rapid development of China's sports industry in the years to come. Some academics have confirmed the importance of core competitiveness to the development of the local sports industry in evaluating core competitiveness. The core competitiveness of these areas will

merge in the future to form a joint force that will compete in a global sports industry.

*2.1.2. Competition Situation.* From a worldwide viewpoint, the sports industries in North America, Western Europe, and Japan are the most developed regions in terms of development. This region's annual production value of sports has risen to become one of their country's most important pillar industries; the total output value of sports amounts to more than 1.5 percent of GDP, making it the country's most important pillar industry. The United States is the most powerful of these countries, and it is also the country with the most prominent manifestations of the characteristics of diversification, commercialization, and globalization. It is also the country with the most competitive sports sector in the world. There are dozens of sports brands that we are all familiar with from our daily lives, and this number is growing. To give you an example, consider sports apparel and supplies. Companies such as Adidas, Nike, and Reebok are popular. Other popular sports clothing and supplies brands include Under Armour, New Balance, North Face, Patagonia, and Columbia. The United States is the dominant force in the world, not to mention in the production of high-tech sports equipment and supplies. Aside from the United States and Japan, other countries with world-renowned sports brands include Germany, the United Kingdom, France, and Switzerland. In comparison to the United States, these countries have relatively tiny economies, which means that the GDP generated by their well-known sports brands is a modest proportion of their total GDP. In addition, the proportion is significant. Even though China's gross domestic product (GDP) has consistently ranked second in the world for many years, it appears that the country's sports business does not yet have a globally recognized brand. As a result of the large increase in labor costs in China as well as the high land price in recent years, we have lost our position as the world's factory. However, this is a temporary phenomenon due to the substantial increase in labor costs in China and the high land price in recent years.

Globalization has accelerated the expansion of the sports sector in recent decades, particularly in the United States. In an era when competitive sports and leisure sports have had a significant impact on people's sports consumption, the sports consumption market has grown significantly, resulting in intense competition in the international sports sector. It may be claimed that worldwide competition in the sports sector is all-encompassing, long-term, and far-reaching because of the availability of talent on the market. In the past, the sports sector was primarily concerned with design. Fashionable design is no longer sufficient in today's world. Take, for example, sportswear as an illustration. In order to reach the perfection of sportswear, high-tech textiles, such as breathable, light, quick-drying, waterproof, windproof, and other application levels, are used in conjunction with reasonable and fashionable design to create products with a large market share. Both are aesthetically pleasing and useful. It can be claimed that the technological content of outdoor sports products is higher than that of

indoor sports products. Mountaineers of the 1950s and 1960s used equipment that was significantly inferior to that used by today's mountaineers. Their lightweight, water-resistant thermal apparel, light, and robust carbon trekking poles, antiglare polarized eyewear, and other products are made with the most up-to-date material technology available anywhere in the world.

Finally, the market environment of the sports sector is also a critical component of worldwide competition in the field of sports. In the sports industry, a mature and active market is the primary driving factor behind the development and expansion of the sports sector. On the contrary, if the market is chaotic and counterfeit items are prevalent, it will surely have a negative impact on the overall health of the sports business. Because of the low cost of counterfeiting, development has a fatal lethality; as a result, it can take advantage of the attractiveness of treasures to draw attention to itself in the marketplace. If people are willing to pay low costs for indistinguishable brand-name knockoffs, it is inevitable that genuine items will find it difficult to compete in this market. Fake items, on the other hand, suffocate the creativity and originality that is the driving force behind the sports sector. Ultimately, the sports sector will have to survive in a low-end and chaotic market in order to continue to exist. As a result, it is necessary to develop a standard. Due to the fact that practically all developed countries have formed their mature and standardized market environments, a healthy sports industry market is the competitive advantage of today's developed and emerging countries, particularly China's sports industry. The market order in our country is incapable of providing a strong foundation for the rapid development of the sports business in our country.

## *2.2. Strategies to Enhance Competitiveness*

*2.2.1. Independent Intellectual Property Rights.* Brands with independent intellectual property rights must first be established in China before they may be developed elsewhere in the world. Currently, China is the world's largest market for sports consumption. Upon regulation, this market will become the most important source of competitiveness for our country's sports business. The establishment of brands with autonomous intellectual property rights must therefore begin with the regulation of the general public and begin by creating your own market, enforcing strict anticounterfeiting measures, and demonstrating a zero-tolerance policy for intellectual property infringement, so that domestic businesses can devote more time, energy, and financial resources to developing their own brands and actively investing in research and development and innovation. Only property owners can utilize their R&D results as capital to operate, for example, by engaging in production and operation through technology equity, technology transfer, and other means. This allows entrepreneurs and researchers to collaborate in the most effective way possible. When it comes to autonomous intellectual property rights, many individuals believe that our country must have its own ideas, creations, and brands in order to compete with foreign

brands. In fact, every company should have its own set of intellectual property rights that are distinct from those of other companies. Intellectual property rights are distinct from one another. A feeling of business, when it comes to a business environment backed by the entire society, is a crucial requirement for success. It is important that intellectual property protection is prioritized while developing a mature and regulated sports sector market.

*2.2.2. The Innovation and Development Vitality of the Sports Industry.* Linkage mechanism was initially a professional word for financial institutions, and it simply indicates that credit funds provide credit support to connected projects or adjacent industrial links in the industrial chain, as defined by the International Organization for Standardization. The project, as well as the entire industry, will have a good impact on the environment. This connection mechanism, for financial institutions, unquestionably protects the security of their cash while also significantly reducing credit risks. Every link in the industrial chain is responsible for maintaining and improving the health and safety of its members, which is impossible to achieve without ensuring the health and safety of all those involved. The linkage mechanism has also been actively introduced in the large scope of the industrial economy to ensure orderly development; that is, in our industrial policy, we must not only support those large and influential enterprises but also support those related enterprises that have an impact on large enterprises. The development status of our country's sports industry is precisely due to the lack of a linkage mechanism at the policy level of the government. It has been discovered by certain academics that the sporting industries in our nation have not yet developed a strong core competitiveness, which is mostly due to the lack of development of industrial clusters and the lack of overall industries. The development plan, a lack of industrial policy support and guidance, a major lack of industry-related management systems, and a lack of an effective incentive mechanism for industrial innovation are all issues that need to be addressed. In fact, one of the most serious shortcomings of our industrial policy is the absence of a connection mechanism, which makes the growth of industrial clusters as well as the general development of the industry extremely difficult.

*2.2.3. Strengthen Cooperation with Internationally Renowned Enterprises.* The most significant benefit that Chinese sports industry businesses have is that they are familiar with, if not in control of, the world's largest consumer market. They are also familiar with their own legislation, regulations, culture, and habits, which gives them a competitive advantage. This is, without a doubt, a problem for those large international corporations seeking to enter the Chinese market. And some international enterprises are known for their innovative designs, high-tech materials or fabrics, cutting-edge business approaches, and global recognition. The two individuals

mentioned above appear to have a great deal of room and opportunity for collaboration. If Li Ning and Nike can work together to develop in China, the prospects for both Li Ning and Nike might be significantly greater than their current development situations. Strangely, despite the fact that nearly all of the world's leading sports brands have established factories in China over the past few decades, no Chinese company has entered into brand strategic cooperation with any of these foreign corporations. Today, when big foreign corporations relocate their plants out of China, it will have a negative impact on us. A considerable number of people were laid off, and the resulting economic downturn in the surrounding cities where the processing plants were concentrated exacerbated the situation. Chinese sports firms should aggressively go out and take advantage of the advantages of well-known foreign enterprises in order to grow and strengthen their own enterprises in today's economic globalization process characterized by the international collaboration that is spreading around the world. With its emphasis on inclusion, Chinese sports culture has established a solid foundation for this type of international cooperation.

### 3. The Proposed Method

Evensen created the Ensemble Kalman Filter (EnKF) to tackle the computing resource difficulty that the classic Kalman filter approach encountered when calculating the prediction error covariance. The EnKF is currently commonly utilized in strongly nonlinear systems to calculate the prediction error covariance. The EnKF state update formula is as follows:

$$x = \frac{1}{m} E1,$$

$$P = \frac{1}{m} AA^T, \quad (1)$$

$$K = P^f H^T (HP^f H^T + R)^{-1},$$

$$A = E \left( I - \frac{1}{m} ll^T \right),$$

where  $E$  is the set of model states,  $x$  is the estimated state value,  $P$  is the state error covariance matrix,  $A$  is a singular matrix,  $A^T$  is the transposed matrix,  $P^f$  is the prediction of  $P$ ,  $m$  is the size of the set,  $K$  represents the Kalman gain matrix,  $H$  represents the observation matrix, and  $R$  represents the observation error covariance matrix.

In the practical application of EnKF, the problem of misleading correlation between spatial observation points and state points, as well as the problem of set nonfull rank, frequently arises, and localization analysis technology is given as a solution to the difficulties mentioned before.



The update equation in the local scope of the  $i$ -th state variable is

$$\begin{aligned} x_i^a &= x_i^f + K_i^l(y^l - H^l x_f^l), \\ A_i^a &= A_i^f(I + S^l S^{lT})^{-0.5}, \\ K_i^l &= \frac{A_i^f S^{lT}(I + S^l S^{lT})^{-1} R^{-0.5l}}{\sqrt{m-1}}, \\ S^l &= \frac{R^{0.5l} H^l A_i^f}{\sqrt{m-1}}. \end{aligned} \quad (2)$$

As is customary in the classical localization analysis procedure, the localization coefficient matrix is often constructed by considering the localized clipping function to be the localization function in the first place. The local clipping function is a piecewise rational function of fifth order that is related to the length scale parameter and changes as the distance between two points increases. It is based on fuzzy mathematics and imitates human thinking by using fuzzy sets, fuzzy relationships, and fuzzy reasoning to judge, synthesize, reason, and process problems that are difficult to solve using conventional methods. Fuzzy analysis theory is used to judge, synthesize, reason, and process problems that are difficult to solve using conventional methods. In the real data assimilation process, the observation error grows as a result of the false correlation in the physical distance between the observation point and the state update point. As a result, the assimilation effect becomes poor as a result of the increased observation error. As a result, this study provides a competitive evaluation model for the sports culture industry that is based on the fuzzy analysis algorithm and is based on the idea of fuzzy analysis.

First and foremost, it is important to construct a fuzzy logic controller in order to perform the assessment process. The database, rule base, fuzzy quantification, reasoning mechanism, and fuzzy discrimination are all components of a general fuzzy logic controller's composition frame, which contains the following: Each component contributes to the fuzzy control process in a unique way. First and foremost, the database serves as a storage bin for all subsets of all input and output fuzzy variables, as well as the membership value of all subsets of all input and output fuzzy variables. Second, the rule base contains a variety of rules in the form of preset language that can be used to infer fuzzy outcomes in the future. Input fuzzy variables that have been determined are quantified using a membership function, and the fuzzy inference process is finished with the help of a rule table that has been built. At the end of the day, fuzzy discrimination is

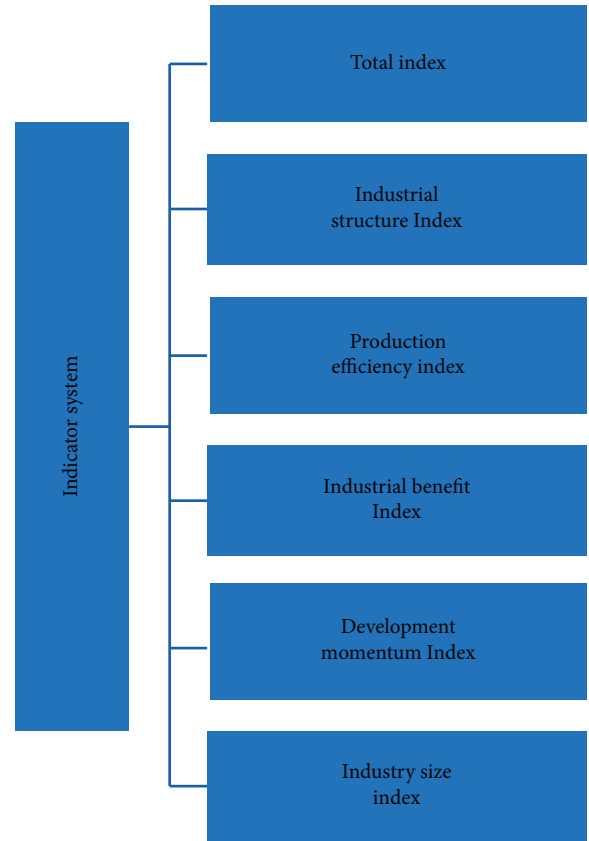


FIGURE 1: Index system.

primarily concerned with converting the inferred fuzzy subsets into accurate weight values that can then be used directly for data assimilation.

The Euclidean distance  $d$  between the observation position and the state update position is employed as the input fuzzy variable in this paper, and the equivalent weight coefficient  $w$  of the observation data is used as the output fuzzy control variable. As a second step, based on actual experience and system requirements, define the basic world and quantitative universe of each variable, in order to calculate the quantitative scale factor of input variable deviation and the scale factor of output control quantity. And the coordinate formula is

$$x = \sqrt{(o_i - v_i)^2 + (o_j - v_j)^2}. \quad (3)$$

The Gaussian membership function expressions for input and output are as follows:

$$d_i(x) = \begin{cases} e^{-x^2/2\sigma^2}, & 0 < x \leq 1, \\ e^{-(x-1.5)^2/2\sigma^2}, & 1 < x \leq 2, \\ \dots \\ e^{-(x-20)^2/2\sigma^2}, & 19 < x \leq 20, \end{cases} \quad d_i(x) = \begin{cases} e^{-(x-1)^2/2\sigma^2}, & 0 < x \leq 1, \\ e^{-(x-0.95)^2/2\sigma^2}, & 1 < x \leq 2, \\ \dots \\ e^{-x^2/2\sigma^2}, & 19 < x \leq 20. \end{cases} \quad (4)$$

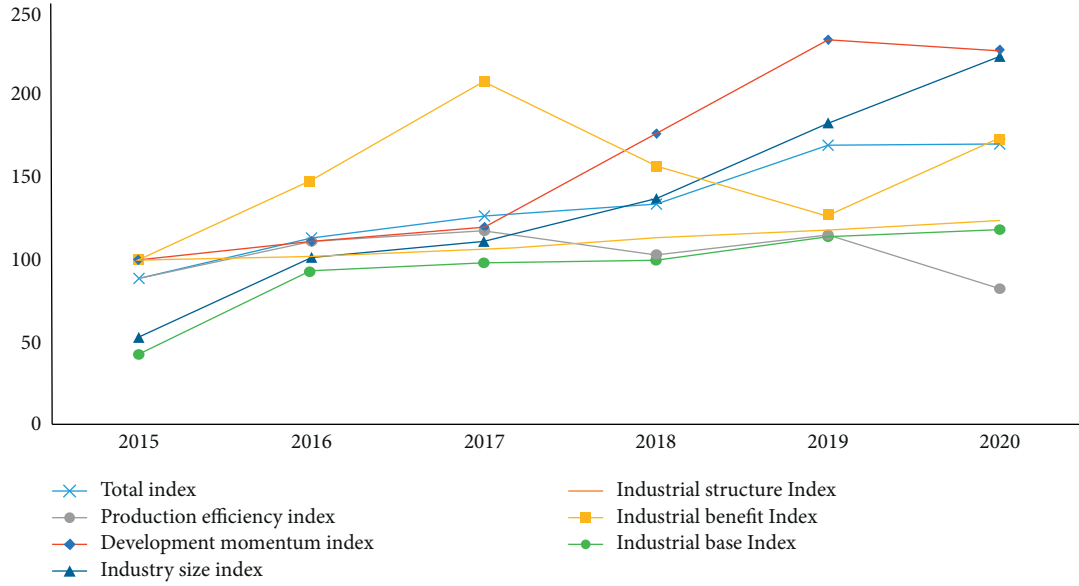


FIGURE 2: Various indicators of Shanghai sports culture industry.

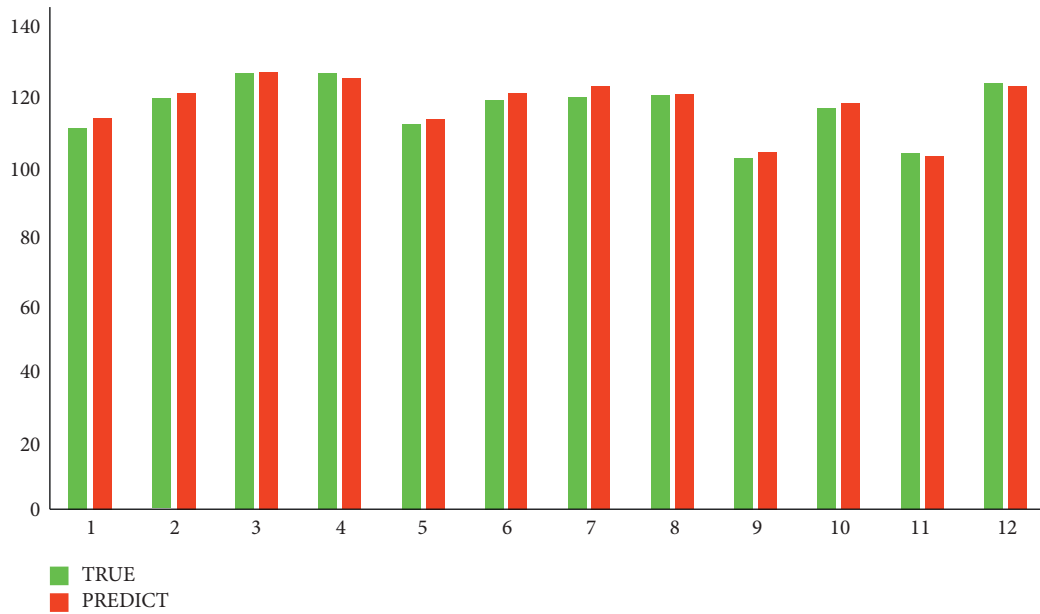


FIGURE 3: Evaluate algorithm prediction performance of our method.

The fuzzy relation matrix is as follows:

$$R = (d_1 \times w_1) \cup (d_2 \times w_2) \cup \dots (d_i \times w_i) \cup \dots (d_m \times w_m). \quad (5)$$

For fuzzy inference, we use the max-min principle as follows:

$$w = d \circ R = \frac{\int \bigvee_{x \in X} (\mu_d(x) \wedge \mu_R(x))}{x} \quad (6)$$

Finally, we perform fuzzy discrimination and data fusion to give the final score of the evaluation.

#### 4. Simulation Results

The sports culture industry in Beijing and Shanghai between 2015 and 2020 was chosen for index measurement and extensive evaluation in order to validate the viability of the created index system and the designed evaluation model in the real application.

First and foremost, this paper constructs an assessment index based on [14, 21, 26], which is depicted in Figure 1, and Figure 2 depicts the change in the law governing Shanghai's sports culture industry index between 2015 and 2020, using the city as an illustration. It can clearly be observed that the

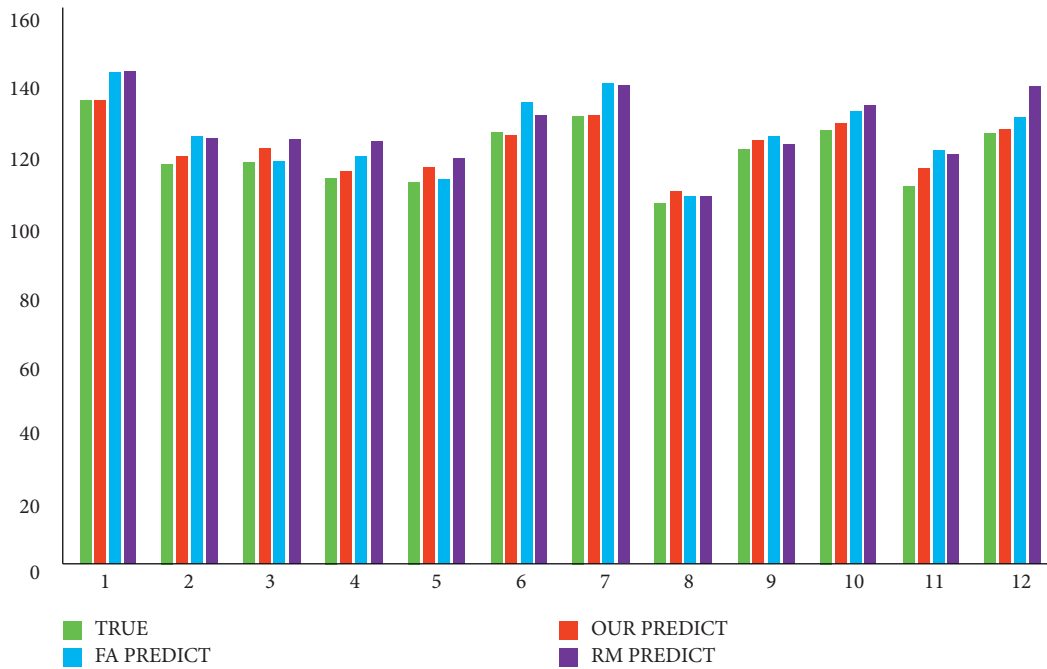


FIGURE 4: Evaluating algorithm prediction performance of OUR, FA, and RM.

competitiveness of Shanghai's sports culture industry as a whole is increasing in importance.

Additionally, the proposed fuzzy analysis technique is evaluated in this article. This research selects an existing expert data set from the cultural industry for use in training the model. The comparison between the output value of the evaluation algorithm in this research and the real value is depicted in Figure 3.

Last but not least, the algorithm developed in this paper is compared with the classic fuzzy analysis algorithm FA and the regression model RM, and the results of the comparison are depicted in Figure 4. As illustrated in Figure 4, the method described in this paper performs much better than the standard evaluation method.

## 5. Conclusion

This study provides a model for evaluating the competitiveness of the sports and cultural industries that are based on a fuzzy analysis algorithm, and it builds a seven-dimensional sports and cultural industry competitiveness evaluation index system that is based on previous research. The experimental data set in this study is drawn from the sports culture industry of representative cities in China, and the superiority of the algorithm suggested in this work is demonstrated by the results. In the future, we will continue to dig into the complexity of the evaluation factors of the competitiveness of the sports cultural industry and explore more effective indicators to evaluate the competitiveness of the sports cultural industry.

## Data Availability

The data used to support the findings of this study are available from the corresponding author upon request.

## Conflicts of Interest

The authors declare that they have no conflicts of interest.

## Acknowledgments

This study was supported by Supporting Fund for Teachers' Research of Jining Medical University, no. JYFC2019RW001.

## References

- [1] J.-H. Huang and K.-H. Peng, "Fuzzy Rasch model in TOPSIS: a new approach for generating fuzzy numbers to assess the competitiveness of the tourism industries in Asian countries," *Tourism Management*, vol. 33, no. 2, pp. 456–465, 2012.
- [2] D. K. Dewangan, R. Agrawal, and V. Sharma, "Enablers for competitiveness of Indian manufacturing sector: an ISM-fuzzy MICMAC analysis," *Procedia-Social and Behavioral Sciences*, vol. 189, pp. 416–432, 2015.
- [3] R. K. Singh and M. K. Sharma, "Selecting competitive supply chain using fuzzy AHP and extent analysis," *Journal of Industrial and Production Engineering*, vol. 31, no. 8, pp. 524–538, 2014.
- [4] M. K. Singh, H. Kumar, M. P. Gupta, and J. Madaan, "Competitiveness of Electronics manufacturing industry in India: an ISM-fuzzy MICMAC and AHP approach," *Measuring business excellence*, vol. 22, 2018.
- [5] C. Wu, X.-y. Zhang, I.-C. Yeh, F.-y. Chen, J. Bender, and T.-n. Wang, "Evaluating competitiveness using fuzzy analytic hierarchy process-A case study of Chinese airlines," *Journal of Advanced Transportation*, vol. 47, no. 7, pp. 619–634, 2013.
- [6] A. Calabrese, R. Costa, and T. Menichini, "Using Fuzzy AHP to manage Intellectual Capital assets: an application to the ICT service industry," *Expert Systems with Applications*, vol. 40, no. 9, pp. 3747–3755, 2013.

- [7] B. Zhalezka and K. Navitskaya, "Multy-criteria fuzzy analysis of regional development," *ECONTECHMOD: An International Quarterly Journal on Economics of Technology and Modelling Processes*, vol. 4, 2015.
- [8] I. Đalić, J. Ateljević, Ž. Stević, and S. Terzić, "An integrated swot-fuzzy piprecia model for analysis of competitiveness in order to improve logistics performances," *Facta Universitatis – Series: Mechanical Engineering*, vol. 18, no. 3, pp. 439–451, 2020.
- [9] D. Huo, Y. Chen, K. Hung, Z. Song, J. Guan, and A. Ji, "Diamond model and the export competitiveness of the agriculture industry from emerging markets: an exploratory vision based on a spatial effect study using a genetic algorithm," *Economic Research-Ekonomska Istraživanja*, vol. 33, no. 1, pp. 2427–2443, 2020.
- [10] Ö. Kabak, F. Ülengin, B. Çekyay, Ş. Önsel, and Ö. Özaydın, "Critical success factors for the iron and steel industry in Turkey: a fuzzy DEMATEL approach," *International Journal of Fuzzy Systems*, vol. 18, no. 3, pp. 523–536, 2016.
- [11] S. Ulubeyli, "Industry-wide competitiveness assessment through fuzzy synthetic evaluation: the case of cement industry," *Journal of Business Economics and Management*, vol. 18, no. 1, pp. 35–53, 2017.
- [12] J. Vaziri and M. A. Beheshtinia, "A holistic fuzzy approach to create competitive advantage via quality management in services industry (case study: life-insurance services)," *Management Decision*, vol. 54, 2016.
- [13] G. Tanriverdi and Ş. Lezki, "Istanbul Airport (IGA) and quest of best competitive strategy for air cargo carriers in new competition environment: a fuzzy multi-criteria approach," *Journal of Air Transport Management*, vol. 95, Article ID 102088, 2021.
- [14] S.-J. Hung, "Activity-based divergent supply chain planning for competitive advantage in the risky global environment: a DEMATEL-ANP fuzzy goal programming approach," *Expert Systems with Applications*, vol. 38, no. 8, pp. 9053–9062, 2011.
- [15] A. Sutoni, "Determination of regional main products with fuzzy logic approach in regional Sula Island of North Maluku Province," in *Proceedings of the 2018 International Conference on Digital Arts, Media and Technology (ICDAMT)*, pp. 18–22, Phayao, Thailand, February 2018.
- [16] Ö. Öz, "Using Boolean-and fuzzy-logic-based methods to analyze multiple case study evidence in management research," *Journal of Management Inquiry*, vol. 13, no. 2, pp. 166–179, 2004.
- [17] H. Nozari, E. Najafi, M. Fallah, and F. H. Lotfi, "Quantitative analysis of key performance indicators of green supply chain in FMCG industries using non-linear fuzzy method," *Mathematics*, vol. 7, no. 11, p. 1020, 2019.
- [18] C. Khompatraporn and T. Somboonwivat, "Causal factor relations of supply chain competitiveness via fuzzy DEMATEL method for Thai automotive industry," *Production Planning & Control*, vol. 28, no. 6–8, pp. 538–551, 2017.
- [19] H. P. Fu, Y. C. Ho, R. C. Y. Chen, T. H. Chang, and P. H. Chien, "Factors affecting the adoption of electronic marketplaces: a fuzzy AHP analysis," *International Journal of Operations & Production Management*, vol. 26, 2006.
- [20] C.-W. Ou, S.-Y. Chou, and Y.-H. Chang, "Using a strategy-aligned fuzzy competitive analysis approach for market segment evaluation and selection," *Expert Systems with Applications*, vol. 36, no. 1, pp. 527–541, 2009.
- [21] J. H. Cheng, C. M. Lee, and C. H. Tang, "An application of fuzzy Delphi and fuzzy AHP on evaluating wafer supplier in semiconductor industry," *WSEAS Transactions on Information Science and Applications*, vol. 6, no. 5, pp. 756–767, 2009.
- [22] L. Jiang, T. Zhang, and Y. Feng, "Identifying the critical factors of sustainable manufacturing using the fuzzy DEMATEL method," *Applied Mathematics and Nonlinear Sciences*, vol. 5, no. 2, pp. 391–404, 2020.
- [23] A. Ortiz de Guinea and L. Raymond, "Enabling innovation in the face of uncertainty through IT ambidexterity: a fuzzy set qualitative comparative analysis of industrial service SMEs," *International Journal of Information Management*, vol. 50, pp. 244–260, 2020.
- [24] C. Kao and S. T. Liu, "Competitiveness of manufacturing firms: an application of fuzzy weighted average," *IEEE Transactions on Systems, Man, and Cybernetics-Part A: Systems and Humans*, vol. 29, no. 6, pp. 661–667, 1999.
- [25] M. K. Hossain and V. Thakur, "Benchmarking health-care supply chain by implementing Industry 4.0: a fuzzy-AHP-DEMATEL approach," *Benchmarking: An International Journal*, vol. 5, 2020.
- [26] J. C. Liu, Y. Li, and J. L. Liu, "Fuzzy comprehensive appraisal of China's offshore wind industry competitiveness based on SWOT," *Advanced Materials Research*, vol. 724-725, pp. 561–567, 2013.
- [27] A. Zangouinezhad, A. Azar, and A. Kazazi, "Using SCOR model with fuzzy MCDM approach to assess competitiveness positioning of supply chains: focus on shipbuilding supply chains," *Maritime Policy & Management*, vol. 38, no. 1, pp. 93–109, 2011.
- [28] J. Stejskal and P. Hajek, "Modelling collaboration and innovation in creative industries using fuzzy set qualitative comparative analysis," *The Journal of Technology Transfer*, vol. 44, no. 3, pp. 981–1006, 2019.
- [29] M. Nilashi, S. Samad, A. A. Manaf et al., "Factors influencing medical tourism adoption in Malaysia: a DEMATEL-Fuzzy TOPSIS approach," *Computers & Industrial Engineering*, vol. 137, Article ID 106005, 2019.
- [30] J. Li, C.-H. Wu, C.-W. Chen, Y.-F. Huang, and C.-T. Lin, "Apply fuzzy DEMATEL to explore the decisive factors of the auto lighting aftermarket industry in Taiwan," *Mathematics*, vol. 8, no. 7, p. 1187, 2020.
- [31] G. Büyüközkan, C. A. Havle, and O. Feyzioğlu, "An integrated SWOT based fuzzy AHP and fuzzy MARCOS methodology for digital transformation strategy analysis in airline industry," *Journal of Air Transport Management*, vol. 97, Article ID 102142, 2021.
- [32] A. B. Naeini, A. Mosayebi, and N. Mohajerani, "A hybrid model of competitive advantage based on Bourdieu capital theory and competitive intelligence using fuzzy Delphi and ism-gray Dematel (study of Iranian food industry)," *International Review*, vol. 3, no. 1-2, pp. 21–35, 2019.

## Research Article

# A Multiobjective Allocation Method for High-Quality Higher Education Resources Based on Cellular Genetic Algorithm

Tianshu He 

*Tonghua Normal University, Tonghua, Jilin 134002, China*

Correspondence should be addressed to Tianshu He; [tians\\_h@thnu.edu.cn](mailto:tians_h@thnu.edu.cn)

Received 1 March 2022; Revised 22 March 2022; Accepted 30 March 2022; Published 18 April 2022

Academic Editor: Punit Gupta

Copyright © 2022 Tianshu He. This is an open access article distributed under the Creative Commons Attribution License, which permits unrestricted use, distribution, and reproduction in any medium, provided the original work is properly cited.

Optimizing the allocation of higher education resources and improving the utilization efficiency of educational resources are of great significance to further promoting the balanced development of higher education quality. In order to rationalize and maximize the efficiency of the allocation of innovation and entrepreneurship education resources in colleges and universities and build an evaluation index system for the input and output of educational resources, this paper proposes to use the improved cytogenetic algorithm educational resources for resource allocation and utilization. The adaptive constraint processing technology is combined with the cytogenetic algorithm to avoid the algorithm falling into local optimum. Our method has achieved good results on high-dimensional functions. The utilization efficiency and allocation efficiency of innovation and entrepreneurship education resources in colleges and universities have increased by 21.33% and 18.92%, respectively, and tend to be in a balanced state, which can optimize the allocation of educational resources.

## 1. Introduction

While higher education has grown significantly in China throughout the 13th Five-Year Plan period, with the gross enrollment rate of higher education increasing from 42.7 percent in 2016 to 54.4 percent in 2020, higher education has reached the stage of universalization in its entirety. General Secretary Xi Jinping stated that the demand for higher education, as well as the need for scientific knowledge and great skills, is more pressing than ever before for the growth of the Party and the country [1–4]. It is a major concern of the Party and the state that higher education develops in a high-quality manner, as this will undoubtedly necessitate and attract more resources to invest. Improving the efficiency of resource allocation is a concrete manifestation of the modernization of higher education governance as well as an important means of achieving the modernization of higher education governance. The establishment of a performance evaluation mechanism for higher education is an essential step toward furthering the reform of higher education, according to the Ministry of Education's 13th Five-Year Plan for Scientific and Technical Development of

Higher Education, which was issued in 2016 [5, 6]. Promotion of first-class construction of our universities should be based on performance, according to the plan. Performance should be used as a lever to coordinate the overall construction of universities as well as the construction of individual disciplines [7]. In this context, the development of a comprehensive index system for evaluating the efficiency of higher education resource allocation, the scientific and precise implementation of the evaluation of resource allocation efficiency, and the formation of a data-driven education resource allocation orientation are all of great theoretical and practical importance in order to further promote a more reasonable and efficient allocation of higher education resources [8–12].

The input and output of education resources are the primary focus of research on the efficiency of resource allocation in education [13]. In order to increase the efficiency with which colleges and universities are run, it is necessary to optimize education resource allocation. The input direction and quantity of education resources are modified and optimized under the guidance of college and university development and discipline construction in order to achieve

this [14, 15]. One of the most important factors in the development of high-quality higher education, the attainment of educational justice, and the improvement of public perceptions about higher education is making the most efficient use of educational resources. As the fact that China places a high value on innovation and entrepreneurship education in colleges and universities and that the total amount of educational resources invested in this area continues to grow year after year, there are still issues to be addressed, such as a lack of adequate investment in resources, unequal allocation, and inefficient utilization, in order to promote an innovation-driven development strategy and alleviate employment pressure [16–20]. The subject of how to rationalize and maximize the efficiency of resource allocation for innovation and entrepreneurship education in colleges and universities has so piqued the interest of people from all walks of life, who have been debating it for quite some time [17, 18].

At the moment, data envelopment analysis is most commonly employed in the evaluation of resource allocation efficiency in many types of schools, and it is widely utilized because of its low preconditions and ease of operation. It is frequently used because of its low preconditions and ease of operation [19, 20]. From the perspectives of policy changes, influencing factors, double-class construction, regional economy, and technical support, domestic researchers have conducted theoretical and empirical studies on the connotation of educational resources and their characteristics, as well as the problems associated with optimal resource allocation. They have also proposed corresponding recommendations for optimal resource allocation. In-depth examination of existing research findings reveals that the majority of the research content is concerned with broad educational resource allocation, with little attention being paid to the allocation of educational resources in colleges and universities, as well as other factors [21–26]. On the one hand, research objects such as universities directly under the Ministry of Education, double first-class universities, and higher vocational institutions receive the majority of attention; on the other hand, research dimensions such as production efficiency, loss efficiency, and allocation efficiency receive the least attention; and on the third hand, studies on ordinary local universities and universities in single provinces receive the least attention. The researchers' primary focus in terms of research methodologies is linear programming methods that use data envelopment analysis to develop CCR-BCC models and evolutionary algorithms that employ genetic algorithm for research [27].

There have been a number of early stage studies undertaken by foreign researchers that have yielded extensive findings in the evaluation of resource allocation efficiency at various levels and types of education [28]. They have then applied their findings in a wide range of practices to improve the overall quality of higher education, including allocation of education funds. The overall efficiency of 45 colleges and universities in the United Kingdom was evaluated using the DEA approach, and the system's rationality for evaluating the efficiency of college operation was confirmed by certain scholars using the method. Several additional researchers

used the DEA approach to analyze the relative efficiency of 45 Canadian universities, and they discovered that the majority of them had high efficiency scores, which is regarded to be a novel way to comprehend the efficiency of Canadian higher education institutions. Based on multiple input-output indicator systems, literature [22] discovered that Australian universities have relatively good operational efficiency compared with other institutions around the world [29–35].

The following recommendations are made in response to the problems identified in the preceding study: develop an education resource input and output evaluation index system, propose a multiobjective function model to improve the efficiency of education resource utilization and allocation, and propose the optimal solution for resource allocation in the multiobjective function model sphere of education resource utilization efficiency and allocation efficiency to achieve the optimization of education resources [36–40].

## 2. Education Resource Allocation Optimization and Algorithm Design

*2.1. Construction of Education Resource Evaluation Index System.* Education efficiency is one of the metrics used to assess the success of a school's educational program. The optimal allocation of educational resources involves determining how to reasonably allocate the limited resources of colleges and universities in order to achieve the educational efficiency of producing the greatest amount of educational output with the least amount of input per unit of time. The education system is a complicated system with a large number of different inputs and various outputs, making it difficult to quantify and measure the link between the inputs and outputs. As a result, in order to improve the efficiency of education while also optimizing resource allocation, it is important to first develop the education resource index system as well as a multiobjective optimization mathematical model.

It is necessary to choose indicators from two dimensions of resource input and output before constructing the education resource input and output index system. The education resource input and output index system is built around two problems: whether the above evaluation index system can completely support the above evaluation index system and whether the above evaluation index system can completely support the above evaluation index system. Education resources input and output index system is shown in Table 1.

In the index system of education, we can see that there are two primary indicators of educational resources input and output, six secondary indicators such as human resources and physical resources, and twelve tertiary indicators such as the number of full-time and part-time teachers and administrative teachers in Table 1.

*2.2. Multiobjective Optimization Analysis and Model Construction.* The following two objectives are given in order to maximize the allocation of resources:

TABLE 1: Education resources input and output index system.

		Tertiary measurement indicators
Education resource input indicators	Human resources	Number of full-time and part-time instructors
		Number of administrative faculty
	Physical resources	Number of off-campus faculty with corporate background
		Total value of teaching instruments and equipment/million yuan
Financial resources	Area of practice platform room/sqm	
	Area of educational base/m <sup>2</sup>	
Education resource output sub-table	Talent cultivation	Special funding investment/million yuan
		Number of educated students
	Scientific research	Number of enterprises established by students/pc
		Number of prizes won in academic competitions at or above provincial level/item
Social service	Total number of academic papers, publications, and subjects/item	
	Production value of scientific and technological achievements/million yuan	

- (1) In order to increase the efficiency with which resources are utilized, that is, to organize limited resources in such a way that the maximal educational product is brought into play.
- (2) To increase the efficiency with resources, that is, to maximize the ratio of educational resources to input resources while also taking into account the complexity and specificity of each resource as well as the degree to which it influences educational outcomes, in order to ensure that each resource is effectively allocated to the most adapted aspect of the curriculum.

First and foremost, this article investigates ways to increase the efficiency with which resources are utilized in the context of education.

Several factors influence the allocation of education resources in colleges and universities, and their allocation problems are classified as nonlinear allocation problems. The ultimate goal is to maximize educational outcomes, and the efficiency of resources utilization is defined as the ratio of educational output to educational input.

$$U = \frac{\sum_{j=1}^m u_j o_j}{\sum_{i=1}^n \sigma_j i_j} \quad (1)$$

in which  $i$  and  $j$  represent the elements of educational resources and educational achievement, respectively,  $o_j$  and  $i_j$  are the output and input of educational resources, respectively, and  $u_j$  and  $\sigma_j$  are the weights of the input and output indicators. With a higher value  $U$ , there is a higher input-output ratio, and with a better utilization efficiency of educational resources, there is a more acceptable combination of educational production variables.

According to the resources input of colleges and universities, the education resources output index system is constructed in order to construct seven resources allocation efficiency indexes, including the teacher-student ratio, the average number of administrative teachers, the average number of off-campus teachers with enterprise background, the average value of teaching instruments and equipment, and the average value of teaching instruments and

equipment, among others. The following is an expression of the objective function of the  $K$ th university's resource allocation for educational purposes:

$$A_{ki} = \frac{x_k + \Delta x_k}{s_k} \quad (k = 1, 2, \dots, K)$$

$$s.t. \quad A_{ki} \leq 1 \quad (i = 1, 4)$$

$$0 \leq A_{ki} \leq 1 \quad (i = 2, 3)$$

$$A_{ki} > 1 \quad (i = 5, 6, 7),$$
(2)

in which  $s_k$  is the number of students in the  $k$ th university,  $x_k$  and  $\Delta x_k$  denote the average value of each resource element in the  $k$ th university, and  $\Delta x_k$  denotes the change of each resource element in the  $k$ th university.

Considering the objective function of (1) and (2) together, we get the multiobjective optimization function, which is as follows:

$$\max U_k = \frac{\sum_{j=1}^m u_j o_j}{\sum_{i=1}^n \sigma_j i_j},$$

$$\max F_k = \sum_{i=1}^n \sigma_j A_{k,i},$$
(3)

in which  $\max U_k$  is the maximum value that should be sought for each university's educational resource utilization efficiency, and maximum educational resource allocation efficiency  $\max U_k$  is the maximum value that should be sought for each university's educational resource allocation efficiency.

The degree of influence of resource input index  $I_1, I_2, \dots, I_7$  and output index  $O_1, O_2, \dots, O_5$  on education is different; therefore, it is necessary to calculate the weights of each factor by the full weight method, and based on the calculation results, expert opinions are solicited on the rationality and validity of the evaluation index weights by using Delphi method, and after two rounds of solicitation, feedback, and revision of the closed-loop process, the final weights of resource input and education resource output

indexes are obtained, as shown in Tables 2 and 3, respectively.

**2.3. Cellular Genetic Algorithm.** A minimization optimization problem with equation constraints and inequality constraints can be represented mathematically in the following way, without sacrificing generality or efficiency:

$$\begin{aligned} \min f(x), x &= (x_1, x_2, \dots, x_n) \\ \text{s.t. } g_i(x) &\leq 0, \quad i = 1, 2, \dots, q \\ h_j(x) &= 0, \quad j = 1, 2, \dots, m, \end{aligned} \quad (4)$$

in which  $f(x)$  is the objective function,  $g_i(x)$  is the  $i$ -th inequality constraint, and the  $j$ -th equation constraint is  $h_j(x)$ .

As indicated in the example of equation constraints, the general strategy is to change the equation constraints into inequality constraints by assigning a very tiny constraint tolerance to the equation constraints, as illustrated in the following example:

$$\begin{cases} h_j(x) \leq \delta \\ -h_j(x) \leq \delta' \end{cases} \quad (5)$$

in which  $\delta$  is the tolerance of the equation constraint, which is typically represented by the value 0.0001 in most cases.

The notion of constraint violation degree is proposed in order to more correctly express the distance between people in a population and the feasible domain; the greater the value of this concept is, the further the individual is from the feasible domain. The expression formula for the degree of constraint violation is presented as follows:

$$\psi(x) = \sum_{i=1}^p \max(0, g_i(x)) + \sum_{l=1}^q \max(0, |h_l(x)| - \delta). \quad (6)$$

The  $\varepsilon$  comparison criterion, which is made of the three criteria listed below, is used to compare feasible individuals with infeasible individuals. For example, to obtain the minimal value, the following three criteria are used:

- (1) Smaller goal function value is selected when both individuals are practicable.
- (2) In the event that both individuals are infeasible, the smaller constraint violation is chosen.
- (3) The feasible individual is selected if the constraint violation degree of one of the infeasible individuals is less than or equal to; otherwise, the feasible individual is selected if the constraint violation degree of one of the infeasible individuals is more than or equal to.

The following is the  $\varepsilon$  setting formula:

$$\varepsilon(\text{gen}) = \begin{cases} \frac{\varepsilon(\text{gen} - 1)}{1.035}, & \varepsilon > 10^{-6} \\ 0, & \varepsilon < 10^{-6} \end{cases}, \quad (7)$$

where gen is the evolutionary algebra  $\varepsilon(0) = 1$ .

The drawback of the method is the low convergence accuracy and lack of diversity for complex constrained problems.

An algorithm of high quality that was developed by merging cellular automata and genetic algorithms is the cellular genetic algorithm (also known as the cellular genetic algorithm). Its fundamental principle is to distribute the population randomly in a two-dimensional topology, which restricts the competition and hybridization behavior of individuals to a local range, thereby ensuring the diversity of the population and preventing it from falling into local optimal solutions too quickly. The genetic operation of the universal cellular genetic algorithm is illustrated in Figure 1.

When dealing with limited optimization issues, the differential evolution algorithm is one of the most effective techniques available. It primarily makes use of the distance between persons as well as the directional distance while performing direct search on a population of people.

Here are three general differential evolution algorithms with their respective variation techniques represented.

$$\frac{\text{DE}}{\text{rand}/1}$$

$$V_{i,j}^t = X_{i,j}^t + F(V_{r_1,j}^t - V_{r_2,j}^t),$$

$$\text{DE}/\text{best}/1$$

$$V_{i,j}^t = X_{\text{best},j}^t + F(V_{r_1,j}^t - V_{r_2,j}^t),$$

(8)

$$\frac{\text{DE}}{\text{current} - \text{to} - \text{best}/1}$$

$$V_{i,j}^t = X_{i,j}^t + F(V_{\text{best},j}^t - V_{i,j}^t) + F(V_{r_1,j}^t - V_{r_2,j}^t),$$

in which  $F$  represents the scaling factor and  $i, r_1$ , and  $r_2$  represent random integers in  $[1, NP]$  and are not equal. The variation of RAND has good global search ability and can effectively maintain the diversity of the population, the variation of BEST takes the better individuals in the current population as the base vector and has good convergence ability, the variation of CURRENT – TO – BEST has good balance for the maintenance of population diversity, and the current-to-best variation has a good balance between the maintenance of population diversity and the enhancement of population convergence.

It is proposed that, in order to improve upon the shortcomings of the standard comparison criterion, the revised standard comparison criterion 10 published in the literature 10 and the  $\varepsilon$  adaptive adjustment method be used. The judgment criterion is as follows:

- (1) Lower goal function value is selected when both individuals are practicable.
- (2) The option can be separated into two categories when one person is a feasible individual and the other is an infeasible individual. It is preferable to choose the infeasible individual whose constraint violation degree is less than; alternatively it is



TABLE 2: Weight of education input resources indicators.

		Tertiary measurement indicators	Weight
Education resource input indicators	Human resources	Number of full-time and part-time instructors	0.18
		Number of administrative faculty	0.06
		Number of off-campus faculty with corporate background	0.09
	Physical resources	Total value of teaching instruments and equipment/million yuan	0.15
		Area of practice platform room/sqm	0.16
		Area of educational base/m <sup>2</sup>	0.12
	Financial resources	Special funding investment/million yuan	0.24

TABLE 3: Weight of education output resources indicators.

		Tertiary measurement indicators	Weight
Education resource output sub-table	Talent cultivation	Number of educated students	0.17
		Number of enterprises established by students/pc	0.21
		Number of prizes won in academic competitions at or above provincial level/item	0.22
	Scientific research	Total number of academic papers, publications, and subjects/item	0.15
	Social service	Production value of scientific and technological achievements/million yuan	0.25

preferable to choose the feasible individual whose objective function value is less than.

- (3) The individual whose objective function value is the smallest chosen in cases when both individuals are

infeasible individuals and if both individuals have a constraint violation degree less than  $s$ .

The adaptive equation is as follows:

$$\varepsilon(t) = \begin{cases} \varepsilon(0) \times e^{-a \times (t/Te)}, & t \leq Te \\ 0, & t > Te \end{cases}, \varepsilon(0) = 0.6 \times \sum_{i=1}^N \frac{G(X_i)}{N}, \quad N = 1, 2, \dots, N, \quad (9)$$

where  $Te$  represents the truncated evolutionary algebra, which can be used to adjust the size of  $\varepsilon(t)$ , where  $a = a_{\min} + T \times (a_{\max} - a_{\min})$ , and  $T$  represents the proportion of viable individuals in the population.  $Te$  is generally set to 1000 when the evolutionary algebra is 1000, and this value will also be used in this paper.

### 3. Experiment Result

In conjunction with the resources index system, a multi-objective function is used, in which each particle represents a configuration scheme, the individual optimal solution  $y$  represents the optimal configuration scheme sought by each particle, and the population optimal solution  $g$  represents the optimal configuration scheme sought by all particles.

A machine with the following hardware configuration is used to conduct all of the experiments in this paper. Matlab2018 was used to construct the majority of the software, which was run on an Inter Core processor with an i9-10850K, 64 GB of RAM, and a 3.4 GHz main clock.

On the simulation software, the simulation operation is carried out by integrating the multiobjective optimization objective function and the restrictions of the resource configuration. Iteration diagrams of algorithms are represented in Figure 2 following implementation of the algorithm as shown in the previous section.

As can be seen from Figure 2, the optimization method proposed in this paper is more in line with the actual situation. It can be seen from the experimental results that the model improves the efficiency of resource utilization. Figure 3 shows a graph of how efficiently each university used its resources before and after the experiment.

In Figure 3, it is clear that this is the case. The resource utilization efficiency of all colleges and universities has improved, with an average gain of 16.37 percent between before and after the experiment, and the resource utilization efficiency of all colleges and universities is trending toward a more balanced state. Compared with their respective baselines, the resource utilization efficiency of colleges C1, C3, and C11 with lower resource utilization efficiency improved significantly, rising from 0.705, 0.985, and 0.755

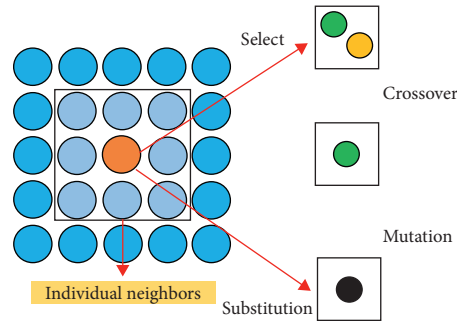


FIGURE 1: The structure of cellular genetic.

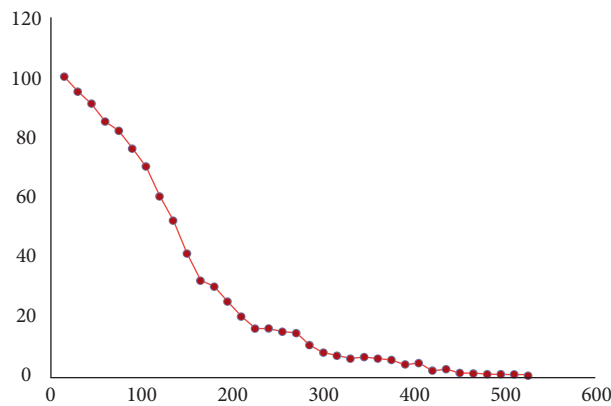


FIGURE 2: Iteration chart.

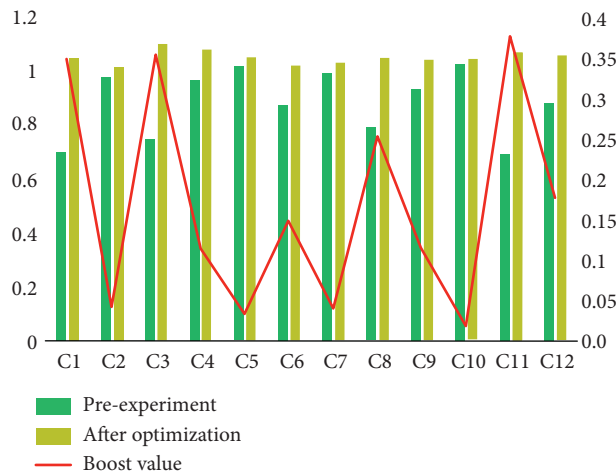


FIGURE 3: Resource utilization efficiency of each university before and after the experiment.

before optimization to 1.055, 1.025, and 1.078 after optimization.

According to Figure 4, the original data of each university, as well as the optimized allocation scheme, are substituted into (3) to calculate the overall resource allocation efficiency of each university before and after optimization, respectively. This is done to determine whether the model improves the resource allocation efficiency.

Figure 4 shows that the difference in resource allocation efficiency between universities prior to the experiment is significant, with a minimum value of 0.127 and a maximum value of 0.32 for the minimum and maximum values, respectively. Following the optimization, the allocation efficiency is 0.188, with an average increase of 42.99 percent, indicating that the optimization of education resource allocation may be achieved by altering the amount and

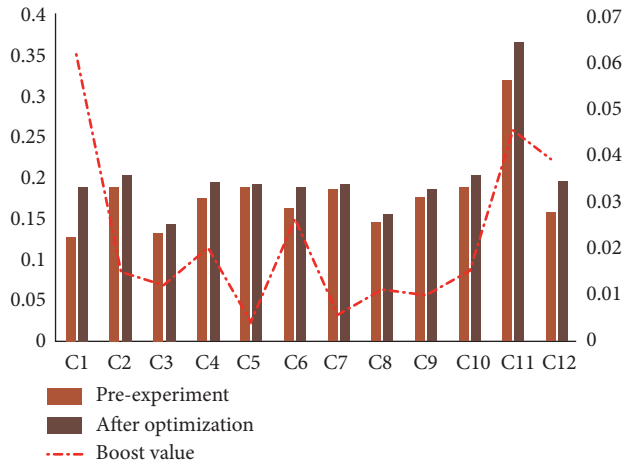


FIGURE 4: Resource utilization efficiency of each university before and after the experiment.

structure of education resources, as demonstrated by the results.

It can be seen from Figure 4 that the optimized educational resource allocation is more reasonable, and its application effect is closer to the actual demand.

#### 4. Conclusion

The optimal allocation of educational resources in colleges and universities is not only related to the development of colleges and universities and the cultivation of regional talents but also related to the improvement of the overall level of national higher education and the scientific utilization of national higher education resources. In order to maximize the allocation of educational resources in colleges and universities, a multiobjective allocation method of high-quality higher education resources based on cytogenetic algorithm is proposed. Schools and universities vary greatly in the allocation of various resources, and there is no clear standard. After optimization, the utilization efficiency and allocation efficiency of educational resources in colleges and universities increased by an average of 21.33% and 18.92%, respectively. In the future research, how to optimize the allocation of educational resources in real time according to the dynamic changes of the external environment has become one of the focuses of the research, which is also a problem that needs to be paid attention to in the future research of this paper.

#### Data Availability

The data used to support the findings of this study are available from the corresponding author upon request.

#### Conflicts of Interest

The author declares that he has no conflicts of interest.

#### References

- [1] M. H. Afshar and R. Hajiabadi, "A novel parallel cellular automata algorithm for multi-objective reservoir operation optimization," *Water Resources Management*, vol. 32, no. 2, pp. 785–803, 2018.
- [2] R. Devarajan, S. C. Jha, U. Phuyal, and V. K. Bhargava, "Energy-aware resource allocation for cooperative cellular network using multi-objective optimization approach," *IEEE Transactions on Wireless Communications*, vol. 11, no. 5, pp. 1797–1807, 2012.
- [3] Q. Liu, R. Mo, X. Xu, and X. Ma, "Multi-objective resource allocation in mobile edge computing using paes for internet of things," *Wireless networks*, pp. 1–13, 2020.
- [4] J. Fan and D. Feng, "Design of cellular manufacturing system with quasi-dynamic dual resource using multi-objective GA," *International Journal of Production Research*, vol. 51, no. 14, pp. 4134–4154, 2013.
- [5] Q. Peng, M. Zhou, Q. He, Y. Xia, C. Wu, and S. Deng, "Multi-objective optimization for location prediction of mobile devices in sensor-based applications," *IEEE Access*, vol. 6, pp. 77123–77132, 2018.
- [6] Y. Hao, Q. Ni, H. Li, and S. Hou, "Robust multi-objective optimization for EE-SE tradeoff in D2D communications underlying heterogeneous networks," *IEEE Transactions on Communications*, vol. 66, no. 10, pp. 4936–4949, 2018.
- [7] Z. Sun, Y. Zhang, Y. Nie, W. Wei, J. Lloret, and H. Song, "CASMO: a novel complex alliance strategy with multi-objective optimization of coverage in wireless sensor networks," *Wireless Networks*, vol. 23, no. 4, pp. 1201–1222, 2017.
- [8] Y. Wang, Y. Wu, F. Zhou, Z. Chu, Y. Wu, and F. Yuan, "Multi-objective resource allocation in a NOMA cognitive radio network with a practical non-linear energy harvesting model," *IEEE Access*, vol. 6, pp. 12973–12982, 2017.
- [9] H. Wu, "Multi-objective decision-making for mobile cloud offloading: a survey," *IEEE Access*, vol. 6, pp. 3962–3976, 2018.
- [10] X. Hao, N. Yao, L. Wang, and J. Wang, "Joint resource allocation algorithm based on multi-objective optimization for wireless sensor networks," *Applied Soft Computing*, vol. 94, p. 106470, 2020.
- [11] Z. Fei, B. Li, S. Yang, C. Xing, H. Chen, and L. Hanzo, "A survey of multi-objective optimization in wireless sensor networks: metrics, algorithms, and open problems," *IEEE Communications Surveys & Tutorials*, vol. 19, no. 1, pp. 550–586, 2016.
- [12] Y. Sun, D. W. K. Ng, J. Zhu, and R. Schober, "Multi-objective optimization for robust power efficient and secure full-duplex wireless communication systems," *IEEE Transactions on Wireless Communications*, vol. 15, no. 8, pp. 5511–5526, 2016.
- [13] A. I. Aravanis, M. R. B. Shankar, P.-D. Arapoglou, G. Danoy, P. G. Cottis, and B. Ottersten, "Power allocation in multibeam satellite systems: a two-stage multi-objective optimization," *IEEE Transactions on Wireless Communications*, vol. 14, no. 6, pp. 3171–3182, 2015.
- [14] Y. Sun, D. W. K. Ng, and R. Schober, "Multi-objective optimization for power efficient full-duplex wireless communication systems," in *Proceedings of the 2015 IEEE Global Communications Conference (GLOBECOM)*, pp. 1–6, IEEE, San Diego, CA, USA, December 2015.
- [15] L. Liu, Q. Fan, and R. Buyya, "A deadline-constrained multi-objective task scheduling algorithm in mobile cloud environments," *IEEE Access*, vol. 6, pp. 52982–52996, 2018.
- [16] A. Starkey, H. Hagra, S. Shakya, and G. Owusu, "A multi-objective genetic type-2 fuzzy logic based system for mobile

- field workforce area optimization,” *Information Sciences*, vol. 329, pp. 390–411, 2016.
- [17] Y. Sun, F. Lin, and H. Xu, “Multi-objective optimization of resource scheduling in fog computing using an improved NSGA-II,” *Wireless Personal Communications*, vol. 102, no. 2, pp. 1369–1385, 2018.
- [18] E. Ahmed, S. Khan, I. Yaqoob, A. Gani, and F. Salim, “Multi-objective optimization model for seamless application execution in mobile cloud computing,” in *Proceedings of the 2013 5th International Conference on Information and Communication Technologies*, pp. 1–6, IEEE, Karachi, Pakistan, December 2013.
- [19] H. Ali, W. Shahzad, and F. A. Khan, “Energy-efficient clustering in mobile ad-hoc networks using multi-objective particle swarm optimization,” *Applied Soft Computing*, vol. 12, no. 7, pp. 1913–1928, 2012.
- [20] N. Gunantara and G. Hendranto, “Multi-objective cross-layer optimization for selection of cooperative path pairs in multihop wireless ad hoc networks,” *Journal of Communications Software and Systems*, vol. 9, no. 3, pp. 170–177, 2013.
- [21] C. Oxendine, M. Sonwalkar, and N. Waters, “A multi-objective, multi-criteria approach to improve situational awareness in emergency evacuation routing using mobile phone data,” *Transactions in GIS*, vol. 16, no. 3, pp. 375–396, 2012.
- [22] H. Dai, H. Zhang, B. Wang, and L. Yang, “The multi-objective deployment optimization of UAV-mounted cache-enabled base stations,” *Physical Communication*, vol. 34, pp. 114–120, 2019.
- [23] X. Hu, Y. Zhang, X. Liao, Z. Liu, W. Wang, and F. M. Ghannouchi, “Dynamic beam hopping method based on multi-objective deep reinforcement learning for next generation satellite broadband systems,” *IEEE Transactions on Broadcasting*, vol. 66, no. 3, pp. 630–646, 2020.
- [24] A. Rachedi and A. Benslimane, “Multi-objective optimization for security and qos adaptation in wireless sensor networks,” in *Proceedings of the 2016 IEEE International Conference on Communications (ICC)*, pp. 1–7, IEEE, Kuala Lumpur, Malaysia, May 2016.
- [25] M. Marks, “A survey of multi-objective deployment in wireless sensor networks,” *Journal of Telecommunications and Information technology*, vol. 5, pp. 36–41, 2010.
- [26] Z. Sun, Y. Liu, and L. Tao, “Attack localization task allocation in wireless sensor networks based on multi-objective binary particle swarm optimization,” *Journal of Network and Computer Applications*, vol. 112, pp. 29–40, 2018.
- [27] M. Arshadi and S. M. Mousavi, “Multi-objective optimization of heavy metals bioleaching from discarded mobile phone PCBs: simultaneous Cu and Ni recovery using *Acidithiobacillus ferrooxidans*,” *Separation and Purification Technology*, vol. 147, pp. 210–219, 2015.
- [28] S. Zarandi, A. Khalili, M. Rasti, and H. Tabassum, “Multi-objective energy efficient resource allocation and user association for in-band full duplex small-cells,” *IEEE Transactions on Green Communications and Networking*, vol. 4, no. 4, pp. 1048–1060, 2020.
- [29] S. Midya, A. Roy, K. Majumder, and S. Phadikar, “Multi-objective optimization technique for resource allocation and task scheduling in vehicular cloud architecture: a hybrid adaptive nature inspired approach,” *Journal of Network and Computer Applications*, vol. 103, pp. 58–84, 2018.
- [30] A. Khalili, M. R. Mili, M. Rasti, S. Parsaeefard, and D. W. K. Ng, “Antenna selection strategy for energy efficiency maximization in uplink OFDMA networks: a multi-objective approach,” *IEEE Transactions on Wireless Communications*, vol. 19, no. 1, pp. 595–609, 2019.
- [31] A. A. Amanatiadis, S. A. Chatzichristofis, K. Charalampous et al., “A multi-objective exploration strategy for mobile robots under operational constraints,” *IEEE Access*, vol. 1, pp. 691–702, 2013.
- [32] D. Vidyarthi and L. Khanbary, “Multi-objective optimization for channel allocation in mobile computing using NSGA-II,” *International Journal of Network Management*, vol. 21, no. 3, pp. 247–266, 2011.
- [33] L. Zuo, L. Shu, S. Dong, C. Zhu, and T. Hara, “A multi-objective optimization scheduling method based on the ant colony algorithm in cloud computing,” *IEEE Access*, vol. 3, pp. 2687–2699, 2015.
- [34] K. Singh, K. Singh, L. H. Son, and A. Aziz, “Congestion control in wireless sensor networks by hybrid multi-objective optimization algorithm,” *Computer Networks*, vol. 138, pp. 90–107, 2018.
- [35] D. G. Reina, J. M. León-Coca, S. L. Toral et al., “Multi-objective performance optimization of a probabilistic similarity/dissimilarity-based broadcasting scheme for mobile ad hoc networks in disaster response scenarios,” *Soft Computing*, vol. 18, no. 9, pp. 1745–1756, 2014.
- [36] A. M. Senthil Kumar and M. Venkatesan, “Multi-objective task scheduling using hybrid genetic-ant colony optimization algorithm in cloud environment,” *Wireless Personal Communications*, vol. 107, no. 4, pp. 1835–1848, 2019.
- [37] L. Wang, Z. Yu, Q. Han, B. Guo, and H. Xiong, “Multi-objective optimization based allocation of heterogeneous spatial crowdsourcing tasks,” *IEEE Transactions on Mobile Computing*, vol. 17, no. 7, pp. 1637–1650, 2017.
- [38] W. Zhang, K. S. Kwak, and C. Feng, “Network selection algorithm for heterogeneous wireless networks based on multi-objective discrete particle swarm optimization,” *KSII Transactions on Internet and Information Systems (TIIS)*, vol. 6, no. 7, pp. 1802–1814, 2012.
- [39] S. Zou, Y. Tang, W. Ni, R. P. Liu, and L. Wang, “Resource multi-objective mapping algorithm based on virtualized network functions: rmma,” *Applied Soft Computing*, vol. 66, pp. 220–231, 2018.
- [40] A. M. Maia, Y. Ghamri-Doudane, D. Vieira, and M. Franklin de Castro, “An improved multi-objective genetic algorithm with heuristic initialization for service placement and load distribution in edge computing,” *Computer Networks*, vol. 194, p. 108146, 2021.